MAY 30 1991

NAS 1.55:3116

NASA Conference Publication 3116

22nd Annual Precise Time and Time Interval (PTTI) Applications and Planning Meeting



Proceedings of a meeting held at
the Sheraton Premiere Hotel
Vienna, Virginia
December 4–6, 1990

NASA

NASA Conference Publication 3116

22nd Annual Precise Time and Time Interval (PTTI) Applications and Planning Meeting

Richard L. Sydnor
Editorial Committee Chairman
Jet Propulsion Laboratory
Pasadena, California

Proceedings of a meeting sponsored by the U.S. Naval Observatory, the NASA Goddard Space Flight Center, the Space and Naval Warfare Systems Command, the Naval Research Laboratory, the National Institute of Standards and Technology, the Army Electronics Technology and Devices Laboratory, the Rome Air Development Center, and the USAF Space Command and held at the Sheraton Premiere Hotel
Vienna, Virginia
December 4–6, 1990

NASA
National Aeronautics and Space Administration
Office of Management
Scientific and Technical Information Division
1991

I

PRECISE TIME AND TIME INTERVAL (PTTI) APPLICATIONS AND PLANNING MEETING

ORDER FORM FOR THE PROCEEDINGS

	Year	Cost	Available	Unavailable
1	1969			X
2	1970	$25.00	X	
3	1971	$25.00		X
4	1972	$25.00	X	
5	1973	$25.00	X	
6	1974	$25.00	X	
7	1975	$25.00	X	
8	1976			X
9	1977			X
10	1978	$25.00	X	
11	1979	$25.00	X	
12	1980	$25.00	X	
13	1981	$25.00	X	
14	1982	$25.00		X
15	1983	$25.00	X	
16	1984	$25.00	X	
17	1985	$25.00	X	
18	1986	$20.00	X	
19	1987	$25.00	X	
20	1988	$35.00	X	
21	1989	$65.00	X	
22	1990	$70.00	X	

Please circle copy(ies) requested and make the check payable to "Treasurer, PTTI". **Please do not add personal names or addresses to the pay line on the check. We cannot accept invoices.** Please return the check and the Order Form to:

Mrs. Sheila Faulkner
Chairman, PTTI Executive Committee
U. S. Naval Observatory
Time Service Department
34th and Massachusetts Avenue, NW
Washington, DC 20392-5100
(202) 653-1460

It is with great regret that we must announce we can no longer absorb the cost of air mailing to international addresses; therefore, the Proceedings will be shipped by Surface Mail. However, if you wish to pay the air mail postage, we will notify you of the cost before mailing. For example, Air Mail to Europe is currently estimated at $27.90 for the first 5 pounds. Each additional pound is $4.00.

When you register for the PTTI Meeting or order the Proceedings, your name is added to the Mailing list to automatically receive future meeting information.

EXECUTIVE COMMITTEE

Sheila C. Faulkner, Chairman
U.S. Naval Observatory

David W. Allan
National Institute of Standards and Technology

Paul Bergschneider
Space and Naval Warfare Systems Command

James A. Buisson
U.S. Naval Research Laboratory

Morton A. Dubinsky
Space and Naval Warfare Systems Command

Hugh S. Fosque
NASA Headquarters

Raymond Granata
NASA Goddard Space Flight Center

Dr. William J. Klepczynski
U.S. Naval Observatory

Dr. Arthur O. McCoubrey
National Institute of Standards and Technology

Dr. John R. Vig
Army Electronics Technology and Devices Laboratory

Dr. H. Beat Wackernagel
USAF Space Command

Dr. Joseph D. White
U.S. Naval Research Laboratory

Dr. Gernot M.R. Winkler
U.S. Naval Observatory

Dr. Nicholas F. Yannoni
Rome Air Development Center

Ms. Nicolette Jardine
U.S. Naval Observatory

OFFICERS

GENERAL CHAIRMAN

PAUL F. KUHNLE

Jet Propulsion Laboratory

TECHNICAL PROGRAM COMMITTEE CHAIRMAN

DR. MARTIN LEVINE

Timing Decisions, Incorporated

ASSISTANT TECHNICAL PROGRAM COMMITTEE CHAIRMAN

S. CLARK WARDRIP

Bendix Field Engineering Corporation

EDITORIAL COMMITTEE CHAIRMAN

DR. RICHARD L. SYDNOR

Jet Propulsion Laboratory

EDITORIAL COMMITTEE MEMBERS

T. Tucker
Jet Propulsion Laboratory
California Institute of Technology

Dr. M. Calhoun
Jet Propulsion Laboratory
California Institute of Technology

P. Clements
Jet Propulsion Laboratory
California Institute of Technology

Dr. G. J. Dick
Jet Propulsion Laboratory
California Institute of Technology

Special Editor for the Hydrogen Maser Workshop
Dr. Derek Morris
National Research Council
Ottowa, Ontario, Canada

PUBLICITY COMMITTEE CHAIRMAN

FRANCIS MULLEN

Frequency and Time Systems, Incorporated

TECHNICAL ASSISTANCE

PAUL KUSHMEIDER

Bendix Field Engineering Corporation

SESSION CHAIRMEN

SESSION I
Dr. G. John Dick
Jet Propulsion Laboratory

SESSION II
Dr. Giovanni Busca
Observatoire Cantonal de Neuchatel

SESSION IIIA
Phillip Talley
The Aerospace Corporation

SESSION IIIB
Dr. Jacques Vanier
National Research Council

SESSION IV
Debra Coleman
Bonneville Power Administration

SESSION V
Dr. Helmut Hellwig
U.S. Air Force/Office of Scientific Research

SESSION VI
Francoise S. Baumont
Observatoire de la Cote D'azur

SESSION VII
Dr. Gernot M.R. Winkler
U.S. Naval Observatory

ARRANGEMENTS

Sheila C. Faulkner
Paul F. Kuhnle
Paul J. Kushmeider

FINANCE COMMITTEE

Dr. William J. Klepczynski
Sheila C. Faulkner

RECEPTIONISTS

The receptionists at the 22nd Annual PTTI meeting were:

Brenda Hicks (U.S. Naval Observatory)
Nicolette Jardine (U.S. Naval Observatory)
Marilyn Levine (Timing Decisions, Incorporated)
Jennifer Stone (Brightline Corporation)
Shirley Swann (Naval Research Laboratory)
Betty Wardrip (Bendix Field Engineering Corporation)
Frances Wright (Naval Research Laboratory)

PTTI ADVISORY BOARD COMMITTEES

1991

OFFICE	NAME	ORGANIZATION
Chairman	Mr. S. Clark Wardrip	BFEC
Vice Chairman	Mr. Martin B. Bloch	FEI
Finance Committee	Mr. Martin B. Bloch, Chairman	FEI
	Mr. S. Clark Wardrip	BFEC
	Mr. James L. Wright	CSC/RC
	Mr. Gary Smith	KODE
Exhibits Committee	Mr. Frances Mullen, Chairman	FTS
	Mr. Gary L. Geil	DATUM
	Mr. Roger J. Hesse	DATUM
	Dr. Martin W. Levine	Timing Decisions
	Mr. Jack McNabb	TRAK
	Mr. Don Mitchell	Austron/FTS
	Mr. William J. Riley	EG&G
	Mr. Ron Roloff	Austron
	Mr. Michael R. Tope	Kinemetrics/Truetime
	Dr. Robert F. C. Vessot	SAO
Guest Speaker Committee	Mr. Robert H. Kern, Chairman	KERNCO
	Professor Carroll O. Alley	University of MD
	Dr. Leonard S. Cutler	HP
	Professor Bradford Parkinson	Stanford University
	Dr. Victor S. Reinhardt	Hughes
	Dr. Samuel R. Stein	Timing Solutions
	Dr. Richard L. Sydnor	JPL
Reports Committee	Mr. Terry N. Osterdock, Chairman	SNI
	Mr. James M. Cloeren	APL
	Mr. Paul F. Kuhnle	JPL
	Mr. Paul J. Kushmeider	BFEC
	Professor Harry Robinson	Duke University
	Mr. Philip E. Talley	Aerospace

NOTE: NON-GOVERNMENT OFFICERS OF THE PTTI ARE AUTOMATICALLY MEMBERS OF THE PTTI ADVISORY BOARD FOR THE YEAR(S) THAT THEY ARE IN OFFICE.

BLANK PAGE

1991 ADVISORY BOARD MEMBERSHIP
Mr. S. Clark Wardrip, Chairman

Bendix Field Engineering Corporation

Professor Carroll O. Alley
University of Maryland
Department of Physics and Astronomy
College Park, Maryland 20742
(301) 454-3405

Dr. James A. Barnes
Austron, Inc.
3300 Mitchell Lane
Boulder, Colorado 80301
(303) 440-7282

Mr. Martin B. Bloch
Frequency Electronics, Inc.
55 Charles Lindbergh Boulevard
Uniondale, New York 11553
(516) 794-4500

Mr. James M. Cloeren
Johns Hopkins University
Applied Physics Laboratory
Johns Hopkins Road
Laurel, Maryland 20707
(301) 953-8821

Dr. Leonard S. Cutler
Hewlett-Packard Company
1651 Page Mill Road
Palo Alto, California 94304
(415) 857-5259

Dr. Henry F. Fliegel
The Aerospace Corporation
Building 120, M5/685
2350E El Segundo Boulevard
El Segundo, California 90245-4691
(213) 336-1710

Mr. Gary L. Geil
DATUM
1363 South State College Boulevard
Anaheim, California 92806
(714) 533-6333

Mr. Roger J. Hesse
DATUM
1363 South State College Boulevard
Anaheim, California 92806
(714) 533-6333

Mr. Robert H. Kern
Kernco, Inc.
28 Harbor Street
Danvers, Massachusetts 01923-0678
(508) 777-1956

Mr. Paul F. Kuhnle
Jet Propulsion Laboratory
4800 Oak Grove Drive
M/S 298
Pasadena, California 90803
(818) 354-2715

Mr. Paul J. Kushmeider
Bendix Field Engineering Corporation
One Bendix Road
Columbia, Maryland 21045
(301) 964-7672

Dr. Martin W. Levine
Timing Decisions, Inc.
P. O. Box 1513
Manchester, Massachusetts 01944
(508) 526-4218

Mr. Jack McNabb
TRAK Microwave
4726 Eisenhower Boulevard
Tampa, Florida 33614-6391
(813) 884-1411

Mr. Donald Mitchell
Austron, Inc.
P. O. Box 14766
Austin, Texas 78761-4766
(512) 251-2313

Mr. Frances Mullen
Frequency and Time Systems, Inc.
34 Tozer Road
Beverly, Massachusetts 01915
(508) 927-8220

Mr. Terry N. Osterdock
Stellar Navigation, Inc.
19075 Skyline Boulevard
Los Gatos, California 95030
(408) 354-0733

Professor Bradford W. Parkinson
Stanford University
Hamsen Labs, Via Palcu
Stanford, California 94305-4085
(408) 395-6521

Dr. Victor S. Reinhardt
Hughes Aircraft
Space and Communications
S12/W322, P. O. Box 92919
Los Angeles, California 90009
(213) 416-0160

Mr. William J. Riley
EG&G, Inc.
35 Congress Street
Salem, Massachusetts 01970
(508) 745-3200

Professor Harry Robinson
Duke University
Department of Physics
Durham, North Carolina 27706
(919) 684-8226

Mr. Ron C. Roloff
FTS/Austron (DATUM Companies)
1930 Isaac Newton Square
Suite 111
Reston, Virginia 22090
(703) 689-4648

Mr. Gary Smith
KODE
1515 South Manchester Avenue
Anaheim, California 92802-2907
(714) 758-0400

Dr. Samuel R. Stein
Timing Solutions Corporation
555 Jack Pine Court
Boulder. Colorado 80304-1711
(303) 443-5152

Dr. Richard L. Sydnor
Jet Propulsion Laboratory
4800 Oak Grove Drive
M/S 298
Pasadena, California 91109
(818) 354-2763

Mr. Philip E. Talley
The Aerospace Corporation
Building 120, M5-686
2350 East El Segundo Boulevard
El Segundo, California 90245-4619
(213) 336-0484

Mr. Michael R. Tope
Kinemetrics/Truetime
3243 Santa Rosa Avenue
Santa Rosa, California 95407
(707) 528-1230

Dr. Robert F. C. Vessot
Smithsonian Astrophysical Observatory
60 Garden Street
Cambridge, Massachusetts 01945
(617) 495-7272

Mr. S. Clark Wardrip
Bendix Field Engineering Corporation
P. O. Box 6147
Vandenberg Air Force Base,
California 93437
(805) 865-3214

Mr. James L. Wright
P. O. Box 4127, CSR 2230
Eastern Test Range
Patrick Air Force Base, Florida 32925
(407) 494-2014

FOREWORD

These Proceedings contain the papers presented at the Twenty Secoond Annual Precision Time and Time Interval Applications and Planning Meeting. The meeting was held at the Sheraton Premiere in Tysons Corner, Virginia this year. A good attendance at the meetings and the banquet was an indication of the continuing interest in the field. We had a number of invited papers, some of which are included in this proceedings. A few papers are missing because they were not received in time for publication or were withdrawn from publication by sponsors. The question and answer periods following each talk are included as usual.

This is the second year that we have had a Poster Session. Acceptance of this session was uniformly positive, both by attendees and by presenters. The advantage of this session is the one-on-one interaction between the presenter and the attendee.

The Hydrogen Maser Workshop, organized by Jacques Vanier, and the Environmental Effects Session, organized by Helmut Hellwig, were outstanding successes due to the efforts of these two gentlemen and to the interest in these aspects of the field.

There were 251 registered attendees, very high for an East Coast meeting.

The objective of these meetings is to provide an opportunity for program planners to meet those who are engaged in research and development and to keep abreast of the state-of-the-art and latest technological developments. At the same time, they provide an opportunity for engineers to meet program planners.

The success of these meetings depends on the efforts of the Program Chairman and the individual Session Chairmen and the organization of the entire meeting by the Chairman of the Executive Committee. Without their unstinting labor, such meetings could not be held.

BLANK PAGE

CONTENTS

Keynote Address

The Past, Present and Future of Atomic Time 1
Professor Norman F Ramsey, Nobel Prize Laureate

SESSION I
The Future of the Art in Atomic Frequency Standards

Chairman: G. John Dick
Jet Propulsion Laboratory

The Classical Microwave Frequency Standards 9
Giovanni Busca, Pierre Thomann, Laurent-Guy Bernier,
Philipe Willemin and Hartmut Schweda, Observatoire de Neuchatel

The Status of Cesium Beam Frequency Standards 19
Dr. Leonard S. Cutler, Hewlett-Packard Co.

State of the Art and Future Directions for the Atomic Hydrogen Maser 29
Dr. Robert F. C. Vessot, Smithsonian Astrophysical Observatory

Trapped-Ion Frequency Standards 53
D. J. Wineland, J. C. Berquist, J. J. Bollinger, W. M. Itano,
D. J. Heinzen, C. H. Manney, F. L. Moore, M. G. Raizen, and
C. S. Weimer, National Institute of Standards and Technology

SESSION II
International Applications of PTTI Technology

Chairman: Giovanni Busca
Observatoire Cantonal de Neuchatel

Inter-Satellite Time Transfer: Techniques and Applications 61
Edoardo Detoma, SEPA S.p.A., Torino, Italy and
S. Clark Wardrip, Bendix Field Engineering Corporation

Current GPS/GLONASS Time References and UTC 87
P. Daly, Department of Electronic and Electrical
Engineering, University of Leeds

USSR National Time Unit Keeping Over Long Interval Using an Ensemble of H-Masers 97
N. B. Koshelyaevsky and S. B. Pushkin, National Scientific and
Research Institute for Physical-Technical and Radiotechnical
Measurements VNIIFTRI, Mendeleevo, Moscow Region, USSR

Time and Frequency Comparisons in Europe by Means of ECS 5 Geostationary Satellite 117
F. Cordara and V. Petitti, Istituto Elettrotecnico
Nazionale Galileo Ferraris, Torino, Italy and A. Cenci, M. Fermi,
and C. Sciarretta, Telespazio S.p.A., Roma, Italy

A Highly Stable Crystal Oscillator Applied to Geodetic VLBI Experiment 131
Hitoshi Kiuchi and Jun Amagai, Communications Research Laboratory, Japan

GPS Time Transfer with Implementation of Selective Availability 145
D. W. Allan, National Institute of Standards and Technology,
M. Granveaud, Observatoire de Paris,
W. J. Klepczynski, U. S. Naval Observatory, and
W. Lewandowski, Bureau International des Poids et Mesures

Time Scale Algorithm: Definition of Ensemble Time and Possible Uses of the Kalman Filter 157
P. Tavella, Istituto Elettrotecnico Nazionale Galileo Ferraris and
C. Thomas, Bureau International des Poids et Mesures

Ultra-stable Hg+ Trapped Ion Frequency Standard 171
J. D. Prestage, G. J. Dick, and L. Maleki,
California Institute of Technology,
Jet Propulsion Laboratory

Design and Industrial Production of Frequency Standards in the USSR 187
Nikolaj A. Demidov and Adolf A. Uljanov,
"QUARTZ" Research and Production Association, USSR

SESSION IIIA
PTTI Technology for the Nineties
Poster Session

Chairman: Phillip F. Talley
The Aerospace Corporation

Long-Term Microwave Power Drift of a Cesium Frequency Standard and its Effect on Output Frequency 209
W. A. Johnson, S. K. Karuza, and F. J. Voit,
The Aerospace Corporation

Rubidium Atomic Frequency Standards for GPS Block IIR 221
W. J. Riley, EG&G Frequency Products, Inc.,
Rubidium Frequency Standards

Precise Frequency Calibration Using Television Video Carriers 231
Edward E. Burkhardt, Burkhardt Monitoring Service

Geodetic Positioning of the Aerospace Electronics Research Lab (ERL) Osborne Time Transfer Receiver (TTR) Using the GPS NAVSTAR Block I Satellites 235
Anthony Liu, The Aerospace Corporation

Precise Measurement Method for Ionospheric Total Electron Content Using Signals from GPS Satellites 243
Michito Imae, Hitoshi Kiuchi, Akihiro Kaneko and Chihiro Miki,
Kashima Space Research Center, Communications Research Laboratory

Application of High Stability Oscillators to Radio Science Experiments Using Deep Space Probes 253
E. R. Kursinski, Jet Propulsion Laboratory
California Institute of Technology

Zero-Crossing Detector with Sub-microsecond Jitter and Crosstalk 269
G. J. Dick, D. F. Kuhnle, and R. L. Sydnor,
Jet Propulsion Laboratory, California Institute of Technology

Hydrogen Masers with Cavity Frequency Switching Servos 283
H. E. Peters, H. B. Owings, and P. A. Koppang,
Sigma Tau Corporation

Frequency Shifts in a Rubidium Frequency Standard Due to Coupling to Another Standard 293
B. Jaduszliwer, R. A. Cook, and R. P. Frueholz,
The Aerospace Corporation

Effect of Thermal Cycling on Stress in Metallic Films on Ceramic Substrates 301
Edward M. Mattison and Robert F. C. Vessot,
Smithsonian Astrophysical Observatory

Sensitivity to the External Temperature of Some GPS Time Receivers 307
W. Lewandowski, Bureau International des Poids et Mesures and
R. Tourde, Observatoire de Paris

GPS Block 2R Time Standard Assembly (TSA) Architecture 317
Tony Baker, ITT Aerospace Communications

Interim Results from the Characterization Testing of the Engineering Development (EDM) Rubidium Clocks for Satellite Applications 325
E. Powers and F. Danzy
Naval Research Laboratory

On the Length of the Drift Region in the Ramsey Cavity 331
P. Thomann, Observatoire Cantonal de Neuchatel

Time and Frequency Measuring Metrological Equipment in the USSR 339
Adolf A. Uljanov, Director-General of Gorky NPO "QUARTZ"

Two-Way Time Transfer Modem 345
I. J. Galysh, P. Landis,
Naval Research Laboratory

SESSION IIIB
Special Hydrogen Maser Workshop

Chairman: Jacques Vanier, Moderator
National Research Council of Canada

Report on the Session **349**
D. Morris, National Research Council

SESSION IV
PTTI Applications in Communications and Power Transmission

Chairman: Debra Coleman
Bonneville Power Administration

Delivery and Application of Precise Timing for a Traveling Wave Powerline Fault Locator System **355**
Michael A. Street,
Bonneville Power Administration

Precise Synchronization of Phasor Measurements in Electric Power Systems **361**
Arun G. Phadke, Virginia Polytechnic Institute and State University

Time Concurrency/Phase-Time Synchronization in Digital Communications Networks **367**
M. Kihara and A. Imaoka, NTT Transmission Systems Laboratories

The Cable and Wireless Approach to Network Synchronization **375**
Robert D. Calvert, Cable and Wireless

International Two-way Satellite Time Transfers Using Intelsat Space Segment and Small Earth Stations **383**
L. B. Veenstra, International Telecommunications
Satellite Organization

The BBC Network Radio Time and Frequency Standard and its Role in the Provision of the Greenwich Time Signal **401**
Jim McIlroy, British Broadcasting Corporation

Synchronizing Computer Clocks Using a Local Area Network **409**
Judah Levine, National Institute of Standards and Technology

SESSION V
Physics of Environmental Sensitivity in Frequency Standards

Chairman: Helmut Hellwig
United States Air Force

Physical Origin of the Frequency Shifts in Cesium Beam Frequency Standards: Related Environmental Sensitivity **419**
C. Audoin, N. Dimarcq, V. Giordano and J. Viennet, Laboratoire de Horloge
Atomique, Unite Propre de Recherche du CNRS, associee a l'Universite Paris-Sud

The Physics of the Environmental Sensitivity of Rubidium Gas Cell Atomic Frequency Standards **441**
W. J. Riley, EG&G Frequency Products
Rubidium Frequency Standards

Physics of Systematic Frequency Variations in Hydrogen Masers **453**
Edward M. Mattison, Smithsonian Astrophysical Observatory

Environmental Sensitivities of Quartz Crystal Oscillators **465**
Fred L. Walls, Time and Frequency Division,
National Institute of Standards and Technology

Local Oscillator Induced Degradation of Medium-Term Stability in Passive Atomic Frequency Standards **487**
G. J. Dick, J. D. Prestage, C. A. Greenhall and L. Maleki,
California Institute of Technology, Jet Propulsion Laboratory

Performance of Soviet and U. S. Hydrogen Masers **509**
A. A. Uljanov and N. A. Demidov, "Quartz" Research and Production Association
E. M. Mattison and R. F. C. Vessot, Smithsonian Astrophysical Observatory
D. W. Allan, National Institute of Standards and Technology
G. M. R. Winkler, U. S. Naval Observatory

SESSION VI
Operational Synchronization and Syntonization

Chairman: Francoise Baumont
Observtoire de 1a Cote D'azur

The National- and International-Wide Prospects of Future Improvements in Position Location and Time Synchronization Systems and Aids **525**
Y. G. Gouzhva, B. N. Balyasnikov, V. V. Korniyenko, I. G. Pushkina and
V. S. Shebshayevich, Leningrad Scientific Research Radiotechnical Institute
V. I. Denisov, "Interradionavigation"
A. P. Reutov, USSR Ministry of Radio Industry

GPS Composite Clock Software Performance **529**
A. L. Satin, W. A. Feess, H. F. Fliegel, and C. H. Yinger,
The Aerospace Corporation

The Use of Precise Ephemerides, Ionospheric Data and Corrected Antenna Coordinates in a Long-Distance GPS Time Transfer **547**
W. Lewandowski, C. Petit and C. Thomas, Bureau International
des Poids et Mesures and M. Weiss, Time and Frequency
Division, National Institute of Standards and Technology

GPS/Loran-C Interoperability for Time and Frequency Applications— A Survey of the Times of Arrival of Loran-C Transmissions via GPS Common Mode/Common View Satellite Observations **559**
B. Penrod, R. Funderburk, Peter Dana—Consultant
Austron, Inc.

LASSO, Two-way and GPS Time Comparisons:
a (Very) Preliminary Status Report **575**
C. Veillet, D. Feraudy, J. M. Torre, J. F. Mangin (OCA)
P. Grudler, F. Baumont (OCA)
J. Gaignebet, J. L. Hatat (OCA)
W. Hanson, A. Clements, J. Jesperson, M. Lombardi (NIST)
D. Kirchner (TUG)
G. Kirchner, H. Ressler, and S. S. Fassi (Space Res. Inst. Graz)
W. J. Klepczynski, P. J. Wheeler, W. Powell, A. Davis (USNO)
M. Granveaud, P. Uhrich (LPTF)

Recent Developments of Loran-C in Europe **583**
S. Leschiutta and E. Rubiola, Politecnico di Torino

On the Line Q Degradation of Hydrogen Masers **599**
L. G. Bernier, G. Busca, H. Schweda, Observatoire
de Neuchatel, Switzerland

KEYNOTE ADDRESS

THE PAST, PRESENT AND FUTURE OF ATOMIC TIME

Norman F. Ramsey
Harvard University
Cambridge, MA 02138, USA

Abstract

The early history of atomic time and frequency standards is reviewed. The most accurate and stable present standards are described. Prospective future improvements are discussed, particularly those with laser cooling and with trapped ions and atoms.

THE PAST

The first successful magnetic resonance experiments were those of Rabi and his associates[1,2] with molecular beams in 1938. The initial experiments measured the interactions of nuclear magnetic moments with external magnetic fields, but radiofrequency spectra were soon observed that depended on internal interactions within molecules[2] or atoms[3,4]. Some of the radiofrequency spectra lines were almost independent of external conditions[5] and could therefore be used as the highly stable periodic component of an atomic clock[6,7]. Rabi, Zacharias and Ramsey at Columbia discussed the possibility of atomic clocks at Columbia as early as 1939 and Rabi discussed these ideas publicly in his 1945 Richtmeyer lecture to the American Physical Society; the first published description of atomic clocks was the New York Times article based on this lecture.

In 1949 Ramsey[8,9] invented the separated oscillatory field method which provided narrower resonances, eliminated first order Doppler shifts and was useable at much higher frequencies. In 1952 Kusch, Lyons Sherwood and others[10] did some initial work on a separated oscillatory field atomic cesium clock, but the work was soon discontinued. In 1954 Zacharias[11] stimulated renewed interest in an atomic cesium clock and began[12] the development of a commercial atomic cesium clock. The first atomic beam apparatus extensively used as an actual frequency standard was constructed in 1955 by Essen and Parry[13]. From 1956 on atomic frequency standards developed rapidly with major contributions coming from a number of laboratories in many different countries[7,14]. Stabilities and accuracies of about 10^{-13} have been achieved with atomic cesium clocks[14] and the second, by international agreement, has been defined as the duration of 9,192,631,770 cesium periods.

Concurrent with the advances in atomic beam clocks, a number other atomic and molecular clocks were developed[7]. Microwave absorption devices using molecular resonances, such such as the NH_3 inversion transition, were developed by Townes and others[7]. Later Townes[15] discovered the maser principle and developed the ammonia maser which operated well but lacked the stability to be competitive.

The combination of Kastler's optical pumping technique[16] with Dicke's use of buffer gases[17] provided strong oscillations free from first order Doppler effects, so optically pumped rubidium can be used as

a frequency standard. Although other atomic clocks have greater accuracy and stability, rubidium clocks are frequently used since they are much lighter and less expensive.

The atomic hydrogen maser was invented by Kleppner and Ramsey[18] and a number of scientists[7] contributed to its improvement. In the hydrogen maser, atoms in the higher hyperfine state of atomic hydrogen are stored in a teflon coated bottle inside a tuned microwave cavity where by stimulated emission they emit coherent highly stable microwave radiation. The stability of a hydrogen maser can be better than 10^{-15} over several hours.

Townes and Schawlow[19] first pointed out the possibility of applying the maser principles at infrared and light frequencies and the first successful laser was made by Maiman[20]. Since then laser developments have occurred at a rapid pace with dramatic improvements in frequency range, power and stability. Major advances came from the suppression of first order Doppler shifts by such techniques as two photon absorption spectroscopy[7] and from the development of successive chains of laser frequencies so that the laser frequencies could be calibrated in terms of cesium.

In recent years a number of major new techniques for trapping and cooling ions have been developed including cooling by collisions with inert gases such as He, laser cooling and sympathetic cooling. Likewise techniques for trapping and cooling neutral atoms have developed at a rapid pace including slowing of atoms with a laser beam, laser trapping of atoms, laser cooling and optical molasses. Since most of these developments hold great promise for the future but are not yet incorporated into current clocks, they will be discussed later in the section on the future.

THE PRESENT

At present different atomic clocks can be chosen to fit the need. When high stability is not required, optically pumped rubidium cells can be chosen for their low cost, small size and light weight; such cells are stable to 10^{-11} over a one month period and more stable for shorter periods. When greater accuracy and stability is required, cesium beam tubes are usually used; they are accurate to better than 10^{-13} over extended time periods. For the highest stability requirements, as in long baseline radio astronomy and navigation in outer space, hydrogen masers are often required; they are stable to better than 10^{-15} over several hours. When optical frequencies need to be measured lasers must be used even though they are not yet absolute standards.

THE FUTURE

Niels Bohr once said, "It is always difficult to make predictions, especially predictions about the future". Long range predictions in a rapidly developing field like that of accurate timing are particularly unreliable because unanticipated new ideas usually occur and greatly change the future. Short term predictions are usually much better because they depend mostly on developments that have already partially occurred. I shall devote most of this section to describing current plans and recent research developments which have particularly promising implications for the future and which are the essential ingredients to rational predictions of both the near and distant futures.

Many improvements are being developed or are in prospect for the atomic clocks currently used. For example, the simple and low cost optically pumped atomic oscillators are being improved by the use of different atoms, by suitable wall coatings which permit the omission of buffer gases[7] and by combining optical pumping techniques with those of atom trapping and cooling.

A number of improvements can be made on the next generation of accurate atomic beam frequency standards[21–24]. Instead of state selection by deflection with inhomogeneous magnetic fields, the atoms may be optically pumped to the desired state. The ends of the separated oscillatory fields cavities can be designed to minimize distributed cavity phase shift[23] and an axial magnetic field may be chosen to minimize Rabi and Ramsey pulling[23]. Beam reversal can be used to evaluate any remaining phase shift between the two oscillatory fields and the excitation can be with counter-propagating waves[21–24]. Although cesium is the atom currently most frequently used in atomic beam frequency standards, other atoms such as Mg are being investigated. Higher excited states may also be used to obtain atomic beam frequency standards at higher frequencies. The atoms in an atomic beam may be laser cooled to reduce the second order Doppler shift. Many of the laser cooling and trapping experiments discussed below are combined laser and atomic beam experiments. Uncertainties in the second order Doppler shift can also be reduced by velocity selection of the beam, but at the cost of a serious reduction in beam intensity.

Many atomic clocks, such as cesium beam tubes, have much better long term accuracy than short term stability in which case the shorter term stability of the clock can be greatly improved by suitably coupling it to a fly wheel oscillator with high short term stability. Crystal oscillators, for example, can be used for the fly wheel oscillator. Very high Q cavities are good for this purpose and superconducting cavities are particularly promising since they are highly stable. Circuits with either optical or electrical feedback from a high Q cavity markedly diminish the noise and increase the short term stability. Consideration is even given to the possibility of using a hydrogen maser as a fly wheel oscillator.

Possible improvements for the hydrogen maser[25] include more stable tuned cavities, electronic cavity tuning, operation at low temperatures, operation in a passive mode and new confinement surfaces, such as superfluid ^{4}He or Fomblin oil. Superfluid helium surfaces have the advantage that they are reproducible since the superfluid helium covers all impurities and does not change its character with time.

Infra-red and optical frequency standards can be improved by the use of narrower lines, by the adaptation to optical frequencies of the separated oscillatory field methods, by improved frequency chains to compare different frequency standards and by the various ion and atom trapping and cooling techniques discussed below.

Dehmelt[26,27] first used electromagnetic ion traps in radiofrequency resonance studies. Penning traps overcome the limitations of the Earnshaw theorem by confining the ions in one direction with an inhomogeneous electric field and in the two other orthogonal directions with a uniform magnetic field. Alternatively, suitable inhomogeneous electric fields can provide focussing in all three directions in Paul or radiofrequency traps which alternately provide focussing and defocussing in each direction but with an average focussing in all directions. Ion traps have the advantage that the observed transition frequencies are approximately independent of the trapping fields. Originally the trapped ions had high kinetic energy (approximately 1 eV) and excessively high second order Doppler shifts. However, Prestage, Dick and Maleki[28] have used a hybrid rf/dc linear ion trap which permits storage of large numbers of ions with reduced susceptibility to the second order Doppler effect caused by the rf confining fields. Alternatively, Cutler[29], Dehmelt[30] and others[30,31] have obtained promising frequency standards by cooling trapped ^{191}Hg ions to 300K by collisions with low pressure helium gas.

Laser cooling, as proposed by Wineland and Dehmelt[27,32] and by Hansch and Schawlow[33], can go to even much lower temperatures by shining intense laser light at the frequency of an allowed optical transition onto a trapped atom or ion slightly below the resonance frequency so the light pressure by the first order Doppler shift is greatest on the ion when it is approaching the light. Dehmelt[34]

and Wineland[27,35] and others[7] have used this technique to cool trapped ions to temperatures of a few micro Kelvin where the second order Doppler shifts are negligible. Laser cooling of ions has been effective with both Penning and electric quadrupole rf traps. If the cooling laser beams act directly on the stored ions being used for time keeping, they must be turned off when the clock frequency is being measured, However, this can be avoided by the process of "sympathetic cooling" in which two different ions are trapped with one being the clock atom while the other is laser cooled; the two kinds of atoms interact sufficiently in the trap for the clock ions to be "sympathetically" cooled by the other ions[36]. Trapped ions have been cooled to the lowest vibrational state of the trap. Laser cooling of trapped ions is a very promising technique for stable clocks with the principal limitation being the low ion density required to avoid space charge effects and the low density in turn reduces the signal to noise ratio.

The extreme limit for low density of ion traps are those with only a single ion[34]. In such such experiments the expected low signal to noise ratio can be improved by the technique of "shelving". In shelving, say with say $^{138}Ba^{+}$, the ion is excited from the $6^2S_{1/2}$ ground state to the $5^2D_{5/2}$ state with two intense laser beams and the transitions between the $5^2D_{5/2}$ state and the $5^2D_{3/2}$ state are induced at the clock frequency. When the ion is "shelved" in the $5^2D_{3/2}$ state the laser induced transitions stop until the ion leaves that state. In this fashion each clock induced transition can affect 10^6 observable fluorescent photons which greatly improves the signal to noise ratio.

In 1985, Phillips[38] and his associates used laser cooling of a focussed atomic beam to slow electrically uncharged atoms and even reverse their velocity. Since the Doppler shift changes as the atom slows down, either the atomic optical frequency or the laser frequency must change for the slowing to continue. Phillips did so by having the atoms pass through a region where the magnetic field gradually changed as the atom moved along its path. Alternatively, Hall[7], Wieman[7] and others[7] have changed or "chirped" the laser frequency as the atom has slowed down. The success of atom cooling permits atoms to be stored in weak traps so there has been a virtual explosion of new ideas and developments in laser trapping of atoms during recent years. Laser forces on neutral atoms can arise either from the gradients of the laser electric field interacting with the induced electric dipole moment of the atom (gradient or dipole force traps) or by the transfer of momentum in the absorption and emission of radiation (spontaneous radiation or scattering force traps), with the gradient traps being intrinsically weaker. When slow atoms are introduced into a region with oppositely directed laser beams along three orthogonal directions at frequencies slightly below the resonance frequency, the atoms will be laser cooled in whatever direction they move. Although such "optical molasses" does not provide a stable trap Chu[39], Pritchard[40], Wieman[40], Cohen–Tannoudji[41] and others[42] have combined optical molasses with either gradient or radiation trapping to trap atoms at about 100 K.

Phillips and his associates[43] in 1988 made the startling experimental discovery that Na atoms could be cooled to lower velocities than had previously been considered to be the theoretical cooling limit. It was thought that there was a theoretical limit, often called the Doppler limit, below which the atoms could not be cooled by laser cooling. This theoretical limit quite reasonably occurs when $k_B T/2 = \hbar\Gamma/4$ where Γ is the spontaneous emission rate from the excited atomic state and k_B is the Boltzmann constant. For Na, this theoretical temperature limit T = 240 μK. In contrast. Phillips and associates[43] found experimentally a cooling to 40 μK. Another theoretical limit to cooling was thought to be the recoil limit which occurs when the recoil energy $(\hbar k)^2/2M$ of the atom of mass M emits a photon of momentum $\hbar k$. Cooling below the Doppler limit has been explained[42–45] by Cohen–Tannoudji, Dalibard, Solomon, Chu and others as due to polarization gradient cooling in a multilevel system and the Sisyphus effect according to which a moving atom is mostly climbing a potential hill of a light shifted doublet ground state sublevel before being optically pumped to the other sublevel. With

polarization gradient cooling Cs atoms have been cooled to 2.5 μK. Aspect, Cohen-Tannoudji and their associates[44,45] have also used a velocity selective process based on coherent trapping of atomic populations into a nonabsorbing coherent superposition of states to achieve transverse cooling of ^{4}He atoms in the triplet metastable state to well below the usual 23 μK one dimensional Doppler cooling limit and the 4 μK recoil limit down to about 2K.

The principal disadvantage of an atom trap is that the strong laser fields that provide the trapping also distort the energy levels and resonance frequencies of the atoms. Usually this makes it necessary to turn the trapping lasers off while the resonance is being studied with a consequent reduction in storage time. One possibility for increasing the effective storage time is to give the atoms a small vertical component of velocity so that they rise up and then fall under gravity, in some cases passing through two coherent oscillatory fields[8] on the way up and down, as recently done successfully by Chu[46] and his associates with microwaves and as planned by others at laser frequencies. In the first succesful fountain experiments the atoms were somewhat heated by giving them the small vertical velocity, but in the future the heating can probably be avoided by slightly shifting the frequency of the vertical cooling lasers so that the optical molasses will move vertically[42,45,46]. Chu[46] also plans to increase the beam intensity for his experiments with an atom funnel based on dissipative optics. As an alternative to the fountain, Wieman[42] has suggested that the atoms can now be cooled to such low temperatures that they can be stored in a magnetic trap so weak that it does not significantly affect the spectrum.

With the impressive recent developments just discussed it is apparent that there are many possibilities both for future improvements of the currently used time and frequency standards and for totally new standards based on trapped ions or atoms. The possibilities are so numerous that it is impossible to predict which ones will be best. But with such promising new techniques already available and with the prospect for further new ideas, the next few years in the field of atomic time should be exciting and productive.

REFERENCES

1. Rabi II, Zacharias JR, Millman S and Kusch P, Phys Rev, 53(1938), 318 and 55(1939), 526.
2. Kellogg JMB, Rabi II, Ramsey NF and Zacharias JR, Phys Rev, 55(1939), 729, 56(1939), 728 and 57(1940), 677.
3. Kusch P, Millman S, Rabi II, Phys Rev, 57(1940), 765.
4. Millman S and Kusch P, Phys Rev, 57(1940), 438.
5. Kusch P and Taub H, Phys Rev, 75(1949), 1477.
6. Rabi II, Phys Rev, 67(1946), 199.
7. Ramsey NF, *History of Atomic Clocks*, Journ of Res of NBS, 88(55)(1983), 301.
8. Ramsey NF, Phys Rev 76(1949), 966 and Phys Today, 33(7)(1980), 25.
9. Ramsey NF, Molecular Beams, Oxford Press, (1956 and 1985).
10. Sherwood JE, Lyons H, McCracken RH and Kusch P, Bull Am Phys Soc, 27(1)(1952), 43. and Sc American 196(2)(1957), 71.

11. Zacharias JR, Phys Rev, 94(1954), 751.

12. Reder FH, USASRDL Tech Rep 2230(AD 265452), (1961).

13. Essen L and Parry VL, Nature, 176(1955), 280, 284.

14. Hellwig H, Evenson KM and Wineland DJ, Phys Today, 31(1978), 23.

15. Gordon JP, Zeiger HZ and Townes CH, Phys Rev, 95(1954), 282.

16. Kastler A, Journ Phys, 11(1950), 225.

17. Dicke RH, Phys Rev, 89(1953), 472.

18. Kleppner D, Goldenberg HM and Ramsey NF, Phys Rev, 126(1962), 603.

19. Schawlow AL and Townes CH, Phys Rev, 112(1958), 1940.

20. Maiman TH, Nature, 187(1960), 493.

21. Derbyshire A, Drullinger RE, *et al*, Proe. Sympos on Frequ Control (IEEE), 39(1985)18.

22. Drullinger RE, Glaze, DJ, Lowe JL and Shirley JH, CPEM Proc (1990) To be published by IEEE.

23. DeMarchi A, Shirley J, Glaze DJ and Drullinger R, IEEE Trans Instrm Meas IM-37(1988) 185 and Proc Sympos on Frequ Contrl 40(1986)428.

24. Audoin C and Vanier J, *The Physics of Atomic Frequency Standards*, Adams Hilger, London(1988).

25. Vessot RFC, Silvera 1, Harvard Smithsonian Center for Astrophysics 3043(1990)1.

26. Dehmelt HG, Phys Rev, 109(1959), 381.

27. Wineland DJ and Itano W, Phys Today, 40(6)(1987), 34 and Science, 237(1987), 612.

28. Prestage JD, Dick, GJ and Maleki L, J Appl Phys 66(1989)1013.

29. Cutler LS, Flory CA, Giffard RP and McGuire MD, Appl Phys B36(1985)137 and B39(1986)251.

30. Major FG and Dehmelt HG, Phys Rev 170(1968), 91.

31. Schaaf H, Schmeling and Werth G, Appl Phys 25(1981), 249.

32. Wineland DJ and Dehmelt HG, Bull Am Phys Soc, 20(1975), 60 and 61.

33. Hansch TW and Schawlow AL, Opt Commun, 13(1975).

34. Dehmelt HG, Bull Am Phys Soc 20(1975) and IEEE Trans & Meas, IM–31(1989), 83; Bergquist JC, Hulet RG, Itano W and Wineland DJ, Phs Rev Lett 57(1986), 1966; Sauer T, Neuhauser W, Blatt R and Toschek P, Phys Rev Lett 57(1986)1696.

35. Wineland DJ, Bergquist JC, Bollinger JJ, Itano WM, *et al*, IEEE Trans Frequ Control (1990).

36. Larson DJ, Bergquist JC, Bollinger JJ, Itano WM and Wineland DJ, Phys Rev Lett 57(1989), 70.

37. Dehmelt HG, Symposium Frequency Standards and Metrology, 4(1989), 286 (Springer Verlag, editor DeMarchi A).

38. Phillips WD, *et al*, J. Opt Soc Am, B2(1985), 1751.

39. Chu S, *et al*, Phys Rev Lett, 55(1985), 48 and 57(1986), 314.

40. Pritchard D and Wieman C, Phys Rev Lett, 57(1986)310.

41. Aspect A, Cohen-Tannoudji C, *et al*, Phys Rev Lett, 57(1986), 1688.

42. Proceedings of the Eleventh and Twelfth Intnl Conf on Atomic Physics.

43. Lett PD, Phillips WD, *et al*, Phys Rev Lett, 61(1988), 169.

44. Aspect A, Cohen-Tannoudji C *et al*, Phys Rev Lett, 61(1988).

45. Dalibard J, Cohen-Tannoudji C *et al*, Jour. Opt. Soc. Am. B2(1985), 1707 and B6(1989), 2023, 2046 and 2112.

46. Kasevich M, Riis E, Chu S and DeVoe RS, Phys Rev Lett, 59(1987), 2631, 63(1989), 612 and 64(1990), 1658.

BLANK PAGE

THE CLASSICAL MICROWAVE FREQUENCY STANDARDS

Giovanni Busca, Pierre Thomann, Laurent-Guy Bernier,
Philippe Willemin and Hartmut Schweda
Observatoire de Neuchâtel
Rue de l'Observatoire 58
CH-2000 NEUCHATEL/Switzerland

1. Introduction

In this paper we present some key problems encountered in the classical microwave frequency standards which are still not solved today. The point of view expressed here benefits from the experience gained both in the industry and in the research lab, on the following classical microwave frequency standards: active and passive H, conventional and laser pumped Cs beam tube, small conventional and laser pumped Rubidium.

The accent is put on the Rubidium standard, the other topics being covered in the following papers. Table 1 presents a simple comparison among the microwave standards.

2. Conventional Rubidium Standards

Models for predicting signal, noise and linewidth are available [1]. However only crude calculations exist concerning the output frequency [2]. The basis of this calculation is a linearization of the equation of the isotopic filter induced optical displacement $\Delta\nu_{op}$ given in REF [3] and a linearization of the equation for light absorption.

The light-shift $\Delta\nu_{LS}$ experienced by the first layer of atoms in the absorption cell can be expressed with small changes from REF [2], as

$$\Delta\nu_{LS} = I_o\,[1-K_o(\theta-\theta_o)]\,K_1(\theta-\theta_o) \qquad (1)$$

where θ is the filter temperature

I_o is the light intensity impinging on the filter

$I_o[1-K_o(\theta-\theta_o)]$ the light intensity at the output of the filter and entering the Rubidium cell,

K_1 a light shift parameter depending upon the spectral shape of the pumping line and

θ_o the filter temperature for which the light shift goes to zero.

With the same meaning of the parameters, considering a mixture of isotopes in the lamp and, for the integrated filter approach, a mixture of isotopes in the cell, we have the general equation giving the frequency vs light intensity and filter cell temperature:

$$\nu = \nu_o - I_o^- \left[1-K_o^- (\theta-\theta_o^-) \right] K_1^- (\theta-\theta_o^-) + I_o^+ \left[1-K_o^+ (\theta-\theta_o^-) \right] K_1^+ (\theta+\theta_o^+) +$$

$$+ \delta_m(\theta-\theta_o^-) + \gamma_m(\theta-\theta_o^-)^2 \qquad (2)$$

where:

ν_o is the unperturbed frequency (independent from the temperature and light intensity)

the index - refers to Rb^{87} isotope

the index + refers to Rb^{85} isotope

θ is the filter-cell temperature

δ_m and γ_m are respectively the linear and quadratic temperature dependence given by the buffer gas mixture [2].

Eq. (2) explicits the fact that the Rb^{87} gives, for normally used cell temperatures > 65°C, a negative light shift; the Rb^{85} gives a positive light shift which never goes to zero.

The parabolic behaviour given in eq. (2) has a minimum for a temperature $\theta = \theta_{min}$ given by

$$\theta_{min} - \theta_o^- = \frac{1 + \dfrac{K_o^+(\theta_o^+ + \theta_o^-)}{p_i^{-1}} - \dfrac{\delta_m}{I_o[\alpha_i K_1^- - (1-\alpha_i)K_1^+]}}{\dfrac{2K_o^-}{p_i^{-1}}\left(p_i - \dfrac{K_o^+}{K_o^-}\right) + \dfrac{2\gamma_m}{I_o[\alpha_i K_1^- - (1-\alpha_i)\,K_1^+]}} \qquad (3)$$

where

$$I_o = I_o^- + I_o^+$$

$$\alpha_i = I_o^-/I_o$$

$$(1-\alpha_i) = I_o^+/I_o \qquad (4)$$

$$p_i = \alpha_i K_1^-/(1-\alpha_i)K_1^+$$

p_i represents the ratio (absolute value) of the negative to the positive light shift, the index i meaning that the ratio is taken at the input of the filter-cell.

Eq. (3) shows that θ_{min} depends upon the total light intensity I_o emitted by the lamp if δ_m and γ_m are different from zero.

The eq. (2) can be expressed in terms of a measurable output parameter, i.e. light intensity I transmitted by the cell.

$$\nu = \nu_o - \alpha_o I\, K_1^- (\theta - \theta_o^-) + (1-\alpha_o)\, I\, K_1^+ (\theta + \theta_o^+) +$$

$$+ \delta_m (\theta - \theta_o^-) + \gamma_m (\theta - \theta_o^-)^2 \qquad (5)$$

where

$$I_o^- \left[1 - K_o^- (\theta - \theta_o^-) \right] = I^-$$

$$I_o^+ \left[1 - K_o^+ (\theta - \theta_o^-) \right] = I^+ \qquad (6)$$

$$I = I^- + I^+$$

$$I^- = \alpha_o I$$

$$I^+ = (1-\alpha_o) I \quad .$$

The meaning of index o is that we are referring to output parameters.

Eq. (5) shows that the frequency is a linear function of the total transmitted light in agreement with experiments [2].

From eq. (5) by differentiating with respect to the transmitted light intensity I one obtains that $\partial\nu/\partial I = 0$ for $\theta = \theta_{LS=o}$ given by:

$$\theta_{LS=0} - \theta_o^- = \frac{\theta_o^+ + \theta_o^-}{p_o - 1} \qquad (7)$$

where $p_o = \dfrac{\alpha_o K_1^-}{(1-\alpha_o) K_1^+}$. (8)

p_o has the same meaning as p_i but referred now to the transmitted total light intensity.

For obtaining good standard performances

$$\theta_{min} = \theta_{LS=0}$$

this relation can be realised by choosing the isotopic ratio in the lamp and in the cell and in addition the buffer gas mixture.

For one commercial Rubidium this occurs at a filter-cell temperature of 75°C [2].

The model shows that the main limitation of the conventional Rubidium is that temperature coefficient and light shift compensation occurs only for a well defined light intensity and well defined cell-filter temperature.

All the parameters occuring in the previous equations are important for a Rubidium drift model.

3. Laser Pumped Rubidium

From experiments in our laboratory, and using a laser power corresponding to the "saturated" light shift [4] the following data are obtained:

a) The light shift vs the laser frequency is $5x10^{-11}$/MHz or a Rubidium stability of $10^{-11}\tau^{-1/2}$ requires a laser stability of $5x10^{-10}\tau^{-1/2}$.

b) The light-shift vs the laser power is: ~ $3x10^{-12}$/%.

c) The laser locked to the Rubidium cell has a cell temperature induced frequency shift of 9 MHz/°C [4].

d) From c) and a) the laser servo produce an additional cell temperature coefficient of $\sim 4.5 \times 10^{-10}/°C$.

e) In the relevant Fourier frequency range (100 Hz - 1 kHz), the laser intensity noise is $> 10^{-6}/\sqrt{Hz}$ while shot noise is $< 10^{-7}/\sqrt{Hz}$.

f) Aging of the laser parameters in single mode operation, locked to the Rb cell, is commonly experienced.

In view of points a) to f) it appears not a simple work to reach the predicted performance [5] $\sigma_y(\tau) = 3 \times 10^{-14} \tau^{-1/2}$.

However when all the previous problem will be solved we will certainly see the realization of the promise of the laser pumping: a very small, low power and high performance Rubidium standard.

4. Cs standards

As a comment to the Table 1 we like to remark that the Cs standard has the lowest intrinsic temperature coefficient, no significant drift and no significant drift mechanism compared to the other standards. In addition, recent advances in a microprocessor controlled electronics [6] have still produced remarkable improvements of the environmental characteristics. One problem to be solved is the aging of the signal due to the degradation of the electron multiplier. This problem exists for high gain ($\sim 10^5$) and low noise figure ($\sim$ 1 dB) multipliers. For low gain and high noise figure multipliers the problems seem solved [7]. However in this case much higher atomic flux is required for obtaining the same short term stability, i.e. the tube lifetime is shortened.

The small optically pumped Cs is appealing. The demonstrated short term stability is $< 10^{-11} \tau^{-1/2}$ [8]. The potential is: small size and light weight. The problems to be solved: the laser frequency noise and laser aging.

5. H-Maser

Relatively to the H-Maser we believe that the problem of the frequency drift is still open. In this context, the cavity pulling has drawn a lot of attention. Today, to our knowledge, 4 different methods of automatic cavity tuning are used for maser in the field: The SE tuning [9], the magnetic relaxation tuning [10], the cavity frequency switching [11] and the auxiliary mode stabilization [12]. Many more have been proposed and tested [2]. As a conclusion we consider that the long term maser frequency drift associated with the cavity pulling is a well known subject due to the high level of precision obtainable in principle by these methods. On the contrary wall shift drift is still very poorly known [13].

From our experience it appears illusory to derive conclusions on wall shift drift vs time a) for masers which are not in continuous operation, b) masers which show a signal amplitude decay which is normally correlated with the line Q decay, c) masers which suffer from magnetic relaxation requiring neck coil current trimming, in order to get the full power operation at a low C field of < 1 mG.

Maser amplitude, line Q and magnetic relaxation should be monitored in addition to the cavity frequency for correct interpretation of the frequency drift data.

As a conclusion wall shift and the associated wall relaxation is still the main problem to be solved.

Acknowledgments

We thank the Swiss Commission CERS, the European Space Agency and the Swiss Federal Office of Metrology for supporting our work on the atomic frequency standards. We acknowledge also the cooperation of Oscilloquartz S.A. for discussing data on Cs beam tubes.

TABLE 1. CLASSICAL μ-WAVE STANDARDS: WHERE DO WE STAND?

	Rubidium		Cesium (small)		H
	Lamp	Laser	magnetic	optical	active
Short-term stability	$\sim 10^{-11}\,\tau^{-1/2}$	?	$10^{-11}\,\tau^{-1/2}$	$3\cdot10^{-12}\,\tau^{-1/2}$	10^{-15} (1000 s)
S/N	85 dB	?	1000	20000	--
Q	10^7	10^7	$2\cdot10^7$	$1\cdot10^7$	$>2\cdot10^9$
Temp. coeff.	10^{-12}/K th. gain: 100		$<10^{-13}$/K		$<3\cdot10^{-14}$/K th. gain: 10^2-10^4
Light-shift coeff.	$5\cdot10^{-11}$/%	10^{-12}/%	--	--	--
Magnetic coeff.	$2\cdot10^{-11}$/G		$<10^{-12}$/G		$<10^{-13}$/G
Long-term stability	10^{-11}/month	?	$3\cdot10^{-12}$/Life		
Life time	>5 years	?	3 ÷ 10 years	?	?

References

[1] J.C. Camparo: Proc. of the 4th Symposium on Frequency Standards and Metrology, Ancona 1988, p. 62.

[2] J. Vanier and C. Audoin: The Quantum Physics of Atomic Frequency Standards (A. Hilger, 1989).

[3] G. Busca, M. Têtu, J. Vanier: Can. J. Phys. 51, (1973), 1379.

[4] J.T. Liu et al.: Proceedings of the 4th European Frequency and Time Forum, Neuchâtel, 13-15 March 1990, p. 157.

[5] J.C. Camparo, R.P. Frueholz: J. Appl. Physics 59, (1986), 3313.

[6] J. Rabian, P. Rochat: Proceedings of the 2nd European Frequency and Time Forum, Neuchâtel, 16-18 March 1988, p. 461.

[7] R.P. Frueholz et al.: Proceedings of the 18th Annual Precise Time and Time Interval Applications and Planning Meeting, (1986), p. 11.

[8] V. Candelier et al.: Proceedings of the 2nd European Frequency and Time Forum, Neuchâtel, 16-18 March 1988, p. 483.

[9] L.J. Rueger, J. Instn. Electronics and Telecom. Engrs 27 (1981) 493.

[10] N. Demidov, A. Uljanov: Design and Industrial Production of Frequency Standards in USSR, these Proceedings, paper no. 13.

[11] H.E. Peters et al.: Hydrogen Masers with Cavity Frequency Switching Servos, these Proceedings, paper no. 22.

[12] G. Busca and L. Johnson: Proceedings of the 1st European Frequency and Time Forum, Besançon, 18-20 March 1987, p. 339.

[13] E.M. Mattison and R.F.C. Vessot: Proceedings of the 41th Annual Frequency Control Symposium, 1987, p. 95.

QUESTIONS AND ANSWERS

Dave Wineland, National Institute of Standards and Technology: Concerning the light shift with the lasers on the rubidium standard; what about chopping the laser light to get rid of the light shift?

Mr. Thomann: Yes, of course that is a method that has already been proposed with normal lamps. It could more easily done with lasers because it is very easy to chop lasers, at least in principle. I don't know of anybody that has tried that, but it is certainly worth trying. One problem is that we have to keep the laser frequency locked at the same time as we chop the intensity. This could be a problem. Of course we don't want to use involved choppers in commercial rubidium standards which are traditionally the cheapest available, but there is a choice: we could make a laboratory standard with elaborate techniques, but for a commercial device one should keep with very simple techniques.

THE STATUS OF CESIUM BEAM FREQUENCY STANDARDS

Leonard S. Cutler
Hewlett-Packard Laboratories
Palo Alto, California

Abstract

There has been a lot of progress in cesium beam frequency standards in the last few years some of which will be reported here. Optical pumping is being pursued actively in a number of laboratories. Optically slowed and cooled beams have been demonstrated as well as traps for cold neutral atoms. The microwave cavity performance with regard to local phase shift at the beam holes has been improved by use of carefully designed and built ring structures for the cavity ends. Work is being done on improvements in electronics with some emphasis on use of digital circuitry and microprocessors. The frequency pulling due to microwave $\Delta M = \pm 1$ transitions (Ramsey pulling) has been analyzed and shown to be important. Status of cesium beam frequency standards in some of the laboratories as well as some of the commercial work will be discussed. Since much of the laboratory work going on involves optical pumping and detection, those items will get the most attention here.

INTRODUCTION

Cesium beam frequency standards occupy an important place in today's technology partially because the unit of time is presently defined by the hyperfine transition in the ground state of Cs_{133} and also because, even though they are highly developed, there is still the potential for considerable improvement in performance.

Factors important to performance include:

1. second order doppler shift
2. cavity phase shifts, end-to-end and local distributed
3. microwave power shift
4. C field homogeneity
5. microwave excitation spectrum symmetry
6. microwave leakage outside the cavity (running waves)
7. pulling by neighboring transitions (Rabi pulling)
8. pulling by $\Delta M = \pm 1$ transitions (Ramsey pulling)

9. pulling by even order modulation distortion

10. noise at even harmonics of modulation frequency on flywheel oscillator

11. defects in the electronic frequency lock servo

These cannot be covered in detail in this paper.

Most of the beam tubes up to the present have used magnetic state separation and a hot wire ionizer detector. The recent availability of diode lasers in the near IR and stabilization techniques have made optical pumping for state separation and detection practical.

Optical pumping has a number of advantages. Much better utilization of the beam can be achieved leading to higher signal to noise ratio for the same cesium flux from the oven. This is due to the velocity selectivity of the magnetic deflection systems. This same velocity selectivity makes correction of the second order Doppler shift (relativistic correction) more uncertain in the magnetic deflection tubes because the velocity distribution of the detected atoms is very dependent on the magnetic field strengths and the tube and magnetic field geometries. The second order Doppler shift is about -1×10^{-13} for the usual beam velocities involved (around 140 m/sec) and is the largest offset outside of that due to the C field and perhaps cavity phase shift in well designed tubes. Since the second order Doppler shift depends on velocity, the line shape will depend on the velocity distribution and will usually be asymmetric leading to a dependence on the microwave modulation waveform and amplitude as well as the microwave power hence good knowledge of the velocity distribution is essential. One other advantage of optical pumping is the absence of strong magnetic deflection fields close to the C field region. This can lead to more homogeneous C fields and consequently better accuracy.

The difference of magnetic moments of the sublevels of the ground state leads to asymmetric population distributions in the magnetic deflection case and consequently pulling from neighboring transitions (Rabi pulling). If $\Delta M = \pm 1$ transitions are present and the populations are asymmetric then Ramsey pulling will occur. With optical pumping and detection, the distribution asymmetries can be made much smaller with consequent reduction in both Rabi and Ramsey pulling.

Finally, if optical cooling is used to obtain slow beams the second order Doppler shift can be made negligibly small since the shift is proportional to temperature and temperatures as low as a few microdegrees Kelvin have already been achieved. In addition, slow beams reduce the Ramsey linewidth and thus improve the precision of the line center determination by the electronics. The reduced linewidth also offers potential improvement in short term frequency stability which can be achieved only if the flywheel oscillator has low enough noise at even harmonics of the modulation frequency.

Fig. 1 shows a fountain experiment with very cold sodium atoms. The atoms in a beam are slowed and then cooled in the "molasses" formed by three intersecting laser beams tuned in frequency below the resonance absorption of the sodium atoms. The cold atoms are then trapped in a magnetic quadrupole trap and finally given a push with a laser pulse to go through the RF cavity. Ramsey linewidth of 2 Hz has been achieved. A similar device would work with cesium. Fig. 2 shows a "funnel" formed from a two dimensional magnetic quadrupole generated by the wire structure. This can provide a continuous beam of cold atoms and thus be very useful for frequency standard work.

In the area of microwave cavity design, local distributed and end-to-end phase shifts are important. In principle, end-to-end phase shift can be measured by beam reversal and many laboratory tubes have this capability. For the measurement to be valid in the presence of local distributed phase shifts, the forward and reverse beams must follow identical trajectories and this requires very careful design and

construction of the tube. Local distributed phase shifts are caused by the presence of running waves (a non-vanishing Poynting vector) due to power being fed to losses. Andrea DeMarchi suggested a ring cavity end shown in Fig. 3 that has vanishing Poynting vector by symmetry at the beam aperture. Here the phase shift should vary as the square of the departure from the symmetry plane and have no variation along it. This is in contrast to the linear variation with departure from the end short found in the usual structures . The symmetry of the ring is very important but it appears that frequency shifts versus position in the beam aperture due to the local distributed phase shift can be kept down to less than 5×10^{-14} for a 3 mm x 3 mm beam with reasonable care in the fabrication. Fairly valid ene-to-end phase shift measurement can then be obtained with this type of structure for the cavity ends. There are many other possible cavity designs based on this symmetry principle.

Pulling by $\Delta M = \pm 1$ transitions, Ramsey pulling, has been analyzed recently in detail (to be published in Journal of Applied Physics). The major part of the effect is fundamentally different from Rabi pulling in which the tails of the adjacent $\Delta M = 0$ transitions, which can be treated independently, just cause a background slope at the center of the desired line and thus lead to a shift. Rabi pulling can be greatly reduced either by detecting the third harmonic of the modulation signal instead of the fundamental or by using other modulation schemes that allow the background slope to be determined. The $\Delta M = \pm 1$ transitions adjacent to the desired 0,0 transition cannot be treated independently since they always have one level in common with the 0,0 transition. They add a component to the transition probability versus frequency of the 0,0 line that has the same periodicity as the normal Ramsey line but has a phase shift. This causes the line center to be offset and cannot be corrected for by any of the means that just detect background slope since the component has no average slope and cannot be distinguished from the Ramsey line itself. If all the level populations are symmetric the effects cancel just as in the Rabi pulling case mentioned above. Since $\Delta M = \pm 1$ transitions are caused by lack of parallelism between the microwave magnetic field and the C field they can be reduced to insignificant levels for reasonable size beams by careful design and construction of the cavity and C field structures.

Electronic defects such as modulation second harmonic distortion, synchronous detector and integrator offsets, modulation signal leakage around the beam tube, microwave spectrum asymmetry, etc. can be measured and corrected by proper design and construction. Low frequency square wave frequency modulation is highly desirable from the even order distortion standpoint. Digital techniques are of great value in reducing many of the defects.

Noise at even harmonics of the modulation frequency are heterodyned with the modulation signal and its harmonics by the beam tube to give a noise signal in the beam tube output at the modulation frequency. This cannot be distinguished from the real tube output and so represents a fundamental limitation to the short term stability. The effect is essentially the same as the pulling due to even order modulation distortion. Present high performance optically pumped laboratory standards are now close to being limited in their performance by the noise performance of available high quality quartz flywheel oscillators so this represents an area that will have to be addressed.

Frequency changes due to microwave power sensitivity can be reduced by power stabilization at the optimum power level. Some causes of power sensitivity are end-to-end cavity phase shift, Rabi and Ramsey pulling and, to a small extent, second order Doppler shift.

LABORATORY STANDARDS

Brief status reports are presented here for some of the laboratories around the world.

PTB at Braunschweig, Germany has done fairly complete evaluations of their tubes, Cs1 and Cs2. These both have longitudinal C fields and use hexapole deflecting magnets. They are flop-out systems and as a result suffer somewhat in short term stability. Both have excellent C field structures. Both have beam reversal capability. The biggest uncertainty reported is that due to end-to-end phase shift, the determination of which is not very good because of the local distributed phase shift in the cavity ends. The overall accuracy estimate is 2×10^{-14} and the difference in their frequencies is 2.5×10^{-14} which is presently unexplained. These standards have the lowest presently reported uncertainty and represent the state of the art for conventional cesium beam standards.

PTB has an experimental tube CSX in which DeMarchi Ring ends were installed on a cavity. The substantially reduced local distributed phase shift error expected was fairly well confirmed and the microwave spectrum was excellent with no visible evidence of $\Delta M = \pm 1$ transitions.

NIST in Boulder, Colorado is working on an optically pumped standard, NIST-7. This used D2 (852 nm) pumping and a cycling transition for detection in the initial experiments. Cavity length is 165 cm and DeMarchi ring ends are used with a longitudinal C field. Measured line width was 65 Hz in good agreement with predictions. The tube microwave spectrum looked very good. It had some slight asymmetry which is not unexpected with D2 pumping. The accuracy has not yet been determined but the goal is 1×10^{-14}. The tube is completely symmetric about the center of its length and thus should be ideal for beam reversal. It will have capability for a number of different pumping schemes. The laser used in the initial experiments has line narrowing produced by enhanced reflection at resonance from an off-axis optical cavity. This is similar to one they developed jointly with the National Research Laboratory of Metrology in Japan.

The Paris Observatory is also working on an optically pumped beam tube but it is not yet to a working stage. It is symmetric about the center of its length and will have capability for beam reversal. The C field will be transverse generated by current carrying rods. The cavity is conventional with a length of 102 cm. Initial experiments will be done with D2 pumping. The staff there has done excellent work on the theory of pumping and detection particularly on the Hanle effect and also experimental work on stabilized lasers.

The Laboratoire de l'Horloge Atomique at Orsay is also working on optical pumping. They have built a tube, Cs III, which has been tested on both D1 and D2 pumping. It has a longitudinal C field and a conventional cavity of length 21 cm with longitudinal microwave magnetic field at the ends. Because of the curvature of the microwave magnetic field due to the mode shape close to the entrance and exit holes in the cavity ends, there are very noticeable $\Delta M = \pm 1$ transitions in the tube microwave spectrum. These have the expected shape of a Ramsey pattern with 180 degrees phase shift between the excitations and linewidth corresponding to the length of the cavity ends. The linewidth of the 0,0 transition is about 500 Hz and demonstrated short term stability was $2 \times 10^{-14}\tau^{-1/2}$ with both D2 and D1 pumping. Considering the short length of the tube, this is an excellent result at this stage of development. The tube has provision for running the optical pumping and detection regions with a magnetic field of several hundred mG to reduce the state trapping associated with the Hanle effect. The microwave spectra with the exception of the $\Delta M = \pm 1$ transitions were excellent. The spectrum with D2 pumping showed slight asymmetry while the D1 spectrum looked very symmetric as expected. The group has also done excellent work on the theory of pumping and detection.

The Communications Research Laboratory (CRL) in Japan has built a conventional cesium standard. It uses hexapole deflection magnets with a transverse C field and a conventional cavity with length 55 cm. The linewidth is about 100 Hz. Accuracy is presently estimated to be 1.1×10^{-13}.

The National Research Laboratory of Metrology in Japan has built an optically pumped tube using D2 pumping. It has a conventional cavity 96 cm in length with a transverse C field. The accuracy is estimated to be 7×10^{-14} and short term stability about $1 \times 10^{-12}\tau^{-1/2}$. They have done very good work on lasers some of it in collaboration with the group from NIST as mentioned above.

Even though the Soviets have primarily pursued hydrogen masers they have had a significant effort in cesium beam standards. They presently have three standards, MTS1, MTS2, and MTS3. MTS3 is currently undergoing evaluation. MTS1 and 3 use dipole optics and MTS2 uses hexapoles. The cavity lengths in MTS1, 2, and 3 are 65, 100, and 194 cm respectively. Accuracy of all three standards is estimated at 1×10^{-13} and short term stability is about $5 \times 10^{-12}\tau^{-1/2}$. They have done a lot of work on C fields and power shifts. They are also working on optical pumping but not much information is available.

A lot of exciting work is going on in cooling and slowing of atoms, most of it being done at NIST in Gaithersburg, Stanford University, and the group at Ecole Normale Superieure in France. Spectacular results have been achieved in cooling cesium atoms to about 2.5 microdegrees Kelvin. Simple experiments with a sodium fountain at Stanford (see Fig. 1) demonstrated a linewidth of 2 Hz. Linewidth with cesium in a similar apparatus should be around 1 Hz. A very simple cesium cell apparatus with two diode lasers at JILA in Boulder, Colorado has already demonstrated a linewidth of 8 Hz. Short term stability could be very good and second order doppler shift extremely small as mentioned in the introduction. With such low temperatures and high densities, spin exchange collisions could be a problem but this remains to be seen.

COMMERCIAL WORK

Frequency and Time Systems (FTS) just announced (Dec. 1990) a new cesium standard, model 4065, that is microprocessor controlled and has servo control of the microwave power and zeeman frequency. It is capable of being remotely controlled. An earlier standard is model 4040, with microprocessor demodulation and integration of the frequency servo signals and control over loop time constant and monitoring of system parameters. It is designed for hands off operation. Another unit is model 4160, militarized and optionally radiation hardened. It too features microprocessor control over some functions. Typical specifications are: 7×10^{-12} accuracy at 25 degrees C and $5 \times 10^{-11}\tau^{-1/2}$ short term stability. An 8 year warranted tube is now available.

Frequency Electronics Inc. (FEI) has designed a new tube with a good microwave spectrum (see Fig. 4). The $\Delta M = \pm 1$ transitions are just visible. No other information is available at this time.

Kernco is developing a GPS block IIR satellite cesium standard that is very small, radiation hardened, and has a 7.5 year warranted life (18 year design) for the beam tube. Specifications include:

weight	19.5 lb
input power	<25 watts
size	4.75" x 5.25" x 16.5"
Short term stability	$3 \times 10^{-11}\tau^{-1/2} + 5 \times 10^{-14}$

NTT has an optically pumped cesium tube under development. It has a cavity length of 21 cm and uses D2 pumping. No details were given on cavity or C field design. The tube includes two ovens which can be operate simultaneously with a detection scheme that allows determination of cavity phase shift

during operation. Short term stability is estimated to be $9 \times 10^{-13}\tau^{-1/2}$. No estimate of accuracy was given.

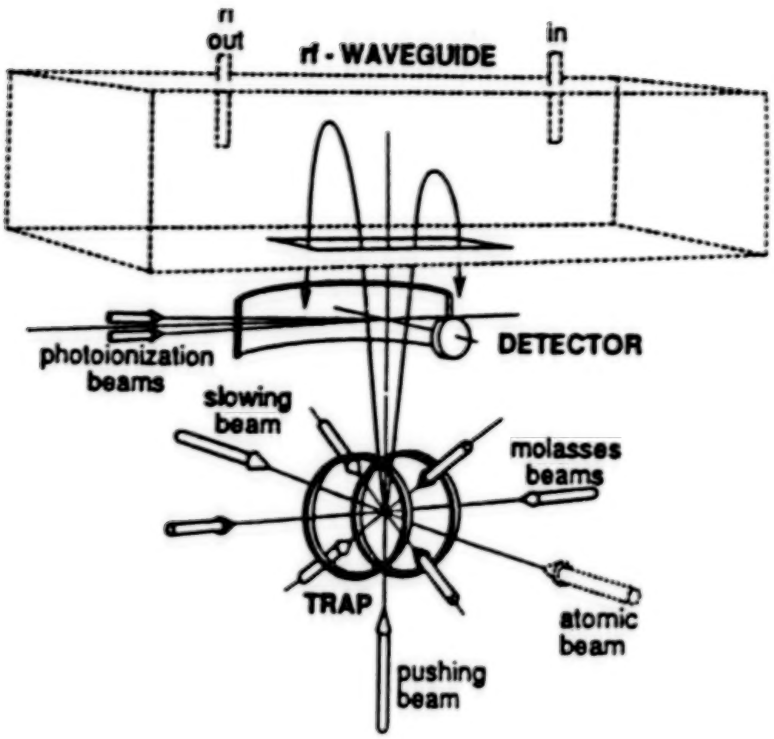
Hewlett-Packard has a new cesium tube in development. It has been optimized by using an accurate ray tracing program and particular attention was paid to reducing $\Delta M = \pm 1$ transitions. It has much better performance in this respect than the high performance tube presently supplied by Hewlett-Packard and equal or better performance in all other respects. The microwave spectrum is shown in Fig. 5.

SUMMARY AND OUTLOOK

Status at the present time for a number of laboratory and commercial standards as well as some of the work leading to the next generation has been presented. Good progress is being made and prospects for the future are bright. Several areas that need emphasis have been pointed out. The present status and future outlook in this writer's conservative view are given in Table 1.

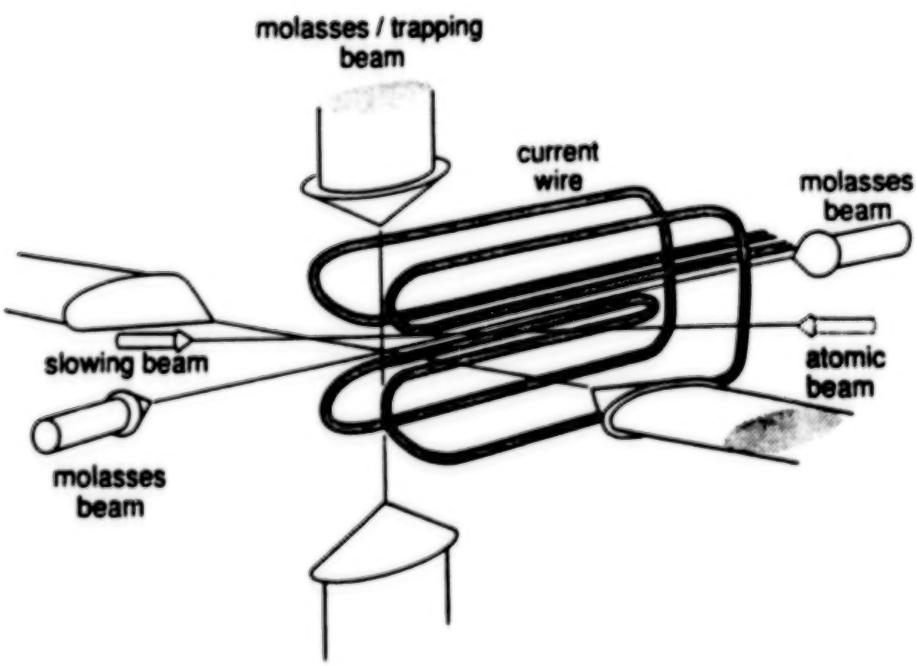
ACKNOWLEDGEMENTS

The author thanks people at the various laboratories and commercial organizations for supplying him the data presented here and apologizes for any omissions or errors.



Sodium atom Fountain. Cold sodium atoms pushed up into the cavity gave linewidth of 2Hz.

Fig. 1



Slow atom Funnel. Wire structure is a two dimensional magnetic quadrupole that provides continuous beam of slow, cold atoms.

Fig. 2

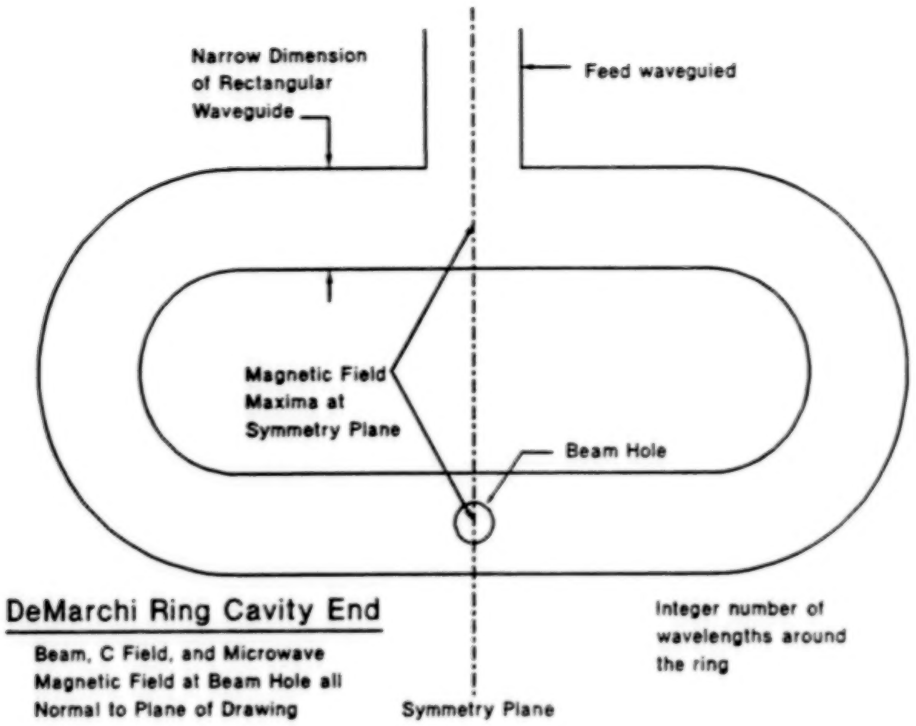
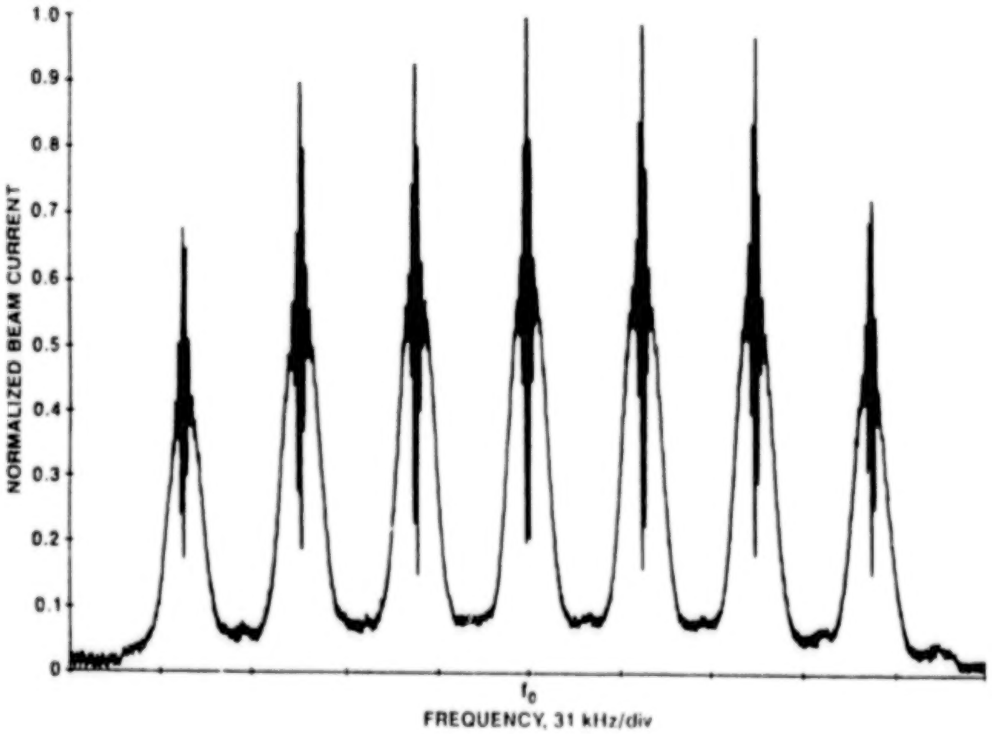
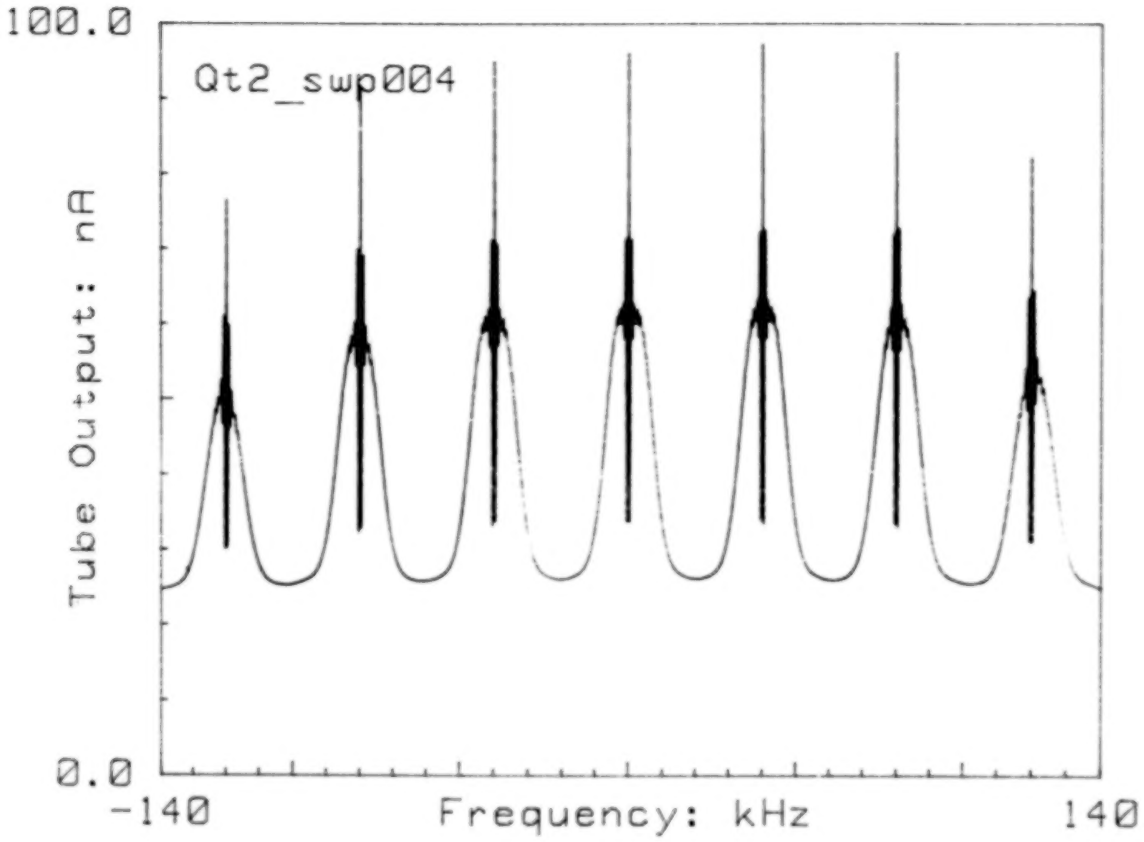


Fig. 3



Microwave spectrum of new Frequency Electronics Inc. cesium beam tube.

Fig. 4



Microwave spectrum of new Hewlett-Packard cesium beam tube.

Fig. 5

BLANK PAGE

STATE OF THE ART AND FUTURE DIRECTIONS FOR THE ATOMIC HYDROGEN MASER

Robert F.C.Vessot
Smithsonian Astrophysical Observatory, Cambridge Massachusetts

ABSTRACT

The present status of technology development for atomic hydrogen masers (H-masers) is reviewed. The limitations to frequency stability and accuracy are discussed with emphasis on the problems associated with cavity resonator instability and the lack of reproducibility and stability of the storage volume wall coating frequency shift. New types of coatings developed in the Soviet Union and better, cavity resonator materials, are expected to make possible frequency at the 10^{-16} level at 10^{4} sec. Better control of systematic effects should extend the long-term stability to levels better than 10^{-15} for intervals beyond one day. Present use of H-masers as flywheel oscillators in timekeeping systems is discussed as is the outlook for the future cryogenic and room temperature H-masers as flywheel oscillators to operate very high resolution frequency discriminators based on the newly evolving technology of trapped and cooled ions and atoms.

1. INTRODUCTION

It is now 30 years since the invention of the atomic hydrogen maser[1] by D. Kleppner and N. F. Ramsey and its technology has matured in several different directions aimed toward a variety of uses and technical requirements.

The principal applications of the H-maser derive from its excellent short term stability. Since the mid 1960s H-masers have been used in widely separated radio telescopes for very long baseline interferometry (VLBI) to control local oscillators and provide timing for data recording. Signals recorded from radio sources are later brought together for correlation to obtain extremely precise angular information of their brightness distributions.

H-masers are now almost exclusively used for tracking spacecraft. Range information is obtained by measuring the time delay of time-coded signals. Range-rate information is obtained by measuring the Doppler shifts of transponded signals. Angle information is derived using the VLBI technique, where simultaneous measurement of spacecraft signals are made at two or more widely separated tracking stations.

Since the H-maser can provide frequency stability at better than 1 part in 10^{14} over intervals of several days, during the past decade it has proven itself as a flywheel oscillator in timekeeping applications. With the advent of the United States' Global Positioning System and the Soviet Union's GLONASS system, a highly precise local time scale can be kept by operating H-maser oscillators as clocks and applying occasional time and frequency corrections from observations of GPS and GLONASS space clocks using the "common-view" technique.

The Soviet Union operates more than a hundred of H-masers as working time and frequency standards in timing centers that serve their vast territories; these clocks are kept synchronized and syntonized by a variety of techniques.

Since this paper is intended to discuss the state of the art it is appropriate to define the nature of the art. The plan of this paper is first to look at the art of obtaining the very best frequency stability over intervals up to about 10^5 seconds, how to cope with the systematic effects that impair maser long term stability, followed by a brief description of the technologies now in use for operating H-masers and, lastly, to offer a view of the future for H-Masers.

2. THE HYDROGEN MASER OSCILLATOR

The H-Maser is an oscillator powered by quantum transitions between two energy levels in the hyperfine structure of atomic hydrogen. At room temperature the population of hydrogen atoms is nearly evenly distributed among four magnetic hyperfine levels designated by F=1, m_F=1, 0, −1 and F=0, m_F=0. These energy levels depend on the relative orientations of the magnetic dipoles associated with the proton and the electron when the atom is in a magnetic field.

In the upper energy level, designated by F=1, the angular momenta of the proton and electron are aligned and added; their magnetic dipoles are also aligned. In this state the total angular momentum can orient itself with a magnetic field in three different directions and the F=1 energy level splits into three components. The F=0 energy level results from the alignment of protons and electrons that cancel their total angular momentum and their magnetic dipoles oppose each other. The energy levels of atomic hydrogen are shown in the upper part of Figure 1.

Figure 1 also shows a schematic diagram of the H-Maser oscillator. Molecular hydrogen at a pressure of about 0.1 Torr is dissociated by an r.f. plasma discharge and collimated into a beam. Atoms in two of the upper magnetic hyperfine energy levels (F=1, m_F= 1, and 0) are selected by passing through a highly inhomogeneous magnetic field generated by a multipole permanent magnet which causes them to move toward the weak field near the axis of the magnet. These atoms are focussed into a storage bulb located in a resonant cavity tuned at the atomic hyperfine frequency. The storage volume confines the atoms to a region where the oscillating magnetic field is in the same phase. Generally , a TE_{011}-mode resonator is used, as shown in Figure 1.

As the atoms proceed from the multipole magnet into the cavity bulb region, the magnetic field they encounter field changes from about 9KGauss radially at the magnet to about one Gauss along the axis of the beam. In this "drift region," the atoms remain in the F=1, m_F=1, and 0 state and will be kept in these states as they proceed along the drift region if the magnetic field they encounter is reduced to the level of the field in the resonator without sudden interruption or change of direction.

The all-important feature of the H-Maser is the surface coating that enables its operation as an oscillator with a narrow resonance linewidth, or high line Q. This is achieved by storing the atoms without appreciable loss of phase coherence from collisions with the wall surfaces or among each other. At room temperature the atoms travel at about 2.5 km/sec, and in a typical two liter storage

vessel, whose collimator provides a one second storage time, a typical atom undergoes 10^5 collisions before leaving the vessel

The frequency of the F=1, m_F =0 to F= 0, m_F =0 transition that powers the oscillator depends on the static magnetic field as $\Delta f_m = 2751\ B^2$ (where B is in Gauss). To avoid frequency shifts from changes of magnetic field, H-Masers are operated at low magnetic fields, usually of about 1 milligauss. To maintain these low fields and to provide a spatially uniform field, with variation at the microgauss level throughout the bulb, magnetic shields are placed about the resonator to attenuate the outside ambient field, and a solenoid is placed within the innermost shield to provide a uniform and controllable field.

The line Q of the H-maser is defined as $Q_l = \pi f_o/\gamma_2$, where f_o is the oscillation frequency and γ_2 is the total rate of loss of phase of the atoms' oscillating dipole moment with respect to the phase of the signal in the resonator. The parameter γ_2 includes loss of phase coherence by escape from the bulb and from recombination to form molecules, also loss of phase coherence from wall collisions, magnetic inhomogeneties and interatomic collisions. Maser oscillation is sustained when the energy released by the incoming atoms resulting from stimulated emission by the microwave fields in the resonator exceeds the energy lost by the resonator. The energy lost includes the the signal delivered to the receiver.

The state of the art of microwave receiving systems for H-masers is an important topic that will require a separate discussion outside the context of this paper.

2.1 FUNDAMENTAL LIMITS OF FREQUENCY STABILITY

The fundamental stability limit for the H-Maser is the same as for other oscillators.[2] Following Kleppner and Ramsey in reference 1, it is given as

$$\sigma_y(\tau) = \frac{1}{Q_l}\sqrt{\frac{kT}{2P\tau}} \tag{1}$$

where $\sigma_y(\tau)$ is the Allan standard deviation of the fundamental limits to frequency stability over time intervals, τ . Q_l is the quality factor of the oscillating system operating at a power level, P, k is Boltzmann's constant, and T is the absolute temperature.

From this expression we see that to obtain the best stability we want high oscillation power and high values of line Q. However these are incompatible situations since high power implies high levels of atomic flux and, consequently, high levels of interatomic collisions.

The power levels normally generated in H-Maser oscillators are low, rarely more than -90 dBm, and the signal-to-noise ratio of the equipment that receives the maser signal has a very significant effect on the maser's short-term stability ($\tau < 100$ sec.). The effect of the added noise on the Allan standard deviations is[3]

$$\sigma_y(\tau) = \frac{1}{2\pi f_o}\left[\frac{FkTB}{P}\ \frac{1+\beta}{\beta}\right]^{1/2} \tag{2}$$

Here F and B are the receiving system noise figure and bandwidth, P as before, is the oscillator power and β is the cavity resonator coupling factor that determines the power delivered to the receiver.

Thermal noise, kT, appears in equation 1 as the noise power within the linewidth of the oscillator and in equation 2 as the effective noise, FkT, within the bandwidth B of the receiver system. In both cases there are advantages to operating a maser at low temperatures.

The maser oscillator's power variation with beam flux is determined by the design of the maser and can be characterized by a quantity q, which depends on the following maser parameter[4]

$$q = \frac{h}{16\pi^2\mu_o{}^2}\ \sigma(\tau)\ v(T)\ \frac{\gamma_t}{\gamma_d}\ \frac{V_c}{\eta V_b}\ \frac{1}{Q_c}\ \frac{I_{tot}}{I}. \qquad (3)$$

Here h is Planck's constant, μ_o is the Bohr magneton, $\sigma(T)$ is the hydrogen atom's spin-exchange collisional cross section, v(T) is the average relative velocity of atoms, γ_d is the rate of loss of phase coherence from the loss of atoms, γ_d is the rate of loss of phase coherence from all causes, including loss of atoms but excluding the effect of interatomic collisions, and Vc/Vb is the ratio to cavity to storage bulb volume, η is the "filling factor", the ratio of the average axial component of the r.f. magnetic field squared to the square of the r.f. magnetic field averaged throughout the cavity. The quantity I_{total} refers to the rate at which the total number of atoms enter the bulb and I is the rate at which atoms in the desired F=1, m_F= 0 state enter the bulb.

Plots of the normalized output power to beam flux are shown in Figure 2, from reference 4, for various values of q. Note that it is possible to stop oscillation by having too many atoms, that smaller values of q provide higher power for a given flux, and that for q > 0.172, the maser will not oscillate.

3. SYSTEMATIC EFFECTS

Figure 3 shows how the Allan standard deviation representing the frequency stability of the H-Maser follows the behavior predicted by the combination of equations 1 and 2 up to a point where systematic effects intrude on the maser's behavior, in this case for intervals beyond 10^4 seconds. The most serious systematic effect is the "pulling" of the oscillation frequency by the mistuning of the cavity resonator. The frequency of oscillation of the aggregate of atoms stored in the maser storage volume includes systematic frequency shifts induced by interatomic collisions and the loss of phase coherence is proportional to these collisional shifts.[5] Another systematic frequency shift that is related to the inter-atomic collision rate is the magnetic inhomogeneity (MI) frequency shift that occurs when the following conditions pertain. 1) When there is an asymmetry in the population of the F=0, m_F = +1 and -1 magnetic hypefine sub-levels of the atoms entering the bulb and 2) when there exits a magnetic field inhomogeneity over the volume of the bulb and 3) when there exists an asymmetry in the distribution of r.f. magnetic fields over the volume of the bulb. Since the inhomogeneity and symmetry requirements, 2 and 3 above, are difficult to fulfill, the MI shift is present in nearly all H-Masers with magnetic state selectors that focus atoms in both the F=1,m_F=1 and m_F= 0 states.

The least well understood systematic frequency shift in the atomic hydrogen maser is the effect of collisions with the surfaces of the storage volume wall, known as the "wall shift". Many questions still remain unresolved resolved about the nature of the collision processes. These include the collision interaction energy, its effect on the advance or retardation of the phase of oscillating dipole moment of the atom and the amount of its phase decorrelation. Surface smoothness, which determines the collision rate, depends on how the coating is applied. The variability of the wall shift from maser to maser is the chief obstacle to achieving frequency accuracy.

Little work on surfaces has been done in Western countries since FEP-120 Teflon was adopted in the mid-1960's. The most significant advance since then has been made in the Soviet Union by Demidov et al.,[6] who report substantial improvement in the reduction of the wall shift by using a new fluoroplastic that they designate as F-10. The eight-to-ten times smaller wallshift of F-10 that, in part, results from its highly superior surface smoothness, allows a correspondingly smaller variability in the wall shift.

The question of long-term frequency stability of the wall shift, as yet, is not resolved. Considerable insight about the present status of this question will be gained by reading the report on the session on wall coatings that appears in these proceedings.

For a more thorough discussion on systematic frequency shifts please see the paper on the physics of such shifts by E. M. Mattison[7] in these proceedings.

3.1 CAVITY RESONATOR MISTUNING

The shift in the output frequency Δf_c from cavity mistuning is given by

$$\Delta f_c = \Delta f_R \, Q_c/Q_l. \qquad (3)$$

where Δf_R is the resonator's frequency offset from the atomic oscillation frequency. We note that the penalty for reducing q by raising Q_c is to make the maser more subject to cavity pulling. Typically, Q_c is about 5×10^4 and Q_l is about 2.5×10^9, so that $\Delta fc = \Delta f_R \times 2 \times 10^{-5}$. For fractional frequency stability at a level of 1 part in 10^{15} we require Δf_R to be kept within 0.07 Hz. For frequency stability at this level, without active frequency control by a servo system, we require good control of the resonator's temperature, and a cavity material with a very low coefficient of thermal expansion, along with excellent mechanical stability. In terms of cavity dimensions for a typical TE_{011}-mode resonator, whose axial tuning rate is about 10 MHz/cm, the axial dimension must be kept constant to less than 7×10^{-9} cm. This is about the diameter of a hydrogen atom! If we assume that we can control temperature at a level of 2×10^{-5} °C we require a linear temperature coefficient smaller than 5×10^{-8} °C. Materials such as Zerodur,[8] Cer-Vit,[9] and ULE[10] are available that have comparable values of thermal coefficients[11] but this is not the whole story. There is also the temperature coefficient of the dielectric constant of the storage bulb, which also causes a frequency shift. The resonator's frequency is affected by everything with which it can interact. This includes the storage bulb within the resonator, all the electronics coupled to the resonator, including the resonator tuning system, and the circuits that couple power to the receiving system.

There is no all-purpose, optimum technique for coping with the resonator frequency drift. When predictability of the frequency drift is important, H- masers designed with the best available materials and techniques for passive stability have been satisfactory. The ageing of Cer-Vit and the other glass-ceramic materials is very predictable, once the initial settling-in of the resonator end covers to their cylinder has taken place, a process that requires some three to six months.[12] To control the effect of cavity pulling there are limits to how far we can increase the value of Q_l, because of the resulting decrease in the available output power and the loss of short-term stability. It is clear that some form control, or of monitoring, of the resonance frequency of the cavity is desirable for long term frequency stability of masers. Three types of active servo techniques have been used.

1. By line Q modulation and searching for a tuning condition, such that Δf_c is zero.[13],[14]

2. By cavity resonance frequency modulation and adjusting the resonator, such that the output signal amplitude is optimized.[15]

3. By introducing signals into the cavity at frequencies away from the oscillation frequency and near the inflection points of the resonator's frequency response.[16] The relative levels of the signals that are sent through the cavity are compared and kept fixed by adjusting the center frequency of the cavity.

Line Q modulation requires a frequency reference with stability comparable to that of the maser being tuned during the period of modulation. Ideally, another maser is employed for this purpose. There are usually sidebands at the modulation frequency in the output signal. This method produces a signal whose frequency depends on the atomic resonance including wall collision shifts. The H-H collisional shifts are cancelled by an offset in the resonator frequency because they are proportional to the collisional line broadening.

Cavity resonance frequency modulation makes possible a H-maser with good stand-alone qualities of frequency stability. As in system No. 1, the modulation signal will be present in the output signal unless some form of compensation is employed. This method adjusts the resonator to the atomic resonance frequency including the wall shift and the H-H collisional shift, which can vary with beam flux .

The last technique mentioned above has been used successfully in masers having very small cavity resonator-storage bulb combinations that have been designed using dielectric loading methods or the lumped capacitor loading.[17] Since using this type of resonator often requires external electronic gain to raise the resonator's quality factor and, under these conditions, the resonator frequency is further subject to the phase stability of the Q enhancing amplifier.

Injecting the probing signals requires scrupulous avoidance of any additional noise or signal at the maser's oscillating frequency to avoid pulling the frequency of the maser oscillation. This method maintains the resonator at some pre-assigned frequency. Beam flux variations will cause changes in output frequency depending on how the resonator frequency is related to the atomic oscillation frequency.

3.2 MAGNETIC FREQUENCY SHIFTS

Systematic frequency shifts from changes in ambient magnetic field result from two different physical processes, 1) a change in the internal magnetic field in the storage volume causing changes in $\Delta f_m = 2751\ B_{int}^2$ and 2) a change in the MI frequency shift, $\delta(\Delta f_{MI})$, resulting from time variations in the spatial uniformity of B_{int}, time variations in the hydrogen density in the bulb, and time variation in the state distribution of atoms entering the bulb.

The first processes results from having finite magnetic shielding capability. Well annealed arrays of high quality shielding material can achieve shielding factors, $S = \delta B_{ext}/\delta B_{int}$ as high as 10^5. If we assume a value for S of 5×10^4, and operate with B_{int} at a level of 5×10^{-4} Gauss we have that

$$\frac{\delta(\Delta fm)}{f} = \frac{5502}{f_o} B_{int} \frac{\delta B_{ext}}{S} = 4 \times 10^{-14} B_{ext}. \quad (4)$$

Given that variation in B_{ext} can be confined to 0.015 Gauss (or a few percent of the earth's ambient field) we can expect systematic fractional frequency variations of about 6×10^{-16}. It is clear that more layers of magnetic shielding can be added, or that a magnetic field compensation servo system can be used, if more severe conditions are encountered.

The second physical process causing magnetically induced frequency shifts is far less straightforward than the process described above. It depends on the inequality of the population difference in the F=1, m_F=+1 and –1 states entering the bulb, the asymmetry of the RF magnetic fields in the storage volume, and the DC magnetic gradient in the storage volume. Under conditions where these populations are not equal and with the almost inevitable lack of RF symmetry and field uniformity in today's equipment, the the output frequency of the maser will vary with beam flux. This causes problems with the flux tuning process described in equation (3), where the frequency shift owing to spin-exchange collisions is assumed to be strictly proportional to the atomic density. (Even in cases where there is no Δf_{MI}, the cavity resonance is still offset in frequency by the amount required to compensate for the spin exchange collision frequency shift, which is proportional to the atomic density.) The stability of the magnetic inhomogeneity shift, Δf_{MI}, will depend on the constancy of the state distribution of atoms and on the interatomic collision rate.

Removal of the MI shift can be done by providing a beam of atoms exclusively in the desired F=1, m_F=0 state or by equalizing the population of atoms in the F=1 m_F=+1 and –1 states. The state distribution of atoms entering the storage volume can be equalized by changing the direction of the axial magnetic field in an alternating manner in the drift region downstream from the state selecting magnet shown in Figure 1. When this field is in the same direction as the field in the bulb, the beam proceeds in the normal states. When the drift region field is inverted under proper conditions, the F=1 states can be inverted. The $m_F = +1$ population then appears in the $m_F = -1$ state. By alternating the direction of the drift region field the average population of the $m_F = +1$ and –1 can be equalized. This technique is used in the Soviet Ch1-75 H-maser.

A more effective, but more complicated method to provide a beam of atoms nearly exclusively in the F=1, $m_F = 0$ state is discussed in section 4.2 of this paper. Using this system the entire population of atoms will generate signal power with one half the rate of interatomic collisions and provide an improvement in the line Q.

3.3 WALL COLLISION FREQUENCY SHIFTS

The most fundamental problem today with the H-maser is the lack of reproducibility and time stability of the wall coating frequency shift. The wall shift is the principal source of maser frequency inaccuracy. Since the wallshift is proportional to the wall collision rate multiplied by the phase shift per collision, ideal coatings should be as smooth as possible and of a material capable of producing the smallest possible phase shift per collision. The original masers built in 1960-1962 used coatings of dimethyl-dichloro-silane (dri-film). In about 1962 Teflon was found to be far superior to dri-film and Teflon has been used since that time.

Coatings of PTFE (poly-tetra-fluoro-ethylene), a long-chain fluorocarbon with a high melting point were originally used. These coatings are difficult to apply and are rarely used today. When a PTFE coating is slowly cooled after melting it crystallizes and has a wallshift with a small temperature coefficient. On the other hand, when it the coating is rapidly cooled after melting, it has a larger wallshift and a larger dependence with temperature. It has zero wallshift at about 82 degrees C.[18] PTFE has rarely been used since 1965.

FEP fluorinated-ethylene-propylene, a branched fluorocarbon with lower melting point than PTFE is far easier to apply that PTFE, and to date, has been the most widely used coating in masers made in the US and Europe.

A far superior coating called "Fluoroplastic F-10" has been developed in the Soviet Union specifically for H-masers.[19] It melts at a lower temperature than PTFE, flows evenly over the surface and has 8 to 10 times lower wallshift than PTFE and FEP Teflon. This new material should substantially improve the accuracy capability of H-masers.

4. A SUMMARY OF TECHNOLOGIES USED IN TODAY'S HYDROGEN MASERS

4.1 HYDROGEN MASER RESONATORS

The most often used resonator operates in the TE_{011} mode. Without appreciable dielectric loading by the bulb, the resonator's typical dimensions are of a cylinder 28 cm dia. x 28 cm long. This allows use of storage bulbs of 2 to 3 liter capacity. Smaller resonators have been made using dielectric loading. These resonators suffer large variations of resonance frequency with temperature owing to the thermal coefficients of dielectric constant of the loading material and require more strenuous autotuning or thermal control than unloaded resonators.

Resonators with smaller dimensions, using lumped capacitance loading to reduce dimensions, are used in passive H-masers and regenerated-Q H-masers. This resonator is in use in the Soviet Ch1-76 H-maser, in some masers built by the Sigma-Tau Standards Corporation (where the idea originated) and in the small regenerated-Q spaceborne masers developed at the Hughes Corporation.

Stabilization of the resonator can be done either by passive means, using materials of high mechanical stability and with very low coefficients of thermal expansion, or by active means, discussed in 3.1. Rough tuning of the resonators is usually done with a mechanical device that in some way slightly alters the internal configuration of the resonators r.f fields. Fine tuning (over a range of a few tens of Kilohertz) is usually done with a varactor coupled to the resonator either directly, as part of a coupling loop or probe, or via a transmission line.

4.2 ATOMIC HYDROGEN STATE SELECTION

The H-maser uses traditional molecular beams techniques with multipole magnets to concentrate atoms in the desired quantum states into a beam aimed into the collimator of the storage volume. Four-pole magnets and six-pole magnets are commonly used. Small diameter four-pole magnets are more efficient in their use of hydrogen than six-pole magnets. Six-pole magnets have focussing properties analogous to optical lenses and can be used to focus a specific range of velocities from the modified Maxwell distribution of velocities of atoms emerging from the source to form a real "image" of the source aperture. While the narrowness of the velocity distribution can be less efficient of hydrogen use, these magnets are useful for operating a state selector that provides a beam of atoms wholly in the desired F=1, $m_F = 0$ state.

A method to provide a beam of atoms nearly exclusively in the F=1, $m_F = 0$ state is shown in Figure 4.[20] Here, the first magnet, in the usual way, focusses a beam into a second magnet of twice the length that, in turn, refocusses the beam as an image of the source aperture at "stop 2" in the figure. An Adiabatic Fast Passage (AFP) radiofrequency transition is made in the space between the magnets to invert the population. Only atoms in the the F=1, $m_F = 0$ states continue through the magnet and on to the bulb.

4.3 MAGNETIC SHIELDS AND FIELD CONTROL

The multilayer magnetic shields in use today appear to be adequate for controlling both the level of magnetic fields and their gradients in the storage volume of H-masers. Systematic frequency shifts resulting from the magnetic conditions in "normal" environments, with variations of a few milliGauss, appear, for the present, to be well enough controlled in most masers. However, as progress continues in the control of other systematic effects other than of magnetic origin, better shielding will be required. A typical example of the shielding factor is $S = \Delta H_{ext}/\Delta H_{int} = 10^5$ for ±0.5 Gauss external variations in ΔH_{ext}. A wider range of cancellation of external magnetic field variations can be achieved with active servo methods by sensing the external field and applying a compensating field.

The control of internal magnetic gradients by multi-section coils so far has proved adequate. Simple degaussing techniques using currents at powerline frequencies to remove remanent fields in the magnetic shields have also been adequate.

Uses of superconducting materials for magnetic shields operated at low temperatures and for conductive coatings of cavity resonators are being considered. The combination of these functions is a very tempting prospect particularly if room temperature, or even low temperature, superconductors become available. Superconducting shields are eminently useful and appropriate for H-masers operating at very low temperatures.

4.4 HYDROGEN SUPPLY, PURIFICATION AND CONTROL

Two types of hydrogen supply systems are presently in use, high pressure gas bottle systems and low pressure sources operating by heating some form of metallic hydride such as Li Al H_4 to release hydrogen. These systems require control of the flow and purification of H_2 before it proceeds to the dissociator. Both regulation of flow and purification are achieved by passing the H_2 through heated metal tubes, plugs, or diaphragms depending on the pressure of the supply.

Gas bottles can be easily vented and refilled to comply with airline transport regulations and are a simple, reliable, low-tech devices requiring only a pressure gauge to give a measure of the gas available.

Metallic hydrides are light in weight, small in volume, do not require a pressure vessel and are thus ideal for spacecraft operation. A metal hydride system is used in the Soviet Ch1-75 H-maser system along with a self-heated thin walled nickel tube for flow control and purification of H_2.

4.5 DISSOCIATORS TO PRODUCE ATOMIC HYDROGEN

In H-masers the dissociation of molecular hydrogen is done by r.f. plasma excitation. The ideal choice of surfaces for the dissociator is one that will not adsorb hydrogen on its surface so as to allow recombination with incoming colliding atoms. Surfaces of glasses that are free of metal oxides and of pure fused silica appear to be the best.

Excitation of the plasma is done by exposure to r.f. fields, either by electrodes that produce predominantly electric fields, or by a coil that produces induced displacement-current fields. The latter method causes less erosion of the glass since it is essentially an electrodeless discharge, but requires a means for starting the discharge such as a spark coil or a miniscule amount of radioactive "α" particle emitter as a "keep alive" to provide ionization to initiate the plasma discharge. The plasma in the glassware presents a variable impedance to the excitation circuit that depends on the hydrogen pressure. This variability can cause difficulties in matching the r.f. power to the plasma. Single transistor oscillator circuits are commonly used, where the glass or quatrz cell containing the plasma is included in the resonant circuit. In these circuits the resonant frequency adjusts itself to changes in

the reactance of the cell when the plasma is started and as the hydrogen pressure is varied. These devices are simple and cheap, but often temperamental and difficult to stabilize.

External r.f. power sources with a wide band match to the plasma cell are less power efficient, but more predictable. Another advantage is that external power sources can be operated at known and fixed frequencies well away from frequencies whose harmonics, if leaked into the maser receiver, could cause problems. The capability of monitoring of incident and reflected power to the plasma is another useful feature.

4.6 VACUUM SYSTEMS AND HYDROGEN SCAVENGING

The use of the ion pump was probably the most significant departure in the evolution of the H-maser from the experimental laboratory environment to the marketplace. Ion pumps are still widely used and some have been specifically designed for pumping hydrogen. For pumping hydrogen the situation is different from the normal ion pump process where a hail of sputtered cathode material particles bury adsorbed gas molecules on surfaces in the pump. Since hydrogen is readily assimilated by the titanium cathodes, in principle there is no need for ionic bombardment and sputtering. However this process is substantially assisted by the scrubbing of the cathodes by the impacting of hydrogen ions. Other species of ions, being heavier, cause the usual pumping by sputtering and burial of gases.

Early ion pumps used in H-masers had cathodes in the form of plates that were attached at their corners and were subject to bending inward and short circuiting to the anodes as the engorged hydrogen warped the plates. This problem was easily cured by adding extra supports to the cathodes. The principal mode of failure if ion pumps in H-masers is related to local stress caused by hydrogen in titanium cathodes.[21] The stress causes spalling and flaking with momentary arcing and eventual short circuiting. Methods for improving the lifetime of operation include annealing of the plates at high temperatures under high vacuum and the selection of high purity titanium.

The use of sorption technology to scavenge hydrogen in H-masers began in 1973 in an effort to reduce the weight of a maser for a space experiment to measure the gravitational redshift,[22] Because sorption cartridges will pump hydrogen almost exclusively at room temperatures the addition of a small ion pump was found to be necessary to pump other gases. This ion pump, which is usually operated at a lower than normal voltage to mimize hydrogen ion bombardment of its cathode, serves to dissociate hydrocarbon gases allowing the freed hydrogen to be pumped by sorption. With sufficient voltage it will operate at an acceptable speed to cope with argon, nitrogen, oxygen etc.

Sorption systems, with an ion pump backup are used in the Soviet Ch1-75 and Ch1-76 H-masers,[23] in the regenerated Q space masers developed at Hughes, and in the Smithsonian Astrophysical Observatory's VLG-12 masers operating with the AFP single state selector. Because of the sensitivity of sorption systems to contamination, use of all-metal seals is recommended in place of elastomer seals.

Sorption cartridges that have reached their pumping capacity can repeatedly be reactivated by applying power to their internal heaters and pumping away the evolved hydrogen. The activation temperatures are high, near 700° C, and provision must be made to prevent damage to other nearby systems during activation. Because this process does not require dissassembly of the maser, there is little liklihood of contamination of the maser's storage volume wall coating during activation.

Precautions are taken in maser vacuum systems to avoid materials with ferromagnetic properties for structures within the innermost magnetic shield. Titanium, copper, aluminium and carefully selected silicon bronze are some of the materials used inside the magnetic shields. Outside of the magnetically sensitive regions, vacuum manifolds are usually made of stainless steel, often with copper Con-Flat seals. Indium seals have been successfully used in conjunction with components made of softer metals such as copper and aluminium.

5. A LOOK TOWARD THE FUTURE OF ATOMIC HYDROGEN MASERS

Atomic hydrogen masers are principally used as flywheel oscillators with outstandingly good short term frequency stability that reaches levels deep in the 10^{-16} domain over time intervals between 1 and 10^5 seconds. Today, on average, the accuracy of frequency reproduction of masers is about 5×10^{-14} and it is clear that H-masers do not compete with cesium beam devices as a primary standards.

The advent of trapped atoms and ions cooled by laser interactions has led to possibilities for frequency discriminators capable of extremely high resolution. These devices will require oscillators having very high frequency stability and capable of producing signals with frequency spectral densities commensurate with, or narrower than, the linewidths of the new discriminators. It is likely that H-masers will be used to supply these signals in future primary frequency standards.

H-masers will continue to be used in applications where the best possible stability is required for intervals beteen 1 second and 10^5 seconds. The limitations imposed by systematic effects that become evident beyond 10^5seconds are now better understood and, as better wall coatings surfaces such as of the Soviet 'Fluoroplastic F-10" material are used, the fundamental limitations to frequency stability and will be improved. Frequency stability at the level of one part in 10^{16} should be attainable in the near future with the best presently available coatings. Further improvement beyond this level should result with even better wall coatings.

The most recent breakthrough in H-maser technology was made in 1986 by operating H-masers at temperatures near 0.5 K using storage volume surfaces of superfluid helium-4. Researchers at the Massachusetts Institute of Technology,[24] the University of British Columbia,[25] and at Harvard University[26] all succeeded in achieving sustained oscillation. These research groups all used very different experimental configurations of cryogenic H-masers.

Cryogenic apparatus for operating apparatus at temperatures near 0.5 K is no longer considered exotic. The use of continuously operated ^{3}He recirculating refrigerators or of dilution refrigerators for operating H-masers is definitely within today's state of the art.

The limits to the stability of cryogenic H-masers still have to be measured. New theoretical quantum mechanical analyses of H-H collisions have been made that predict limitations due to previously unknown processes related only to the storage time of atoms in the maser.[27] Research is now in progress to measure the properties of low temperature hydrogen collisional interactions with hydrogen and helium to test the new theory.

Figure 5 shows the layout of the cryogenic H-maser mentioned in reference 25. Its frequency stability, projected from all known effects of its design is given in Figure 6. This plot includes limitations owing to receiver noise resonator instability, and the instability of the predicted new frequency shifts. A plot of the spectral density of the maser's spectral density of phase fluctuations is shown in Figure 7. This figure shows the white phase noise corresponding to the τ^{-1} behavior of the stability plot shown in Figure 6.6.

6. SOME OBSERVATIONS ON PRESENT AND FUTURE H-MASERS

In this paper the writer has tried to shed some light on the state of the art of atomic hydrogen masers. Since it is only recently that we, in the United States, have had the opportunity to appreciate maser developments made in the Soviet Union, this brief survey is bound to be incomplete.

In comparison with the technological development of other types of frequency standards in the West there has been only a few people involved in H-maser development. In the West it is only recently that development is headed toward designs suitable for small scale production. On the other hand the Soviets have placed far more reliance on H masers as working standards than we have in the West. They have already produced many hundreds of H-masers, and are now offering both active and passive H-masers for sale.

The market for H-masers in the West has, so far, been limited. However applications for masers are growing in number as signals of high frequency stability rather than of high accuracy become more in demand in view of the significant improvements in time transfer offered by two -way time transfer with communication satellites, the Global Positioning System and the Soviet Union's GLONASS system.

The development of H-masers still has a long way to go to reach its full potential as a highly stable oscillator. Improvements in the long term stability of room temperature H-masers are forseen by use of new wall coatings and better control of systematic effects. Cryogenic H-masers wth stability at the 10^{-17} to 10^{-18} level and outstandingly high spectral purity will likely serve as oscillators for operating standards based on future high resolution frequency discriminators using trapped and cooled ions and atoms. The unique quality of the H-maser as an active oscillator, with unparalleled frequency stability for intervals up to 10^5 seconds and excellent long-term predictability of its fre-

quency variation, has led to its successful use as a "flywheel clock" at the U.S. Naval Observatory and at other timing centers.

The outstanding long-term (year-to-year) frequency stability of the ensemble of Soviet H-masers reported by N. B. Kosheyaevsky and S. B. Pushkin[28] and the predictability of the behavior of H-masers discussed by Uljanov, Demidov, Mattison, Vessot, Allan and Winkler,[29] have proven the validity of new strategies for timekeeping. Precise time transfer by operating with common view GPS and Glonass signals makes possible the precise comparison of H-maser frequency over the long-term and enables these devices to serve as excellent flywheel standards.

Further advances in time transfer using active H-masers in orbiting spacecraft to permit time transfer at the few picosecond level will be required to keep up with the performance of future primary standards based on frequency discriminators operating with trapped ion and cooled atoms and ions.

It is clear that the technology of the atomic hydrogen masers, which is now only 30 years old, has still to reach its full maturity.

ACKNOWLEDGEMENTS

The presentation and contents of this paper have benefitted greatly by discussions with my colleague, Dr. Edward M Mattison, with Mr. David W. Allan of the National Institute of Standards and Technology and with Dr. Gernot M. R. Winkler of the U. S. Naval observatory My participation at the PTTI was supported by the Smithsonian Institution's Research opportunities Fund.

REFERENCES

1 D. Kleppner, H. M. Goldenberg , " Theory of the atomic hydrogen maser,"*Phys. Rev.* vol. 126, 603-615, 1962.

2 W A. Edson "Noise in oscillators,"*Proc. IRE* , vol. 48, pp. 1454-1456, 1960.

3 R. Vessot, L. Mueller, and J. Vanier , "The specification of oscillator characteristics from measurements made in the frequency domain," *Proc IEEE*, vol. 54, no 2, pp. 199-207, 1966.

4 D. Kleppner, H. C. Berg, S.B. Crampton, N.F. Ramsey, R.F.C. Vessot, H.E. Peters and J. Vanier, "Hydrogen-maser principles and techniques," *Phys. Rev.* ,Vol 138, Number 4A, 1964

5 S . B. Crampton, "Spin exchange shifts in the hydrogen maser," *Phys. Rev.* vol. 158, pp. 57-61, 1967.

6 N.A. Demidov, E.M. Yezhov, V.A. Feodorov, A.A. Ul'janov. "The search for new materials in the hydrogen generator,"*UDK* 621.317.7.6.089.69.

7 E.M. Mattison, "Physics of systematic frequency variations in hydrogen masers," in these proceedings.

8 Zerodur is a trademark of Schott Glasswork, Inc.

9 Cer-Vit is a trademark of Owens-Illinois, Inc.

10 ULE is a trademark of Corning, Inc.

11 E.M. Mattison and R.F.C. Vessot, "Time and temperature stability of silver-coated ceramics for hydrogen maser resonant cavities," *Proc. 20th Annual Precise Time and Time Interval* (PTTI) *Applications and Planning Meeting*, p. 313, 1988.

12 R.F.C. Vessot and E.M. Mattison, W. J. Klepczynski, I.F. Silvera, H.P. Godfried and R.L. Walsworth, "Results of two years of hydrogen maser clock operation at the U.S. Naval Observatory and ongoing research at Harvard-Smithsonian Center for Astrophysics", *Proc. 17th Annual. Precise Time and Time Interval P.T.T.I Meeting*, Washington, D.C., Dec. 3-5, 1985; pp. 413-431.

13 J. Vanier and R.F.C. Vessot, "Cavity Tuning and Pressure Dependence of Frequency in the Hydrogen Maser," *Applied Physics Letters* Vol. 4, Number 7, 1964

14 J. Vanier, H.E. Peters and R.F.C. Vessot, "Exchange Collisions, Wall Interactions, and Resettability of the Hydrogen Maser," *IEEE Trans. on Instrumentation and Measurement*, Vol. IM-13, Number 4, pp. 185-188, December, 1964

15 H.E. Peters, "Design and Performance of New Hydrogen Masers Using Cavity , Frequency Switching Servos," Sigma Tau Standards Corporation, *Proc. of the 39th Annual Symposium on Frequency Control*, pp. 420-425, 1984

16 C. Audoin, "Fast Cavity Auto-tuning systems for hydrogen masers," *Revue Phys. Appl.* Vol 16, pp. 125-130, 1981.

17 H.E. Peters, "Atomic Standards with reduced size and weight," U.S. Patent Number 4123777, October 31, 1978.

18 R.F.C. Vessot and M.W. Levine, "Studies of Hydrogen Maser Wall Shift for High Molecular Weight Polytetraflourocthylene," *Proc. 24th Annual. Symposium on Frequency Control*, 27-29 , U.S. Army Electronics Command Ft. Monmouth, NJ. pp. 270-276, 1970.

19 N.A. Demidov, E.M. Yezhov, V.A. Feodorov and A.A. Ul'janov, ref. UDK621.317.7.6.089.69]

20 E. M. Mattison, R.F.C. Vessot and W. Shen, "Single-state selection system for hydrogen masers," *IEEE Transactions on Ultrasonics, Ferroelectronics, and Frequency Control*. UFFC-34, No. 6, pp. 622-628, Nov. 1987.

21 N.A. Demidov, E.M. Ezhov and A.A. Ul'janov, "On the duration of hydrogen evacuation by magnetic-discharge pumps," *Instruments and Experimental Techniques*, Vol. 21, pp. 739-740, 1978.

22 R.F.C. Vessot, M.W. Levine, E.M. Mattison, T.E. Hoffman, E. A. Imbier, M. Tetu, G. Nystrom, J. J. Kelt, Jr., H.F. Trucks, and J.L. Vaniman, "Spaceborne hydrogen maser design," *Proc. of the Eighth Ann. Precise Time and Time Interval Applications* and *Planning Meeting*, Washington, D.C., December; pp. 277-354.

23 N. A. Demidov and A. A. Uljanov, "Design and industrial production of frequency standards" in these proceedings.

24 H.F. Hess, G.P. Kochanski, J. M. Doyle, T. J. Greytak, and D. Kleppner, "Spin-polarized hydrogen maser,"*Phys. Rev.* A. Vol. 34, 1602 (1986)

25 M.D. Hurliman, W.N. Hardy, A.J. Berlinsky, and R.W. Cline, "Recirculating cryogenic hydrogen maser,"*Phys. Rev. A*, Vol 34, 1605 (1986).

26 R.L. Walsworth, I. F. Silvera, H.P. Godfried, C.C. Agosta, R.F.C Vessot and E.M. Mattison, "Hydrogen maser at temperatures below 1K," *Phys. Rev. A*, Vol. 34, 2550 (1986).

27 J.M.V.A. Koelmann, S..B. Crampton, H.T.R. Stoof, O.J. Luiten and B.J. Verhaar, "Spin exchange frequency shifts in cryogenic and room-temperature hydrogen masers," *Phys Rev. A*, Vol. 38, Number 7, pp. 3535-3547 (1988)

28 N. B. Koshalyaevsky and S. B. Pushkin "USSR National time unit keeping over long intervals using an ensemble of H-masers" in these proceedings.

29 A. A. Uljanov, N. A. Demidov, E. M, Mattison, R. F. C. Vessot, D. W. Allan and G. M. R. Winkler "A comparison of Soviet and U. S. hydrogen masers" in these proceedings.

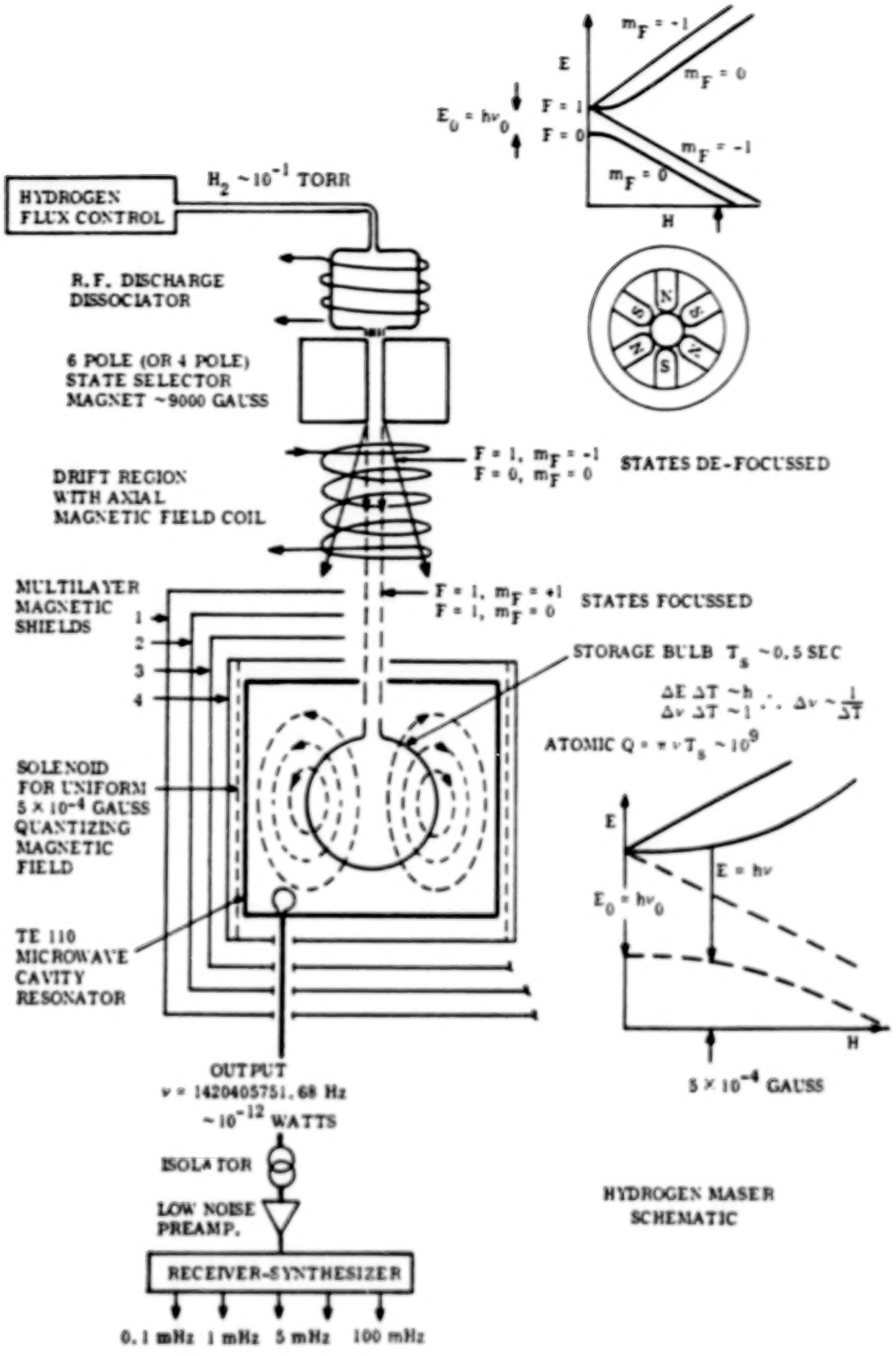


Figure 1. Energy levels of atomic hydrogen and a schematic diagram of the H-maser.

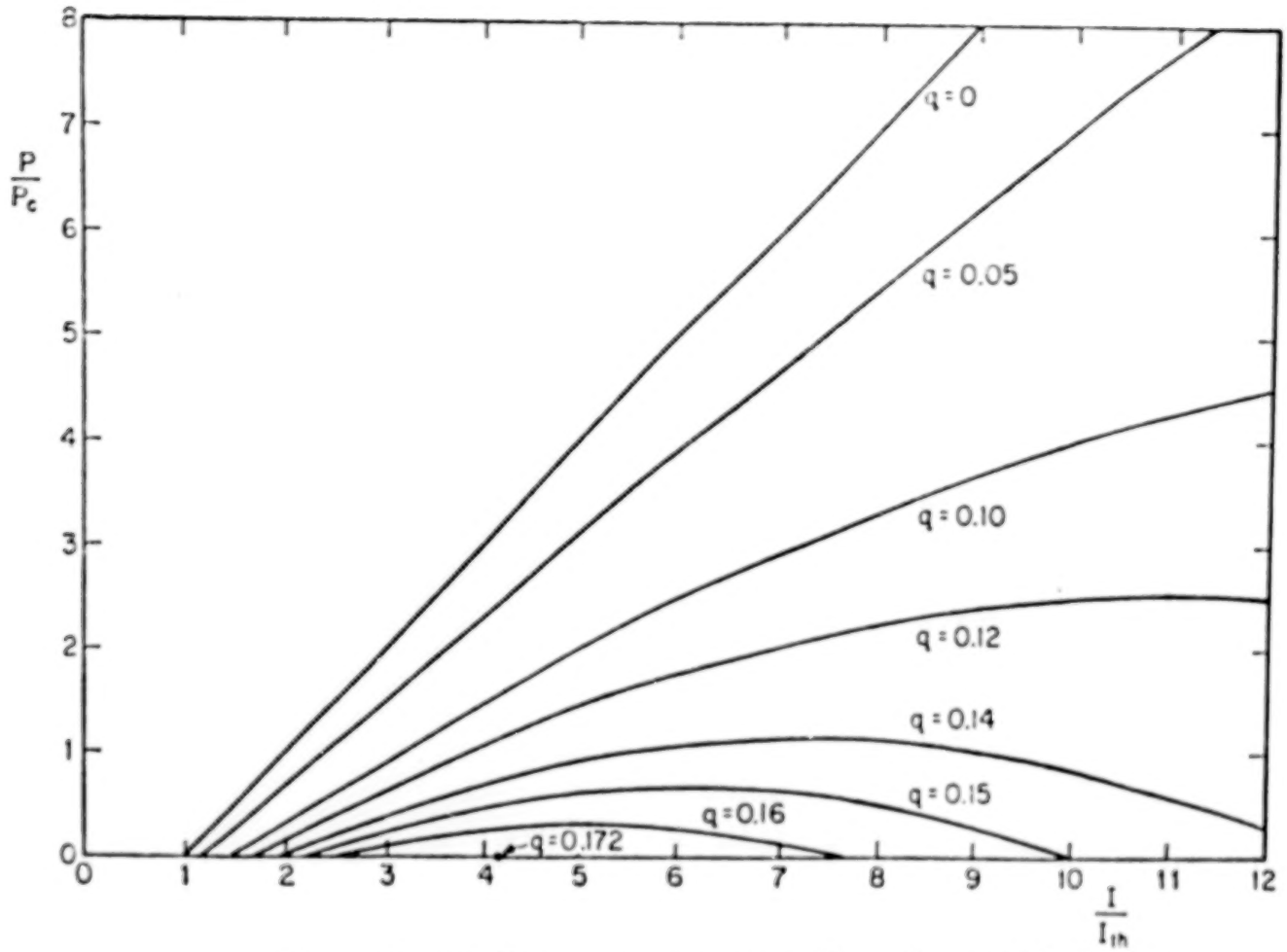


Figure 2. Oscillator power versus flux of atomic hydrogen

**From "Hydrogen Maser Principles and Techniques"
D. Kleppner, H.C. Berg, J.B. Crampton,
N.F. Ramsey, R.F.C. Vessot, H.E. Peters
and J. Vanier, Phys. Rev. 138, May, 1965.**

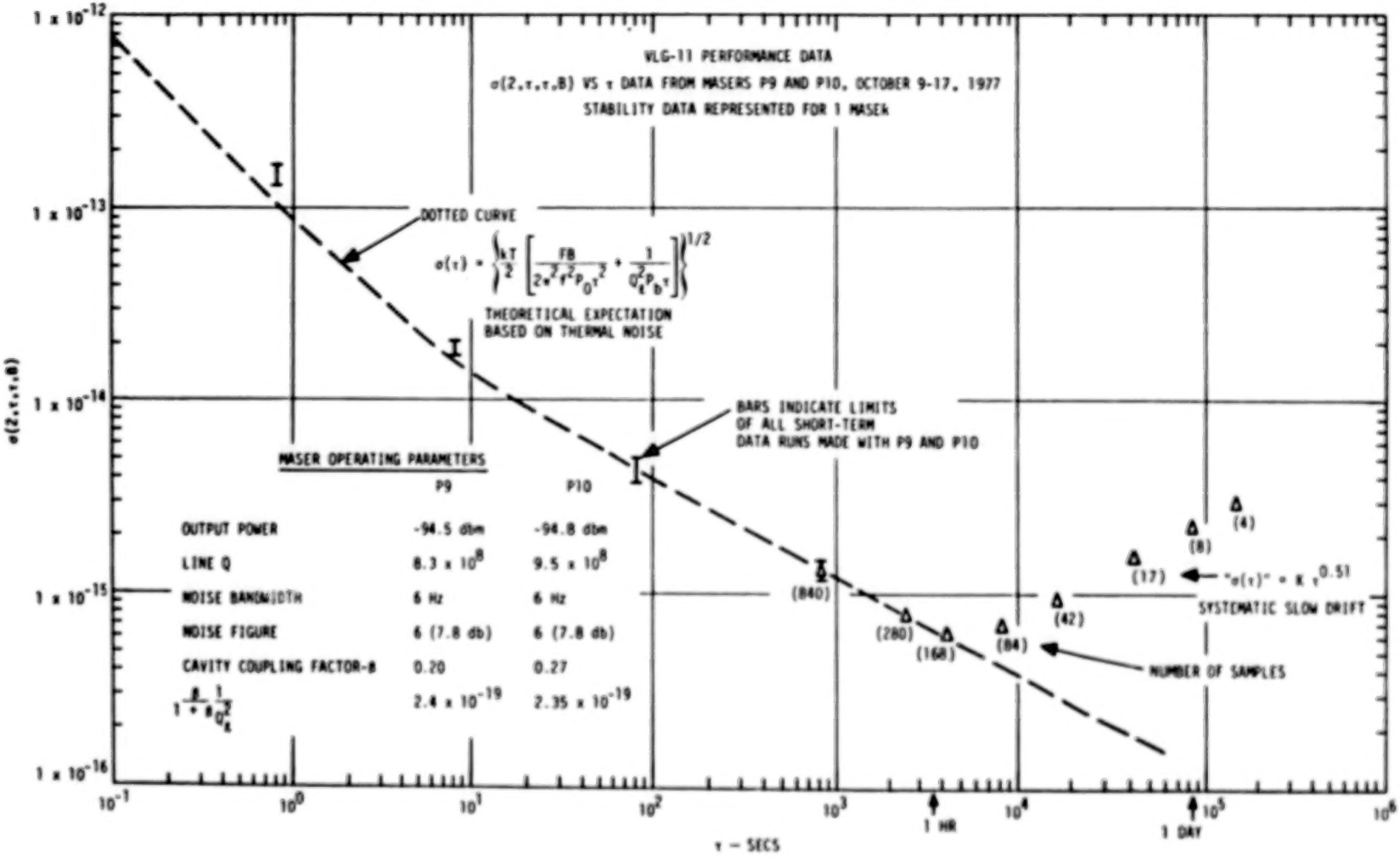


Figure 3. Stability of H-masers showing the effect of systematics.

SCHEMATIC DIAGRAM OF STATE SELECTION SCHEME
TO OBTAIN HYDROGEN ATOMS ONLY IN THE
$F = 1, M_F = 0$ HYPERFINE STATE

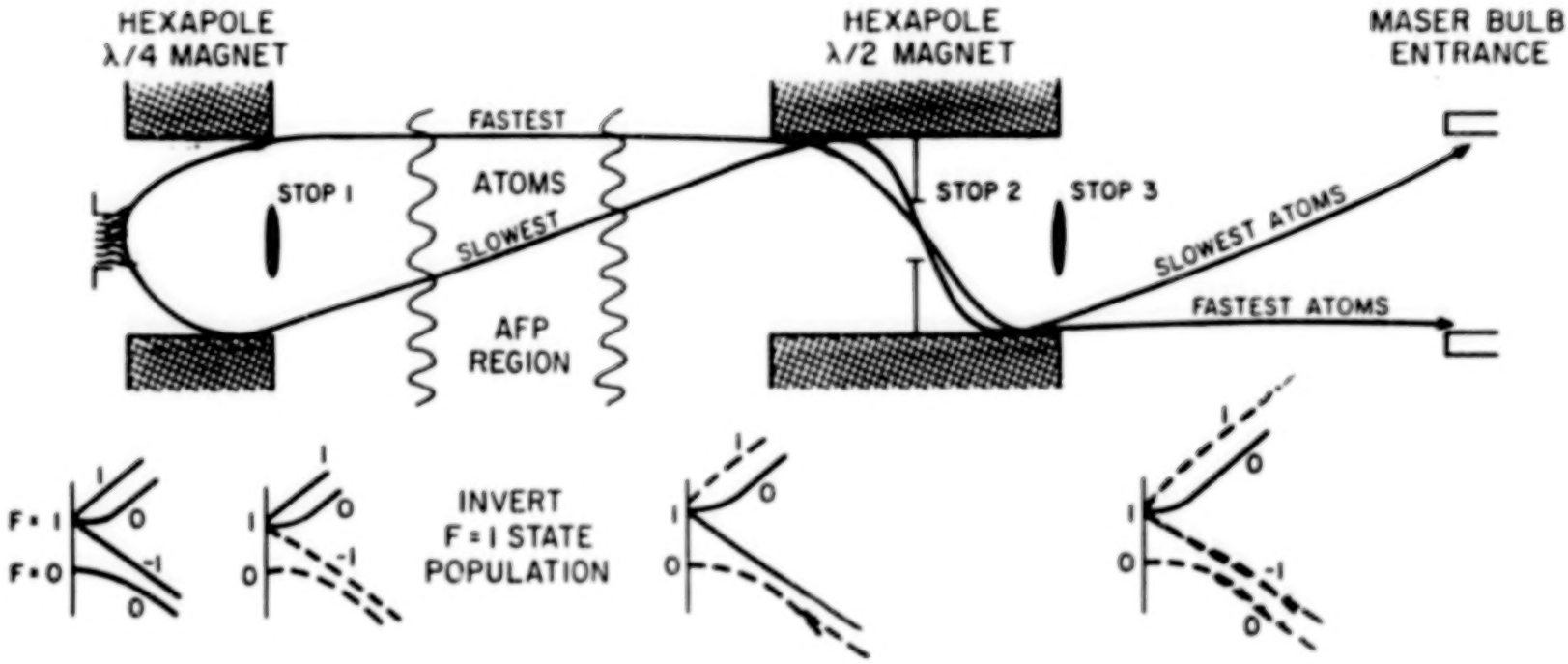
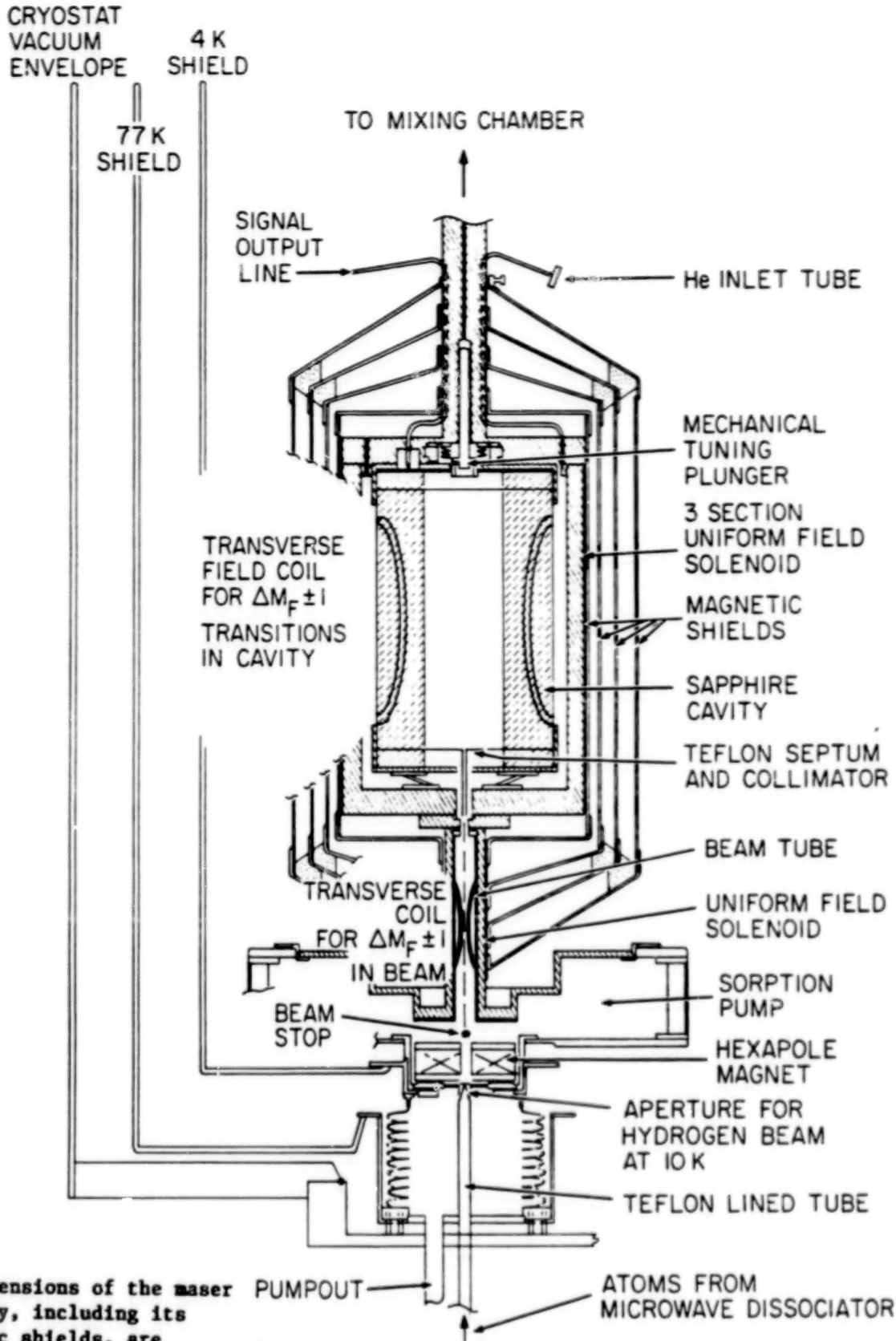


Figure 4.



The dimensions of the maser assembly, including its magnetic shields, are 22.8 cm (9") dia. x 45.7 cm (18") high.

Figure 5. Layout of the cryogenic H-maser.

BLANK

PAGE

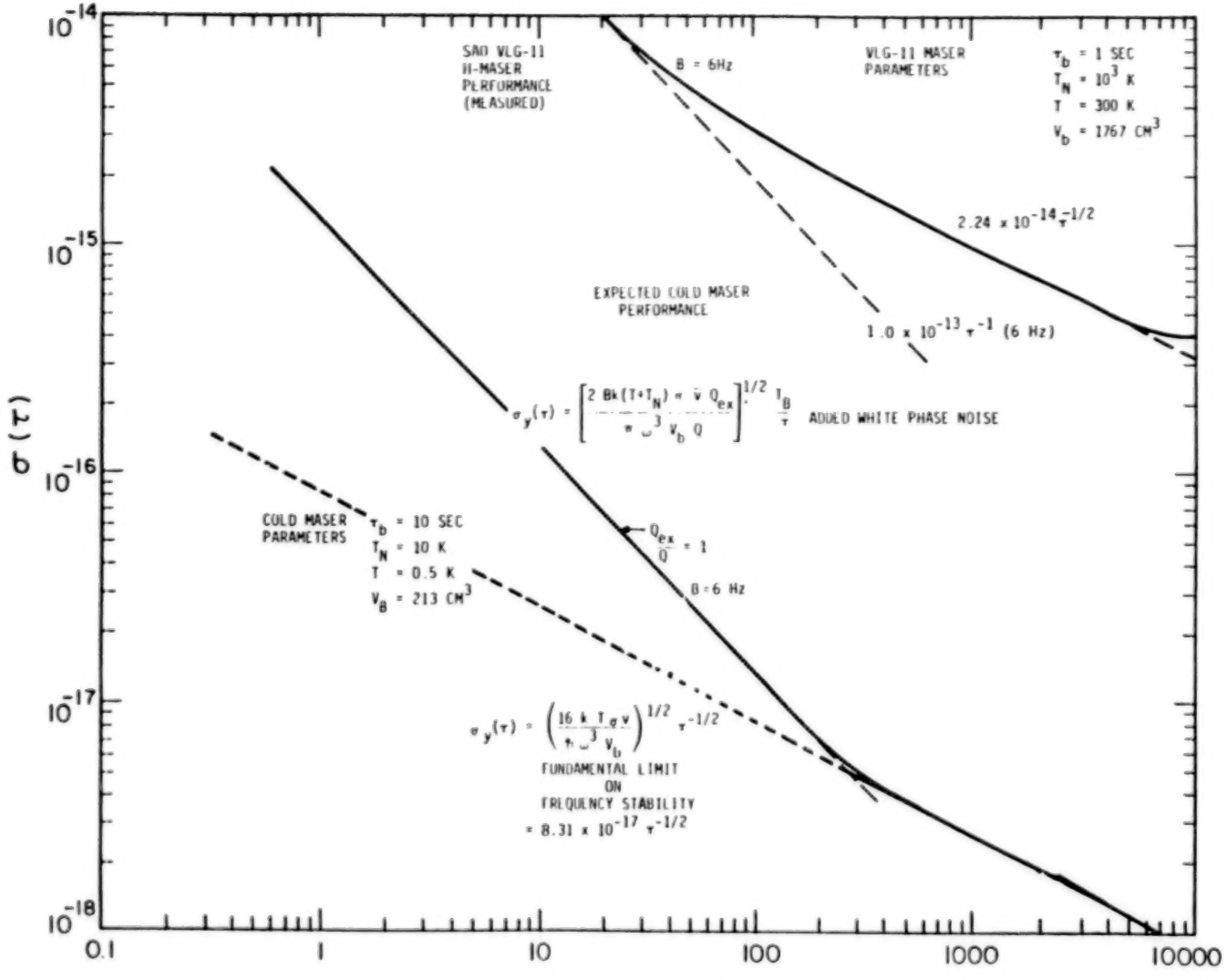


Figure 6. Stability projected for the cryogenic H-maser (shown in Figure 5)

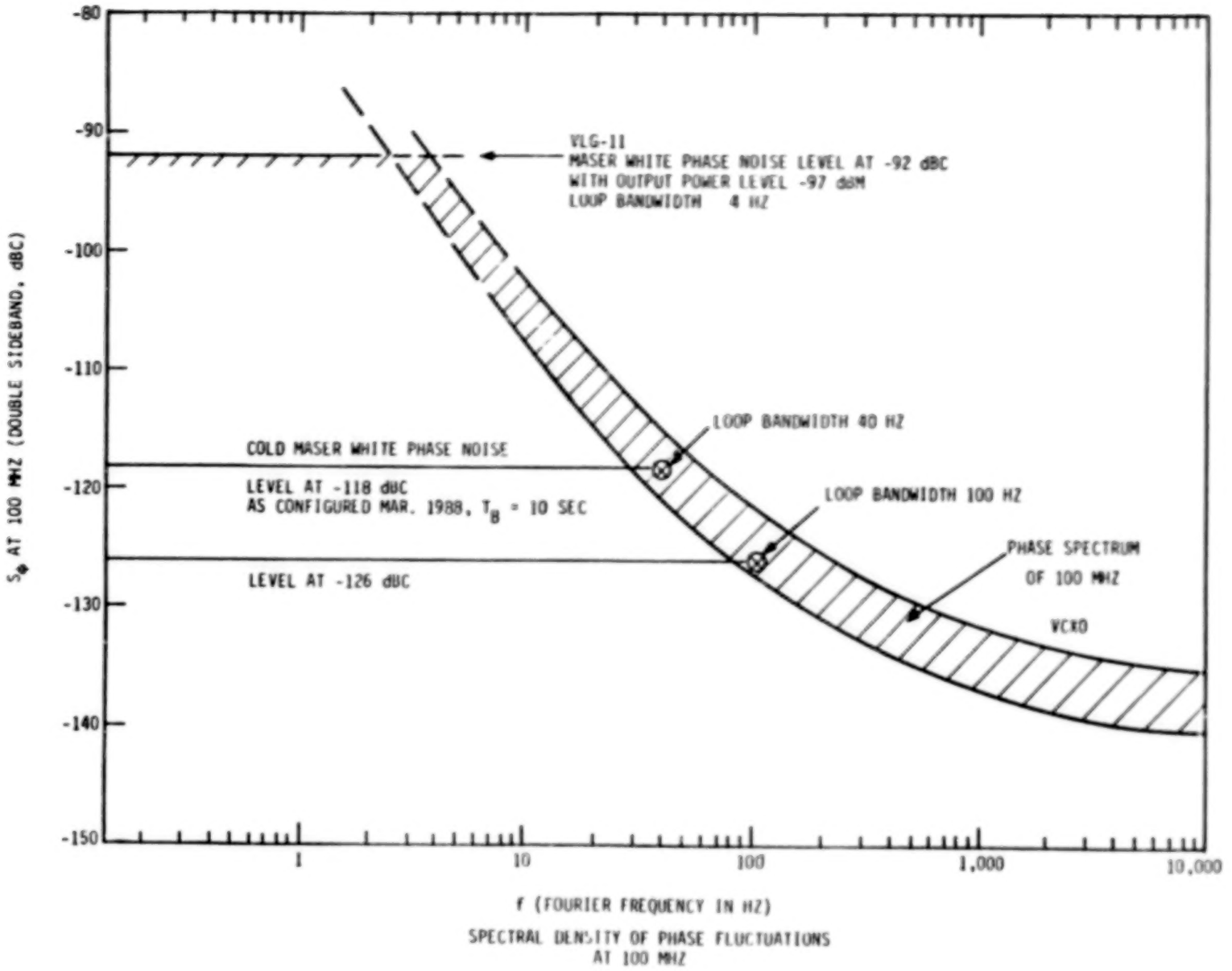


Figure 7. Spectral density of phase fluctuations at 100 MHz for the cryomaser and conventional H-masers.

BLANK PAGE

TRAPPED–ION FREQUENCY STANDARDS*

D. J. Wineland, W. M. Itano, J. C. Bergquist, J. J. Bollinger,
D. J. Heinzen, C. H. Manney, F. L. Moore, M. G. Raizen, and C. S. Weimer
Time and Frequency Division
National Institute of Standards and Technology
Boulder, Colorado 80303

Abstract

Frequency standards based on stored atomic ions are briefly reviewed. Specific examples are chosen to illustrate what is currently possible. Both rf/microwave and optical devices are discussed. The present limitations to existing experiments and possibilities for future improvement are outlined.

INTRODUCTION

The interest in stored ion frequency standards is reflected by the large number of laboratories using the stored–ion technique for high resolution atomic spectroscopy with application to frequency standards. The authors are aware of related work currently being pursued at (in alphabetical order) Communications Research Laboratory (CRL), Tokyo; Hamburg University; Hewlett Packard, San Jose; IBM, San Jose; Imperial College, London; Jet Propulsion Laboratory (JPL), Pasadena; Korea Standards Research Institute, Taejon, Korea; Laboratoire de l'Horloge (LHA), Orsay; Mainz University; Max Planck Institute, Garching; National Institute of Standards and Technology (NIST), Boulder; National Physical Laboratory (NPL), Teddington; National Research Council (NRC), Ottawa; National Research Laboratory of Metrology (NRLM), Tsukuba; Physikalisch–Technische Bundesanstalt (PTB), Braunschweig; and the University of Washington, Seattle. With apologies to many of these laboratories, this paper gives only a brief review of progress toward realizing frequency standards based on stored ions. It is not intended to be comprehensive. The reader is referred to recent proceedings of this conference and those of the Symposium on Frequency Control, the proceedings of the Fourth Symposium on Frequency Standards and Metrology[1], a forthcoming review[2], or the specific laboratories for further information.

Although there is overlap of the work between various groups, historically there has been a natural division in experiments performed in the rf/microwave spectral region versus those in the optical spectrum. One reason for this division has been that the required stable local oscillators have been difficult to provide in the optical domain and relatively easier in the rf/microwave region. This distinction is disappearing because better sources are now required in the rf/microwave region. Another reason for the division is that the ability to generate time (measure the phase of the clock radiation) in the rf/microwave region is straightforward, while it remains a difficult problem for optical frequencies.

*Work of the U.S. Government. Not subject to copyright.

RF/MICROWAVE EXPERIMENTS

The particular ion for an rf/microwave frequency standard should have a high frequency to increase stability (other things being equal). However, a primary consideration seems to be availability of a convenient optical source for use in optical pumping and double resonance detection of the clock transition. In addition, some experiments require a narrow band optical source for laser cooling. Some representative examples of rf/microwave clocks are given below:

A. $^{199}Hg^{+}$ Paul trap frequency standards

In 1973, Major and Werth observed the 40.5 GHz ground-state hyperfine transition of $^{199}Hg^{+}$ with a linewidth of a few hertz[3]. $^{199}Hg^{+}$ has some advantages over other ions as a frequency standard. Its hyperfine transition has a relatively high frequency. Because of its large mass, it has a low second-order Doppler shift at a given temperature.

The detection of the resonance is based on optical pumping. The lowest electronic levels are shown in Fig. 1. An rf-excited lamp containing the ^{202}Hg isotope will emit 194 nm radiation that will drive $^{199}Hg^{+}$ ions in the F=1 hyperfine level of the ground state to the $5d^{10}6p\ ^{2}P_{1/2}$ state. The ions can then decay to either the F=0 or F=1 hyperfine levels. The lamp eventually pumps most of the ions to the F=0 ground state. If microwave radiation near the 40.5 GHz resonance is applied, some ions are driven to the $m_F = 0$ sublevel of the F=1 state. They then can be re-excited to the $5d^{10}6p\ ^{2}P_{1/2}$ state by light from the lamp. When they decay, the 194 nm photons are detected with a photomultiplier tube. Jardino *et al*[4] made the first frequency standard based on this system. They measured $\sigma_y(\tau) = 3.6 \times 10^{-11}\tau^{-1/2}$, for $10 < \tau < 3500$, where τ is the measurement time interval in seconds. This stability was comparable to that of some commercial cesium atomic clocks.

This basic system was developed further by Cutler *et al*[5, 6, 7, 8]. They introduced helium buffer gas to reduce the temperature of the ions to near room temperature. The lamp was turned off when the microwave radiation was applied, in order to avoid light shifts of the microwave resonance frequency. The number of ions was about 2×10^{6}. The resonance linewidth was 0.85 Hz. Fractional frequency fluctuations of 7.6×10^{-15} for integration times of one day have been reported[6].

Prestage *et al*[9] have demonstrated a $^{199}Hg^{+}$ frequency standard based on a linear rf trap. Ramsey's separated oscillatory field method was employed to drive the resonance. In this method, two short rf pulses are applied. This yields a linewidth in hertz of about 1/(2T), where T is the time between the two pulses in seconds. The frequency standard was operated with a linewidth of 0.16 Hz and a Q of 2.5×10^{11}. The short-term stability of the device was $\sigma_y(\tau) = 1.6 \times 10^{-13}\tau^{-1/2}$ for $50 < \tau < 800$.

B. $^{9}Be^{+}$ Penning trap frequency standard

Bollinger *et al*[10, 11] demonstrated the first frequency standard based on laser-cooled ions where the second-order Doppler shift can be significantly reduced. This standard was based on a 303 MHz hyperfine transition in the ground electronic state of $^{9}Be^{+}$. The hyperfine sublevels of the ground state are shown in Fig. 2. The first derivative of the frequency of the transition between the $(m_I = -3/2,\ m_J = 1/2)$ sublevel and the $(m_I = -1/2,\ m_J = 1/2)$ sublevel approaches zero at a value of the magnetic field near 0.8194 T. A frequency-doubled cw dye laser was used to generate 313 nm radiation to laser-cool and optically detect the ions.

In the most recent version of the $^9Be^+$ frequency standard, sympathetic laser cooling was used[12]. Magnesium ions were trapped at the same time and were continuously laser cooled. The Coulomb interaction between the ions kept the $^9Be^+$ ions cold continuously. The number of $^9Be^+$ ions was about 5000 to 10,000. The 313 nm radiation source was tuned so that most of the ions would be pumped to the ($m_I = 3/2,\ m_J = 1/2$) ground-state sublevel in a few seconds. The 313 nm radiation was then turned off. Ions in the ($m_I = 3/2,\ m_J = 1/2$) sublevel were transferred to the ($m_I = 1/2,\ m_J = 1/2$) sublevel and then to the ($m_I = -1/2,\ m_J = 1/2$) sublevel by two successive rf pulses. The Ramsey method was then used to drive some of the ions to the ($m_I = -3/2,\ m_J = 1/2$) sublevel. Then rf pulses were applied in the reverse order, to bring ions which had remained in the ($m_I = -1/2,\ m_J = 1/2$) sublevel back to the ($m_I = 3/2,\ m_J = 1/2$) sublevel. The 313 nm source was then turned back on and the fluorescence intensity was measured. The intensity was proportional to the ($m_I = 3/2,\ m_J = 1/2$) population. If ions were left in the ($m_I = -3/2,\ m_J = 1/2$) sublevel, there was a decrease in the intensity. The time between the two rf pulses was as long as 550 s, although 100 s was more typical. With T=550 s, the width of the resonance was 900 μHz. The stability was better than $3 \times 10^{-12}\tau^{-1/2}$. However, a frequency shift with changes in pressure was observed[12]. This limited the long-term stability of the standard to about 3×10^{-14}. The uncertainty of the second-order Doppler shift was only 5×10^{-15}.

C. Other work

Other ions have been investigated for use in microwave frequency standards. Lasers have been used for optical pumping and detection of hyperfine transitions in several other ions, including $^{25}Mg^+$ [13], $^{137}Ba^+$ [14], $^{135}Ba^+$ [15], and $^{171}Yb^+$ [16]. Frequency standards based on $^{137}Ba^+$ [17] and $^{171}Yb^+$ have been reported[18].

OPTICAL FREQUENCY STANDARDS

An optical standard has the chief advantage that, if the transition linewidth and signal-to-noise ratio can be maintained, the stability of the standard improves linearly with the increase in frequency of the atomic transition used for the reference. This factor of improvement can be as much as 10^4. Conversely, by going to higher frequency, we can sacrifice some signal-to-noise ratio by using smaller numbers of ions and still maintain good stability. This is important because in general, the second-order Doppler shift is reduced as the number of ions is reduced. The penalty for using optical frequencies is that the required local oscillators (lasers) are more difficult to produce and the measurement of frequencies and the phase of the oscillation is difficult. Nevertheless, it seems that this approach will ultimately yield fundamental improvements in performance and several labs are pursuing these experiments.

High resolution experiments have been reported in Ba^+ [19, 20, 21], Yb^+ [18, 22], and Sr^+ [23] and Hg^+. As an example, we briefly discuss the experiment on Hg^+ at NIST.

A. Hg^+ single-ion optical spectroscopy

Hg^+ has a level structure which seems to be suitable for an optical frequency standard. The $5d^96s^2$ $^2D_{5/2}$ state is metastable, with a lifetime of about 90 ms. The 194 nm transition from the ground $5d^{10}6s$ $^2S_{1/2}$ to the $5d^{10}6p$ $^2P_{1/2}$ state can be used for laser cooling and for electron shelving detection[24]. Near

zero field, some hyperfine components of the 281.5 nm transition in $^{199}Hg^+$ are nearly independent of magnetic field. One of these is the transition from $F = 0$ in the ground state to $(F = 2,\ m_F = 0)$ in the upper state. Recently, Bergquist *et al*[25] observed this transition with a linewidth of under 80 Hz. The resonance line Q is over 10^{13} and is the highest ever observed in an atomic or molecular transition. The laser frequency was servoed to the single-ion resonance for periods of several minutes[25].

FUTURE

In general, the second-order Doppler shift increases as the number of ions is increased. This effect can be reduced by using a linear trap geometry[26] as has recently been demonstrated by Prestage, *et al*[9]. For more than one ion in a linear rf or Penning trap the second-order Doppler shift can be reduced to its minimum value by stacking a line of individual ions along the trap axis of symmetry[27, 28, 29]. This may provide a microwave or optical frequency standard with an extremely small second-order Doppler shift[28].

Throughout the history of high resolution trapped-ion spectroscopy, the most difficult systematic perturbation to eliminate has been the second-order Doppler shift. If this shift is reduced, other systematic effects may become more important. A surprising result (to us) was the large pressure shift measured on the $^9Be^+$ hyperfine transition[12, 28]. This may be caused by sticking of molecular background gas ions to the $^9Be^+$ ions. These kinds of shifts should also be investigated in other ions.

As the systematic shifts of the ion clock transitions are reduced, the demands on local oscillator spectral purity become more stringent. This is apparent in the experiments on Hg^+ and Be^+ microwave/rf transitions and is the most important limitation in the Hg^+ optical experiments.

Although the light sources for optical pumping, detection, and laser cooling can be difficult to produce, we anticipate that simple, cheap, solid state optical sources in the ultraviolet will eventually become available. This development will probably be driven by the optoelectronic industry rather than developers of clocks, but there is such a large effort to develop shorter wavelength solid state sources that there is reason to be optimistic.

Certainly, the new laser-cooling schemes will result in significant advances for neutral atom clocks[30]. It appears that the main advantage of the new cooling schemes is not the further reduction in the second-order Doppler shift, but the dramatically increased control over the positions and velocities of the atoms. Neutral atom clocks can work with much larger numbers of atoms and can therefore have high signal-to-noise ratio and stability. These experiments have the added advantage that diode lasers for optical pumping and laser cooling are available now. Therefore the ion trappers will have competition from these neutral atom experiments. Although there is no clear overall advantage to either approach, we expect to see dramatically improved frequency standards for both neutral atom and trapped ion experiments.

ACKNOWLEDGMENTS

The work at NIST has been supported by the Air Force Office of Scientific Research and the Office of Naval Research.

REFERENCES

1. *Frequency Standards and Metrology*, A. De Marchi, Ed., Berlin: Springer– Verlag, 1989.

2. W. M. Itano, Proc. IEEE, Special Issue on Time and Frequency, to be published.

3. F. G. Major and G. Werth, *High–resolution magnetic hyperfine resonance in harmonically bound ground–state ^{199}Hg ions*, Phys. Rev. Lett., vol. 30, pp. 1155–1158, 1973.

4. M. Jardino, M. Desaintfuscien, R. Barillet, J. Viennet, P. Petit, and C. Audoin, *Frequency stability of a mercury ion frequency standard*, Appl. Phys., vol. 24, pp. 107–112, 1981.

5. L. S. Cutler, R. P. Giffard, and M. D. McGuire, *A trapped mercury 199 ion frequency standard*, in Proc. 13th Annu. PTTI Applications and Planning Meeting, NASA Conf. Publ. 2220, pp. 563–573, 1981.

6. L. S. Cutler, R. P. Giffard, P. J. Wheeler, and G. M. R. Winkler, *Initial operational experience with a mercury ion storage frequency standard*, in Proc. 41st Annu. Frequency Control Symp., AD–A216858, pp. 12–17, Springfield, VA: Natl. Technical Information Service, 1987.

7. L. S. Cutler, R. P. Giffard, and M. D. McGuire, *Thermalization of 199Hg ion macromotion by a light background gas in an rf quadrupole trap*, Appl. Phys. B, vol. 36, pp. 137–142, 1985.

8. L. S. Cutler, C. A. Flory, R. P. Giffard, and M. D. McGuire, *Doppler effects due to thermal macromotion of ions in an rf quadrupole trap*, Appl. Phys. B, vol. 39, pp. 251–259, 1986.

9. J. D. Prestage, G. J. Dick, and L. Maleki, *Linear ion trap based atomic frequency standard*, IEEE Trans. Instrum. Meas. (in press)

10. J. J. Bollinger, W. M. Itano, and D. J. Wineland, *Laser cooled $^{9}Be^{+}$ accurate clock*, in Proc. 37th Annu. Frequency Control Symp., AD–A136673, pp. 37–41, Springfield, VA: Natl. Technical Information Service, 1983.

11. J. J. Bollinger, J. D. Prestage, W. M. Itano, and D. J. Wineland, *Laser–cooled–atomic frequency standard*, Phys. Rev. Lett., vol. 54, pp. 1000–1003, 1985.

12. J. J. Bollinger, D. J. Heinzen, W. M. Itano, S. L. Gilbert, and D. J. Wineland, *A 303–MHz frequency standard based on trapped Be^{+} ions*, IEEE Trans. Instrum. Meas. (in press).

13. W. M. Itano and D. J. Wineland, *Precision measurement of the ground–state hyperfine constant of $^{25}Mg^{+}$*, Phys. Rev. A, vol. 24, pp. 1364– 1373, 1981.

14. R. Blatt and G. Werth, *Precision determination of the ground–state hyperfine splitting in $^{137}Ba^{+}$ using the ion–storage technique*, Phys. Rev. A, vol. 25, pp. 1476–1482, 1982.

15. W. Becker and G. Werth, *Precise determination of the ground state hyperfine splitting of $^{135}Ba^{+}$*, Z. Phys. A, vol. 311, pp. 41–47, 1983.

16. R. Blatt, H. Schnatz, and G. Werth, *Precise determination of the $^{171}Yb^{+}$ ground state hyperfine separation*, Z. Phys. A, vol. 312, pp. 143–147, 1983.

17. H. Knab, K. D. Niebling, and G. Werth, *Ion trap as a frequency standard: Measurement of Ba^{+} frequency fluctuations*, IEEE Trans. Instrum. Meas., vol. IM–34, pp. 242–245, 1985.

18. R. Casdorff, V. Enders, W. Neuhauser, P. E. Toschek, and R. Blatt, *Frequency standards based on trapped Yb^+ ions*, in International Conf. on Quantum Electronics Technical Digest Series 1990, vol. 8, pp. 218–219, Washington, DC: Optical Society of America, 1990.

19. P. E. Toschek, *Lumino-refrigeration*, Ann. Phys. Fr., vol. 10, pp. 761–775, 1985.

20. G. Janik, W. Nagourney, and H. Dehmelt, *Doppler-free optical spectroscopy on the Ba^+ mono-ion oscillator*, J. Opt. Soc. Am. B, vol. 2, pp. 1251–1257, 1985.

21. W. Nagourney, N. Yu, and H. Dehmelt, *Laser spectroscopy of a single barium ion using 'shelving'*, in Frequency Standards and Metrology, A. De Marchi, Ed., Berlin: Springer-Verlag, 1989, pp. 312–318; Opt. Commun. vol. 79, pp. 176–180, 1990.

22. H. A. Klein, A. S. Bell, G. P. Barwood, P. Gill, and W. R. C. Rowley, *Studies of laser-cooled trapped Yb^+*, IEEE Trans. Instrum. Meas. (in press).

23. J. D. Sankey and A. A. Madej, *A single trapped strontium ion: A first step towards an improved frequency standard*, IEEE Trans. Instrum. Meas. (in press).

24. H. G. Dehmelt, *Mono-ion oscillator as potential ultimate laser frequency standard*, IEEE Trans. Instrum. Meas., vol. IM-31, pp. 83–87, 1982.

25. J. C. Bergquist, W. M. Itano, F. Elsner, M. G. Raizen, and D. J. Wineland, *Single ion optical spectroscopy*, in Proc. Conference on Light Induced Kinetic Effects, L. Moi and E. Arimondo, Eds. (in press).

26. D. A. Church, *Storage-Ring Ion Trap Derived from the Linear Quadrupole Radio-Frequency Mass Filter*, J. Appl. Phys., vol. 40, pp. 3127–3134, 1969.

27. H. Dehmelt, *Introduction to the Session on Trapped Ions*, in Frequency Standards and Metrology, A. De Marchi, Ed., Berlin: Springer-Verlag, 1989, p. 286.

28. D. J. Wineland, J. C. Bergquist, J. J. Bollinger, W. M. Itano, D. J. Heinzen, S. L. Gilbert, C. H. Manney, and M. G. Raizen, *Progress at NIST towards absolute frequency standards using stored ions*, IEEE Trans. Ultrason. Ferroelec. Freq. Control, vol. 37, pp. 515–523, 1990.

29. H. Walther, private commun.

30. C. Cohen-Tannoudji and W. D. Phillips, *New Mechanisms for Laser Cooling*, Physics Today, vol. 43, no. 10, October, 1990, p. 33; see also, for example, the recent collection of papers in: Journal of the Optical Society of America, vol. B6, 1989.

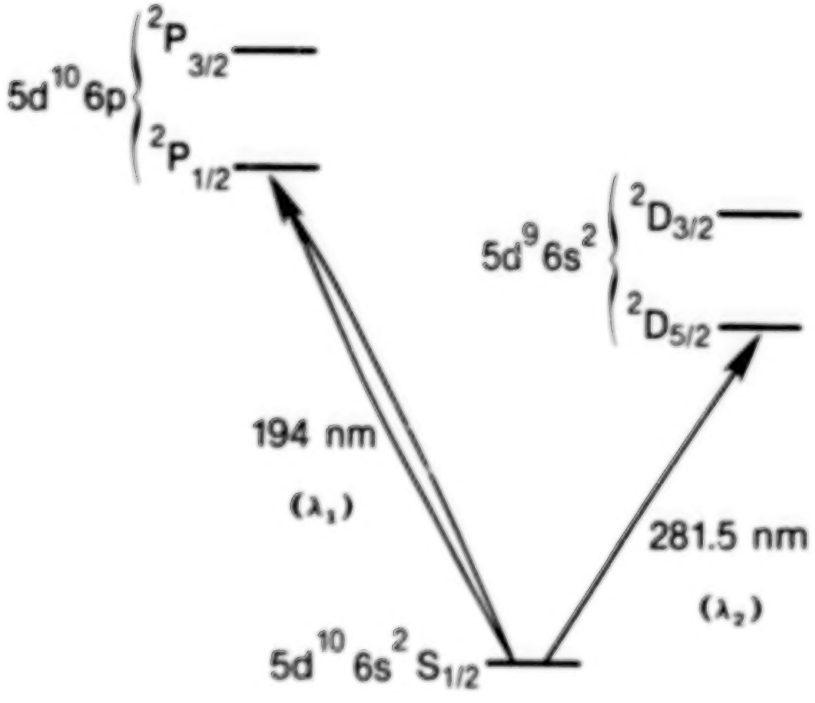


Fig. 1. Electronic energy levels of Hg^+. The ground electronic state of the $^{199}Hg^+$ isotope is made up of two hyperfine levels, separated by 40.5 GHz. Some microwave frequency standards are based on this transition. An optical frequency standard might be based on the 281.5 nm transition.

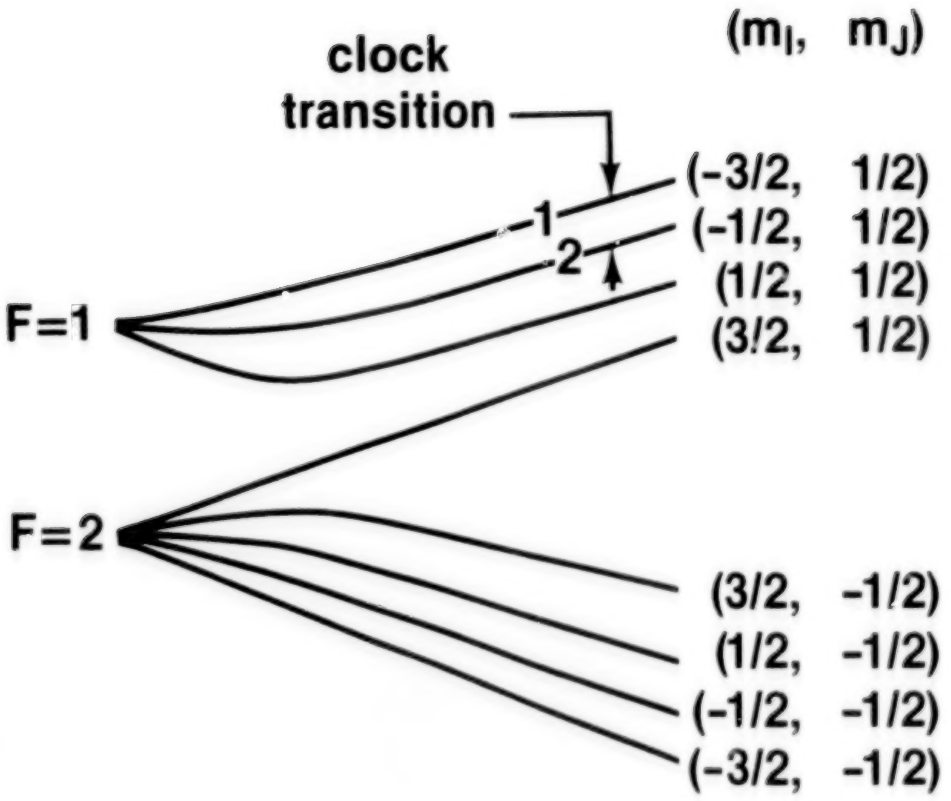


Fig. 2. $^{9}Be^{+}$ energy levels in a magnetic field. The frequency standard is based on the 303 MHz "clock transition" between the levels labeled "1" and "2."

INTER – SATELLITE TIME TRANSFER: TECHNIQUES AND APPLICATIONS

E. Detoma
SEPA S.p.A., Torino (Italy)

S.C. Wardrip
Bendix Field Engineering Corporation
NASA/Vandenberg AFB, California (USA)

Abstract

The role of the NASA Tracking and Data Relay Satellite System (TDRSS) is to increase the volume and frequency of communication between an orbiting spacecraft and the Earth, while at the same time providing command and tracking functions with extended coverage via a network of orbiting satellites and one or more ground stations. The same concept is currently being studied and is planned by the European Space Agency (ESA) under the name of Data Relay Satellite System (DRSS).

TDRSS is an answer to the increasing complexity of new satellites and space missions that, especially in the field of scientific and application satellites, are placing increasing requirements in terms of mission support.

New satellites, designed for scientific missions, such as astronomical observatories, or earth applications, for remote sensing, geodesy and precise navigation, are relying on precise onboard clocks to accomplish their missions.

All these spaceborne clocks require precise synchronization to some external ground reference, synchronization that must be provided as a part of the standard mission support. Since mission support is the primary role for the TDRS systems, synchronization must be provided through the same links used for telemetry, command and data acquisition.

There have been many time transfer experiments, and the techniques are well known and established throughout the years. A number of experiments have evolved into operational services now available worldwide and, in the case of the GPS, even to satellites in low earth orbit.

However, the requirement to provide timing support as a part of the standard support to the space missions, has resulted in NASA providing timing services to user spacecraft directly via the TDRSS. The same service is being considered for the new Advanced TDRSS (ATDRSS) and the ESA Data Relay Satellites (DRS).

We will start with a brief review of the well known time transfer techniques that have been studied and tested throughout the years. We will then discuss the applicability of time transfer techniques to a timing service as provided through a TDRS/DRS System, the problems related to the choice of the timing signal within the constraints imposed by the existing systems, and the possible practical implementations, including a description of the time synchronization support via TDRSS to the Gamma Ray Observatory (GRO).

TIME TRANSFER: DISSEMINATION AND SYNCHRONIZATION

In general, the knowledge of the relative time offsets between two or more clocks is desired. This requires the comparison of the readings of the clocks. If the clocks are remotely located this may be difficult, depending on the degree of synchronization required by the measurement.

We will refer to the exchange of timing information between two or more clocks, an exchange leading to the determination of the clocks respective offsets in time, as the *synchronization* procedure.

When the time information is transmitted or broadcasted to two or more users it is called *"time dissemination"*, and it is generally performed by transmitting time coded information (time codes).

Dissemination by itself does not imply the presence of a clock at the user site: the user can simply get its time from the decoded message. Synchronization, being the measure of the offset between two clocks, always requires a clock at the user site.

Since, in many occasions, the two procedures are used together (sometimes just to reduce the initial ambiguity of the synchronization procedure) they are both, in general, referred to as *"time transfer"* procedures.

Radio or optical signals have been used to transfer time over long distances. In both cases, a timing signal or marker must be modulated on the electromagnetic wave acting as the carrier.

Usually an event marker is used to synchronize clocks. This can be a pulse, or the zero crossing of a sine wave, or a particular status of a Pseudo Random Noise (PRN) Code. The time mark, sometimes referred to as a "tick", must be identifiable and precisely resolved in time. If a pulse is used as a timing marker, usually its leading edge is taken as the on-time reference, and the sharpest rise time is desirable. If the zero crossing of a sine wave is used, the higher the frequency the better the timing resolution for a given Signal to Noise (S/N) ratio. But this requires a better "a priori" knowledge of the relative position of the two clocks being synchronized, since the number of zero crossing per unit of time increases with the frequency; this presents another problem: *ambiguity resolution.*

Time dissemination usually relies on the transmission of full numeric coded information. The process of transmitting such information generates an RF spectrum that is far from optimum for synchronization. Moreover, the unavoidable delays and jitters of the coding/decoding equipment adds uncertainty to the measurements and finally degrades the precision and accuracy of the time transfer.

However, being able to read the time from the received message, without reasonable ambiguity, the user does not need its own clock to keep time: usually a time code reader and display unit is all that is required.

USE OF SATELLITES FOR TIME SYNCHRONIZATION

Satellites have been used for decades now for time synchronization. They are useful, since they can extend the limits of precise time synchronization far beyond the horizon. VLF and LF transmissions (notably OMEGA and LORAN) have been used in the past to convey time information over the horizon, but they have limited capabilities. LORAN can achieve the greatest precision only within the limits of groundwave propagation, a few hundred kilometers. OMEGA has worldwide coverage, but relatively poor performances for timing, only a few tens of microseconds.

The simplest technique using a satellite for time transfer (synchronization or dissemination) is the *one-way technique* (Fig. 1); the satellite is used as a radio relay, or transponder. The signal is transmitted from A to the satellite and from the satellite relayed back to B, which is located well beyond the line of sight of A.

The synchronization equation (see Fig. 1 for symbols) is:

$$E = \text{time}(A) - \text{time}(B) = T_D - T_M$$

and, since T_M is measured, then T_D must be estimated, or computed, given the orbit of the satellite and the location of A and B. Uncertainties in the satellite orbit and ground locations of A and B are the main causes of error for the one-way technique.

Many variations of this technique exist. In one, a clock onboard the satellite replaces the ground transmitting station. Synchronization can even be accomplished, when two stations are simultaneously in view of the satellite, without having a real clock on the satellite, provided that some kind of easily identifiable pulse is transmitted by the satellite (*passive synchronization*)[14].

Using this technique (Fig. 2), two ground clocks can be synchronized by comparing the times of arrival of the same pulse emitted by the satellite[14]. This method is a natural extension of the passive TV synchronization method, widely used to synchronize clocks on a national scale in many countries.

Let the satellite emit a pulse at an arbitrary time t_0. The propagation delay from the satellite to "A" is $T_D(A)$, and from the satellite to "B" is $T_D(B)$; these delays must be known by computing the range at t_0 and applying corrections for tropospheric and ionospheric delays (Fig. 2).

At the location of the clock "A", the pulse emitted by the satellite is received at $T_M(A)$; computing $T_D(A)$, "A" is able to evaluate t_0 in its own time scale.

The same occurs at the location of the clock "B"; another evaluation of t_0 is carried on, but this time it is in the "B" time scale. Obviously the two will not be identical, because of the error E between the two clocks: the difference between the two determinations of t_0 will give a measure of E.

It can be proven that uncertainties in the ephemeris of the satellite, which produce errors in the range estimates, are greatly reduced by the differencing technique[14], resulting in smaller errors in the time synchronization. This fact has been successfully exploited in the "common-view" technique using GPS satellites[15].

If the satellite carries a stable *oscillator onboard*, it may produce a repetitive stream of pulses, with no requirement placed on the degree of synchronization of these pulses with any time scale. As long as these pulses are stable in frequency, and a count is maintained onboard the satellite (and eventually transmitted via telemetry to the ground stations), then the previous synchronization scheme can be extended to clocks not in common-view of the satellite (Fig. 3).

The onboard satellite oscillator acts as a flywheel only for the time required by the satellite to fly between one site and another. Its frequency must be stable only over this limited amount of time. This makes possible to use this technique to synchronize precise atomic oscillators with simple onboard crystal oscillators.

This is the satellite extension of a technique proposed several years ago by Besson, of using aircraft to carry around flying clocks. In 1971, Joseph Hafele of Hewlett Packard and others were the first to fly cesium clocks around the world to prove the Special Theory of Relativity. Aircraft have been

used also in other experiments (involving relativity) by C. Alley and co-workers at the University of Maryland.

If the oscillator is stable, and the counting devices following the oscillator itself have provisions to be synchronized to an external time scale (for instance, UTC), then the satellite can broadcast precise time in the form of pulses (markers) with related coded information (Fig. 4), in such a way that is possible:

- one-way time dissemination;
- one-way absolute synchronization (referenced to the onboard time scale, so that a user needs only to receive the satellite transmission to precisely set and synchronize his clock);
- one-way relative synchronization (between two users, either in common view or not, using the stability of the satellite clock as a time flywheel).

These techniques were widely used with the TRANSIT/NNSS satellite system and in the GPS/NAVSTAR, as a timing spin-off from the implementation of satellite navigation systems.

However, all the preceding techniques:

- One-way, satellite acting as a repeater;
- Passive synchronization;
- Satellite carrying an oscillator;
- Satellite carrying a clock;

rely on computed ranges and propagation delays to achieve time transfer: this is a basic limitation of these techniques. A method to accurately measure the propagation delay is very desirable, especially if this can be done with the same precision by which time events are measured.

This is the idea behind the *two-way synchronization* techniques. Both stations, "A" and "B", are active, transmitting their own time signals and receiving the signals transmitted by the other (Fig. 5).

If the satellite is really stationary, when "A" receives the pulse transponded back by "B", then "A" has a measurement of twice the propagation delay between "A" and "B". Here we suppose that the two paths (from "A" to "B" and "B" to "A") are truly reciprocal and this, in practice, may not be the case.

Now that a direct measure of the propagation delay is available at "A", this can be transmitted back to "B" and "B" uses the delay to correct its timing measurements and retrieve the synchronization error E, instead of having to compute the delay from range measurements.

In practice, things are more complicated, but the method is one of the most accurate and precise ever being used for time synchronization. Only laser-based synchronization methods, thanks to their higher bandwidth, can achieve better resolution and accuracy. The disadvantage is related to the fact that a complete transmitting/receiving equipment must be available at the two sites.

This was a bit of a problem in the past, when satellite communication meant bulkier antennas and apparatus. However, with the present day technology, this is feasible with smaller VSAT antennas and Direct Broadcasting Satellites, and indeed experiences have already been taken place in the United States, at the NIST and at the U.S.N.O.

Laser communication links present a wider bandwidth than is possible with RF links. However, they are not as much as efficient in terms of signal to noise ratio. Moreover, a light signal can be relayed back by a mirror or by a retroreflector. Precision pointing of a mirror in space is a difficult task. The retroreflector provides an easy and accurate reference direction of reflection, the only problem being that the light is reflected exactly back to the transmitter site. The problem can be solved by placing a photon detector, a stable oscillator and an event counter onboard the satellite, in addition to the retroreflector array.

Every user (Fig. 6) transmits an intense pulse of light at a known time; which can be precisely measured against the local time scale. The pulse transmitted by the user "A" arrives at the satellite, detected by the photodetector and time tagged in the local time scale of the onboard clock. At the same time, the retroreflector array reflects part of the original pulse energy back to the ground, when it is detected and the round trip time measured accurately.

Since the transmit time and the propagation delay are known, the time of arrival of the transmitted pulse at the satellite can be computed in the station "A" time scale. Also, the transmitted pulse arrival time is measured in the satellite time scale "S" and, by taking into account the propagation delay, we have a measurement of the synchronization error $E(A - S)$ between the time scale of "A" and the satellite.

Another user "B", shortly after "A", makes a measurement, performing the same procedure, and is able to recover $E(B-S)$. By taking the difference between the two measurements yields the synchronization error between "A" and "B". The time scale of the satellite disappears in the differencing.

The frequency stability of the onboard oscillator, in the short time between the arrival of the pulse from "A" and the arrival of the pulse from "B", must be such as to not degrade the timing accuracy of the measurement. If the time elapsed between the arrival at the satellite of the two pulses is only a few hundred milliseconds, it can be shown that a good crystal oscillator can provide enough stability not to degrade the synchronization at the subnanosecond level.

This technique has been implemented in the **LASSO** (LAser Synchronization from Stationary Orbit) concept. A first attempt to carry a LASSO package into orbit was done with the SIRIO-2 satellite and failed, due to a launching accident. Later, a LASSO package was successfully orbited onboard the ESA Meteosat–P2 satellite.

The LASSO experiment was proposed by M. Lefebvre et al. of the Centre National d'Etudes Spatiales (CNES), Toulouse (France). Based on a presentation at the 1972 COSPAR meeting in Madrid, the European Space Agency (ESA) accepted a proposal from the Bureau International de l'Heure (BIH) to pursue a related space mission.

The aim of the LASSO technique is to provide a repeatable, near–real–time method for long distance (intercontinental) clock synchronization, with nanosecond accuracy.

The LASSO payload is composed of retroreflectors, photodetectors for sensing light at two wavelengths (from ruby and doubled Nd–YAG laser emitters) and an ultrastable oscillator to time–tag the arrival of laser pulses; these time–tags or "datations" are transmitted to the ground via telemetry.

The LASSO technique is based on the use of laser ground stations firing monochromatic light pulses at predicted times, directed toward the synchronous satellite. An array of retroreflectors onboard the spacecraft sends back a fraction of the received signal to the originating laser station, while an electronic device onboard the spacecraft detects and time-tags the arrival of the laser pulses.

Each station measures the time of transmission and the two-way propagation delays of the laser pulses, and computes the one-way propagation time between the station and the spacecraft. Then, the offsets between the clocks that provide the time reference at each of the laser stations can be computed from the data collected at the spacecraft and at the ground stations.

With reference to the timing diagram (Fig. 6) for two stations, we have (corrections are neglected):

$$E = (Td_A - Td_B) + (Tp - A - Tp_B) - (Ts_A - Ts_B)$$

where:

- E is the time offset between the two clocks at the stations A and B;
- Td_i are the transmission times of laser pulses from the station i [i =A, B];
- Tp_i are the propagation delays between each station and the spacecraft [i = A, B];
- Ts_i are the times of arrival onboard the satellite of the laser pulses transmitted from the station i [i =A, B];

If: Tr_i are the return times of laser pulses transmitted from the station i [i =A, B],

then the propagation delays Tp_i can be easily computed as:

$$Tp_i = \frac{Tr_i - Td_i}{2} \qquad [i = \mathrm{A},\ \mathrm{B}]$$

Substituting, we finally obtain the synchronization equation:

$$E = \frac{(Td_A - Td_B)}{2} + \frac{(Tr_A - Tr_B)}{2} + (Ts_A - Ts_B)$$

An interesting variation to the LASSO scheme for optical time transfer was proposed in the past[11]. The idea was to reverse the locations of the optical transmitter and receiver. In the LASSO experiment the transmitting lasers were located on the ground, and the satellite carried orbiting retroreflectors. The proposal to reverse the roles, putting the laser in orbit and inexpensive retroreflectors and detectors on the ground, was aimed to reduce the cost to the user, in hope of providing time dissemination available at metrology centers around the world, and to allow geodetic users of the system to cover wide areas with passive retroreflectors at minimum cost. The difficulty lies in pointing the orbiting laser with the required accuracy. As far as we know, the technique was never pursued, even if it is an interesting concept.

INTERSATELLITE LINKS FOR TIME SYNCHRONIZATION

The Tracking and Data Relay Satellite System (TDRSS) is designed to provide Tracking and Data Relay Service to User Satellites, generally in Low Earth Orbit (LEO), using a constellation of geosynchronous satellites (two operational, TDRS West and East, plus an in-orbit spare) and two ground stations, both located at White Sands, New Mexico.

Fig. 7 (from Ref. 1) shows the geometry involved in the TDRS System. A signal is transmitted (from the user LEO satellite) to one of the two operational TDR satellites which transponds the signal to the TDRSS NASA Ground Terminal (NGT) at White Sands (Fig. 12). The same path is followed in reverse by a signal transmitted from the ground to the user LEO satellite via TDRSS.

When ground stations were used to provide tracking, command, telemetry and data acquisition support to the space missions, an extensive world wide network was required to provide continuity of coverage. In those days, the signals traveling from ground to the satellite (tracking and command) were referred to as the "uplink". Conversely, signals traveling from the satellite to ground (tracking, telemetry and data) were referred to as downØlink communications.

This is not so obvious with TDRSS. First, the signal from NGT to the satellite travels upward to the TDR satellite, and then downward to the user satellite, which is in low Earth orbit below the TDRS. Conversely, from the satellite to ground, the signal travels upward to the TDR satellite, then downward to NGT. To avoid confusion, the convention adopted was to refer to the communication link from NGT to the user satellite via TDRS as the forward link, and to the link from the user satellite to NGT via the TDRS as the return link. The TDRS is basically a transponder.

The TDRS is transparent as regard to the communication of data between the user LEO satellite and NGT. However, while the NASA TDRSS was designed to provide Tracking and Data Relay Support to Earth Orbiting Missions, it was not designed to support time and frequency transfer to a User Satellite.

The first satellite needing such a service is an astronomical observatory, the Gamma Ray Observatory (GRO). GRO requires a time-tag of data collected onboard to within 100 microseconds of Universal Time Coordinated (UTC) time scale. Since the onboard oscillator is a crystal oscillator, it needs periodical calibrations, which must be performed from the ground, via the command and telemetry link. To correct the oscillator, however, its phase, frequency offset and aging must be precisely measured with respect to UTC, or against a ground clock referenced to UTC by external means.

In 1975-1976 the Timing Systems Section of the Network Engineering Division at GSFC was charged with this problem. The Applied Physics Laboratory (APL) of the Johns Hopkins University was tasked to aid with a study of possible solutions. The study resulted in what is referred as the DATA INTERFACE APPROACH: to synchronize user spacecraft clocks via the Tracking and Data Relay Satellite System. The technique chosen was the two-way technique.

NOTE: Notice that the User Clock may be either onboard a User Satellite or on the ground: i.e., the technique can be used to also synchronize a second ground station[3] or any Remote Clock, provided that a TDRS-compatible transponder is available at the site[4].

In the two way time synchronization technique[3], two clocks, located at A and one at B (Fig. 5) exchange the time information through a satellite communication link. The time information can be in the form of pulses, bursts of pulses, continuous sine signals or Pseudo Random Noise codes (PRN codes). The basic equation giving the time difference between the two clocks is[1]:

$$E = \frac{[T_1 - T_0] - [T_3 - T_2]}{2} + \delta E \quad \text{(corrections)} \tag{1}$$

where: E is the time offset between the clocks in A and B [actually $E = T(B) - T(A)$];
T_1 and T_3 are the times of reception of the time signal transmitted at the times T_0 and T_2 by A and B.

The corrections δE take into account several factors affecting the synchronization process: the difference in the forward and return paths (from A to B and from B to A) due to the satellite motion and to the Earth rotation, the atmospheric propagation delays (troposphere and ionosphere) and the equipment delays.

Usually a pulse at the rate of 1 pulse per second is the electrical output of a standard clock; the resulting 1 second ambiguity can be easily resolved by looking at the time readout, since one second change in the display is easy to observe, and numerical information can be easily coded, transmitted and decoded as digital data in a one second frame.

The 1 pps pulse output constitutes the time mark of the clock, used to resolve time intervals smaller than 1 second: usually the leading edge of the pulse itself is taken as the on-time reference to increase the resolution of the measurement.

The synchronization procedure used in the TDRSS determines coarse and fine spacecraft clock error with respect to UTC. Coarse error is determined from the spacecraft clock time code to one second resolution; fine error is defined as the residual synchronization error within the 1 second ambiguity period.

> We will show, however, that, by relating the ambiguity to the repetition period of the timing pulses used as the time signal, some simplification in the hardware and in the operations may be obtained (see the HYBRID TECHNIQUE).

To perform the ranging measurements (a primary function of the TDRSS is to provide orbital support to the missions), a Pseudo-Random Noise (PRN) Code is generated at the TDRSS Ground Station and modulated on the forward RF link together with the command data for the user spacecraft.

There, the code is received, demodulated and the code epoch precisely measured to reconstruct a second code with the same characteristics of the received code, but with a different bit pattern. Exact time synchronization between the two codes is maintained. This second code is sent back to White Sands via TDRSS.

Being precisely synchronized to the forward-link ranging code, the return-link code provides an easy way to measure the two-way propagation time, so that an estimate of the one-way range between White Sands and the User Satellite is obtained. Since the range from White Sands to the relaying TDR satellite is precisely known (or continuously measured using the same technique), the range from the TDR satellite to the User Satellite is also known.

Even if ranging is not performed continuously, the forward and return PRN codes are present. The PRN codes are an ideal timing signal for time transfer, because of the optimum use of the available bandwidth, the good rejection of external interferences (man-made or natural) and the extreme resolution of the timing measurements due to the high repetition rate of the chip period.

The TDRSS PRN code is periodic, with a code period of about 85 ms, i.e., the code repeats itself every 85 ms. This is the time interval ambiguity associated with the PRN code. Once per cycle, the

code generator steps over one easily identifiable state, the so called "All 1's" state, since every tap on the feedback logic of the shift register generating the PRN code is at logic level 1. Notice that an "all 0's" state cannot exist in a PRN code generator, otherwise the code itself will be trivial, being locked in a zero state condition.

In the TDRSS time transfer techniques using PRN codes, the timing signal (or time reference ticks) exchanged between the two clocks to perform the synchronization is the "All 1's" state of the PRN code, and the reference time is measured accordingly on the rising edge of the "All 1's" pulse from the local generator, when the received and locally generated codes are correlated (when receiving), or on the rising edge of the "All 1's" pulse from the local generator when transmitting.

Basically, the APL approach was to use a two-way time synchronization technique, after an initial coarse synchronization was performed to resolve the one second ambiguity. Time tagging of the "All 1's" pulses was required to identify the selected pulse (with about 80 ms ambiguity due to the PRN code repetition rate) within the 1 second coarse synchronization interval. The identification was carried on using the telemetry data stream, since, in principle, epoch timing, telemetry data and frame rates and clocks ticks are asynchronous.

Several techniques were considered[5], including one-way time transfer; however, the improved performances related to the implementation of the two-way technique were evident, and it was decided to implement a synchronization scheme based on the two-way technique, which in its basic form is shown in Fig. 8.

Going deeper into the details of the actual implementation, two situations were taken into account, due to the fact that the return PRN code can be locked to the forward PRN code whether or not a TDRSS ranging function is being performed.

The non-ranging situation requires only an additional time interval measurement onboard the User Spacecraft to measure the transmission time of the reference mark of the transmitted code. This additional measurement must be relayed back to Earth via the telemetry. The remaining of the computations are essentially identical.

Return PRN Code locked to the Forward Code (Technique 1)

The first technique considered assumes that the Return PRN Code (generated onboard the User Satellite) is locked to the Forward Link PRN Code. In Fig. 9 (from Ref. 5) this is shown schematically. To avoid confusion in reading the figure, consider that the second number used in the suffix of the indicated quantities refers only to the number of consecutive measurements performed, and can be ignored, since, in principle, the two-way time transfer can be carried on in one measurement frame.

Defining:

$D_1 = D_{11}$ = transmission time of the timing reference from the master (ground) station;

$D_2 = D_{21}$ = time of reception/transmission of the timing reference at the user;

$D'_3 = D'_{31}$ = time interval elapsed from the time of transmission to the reception of the timing signal at the master site.

NOTE: D'_3 is the two-way propagation delay; the "absolute' time of reception of the timing mark in

the master time scale is actually $D_3 = D'_3 + D_1$.

If E_1 is the time offset between the two clocks, we can write:

$$D_1 + t_f = E_1 + D_2 \tag{2}$$

and:

$$D_1 + D_3 = E_1 + D_2 + t_r \tag{3}$$

where t_r and t_f are the forward and return propagation delays.

If the geometry is completely reciprocal, t_r and t_f would be equal and the eqs. (2) and (3) can be simply added to obtain:

$$E_1 = \frac{D_1 + D_3}{2} - D_2 \qquad [D_3 = D_1 + D'_3] \tag{4}$$

which is the basic two-way time synchronization equation, shown also in Fig. 6.2. However, considering the satellite motion and the resulting Doppler effect, we know that this is not true, and in general t_f will be different from t_r.

If this is the case, we can simply use the eq. (2) and write:

$$E_1 = t_f - (D_2 - D_1)[\text{for the technique 1}] \tag{5}$$

The first approximation to evaluate t_f, yielding the classical two-way time synchronization equation (4), assumes full reciprocity, neglecting any satellite motion. In this case, t_f is obtained directly from the two-way propagation delay D'_3.

For the TDRSS synchronization, as in other cases, a more complicated model for the satellite motion is assumed, but this will not be described here.

Return PRN Code not locked to the Forward Code (Technique 2)

The second technique considered is more general, and assumes that the Return PRN Code (generated onboard the User Satellite) is not locked to the Forward Link PRN Code. In Fig. 10 (from Ref. 5) this is shown schematically. Again, to avoid confusion in reading the figure, the second number used in the suffix refers only to the number of consecutive measurements performed, and can be ignored in the following discussion.

Defining: $D_1 = D_{11}$ = transmission time of the timing reference from the master (ground) station;

$D_2 = D_{21}$ = time of reception of the timing reference at the user;

$D_4 = D_{41}$ = time of transmission of the timing reference from the user;

$D'_3 = D'_{31}$ = time of reception of the timing reference at the master site, elapsed from the transmission time

NOTE: D'_3 is the two-way propagation delay; the "absolute" time of reception of the timing mark in the master time scale is actually $D_3 = D'_3 + D_1$

If E_2 is the time offset between the two clocks, we can write:

$$D_1 + t_f = E_2 + D_4 \tag{6}$$

and

$$D_1 + D'_3 = E_2 + D_2 + t_r \tag{7}$$

The suffix "2" of E_2 denotes only the time offset as computed using technique 2. If total reciprocity of the forward and return propagation delays cannot be assumed, we can only write:

$$E_2 = t_f - (D_4 - D_1) \tag{8}$$

Again, t_f must be computed separately, under the assumptions given above.

The TDRSS PRN code generator chip rate and code length result in a repetition period for the full code of about 85 ms; as a consequence, this is also the repetition period of the "All 1's" state of the code.

To identify the "All 1's" state used as the timing marker for the synchronization, a range gating system using the telemetry frame was used. This resulted in some problems, related to the decoding delay of the telemetry frame which, in the TDRSS, is convolutionally encoded on the carrier. This unpredictable delay may create some ambiguity in the "All 1's" state identification, when the two occur very close together.

The problem was solved by adding a second telemetry identifier and resulted in an increase in the complexity of the hardware used to implement the technique.

An error budget was estimated[5] as follows:

SOURCE	ERROR assuming given errors are 1 σ values	ERROR assuming given errors are 3 σ values
Measurements and calculations	6 ns	6 ns (*)
Differential delay at User Satellite	7 ns	20 ns
Differential delay at Master site	7 ns	20 ns
Differential delay of Satellite	10 ns	30 ns
Non-reciprocity in propagation effects	5 ns	5 ns (*)
TOTAL R.M.S.	16 ns	42 ns

NOTE (*): No averaging is assumed

In 1982 a second proposal was put forward by the Gamma Ray Observatory Project Office, regarding the possibility to passively monitor the Gamma Ray Observatory onboard clock simply by using the telemetry return link[7].

The idea was to implement a one-way time transfer technique, based on the telemetry link, with the following budget:

	ERROR SOURCE	R.M.S. ERROR
(a)	GRO clock quantization error	0.28 μs
(b)	Spacecraft delay	—
(c)	Orbit determination error	2.00 μs
(d)	TDRS transponder delay	—
(e)	WSGT equipment delay	1.00 μs
(f)	Telemetry clock reconstruction error	2.00 μs
(g)	NGT quantization error	0.29 μs
(h)	NGT clock error	1.00 μs
	TOTAL R.M.S. ERROR	$\approx$ 3.20 μs

This figure for the total R.M.S. error was considerably higher than that given by the data interface approach. Nevertheless, if maintained, the telemetry interface approach would have been able to satisfy the requirements of the GRO spacecraft with much less hardware and complexity than the more sophisticated APL proposal.

However, the technique was not accepted, because of the risk involved in the decoding of the telemetry data stream: in some of the bit and frame synchronizers used at the time, random slippages of one bit occurred in the clock reconstruction.

Some variations on the schemes proposed for the DATA INTERFACE APPROACH can be envisaged, e.g. by reducing the hardware complexity while maintaining the accuracy of the two-way technique.

> The use of a Hybrid Technique was suggested by the fact that, after the two clocks (NGT and user) are synchronized, no need exists to carry on the pulse identification process using range gates and telemetry frame information.

How well two clocks need to be synchronized for this statement to be true?

> It can be shown that two clocks (Master and User) need only to be synchronized to within T/4 seconds, where T is the "All 1's" repetition period (i.e., the repetition period of the PRN code).

Since, for TDRSS, $T \approx 80$ ms, then the two clocks need only a initial coarse synchronization within 20 ms. This is well within the capability of a One–Way Time Transfer technique, such as the Telemetry Interface Approach. Therefore, the synchronization of the User Clock (either on a Satellite or on the Ground) can be carried on in two steps:

1. COARSE SYNCHRONIZATION: One can use the Telemetry Interface Approach or any other suitable, simple technique to synchronize the User Clock at the 20 ms level (T/4): the One–Way technique is advisable.

The One–Way technique has a definite advantage over trying to perform the full Telemetry Interface approach, since all the propagation delays need not be measured more accurately than a few ms. Range computation from the orbital elements, prediction of atmospheric delays and other delays associated to the equipment may all be neglected.

2. FINE SYNCHRONIZATION: Once the coarse synchronization has been performed, using whatever technique is available and convenient, and the two clocks are synchronized within 20 ms, there is no need to identify the "All 1's" pulses.

In this way we should be able to exploit the full capability and accuracy of the Two–Way technique, without the trouble to use the identification procedure (using the telemetry frame marks) and even without the ranging gates, *as long as we rely upon the short term stability ($\tau \leq 1$s) of the clock that generates the PRN code.*

> This approach simplifies the hardware to be built and allows the fine synchronization procedure (2) alone to be used, if the User Clock is maintained to within T/4 seconds.

From an operational point of view, the coarse synchronization must be carried on only initially, when the clock is first switched on. After that, this technique need only be used if a major malfunction should occur and coarse synchronization is lost.

> However, for normal timekeeping, only the fine synchronization procedure is to be used.

This adds a substantial simplification to the operational requirements and limits the amount of data to be handled.

The following description is intended to present a possible implementation of the Hybrid synchronization technique. Equipment delays are considered as known quantities, and, in any case, measurable and stable to within the required accuracy. To simplify the equations these delays are, at present, ignored. The coarse synchronization technique will not be addressed, since it is straight forward in its execution; only the two–way fine synchronization will be described.

The reference pulses exchanged between the Master clock (NGT) and the User are the "All 1's" occurrences of the PRN code. The "All 1's" repetition period is T, and it can be shown that, to

avoid any ambiguity in recovering the time offset E between the two clocks, these should be initially synchronized with an overall error not to exceed T/4. This is a condition that is readily achievable using ordinary synchronization techniques, and should not present a problem.

During a preliminary investigation, several modes of operation were studied, depending on whether or not the "All 1's" reference mark would or would not be readily available at NGT. In the following it is assumed that the "All 1's" state indicator is available at the master site (NGT): and, as such, various techniques using ranging signals or ground bilateration transponders will not be addressed. In the mode considered here, the "All 1's" signal is available both at the Master Clock and at the User Clock (Fig. 11).

The first occurrence of the "All 1's" after the local second tick at the Master (NGT) occurs at a time T_1, and T is the "All 1's" repetition period. The signal is received at the User at the time T_5 and it is transponded back to NGT, where it arrives at the time T_4 (Fig. 11).

Neglecting the effect due to the satellite motion, the clock offset E is given by the two-way synchronization equation as:

$$E = \frac{T_4 + T_1}{2} - T_5 \tag{9}$$

If T_3 is the first occurrence of the received "All 1's" after the second tick at NGT and T_2 is the first occurrence of the transponded "All 1's" at the User, again after the local second tick, we can write:

$$T_4 = T_3 + n \cdot T \qquad T_5 = T_2 + \frac{n}{2} \cdot T \tag{10}$$

where n is an integral number of cycles of T. Substituting into eq.(9) we have:

$$E = \frac{T_3 + T_1}{2} - T_2 \tag{11}$$

which avoids the use of the range gates to enable the measurements and the identification of T_3 and T_1; a counter is simply started by the local second tick and stopped by the "All 1's" occurrence. However, *special care must be exercised* to handle the modulo–T arithmetic implicit in eq. (11).

The two clocks must be synchronized initially to within T/4 to avoid any ambiguity. Synchronization to T/2 is required because of the division by 2 in eqs. (9) and (11), while initial synchronization to T/4 is further required to give the correct sign to the computed offset (otherwise $E = -5\mu s$ and $E = T/2 - 5\mu s$ are completely equivalent, since a residual ambiguity of T/2 still exists on the computed offset E).

As in the Data Interface Approach (APL), the correction to the basic synchronization equation for the satellite motion is obtained from successive differences in the round trip propagation delays, using the T_3 and T_1 measurements.

The equations will remain the same as those provided for the Data Interface Approach. It can be shown that the linear range variation model is a valid assumption only as a first order approximation; however, it is considered to be fairly effective in dealing with Doppler estimation[11].

The error budget remains essentially identical to the figures quoted for the Data Interface Approach. The main difficulty is related to the calibration of the equipment delays; this remains the main factor

limiting the overal accuracy of the Two-Way techniques in general.

In the Hybrid Technique, the coarse and fine synchronization procedures are *completely independent*: as a consequence, the practical implementation of the technique can be broken into steps:

- satellites requiring only coarse time (and maybe these are the majority) *can use the coarse synchronization procedure alone*;
- a satellite requiring more accurate time, will require full synchronization capability: however, in this case, and as long as the clock onboard is kept "on time", the *fine synchronization procedure alone* can be used. The coarse synchronization is to be used only *to set the clock* when it is first switched on, or in the event that some malfunction occurs and time is completely lost at the remote clock;
- to synchronize a *ground clock* the fine synchronization technique alone can be used, since the clock can be kept on coarse time very easily with any other simple and inexpensive techniques already available (LORAN, HF Standard Transmissions, even, in some countries, with radio broadcasted time codes).

The capability to *support a multi-user environment* is stressed by the Hybrid technique. Since no range gates are required (depending upon the relative position of each user), many users can take simultaneous measurements. Then, the time differences can be computed against a single measurement for the forward "All 1's" state and multiple measurements (one per user) for the return state indicators.

Even in this case the coarse synchronization needs only to be used in the event of a malfunction: this feature will help to reduce the operational requirements and, as a consequence, the operational costs.

ADVANCED TDRS PROGRAMS

In the United States, plans are under study to implement an advanced version of the TDRSS; the Advanced TDRSS, or ATDRSS for short, will retain the same basic features of the current TDRSS, having incorporated the timing support in the basic specifications for the system (Ref. 12, para. 5.1, and Ref. 13, para. 3.5.2):

> "... ATDRSS tracking service will provide measurements from which estimates of the USAT (User Satellite) orbit, oscillator frequency bias, and clock bias will be determined."

At the AGT (ATDRSS Ground Terminal), time will be provided to the ranging and communications systems by a Common Time and Frequency System (CTFS), based on a redundant set of cesium frequency standards and time code generators (Ref. 13, sect. 6).

The ATDRSS will support the following time transfer services via the available tracking links via the SMA (S-band, Multiple Access), SSA (S-band, Single Access), KuSA and KaSA (Ku- and Ka-band Single Access) telecommunications channels (Ref. 12, para. 3.5):

- Two-way time transfer, supported via the two-way tracking service;

- One-way time transfer, via the one-way return link tracking service.

In the two-way mode, the time transfer measurement is performed with the following sequence (Ref. 12, para. 5.2.1.d):

1. The AGT measures the elapsed time between a reference CTFS time epoch and the next outgoing forward link range channel PN epoch. The AGT measures the elapsed time between the same reference CTFS epoch and the first return link PN epoch to arrive after the outgoing forward link PN epoch.
2. The USAT places a time tag ir the return service data, referring to the departure time of the PN epochs.

The following specifications apply to the ATDRSS two-way time synchronization (Ref. 12, para. 5.3.1.c and para. 5.3.1.d):

- Time Transfer (TT) Measurements Resolution (this is called "granularity" in the specifications): < 200 ns
- TT Measurements r.m.s. Error (also referred as jitter in the specifications): < 25 ns
- Systematic Errors

  contribution from ATDRSS: $< \pm 35$ ns
  contribution from AGT: $< \pm 30$ ns

  [these are the same requirements as for the two-way ranging specifications]
- ATDRSS Delay Compensation [Delay Calibration]: to be provided as part of the timing service
- Time Tagging Accuracy

  for ranging data: $< \pm 1$ μs of CTFS epochs
  for Doppler data: $< \pm 25$ ns of CTFS epochs
  for time transfer data: $< \pm 5$ μs of CTFS epochs
- Timing Accuracy: the reference CTFS epoch times shall have a systematic error $< \pm 5$ μs relative to UTC, and shall be traceable to UTC time within ± 100 ns

For the one-way synchronization, the system specifications state (Ref. 12, para. 5.2.2.c) the following procedure:

1. The USAT will place time tags in the return service data.
2. The AGT shall format the user return service data into NASCOM (NASA Communications Network) data blocks.
3. The AGT shall place time tags in NASCOM data blocks.

In Europe and Japan, other compatible (at least for the S-band service) Tracking and Data Relay Satellites are under study: those are the ESA DRS (Data Relay Satellite) and the Japanese JDRS, planned for the mid-90s.

In Europe, a significant development may delay the planned launch of the first ESA DRS-1: the Advanced Relay and Technology Mission (ARTEMIS) project is well under way, and has been given priority by ESA over the DRS program. The first launch of ARTEMIS (as DRS-0) is scheduled in 1992.

ARTEMIS is a communication technology demonstration satellite, for advanced data relay and land mobile applications. The payloads will be:

- a laser optical data relay communication experiment (SILEX), for high data rate communications;
- an S-band, multiple access data relay payload, for medium data rates, intended to be compatible with the Multiple Access (MA) S-band service provided by TDRSS and ATDRSS;
- an L-band payload, intended for mobile services;
- a number of spacecraft technology experiments, such as ion propulsion and Ni-H batteries;
- an EHF propagation payload, to study propagation effects at high frequencies.

After a nominal 3 years experimental phase, ARTEMIS is intended to become part of the ESA DRS System as DRS-0. Several technologies carried onboard ARTEMIS are interesting: as far as timing is concerned, certainly the SILEX payload may offer unique capabilities to exercise new techniques for intersatellite time transfer.

ACKNOWLEDGEMENTS

The authors wish to thank Mr. E. Saggese of Space Engineering (Rome, Italy), for the useful information and discussions on the European programs, and also Mr. Tony Comberiate of the NASA Goddard Space Flight Center for information on the TDRSS and ATDRSS programs.

REFERENCES

1. G. Whitworth, J.W. McIntyre and R.E. Downs, "TIME MAINTAINANCE OF USER CLOCKS VIA THE TRACKING AND DATA RELAY SATELLITE SYSTEM", Proceedings of the 14th Precise Time and Time Interval (PTTI) Meeting, NASA/DoD [NASA-GSFC, December 1982], pp. 39-55, NASA Conference Publication 2265.
2. J.W. Cunningham, D.E. Manion, "TDRSS ORIENTATION AND SYSTEM DATA FLOW, COURSE 880 — TEXTBOOK", Rev. 3, NASA/GSFC, Network Test and Training Facility (NTTF), Publication STDN No. 1151.2 (June 1983).
3. E. Detoma, "SYNCHRONIZATION OF REMOTE CLOCKS BETWEEN NGT AND NTTF: A SURVEY OF AVAILABLE TECHNIQUES", Bendix Field Engineering Corporation Internal Report (August 1987).

4. A.R. Chi, E. Byron, "TWO-WAY TIME TRANSFER EXPERIMENT USING A SYNCHRONOUS SATELLITE", Proceedings of the 7th Precise Time and Time Interval (PTTI) Meeting, NASA/DoD, pp. 357-377.

5. E. Byron, G.P. Gafke, J.W. McIntyre, "PHASE I STUDY AND DESIGN OF TECHNIQUES FOR PRECISE TIME TRANSFER VIA THE TRACKING DATA RELAY SATELLITE SYSTEM (TDRSS)", Progress Report, APL/JHU Space Communications Group, Special Report CSC-0-322 (Sept. 25, 1976).

6. J.A. Hrastar, "A TIME UPDATE SYSTEM FOR THE GAMMA-RAY OBSERVATORY", NASA/GSFC Internal Report 403-122-001 (May 1982).

7. For the telemetry interface approach see the following documents:

   - E.P. Greene, "PASSIVE MONITORING APPROACH TO GRO SPACECRAFT CLOCK SYNCHRONIZATION", NASA/GSFC Internal Memorandum, (July 02, 1982).
   - E.P. Greene, "PASSIVE MONITORING APPROACH TO GRO SPACECRAFT CLOCK SYNCHRONIZATION", NASA/GSFC Internal Memorandum, (July 20, 1982).
   - S. Tompkins, "PASSIVE GRO TIME CORRELATION IMPLEMENTATION IN MSOCC", NASA/GSFC Internal Memorandum (February 1983).
   - S. Tompkins, "GRO TIME CORRELATION EXPERIMENT TEST PLAN", NASA/GSFC Internal Memorandum (February 1983).

8. For the hybrid technique see the following documents:

   - E. Detoma, "TWO-WAY TIME SYNCHRONIZATION VIA THE TDRSS", NASA/GSFC Internal Memorandum (December 24, 1981).
   - E. Detoma, "SATELLITE OR GROUND USER CLOCK TIME SYNCHRONIZATION VIA THE NASA TDRSS: THE HYBRID TECHNIQUE", NASA/GSFC — BFEC Internal Report (April 1983).
   - E. Detoma, "COMPARISON OF DIFFERENT TECHNIQUES TO PERFORM CLOCK SYNCHRONIZATION VIA THE TDRSS", NASA/GSFC — BFEC Internal Report (April 1983).

9. E. Detoma, S. Leschiutta, "THE SIRIO-1 TIMING EXPERIMENT", Proceedings of the 11th Precise Time and Time Interval (PTTI) Meeting, NASA/DoD [NASA-GSFC, December 1979], pp. 521-556, NASA Conference Publication 2129.

10. E. Detoma, S. Leschiutta, "TWO-WAY SEQUENTIAL TIME SYNCHRONIZATION: PRELIMINARY RESULTS FROM THE SIRIO-1 EXPERIMENT", Proceedings of the 12th Precise Time and Time Interval (PTTI) Meeting, NASA/DoD [NASA-GSFC, December 1980], pp. 329-348, NASA Conference Publication 2175.

11. V.S. Reinhardt, D.A. Premo, M.W. Fitzmaurice, S.C. Wardrip, P.O. Cervenka, "NANOSECOND TIME TRANSFER VIA SHUTTLE LASER RANGING EXPERIMENT", Proceedings of the 9th Precise Time and Time Interval (PTTI) Meeting, NASA/DoD [NASA-GSFC, December 1977], pp. 319-342, NASA Technical Memorandum TM-78104.

12. "PHASE B ADVANCED TRACKING AND DATA RELAY SATELLITE SYSTEM (ATDRSS) SERVICE REQUIREMENTS SPECIFICATIONS", NASA/GSFC Document S-500-1 (20 November 1989).

13. "PHASE B SPACE NETWORK (SN) OPERATIONS CONCEPT IN THE ADVANCED TRACKING AND DATA RELAY SATELLITE SYSTEM (ATDRSS) ERA", NASA/GSFC Document S-500-3 (20 November 1989).

14. E. Detoma, "PROPOSTA DI UN METODO DI SINCRONIZZAZIONE PASSIVA DI OROLOGI ATOMICI DISTANTI UTILIZZANTE SATELLITI ARTIFICIALI", Tesi di Laurea (Universita' degli Studi di Torino, Luglio 1977).

15. M. Weiss, "COMMON-VIEW TIME TRANSFER AND THE NBS SATELLITE SERVICE", NBS Seminar on Frequency Stability and Its Measurement (Boulder, CO. — July 24-26, 1984).

Fig. 1 - ONE-WAY TIME TRANSFER

Fig. 2 - PASSIVE SYNCHRONIZATION

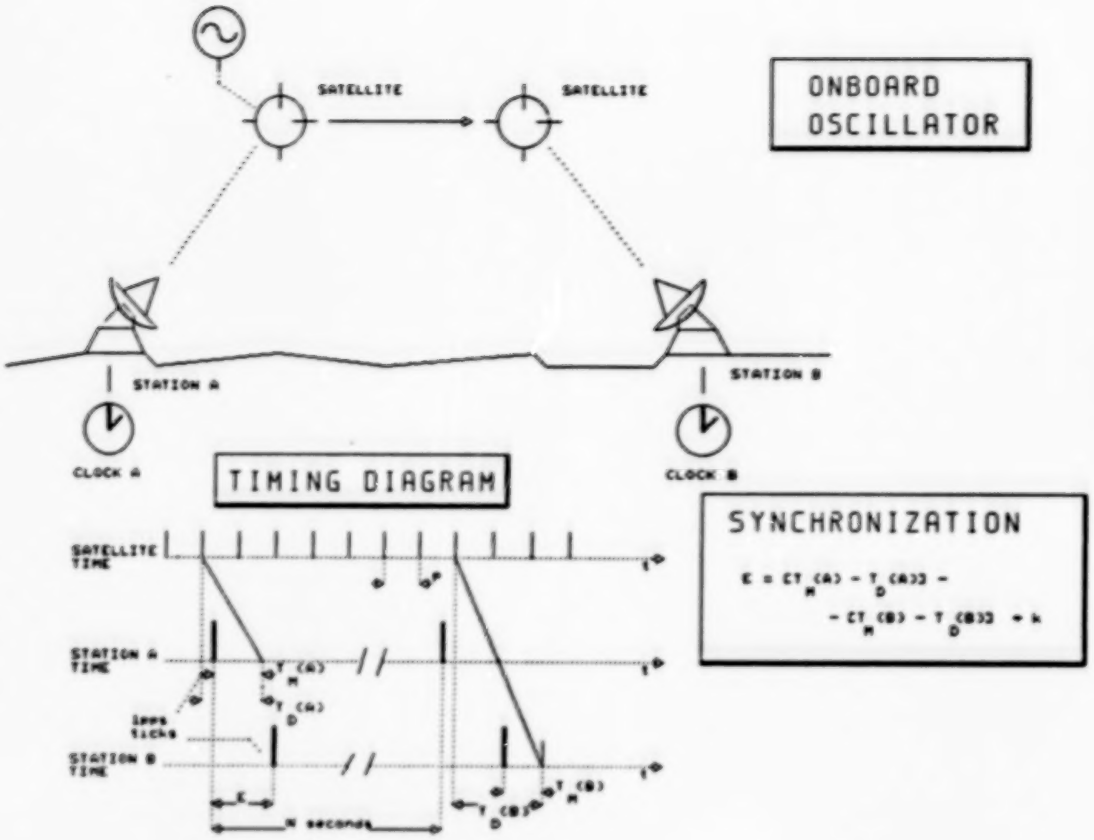


Fig. 3 - SYNCHRONIZATION WITH ORBITING OSCILLATOR

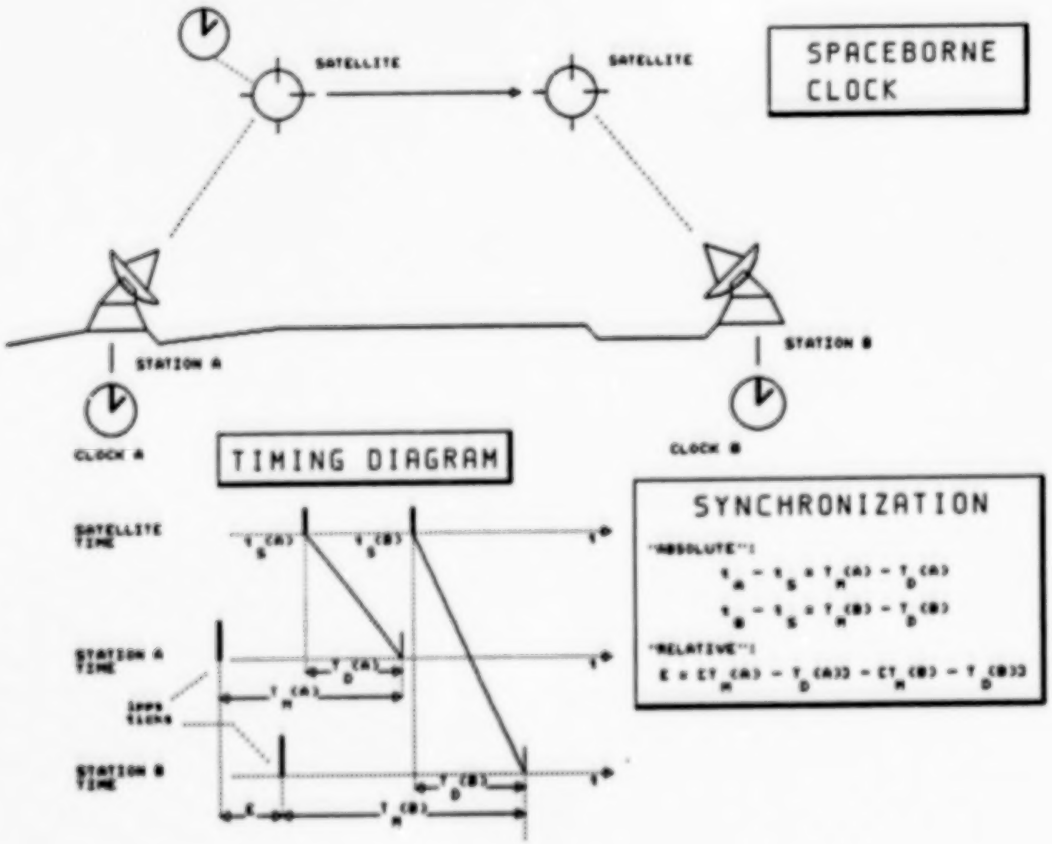


Fig. 4 - TIME TRANSFER WITH ORBITING CLOCK

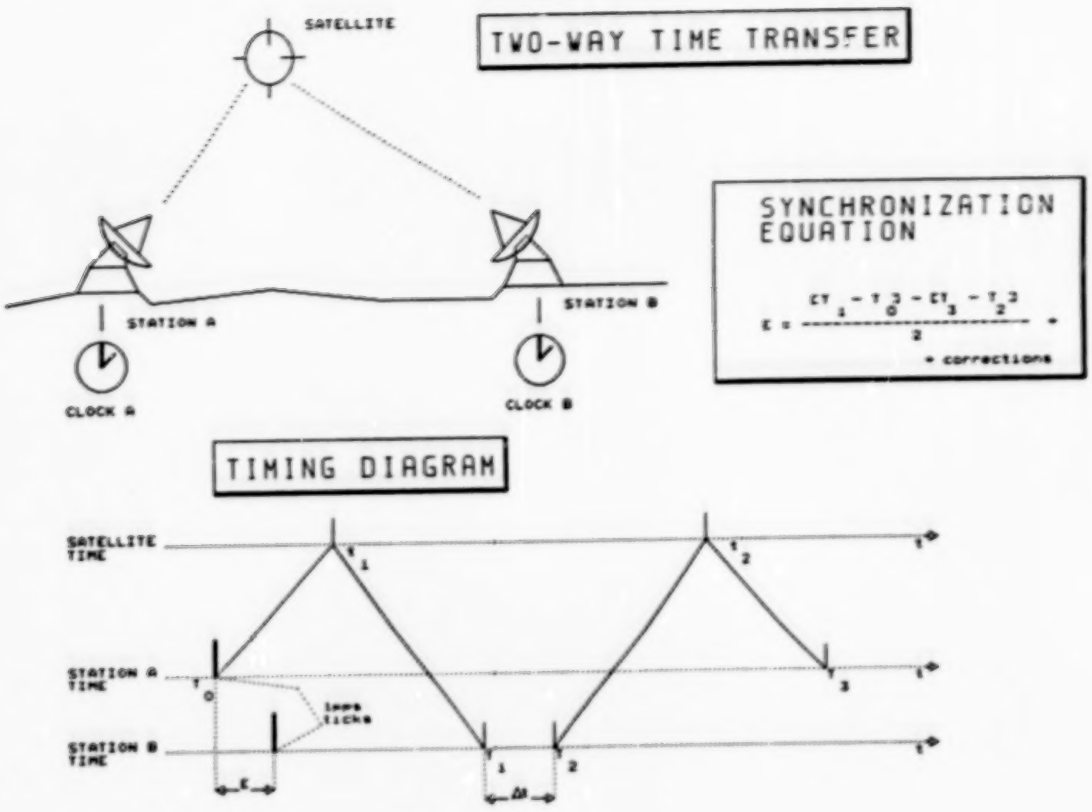


Fig. 5 - TWO-WAY SYNCHRONIZATION

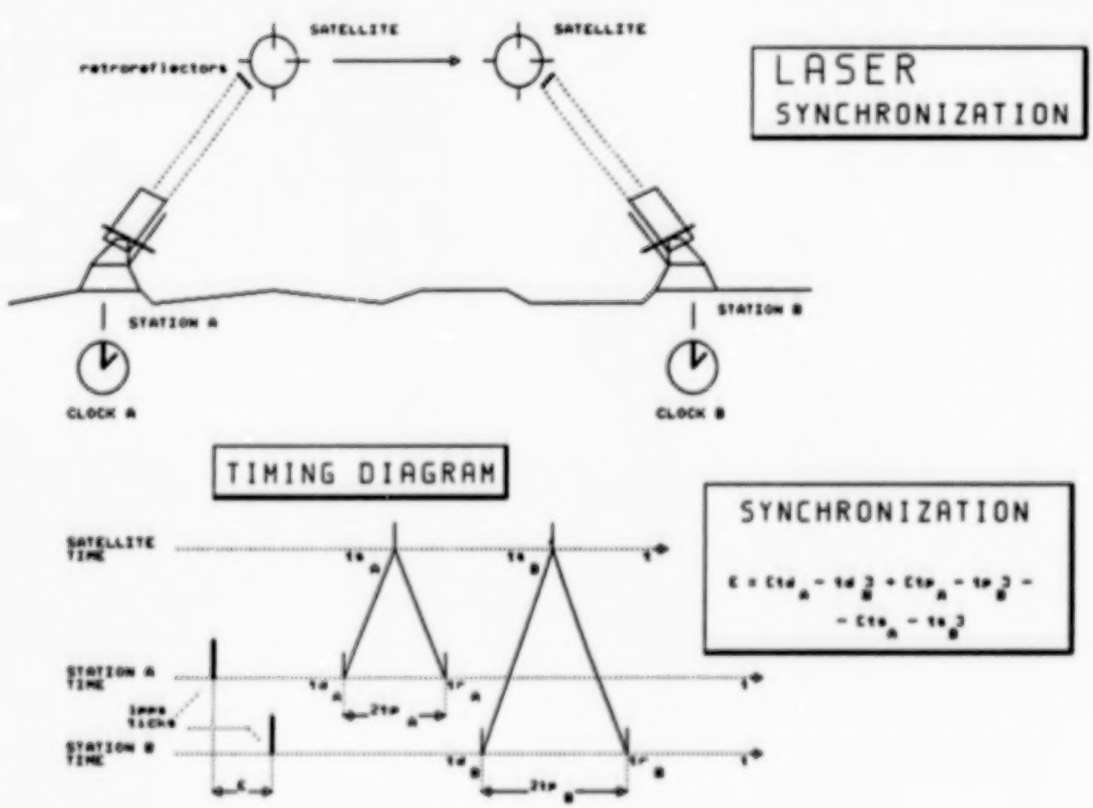


Fig. 6 - LASER SYNCHRONIZATION (LASSO)

Fig. 7 - Tracking and Data Relay Satellite System (TDRSS) Orbital Geometry (from ref. 1)

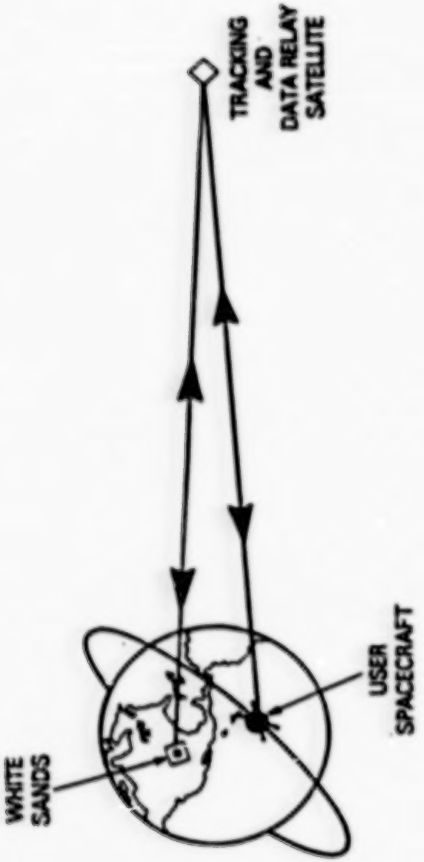


Fig. 8 - TDRSS two-way synchronization: simplified timing diagram (from ref. 1)

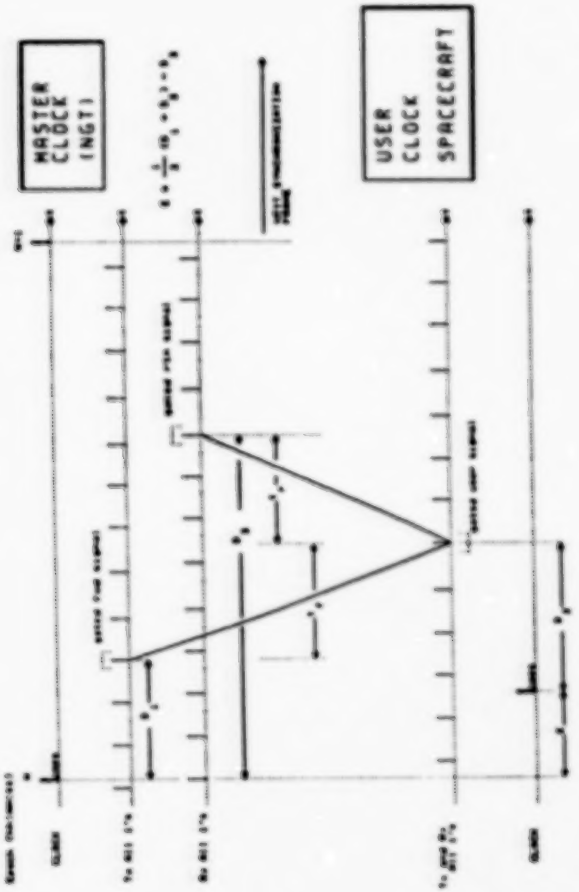


Fig. 9 - TDRSS two-way synchronization - Technique 1: basic timing diagram (from ref. 6)

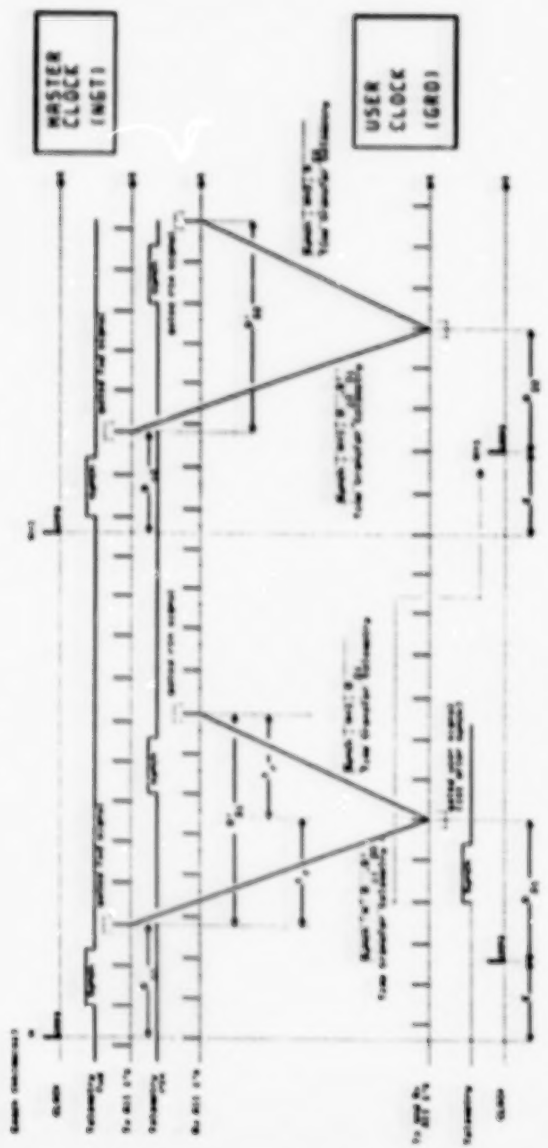


Fig. 10 - TDRSS two-way synchronization - Technique 2: basic timing diagram (from ref. 6)

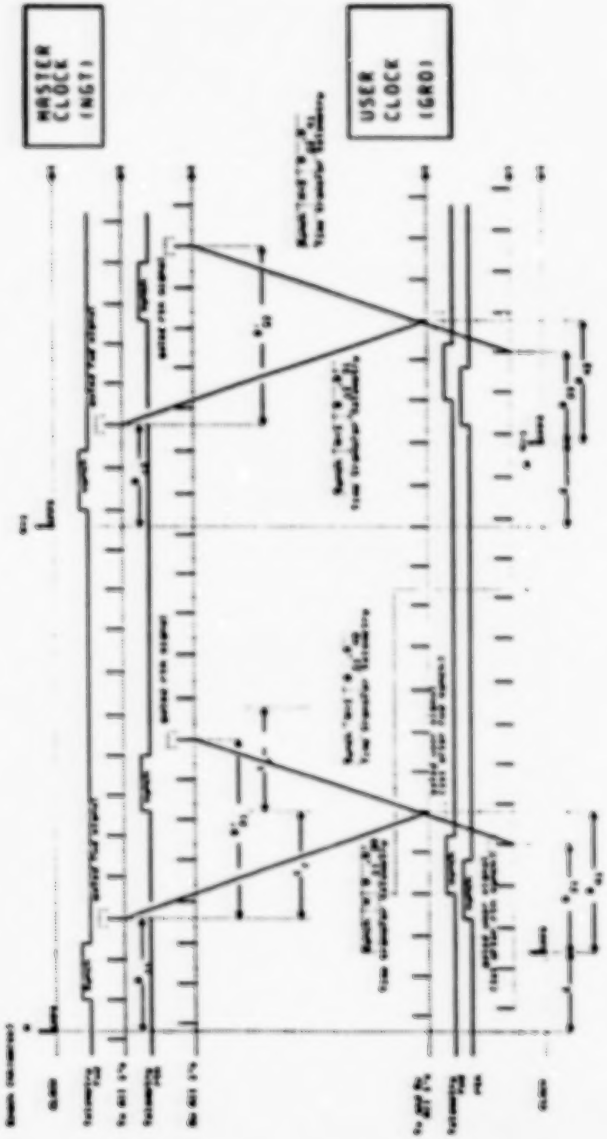


Fig. 11 - Hybrid method. Fine synchronisation computations carried on with modulo-2 arithmetic (from ref. 9)

Fig. 12 - The TDRSS Spacecraft

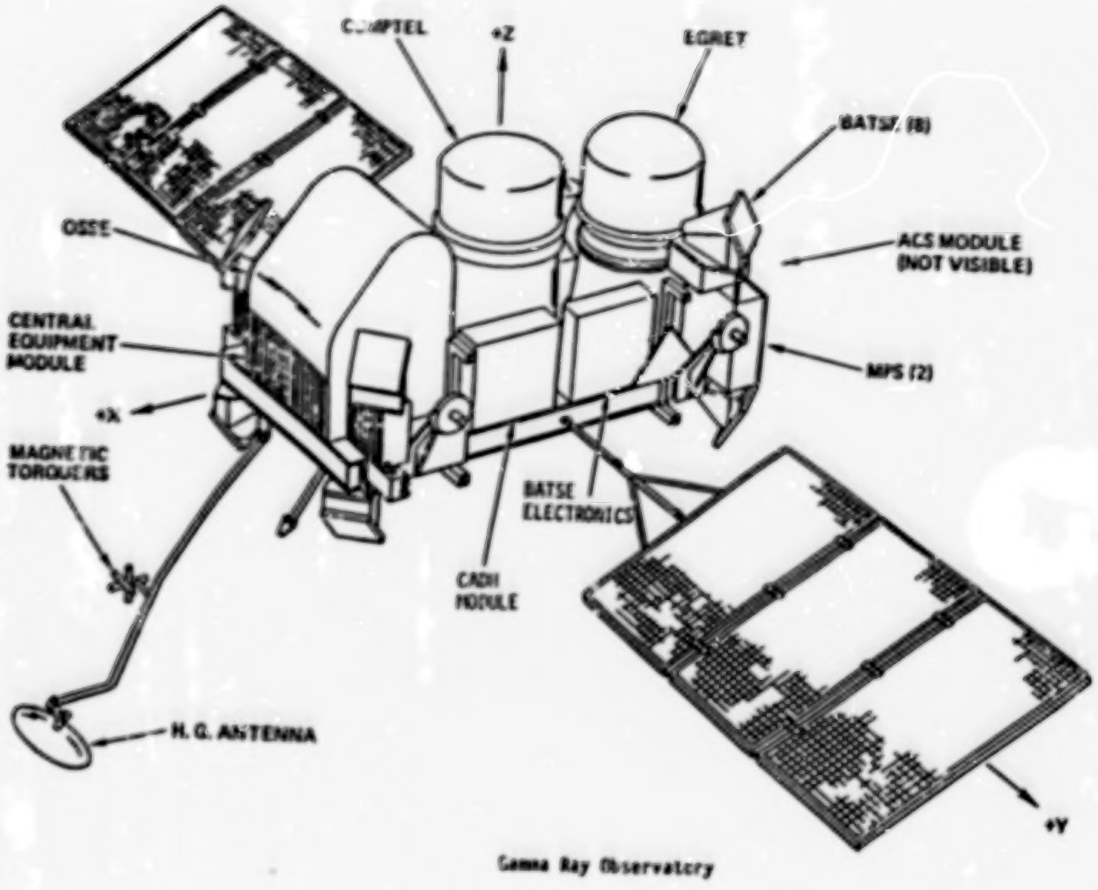


Fig. 11 - The Gamma Ray Observatory (GRO)

CURRENT GPS/GLONASS TIME REFERENCES AND UTC

P Daly

Department of Electronic and Electrical Engineering
University of Leeds, Leeds LS2 9JT, United Kingdom

Abstract

The world's two global satellite navigation systems, GPS and GLONASS, will both become operational during the early 1990's. Each will offer, independently of the other, precise location and time transfer continuously anywhere in the world and indeed in space itself. Many potential users, in particular the civil aviation community, are keenly interested in a joint GPS/GLONASS operation since it would offer substantial advantages in defining and maintaining the integrity of the navigation aid. The question arises of compatibility of GPS/GLONASS from the point of view of satellite on-board clocks, their system references, their national standards and ultimately UTC. Results are presented on the characterisation of GLONASS system and spacecraft clocks as compared to their Navstar GPS counterparts.

INTRODUCTION

GLONASS provides worldwide time dissemination and time transfer services in the same manner as Navstar GPS with both exhibiting substantial advantages over other existing timing services. Time transfer is both efficient and economic in the sense that direct clock comparisons can be achieved via GLONASS between widely separated sites without the use of portable clocks. Event time tagging can be achieved with the minimum of effort and users can reacquire GLONASS time at any instant due to the continuous nature of time aboard the satellites.

The first release from the Soviet Union of detailed GLONASS information occurred at the International Civil Aviation Organisation (ICAO) special committee meeting on Future Air Navigation Systems (FANS) in Montreal in May 1988 [1]. In full operation GLONASS will have 24 satellites in orbit, 8 satellites separated by 45 degrees in phase in each of three planes 120 degrees apart. During the present pre-operational phase only two of the planned orbital planes have been occupied. Currently eight GLONASS satellites are in full operation, four each in planes 1 and 3 (see Table 1); this gives single satellite coverage at most locations almost 24 hours a day.

SAT ID	COSMOS	GLONASS	CHN	L1/MHz	PLANE
1988-43A	1946	34	12	1608.7500	1
1988-43C	1948	36	24	1615.5000	1
1988-85C	1972	39	10	1607 6250	3
1989- 1A	1987	40	9	1607.0625	1
1989- 1B	1988	41	6	1605.3750	1
1990-45A	2079	44	21	1613.8125	3
1990-45B	2080	45	3	1603.6875	3
1990-45C	2081	46	15	1610.4375	3

Current Active GLONASS Satellites 30-11-90.
Table 1

The only new satellites to appear during 1990 have been the three with international identifiers 1990- 45A,B and C.

TIME FROM GPS/GLONASS

Time transfer from GPS/GLONASS is achieved in a straightforward manner, Figure 1. Each satellite transmits signals referenced to its own on-board clock. The Control Segment monitors the satellite clocks and determines their offsets from the common GPS/GLONASS system time. The clock offsets are then uploaded to satellites as part of their transmitted data message. A user at a known location receives signals from a satellite and by decoding the data stream modulated on to the transmission, is able to obtain the position of the satellite, as well as the satellite's clock offset from the common system time. Hence the signal propagation time can be calculated at any instant. The time at which the signals are transmitted is also contained in the data message; by combining this with the propagation time and correcting first for atmospheric effects and other delays and then for the satellite's own clock offset, the user can effect transfer to GPS/GLONASS system time. Correction to an external time scale (such as UTC(USNO) or UTC(SU)) is then possible since the relevant offset is one of the transmitted data parameters. Any other user who has the same satellite visible is also able to transfer to the same common time scale.

SATELLITE CLOCK OFFSETS

GLONASS clock offsets are transmitted as part of each satellite's ephemeris data once every half-hour. The clock information arrives in the form of two parameters (i) the SV clock phase offset from GLONASS system time, a0 and (ii) the SV clock fractional frequency offsets from the GLONASS system reference, a1. The clock offset a2, the second rate of change of phase used in GPS, is not employed by GLONASS as the half-hour update makes this unnecessary.

GLONASS does transmit one additional timing parameter - the phase offset between system time and its reference standard, A0. This last offset is normally only updated once a day. There is again a parallel here between the two satellite navigation systems as GPS also transmits a phase offset between GPS system time and its reference standard, UTC(USNO). The added complication in the case of GLONASS is that the reference standard has not been fixed with time. In the official Soviet documentation, this parameter is described as "..... correction to the system time scale relative to the time scale to which the ephemeris and satellite synchronisation parameters are calculated". At certain times, this latter reference standard has been UTC(SU) but at other times a second (and different standard) has been employed probably for experimental purposes. In the absence of any solid information, this second reference standard is described (by us) as Moscow Time. Perhaps a more appropriate name would be "auxiliary reference standard". Table 2 shows the range and resolution of the GLONASS clock correction parameters.

GLONASS	*Bits**	Scale	Range	Resolution	Units
a0	22	2^{-30}	$\pm 2\times10^{-3}$	9×10^{-10}	s
a1	11	2^{-40}	$\pm 9\times10^{-10}$	9×10^{-13}	s/s
A0	28	2^{-27}	± 1	7×10^{-9}	s

* MSB = sign bit.

GLONASS clock correction parameters

Table 2

GPS/GLONASS TIME TRANSFER MEASUREMENTS

A series of measurements has been conducted of the difference between UTC(USNO) and both GPS and GLONASS system times. A prototype single channel GLONASS/Navstar GPS receiver [2] allows time comparisons between system times and a 1 pps reference synchronised to UTC(USNO). The Navstar system time / UTC(USNO) comparison is used as a calibration of the measurement since the offset between GPS time and UTC(USNO) is already known - it is transmitted as part of the GPS data message.

DATE	SATELLITE	READINGS (1/SEC)	AVERAGE OFFSET/ns	STANDARD DEVIATION/ns
26/10/90	NAVSTAR 2	2336	-194	76
26/10/90	NAVSTAR 3	2157	-195	49
26/10/90	NAVSTAR 6	3413	-242	54
26/10/90	NAVSTAR 9	4850	-228	72
26/10/90	NAVSTAR 11	4312	-185	55
26/10/90	NAVSTAR 12	3058	-214	51
26/10/90	NAVSTAR 13	4300	-192	58
26/10/90	NAVSTAR 19	538	-205	50
26/10/90	GLONASS 34	3224	5425	58
26/10/90	GLONASS 36	4291	5444	64
26/10/90	GLONASS 39	3052	5449	60
26/10/90	GLONASS 40	4111	5437	71
26/10/90	GLONASS 41	4484	5436	54
26/10/90	GLONASS 44	4130	5478	65
26/10/90	GLONASS 45	3585	5436	62
26/10/90	GLONASS 46	4828	5437	55

Navstar and Glonass system time offset from UTC(USNO).
Table 3.

Table 3 shows a set of measurements over a typical 24 hour period on 26 October 1990. Each individual measurement lasts 180 seconds; satellites are accessed many times in the course of the day during which time they complete 2.125 orbits. The data has been corrected for tropospheric, relativistic and earth rotation effects but not for ionospheric effects. Only two of the available GPS block II satellites were used; the absence of "Selective Availability" on both at this time is noticeable. Both sets of data are consistent in the sense that all eight satellites individually produce results which differ from the average by much less than the standard deviation. Current research is aimed at reducing the uncertainty in these measurements to the order of 10 ns.

GLONASS TIME SCALES & UTC(SU)

Data which relates UTC(USNO) timing edges to both GPS and GLONASS system and reference times (such as is presented in Table 3 for 26 October 1990) are routinely averaged on a daily basis over the ensemble of available satellites. These daily values can then be related to GPS/GLONASS reference times through the transmitted offsets. The end result is a set of daily averaged values of the difference between the local estimate of UTC(USNO) and the GLONASS reference time which can be either UTC(SU) or Moscow time. Figure 2 shows a plot of UTC(USNO) against UTC(SU)/Moscow Time over a period of more than 2 years starting in mid-1988 and finishing towards the end of 1990. Superimposed on the Leeds University data are the 10-day values of UTC(USNO) - UTC(SU) as produced independently [3] by the BIPM in Paris. The plot shows clearly the two phases of operation - GLONASS was referred to Moscow time during the second half of 1988 and the first half of 1990; the reference time was UTC(SU) during the whole of 1989 and the second half of 1990. The step in reference time at the end of 1989 was -1.5 microseconds, followed by an equal and opposite step on 20 June 1990. The slopes of the two sets of data during the first half of 1990 would lead one to conclude that the Moscow Time reference is offset from UTC(SU) in phase by around 1.5 microseconds but very close to UTC(SU) in frequency.

As mentioned previously, a step in the GLONASS reference time from Moscow Time back to UTC(SU) took place on 20 June 1990. Coincidentally, GLONASS system time was also reset to a value very close to UTC(SU) itself. The means of observing these changes is illustrated in Figure 3. The continuous measurement of GLONASS system time with reference to UTC(USNO) showed up the step change in the former as it occurred. Soon afterwards the transmitted SV offsets from GLONASS system time also reflected the same change. By referring the SV phase offsets to the same reference time (12:00 GMT on 20 June), the change in the averaged SV offsets was computed to be

+38.147 μs (standard deviation 16 ns). The difference between UTC(USNO) and GLONASS system time obtained at the Leeds University ground station averaged over the previous and following 24 hours amounted to +38.140 μs (standard deviation 64 ns).

As a result of the confirmed change in system time together with the step in reference time, it was possible to conclude that the opportunity had been taken on 20 June by the control segment both to synchronise GLONASS reference time once again to UTC(SU) and to bring system time to within +/- 1 μs of UTC(SU). It will be recalled that GPS system time is constrained to lie within +/- 1 μs of UTC(USNO).

Since January 1990 data has been provided by Leeds University to the BIPM in Paris [3] in the following format:-

1) Daily measurements at the University of Leeds averaged over the available ensemble of GLONASS satellites of UTC(USNO) against GLONASS system time.

2) Daily measurements at the University of Leeds averaged over the available ensemble of GPS satellites of UTC(USNO) against GPS system time.

3) Daily values of the difference between GLONASS system time and the GLONASS reference time contained in the satellite data message.

Daily values of the difference between GPS system time and UTC(USNO) are transmitted by GPS satellites and can be used to validate the data obtained in 2). This validation is an important feature of the measurement as most of the measurement equipment is common to both GPS and GLONASS. By means of the transmitted offsets, A0, it is possible to deduce a value for UTC(USNO) - UTC(SU) obtained by the satellite navigation systems GPS and GLONASS with an uncertainty of less than 100 ns.

GLONASS CLOCK PERFORMANCE

Data on the performance of certain GLONASS satellites has already been published. Over the years 1986-1989 a steady improvement in performance has been demonstrated with clocks on-board spacecraft launched during 1989 showing the qualities of high-quality Cesium standards of roughly the same level of performance as the GPS block I Cesiums.

It is all the more interesting to look at the behaviour of the most recently launched (19 May 1990) satellites - GLONASS 44,45 and 46, (1990 - 45A,B and C). These spacecraft have been operational in space for about 4 months. The clock phase and frequency offsets (a0 and a1) for GLONASS 44 are shown in Figure 4 averaged out once per day over a period of nearly 140 days. There is a curious cyclic variation in the frequency data whose period is around 8 days (the period of satellite ground track repeat). This behaviour is also observed in the frequency offset plots of both GLONASS 45 and 46 and is probably due to thermal effects or modelling effects of the spacecraft orbits and clock; no such cyclic changes have yet been observed in data obtained from earlier satellites.

The phase data displays the quadratic behaviour arising from a fixed frequency offset and drift. When these two are removed, the resulting data points produce an Allan variance plot shown in Figure 5, typical of a high-quality space-borne Cesium clock with a flicker noise floor of 5 times e - 14. For the purposes of comparison, an Allan variance plot for one of the better GPS Cesiums (PRN 13) is found in Figure 6.

CONCLUSIONS

On the basis of daily measurements made of a local reference and satellite system times, it is clear that one can produce consistent results averaged over an ensemble of available spacecraft. It is routinely possible to deduce values of UTC(USNO) - UTC(SU) on a daily basis to precisions of less than 100 ns. These levels of uncertainty can without doubt be reduced once the most common sources of error have been accounted for.

At the time when measurements were first calibrated in the University of Leeds GLONASS system time was referred to Moscow time (auxiliary time reference) and remained in this state from the middle till the end of 1988. During the whole of 1989, system time was then referred to UTC(SU). A second period of reference to the "auxiliary standard" began at the start of 1990 and continued for six months. The direct linking between GLONASS system time and UTC(SU) was resumed during June 1990 and has continued in this state until the present (end November 1990). Data on both reference clocks indicate that the "auxiliary time reference" is related to UTC(SU) by a straightforward phase offset; there seems to be very little difference in frequency between the two standards. Now

that both Navstar GPS and GLONASS are both referred to their respective national time standards, UTC(USNO) and UTC(SU) respectively, the prospects for international time transfer and coordination of UTC by satellite are very encouraging.

Allan variance frequency stability profiles of the most recently launched GLONASS spacecraft (1990- 45A,B and C) indicate the continued use of high-quality Cesium beam standards on board. Daily values of the fractional frequency offsets of these recent satellites demonstrate an unusual and unexplained cyclic change with period around 8 days.

REFERENCES

[1] T G Anodina :
Working Paper -
"Global Positioning System GLONASS", Special Committee on Future Air Navigation Systems (FANS/4), International Civil Aviation Organisation (ICAO), Montreal, 2-20 May, 1988.

[2] S A Dale, I D Kitching and P Daly :
"Position-Fixing using the USSR's GLONASS C/A Code", IEEE PLANS' 88 (Position Location & Navigation Symposium), Orlando, 29 November - 2 December, 1988, pp 13-20.

[3] Bureau International des Poids et Mesures (BIPM Monthly Circular T) Pavillon de Breteuil, F-92312 Sevres Cedex, France.

TIME TRANSFER FROM GLONASS

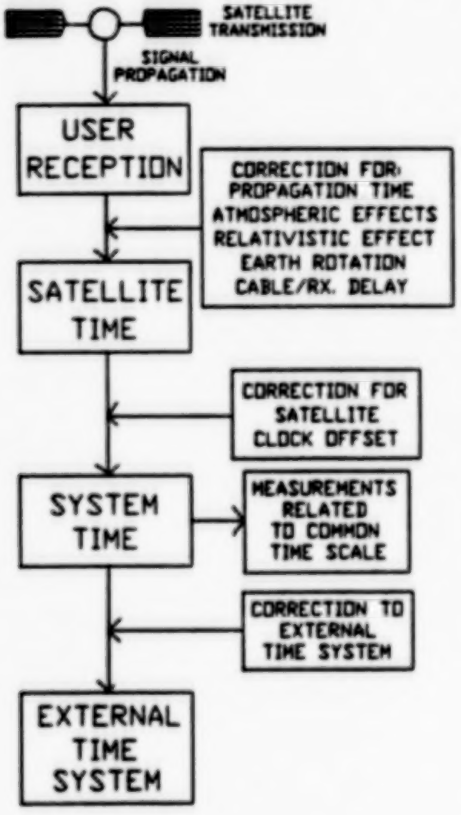


FIGURE 1

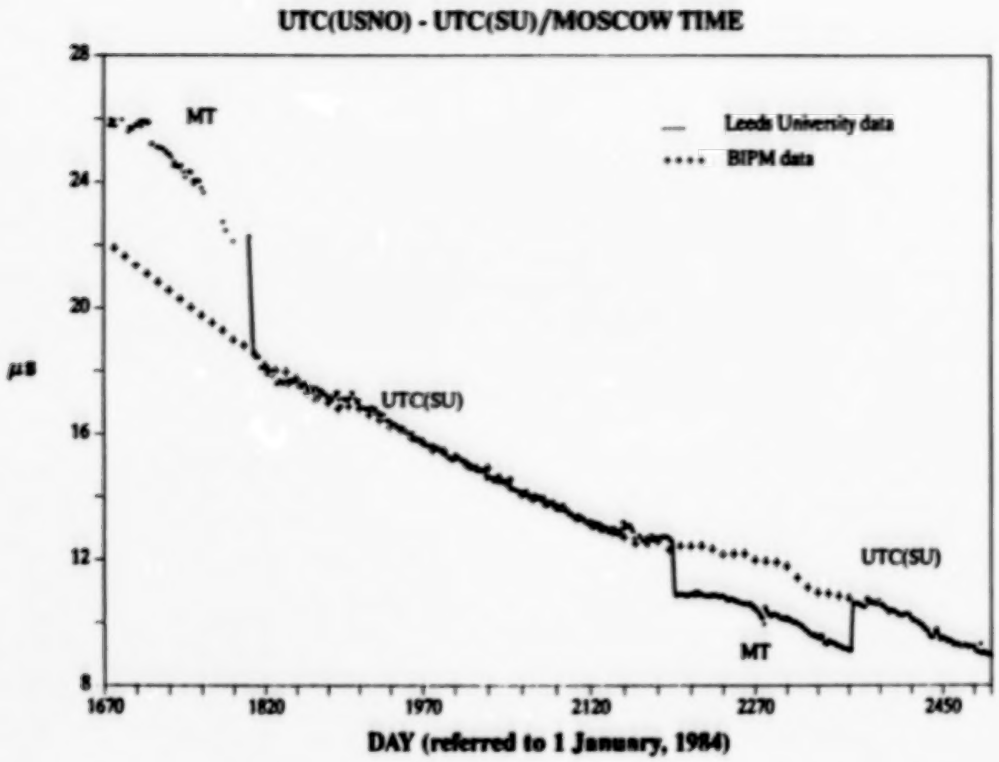
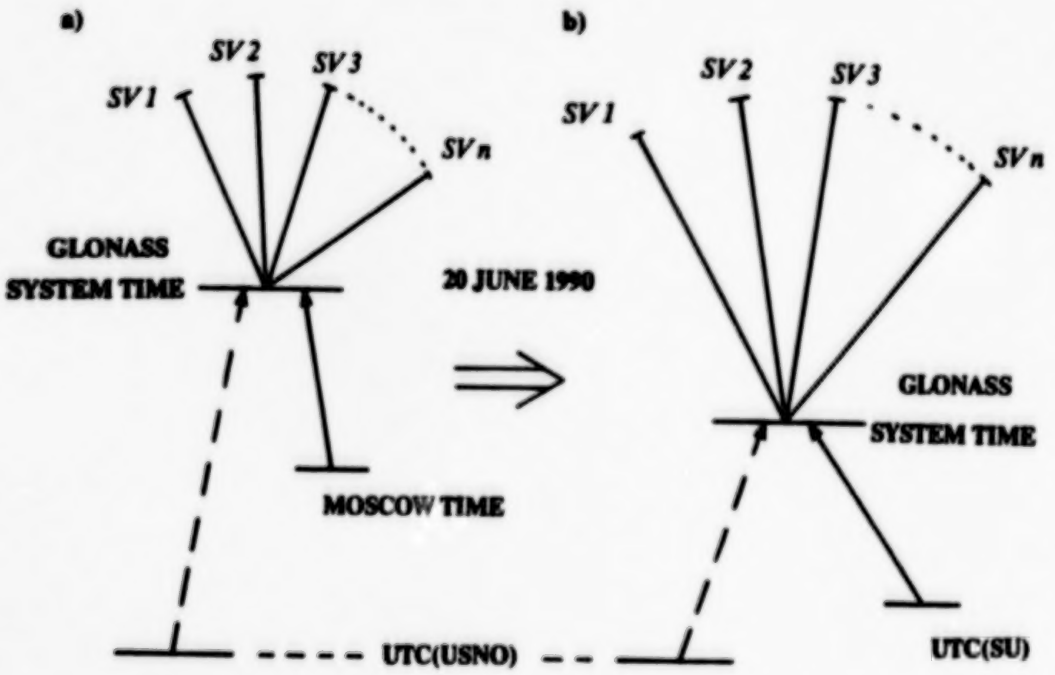


FIGURE 2



GLONASS TIME REFERENCES

FIGURE 3

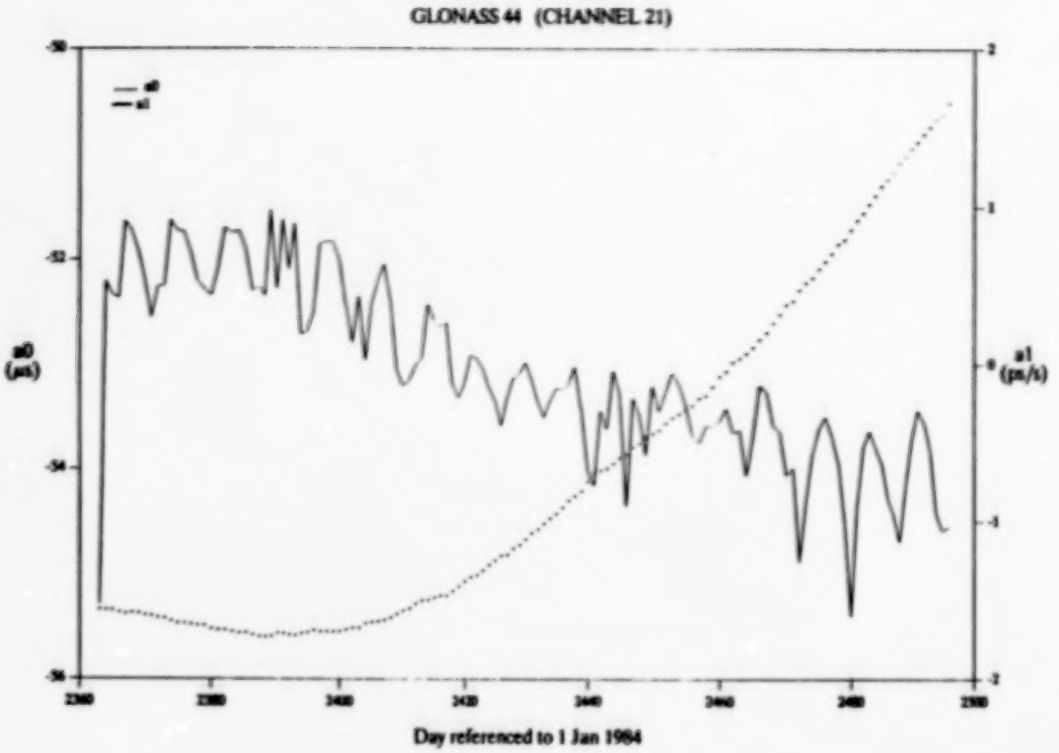


FIGURE 4

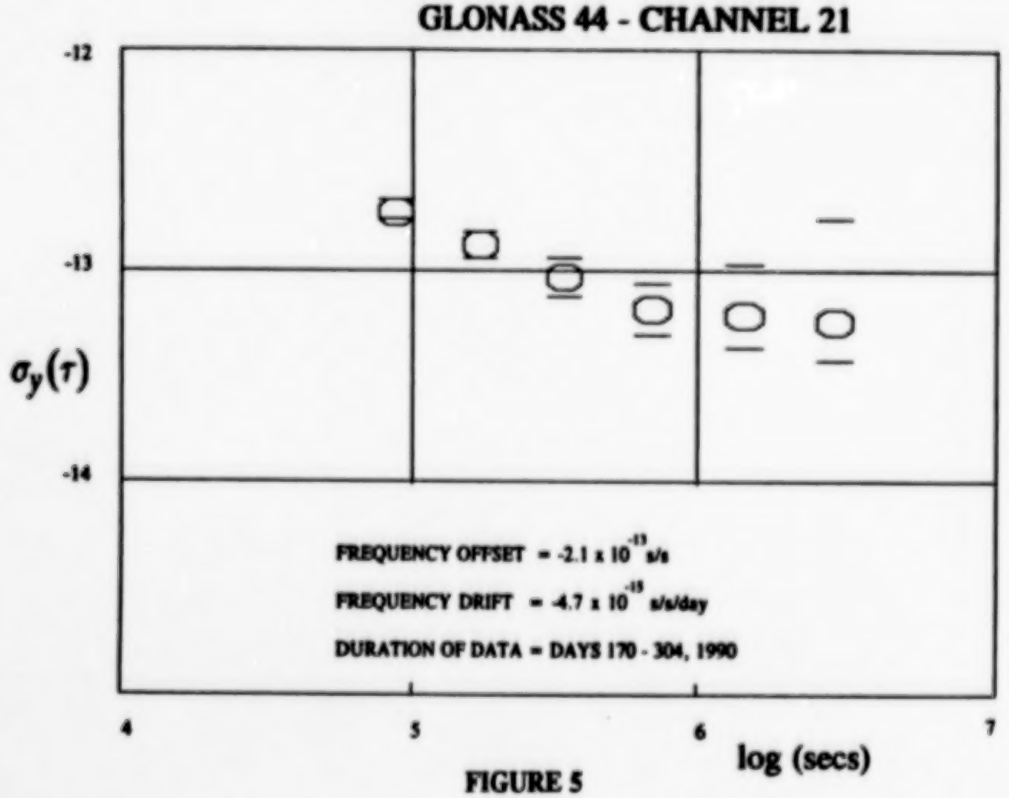


FIGURE 5

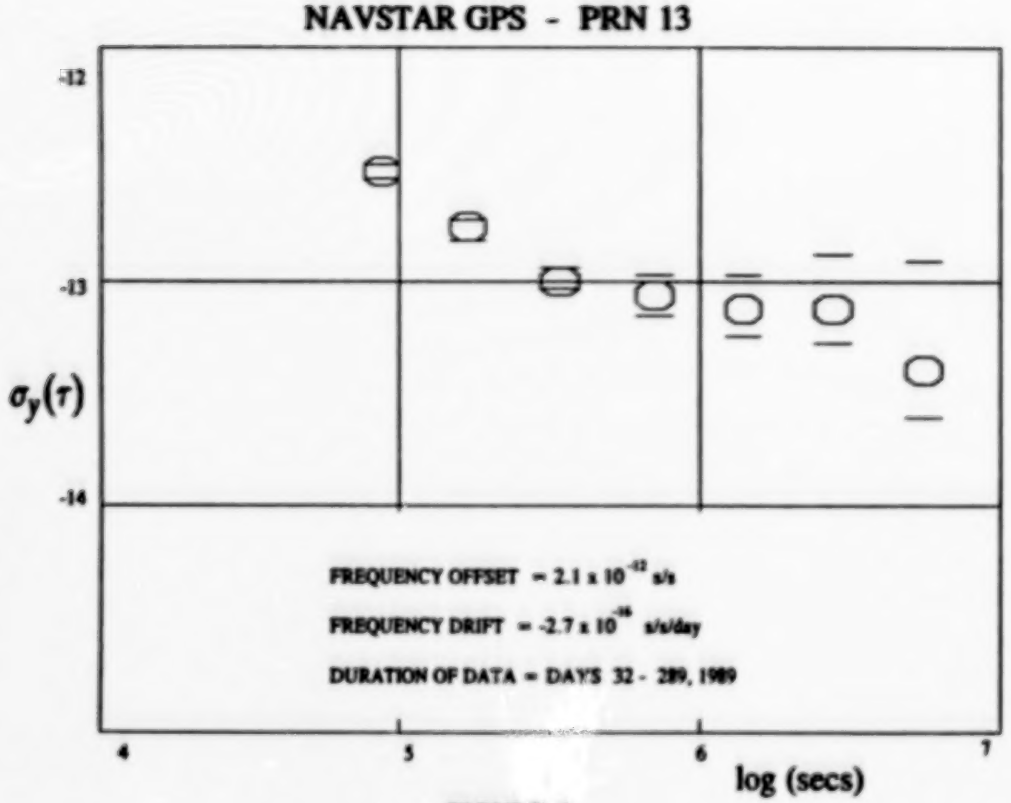

NAVSTAR GPS - PRN 13
-12
-13
-14
$\sigma_y(\tau)$
FREQUENCY OFFSET = 2.1 x 10^-12 s/s
FREQUENCY DRIFT = -2.7 x 10^-16 s/s/day
DURATION OF DATA = DAYS 32 - 289, 1989
4
5
6
7
log (secs)

FIGURE 6

QUESTIONS AND ANSWERS

Carroll Alley, University of Maryland: I have had an extensive briefing in Moscow on the GLONASS system. The satellites have a large array of corner reflectors and they are tracked with high precision by laser ground stations. They told me that whenever the orbit gets off by 20 centimeters, they make a correction.

Professor Daly: I have a question — Do you believe the 20 centimeters?

Professor Alley: Yes.

Profesor Daly: People that are familiar with GPS orbits, and I am not an expert on the subject, would not claim the same certainty for GPS orbits.

Professor Alley: I agree with that too.

Professor Daly: I rest my case.

BLANK PAGE

USSR NATIONAL TIME UNIT KEEPING OVER LONG INTERVAL USING AN ENSEMBLE OF H-MASERS

N.B.Koshelyaevsky, S.B.Pushkin
National Scientific and Research Institute
for Physical–Technical and Radiotechnical Measurements
VNIIFTRI, Mendeleevo, Moscow region, 14570, USSR

... all is as one day with God,
and time only is measured unto men.
(the Book of Mormon, Alma, 40:8)

INTRODUCTION

Because of lack of official information on the USSR State Time and Frequency Service (STFS) for a long time we shall illuminate it in the first part of this report. The second part of the report will deal with a problem mentioned in a head line.

The STFS is responsible for time and frequency measurement unification both in the field of atomic, TA(SU) and UTC(SU) and universal time UT1(SU) over the whole territory of the USSR. The scientific head of STFS is the Main Metrological Center, it is situated in Mendeleevo near Moscow.

The National Primary Time and Frequency Standard (NPTFS) of the USSR is the instrumentational basis for independent realization of the national unit of time interval — second — in a full agreement with its definition in the SI system and also for the national time scale generation. Then the unit of time interval and time scale information are disseminated to secondary standards (SS), Fig. 1, each of them can keep autonomously the time unit and time scale. The most widespread links for time comparisons between SS themselves and between SS and NPTFS are as follows: micrometeorite (MM) link, portable clock, usually on the basis of HP Cs standard, and beginning from 1988 — on the basis of a small sized H–maser, Fig. 2, and beginning from the second part of 1989 signals of GLONASS system in a "common view" mode. For short range time comparison TV signals are usually used.

The independent realization of the time interval unit is performed by means of three laboratory Cs primary standards, Figures 3 through 5. One can find the detailed information on these instrument in References 1 through 3. At the moment we note only that all the above mentioned instruments have classical, but to some extend various design with magnetic state separation and their accuracy is evaluated at present to be about $\leq 2 \times 10^{-13}$. We don't use the primary Cs like a clock but from time to time put it into operation for frequency comparison with an ensemble of continuously running H–masers.

At NPTFS we usually use about 15 commercial H-masers of CH1–70, CH1–80 types, Figs. 6 & 7. These were designed and manufactured by NPO "QUARTZ" from Nizhnij Novgorod. The actual values of

H-masers output frequencies are intentionally different from each other by more than 1×10^{-13}, but using proper corrections they are recalculated to the same value. The frequency stability of the new H-masers of CH1-80 type is significantly better than that of the CH1-70. The common drawbacks of all our timekeeping instruments are lack of reliability, especially in a clock mode. This prevents applications of time scale algorithm which need continuous statistical weighting over long intervals. In Figs. 8 and 9 one can see ten days averaged relative frequency changes for some of H-masers.

Every hour the output signals (1 pps & 5MHz) from the above mentioned H-masers are compared with each other using time interval meter of 0.3 ns resolution. The 1 pps signals are directly compared, the phase deviation of 5 MHz signal is preliminary multiplied 100 times and then it produces another set of 1 pps signals. The latter is used for frequency evaluations over short intervals, up to several days, while scale measurements are based on the former set of 1 pps signals.

On the basis of such a comparisons the relative frequencies of time keeping instruments are determined, and from 3 to 7 H-masers with the most uniform performance are used for time scale generation. All H-masers have the same statistical weight. If a maser changed its frequency we exclude it from the group, and vice versa, if the frequency of H-maser is quite stable over the period from 2 to 4 weeks it may be returned to the group. In such a way we generate TA(SU) time scale. The present unit of time interval is not matched to a current primary Cs value. It means that since initial matching unit of time TA(SU) is a free time scale supporting by an ensemble of continuously operating H-masers.

The UTC(SU) time scale has the time unit the same as TA(SU), it is shifted by a constant value and "leap" second is inserted into it in accordance to IERS circulars.

All SS, Fig. 1, have from 4 to 8 H-masers of CH1-70 type. Each of SS generates an autonomous time scale TA(SS) which is based on constant time unit. This time unit was established at the beginning of SS operation and is kept constant on the basis of internal comparisons of the individual H-masers. Apart from it, each SS taking into account the results of TA(SU) - TA(SS) comparisons generates UTS(SS), which is matched as precise as possible to UTC(SU).

Up to now the main operational link for time comparison between standards in STFS is MM link[5]. We shall show its characteristics on the basis of TA(SU) - TA(Khark) time comparison results, Fig. 11. If one exclude systematic frequency changes between TA(SU) and TA(Khark) and try to estimate RMS deviation between actual readings and two months averaged values (usually 8 sessions), Figs. 12 and 13, one may find $1\sigma \leq 40$ns. Comparison of the data in a triangle Moscow - Kharkov - Uzhgorod shows the accuracy of this link to be about 20 ns[6].

At the middle of 1989 we started experiments on time comparison via GLONASS in a "common view" mode. At present we have two navigational single frequency receivers, Figs. 14a & 14b, from which we succeeded to extract the time information. The time resolution of these instruments including additional time interval meter is 1 ns. Fig. 15 displays the results of the simultaneous measurements of the same satellites at two receivers. One may see a high phase stability and resolution of the whole instrument. The delay time difference does not exceed 6.8 ± 1.3ns, and its rate does not exceed 0.05 ± 0.1ns/day.

At Fig. 16 one can see results of time comparison at the distance of about 50 km between UTC(SU) and another secondary standard equipped with 4 H-masers. All links: GLONASS, TV and clock give the coinciding in the limit of uncertainty estimation of frequency, but differ in time scales to some extent. Frequency estimations are follows: GL — $(1.16 \pm 0.16) \times 10^{-14}$, TV — $(1.16 \pm 0.39) \times 10^{-14}$, Clock — $(0.69 \pm 0.55) \times 10^{-14}$. RMS deviation of readings from the fitted line about 25 ns for GL and about 35 nS for TV.

One may see quite the same picture for the first GLONASS experiment at the distance of more than 4000 km between Mendeleevo and Irkutsk, Fig.17 — the values of frequency difference determined by GLONASS and by the clock coincide, but there is a gap about 100 nS in scales. The relatively large readings scattering, $1\sigma \approx 58$ns, is due to lack of experience at the first stage of this activity. In Fig. 18 one can see modern results which show nice agreement with clock time scale comparison and better precision, $1\sigma \approx 22$ns.

In the second part of this report we would like to analyze the frequency stability of TA(SU) over the interval of several years.This analysis will be based on time comparisons of TA(SU) with TAI and on frequency comparisons with national primary Cs standards.

The main time link between TA(SU) and TAI is common reception of Loran C 7970 W station emitting from Sylt in Paris Observatory (OP) and Pulkovo Observatory near Leningrad. Pulkovo Observatory is connected with TA(SU) via MM link. In addition from time to time we compare our scale using portable clock.

Fig. 19 displays the time scale difference TAI – TA(SU) for the period of 1985–1989. The Loran C and clock data are taken from Circular T BIPM. Both dependences have a parabolic shape, they coincide qualitatively and quantitatively. Such a parabolic shape says that we have a certain frequency drift rate. The regression analysis gives us the following estimation for this rate: $(7.5 \pm 0.2) \times 10^{-14}$/1000 days for Loran C 7970 W and $(8.8 \pm 1.0) \times 10^{-14}$/1000 days for clock transportation. The result of clock transportation is not so precise due to lack of comparisons and low precision of some part of comparisons, these are comparisons with labs, which time links with OP have not enough precision.

Besides we have an extra link via reception Loran C 7990Y station in Kharkov and MM link between our labs. For these calculations we use the USNO Circular series 4 and the BIPM Circular T. This result presented in Fig. 20. It looks quite similar to Fig. 19 and gives the following frequency rate estimation — $(10.3 \pm 0.2) \times 10^{-14}$/1000 days.

Summarizing these results we may say that the unit of time interval in the TA(SU) system which is based on the ensemble of H-masers has a systematic rate $\leq 10^{-16}$/day with regard to more stable units in the TAI system.

Taking into account this rate we show in Fig. 21 the residual frequency deviation of TA(SU) smoothed by moving average over interval of two months. We can't consider these dependences completely correlated, so it means that the resolution of the experiment was not sufficient for precise detection of TA(SU) frequency changes. Nevertheless it gives us an opportunity of estimating relative frequency instability at the interval of 2 months 3×10^{-14}.

One may be interested in the following: is such a frequency drift of the H-maser ensemble unique? We have the most reliable data on atomic time scale TA(Khark) which is based on the ensemble of the same H-masers for more than 5 years. The data of time comparisons displayed at Fig. 11 show the systematic relative frequency drift between TA(SU) and TA(Khark) with the rate about $\approx (14.5 \pm 0.2) \times 10^{-14}$/1000 days. Then if TA(SU) has the rate about $\sim 8 \times 10^{-14}$/1000 days relative to TAI, TA(Khark) is $\sim -6 \times 10^{-14}$/1000 days. So we may consider such a rate to be typical for a free ensemble of H-masers.

If we remove this constant rate from above mentioned results and apply two-months moving average procedure the residual frequency changes are displayed at Fig. 22. Supposing that TA(SU) and TA(Khark) are equally stable we get an estimation of relative frequency stability of about $\leq 2 \times 10^{-14}$.

If one compare changes of TA(SU) time unit against the national primary Cs standard, Fig. 23, it

becomes obvious that TA(SU) time unit has a relative drift of about $(3.3 \pm 1.6) \times 10^{-14}$/1000 days. The value of this drift is less than half that against TAI.

As far as we discuss such a small frequency changes it is interesting how stable are other laboratories contributing to TAI scale generation. Fig. 24 presents the modified TAI - TA(k) differences for NIST, NRC, PTB, SU and USNO laboratories. The modifications introduce to the scale a constant time shifting and a proper constant frequency adding in order to clarify the scale features. One may look at the obvious similarity in scales — all the scales change the time unit in the same direction — the second becomes shorter, Fig. 25. The relative rate of this changing depends on the laboratory and is as follows: $(16.6 \pm 0.2) \times 10^{-14}$/1000 days, $(14.5 \pm 0.4) \times 10^{-14}$/1000 days, $(2.8 \pm 0.1) \times 10^{-14}$/1000 days, $(8.9 \pm 0.2) \times 10^{-14}$/1000 days, $(14.8 \pm 0.3) \times 10^{-14}$/1000 days. Such a correlation is not our "achievement", the existence of correlations between individual clock and scales was shown in References 8 and 9. We can't explain this phenomenon, but we hope it should force the time and frequency community to think once more what have happened, what is the actual value of stability of national time scales, and what is the best clock?

ACKNOWLEDGEMENT

First of all authors would like to acknowledge the Executive Committee of the PTTI meeting for the warm invitation to give an invited talk, and the PTTI Board for financial support.

This report reflects the state of art of NTFS and is based on industrious work of many persons to whom we are indebted. We acknowledge the head of MMC Dr.V.Tatarenkov, for his support and interest in this work, all our colleagues who are responsible for proper directions: G.Yolkin — primary Cs standards, B.Gaigerov — H-masers, MM link — S.Shustrov, GLONASS — A.Al'shina and G.Cherenkov. We couldn't get such nice results on time scale comparison without friendly cooperation with our colleagues from SS in Irkutsk, Kharkov and Uzhgorod which are headed by N.Tel'puhovsky, A.Tkachuk, and L.Kouharenko to whom we would like to express our thanks.

REFERENCES

Note that the editor does not have Cyrillic characters available. The references below in **bold font** *are transliterated from the original, more or less accurately.*

1. **V. G. Ilyin i dr., Izmeritelynaya technika, No. 10, 43, 1976**
   Yu. G. Abashev i dr., Izmeritelynaya technika, No. 2, 18, 1986

2. Yu. G. Abashev et al., Proceedings of the Fourth Symposium on Frequency Standards and Metrology, 374, Ancona, Italy, September 5-9,1988.

3. Comite Consultative pour la Definition de la Second, 11th session, Working document submitted to the 11th session, CCDS/89-6bis, 1989, Pavillon de Breteuil.

4. **B. L. Kasheev i dr., III Vsesoyuznyayi symposium po issledovaniyam v oblasti ismerenyi vremeni i chastoty, tezisy dokladov, 153, 23-26 oktyabrya 1990, Moskva, 1990**

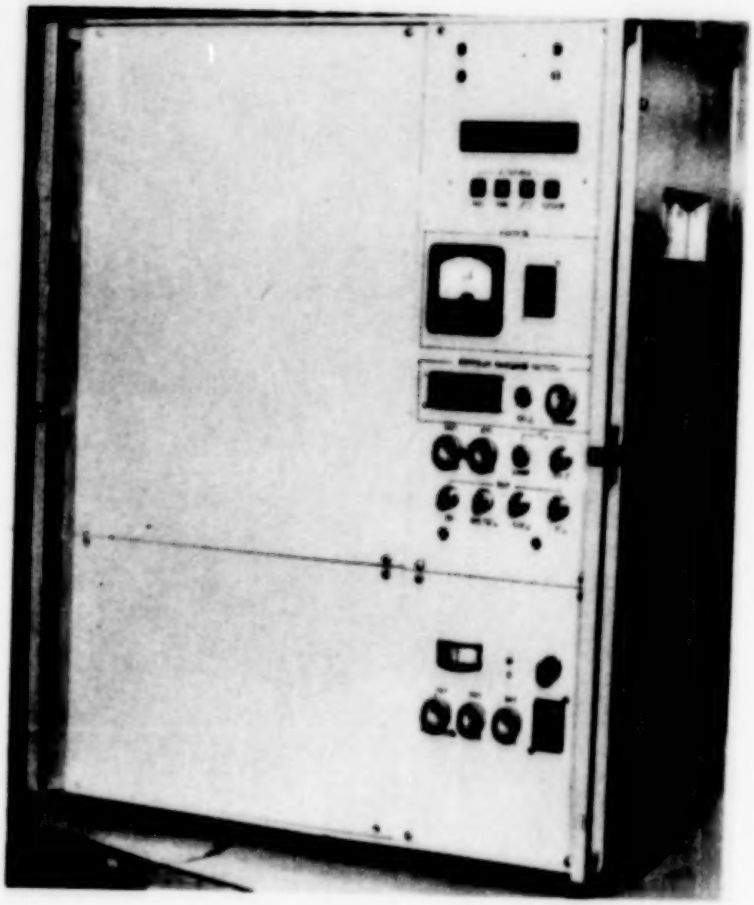
5. **A. P. Alyashyna, S. B. Pushkin, N. B. Koshelyaevsky, VII Vsesoyuznaya nauchno–tekhnicheskaya konferentsia "Metrologia v radiozektronike", tezisye dokladov, 254, Moskva, 1988**

6. N.B.Koshelyaevsky, S.B.Pushkin, G.T.Cherenkov, Soviet–West German Workshop "Scientific and industrial cooperation in the use of global navigation satellite system GLONASS", to be published.

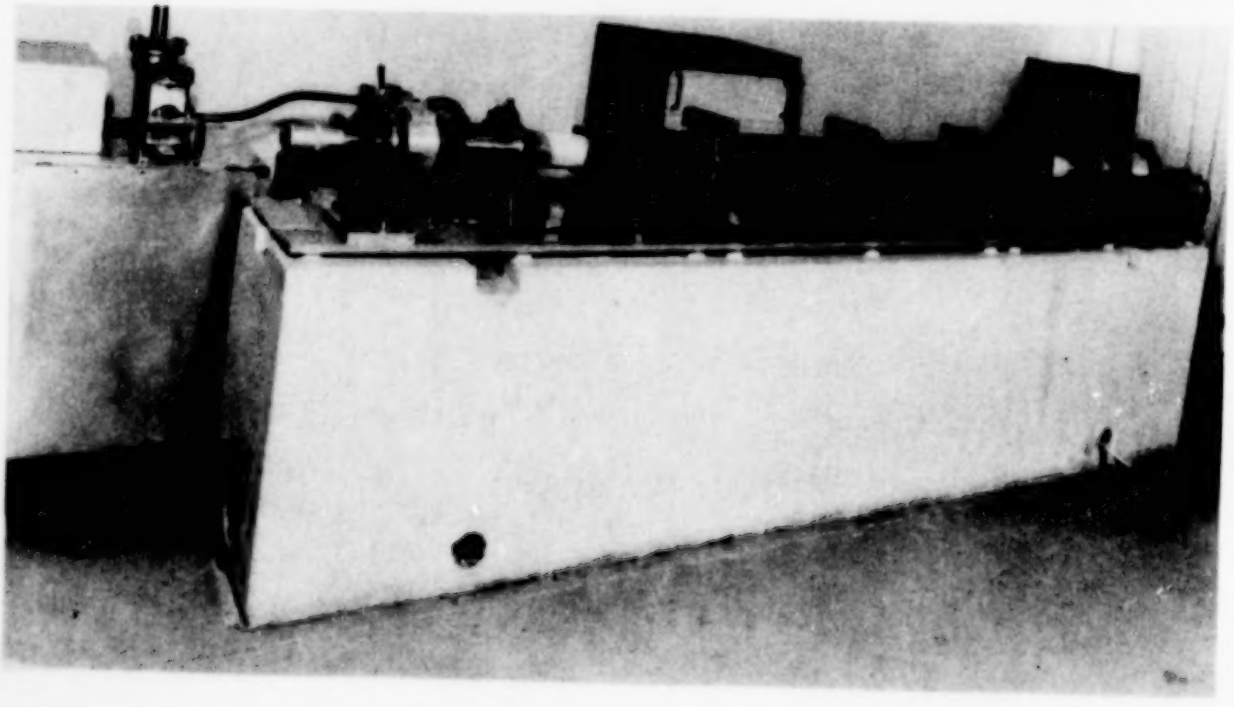
7. Proceedings of the Third International Timescale Algorithm Symposium, 137, 12–13 September 1988, Turin, Italy.

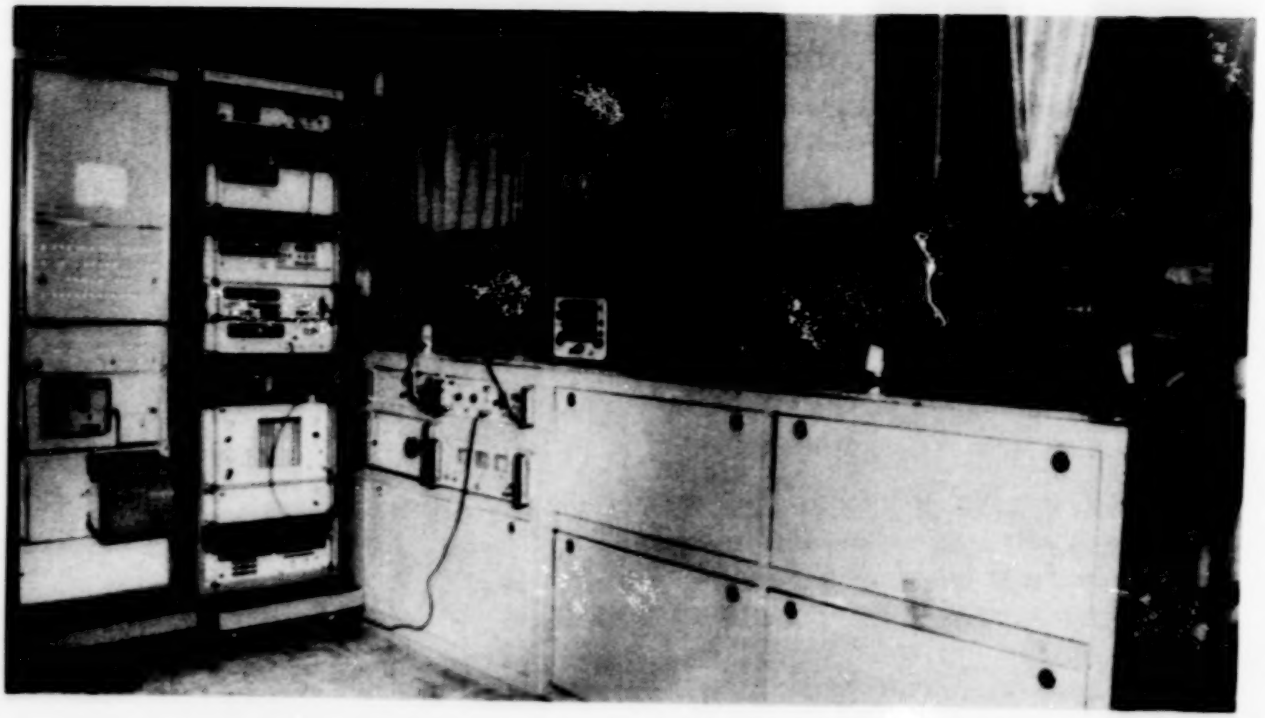
8. Commite Consultative pour la Definition de la Second, 11th session, Declaration S2 (1989).

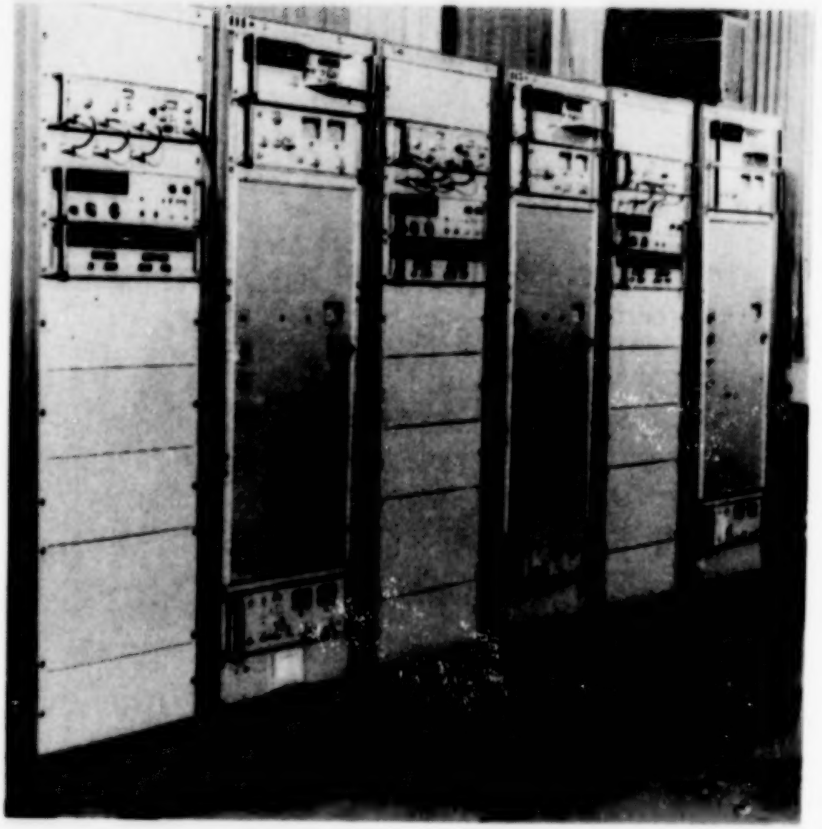

LC 7970Y
Pulkovo
Moscow
Sverdlovsk
Novosibirsk
Kharkov
Irkutsk
Khabarovsk
Uzhgorod
TV
LC 7990Y
LC 9970X
1000 km
NPTFS
SS
MM link

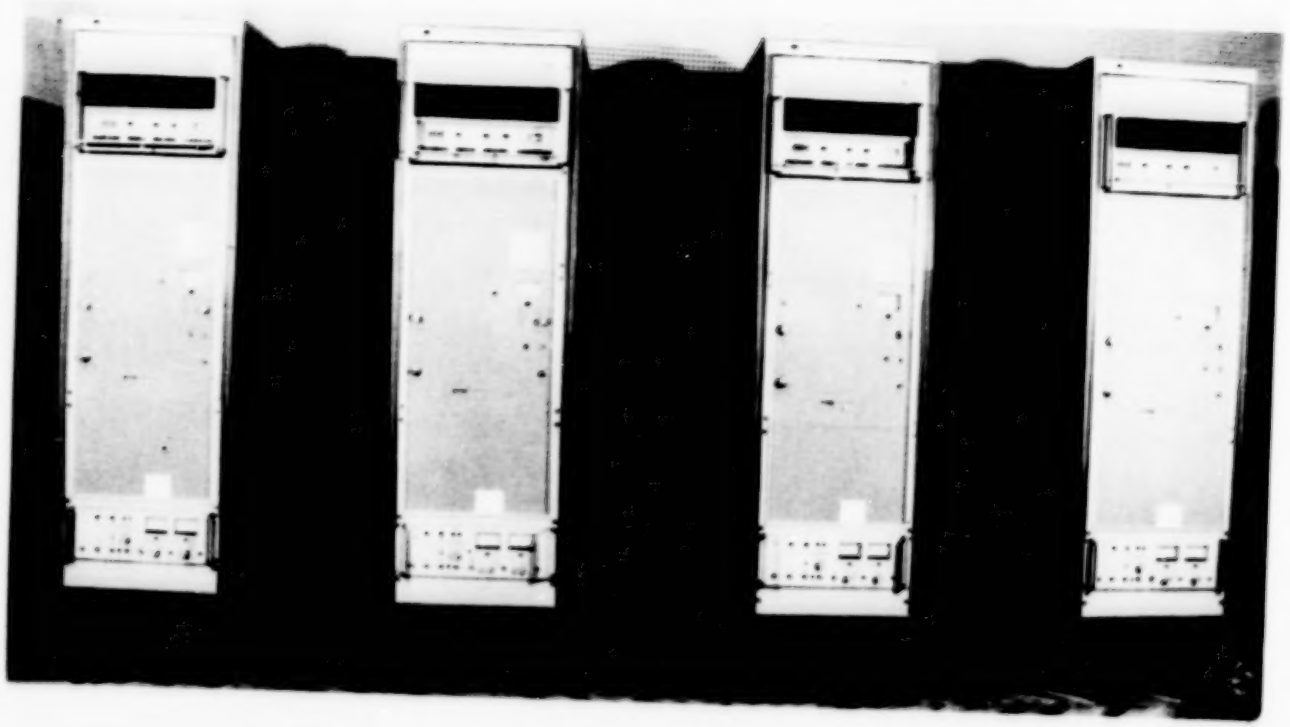


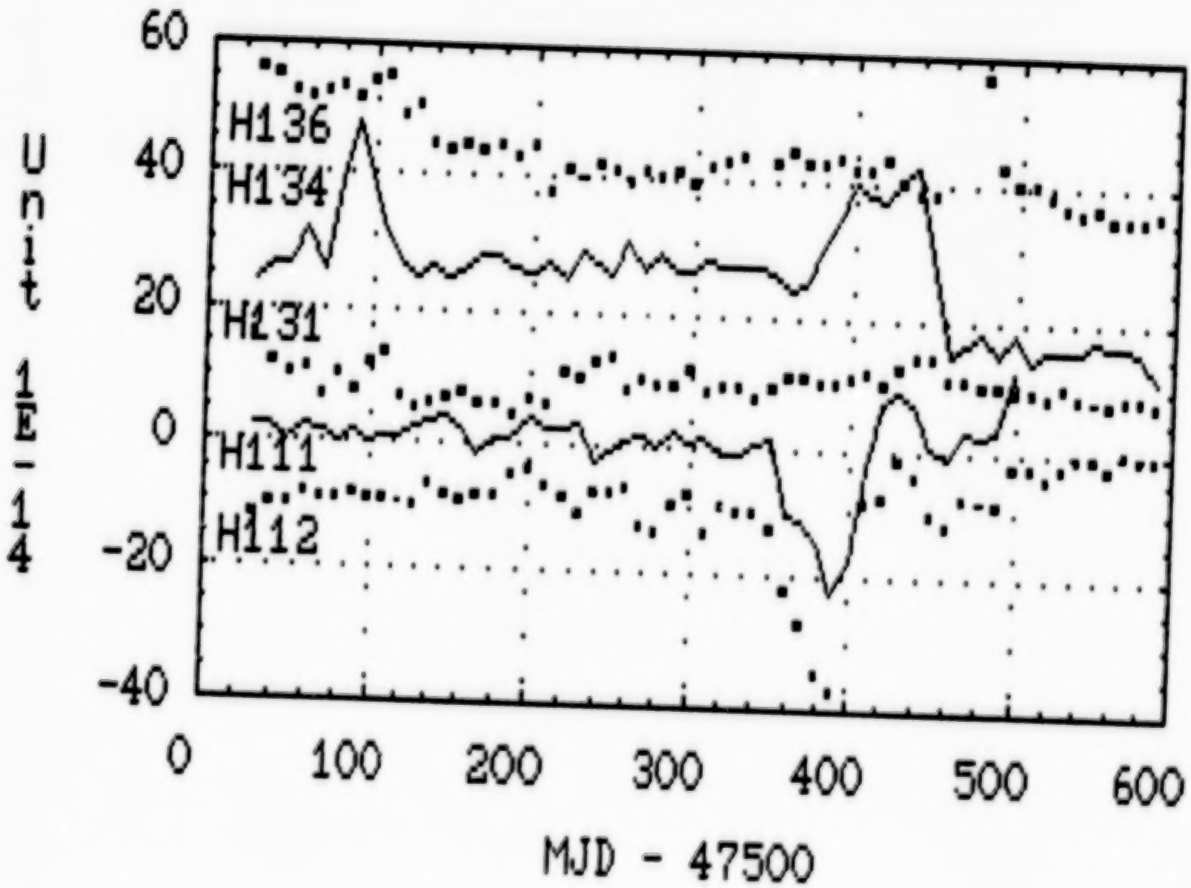

133
Cs

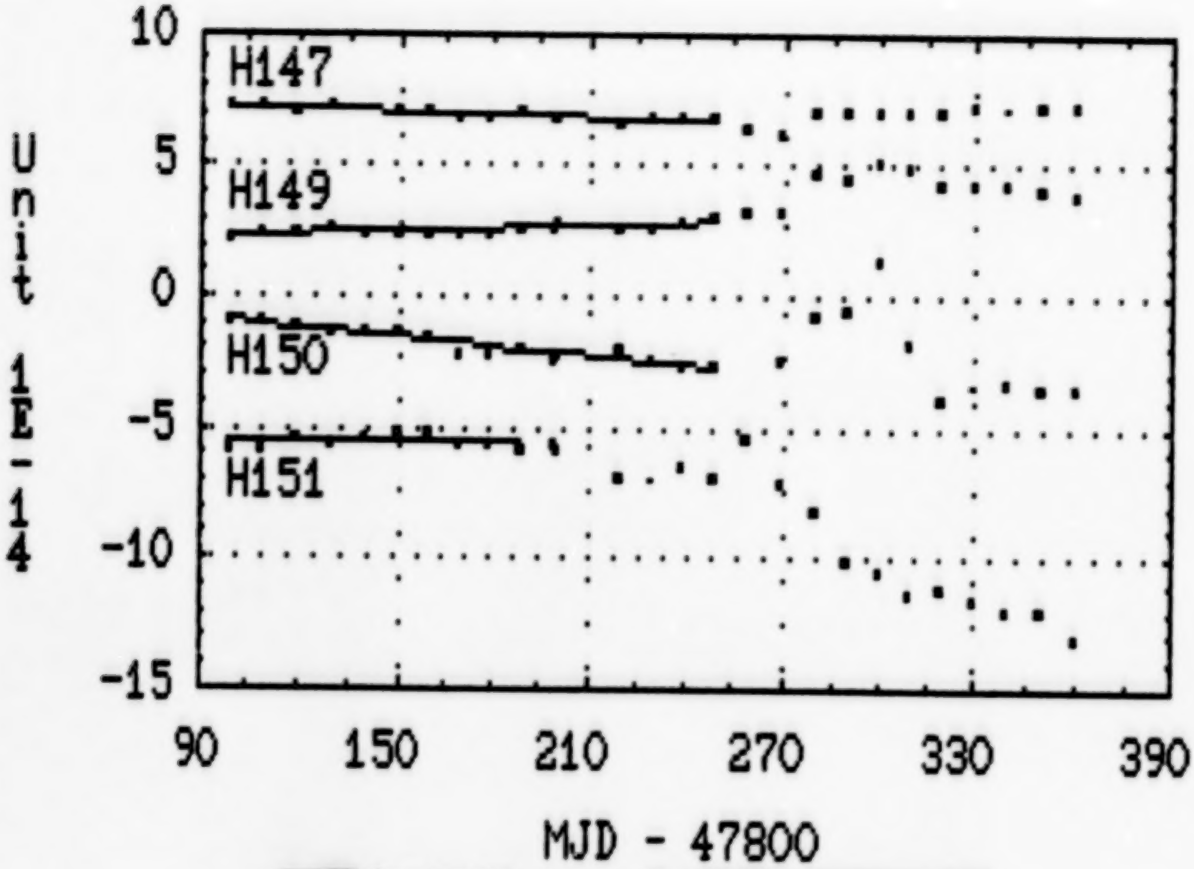


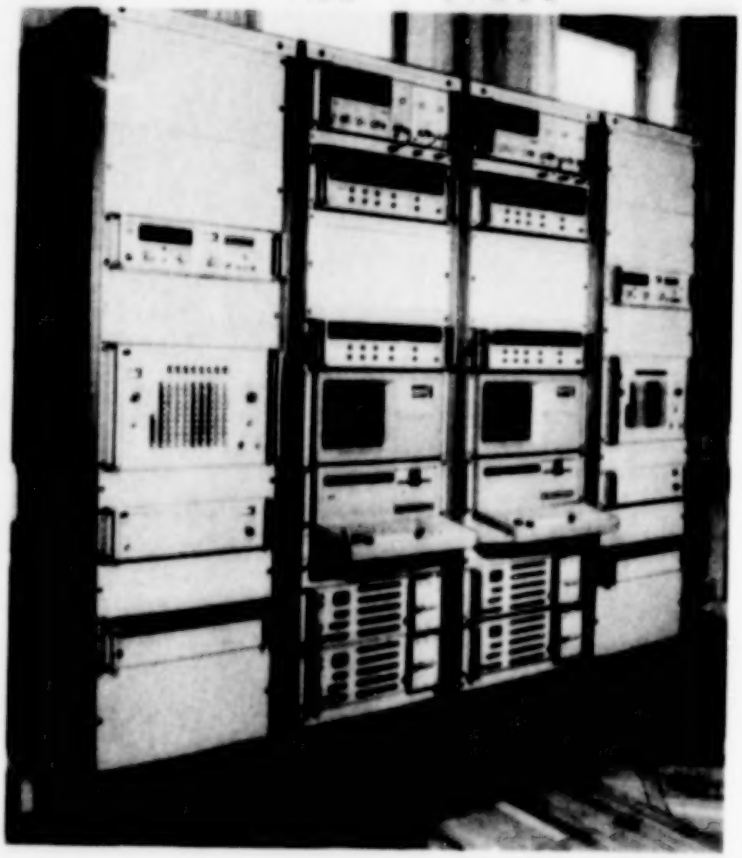


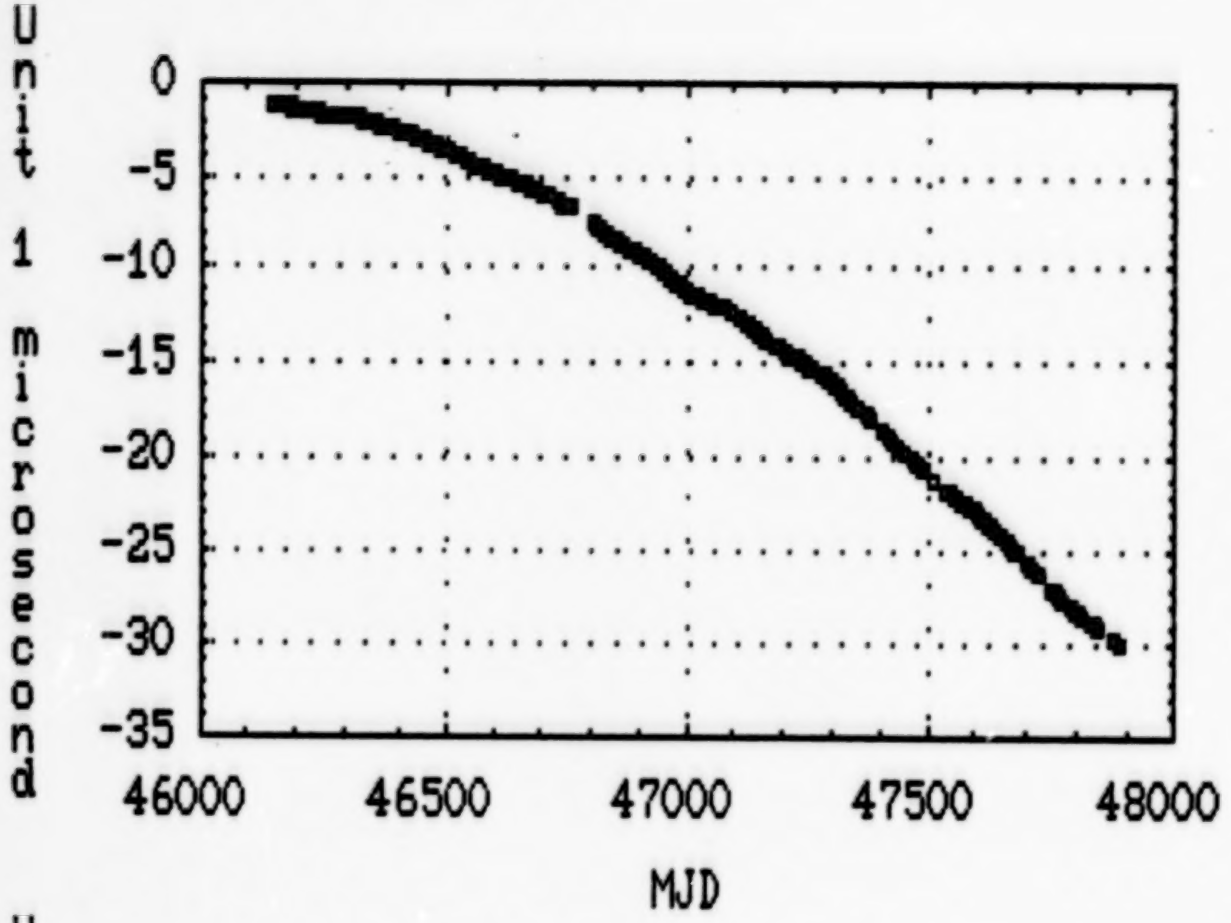


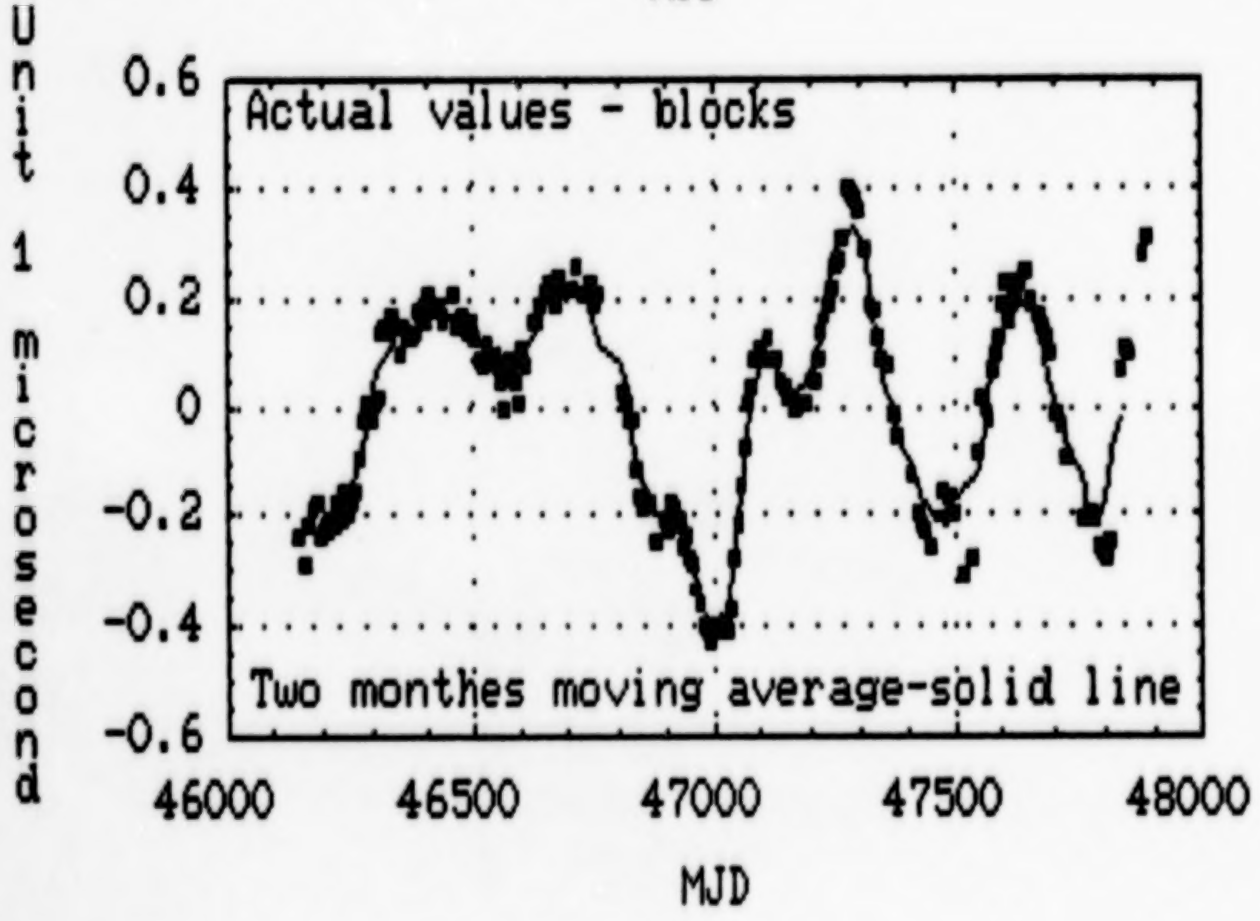


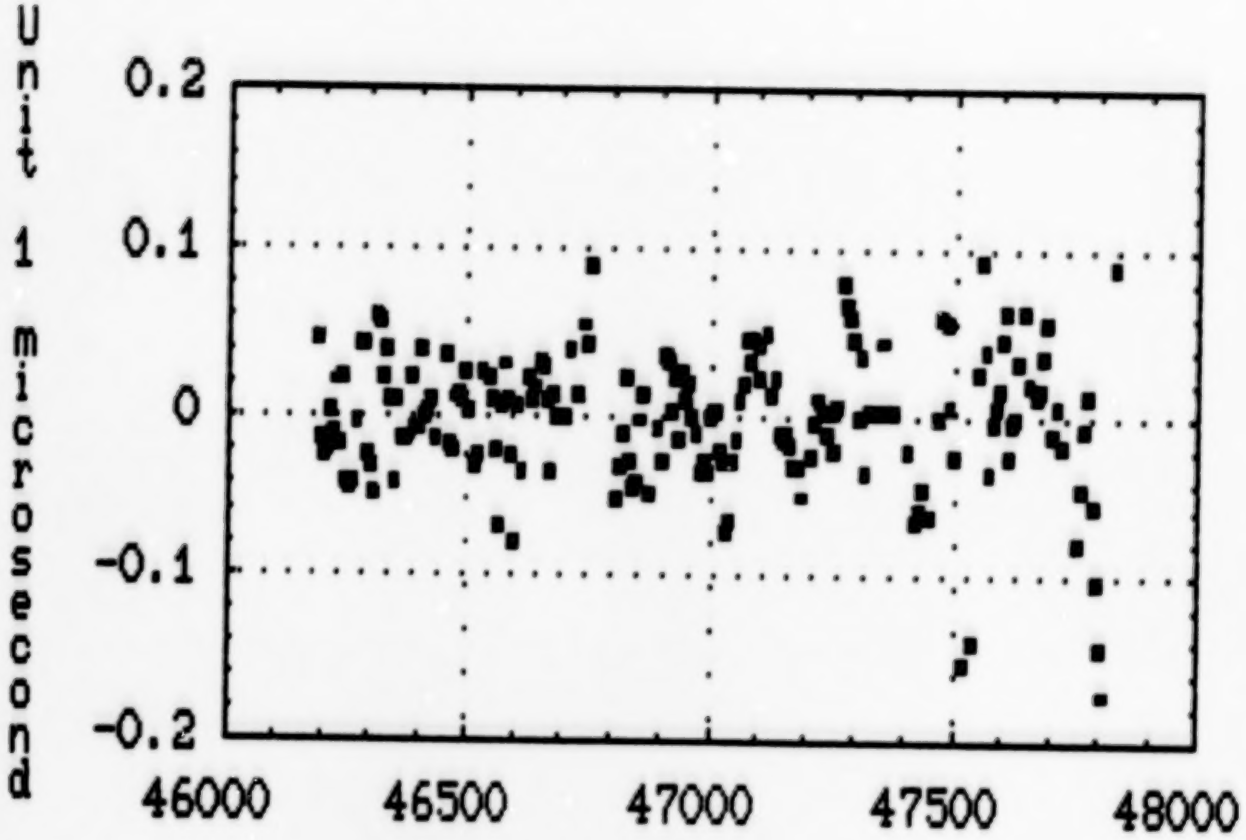

60
40
20
0
-20
-40
H136
H134
H131
H111
H112
0
100
200
300
400
500
600
MJD - 47500
Unit 1E-14

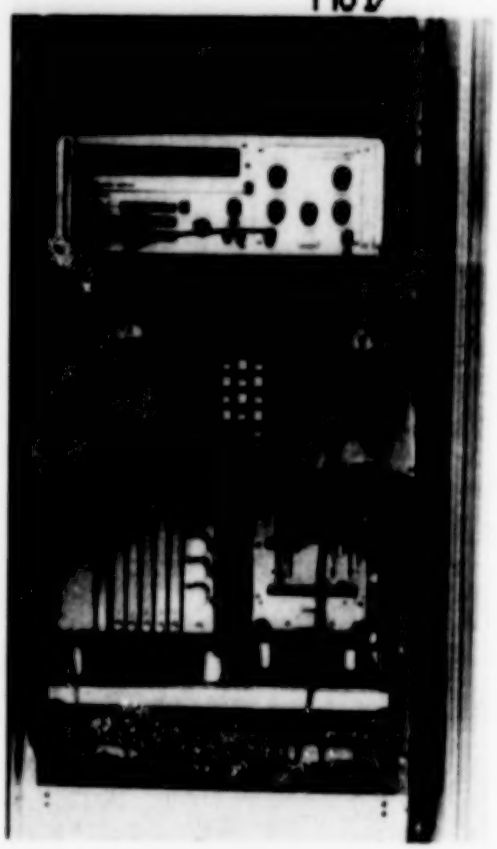

10
5
0
-5
-10
-15
H147
H149
H150
H151
Unit 1E-14
90
150
210
270
330
390
MJD - 47800

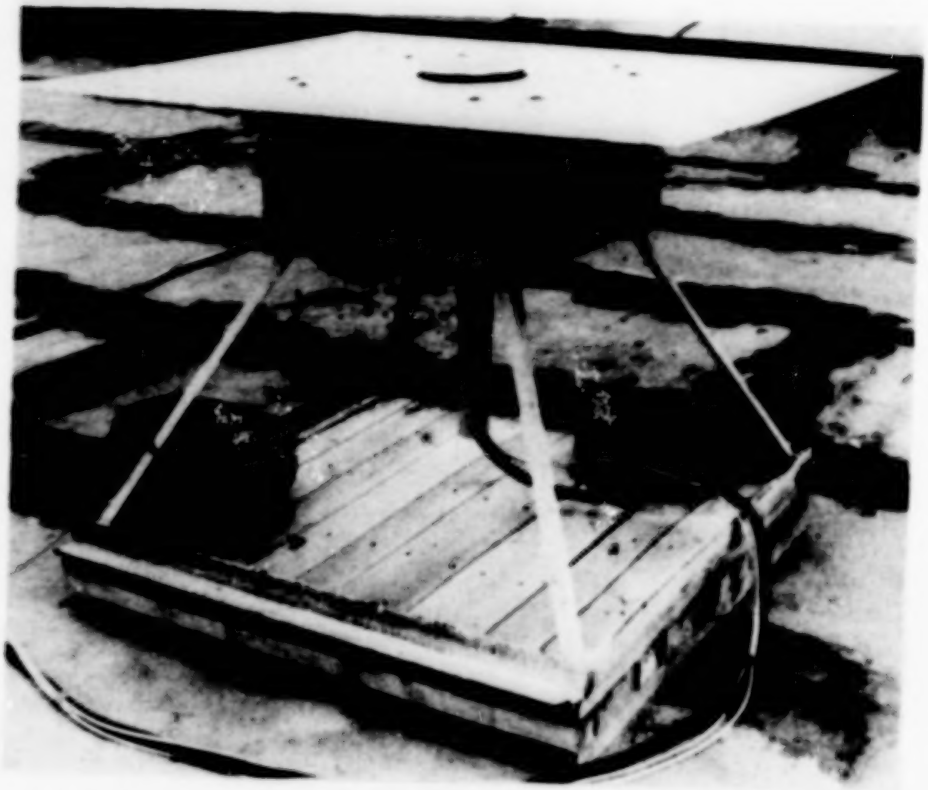


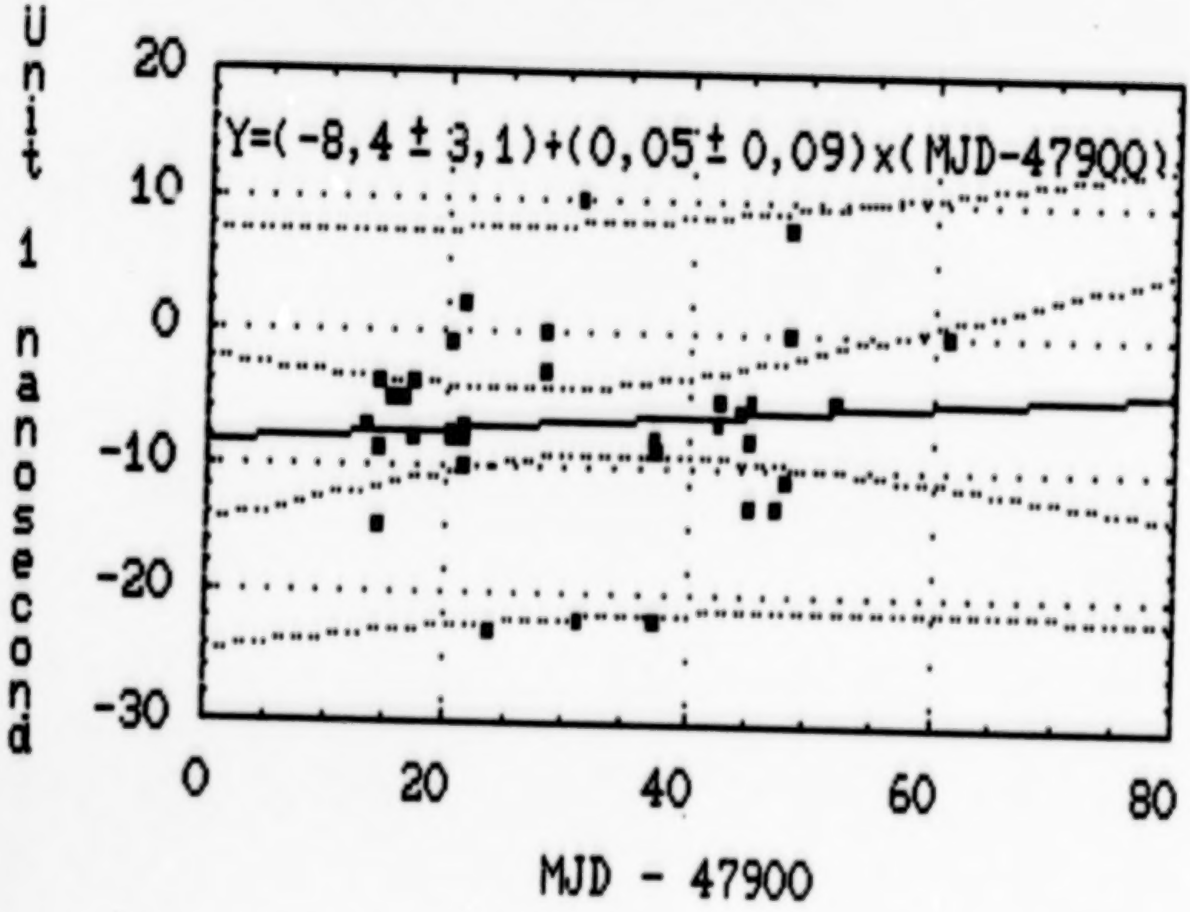

Unit 1 microsecond
0
-5
-10
-15
-20
-25
-30
-35
46000
46500
47000
47500
48000
MJD

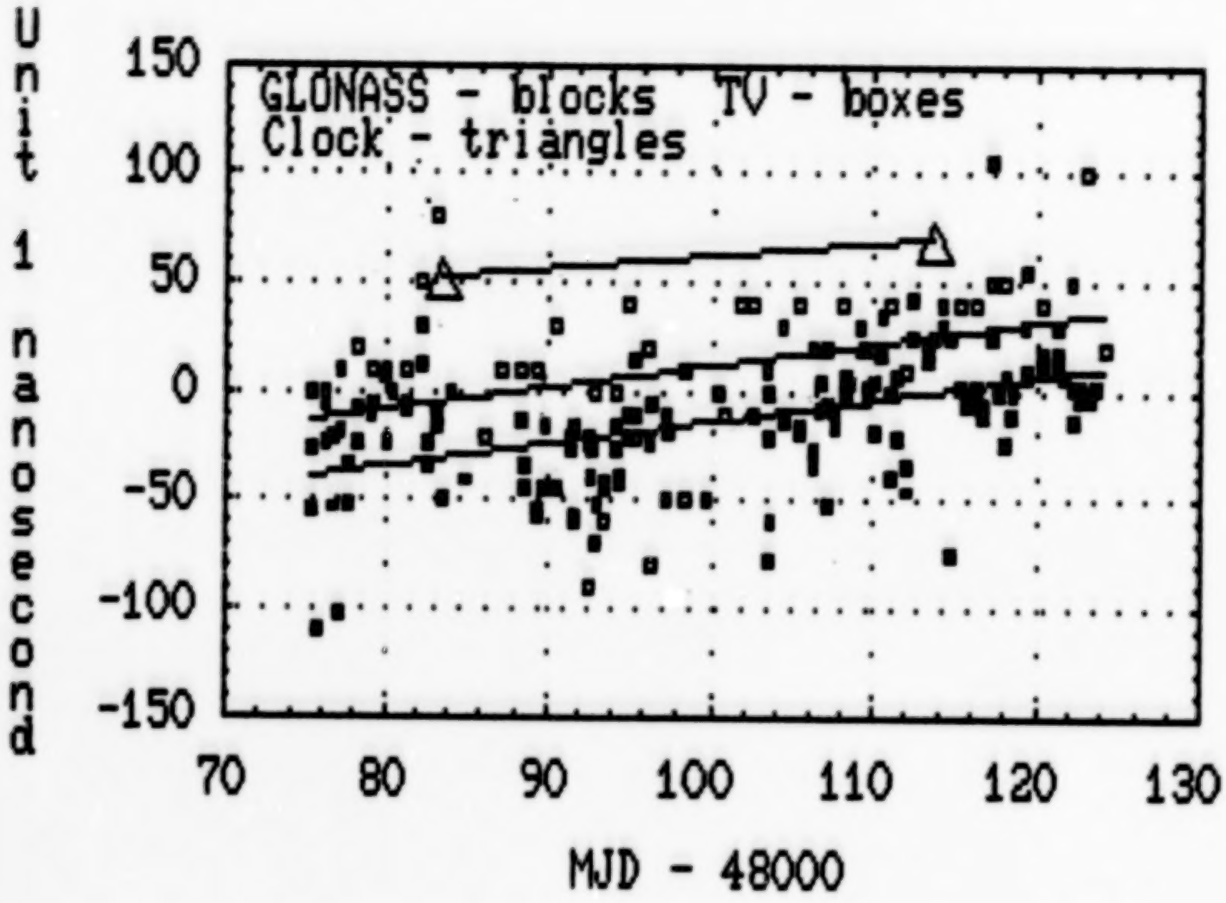

Unit 1 microsecond
0.6
0.4
0.2
0
-0.2
-0.4
-0.6
Actual values - blocks
Two monthes moving average-solid line
46000
46500
47000
47500
48000
MJD

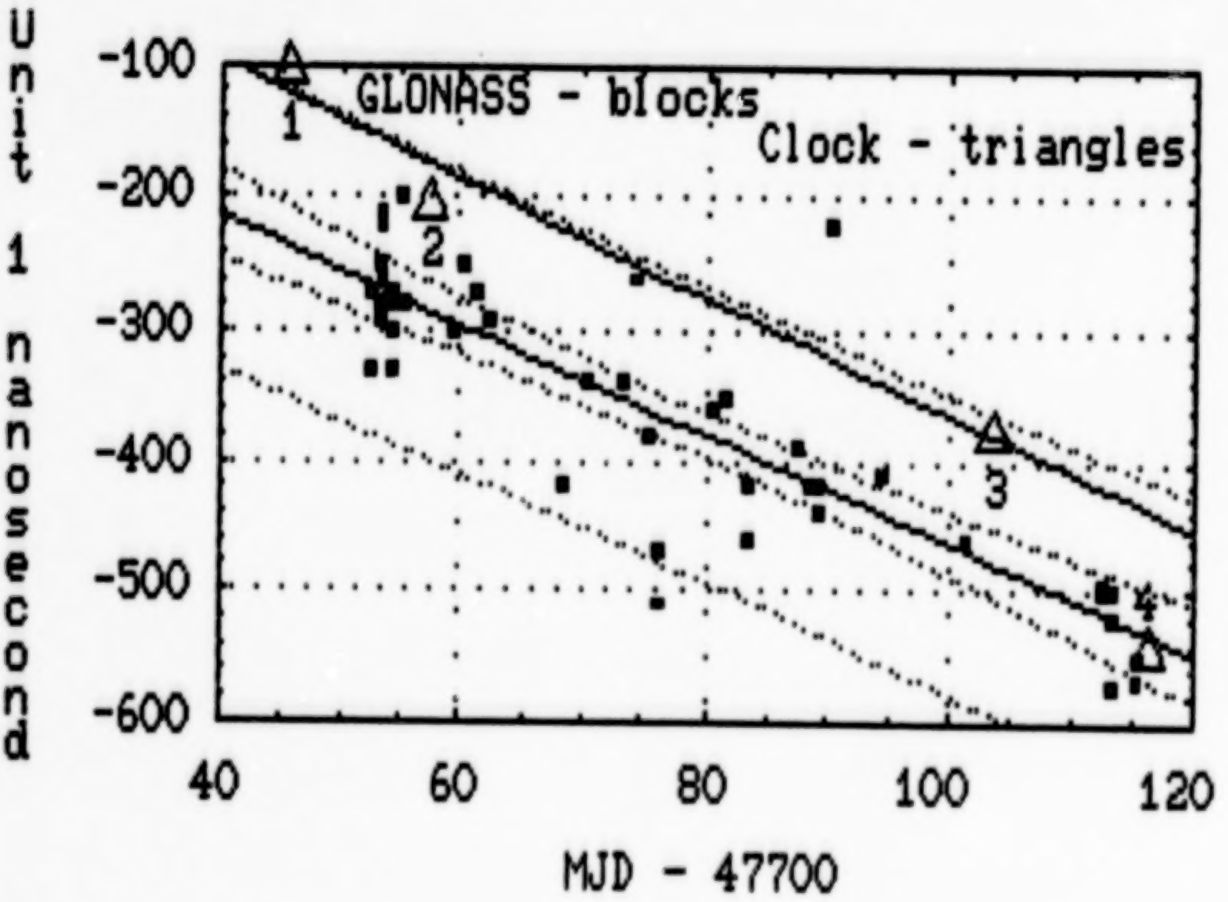

Unit 1 microsecond
0.2
0.1
0
-0.1
-0.2
46000
46500
47000
47500
48000
MJD

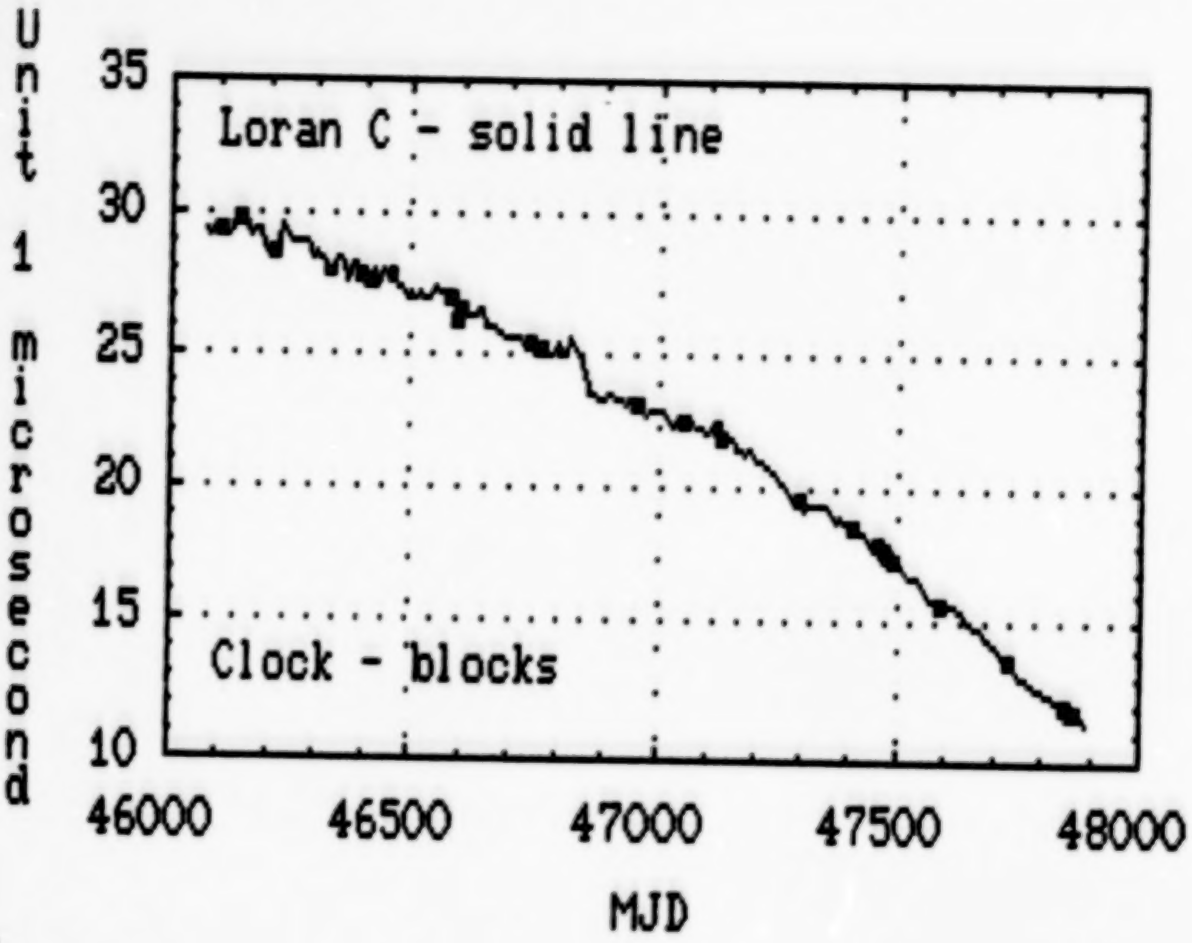


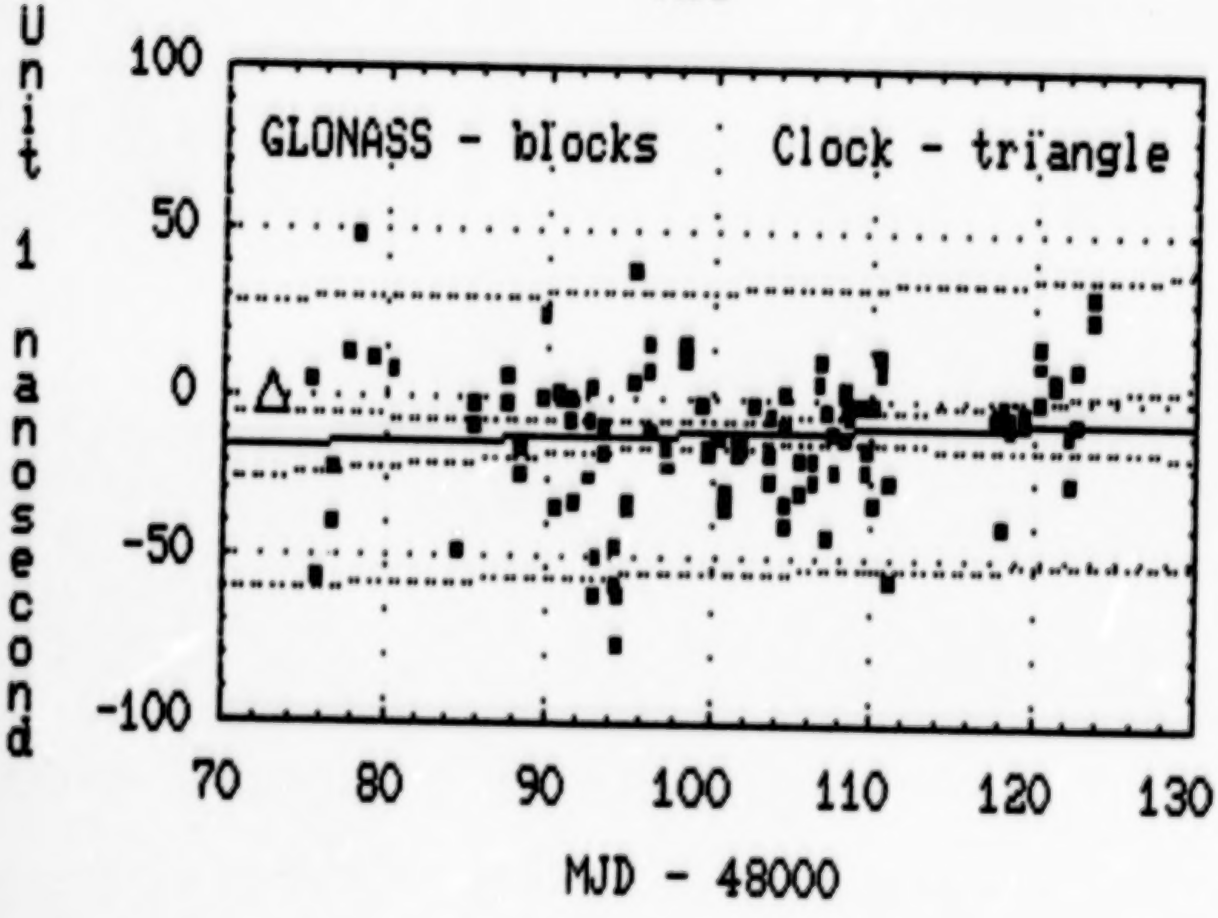


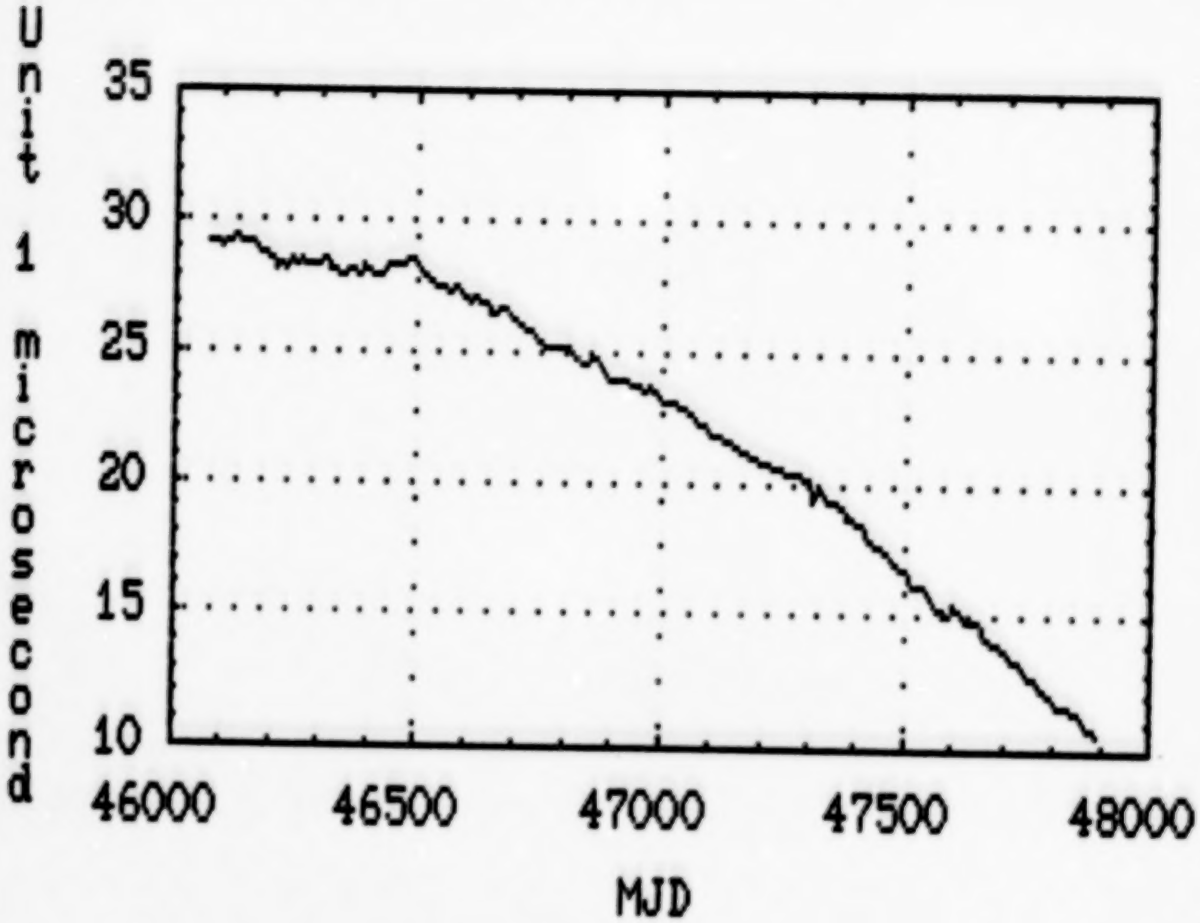

Y=(-8,4 ± 3,1)+(0,05 ± 0,09)x(MJD-47900)
20
10
0
-10
-20
-30
0
20
40
60
80
MJD - 47900
Unit 1 nanosecond

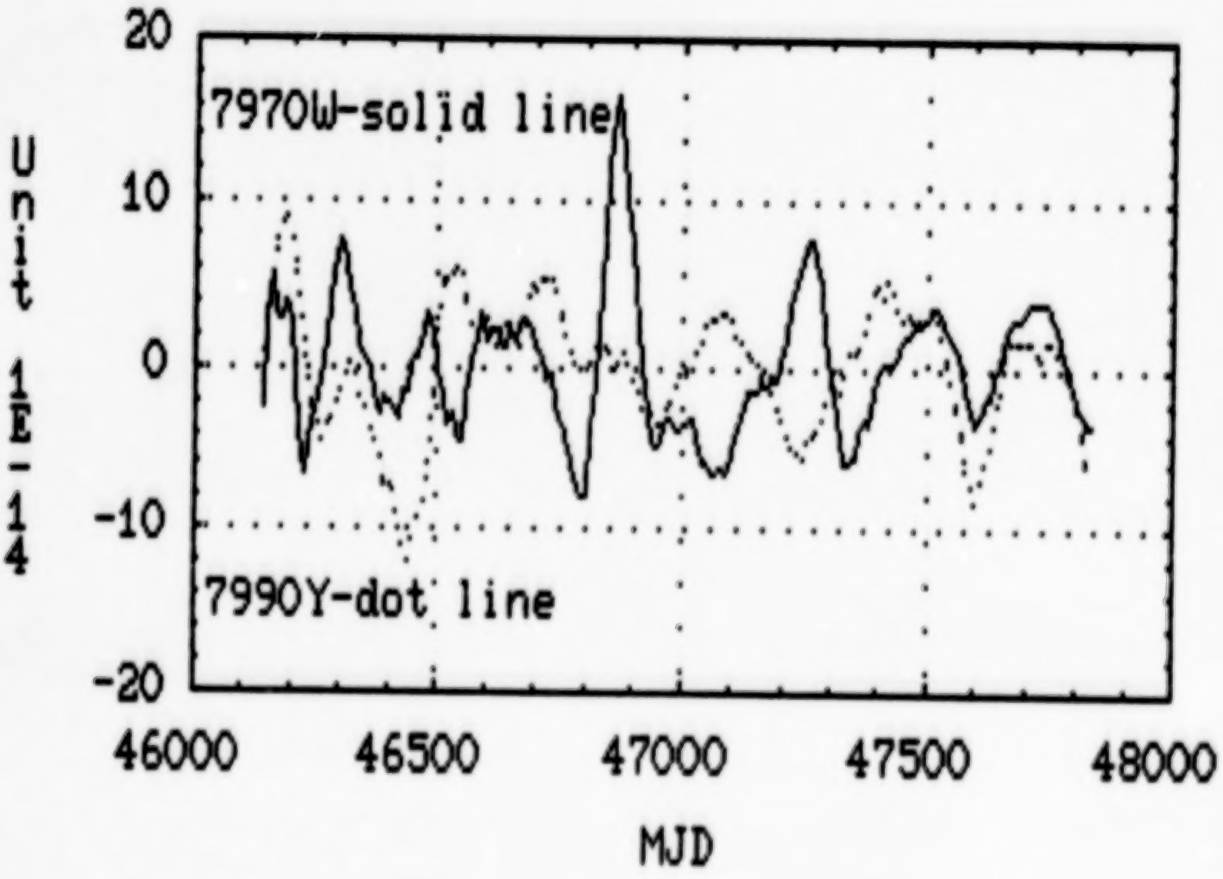

GLONASS - blocks TV - boxes
Clock - triangles
Unit 1 nanosecond
150
100
50
0
-50
-100
-150
70
80
90
100
110
120
130
MJD - 48000

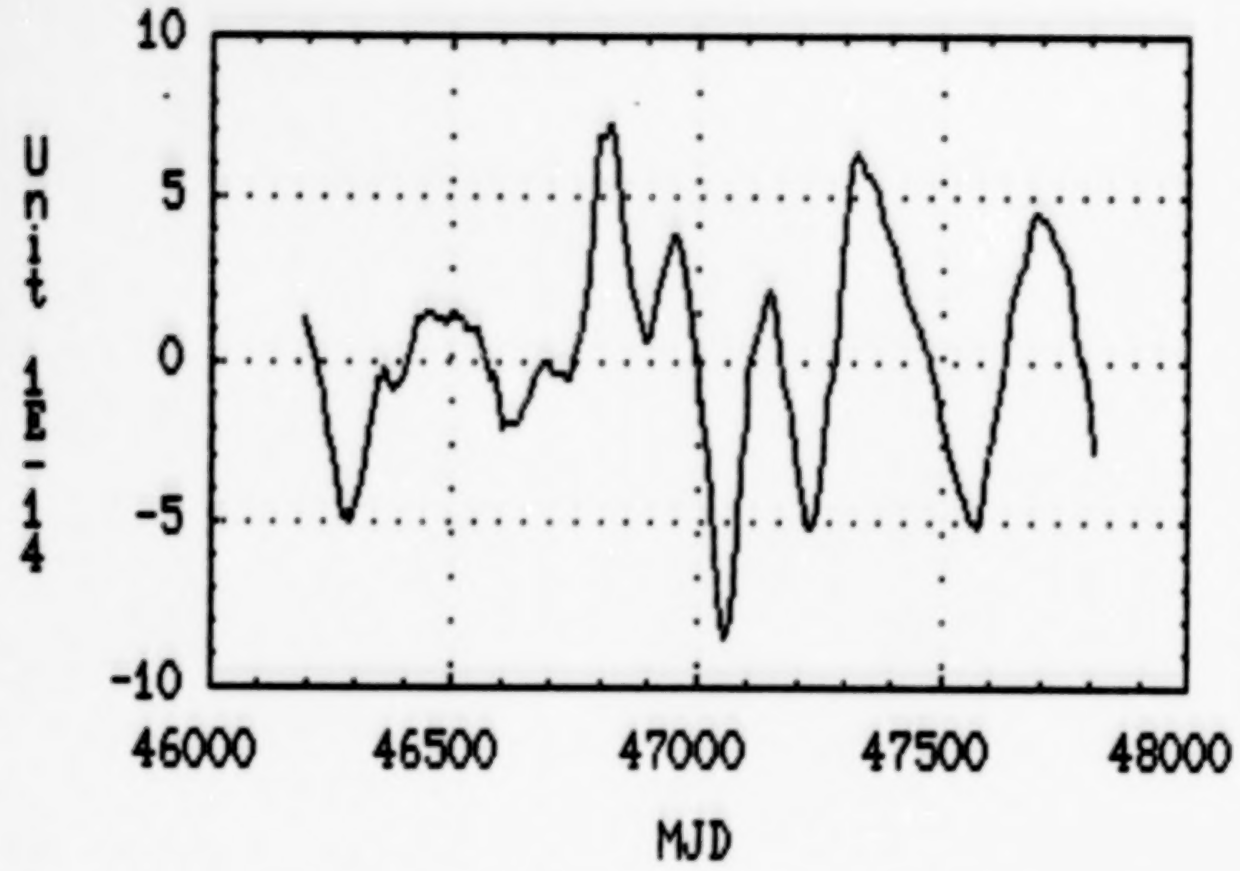

GLONASS - blocks
Clock - triangles
Unit 1 nanosecond
-100
-200
-300
-400
-500
-600
1
2
3
4
40
60
80
100
120
MJD - 47700

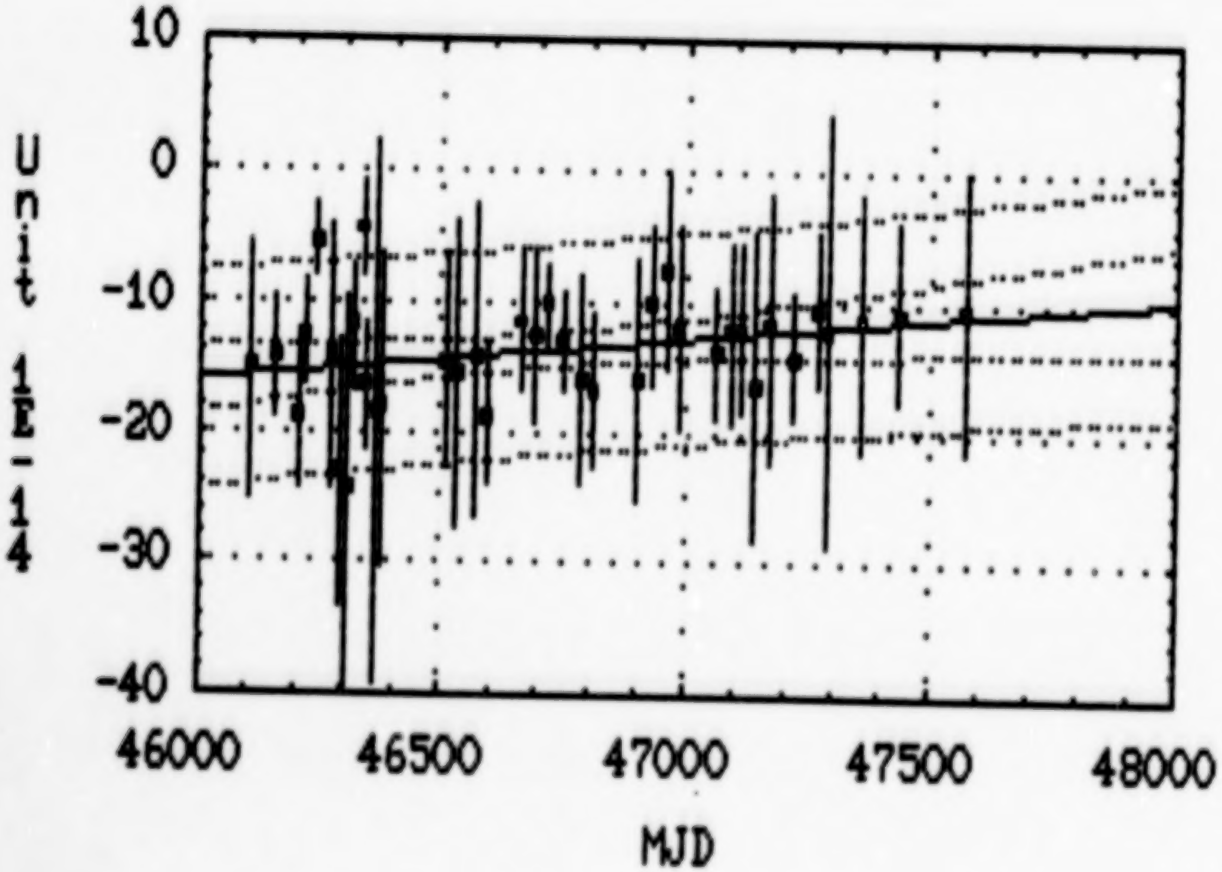

Unit 1 microsecond
35
30
25
20
15
10
Loran C - solid line
Clock - blocks
46000
46500
47000
47500
48000
MJD

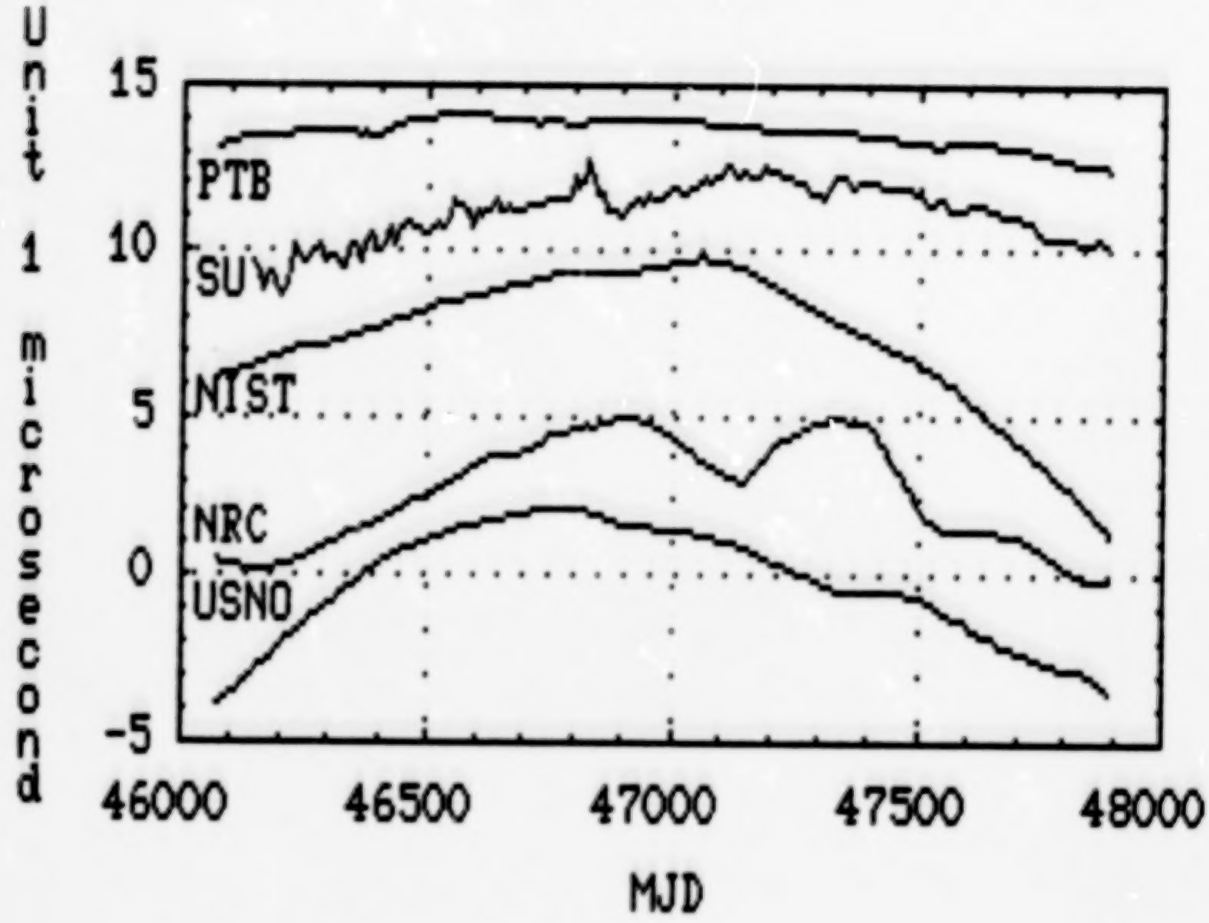

Unit 1 nanosecond
100
50
0
-50
-100
GLONASS - blocks
Clock - triangle
70
80
90
100
110
120
130
MJD - 48000

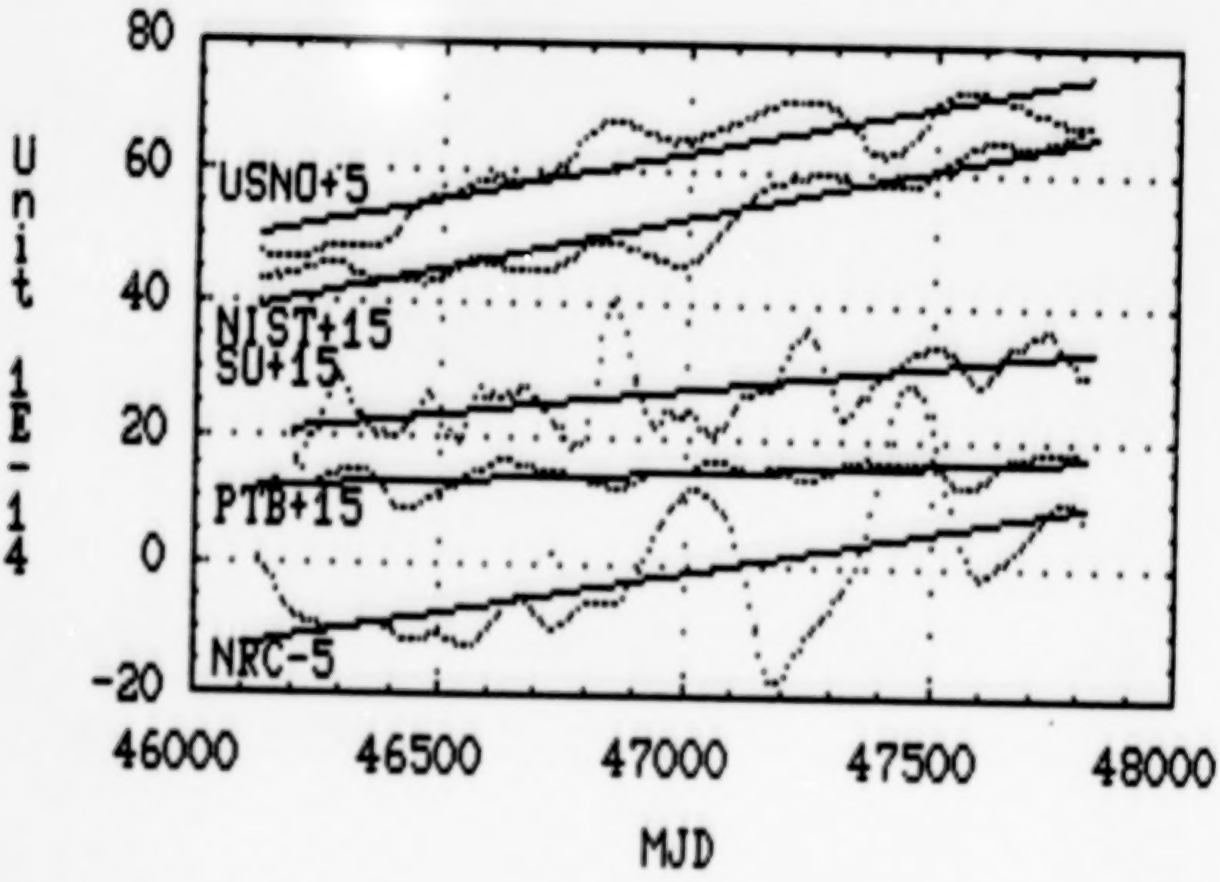

Unit 1 microsecond
35
30
25
20
15
10
46000
46500
47000
47500
48000
MJD


Unit 1E-14
20
10
0
-10
-20
7970W-solid line
7990Y-dot line
46000
46500
47000
47500
48000
MJD


10
5
0
-5
-10
Unit 1E-14
46000
46500
47000
47500
48000
MJD


10
0
-10
-20
-30
-40
Unit 1E-14
46000
46500
47000
47500
48000
MJD


Unit 1 microsecond
15
10
5
0
-5
PTB
SUW
NIST
NRC
USNO
46000
46500
47000
47500
48000
MJD


Unit 1E-14
80
60
40
20
0
-20
USNO+5
NIST+15
SU+15
PTB+15
NRC-5
46000
46500
47000
47500
48000
MJD

QUESTIONS AND ANSWERS

Carroll Alley, University of Maryland: Dave, did you visit there yourself?

Mr. Allan: Yes, I was there last September.

Professor Alley: How do they transport the Hydrogen Masers?

Mr. Allan: With difficult. They are not small. They have taken them on several trips — to TAI in Paris, to other sites that they have around the world. I don't know how difficult it is. The one maser that I saw there was probably transportable by two people. Our colleagues here could probably answer that if you asked them. They have two small maser models, I am not sure which one it is, but they were developing one while I was there that had a dynamic magnetic field servo with an attenuation factor of about 200,000. It looked like it would make a beautiful portable clock. It was fairly small.

Unidentified Questioner: David, what do you know about their passive masers?

Mr. Allan: We will show the data tomorrow night on their passive masers. I think it is fairly new for them, most of the masers that they have made are active masers. The stability is comparable to some that we have built, better than some, but not as good as others.

Harry Peters, Sigma Tau: I thought that it would be an appropriate question to ask whether these masers in the ensembles are being automatically spin-exchange tuned or otherwise tuned to achieve this stability.

Mr. Allan: Yes, they are.

Unidentified Questioner: In the chart that showed the various links, it showed the different sites where they have the hydrogen masers. How many masers do they have at each site? Do they all have the same number of clocks?

Mr. Allan: The paper said that they have up to eight hydrogen masers at each of those secondary sites.

Mr. Thomann, Neuchatel Observatory: Do we know whether they have the same design of masers at Gorky and at VNIIFTRI, and is the material for coating of the bulbs the same?

Dr. Demidov: All the coatings since 1975 have been made with F10.

BLANK PAGE

TIME AND FREQUENCY COMPARISONS IN EUROPE BY MEANS OF ECS 5 GEOSTATIONARY SATELLITE

F. Cordara, V. Pettiti
Istituto Elettrotecnico Nazionale Galileo Ferraris
Corso Massimo d'Azeglio, 42 - 10125 Torino, Italy
Tel. 011/3488933

A. Cenci, M. Fermi, C. Sciarretta
Telespazio S.p.A.
Via Tiburtina, 965 - 00156 Roma, Italy
Tel. 06/406931

Abstract

A time synchronization experiment between some European laboratories using the passive television method applied to the signals broadcasted by Eutelsat I-F5 telecommunication satellite was completed in 1990.

The results obtained in the last period, when also range measurements from a Telespazio ground station were performed, are analyzed to evaluate the accuracy level of the time comparisons corrected for the effect of the satellite movement with position data obtained either from the European Space Agency (ESA) or from orbit determination with range data entered into GEODYN program of NASA/GSFC.

1 - Introduction

A time synchronization experiment between the time scales of eight European laboratories using the passive television method |1| applied to the RAI Uno signals transmitted at 11.01 GHz by Eutelsat I-F5 (ECS-5 in the sequel) telecommunication satellite placed in a geostationary orbit at 10° East longitude, was completed in February 1990.

The aim of this experiment, developed in the frame of Euromet Project P88/169, was to investigate in the capabilities of these techniques in order to establish a synchronization system covering several countries in Europe, yielding good precision in time and frequency calibration with relatively low cost equipment |2,3|.

The laboratories involved in the last period of the experiment are reported below together with their receiving stations coordinates:

Laboratory	Latitude	Longitude	Height (m)
AOS - Astronomical Latitude Observatory BOROWIEC, POLAND	52°16'37.0"N	17°04'23.7"E	129
ASMW - Amt für Standardisierung, Meßwesen und Warenprüfung - BERLIN, GERMANY	52°27'14"N	13°37'01"E	50
FUC - Telespazio S.p.A. FUCINO, ITALY	41°58'41.3"N	13°35'57.1"E	671
IEN - Istituto Elettrotecnico Nazionale TORINO, ITALY	45°00'53.6"N	07°38'20.1"E	297
STA - Swedish Telecommunication Administration - STOCKHOLM, SWEDEN	59°09'54.2"N	18°08'13.5"E	109
TP - Ustav Radiotechniky a Elektroniky PRAHA, CZECHOSLOVAKIA	50°07'53"N	14°27'09"E	300
TUG - Technische Universität GRAZ, AUSTRIA	47°04'01.5"N	15°29'35.5"E	534
VSL - Van Swinden Laboratorium DELFT, THE NETHERLANDS	51°59'58.9"N	04°22'50.7"E	60

The receiving stations used, with the exception of the Telespazio - Fucino ground station, were made of commercial TV satellite receivers and antennas with diameters varying from 0.9 to 3 m.

The daily measurement schedule followed in each laboratory consisted, up to January 1990, in two sets of 25 time interval measurements, twelve hours apart, between the local UTC and the trailing edge of the first field synchronizing pulse of the video signal. Since January 1990, when the range measurements from the Telespazio ground station were also performed, the measurement schedule was updated to have more synchronization results.

In Fig. 1 are reported the comparison results between UTC(IEN) and the time scales of TUG, STA and TP obtained via ECS 5 for the period November 1989 - February 1990 corrected for the satellite position data supplied by the European Space Agency (ESA). In the figure are also reported the differences every ten days computed from BIPM Circulars T, in the case of TP, or the daily differences computed via GPS common-view in the case of STA and VSL.

As reported in previous works on this subject |2,3|, it can be seen that a precision of some hundreds of nanoseconds can be achieved by correcting for the satellite position parameters supplied by the control station with an uncertainty of some kilometers.

The peak-to-peak fluctuations of the synchronization results are also strictly dependent on the baselines between the laboratories involved that varied from some hundreds of kilometers up to 1700 kilometers in the IEN/STA

link. The differences between the synchronization results, obtained with ECS 5 and the synchronization systems already established, are mainly due to an insufficient evaluation of the differential delay of each pair of receiving equipment. This is more evident in the case of UTC(IEN) - UTC(TP) where the uncertainty reaches 1.5 us, due also to the synchronization link used to relate TP to UTC (long distance terrestrial television link).

Since November 1989, the daily measurement schedule was changed to verify if the diurnal effects due to the satellite movement, still present in the synchronization results, could be reduced computing the time differences at half-sideral day intervals, but no appreciable improvement was obtained with this procedure.

2 - Range measurements

From January 30 to February 20, 1990, range measurements were performed every hour at the Telespazio-Fucino groundstation where the RAI Uno signals are transmitted to ECS 5. A portable cesium clock was also installed at Fucino as a local reference to perform every hour synchronization measurements with the other time scales.

The equipment set-up is shown in Fig. 2; each measurement sequence started with the time difference between the local 1 PPS reference UTC(FUC) and the first selected TV synchronizing pulse received from the satellite and was followed by a range measurement beginning after a 300 ms delay for instrumentation reasons. This measurement was stopped by a TV pulse from ECS 5 after nearly 250 ms (Fig. 3). The measurement resolution was 0.5 ns. The range values measured at Fucino have been reported in Fig. 4 together with the range computed for Fucino from ECS-5 orbital parameters supplied by ESA-Redu control station. The differences between the two sets of range data are reported in Fig. 5 where a maximum difference of about 1 km can be observed. This is mainly due to the uncertainty of the ESA parameters and, to a lesser extent, in having disregarded the satellite transponder delay. The typical standard deviation of a set of 25 range measurements, using the synchronizing pulses, was 1 meter.

In Fig. 6 are reported the synchronization results between UTC(IEN) and UTC(FUC) for February 1990 and, with crosses, the average of a pair of adjacent synchronization data at a half-sideral day interval. A considerable reduction of the daily fluctuations is obtained but a long-term excursion of ± 1 us is still present. Looking at ECS longitude data for the same period (Fig. 7), with the same averaging process applied, it can be noticed that the excursion seen before matches very well the longitude-drift of the satellite. These synchronization results have been therefore corrected only for the effect of the mean longitude variation obtained from ESA position data and for the differential delay of the two stations (Fig. 8). In the same graph is reported with a dashed line the mean rate of the cesium clock at Fucino during the

experiment versus UTC(IEN) that was of +96 ns/d; the mean rate evaluated by means of ECS-5 has been found equal to +92 ns/d. The residual daily fluctuation of the order of 200 nanoseconds peak-to-peak, is of the same order of that obtained averaging synchronization data at 12 hour interval.

The bias of about 0.6 us between the two curves is due to the fact that it was not possible to evaluate separately the receiving and transmitting delay of the Fucino groundstation and that the delay of the Test Loop Translator, used for the measurement of the total delay, is not known.

The total delay of the Fucino transmitting and receiving station, measured during the experiment, was found equal to 3.918 us with an uncertainty of $\pm$ 7 ns.

The delay of the IEN station, measured by means of a satellite simulator, as described in |3|, was found equal to 0.851 us with an uncertainty of $\pm$ 15 ns. The long-term stability of this delay has also been investigated for six months after having stabilized the temperature inside the satellite simulator within $\pm$ 1 K.

The measurement results, reported in Fig. 9 together with the outdoors temperature, show a correlation between the temperature and the delay variation.

3 - Orbit determination of ECS 5

The precise orbit determination of ECS 5 geostationary satellite has been performed at Telespazio using the range measurements collected in the period January 30 - February 20 1990 and discussed in the previous section. The travel times of TV synchronization signal, from Fucino ground station to ECS 5 satellite and back, have been preprocessed, converted into one way range measurements and formatted into a suitable format for GEODYN program to compute satellite orbit.

GEODYN is a NASA/GSFC program routinely used at Telespazio to analyze laser ranging data to LAGEOS and other geodetic satellites for precise orbit determination and geodetic parameter estimates. This program represents the state-of-the-art in modelling forces acting on satellites and has the capability to process various types of observations.

The model implemented into GEODYN to analyze the data is summarized in table 1. In our model we took into account the gravity of the Earth, with its spherycal harmonics for some low degree and order terms, together with the gravitational forces due to the Sun and the Moon. Furtherly, we took into account perturbation due to the solar radiation pressure.

Due to the limited tracking geometry, we were not able to estimate the full state vector of the satellite. In fact ranging measurements from one station only do not allow the estimate of the eccentricity and the inclination of the satellite |4|, for this reason we fixed these elements at the a priori values provided by ESA.

Table 1 - GEODYN setup for the ECS 5 orbit determination

ECS 5 CONSTANTS		
	Satellite Mass	656.5 kg
	Satellite Area	20.42 m^2
	Nominal Reflectance Coefficient	1.2
KINEMATICAL MODEL		
	Precession	IAU 1976
	Nutation	IAU 1980
	Lunar and Planetary Ephemeris	JPLDE118
	Reference System	1950.0
	Earth Semi Major Axis	6378144.11 m
	Flattening	1/298.255
DYNAMICAL MODEL		
	Gravity field	GEM-T1(8x8)
	h_2, l_2	0.6040, 0.0852
	GM	$3.98600440 \times 10^{14}$ m^3/s^2
	Gravity from Sun and Moon	applied
METHOD OF ANALYSIS		
	Single-arc with variable length	
COMMON PARAMETERS ESTIMATED IN THE SOLUTION		
	No common parameters estimated in the solution	
ARC PARAMETERS ESTIMATED IN THE SOLUTION		
	- Four Keplerian elements, Eccentricity and Inclination fixed at the a priori values	
	- Solar radiation coefficient	

The entire data set has been divided into two subsets which were analyzed separately. The first subset lasts from the 29th of January to the 7th of February at 00:00 UTC, while the second one lasts from the 7th of February at 12:30 UTC to the end of the data collection. The analysis of the entire data set was not possible because some manoeuvres have been made on the satellite. Furtherly in the morning of the 7th of February some improvements in the data acquisition system were applied.

Some results from data analysis are summarized in table 2, where in the first column DATA1 refers to the first data subset and DATA2 to the second.

Table 2 - Results of ECS 5 orbit determination

	N. of obs.	Accepted obs.	Mean of orbit resid. (m)	RMS of orbit resid. (m)	RMS of poly.-resid. (m)
DATA 1	4000	3995	0.0	1.6	1.4
DATA 2	6275	6147	0.0	1.1	0.64

The second column gives the total number of observations relevant to the two data sets, while the third refers to the observations not edited after fitting the range data with the estimated orbit of the satellite. The fourth and the fifth columns give respectively the average and the RMS of the orbit residuals. Let us note that the orbit fit seems quite good. The RMS, given in the sixth column, are referred to the residuals obtained by fitting with a polynomial the orbit residuals. Therefore they give an indication of the "single shot" measurement noise. The reduction of the noise of the observations after the improvement of the data acquisition system is evident. Let us now discuss briefly about the errors associated with the estimated orbit. The RMS of orbit residuals at the 1 m level does not mean that the state vector of the spacecraft is known at the same level of precision.

The estimated formal errors in the satellite position and velocity are given in table 3. The improvement in the DATA 2 estimates is mainly due to the more robust statistics of the second data subset.

Table 3 - Scaled formal errors

	RMS of position (m)	RMS of velocity (m/s)
DATA 1	388	0.028
DATA 2	95	0.007

Table 4 shows a comparison between Telespazio and ESA estimates. The differences are of the order of few kilometers which is what could be expected taking into account the errors associated to the ESA estimates which are of the same order of magnitude.

Significant reduction of the satellite position errors could be achieved by improving the statistics and geometry of the observations (e.g. with multiple tracking stations, the use of very accurate pointing angle observations, longer tracking period etc.).

Table 4 - ESA vs. Telespazio (TPZ) estimates comparison

DATA 1

	ESA	TPZ	TPZ-ESA
x(m)	34938980.3	34941001.7	2021.4
y(m)	-23574697.3	-23571733.1	2964.2
z(m)	45867.6	45366.1	-501.5
$\dot{x}$(m/s)	1720.424	1720.196	-0.228
$\dot{y}$(m/s)	2549.790	2549.943	0.153
$\dot{z}$(m/s)	1.821	1.887	0.066

DATA 2

	ESA	TPZ	TPZ-ESA
x(m)	38164955.1	38160760.5	-4194.6
y(m)	-17887232.7	-17895895.3	-8662.6
z(m)	30435.4	30611.6	176.2
$\dot{x}$(m/s)	1305.610	1306.237	0.627
$\dot{y}$(m/s)	2785.039	2784.751	-0.288
$\dot{z}$(m/s)	0.679	0.635	-0.044

The results so far obtained are very promising. They suggest that the method of passive TV ranging is a quite good method for geostationary satellite tracking with an intrinsic precision better than 1 m. This precision is impressive, if compared with that obtained with the actual ranging based on VHF or S Band tracking, in particular considering the simplicity and economy of the used system.

4 - Use of Telespazio position data to correct the synchronization results

The position data of ECS 5 obtained from the range measurement with the procedure explained above, have been used to correct the synchronization data obtained for the period January 30 - February 20, 1990 for some of the laboratories involved, namely TUG, STA, VSL. The results, which are reported in Fig. 10, have also been corrected for the differential receiving delays: an accurate evaluation was possible in the case of TUG, STA and VSL because the GPS measurements were used to estimate the difference between the time scales and consequently to compute the mean differential delay for a satellite position given by GEODYN program. The GPS comparisons between the aforementioned laboratories have also been reported in Fig. 10.

In table 5 some figures are given to compare the performances of the ECS 5 synchronization system to the GPS common view:

Table 5 - ECS 5 versus GPS time scales comparisons - February 1990

	UTC(IEN)-UTC(TUG)	UTC(IEN)-UTC(VSL)	UTC(IEN)-UTC(STA)
mean rate (GPS)	+35 ns/d	+15 ns/d	+13 ns/d
mean rate (ECS 5)	+48 ns/d	+11 ns/d	+23 ns/d
std. dev. of residuals	83 ns	78 ns	100 ns
n. of samples	95	36	32

From the mean rates reported above, it can be seen that frequency comparisons with an accuracy of some parts in 10^{-13} for observation times of 20 days have been achieved in this synchronization experiment.

5 - Conclusions

The results obtained in the synchronization experiment between some European Laboratories, based on the passive television method applied to the signals received from Eutelsat I-F5 (ECS 5) geostationary satellite and on range measurements from one station, always using TV signals, have shown that:

- it is possible to determine the satellite position from the range measurements with an accuracy of 1 km or better;
- using these position data to correct the synchronization results, time comparisons on long baselines with a precision of 100 ns (1 σ) can be performed;
- an accuracy of some parts in 10^{-13} in frequency comparisons can be achieved, over observation times of 20 days, using the same correction procedure.

References

|1| J. Tolman, V. Ptacek, A. Soucek, R. Stecher: Microsecond clock comparison by means of TV synchronizing pulses - IEEE Transactions on Instrumentation and Measurement, Vol. IM-16, n. 3, September 1967.

|2| O. Buzek, J. Cermak, J. Vondrak, F. Cordara, V. Pettiti, P. Tavella: Synchronization of time scales by television method using ECS satellites - Preliminary results - Proc. of 3rd European Time and Frequency Forum, pp. 204-214, Besançon, March 1989.

|3| V. Pettiti, F. Cordara, P.G. Galliano: Status report on a synchronization experiment between European Time Scales using ECS geostationary satellite - Proc. of 21st Annual Precise Time and Time Interval Applications and Planning Meeting, pp. 323-340, Redondo Beach, November 1989.

|4| E.M. Soop: Introduction to geostationary orbits - European Space Agency, SP-1053, November 1983.

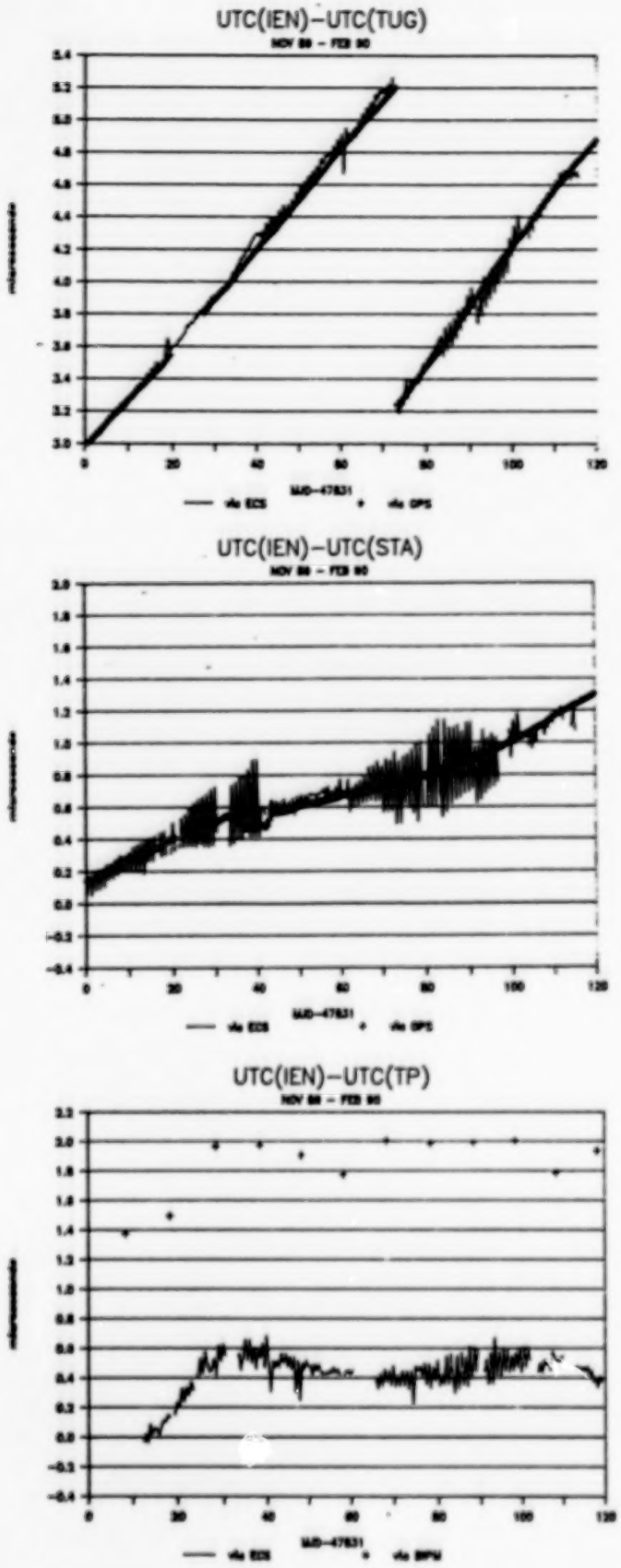


Fig. 1 – Time scales comparisons by means of ECS 5 satellite.

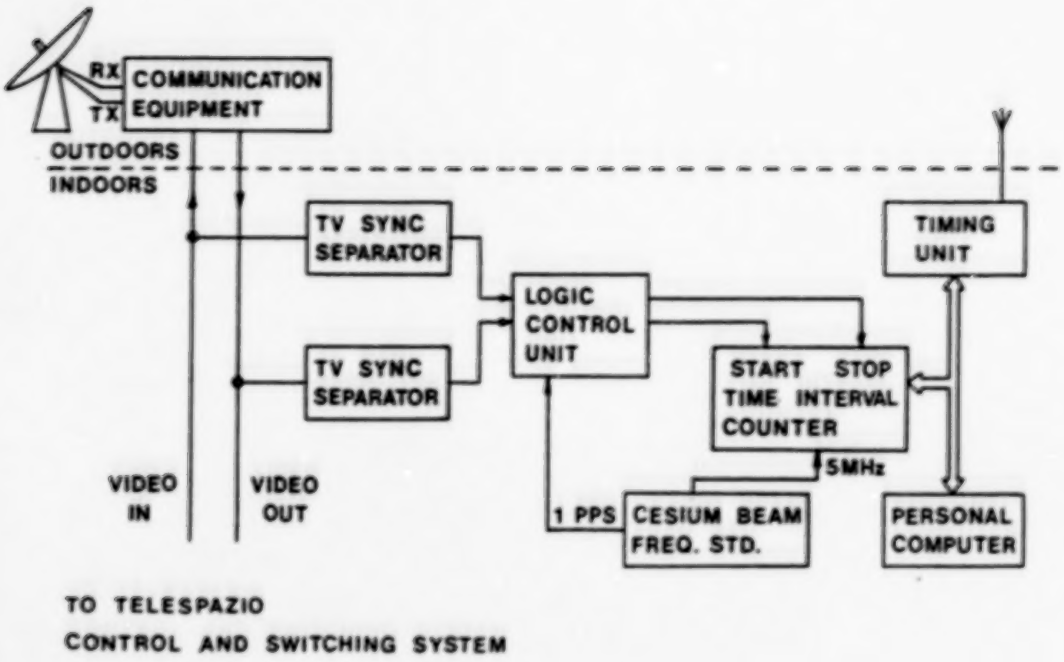


Fig. 2 - Equipment set-up for range measurements at Fucino Telespazio groundstation.

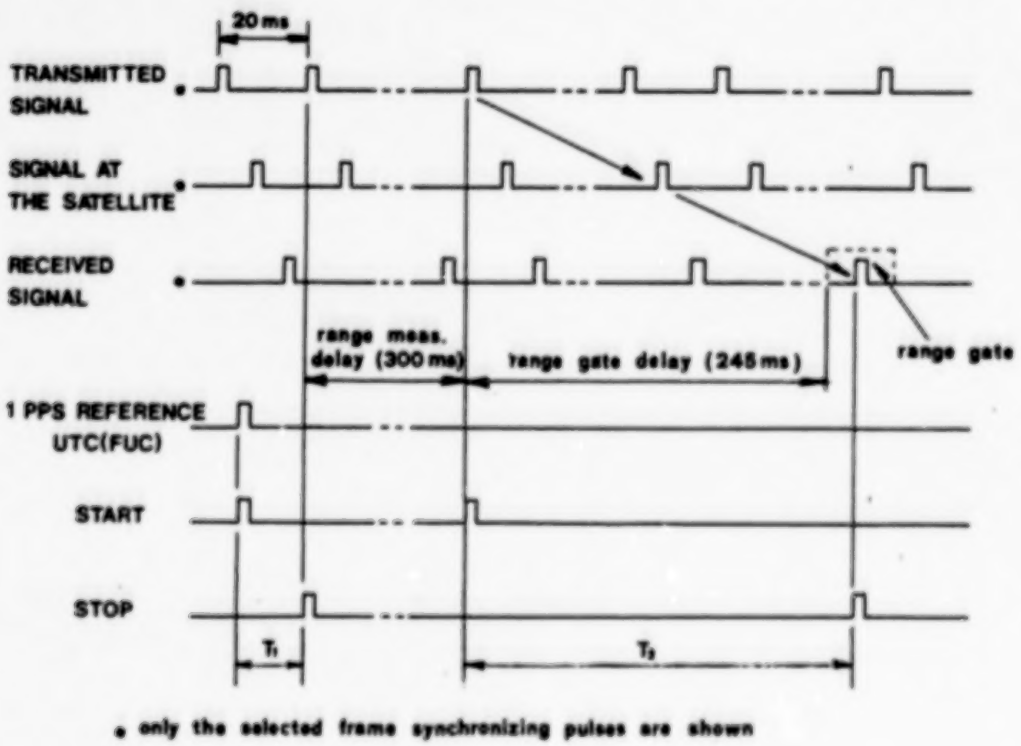


Fig. 3 - Range and syncronization measurements sequence.

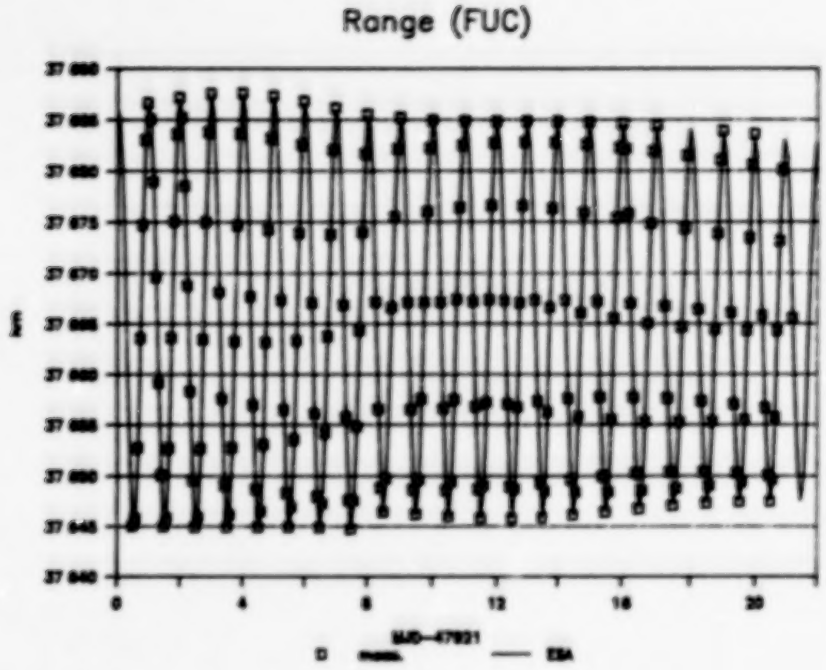


Fig. 4 - ECS 5 range measurements vs. computed range data (ESA) - February 1990.

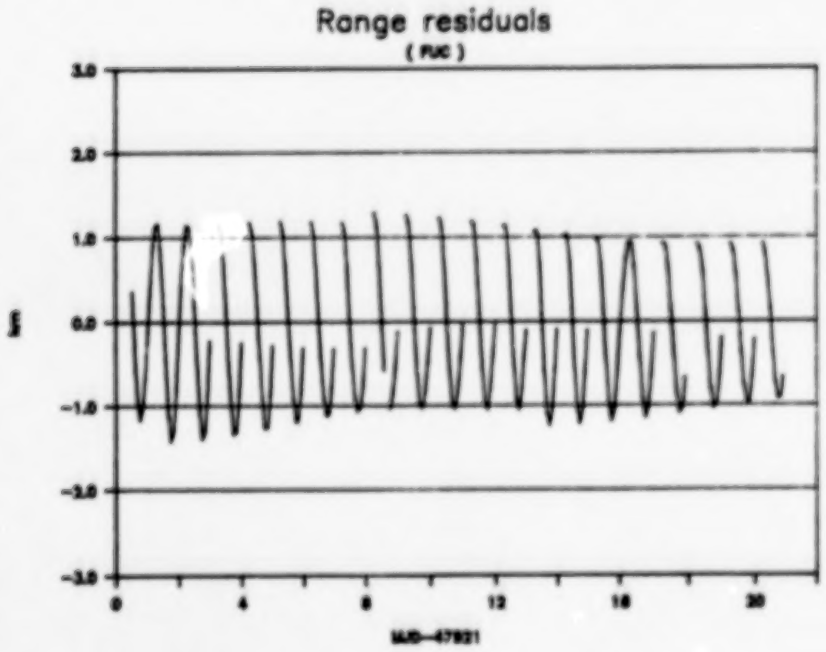


Fig. 5 - ECS 5 range residuals - February 1990.

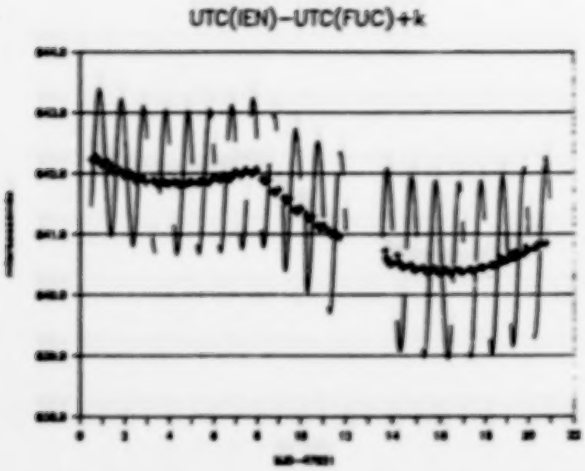


Fig. 6 - IEN-FUC synchronization results - February 1990 (+ averaged values).

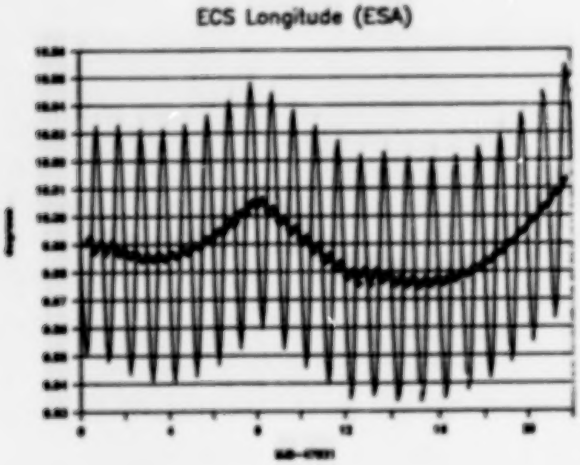


Fig. 7 - ECS 5 longitude from ESA - February 1990 (+ averaged values).

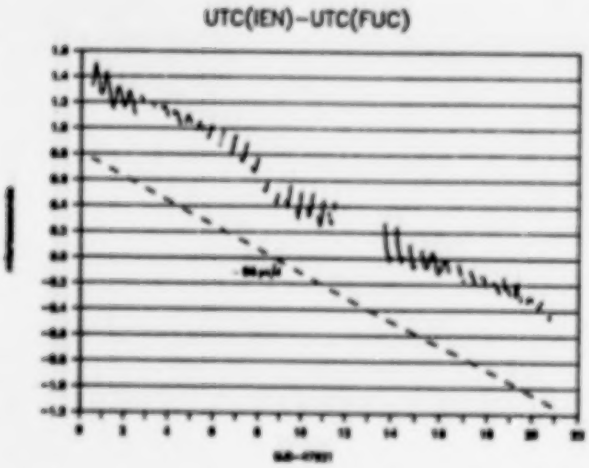
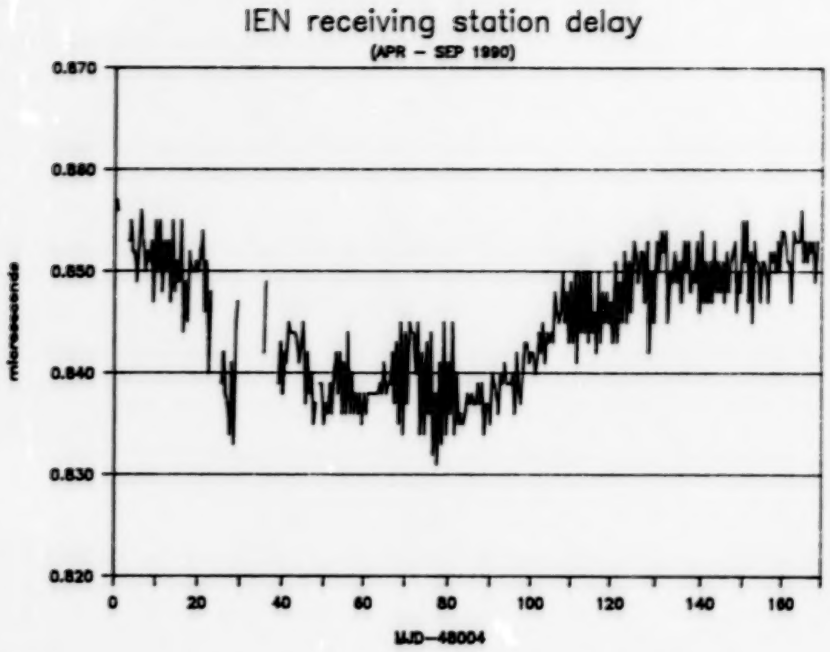


Fig. 8 - IEN-FUC corrected for the effect of longitude variations (— mean rate of the Fucino clock).



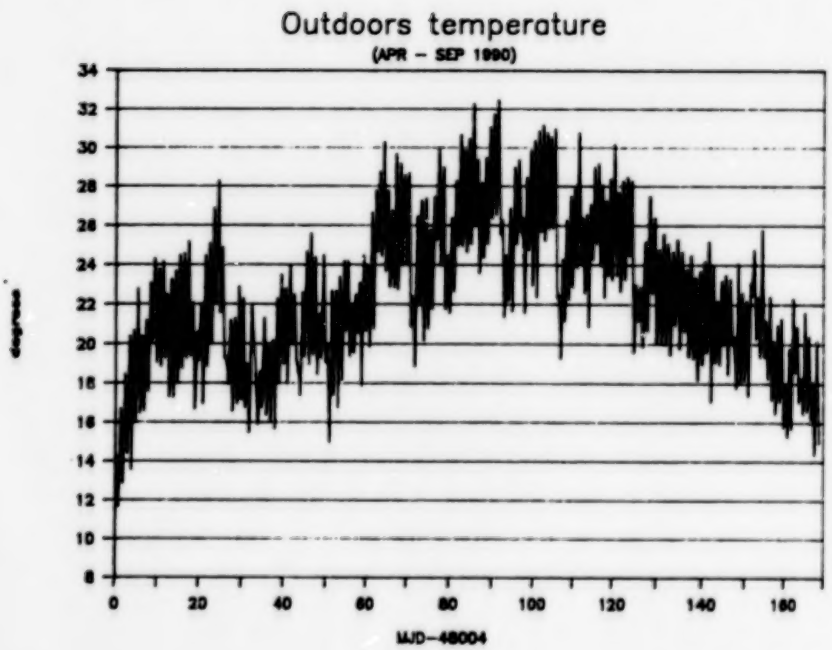


Fig. 9 - Long term delay measurements of the IEN receiving station.

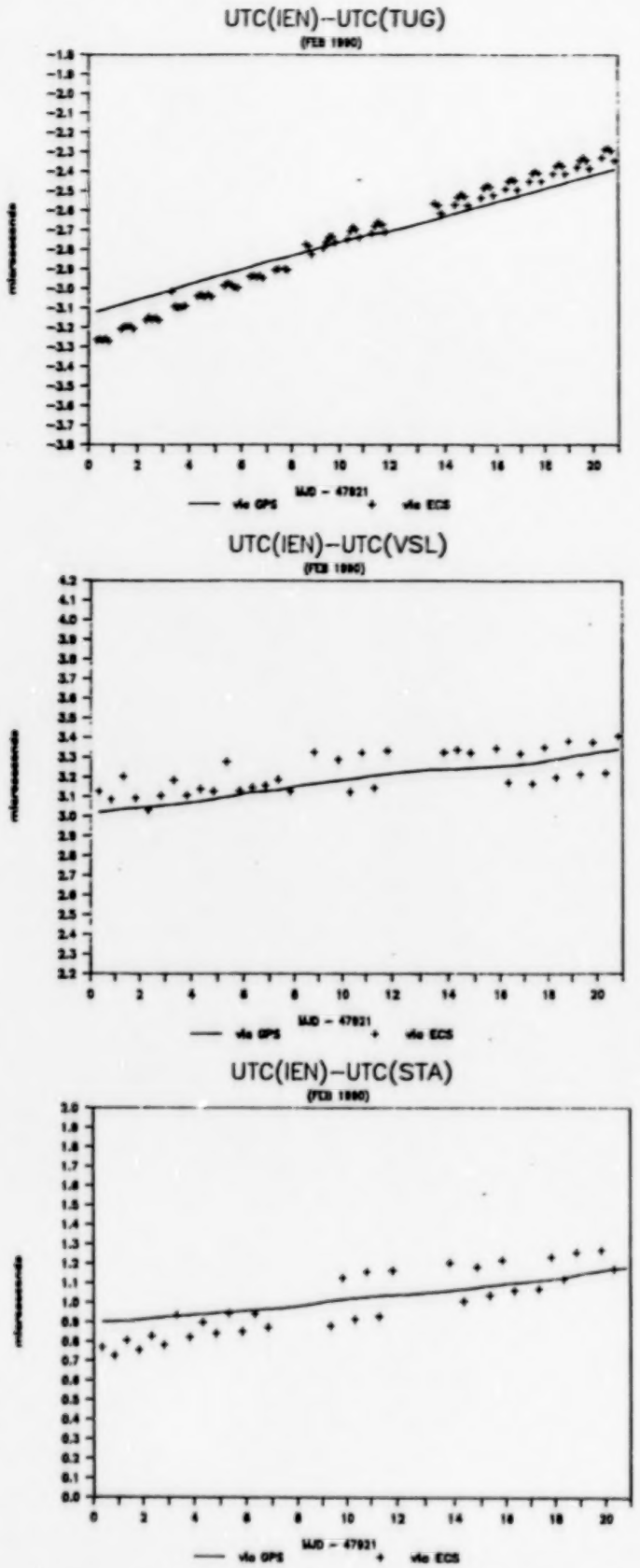


Fig. 10 - ECS 5 synchronization results corrected for Telespazio position data.

A HIGHLY STABLE CRYSTAL OSCILLATOR APPLIED TO GEODETIC VLBI EXPERIMENT

Hitoshi KIUCHI and Jun AMAGAI
Kashima Space Research Center, Communications Research Laboratory
893-1 Hirai, Kashima, Ibaraki 314 Japan

ABSTRACT

Instead of a hydrogen maser, a carefully selected Crystal oscillator which is phase locked to a Cesium (Cs) frequency standard for time range of more than 100 seconds is adopted to the time and frequency standard of a geodetic VLBI experiment. The domestic VLBI experiment with 55km baseline using the Crystal oscillator at one end was made in Japan and the obtained error of the baseline vector components were 4cm, and that of the baseline length was 3cm. This system may be operated after only 2 hours warm up. These results coincides with those of conventional geodetic Laser ranging and VLBI using a hydrogen maser within the formal error. A VLBI experiment with over 1000km baselines were carried out successfully from October 1988, and over 11000km baseline between Japan and Antarctica was carried out successfully in January 1990.

1. INTRODUCTION

Very long Baseline Interferometry (VLBI) is one of the most accurate modern positioning techniques. Although it was initially developed by astronomers as a tool to improve the angular resolution of radio telescopes, it was realized that it would also be an ideal geodetic instrument. In usual VLBI experiments made for geodetic purpose, each antenna receives signals from a radio source for a hundred seconds or more in one observation. This observation is repeated changing between dozen or more radio sources during a nominal 24-hour session. A single experiment therefore consists of a hundred or more observations. The frequency standard of VLBI must be stable over a long time range (more than 100sec) as well as a short range (less than 100sec). Short time range stability is essential for maintaining the coherence and long time stability is necessary for regulating the time of observations. The hydrogen maser oscillator satisfies these requirements and this is a reason for its use for VLBI. However, resent technology has improve the stability of Crystal oscillator (AT-cut resonator of the BVA style). The possibility of Crystal oscillator as a frequency standard of VLBI will now be discussed. A hydrogen maser frequency standard with stability better than 10^{-14} has been playing an important role in the VLBI experiments. Maintaining the coherence of the receiving signal of each station is one of the most important factors in VLBI data acquisition. While the stability of the atmosphere which causes phase scintillation, is about 10^{-13} as measured by VLBI. The atmospheric scintillation degrades the coherence of VLBI data, which is independent of the phase fluctuation of hydrogen maser. Research work in the Crystal oscillators

has made remarkable progress in recent years, and the stability of the selected Crystal oscillators reaches $\sigma y(\tau < 100sec) = 3x10^{-13}$, a value comparable to the stability of the atmosphere. Therefore the potential for obtaining a good fringe by using the Crystal oscillator instead of the hydrogen maser exists. The main purpose of the new frequency reference system development was to contract a highly transportable time and frequency standard for VLBI, and in our case we adopted a Crystal oscillator for VLBI frequency reference. The Crystal oscillator has advantages for space technology application (Space VLBI etc.), and transportable VLBI because it satisfies the requirements of small size, light weight, and aseismatic structure.

A new frequency system which constructed a Crystal oscillator whose phase is locked to that of a Cesiumfrequency standard (Crystal-Cesium system) has been developed for time ranges of over 100 seconds, as the stability of Cesium frequency standard is better than that of a Crystal oscillator for long term ranges. First of all, zero and short baseline interferometer experiments were carried out to assess the performance of the Crystal-Cesium system and to find the optimum data analysis method for using Crystal-Cesium system. Secondly, the 55km baseline (a reference baseline in Japan, which has been measured 5 times by VLBI and other methods) VLBI experiment was made in order to provide a comparison with conventional results and to determine optimum integration time for this system. As a result of these experiments, the baseline vector was obtained with an error of 4.3cm on each component, and 3.4cm on its length.

2. Potential of the Crystal oscillator as the VLBI frequency standard

The stability of frequency standard in a short time period is an important factor in maintaining the coherence of received signals in VLBI experiments. However VLBI observation from the ground always suffer from the atmospheric scintillation effect, resulting in a loss of coherence. Therefore the stability of the atmosphere determine the limit of requirement for that of frequency standard in a short time range. The stability of atmosphere was measured to about $1x10^{-13}$ at 100sec by domestic VLBI (Fig.1), this result being almost same as those of Rogers and our measurements (Table 1). The stability of hydrogen maser is $1x10^{-14}$ at 100 sec and it is stable enough compared with the atmosphere, while recent technology progress has provided a stability of $3x10^{-13}$ for Crystal oscillators, which is almost the same as the atmosphere's stability. A Crystal oscillator is strongly proposed as a frequency standard for VLBI in a short time range.

The requirements for the VLBI frequency standard are as follows;

(1) To keep the signal coherence during integration time.

(2) Phase variance of the clock instability should be better than accuracy of the measurement.

The coherence loss Lc due to the instability of frequency standard in 100sec integration time is estimated by Eq.1.

$$Lc=\omega o^2(\alpha p/6 + \alpha f/12*T + \sigma y^2/57*T2) \quad \text{.....} \quad (1)$$

where Lc: loss of coherence

ωo: angular frequency of local oscillator

(8080MHz in X band) [rad/sec]

αp: Allan variance of white phase noise at 1 sec

$(1x10^{-13})^2$: hydrogen maser at Kashima

αf: Allan variance of white frequency noise at 1 sec

$(7x10^{-14})^2$: hydrogen maser at Kashima

σy^2:Constant Allan variance of flicker frequency noise

$(5.5x10^{-15})^2$: hydrogen maser at Kashima

$(3x10^{-13})^2$: selected Crystal

T: Integration time [sec]

The stability of the hydrogen maser at Kashima is shown in Fig.2. According to Eq.1, the calculated losses for hydrogen maser and Crystal oscillator at an integration time of 100sec are $1.23x10^{-4}$ and 0.041 respectively, and compared with the loss due to 1 bit sampling (Loss=0.36) at data acquisition they are small enough to be ignored. Long term stability of the frequency standard is necessary for regulating the results of each observation when analyzing them. Though the long term stability of the Crystal oscillator is not acceptable for VLBI, the high performance Cesium frequency standard has a superior stability in a long term ($\sigma y(\tau>100) <= 3x10^{-13}$). But if only Cesium is used in VLBI experiments, it is impossible to keep the coherence of the X band signal, as the stability of Cesium is worse than $\sigma y=10^{-12}$ in short term during signal integration. Hence a frequency standard, which has the stability of the Crystal in a short time range and that of Cesium in a long time range, is needed to satisfy the requirements of VLBI and can be realized by using a Crystal oscillator with its phase locked to the Cesium frequency standard in a long time range.

The required stability of this equipment is the shaded area in Fig. 3. Stability measurements with Zero Baseline Interferometry and the short baseline VLBI experiment were made.

3. The stability measurement with Zero Baseline Interferometry

Stability was measured with Zero Baseline Interferometry (ZBI) (Fig.4). This method used the K-3 VLBI system which was developed at CRL. System noise of this method is very low and this measurement is realistic method for VLBI experiments, because the performance of the oscillator is measured in the same configuration. In VLBI, the geodetic reference point is the intersection point of axes of Azimuth(Az) and that of Elevation(El), and is a stationary point. In ZBI method, both receiving systems are mounted on a same antenna. In this case, the baseline length is zero, because the geodetic reference point is common for both systems.

The common noise generated by Noise Diode is injected to both X band feeder systems. The reference signal is supplied to one system by a hydrogen maser and to the other by the test

frequency system(DUT : Device Under test). A cross correlation was made between the two systems in real time by using the K-3 VLBI correlation processor. Then the resulting stability was equivalent to both references. In this case, the DUT's are a Cesium, a Crystal and the Crystal-Cesium system. This method is a modified DMTD (Double Mixer Time Difference) method. The results are shown in Fig.5, which shows the detected fringe phase in the X band. It is possible to find out the long term characteristics in stability of the frequency standard. The result of using Crystal oscillator (Fig.5a) shows random walk over the long term caused by the external temperature change. When using Cesium frequency standard (Fig. 5b), the fringe phase is stable in the long term. And in case of using a Crystal-Cesium system frequency standard (Fig.5c), the fringe phase is as stable as when using only a Cesium frequency standard. Fig.6 shows the observed delay in X band. This detected fringe phase is the respective instrumental delay of two systems. It is possible to find out the capability for keeping coherence. When using Crystal oscillator (Fig.6a), it is possible to get a good fringe, and the determined delay is stable. When a Cesium frequency standard is used (Fig.6b), the determined delay changed as much as 100 nsec, and thus it is impossible to keep the coherence in the X band. This means the Cesium frequency standard is not suitable for the frequency standard of VLBI in the X band. The results from the Crystal-Cesium system (Fig.6c) have the same characteristics as those from when only the Crystal oscillator was used.

Fig.7 shows that the coherence depends on integration time, and it is calculated directly from the correlated data. It is possible to tell coherence from this Figure.

Fig.8 shows the stability of the Crystal-Cesium system, which is measured by the detected fringe.

These results show that the Crystal oscillator has a good short term stability but it is inferior to the Cesium frequency standard in the long term, while a Cesium standard has a excellent long term stability but it is unusable for X band VLBI experiments. The Crystal-Cesium system is very close to meeting requirements.

4. Estimation of the optimum integration time for the Crystal-Cesium system

The SNR of VLBI is calculated by Eq.2.

$$SNR=[\pi*Sc/8k]*[D1*D2*SQRT(\eta1*\eta2)/SQRT(Ts1*Ts2)]*SQRT(2BT)*\rho \quad .....(2)$$

where Sc : correlated flux of source k : Boltzman constant
D : diameter of the antenna η : antenna efficiency
Ts : system temperature B : band width
T : integration time

$\rho=(2/\pi)*0.6*SQRT(3/4)$

: : :..... Fringe stopping loss
: :..... Scintillation loss
:..... 1 bit sampling loss

The coherence loss is expressed by Eq.1. There is an optimum integration time which gives the maximum SNR*coherence, and an estimate of this suitable integration time is shown in Fig.9. Fig.9 (a) shows the estimated SNR*coherence were a fixed Cesium stability ($\sigma y(1)=3x10^{-12}$) and variable Crystal stability are used. Fig. 9(b) shows the opposite situation (fixed Crystal stability and variable Cesium stability), where fixed Crystal stability is $\sigma y(1)=4x10^{-13}$. The optimum integration time depends on the stability of the Crystal oscillator and that of the Cesium frequency standard. When using high performance commercial Cesium, the SNR*coherence has a maximum value at about 120 sec integration time. As in this case the clock error is less than 0.05 nsec, it can be said that the optimum integration time is 120sec for this system. It is possible to use the data with SNR better than 7 for VLBI data analysis. In other words, the Crystal-Cesium system, which can get SNR of better than 7 in 120 sec integration time can be used with the VLBI antenna pair.

5. The 55km baseline experiment

An experiment with the 55km baseline, which is regarded as a reference VLBI baseline in Japan, was made immediately after JEG-5(fifth Geodetic VLBI experiment between Tsukuba GSI : Geographical Survey Institute, and Kashima CRL using hydrogen masers at both stations) and the schedule of JEG-5 was repeated, in order to avoid problems arising from the change of the propagation media error. A Crystal, a Cesium frequency standard and a PLL circuit were transported from Kashima to Tsukuba 2 hours before the start of the experiment. The 26m Az-El type Radio telescope at CRL Kashima and the 5m Az-El type Radio telescope at GSI Tsukuba were used. Both Radio telescopes are equipped with the K-3 VLBI system. A hydrogen maser frequency standard is used as the reference signal at Kashima station and the Crystal-Cesium system is used at Tsukuba station. Other parts of the system were the same as the JEG-5 experiment. The experiment was done for 24 hours, and the cross correlation was made in Kashima. The results are shown in Table.2. In order to compare the accuracy dependence for the integration time, the results for the following three cases were analyzed.

case I : Same integration time as JEG-5
(80 to 300sec integration time which depends on the source flux)
case II : Integration time fixed for 120sec.
case III : Integration time fixed for 60sec.

The most accurate result is obtained with a 120sec integration time (case II). In case I, some correlated peak (fringe phase) on delay rate is detectable, and shows that the rate changed within the integration time. In case III, it is impossible to get SNR better than 7 at the weak radio sources. The difference between the result with the hydrogen maser(JEG-5) and that of the Crystal-Cesium system (case II) is less that 4.3cm in baseline vector and 3.4cm in baseline length.

6. Application of the Crystal-Cesium system to the 1000km+ baseline VLBI experiments

The over 1000km baseline VLBI experiments were made from October 1988. The first experiment between Kashima and Wakkanai, the northernmost part of Japan. In this experiment, the highly transportable VLBI station which consists of a 3m antenna, the antenna control unit, the K-4 VLBI system and the Crystal-Cesium system, was operated in Wakkanai. This system is the smallest VLBI data acquisition system in the world. Generally the measured accuracy of VLBI worsens as antenna size decreased, but this system has overcome the problem through the wide bandwidth receiving. The receiving bandwidth (273MHz effective band width) is twice as wide as the normal X band bandwidth (128MHz) in CDP experiment. The K-4 VLBI system is a data acquisition system which was developed at CRL for application in transportable VLBI station. The direction of the baseline vector was approximately North-South. Good fringes and the good results were obtained from this system. The baseline vector was obtained with errors of 5.1cm in the X, 3.8cm in the Y, 6.2cm in the Z components, and the an error of 1.5cm in its length on VLBI coordinate. The errors of 1.4cm in the North-South component, 1.0cm in the East-West component (horizontal components) and 8.7cm in vertical component were obtained. The results show that sensitivity in horizontal components is good, making analysis of plate motion possible, and also shows the effectiveness of the Crystal-Cesium system for VLBI frequency standard even for VLBI experiments with baselines over 1000km.

In January 1990, the Antarctica VLBI was carried out. The equipments were same as the Wakkanai VLBI experiment eliminate the antenna system. The Crystal-Cesium system was operated in Antarctica, and we can get the good geodetic results. The baseline vector was obtained with errors within 20cm.

7.DISCUSSION & CONCLUSION

Instead of a hydrogen maser, a carefully selected Crystal oscillator which is phase locked to a Cesium frequency standard for time ranges 100 seconds is adopted to the time and frequency standard of a geodetic VLBI experiment. The stability of the atmosphere is about 10^{-13}. The atmospheric scintillation degrades the coherence of the VLBI data, which is independent of the phase fluctuation of hydrogen maser. It is impossible to avoid to this effect even if a hydrogen maser is used. Research work in the Crystal oscillators has made remarkable progress in recent years, and the stability of selected Crystal oscillators reaches 3×10^{-13}, a value comparable to the stability of the atmosphere. Therefore the potential for obtaining good fringes by using the Crystal oscillator instead of the hydrogen maser exists. But the Crystal oscillator is inferior to a Cesium frequency standard in long term stability. A frequency standard, which has the stability of the Crystal in a short time range and that of Cesium in a long time range, is needed to satisfy the requirements of VLBI and can be realized by using a Crystal oscillator with its phase locked to the Cesium frequency standard in a long time range. The main purpose of the new frequency reference system development was to contract a highly transportable time and frequency standard for VLBI. The

Crystal oscillator has advantages for space technology application (Space VLBI etc.), and transportable VLBI because it is satisfies the requirement of small size, light weight, and aseismatic structure.

This system can be used for VLBI frequency standard, and it has advantages for use with a transportable VLBI system, but its accuracy is worse than that of a hydrogen maser system. Although ambient temperature control was not considered, external temperature control is desirable to keep the stability of the Crystal in Flicker in using the Crystal oscillator, as it has a strong dependency on temperature. We expect to develop the Crystal oscillator which has a stability better than 1×10^{-13}. The coherence loss caused by this stability is 0.0045, which is small enough for keeping coherence.

The domestic VLBI experiment with 55km baseline using the Crystal oscillator at one end was made in Japan and the obtained error of the baseline vector components were 4cm, and that of the baseline length was 3cm. This system may be operated after only 2 hours warm up. These results coincide with those of conventional geodetic Laser ranging and VLBI using a hydrogen maser within the formal error. A VLBI experiment using this system with over 1000km baseline was carried out successfully in Oct. 1988 and over 11000km baseline between Japan and Antarctica was carried out successfully in Jan. 1990.

ACKNOWLEDGEMENT

The Crystal oscillator was specially selected by the OSCILLOQUARTZ company in Switzerland for our experiment. We would like to express our thanks to Dr. Schlueter, the director of OSCILLOQUARTZ. We are indebted to the staff members of Geographical Survey Institute in the domestic experiment.

REFERENCE

[1] Rogers, A.E.E.; "The sensitivity of a Very long baseline interferometer", Radio Interferometry Techniques for Geodesy, NASA Conference Publication 2115, 1980.

[2] Kiuchi,H., J. Amagai, S. Hama, T. Yoshino, N. Kawaguchi, and N. Kurihara; "Instrumental Delay Calibration by Zero Baseline Interferometry for International VLBI Time Comparison". J. Rad. Res. Labs., 34, 143, 115-139, Nov. 1987.

[3] Amagai, J., H. Kiuchi, and N. Kawaguchi; "Short baseline experiment using the highly transportable VLBI station", IEEE-IM Special issue, Apr. 1989.

[4] Rogers, A. E. E. ; "Coherence Limits for Very-Long-Baseline Interferometry", IEEE trans., IM-30, 4, 283-286, Dec. 1981.

[5] Kawaguchi, N. ; "Coherence loss and delay observation error in Very-Long-Baseline Interferometry" , J. Rad. Res. Labs., 30, 129, 59-87, Mar. 1983.

[6] Morikawa, T., Y. Ohta, and H. Kiuchi; " Development of hydrogen masers for K-3 VLBI system". PTTI, 1984.

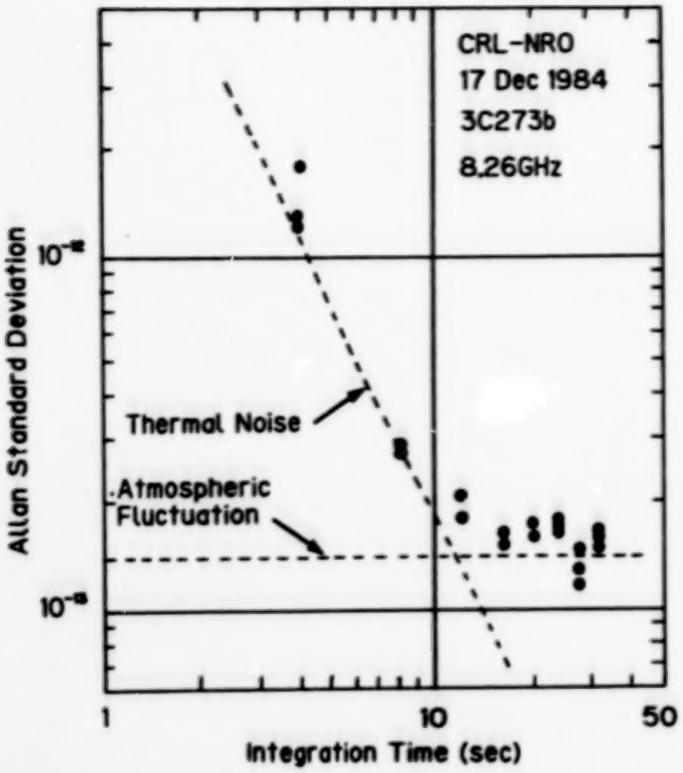


Fig. 1 Atmospheric fluctuation in Allan standard deviation

This is the result of the domestic VLBI between CRL-NRO (Nobeyama Radio Observatory) in Dec. 1984. X-axis shows the integration time and Y-axis shows the stability in Allan variance.

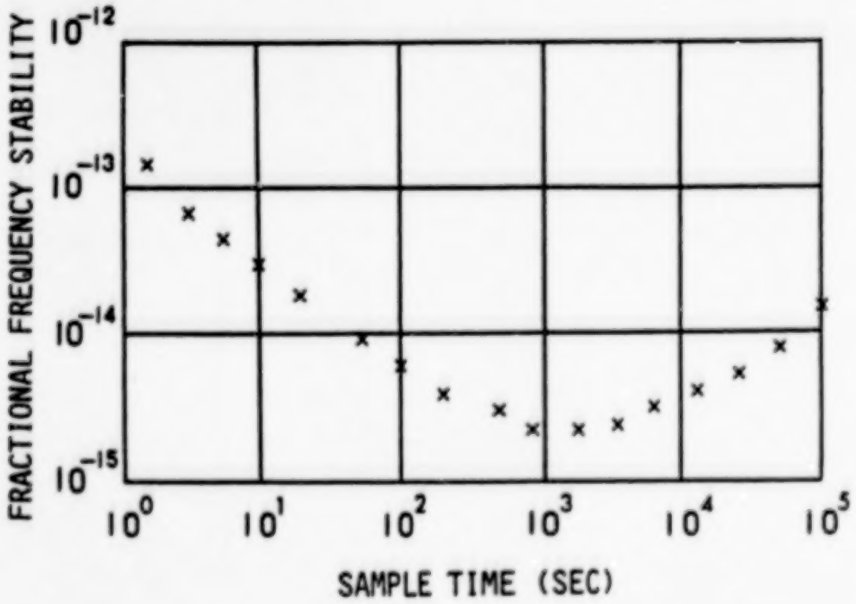


Fig. 2 Stability of the hydrogen maser in Kashima station

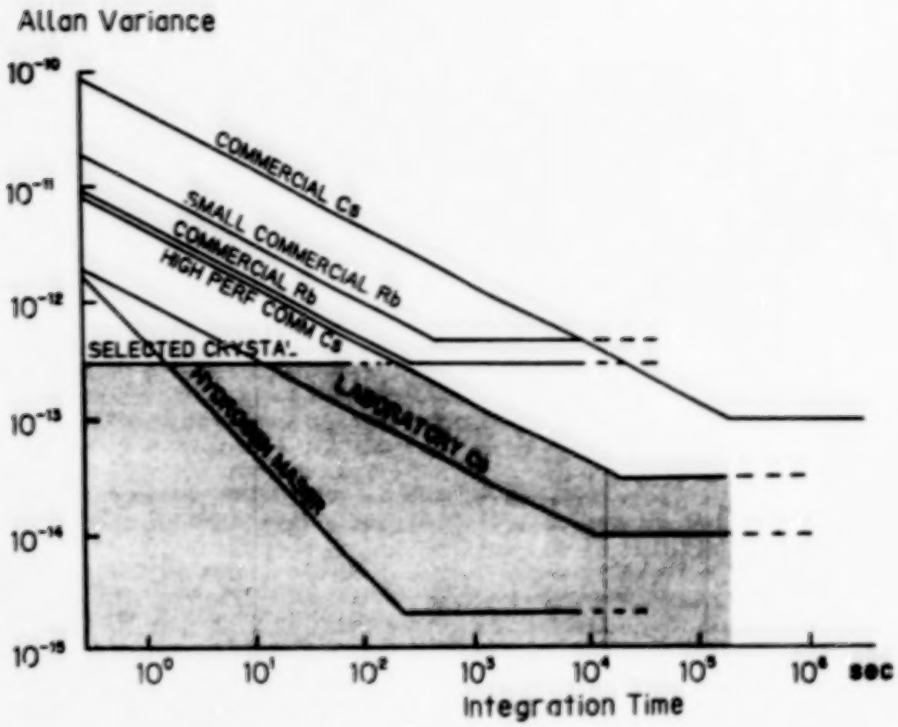


Fig. 3 Required stability



Fig. 4 Block diagram of the stability measurement system

BLANK

PAGE

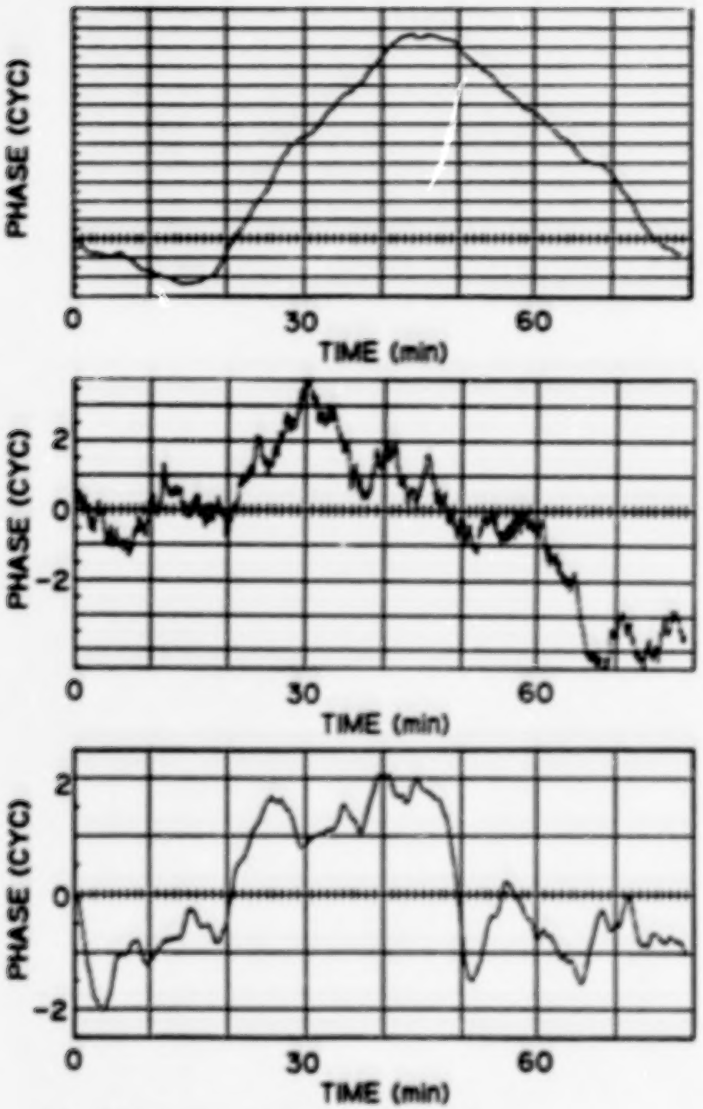


Fig. 5 Variation of the correlated phase
(in regular order)
(a) The result of using a Crystal oscillator only
(b) The result of using a Cesium standard only
(c) The result of using a Crystal-Cesium system

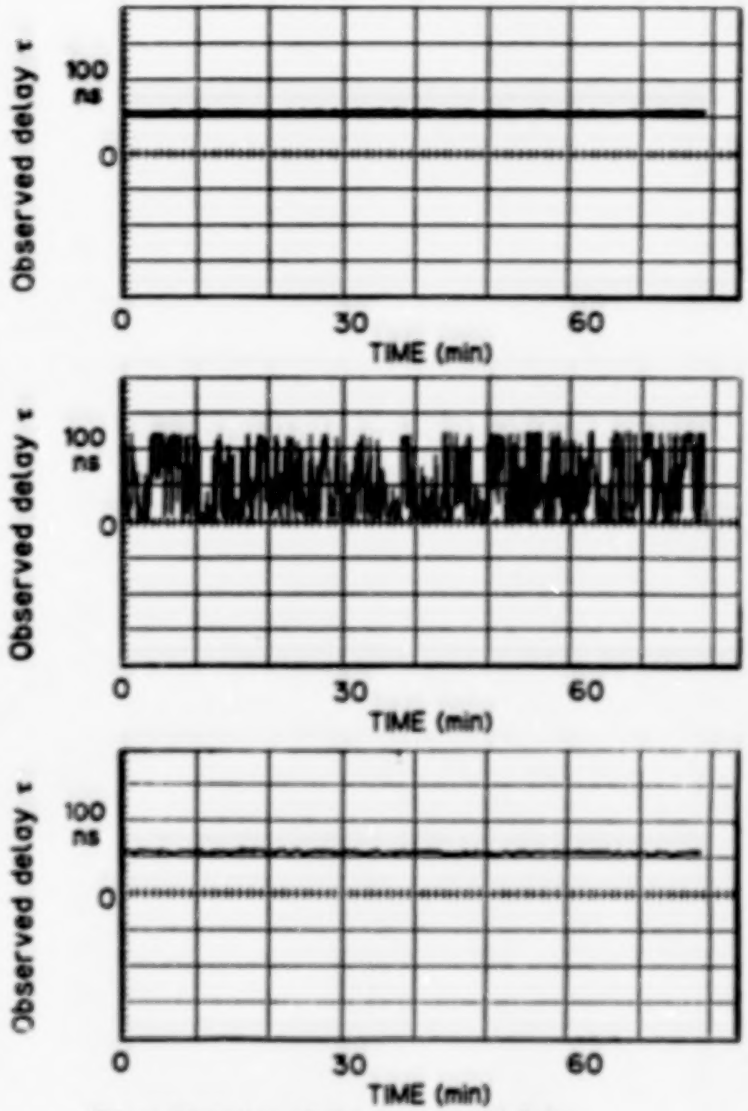
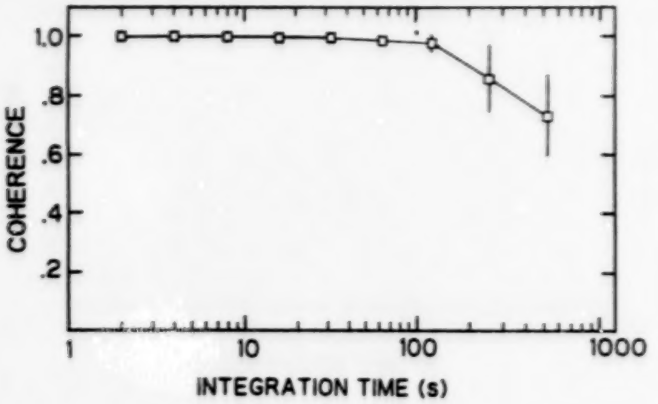
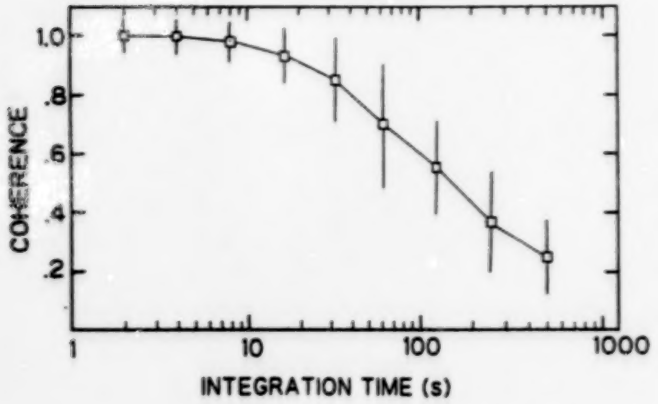


Fig. 6 Variation of the determined delay
(in regular order)
(a) The result of using a Crystal oscillator only
(b) The result of using a Cesium standard only
(c) The result of using a Crystal-Cesium system





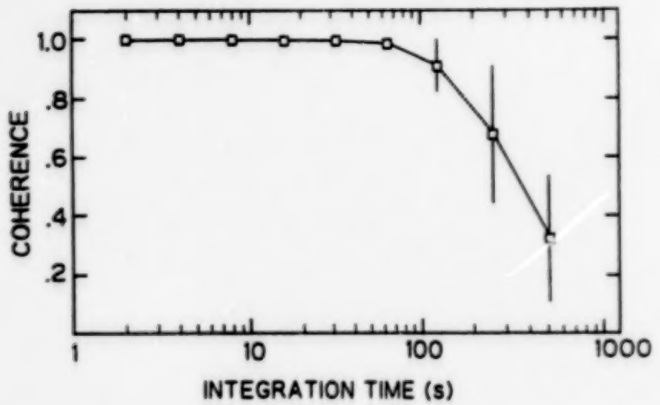


Fig. 7 Coherence
(in regular order)
(a) The result of using a Crystal oscillator only
(b) The result of using a Cesium standard only
(c) The result of using a Crystal-Cesium system

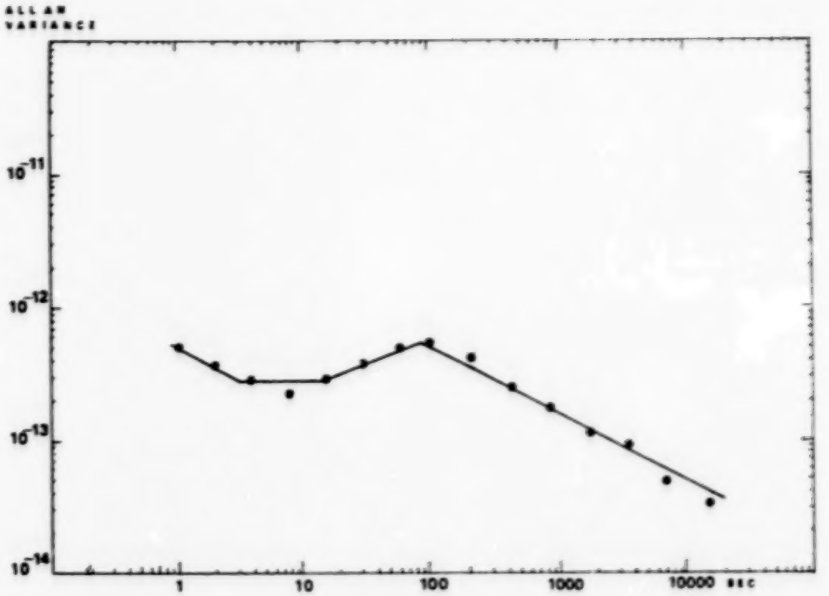


Fig. 8 Stability of the Crystal-Cesium system

Fixed stability of the Cesium Frequency Standard [$\sigma_y(\tau=1) = 3\times10^{-12}$]

Stability of Crystal oscillator $\sigma_y(\tau=1)$	Maximum SNR point in Integration Time
3×10^{-13}	190 [sec]
4×10^{-13}	184
5×10^{-13}	177
6×10^{-13}	169

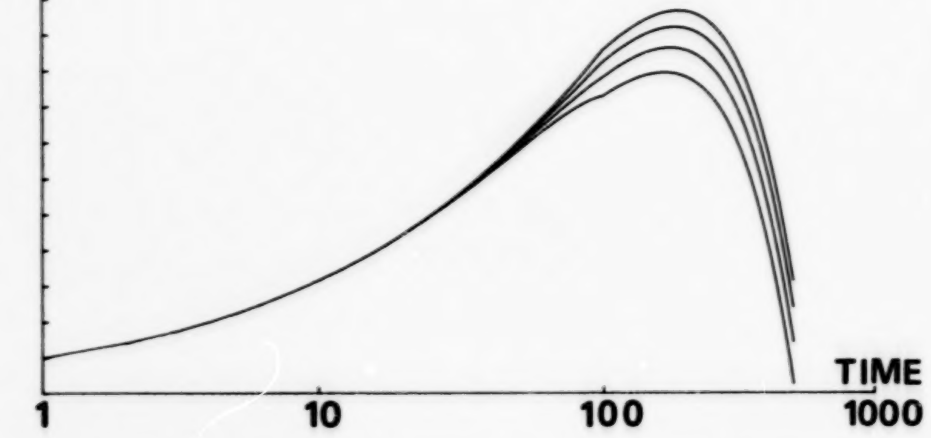


Fig. 9 (a) Estimated SNR* coherence (fixed Cesium stability)

Fixed stability of the Crystal Oscillator [$\sigma_y(\tau=1) = 4\times10^{-13}$]

Stability of Cesium Frequency Standard in $\sigma_y(\tau=1)$	Maximum SNR point in Integration Time
3×10^{-12}	184 [sec]
4×10^{-12}	118
5×10^{-12}	100

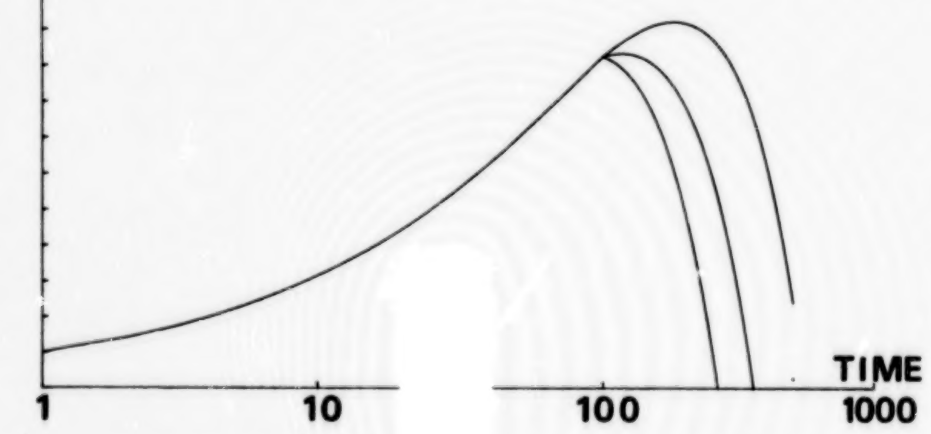


Fig. 9 (b) Estimated SNR* co[illegible]ce (fixed Crystal stability)

Table 1 Atmospheric fluctuation in Allan standard deviation

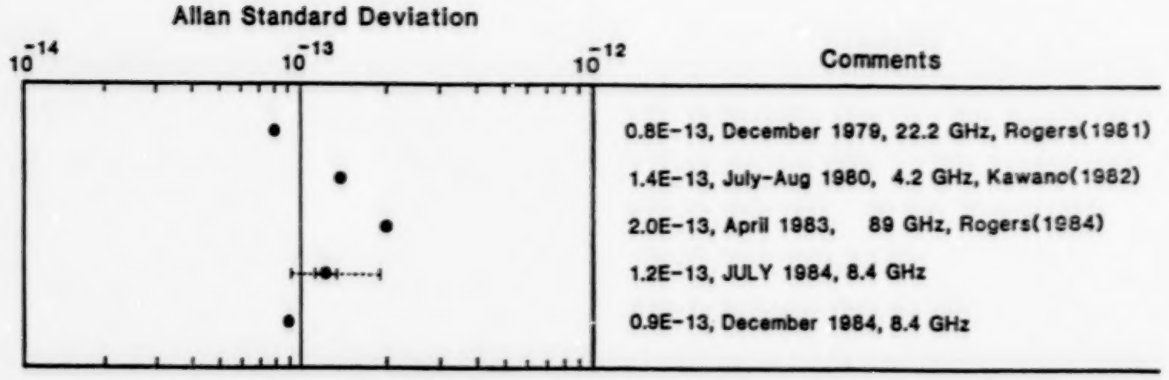


Table 2 Observed baseline components in 55km baseline experiment

	X	σ_x	Y	σ_y	Z	σ_z	B	σ_B
JEG-5	-3957171.259	0.020	3310237.094	0.017	3737709.499	0.022	54548.556	0.007
CASE-I	-3957171.290	0.089	3310237.040	0.082	3737709.506	0.093	54548.502	0.026
CASE-II	-3957171.302	0.075	3310237.085	0.061	3737709.514	0.077	54548.522	0.021
CASE-III	-3957171.377	0.112	3310237.141	0.099	3737709.596	0.110	54548.522	0.031

* in [m]

JEG-5 : Using Hydrogen maser. Integration time(80 to 300sec) is dependent on source.

CASE-I : Integration Time is same as using Hydrogen Maser(80 to 300sec).

CASE-II : Integration Time is fixed in 120sec.

CASE-III : Integration Time is fixed in 60sec.

QUESTIONS AND ANSWERS

Professor S. Leschiutta, University of Turin: First, what was the type or model of crystal oscillator used, and second, what order of servo loop and, if a simple loop, what was the time constant?

Mr. Hamma: The oscillator was a BVA oscillator from Oscilloquartz. (Editors note: The following answer was not available at the meeting, but was obtained later by private communication.) The loop was a quadratic one (second order) with $\tau_1 \simeq 100$ seconds and $\tau_2 \simeq 250$ seconds.

GPS TIME TRANSFER WITH IMPLEMENTATION OF SELECTIVE AVAILABILITY

D. W. Allan
National Institute of Standards and Technology
Boulder, Colorado 80303, U.S.A.

M. Granveaud
Observatoire de Paris
61, av. de l'Observatoire
75014 Paris, France

W. J. Klepczynski
U.S. Naval Observatory
Washington, DC 20392–5100, U.S.A.

W. Lewandowski
Bureau International des Poids et Mesures
Pavillon de Breteuil
F–92312 Sèvres Cedex, France

Abstract

The international community of time metrology is facing a major challenge with the Selective Availability (SA) degradation of GPS satellite signals. At present there are 6 Block I satellites and 8 Block II satellites operating. According to the policy of the U.S. Department of Defence the Block I satellite signals will not be degraded, but these satellites are old with a finite life. The Block II satellites, which have all been launched since 1988, were subject to Selective Availability from March 25, 1990. The effect of SA should be to limit precision to about 100 meters for navigation and 167 ns for timing.

A study has been conducted in order to understand the nature of the actual introduced degradation, and to elaborate the means of removing the effects of this degradation on time transfer. This study concerns the time extraction from GPS satellites at NIST, USNO and Paris Observatory, and the comparison of atomic clocks between these laboratories by common view approach. The results show that when using the data taken over several days the time extraction can be achieved with uncertainty of a few tens of nanoseconds, while strict common–view has removed entirely the effects of SA during the periods under study.

INTRODUCTION

Over the past ten years non–degraded GPS satellite signals have become the principal tool for national and international comparisons of atomic clocks. Using GPS, time transfer is now ten times more

accurate than it was using LORAN-C. The introduction of GPS has led to a major improvement of world wide time metrology in precision, accuracy and coverage. With GPS, time comparisons are performed with an accuracy of a few nanoseconds for short baselines (up to 1000 km) and 10 to 20 nanoseconds for intercontinental distances. This makes it possible to compare the best standards in the world at their full level of performance: for integration times of only 10 days, the frequency differences between atomic clocks are measured at the level of one part in 1014. The most recent studies[1, 2] show further improvements.

Thus, GPS has brought a major contribution to such activities as the establishment of International Atomic Time (TAI), the realisation of the NASA's JPL Deep Space Network (DSN) and the studies of millisecond pulsars. All this was done with an undegraded GPS, free of Selective Availability.

Unfortunately, since the GPS concept was born in 1973, different ways to prevent civil users having access to the entire accuracy of the system have always been under consideration[3, 4]. The type of degradation of GPS signals, called Selective Availability (SA), have now been approved. On the 25th of March 1990 SA was officially implemented on Block II satellites. The effect of SA should be of about 167 ns for timing.

The 6 Block I satellites are not affected by SA but they are old and in 1993, when GPS will be declared fully operational, these satellites will probably be turned off and the whole constellation will be composed of Block II satellites, all affected by SA. Does this represent a disaster for time metrology and the return to LORAN-C epoch? Perhaps not.

The SA affects direct access to GPS time most severely. This access is degraded by a factor of up to ten. Even with SA, however, the GPS time is distributed with uncertainty better than 1 microsecond which is satisfactory for many non-metrological applications. In addition, as this study shows it, a smoothing over a period of several days removes most of the SA effects, and reduces the uncertainty of access to GPS time to several tens of nanoseconds.

One major problem could be the impact of SA on high accuracy time comparisons. Here again an appropriate treatment of data can entirely remove the degradation of the GPS signal. The realisation of a strict common-view between two laboratories (synchronization of observations within 1 second) completely removes the phase jitter of satellite clock. The elimination of the impact of ephemerides degradation is much more arduous: this requires delayed access to precise ephemerides for correcting the degraded broadcast ephemerides.

Yet, the official implementation of SA has reserved us two pleasant surprises: as this study shows, the broadcast ephemerides appear not to be degraded, and on the 10th of August 1990 SA was removed from Block II satellites.

DEGRADATION OF GPS SIGNALS

The degradation of GPS signals is linked with the history of the development of GPS. At first the project was no more than the reservation of P-code for authorized users with ultimate uncertainty of real-time positioning of 16 m. It was intended that C/A-code would be accessible to all users and would have a capacity of 100 m for real-time positioning. After the launch of first GPS satellites it became clear that the performance of C/A-code is much better than expected: instead of the announced 100 m uncertainty, users equipped with cheap C/A-code receivers were able to easily obtain 30 m. This has lead the DoD to review its policy concerning availability of GPS to the general

public.

The concept of Selective Availability was born with the intention of degrading the positioning accuracy for Standard Positioning Service (SPS) users to 120 m[3]. All Block II satellites are subject to SA. In addition to SA, an Anti-Spoofing (A-S) mode of operation can be activated. This is a method of protecting military operations against adverse imitations of P-code by encryption of P-code. The encrypted P-code is denoted Y-code. The A-S does not affect C/A-code. Receivers equipped with the utility to remove the effects of S/A and A/S are called Precise Positioning Service (PPS) receivers.

According to the information accessible to the civil community, SA should consist of:

1. a phase jitter of the satellite clocks, the effect of which can be removed by a strict common view for time transfer, and
2. a changeable bias in the broadcast ephemerides.

The net of the two SA effects is about 100 meters for navigation and 167 ns for timing. Some of the bias in the ephemerides will cancel in common view. The smaller the baseline the more the cancellation.

Since the concept of limiting access to P-code to PPS users only was withdrawn and SA was introduced instead, P-code receivers have became available on the market for the general public. However these owners of P-code receivers are unable to eliminate the errors added by SA to GPS signals; the only advantage they keep is that of using two frequencies L1 and L2 in the codeless mode to measure ionospheric delay. The PPS users remove degradation by employing SA decription techniques. Table I and II give the approximate performances of GPS in terms of the information available to the civil community.

Table I. Effects of SA on positioning

OPERATING MODE		PPS USERS		SPS USERS	
SA	A-S	P(Y)-CODE	C/A-CODE	P-CODE	C/A-CODE
OFF	OFF	16 m	30 m	16 m	30 m
ON	OFF	16 m	30 m	100 m	120 m
OFF	ON	16 m	30 m	?	30 m
ON	ON	16 m	30 m	?	120 m

Table II. Effects of SA on the dissemination of *GPS time*

OPERATING MODE		PPS USERS		SPS USERS	
SA	A-S	P(Y)-CODE	C/A-CODE	P-CODE	C/A-CODE
OFF	OFF	15 ns	40 ns	15 ns	40 ns
ON	OFF	15 ns	40 ns	142 ns	167 ns
OFF	ON	15 ns	40 ns	?	40 ns
ON	ON	15 ns	40 ns	?	167 ns

We have observed in the past several exercises which might have been the tests of SA. Here we give a brief description of them together with the officially implemented SA.

A) Exercise of September 29 to October 2, 1989. During these 4 days the signals of Block I satellites were perturbed. This exercise, which may have been a test of SA showed a phase jitter of the satellite clocks and a degradation of ephemerides. In it,

- the slopes of linear fit to a 13-minute track increased from the usual 15 ps/s to 100 ps/s. These slopes were different for simultaneous observations in different laboratories. For example, for PRN 13 observed on September 29, 1990 at 19h18m UTC, the slope was of −105 ps/s at OP and −26 ps/s at NIST. This would indicate a bias in ephemerides,
- the comparison by common-view of UTC(OP) with UTC(PTB) (distant of about 700 km) had a standard deviation of 15 ns instead of the usual several nanoseconds, but comparison of UTC(OP) with UTC(NIST) (distant of about 7500 km) had a standard deviation of 100 ns instead of the usual 15 ns. This indicates an error in ephemerides which can partially be cancelled over short distances.

B) Exercises on PRN 14. During several months before implementation of SA the first satellite of Block II, PRN 14 was submitted for short times to degradation which seemed to consist only in phase jitter.

C) "March—August 1990" Implementation of SA. On March 25, 1990 all satellites of Block II were subjected to Selective Availability (see Fig. 1). The discrepancy of UTC(USNO) — GPS time values has increased by a factor of ten. As during the exercise of September 29 — October 2, 1989 the slopes of 13-minute tracks have increased by approximately the same amount. However the slopes were quite similar for simultaneous observations from different laboratories. For example, for PRN 14 observed on March 30, 1990 at 6h30m UTC, the slope was −107 ps/s at OP and −113 ps/s at USNO. The slight difference between these two slopes is certainly due to local conditions of observations such as multipath propagation, rather bad estimation of ionospheric delays. ... Moreover, the common-view comparisons entirely removed the SA. This means that the SA consisted manly of a phase jitter of satellite clocks without ephemeride degradation. The SA introduced on March 25 was suspended between June 24 and 30, July 8 and 14. On August 10, 1990 it was removed and has not yet, at the time of the meeting, been reimposed.

DISSEMINATION OF TIME

The GPS is primarily a tool of time dissemination. Many users employ the GPS to acquire GPS time or UTC for use in real time or in post-processing. Real-time access to GPS time can easily be realized with an uncertainty of 100 ns when SA is off. With some post-processing this value can be considerably reduced.

What happens when SA is activated can be seen on Fig. 1. Real-time access to GPS time by a single space vehicle can be realized with an uncertainty of several hundreds of nanoseconds. This is satisfactory for some applications. A more accurate access to GPS time can be obtained with postprocessed smoothed data. The results depend of the length of the smoothed period. From the results given by Table III we can conclude that the effects of SA on time dissemination can be reduced to the level of 30 ns when smoothing (Vondrak smoothing[9] the data over 10 days (see also Fig. 2). Smoothing over 1 day gives about 100 ns and over 3 days about 50 ns. Moving average of one day and three days provides similar results.

ACCURATE TIME COMPARISONS VIA COMMON VIEW

In time metrology there is a need for accurate comparisons of remote atomic clocks. Ideally the method of comparison employed should not obscure the performance of the clocks. The simultaneous observations of GPS satellites, known as the common-view approach, has proved to be very close of this ideal[1, 2, 5]. Moreover during the implementation of SA, precisely synchronised common-views entirely remove the effects of satellite clock phase jitter. The common-view approach also reduces the effect of ephemeride degradation[6].

During this study for Block II satellites we used strict common-views with synchronization to 1 second (assuming that both receivers use the same reference time for monitoring the tracks), and the tracks of the full standard length of 13 minute. We have used raw data with no correction for broadcast ephemerides or ionospheric model. The antennas coordinates were corrected [7,8]. The values of UTC(OP)–UTC(USNO) are smoothed (Vondrak smoothing[9]) over the periods of ten days. The results are given by Table IV, and are illustrated by Fig. 3.

Clearly, strict common-views completely eliminate the effects of SA, which means that there is no ephemeride degradation. The distance between OP and USNO being about 6000 km, a large error in ephemerides would introduce a major discrepancy. The slight difference, a few nanoseconds, between the results of Block I and Block II comes from the use of different ensembles of satellites. This can be the effect of broadcast ephemerides, model of ionosphere, multipath propagation...

The results of another common-view comparison of two distant laboratories (OP and NIST) during implementation of SA can be found in[2].

CONCLUSIONS

This study shows that the March—August 1990 implementation of SA consisted only of satellite clock phase jitter, and can be entirely removed by strict common-views. The satellite ephemerides were not degraded. This is fortunate for time metrology, and brings the hope that even degraded GPS signals will allow high accuracy time comparisons without painful and time-wasting correction of ephemerides.

At present, however, there is no certainty that SA will continue to be implemented in this way. The exercise of September 29—October 2 1989 shows that the degradation of ephemerides is possible. For this reason the community of time metrology is well-advised to continue its efforts in studying possible techniques for the correction of degraded ephemerides. Various approaches are now being considered [6]. These include the use of precise ephemerides or the use of the differences between broadcast undegraded and broadcast degraded ephemerides if provided by OCS. At present the delay of three months with which precise ephemerides are accessible is a major obstacle to their use on an operational basis. Additionally, the use of precise ephemerides requires the record of broadcast ephemerides in some laboratories around the world (one per area). At present the broadcast ephemerides are recorded regularly at BIPM (Sèvres, France) and NIST (Boulder, Colorado).

The implementation of SA is a severe drawback in terms of direct access to time, but for delayed dissemination of time the effects of SA can be considerably reduced.

REFERENCES

1. B. Guinot, W. Lewandowski, C. Thomas, *A review of Recent Advances in GPS Time Comparisons*, in Proc. 4th European Time and Freq. Forum, pp. 307–312,1990.

2. W. Lewandowski, G. Petit, C. Thomas, M. Weiss, *The use of Precise Ephemerides, Ionospheric Data and Corrected Antenna Coordinates in a Long Distance GPS Time Transfer*, in Proc. 22nd PTTI (this volume), 1990.

3. M. J. Ellett, *Civil Access to the Precise Positioning Service of the NAVSTAR GPS*, in Proc. 18th PTTI, pp. 353–361, 1986.

4. W. J. Klepczynski, L. G. Charron, *The Civil GPS Service*, in Proc. 20th PTTI, pp. 51–64, 1988.

5. D. W. Allan, M. Weiss, *Accurate Time and Frequency Transfer during common-view of a GPS satellite*, in Proc. 34th Ann. Symp. on Freq. Cont., pp. 334–346, 1980.

6. W. Lewandowski, M. A. Weiss, *The Use of Precise Ephemerides for GPS Time Transfer*, in Proc. 21st PTTI, pp. 95–106, 1989.

7. B. Guinot, W. Lewandowski, *Improvement of the GPS Time Comparisons by simultaneous relative positioning of the receiver antennas*, Bulletin Géodésique, 63, pp. 371–386, 1989.

8. W. Lewandowski, R. J. Douglas, W. J. Klepczynski, W. Strange, J. Suter, M. Weiss, *Positioning of GPS antennas in Time Keeping Laboratories of North America*, in Proc. 43rd Symp. on Freq. Cont. pp. 218–224, May 1989.

9. J. Vondrak, Bull. Astron. Inst. Czechoslovakia, 20, 349,1969.

LIST OF ACRONYMS AND ABBREVIATIONS

A-S	Anti-Spoofing
BIPM	Bureau International des Poids et Mesures
CV	Common-View
C/A-Code	Coarse/Acquisition Code
DoD	United States Department of Defence
GPS	Global Positioning System
JPL	Jet Propulsion Laboratory
OCS	GPS Operational Control Segment
OP	Paris Observatory
NASA	National Aeronautic and Space Agency
NIST	National Institute of Standards and Technology
P-Code	Precision Code
PPS	Precise Positioning Service
PTB	Physikalisch-Technische Reichsanstalt
SA	Selective Availability
SPS	Standard Positioning Service
SV	Space Vehicle
USNO	US Naval Observatory
UTC	Coordinated Universal Time

Table III. 10-days smoothed values of UTC(k) - *GPS time*.
Unit: 1 nanosecond.

UTC(OP) - *GPS time*

Date 1990	By Block I 28 SV	By Block II 64 SV	Block I -Block II	SA on Block II
May 18	-318	-352	34	ON
May 28	-252	-266	14	ON
June 7	-141	-135	-6	ON
June 17	-12	-21	9	ON
June 27	116	112	4	ON
July 7	123	98	25	ON
July 17	-16	15	-31	ON
July 27	-137	-126	-11	ON
Aug. 6	-162	-137	-25	ON
Aug. 16	-92	-96	4	OFF
Aug. 26	27	33	-6	OFF

UTC(USNO) - *GPS Time*

Date 1990	By Block I 45 SV	By Block II 12 SV	Block I -Block II	SA on Block II
May 18	-105	-111	6	ON
May 28	-52	-88	36	ON
June 7	28	0	28	ON
June 17	128	142	14	ON
June 27	232	232	0	ON
July 7	254	238	16	ON
July 17	111	115	-4	ON
July 27	-40	-34	-6	ON
Aug. 6	-120	-120	0	ON
Aug. 16	-118	-118	0	OFF
Aug. 26	-38	-33	-5	OFF

Table IV. UTC(OP) - UTC(USNO) by common-view.
Unit: 1 nanosecond.

Date 1990	by Block I 7 CV	by Block II 3 CV	Block I -Block II	SA on Block II
Mar. 9	-790	-788	-2	OFF
Mar. 19	-706	-709	3	OFF
Mar. 29	-577	-574	-3	ON
Apr. 8	-485	-482	-3	ON
Apr. 18	-410	-410	0	ON
Apr. 28	-365	-365	0	ON
May 8	-296	-293	-3	ON
May 18	-213	-215	2	ON
May 28	-215	-211	-4	ON
June 7	-171	-169	-2	ON
June 17	-160	-157	-3	ON
June 27	-140	-140	0	ON
July 7	-148	-149	1	ON
July 17	-144	-147	3	ON
July 27	-112	-111	-1	ON
Aug. 6	-61	-58	-3	ON
Aug. 16	-6	-5	-1	OFF
Aug. 26	-51	-48	-3	OFF

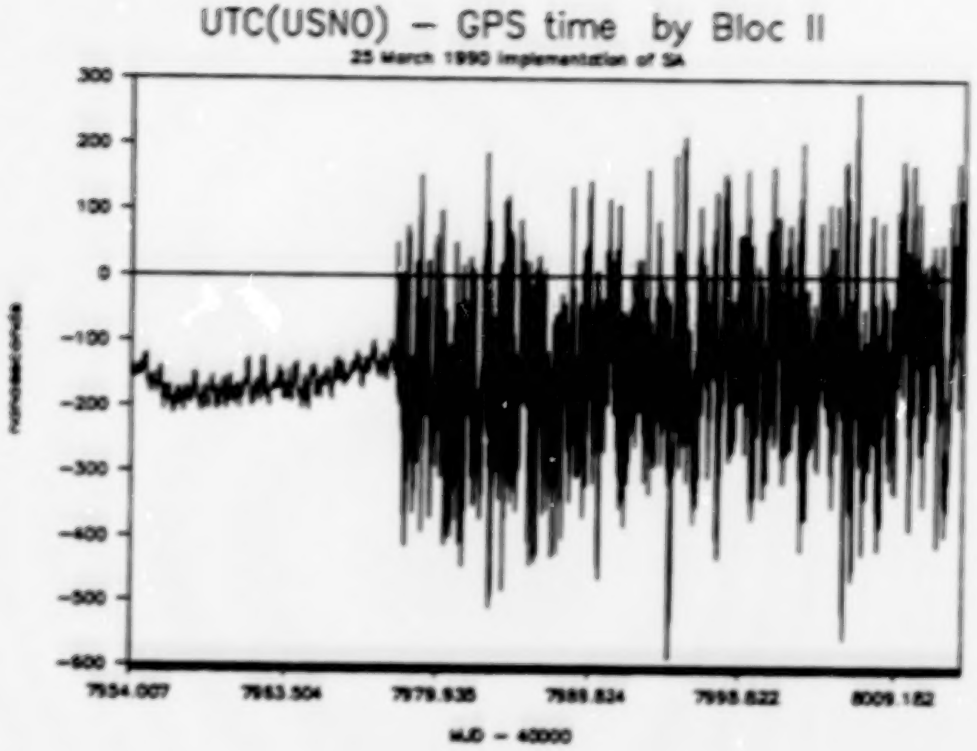


Figure 1. Implementation of SA on 25 March 1990 as seen from the US Naval Observatory.

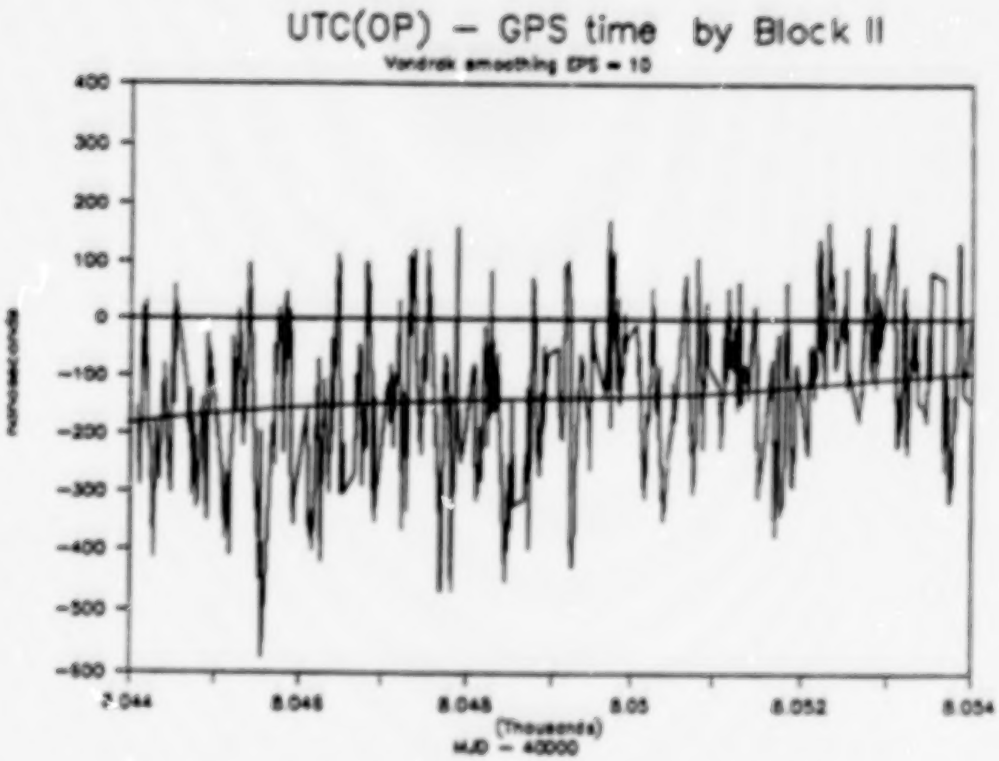
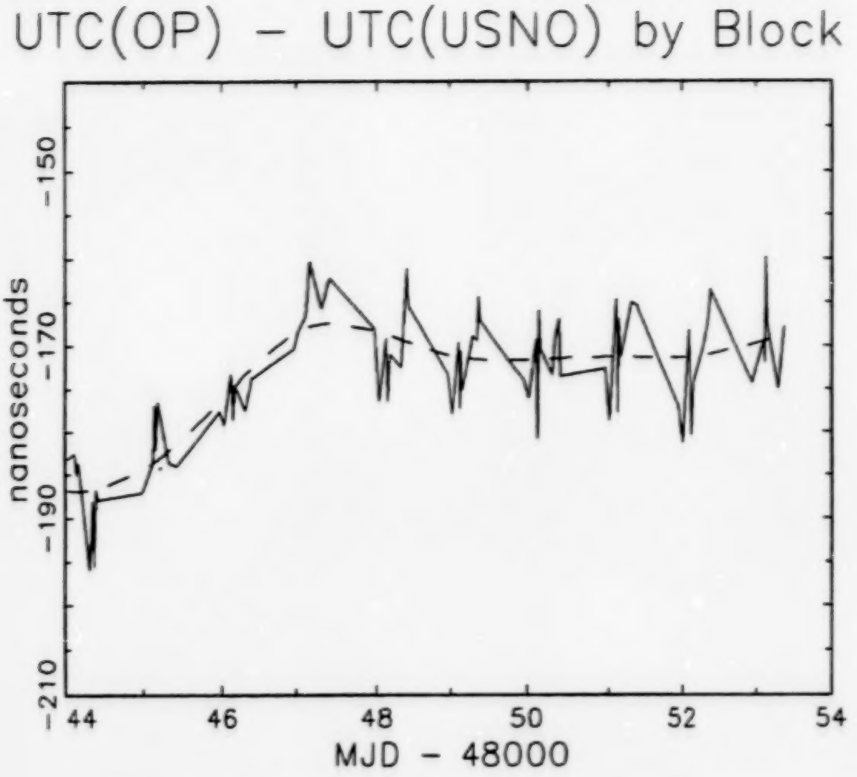


Figure 2. Values of UTC(OP)-GPS time by Block II satellites smoothed over a periods of 10 days.



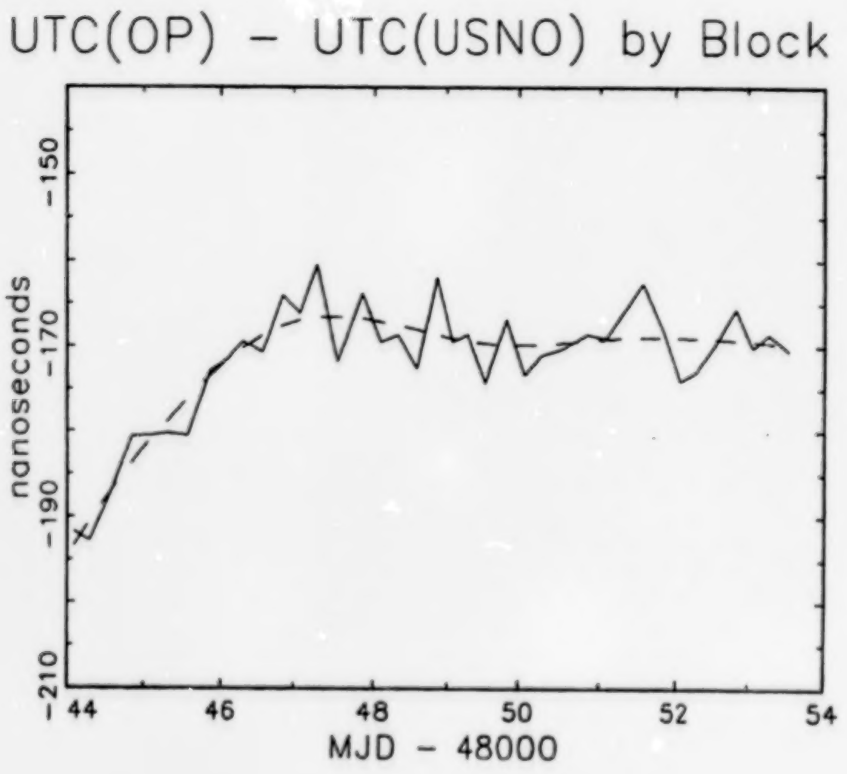


Figure 3. Common-views between Paris Observatory and US Naval Observatory (distante of about 6000km) over a periode of 10 days. Dashed lines represent smoothing.

QUESTIONS AND ANSWERS

Unidentified Questioner: What smoothing algorithm did you use?

Mr. Lewandowski and David Allan: The data that you saw used Vondrak smoothing before the SA, but the actual smoothing on the one day, three day and ten day samples was just simple averaging.

Dr. Gernot Winkler, U.S Naval Observatory: The noise is not white, and it is not Gaussian. Under these conditions, averages are not the optimum estimator of the center of the distribution. I have made some tests using simply the median of neighboring values, and if you have sufficient numbers of observations, and of course we will have more with more satellites, this becomes much more effective.

Professor Carroll Alley, University of Maryland: Is there any evidence of periodicity in the noise? What is the shortest time between which you can do these comparisons?

Mr. Lewandowski: The time between observations was 30 minutes. We were just looking for common view time comparisons.

Unidentified Questioner: In view of the political environment, is there any change in the SA policy?

Mr. Lewandowski: No one knows! At least they are not saying!

BLANK PAGE

TIME SCALE ALGORITHM: DEFINITION OF ENSEMBLE TIME AND POSSIBLE USES OF THE KALMAN FILTER

Patrizia Tavella
Istituto Elettrotecnico Nazionale Galileo Ferraris
Strada delle Cacce, 91
10135 Torino
Italy

and

Claudine Thomas
Bureau International des Poids et Mesures
Pavillon de Breteuil
92312 Sèvres Cedex
France

Abstract

The work reported in this paper takes place in a general theoretical overview concerning the generation of an ensemble time scale. Different algorithms can be designed to match the particular needs of users and the available sets of clocks and time measurements. In all cases however, the statistical treatment of clock data requires at least:

- ***the definition of an average time scale,***
- ***the specification of a procedure to optimize the contribution of each clock,***
- ***the implementation of a filter on each clock frequency to provide a means of prediction.***

Here, the comparative study of two time scale algorithms, devised to satisfy different but related requirements, is presented. They are ALGOS(BIPM), producing the international reference TAI at the Bureau International des Poids et Mesures, and AT1(NIST), generating the real–time time scale AT1 at the National Institute of Standards and Technology. In each case, the time scale is a weighted average of clock readings, but the weight determination and the frequency prediction are different because they are adapted to different purposes.

The possibility of using a mathematical tool, such as the Kalman filter, together with the definition of the time scale as a weighted average, is also analysed. Results obtained by simulation are presented.

INTRODUCTION

To keep time is to accumulate, without discontinuity, time scale units as close as possible to the SI second as defined in 1967 by "the duration of 9192631770 periods of the radiation corresponding to

the transition between the two hyperfine levels of the ground state of the cæsium atom"[1].

Time laboratories have at their disposal commercial cæsium clocks. But physical devices can fail, so these laboratories are inevitably led to keep not one, but several clocks which are together treated as an ensemble. Clock readings are then combined through an algorithm designed to raise the stability, accuracy and reliability of the time scale above the level of performance of any individual clock in the ensemble.

In the design of a time scale algorithm there is no general solution. Rather the fundamental ingredients should be artfully mixed to match the available time measurements and the needs of the user. Some of these ingredients are the definition of an average time scale, the specification of a weighting procedure, the determination of a means to predict clock frequencies and the implementation of a filter on measurement noise.

In this paper the key point of the definition of the time scale is highlighted for different algorithms. In a first section, we propose the comparative study of two time scale algorithms: ALGOS(BIPM)[2], producing the international reference, TAI, at the Bureau International des Poids et Mesures, and AT1(NIST)[3], generating the real-time time scale, AT1, at the National Institute of Standards and Technology. Though the weight determination and the frequency prediction are different, because they are adapted to different purposes, these two algorithms rely on the same definition of the time scale.

In a second section we emphasize the possible use of the Kalman filter for a time scale. This mathematical tool is first briefly presented and then shown as being valuable help in the efficient processing of clock data. Here we show with three examples of algorithms based on Kalman filtering[4, 5, 6] that this technique can be unpowerful for the elaboration of a time scale if an equation of definition is not set. Finally, our own view of how to take advantage of the Kalman filter is given together with results obtained from simulated clock data.

Note: In what follows symbols are defined as:

t: date of the time scale update,
H_i: clock identification,
$h_i(t)$: reading of clock H_i at date t
(this quantity is not directly accessible by experiment),
p_i: weight assigned to clock H_i,
$x_i(t)=TA - h_i(t)$: clock $H - i$ time offset from the time scale
TA under computation
(this quantity gives user access to the time scale),
N: clocks number,
$x_{ij}(t) = h_j(t) - h_i(t) = x_i(t) - x_j(t)$: measurement between clock H_j and clock H_i at date t,
τ: time interval between two measurement cycles.

1. COMPARATIVE STUDY OF ALGOS(BIPM) AND AT1(NIST)

The detailed analysis of the comparison of the two algorithms, ALGOS(BIPM) and AT1(NIST), has been published elsewhere[7]. Here we give only the main features of that study in order to focus on the definition of the time scale in these two cases.

1–1 ALGOS(BIPM)

ALGOS(BIPM) produces the international reference, TAI (temps atomique international), at the Bureau International des Poids et Mesures (Sèvres, France). The requirement here is for extreme reliability and long-term stability. To this end, TAI relies on a large number of clocks of different types, located in different parts of the world and connected in a network allowing the precise exchange of time data. Although measurements are performed at intervals of τ=10 days, the definitive update of TAI is obtained from an iterative and post-processed procedure which treats, as a whole, two-month blocks of data and so ensures long-term stability[2, 7]. One important consequence is that TAI is a deferred-time time scale.

The first step in the establishment of TAI is the computation of a free atomic time scale, EAL (échelle atomique libre), obtained as a weighted average of clock readings. TAI is then derived from EAL with a frequency steering in order to ensure accuracy. For each date t of the two-month interval of computation [t_0, t_0 + 60 days], EAL is defined as:

$$EAL(t) = \frac{\sum_{i=1}^{N} p_i[h_i(t) + h'_i(t)]}{\sum_{i=1}^{N} p_i}. \qquad (1)$$

In this equation, p_i is the weight assigned to clock H_i, and $h'_i(t)$ is a time correction applied at date t to ensure time and frequency continuity of the scale when the weights of clocks or the total number of clocks is changed[8]:

$$h'_i(t) = x_i(t_0) + B_{ip} \cdot (t - t_0), \qquad (2)$$

here $B_{ip}(t)$ is the frequency of clock H_i, relative to EAL, predicted for the period t_0, t.

From equation (1) and the above notations, we get the system of equations:

$$\begin{cases} \sum_{i-1}^{N} p_i x_i(t) = \sum_{i=1}^{N} p_i h'_i(t) \\ x_{ij}(t) = x_i(t) - x_j(t) \end{cases} . \qquad (3)$$

The time measurements are chosen to be non-redundant so that the system (3) is deterministic with N equations and N unknowns and so is exactly solvable at each date t. The results are the quantities $x_i(t_0 + n\tau)$ with n = 0, 1, 2, 3, 4, 5 and 6 for each clock H_i. Clock H_i frequency $B_i(t_0 + 60$ days) for the two-month interval under computation is obtained as the least squares slope of the quantities $x_i(t_0 + n\tau)$.

The detailed and complete description of the weighting procedure is described elsewhere[7]. The general principle is that the weight assigned to clock H_i is set to be inversely proportional to the frequency variance of the clock over six two-month samples. This ensures the long-term stability of EAL and allows deweighting for seasonal fluctuation. An upper limit of weight and a system for the detection of abnormal behaviour are also in use in ALGOS(BIPM).

The frequency prediction is a one step linear prediction[7], the supposition being that each clock most likely behaves in the present two-month interval as it did in the previous one. This is the optimal estimate for random walk frequency modulation, which is the predominant clock noise for two-month averaging time.

1–2. AT1(NIST)

The AT1 time scale, developed at the National Institute of Standards and Technology (Boulder, Co, USA) is used for scientific studies. The basic requirement is to provide definitive access to the time scale in near real time, with no post-processing or reprocessing. It is an average time scale derived from measurements taken from about 10 commercial clocks located on the site. The AT1(NIST) algorithm estimates time, adaptative weight and frequency[3] for each contributing clock at each measurement cycle, at present $\tau = 2$ hours.

The equations for computing the time scale at date t are based on predicted values $\hat{x}_i$ and $\hat{y}_i$ for the time and frequency of each clock. The predicted time difference $\hat{x}_i(t)$ of clock H_i relative to AT1, for the date t, involves the time offset $x_i(t-\tau)$ obtained from the previous computation and the frequency $\hat{y}_i(t-\tau)$ estimated at date $t-\tau$ and predicted for the next τ period. This is written as:

$$\hat{x}_i(t) = x_i(t-\tau) + \hat{y}_i(t-\tau) \cdot \tau. \tag{4}$$

This equation is completely similar to (2) in the description of ALGOS(BIPM) if $t - t_0$ is set equal to τ.

The definition of the time scale itself is written as:

$$x_i(t) = \frac{\sum_{j=1}^{N} P_j[\hat{x}_j(t) - x_{ij}(t)]}{\sum_{j=1}^{N} P_j}. \tag{5}$$

where $x_{ij}(t)$ is the non-redundant set of time measurements.

A trivial transformation of (5) leads to:

$$x_i(t) = \frac{\sum_{j=1}^{N} P_j[\hat{x}_j(t) - x_j(t)] + x_i(t)}{\sum_{j=1}^{N} P_j}, \tag{6}$$

so that we get the system of equations:

$$\begin{cases} \sum_{j=1}^{N} P_j x_j(t) = \sum_{j=1}^{N} P_j \hat{x}_j(t) \\ x_{ij}(t) = x_i(t) - x_j(t) \end{cases}. \tag{7}$$

This is a system of N equations with N unknowns, equivalent to system (3) for ALGOS(BIPM).

The analogy in the definition of EAL and AT1 time scales is then complete.

Weights p_i appearing in (5), designed to ensure stability, have been determined in the previous computation at date $t-\tau$ with an exponential filter over the time deviations between predicted and estimated time differences of the last N_τ periods[3]. The time constant N_τ is usually set at 20 to 30 days. These time deviations are also corrected for the bias introduced by the correlation between the clock itself and the average time scale[3]. A detector of abnormal behaviour and an upper limit of weight[7] exist also in AT1(NIST).

The predicted frequency $\hat{y}_i(t)$ comes from an exponential weighted average of past and present mean frequencies. The time constant of this exponential filter being characteristic of the statistical behaviour of each contributing clock.

Conclusions

The ALGOS(BIPM) and AT1(NIST) algorithms rely on the same basic definition of the time scale, generated as a weighted average of clock readings. They also present other common features: measurements of time differences are treated as having negligible uncertainties and clocks are supposed uncorrelated among them.

The appropriate way to determine clock weights and to predict clock frequencies depends essentially on the available measurements (number of clocks, measurement sampling) and on the properties required for the resulting time scale (real-time updating or deferred-time post-processing).

2. TIME SCALES BASED ON KALMAN FILTERING

2-1 KALMAN FILTERING OUTLINE

The Kalman filter, which is used in many signal processing applications, is a tool well-adapted for stochastic estimation and prediction. It is a recursive and linear filter, optimal in the sense of least squares estimation[9, 10].

Its property of recursivity makes of this filter an interesting tool for help in the elaboration of a time scale: it allows a definitive treatment at each measurement cycle and provides a means of prediction for the next step. The system under estimation, in the case of a time scale, includes clock time offsets and clock frequencies. The evolution with time of these quantities can easily be represented by a linear model, linearity being a necessary condition for application of the Kalman filter theory. In addition measurement noise and correlation among clocks can naturally be inserted in the model whereas it is not the case for the two previous algorithms.

Here is a brief description of how Kalman filtering operates. The intention is to avoid equations which can be found elsewhere[10] but rather present basic ideas in the schematic way of Fig. 1 and 2.

Consider a dynamical system which evolves linearly with time. At date t its state is represented by a vector $X(t)$. We wish to estimate this vector using measurements, obtained with a τ measurement cycle, for times preceding date t. Suppose that the system state was estimated at date $t-\tau$ by the vector $X(t-\tau/t-\tau)$, a quantity which must be read as **estimate of X at date $t-\tau$ knowing**

all the measurements up to date $t - \tau$. This estimate has an error given by a covariance matrix $\Gamma(t - \tau/t - \tau)$ and represented on Fig. 1.

According to the model of evolution and to the noise of the model given by the covariance matrix $Q(t)$, the transition step of the Kalman filter (Fig. 1) allows us to estimate the predicted state of the system at date t, knowing all the measurements up to date $t - \tau$: the vector $X(t/t - \tau)$. The error on the estimation of this vector is given by the matrix $\Gamma(t/t - \tau)$, which includes the matrix $Q(t)$. This error is larger than the error at date $t - \tau$, mainly because the model is not perfect (see Fig. 1).

We now represent a new measure by a vector $Z(t)$ which is affected by an error given by the matrix $R(t)$ and represented on Fig. 1. From the predicted state at date t and this new information, the Kalman filter computes a new estimate of the state of the system according to an "update adjustment" described in Fig. 2. This new estimate is represented by the vector $X(t/t)$ affected by a covariance matrix $\Gamma(t/t)$, the trace of which has been minimized.

The update adjustment of Fig. 2 builds the new estimate from the old one and from the innovation weighted by the Kalman gain. The innovation represents the new information contained in the last measurement: it is simply the difference between the real measure and a predicted measure, expected from the predicted state at t knowing $t - \tau$. The Kalman gain $K(t)$ is given by a complex expression involving all the errors which affect the system, mainly Γ, Q and R[10]. Qualitatively, if the measurement $Z(t)$ is very good, that is, affected by a very small error, the Kalman gain at date t will be large so that the new estimate of the system state will largely rely upon the new observation. On the contrary, if the measurement is very bad, the adjustment process of the Kalman filter will tend to ignore it.

At last one more detail: the noises which are involved in the Kalman recurrence must be white noises.

2–2 EXAMPLES OF APPLICATION OF THE KALMAN FILTERING TO THE COMPUTATION OF A TIME SCALE

The first attempt to apply the Kalman filter to the problem of time scales was performed by Tryon and Jones in 1982[4]. Their system is an ensemble of N clocks. The system state $X(t)$ has 2N components: the N clock time offsets $h_i(t)$ and the N clock frequencies $y_i(t)$ relative to an ideal time scale. The model integrates each clock time and frequency affected by white frequency noise and random walk frequency modulation. The measurement vector $Z(t)$ is composed of the (N-1) time differences, measured between each clock and the reference clock. The measurement noise is supposed to be negligible. The result of the Kalman recursivity is an estimate of how each clock departs from an ideal time scale, but it is found that the error of this estimate always increases with time. This non-convergence of the covariance matrix Γ arises from the lack of observability of the system: N quantities $h_i(t)$ being estimated from only (N-1) measurements. In this case the Kalman filter is an efficient tool for filtering the data noise but, isolated, it does not have the power to build an average time scale.

Another example is the approach developed by Stein[5], where a Kalman filter is applied on the time measurements $x_{ij}(t)$ themselves, to smooth out the white phase noise. These filtered measurements are then used to predict the time offset of a given clock, relative to the ensemble time, in (N-1) different ways, each way passing through another clock of the ensemble. The definitive estimate of this time offset comes from a weighted average of these different predictions. The weighted average is defined by (3) or (5) and computed with a static and robust Kalman filter.

The Kalman filter is also used for time scales as a complement to the AT1(NIST) algorithm for frequency step detection. This work, proposed by Weiss and Weissert[6], utilizes the results $x_i(t)$ of AT1 in order to realize pseudo-measurements of the frequency of each clock relative to the ensemble time. The white noise of these pseudo-measurements is filtered and so gives access to the random walk component of each frequency and to the variance of this estimation. They are then tested for possible step.

2.3 A NEW PROPOSAL FOR USING THE KALMAN FILTER IN TIME SCALE GENERATION

Here we propose a new approach for using the Kalman filter in time scale generation and present results obtained with simulated clock data.

We start with the same hypothesis and defining equations as were used for ALGOS(BIPM) and AT1(NIST).

Suppose an ensemble of N clocks, the frequencies of which are uncorrelated. One clock is chosen as the reference. Each day N-1 time measurements are performed (τ = 1 day). Suppose also that the white phase noise of the measurements is smoothed out before the main computation of the time scale so that it can be treated as negligible. The ensemble time scale is defined by (3) or (5) as:

$$x_j(t+\tau) = \frac{\sum_{i=1}^{N} P_i[\hat{x}_i(t+\tau) - x_{ij}(t+\tau)]}{\sum_{i=1}^{N} P_i} \tag{8}$$

with: $\hat{x}_i(t+\tau) = x_i(t) + \hat{y}_i(t) \cdot \tau$, similar to (4),

where $\hat{y}_i(t)$ is the predicted frequency for the interval $[t,\ t+\tau]$.

The weight p_i and the predicted frequency $\hat{y}_i(t)$, relative to the time scale, of each clock are chosen outside the main computation to ensure the best long-term stability.

Now we wish to improve the short-term stability of the scale. For this purpose we use N-1 Kalman filterings, each of them operating on just two clocks, the reference clock H_j and another one chosen among the ensemble H_i. This decoupling supposes that the N-1 pairs of clocks are uncorrelated, which is theoretically not true, as the same reference clock is involved in each pair. However, one can choose the least noisy clock as reference and suppose the coupling to be small. Anyway the correlation of the N-1 pairs can be easily inserted in a Kalman filter operating on all the pairs together.

For each Kalman filter, the state of the system is composed of a single quantity, the frequency $y_{ij}(t)$ at date t of clock H_i relative to the reference clock. The model of evolution of the system is written as:

$$y_{ij}(t+\tau) = y_{ij}(t) + \alpha_{ij} \ , \tag{9}$$

where α_{ij} is white noise driving the random walk frequency modulation of the clock. The Q matrix is reduced here to the variance of the white noise α_{ij}.

Frequency measurements are deduced from time measurements with the equation:

$$z_{ij}(t+\tau) = \frac{x_{ij}(t+\tau) - x_{ij}(t)}{\tau} = y_{ij}(t+\tau) + \beta_{ij} \tag{10}$$

and are affected with white frequency modulation β_{ij}, with variance R.

The application of the Kalman filter leads to an estimation of the random walk component of the frequency $y_{ij}(t+\tau)$ of clock H_i relative to clock H_j while smoothing out the white frequency modulation.

Now, the filtered estimate $y'_{ij}(t+\tau)$ of the frequency $y_{ij}(t+\tau)$ can be introduced in the equation of definition of the time scale as:

$$x_j(t+\tau) = \frac{\sum_{i=1}^{N} P_i[x_i(t) + \hat{y}_i(t)\cdot\tau] - \sum_{i=1}^{N} P_i[x_{ij}(t) + y'_{ij}(t+\tau)\cdot\tau]}{\sum_{i=1}^{N} P_i} \tag{11}$$

or

$$x_j(t+\tau) = \frac{\sum_{i=1}^{N} P_i[x_i(t) - x_{ij}(t)]}{\sum_{i=1}^{N} P_i} + \frac{\sum_{i=1}^{N} [\hat{y}_i(t) - y'_{ij}(t+\tau)\cdot\tau]}{\sum_{i=1}^{N} P_i} \tag{12}$$

The first term of (12) is $x_j(t)$, the time offset of the reference clock H_j with respect to the average time scale. The second term is the weighted average of estimations of the frequency of clock H_j relative to the time scale, obtained through clock H_i and the filtered frequency of clock H_i relative to clock H_j; it is then the frequency of the reference clock H_j relative to the average time scale at date $t+\tau$.

Our proposal consists in filtering the white frequency modulation to estimate the random walk component of the frequency of a clock relative to another clock and then introducing this filtered frequency in the definition of the average time scale. This approach is thus opposite to that developed by Weiss and Weissert[6].

This new procedure has been investigated with simulated clock data: 6 clocks were simulated with different levels of white frequency modulation and random walk of frequency for a 300-day period. One clock has better short-term and long-term stability than the others: this is chosen as the reference clock. The frequency stability for the 5 pairs of clocks is given on Fig. 3. After filtering of the white frequency modulation, the short-term frequency stability for each pair of clocks is largely improved, as shown on Fig. 4. The efficiency of the filtering is presented on Fig. 5 for a given pair of clocks: the white frequency modulation is smoothed out, leading to the extraction of the random walk component of the frequency of one of the clocks relative to the other.

For the computation of the time scale, the weight p_i of clock H_i is chosen to be the reciprocal of its Allan variance computed over 30 days. The predicted frequency of clock H_i relative to the time scale, $\hat{y}_i$, is the average of the previous 30-day frequency data. This averaging time is chosen to improve the long-term stability of the average time scale.

The frequency stability of the resulting time scale, computed either with raw data or after implementation of the Kalman filtering procedure, is presented on Fig. 6: the average time scale obtained with filtered data has a lower level of white frequency modulation and so is more stable using averaging time in the range 1–30 days. After a 30-day averaging time, the random walk frequency noise is predominant and the two time scales have the same behavior.

CONCLUSIONS

The first step of the construction of a time scale is the definition of the ensemble time. For most time scale algorithms used in timing centers, the ensemble time is a weighted average of clock readings. The determination of the contribution of each clock and the mode of prediction of its frequency relative to the time scale are chosen in order to match special user needs and available time measurements.

The Kalman filter is a tool well adapted to time scale generation once the definition of the ensemble time has been given. It helps to smooth out the white phase noise of the time measurements. Its use for filtering the white frequency modulation of the clocks themselves is a new approach. In this case the time scale is built with the random walk component of the frequencies of the clocks relative to a single clock chosen as reference. The short-term stability of the resulting time scale is then significantly improved.

REFERENCES

1. Resolution 1 of the 13th Conférence Générale des Poids et Mesures, 1967–1968.

2. B. Guinot and C. Thomas, *Establishment of International Atomic Time*, BIPM Annual Report 1988, Part D, pp. D1–D22.

3. F. B. Varnum, D. R. Brown, D. W. Allan and T. K. Peppler, *Comparison of time scales generated with the NBS ensembling algorithm*, Proc. of the 19th Annual Precise Time and Time Interval (PTTI) Applications and Planning meeting, 1987, pp.13–23.

4. R. H. Jones and P. V. Tryon, *Continuous time series models for unequally spaced data applied to modeling atomic clocks*, Siam J. Sci. Stat. Comput., vol.8, nx1, 1987, pp. 71–81.

5. S. R. Stein, A. Gifford and L. A. Breakiron, *Report on the time scale algorithm test bed at USNO*, Proc. of the 21st Annual Precise Time and Time Interval (PTTI) Applications and Planning Meeting, 1989, pp. 269–288.

6. M. A. Weiss and T. Weissert, *A new time scale algorithm: AT1 plus frequency variance*, Proc. of the 21th Annual Precise Time and Time Interval (PTTI) Applications and Planning meeting, 1989, pp. 343–358.

7. P. Tavella and C. Thomas, *Comparative study of time scale algorithms*, submitted to Metrologia, April 1990.

8. B. Guinot, *Some properties of algorithms for atomic time scales*, Metrologia, 24 1987, pp. 195–198.

9. R. E. Kalman and R. Bucy, *New results in linear filtering and prediction theory*, Transactions of the ASME, Journal of Basic Engineering, 83D, 1961, pp. 95–108.

10. S. A. Tretter, *Introduction to discrete-time signal processing*, Ed. John Wiley & Sons, 1976, Chapters 13 & 14.

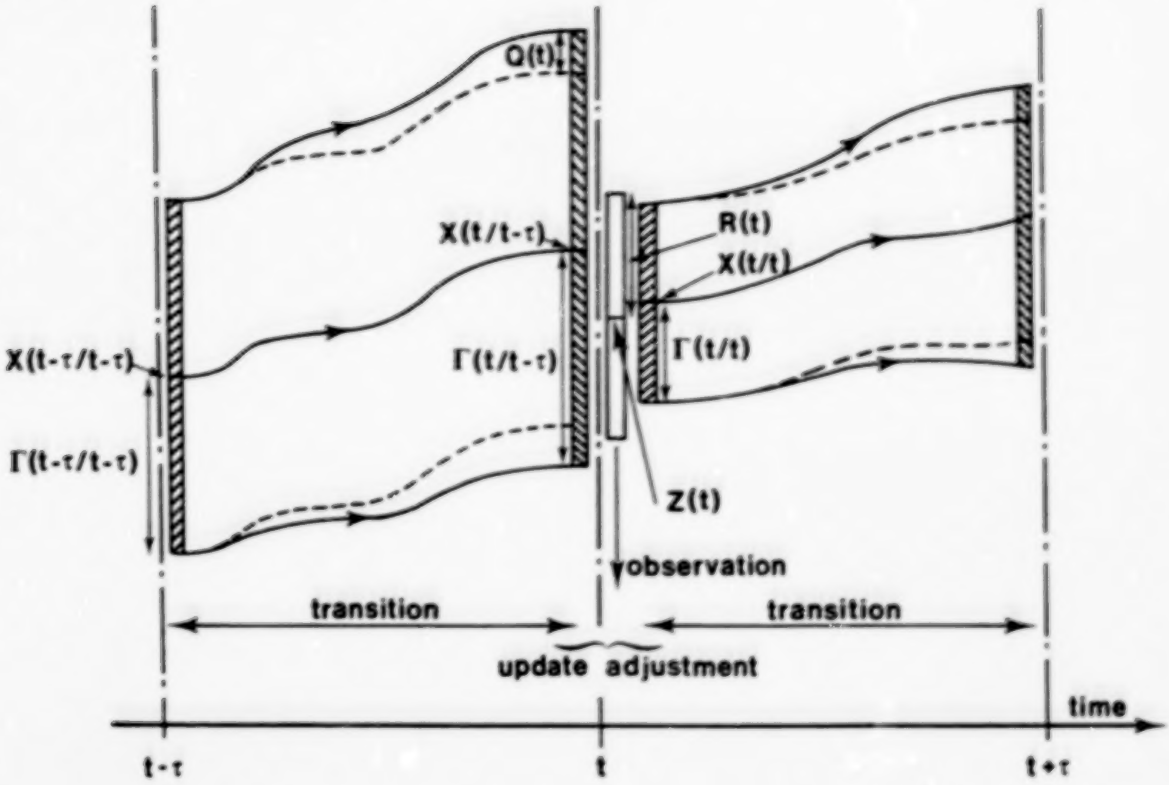


FIGURE 1: Recursive procedure for the Kalman filter.

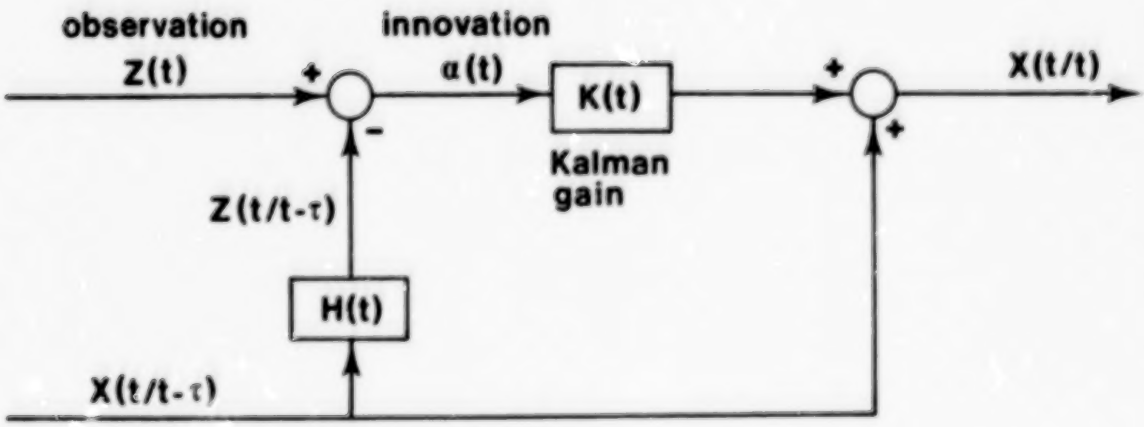


FIGURE 2: Schematic description of the adjustment process for the Kalman filter, leading to the updated estimation of the state of the system (The H matrix, not specified in the text, is the 'observation matrix' which links the vector of the system state, X, to the vector of measurement, Z. If all the quantities under estimation are observable, H is the matrix Identity).

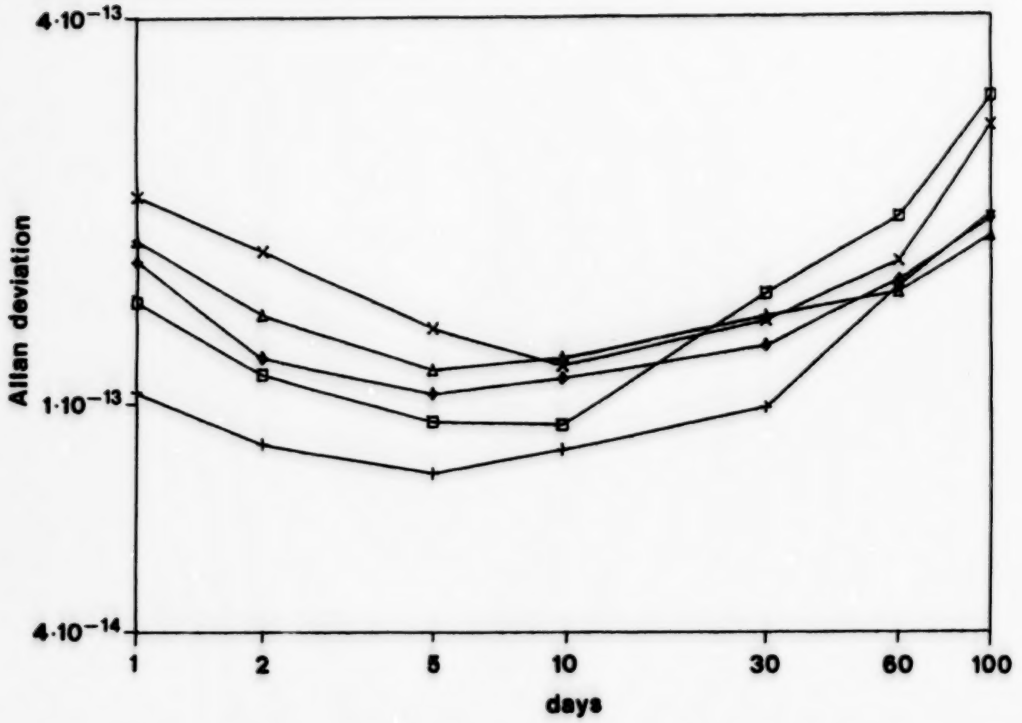


FIGURE 3: Allan deviation for five pairs of clocks. The clocks are simulated with different levels of white frequency modulation and random walk frequency modulation.

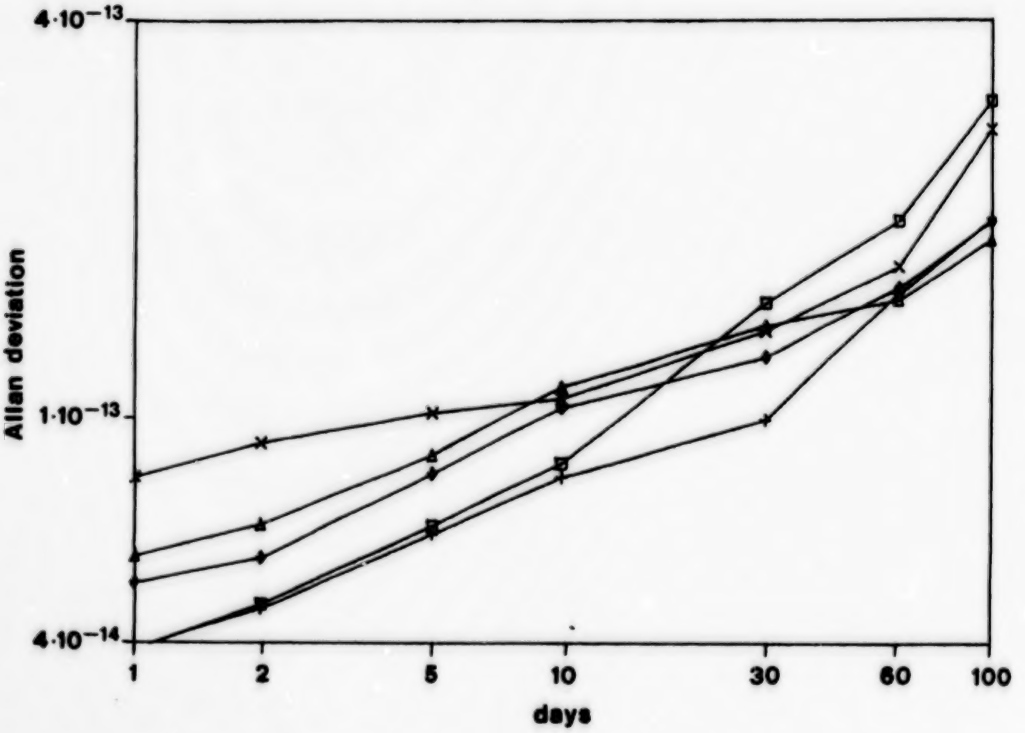


FIGURE 4: Allan deviation of the same pairs of clocks as in Fig. 3, after aplication of a Kalman filter for smoothing out the white frequency modulation.

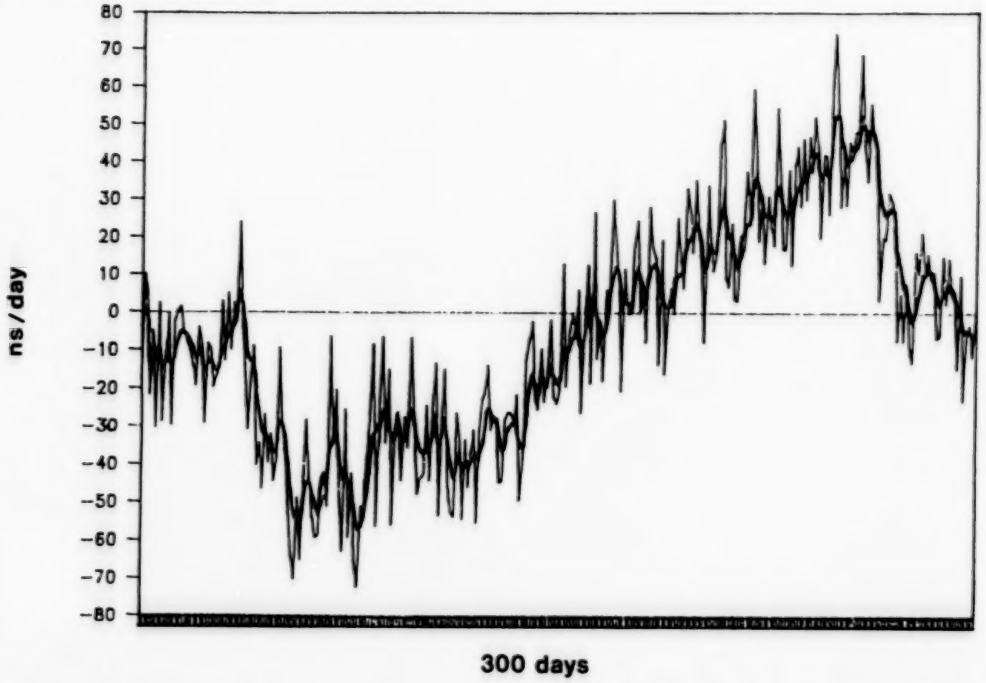


FIGURE 5: Example of Kalman estimation of the random walk component of the frequency:

measured frequency
estimated frequency

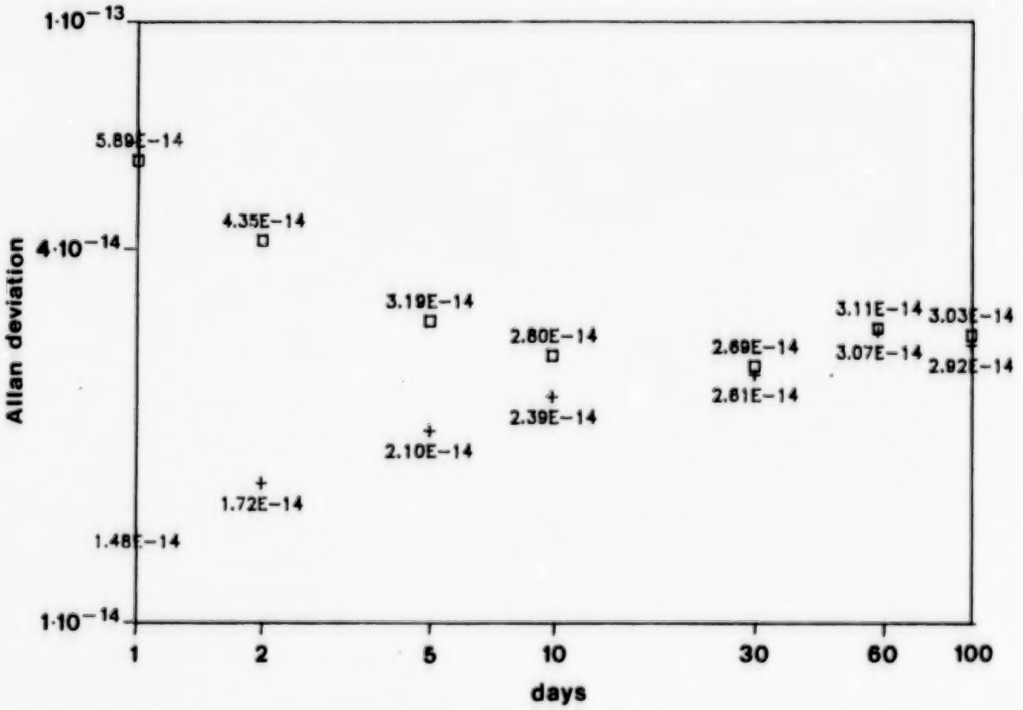


FIGURE 6: Stability of the average time scales obtained with simulated clock data:

raw clock data,
filtered clock data.

QUESTIONS AND ANSWERS

Unidentified Questioner: Was your data tested for periodicity, such as for the apparent ten day period in the graph? Was any Chi square test performed? Was the noise tested for whiteness and Gaussian behavior?

Ms. Tavella: Each type of noise was obtained from random white noise.

BLANK PAGE

ULTRA-STABLE Hg^+ TRAPPED ION FREQUENCY STANDARD*

J. D. Prestage, G. J. Dick, L. Maleki

California Institute of Technology, Jet Propulsion Laboratory
4800 Oak Grove Drive
Pasadena, California 91109

Abstract

We are developing a fieldable trapped ion frequency standard based on $^{199}Hg^+$ ions confined in a hybrid rf/dc linear ion trap. This trap permits storage of large numbers of ions with reduced susceptibility to the second-order Doppler effect caused by the rf confining fields. In preliminary measurements we have obtained a stability of $2—3 \cdot 10^{-15}$ for 10,000 second averaging times. These measurements were carried out with a 120 mHz wide atomic resonance line for the 40.5 GHz clock transition with a second order Doppler shift from the rf trapping field of $6 \cdot 10^{-13}$.

INTRODUCTION

Atomic frequency standards with high stability for averaging times τ longer than 1000 seconds are necessary for a variety of astrophysical measurements and long baseline spacecraft ranging experiments. The millisecond pulsar, PSR 1937+27, shows stability in its rotational period that exceeds that of all man-made clocks for averaging times longer than 6 months. Comparison of this pulsar period with an earth based clock of stability $1 \cdot 10^{-15}$ over averaging periods of one year is expected to show the effects of very low frequency gravitational waves[1,2]. Spacecraft ranging measurements across the solar system would be improved with earth based clocks whose stabilities exceeded $1 \cdot 10^{-15}$ for averaging times of 10^4 to 10^5 seconds. This clock performance would also improve gravity wave searches in spacecraft ranging data. Another use for long term stable clocks in NASA's Deep Space Network would be in maintaining syntonization with UTC.

We are developing a fieldable frequency standard based on $^{199}Hg^+$ ions confined in a linear ion trap which should show good long term frequency stability. Typically the largest source of frequency offset stems from the motion of the ions caused by the trapping fields via the second-order Doppler or relativistic time dilation effect. Though a large ion number is desirable for good signal to noise, the frequency offset which also grows with the number of ions forces us into a trade-off situation where fewer ions are trapped in order to reduce the (relatively) large offset and frequency instabilities which may result.

*This work represents the results of one phase of research carried out at the Jet Propulsion Laboratory, California Institute of Technology, under contract sponsored by the National Aeronautics and Space Administration.

In a conventional hyperbolic or Paul trap ions are trapped around the point node of the rf electric field at the center (Fig. 1). The strength of the electric field and the resulting micromotion of the trapped particles grows linearly with distance from this node point. As ions are added the size of ion cloud grows until the second order Doppler shift arising from the micromotion in the trapping field dominates the second order Doppler shift from the ion's thermal motion at room temperature. For typical operating conditions [3,13] a spherical cloud containing $2 \cdot 10^6$ mercury ions shows a 2nd order Doppler shift of $2 \cdot 10^{-12}$, a value some ten times larger than that for mercury ions undergoing room temperature thermal motion.

In order to increase the number of stored ions with no corresponding increase in second-order Doppler shift from ion micromotion we have designed and are currently testing a hybrid rf/dc linear ion trap. This trap confines ions along a line of nodes of the rf field (Fig.2). The trapping force transverse to the line of nodes is generated by the ponderomotive force as in conventional Paul traps while the axial trapping force is provided by dc electric fields [3-7].

We can compare the second-order Doppler shift, $\Delta f/f$ generated by the trapping fields for a cloud of ions in a linear trap and a conventional Paul trap [3,4] assuming that both traps are operated so that the ions have the same secular frequency ω. When the same number of ions N, are held in both traps the average distance from an ion to the node line of the trapping field is greatly reduced in the linear trap. Since the perpendicular distance from the line of nodes determines the magnitude of the rf trapping field the 2nd order Doppler shift of an ion's transition frequency due to motion in the trapping field is reduced from that of a conventional point node trap. If R_{sph} is the ion cloud radius in the Paul trap and L is the ion cloud length in the linear trap the Doppler shift in the two traps are related by[3]

$$\left(\frac{\Delta f}{f}\right)_{lin} = \frac{5}{3}\frac{R_{sph}}{L}\left(\frac{\Delta f}{f}\right)_{sph}. \tag{1}$$

As more ions are added to the linear trap this shift will increase. It will equal that of the spherical ion cloud in a hyperbolic trap when

$$N_{lin} = \frac{3}{5}\frac{L}{R_{sph}}N_{sph}. \tag{2}$$

Equations (2) and (3) are valid when the ion cloud radii, R_{lin} and R_{sph}, are much larger than the Debye length which is the characteristic plasma density fall off length at the ion cloud edge and is about 0.4 mm for typical Hg^+ ion plasmas used in frequency standard work [3,13].

In addition to its larger ion storage capacity the dependence of the second-order Doppler shift on trapping parameters in a linear trap is very different from that in a conventional Paul trap. For many ions in a Paul trap this shift is given by[3,10]

$$\left(\frac{\Delta f}{f}\right)_{sph} = -\frac{3}{10c^2}\left(\frac{N\omega q^2}{4\pi\epsilon_o m}\right)^{2/3} \tag{3}$$

where ω is the secular frequency for a spherical ion cloud containing N ions each with charge to mass ratio q/m. c is the speed of light and ϵ_o is the permittivity of free space. Ions in a linear trap show a 2nd order Doppler shift from the motion generated by the rf confining field given by[3]

$$\left(\frac{\Delta f}{f}\right)_{lin} = -\left(\frac{q^2}{8\pi\epsilon_o mc^2}\right)\frac{N}{L} \tag{4}$$

where L is the length of the ion cloud.

In contrast to the spherical case as described Eq.(3), this expression contains no dependence on trapping field strength, as characterized by ω, and depends only on the linear ion density N/L. If for example, the rf confining voltage increases and consequently the micromotion at a given point in space increases, the ion cloud radius will decrease so that the second-order Doppler shift from ion micromotion remains constant. Similar statements can be made about variations in any parameter that effects the radial confinement strength [4].

The sensitivity of the finite length linear trap to variations in radial trapping strength (characterized by ω) is [4]

$$\frac{\delta\left(\frac{\Delta f}{f}\right)_{lin}}{\left(\frac{\Delta f}{f}\right)_{lin}} = -2\frac{R_t}{L}\frac{\delta\omega}{\omega}, \tag{5}$$

and to variations in endcap voltage is

$$\frac{\delta\left(\frac{\Delta f}{f}\right)_{lin}}{\left(\frac{\Delta f}{f}\right)_{lin}} = 2\cdot\frac{R_t}{L}\frac{\delta V_e}{V_e} \tag{6}$$

where R_t is the trap radius. The Paul trap shows a corresponding sensitivity to trap field strength variations

$$\frac{\delta\left(\frac{\Delta f}{f}\right)_{sph}}{\left(\frac{\Delta f}{f}\right)_{sph}} = -\frac{2}{3}\frac{\delta\omega}{\omega}. \tag{7}$$

A comparison of Eqs. (5) and (7) shows the linear trap based frequency standard to be less sensitive to variations in trapping field strength than the Paul trap by a factor of $3R_t/L$. For the trap described in the next section this factor is about 1/3.

LINEAR TRAP DESCRIPTION

Our linear trap is shown in Fig. 3. The operation of the trap as a frequency standard is similar to previous work [9,10]. The ions are created inside the trap by an electron pulse along the trap axis which ionizes a neutral vapor of ^{199}Hg. A helium buffer gas (2×10^{-3} Pascal or 1.5×10^{-5} torr) collisionally cools the ions to near room temperature. Resonance radiation (194 nm) from a ^{202}Hg discharge lamp optically pumps the ions into the F=0 hyperfine level of the ground state. This UV light is focused onto the central 1/3 of the 75 mm long ion cloud. The thermal motion of the ions along the length of the trap will carry all the ions through the light field so that pumping is complete in about 1.5 seconds for typical lamp intensities.

To minimize stray light entering the fluorescence collection system this state selection light is collected in a Pyrex horn as shown in Fig. 3. The placement of the LaB_6 electron filament is also chosen to prevent light from the white hot filament from entering the collection system. Its placement and relatively cool operating temperature together with good filtering of the state selection/interrogation

UV light in the input optical system have allowed frequency standard operation without the use of a 194 nm optical bandpass filter in the collection arm. This triples data collection rates since such filters typically have about 30% transmission for 194 nm light.

Microwave radiation (40.5 GHz) propagates through the trap perpendicular to the trap axis thereby satisfying the Lamb-Dicke requirement that the spatial extent of the ion's motion along the direction of propagation of the microwave radiation be less than a wavelength. This radiation enters the trap region through the Pyrex horn (see Fig. 3) and propagates in the opposite direction to the UV state selection/interrogation light. This allows fluorescence collection in both directions perpendicular to the plane of the page in Fig.3. For the resonance and stability data shown below fluorescence was collected in only one of these two directions.

FREQUENCY STANDARD OPERATION

We have used Ramsey's technique of successive oscillatory fields to probe the approximately 40.5 GHz clock transition in $^{199}Hg^{+}$ ions confined to the linear trap described above. In these measurements the 40.5 GHz signal is derived from an active Hydrogen maser frequency source as shown in Fig. 4. A representative resonance line used in the $^{199}Hg^{+}$ clock transition is shown in Fig. 5. State selection and interrogation is accomplished during the 1.5 seconds following the lamp turn on. It is, of course, necessary to switch the light level to near zero to prevent light shifts and broadening of the clock transition. A background light level of about 300,000 per 1.5 second collection period has been subtracted to generate the resonance shown. The successive oscillatory field pulses consist of two 0.4 second microwave pulses separated by 3.5 second free precession period. The data shown is an average of ten 4 Hz wide scans with a 15 mHz frequency step size.

To determine the frequency stability of the overall system of ions, trap, microwave source, etc., we have locked the output frequency of the 40.5 GHz source to the frequency of the central peak of the resonance shown in Fig. 5 in a sequence of 2048 measurements. The time required for each measurement is about 6.9 seconds and the loop response time was 5 measurement cycles. By averaging the frequencies of 2^N adjacent measurements (N=1,2,..,10) we form the modified Allan variance. Two such stability measurements are shown in Fig.6. The frequency stability presented here has been extended to longer averaging times than previously reported [8] primarily through the addition of a triple layer of magnetic shields. Fig. 9 compares the present stability to other frequency standards including the active hydrogen masers used in JPL's Deep Space Network.

LOCAL OSCILLATOR REQUIREMENTS

One of the factors that can degrade the performance of passive atomic frequency standards is frequency fluctuations in the local oscillator (L.O.). The limitation due to this effect continues to the longest times, having the same $1/\sqrt{\tau}$ dependence on measuring time τ as the inherent performance of the standard itself. The cause of this effect is time variation of the sensitivity to L.O. fluctuations due to the interrogation process. This limitation was evaluated in a recent calculation for sequentially interrogated passive standards[10]. Since our trapped ion standard is of this type, the analysis should be directly applicable.

Additionally, effects inherent in operation of the feedback loop introduce a $1/\tau$ limitation to standard

performance which depends on the attack time t_a of the feedback loop.

Roughly speaking, the analysis shows that the local oscillator must have frequency stability at least as good as that of the standard itself, for a measuring time equal to the interrogation cycle time t_c. However, the effect may be reduced by use of a short dead time t_d and double-pulse interrogation. In that case, the instability induced by an L.O. with constant (flat) variance $\sigma_{LO}(\tau)$, is given approximately by [11,13]

$$\sigma_y(\tau) \approx \left(\frac{t_d}{t_c}\right) \sigma_{LO}(t_c) \sqrt{\frac{t_c}{\tau}}. \tag{8}$$

This instability will add in quadrature to that inherent in the standard itself. Thus, our trapped mercury ion frequency source with a performance of $\sigma_y(\tau) = 1.7 \cdot 10^{-13}/\sqrt{\tau}$, a cycle time of $t_c = 6.5$ seconds, and dead time of $t_d = 3.5$ seconds requires an L.O. with performance approximately given by $\sigma_{LO}(6.5) < 6.5/3.5 \cdot 1.7 \cdot 10^{-13}/\sqrt{6.5} \approx 1.24 \cdot 10^{-13}$. Longer cycle times and higher performance would place a more stringent burden on the L.O.

A crystal quartz L.O. with stability of $\sigma_y(\tau) \approx 1 \cdot 10^{-13}$ from 1 to 100 seconds is available commercially and could be combined with the trapped ion standard. Adding the instability given by Eq. 8 for this oscillator in quadrature with that for the trapped ion source itself predicts a combined stability of $\sigma_y = 2.2 \cdot 10^{-13}/\sqrt{\tau}$. With a loop attack time of $t_a = 35$ seconds, this performance would be achievable for times $\tau > (t_a \cdot 1/1.7)^2 = 425$ seconds.

While operation at the highest performance levels may place unattainable requirements on available crystal quartz local oscillators, application with a hydrogen maser, or other ultra-high stability source such as a high-Q cryogenic oscillator, could enable long term performance beyond 10^{-15}. However, in such an application, the hydrogen maser's frequency would not be steered to that of an independently operating trapped ion source. The maser's output signal would instead be used itself to interrogate the Hg^+ transition. Information thus gathered would be used to compensate for long term variation in the maser frequency.

SOURCES OF FREQUENCY INSTABILITY

We have measured the second order Doppler shift induced by the micromotion in the trapping fields in two ways—by measuring the ion cloud radius and by measuring the ion frequency as the ion number decays. Fig. 8 shows fluorescence from the ions as a masked PMT is swept across the focal plane of the imaging/collection system. Spatial variations in background light has been eliminated by subtracting light levels measured with ions in the trap from light levels with no ions present. Assuming a cylindrical ion cloud, a ray tracing analysis of the light falling on the PMT aperture shows that a 1.5 mm radius ion cloud gives a good fit to the experimental data (see Fig.8). With this ion cloud radius, trap operation at 50 kHz transverse secular frequency will yield a second order Doppler shift from the trapping field of $6 \cdot 10^{-13}$ [8].

An independent measurement of this frequency shift is shown in Fig. 9. This figure shows the time variation of the output frequency of the 40.5 GHz source when servoed to the $^{199}Hg^+$ clock transition. At the time shown by the arrow the electron pulse which fires at each measurement cycle is stopped. From that point on the number of ions in the trap is diminishing as the frequency is continuously tracked. Near the end of the run there are very few ions in the trap, though, enough to give a weak lock and a determination of the ion resonance frequency in the limit of low ion number where trapping field shifts approach ordinary thermal second order Doppler shifts [8]. The approximately 25 mHz

frequency shift in going from many ions to few ions is in good agreement with the $6 \cdot 10^{-13}$ value obtained from the ion cloud radius measurement described above. There was no active ion number stabilization used in any of the measurements described here.

The fractional sensitivity of the $^{199}Hg^{+}$ clock transition to magnetic field variations is nearly 1000 times less than that of hydrogen at the same operating field. For the present measurements the field was set at 5μT (50 mG). At this operating field the unshielded atomic sensitivity is $2.5 \cdot 10^{-13}$ per mG. To reach $5 \cdot 10^{-16}$ frequency stability the current in the Helmholtz field bias coils must be stable to $5 \cdot 10^{-5}$. To prevent ambient field disturbances from influencing the ion frequency the trap region is surrounded by a triple layer magnetic shield of shielding factor 10,000.

CONCLUSIONS

We have demonstrated the increased signal-to-noise and very good stability inherent in a linear ion trap based frequency standard. Clock operation with line $Q = 3.3 \cdot 10^{11}$ has achieved performance of $2-3 \cdot 10^{-15}/\sqrt{\tau}$ for $\tau = 10{,}000$ seconds. Line Q's as high as $1.3 \cdot 10^{12}$ have been measured [8], indicating consequent performance for this trap as high as $5 \cdot 10^{-14}/\sqrt{\tau}$ for $\tau > 150$ seconds. The requirement for local oscillator stability required to achieve this performance is quite stringent. However, controlling a hydrogen maser or cryogenic oscillator for long term stability improvements seems straightforward.

ACKNOWLEDGEMENT

We wish to thank Dave Seidel for taking the ion cloud radius optical data, Randy Berends for making ^{202}Hg lamps and Bob Tjoelker for carefully reading this manuscript.

REFERENCES

[1] D. W. Allan, "A Study of Long Term Stability of Atomic Clocks", *Errata Proc. 19th Annual Precise Time and Time Interval (PTTI) Applications and Planning Meeting*, 375–380, 1987.

[2] M. M. Davis, J. H. Taylor, J. M. Weisberg,and D. C. Backer, "High-precision timing observations of the millisecond pulsar PSR1937+21", *Nature* **315**, 547-550, 1985.

[3] J. D. Prestage, G. J. Dick, L. Maleki, "New Ion Trap for Frequency Standard Applications", *J. Appl. Phys.* **66**, No. 3, 1013–1017, August 1989.

[4] J. D. Prestage, G. R. Janik, G. J. Dick, and L. Maleki, "Linear Ion Trap for Second-Order Doppler Shift Reduction in Frequency Standard Applications",in *IEEE Trans. Ultrason. Ferroelec. Freq. Contr.*, **37**, 535-542, 1990.

[5] G. R. Janik, J. D. Prestage, and L. Maleki, "Simple Analytic Potentials for Linear Ion Traps", *J. Appl. Phys.* **67**, No. 10, 6050–6055, May 1990.

[6] H. G. Dehmelt, "Introduction to the Session on Trapped Ions," *Proc. 4th Symp. Frequency Standards and Metrology*, 286, 1989.

[7] D. J. Wineland, J. C. Bergquist, J. J. Bollinger, W. M. Itano, D. J. Heinzen, S. L. Gilbert, C. H. Manney, and C. S. Weimer, "Progress at NIST Toward Absolute Frequency Standards Using Stored Ions", in *Proceedings of the 43rd Ann. Symposium on Frequency Control*, 143–150, 1989.

[8] J. D. Prestage, G. J. Dick, and L. Maleki, "Linear Ion Trap Based Atomic Frequency Standard", to appear in *IEEE Trans. Instr. Meas.*, April, 1991.

[9] J. D. Prestage, G. J. Dick, and L. Maleki, "The JPL Trapped Ion Frequency Standard Development, *Proc. 19th Annual Precise Time and Time Interval (PTTI) Applications and Planning Meeting*, 285–297, 1987.

[10] L. S. Cutler, R. P. Giffard, P. J. Wheeler, and G. M. R. Winkler, "Initial Operational Experience with a Mercury Ion Storage Frequency Standard", in *Proc. 41st Ann. Symp. Freq. Control, IEEE Cat. No. 87CH2427-3*, 12–19, 1987.

[11] G. J. Dick, "Calculation of Trapped Ion Local Oscillator Requirements," *Proc. 19th Annual Precise Time and Time Interval (PTTI) Applications and Planning Meeting*, 133–146 1988.

[12] C. Audoin, V. Candelier, and N. Dimarcq, "A Limit to the Frequency Stability of Passive Frequency Standards," to appear in *IEEE Trans. Instr. Meas.*, April, 1991.

[13] L. S. Cutler, R. P. Giffard, and M. D. McGuire, "Thermalization of ^{199}Hg Ion Macromotion by a Light Background Gas in an RF Quadrupole Trap", *Appl. Phys. B* **36**, 137–142, 1985.

[14] M. Jardino, M. Desaintfuscien, and F. Plumelle, "Prospects for a Mercury Ion Frequency Standard", *Jour. De Physique*, **C8**, 327–338, 1981.

FIGURE CAPTIONS

Figure 1 A conventional hyperbolic RF ion trap. A node of the RF and DC fields is produced at the origin of the coordinate system shown.

Figure 2 The rf electrodes for a linear ion trap. Ions are trapped along the line of nodes of the rf field with reduced susceptibility to second-order Doppler frequency shift.

Figure 3 Linear Ion Trap Assembly View. The trap is housed in a 3.375" vacuum cube. State selection light from the ^{202}Hg discharge lamp enters from the right, is focused onto the central 1/3 of the trap and is collected in the horn. Fluorescence from the trapped ions is collected in a direction normal to the page.

Figure 4 Schematic of measurement system where the $^{199}Hg^{+}$ clock frequency is compared to an H-maser frequency.

Figure 5 $^{199}Hg^{+}$ clock transition as measured with successive oscillatory fields method. This line shape results from two 0.4 second microwave pulses separated by a 3.5 second free precession period. The central line is about 120 mHz wide.

Figure 6 Two measurments of the $^{199}Hg^{+}$ clock transition stability for the 120 mHz resonance line of Figure 5. Fractional frequency stability is $2 \cdot 10^{-13}/\sqrt{\tau}$ for $35 < \tau < 10,000$ sec.

Figure 7 Comparison of the currently demonstrated $^{199}Hg^{+}$ stability with other frequency standards used in JPL's Frequency Standards Laboratory.

Figure 8 The ion cloud diameter as determined by sweeping a masked photomultiplier across the focal plane of the UV light imaging/collection system. The data displayed is collected light vs. detector position.

Figure 9 A direct measure of 2nd order Doppler shift due to ion motion in the rf trapping fields. As the ion number (and hence ion cloud radius) diminishes the clock frequency increases. A net frequency shift of 25 mHz ($6 \cdot 10^{-13}$) is shown.

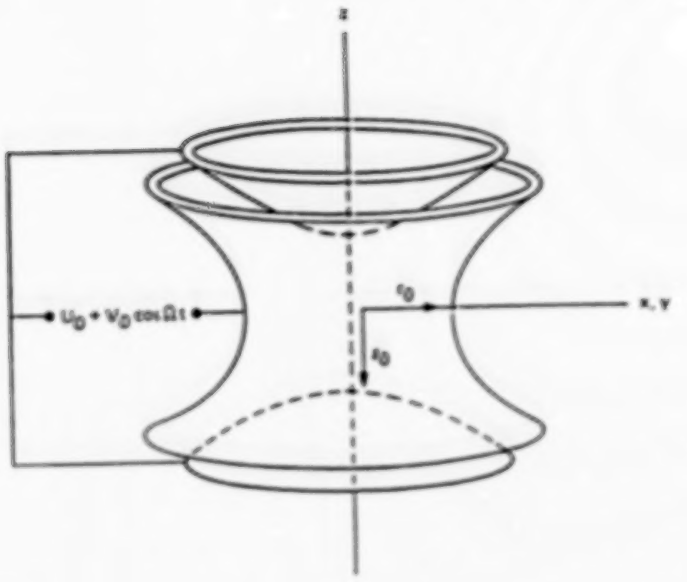


Figure 1 A conventional hyperbolic RF ion trap. A node of the RF and DC fields is produced at the origin of the coordinate system shown.

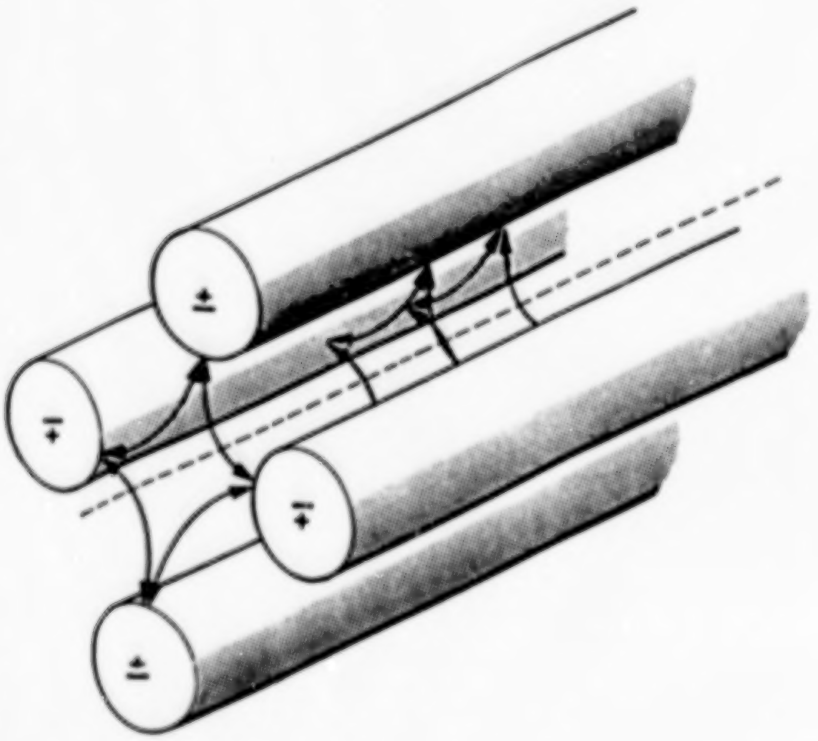


Figure 2 The rf electrodes for a linear ion trap. Ions are trapped along the line of nodes of the rf field with reduced susceptibility to second-order Doppler frequency shift.

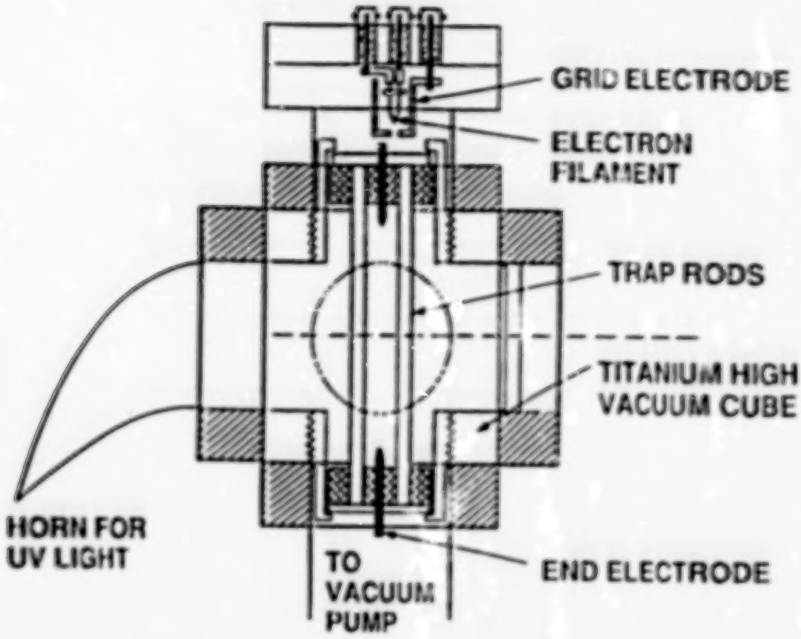


Figure 3 Linear Ion Trap Assembly View. The trap is housed in a 3.375" vacuum cube. State selection light from the ^{202}Hg discharge lamp enters from the right, is focused onto the central 1/3 of the trap and is collected in the horn. Fluorescence from the trapped ions is collected in a direction normal to the page.

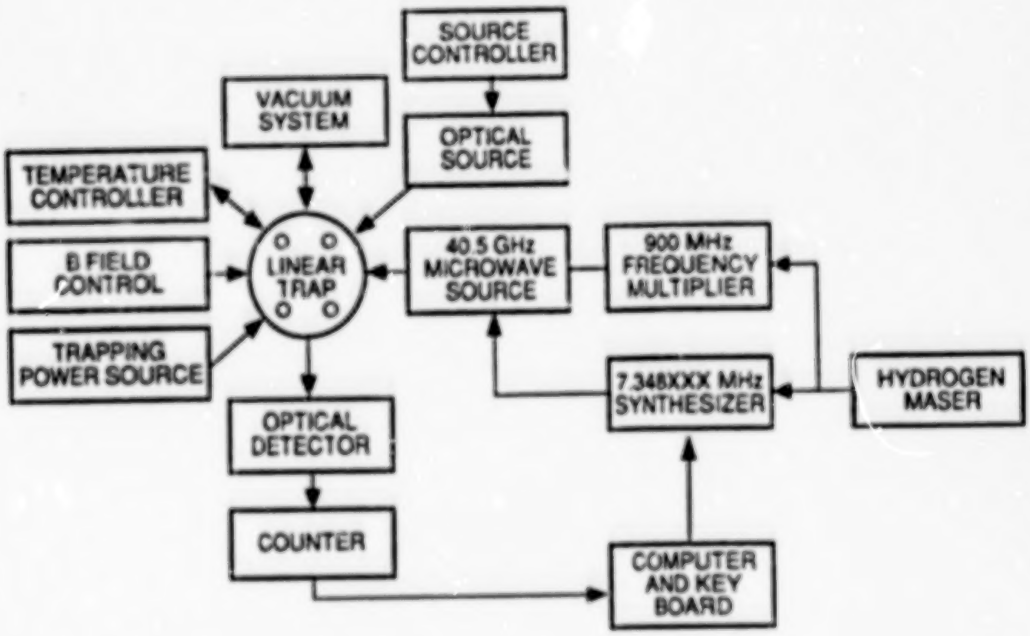


Figure 4 Schematic of measurement system where the $^{199}Hg^{+}$ clock frequency is compared to an H-maser frequency.

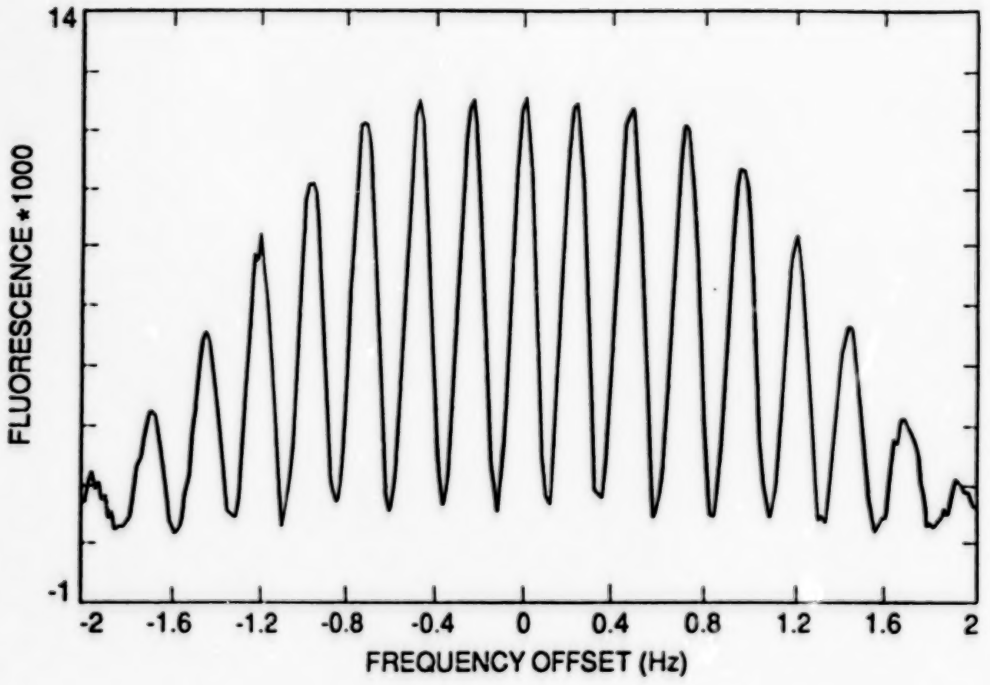
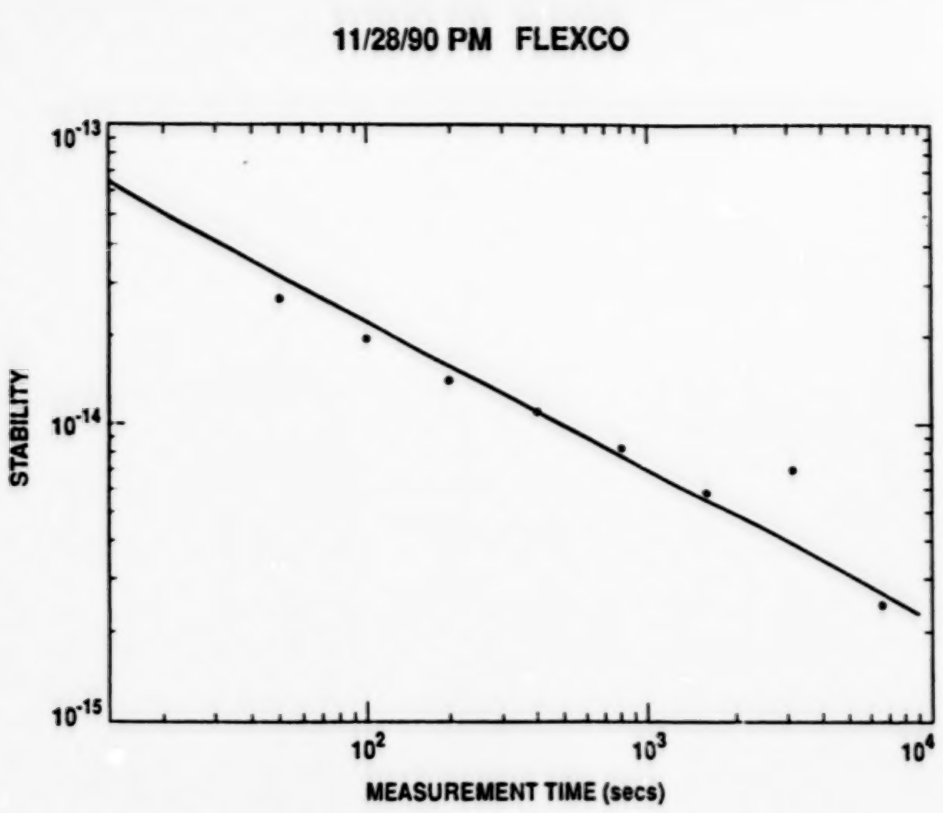


Figure 5 $^{199}Hg^{+}$ clock transition as measured with successive oscillatory fields method. This line shape results from two 0.4 second microwave pulses separated by a 3.5 second free precession period. The central line is about 120 mHz wide.



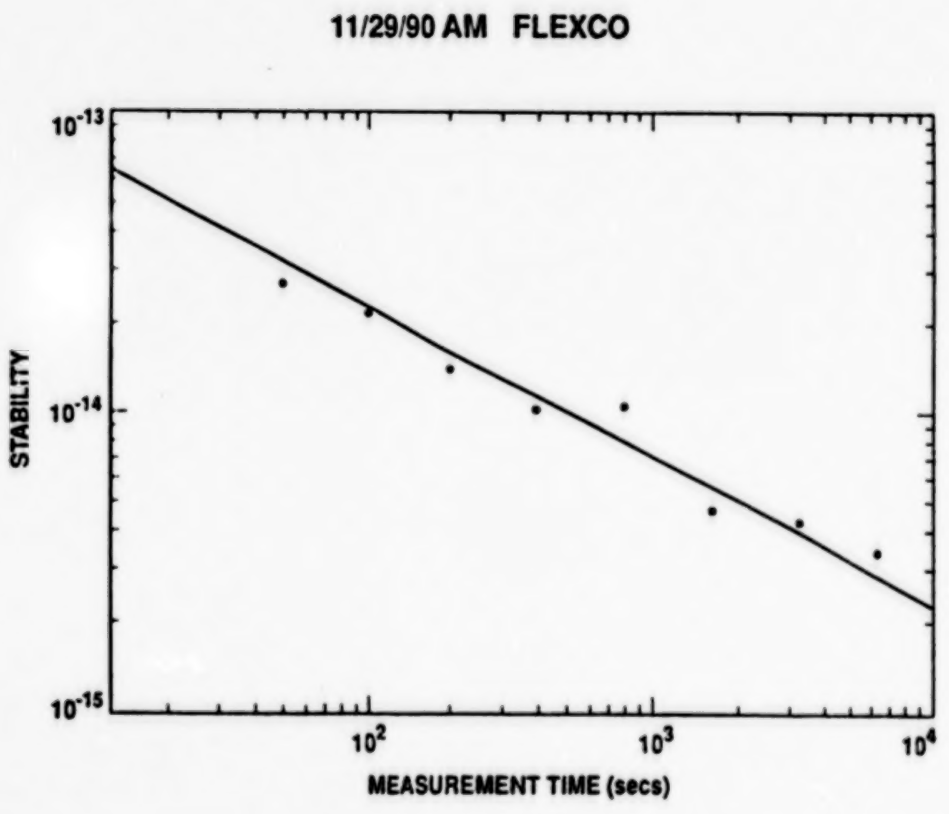


Figure 6 Two measurments of the $^{199}Hg^{+}$ clock transition stability for the 120 mHz resonance line of Figure 5. Fractional frequency stability is $2 \cdot 10^{-13}/\sqrt{\tau}$ for $35 < \tau < 10{,}000$ sec.

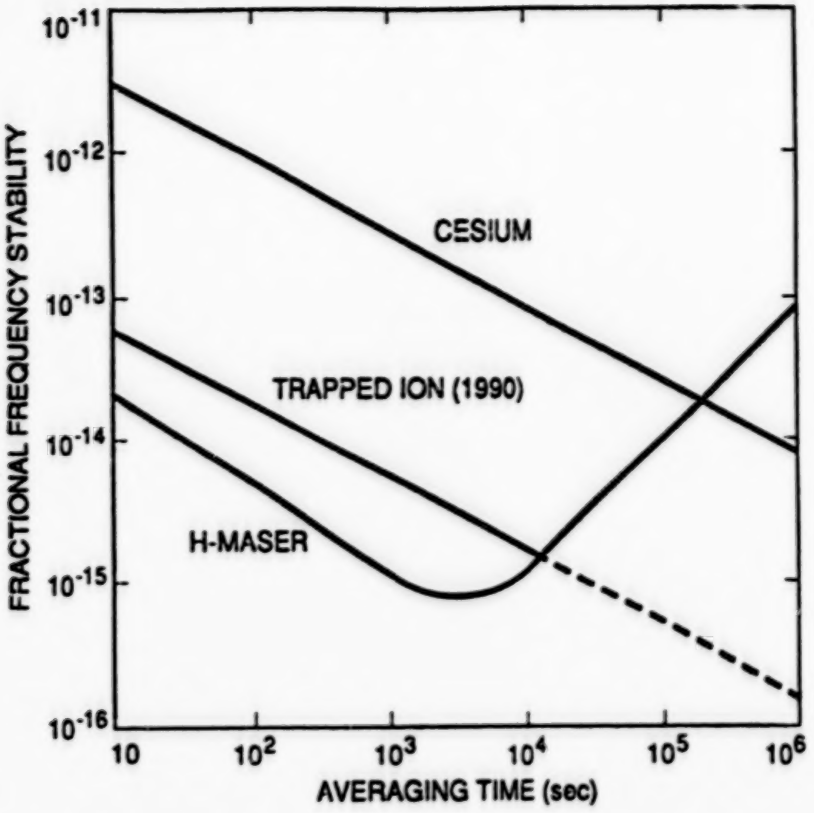


Figure 7 Comparison of the currently demonstrated $^{199}Hg^{+}$ stability with other frequency standards used in JPL's Frequency Standards Laboratory.

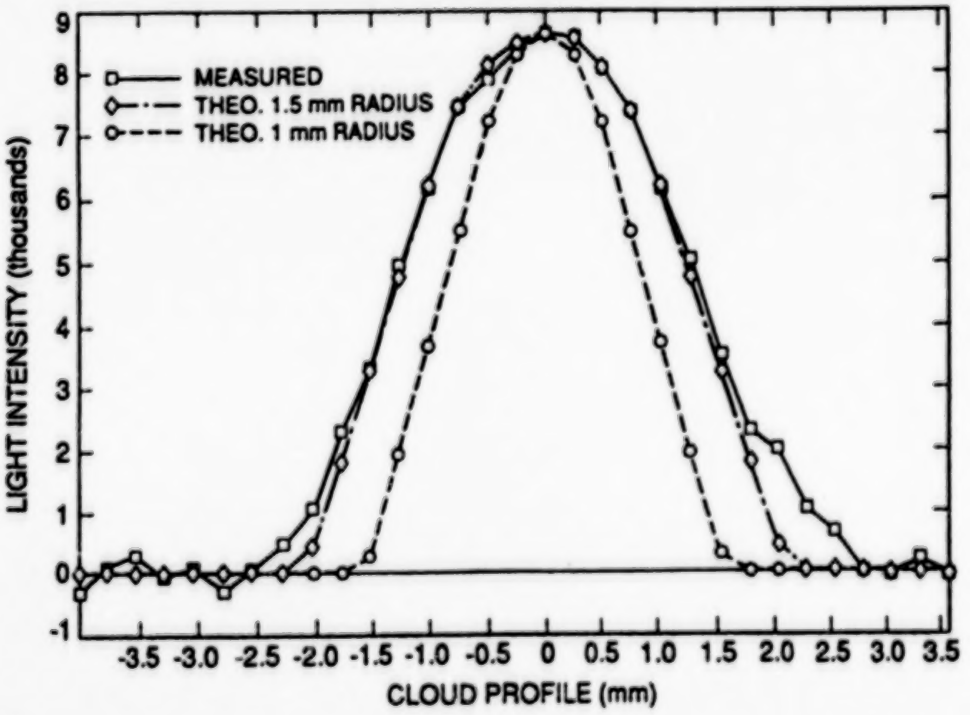


Figure 8 The ion cloud diameter as determined by sweeping a masked photomultiplier across the focal plane of the UV light imaging/collection system. The data displayed is collected light vs. detector position.

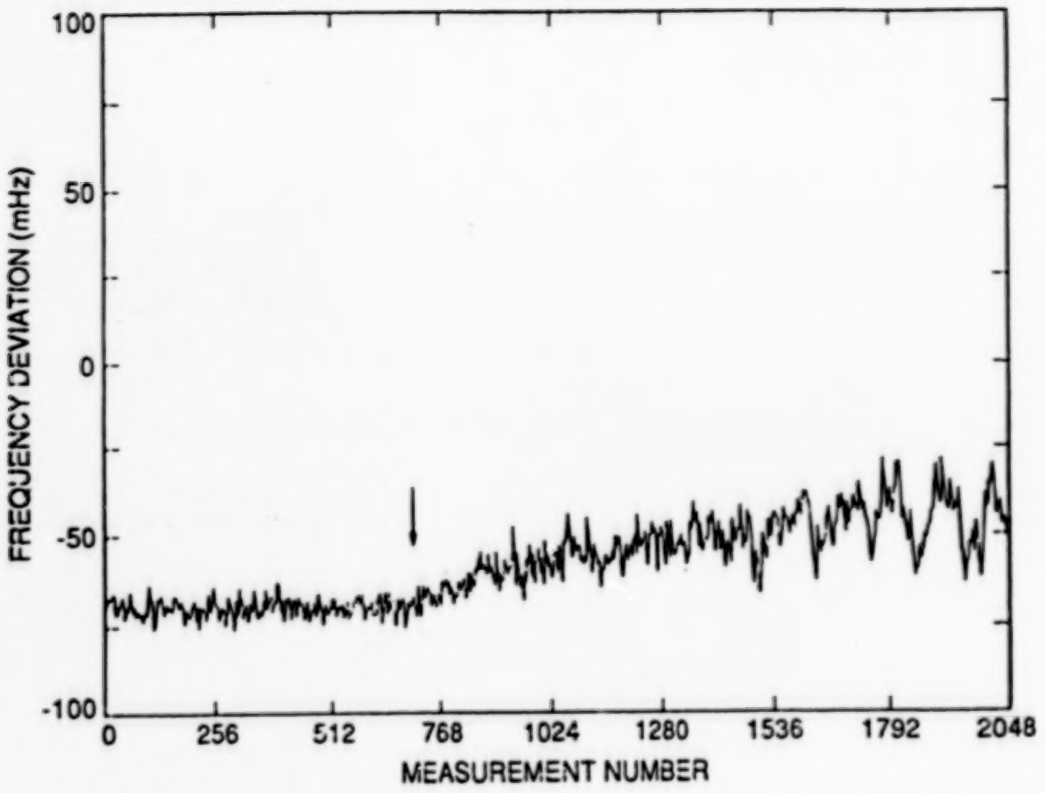


Figure 9 A direct measure of 2nd order Doppler shift due to ion motion in the rf trapping fields. As the ion number (and hence ion cloud radius) diminishes the clock frequency increases. A net frequency shift of 25 mHz ($6 \cdot 10^{-13}$) is shown.

QUESTIONS AND ANSWERS

Dr. Thomann, Neuchatel Observatory: How good a candidate would that be for a primary standard?

Dr. Prestage: As we run it the second order doppler shift is probably the limiting effect. Accuraccy of 1×10^{-13} would be reasonable.

Dr. Thomann: By sacrificing some signal to noise you could improve the second order doppler effect significantly?

Dr. Prestage: Yes, we could.

BLANK PAGE

DESIGN AND INDUSTRIAL PRODUCTION OF FREQUENCY STANDARDS IN THE USSR

N.A. Demidov and A.A. Uljanov
"QUARTZ" Research and Production Association

Abstract

Some aspects of research development and production of quantum frequency standards, carried out in "QUARTZ" Research and Production Association (RPA), Gorky , USSR, have been investigated for the last 25–30 years. During this period a number of rubidium and hydrogen frequency standards, based on the active maser, have been developed and put into production. The first industrial model of a passive hydrogen maser has been designed in the last years.

Besides frequency standards for a wide application range, RPA "QUARTZ" investigates metrological frequency standards — cesium standards with cavity length 1.9 m and hydrogen masers with a flexible storage bulb.

HYDROGEN MASERS

The first hydrogen maser industrial model CH1–44 was developed in 1968. It was a bulky facility with ion pumps and a glass ceramic cavity. This maser frequency stability was better than 5×10^{-13} per day. Thanks to these early instruments the company has got an experience to work with hydrogen masers, it has investigated their behavior, defined the requirements to maser main units and made technological base for their commercial production. Totally 10 units of this type were produced.

The second hydrogen maser model CH1–70 was designed in 1974. Its metrological and operating characteristics were significantly improved: it decreased dimensions and weight, frequency stability better than (2 to 3) $\times 10^{-14}$ per 100 s to 1h measurement intervals. The maser view is shown in Fig. 1, and its schematic structure is given in Fig. 2. The design peculiarity is a special 3–section ion pump, that separately evacuates the storage bulb, state selector magnet and cavity. A separate storage bulb and cavity vacuum system complicate the maser design, but due to this a better vacuum in the storage bulb is achieved. Our experience showed that the wall shift stability and residual gas level in the storage bulb could be correlated. The maser vacuum system uses all–metal seals.

Cavity mechanical resistivity to shocks, vibrations, and stress relaxations significantly influence the hydrogen maser parameters. Our investigations allowed us to solve a number of design and technological problems that reduced these factors to 10^{-15}. Particularly, in masers of this type, frequency dependence on external pressure was 1×10^{-15} per 50 mm Hg.

The cavity frequency drift is the most critical factor in long–term measurements. It was of order (+1.5 to + 3) $\times 10^{-13}$ per day for CH1–44 model and had a tendency to continuous decrease with time. It proved to be related to thermodynamic equilibrium achievement in cavity material. The

drift value in masers with glass ceramic and fused quartz cavities largely depends on oven operating temperature and previous cavity thermal processing. The special thermal processing technology for the CH1–70 maser cavities, made of S0–115M astroglass ceramic, allowed us to minimize the frequency drift down to $< 1 \times 10^{-14}$ per day in the majority of the instruments.

Storage bulbs are coated by fluoroplastics (teflon). They are more insensitive to atomic hydrogen and provide a less spectral line shift and a broadening. For this purpose, until 1975 in the USSR fluoroplastic suspension F–4(tetrafluoroethylene homopolymer) was used, providing a frequency shift of –0.034 Hz for bulbs with 15.7 cm in diameter at temperature +50 °C. As it was found, the wall shift and the spectral line Q factor greatly depend on smoothness of polymer surface structure. Further progress was noted, when fusible fluoroplastics were offered for bulb coating. The best results were received from fluoroplastic F–10, that provided the frequency shift -0.005 Hz and $Q \approx 2.5 \times 10^9$[1].

CH1–80 frequency standard represents this maser modification; it has improved electronics and is produced by "QUARTZ" RPA up to now. The basic instrument characteristics are shown in Fig. 3. The company has delivered 150 instruments on the whole, and all of them are actually operating, thanks to our maintenance and repair service.

These instruments are actively used by the National Time and Frequency Service, they proved to be useful in Very Long Baseline Interferometry, etc. Time and frequency references, located in European and Asiatic parts of the USSR, are based on these instruments[2].

Today we have extensive statistical data, confirming maser high long–term frequency stability in automatic cavity tuning mode—systematic frequency drifts are less than 1×10^{-13} per 1 year. According to National Scientific and Research Institute for Physical, Technical and Radiotechnical Measurements (VNIIFTRI), the measurement data, taken in January–May interval of 1990, the frequency drift of four CH1–80 instruments was less than 1×10^{-16} per day[3].

The instruments of this type, operating in automatic cavity tuning mode with digital system, have lifetimes of 3 years and more. In this mode the atomic beam intensity is modulated. When the automatic cavity tuning system is switched off, the beam intensity decreases and the instrument lifetime is not less 5 years. The main limiting factor of lifetime is the ion pump, and — very seldom— the discharge bulb of atomic hydrogen source made of quartz glass. The ion pump lifetime can be increased by titanium pump plates replacement.

The CH1–75 frequency standard is the last model of this family, released in 1986. Its maser, given in fig.4, has 480×550×680 mm dimensions and weight 90 kg.

The sorption pump design with titanium compact chip as a getter allowed the increase of reliability and lifetime of the beam–forming system with simultaneous weight, dimension and power consumption decreasing. The use of titanium chip excludes maser vacuum system contamination due to getter destruction at continuous operation for long periods. In this case sufficiently large getter particles form a fine grid[4]. The sorption pump external view is shown in Fig. 5. The sorption pump contains about 1 kg of getter, that provides the instrument lifetime for over 5 years. The pump is equipped with the tungsten heater. The chip surface is activated at 800 °C temperature and vacuum better than 10^{-15} mm Hg. Gases not absorbed by the getter can be pumped out by a small ion pump with (1–2) l/s productivity. The similar pump provides vacuum in the microwave cavity.

The small distance between the selective magnet and the storage bulb makes the task of creation an effective selective system more difficult. Quadrupole and hexapole magnet efficiencies were also investigated. As a result, we used quadrupole magnet with its length–to–channel diameter ratio 40.

The magnet had an external diameter of 30 mm, a channel diameter of 1.6 mm, and a length of 75 mm. The magnetic induction on the pole tips is 1 T. The atomic hydrogen source is made of a superpure quartz glass. Its structure is given in Fig. 6. Vacuum seals are provided by indium gaskets, located directly on the source glass flange and fixed by a nut, made of springy bronze. The multichannel collimator is made of a Pyrex glass. Channel diameter is 0.01 mm, the external diameter is 0.5 mm, and the length is 0.8 mm. The compound $LaNi_5H_x$ is used for keeping molecular hydrogen. The $LaHi_5H_x$ is characterized by high hydrogen partial pressure (2 to 5 atm) at +(20-50)° C. 250 grams of the compound contains 18 liters of hydrogen at normal pressure. It is sufficient for maser continuous operation for more than 40 000 hours.

The multizone two-stage oven has the temperature control factor 10^4. The instrument temperature coefficient of frequency is less than 5×10^{-15}/°C.

Magnetic field stabilization in the storage bulb area is provided by a five-layer 81 HMA permalloy shield of 0.35 to 0.5 mm thickness. The shielding dynamic factor of the system with 5 magnetic shields is of order 3×10^4. For the further increasing of a shielding factor a system of "active" magnetic field stabilization was developed[5], where a ferroprobe is used as a sensitive element. With the help of this "active" stabilization system the shielding factor over 10^5 is achieved.

Crystal oscillator frequency tuning to spectral line frequency is accomplished in the automatic frequency control unit, having an ordinary block-diagram. The large multiplication factor for the first multiplier stages and optimal operating modes for all assemblies allowed us to minimize the common phase temperature coefficient of the automatic frequency control unit to 0.01 ns/°C. It permits the achievement of maser frequency stability 10^{-15} without temperature control of the AFC unit.

The instrument has a built-in frequency comparator, providing frequency and phase comparison, and also manual and automatic cavity tuning when a reference signal with characteristics similar to a maser is used. Current time indication and assembly diagnostics are performed with the help of the control unit, containing a reversible frequency counter, a control assembly, and a digital-to-analog converter.

The 5 and 100 MHz output signal frequency stability of CH1-75 is (2 to 3) $\times 10^{-13}$ per s and lowers to (1 to 2) $\times 10^{-15}$ per 10^3 to 10^4s measurement interval. With automatic cavity tuning system in operation, the frequency stability is equal to (2 to 3) $\times 10^{-15}$ per day. Presently this instrument is in serial production.

PASSIVE HYDROGEN MASER

From early days of hydrogen standards and up to now much attention has been paid to problems of improving hydrogen frequency standard characteristics, concerning their weight and dimensions, operation in severe conditions, as these standards can be used in modern global navigational systems and in transportable clocks for time scale synchronization with nanosecond accuracy. Due to new materials, technical decisions and vacuum facilities hydrogen maser dimensions depend on microwave H_{011}-mode cavity size with height and diameter about 280 mm.

The major decision for minimizing dimensions and weight of a hydrogen frequency standard can be found in decreasing microwave cavity size. However, it leads to lowering its Q-factor, impossibility of self-excitation, and as a result the maser can work only in amplification mode—that is, the quantum discriminator mode. The idea of spectral line indication by detecting a frequency-modulated

signal passing through the microwave cavity, promoted the creation of small-sized hydrogen frequency standards[6]. In addition to minimizing the instrument size, hydrogen maser passive mode of operation improves a long-term stability and a lifetime due to atomic beam intensity reduction.

The quantum hydrogen discriminator uses two types of small-sized cavities with quasi-H_{011} modes: cavities with partial dielectric filling[7] and the so-called special axial-symmetric (SAS) cavity with metal plates around the storage bulb, intended for use in hydrogen masers[8,9].

Metal-dielectric cavities have a rigid construction, capable of resisting extremely high levels of shock and vibration, but the lack of industrial production in USSR, high cost and processing difficulties limit the application of industrial instruments. This was the reason to choose a SAS-cavity for the industrial instrument, that is more simple in production and where less expensive materials can be used.

The main problem at SAS-cavity development was to design a rigid construction of metal plates, isolated from cavity walls, as was proposed in [8,9]. We tested different methods of metal evaporation, paste burning-in on a quartz storage bulb, fine metal strips gluing and so on. But these techniques did not give good results. The first two methods showed a low cavity Q-factor of 4×10^3. The third one did not provide sufficient construction reliability, due to different thermal coefficient for quartz glass and metal. The problem was solved by the developing of the original cavity construction[10], where plates were attached to the cavity face walls by metal non-isolated jumpers. The cavity structure is manufactured simultaneously with the cavity base and is characterized by sufficient rigidity, high Q-factor and good producibility.

The offered SAS-cavity design is used in CH1-76 passive hydrogen maser (Fig.7). The cavity is made of D16 aluminum alloy with silvered walls and has a Q-factor of 12×10^3 and internal diameter of the cylinder of 128 mm and of the plates of 62 mm. This provides amplification over 8 dB. The storage bulb, coated by fluoroplastic F-10, has a relatively small volume 0.45 l, in this case spectral line Q-factor can reach 1×10^9. The cavity is surrounded by four magnetic shields. The three internal shields are made of permalloy 81HMA of 0.5 mm thickness. They are placed in vacuum, and additionally perform the function of heat reflecting screens.

The fourth magnetic shield is made of 79HM permalloy of 1 mm thickness. It shields completely the discriminator and represents a load-carrying structure. The shielding dynamic factor is more than 8×10^4. The atomic hydrogen source located in the fourth magnetic shield, has a ring-shaped magnet, providing continuously variable magnetic field configuration in interdrift space. This prevents a Zeeman sublevel population change. Besides,the magnet improves HF discharge operating mode. The quantum hydrogen discriminator oven has a stage with two independent control zones. The oven heater windings are located at the external cavity side. Total power dissipated by the ovens is equal to 1 W at normal conditions and cavity temperature of 50°C. The quantum hydrogen discriminator is made in the form of tube with 222 mm in diameter, 520 mm in length and 19.5 kg in weight.

The construction of the above-mentioned cavity with relatively thin and long jumpers is not enough resistant to shocks and vibrations. This disadvantage is eliminated in our "magnetron" construction of the SAS-cavity[11]. Here metal plates are fixed to the lateral surface of the cavity, manufactured from a monolithic piece, that provides its high mechanical rigidity and reliability (Fig. 8).

The short-term frequency stability of the passive hydrogen frequency standard depends on conversion transconductance (figure of merit) of the quantum hydrogen discriminator, and its long-term stability is determined by spectral line stability and AFC system accuracy. The limiting factors for long-term spectral line stability are the same as for an active maser, and they permit the achievement of high

metrological characteristics.

The CH1-76 passive hydrogen standard block-diagram (Fig. 9a) was designed on the base of the block-diagram for one modulation frequency, offered in article [12]. The advantage of this diagram is in use of "noise" local oscillator, that eliminates the influence of spurious signal, passing from 20.405 MHz synthesizer to the IF amplifier channel[13]. In the passive hydrogen standard a separate crystal oscillator with 90MHz frequency, multiplied up to 1440 MHz, is used as a local oscillator of this type.

Usually the CH1-76 frequency stability is determined by the expression $\sigma = 1 \times 10^{-12}/\tau^{1/2}$ at $1 < \tau < 10^4$ s. Frequency stability is equal to 1×10^{-14} per day and is limited by transients in electronic assemblies. Further improvement of electronic assemblies gives us a hope to reach frequency stability for the specified quantum hydrogen discriminator of (3 to 5) $\times 10^{-15}$ per day. The temperature coefficient of frequency is less than 2×10^{-14}/°C. Frequency shift at magnetic field variation in the range of $\pm 2 \times 10^{-4}$ T is less than (3 to 5) $\times 10^{-14}$. The CH1-76 frequency standard is characterized by a good long-term frequency stability. For measurement intervals of several months the frequency drift is (1 to 3) $\times 10^{-16}$ per day (Fig. 10)[14].

The CH1-76 frequency standard has a satisfactory mechanical rigidity and maintains high metrological characteristics under severe mechanical conditions. It was proved by its tests as transportable clocks. The standard dimensions are 280×480×555 mm (height, width, depth), a weight of 53 kg, power consumption of 70 W from +27 V power supply (Fig. 9b).

HYDROGEN MASER WITH FLEXIBLE STORAGE BULB

The absolute frequency of the hydrogen maser is generally determined by a wall-shift measurement accuracy. Nonreproducibility of coating characteristics in the traditional method of wall-shift measurement gives an accuracy of (1 to 2) $\times 10^{-12}$. The further improvement of the wall shift measurement accuracy can be achieved by the design of a hydrogen maser with a flexible storage bulb. Its use eliminates basic limitations in accuracy measurement, as the same bulb surface is present during the measurements at bulb volume change. The use of a flexible storage bulb allows us to control a wall shift during its operation. In its turn it permits the increase in long-term frequency stability of a hydrogen maser. Many authors attempted to develop a hydrogen maser with a flexible storage bulb, but because of great manufacturing problems they failed.

As a result of our tests we came to the conclusion, that the construction with the flexible storage bulb part outside the microwave cavity is preferable. The optimization of the storage bulb shape and size allowed us to achieve the characteristics of the hydrogen maser with a flexible bulb similar to CH1-70 standard specifications. The problem of the bulb volume reproduction with high accuracy was solved by reinforcing its flexible part with a quartz or alumosilicate glass cloth[15]. The hydrogen maser design with a flexible bulb, developed in 1985, is shown in Fig. 11.

Starting from 1986 continuous measurements are taken. During this period the quantum hydrogen maser with a flexible bulb showed a high reliability. The bulb volume was changed more than one hundred times and no changes were noticed in the flexible part. The frequency measurement of the hydrogen maser with the flexible storage bulb and its volume change gave us the opportunity to determine hydrogen atom nondisturbed transition frequency with high precision.

The test results are summarized in Table 1.

		Table 1.		
Coating material	Wall shift, Hz at 50°C D=15.7 mm	Bulb number	f=1420405751 Hz	Data reference, year
F–4DU	-0.0242 ± 0.0014	10	,,,.7682 ± 0.0014	[18], 1976
F–4D	-0.034 ± 0.004	6	,,,.77 ± 0.005	[19], 1977
TFE–42	-0.0337 ± 0.001	11	,,,.768 ± 0.002	[20], 1970
FEP–120	-0.022 ± 0.001	6	,,,.77 ± 0.003	[21], 1971
F-10		flexible bulb	,,,.709 ± 0.0005	1988

The received frequency value $f_0 = 1420405751.7709 + 0.0005$ Hz is in good agreement with f_0 measurement results, received by bulb replacing method. We hope to improve a wall shift and f measurement accuracy to better than 1×10^{-13} by the further flexible bulb modification, a better bulb volume control, a more pure and uniform bulb coating and the test accuracy of order 10^{-15}.

RUBIDIUM FREQUENCY STANDARDS

The concept of rubidium standard design was adopted in the 1970's and includes two trends:

- rubidium frequency standards,
- measuring rubidium frequency and time standards.

The first trend represents the commercial rubidium standards CH1–43(1968), CH1–50(1971), CH1–72(1981), CH1–77(1987). The second trend includes the instruments, which are used by metrological services of industrial plants. The instruments of this type are CH1–48(1971), CH1–69(1976), CH1–78(1987). At present time three models of rubidium frequency standards are produced: CH1–78, SCHV–74 and RSCH–77 (Fig. 12). The instruments have traditional block–diagrams, but the design and manufacturing technology of the rubidium quantum discriminator are original and asserted by certificates of authorship. It refers to optical pump source design with a cylindrical gas–discharge tube, located in an evacuated bulb (Fig. 13).

This design decision provides low power consumption (700–800 mW), and allows placement of the quantum elements (absorption cells, filters, pump source) in one temperature–controlled volume. It provides low temperature coefficient of frequency for the instruments.

The tests showed, that the basic aging process of the gas–discharge tube can be explained by surface conductance, caused by the influence of HF discharge plasma on glass surface when alkali metal vapor is used. In its turn it creates a systematic frequency drift due to a light beam shift and shortens the lifetime of the gas–discharge tube. To decrease the influencs of these factors, the rubidium

standard utilizes the reduction mode. When the instrument is turned on, the gas-discharge tube is warmed up in a short time up to the temperature (200-250)°C. The conductive film, formed on the internal tube surface, is broken and gas-discharge is ignited in the normal way. The reduction mode allowed us to increase a gas-discharge tube lifetime and improve the metrological parameters of the rubidium standard. The original manufacturing technology of quantum elements is characterized by the absorption element material (rubidium-87 and potassium alloy, filled with argon under 1 mm Hg pressure), by buffer gas pressure calibration technique in an absorption cell according to signal frequency offset of atomic resonance (calibration accuracy (3 to 4) x 10^{-11} and some other technical decisions. All of them provided sufficiently high metrological characteristics of the rubidium standard and its stability under hard environmental and mechanical conditions.

The rubidium standard production is provided by complete special technological equipment, developed and manufactured by domestic plants.

The main specifications of CH1-78 standard are given in Table 2.

METROLOGICAL CESIUM FREQUENCY STANDARD

In 1980 RPA "QUARTZ" developed the MC-3 cesium frequency standard for National time and frequency state service[17].

The cesium atomic beam tube (Fig. 15) consists of Ramsey microwave cavity with drift space length 194 cm and interaction area length of 1 cm each, transverse field Hc, formed by four bars, a three-layer magnetic shield (internal rectangle), two mobile source-detector units (one at each side of the atomic beam tube), and two-pole selective magnets. All of them are enclosed in a vacuum system, evacuated by two 250 l ion pumps (vacuum 5 x 10^{-6} Pa).

The beam is of ribbon type, formed by multichannel collimator with transversal dimensions 9×0.5 mm. The beam optics uses selective magnets with a center slot and valves, placed across the beam center. The center beam frequency of Ramsey resonance can reach (48-65) Hz depending on the light source and the detector position. The field strength is of the order Hc≈ 5.25 A/m. The maximum field nonuniformity is 0.5%, it is tested by eight Zeeman coils, located along the beam axis. The used signal makes up 80% of full current beam on the detector; figure of merit is F≈30.

The nonexcluded systematic error is of the order 1×10^{-13}. The basic investment to this value is made by a distributed phase shift in microwave cavity, magnetic field gradients at the atoms flying into and out of H-field, and the presence of dissipated microwave power.

The latter can be found out in the limits 1×10^{-13} as a function of H-field direction and microwave power level. The cesium frequency standard uses the digital system of output signal automatic frequency control according to the cesium transient frequency. Square-pulse modulation frequency with modulation interval 4 s is used, that is achieved by the synthesizer frequency change. At the moment of synthesizer frequency changing the digital voltmeter is disabled and doesn't perform readouts to exclude transient process influence on tuning frequency.

In the control unit the error signal from atomic beam tube output is summed and averaged for the specified modulation period number. This signal is used for shaping the frequency correction signal of the hydrogen maser synthesizer. The time of error signal averaging and compensating and correspondingly the interval between corrections can be changed from 10 s to 1 hour. Figure 16 shows the results of MCs-3 standard frequency comparison with the group hydrogen keeper specifications

received by VNIIFTRI. The frequency reproducibility is 5×10^{-14} for the measurement interval up to 16 hours[16].

At present the time intensive research on cesium atomic beam tube modification, providing minimum nonexcluded systematic error, is being in process. The main tasks of this modification are the use of ring–shaped microwave cavity, the creation of H longitudinal field, elimination of microwave power scattering, and minimizing average speed of beam atoms.

Fig.16. Table 2.

CH1–78 measuring rubidium frequency time standard specifications.

Specifications	CH1–78a	CH1-78b
1. Output frequency values, MHz	5; 1; 0.1	5; 1; 0.1
2. Drift per 1 month	6×10^{-12}	3×10^{-11}
3. Allan variance per:		
1 s	7×10^{-12}	7×10^{-12}
10 s	3×10^{-12}	3×10^{-12}
1 day	7×10^{-13}	2×10^{-12}
4. Frequency reproducibility & relative accuracy	5×10^{-12}	5×10^{-12}
5. Mean temperature coefficient of frequency	8×10^{-13}	8×10^{-13}
6. Measurement accuracy per:		
1 s	1.4×10^{-11}	1.4×10^{-11}
10 s	1.4×10^{-12}	1.4×10^{-12}
100 s	1.4×10^{-12}	1.4×10^{-12}
7. Operating temperature range, °C	0...+50	0...+50
8. Power consumption, VA		
220 V (50 Hz)	43	43
27 V	35	35
9. Weight, Kg	17	17

REFERENCES

1. N.A. Demidov, E.M. Ezhov, V.A. Phedorov and others. *Frequency wall-shift investigation in hydrogen maser in new materials* Proc. VNIIFTRI Issledovaniya v oblasty izmereny vremeny i chastoty. Moscow, 1978, v.37(67), P.81–85

2. S.B. Pushkin, R.B. Sharikov. *Analysis of metrological characteristics of the National Time and Frequency Service reference.* Proc. VNIIFTRI. Issledovaniya v oblasty izmereny vremeny i chastoty. Moscow, 1989, P.3–8

3. B.A. Gaigerov, N.D. Zhestkova, N.B. Koshelyaevsky and others. *Basic metrological characteristics of "Chajka-Cheget" instruments complex used in the National Time and Frequency Service* Fhes. of papers of IVth all-union symp. Issledovaniya v oblasty izmereny vremeny i chastoty. VNIIFTRI, Moscow, 1990–P.4

4. S.L. Gordeev , N.A. Demidov , E.M. Ezhov. *Getter pump gas absorber for hydrogen pumping out* A.s. 918.510. USSR Bjulleten Izobreteny , 1982, N 13

5. G.A. Elkin, A.I. Bojko, N.D. Zhestkova. *Stabilization of direct magnetical field in hydrogen maser* Thes. of papers of Vth all-union confer. "Metrologiya v radioelectronice" VNIIFTRI, Moscow, 1981, P.88

6. F.L. Walls , H. Hellwig. *A new kind of passively operating hydrogen frequency standards* Proc.30th Ann. Symp. Freq. Contr., 1976, P.473–480

7. E.S. Salisky, N.A. Weakliem. *An Operating Development Modes Spacecraft Hydrogen Maser* Proc. 32th Ann. Freq. Contr. Symp., 1978, P.499–505

8. H.E. Peters. *Small, very small and extremely small hydrogen maser* Proc. 32th Ann. Freq. Contr. Symp. , 1979, P.469

9. V.A. Bochkov , B.A. Gaigerov , V.P. Korolyov and others. *Hydrogen maser with smallsize cavity* Radiotekhnika i electronica , 1981, VXXVI, N 11–P.2471

10. A.A. Belyaev , N.A. Demidov , S.B. Povalyashko . *Hydrogen discriminator* A.s. N 1.336.881 USSR. Otkritiya.Izobreteniya N 33,1987

11. A.A. Belyaev , N.A. Demidov , Makarychev. *Hydrogen maser* A.s. N 1.459.568 USSR. Otkritiya. Izobreteniya, N 6,1989

12. G. Bursa, H. Brandenberger. *Passive H-maser* Proc.33rd Ann. Freq. Contr. Symp., 1979, P.563–568

13. N.A. Demidov , B.A. Sakharov . *Passive H-maser* A.s.N 1.258.212 USSR. Otkritiya. Izobreteniya. N 34 1986

14. A.S. Perlin , V.P. Egorov , N.V. Korolyova . *The results of hydrogen maser behavior research comparing to the National Time and Frequency Service reference.* Thes. of IVth all-union symp. Issledovaniya v oblasty izmereny vremeny i hastoty. VNIIFTRI. Moscow, 1990, P.13.

15. N.A. Demidov , V.A. Phedorov , V.I. Phedoseev. *Flexible storage bulb for hydrogen maser* A.s. N 1.137.947 USSR. Otkritiya. Izobreteniya, 1985, N 4

16. L.I. Polyakova, V.Yu. Runov, Yu.V. Timofeev and others. *The results of research of metrological Cesium frequency standard* Thes of papers Vth all-union conf."Metrologiya v radioelectronike" VNIIFTRI Moscow, 1984, P.253–255

17. Yu.G. Abashev, G.A. Elkin, Yu.V. Timofeev. *The results of the cesium frequency reper MCs-3 used in the National Time and Frequency Service.* Thes. of papers IVth all-union conf. "Metrologiya v radioelectronike" VNIIFTRI, Moscow, 1984, P.253–255

18. N.D. Zhestkova, G.A. Elkin, V.T. Zemscova. *The hydrogen reper of frequency and determination of absolute frequency* Izmeritelnaja tekhnika. , N10, 1976, P.50–51.

19. N.A. Demidov, E.M. Ezhov, A.A. Uljanov and others. *A frequency wall-shift investigation in the hydrogen maser.* Izmeritelnaja tekhnika , N7, 1977, P.45–47.

20. H. Hellwig, R.F.C. Vessot, M.W. Levin and others. *Measurement of unperturbed hydrogen hyperline transition frequency* IEEE Trans. on Instrum. and Measur.

21. D. Morris Metrologia , v7, N4, 1971, P.162–166.

BLANK

PAGE



Fig.1. CH1-70 hydrogen maser.

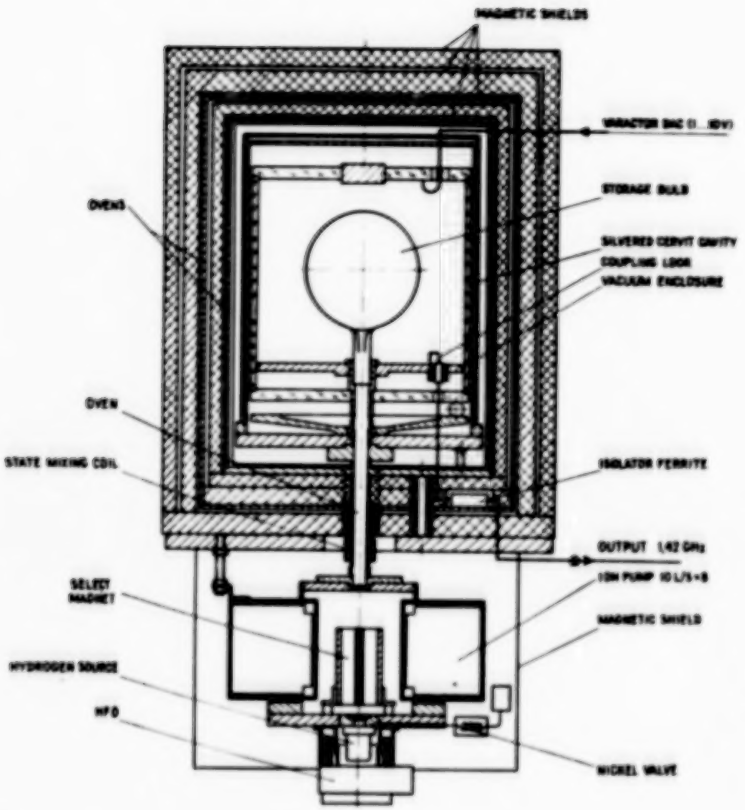


Fig.2. CH1-70 hydrogen maser schematic.

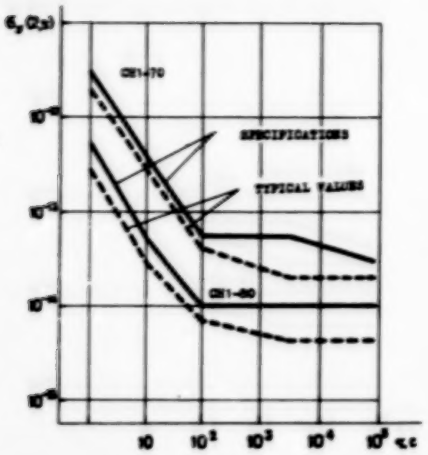
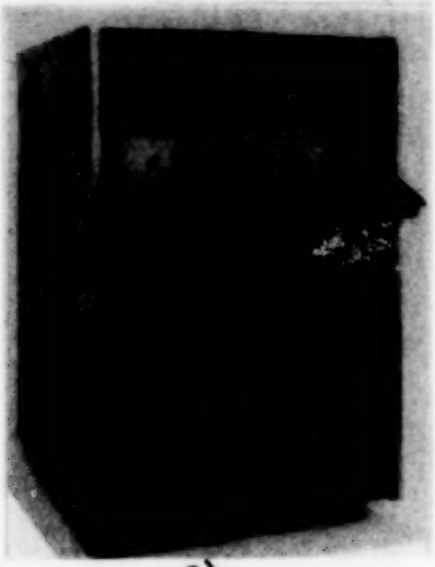


Fig.3. Frequency stability per 1, 10,100 s, 1 h and 24 h. Additional frequency shift change: less than $1.5*10^{-14}$ for CH1-70 and less than 10**(-14) for CH1-80. at 1 C ambient temperature



a)

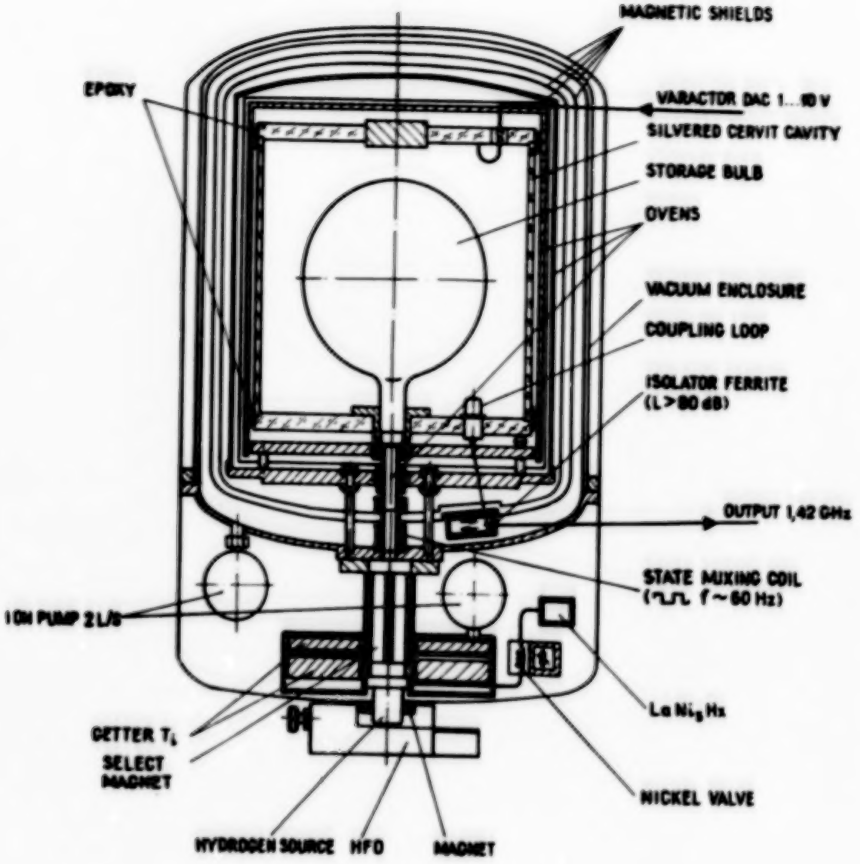


Fig.4. CH1-75 hydrogen maser:
a) photo; b) schematic design.

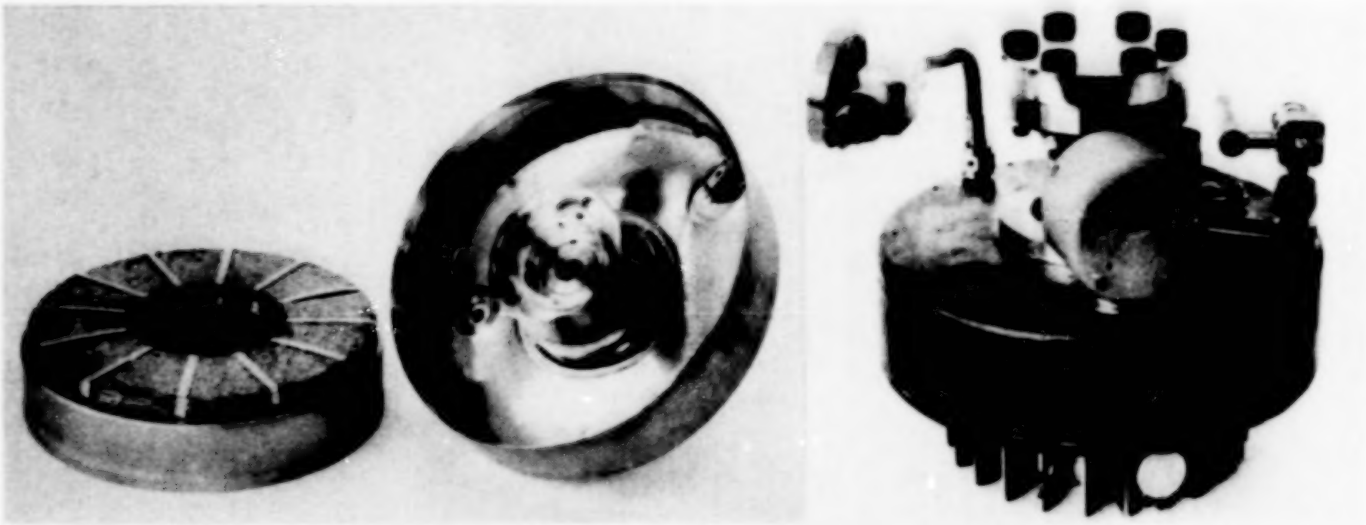


Fig.5. Getter pump of hydrogen masers CH1-75, CH1-76.



Fig.6. Quartz discharge bulb of hydrogen masers CH1-75, CH1-76.

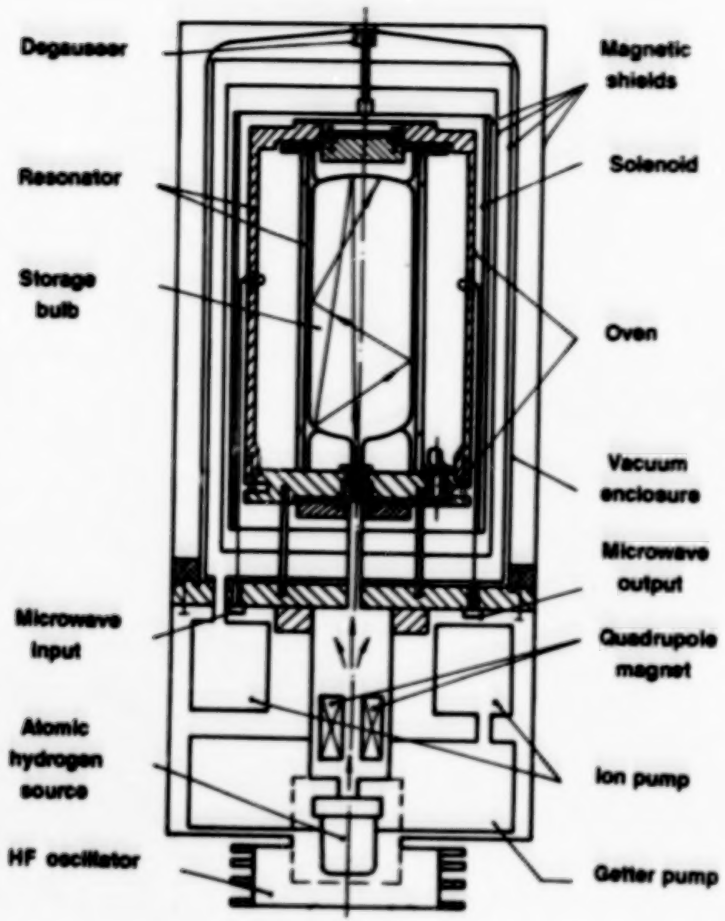




Fig.7. CH1-76 hydrogen maser:
a) schematic design;
b) assambling without vacuum tank, magnetic shields and cavity cylinder.

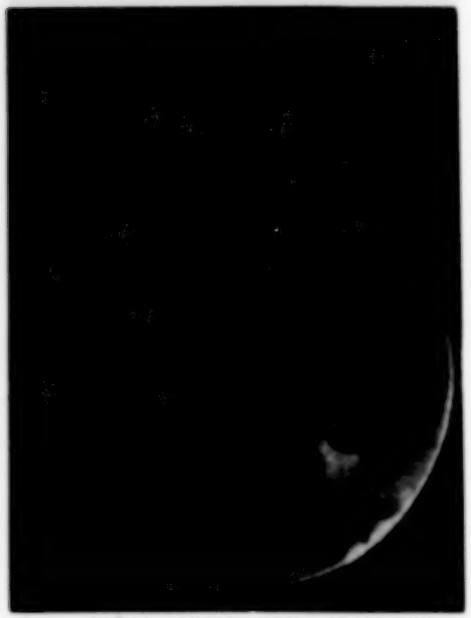


Fig.8. Photo of "megnetronic" cavity.

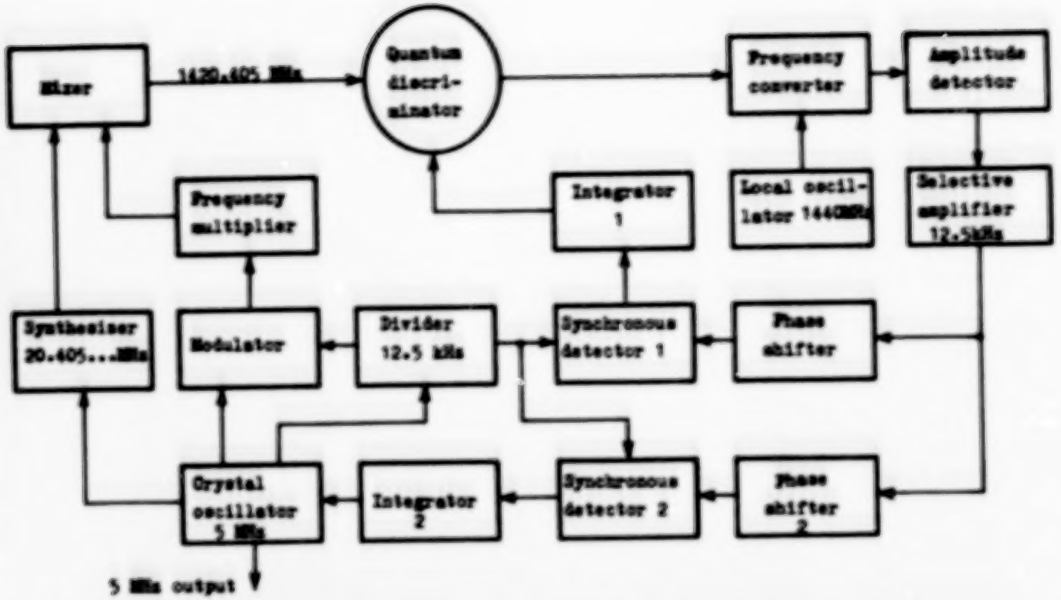


Fig.9. CH1-76 passive hydrogen maser : a)block-diagram b) photo.



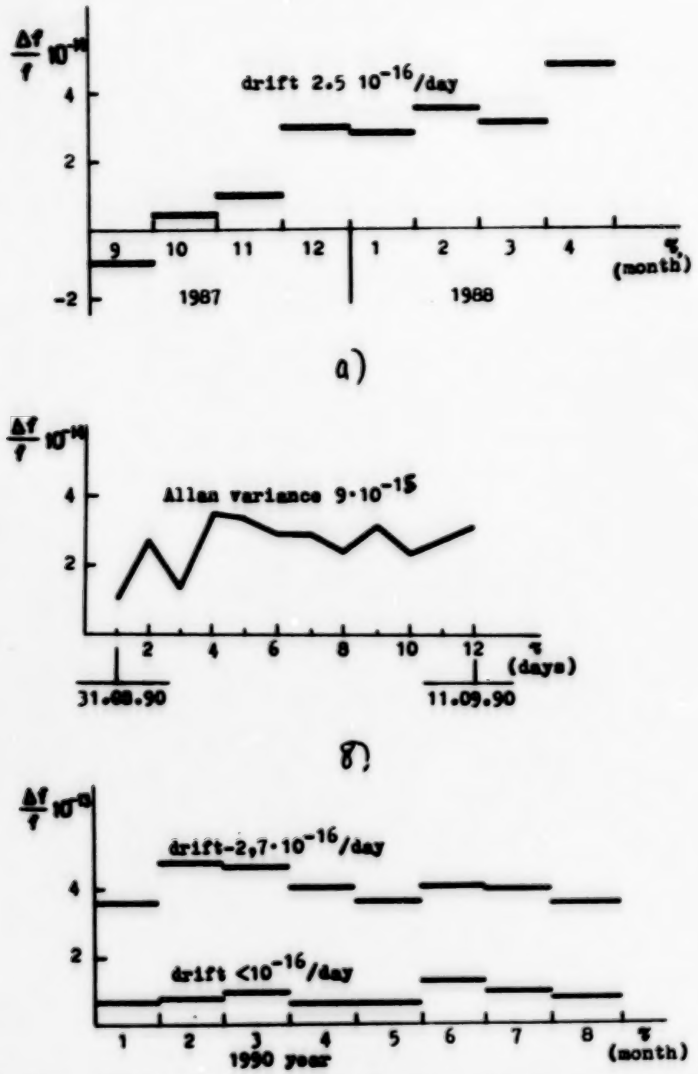


Fig.10. The exemples of output frequency behaviour of the CH1-76 commercial instruments in relation to a group of active masers: a) averaging per month; b) averaging per day; c) long-term stability analysis results of two CH1-76 (obtained in Leningrad Scientific Research Radio Technical Institute [14]).

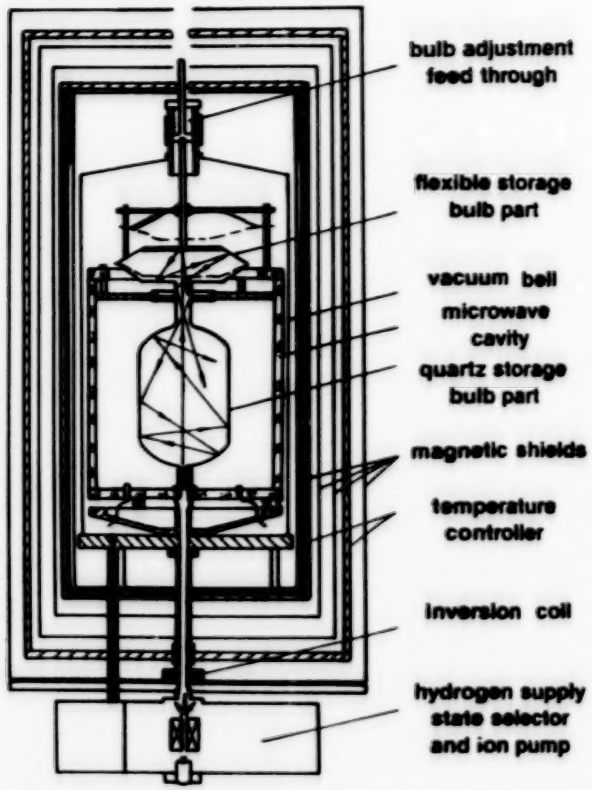


Fig.11. The hydrogen maser with flexible storage bulb.

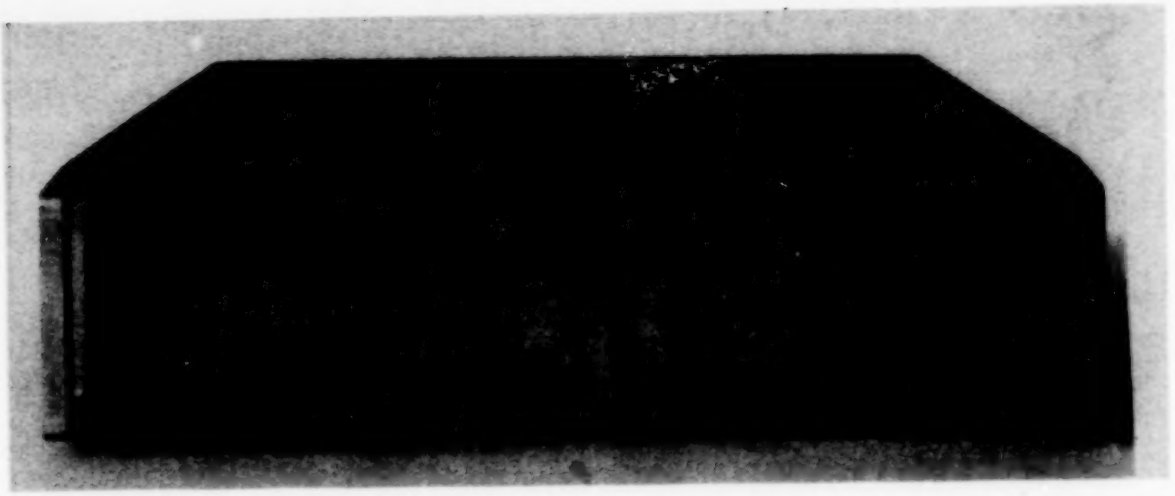


Fig.12. CH1-78 rubidium frequency standard.

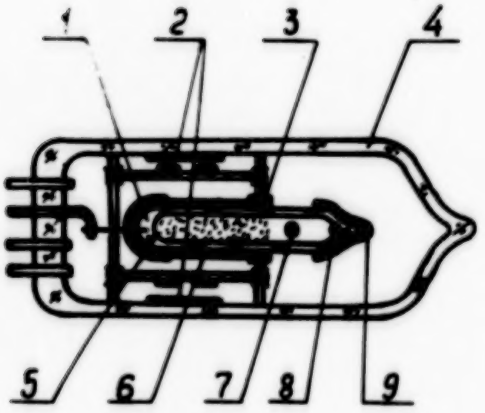
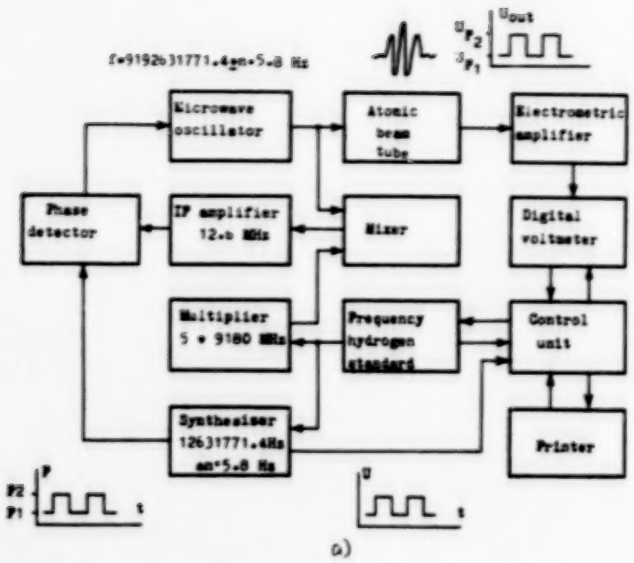
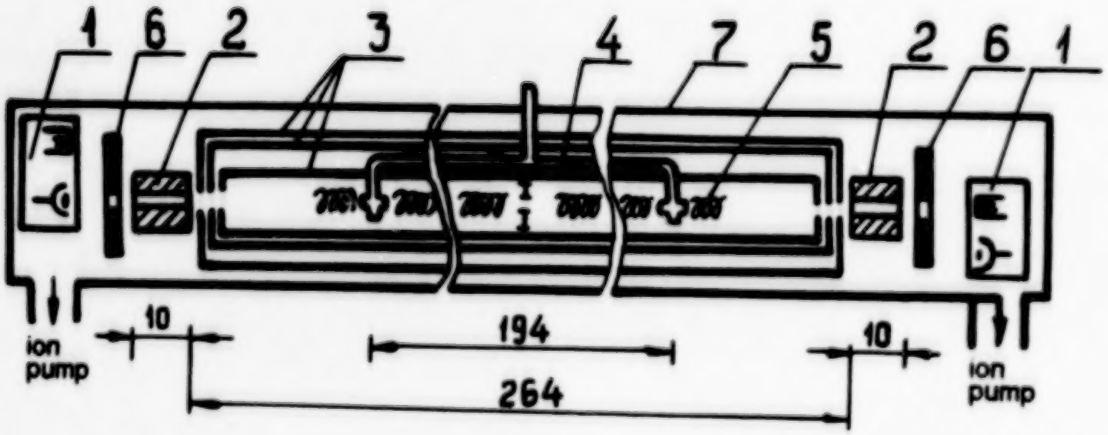


Fig.13. The gas-discharge lamp of optical pumping source for rubidium frequency standards:
1) gas-discharge lamp 2) getting reflector
3,5) heater contact 4) vacuum envelope 6) heater
7) starting electrode 8) Rubidium-87
9) high frequency electrode.



а)



б)

Fig.14. MCs-3 - metrology cesium frequency standard:
a) block-diagram;
b) the Cs atomic beam tube schematic design.
1) beam source and detector 2) state selecting magnets 3) magnetic shields 4) microwave cavity 5) LF-coils 6) graphite 7) vacuum envelope



Fig.15. Relative frequency difference between MCs-3 and ensemble hydrogen clocks of the National Time and Frequency Service.

Table 2.

Table 1.

Coating material	Wall shift, Hz at 50°C D=15.7 mm	Bulb number	f=1420405751 Hz	Data reference, year
F-4DU	-0,0242 ±0,0014	10	..,7682 ±0,0014	[18], 1976
F-4D	-0,034 ±0,004	6	..,77 ±0,005	[19], 1977
TFE-42	-0,0337 ±0,001	11	..,768 ±0,002	[20], 1970
FEP-120	-0,022 ±0,001	6	..,77 ±0,003	[21], 1971
F-10		flexi-ble bulb	..,7709 ±0,0005	1988

The received frequency value f_o =1420405751.7709+0.0005 Hz is

QUESTIONS AND ANSWERS

Albert Kirk, Jet Propulsion Laboratory: The Allan variance data that you showed—was that taken while the maser was autotuning?

Dr. Demidov: Yes

LONG-TERM MICROWAVE POWER DRIFT OF A CESIUM FREQUENCY STANDARD AND ITS EFFECT ON OUTPUT FREQUENCY

W. A. Johnson,
S. K. Karuza, and F. J. Voit
Electronics Research Laboratory
The Aerospace Corporation
P. O. Box 92957
Los Angeles, CA 90009

Abstract

It has been shown previously that the long-term frequency stability of a cesium (Cs) frequency standard is affected by variations in the standard's internal microwave power source [1,2]. Studies were performed on a commercial Cs frequency standard for a period of 20 days, to determine the stability of its microwave power source. The results were then analyzed statistically, and the effects of microwave power drift on the standard's frequency stability were calculated.

INTRODUCTION

Studies were performed in our laboratory on cesium (Cs) frequency standards (clocks) made by different manufacturers, to determine the effect of microwave power variations on the output frequency of the standard at different settings of the C-field current. Figure 1 is a block diagram of the test set-up. The results were reported in [3,4]. In one particular Cs frequency standard, we wanted to determine the stability of its own internal microwave power source and the effect of this stability on the frequency stability of the standard.

During the last 20 days of the experiment the zero offset of the microwave power meter was recorded manually. These data were then used to correct the actual measured microwave power values by enabling power meter drift to be eliminated. These results are reported herein. We note that because we have many components in series with the clock electronics, we cannot say that the power variations we measured are completely attributable to the clock itself. It is likely that the resulting power variations are somewhat worse than would be the case for a normal clock configuration.

MEASUREMENTS

During the 20-day measurement period there were three separated data runs lasting approximately 3, 6, and 10 days. At the beginning of each run the power meter was zeroed. Because we could not zero the meter during a run without stopping the program, we periodically increased the microwave attenuator setting by 60 dB and read the meter's output in microwatts. During the data taking, the power level into the meter was on the order of 50 μW. Sixty dB below this is thus 50×50^{-6} μW, which is very much less than the smallest nonzero power (0.01 μW) that the system can read. Thus, increasing the attenuation by 60 dB was equivalent to terminating the meter with a load; indeed, it was probably better, because no microwave connections were changed. The measured power offsets are plotted in Figure 2.

Each of the three data runs consisted of the following steps:

1. Set the C-field at a low value (6 to 8 mA) and the power at the optimum value (i.e., for maximum beam current) of -12.5 dBm.
2. Measure the beat frequency over some long averaging time T.
3. Increase the power level by 1 dB to -11.5 dBm.
4. Measure the beat frequency over T again.
5. Increase the C-field current by some prescribed amount (typically 1 mA in our data sequence).
6. Measure the beat frequency over T again.
7. Change the power back to -12.5 dBm.
8. Measure the beat frequency over T again.
9. Increase the current again.
10. And so on.

The last C-field current is typically 22 mA.

Each time either the C-field current or the microwave power is changed, there is a waiting period of approximately 5 minutes before data taking begins. This wait ensures that if the clock loop goes out of lock, it will have more than adequate time to relock. For the particular clock measured, the maximum time to acquire relock is about 2 minutes. It is during these 5-minute waits that the power meter's zero offset is read. Figure 2 is a plot of these zero offsets as a function of time. Note that the offsets are all either zero or negative. A negative value for the offset means that all powers measured are actually larger by the amount of the offset.

Figure 3 is a plot versus time of the two measured power levels. The corrected power data were fit with a second-order function, i.e., $a_0 + a_1 t + a_2 t^2$. Figure 4 is a plot versus time of the high and low power-level fits, and Figure 5 is a plot, versus time, of the difference between the two fits. Figures 6 and 7 are plots of the residuals that are left after the fit curve is subtracted from the corrected power data.

To determine the contribution of the power measurement equipment, the stability of the actual power meter used to obtain the data was measured. Figure 8 is a block diagram of the measurement system. Figures 9 and 10 show the results of two long data runs, one for about 10 days and the other for about 16 days. Each data point is for an averaging time of about 2.8 hr. Note that the standard deviation of each data set is much less than the standard deviations in Figures 6 and 7. The data-point separation in time for Figures 6 and 7 varies, but it is close as 0.14 days (3.36 hr) and this is comparable to that in Figures 9 and 10. The conclusion is that drifts in the power meter, in its calibrator, and in the power measurement head contribute negligibly to the measurements plotted in Figures 6 and 7.

DATA STATISTICS

Because of the very regular manner in which the data were taken, there occurred systematic time separations in the data of 0.14 and 0.41 days. The data could also be averaged to give results for 0.82 and 2.5 days. These data were then analyzed statistically. The results are summarized in Table I. Column 1 is the time τ between measurements. Column 3 is the Allan standard deviation of the power as a function of τ. Column 2 is the number of data points used to calculate the results in Column 3. Figure 11 is a plot of the change in clock output frequency for a 1-dB change in microwave power as a function of the C-field setting. The factor 8×10^{-13} comes from Figure 11 and represents about the worst C-field-setting coefficient of frequency change per dB of power change over the Zeeman frequency range 25 to 51.5 kHz. Column 4 is approximately the maximum Allan standard deviation that would be caused by the power changes in column 3. Column 5 has calculated values of $3.55 \times 10^{-11}/\sqrt{\tau}$; this equation is derived from Figure 12, which is a plot of the Allan standard deviation of the Cs clock as measured against our HP-50613-004 standard.

CONCLUSIONS

One can conclude from the data in Table I, as plotted in Figure 13, that even if the C-field is set far away from an optimum setting, the effect of changes in microwave power on the Allan standard frequency deviation will be small for periods of less than 2.5 days. Even at 2.5 days, the Allan standard frequency deviation that results from beam tube noise is still about twice what would result from microwave power changes in this particular standard. Thus, if the Allan standard deviation of the power remained about constant, the Allan standard frequency deviation due to beam tube noise and that due to microwave power variations would be about equal at 10 days.

ACKNOWLEDGMENT

The authors thank Mr. Michael Meyer of The Aerospace Corporation for editing and preparing this paper.

REFERENCES

1. A. De Marchi, "Rabi Pulling and Long-Term Stability in Cesium Beam Frequency Standards," *IEEE Trans. Ultrasonics, Ferroelectronics, and Frequency Control UFFC-34* (6), 598–601 (November 1987).

2. A. De Marchi, "New Insights into Causes and Cures of Frequency Instabilities (Drift and Long-Term Noise) in Cesium Beam Frequency Standards," *Proc. 41st Frequency Control Symposium, 1987*, pp. 54–58.

3. S. K. Karuza, W. A. Johnson, and F. J. Voit, "Determining the Effects of Microwave Power and C-field Setting on the Frequency of a Cesium Atomic Frequency Standard," *Proc. 3rd European Time and Frequency Forum (Besancon, France, 21–23 March 1989)*, pp. 69–72.

4. S. K. Karuza, W. A. Johnson, J. P. Hurrell, and F. J. Voit, "Determining Optimum C-field Settings that Minimize Output Frequency Variations in Cesium Atomic Frequency Standards," presented at the 21st Annual Precise Time and Time Interval (PTTI) Applications and Planning Meeting, Redondo Beach, Calif., 30 November 1989.

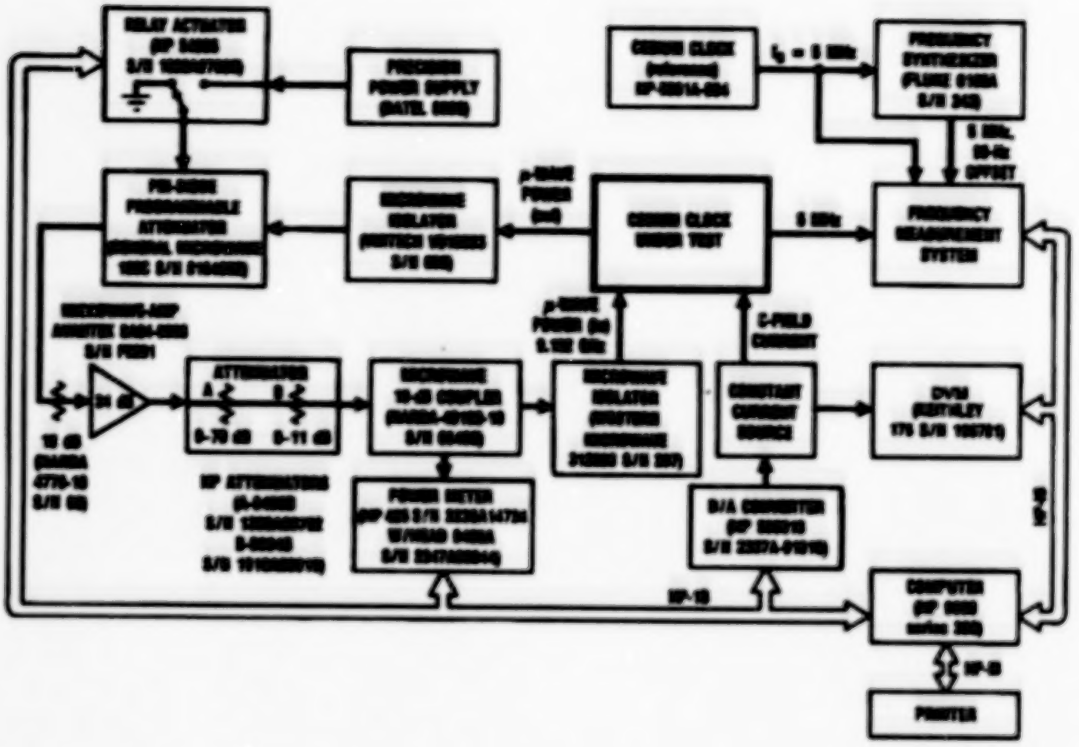


Figure 1. Block Diagram of the C-field Measurement System for a Cs Frequency Standard

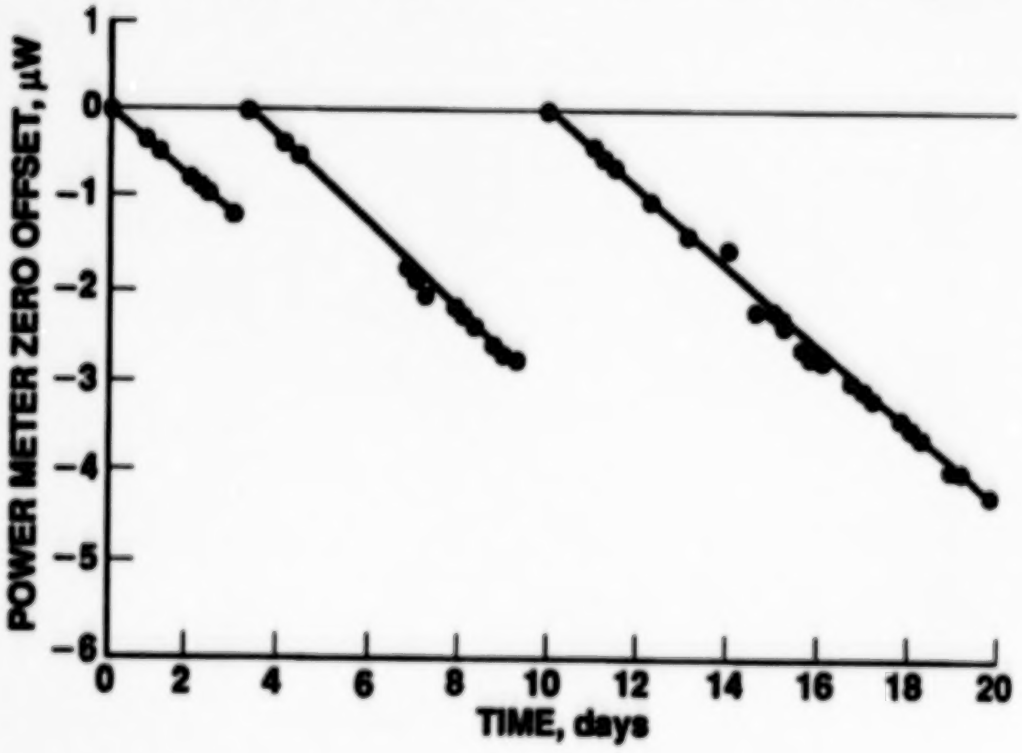


Figure 2. Plot of the Power Meter Zero Offset as a Function of Time

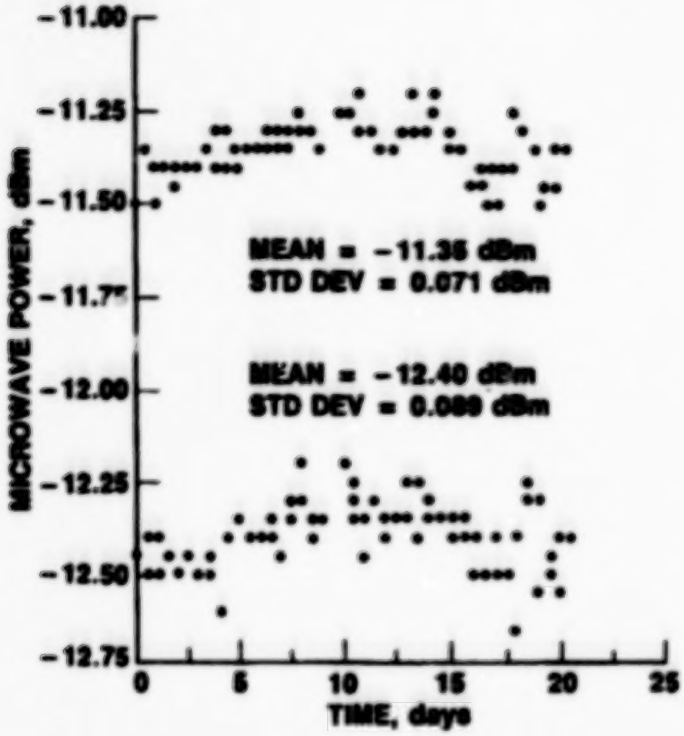


Figure 3. Plot of the Two Measured Power Levels as a Function of Time

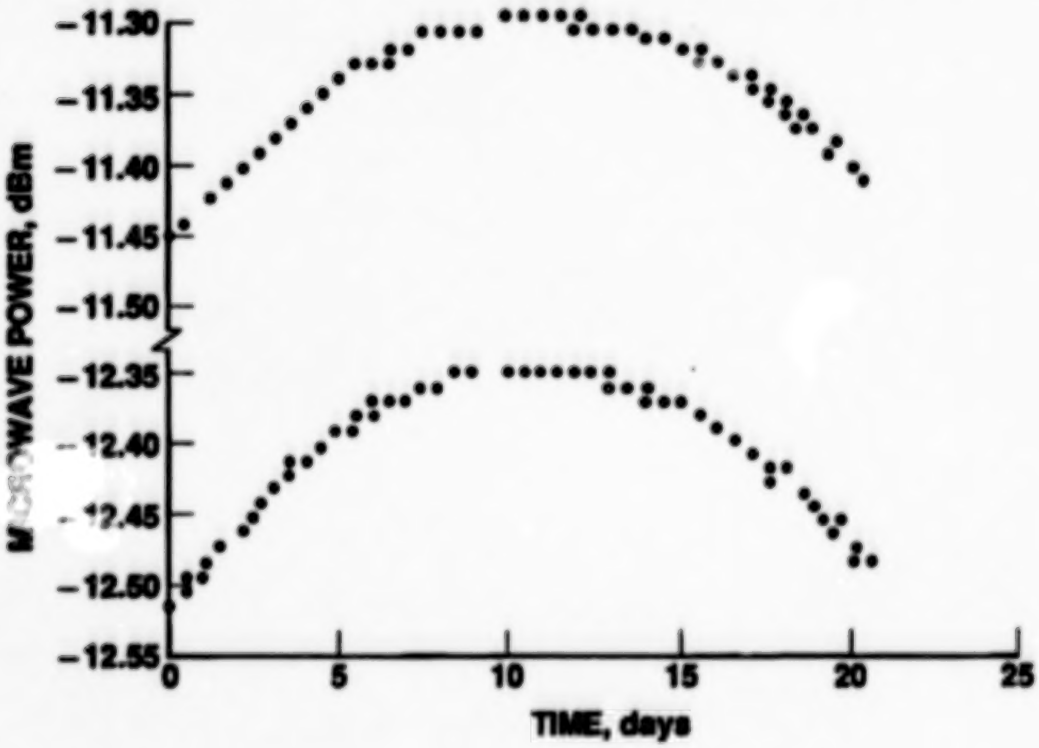


Figure 4. Plot of the Curve Fits of the Two Measured Power Levels as a Function of Time

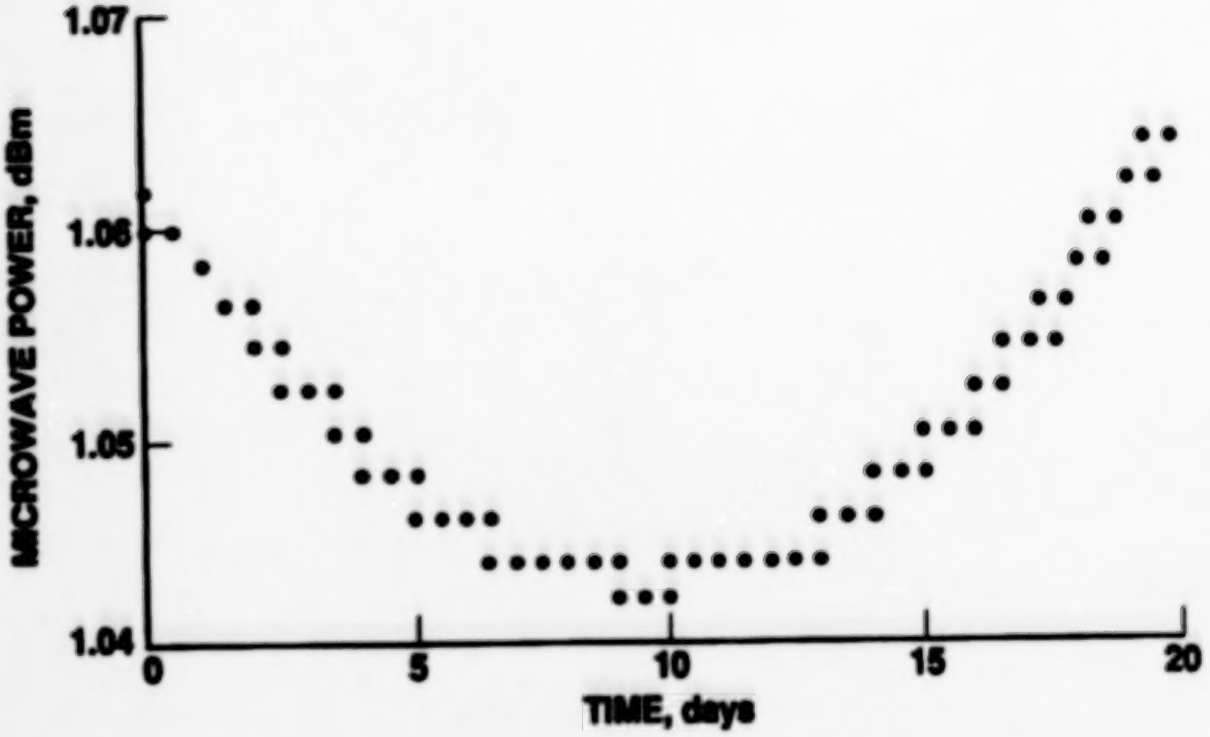


Figure 5. Plot, as Function of Time, of the Difference of the Two Fits to the Power Data

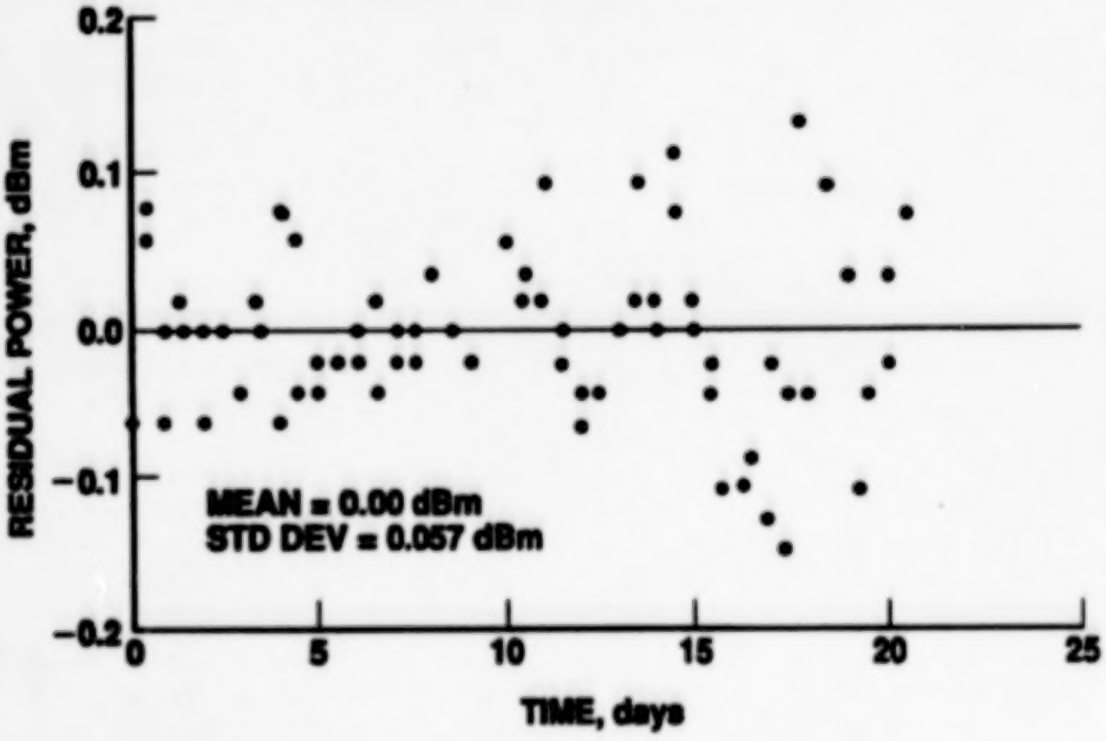


Figure 6. Plot, as a Function of Time, of the High-Power Residuals that Remain after the Fit Curve is Subtracted

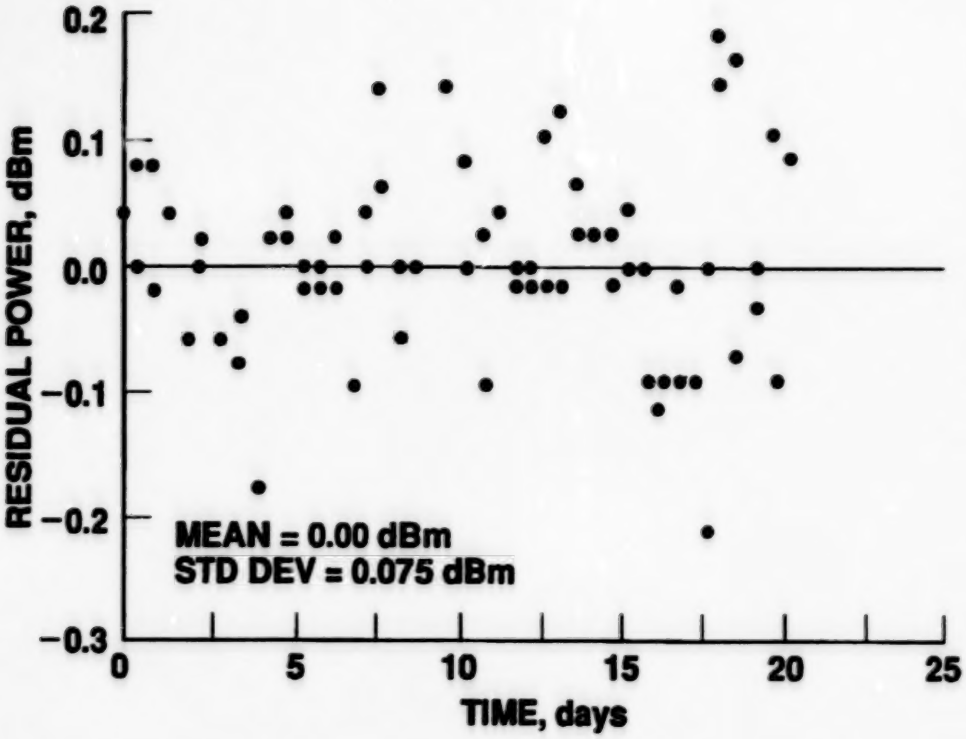


Figure 7. Plot, as a Function of Time, of the Low-Power Residuals that Remain after the Fit Curve is Subtracted

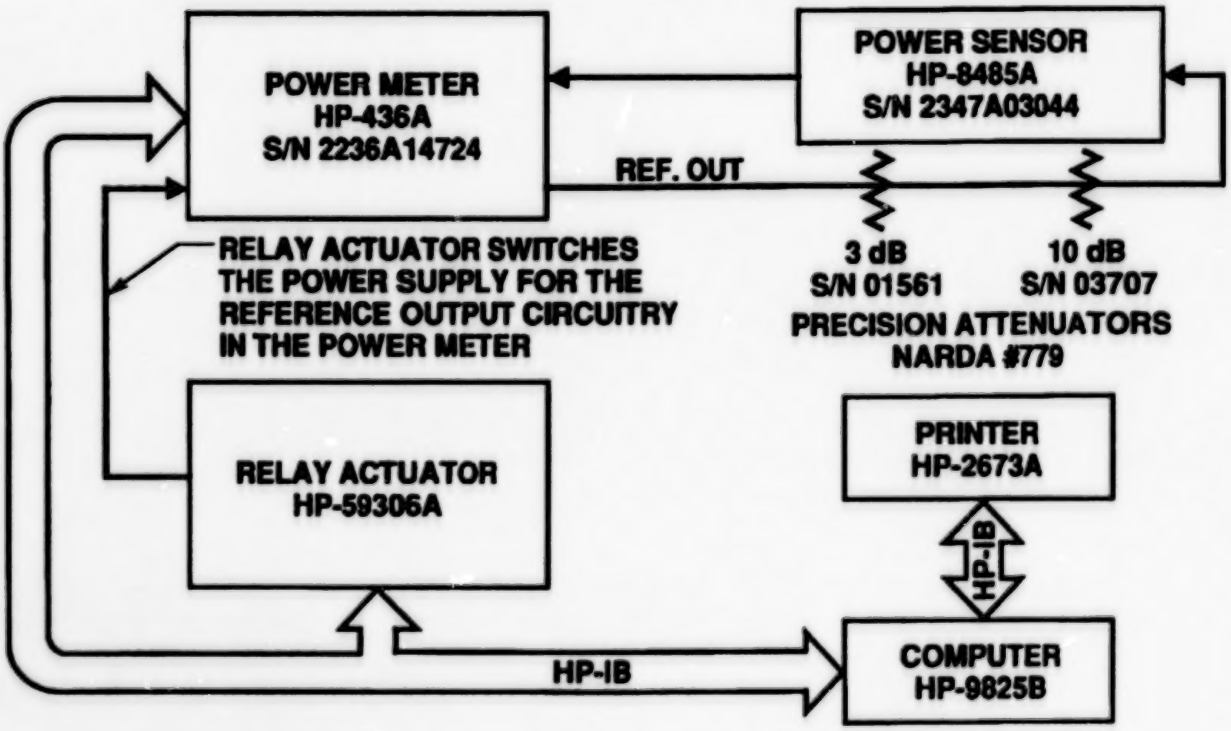


Figure 8. Block Diagram of the Power Meter Measurement System

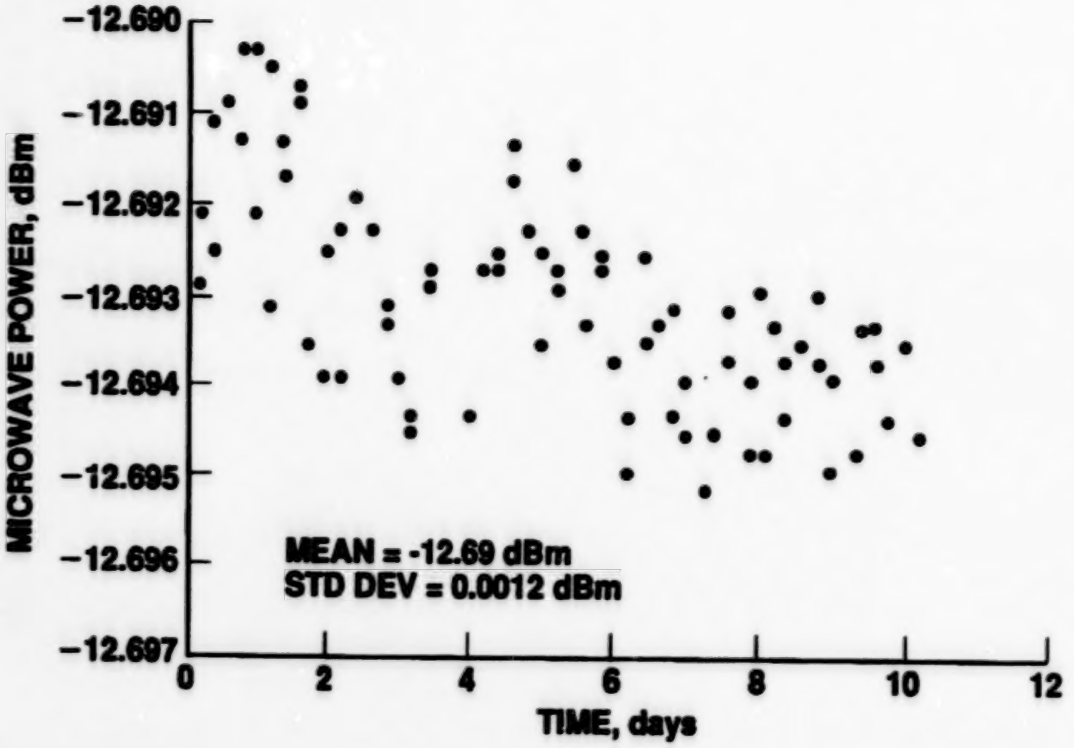


Figure 9. Plot of the Stability of the Power Meter for a 10-Day Run

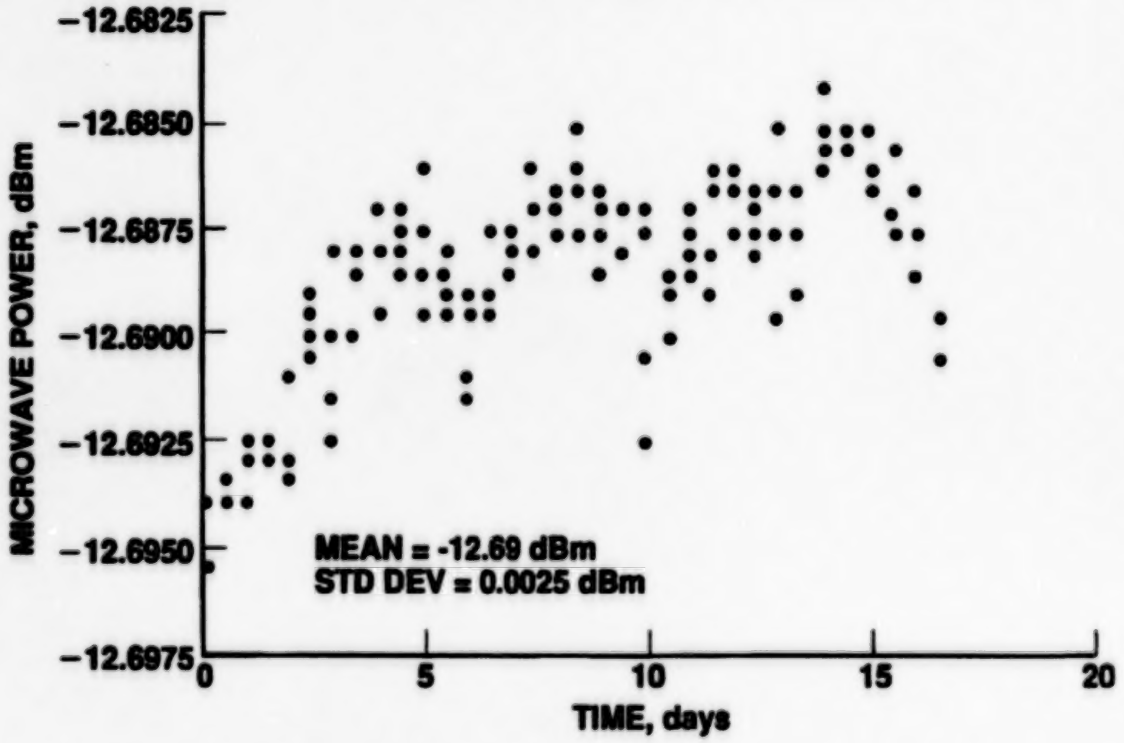


Figure 10. Plot of the Stability of the Power Meter for a 16-Day Run

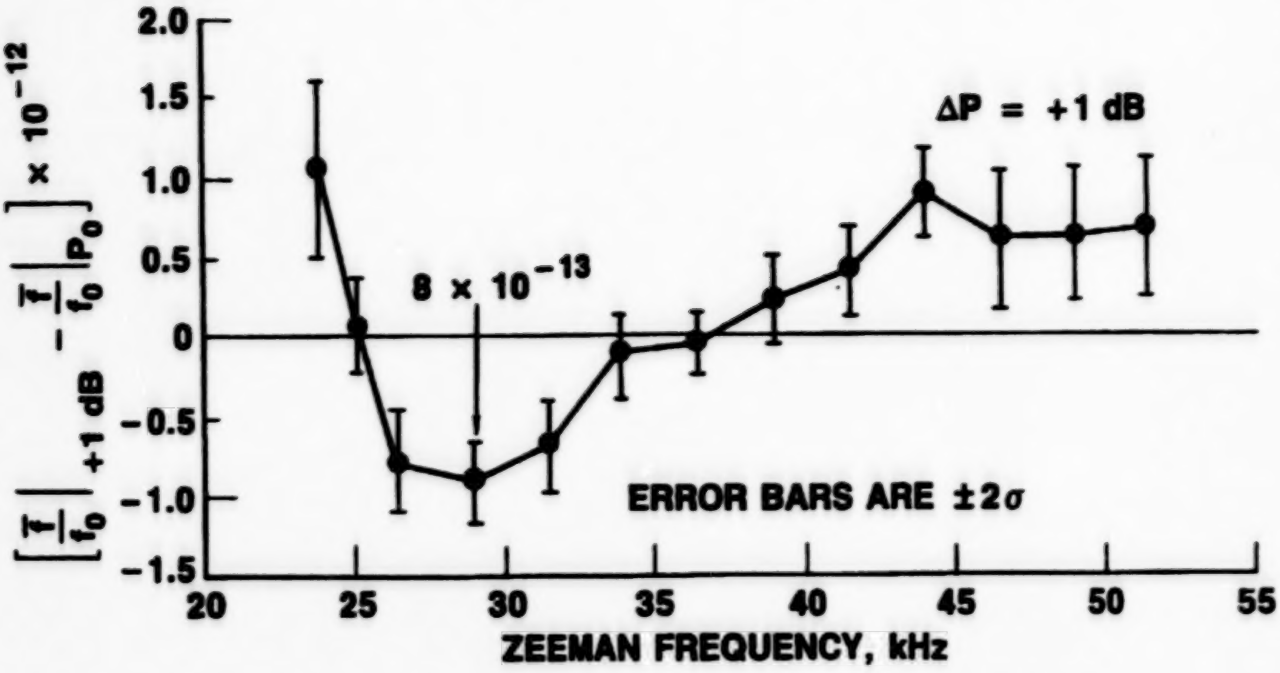


Figure 11. Difference of the Average Frequencies of the Cs Frequency Standard as aFunction of C-field for a Microwave Power Change of +1 dB above the Optimum Power Level P_0

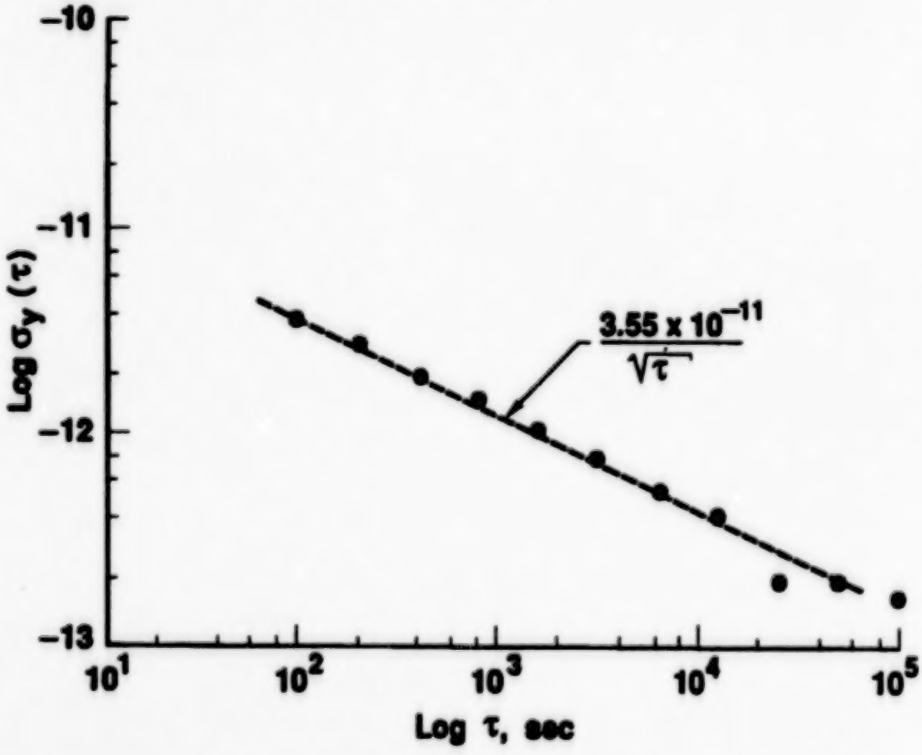


Figure 12. Plot, as a Function of Sampling Time, of the Allan Standard Frequency Deviation of the Cs Frequency Standard

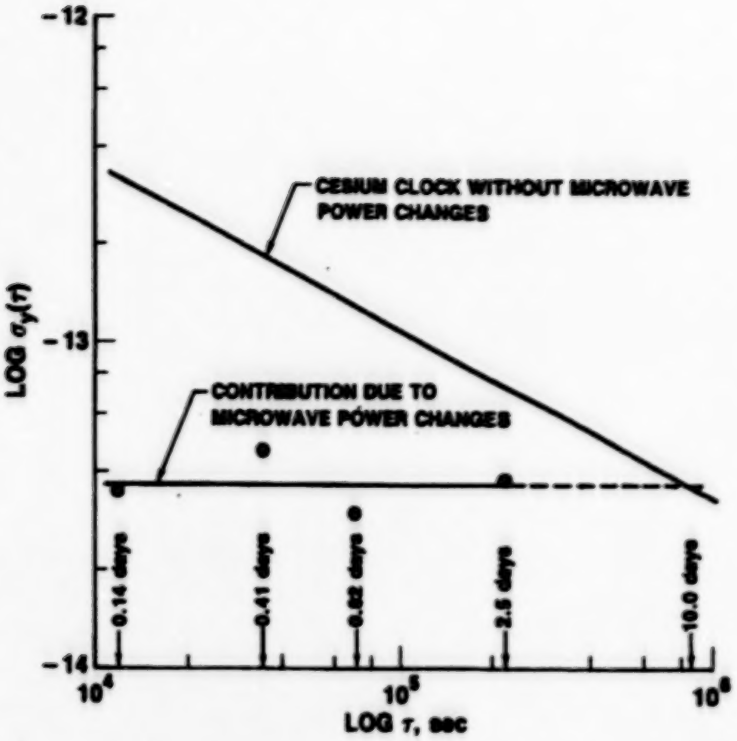


Figure 13. Plot of the Calculated Contribution of Microwave Power Changes to the Allan Standard Frequency Deviation of the Cs Frequency Standard

Table 1. Measurement Data

POWER DATA			FREQUENCY DATA	
TIME (τ), days	No. OF POINTS	ALLAN STD DEV $[\sigma_p(\tau)]$, dBm	ALLAN STD DEV $[\sigma_y(\tau) = \sigma_p(\tau) \times 8 \times 10^{-13}]$	$\frac{3.55 \times 10^{-11}}{\sqrt{\tau}}$
0.14	128	0.04390	0.3512×10^{-13}	3.228×10^{-13}
0.41	64	0.05794	0.4635×10^{-13}	1.886×10^{-13}
0.82	26	0.03719	0.2975×10^{-13}	1.334×10^{-13}
2.50	12	0.04807	0.3846×10^{-13}	0.7638×10^{-13}

BLANK PAGE

RUBIDIUM ATOMIC FREQUENCY STANDARDS FOR GPS BLOCK IIR

W. J. Riley
EG&G Frequency Products
Salem, MA 01970

Abstract

EG&G, Inc. has been selected to provide the Rubidium Atomic Frequency Standards (RAFS) for the GPS Block IIR NAVSTAR satellites. These satellites will replenish and upgrade the space segment of the Global Positioning System in the mid 1990s. The EG&G GPS RAFS Rb clocks are the latest generation of the high-performance rubidium frequency standards described at this conference in 1981, 1983, 1985, and 1987. They offer an aging rate in the low $pp10^{14}$/day range and a drift-corrected 1-day stability in the low $pp10^{14}$ range. The Block IIR version of these devices will have improved performance, higher reliability, smaller size, and greater radiation hardness.

The GPS Block IIR atomic clocks have a "natural frequency" configuration whereby they output a frequency of about 13.4 MHz that is a submultiple of the atomic resonance of Rb (or Cs). The RAFS operates at a low, fixed C-field for increased stability. The unit has been repackaged into a smaller 4.6" x 8.5" x 5.8" outline, but is somewhat heavier (12 lbs.) because of additional radiation shielding. Elimination of the ground tuning logic and the secondary loop synthesizer (with its ovenized crystal oscillator) has reduced the RAFS complexity and improved its reliability to 0.80 for the 7.5-year mission. The RAFS power consumption is only 13 W at +20°C in vacuum.

This paper describes the GPS Block IIR RAFS design, including the changes and improvements made, and the test results obtained, since the last report at this conference in 1987.

INTRODUCTION

The GPS Block IIR NAVSTAR satellites will replenish the Rockwell Block II satellites currently being deployed. General Electric Astro Space Division is the prime USAF contractor for this program, ITT Aerospace/Communications Division is the navigation payload subcontractor, and EG&G has been selected to supply the rubidium atomic frequency standards. A major new feature of the Block IIR satellites is crosslink ranging that can be used to exchange clock correction data between satellites without ground segment control, thus providing a high degree of autonomy. Information regarding the EG&G GPS RFS design and performance has been previously presented at this meeting[1, 2, 3, 4]. This paper updates that information with the Block IIR changes and recent test results.

REQUIREMENTS

The requirements for the GPS Block IIR Atomic Frequency Standards are given in the USAF Space Division Technical Requirements Document[5] and the ITT Specification[6]. A summary of those

requirements is shown in Table 1. The navigation performance of the GPS system depends critically on the stability of the atomic clocks on board the NAVSTAR satellites. The rubidium frequency standard chosen for the GPS Block IIR application is the high performance unit developed at EG&G especially for this application. This clock has the highest stability of any available device, while also having the practical size, weight, power, reliability, and life advantages of an RFS.

The stability requirements for the Block IIR atomic clocks are shown in Table 2, along with the range error predicted from the measured frequency stability of the EG&G GPS RFS. This high-performance rubidium clock is able to meet the stringent 1- and 14-day autonomous timing requirements.

BLOCK DIAGRAM

The most important new design feature of the Block IIR RAFS is the "natural frequency" approach to integrating the clock and secondary loop synthesizer into a Total Navigation Package. The same synthesis hardware that provides frequency adjustments and selective availability also converts the Cs or Rb AFS frequency to 10.23 MHz for the navigation payload. This concept eliminates the RFS secondary loop and ground tuning sections, reducing size, weight, power, and complexity, while improving performance, radiation hardness, and reliability.

A block diagram of the RAFS is shown in Figure 1. A voltage controlled crystal oscillator (VCXO) provides the output via an amplifier and crystal filter. The VCXO also excites the Rb physics package via an rf multiplier chain. A servo amplifier processes the discriminator signal from the physics package to lock the VCXO to the Rb resonance. A lamp exciter, C-field source, and temperature controllers support the physics package operation. A power supply operates the unit under telemetry control, while monitor signals indicate the RAFS status. This arrangement is a simplified "natural frequency" configuration that eliminates the secondary loop synthesizer and ground tuning interface by operating the unit at fixed, low C-field and outputting an exact submultiple of the Rb atomic frequency.

PHYSICS PACKAGE

The GPS Block IIR RAFS physics package design is based on classical rubidium gas cell frequency standard principles. This approach gives the highest performance consistent with allowable size. The discrete isotopic filter cell gives zero light shift (ZLS) over a range of light intensity and a high S/N ratio. This permits operation at a relatively low light level, thus reducing temperature and rf power dependencies. The characteristics of the lamp, filter, and absorption cells are described in Reference 1. The lamp operates in the Kr-Rb mixed mode and is excited with 0.45 W of rf power at 105 MHz. The lamp output is free from self-reversal. Lamp life is assured by tight heat sinking, alkali resistant glass, high vacuum processing, small envelope surface area, and calorimetric measurement of rubidium fill.

The filter cell operates in a separate oven whose temperature is adjusted for ZLS. The filter cell buffer gas and pressure are chosen to give optimum signal and lowest TC under ZLS conditions.

The absorption cell buffer gases are chosen for narrow linewidth and low TC. The mix ratio is adjusted for a slightly positive TC to partially compensate for the filter cell TC. The nominal fill pressure is determined by the 13.40134393 MHz output frequency and is sufficient to reduce the wall relaxation rate without excessive buffer gas collisional broadening. The absorption cell length is optimized for maximum signal at the chosen light intensity and temperature, the latter being the coolest practical

for operation at an upper baseplate temperature of +50°C.

A cross-sectional view of the GPS Block IIR RAFS physics package is shown in Figure 2. The three ovens are supported by a fiberglass structure that makes effective use of the vacuum environment for thermal insulation. The low thermal conductivity mounting and leads, and low emissivity ovens, reduce heat losses so that the entire physics package requires only 1.8 W of oven power under normal operating conditions.

A lens is used to collimate the lamp output and provide a uniform light distribution. A two-section C-field coil configuration is used to provide a uniform magnetic bias field. The absorption cell is well-bonded to its oven to avoid temperature gradients, and sapphire oven windows are used for high thermal conductivity. These features help to ensure a homogeneous absorption line. Precisely registered, thin, double-layer foil oven heaters are used to provide a low residual magnetic field.

The microwave cavity is excited with an E-probe and has slotted end covers that support the desired TE_{111} mode while allowing light transmission without significant microwave leakage. The SRD multiplier is mounted against the cavity and shares its stabilized thermal environment. The physics package includes two 0.025 inch Hipernom cylindrical magnetic shields.

ELECTRONICS

The RAFS electronic circuits determine, to a large extent, the overall frequency stability that is achieved.

Temperature Controllers: The temperature controllers are dc thermistor bridges and dissipative regulators, with static thermal gains of about 2000. The oven demand power is determined by the 1-hour warmup requirement. Vacuum conditions not only reduce oven losses, but also raise the thermal gains and servo stability margins.

Lamp Exciter: The lamp exciter is a Clapp rf power oscillator with the Rb lamp located inside the series-tuned coil. The lamp network presents a range of loads as a function of lamp mode, and the circuit has been characterized under these various conditions to ensure proper operation. Starting may require the exciter to redistribute condensed rubidium inside the lamp by rf induction heating. Ignition takes place when sufficient voltage exists across the lamp coil. The running condition is stabilized against environmental changes and supply ripple by a current regulator circuit.

Preamplifier: The photodetector preamplifier is a one-stage configuration with dc and ac transimpedances of 100 kΩ and 5 MΩ, respectively. The ac gain is broadly peaked at the fundamental modulation frequency. The signal-to-noise ratio (S/N) and stability of the RAFS are determined primarily by the strength of the Rb discriminator signal and the level of white frequency noise. The latter is predominately due to shot noise at the photodetector. The dominant source of preamplifier noise is op amp input voltage noise flowing through the shunt resistance of the photodetector, and, because of the low leakage of the EG&G photodiode, this noise contribution is small. S/N data for the GPS Block IIR RAFS are as follows:

DC Photocurrent	100 μA	Discriminator Signal	240 pA per $1\text{x}10^{-10}$
Shot Noise	5.7 pA/$\sqrt{\text{Hz}}$	White Freq Noise PSD	$5.8\text{x}10^{-24}\text{Hz}^{-1}$
Preamplifier Noise	0.9 pA/$\sqrt{\text{Hz}}$	Predicted Stability	$1.7\text{x}10^{-12}\tau^{-1/2}$
Total Noise	5.8 pA/$\sqrt{\text{Hz}}$	Measured Stability	$2.8\text{x}10^{-12}\tau^{-1/2}$ (inc ref noise)

Magnetic Bias Supply: The magnetic bias supply is an active current source that operates the Rb physics package at a low, fixed C-field to minimize its magnetic dependence. The reference voltage for the C-field supply is derived from a precision low-TC, rad-hard Zener diode. The C-field current is boosted during lock acquisition to avoid the possibility of lockup on a Zeeman response.

RF Chain: The rf multiplier chain consists of a 13.40134393 MHz VCXO, a phase modulator, a diode tripler, a push-push doubler, and a x85 step recovery diode (SRD) multiplier. The low noise of the Rb reference permits a tight lock loop that allows the use of a low-complexity, nonovenized crystal oscillator. An ALC loop is used to maintain constant drive to the SRD multiplier. This approach gives high stability and spectral purity with minimum complexity. Particular care is taken to avoid frequency offsets caused by AM and PM modulation distortion. A pure modulation waveform is generated by passive integration of a precision squarewave, and highly linear phase modulation is obtained by applying small excursions to a hyperabrupt varactor diode in an all-pass phase modulator configuration.

A new feature of the Block IIR design is the inclusion of a high-Q helical resonator rf bandpass filter ahead of the SRD multiplier. This greatly improves the spectral purity and helps to avoid frequency offsets due to spurious components on the microwave spectrum. The SRD multiplier uses a low capacitance diode in a shunt mode with an external dc bias resistor that is used to adjust the microwave power level to the optimum value.

RF Output Amplifier: The rf output amplifier must not only provide the +18 dBm, low-distortion RAFS output, but must also maintain a phase-continuous output under transient radiation. During transient radiation, the active devices of the VCXO and output amplifier are subject to upset. Short-term ($\leq$1 μsec) flywheeling is provided by the LC output tank. Medium-term ($\leq$100 μsec) flywheeling is provided by a crystal bandpass filter ahead of the output stage. The output stage recovers before the energy in its tank is dissipated. The VCXO crystal resonator itself keeps vibrating during the radiation, and the VCXO circuit recovers within the ringing interval of the crystal filter.

Power Supply: The power supply consists of an input filter, a dc/dc converter, and three linear regulators. The dc/dc converter uses a single-ended flyback configuration that provides both dc isolation and regulation. The +28 V output is used directly as the heater supply while the +5 and $\pm$15 V supplies are further stabilized by precision linear regulators before supplying the logic and analog circuits. Under normal operating conditions in vacuum, the RAFS circuits consume under 10 W. The total dc input is 33 W demand during warmup and 13 W steady-state at +20°C baseplate.

MECHANICAL PACKAGING

The RAFS outline is shown in Figure 3. The height was reduced by about one inch by eliminating the secondary loop and ground tuning circuitry, and particularly by the removal of the large ovenized secondary loop crystal oscillator. The length and width were increased slightly because of the addition of tantalum covers on the four sides for radiation shielding. The number of mounting feet was increased from four to eight, and the command/monitor connector was changed to a smaller size.

Packaging Layout: The RAFS packaging is shown in Figure 4. The outer magnetic enclosure and the side and top covers have been removed in the right photograph to expose the electronic boards and other subassemblies in cavities of the chassis. The primary objectives in this packaging design are ruggedness, thermal transfer, access for assembly and inspection, EMI shielding, radiation shielding, and light weight.

The main chassis provides the thermal and structural interface for the various assemblies and printed circuit boards (PCBs). It is a one-piece, machined aluminum box-like structure with a solid baseplate and four vertical walls. The walls have integral stiffening ribs/partitions that form compartments on the outer surfaces. There are ten PCBs mounted in these compartments. The boards are located around the structure to minimize the length of wiring runs and crosstalk. The partitions between the compartments stiffen the wall, provide EMI shielding between the PCBs and provide a mounting surface for heat sinks for components with high power dissipation.

The four walls of the chassis form a central cavity that contains several assemblies. The physics package is mounted at the bottom on the baseplate of the structure. The lamp exciter and helical resonator assemblies are attached to the physics package before installation into the structure. The electrical connections are made with nonmagnetic semi-rigid coaxial cables. The rf output connector is located on the structure wall so that it protrudes directly into the output amplifier compartment.

Filter boxes are mounted at the power and monitor connectors to eliminate radiation to or from exposed leads. EMI gaskets are used under the connector flanges. All leads pass through feedthrough filter capacitors, and the assembly is located near the power supply to minimize exposed lead length. There are also feedthrough filter capacitors in partitions in the chassis where needed for EMI suppression. The electronic compartments have aluminum covers fastened against the chassis with closely spaced screws for containment of EM radiation. The four sides and the top also have covers of tantalum for nuclear radiation shielding. An outer magnetic enclosure is used to provide additional magnetic shielding.

RADIATION HARDENING

Radiation hardening is a critical aspect of the GPS Block IIR RAFS requirements, and one that has received much attention during the design effort. The RAFS design has undergone detailed radiation hardening analysis by GE, with the assistance of EG&G, GE, ITT, and JAYCOR. Critical parts and subassemblies have also been subjected to radiation testing. In particular, the Rb physics package has been subjected to total gamma dose testing, and the VCXO and RF output chain has been subjected to transient radiation testing. This analysis and test have shown that the design can meet the stringent clock performance requirements under both the natural and manmade radiation environments.

RELIABILITY

The predicted MTBF of the overall GPS Block IIR RAFS is 298,000 hours, and 348,000 hours excluding those components (such as monitors) that do not contribute to a mission failure. This corresponds to reliability values of 0.80 and 0.83, respectively, for a single Rb clock over the 7.5-year mission duration. Each satellite is expected to have one active and one hot-standby rubidium clock, and one cesium clock as a cold-standby unit.

TEST RESULTS

Two additional GPS RFS prototype units (S/Ns 3 and 4) were built as part of the GE proposal effort. These units have the original mechanical configuration, but incorporate the changes associated

with the 13.4 MHz "natural frequency" approach. Test data for all the EG&G GPS RFS units show excellent performance that exceeds the Block IIR requirements.

Stability: All of these RFS units have consistently shown drift-corrected Allan variance stabilities at or below $\sigma_y(\tau) = 3\text{x}10^{-12}\tau^{-1/2} + 1.5\text{x}10^{-14}$ when measured against the NRL hydrogen maser. One-day stabilities in the high 10^{-15} range are typical. An example of a recent NRL 107-day stability run at constant temperature for S/N 4 is shown in Figures 5 and 6. The stability is about 10^{-14} between 10^5 and 10^6 seconds. The higher level of white FM at shorter averaging times is due to the measuring system.

Aging: The GPS RFS units have shown aging $\leq 5\text{x}10^{-14}$/day. The aging is always negative, tends to decrease gradually with undisturbed operating time, and is consistently smooth and highly modelable.

Temperature Stability: The average TCs of S/Ns 3 and 4 were measured at EG&G to be about $-0.7\text{x}10^{-13}$/°C and $+0.4\text{x}10^{-13}$/°C, respectively, over a baseplate temperature range from +20°C to +45°C. S/N 4 was then re-optimized for operation from +15°C to +20°C, where it displayed an average TC of about $+0.6\text{x}10^{-13}$/°C. The steady-state TC is always smooth, hysteresis-free, and quite modelable.

A test was conducted to measure the clock error caused by orbital temperature variations. S/N 4 was subjected to a +15°C to +20°C triangular temperature profile having a 12-hour period. The resulting time error was about ±2 nsec, well within the operational requirements.

Power: The steady-state power versus temperature characteristic of EG&G GPS RFS S/N 4 was measured as a function of baseplate temperature from −15°C to +35°C. The power was 12.6 W at +20°C and varied by about −50 mW/°C.

Retrace: A series of power on/off retrace tests were conducted on S/N 1 at NRL. This 58-day test included 4 retrace cycles, with off periods from about 2 to 10 days. This retrace record is unique because it is the only such record known for an RFS of such high stability against such a high stability reference. The measurement noise is therefore very low, even in relation to the low retrace values. The retrace record is also interesting in that the RFS frequency seems to "freeze" during the off period (with a slight tendency for the frequency to reverse). This indicates that the dominant aging mechanism depends on elevated internal operating temperature. The most likely such mechanism is redistribution of rubidium within the lamp. This process would indeed literally "freeze" while the unit was off. The overall record shows gradual settling, and seems to be the same as it would have been without the off-periods (if they were simply cut out of the record).

The retrace behavior of the unit was excellent, ranging from essentially zero (for 2 days off) to about $3\text{x}10^{-13}$ (for 10 days off). These results are consistent with similar retraces conducted on GPS RFS S/N 2 as part of a total gamma dose physics package radiation test (see below). This RAFS design easily complies with the $5\text{x}10^{-12}$ retrace requirement, and the warm-up time required to achieve this retrace is less than the 3 days specified.

Radiation: A total gamma dose radiation test was conducted on the RAFS physics package. The objective of the test, conducted jointly by EG&G Frequency Products and GE Astro Space, was to determine the effects of total dose gamma radiation on the frequency, photodetector current, and other characteristics of the high-performance Rb physics package. Most of all, the test was run to rule out any unexpected effects. Measurements were made before and after doses of 7, 21, and 70 krads(Si) of gamma radiation from a Co^{60} cell. No significant frequency shifts or other changes in performance were observed within the limit of about $1\text{x}10^{-11}$ set by the drift and retrace effects (primarily due to

the disassembly and reassembly of the RAFS before and after each irradiation). Since these exposures represent x1, x3, and x10 of the total dose expected from natural radiation during the 7.5-year life of the GPS satellite, during which the RAFS can be expected to have a total frequency shift of about $1x10^{-10}$, this test has confirmed that the effect of the radiation on the Rb physics package is negligible.

PROGRAM STATUS

The development phase of the GPS Block IIR RAFS program is nearly complete. Critical Design and Manufacturing Readiness Reviews have been held, and most data items are complete. A brassboard unit of the new design configuration has been built and is undergoing acceptance testing. After the production go-ahead, Block IIR Rb clock deliveries are scheduled to begin in June 1992.

ACKNOWLEDGMENTS

The recent work on this EG&G high performance rubidium frequency standard has benefited from the contributions of many persons both within and outside the EG&G organization. Prominent among the former are S. Goldberg, T.J. Lynch, K.D. Lyon, and J.R. Vaccaro. Among the latter, the author wishes to acknowledge radiation hardening consultation by D.H. Swant of GE and systems engineering by A.P. Baker of ITT. We also wish to thank the NRL Space Applications group for their continued test support.

REFERENCES

1. W.J. Riley, "A Rubidium Clock For GPS," Proceedings Of The 13th Precise Time And Time Interval (PTTI) Applications And Planning Meeting, pp. 609-630, December 1981.

2. T.J. Lynch and W.J. Riley, "Test Results For GPS Rubidium Clocks," Proceedings Of The 15th Precise Time And Time Interval (PTTI) Applications And Planning Meeting, pp. 269-280, December 1983.

3. S. Goldberg, T.J. Lynch and W.J. Riley, "Further Test Results For GPS Rubidium Clocks," Proceedings Of The 17th Precise Time And Time Interval (PTTI) Applications And Planning Meeting, pp. 145-155, December 1985.

4. F. Danzy and W. Riley, "Stability Test Results For GPS Rubidium Clocks," Proceedings Of The 19th Precise Time And Time Interval (PTTI) Applications And Planning Meeting, pp. 267-274, December 1987.

5. "GPS Block IIR Space Segment Technical Requirements Document," CWNZ-87-500, 12/31/87.

6. "Performance Specification, Atomic Frequency Standard (AFS)," ITT Defense Communications Division Dwg. No. 30072-0134, Rev. N, 1/15/90.

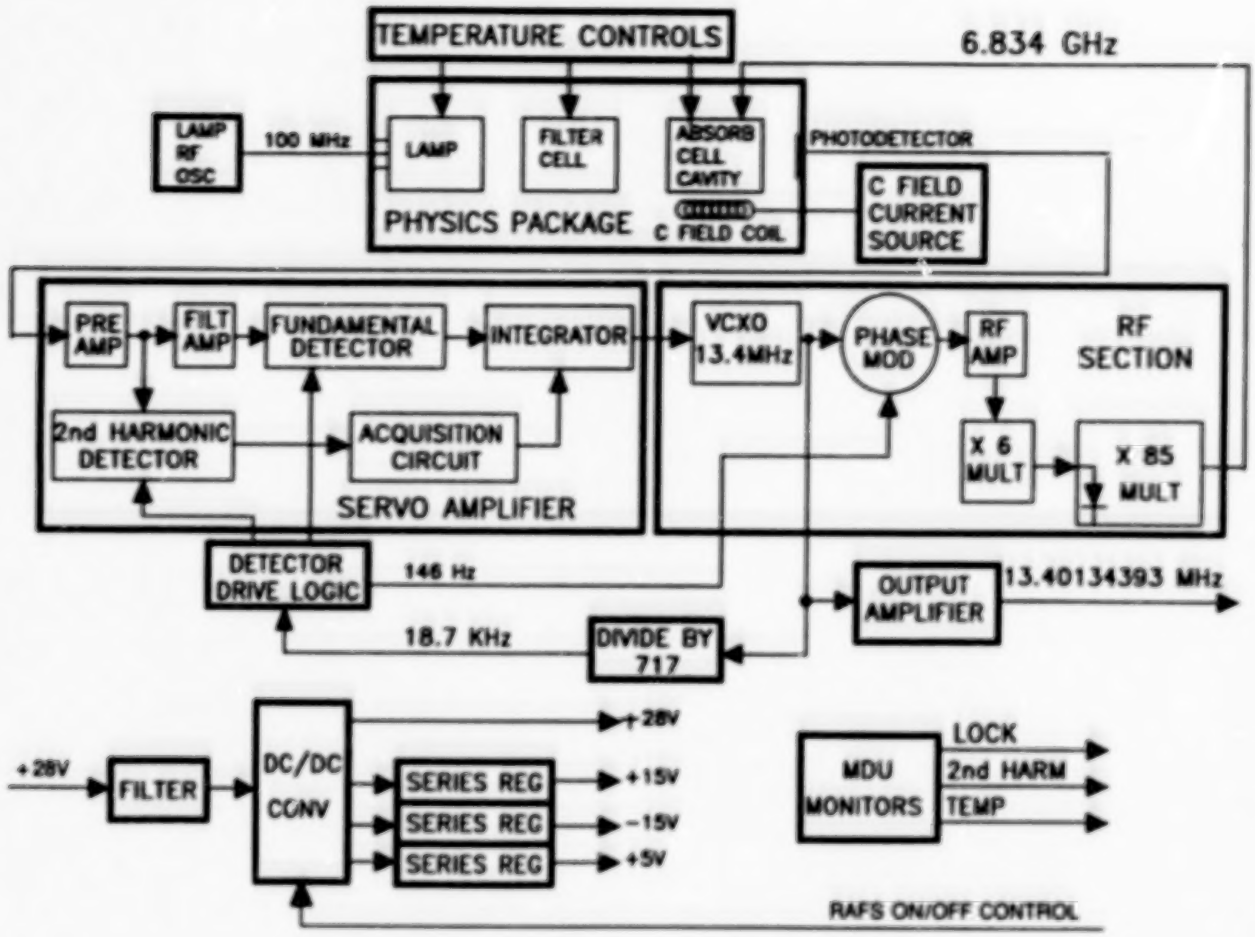


Figure 1. Block Diagram of GPS Block IIR RAFS.

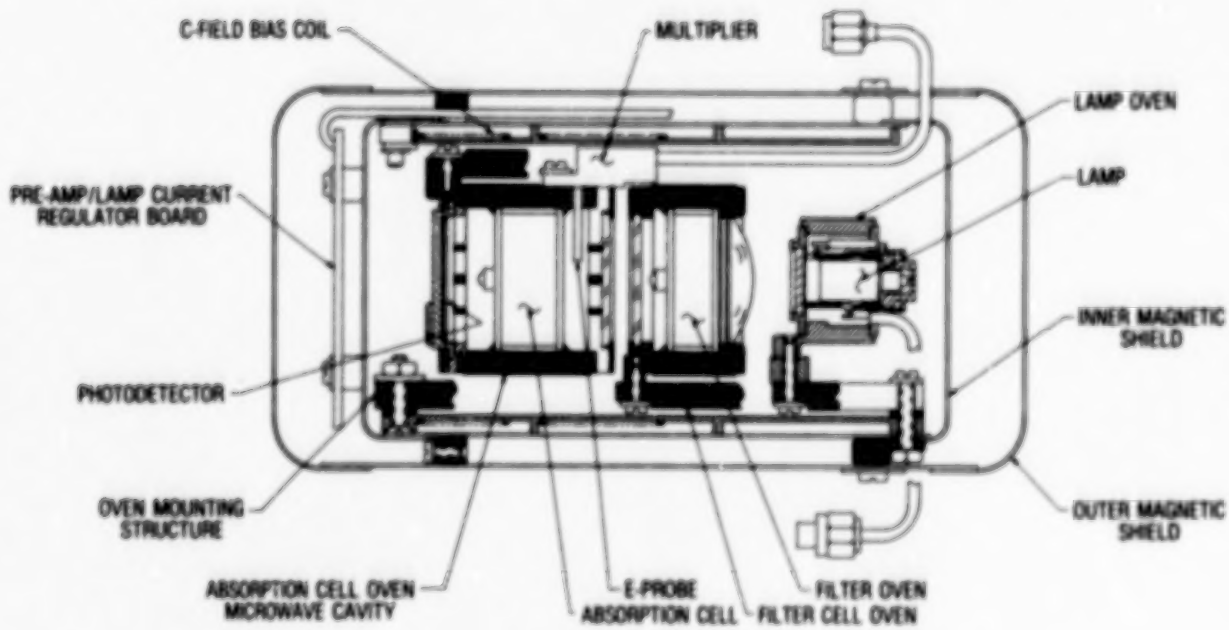


Figure 2. Physics Package Cross-Section.

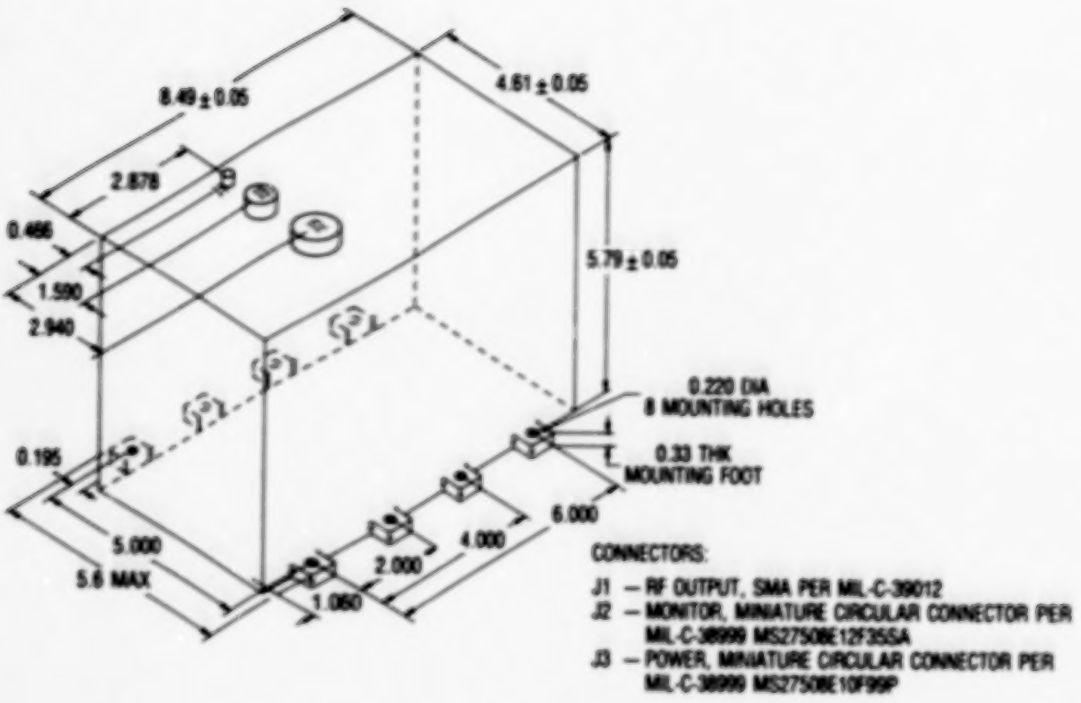


Figure 3. RAFS Outline.

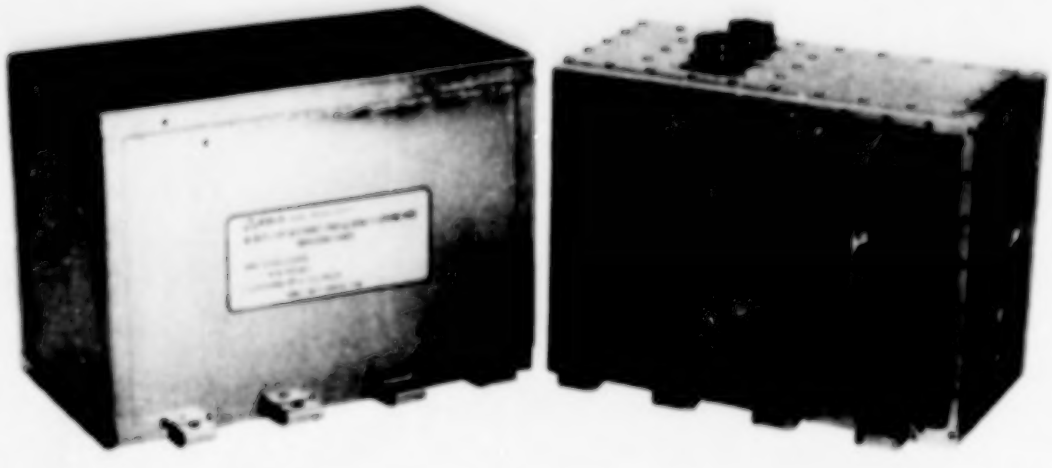


Figure 4. Photographs of GPS Block IIR RAFS.

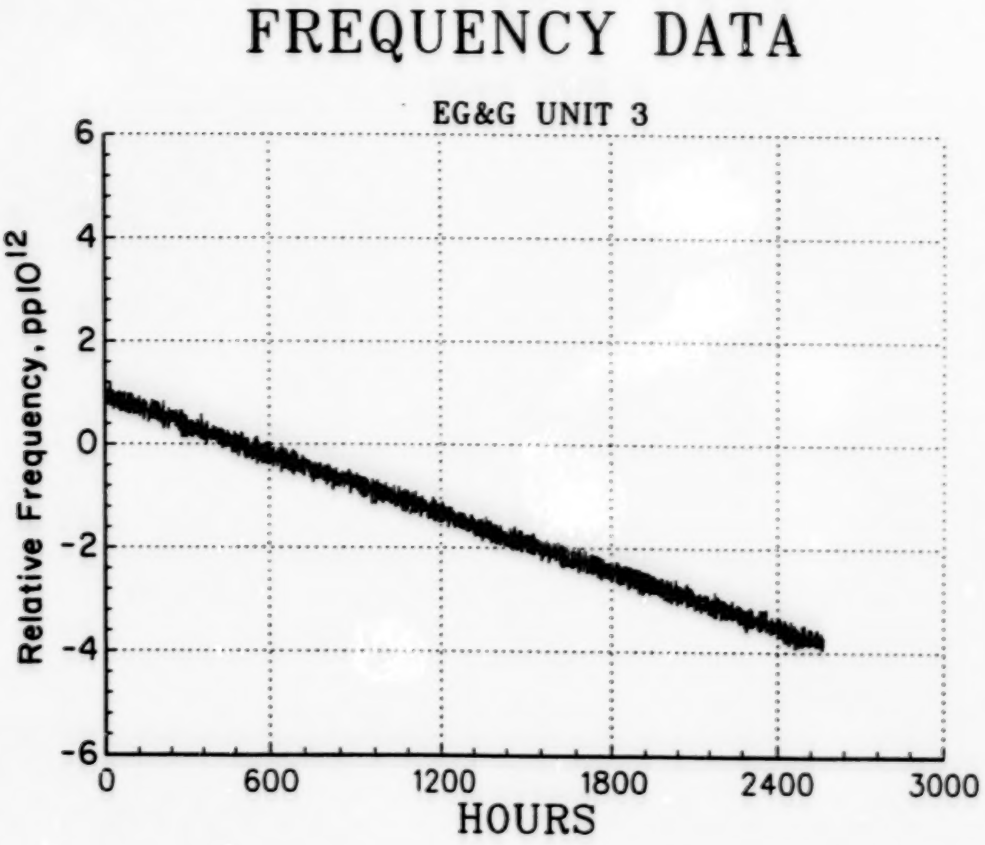
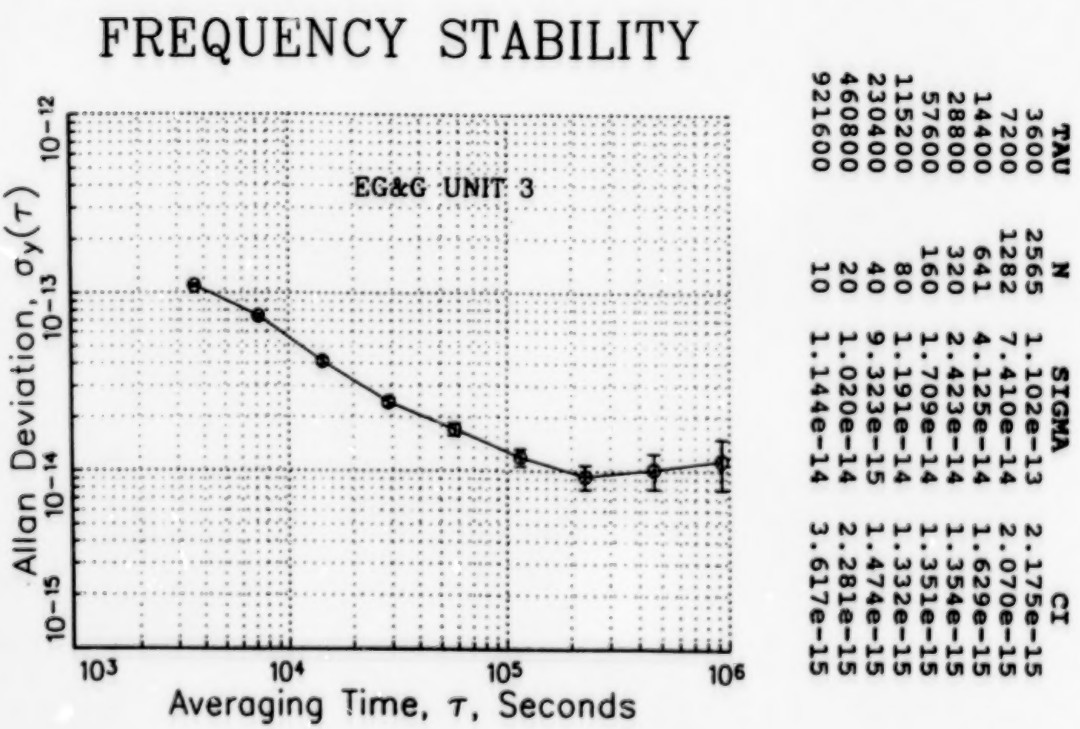


Figure 5. S/N 4 Frequency Record.



TAU	N	SIGMA	CI
3600	2565	1.102e-13	2.175e-15
7200	1282	7.410e-14	2.070e-15
14400	641	4.125e-14	1.629e-15
28800	320	2.423e-14	1.354e-15
57600	160	1.709e-14	1.351e-15
115200	80	1.191e-14	1.332e-15
230400	40	9.323e-15	1.474e-15
460800	20	1.020e-14	2.281e-15
921600	10	1.144e-14	3.617e-15

Figure 6. S/N 4 Stability.

PRECISE FREQUENCY CALIBRATION USING TELEVISION VIDEO CARRIERS

Edward E. Burkhardt
Burkhardt Monitoring Service
P.O. Box 1411
Glen Allen, Virginia 23060

Abstract

The availability of inexpensive and quick precise frequency calibration methods is limited. VLF and GPS do offer precise calibration. However, antenna placement, cost of equipment, and calibration time place many restrictions on the user.

The USNO maintained line-10 television Time of Coincidence (TOC) of station WTTG, channel 5, Washington, DC requires a frequency stable video carrier. This video carrier, 77.24 MHz, is controlled by the same cesium beam standard controlling the TOC of line-10.

Excellent frequency comparisons against this video carrier have been accomplished at 95 miles (153 km). With stable propagation and a three foot wire antenna, a part in 10^9 can be determined in a few minutes.

Inexpensive field equipment with a synthesized 1 kHz offset from the video carrier offers parts in 10^{11} calibrations in a few minutes using an oscilloscope as a phase comparator.

INTRODUCTION

The accuracy of precise time and time interval (frequency) has increased at a phenomenal rate over the years. Atomic standards and modern means of communications now provide us values not dreamed of a few decades ago. The scientific and military worlds are tied together to within a few nanoseconds. While those of us involved in the PTTI arena apply precise accuracies to our everyday work, a large segment of the general population that needs PTTI has been left behind. This lag has left thousands of daily users where they were thirty years ago at a part in 10^7 using WWV on shortwave. Low frequency phase tracking, Loran-C, GPS/GLONASS and the like are not easily accessible tools for many in the general communications fields.

METHODS AND LIMITS

The following means of dissemination, while able to provide PTTI results, have limiting factors to the general user. The following factors are typical for general communications personnel:

VLF (3-30 kHz), 10^{-11} or better, requires expensive receivers and special antennas. Calibration time is in hours, full knowledge of diurnal phase changes is necessary.

LF (30-300 kHz), 10^{-11} to 10^{-13}, requires expensive receivers and timing equipment. European users can use stabilized broadcast carriers (90-200 kHz).

MF (300 kHz-3 MHz), limited to 10^{-7} unless daytime groundwave signals are available, low cost receivers. While phase stable standard broadcast stations (0.54-1.6 MHz) could be used, none are currently in operation (North America).

HF (3-30 MHz), limited to 10^{-7} unless groundwave signals are available, low cost receivers.

VHF (30-300 MHz), 10^{-12} (see below), low cost receivers.

UHF (300 MHz-3 GHz), 10^{-12}, low to high cost receivers, generally line of sight range and subject to phase jitter proportional to frequency increase. Satellite signals subject to orbital changes, GPS is too expensive.

SHF (3-30 GHz), 10^{-12}, medium to high cost receivers, generally limited to line of sight and subject to phase jitter proportional to frequency increase. Satellite signals subject to orbital changes.

LINE-10 (TELEVISION), 10^{-11}, medium to high cost receivers, currently available only on WTTG, channel 5, Washington, DC. Requires clock comparison of specific line 10 television pulse that occurs every 1,001 seconds. Meaningful calibrations require an hour or longer under stable propagation conditions.

COLOR SUBCARRIER, 10^{-11}, medium cost receivers, now generally unreliable due to network routing changes, satellite orbital changes, and the mode of station operation.

NIST AUTOMATED COMPUTER TIME SERVICE, 10^{-6} to 10^{-8}, low cost, but requires computer, modem, and several long distance telephone calls. Time period for calibration is 20 minutes to 24 hours depending on needs.

USAGE DEMANDS

While timing demands to a millisecond can be met by many of the above discussed methods, by far the greatest need of the general communications worker is frequency calibration. The workhorses of the communications industry are the digital counter and digital synthesizer (service monitor). Affordable test equipment capable of parts in 10^8 or better are generally found in use. The demand of setting operating frequency to a few parts in 10^9 has become commonplace in industry. Unfortunately, field verification of test equipment time bases can not be accomplished in an easy and affordable manner. These general users are in need of a low cost, propagation stable, and quick and easy to use precise frequency source.

PRECISE TELEVISION VIDEO CARRIERS

At the present time USNO operates a phase stable video carrier on station WTTG, l 5, Washington, DC. This station's 100 kW transmitter can be used up to 150 miles (240 km) short wire antenna as a reliable precise frequency source at its operating frequency of 77.24 MH h the addition of other select television stations throughout the United States operating precis olled video carriers, large percentages of the general population can be supplied with the needed frequency calibration source. Precise operation by a single station in each of the top 10 telev markets of:

New York City, Los Angeles, Chicago, Philadelphia, San Francisco, Boston, Detroit, Dallas-Ft. Worth, Washington, DC, and Houston will provide service to better than one-third the country's population. The addition of markets 11-20: Cleveland, Atlanta, Minneapolis-St. Paul, Miami, Seattle-Tacoma, Pittsburgh, Tampa-St. Petersburg, St. Louis, Denver, and Phoenix will include better than 45 percent of the general population.

CONSIDERATIONS AND OBSERVATIONS

The selection of the lower numbered television channels (2-6) operating 55.25 through 83.26 MHz is preferred due to their longer signal range and better propagation phase stability, just to name a few factors. Identification that the system is operating precisely can be accomplished by a carrier phase change lasting a few seconds occurring every five minutes. Such an identification phase change would not affect the received picture if this phase change transition is on the order of 50 ms. Such identification phase changes may be accomplished with reactance phase changes in the transmitter far isolated from the primary frequency source. Video carriers controlled by in-house cesium or rubidium standards can be directly compared by normal methods such as VLF and GPS.

The WTTG phase stable carrier has been observed for a number of years at a location 95 miles away. A high stability quartz frequency standard is continuously phase compared against WWVB operating at 60 kHz. This quartz oscillator drives a synthesizer with an output 1 kHz removed from the WTTG video carrier (77.239 vs. 77.24 MHz). A communications receiver supplies the detected 1 kHz beat note to a dual trace oscilloscope. The second oscilloscope input also has a 1 kHz input derived from a divided output of the quartz oscillator. Frequency differences between the WTTG carrier and the local quartz oscillator are noted as drift displays on the dual trace oscilloscope. At WTTG's frequency of 77.24 MHz a 1×10^{-9} difference results in a cycle beat once per 12.94 seconds. Careful expanded-scale oscilloscope observations provide parts in 10^{11} in 10 minutes. Short-term propagation phase changes are easily recognized and can be ignored. The video carrier can also be compared using the zero beat method, but accuracy errors become a factor during signal level fades and propagation phase changes.

Low cost VHF receivers and easily constructed video carrier offset phase lock loop generators operating from the user's time bases can make this precise frequency calibration method ideal for those within range of any television station operating with a precise video carrier.

BLANK PAGE

Geodetic Positioning of the Aerospace Electronics Research Lab (ERL) Osborne Time Transfer Receiver (TTR) using the GPS NAVSTAR Block I Satellites

Anthony S. Liu
Aerospace Corp.
El Segundo, California

Abstract

Aerospace has routinely processed the Osborne Time Transfer Receiver (TTR) data for the purpose of monitoring the performance of ground and GPS atomic clocks in near real-time with on-line residual displays and characterizing clock stability with Allan Variance calculations. Recently, Aerospace added the ability to estimate the TTR's location by differentially correcting the TTR's location in the WGS84 reference system. We exercised this new feature on a set of TTR clock phase data and obtained sub-meter accurate station location estimates of the TTR at the Aerospace Electronic Research Lab (ERL).

BACKGROUND

The Osborne Time Transfer Receiver's (TTR) primary function is to provide a means to monitor a local laboratory frequency standard by comparing this standard to GPS system time using the GPS Navstar satellites. In order to accomplish this task, it is necessary to set up initially, the local receiver coordinates into the receiver's memory. This initialization is assisted by using the built-in positioning capabilities of the receiver whereby real-time location estimates are obtained during user specified tracks. The TTR is a single channel Clear Acquisition (CA) receiver, thus the real time estimates of location are obtained sequentially in time from each satellite. This operation is in contrast to position receivers designed to receive signals from four or more satellites simultaneously using the Precise (P) Code, which is an order of magnitude more accurate than the CA code. The lack of simultaneity of the measurements further degrades the position estimates from the TTR. Therefore the initially entered station coordinates are only first estimates and subject to error.

These deficiencies are unessential to the receiver's operation as a time transfer device, and consequently the TTR has been most useful and helpful in quickly detecting atomic clock anomalies not only in the laboratory standard, but also, satellite atomic clocks themselves. This latter ability is due to the high precision and stability of the laboratory clock.

The initially entered receiver locations were obtained by observing the TTR's solution on a daily basis for several days. Since no consistent daily solution could be obtained, the locations were finally selected and entered by a trial and error method. The receiver's initial position errors are clearly manifested in the clock phase difference measurements as pronounced systematic diurnal signatures in some the satellites, (Satellites ID PRN 9 and PRN 3) as seen in figure 1. The long non-diurnal systematic effects

observed for each satellite seen in this figure is the effect of clock steering (confirmed by independent data from USNO) performed by the GPS control segment. The clock steering is necessary to keep GPS system time to within a microsecond of USNO time.

The program which was used to monitor atomic clock performance and characterize clock stability by computing the Allan Variance was modified with additional code for an iterative least squares procedure. The initial estimate is refined by inputting the time difference measurements from the receiver as data into this least squares program and thus derive a better estimate for the station coordinates. Since the original station entries are referenced to the WGS84 geodetic coordinates as given by the TTR, and the broadcasted ephemerides are also based on the WGS84 system, the resulting least squares corrections will be referenced to the WGS84 coordinates.

ANALYSIS

We note that the Δr, the range difference (i.e.time difference measurement error times the speed of light) is merely the negative sum of the projections of the South, East and height components of the station error into the line of sight from the station to the satellite. A derivation of this is given in the Appendix section.

$$\Delta r = -\cos AZ \cos el(\text{ South error}) - \sin AZ \cos el(\text{ East error}) - \sin el(\text{ Height error}) \quad (1)$$

where (el) and (AZ) are the observe elevation and azimuth angles. Azimuth is defined as measured from North round by East. or:

$$\Delta r = -\cos AZ \cos el(R\Delta\phi) - \sin AZ \cos el(R\cos\phi\Delta\lambda) - \sin el(\Delta h) \quad (2)$$

where Δh, $\Delta\phi$ and $\Delta\lambda$ are the respective height correction above a reference geoid, and corrections in latitude and longitude of the TTR. The system of normal equations necessary for a least squares solution is given by equation (3), where the left hand side contains the data, and the right hand side consists of the station's South, East and height errors to be determined from the data. Each row of the matrix of normal equations $\|A\|$ is formed from the coefficients of equation (2). A vector of measurements, $|\Delta\vec{r}|$, is formed from the data set, Δr. The solution proceeds in an iterative two step procedure. The data are first fitted to a polynomial up to sixth degree in time to remove the clock phase wander and other systematic effects. The remaining difference, Δr, is used in a standard least squares solution for the station off-sets in the South, East, and height directions, as follows:

$$\begin{pmatrix} (\text{South error}) \\ (\text{East error}) \\ (\text{Height error}) \end{pmatrix} = \left[\|A\|^T\|A\|\right]^{-1}\|A\|^T|\Delta\vec{r}| \quad (3)$$

As many as 15 iterations are necessary to converge the final solution. Each iteration includes a reestimation of the polynomial to separate out the clock wander and steering effects from the station location estimation.

DATA DESCRIPTION AND RESULTS

A span of clock phase difference data between 2/8/90 to 4/19/90 from the TTR5 was selected for the receiver coordinate adjustment. This data also contained the elevation and azimuth angles as computed by the TTR5, which are needed in equation (2). The iterative least squares correction for the coordinates is obtain by computing the weighted correction from each NAVSTAR. At the end of each iteration, the sum of the average data residual (standard deviation or s.d.) from each NAVSTAR is computed, and the iteration ceases when this sum reaches a minimum. The result and solution from this procedure are summarized in Table 1.

As seen in this table, the final post-fit data s.d. from each NAVSTAR are substantially reduced from the initial pre-fit data s.d. The columns labelled "corrections" are the final corrections determined from data from each NAVSTAR, and show considerable scatter from NAVSTAR to NAVSTAR (e.g. -11.726 meters of West error for NAVSTAR 9). The individual s.d. for each NAVSTAR for each coordinate component are listed under the column labelled "sig". The final solution for the South, East, height correction components and the associated composite s.d from all the NAVSTARs are listed under the columns labelled "weighted mean" and "composite sigma" respectively. The corrections are 7.366m South, 5.612m West and 16.12m low.

These formal s.d. need to be multiplied by a factor of about 6 to 7 corresponding to the postfit average data residual as described by the data s.d. The covariance implicit in equation (3) assumes a data sigma of one meter, whereas it is more appropriate to use the actual data sigma of about 7 meters. Consequently, the more realistic uncertainties are 0.60 meters, 0.39 meters and 0.36 meters in the respective coordinates. Finally, when the linear corrections are converted to arc second measure, the corrections are 0.2382" South in latitude and 0.2187" West in longitude.

When these corrections are used in equation (2) to compensate the data for station error, a marked improvement is seen when Figure 2 is compared to Figure 1. The most noticeable effect is the reduction in the diurnal phase errors for NAVSTAR PRN 9 and 3 as well as moderate error reduction for the other NAVSTAR PRNs.

For further confirmation of the validity of these results, we performed a "blind test" verification by using the corrective factors derived from data between 2/8/90 to 4/19/90 into a data span not used in the solution. We selected a earlier set between 10/3/89 to 11/12/89. The result of this test is shown in Figures 3 and 4. Figure 3 shows the errors when the station correction is left out. As can be seen, sizable errors for PRNs9 and 3 are there and of the same magnitude as seen in Figure 1, where the station corrections are also left out. In Figure 4, where the corrections are applied, significant reductions in the diurnal errors especially for PRNs 9 and 3 are achieved. As an additional note, the data selected were time differenced measurements between the Aerospace laboratory standard and each of the NAVSTAR clocks. Hence, as can been seen in Figures 3,and 4, the individual satellite clock behavior is exhibited. A summary of each of the clock's frequency labeled as FRQ and aging labeled as DFQ between each satellite and the laboratory is shown in the upper right hand corner of the figure. The units for frequency difference between laboratory standard and satellite clock are in picoseconds/second and the aging factor are in nanoseconds/days^2.

SUMMARY AND CONCLUSION

A few meters of TTR location input error will result in noticeable effects in the data. Significant improvements resulted when station corrections of 0.2382" South in latitude, 0.2187" West in longitude and -16.12 meters in receiver height are applied. The results here show that the TTR with CA coded data provides sufficient precision for the receiver to act as a WGS84 position locator with sub-meter accuracy as well as a time-transfer device.

APPENDIX

For the purpose of differentially correcting the station coordinates, we formulate the rectangular station components for a spherically shaped earth,

$$\begin{aligned} X &= (R+h)\cos\phi\cos\lambda \\ Y &= (R+h)\cos\phi\sin\lambda \\ Z &= (R+h)\sin\phi \end{aligned}$$

where R, h, ϕ and λ are the respective radius, height above a reference geoid, geocentric latitude and longitude of the TTR.
We define a set of unit vectors $\vec{L}$, $\vec{A}$, $\vec{D}$ as:

$$\begin{array}{lll} L_x = \cos\phi\cos\lambda & A_x = -\sin\lambda & D_x = -\cos\lambda\sin\phi \\ L_y = \cos\phi\sin\lambda & A_y = \cos\lambda & D_y = -\sin\lambda\sin\phi \\ L_z = \sin\phi & A_z = 0 & D_z = \cos\phi \end{array} \tag{1}$$

so that errors in the rectangular components are related to errors in the spherical components through the matrix equation as:

$$\begin{pmatrix} \Delta X \\ \Delta Y \\ \Delta Z \end{pmatrix} = \begin{pmatrix} L_x & A_x & D_x \\ L_y & A_y & D_y \\ L_z & A_z & D_z \end{pmatrix} \begin{pmatrix} \Delta h \\ R\cos\phi\Delta\lambda \\ R\Delta\phi \end{pmatrix} \tag{2}$$

In order to obtain the errors ΔX_h, ΔY_h, and ΔZ_h in a local horizon tangent plane, with the normal to the plane in the local zenith direction, we need to rotate ΔX, ΔY, ΔZ by a rotation matrix:

$$\begin{pmatrix} \Delta X_h \\ \Delta Y_h \\ \Delta Z_h \end{pmatrix} = \begin{pmatrix} -D_x & -D_y & -D_z \\ A_x & A_y & A_z \\ L_x & L_y & L_z \end{pmatrix} \begin{pmatrix} \Delta X \\ \Delta Y \\ \Delta Z \end{pmatrix} \tag{3}$$

Substituting ΔX, ΔY, ΔZ from equation (2) into (3), we obtain:

$$\begin{pmatrix} \Delta X_h \\ \Delta Y_h \\ \Delta Z_h \end{pmatrix} = \begin{pmatrix} -D_x & -D_y & -D_z \\ A_x & A_y & A_z \\ L_x & L_y & L_z \end{pmatrix} \begin{pmatrix} L_x & A_x & D_x \\ L_y & A_y & D_y \\ L_z & A_z & D_z \end{pmatrix} \begin{pmatrix} \Delta h \\ R\cos\phi\Delta\lambda \\ R\Delta\phi \end{pmatrix} \tag{4}$$

which reduces simply to:

$$\begin{pmatrix} \Delta X_h \\ \Delta Y_h \\ \Delta Z_h \end{pmatrix} = \begin{pmatrix} 0 & 0 & -1 \\ 0 & 1 & 0 \\ 1 & 0 & 0 \end{pmatrix} \begin{pmatrix} \Delta h \\ R\cos\phi\Delta\lambda \\ R\Delta\phi \end{pmatrix} \tag{5}$$

The topocentric rectangular measurement error vector, $\Delta\vec{\rho}$, with components, Δu, Δv, Δw, is the negative of the station error vector $\Delta\vec{R}$, (assuming no errors for the NAVSTARs' position).

$$\Delta\vec{\rho}(\Delta u, \Delta v, \Delta w) = -\Delta\vec{R}(\Delta X_h, \Delta Y_h, \Delta Z_h) \tag{6}$$

A triad of unit vectors in the topocentric system is defined for the observed elevation (el) and azimuth (AZ) angles as follows:

$$\begin{array}{lll} L_{xh} = -\cos el \cos AZ & A_{xh} = \sin AZ & D_{xh} = \cos AZ \sin el \\ L_{yh} = \cos el \sin AZ & A_{yh} = \cos AZ & D_{yh} = -\sin AZ \sin el \\ L_{zh} = \sin el & A_{zh} = 0 & D_{zh} = \cos el \end{array}$$

so that:

$$\begin{pmatrix} \Delta u \\ \Delta v \\ \Delta w \end{pmatrix} = \begin{pmatrix} L_{xh} & A_{xh} & D_{xh} \\ L_{yh} & A_{yh} & D_{yh} \\ L_{zh} & A_{zh} & D_{zh} \end{pmatrix} \begin{pmatrix} \Delta r \\ r\cos el \Delta AZ \\ r\Delta el \end{pmatrix} \tag{7}$$

The inverse is then:

$$\begin{pmatrix} \Delta r \\ r\cos el \Delta AZ \\ r\Delta el \end{pmatrix} = \begin{pmatrix} L_{xh} & L_{yh} & L_{zh} \\ A_{xh} & A_{yh} & A_{zh} \\ D_{xh} & D_{yh} & D_{zh} \end{pmatrix} \begin{pmatrix} \Delta u \\ \Delta v \\ \Delta w \end{pmatrix} \tag{8}$$

Noting the relationship between $\Delta\vec{\rho}$ and $\Delta\vec{R}$ in equation (6), and substituting (5) into (8) we get for first component, the range expression, Δr as:

$$\Delta r = -\cos AZ \cos el(R\Delta\phi) - \sin AZ \cos el(R\cos\phi\Delta\lambda) - \sin el(\Delta h) \tag{9}$$

or:

$$\Delta r = -\cos AZ \cos el(\text{ South error}) - \sin AZ \cos el(\text{ East error}) - \sin el(\text{ Height error}) \tag{10}$$

AEROSPACE ELECTRONIC LAB TTR
LEAST SQUARES STATION ADJUSTMENT
(meters)

ITERATIVE SOLUTIONS FOR EACH NAVSTAR PRN

	stnd deviation							
	pre-fit residual	post-fit residual	final South correction		final East correction		final Height correction	
PRN			correction	sig	correction	sig	correcton	sig
6	6.809	6.415	-2.776	1.115	- 1.013	0.971	1.667	0.568
9	9.298	7.350	-0.215	0.116	-11.726	0.801	-0.624	0.083
11	7.146	6.557	-6.023	0.430	5.883	0.410	1.002	0.150
12	6.044	5.888	1.054	0.203	-2.926	0.209	-0.768	0.108
13	4.640	3.691	-2.125	0.331	-0.064	0.081	1.285	0.206
3	7.690	6.570	1.857	0.179	0.234	0.081	-0.661	0.102

WEIGHTED SOLUTION

South Correction		East Correction		Height Correction	
weighted mean	composite sig	weighted mean	composite sig	weighted mean	composite sig
-7.366	0.600	-5.612	0.387	-16.122	0.360

AEROSPACE ELECTRONIC LAB TTR
STATION LOCATION

	Latitude			Longitude			Height
Old value:	+33deg	54min	54.5778sec	241deg	37min	13.5410sec	25.00 meters
Correction:			-0.2382sec			-0.2187sec	-16.12 meters
New value:	+33deg	54min	54.3396sec	241deg	37min	13.3223sec	8.78 meters

TABLE 1.
Summary of solutions and estimates of TTR5
station location in WGS84 reference system

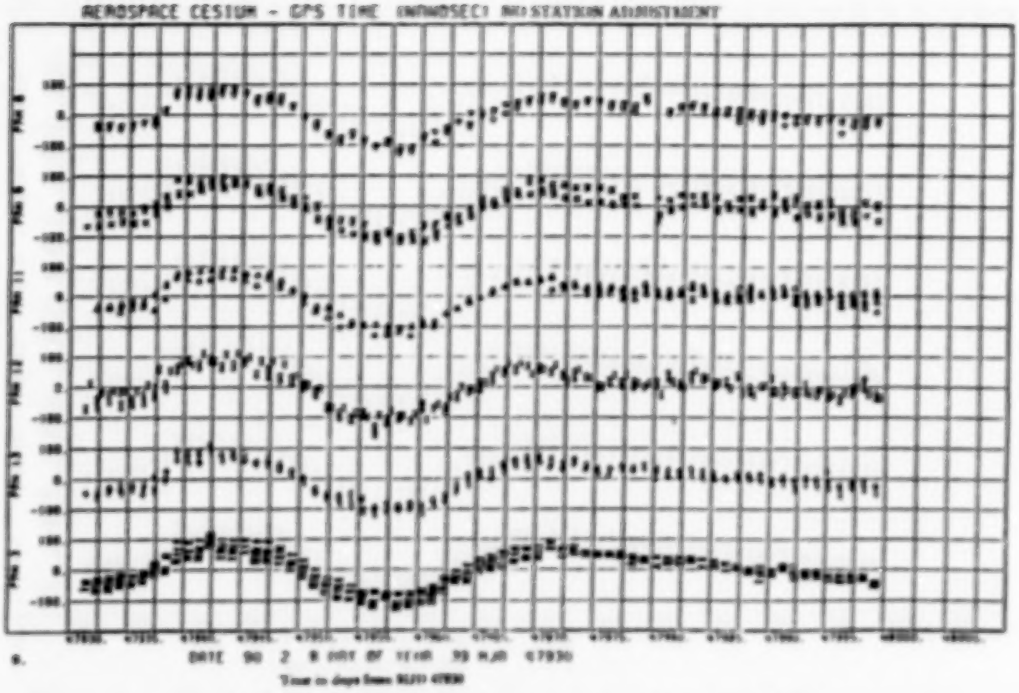


Figure 1. Clock phase residuals between ground cesium and GPS system time via each NAVSTAR PRN. Same systematic effect for satellite is due to GPS time steering. Diurnal "scatter" is due to station location error.

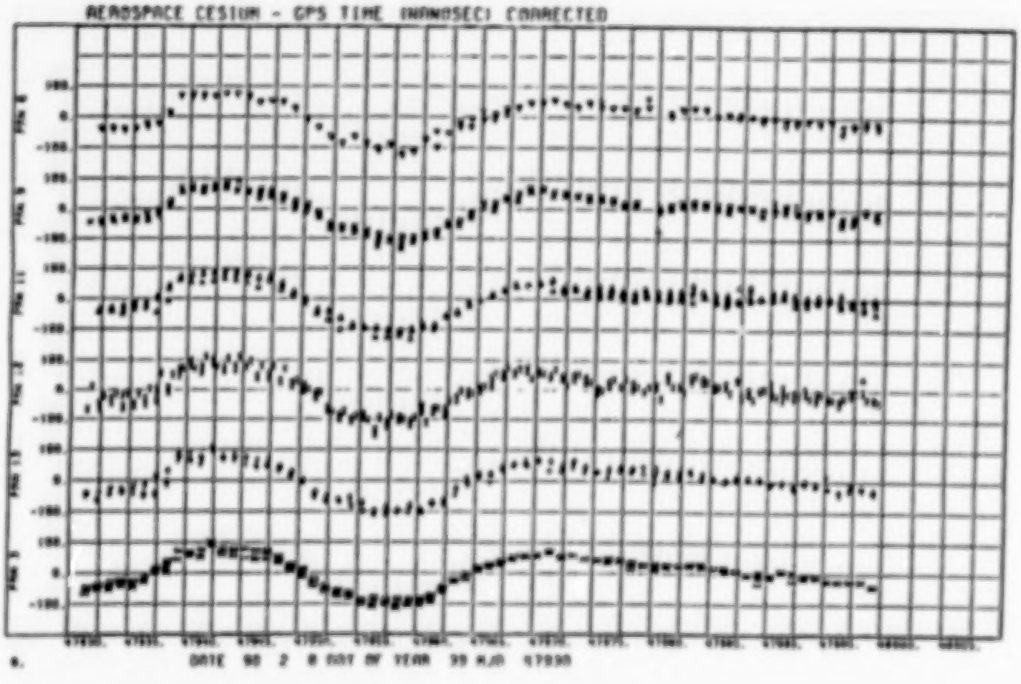


Figure 2. Clock phase residuals between ground cesium and GPS system time via each NAVSTAR PRN. Diurnal "scatter" considerably reduced from Figure 1. Reduction is due to corrected station location.

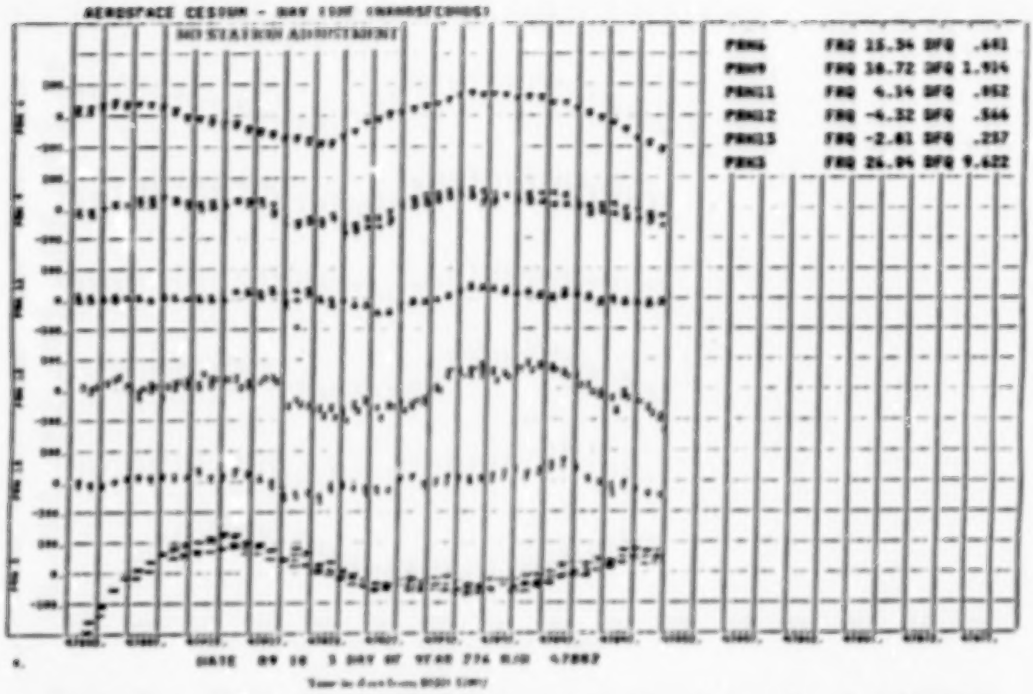


Figure 3. Clock phase residuals between ground cesium and each NAVSTAR PRN. The individual satellite clock variations are apparent. The table on the upper right corner of figure lists the frequency offset (FRQ) in units of picosec/sec. and ageing (DFQ) in units of nanosec/days^2. Diurnal "scatter" is due to station location error.

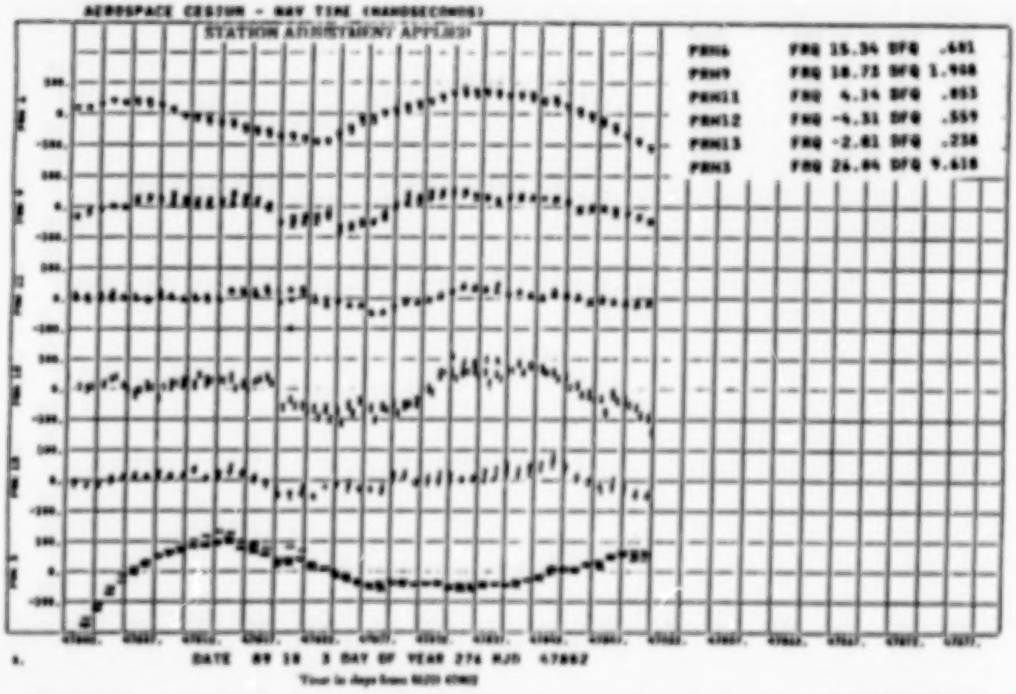


Figure 4. Clock phase residuals between ground cesium and each NAVSTAR PRN. The table on the upper right corner of figure lists the frequency offset (FRQ) in units of pjcosec/sec. and ageing (DFQ) in units of nanosec/days^3. Diurnal "scatter" considerably reduced by using same station locations values as used in Figure 2. and listed in Table 1.

PRECISE MEASUREMENT METHOD FOR IONOSPHERIC TOTAL ELECTRON CONTENT USING SIGNALS FROM GPS SATELLITES

Michito IMAE, Hitoshi KIUCHI, Akihiro KANEKO Shin'ichi HAMA and Chihiro HIKI
Kashima Space Research Center
Communications Research Laboratory
893-1, Hirai, Kashima-machi, Ibaraki, 314 Japan

ABSTRACT

Communications Research Laboratory (CRL) has developed a GPS codeless receiver called "GTR-2" for measuring total electron content (TEC) along the line of sight to the GPS satellite by using the cross correlation amplitude of the received P-code signals carried by L1(1575.42MHz) and L2 (1227.6MHz). This equipment has the performance of uncertainty in the measurement of TEC of about 2×10^{16} electrons/m^2 when a 10 dBi gain antenna was used.
To increase the measurement performance, CRL is planning an upper version of GTR-2 called GTR-3 which uses the phase information of the continuous signals obtained by making a cross correlation or multiplication of the received L1 and L2 P-code signals.
By using the difference of these measured phase values, we can estimate the ionospheric delay with the ambiguities of the periods of L1+L2 and L1 -L2 signals. As the periods of these signals are about 3 ns and 0.3 ns respectively, then this method has the possibility of TEC measurement with the uncertainty of 1 or 2 times of 10^{15} electrons/m^2 of TEC.
Additionally to the precise measurement of TEC, this method has the ability of the precise measurement of the pseudo-range between the GPS satellite and the receiver for the precise positioning.

1. INTRODUCTION

Several kinds of GPS codeless receiving systems for the precise relative positioning [1-4] are developed and they use the dual frequency signals transmitted from GPS for the calibration or correction of the ionospheric propagation delay. To make this correction of ionospheric delay, they must make the measurements of the pseudo-range for L1 and L2 signals individually.
CRL has developed a TEC measurement system using the amplitude of cross correlation of the received L1 and L2 P-code signals[5]. This method is very simple, but its precision is principally based on the duration of P-code signal, so it is difficult to obtain sub-ns level of ionospheric delay correction. To realize more precise ionospheric delay correction, CRL is planning to build a ionospheric TEC measurement equipment by using the method described in this paper.

2. IONOSPHERIC GROUP DELAY AND PHASE DELAY

In the meaning of first order approximation, the ionospheric group delay $\Delta t_{group}(f_c)$ and phase delay $\Delta t_{phase}(f_c)$ caused on the electro-magnetic waves which transverse the

ionosphere are expressed by the following equations (1) and (2) respectively.

$$\Delta t_{group}(f_c) = 134 \cdot N_e / f_c^2 \quad (ns), \qquad (1)$$
$$\Delta t_{phase}(f_c) = -134 \cdot N_e / f_c^2 \quad (ns). \qquad (2)$$

Where N_e is ionospheric total electron content for the line of site to the satellite in electrons/m^2, and f_c is the carrier frequency of signal in Hz. Namely the group delay and the phase delay hav same magnitude, but the group delay has a positive value while the phase delay has a negative value.
Ne for the vertical path changes from about 1×10^{18} to 1×10^{16} [electrons/m^2] at the day time of solar maximum and at the night time of solar minimum, and it changes complicatedly from time to time. Therefore we can say that the ionospheric delay is one of the largest error sources for the precise positioning and the time transfer by using space techniques.

3. IONOSPHERIC TOTAL ELECTRON CONTENT MEASUREMENT USING GPS SATELLITE

3.1 Conventinal measurement methods

As the ionospheric delay depends on the carrier frequency mentioned in the previous section, so the conventional calibration or correction methods used in the precise relative positioning by GPS satellite are using the relative delay time between the L1 and L2 signals. To get the relative delay time, especially in the case of the GPS codeless receivers, one makes the reconstruction of the clock signal of P-code and/or carrier signal of L1 and L2 signal individually. Namely one must have the pseudo-range measurement circuits for L1 and L2 signals individually. In addition, in the case of carrier reconstruction method, the measurement precision is very high but the ambiguity resolution is difficult because the wave length of the carrier signal is very short.
One of the other methods by using the GPS signals for the TEC measurement is the GTR-2 method which is developed at CRL and BIPM. It uses the cross-correlation or multiplication amplitude of L1 and L2 P-code signals. As the measurement precision of GTR-2 method is proposed to duration of the P-code clock signal and inversely proposed to the square root of signal-to-noise ratio (S/N), one must use a high gain antenna to improve the precision.

3.2 Principle of GTR-3

As the L1 and L2 P-code signals transmitted from the GPS satellite have a same code pattern for each GPS satellite and all of the carrier frequencies and the code clock frequencies are synthesized from same onboard frequency reference, then we can express the L1 and L2 P-code signals by the following equations when they are transmitted from the satellite;

$$x_{p1}(t) = P(t)\cos(2\pi f_{L1} t), \qquad (3)$$
$$x_{p2}(t) = P(t)\cos(2\pi f_{L2} t), \qquad (3')$$

where P(t) is a binary pseudo-random-noise sequence which has an amplitude of ± 1, and f_{L1} and f_{L2} are the carrier frequencies of L1 and L2 signals.
The received P-code signals referred to receiver clock are denoted by the following equations (4) and (4'), and figure 1 shows the schematic description of them.

$$t_1 = \phi_1/(2\pi F_1)$$
$$\simeq \Delta t_c - 134N_e/(f_{L1}f_{L2}) - N_1T_0 - (1/4+n_1)T_1, \quad (9)$$
$$t_2 = \phi_2/(2\pi F_2)$$
$$= \Delta t_c + 134N_e/(f_{L1}f_{L2}) - N_2T_0 - (1/4+n_2)T_2, \quad (9')$$

where

$T_1 = 1/F_1 \sim 0.357$ns,
$T_2 = 1/F_2 \sim 2.875$ns,
$F_1 = f_{L1}+f_{L2} = 10.23$MHz x 274 $= F_0$ x 137,
$F_2 = f_{L1}-f_{L2} = 10.23$MHz x 34 $= F_0$ x 17,
$F_0 = 20.46$MHz :maximum common frequency for F_1 and F_2,
$T_0 = 1/F_0 \sim 48.88$ns,
N_1, N_2, n_1, n_2 ;positive integer numbers (ambiguities),
$0 \leqq n_1 < 137$, and $0 \leqq n_2 < 17$.

From (9),(9'), we can estimate TEC and psudo-range,

$$N_e = \{(t_2-t_1)+(N_2-N_1)T_0+(1/4+n_2)T_2-(1/4+n_1)T_1\}f_{L1}f_{L2}/268 \quad (10)$$
$$\Delta t_c = \{t_1+t_2+(N_1+N_2)T_0+(1/4+n_1)T_1+(1/4+n_2)T_2\}/2, \quad (11)$$

with the ambiguities of n1, n2, N1, N2.

Generally, the ambiguity resolution is difficult because durations of L1+L2 signal and L1-L2 signal are very short, but in the case of GTR-3, we can use the rough estimation of TEC obtained by the GTR-2 method and also use the frequency relation between F1 and F2, the maximum common frequency of them is 20.46 MHz, so we can solve the ambiguities easily.

3.3 ESTIMATION OF MEASUREMENT PRECISION AND EXAMPLE OF RECEIVER DESIGN

Table 1 shows the estimated precisions of TEC and pseudo-range measurement using GTR-3 method. The received powers of the L1 and L2 P-code signals are assumed the minimum values of the GPS specifications. And an omni-directional antenna which has a gain of +3 dBi is assumed for the receiving antenna. In this case, the estimated measurement precisions are expected to be about 1.2×10^{15} for TEC and 2.5 cm for pseudo-range measurement respectively. These values of precision are not including the stabilities of the satellite reference clock and the receiver clock.
Figure 4 shows the block diagram based of the GTR-3 method. It has a very simple construction and similar to the GTR-2, but to keep the phase information of the received signals, all of the local signals for frequency conversion in the receiver are synchronized to the receiver reference clock. The received L1 and L2 signals are frequency converted to the IF signals and made a multiplication by using an analogue multiplier. The output signal of the multiplier have the continuous signals corresponding to the L1+L2 signal and the L1-L2 signal described in previous section. As they have about ± 9kHz for the L1+L2 signal and ± 1kHz for the L1-L2 signal of doppler frequency shift due to the satellite motion, then they are finally frequency converted to the signals which have the center frequencies of 10 kHz to be read by the analogue-to-digital converters which have the clock rate of 40kHz. The obtained digital signals are signal-processed by micro-computer to calculate the phases or the zero-crossing timing.
The receiving system based on this concept is now under development at CRL, and

$$y_{P1}(t) = P(t-\Delta t_{g1})\cos\{2\pi f_{L1}(t-\Delta t_{p1})\}, \quad (4)$$
$$y_{P2}(t) = P(t-\Delta t_{g2})\cos\{2\pi f_{L2}(t-\Delta t_{p2})\}, \quad (4')$$

where,

$\Delta t_g(f_{Ln}) = \Delta t_s+\rho/c+\Delta t_{trop}+\Delta t_{gion}(f_{Ln})$:pseudo-delay for modulation term,
$\Delta t_p(f_{Ln}) = \Delta t_s+\rho/c+\Delta t_{trop}+\Delta t_{pion}(f_{Ln})$:pseudo-delay for carrier term,
Δt_s :time diference between satellite clock and receiver reference clock,
Δt_{trop} :tropospheric propagation delay,
for n=1 and 2.

By making the multiplication of y_{P1} and y_{P2} using a multiplier which is illustrated in figure 2, we get continuous signals or de-spread signals at the output port of the multiplier. Equation (5) denotes the formula expression of this multiplication of y_{P1} and y_{P2}, and figure 3 shows the spectrum diagram of the received L1 and L2 P-code signals and the result of their multiplication.

$$\begin{aligned} z(t) &= y_{P1}(t)y_{P2}(t) \\ &= P(t-\Delta t_{g1})P(t-\Delta t_{g2})\cos\{2\pi f_{L1}(t-\Delta t_{p1})\}\cos\{2\pi f_{L2}(t-\Delta t_{p2})\} \\ &= A(t)[\{\cos(2\pi F_1 t-\phi_1)+\cos(2\pi F_2 t-\phi_2)\}] \end{aligned} \quad (5)$$

where

$A(t) = P(t-\Delta t_{g1})P(t-\Delta t_{g2})$,
$F_1 = f_{L1}+f_{L2}$,
$F_2 = f_{L1}-f_{L2}$,
$\phi_1 = 2\pi f_{L1}\Delta t_{p1}+2\pi f_{L2}\Delta t_{p2}$, $\phi_2 = 2\pi f_{L1}\Delta t_{p1}-2\pi f_{L2}\Delta t_{p2}$,
$\Delta t_c = \Delta t_s+\rho/c+\Delta t_{trop}$.

The A(t) in the equation (5) is expressed by equation (6)[6].

$$\begin{aligned} A(t) = B(\Delta t_{g1}-\Delta t_{g2}) &+\{\text{compornents of P-code clock}\} \\ &+\{\text{un de-spread part}\} \end{aligned} \quad (6)$$

The first term represents the dc compornent which is proporsed to the relative delay between the L1 and L2 P-codes due to the ionosphere, the second term denotes the P-code clock and its higher order compornents, and the third term denotes the compornent which can not be de-spread.
From equation (5) and (6), we can obtain the continuous signals at the outputs of the band-pass filters in the figure 2 and they are expressed by

$$z_1(t) = B(\Delta t_{g1}-\Delta t_{g2})\cos(2\pi F_1 t-\phi_1), \quad (7)$$
$$z_2(t) = B(\Delta t_{g1}-\Delta t_{g2})\cos(2\pi F_2 t-\phi_2). \quad (7')$$

The phase tesrms in equation (7) and (7') are discribed as the followings;

$$\phi_1 = 2\pi F_1\Delta t_c-134N_c2\pi F_1/(f_{L1}f_{L2}), \quad (8)$$
$$\phi_2 = 2\pi F_2\Delta t_c+134N_c2\pi F_2/(f_{L1}f_{L2}). \quad (8')$$

Finally we get the epocks of the zero-crossing point of $z_1(t)$ and $z_2(t)$, t_1 and t_2, and they are denoted by

being made the preliminary receiving tests, and the results will be shown in the other occasion.

4. CONCLUTIONS

In this paper the principle of the method for precise TEC measurement by using the signal phase informations of continuous signal of L1+L2 and L1-L2 obtained by making multiplication of received L1 and L2 P-code signal from GPS satellite. As the hard-wear construction is very simple and it also has the possibility of cm level of the pseudo-range measurement, then it is expected to be used not only for the precise TEC measurement but also for the precise relative positioning receiver. And the ambiguity resolutionin the measurement of TEC and pseudo-range will be made comparatively easily by using rough estimation of TEC obtained by the GTR-2 method and also the frequency relationbetween L1+L2 and L1-L2 frequencies.

References

[1] Ladd J.W. et al,"The macrometer Dual-B and Interferometric Surveyor", Proc. of 1st International Symposium on Precise Positioning with the Global Positioning System, 1985.

[2] MaCdoran P.F. et al,"Codeless Systems for Precise Position with the "NAVSTAR-GPS", Proc. of 1st International Symposium on Precise Positioning with the Global Positioning System, 1985.

[3] Stansell T.A. et al,"The First Wild-Magnavox GPS Satellite Surveying Equipement: WM-101", Proc. of 1st International Symposium on Precise Positioning with the Global Positioning System, 1985.

[4] Sugimoto Y. et al,"Development of GPS Positioning System PRESTER", Proc. 1988 Conference on Precision Electromagnetic Measurements, 1988.

[5] Imae M. et al,"A Dual Frequency GPS Receiver Measuring Ionospheric Effects without Code Demodulation and Its Application to Time Comparisons", Proc. of 20th PTTI, 1988.

[6] Spilker J.J,"Digital Communication by Satellite", Printice-hall, 1977.

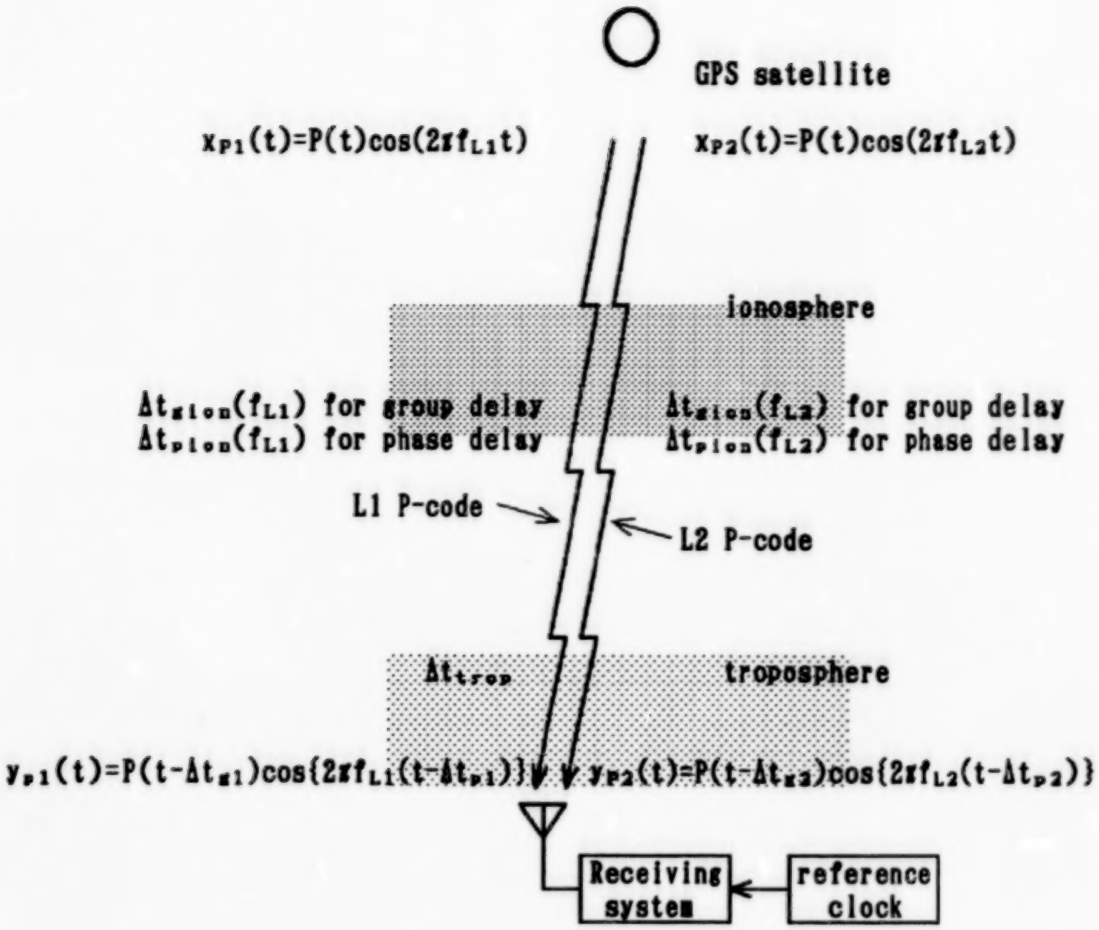


Figure 1. Schematic expression of psudo-range.

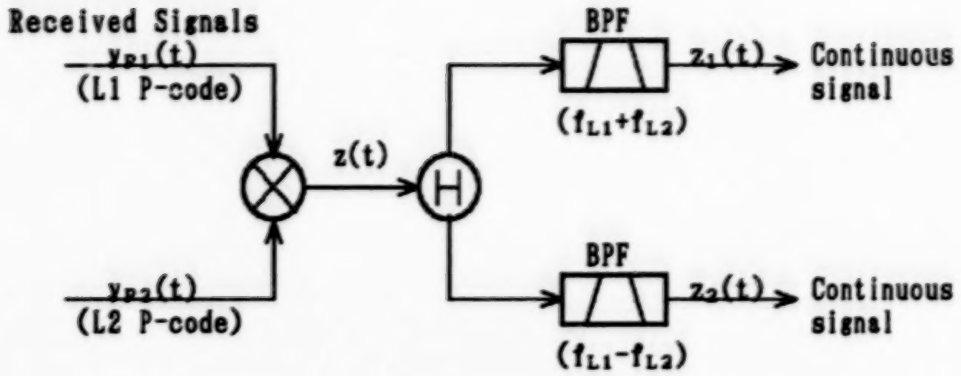


Figure 2. Principle of measurement method.

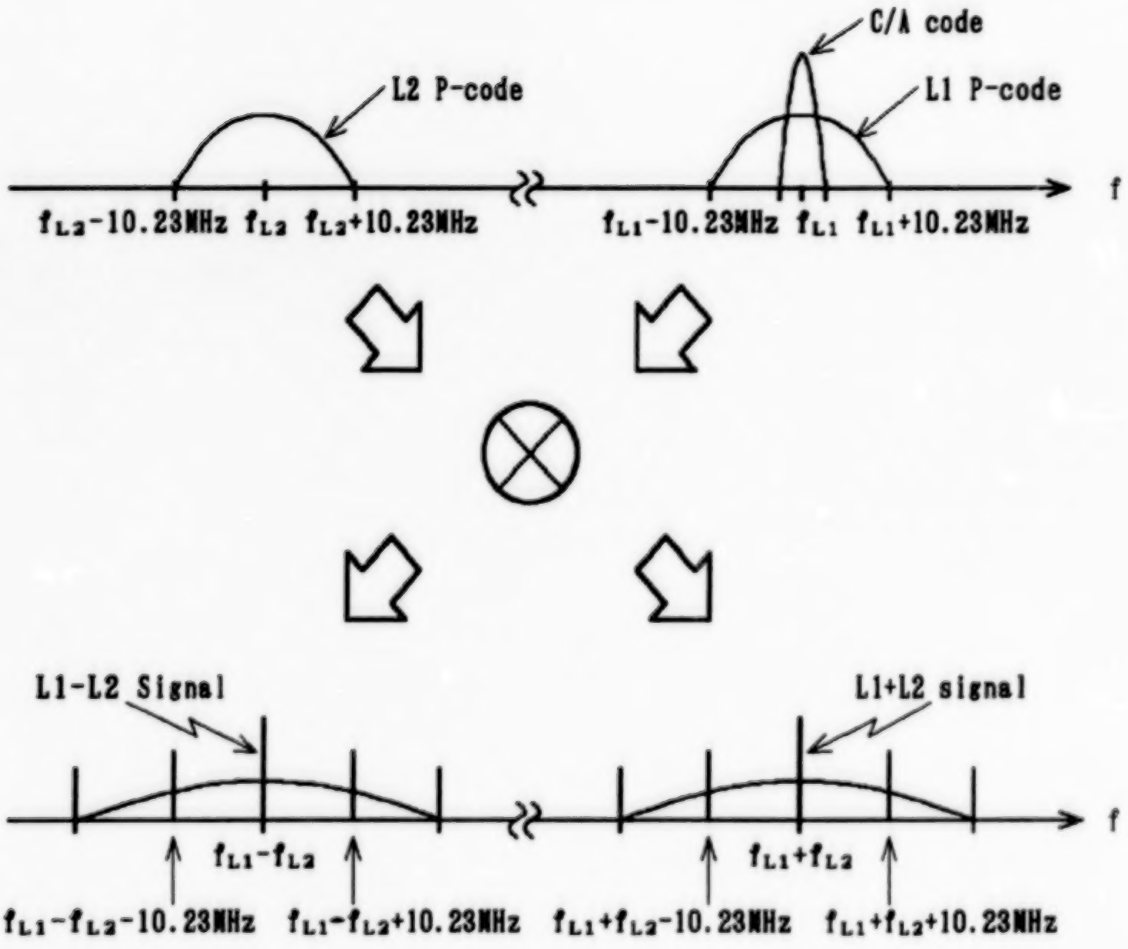


Figure 3. Schematic spectrum diagram of received signals and results of their multiplication.

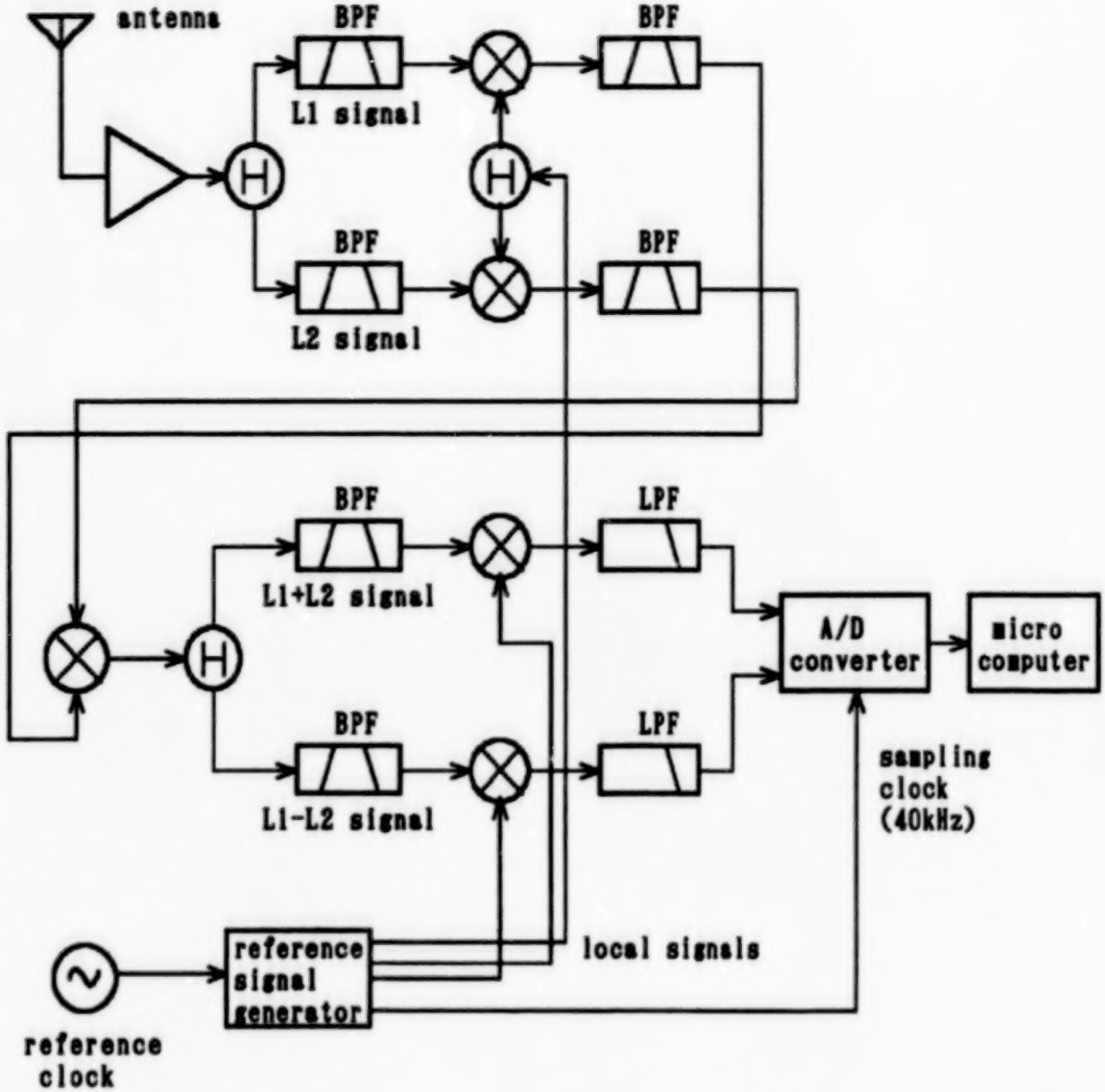


Figure 4. Block diagram of receiving system which is under development at CRL.

Table 1. Estimation of performance of TEC and psudo-range measurements.

	L1 P code	L2 P code
received power	>-133 dBm	>-136 dBm
antenna gain (omni-directional)	+3 dBi	+3 dBi
system noise (No)	-174 dBm/Hz	-174 dBm/Hz
carrier-to-noise ratio (C/No) at input of multiplier	>+44 dBHz	>+41 dBHz
carrier-to-noise ratio (C/No) at output of multiplier	>+12 dB·Hz	
bandwidth of zero-crossing detection for t_1 and t_2	2 Hz	
measurement precision of t_1	~0.02 ns	
measurement precision of t_2	~0.16 ns	
estimation precision of TEC	~1.2×10^{15} electrons/m^2	
estimation precision of psudo-range	~2.5 cm	

BLANK PAGE

APPLICATION OF HIGH STABILITY OSCILLATORS TO RADIO SCIENCE EXPERIMENTS USING DEEP SPACE PROBES

E. R. Kursinski
Jet Propulsion Laboratory
California Institute of Technology
Pasadena, California 91109

Abstract

The microwave telecommunication links between the earth and deep space probes have long been used to conduct radio science experiments which take advantage of the phase coherency and stability of these links. These experiments measure changes in the phase delay of the signals to infer electrical, magnetic and gravitational properties of the solar system environment and beyond through which the spacecraft and radio signals pass. The precision oscillators, from which the phase of the microwave signals are derived, play a key role in the stability of these links and therefore the sensitivity of these measurements. These experiments have become a driving force behind recent and future improvements in the Deep Space Network and spacecraft oscillators and frequency and time distribution systems.

Three such experiments which are key to these improvements are briefly discussed here and the relationship between their sensitivity and the signal phase stability is described. The first is the remote sensing of planetary atmospheres by occultation in which the radio signal passes through the atmosphere and is refracted causing the signal pathlength to change from which the pressure and the temperature of the atmosphere can be derived. The second experiment is determination of the opacity of planetary rings by passage of the radio signal through the rings. Because the signal is coherent, the diffraction effects can be removed resulting in resolutions of 10's to 100's of meters in the radial direction depending on a number of factors including the coherence time of the microwave signal. The third experiment is the search for very low frequency gravitational radiation. The fractional frequency variation of the signal is comparable to the spatial strain amplitude the system is capable of detecting. A summary of past results and future possibilities for these experiments are presented.

INTRODUCTION

Microwave telecommunication links between the earth and deep space probes have been used since the beginning of space travel for communication and navigation. The phase stability required for these functions provided the opportunity for radio science experiments measuring changes in the signal phase and group delay to infer electrical, magnetic and gravitational properties of the solar system and beyond. The sensitivity of these measurements is ultimately limited by the precision oscillators from which the phase of the microwave signal is derived. These experiments have become a driving

force behind recent and future improvements in the reference oscillators and frequency distribution systems in NASA's Deep Space Network (DSN) and planetary space probes. The purpose of this paper is provide some insight into the source of these and future requirements.

Three experiments have been chosen for this discussion which collectively push spacecraft and ground oscillator performance. The first is the remote sensing of planetary atmospheres by occultation technique where the radio signal passes through a planet's atmosphere and is refracted causing the optical path length of the signal to change from which the pressure and temperature of the atmosphere can be estimated. The second experiment is the determination of the microwave opacity of planetary rings through the changes in the signal amplitude and phase induced during the signal's passage through the rings. The third experiment is the search for very low frequency gravitational radiation. The fractional frequency variation of the signal is comparable to the spatial strain amplitude of the gravitational waves which the system is capable of detecting.

The instrument consists of the combined radio systems of the spacecraft and ground tracking stations and is operated in one of two configurations. The first is referred to as the "one-way" or noncoherent doppler (or bi-static radar) mode where independent reference oscillators are used at the earth and the spacecraft. In the "two-way" or coherent doppler mode, only an earth-based reference oscillator is used. A coherent signal is transmitted from the earth, received at the spacecraft by a transponder and then retransmitted to the earth. Upon reception at the earth, the signal's frequency is essentially differenced with an estimate of the original transmitted frequency derived from the same reference oscillator. The two-way mode provides the more sensitive measure of signal phase owing to the stability of the hydrogen masers at each DSN tracking complex. However, for the two-way mode to function properly, the transponder must acquire and maintain phase lock on the uplink signal which is difficult when rapid signal dynamics exist making the one-way mode preferable for occultation measurements. This mode places tight requirements on the phase stability of the oscillator on-board the spacecraft.

ATMOSPHERIC OCCULTATIONS

The atmospheric occultation technique was first conceived in the early 1960's and first used to successfully characterize a planetary atmosphere with Mariner IV at Mars [1,2]. It has characterized the pressure and temperature of the atmospheres of all the major bodies in the solar system with the exception of Pluto. This technique is an optics experiment where the atmosphere acts as a lense whose properties are inferred from the perturbations induced in the light passing through it. As viewed from the earth, the spacecraft passes behind the planetary atmosphere and the refraction generated increase in the signal's optical path length is measured *via* the signal phase (see Figures 1 and 2).

Given the atmospherically induced phase shift versus time, as well as an accurate knowledge of the trajectory and gravity field of the planet, the recovery of the atmospheric pressure and temperature proceeds as follows [3]:

1. The asymptotic paths of the signal into and out of the atmosphere are computed based on the bending angle required to generate the measured atmospheric frequency shift.
2. The bending as a function of altitude is transformed into refractivity vs altitude via an Abel transform.

3. The number density profile is recovered from the refractivity profile using the fact that the measured refractivity is proportional to the refractivity per molecule times the number of molecules along the signal's path.

4. The pressure is determined by integrating the weight in the column of atmosphere above each altitude and setting the pressure such that it supports this weight (condition for hydrostatic equilibrium).

5. The temperature profile is computed from the equation of state (ideal gas law in the simplest case) using the number density and pressure profiles derived in steps 3 and 4.

Steps 3 and 4 require some knowledge of the average atmospheric constituents which is provided by other instrumentation on the spacecraft and the earth. From these steps it is clear that errors in phase map sequentially into errors in bending angle, refractivity, number density, pressure and temperature. A direct analytical solution of this error propagation does not exist although the author is presently pursuing this task. Simulations have generally been used instead to estimate the effects of the oscillator noise.

The minimum detectable bending angle provides an indication of the sensitivity of the technique. For small bending angles, the doppler shift due to bending is approximately:

$$F_{doppler} = F_0 \Theta v / c \tag{1}$$

where F_0 is the nominal microwave frequency, Θ is the bending angle in radians, v is the component of the spacecraft velocity in the plane of the sky and c is the velocity of light in a vacuum. The minimum detectable bending angle occurs when this doppler shift exceeds the uncertainty in the signal frequency. Given a 10^{-12} oscillator and a 10 km/sec plane of the sky velocity (typical numbers for Voyager), bending angles as small as 30 microradians can be detected.

In high altitudes, the technique is limited by the presense of sufficient material to cause measurable bending and phase shift. In the Voyager case, a typical upper altitude limit is 0.1 to 1 millibar with temperature uncertainties estimated to be around 10 Kelvin. Figure 3 contains the vertical temperature vs pressure profiles for the inbound and outbound occultations of Uranus [4]. One noteworthy exception to this upper limit was the occultation of Triton, the large moon of Neptune, in which the sensitivity was pushed another order of magnitude by least squares fitting the entire measured phase profile to the phase shift due to an isothermal atmosphere. The recovered surface pressure and isothermal temperature of Triton were 16 ±3 microbars and 48 Kelvin ±5 respectively dominated by the uncertainty in the oscillator phase over the ten second occultation [5].

In lower altitudes the trajectory often limits the maximum bending angle where the deepest penetration into the atmosphere occurs. For the Pioneer Venus orbiter, the maximum depth is limited to 40 km above the surface where the bending angle exceeds a critical refraction angle below which the ray does not reemerge from the atmosphere. Absorption by atmospheric constituents such as ammonia can also limit the penetration depth. Maximum pressure levels of a few bars were typically achieved by Voyager.

To first order the pressure and number density (and therefore refractivity) of an atmosphere increase exponentially with decreasing altitude and the dependence is exactly exponential in a region where the temperature is constant (isothermal). This dependence is characterized by a scale height, the change in altitude over which the parameter of interest changes by a factor of e, the base of the natural

logarithm. The sensitivity of the measurements to the oscillator phase uncertainty primarily depends on the refractivity scale height of the atmosphere and the geometry of the occultation. In order to make a useful measurement, the exponential increase in refractivity and therefore signal phase delay as the ray descends through the atmosphere must grow faster than the increase in uncertainty in the estimated oscillator phase. A relevant figure of merit is the stability of the oscillator over the time required for the raypath to descend a scale height in the atmosphere. In the upper atmosphere, this time typically ranges from one to 10 seconds. Deeper in the atmosphere, as the bending increases, the vertical descent of the ray slows significantly. However, the phase delay through this region of the atmosphere is large relative to the oscillator uncertainty and the greatest errors are typically in the upper tenuous regions of the atmosphere as indicated in Figure 3.

Another relevant vertical dimension is the radius of the first Fresnel zone of the occulted ray. This is used as an estimate of the diffraction limited cross section of the geometric ray and sets the vertical resolution of the recovered profiles. In reality, the diffraction can be modeled to some degree and finer vertical structure can be inferred. This sets the maximum signal detection integration time which is typically on the order of 0.1 seconds. Generally both oscillator stability and SNR are limiting factors on this time scale.

The occultation length is also important because it represents the total span over which the signal's phase must be estimated. Shorter, faster occultations are desirable simply because the oscillator phase has less time to wander. Occultation lengths have ranged from 10 seconds for Triton to a few thousand seconds for the large outer planets.

To gain further insight, it is useful to consider the effect of the oscillator phase uncertainty on the altitude at which a certain temperature accuracy can be achieved. The phase uncertainty due to the oscillator must be some small fraction of the phase shift caused by the atmosphere. For each factor of ϵ of improvement in the oscillator's stability, the altitude at which the same phase ratio would be achieved would increase by a scale height. In comparison with the 1×10^{-12} class Voyager oscillator, use of the currently available 1×10^{-13} crystal oscillators [6] would result in an altitude increase of 2.3 ($= \ln(10)$) scale heights assuming a common occultation geometry and spectral shape for the noise. This assumption of similar spectral shape is valid because both oscillator types exhibit flicker frequency noise over the relevant time scales [6]. Given a Voyager-like range of pressure sensitivity from tenths of millbars to a few bars (~ 9 scale heights), this stability would increase the sensitivity to low pressures by an order of magnitude and the total range of altitudes covered by ~25%. For a tenuous atmosphere like Mars the increase in altitude range covered would be even more dramatic. Given a 10 km scale height and the expected altitude sensitivity range of 60 km with the 10^{-13} Mars Observer oscillator (Dave Hinson personal communication), a Voyager class oscillator would have reduced this to 37 km indicating the improved performance will result in a 60% increase in the altitudes covered.

Using these same assumptions of common geometry and spectral shape, a similar argument can be made concerning the pressure and temperature uncertainty at any altitude. Assuming that the 5 step process of atmospheric temperature recovery can be represented by an equivalent linear filter, which appears to be the case based on preliminary results by the author, the pressure and temperature uncertainty as a function of altitude will be identical except for the constant scale factor between the noise levels of the two oscillators. Therefore, an improvement of an order of magnitude in the Allan deviation of an oscillator would result in an improvement by this same factor in the accuracy of the recovered pressure and temperature accuracy at all altitudes.

RING OCCULTATIONS

Radio occultations of the ring systems of Jupiter, Saturn, Uranus and Neptune were performed with Voyager of which the Saturnian and Uranian rings provided positive, detailed results. The rings act as huge diffraction gratings whose complex microwave opacities as well as particle densities and size distributions are characterized by the occultation measurements. The opacity measurements are complex in that they provide information on both signal amplitude and phase changes caused by the ring material.

This instrument has a large dynamic range due to the signal to noise ratio (SNR) at the receiver which places limits on sensitivity range and accuracy of the detected opacity profiles [7]. In order to avoid degrading this performance, the signal and receiver local oscillator phase noise spectral densities due to the reference oscillators from which they are generated must be kept below the thermal noise associated with the SNR where possible. The range of Fourier frequencies of interest for Voyager was typically within ±3 kHz of the carrier frequency covering the angular extent of signal reception by the main lobe of the spacecraft antenna pattern [8].

Concerning diffraction limitations, the uncorrected radial resolution of a radio opacity profile is coarser by factors of hundreds than an optical stellar occultation measurement made with a common viewing geometry due to the relatively long microwave wavelengths. However, the occulted radio signal is coherent allowing the diffraction to be dramatically reduced resulting in resolutions comparable to the optical measurements. Figure 4 shows a near-classic example of a diffraction pattern observed in a ring occultation profile near a sharp edge. Figure 5 provides an excellent example of the effectiveness of the diffraction removal process for Saturn's F-ring. This process has been thoroughly analyzed in [7] and most of what follows is a summary of those results.

This process can be thought of as an inverse transform where the actual opacity of the rings is recovered from the diffraction limited measurements of the opacity. As in the case of a Fourier transform, the finite transform length of the data segment limits the resolution, spatial resolution in this case, of the inversion. A number of factors such as trajectory knowledge and finite antenna pattern footprint on the ring plane can limit the ultimately achievable radial resolution. The achievable resolution is approximately

$$\Delta R_w \cong 2F^2/W \tag{2}$$

where ΔR_w is the radial resolution, F is the Fresnel "scale" and W is the spatial length of the data segment to be inverted. F is radius of the first Fresnel zone in the ring plane divided by square root of 2 and is the characteristic length of a spatial cycle of the diffraction oscillations apparent in the uncorrected occultation results such as those in Figures 4 and 5.

In order for this inversion process to reduce the effects of diffraction, the phase of the unperturbed signal must be known to a fraction of a cycle across the data segment to be inverted. As in the case of an atmospheric occultation, this phase is not precisely known and must be estimated during periods where the direct signal is not visible through the rings. The actual signal phase will gradually wander away from the estimate and at some point the criterion of phase knowledge to a fraction of a cycle can not be maintained. The radial resolution at this point is the resolution ultimately available using this oscillator, essentially by limiting the data segment length in the inversion process.

Having said this, it is important to note that the Saturn and Uranus ring systems are very different

in terms of the radial extent of their individual rings. Saturn has the only ring system in the solar system with microwave opacities over large radial segments such that the direct signal is not be visible for 10's to 100's of seconds during an occultation. In contrast, the Uranian rings are relatively narrow in radial extent separated by large gaps of free space. Typical values range from 2 to 10 km for rings other than the epsilon ring which had a 75 km radial width measured by the egress occultation [9]. These occultations last from a fraction of a second up to a few seconds requiring only that the signal phase be coherent over these relatively short periods.

To provide insight to the relationship between stability and radial resolution, consider the following approximate analysis. An approximate expression relating the coherent integration time, T, and the Allan variance of a reference frequency standard is given by [10]

$$T = 1/[\omega_0 \sigma_y(T)] \tag{3}$$

where $\sigma_y^2(T)$ is the Allan variance and ω_0 is the link frequency in radians per second. The equivalent data segment length corresponds to the radial distance which the raypath moves in the ring plane over this time. Once this width is known, equation 2 can be used to estimate the achievable radial resolution. Figure 6 contains a chart of Allan deviation *vs* integration time, on which four curves are drawn, the Allan deviation performance curves of three oscillators and a line representing phase coherence *vs* integration time for X-band. The radial resolution axis under the integration time axis has been converted from coherence time to effective data segment length and then radial resolution for the Voyager-1 Saturn F-ring occultation geometry. The radial resolution at the intersection of an oscillator performance curve with the coherence curve indicates the oscillator limited resolution providing a simple method for comparing the relative merits of different standards for this application.

A more precise analysis of the effects of oscillator phase noise must consider each noise type (white frequency, flicker frequency etc.) explicitly and must take into account whatever detrending of the phase wander is done in the diffraction removal process. Because it is analytically tractable, the effect of a white frequency noise process on the diffraction removal inversion has been characterized using the phase structure function [7]. The resulting phase limited resolution is:

$$\Delta R_\phi = \Delta R_w \left[\frac{b^2/2}{e^{-b} + b - 1} \right] \tag{4}$$

where $b = \omega_0^2 \sigma_y^2 W / 2\dot{\rho}_0$, $\omega_0 = 2\pi f_0$, $\sigma_y^2(1)$ is the one second Allan variance, W_{eff} is the effective physical width of the data segment to be inverted, and $\dot{\rho}_0$ is the radial velocity in the ring plane. Figure 7 is a plot of equation 4 for different ring occultation geometries at Saturn and Uranus and indicates how the finite oscillator stability degrades the potential radial resolution. The dashed lines in the figure indicate where data processing requirements become prohibitive. The approximate result in Figure 6 provides results within 50% of the white frequency noise estimates in [7].

GRAVITATIONAL WAVE SEARCH

The experiments attempting to detect signatures of very low frequency gravitational radiation in the spacecraft Doppler records place the tightest performance goals on the ground based frequency standards. Theory predicts the presence of distinctive three pulse signatures in the received frequency of

the spacecraft signal produced by the gravitational radiation propagating through the solar system [11]. The instrument is configured in the two-way doppler mode to take advantage of the phase stability of the hydrogen maser frequency standards residing at each DSN tracking complex. It functions essentially as one arm of an interferometer stretched across the solar system. The earth based tracking system at one end is both the transmitting and receiving node of the interferometer and the spacecraft at the other end acts as a reflector. The difference between the frequencies of the transmitted and received signals is generated at the tracking station providing a data set in which to search for 3-pulse signatures.

The instrument's sensitivity is ultimately limited by the stability of the frequency standard over the signal integration time as well as the round trip light time (RTLT) of the signal's passage to and from the spacecraft. The characteristic stability of the hydrogen masers causes the most sensitive region of the instrument to run from approximately 0.0001 to 0.01 Hz where the high frequency limit is set by the thermal noise of the earth-spacecraft microwave link and the lowest detectable frequency by the response function to gravitational radiation (approximately 3/RTLT) [12]. These limits are both tied to the RTLT. A more distant spacecraft such as Pioneer 10 with a 12.25 hour RTLT will have a very low frequency cutoff but also a relatively small high frequency cutoff due to a low SNR.

In terms of detection of gravitational radiation bursts, the Allan deviation of the detrended received signal frequency residuals provides a useful figure of merit indicating the burst strain amplitude sensitivity of the instrument. For sinusoidal sources, the normalized frequency power spectral density provides a relevant figure of merit. A key sensitivity factor is the resolution of the frequency spectrum which can be microhertz or less for data sets acquired continuously over weeks improving the sensitivity to periodic sources over bursts by a factor of 10 or more. The span of continuous data acquisition is typically limited to a few weeks when spacecraft are near solar opposition because the signal phase scintillations due to the interplanetary plasma are minimal [13].

The present system utilizes S-band signals to and from the spacecraft at 2.1 and 2.3 GHz respectively. Measurements made in this configuration in December of 1988 with Pioneer 10 indicate an instrument sensitivity of 2.8×10^{-13} for bursts and a 90% probability of detection for periodic sources of 4×10^{-14} presumably limited by variations in the solar wind [12]. Future measurements will be conducted with higher frequency links to reduce plasma effects. The first measurements will be made using an X-band uplink and downlink (7.1 and 8.4 GHz respectively) system with the Galileo spacecraft in May of 1991. These X-band frequencies should reduce the plasma effects by more than an order of magnitude relative to the S-band system. This first test occurs only 6 months after Galileo's first flyby of the earth. While the relatively short RTLT of this geometry will severely limit the low Fourier frequency sensitivity of the instrument, the SNR will be very high maximizing the high frequency sensitivity. The total contribution of the transmitting and receiving equipment of the DSN in this X-band configuration should be no more than 5×10^{-15} for time scales of 1000 to 3600 seconds with the hydrogen masers contributing no more than 2×10^{-15} [14]. It is also important to realize that stable distribution of the reference frequency over a kilometer or more from a maser to the antenna is not trivial and has led to a research and implementation effort utilizing near-zero temperature coefficient fiber optic cable [15].

A proposal has been written to conduct a Ka-band uplink and downlink experiment (34 and 32 GHz respectively) near the end of the century using the Cassini spacecraft while en route to Saturn. These higher frequencies would reduce the interplanetary plasma instabilities at X-band by another order of magnitude. The potential instrument stability has been estimated as approximately 1×10^{-15} at 1000 seconds [16] with the hydrogen maser performance contribution estimated to be 4×10^{-16} based

on assumed improvements in spin rate selection and magnetic screening as well as phase locking the maser to a trapped ion frequency standard.

OSCILLATOR REQUIREMENTS

These three experiments have been discussed together to provide a sense of the wide range of scales the spacecraft and DSN oscillators must cover. For the two occultation experiments, the spacecraft oscillator must provide stability over time scales covering approximately 7 orders of magnitude from ±3 kHz on either side of the carrier frequency to durations of more than 1000 seconds. The frequency standards at the DSN tracking complexes must provide stable references over this range as well as still longer spans covering the round trip passage of the signals across the solar system. These time scales are summarized in Figure 8.

FLIGHT OSCILLATORS

The goal for the performance of flight oscillators is really open-ended, the more stable the oscillator, the better the measurements will be. In reality, one must take into account present oscillator technology capabilities in specifying oscillator performance for these experiments. The choice of spacecraft oscillators is very constrained by size, weight, power, reliability and cost considerations which, when combined with the time scales of interest, have thus far made high performance crystal oscillators the references of choice.

In looking to the future, it is interesting to note that with the completion of the Voyager grand tour all planets except Pluto have been visited by spacecraft. Therefore one can expect that most planetary spacecraft will remain at a planet to provide a more in depth characterization of the planet. Orbiting spacecraft must have lower velocities relative to the planets under observation than the Voyagers in order to remain in orbit, implying that future outer planet atmospheric and ring occultations will generally be slower and therefore more sensitive to oscillator phase instability. The Galileo orbiter which will begin orbiting Jupiter in December of 1995 provides an excellent example. The oscillator on board is a spare Voyager oscillator with 10^{-12} performance causing only the first Jovian occultation to rival the Voyager accuracies because the subsequent occultations will be longer and slower.

The Cassini orbiter will characterize the atmospheres of Saturn and Titan and the rings with occultation measurements while in orbit around Saturn. To improve upon the Voyager results, the desire for more accurate atmosphere and ring measurements will of course lead to placing a more stable oscillator on-board. It does appear that this need will be met simply because the Cassini oscillator will presumably have at least the performance of the Mars Observer oscillator. In addition, a stable oscillator will also be placed on the Huygens' probe to provide a stable radio link frequency to measure the velocity of descent of the probe into the Titan atmosphere to characterize winds in the Titan atmosphere.

There are some applications for still longer time scales which haven't been discussed here. Recovery of a planet's gravity field can be accomplished with one-way doppler measurements if the flight oscillator is sufficiently stable. This can be desirable in situations where gravity field and occultation measurements are simultaneous creating a conflict between the desire for the one way versus two way doppler configuration. A related application is the proposed Solar Probe mission which would pass within

a few solar radii of the sun over a 14 hour period making a series of gravity related measurements. The proposed configuration would utilize a flight hydrogen maser to provide the necessary stability. This could also provide an application for a flight trapped ion standard whose performance could conceivably rival that of the maser over this time scale.

GROUND OSCILLATORS

In creating the ground oscillator requirements, it is important to realize that the ground based oscillators can be expected to provide better overall performance than the flight oscillators because they are not limited by the same constraints imposed on the spacecraft equipment. In addition, because of long flight times to the outer planets (such as the seven year trip for Cassini to reach Saturn), ground oscillators can potentially take advantage of more current technology not available when the flight instrumentation was designed and implemented. Therefore the goal of the noise power of ground oscillators in the DSN has been set at 10 dB below that of the downlink signal which is limited by a combination of the flight oscillator, the downlink SNR and any uncalibrated propagation effects. This was achieved for the Voyager Neptune encounter due to the relatively low received signal SNR and the 10^{-12} performance of the 15 year old Voyager oscillator. For Mars Observer (MO), however, the exceptional performance of the flight oscillator will be comparable to that of the hydrogen maser (possibly even exceeding it) for time scales near 1 second making it difficult to achieve this 10 dB goal as indicated in Figures 9 and 10.

TROPOSPHERE

In discussing these requirements it is important to consider other noise sources which can mask the stability of the frequency standards. One particular source worthy of mention here is the phase instability caused by the passage of signals through the earth's troposphere. A simple model of the troposphere indicates a level of instability that, without calibration, will significantly exceed the hydrogen maser stability over time scales less than about a day [17]. A particular case of relevance is the previously mentioned Ka-band gravitational wave search sensitivity estimate which assumes 95% calibration of the troposphere. Present crystal oscillator performance is also becoming comparable to these phase instabilities and will require partial calibration of the earth's troposphere to take full advantage of the oscillator's performance. An interesting application of a very stable flight oscillator has been proposed where the troposphere effects can be removed using simultaneous one and two-way up and downlinks when the flight oscillator stability exceeds the instabilities due to the troposphere [18]. This technique could potentially be applied to all three experiments described here although maintaining the two-way links during the occultations might pose significant technical difficulties. The DSN is presently studying the possibility of deep space tracking stations in orbit around the earth which would potentially eliminate the troposphere from the signal path but would introduce gravity induced orbital perturbations into the signal phase data.

CONCLUSION

In conclusion, I hope that this has provided some insight into these scientific applications and how they utilize phase stability. With the tremendous success of the Voyager radio science experiments which

have proven themselves as powerful tools for characterizion of planetary systems and the tantalizing prospect of gravitational radiation detection, these experiments should continue to be a part of future planetary space probes and their symbiontic relationship with the developers of frequency standards should also continue to provide a unique set of applications for future frequency standard research and development.

REFERENCES

[1] A. Kliore et al., "Occultation Experiment: Results of First Direct Measurement of Mar's Atmosphere and Ionosphere", Science 149, 1243–1248, 1965

[2] G. Fjeldbo and V.R. Eshleman, "The Atmosphere of Mars Analyzed by Integral Inversion of the Mariner IV Occultation Data", Planet. Space Sci., Vol. 16, pp. 1035–1059, 1968

[3] G. Fjeldbo, A. J. Kliore and V. R. Eshleman, "The Neutral Atmosphere of Venus as Studied with the Mariner V Radio Occultation Experiments", The Astronomical Journal, Vol. 76, No.2, pp. 123–140, March 1971

[4] G. F. Lindal et al., "The Atmosphere of Uranus: Results of Radio Occultation Measurements With Voyager 2", Journal of Geophysical Research, Vol. 92, No. A13, pp. 14987–15001, December 30, 1987

[5] G. L. Tyler et al., " Voyager Radio Science Observations of Neptune and Triton", Science, Vol. 246, pp.1466–1472, 15 December 1989

[6] J. R. Norton, "Ultrastable Quartz Oscillator for Spacecraft", Proc. of 21st Annual Precise Time and Time Interval Planning Meeting (PTTI), Nov. 28–30, 1989, pp. 509–518

[7] E. A. Marouf, G. L. Tyler and P. A. Rosen, "Profiling Saturn's Rings by Radio Occultation", Icarus, Vol. 68, pp. 120–166, 1986

[8] E.R. Kursinski and S.W. Asmar, "Radio Science Ground Data System Requirements for the Voyager Neptune Encounter", submitted to The Telecommunications and Data Acquistion Progress Report Dec. NASA JPL Pasadena California

[9] D. L. Gresh et al., "Voyager Radio Occultation by Uranus' Rings. I: Observational Results", Icarus, Vol. 78, pp. 131–168, 1989

[10] W.K. Klemperer, "Long-baseline radio interferometry with independent frequency standards", Proc. IEEE, vol. 60, pp. 602-609, May 1972

[11] F.B. Estabrook and H.D. Wahlquist, GRG 6, 439 (1975)

[12] J. D. Anderson et al., "Application of Hydrogen Maser Technology to the Search for Gravitational Radiation", Proc. of 21st Annual Precise Time and Time Interval Planning Meeting (PTTI), Nov. 28–30, 1989, pp. 259–268

[13] J. W. Armstrong, R. Woo and F. B. Estabrook, "Interplanetary Phase Scintillation and the Search for Very Low Frequency Gravitational Radiation", The Astrophysical Journal, Vol. 230, pp. 570–574, June 1, 1979

[14] E.R. Kursinski, "High Stability Radio Links", NASA Conference Publication 3046: Relativistic Gravitational Experiments in Space, June 28–30, 1988, pp. 171–178

[15] P. F. Kuhnle, "NASA/JPL Deep Space Network Frequency and Timing", Proc. of 21st Annual Precise Time and Time Interval Planning Meeting (PTTI), Nov. 28–30, 1989, pp. 479–490

[16] A.L. Riley et al., "Cassini Ka-band Precision Doppler and Enhanced Telecommunications System Study", Jointly sponsored by NASA/JPL, Pasadena CA, USA and Agenzia Spaziale Italiana, Roma, Italia, Jan. 22, 1990, pp. 13–20

[17] R. N. Truehaft, "Tropospheric Limitations to the Stability of Radio Metric Delay Measurements", Proc. of 21st Annual Precise Time and Time Interval Planning Meeting (PTTI), Nov. 28–30, 1989, pp. 233–238

[18] R.F.C. Vessot and M.W. Levine, "A Time Correlated Four-Link Doppler Tracking System", A Close-up of the Sun, ed. M. Neugebauer and R.W.Davies, JPL Publication 78–70, pp. 457–497, Sept. 1978

[19] E.A. Marouf and G.L. Tyler, "Microwave Edge Diffraction by features in Saturn's Rings: Observations with Voyager 1", Science, Vol. 217, no. 4556, pp. 243–245, July 16, 1982

[20] G. L. Tyler et al., "The Microwave Opacity of Saturn's Rings at Wavelengths of 3.6 and 13 cm from Voyager 1 Radio Occultation", Icarus, Vol. 54, pp. 160–188, 1983

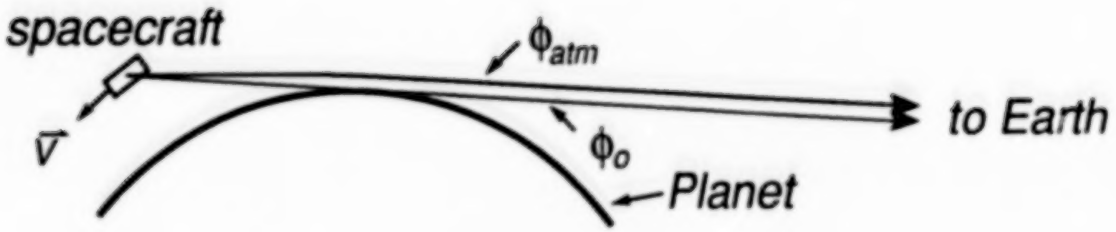


Figure 1: Atmosphere occultation geometry

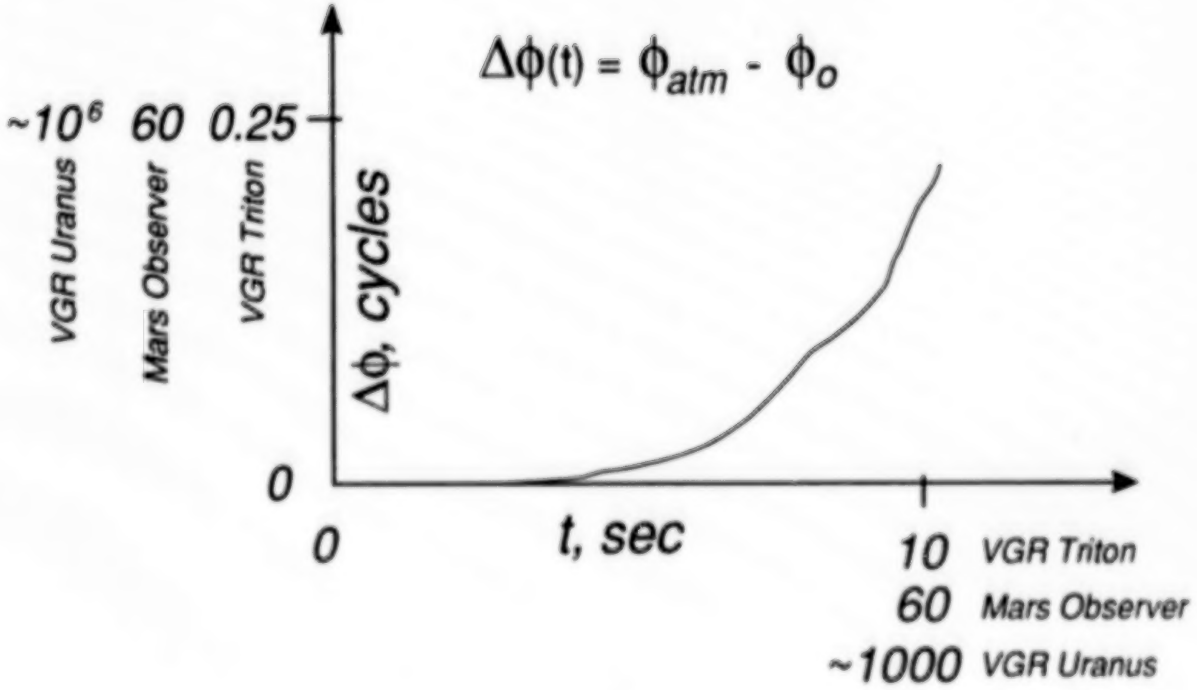


Figure 2: Atmosphere induced phase shift

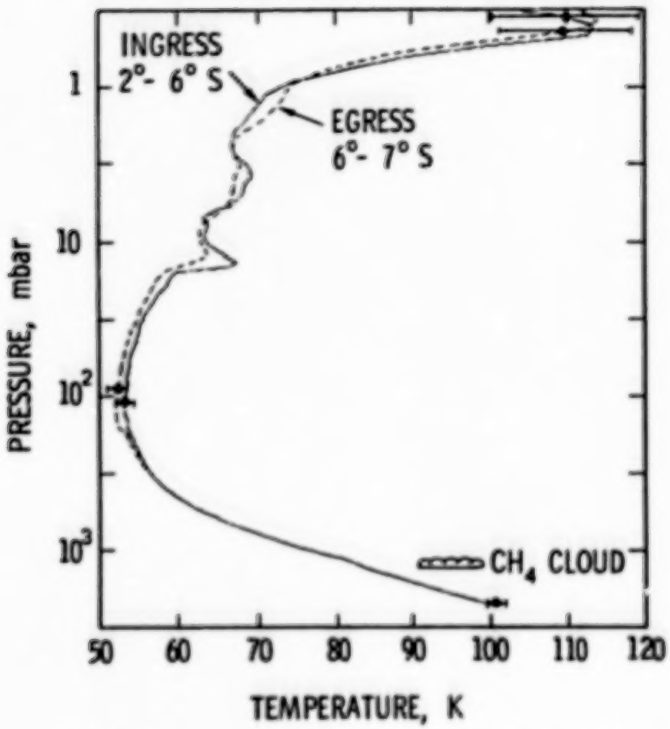


Figure 3: Vertical temperature vs pressure profile for Uranus recovered from radio occultation measurements (Figure from [4])

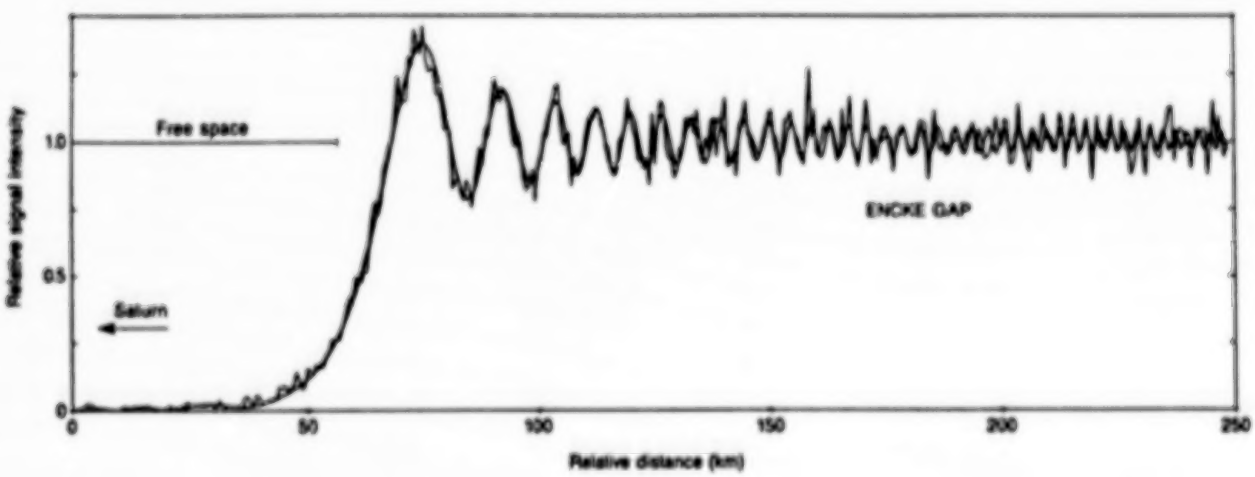


Figure 4: Diffraction effects in radio occultation data caused by the edge of Saturn's Encke gap. Smooth curve shows theoretical diffraction from abrupt edge fitted to irregular curve of measured signal intensity. (Figure from [19])

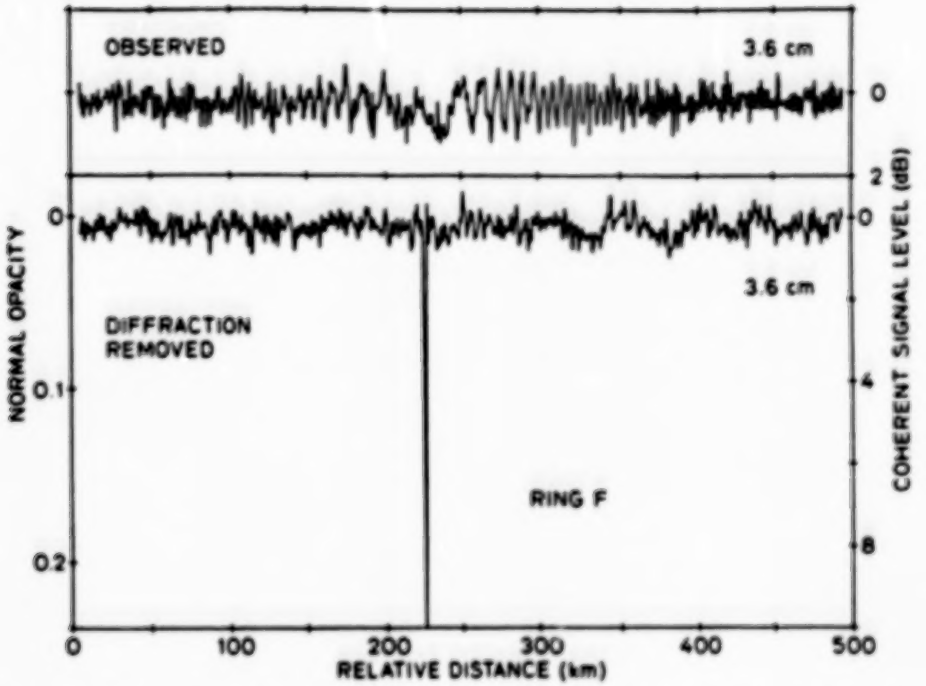


Figure 5: Effect of diffraction removal on observed opacity of Saturn's F-ring (Figure from [20])

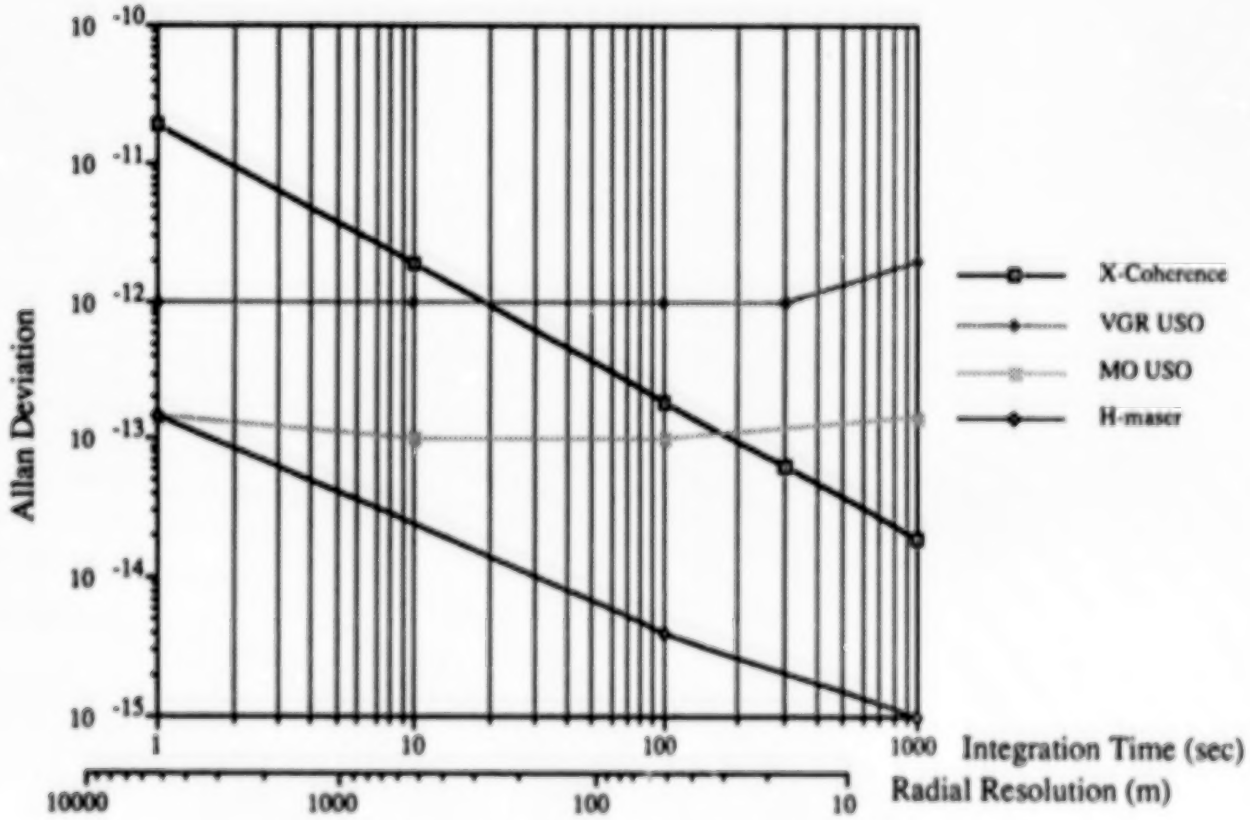


Figure 6: Limitation of Saturn F-Ring radial resolution at X-band due to oscillator stability

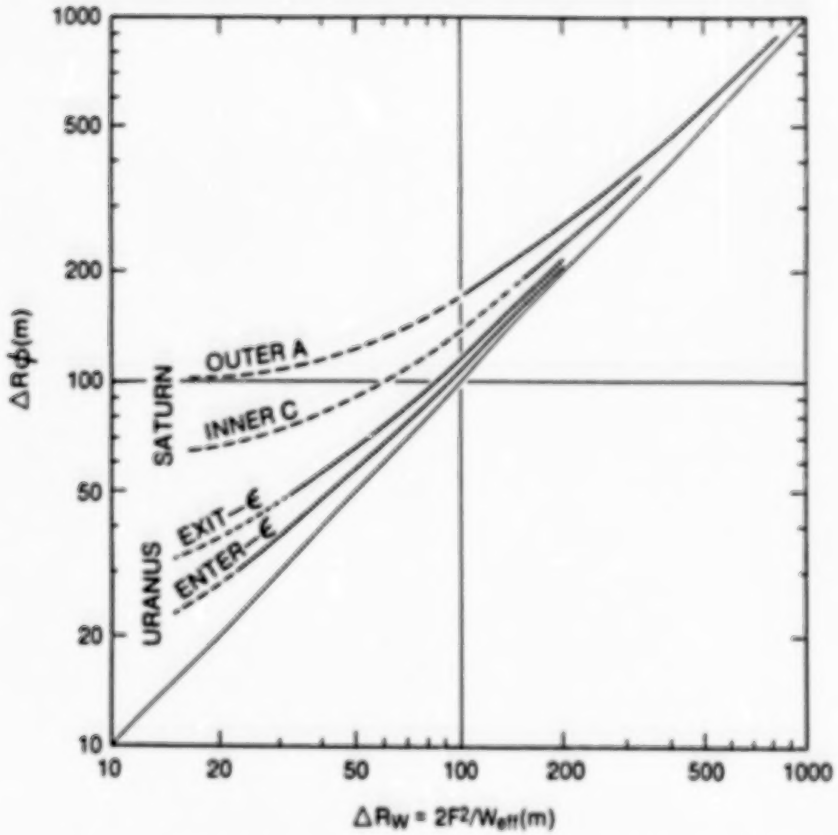


Figure 7: Comparison of the limitation of oscillator phase instability on the radial resolution of recovered ring opacity profiles for the cases of Voyager 1 at Saturn and Voyager 2 at Uranus assuming white frequency noise with $\sigma_y(1)=4x10\text{-}12$. At Saturn, the phase instability limiting resolution is about 200 m. At Uranus, this limit is about 30 and 45 m at occultation entry and exit of the epsilon ring. The difference is due to the different occultation geometries for the two planets. (Figure from [7])

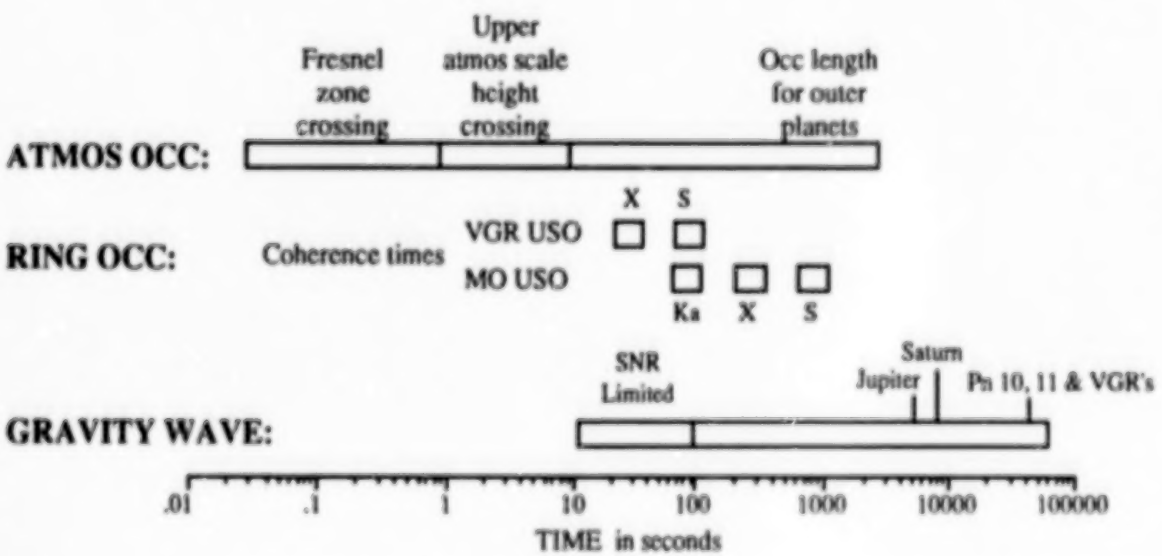


Figure 8: Time Scales of Interest

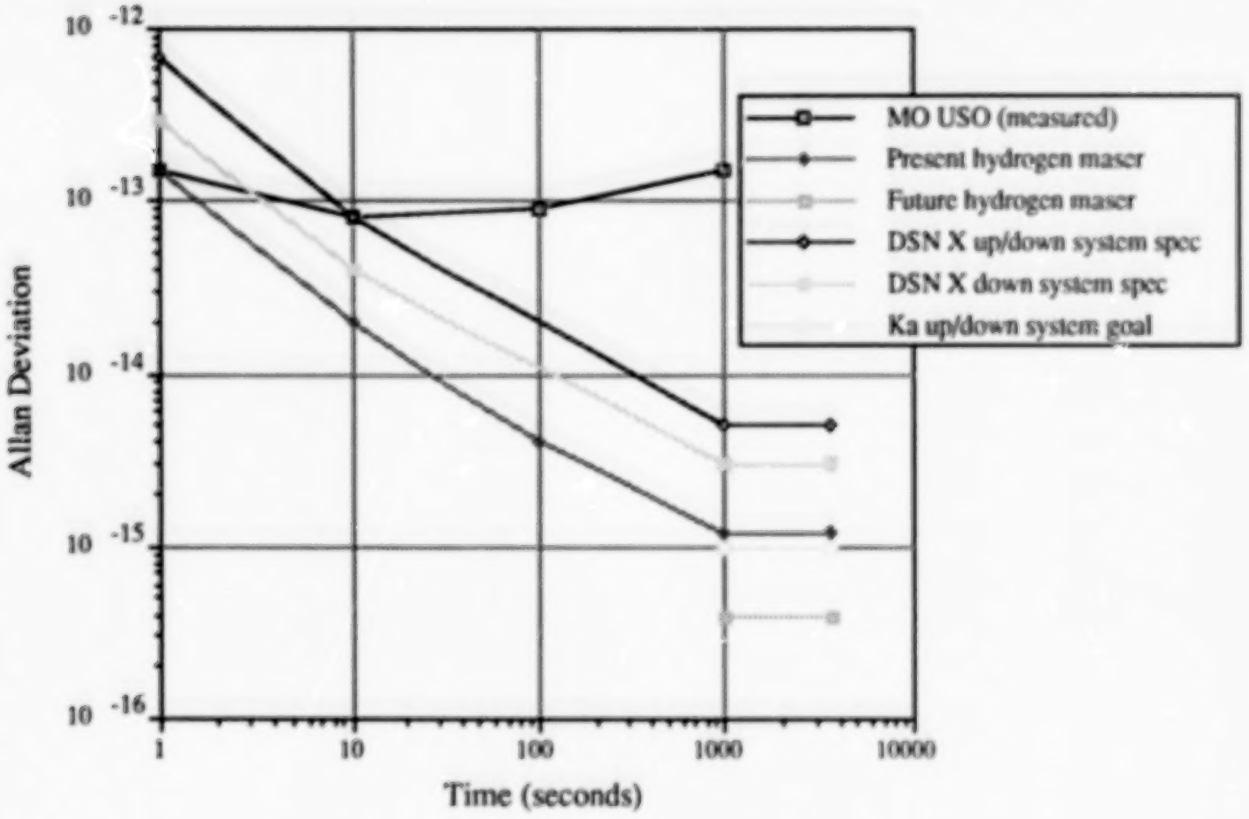


Figure 9: Present and Future Stability Performance

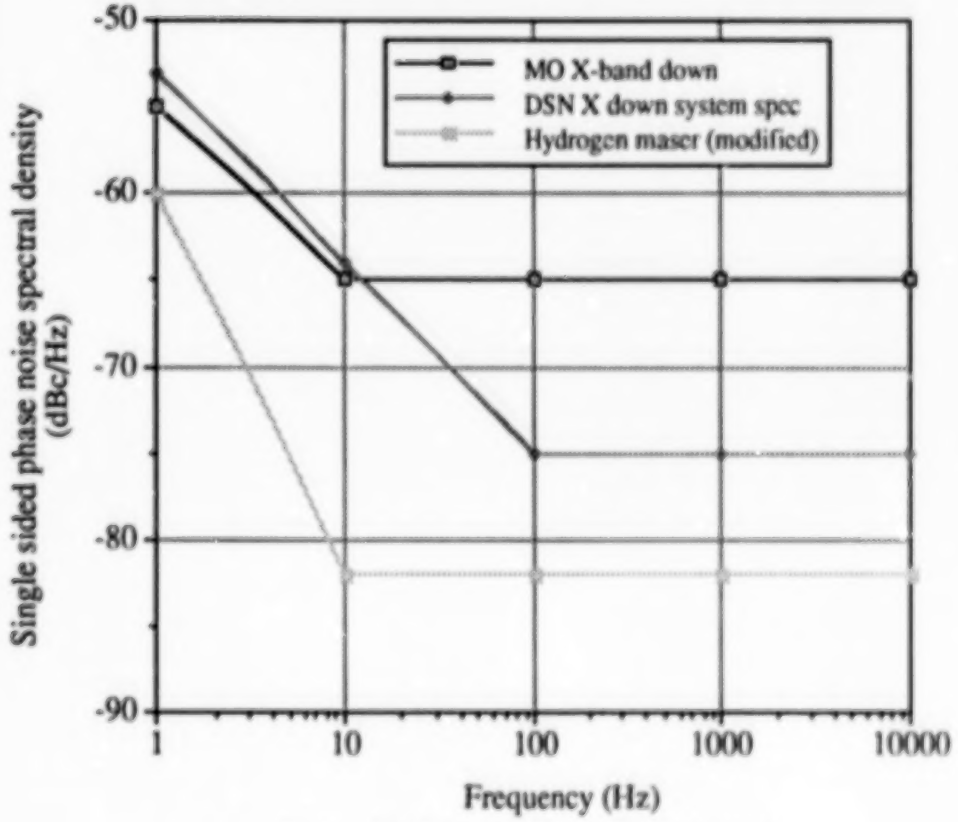


Figure 10: Spectral Purity Performance

ZERO–CROSSING DETECTOR WITH SUB–MICROSECOND JITTER AND CROSSTALK*

G. J. Dick; P. F. Kuhnle; R. L. Sydnor
California Institute of Technology
Jet Propulsion Laboratory
4800 Oak Grove Drive
Pasadena, California 91109

Abstract

A zero–crossing detector (ZCD) has been built and tested with a new circuit design which gives reduced time jitter compared to previous designs. With the new design, time jitter is reduced for the first time to a value (4.2×10^{-8} seconds for a 1 Hz input signal and a 1 second measuring time) which approaches that due to noise in the input amplifying stage. Additionally, with fiber–optic transmission of the output signal, crosstalk between units has been eliminated. Incorporation of commercially available double–balanced mixers allowed two $\approx$ 100 MHz signals differing by 1 Hz to be compared, giving an Allan Deviation of 1.17×10^{-15} at a 1 second measuring time. The measured values are in good agreement with circuit noise calculations and approximately ten times lower than that for ZCD's presently installed in the JPL test facility. Crosstalk between adjacent units was reduced even more than the jitter. Where the old units showed crosstalk of $> 10^{-4}$ seconds between units, no crosstalk could be detected between the new ZCD's, even when operating from the same power supply.

BACKGROUND

A limitation on the present capability to characterize frequency sources with ultra–high stability is the performance of the zero crossing detector (ZCD) which is used to measure the frequency difference between two such standards.[1, 3] The ZCD functions to transform a $\approx$ 1 Hz sine–wave beat frequency between the sources into a square wave or train of pulses that can be characterized by a conventional counter. While the capability of the presently available system was sufficient to characterize sources until now, new standards are now available with much higher stability at short measuring times. These new standards cannot be characterized using the present performance of the ZCD.

Present ZCD's show a time jitter of approximately 10^{-6} seconds. Noise in the mixers used to generate the beat frequency between the oscillators is much smaller ($< 10^{-7}$ seconds) than the ZCD jitter, while the stability of available counters is very high, with jitter of the order of 10^{-9} seconds.[4]

*This work was carried out at the Jet Propulsion Laboratory, California Institute of Technology, under a contract with the National Aeronautics and Space Administration.

The present ZCD's also suffer from severe crosstalk problems, so that the output signal from one unit can induce a time offset in an adjacent unit by as much as 10^{-4} seconds. If the time jitter and crosstalk in the ZCD's could be reduced below 10^{-7} seconds, thus matching the performance of available low noise mixers, the new standards such as the Superconducting Cavity Maser Oscillator (SCMO) could be characterized without limitation by fluctuations in the measuring system.

PRESENT TECHNOLOGY: NOISE

Figure 1 shows a schematic of the presently used units. A low noise amplification stage filters the 1 Hz input signal and increases its amplitude as much as possible without clipping. This large signal drives a special-purpose "open loop" operational amplifier stage which operates to transform the sine wave signal to a square wave with relatively short rise and fall times. Since this second stage operates without feedback limitation to its frequency response, and since the slew rate at its input is low, a latching circuit must be included to prevent noise-induced double triggering which would otherwise occur.

Amplitude noise in the first two stages introduces a time jitter into the signal which may be estimated as follows. Suppose the signal at the input to any stage has a slew rate of $\mathcal{S}$ (volts/second) and that the stage has an equivalent input noise of N (volts/$\sqrt{\text{Hz}}$) and a bandwidth of B (Hz). In this case an input amplitude jitter of $N\sqrt{B}$ (volts) will give rise to a time jitter of $N\sqrt{B}/\mathcal{S}$ (seconds). While the slew rate at the input to the first stage is low, the bandwidth of that stage is very low, thus allowing excellent overall performance, if that stage were the only limitation. However, the second stage must have a very wide bandwidth in order to give the short rise time required for proper operation of the counter. For example, second stage may require a bandwidth 10^5 times larger than the first stage, while the slew rate at its input has been increased only 15 times by the gain of the first stage. Thus it introduces $\sqrt{10^5}/15 \approx 20$ times as much time jitter as the first stage and prevents good performance in the ZCD.

PRESENT TECHNOLOGY: CROSSTALK

Crosstalk between units and phase offsets which are sensitive to details of circuit interconnections arise in the present units due to parasitic ground currents at the signal frequency. Figure 2 shows an overall schematic of the present ZCD system and identifies the parasitic ground-wire resistances. The very low frequency of the signal (1 Hz) means that skin-depth shielding effects, which usually tend to isolate AC signals, are absent. Output signals must be large enough so they can be transmitted substantial distances without degradation. This results in a substantial output current at a frequency identical to that of the input signal.

The present units are characterized by an output voltage of 2.5 V, a termination of 50 Ω, and an input slew rate of $\mathcal{S} \approx 1$ V/second. The resulting output current of $I = 2.5/50 = .05$ A can give rise to an input voltage offset of 50 μV for parasitic resistances of only .001 Ω. For an input slew rate $\mathcal{S} = 1$ V/second, a 50 μs time offset will result. However this offset depends on details of the configuration and so makes the whole system extremely sensitive to any kind of physical perturbation. Furthermore, if two or more units are operated in physical proximity to each other, and if the signals in these units have slightly different frequencies, the phase between the two will vary with time. This will induce a large, time-varying phase offset in adjacent units which can corrupt the measurements being made.

NEW DESIGN: NOISE

Operational amplifiers are available with an equivalent input voltage noise density of 4 nV/$\sqrt{\text{Hz}}$ for frequencies above 1 Hz.[5] For a first stage input slew rate of $\mathcal{S} = 1$ V/second or greater, and a bandwidth of $B_1 = 1$ Hz, this makes possible an RMS jitter of .004 μs for the contribution of that stage. If noise due to each subsequent stage can be kept at or below this value, a ZCD circuit could be constructed with jitter substantially less than 0.1 μs. Overall performance would then be limited by the performance of available mixers.

However, the rise time τ from the final stage of the ZCD must be very short, preferably $\tau < 0.1\mu$s and so must have a large bandwidth given approximately by $B > 1/(2\pi\tau)$. While, as previously discussed, a very large bandwidth in the second stage B_2 will result in increased jitter, this bandwidth may be made somewhat greater than that of the first stage before the second-stage contribution to the jitter matches that of the first stage. This is because the slew rate has been increased by gain of the first stage G_1, thus allowing a greater equivalent input voltage noise at the second stage without increasing the time jitter. If both stages have equivalent (white) input noise, the contribution of the second stage will be less than that of the first as long as

$$B_2 < B_1 G_1^2. \tag{1}$$

All stages after the first must have a built-in limiting action because otherwise their voltage swings would be larger than allowed by available power supplies. It is possible to construct limiting amplifier stages with reduced bandwidth which are well behaved in their operation if the gain of the stage is not too large. Since the slew rate $\mathcal{S}$ is increased in proportion to the gain G of the stage, the requirement for well-behaved operation is that the time for the output voltage to slew to its limit V_{max} must be allowed by the bandwidth B of the stage. This condition on the gain of the second stage can be written;

$$\frac{G_2 \mathcal{S}_2}{V_{max}} < 2\pi B_2 \tag{2}$$

where $\mathcal{S}_2$ is the slew rate at the input to the second stage. Since the slew rate is increased by the gain of any given stage, $\mathcal{S}_2 = G_1 \mathcal{S}_1$ and we can write the gain condition for the second stage as

$$G_2 < \frac{2\pi B_2 V_{max}}{\mathcal{S}_1 G_1}. \tag{3}$$

The conditions to reduce the noise contribution of the nth stage to a value below that of the first stage can similarly be written in terms of a product over the gains of previous stages;

$$B_n < B_1 \prod_{i=1}^{n-1} G_i^2 \tag{4}$$

and

$$G_n < \frac{2\pi B_n V_{max}}{\mathcal{S}_1 \prod_{i=1}^{n-1} G_i}. \tag{5}$$

Note that the gain G_n is calculated in terms of the bandwidth B_n actually chosen.

Figure 3 shows a block diagram of a four stage ZCD with gains and bandwidths calculated subject to equations (5) and (6). In order to reduce overall noise to a value comparable to that due to the first stage alone we have found it necessary to add two intervening stages in between the first stage and the "wide open" stage compared to the old design shown in Figure 1. This new design allows an overall jitter of less than 0.1 μs.

NEW DESIGN: CROSSTALK

In order to eliminate the effect of output ground loop currents on the input signal, we have modified the design to eliminate both input and output ground loop currents. As shown in Fig. 4, the high current output driver has been replaced by a fiber–optic transmitter. While the transmitter requires substantial drive current (.030 A) these currents are completely contained within the chassis and power supply of the ZCD itself, and do not necessarily flow throughout the room as was previously the case. The fiber optic signals themselves cause no interference at all, and are themselves not subject to degradation by other electrical interference signals. The fiber optic receiver is connected directly to the counter input.

Ground loops at the input to the ZCD have also been eliminated. Even though the RF signals into the mixer are necessarily grounded at the outer coaxial connection, the dual–transformer design of the mixer allows a floating output (1 Hz) signal.[6] As shown in Fig. 4, all external ground loops are thus eliminated, leaving only those (not shown) which are due to power supply connections or internal to the ZCD circuitry itself. In this design the mixer is physically mounted within the ZCD module.

TEST RESULTS–NOISE

Two zero–crossing detectors have been built and tested which is based on the design shown in Figure 3. Preliminary tests using a common 1 Hz input signal with an amplitude of 400 mV P-P showed an Allan Deviation of frequency variations

$$\sigma_\nu(\tau) = 4.2 \times 10^{-8}\text{Hz} \tag{6}$$

for the two units together at a measuring time of $\tau = 1$ second. Double balanced mixers[6] were then added to the circuitry to allow comparison of two RF signals at 100 MHz. Test results shown in Fig. 5 show that the short term performance approaches a measurement floor for the Allan Deviation of relative frequency variation $\delta y = \delta\nu/\nu_o$ given by

$$\sigma_y(\tau) = \frac{1.17 \times 10^{-15}}{\tau} \tag{7}$$

for two units together. This value is approximately ten times lower than that for ZCD's presently installed in the JPL test facility. Because "bare" ZCD noise at $\nu_o = 100$ MHz would only be

$$\sigma_y(\tau) = 4.2 \times 10^{-8}/10^8 = 4.2 \times 10^{-16} \tag{8}$$

at $\tau = 1$ second, most of this noise is apparently due to the mixers. The increase above the limiting value at longer times ($\tau > 10$ seconds) is probably due to temperature fluctuations. The units were not thermally isolated but were subject to a typical laboratory thermal environment.

At the time of the tests there were not available RF signals at 100 MHz signals with a stability greater than $1 \times 10^{-14}/\tau$, and so to measure the contribution of the ZCD's themselves, the two units were independently attached to the same source, and the time jitter between their output pulses was measured. In this way noise on the input signals was largely cancelled while noise due to the individual mixers and ZCD's was not.

DETAILED NOISE ANALYSIS

We consider three types of noise as contributing substantially to the overall performance of the ZCD: Flicker voltage noise in the first stage of the ZCD, white noise from all stages, and flicker phase noise in the RF mixer. Throughout this section we assume a slew rate of $\mathcal{S} = 1$ V/second, recognizing that the actual value may be up to $\mathcal{S} = 3$ V/second, giving somewhat lower time jitter for the same voltage fluctuation.

Following the conventions of IEEE Standard PAR–P–1139, we define the parameters;

$$D = \frac{1.038 + 3\ln(2\pi f_h \tau)}{4\pi^2} \tag{9}$$

and

$$E = \frac{3 f_h}{4\pi^2} \tag{10}$$

where f_h is the upper cutoff frequency and τ is the measuring time; so that the Allan Variance of frequency fluctuations $\delta\nu$ may be written:

$$\sigma_\nu^2(\tau) = D[f S_\phi(f)]\tau^{-2} \tag{11}$$

for flicker phase noise, and

$$\sigma_\nu^2(\tau) = E[S_\phi(f)]\tau^{-2} \tag{12}$$

for white phase noise, where f is the fluctuation frequency, ν_o is the RF frequency, and $S_\phi(f)$ is the spectral density of phase fluctuations. We also use an Allan Deviation defined by

$$\sigma_\nu(\tau) = \sqrt{\sigma_\nu^2(\tau)}. \tag{13}$$

Using a 1 Hz cutoff frequency and $\tau = 1$ second measuring time, we approximate the constants by $D = .166$ and $E = .0756$.

Because of their nonlinear nature, it is not clear how to treat the flicker noise for ZCD stages after the first (linear) stage. However, the effect of low frequency noise in these subsequent stages is apparently reduced by the gain of the first stage, and so we will ignore their contribution. The manufacturer indicates a flicker voltage noise for our configuration of 6 nV/$\sqrt{f}$ (/$\sqrt{\text{Hz}}$) RMS. For a slew rate of $\mathcal{S} = 1$ V/second, this results in an RMS time jitter of 6×10^{-9} seconds in a 1Hz bandwidth at an offset of $f = 1$ Hz, a phase jitter for the 1Hz signal larger by 2π, and a spectral density of phase fluctuations given by

$$S_\phi(f) = \left[2\pi \times 6 \times 10^{-9}\text{V}/\mathcal{S}\right]^2 / f. \tag{14}$$

The measurements reported earlier measured the combined deviation for two nominally identical ZCD's. For the operational frequency $\nu_o = 1$ Hz of these tests of two "bare" ZCD's, Eqs. 11 and 13 combine with twice the value given by Eq. 14 to predict a Deviation at $\tau = 1$ second of

$$\sigma_\nu(1) = 2.17 \times 10^{-8}\text{Hz}. \tag{15}$$

The contribution due to white amplifier noise is approximately the same size. The design procedure for the ZCD given an earlier section allows similar white noise contributions for each succeeding stage, for an effective value 4 times larger than that for a single stage. Thus the manufacturer's specification of 4 nV/$\sqrt{\text{Hz}}$ RMS for each device gives rise to an effective spectral density of

$$S_\phi(f) = 4 \times \left[2\pi \times 4 \times 10^{-9}\text{V}/\mathcal{S}\right]^2. \tag{16}$$

Combining this result with Eqs. 12 and 13 gives a contribution to the two-device test of

$$\sigma_\nu(1) = 1.96 \times 10^{-8}\text{Hz} \tag{17}$$

for the white noise of the ZCD.

The combined results of flicker and white amplifier noise compare very favorably to the measured value for tests of the bare ZCD which gave a value previously discussed of $\sigma_\nu(\tau) = 4.2 \times 10^{-8}$ Hz at $\tau = 1$ second measuring time.

The contribution due to the double-balanced mixer to RF tests can be similarly evaluated on the basis of Eqs. 11 and 13. Addition of the mixers caused the frequency deviation to more than double, increasing from 4.2×10^{-8} Hz to 1.17×10^{-7} Hz at $\tau = 1$ second averaging time. This increase implies a flicker phase noise (per mixer) of -135 dB/f ($/\sqrt{\text{Hz}}$). This value compares favorably to -140 dB/f ($/\sqrt{\text{Hz}}$), the lowest measurement system noise reported to date.[7]

TEST RESULTS–CROSSTALK

Figures 6 and 7 show the results of identical crosstalk measurements on the old and new ZCD's, respectively. Here, in each test a (buffered) 100 MHz signal from a hydrogen maser provided a reference for each of two ZCD's, while the test signals for each unit differed by approximately 0.01 Hz. The beat frequencies characterized were 1 Hz and $\approx$ 1.01 Hz. We show results for the channel in each case with a beat frequency of exactly 1 Hz, as generated by an offset generator from the original 100 MHz signal. The two units in each case had a common ground and were powered by a single power supply.

A comparison of the figures shows that, under these conditions, the old units show a sinusoidal variation of the time residuals for the 100 MHz signal of more than 10^{-12} seconds and a false peak in the Allan Deviation of nearly 3×10^{-14} at a measuring time of $\tau \approx 30$ seconds. The sinusoidal variation in the time residuals indicates a crosstalk between ZCD's of 10^{-12} seconds increased by the frequency ratio 10^8 Hz/1 Hz, or 10^{-4} seconds. The new units, as shown in Fig. 7, show no observable crosstalk, but instead allow the performance of the offset generator to be properly characterized.

DISCUSSION

Characterization of the instabilities in frequency sources requires a means of analyzing the frequency variations of the source under test while using another oscillator as a reference. For sources with ultra-high stability, this is typically done by offsetting the RF output frequency of one of the sources by a very small difference frequency ν_d, (typically $\nu_d = 1$ Hz) and then combining the output signals from the two sources in a semiconducting "double balanced" mixer to give an output at the difference frequency (1 Hz).

In this circumstance any frequency variation $\delta\nu_o$ in the source under test gives rise to an identical variation in the difference frequency,

$$\delta\nu_d = \delta\nu_o \tag{18}$$

and a correspondingly larger variation in relative frequency variation;

$$\frac{\delta\nu_d}{\nu_d} = \frac{\nu_o}{\nu_d}\frac{\delta\nu_o}{\nu_o} \tag{19}$$

if the RF output frequency ν_o is much larger than the difference frequency ν_d.

For example, for a 100 MHz output frequency and 1 Hz difference, the fractional uncertainty is increased by ν_o/ν_d = 100MHz/1Hz= 10^8 times. Thus, if the standards have a stability of $\delta f/f = 10^{-13}$, the 1Hz beat frequency will show a much larger variation of $\delta f/f = 10^{-5}$.

Measurement of the difference frequency ν_d is obtained by measurement of its period. If the time jitter of the ZCD is δt_z, and the time of measurement is τ, an uncertainty in the difference frequency ν_d is introduced

$$\frac{\delta\nu_d}{\nu_d} = \frac{\delta t_z}{\tau} \tag{20}$$

which in turn results in an uncertainty in the measured frequency of the standard ν_o given by

$$\frac{\delta\nu_o}{\nu_o} = \frac{\nu_d}{\nu_o}\frac{\delta\nu_d}{\nu_d} = \frac{\nu_d}{\nu_o}\frac{\delta t_z}{\tau}. \tag{21}$$

Equation (21) shows that a limit is placed on our measurement capability by ZCD jitter which decreases linearly with increasing measuring time τ. This limit also depends on the operating frequency ν_o of the frequency sources which are being characterized, and the beat frequency ν_b used to drive the ZCD. The highest available operating frequency for available frequency sources is typically 100 MHz. Increased operating frequencies may be available in the future, but for the present, the cost of transmitting and conditioning higher frequencies would be substantially greater than for 100 MHz signals. The difference frequency ν_d is operated at 1 Hz to allow measurements to be made at least every second. It is important to be able to characterize standards at short measuring times, and a lower limit $1/\nu_d$ to the time of characterization is determined by the difference frequency ν_d.

Thus there are important reasons why the operating frequency is not higher than 100 MHz and the difference frequency is at least as high as 1 Hz. Taking these values as given and using Eq. (21), the 1μs jitter of present ZCD's limits our measuring capability to

$$\frac{\delta\nu_o}{\nu_o} = \frac{10^{-14}}{\tau}. \tag{22}$$

Until recently, hydrogen maser standards presented the best possible stability for all time periods from 1 second to approximately 10,000 seconds.[8] The short term stability of hydrogen masers is approximately given by $\delta f/f = 10^{-13}/\tau$. Because these values are 10 times larger than that given by Eq. (22), the hydrogen maser standards can be well characterized using the old ZCD's.

However, newly developed superconducting standards are 10 times more stable than the hydrogen masers at short measuring times.[9] These standards show a stability of less than 1×10^{-14} at 1 second and so could not be well characterized at an operational frequency of 100 MHz. However, results reported here represent a ten-fold improvement over that given in Eq. (22), allowing such characterization of the new standards for the first time.

ACKNOWLEDGEMENTS

The authors would like to thank P. DeLaere for engineering contributions, and R. T. Wang for assisting in the measurements.

REFERENCES

[1] Calculation of the statistics of zero crossings for a sine wave with added noise can be found in *Probability, Random Variables, and Stochastic Processes*, Athanasious Papoulis, McGraw-Hill, New York (1965); also see discussion on "sine-wave-comparator amplifiers" by R. Kelner, J. W. Gray, E. F. MacNichol, Jr. in *MIT Radiation Laboratory Series* **19** "Waveforms," pp. 345-355, Boston Technical Lithographers, Boston (1964).

[2] "Low Noise Buffer Amplifiers and Buffered Phase Comparators for Precise Time and Frequency Measurement and Distribution," R. A. Eichinger, P. Dachel, W. H. Miller, and J. S. Ingold, *Proceedings, 13th Annual Precise Time and Time Interval (PTTI) Applications and Planning Meeting*, 263-279 (1981).

[3] "High stability buffered phase comparator," W. A. Adams, and V. S. Reinhardt, U. S. Patent 4,425,543 (1984).

[4] "A Method for Using a Time Interval Counter to Measure Frequency Stability," C. A. Greenhall, *IEEE Trans. Ultrasonics, Ferroelectrics, and Frequency Control* **36** 478-480 (1989).

[5] Linear Technology LT1028 Ultra-Low Noise Precision High Speed Operational Amplifier.

[6] Hewlett Packard Double-Balanced Mixer Model 10514/C. 1/f noise performance is specified as being "typically less than 100 nV/$\sqrt{Hz}$ at 10 Hz." The 1/f character of this noise would result in noise amplitude of approximately 316 nV/$\sqrt{Hz}$ at 1 Hz. Our measurements indicate actual noise levels are approximately 3 times lower than this value.

[7] "Extending the Range and Accuracy of Phase Noise Measurements," F. L. Walls, A. J. D. Clements, C. M. Felton, M. A. Lombardi, and M. D. Vanek, *Proceedings, 42nd Annual Symposium on Frequency Control*, 432-441 (1988),

[8] See, for example, "Operating and Environmental Characteristics of Sigma Tau Hydrogen Masers used in the Very Long Baseline Array (VLBA)," T. K. Tucker, *Proceedings, 20th Annual Precise Time and Time Interval (PTTI) Applications and Planning Meeting*, 325-336 (1989).

[9] "Improved Performance of the Superconducting Cavity Maser at Short Measuring Times" R. T. Wang and G. J. Dick, *Proceedings, 44th Annual Symposium on Frequency Control*, 89-93 (1990).

Figure Captions

Figure 1 Block diagram of existing JPL zero-crossing detector design which has been in use for many years. Stage one must be a purely amplifying and filtering stage (no limiting) in order to provide a well-defined noise bandwidth for the measurements taken. The JPL units use a μa709-type operational amplifier for the second stage to allow a high switching speed with low noise.

Figure 2 Block diagram of the measurement system including parasitic resistances in the various signal and power paths. Since the output current is substantial, and with a frequency identical to that of the input, output-input coupling corrupts the phase of the input signal. Crosstalk between units similarly results in phase shifts at adjacent units which is dependent on the phase difference between the signals at the two units. Because the frequency is so low (1 Hz), penetration depths are large and parasitic resistances alone can be used to estimate this coupling.

Figure 3 Block diagram of the new ZCD design. Multiple limiting stages with increasing slew rates and bandwidths allow an overall time jitter which is not appreciably larger than that due to noise contributions of the first stage alone. Since input signals with varying amplitudes must be accommodated, circuit bandwidths in stages 2 and 3 have been chosen to allow slew rates up to three times higher than the values given.

Figure 4 Block diagram of the RF frequency measurement system including the new ZCD. Ground loops involving both input and output signals are eliminated. Signal input uses symmetric outputs from a double-balanced mixer. Signal output is by means of fiber optic coupling, which eliminates the large ground loop currents associated with high-level signal output.

Figure 5 Results of a test of two of the new ZCD's. Measured stability is expressed in terms of an inferred Allan Deviation of relative frequency variation for the 100 MHz signal sources being compared. The values, on a per unit basis, would be smaller by $1/\sqrt{2}$ than those shown. Short term performance of $10^{-15}/\tau$ corresponds to a time jitter of 10^{-7} seconds, a value 10 times lower than that for ZCD's previously available. Longer term instabilities are somewhat higher, probably due to thermal fluctuations. The units were not thermally isolated, but subject to ordinary laboratory thermal environment. Because RF signals were not available with noise as low as these circuits, identical RF signals were fed to the mixers for each ZCD, and the differential jitter was measured. In this way, the noise of the source is largely cancelled, while noise in the mixers and ZCD's themselves does not.

Figure 6 Measurement of crosstalk between two of the older ZCD's. Here the RF ($\approx$ 100 MHz) signals to the unit being characterized differed by exactly 1 Hz while the signals to an adjacent unit differed by $\approx$ 1.01 Hz. The effect of the resultant 100 second beat between the signals is very apparent here, showing a sinusoidal time residual variation of more than 10^{-12} seconds. The rise in Allan Deviation for time periods approaching 100 seconds is due to this time variation and is more than 30 times larger than the actual deviation between the signals.

Figure 7 Crosstalk test of the new ZCD's using exactly the same setup as described in the previous figure. There is no evidence of crosstalk with a $\approx$ 100 second period. The offset generator which was used to generate the 100 MHz + 1 Hz RF signal is the limiting factor in this test ($\approx 1 \times 10^{-14}$ at $\tau = 1$ second).

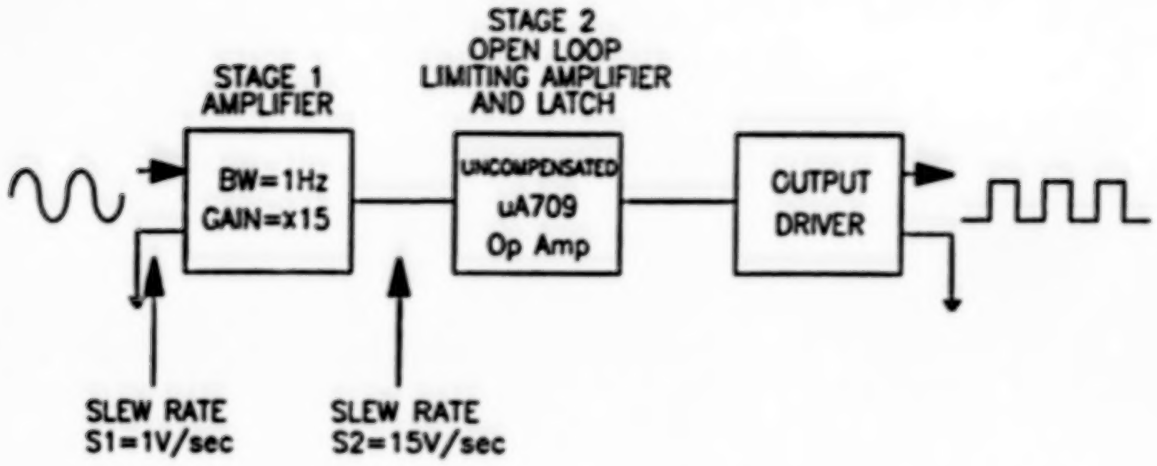


Figure 1. Block diagram of existing JPL zero-crossing detector design which has been in use for many years. Stage one must be a purely amplifying and filtering stage (no limiting) in order to provide a well-defined noise bandwidth for the measurements taken. The JPL units use a μa709-type operational amplifier for the second stage to allow a high switching speed with low noise.

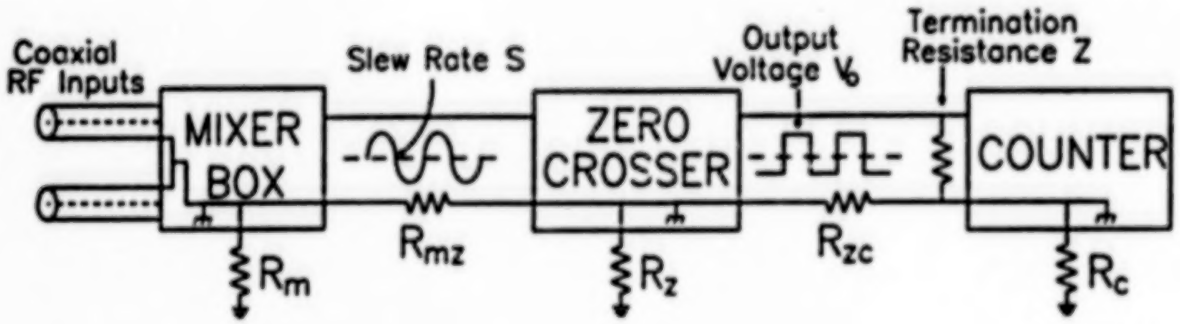


Figure 2. Block diagram of the measurement system including parasitic resistances in the various signal and power paths. Since the output current is substantial, and with a frequency identical to that of the input, output-input coupling corrupts the phase of the input signal. Crosstalk between units similarly results in phase shifts at adjacent units which is dependent on the phase difference between the signals at the two units. Because the frequency is so low (1 Hz), penetration depths are large and parasitic resistances alone can be used to estimate this coupling.

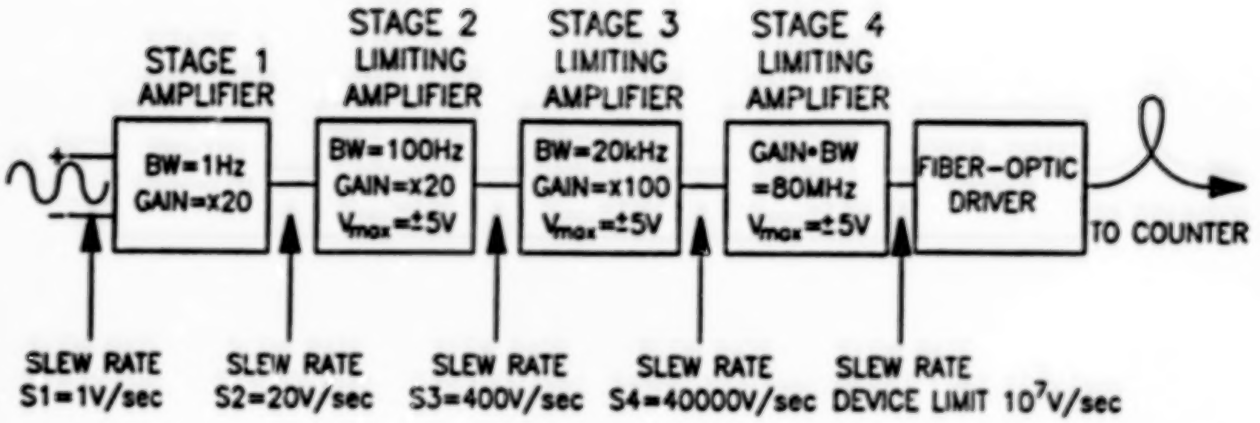


Figure 3. Block diagram of the new ZCD design. Multiple limiting stages with increasing slew rates and bandwidths allow an overall time jitter which is not appreciably larger than that due to noise contributions of the first stage alone. Since input signals with varying amplitudes must be accommodated, circuit bandwidths in stages 2 and 3 have been chosen to allow slew rates up to three times higher than the values given.

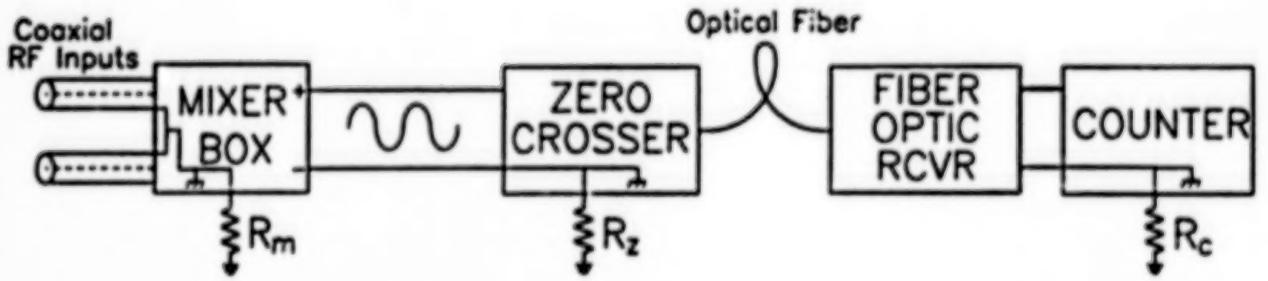


Figure 4. Block diagram of the RF frequency measurement system including the new ZCD. Ground loops involving both input and output signals are eliminated. Signal input uses symmetric outputs from a double-balanced mixer. Signal output is by means of fiber optic coupling, which eliminates the large ground loop currents associated with high-level signal output.

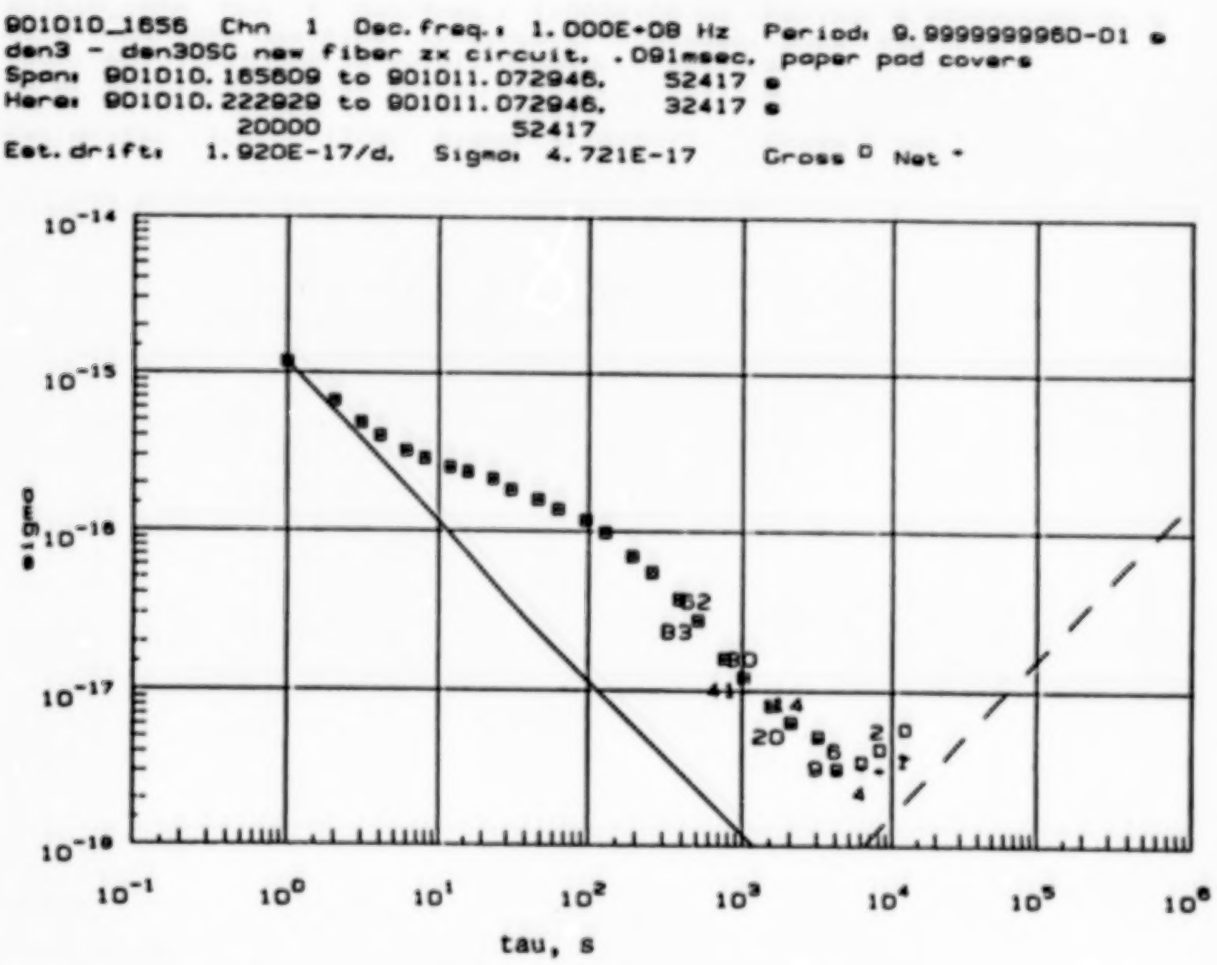
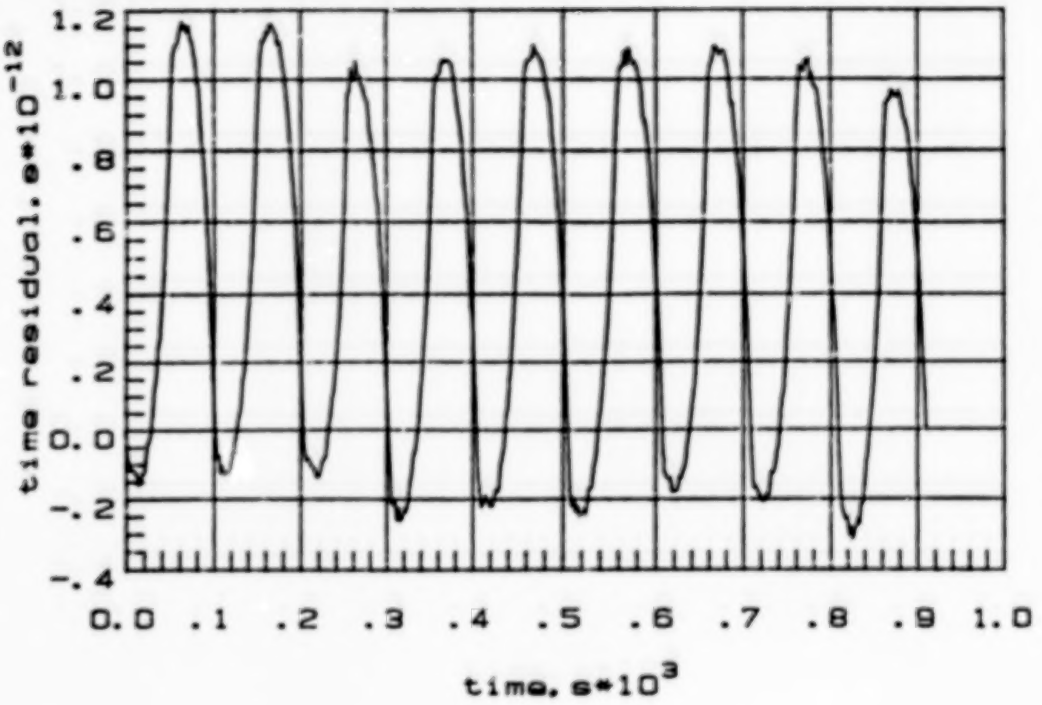


Figure 5. Results of a test of two of the new ZCD's. Measured stability is expressed in terms of an inferred Allan Deviation of fractional frequency variation for the 100 MHz signal sources being compared. The values, on a per unit basis, would be smaller by $1/\sqrt{2}$ than those shown. Short term performance of $10^{-15}/\tau$ corresponds to a time jitter of 10^{-7} seconds, a value 10 times lower than that for ZCD's previously available. Longer term instabilities are somewhat higher, probably due to thermal fluctuations. The units were not thermally isolated, but subject to ordinary laboratory thermal environment. Because RF signals were not available with noise as low as these circuits, identical RF signals were fed to the mixers for each ZCD, and the differential jitter was measured. In this way, the noise of the source is largely cancelled, while noise in the mixers and ZCD's themselves does not.



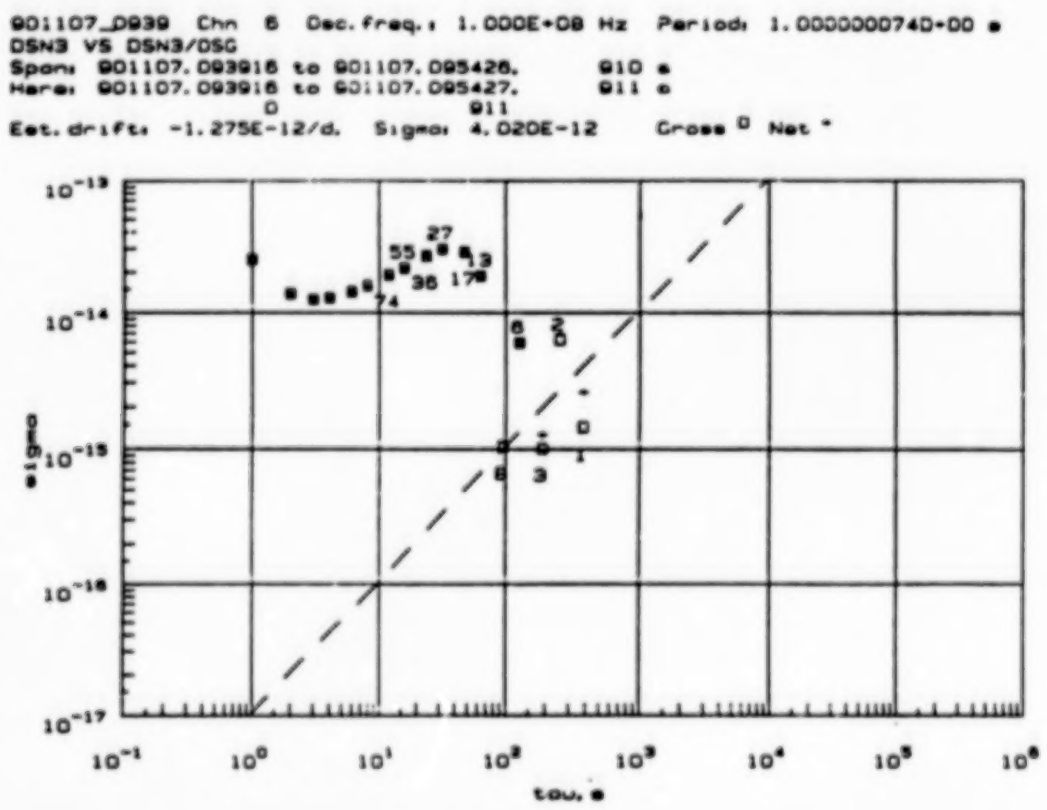
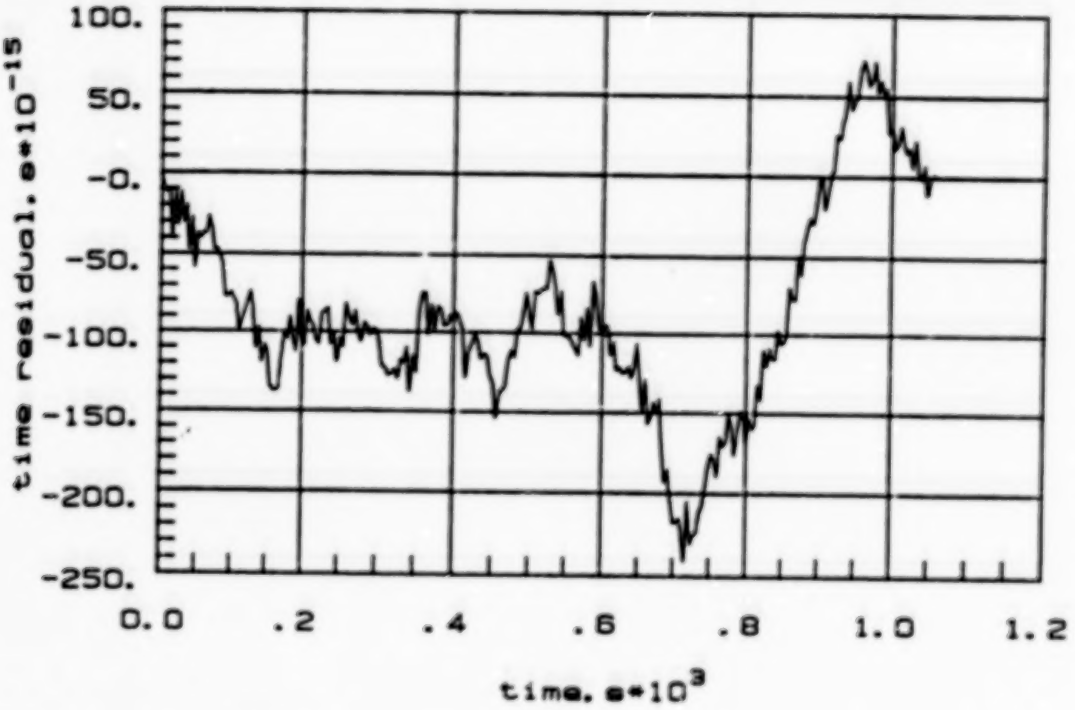


Figure 6. Measurement of crosstalk between two of the older ZCD's. Here the RF (≈ 100 MHz) signals to the unit being characterized differed by exactly 1 Hz while the signals to an adjacent unit differed by ≈ 1.01 Hz. The effect of the resultant 100 second beat between the signals is very apparent here, showing a sinusoidal time residual variation of more than 10^{-12} seconds. The rise in Allan Deviation for time periods approaching 100 seconds is due to this time variation and is more than 30 times larger than the actual deviation between the signals.



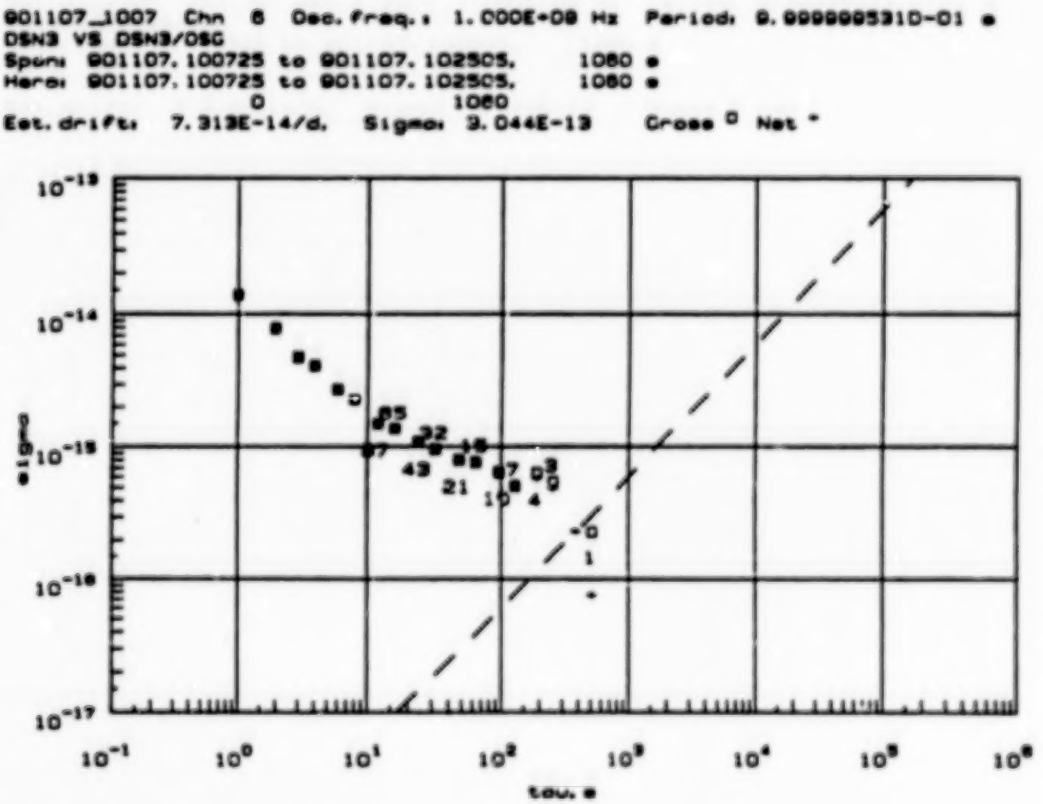


Figure 7. Crosstalk test of the new ZCD's using exactly the same setup as described in the previous figure. There is no evidence of crosstalk with a ≈ 100 second period. The offset generator, which was used to generate the 100 MHz + 1 Hz RF signal, is the limiting factor in this test ($\sigma(\tau) \approx 1 \times 10^{-14}/\tau$).

HYDROGEN MASERS WITH CAVITY FREQUENCY SWITCHING SERVOS

H. E. Peters, H. B. Owings and P. A. Koppang
Sigma Tau Standards Corporation
1711 Holt Road
P. O. Box 1877
Tuscaloosa, AL 35403

Abstract

The stability of the free-running hydrogen maser is limited by pulling of the unperturbed hydrogen transition frequency due to instability of the cavity resonance frequency. Two automatic approaches to cavity stabilization have been used successfully in field operable atomic hydrogen masers in the past. One method is based upon the "spin-exchange" tuning procedure and was used in masers constructed at NASA's Goddard Space Flight Center.[1, 2] The other method is the cavity frequency switching servo used on Sigma Tau Standards Corporation (STSC) hydrogen masers.[3, 4, 5]

While automatic spin-exchange tuning is in principle the more basic and accurate method, the required beam intensity switching and the long servo time constant result in reduced stability for measuring intervals up to 10^6 seconds. More importantly, the spin-exchange tuning method requires a second stable frequency source as a reference, ideally a second hydrogen maser, to get the best results.

The cavity frequency switching servo, on the other hand, has very little effect on the maser short term stability, and is fast enough to correct for cavity drift while maintaining the cavity at the spin-exchange tuned offset required to minimize instability due to beam intensity fluctuations. Not only does the cavity frequency switching servo not require a second stable frequency source, but the frequency reference is the atomic hydrogen radiated beam signal, so that no extra RF connections need be made to the cavity, and externally generated signals that would perturb the hydrogen atom need not be transmitted through the cavity.

In this paper we will discuss the operation of the cavity frequency switching stabilization method and will illustrate the transient response of the servo and certain other aspects of the technique that have potential for achieving improved basic accuracy. We also will give stability results obtained between masers at STSC and long term stability data obtained with STSC hydrogen masers at the United States Naval Observatory.

INTRODUCTION

The stability of the hydrogen maser for measuring intervals beyond 1000 seconds is primarily limited by cavity pulling. For very long term stability and for long term intrinsic reproducibility and accuracy, variation in the wall shift is also of serious concern. (Accuracy as defined by first, a realistic error budget and second, substantiation of the accuracy factors by reproducible measurements between standards.)

Cavity pulling can be reduced to a minimum by carefully spin- exchange tuning the cavity[6] and then stabilizing the cavity at the spin-exchange tuned frequency by use of the cavity frequency switching

servo. Results given in this paper illustrate the performance obtained at present using this technique. Further development of the cavity frequency switching technique at STSC indicates substantial improvements in stability can still be made, and further that use of this cavity stabilization method will provide the means to achieve improved accuracy.

The determination of the wall shift requires the operation of hydrogen masers with different size storage bulbs that are coated with chemically identical materials and processed with carefully controlled procedures. The accuracy previously achieved has been in the 1 or 2 parts in 10^{12} region.[6] We believe this may be reduced by an order of magnitude or more by use of improved techniques, particularly the use of the cavity frequency switching servo, as well as improved wall coating materials and computer instrumentation techniques.

THE CAVITY FREQUENCY SWITCHING SERVO

The operation of the cavity automatic frequency tuning system (the "cavity servo") is based upon switching the cavity resonance frequency between two frequencies approximately equally spaced about the maser oscillation frequency. The two frequencies are about one half the cavity resonance width apart and are switched at a rate that is slow compared to the cavity field decay time constant but fast in comparison with the atomic relaxation rate.

The modulation (switching) rate and the relative duration of the high and low frequencies are controlled by a digital circuit called the Modulation Period Generator (MPG). The voltage on a varactor diode coupled to the cavity is switched between two precisely controlled voltages by the MPG, thereby changing the cavity frequency.

When the maser frequency is located at the crossover point of the two cavity resonances, there is no amplitude modulation on the maser signal coupled from the cavity; but when the signal is not at this point, there is an amplitude modulation, and this is detected on the receiver IF signal. The modulation envelope is processed in a phase sensitive "Synchronous Detector" circuit that sends up or down correction commands to a "Cavity Register." The cavity register integrates the up or down signals and produces a voltage which corrects the cavity average frequency. Two ways of controlling the cavity average frequency have been used successfully.

In early STSC masers the register voltage changed the temperature of the cavity by applying a bias to the temperature control circuit. Since the STSC masers have metal cavities with quite linear frequency variation with temperature, this method results in a well controlled servo, but the response is relatively slow due to the large thermal mass of the cavity assembly.

In the most recently constructed STSC masers the cavity frequency is controlled by applying the register voltage to a second varactor diode coupled to the cavity. The servo time constant is then not limited by the cavity thermal response. The varactor control method has the capability of compensating very quickly for systematic cavity disturbances, while the temperature variation method has the advantage of maintaining the cavity assembly, coupling components and storage bulb at a constant temperature.

For future experimental work the masers can be changed rather quickly between either the temperature control or the varactor control method. This can prove very valuable in measurements to establish temperature coefficients of systematic variables, oscillation parameters, or fundamental temperature dependencies such as the second order Doppler shift or wall shift.

SPIN-EXCHANGE TUNING USING THE CAVITY FREQUENCY SWITCHING SERVO

One of the unique features of the cavity frequency switching servo is the method used to establish and maintain the maser cavity at the spin-exchange tuned frequency. Cavity pulling and atom-atom spin exchange pulling of the maser output frequency both depend in a nearly linear, monotonic fashion upon the density of atoms within the storage bulb. There is a unique cavity offset from the unperturbed transition frequency where the maser frequency is independent of beam intensity. This is the basic concept in all spin-exchange tuning methods.

In the usual method of spin-exchange tuning, the output frequency of the maser to be tuned is compared with another stable reference source, optimally another hydrogen maser. Curves of output frequency versus cavity frequency are plotted at different beam intensities (source pressure settings) and the point at which the curves cross establishes the proper cavity setting.

With the cavity frequency switching servo, the cavity is automatically held at the cross-over point of the two resonances. This is a stable point, but not necessarily the cavity average frequency (if the cavity Q's and coupling factors are exactly equal the tuned cavity position would be the average of the two cavity resonances).

However, with the cavity switching continuously between two frequencies, the average pulling effect experienced by the radiating atoms is not just a function of the two frequencies (and the resonance shape at the two frequencies), but is also a function of the time spent at each frequency. So by controlling the relative time spent at the high frequency in relation to the low frequency, the time average cavity resonance frequency experienced by the radiating atoms can be varied, and a spin-exchange compensation point can be established in a manner very similar to the conventional method of establishing a fixed cavity offset frequency.

A full analysis of the physics of the hydrogen maser using the cavity frequency switching system will not be presented here, but the well behaved linear relationship between modulation periodicity and the effective cavity frequency is easily demonstrated experimentally.

The data presented in Figure 1 illustrates the spin-exchange cavity tuning of a STSC hydrogen maser. The maser being tuned is referenced to a second STSC maser and the ordinate in Figure 1 is the fractional frequency difference between the masers. The abscissa gives the number set in the modulation period generator (MPG), which has a maximum range of 0 to 99999 corresponding in this maser to a change of 16 kHz in cavity frequency. The MPG number range in Figure 1 is 50000 to 59000, which corresponds to a range in cavity frequency of 1.44 kHz.

The two curves in Figure 1 show the results obtained by varying the MPG number using two different values of the source pressure. The spin-exchange tuned position is the point at which the two curves cross. The frequency data were obtained with a precision of 2 to 3 parts in 10^{15} and the least significant digit of the MPG represents 0.16 Hz, which is equivalent to a maser frequency change for the low pressure curve of 1.60 parts in 10^{15}. The maser would be tuned to better than one part in 10^{14} by setting the MPG within 6 digits of the crossover point. To the extent of the stability of the cavity servo and maser oscillation parameters, the cavity will be tuned to this precision whenever the cavity tuner is on and stabilized.

CAVITY SERVO TRANSIENT RESPONSE

The transient response of the cavity servo following a step offset in the cavity register is shown in Figure 2. This curve illustrates the cavity response when the system uses a varactor diode as the frequency varying element. Here the full scale ordinate is $\pm 5 \times 10^{-13}$ and the abscissa is time in seconds.

The reference maser and the maser to be tested were initially stable, and then the cavity register of one maser was offset by an amount to change the output frequency in one direction by 3 parts in 10^{13}. The cavity servo returned the cavity to the tuned position during a transient period, after which the register was again offset, this time in the negative direction. After another transient period the maser had again returned to the tuned position within the frequency resolution of the test.

From Figure 2 the time constant of the cavity servo can be obtained and in the present case it is approximately 2,000 seconds. While Figure 2 shows the maser frequency transient response when the register voltage (cavity varactor voltage) is purposely offset, Figure 3 illustrates the servo response when a relatively large change in cavity temperature is purposely set in the thermal control system.

There is a tapped resistor array in the cavity temperature control system through which temperature changes to the cavity can be made from the maser control panel. In Figure 3a the maser was stable at the beginning, and then a cavity temperature change of approximately $-0.05°C$ was made. This corresponds to a thermally induced offset in maser frequency of approximately 1.55×10^{-11}. The cavity servo responded at the maximum rate, and after approximately 11 hours reached equilibrium at the new temperature.

In Figure 3b the cavity temperature was raised by $+0.05°C$, back to the original temperature, and the cavity servo again corrected for the change in a similar time period. At the end of Figure 3b the maser frequency was measured and was found to be within 5×10^{-15} of the original frequency. From the known cavity frequency response to temperature variation, this corresponds to returning to the original temperature to within approximately $1.6 \times 10^{-5}°C$.

After the transient at the end of Figure 3a the maser did not quite reach the original frequency, the slope of the phase curve gives a frequency offset of $+3.4 \times 10^{-14}$ (the sign of the slope is reversed in this plot). This illustrates that there are temperature dependent factors other than cavity frequency that influence the output frequency.

The second order Doppler shift accounts for part of the difference, namely 0.7×10^{-14}. The temperature coefficient of wall shift is the wrong sign to account for the remainder, so we may assume there are thermal variations in the cavity parameters (Q_c, n', coupling or filling factor for example) or electronic component temperature sensitivities. Cavity spin-exchange tuning was not checked during the test.

The corrections indicated on the cavity register after the transients shown in Figure 3 were approximately 1/2 of full scale. On the basis of current maser data, this is a relatively huge correction that would occur only after several years of operation, and the drift associated with this rate is typically less than 10^{-14} per year.

THE WALL SHIFT

Due to the use of automatic cavity tuners on all STSC hydrogen masers, we have a precise means of separating cavity drift from other frequency perturbing influences, including possible variation in the wall shift. It has been our experience that the frequencies of new hydrogen masers drift upward during the first few months of operation relative to masers that have been operating for much longer periods. The change is on the order of 1×10^{-14} per day at first, even though the cavity tuners are operating properly.

After extensive testing of electronic systems and searching for drift of cavity parameters or other systematic variables, the most plausible conclusion appears to be that the wall shift decreases with time when the bulb is first exposed to atomic hydrogen. By the time the masers have been fully tested and prepared for delivery (typically 2 to 3 months after first operation) the relative drift upward decreases to a few parts in 10^{15} per day, well within specifications. However, tests of six masers delivered to the United States Naval Observatory and one maser delivered to NIST indicate that there is a residual drift upward relative to international standards.

One plausible reason for the drift is that, upon exposure to the atomic hydrogen beam, the atoms interact with and remove contaminants on the Teflon surface. Atomic hydrogen is a free radical and very reactive. Many of the possible contaminants probably do not cause first order transitions, but introduce anomalous phase shifts which go away with time.

Another possible reason for the initial drift is that the Teflon surface may be in the process of stabilization of its physical phase. It is quite reasonable that this clean-up, or phase stabilization, is the reason that the older masers have very little relative drift in frequency — the material of the wall is no longer changing — which implies that the storage bulb surfaces are relatively pure, phase stable substances, namely Teflon.

While experimental errors in storage bulb geometrical factors such as the macroscopic surface to volume ratio or the microscopic smoothness of the coating introduce errors in wall shift determinations using traditional procedures[6], properties such as the temperature coefficient of the phase shift per collision should be relatively reproducible if the wall material is a pure substance.

It is important to note here that the wall shift of Teflon FEP-120 goes to zero and reverses sign at a temperature near 100 °C.[6] In view of this it is very possible that hydrogen masers, fitted with different size bulbs and operated at different temperatures for periods of time long enough to allow the bulb coatings to become clean and stable, could very likely provide a means for experimentally determining the temperature at which the wall shift becomes zero.

STSC hydrogen masers can be fitted with bulbs ranging from under 7 cm to over 16 cm. It is also possible to operate these masers over a wide range of precisely controlled temperatures. It is therefore possible to envision the continuous operation of field operable hydrogen masers under conditions such that the wall shift is negligible and other perturbations to the hydrogen atom have been accurately accounted for. This is one of the interesting experimental goals of Sigma Tau Standards Corporation.

SIGMA TAU MASER STABILITY

Figure 4 shows the relative stability of two STSC hydrogen masers as measured at the company. The masers were located in a laboratory environment with the temperature controlled within ±1°C by

the building air conditioner. These data are typical of the stability realized for the 21 masers of the current design for measuring intervals up to 100,000 seconds in a relatively well controlled laboratory environment.

All the STSC hydrogen masers constructed to date have been built for sale to various customers, so they have not been present at STSC for long enough periods to characterize the very long term stability. However, through the courtesy of the United States Naval Observatory, data has been provided showing the stability of NAV-2, one of the STSC masers located at the observatory, relative to the BIPM.

Data on the relative phase variation of the other NAV series masers (STSC masers) versus other Naval Observatory standards has also been obtained during the above period, and from this data we have calculated the relative stability of several of the six hydrogen masers STSC has delivered to the Observatory.

Figure 5 shows the frequency of four STSC masers over a period of 90 days. The frequency starting points on the vertical axis are synthesized and arbitrary. The important feature in Figure 5 is the excellent long term stability. All four of the masers are increasing smoothly in frequency relative to the BIPM at approximately 2 part in 10^{15} per day. The masers are typically varying amongst themselves by 1 part in 10^{15} per day or less.

CONCLUSION

While the present performance of STSC hydrogen masers is excellent, we feel that it can still be improved significantly. Research and development is continuing at STSC and new discoveries are being made continuously. One of the purposes of this paper is to illustrate that the state of the art in hydrogen maser technology has not reached a plateau.

The first maser using the cavity frequency switching servo was delivered only five years ago and the design has been changed very little in the 25 hydrogen masers of this type that have been produced since then. Tests done in the course of construction indicate that the cavity coupling, Q, and other oscillation parameters of these masers can be improved. We do not understand at present the source of a residual temperature coefficient of frequency that is typically about a part in 10^{14} per °C (ambient) and it is likely that further experimentation can show the way to improve upon this.

We have the ability at present to spin-exchange tune the masers very precisely at different cavity temperatures and should be able to characterize the frequency dependence on wall shift at different temperatures, using different bulb sizes and different wall coatings, and watch the relative frequencies over extended operating periods.

Using the state of the art in cavity tuning and spin-exchange tuning as well as the ability to determine precisely the frequency of masers fitted with different size storage bulbs with improved coatings as a function of temperature and time, we hope to be able to provide significant improvements in intrinsic reproducibility and fundamental accuracy in the future.

ACKNOWLEDGEMENTS

The authors thank the United States Naval Observatory for making performance data available on the NAV - series masers located at the USNO in Washington, DC.

REFERENCES

1. H. E. Peters, T. E. McGunigal and E. H. Johnson, *Hydrogen Standard Work at Goddard Space Flight Center,* Proceedings, 22nd Symposium on Frequency Control, 1968.

2. Harry E. Peters, *Characteristics of Advanced Hydrogen Maser Frequency Standards,* Proceedings, 5th Annual PTTI Meeting, 1973.

3. H. E. Peters, *Design and Performance of New Hydrogen Masers Using Cavity Frequency Switching Servos,* Proceedings, 38th Symposium on Frequency Control, 1984.

4. H. E. Peters and P. J. Washburn, *Atomic Hydrogen Maser Cavity and Bulb Design Optimization,* Proceedings, 16th Annual PTTI Meeting, 1984.

5. H. E. Peters, H. B. Owings and P. A. Koppang, *Atomic Hydrogen Masers with Self Auto-Tune System and Magnetic Field Cancellation Servo,* Proceedings, 20th Annual PTTI Meeting, 1988.

6. Vanier, J & Audoin, C, *The Quantum Physics of Atomic Frequency Standards,* Bristol, Adam Hilger, IOP Publishing LTD, 1989.

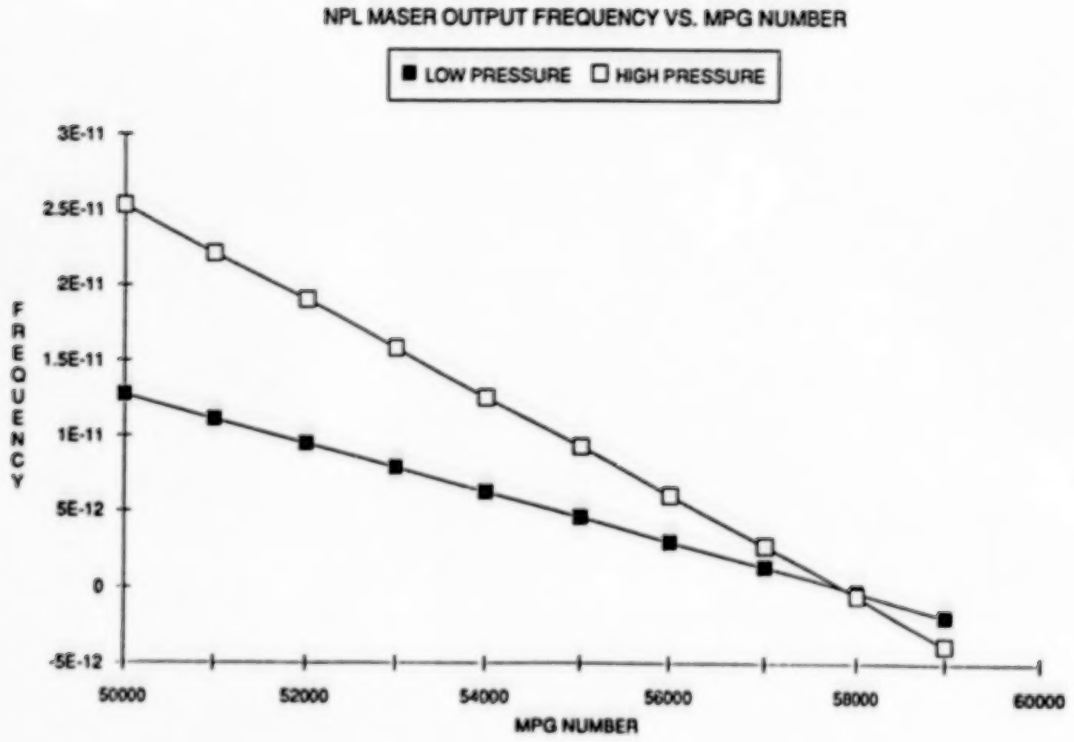


Figure 1. Spin-exchange tuning a STSC hydrogen maser equipped with a cavity frequency switching servo.

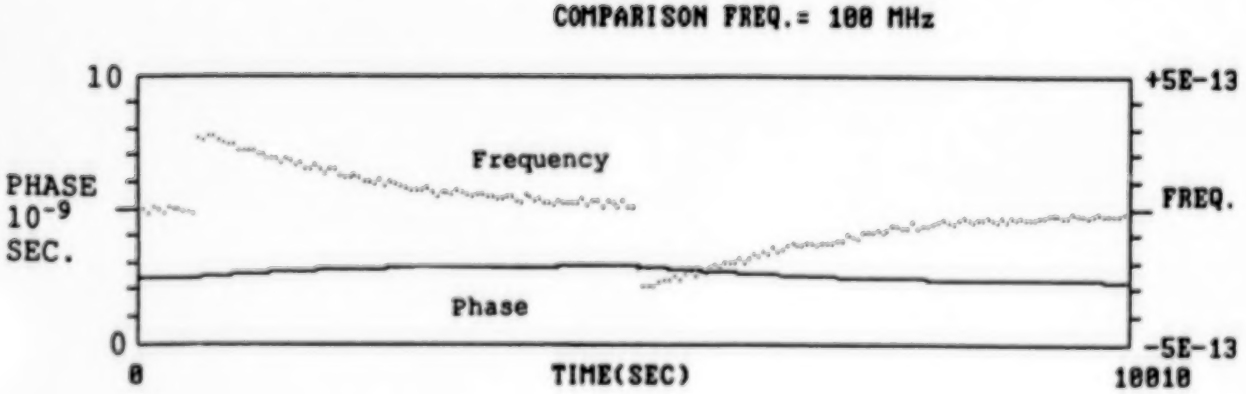


Figure 2. STSC cavity switching servo transient response.

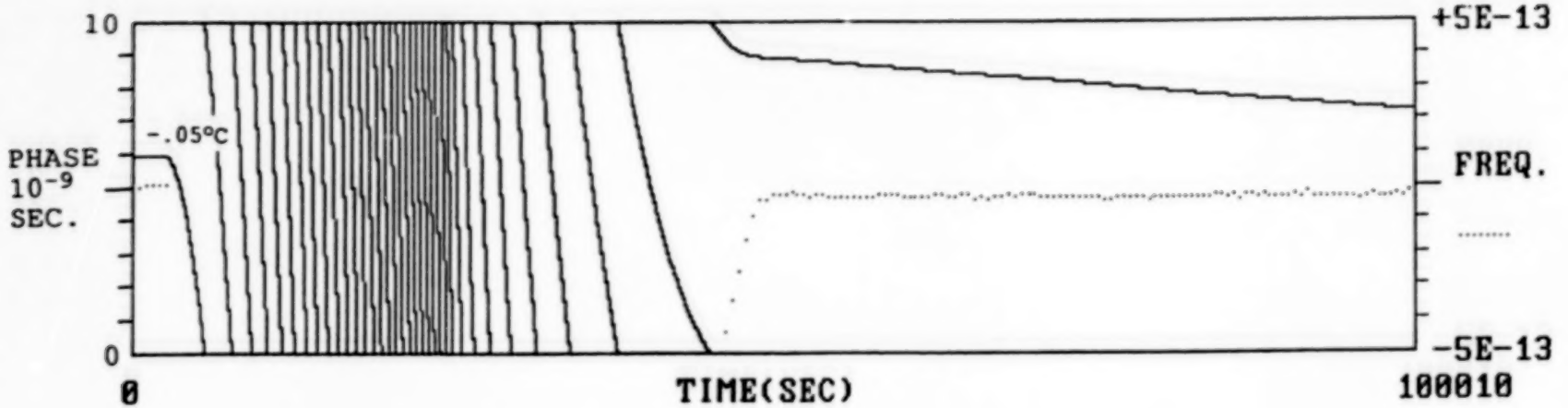


Figure 3a. Servo transient response to a decrease in the cavity thermal control set point using a varactor for the servo frequency control.

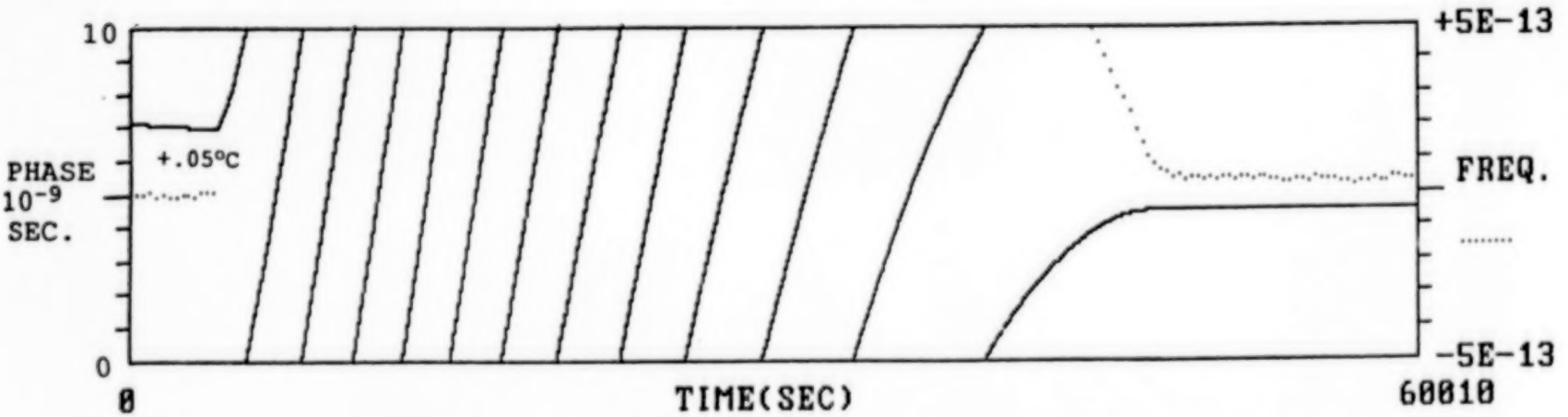


Figure 3b. Servo transient response to an increase in the cavity thermal control set point (resetting to the temperature at the beginning of Figure 3a.)

TAU= 400010

COMPARISON FREQ.= 100 MHz

ST1= 1.131462E-13 (29998)	ST500= 2.013786E-15 (59)
ST2= 6.224469E-14 (14999)	ST1000= 1.567694E-15 (400)
ST5= 2.944684E-14 (5999)	ST2000= 1.632116E-15 (200)
ST10= 1.765867E-14 (2999)	ST5000= 1.616498E-15 (80)
ST20= 1.86276E-14 (1499)	ST10000= 1.407244E-15 (40)
ST50= 6.369869E-15 (599)	ST20000= 1.107939E-15 (20)
ST100= 4.402457E-15 (299)	ST50000= 1.967648E-15 (8)
ST200= 2.65002E-15 (149)	ST100000= 1.717134E-15 (4)

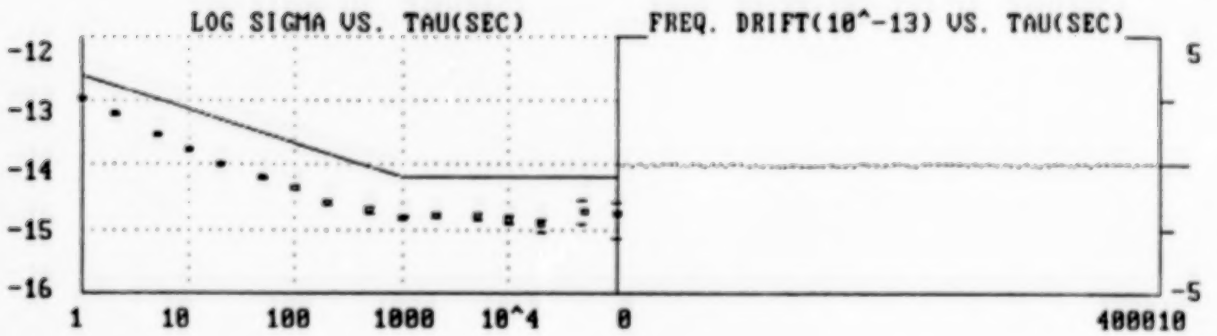


Figure 4. STSC measurement of maser stability.

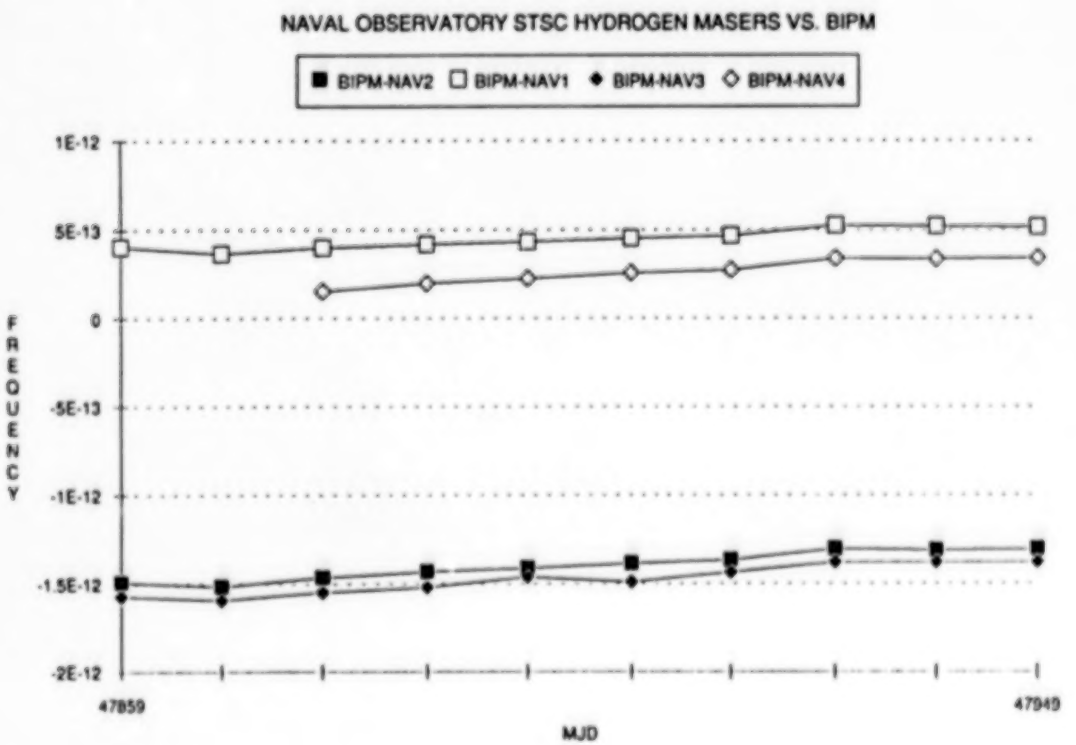


Figure 5. Long term stability of Nav- series hydrogen masers.

FREQUENCY SHIFTS IN A RUBIDIUM FREQUENCY STANDARD DUE TO COUPLING TO ANOTHER STANDARD

B. Jaduszliwer, R. A. Cook and R. P. Frueholz
Chemistry and Physics Laboratory
The Aerospace Corporation
P.O.Box 92957, Los Angeles, CA 90009

Abstract

Highly reliable timing systems, such as used on board satellites, may incorporate a hot standby atomic clock besides the active one. RF couplings between them may affect the performance of the active clock. We have investigated the effect of such couplings between two rubidium atomic clocks, and found that they will add an oscillatory term to the Allan Variance of the active clock, degrading its frequency stability, and that under certain circumstances they may also shift the active clock's operating frequency. We discuss these two effects in detail, and establish the level of isolation required to render them negligible.

INTRODUCTION

In a highly reliable timing system, it may be desirable to have two atomic frequency standards operating at all times, so that if one of them malfunctions, the other one can take over the timing function without a warm-up time lag. Also, cross checks might be performed to verify performance. Since both standards could be installed close to each other, sharing power, ground and control wiring, the possibility of RF couplings between them causing frequency shifts in the unit being used as the systems's frequency reference, or impairing its frequency stability, must be addressed. As an example, the current architecture of GPS Block IIR satellites envisions two atomic frequency standards being powered simultaneously, one as the active reference clock and the other one as a hot standby; under most circumstances, both would be rubidium atomic frequency standards (RAFS). In the satellite environment, potential couplings are definitely a concern. In order to assure that the system performance will remain within acceptable bounds, the effect of these couplings must be evaluated and the level of isolation between clocks required to keep coupling effects acceptably small must be determined.

We have conducted an experimental program to determine the magnitude and characteristics of the effects of RF coupling between two powered Rubidium Atomic Frequency Standards (RAFS) by measuring frequency shifts and Allan Variances of the active clock output as a function of the power coupled in from the hot standby clock, and the frequency offset between both clocks. The results presented and discussed in this report have been obtained with EFRATOM FRK-L RAFS, which were available in our laboratory.

EXPERIMENTAL APPROACH

Since the type and strength of the possible couplings between clocks will depend on the details of their construction, as well as on their relative positions and orientations, wiring, etc., an evaluation of the actual effects of those possible couplings on system performance would be extremely difficult except on the final assembled hardware. The approach we have decided to take instead is to identify the worst possible coupling modes, measure the effects of those couplings on clock performance, and then determine the level of isolation required between clocks to insure that system requirements will be met.

Preliminary analysis and experimentation indicated that direct coupling of the output of the standby clock into the control input of the voltage-controlled quartz crystal oscillator (VCXO) of the active clock results in the highest impact on the active clock's performance. We have investigated the behavior of the active clock in this configuration, using the experimental arrangement shown in Figure 1. The output of the standby RAFS is fed, after suitable attenuation, into the active RAFS's VCXO control point; the frequency offset Δf between the two RAFS and the power level coupled in, P_c, can be varied. The output frequency of the active RAFS is measured using standard heterodyning techniques. An Oscilloquartz BVA VCXO is used as the frequency reference for the frequency synthesizer and counter for integration times τ of up to 10^3 s. Some of our results have been extended to 10^4 s integration times by replacing the BVA VCXO by an FTS Model 5000 Cesium Beam Atomic Frequency Standard (CAFS). Using this setup, we can measure active RAFS frequency shifts δf and Allan Deviations $\sigma_y(\tau)$ as a function of Δf and P_c.

FREQUENCY SHIFTS

The fractional frequency shift $\delta f/f$ of the output of the active RAFS was measured with the standby RAFS offset by $\Delta f/f \approx 10^{-9}$, 10^{-10} and 10^{-11}. The level of the standby RAFS signal coupled at the VCXO control point was adjusted using the 0-80 dB variable attenuator shown in Figure 1. Each frequency shift measurement was corrected for drift by measuring the frequency of the uncoupled active RAFS immediately before and after it. Figure 2 presents the measured frequency shifts for the three nominal standby RAFS offsets, versus the peak-to-peak coupled signal level, in a log-log plot. The two short lines at the center of the plot indicate the expected slopes for a shift proportional to the coupled power (full line) and the coupled amplitude (dashed line). Clearly, the data support a shift proportional to the power. Figure 3 shows the frequency shifts measured for each one of the three offsets versus the coupled signal power into the 50Ω termination at the VCXO control point. Each data set was fitted by a linear $\delta f/f \approx \alpha P_c$ law; the slopes are $\alpha \approx 4.9$, 5.2 and 5.5×10^{-11}/mW for $\delta f/f \approx 10^{-11}$, 10^{-10} and 10^{-9}, respectively. The differences between the coefficients are not significant, indicating that the frequency shifts are independent of the offset between the two RAFS. The averaged frequency shift coefficient for RF power applied at the VCXO control point is $\alpha \approx 5.2 \times 10^{-11}$/mW.

The fact that the frequency shift is independent of the frequency offset between the clocks and is also present when the active clock output is fed back into its own VCXO, in which case $\Delta f = 0$, suggests some type of non-linear rectification of the coupled signal as a likely origin of the power-dependent frequency shift, with the small DC voltage thus generated coupling into the RAFS frequency control loop before the integrator.

FREQUENCY STABILITY MEASUREMENTS

The experimental arrangement shown in Figure 1 was also used to measure the Allan Variance of the active RAFS as a function of standby RAFS offset and coupled signal level. The baseline Allan Deviation of the active RAFS was first measured with the standby RAFS unpowered, and then measured again with the powered standby RAFS on the table, in the same position as for all subsequent measurements, but disconnected from the active RAFS; the lack of change in $\sigma_y(\tau)$ indicates that no significant unintended couplings between the two RAFS were present. Figures 4 and 5 show the changes induced in $\sigma_y(\tau)$ by decreasing levels of signal being coupled at the control point of the active RAFS VCXO, with the standby RAFS offset by $\Delta f/f \approx 10^{-9}$ and 10^{-10}, respectively. In each case, for high coupled power we see dramatic oscillations in the $\sigma_y(\tau)$ data, which gradually disappear as more attenuation is inserted between the two RAFS. When the coupled power is attenuated by 50 to 70 dB, the baseline $\sigma_y(\tau)$ has largely been recovered.

The period T of the oscillations can be estimated from the 10 dB attenuation data to be approximately 80 s for $\Delta f/f \approx 10^{-9}$ and 540 s for $\Delta f/f \approx 10^{-10}$. It is easy to show that in each case the period is the reciprocal of the frequency offset between the clocks, corrected for the aforementioned power shift:

$$T = \frac{1}{\Delta f + \alpha P_c f}, \tag{1}$$

where α is the frequency shift coefficient discussed in the preceding section. Using (1), for 10 dB attenuation we obtain $T = 75$ s and $T = 520$ s for nominal fractional offsets 10^{-9} and 10^{-10} respectively, in good agreement with the estimated periods. The cause of these oscillations is discussed in the last section. Longer term $\sigma_y(\tau)$ data obtained using an FTS CAFS as the frequency reference shows that the oscillatory behavior described above also obtains for longer averaging times.

SIMULATED–SWITCH CONFIGURATION

We have also explored a second configuration, shown in Figure 6, in which the highly attenuated output of the standby clock is connected directly to the output of the active clock. This configuration simulates the situation likely to be encountered in a space vehicle, where a switch operated by telemetry connects the active clock to the rest of the timing system, while inserting a large (but, for a real switch, finite) attenuation between the standby clock and the rest of the timing system.

Measurements of the frequency of the active clock showed it to be independent of both the offset between clocks and the signal level being coupled from the standby clock. This is understandable, since the signal coupling was done outside the active clock; thus, there is no reason to expect its frequency to shift in any way. On the other hand, frequency stability measurements showed exactly the same type of oscillations in the Allan Deviation as observed in the first configuration. The period was still the reciprocal of the frequency offset between clocks, but this case Δf did not need to be corrected for the coupled–power frequency shift.

In order to determine whether these oscillations involved any interaction of both signals within the active clock, we inserted a unity–gain buffer amplifier between the active clock output and the connection point. This insertion transmitted forward the signal from the active clock without change, but added at least 33 dB of attenuation to any back–coupling of the signal of the standby clock into the

active clock via its output connector. Since the oscillations in the Allan Deviation were not affected by this insertion, we must conclude that those oscillations simply reflect the presence in the clock signal of an admixture of a second coherent signal at a slightly different frequency, as discussed in the next section.

EFFECT OF A "BRIGHT LINE" OF FREQUENCY FLUCTUATIONS

The relationship between a signal's Allan Variance $\sigma_y^2(\tau)$ and its one-sided spectral density of frequency fluctuations, $S_y(f)$, is given[1] by:

$$\sigma_y^2 = 2\int_0^\infty S_y(f)\frac{sin^4(\pi f\tau)}{(\pi f\tau)^2}df. \tag{2}$$

For the situation described in the previous section, where the clock signal contains an admixture of a second coherent signal, offset by Δf,

$$S_y(f) = (r^2/2)\delta(f-\Delta f) \tag{3}$$

where r is the amplitude coupling coefficient. Inserting this expression for $S_y(f)$ into (2), we obtain for the Allan Deviation

$$\sigma_y(\tau) = r\frac{sin^2(\pi\Delta f\tau)}{\pi\Delta f\tau}, \tag{4}$$

which oscillates with period $1/\Delta f$, as shown in Figure 7. This oscillatory behavior is similar to what we have measured in both of our test configurations. The similarity can be made more evident by adding a white-noise FM contribution to $S_y(f)$, to obtain

$$\sigma_y(\tau) = \left[\frac{10^{-22}}{\tau} + r^2\frac{sin^4(\pi\Delta f\tau)}{(\pi\Delta f\tau)^2}\right]^{1/2}. \tag{5}$$

This Allan Deviation is plotted in Figure 8, and displays a dependence on τ quite similar to what we have observed. The most noticeable difference is that the oscillations in the measured $\sigma_y(\tau)$ are damped out faster than τ^{-1}. This is quite likely due to the fact that Δf, which here was treated as a fixed parameter, is actually a stochastic variable.

CONCLUSIONS

This study has shown that the presence of a second, standby atomic frequency standard in a timing system will add an oscillatory term to the system's Allan Variance, thus impairing the system's performance. These oscillations can be fully understood in terms of the linear superposition of the outputs of the two sources, without invoking any clock-dependent mechanism, and so this conclusion

has very general validity. The amplitude of these oscillations will depend on the strength of the coupling of the signal from the standby with the signal of the active clock, and can be made negligible by inserting adequate isolation between them. For the configurations we have explored, and for the two Efratom RAFS we have used in this study, 70 dB was an adequate level of isolation.

Our study has also shown that under certain circumstances, the output frequency of the active atomic clock may be shifted by coupling the output of the standby clock. This result depends sensitively on the actual hardware and mode of coupling; in the conditions of our study (Efratom RAFS in a worst possible case configuration, with the standby clock output connected to the voltage control point of the active clock VCXO), the frequency shift was independent of clock offset and dependent only on the power level being coupled. The coupling coefficient was of the order of 5×10^{-11}/mW, so that the level of isolation required to reduce the Allan Variance oscillations to acceptable levels (approximately 70 dB) is more than adequate to make this frequency shift negligible.

REFERENCE

1. J. A. Barnes, A. R. Chi, L. S. Cutler, D. J. Healey, D. B. Leeson, T. E. McGunigal, J. A. Mullen, W. L. Smith, R. L. Sydnor, R. F. C. Vessot and G. M. R. Winkler, *Characterization of Frequency Stability*, IEEE Trans. Instr. and Meas., IM-20, 105 (1971).

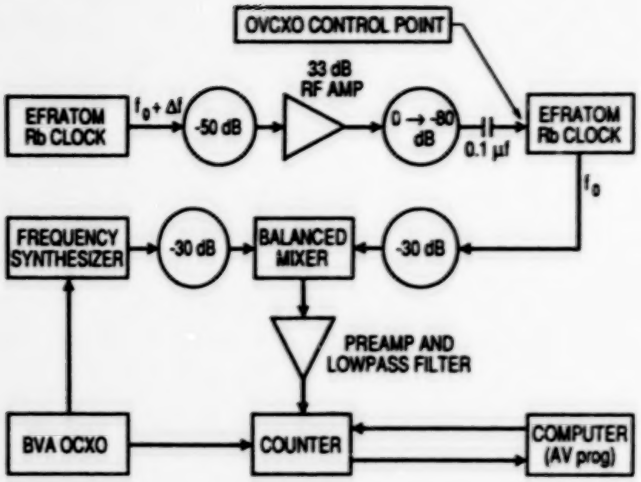
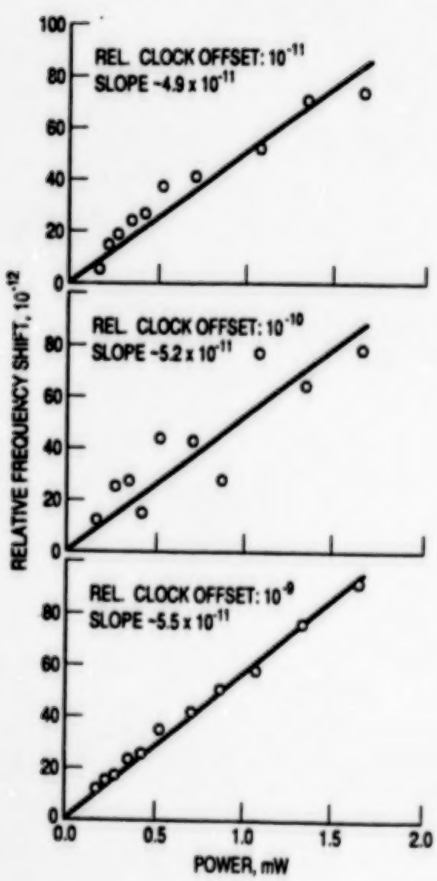


Figure 1

Worst-case test configuration. The standby clock signal, offset by Df, is injected at the VCXO voltage control pin of the active clock. A 80 dB variable attenuator allows control of the signal level. The Allan Variance and frequency shift of the active clock are measured using standard heterodyning techniques.



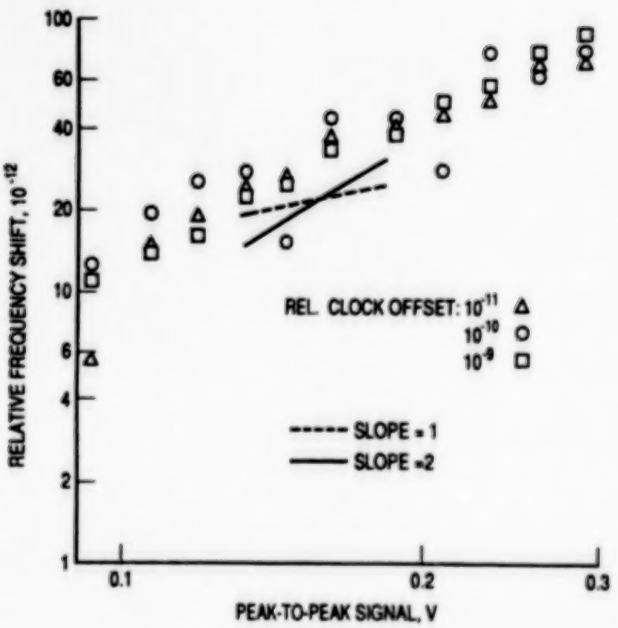


Figure 2

Relative frequency shift of the active clock vs. injected signal level, for three different frequency offsets between standby and active clocks, in a log-log plot. The two lines display the slopes for amplitude- or power-dependent shifts.

Figure 3

Relative frequency shift of the active clock vs. coupled power level, for three different offsets between standby and active clocks. The lines are one-parameter fits; the slopes give the coupled-power shift coefficient. The differences between the slopes are not significant.

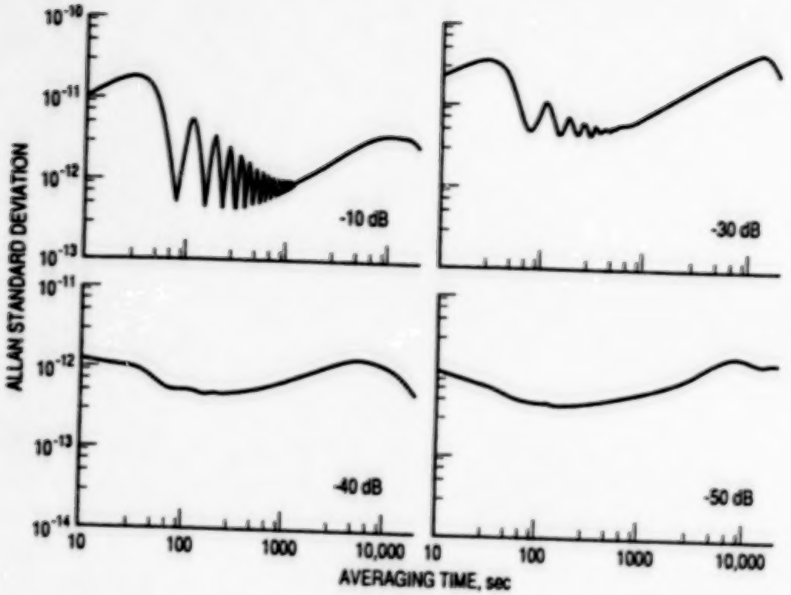


Figure 4

Allan Deviation of the active clock, with the standby clock offset by 1 x 10^{-9}, for increasing attenuator settings. With 50 dB attenuation, the measured Allan Deviation is very close to the baseline.

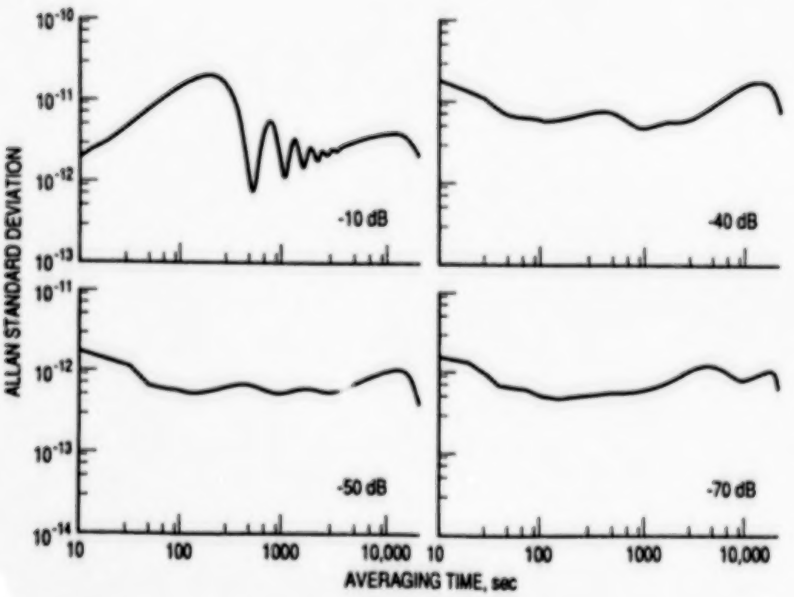


Figure 5

Allan Deviation of the active clock, with the standby clock offset by 1 x 10^{-10}, for increasing attenuator settings. With 70 dB of attenuation, the measured Allan Deviation is very close to baseline.

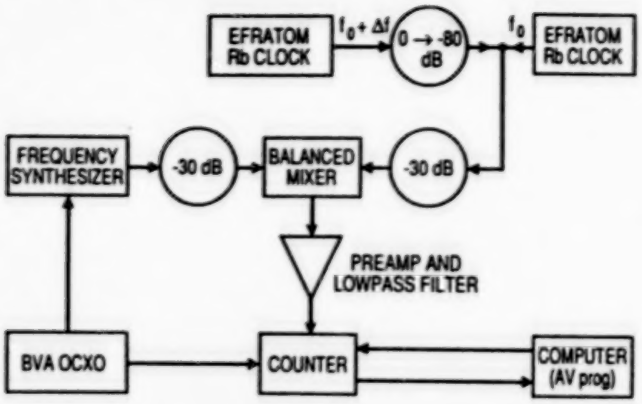


Figure 6

"Simulated switch" configuration. The output of the standby clock is connected to the output of the active clock through an attenuator, representing the "open" side of a switch connecting both clocks to the rest of the timing system on board a satellite. The measuring system is the same one used for the worst-case configuration measurements.

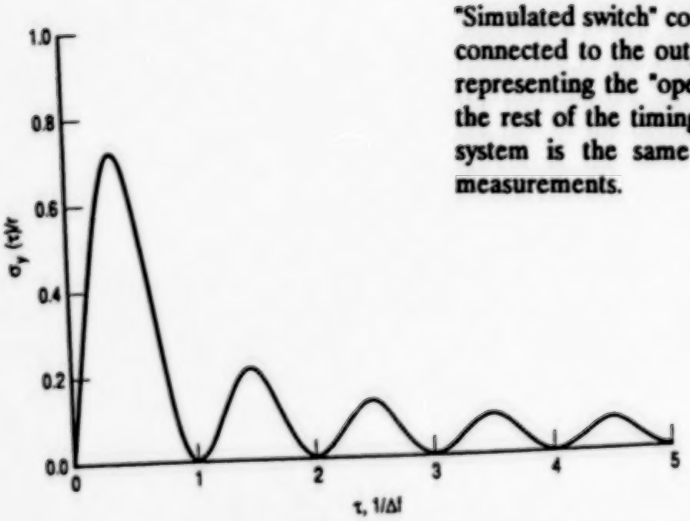


Figure 7

Allan Deviation due to a "bright line" source of fractional frequency fluctuations (normalized by the amplitude coupling coefficient r) vs. averaging time, in units of reciprocal frequency offset Df.

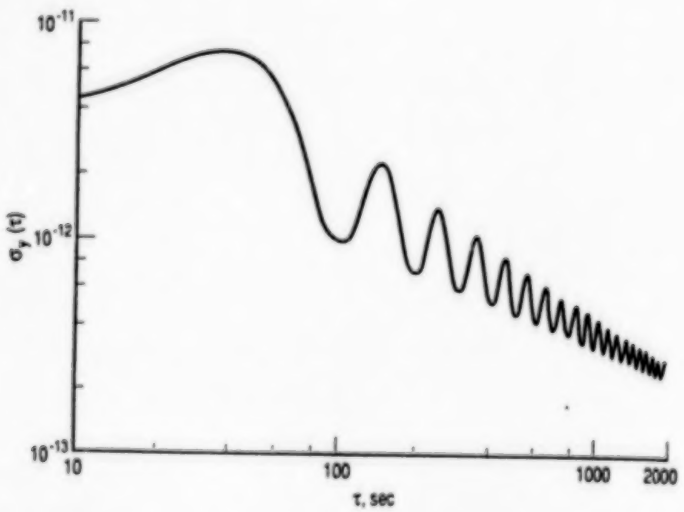


Figure 8

Allan Deviation calculated for a spectral density of frequency fluctuations consisting of the sum of a white noise FM term and a "bright line" term.

EFFECT OF THERMAL CYCLING ON STRESS IN METALLIC FILMS ON CERAMIC SUBSTRATES

Edward M. Mattison and Robert F.C. Vessot
Smithsonian Astrophysical Observatory
Cambridge, Massachusetts

INTRODUCTION

The hydrogen maser is the most stable frequency standard currently available for averaging intervals of hours to weeks. A major contributor to maser frequency variations is the maser's microwave resonant cavity: by means of the cavity pulling effect, a change in the cavity's resonance frequency produces a proportional change in the maser's output frequency. To minimize variations in the cavity's dimensions, and thus in its resonance frequency, maser cavities are often constructed of a low-expansivity glass-ceramic material coated on its inner surface with a conducitive metallic film. We have previously shown[1] that silver films like those used in SAO maser cavities develop tensile stress when cooled to room temperature after being fired onto the cavity, and that the stress in such films relaxes with time at a rate proportional to the level of stress. Stress relaxation in maser cavity coatings can alter the shape, and hence the resonance frequency, of the cavity, resulting in a slow variation in the maser's output frequency.

In the present work we have investigated the possibility of reducing or reversing the initial tensile stress by precooling the coated cavity material. We hypothesize that cooling the material well below its normal working temperature and then warming it to its normal temperature would result in a lower tensile stress or even a compressive stress. Under such a condition stress relaxation, and thus any consequent frequency drifts, might be reduced or reversed.

EXPERIMENT DESCRIPTION

MATERIAL SAMPLES AND MEASUREMENT SYSTEM

Measurements were made on eight samples of silver-coated low-expansion materials; these were among the samples whose shapes had been measured over a span of approximately eight years in the previous work on stress relaxation[1]. The samples are approximately 3.94 inches long, 0.75 inches wide, and 0.25 inches thick; they are optically polished on one face and coated with silver on the opposite face. Details of the sample preparation are given in reference 3. The substrate materials and film thicknesses for the samples are shown in Table 1.[2]

The silver film stress was determined from measurements of the sample shapes. The bending of the samples relative to a reference optical flat was measured by an optical interferometer equipped with a phase measuring adaptor. The adaptor digitized the interferograms formed by the interferometer and transferred the data to a computer, which analyzed the sample shapes using curve-fitting software.

Table 1 -- Sample Materials

Plate	Material	Coating Thickness (.001 inch)
4	Zerodur	6.25
6	Cervit	uncoated
7	Cervit	4.88
9	Cervit	4.20
11	Cervit	1.00
24	ULE	4.37
28	ULE	1.95
30	ULE	1.05

EXPERIMENTAL PROTOCOL

The measurements were carried out during the period 25-28 June 1990. To obtain a knowledge of the samples' shapes before chilling, we first measured the sample shapes near room temperature. During measurement the samples were housed in an insulated, temperature-controlled chamber. The chamber's air temperature was measured using a calibrated thermistor driven by a constant current supply. To determine the incremental rate of change of coating stress with temperature and thus to be able to correct for small temperature variations, we measured the samples at approximately 25°C and 33°C, allowing several hours for the samples to equilibrate at each temperature.

Following the baseline curvature measurements, we removed the samples from the measurement chamber. A soft black deposit that had been deposited by vapor emitted by the chamber's insulation was removed by gentle wiping with acetone. Also, a deposit of adhesive on sample 11 from a strip of double sided tape was removed by rubbing with Alconox cleaner dissolved in water. Care was taken not to distort the samples during cleaning. We then immersed plates 4, 7, 11, 24, and 28 in liquid nitrogen for approximately 1.5 hours, after which we returned all of the plates to the sample chamber and measured their shapes several times during the following three days, at 25°C and 33°C.

DATA ANALYSIS

The shape analysis program determines the shape of the samples from the digitized interferogram. The fringe pattern produced by the interferometer is a function of the optical path difference (OPD) between the sample and a reference optical flat, and thus contains the sample shape. The program expresses the sample's shape by fitting a set of orthogonal Zernike polynomials to the OPD pattern. The coefficients of the first two polynomials, C_1 and C_2, express the average tilt of the sample relative to the flat, while the third Zernike coefficient, C_3, is proportional to the sample's curvature, referred to in optics terminology as "focus".

The sample curvature K is given by

$$K = \frac{4\,C_3}{r_o^2} \qquad (1)$$

where r_o is the radius of the circle that circumscribes the (rectangular) interferogram.

The stress σ in the silver film parallel to the surface of the sample is proportional to the sample curvature[1]:

$$\sigma = K \frac{E}{6(1-\nu)} \frac{t_s^2}{t_f} \qquad (2)$$

where E and ν are the Young's modulus and Poisson's ratio, respectively, of the substrate material, t_s is the thickness of the substrate, and t_f is the film thickness. Because the samples were not completely flat in their unstressed state prior to being silver coated, the value of K in Eq. 2 must be the difference between sample's measured curvature and its initial (precoating) curvature.

The film stresses calculated from the fitted Zernike coefficients are plotted against elapsed time in Fig. 1.

DISCUSSION OF RESULTS

ACCURACY OF ZERNIKE POLYNOMIAL FIT

In calculating the sample curvature and film stress from the third Zernike coefficient, C_3, we assume that a three-parameter Zernike fit well represents the shape of the sample. A measure of that assumption is given by comparing $C_3(3)$ and $C_3(8)$, the values of C_3 resulting from a three-parameter Zernike fit and an 8-parameter fit, respectively. For samples 4, 6, 7, 9, 11, and 28 these coefficients generally agree to within about 10 to 15 percent, indicating that the three-parameter fit represents the sample shape well. For samples 24 and 30, however, $C_3(3)$ and $C_3(8)$ differ by up to roughly 50% for some measurements. Examination of the sample profiles given by the curve-fitting program show that sample 24 has a significant amount of asymmetrical curvature, which is represented by Zernike functions higher than order 3. Sample 30 has very little curvature, as indicated by small values of C_3, and its shape is only partially represented by the third Zernike polynomial.

EFFECT OF CHILLING: LIMITING FILM STRESS

Figure 1 reveals many similarities in the behavior of the coatings. The baseline measurements before chilling the samples show that all of the coatings had surface stresses of between roughly -1×10^7 and -2×10^7 N/m^2 at a temperature of 25°C. (The interferogram radius for plate 7's baseline measurement at 25°C was inadvertently not obtained from the program, so the coating stress could not be calculated for that measurement.) Negative stress values represent tensile film stresses. All of the coated samples were under tensile stress before being chilled.

After the plates 4, 7, 11, 24, and 28 were immersed in liquid nitrogen and rewarmed to room temperature, their film stresses were between $+2.0 \times 10^7$ and $+2.5 \times 10^7$ N/m^2. (Plate 30 was not chilled because its baseline curvature was not well defined, and plate 9 was preserved as an undisturbed sample.) The consistency of the post-chilling stress confirms that the film stress is limited by the yield strength of the silver material. The yield strength of bulk silver[3] ranges between 1.0×10^7 N/m^2 and 5.4×10^7 N/m^2. Thus the maximum stress resulting from chilling and warming the samples is consistent with the yield strength of silver.

INCREMENTAL STRESS CHANGE WITH TEMPERATURE

The existence of a limiting value for the film stress is also indicated by measurements of the incremental change in stress with temperature. When the samples were raised monotonically from 25°C to 33°C after chilling, the film stress increased by an amount substantially smaller than the corresponding increase observed in the baseline (prechilling) measurements. When the temperature was then returned to 25°C, the stresses decreased by amounts comparable to, although smaller than, the baseline changes. The rates of change of stress with temperature are given in Table 2.

Table 2 -- Rate of Change of Film Stress with Temperature

	$d\sigma/dT$ (10^5 Nm^{-2} $°C^{-1}$)		
Plate	25°C→33°C Prechilling	25°C→33°C Postchilling	33°C→25°C Postchilling
4	8.2	2.0	7.0
7	---	0.096	7.9
11	6.0	0.41	4.9
24	6.5	1.3	4.9
28	7.8	3.1	6.2
Not chilled:			
9	7.4	6.4	6.3
30	6.4		6.7

The measurements $d\sigma/dT$, together with the existence of a limiting film stress, have implications for maser performance. A coated maser cavity brought monotonically to room temperature from its firing temperature will have a tensile coating stress limited to approximately $2x10^7$ Nm^{-2}. Because the incremental rate of change of film stress with temperature is roughly $+6x10^5$ Nm^{-2} $°C^{-1}$, raising the cavity's temperature by approximately 30°C ($\approx 2x10^7/6x10^5$) is expected to reduce the film stress roughly to zero. Lowering the stress in this way reduces any cavity deformation due to stress relaxation, and thus reduces or eliminates the contribution of film stress to long-term frequency drift. SAO masers operate with a cavity temperature of 50°C, 30°C above room temperature, which satisfies the criterion for stress reduction.

STRESS CHANGE WITH TIME

The data of Fig. 1 indicate that the stress in the post-chilled films decreased over the period of observation. This agrees with earlier measurements[1] that showed that the stress in the coatings relaxed at a rate proportional to the internal stress. The stress in plate 9, which had not been chilled, decreased slightly in magnitude (became less negative). The data for plate 30 do not indicate a temporal stress change; this may be due to the small initial stress, or to the marginal representation of sample curvature by C_3. In order to obtain quantitatively significant values for the stress change with time, measurements over considerably longer periods would be needed.

CONCLUSIONS

The measurements confirm the hypothesis that prechilling metal-coated substrates can decrease or reverse the internal film stress, and that the stress is limited by the yield strength of the film material. Thus improper temperature treatment of hydrogen maser cavities can result in high coating stress and consequent frequency drift due to long-term stress relaxation. However, as discussed above, proper temperature cycling prior to operation can reliably reduce the surface stress in hydrogen maser cavities to a level where stress relaxation is not an important factor in maser frequency stability.

ACKNOWLEDGEMENTS

We thank R. Sumner, University of Arizona Optical Sciences Center, for his assistance during this work.

REFERENCES

[1] E. M. Mattison and R.F.C. Vessot, "Time and temperature stability of silver-coated ceramics for hydrogen maser resonant cavities," *Proc. 20th Annual Precise Time and Time Interval (PTTI) Applications and Planning Meeting*, p. 313 (1988).

[2] Zerodur is a trademark of Schott Glasswork, Inc.; Cervit is a trademark of Owens-Illinois, Inc.; and ULE is a trademark of Corning, Inc.

[3] J.L. Everhart, W.E. Lindlief, J. Kanegis, P.G. Weissler, and F. Siegel, "Mechanical properties of metals and alloys", NBS Circular C447. U.S. Government Printing Office, 1943.

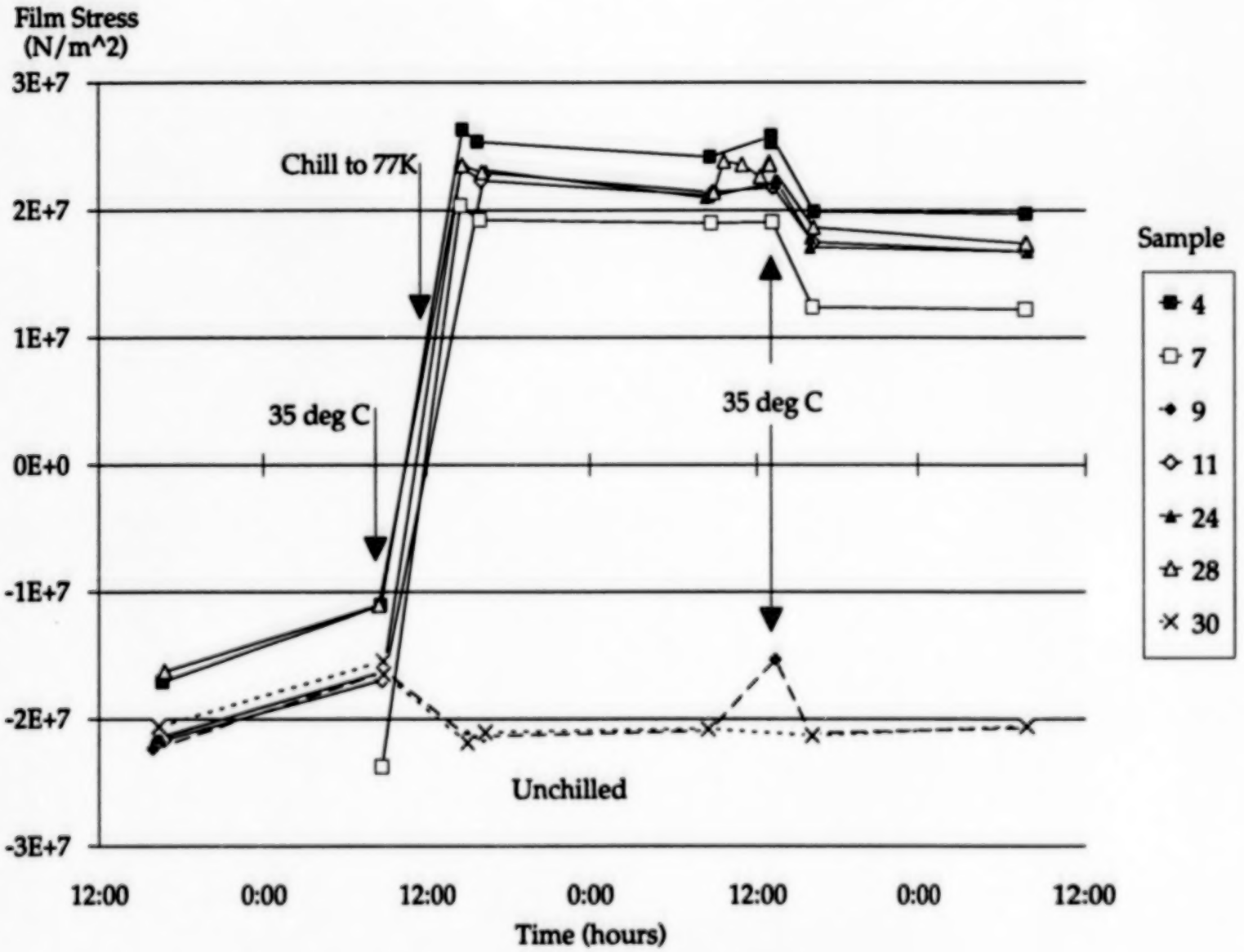


Fig. 1. Film stress as functions of time and temperature cycling
(Measurements at 25°C except as noted)

SENSITIVITY TO THE EXTERNAL TEMPERATURE OF SOME GPS TIME RECEIVERS

W. Lewandowski
Bureau International des Poids et Mesures
Pavillon de Breteuil
F–92312 Sevres Cedex, France

and

R. Tourde
Observatoire de Paris
61, av. de l'Observatoire
75014 Paris

Abstract

It has been assumed until recently that GPS time receiver units (receiver+cables+antenna) have good stability and do not affect time transfer by more than 1 ns. Differences of a few nanoseconds sometimes observed during calibration campaigns have been attributed to external causes, such as multipath propagation, rather than to variations within the hardware.

The characteristic feature of most comparisons of GPS time receivers is their short duration. Normally the comparison takes place, at most, over one week. To observe the behaviour of GPS time receivers over a period of several months, an experiment has been organised involving three receivers of two types. All three were connected to the same atomic clock.

An unexpected sensitivity to external temperature was found in one type of receiver. This effect proved to be a function of the length and type of the antenna cable. In the most unfavourable case the sensitivity was 1.8 ns/°C.

INTRODUCTION

The GPS time receivers used for the purposes of time metrology have enjoyed until recently the excellent reputation of keeping one nanosecond whatever the environmental conditions. Several campaigns of differential calibration[1, 2, 3] have been conducted under this assumption. During these campaigns the receivers were compared typically over an interval of one or two days. These campaigns were rarely repeated in the same location. On the other hand, time laboratories are equipped in most of the cases with single GPS receiver. There have been only few opportunities to compare GPS time receivers for a period exceeding one week. Differences of a few nanoseconds sometimes observed during these comparisons have been attributed to external causes, as for instance multipath propagation,

rather than to changes within the hardware. In only one case have two GPS receivers of different type been compared over a period of some months[4]. The differences between these receivers did not show fluctuations, however an inconsistency in the software of two receivers was noticed.

The experiment described in this paper was organized in order to observe the long-term behaviour of GPS time receivers. It covered the period November 22, 1989 — April 10, 1990. Three receivers of two types were involved. A sensitivity to the external temperature of one type of the receiver is demonstrated.

RECEIVERS

The experiment involved three C/A Code GPS time receivers, of two types used currently in numerous time-metrology laboratories. The receiver denoted R1 is of the first type, the receivers denoted R2 and R3 are of the second one. These two types of receiver are manufactured by two different makers and there are three major differences between them:

(a) Original design: the first type of receiver was designed for accurate time transfer; the second one was designed originally for differential geodesy and was later adapted for accurate time transfer.

(b) Internal delay: the first type has internal delay of about 50 ns, the second type one of about 400 ns.

(c) Frequency transmitted from the antenna to the receiver through the cable: the first type down-converts at the antenna level from the L1 frequency (1575.42 MHz) to 75 MHz and sends this signal by cable to the receiver. The second type transmits at 1575.42 MGHz directly to the receiver.

The second type of receiver (R1 and R2), as this experiment proves, shows sensitivity to the external temperature.

ANTENNA CABLES

Throughout the entire duration of this experiment, receiver R1 operates with a coaxial cable (type RG213U) of 33 m length provided by the maker.

Receivers R1 and R2 operate with different coaxial cables, all provided by the maker: 100 m (type H100 super low loss), 72 m (type H100 super low loss), 30 m (type RG213U low loss).

For simplicity of notation we will associate with the name of the receiver the length of the cable with which it was operated.

The table below gives the principal characteristics of these cables.

Length [m]	Type	Characteristic impedance [Ohms]	Attenuation at 1575 MGHz [dB/100m]	Operating temperature [°C]
100	H100 super low loss	50	15	−40 +80
72	H100 super low loss	50	15	−40 +80
33	RG58CU	50	40	−40 +80
30	RG213U low loss	50	30	−40 +80

ORGANIZATION OF THE EXPERIMENT

The three receivers use separate antennas located on the same roof. The differential coordinates of the antenna phase centres are known with uncertainties of a few centimetres.

The three receivers are programmed with the same schedule including 26 tracks per day.

The receivers are connected to the same master clock generating UTC(OP). The comparison consists in the computation, for each track i, of the time differences:

$$dt(i) = [\text{UTC(OP)} - \text{GPS}]\text{Rec.A} - [\text{UTC(OP)} - \text{GPS}]\text{Rec.B} ,$$

or, using abbreviations,

$$dt(i) = \text{Rec.A} - \text{Rec.B} ,$$

and then in computing the daily mean DT of dt(i).

RESULTS

The comparison of the three receivers is realized in several steps illustrated by Figures 1 through 4:

Figure 1 — First comparison (November 22, 1989 to January 12, 1990). Receiver R2 operates with the 100 m coaxial cable: receiver R3 operates with the 30 m coaxial cable. Differences between R2(100m) and the other two receivers reach a peak to peak value of 20 ns. Receivers R1(33m) and R3(30m) differ, peak to peak by 3.2 ns with a standard deviation of 0.6 ns over a 50–day period of comparison. The deviations of R2(100m) are strongly correlated with external temperature.

Figure 2 — Second comparison (January 13 to 22, 1990). The cables and antennas connected to R2 and R3 are interchanged. Receiver R3(100m) is now sensitive to the temperature.

Figure 3 — Third comparison (January 23 to March 20 1990). Receiver R2 now operates with the 72 m cable and R3 is connected to its original 30 m cable. A sensitivity to the temperature is observed for R2(72m), but is less strong than that for R2(100m). The differences peak to peak between R1(33m) and R3(30m) reach 2.4 ns; the standard deviation for the 56-day period of experiment is 0.6 ns.

Figure 4 — Fourth comparison (March 21 to April 10, 1990). Receiver R2 operates with the 30 m cable. The standard deviation between R2(30m) and R1(33m) is found to be 0.3 ns for a 20-day period of comparison. Peak to peak differences of 3.5 ns between R3(30m) and two other receivers are observed; these differences are correlated with temperature.

The observations described in the above comparisons show that standard deviations of daily means depend on the sensitivity to temperature of the receivers used: they decrease when sensitivity is reduced. Figure 5 shows the differences of individuals values $dt(i)$ between R2(100m) and R1 during one day: November 24, 1989. We observe a clear correlation with temperature. This effect induces an increase of the daily mean standard deviations.

CONCLUSIONS

1. The data obtained from receivers R2 and R3, both of the second type, are correlated with the external temperature.
2. This correlation depends upon the antenna cable. With the 100m cable (type H100 super low loss) recommended by the maker, the variation reaches 1.8 ns/xC.
3. Errors arising from changes in external temperature should be reduced to less than 1 nanosecond over the domain of usual temperatures for harmonization with other instrumental errors and potentialities of GPS: this achievement needs the sensitivity to be reduced to 20ps/xC.
4. Time-metrology laboratories should be equipped with at least two GPS time receivers (preferably three) to detect abnormal behaviours linked for instance with environmental conditions.

REFERENCES

1. J. A. Buisson, O. J. Oaks and M. J. Lister, *Remote Calibration and Time Synchronization (R-CATS) Between Major European Time Observatories and the US Naval Observatory using GPS*, in Proc. 17th PTTI meeting, pp. 201-222, 1985.
2. W. Lewandowski, M. A. Weiss and D. Davis, *A calibration of GPS Equipment at Time and Frequency Standards Laboratories in the USA and Europe*, in Proc. 18th PTTI meeting, pp. 265-279, 1986, [also in Metrologia, 24, pp. 181-186, 1987].
3. M. A. Weiss and D. Davis, *A Calibration of GPS Equipment in Japan*, in Proc. 20th PTTI meeting, pp. 101-106, 1988.
4. D. Kirchner, H. Bessler and S. Fassl, *Experience with two collocated C/A code GPS receivers of different type*, in Proc. 3rd European Time and Freq. Forum, pp. 94-103, March 1989.

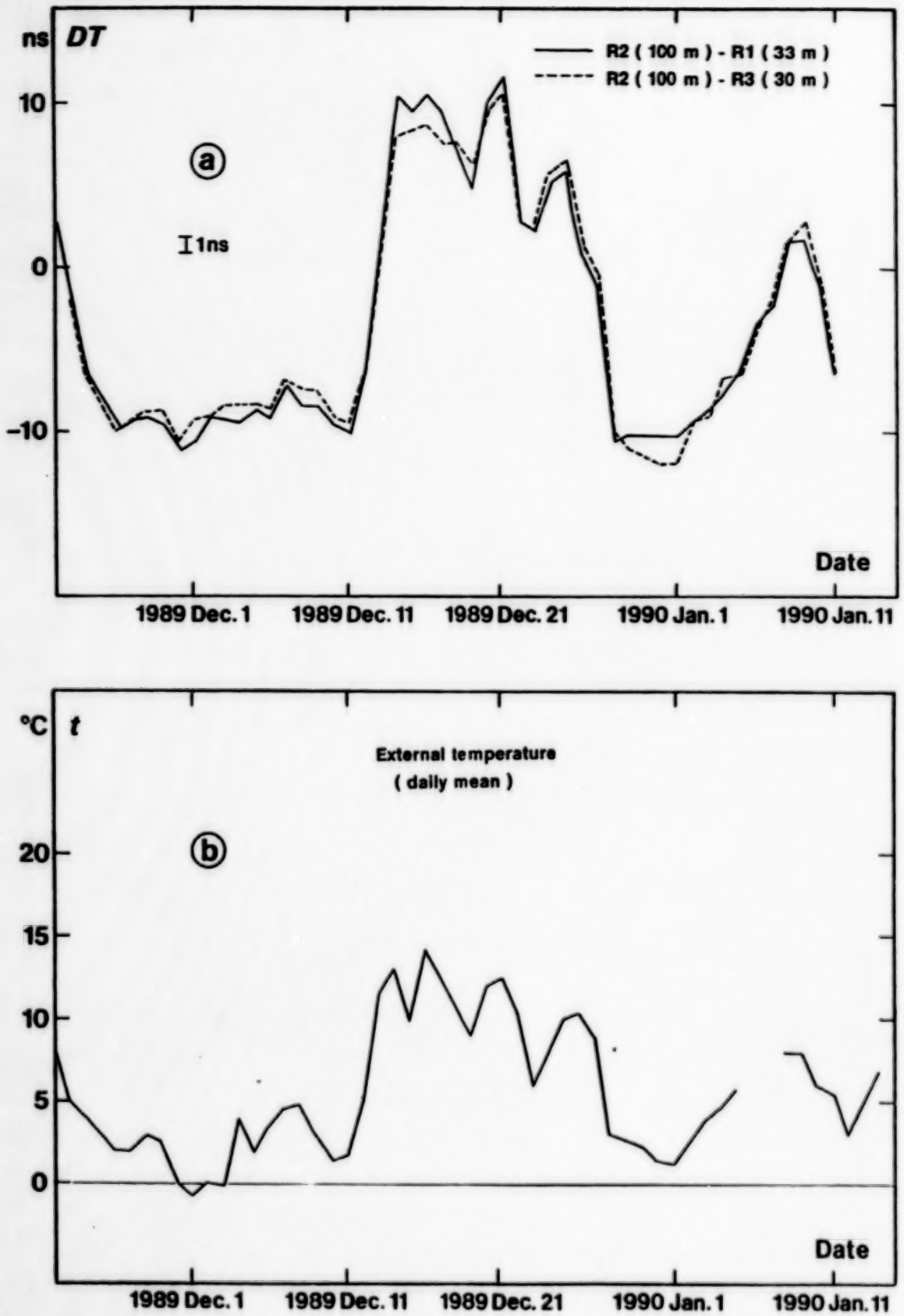
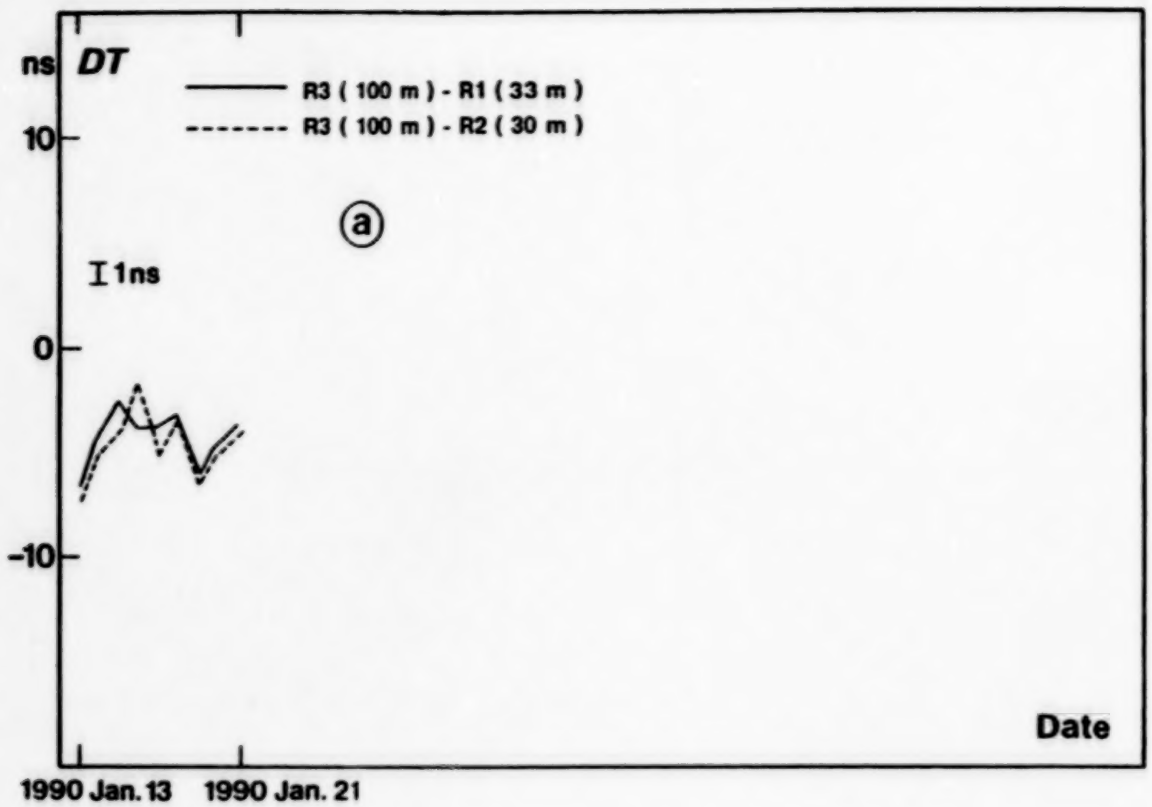


Figure 1. First comparison.



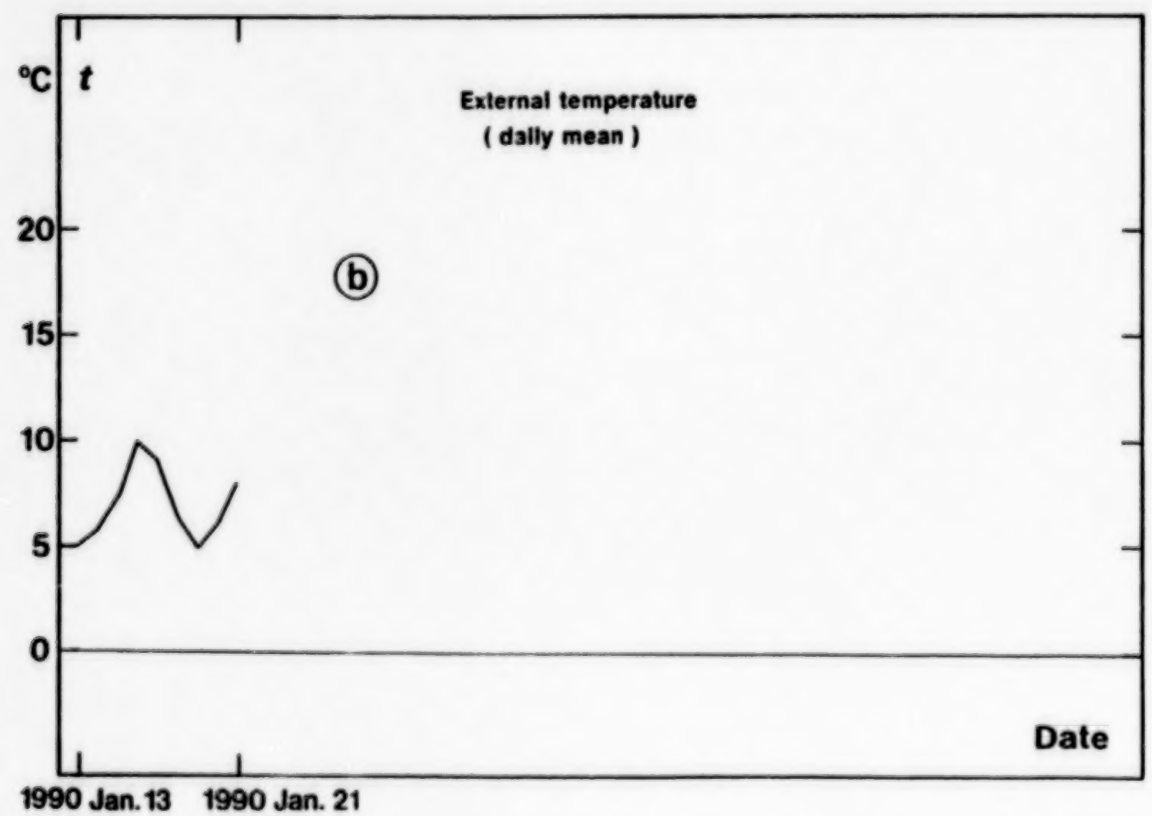


Figure 2. Second comparison.

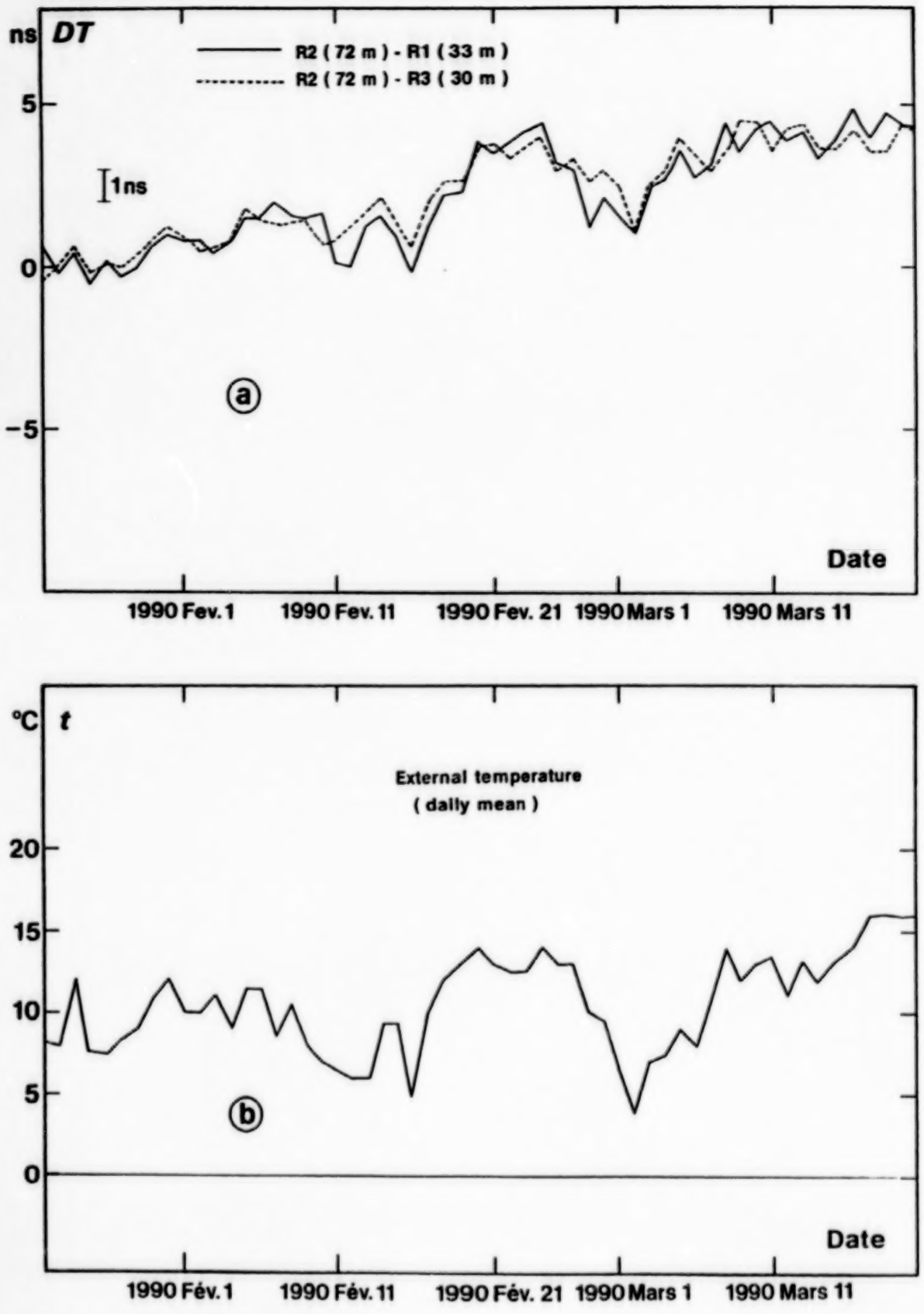
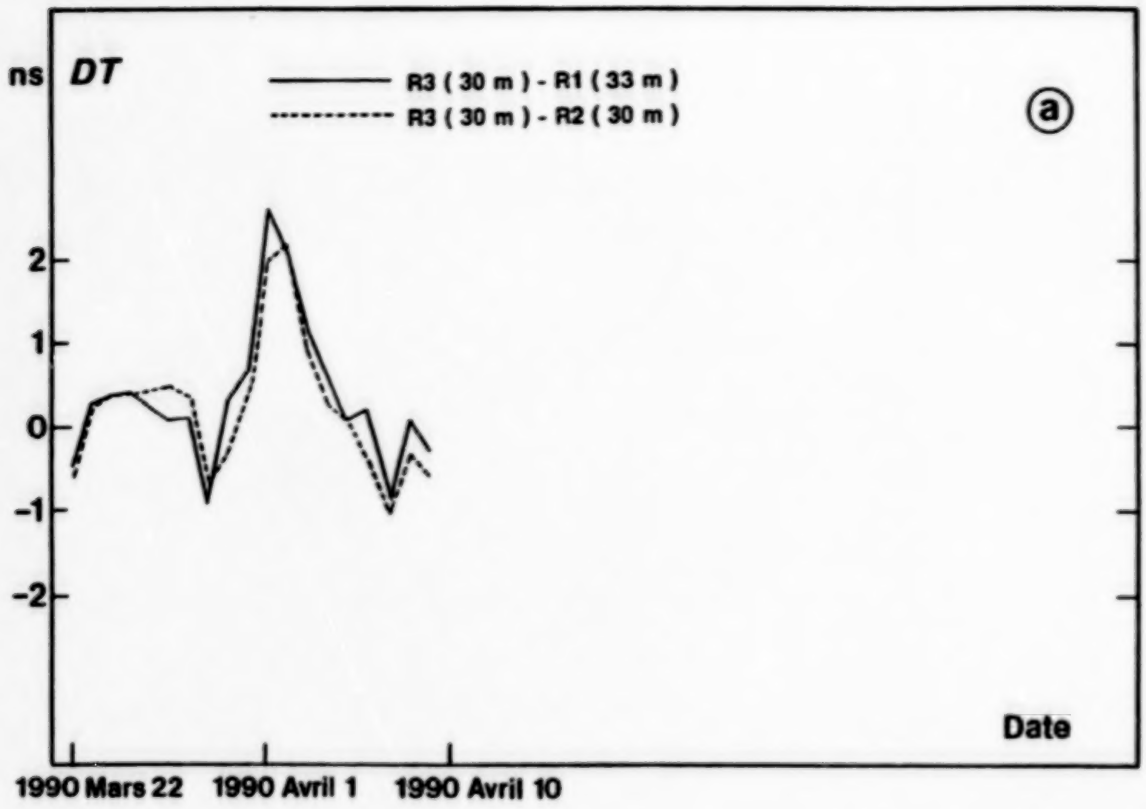


Figure 3. Third comparison.



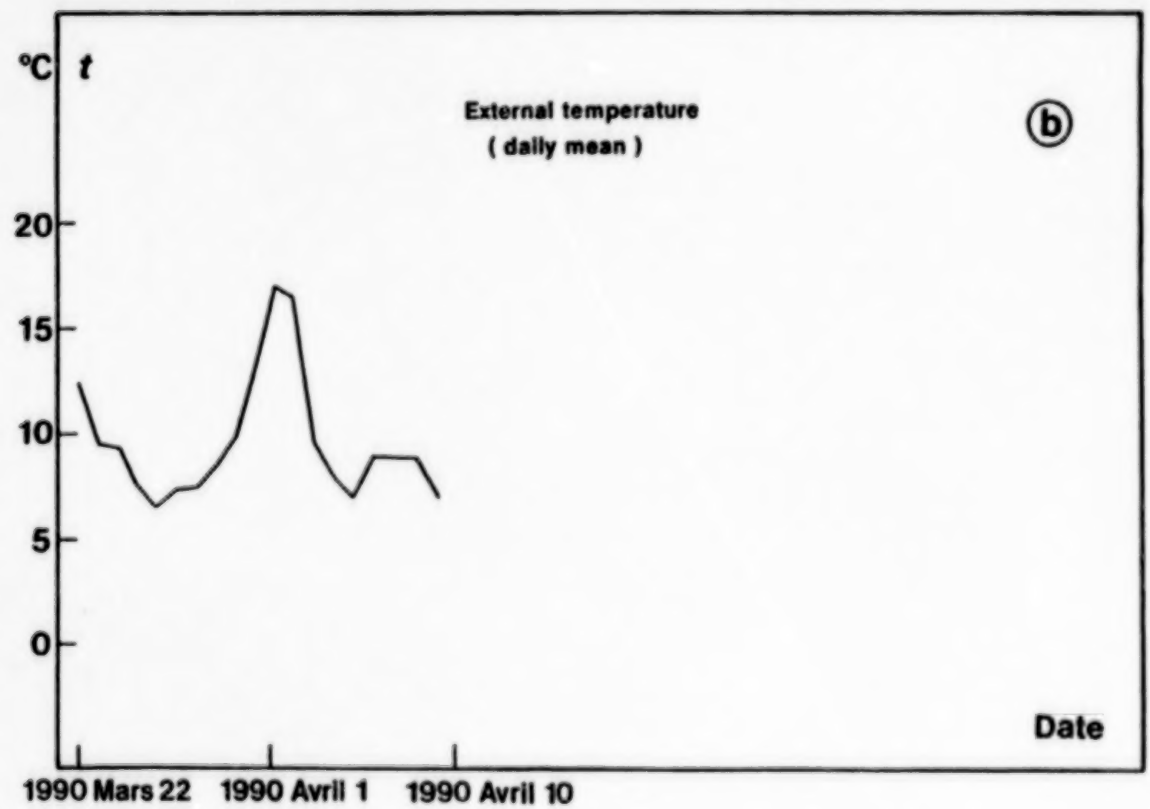


Figure 4. Fourth comparison.

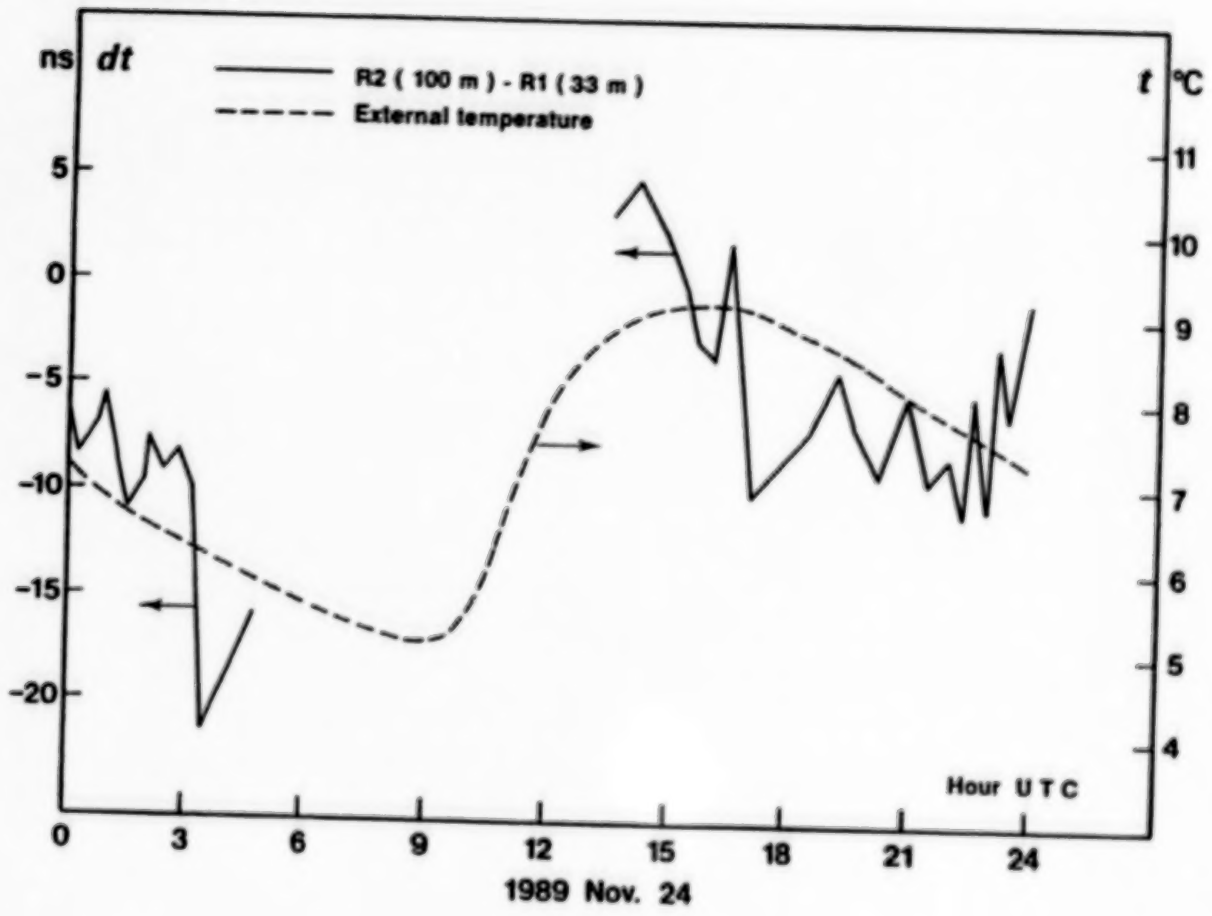


Figure 5. One day period of comparison between receivers R2(100m) and R1(33m).

BLANK PAGE

GPS BLOCK 2R TIME STANDARD ASSEMBLY (TSA) ARCHITECTURE

Anthony P. Baker
ITT Aerospace Communications
Nutley, NJ

Abstract

The underlying philosophy of the GPS 2R TSA architecture is to utilize two frequency sources, one fixed frequency reference source and one system frequency source, and to couple the system frequency source to the reference frequency source via a sample data loop. The system source is used to provide the basic clock frequency and timing for the space vehicle (SV) and it uses a VCXO with high short term stability. The reference source is an atomic frequency standard (AFS) with high long term stability. The architecture can support any type of frequency standard. In the system design rubidium, cesium, and H2 masers outputting a canonical frequency were accommodated. The architecture is software intensive. All VCXO adjustments are digital and are calculated by a processor. They are applied to the VCXO via a DAC.

DESCRIPTION OF TSA ARCHITECTURE

The GPS 2R TSA architecture is illustrated by Figure 1. An AFS is used as a reference frequency source. It operates with a fixed, minimum C field and provides an output frequency that can easily be multiplied to the resonant frequency of the particular AFS being utilized. It contains no frequency synthesizers or extra feedback loops and no frequency adjustments. The nominal output frequency of

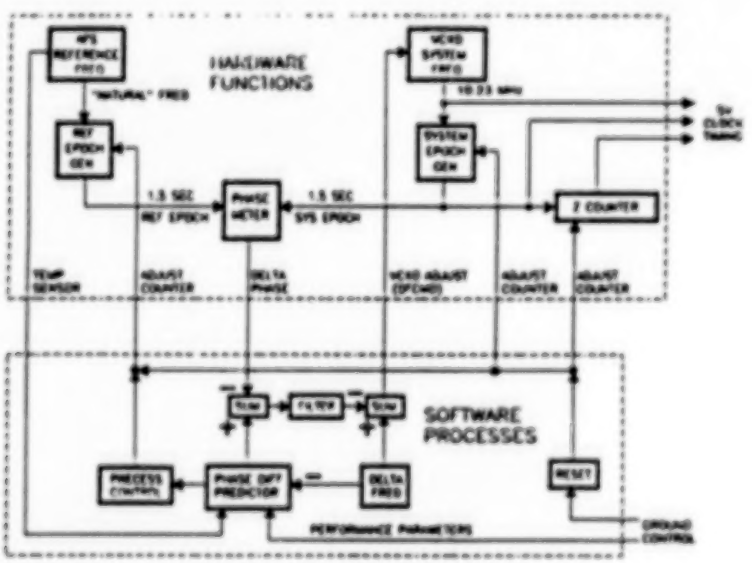


FIGURE 1 TSA ARCHITECTURE

the AFS is not critical; in this implementation it is 13.4 MHz. A stable VCXO is used as an system frequency source. Its nominal frequency is 10.23 MHz (GPS frequency) adjustable in 1 micro Hz steps over a range of 10 Hz to accommodate aging and selective availability (SA). The AFS and VCXO outputs are divided to obtain 1.5 second "epochs". These epochs are compared in a phase meter and the measured phase difference between the AFS and the VCXO epochs is compared to the predicted phase difference generated by a software phase difference predictor. The result of the comparison is a loop error signal that represents the difference in phase between the VCXO and the AFS. The loop error signal is converted by the processor to a VCXO control voltage (DFCMD) which is applied to the VCXO (after compensation for VCXO non linearity) to remove the phase difference. The loop filter smooths the phase meter output (a running average) and provides a software controlled, loop time constant. The loop time constant is normally quite long but switches to a short time constant when fast frequency corrections are required. DFCMD is generated every 1.5 seconds. The frequency of the VCXO can also be dithered by adjusting the DFCMD and compensating the output of the phase difference predictor.

The phase difference predictor uses AFS and VCXO performance algorithms stored in the processor to adjust the phase difference prediction to take into account the actual frequency of the AFS, its frequency drift (in the case of a rubidium AFS), its temperature sensitivity, relativistic and gravitational effects, and the non-linear response of the VCXO to control voltages. Since the AFS is asynchronous to GPS time, the phase difference predictor also keeps track of the precession between the epochs generated from the AFS frequency and the epochs generated from GPS time. Since the divider in the reference epoch generator only divides by whole numbers, keeping track of precession is a book keeping process until it reaches a value close to the value of the AFS period. When this value is reached, the divider in the reference epoch generator is adjusted by a whole count. The non linear response of the VCXO to control voltage changes and DAC non-linearity are taken into account when the DFCMD is generated. The VCXO characterization ensures that VCXO tuning is at the center of the tuning range of the DAC so that there is sufficient range to take care of VCXO aging and SA. The Z counter indicates real time by counting the reference epochs.

DESIGN CONSTRAINTS UPON TSA ARCHITECTURE

Performance specifications impose various design constraints upon the architecture. The requirement that the TSA be capable of operating for 6 months without ground assistance has the most severe impact on the design. It requires that the performance of the AFS (and to some extent the VCXO) be predictable to close tolerances for 6 months. In order to meet this requirement the AFS performance must be modeled prior to launch and the model stored in processor memory for use during orbital operation. It must also be possible to update these characteristics as a result of ground measurements. The impact of other specifications are, for the most part, minimal. Radiation and prompt dose specifications require the use of tantalum shielding and CMOS SOS technology for selected circuits and require that the AFS output use tuned circuits to "flywheel" through nuclear upsets. Specially designed circuits are also required to convert from the analog to the digital domain. The most significant constraints are listed below.

- Ensure TSA operation for 6 months without ground assistance.
- Ensure that there can be no undetected failure.
- Operate through single event (random) upsets.

- Make TSA radiation and nuclear event resistant.
- Provide for ground control override of all autonomous actions.
- Provide dual redundancy.

IMPLEMENTATION OF TSA ARCHITECTURE

The TSA system design is illustrated by the hardware diagram of Figure 2. Dual redundancy is used throughout for reliability reasons except that three AFS are used; two rubidium (RAFS) and one cesium (CAFS). It is intended that two rubidium standards be powered up at all times. One standard will be on-line and the other will be a hot standby. Failure of the on-line standard (reference frequency source) will result in an automatic switchover to the hot standby. Switchover is accomplished without effecting the navigation mission of the SV because the high stability VCXO will "free run" during switchover and the hot AFS will be synchronized to the VCXO before it takes over as the reference frequency source. Monitor circuits ensure that AFS failure can be detected prior to significant performance degradation. The CAFS will be on cold standby for redundancy reasons but can also be used as a hot standby. Recovery from failure of other components requires ground help. The

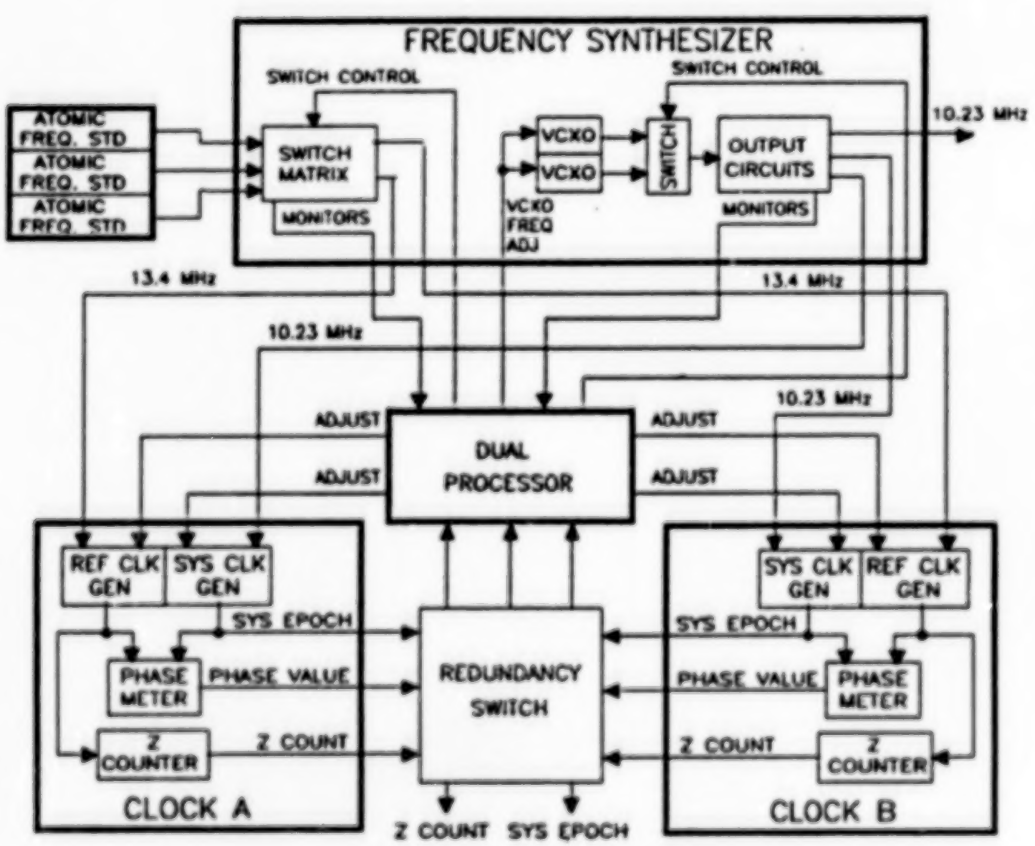


FIGURE 2 TSA SYSTEM BLOCK DIAGRAM

SV epoch generator hardware divides the outputs of the reference and system frequency sources to obtain reference and system clocks (1.5 second epochs). The dividers are programmable and resetable for initialization and adjustment purposes. A phase meter measures the phase difference between the system epoch and the reference epoch and outputs a digital value which represents coarse (¿ one AFS period) and fine phase difference between them. The measured phase is compared to the phase predicted by software and the difference is converted by the DFCMD generator to a frequency control signal that is applied to the VCXO which adjusts the VCXO frequency to remove the phase difference. The Z counter keeps track of real time by counting the reference epochs. Software provides adjustments to the epoch generators for initialization and clock correction and hardware monitors provide inputs to software diagnostics so that no undetected failures can occur.

The TSA software design is illustrated in Figure 3. The software predicts the phase difference between the reference and system clocks at each epoch using AFS performance models and AFS frequency data stored in the processor. In this implementation it must take into account the actual AFS frequency, AFS frequency drift, and AFS temperature. It reads the measured phase and compares it to the predicted phase. Phase error is converted to VCXO frequency control words (DFCMD) that are applied to the DAC in the VCXO which causes the VCXO to change frequency and thus remove the phase error. The DFCMD value is adjusted in accordance with a model stored in the processor to remove non linearities in the transfer function between the DFCMD and the output frequency change of the VCXO. The DFCMD is also adjusted to produce VCXO output frequencies in accordance with an SA algorithm that is related to the Z count. The software also maintains a software Z count to ensure that the hardware Z count is correct. AFS performance models and other performance

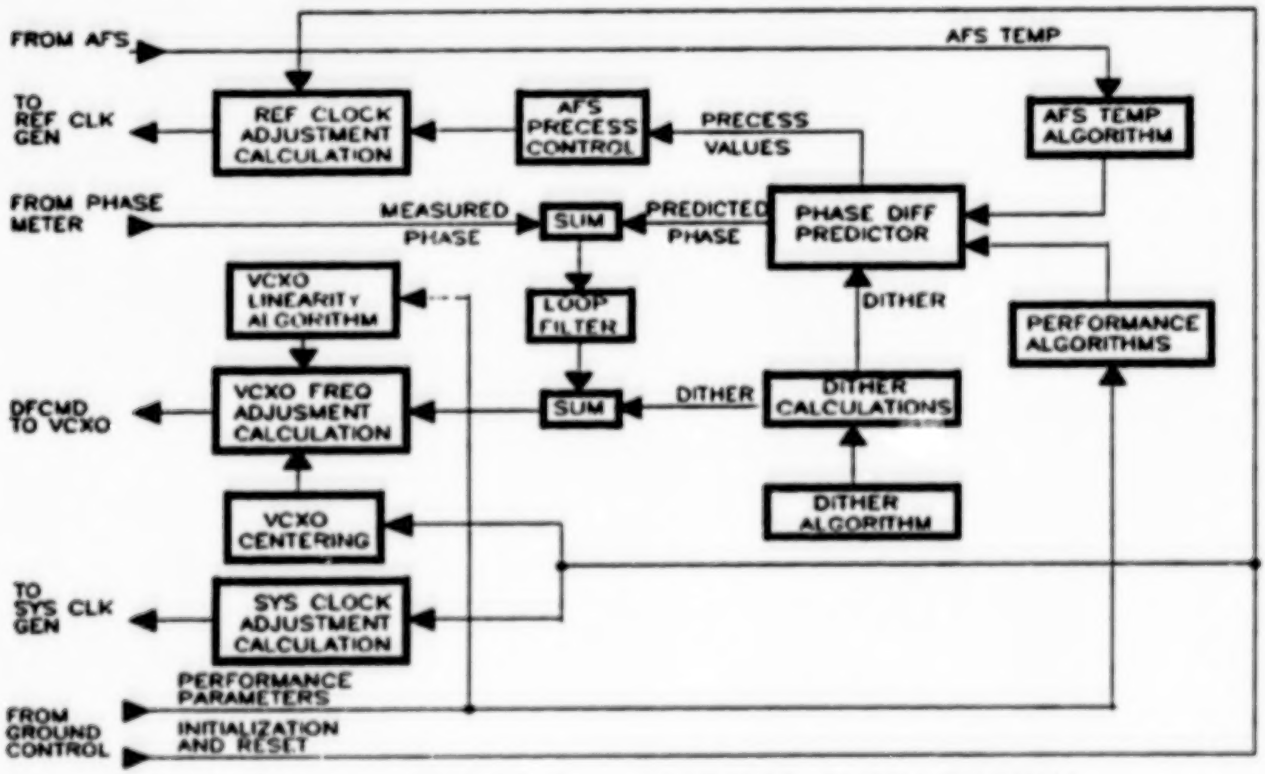


FIGURE 3 SOFTWARE BLOCK DIAGRAM

data are calculated prior to launch from careful measurements of the performance of the AFS and VCXO. These models and data are uploaded with other SV software during initialization. The models

and data are updated as required during orbital operations based upon ground measurements of in-orbit performance. The models and data parameters remain valid for more than 6 months although corrections may be provided to the user (in the user message) as a result of inter satellite measurements (cross link measurements).

TSA SYSTEM INTEGRITY

Numerous hardware monitors provide information to the processor so that there is no possibility that a single failure of a TSA component can go undetected. Improper monitor reading cause a fault alarm to be issued. Figure 4 illustrates the hardware monitoring arrangement. The following hardware monitors are provided:

- AFS activity detector. Detects AFS output.
- VCXO activity detector. Detects VCXO output.
- AFS lock status. Detects if AFS loop is locked.
- Reference and system epochs.
- Second harmonic level. Detects level of AFS modulating signal.
- Z counter. Value of Z count
- Phase meter (S/W looks for phase jumps and erroneous precession).
- Nuclear event detector.
- AFS temperature. Measures AFS baseplate temperature
- Cross link measurements

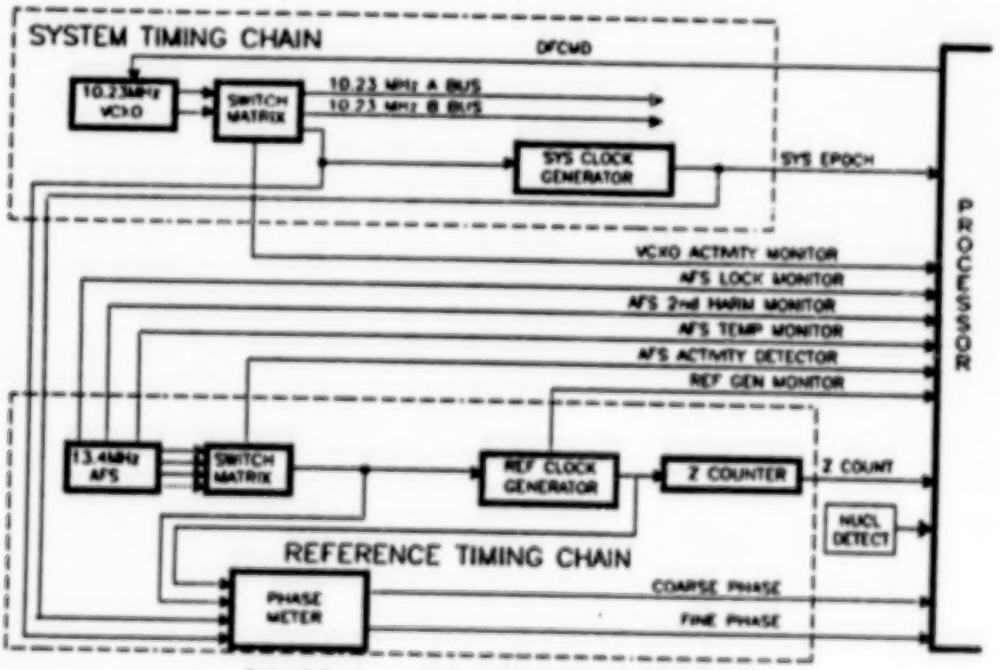


FIGURE 4 TSA INTEGRITY MONITORING

The first four of the above monitors are go, no-go detectors which indicate failures of the AFS, VCXO, and system and reference clocks directly. In the case of the system and reference epochs, software also maintains a watchdog timer. If the epochs do not occur within a specified period of time, an alarm is issued regardless of the status of the hardware monitors. The second harmonic detector will also indicate AFS failure; in addition, it will often provide an early warning of AFS failure conditions. If the level changes 20% with respect to a running average (calculated by software), experience has shown that it is probable that something is going wrong with the AFS even if its output remains unaffected. The value of previous Z counts is stored by software. At each epoch one is added to the previous Z count and the result is compared to the current Z count. Mismatches not accompanied by other alarms indicate that a logic upset has occurred.

The phase measurements are the most indicative of the health of the TSA. Phase values can indicate catastrophic failure, logic upsets, and health that is slowly deteriorating. A single, fixed phase jump that continues for more than on or two epochs is an indication that a logic upset has occurred. Erratic and continuous phase errors indicate a component failure. Phase values that indicate a precession that is different from the expected precession are indicative of AFS frequency changes. This can be detected before system performance is affected. Phase changes are likely to be the first indication that there is a problem and thus ensure that action can be taken within one or two epochs.

The nuclear event detector and AFS temperature monitor are not strictly TSA integrity monitors. The nuclear event detector confirms the cause of upset and therefore is useful in determining recovery actions. The temperature monitor is used by the phase predictor when it is calculating expected phase since the frequency of the AFS varies slightly with temperature. However, out of range, non cyclic, or erratic temperature changes indicate something is wrong with the AFS. Cross link measurements between insight Block 2R satellites also provides an important integrity check. They are made hourly and will indicate slow or fast time changes that have not been predicted.

System integrity is software intensive. No hardware recovery or alarm action takes place directly. Software takes appropriate action on the basis of monitor inputs. The software also maintains the usual internal range checks and time outs to ensure that the software is operating correctly. Any fault alarm will cause the software to enter a diagnostic routine which determines what has failed and whether it is possible to recover autonomously without affecting performance. If it is possible to recover autonomously the TSA does so. If not an alarm is placed in the user message. A complete description of autonomous recovery is not covered in this paper, but, in general, if the failure is limited to the AFS, or if the upset is limited to either the system or reference timing autonomous recovery is possible.

PREDICTED TSA PERFORMANCE PARAMETERS

Engineering models and prototypes of the frequency standards and other TSA functions have been built and initial tests completed. Analysis of the test results leads me to believe that the following performance can be achieved.

- Short Term Frequency Stability: VCXO 1×10^{-12}; CAFS 3×10^{-11}; RAFS 3×10^{-12}
- Long Term Frequency Stability: CAFS 5×10^{-14}; RAFS $1 \times 1-^{-14}$
- TSA User Range Error (24 hour,1 Sigma): CAFS 2.6 m; RAFS 1.8 m

- Frequency Drift (RAFS): Removed by modeling
- Temperature Sensitivity: RAFS 1×10^{-13} change in freq per degree C
  (Decreased to 2.4×10^{-14} by modeling)
  CAFS Negligible
- AFS Reliability: Better than 0.75
- Power Consumption: CAFS 20 watts; RAFS 14 Watts
- Weight: CAFS 26 LBS; RAFS 12 LBS

IMPROVEMENTS TO THE TSA DESIGN

The TSA is no exception to the rule that all designs can be improved. Possible future improvements to the TSA that can be made as a result of experience gained on this design range from minor enhancements to complete redesigns. The software intensive nature of the design presents possibilities for increased use of autonomous recovery and improved availability due to autonomous redundancy management. Minor changes (in the technical sense) to the hardware and software would permit autonomous recovery from many TSA hardware failures and all TSA hardware upsets. These changes are:

- Add a hot standby VCXO so that VCXO and AFS switchover is possible.
- Duplicate or time share the phase measurement circuitry.
- Provide software controlled management of hot standby VCXO.
- Add software diagnostic routines to locate upsets and failures.
- Add software performance analysis routines to characterize operation.
- Reduce the number of AFS from three to two.

The first three of the above changes increases availability by incorporating autonomous hardware redundancy management of the AFS and VCXO hardware. Duplicating or time sharing the phase measurement circuitry permits monitoring and assessing the performance of the AFS and VCXO hot standbys. The fourth change would increase availability by permitting autonomous recovery from TSA logic upsets. It provides for the effective use of the first three changes. The fifth change provides the means to model the performance of the TSA during operation thus improving the ability of the phase predictor to predict phase. The last change recognizes 17 years of improvements made in the reliability of atomic frequency standards and the improved availability as a result of autonomous AFS switching.

Another improvement would be to develop a nuclear upset proof digital frequency synthesizer. The original TSA system design incorporated a digital frequency synthesizer to generate the 10.23 MHz and to provide SA. This approach was abandoned and a VCXO used in its place because an nuclear upset proof synthesizer was not available. It seems likely that technology has advanced to the point where such a synthesizer is now possible. Synthesizers permit a single AFS to drive both the reference and system clocks, further improving availability, and SA functions are simplified.

In the present design, many TSA functions are included as part of other functions. Hardware functions are located in the Mission Data Unit (MDU) and the TSA software is located in the mission processor. Also, the system epoch generator is part of the P code generator. The current hardware configuration evolved from previous GPS designs but is not the best way to ensure TSA performance and producibility and results in complex MDU hardware and mission processor software. The TSA should be configured into three functions; AFS, VCXO, and TSA logic. The TSA logic should include its own processor. Such a configuration would simplify the MDU and mission processor software, reduce VCXO redundancy by 2, permit separate testing of the MDU and TSA, and improve the producibility of both the TSA and the MDU.

INTERIM RESULTS FROM THE CHARACTERIZATION TESTING OF THE ENGINEERING DEVELOPMENT (EDM) RUBIDIUM CLOCKS FOR SATELLITE APPLICATIONS

Edward D. Powers, Jr.
Fredrick Danzy
Naval Research Laboratory
Code 8321
4555 Overlook Avenue, Southwest
Washington, D.C. 20375–5000

Abstract

This paper presents some interim results from the environmental testing program to evaluate the Engineering Design Model (EDM) of the EG&G Spaceborne Rubidium Clock. This effort is in support of the GPS BLOCK IIR program and is intended to characterize the performance of EG&G design for BLOCK IIR satellite applications. Two EG&G EDM units are currently under test at NRL's Clock Test Facility to measure the long–term frequency stability, drift, and frequency versus temperature characteristics.

INTRODUCTION

The Global Positioning System (GPS) provides users with precise position and timing information, and will have a constellation of 21 satellites, with 3 on orbit spares, expected to be completed by the mid 1990's. It is anticipated that GPS BLOCK IIR (Replacement) satellites will be needed during the second half of this decade. The GPS BLOCK IIR satellites will carry two EG&G Rubidium Atomic Frequency Standards (AFS) and one Kernco Cesium AFS.

Because the AFS is of such importance to GPS, an AFS development program was begun for the GPS program. An alternative source rubidium AFS project was started by the GPS Program Office and Rockwell in 1979 to insure the supply of space–qualified AFS's. As part of this program EG&G built two prototype Rubidium AFS's, units 1 and 2[1, 2]. These two units were later modified[3]. In 1987, NRL and EG&G presented a paper describing the results of testing done at NRL on these two prototype units[4]. The data presented demonstrated a frequency stability and drift rate better than that of any other Rubidium AFS ever tested at NRL.

Several years later in support of the GPS IIR program, EG&G built two additional rubidium AFS's, units 3 and 4. EG&G implemented several design changes in units 3 and 4. These changes included elimination of the synthesizer and a rearrangement of sub–assemblies which have lead to a more

compact design. Units 3 and 4 output frequency, 13,401,343 Hz, is the 510th sub-multiple of the 6,834,682,000 Hz rubidium transition frequency. This allows for elimination of the synthesizer. NRL is doing detailed developmental testing on these four rubidium AFS's in support of the GPS BLOCK IIR program. The purpose of this testing is to assist EG&G, the spacecraft manufacturer, and the GPS Program Office in refining the design and to document the performance of the AFS in the expected space environment. The interim test results of the GPS BLOCK IIR Rubidium AFS are reported in this paper.

NRL CLOCK TEST FACILITY

The Naval Research Laboratory (NRL) has served as the primary development and test facility for all GPS AFS's since the initial concept of GPS. In 1985, the NRL Clock Test Facility was completed and includes a fully-automated 48 channel dual-mixer phase measurement system which records both phase and 900 analog measurements every hour[5]. Shorter-term phase measurements are made using a 12 channel dual mixer system with a 30 channel analog data logger. The primary frequency reference NRL for all phase measurements is one of 5 Hydrogen Masers at NRL[6]. For space environmental testing, NRL has 12 Thermally-controlled high Vacuum Chambers (TVAC). Additional measurements made at the NRL Clock Test Facility include phase noise, spectral purity, vibration, and AC and DC magnetic fields susceptibility measurements.

FREQUENCY STABILITY TESTING

The GPS BLOCK IIR Rubidium AFS's frequency stability specification is defined in terms of Allan Variance[7]. The frequency stability requirement is for performance better than $3.0 \times 10^{-12}/t^{1/2} + 5.0 \times 10^{-14}$ with the frequency drift removed, while operating in a vacuum of less than 1×10^{-5} torr, at a constant temperature. The frequency drift should be less than 5.0×10^{-14}/day after 30 days of continuous operation under constant environmental conditions in vacuum. This performance specification equals the typical performance shown by EG&G units 1 and 2 in testing done at NRL[4]. The development goal is the for long-term frequency stability to be better than 1.0×10^{-14} at sample times greater than one day.

Figure 1 shows frequency stability data with and without drift removed collected from unit 3. This test took place over a 107-day period in TVAC at a constant temperature of 28 C. Also shown in figure 1 is NRL reference maser's long-term frequency stability and the phase measurement systems noise floor. Figure 2 shows a normalized frequency offset plot of unit 3. A peak-to-peak deviation of 80 nanoseconds can be seen in figure 3 which is a drift removed phase plot with a frequency drift of -4.45×10^{-14}/day removed. Unit 4 when tested under similar conditions exhibits comparable performance.

TEMPERATURE SENSITIVITY TESTING

An integral part of the planned GPS BLOCK IIR satellite operation incorporates a computer model used to remove the fluctuations in phase due to frequency offset, frequency drift and frequency fluctuations due to thermal changes on board the satellite. Because no active temperature control of the

Rubidium AFS is planned, the exact thermal sensitivity of the AFS must be well understood for this computer model to remove these sensitivity.

Initial temperature sensitivity measurements were made on unit 4 in which the temperature was changed every 6 hours in 5 degree C steps, from 10 C to 35 C and then back to 10 C. Frequency changes ranging from less than 1.0 X 10 -13/C up to 5.0 X -13/C can be seen in figure 4.

Later, EG&G modified unit 4 so that its operating temperature range more closely matched that of the preliminary predicted thermal profile of the spacecraft. Figure 5 shows the results of the latest thermal sensitivity testing done on unit 4 after modification. This test profile called for the temperature to be changed every 8 hours in 0.5 C steps from 15.5 C to 21.5 C and then back to 15.5 C. Analyzing the data from figure 5 points out that between 17.5 C to 21.5 C, the frequency changes were less than 5.0 X 10 -14 /C, while the change in frequency between 15.5 C to 17.5 C was as great as 3.3 X 10 -13/C.

Unit 3 was subjected to a 12-hour thermal cycle with a 3 C peak-to-peak deviation. This 12-hour thermal cycle was chosen to roughly simulate a 12-hour temperature cycle due to the GPS orbit. Temperature sensitivity ranged from 4.0 X 10 -13/C at 17 C to less than 1.0 X 10 -13/C at 27 C.

FUTURE TESTING

Because on-orbit modeling of the EG&G Rubidium AFS is such a vital part of the GPS BLOCK IIR satellite operation concept, a thorough understanding of how closely the clock can be characterized on the ground prior to launch is imperative. The variability between AFS's manufactured will need to be investigated to see the impact it will have on this model.

The best test for evaluating the thermal sensitivities of the Rubidium AFS would be to use the exact thermal profile expected in space. When the GPS BLOCK IIR spacecraft manufacturer completes their predicted thermal profile analysis for the spacecraft, NRL will use this information to derive new tests that more closely corresponds to what the Rubidium AFS will see in space. Additional testing will include a detailed look at the temperature sensitivity of the Rubidium AFS over a much wider range, the repeatability the temperature sensitivities over time, and a detailed analysis of the effect of temperature on drift.

REFERENCES

1. W. J. Riley, *A Rubidium Clock for GPS,* Proceedings of the 13th Annual Precise Time and Time Interval (PTTI) Application and Planning Meeting, pp 609-630, December 1981.

2. T.J. Lynch and W. Riley, *Test Results for Prototype GPS Rubidium Clock,* Proceedings of the 15th Annual Precise Time and Time Interval (PTTI) Application and Planning Meeting, pp 269-280, December 1983.

3. S. Goldberg, T.J. Lynch and W.J. Riley, *Further Test Results for Prototype GPS Rubidium Clock,* Proceedings of the 17th Annual Precise Time and Time Interval (PTTI) Application and Planning Meeting, pp. 145-155, December 1985.

4. F. Danzy and W. Riley, *Stability Test Results for GPS Rubidium Clocks,* Proceedings of the 19th Annual Precise Time and Time Interval (PTTI) Application and Planning Meeting, pp 267-274.

5. S.R. Stein and G.A Gifford, *Software for Two Measurement Systems,* Proceedings of the 38th Annual Symposium on Frequency Control, pp. 483–486, June 1984.

6. G.A. Gifford, J.D. White and H.E. Peters, *Hydrogen Maser Research and Development at Sigma Tau Standards and Test of Sigma Tau Standards Masers at the Naval Research Laboratory,* Proceedings of the 17th Annual Precise Time and Time Interval (PTTI) Application and Planning Meeting, pp. 105–128, December 1985.

7. D.W. Allan, *Statistics of Atomic Frequency Standards,* IEEE Proceedings 54, No. 2, pp.221–230, February 1966.

Frequency Stability
EG&G#3

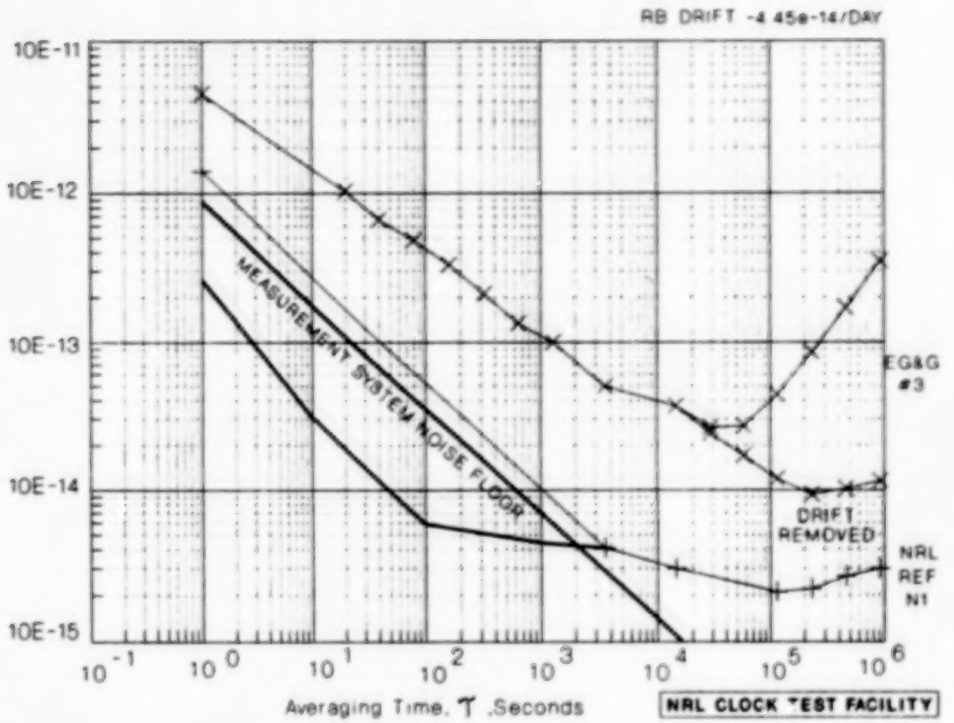


Figure 1

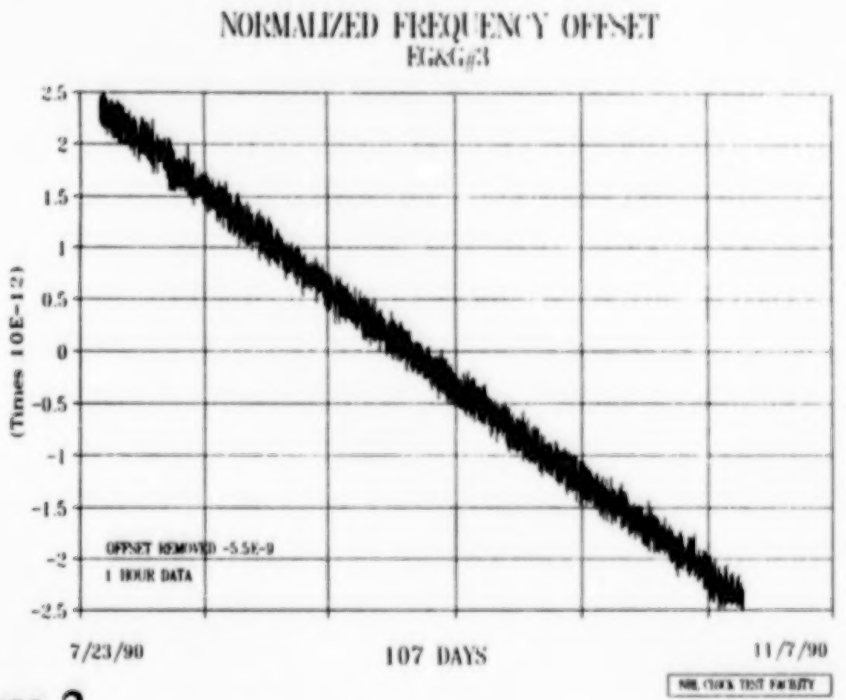


Figure 2

BLANK

PAGE

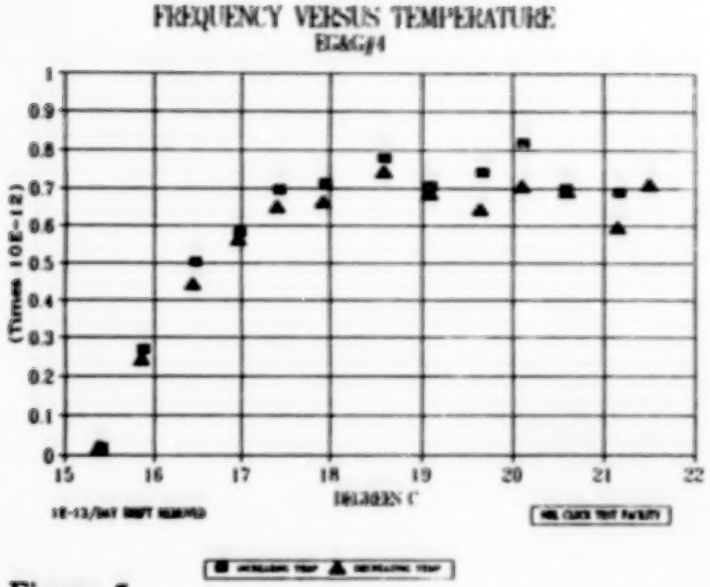


Figure 5

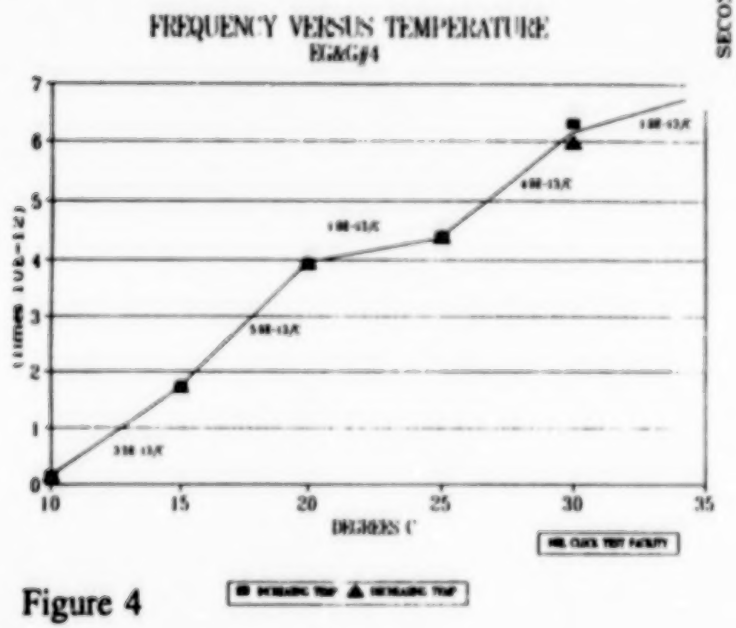


Figure 4

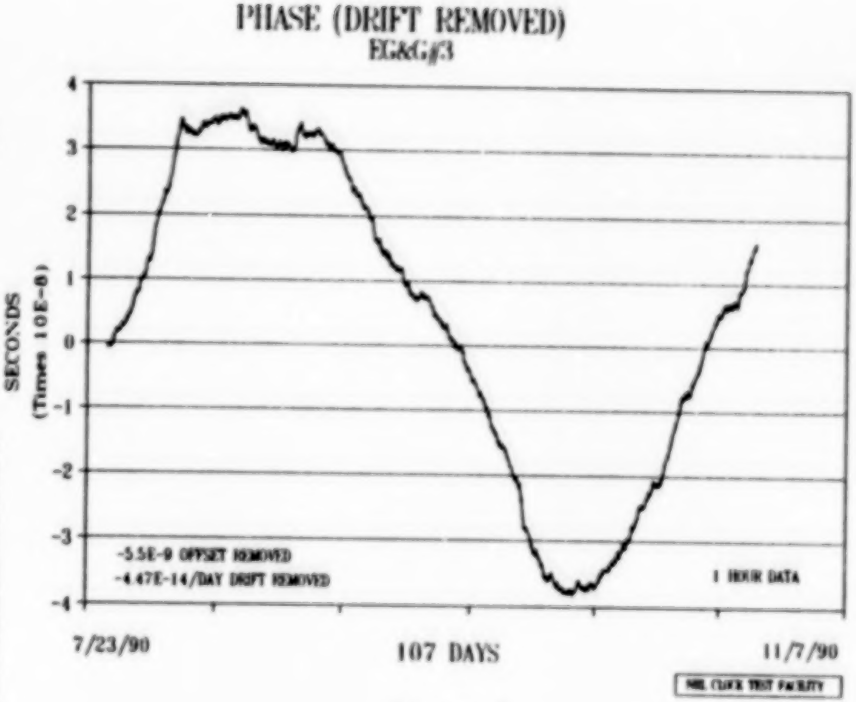


Figure 3

330

ON THE LENGTH OF THE DRIFT REGION IN THE RAMSEY CAVITY

Pierre THOMANN
Observatoire Cantonal de Neuchâtel
Neuchâtel, Switzerland

Abstract

The interaction of atoms in a beam with the microwave field in a separated field geometry such as a Ramsey cavity is generally described in terms of the three regions traversed successively by the atoms, namely two interaction regions of length ℓ separated by a "drift", or "free precession", region of length L. For a monokinetic beam of velocity v, the linewidth of the central fringe in the Ramsey resonance pattern is usually expressed as $\Delta\omega = \pi\, v/L$.

A more detailed calculation shows, however, that the linewidth is equal to $\pi\, v/L^*$, where the equivalent drift L^* is larger than L by an amount of the order of ℓ/L. The correction depends on the field distribution in the interaction regions. Its origin lies in the fact that atomic precession is not limited to the field-free regions but also occurs in the interaction regions, where atomic coherence builds up or decreases continuously.

Although the correction to the equivalent length of the drift region is small, it may be relevant to the evaluation of the second-order Doppler effect bias in primary cesium-beam standards to the extent that the atomic velocity is deduced from the lineshape and from the geometrical parameters of the cavity. It is shown that in current and projected standards with atoms of average thermal velocity, use of corrected dimensions may lead to a change of the calculated bias of the order of 10^{-14}, which is significant at the levels of accuracy considered nowadays.

1. INTRODUCTION

The velocity distribution of atoms in atomic beam standards often needs to be known with considerable accuracy because of its relevance to the determination of the second-order Doppler shift $\delta\nu_D = -(v/c)^2/2$. Several methods have been proposed and used to determine the velocity distribution [1-6]. Most of the methods actually yield a transit-time distribution, through an analysis of the Ramsey pattern lineshape [6], the power dependence of the transition probability at resonance [5], or through the response to RF pulses of varying periodicity [2]. In order to deduce the average velocity and the velocity distribution from such transit-time information, one must know precisely what physical length has been travelled during the measured transit-time. It is often assumed that the relevant length is the separation L between the end of

the first interaction region and the beginning of the second. The following calculation of the linewidth of the central fringe of the Ramsey pattern takes into account the non-zero length ℓ of the interaction regions, which is usually neglected. The calculated linewidth is indeed affected by the finite interaction length, the amount of the correction being of order ℓ/L and depending somewhat on the RF field profile inside the interaction regions.

2. CALCULATION OF THE EFFECTIVE LENGTH

The purpose of the calculation is to establish a precise relationship between the linewidth of the resonance curve, which is directly accessible to measurement, the length of the Ramsey cavity, which is known by construction, and the atomic velocity which is the parameter to be determined. For the sake of simplicity a monokinetic beam of velocity v will be considered; the results can then be extended to actual velocity distributions.

The two levels of the clock transition (F = 4; m = 0 and F = 3; m = 0 in the case of cesium) are coupled to a near-resonant RF magnetic field. We write the familiar Bloch equations for the three components of the magnetic dipole (fictitious spin 1/2) associated to this two-level system. It is convenient, as usual, to write these equations in a frame rotating with the resonant part of the RF-field, and to neglect the fast oscillating antiresonant part. The equations of motion then read

$$\dot{x} = \alpha y \tag{1a}$$

$$\dot{y} = -\alpha x - \beta(t) z \tag{1b}$$

$$\dot{z} = \beta(t) y \tag{1c}$$

where x and y are the transverse components of the fictitious dipole in phase and in quadrature with the RF-field; z is the longitudinal component of the fictitious dipole and the population inversion of the real two-level system ($z = 1$ if $F = 4$, $m = 0$; $z = -1$ if $F = 3$, $m = 0$).

The detuning α is the difference between RF frequency and atomic frequency: $\alpha = \omega_{RF} - \omega_o$; $\hbar\beta(t) = \mu_B B(t)$ is the coupling energy between atom and RF-field ($B(t)$ is the amplitude of the RF field, directed along Ox in the fictitious dipole space).

Since there is no relaxation in this system, the representative vector is of constant length ($x^2(t) + y^2(t) + z^2(t) = 1$ at all times) and its motion is a rotation about the instantaneous rotation vector $\vec{\Omega}(t) = (\beta(t), 0, -\alpha)$.

We will consider the two standard configurations of Ramsey cavities used in cesium standards, namely the E-bend cavity where the RF field amplitude is constant in each interaction region, and the H-bend cavity where the RF field amplitude has a sine envelope. The corresponding time sequences for $B(t)$ are shown in Fig. 1.

2.1 E-BEND CAVITY, EXACT SOLUTION

Since the amplitude of the RF field is constant, B is time-independent during each of the three parts of the evolution and the equations of motion can be integrated analytically in a standard manner [7]. The quantity of interest is the population inversion z at time $T_P + 2T_R$, as a function of the detuning α. For small detunings the exact solution can be expanded in power series of the ratio α/β of the detuning to the Rabi frequency at resonance. Optimum RF power is assumed ($\beta T_R = \pi/2$); for detunings such that $|\alpha T_P| \leq \pi/2$, we have $|\alpha|/\beta \leq \ell/L$.

The usual expression for the lineshape near resonance is the zero order term of the expansion:

$$z\,(T_P + 2T_R) \cong - \cos\,(\alpha T_P) \qquad (2)$$

The approximate linewidth $\Delta\omega$ (FWHM) is equal to π/T_P and the atomic velocity is related to the linewidth by

$$v = \frac{L}{T_P} \cong \frac{L\Delta\omega}{\pi} \qquad (3)$$

If, however, terms of order 1 in α/β are kept in evaluating z, the main change is a narrowing of the fringe spacing and width:

$$z\,(T_P + 2T_R) = - \cos\left[\,\alpha\,(T_P + \frac{4}{\pi}\,T_R)\,\right] \qquad (4)$$

The linewidth is now $\Delta\omega = \pi/T^*$, where the effective transit-time T^* is equal to $T_P + \frac{4}{\pi}\,T_R$.

The distance travelled by the atoms during the effective transit-time T^* is what we call the effective length L^* of the Ramsey cavity

$$L^* = L + \frac{4}{\pi}\,\ell \quad , \qquad (5)$$

to which the velocity is now related by

$$v = \frac{L^*\Delta\omega}{\pi} \quad . \qquad (6)$$

Equation (4) means that the time interval over which the phase of the atomic dipole and the phase of the RF field are allowed to drift apart between the two atom-field interactions extends beyond the field-free interval to include part of the interaction times. The transit-time which can be inferred from the width of the central fringe in the simple case of a monokinetic beam is thus

the time $T^\bullet$ to travel $L^\bullet$, the effective length, instead of the time T_P to travel L in the approximate derivation. Consequently the velocity that can be deduced from this effective time of flight is higher by a factor $1 + \frac{4}{\pi}\frac{\ell}{L}$ (eq. (5)). It may be expected that a similar correction will apply in the case of a real beam when converting the transit-time distribution into a velocity distribution (see also below).

2.2 APPROXIMATE INTEGRATION OF THE BLOCH EQUATIONS

The origin of the additional transit time can best be seen by integrating directly the equations of motion of the fictitious spin 1/2. Although an exact integration is possible in the case of a constant field amplitude, one can settle for an approximate integration where terms of order two in α/β are neglected. This procedure will also allow us to evaluate the effective transit-time and length of an H-bend cavity where the field amplitude is not constant and no analytical solution to eqs. (1) can be found.

We find that the FWHM linewidth, i.e. twice the detuning required for the final inversion to be equal to zero, can be expressed as

$$\Delta\omega = \frac{\pi}{T^\bullet} \quad , \tag{7}$$

$$\text{with } T^\bullet = T_P + 2\int_0^{T_R} \sin\left[\int_0^t \beta(t')\,dt'\right] dt \tag{8}$$

Introducing the explicit field profile $\beta(t)$ (Fig. 1) in the integral, we get

$$\text{E-bend cavity:} \quad T^\bullet = T_P + \frac{4}{\pi} T_R \tag{9}$$

$$\text{H-bend cavity:} \quad T^\bullet = T_P + \sqrt{2}\ J_o(\pi/4)\ T_R \tag{10}$$

The E-bend result is identical to the exact result (eq. (5)) and thus validates the approximate integration procedure used to derive eq. (8).

3. DISCUSSION

The implication of the results above for the second order Doppler shift bias depends on the average atomic velocity and the geometry of the Ramsey cavity. In an optically pumped standard with L = 1 m, $\ell = 10^{-2}$ m, v_{rms} = 300 m/s, the Doppler biases calculated with L and $L^\bullet$ would differ by $1.3 \cdot 10^{-14}$, a value that cannot be neglected anymore.

The linewidth of the central fringe is of course not the only way of measuring transit-times. It seems obvious, however, that the effective transit-time and length described here are the relevant parameters in relating spectral features of the atomic resonator to the atomic velocity or velocity distribution.

The practical case of a velocity distribution introduces a complication in that the optimum power condition assumed in the monokinetic case can no longer be satisfied by all atoms. This has a consequence on the lineshape but it can be shown that the effect on the effective transit time is zero if the transit-time distribution is symmetric. As an illustration of this point we compare the monokinetic results (eqs. (9) and (10)) with results [9] obtained by computing the linewidth of the Ramsey pattern for a real, asymmetric, velocity distribution with a width equal to ~ 10% of average velocity. In the H-bend case, the equations of motion were integrated numerically:

$$\text{E-bend:}\begin{cases} L^{\bullet}\ \text{(monokinetic, eq. 9)} & = L + 1.27\ \ell \\ L^{\bullet}\ \text{(velocity distribution)} & = L + 1.28\ \ell \end{cases}$$

$$\text{H-bend:}\begin{cases} L^{\bullet}\ \text{(monokinetic, eq. 10)} & = L + 1.20\ \ell \\ L^{\bullet}\ \text{(velocity distribution)} & = L + 1.23\ \ell \end{cases}$$

Considering that in the H-bend case ℓ/L was .03, the agreement is within the precision of the monokinetic estimate where terms ~ $(\ell/L)^2$ have been neglected.

CONCLUSION: The concept of effective transit-time and effective length of a Ramsey cavity has been pointed out. The use of these effective parameters in determining atomic velocities may lead to a significant improvement in the evaluation of the second order Doppler bias in atomic beam primary standards.

Acknowledgment. This work was supported by the Swiss Federal Office of Metrology, Wabern, Switzerland.

References

[1] A.G. Mungali, Metrologia 7, 49 (1971).

[2] H. Hellwig et al, Proc. 27th Annual Symposium on Freq. Control, Fort Monmouth, NJ (1973), p.357.

[3] S. Jarvis, Metrologia 10, 87 (1974).

[4] D.A. Howe et al, Proc. 28th Annual Symposium on Freq. Control (1974), p. 362

[5] T. Heindorff et al, PTB Mitteilungen 94, 318 (1984).

[6] J.-S. Boulanger, Metrologia 23, 37 (1986).

[7] J. Vanier, C. Audoin: The Quantum Physics of Atomic Frequency Standards p. 628 (Hilger, 1989).

[8] N. Ramsey: Molecular Beams (Oxford Univ. Press, 1956).

[9] A. Bauch, private communication.

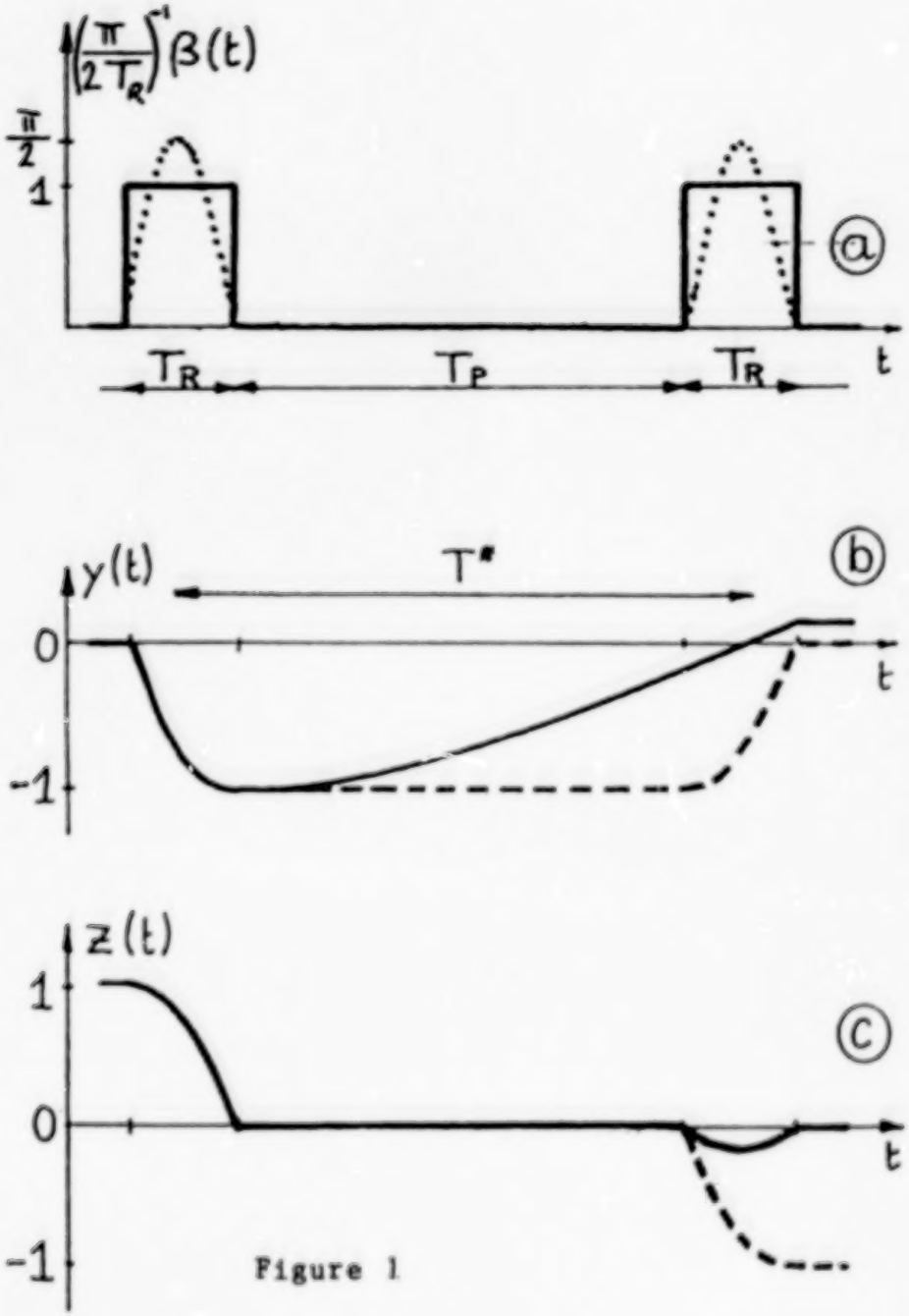


Figure 1

a) Time-dependence of the RF magnetic field B(t) (in Rabi frequency units). Solid line: E-bend cavity; dotted line: H-bend cavity.

b, c) Time-dependence of the atomic dipole y(t) (b) and of the population inversion z(t) (c)

Solid lines: $-aT^* = \frac{\pi}{2}$; dashed lines: $a = 0$

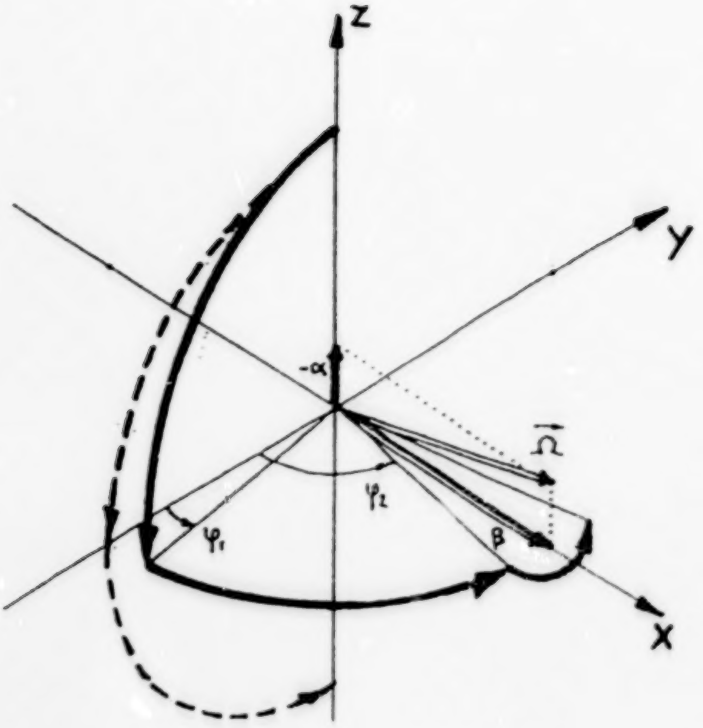


Figure 2: Path of the fictitious spin $\frac{1}{2}$ vector on the Bloch sphere. Solid lines: $-\alpha T^* = \frac{\pi}{2}$; dashed line: $\alpha = 0$.

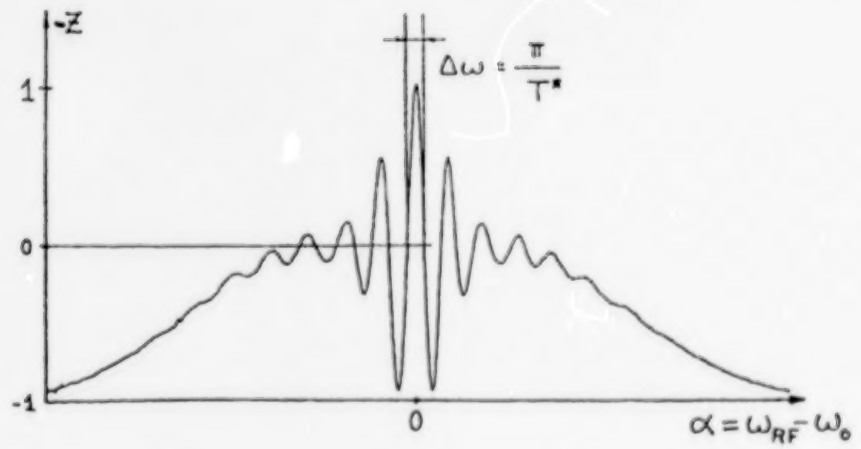


Figure 3: Typical Ramsey fringe pattern and linewidth.

BLANK PAGE

TIME AND FREQUENCY MEASURING METROLOGICAL EQUIPMENT IN THE USSR

Adolph A. Uljanov, Director–General
of Gorky Research and Production
Association "QUARTZ"

Abstract

The complex of the means of providing time and frequency traceability in the USSR includes the system of time and frequency standards of the National Time and Frequency Calibration Service, time and frequency transfer facilities and local time and frequency standards. Control on measurement correctness is performed by the All–Union State Standard calibration service.

The hardware of most of the above–mentioned systems is provided by the instruments developed by our institute. A common scientific and technological approach allowed us to create a unified system of time — frequency equipment composed of widely used serial instruments, sets, automated systems and complexes. Primary frequency standards of different classes, time and frequency references and instruments are based on the unified system. CH1–70 hydrogen frequency standard and its CH1–70A, CH1–80 modifications are used in the group time and frequency standards. Measuring time and data processing techniques, and also instrumentation specifications on the results of 10–year operation are given in the report. The existing system provides time–frequency measurements with $2 \times 10^{-13} \pm 1 \times 10^{-14}$ ***accuracy.***

Metrological equipment, providing traceability of frequency– time measurements in the USSR, comprises:

- a system of frequency–time standards located in different regions of the country;
- equipment for transmission time and frequency units using different communication links;
- reference and working measuring instruments of the consumers.

The system operation, control and also measurement inspection are performed by the National time and frequency service and the National calibration service of Gosstandard USSR.

The major part of the above–mentioned complexes and systems includes instruments developed by our association during the last 15 years. A common scientific and technological approach allowed to create a unified system of frequency–time measuring equipment composed of widely used serial instruments, sets, automated measuring systems and complexes. This unified system includes CHO–100 primary

frequency–time standard of the Main Verification Center of the National time and frequency service, CH0–101, CH0–101B secondary frequency–time standard, CH0-200 reference measuring instruments.

The principle of operation of these instruments is based on time and frequency keeping by the group of hydrogen masers. In this case high precision measurements, achieved by averaging or approximation to the best maser characteristics, and their reliable data are provided.

The frequency and time scale adjustment defined by the comparison between the National frequency–time standard and the given time keeper are taken into consideration in measurements. A multichannel automated measuring system provides the mutual comparison of frequency difference and frequency stability measurement for each pair of hydrogen masers in the group for different time intervals from 1 s up to 1 month. By mutual comparison the measuring system calculates characteristics of each hydrogen maser. Taking into account Allan variance measurement data over short time intervals from 1 s up to 1 day, one performs the choice of the best hydrogen maser as reference, weight estimation of each maser in the group and its operation check. According to the frequency drift measurement the data of each hydrogen maser at intervals per 1 day and more the mean frequency and time scale value of the group in relation to the National frequency standard and also frequency drift and time scale adjustments of each hydrogen maser in relation to the group are defined. The above mentioned data allows to save the history of the group in case of hydrogen maser operation failure or measurement continuity break.

Measurement, data processing and adjustment storage provide sine-wave signals in a wide frequency range and also time scale and various pulse signals at the device output with characteristics approximate to the National standard system.

The output signal accuracy in relation to the National standard depends on the internal and external measurement precision and hydrogen maser frequency stability.

The order of operation of all complex devices is programmed by the software algorithm. All the measurement and diagnostic data are displayed periodically every hour or at any time by the user request.

The consumer may order different equipment: both separate instruments and several measuring systems, including time keepers, complexes or automated measuring systems.

The above-mentioned complexes and systems use the hydrogen maser, type CH1-70 (1980), or its later modification (1987) CH1-80. A detailed discussion of the hydrogen maser characteristics is given in the paper, authored by Dr. Demidov and me for this conference [1]. According to the results of the 10-year operation the frequency-time secondary standards the type CH0-101, in different time and frequency services demonstrate relative time and frequency keeping accuracy about the order of 1to 5×10^{-14} over time intervals from 1 month and more. This information is described in detail in the paper written by Dr. Koshelyaevsky, USSR National time and frequency service expert.

At present the improvement in measurement precision is quite possible with the advent of a new generation of frequency measuring equipment, based on CH1-75, CH1-76 hydrogen masers, CH7-45 frequency comparator and CH7-48 phase comparator, I4-10 time interval meter, frequency precision summer, RUS-39 distribution amplifier and others.

The design and characteristics of CH1-75, CH1-76 hydrogen masers are given in paper [1]. The information on the rest measuring equipment is given shortly below.

Ultrastable frequency signal measurements in the frequency and time domains are provided by conversion of reference and measured signal frequencies. Frequency and phase comparators, spectrum analyzers are based on this principle of operation. In these instruments by frequency conversion a multiplied signal, which is a difference of reference and measured frequencies, is separated, then analyzed by a frequency counter, a time-interval meter or by a narrow-band filter. Mutual spectrum-to-frequency stability conversion and vice versa are also possible. These methods are discussed in detail in papers [2] and some of them have been used in our frequency-time measuring equipment.

The CH7-45 frequency comparator is intended for measuring 5 MHz and 100 MHz signal frequency difference and frequency and phase stability (with external heterodyne input frequency range 2 – 100 MHz). The comparator allows to measure characteristics of crystal oscillator and frequency — time standards and operates in time and frequency measuring systems. The measuring and data calculation processes are performed by a built-in microprocessor, and results are indicated on the liquid-crystal display in the convenient form.

The instrument frequency stability which is defined by the sensitive level of the comparator, is better than 1×10^{-13} for 1 s time interval and better than 1×10^{-15} for 1 h and more. The input frequency difference relative to multiplication factor is $K = 10^3$, 10^4, 10^5; passbands are 10, 30, 100, 300 Hz, 1, 10 kHz; measuring time intervals are from 10 s to 3600 s.

The CH7-48 phase comparator comprises four parallel channels. It is intended for operation in multichannel frequency measuring systems. The input frequency is 5 MHz or 100 MHz. The instrument frequency stability is better than 1×10^{-15} for 1 h.

The I4-10 time interval meter is designed for precision measurement of time interval between two pulses and time pulse parameters. The principle of operation of this meter is based on the method of "charge-discharge capacity by stable currents". The systematic error of measurement is 1 ns. The time resolution is 0.1 ns for time interval 0 – 10 s. The I4-10 operates with pulses of any polarity up to 10 V amplitude and the repetition rate up to 10 MHz. For repetitive sequences it has the measuring mode with noise time base modulation and averaging factor up to 10 which allows to increase the time resolution up to 5 – 10 ps.

Sine-wave and pulse signal distributing amplifiers are designed to provide all systems of the measuring complex and also external equipment with highly stable standard frequency signals. The amplifiers have a low internal noise, a high temperature stability and a high isolation between channels.

The basic characteristics of The RU3-39 sine-wave signal distribution amplifier:

- operating frequencies: 1, 5, 10, 100 MHz;
- input voltage: 0.3 V - 1.5 V;
- input and output resistance: 50 Ohm;
- instrument frequency stability not more than 2×10^{-13} per 1 s;
- temperature stability 0.02 ns/deg.C;
- isolation between channels 100 dB.

The instrument has two distribution channels with distribution factor 1:10.

The basic characteristics of pulse signal amplifier:

- the number of inputs - 6;
- the number of outputs - 16;
- switching in any combination;
- input and output signals - TTL square pulses at 50 Ohm load with 0 - 10 MHz repetition rate;
- the time scattering of signals, formed from one input - not more than ±1 ns.

Time-scale corrector is designed to convert discrete calibrated phase shift to 5 MHz reference signal to provide adjustable coordinate time scale. The instrument is used, mainly, in the time-scale shaping systems of the frequency-time standards. Its principle of operation is built on the pulse sequence summation method, widely used in the frequency synthesis technique. The instrument allows to perform discrete signal phase correction in 0.1 ns–100 ns range with 0.1 ns minimum steps. The basic instrument error — temperature phase shift— not more than 0.05 ns/deg.C.

The frequency precision summer permits to synthesize a signal, the frequency of which is equal to the mean weighted frequency of the group from 2 to 4 5 MHZ highly stable reference signals. It is designed to form and generate average frequency and time scale signal of the group frequency-time standards.

The principle of operation of this instrument is based on the crystal oscillator automatic frequency control by the sum of signals passed from the frequency discriminators. Each discriminator compares crystal oscillator frequency with the frequency of one of the summed signals. The CH7-48 phase comparator is used to improve sensitivity.

The basic summer characteristics:

- instrument frequency instability — 2×10^{-13} per 1 s, 4×10^{-15} per 100 s, 1×10^{-15} per 1 h and more;

All the above-mentioned instruments may be integrated into measuring systems controlled by a computer via IEC 625 bus.

On the base of the above-mentioned instruments and other auxiliary equipment a new generation of frequency-time keepers and standards has been developed. This very generation also uses the group principle of time and frequency keeping and the basic techniques to control the instruments.

Unlike the currently used equipment, a new generation of instruments provides output signals on the basis of converted mean weighted frequency; the assessment and quality control criteria of masers and measuring equipment have been added using the latest measuring techniques and processing of larger data arrays; besides the RF-cavity operating temperature in the hydrogen frequency keepers has been reduced that decreases frequency drift of CH1-75 hydrogen masers by 3 – 4 times. The research on new frequency standards has confirmed a substantial improvement of their characteristics in comparison with the currently available models. They have demonstrated frequency and time scale keeping accuracy not more than 2×10^{-14} or less for intervals up to 1 month.

The use of such frequency standards in the last ten years shows that the improvement of their characteristics by 2 – 3 times compared to the characteristics achieved under the workshop conditions may be possible.

References

1. N.A.Demidov, A.A.Uljanov, *Design and industrial production of frequency standards in the USSR*, XXII PTTI meeting, December 4-6, 1990, Tysons Corner, Virginia, USA.

2. J.Rutman, *Characterization of frequency stability transfer function approach and its application to measurement via filtering of phase noise.* IEEE Transactions on Instrumentation and Measurement v.IM-23 March 1974, p.40-48.

BLANK PAGE

Two-Way Time Transfer Modem

Ivan J. Galysh, Paul Landis
Naval Research Laboratory
Washington, DC

Introduction

NRL is developing a two-way time transfer modem that will work with very small aperture terminals (VSAT), commercial satellites, and an atomic clock. The two-way method has been chosen because of its performance and insensitivity to the position of the receivers and satellites. Precision, stability, accuracy, and versatility are the primary design considerations of this modem. The modem is designed to use many off the shelf components.

Design

The modem can be broken up into several sections, analog box, digital card, and computer (Figure 1). The analog box handles the interface between the VSAT and the digital card. The 5 MHz and 1PPS interface are also implemented in the analog box. There are two digital and two analog test ports. The two digital test ports allow the user to monitor various signals in the digital card. Signals to be viewed are selectable through software. The analog ports are driven by a pair of 12-bit digital to analog converters (DAC). The DACs are driven by the computer.

The second section of the modem is the digital card. The digital card contains the hardware needed to track the carrier and code and make the time of arrival measurements. The card also handles the transmission of data and 1PPS.

The third section of the modem is a personal computer with a digital signal processor (DSP) that controls the digital card and analog box. The computer in this implementation is a MS-DOS compatible computer. The computer is configured as a keyboard, display, and storage interface for the DSP. The DSP used is Texas Instrument's TMS320C30 that runs at 16 MIPS and up to 33 MFLOPS. The DSP may seem to be overkill, but the reason for using such a powerful processor is to leave room for other functions that may be added later. Another reason for choosing this DSP was that a C compiler was available for it to make code writing much easier.

Acquisition

The modem performs a two dimensional search to acquire a signal. One dimension is a time search. This search is to lock the receiver's code generator to the incoming signal's code. The other dimension is the frequency search. The frequency search is performed by reading 64 data samples at a high

rate from the correlators and performing a Fast Fourier Transform FFT on the data and storing the largest magnitude and the bin that it is in. Next, the code generator for the receiver is shifted and another frequency search is performed. This process is repeated over the entire code length. This process allows the modem to find the point where the codes and the frequency produce a maximum correlation. The next step is to match the codes and frequency offset. Once the largest peak is found the receiver's code is aligned with the incoming signal.

Tracking

In the tracking mode, the numerically controlled oscillators used for the carrier and code are adjusted 608 times a second. The DSP first reads the correlators to determine the error signal. The information is then processed through the digital filters. The error information from the digital filters is then used to adjust the numerically controlled oscillators.

Data Transmission

Information can be exchanged between modems. The DSP converts the data into a serial stream. The start of the data is synchronized to the 1PPS. Refer the 1989 PTTI paper for details on the data format.

Time of Arrival Measurement

Data is sampled from the correlators at a 608 Hz rate. The code cycles at the same rate and generates an epoch pulse. Time of arrival measurements are made on each sample. As shown in Figure 2, the time of sample resolution is 40 ns. The time of arrival measurement (TOM) occurs on that boundary and the epoch occurs somewhere within the 40 ns. The slope of the line is the phase slope of the receiver's code. The phase 'y' is measured phase at 'TOM'. To determine the time of arrival (TOA), the TOM and y are measured at the occurrence of the epoch. The measurements, along with the known slope, are entered into the line equation (Figure 2) and the TOA is found. Of the 608 TOAs found, one of them occurred on the 1PPS. To better the resolution of the TOA, the 608 points are curve fitted with the 1PPS point in the middle. The curve fit helps reduce the noise in the measurements and gives the TOA for the 1PPS better resolution.

Conclusion

One modem prototype is built and is being debugged. The modem has acquired and tracked signals and made time of arrival measurements. The next step is to get the communications software working and develop the control software for the system. The last step is to test the system and evaluate it.

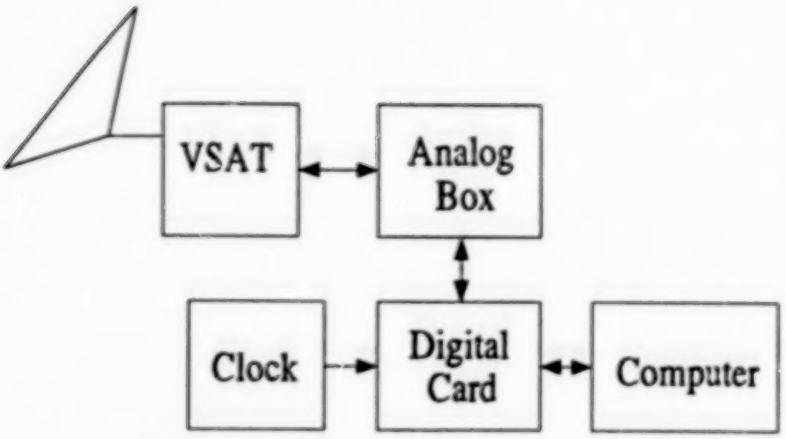


Figure 1 Modem Block Diagram

Time of Arrival Measurement

25 MHz / 2.5 MHz = 10 steps/sawtooth

2.5 Mhz = 400 ns.

Resolution = 400ns/ 2^{12} ~ 100psec

TOA = TOM - y/m

m = phase slope
y = phase at TOM
TOA = time of arrival
TOM = time of measurement

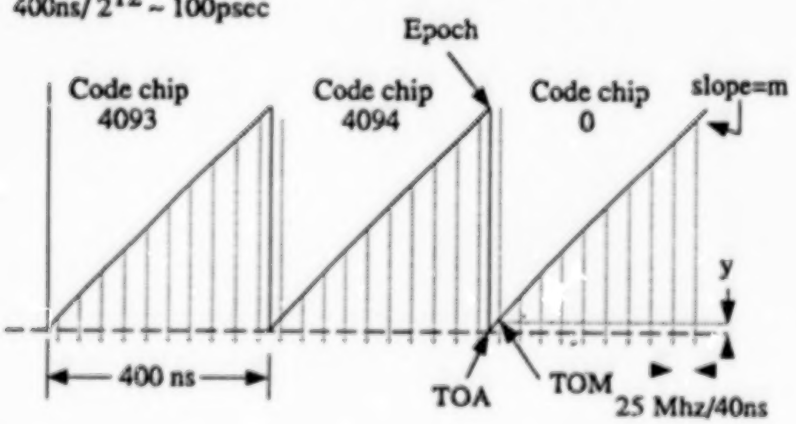


Figure 2 Time of Arrival Measurement

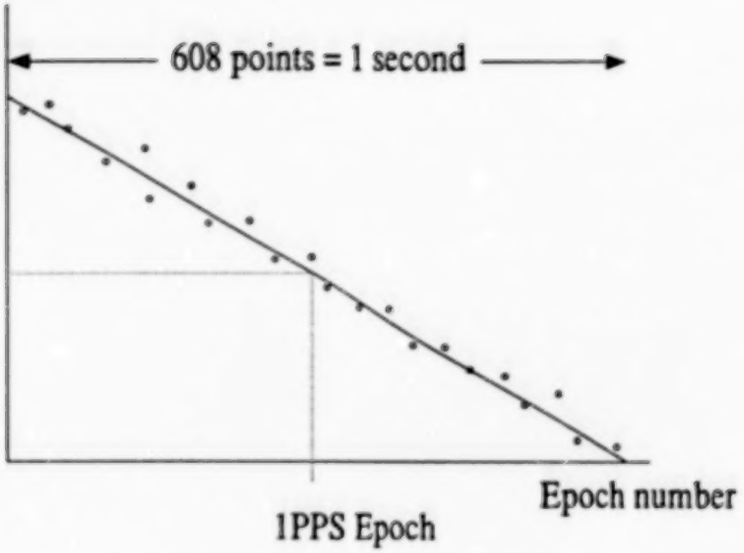


Figure 3 Curve Fit of TOA's

SPECIAL HYDROGEN MASER WORKSHOP[1]

Held on Wednesday, December 5, 1990

Report by
D. Morris
Institute for National Measurement Standards
National Research Council
Ottawa, Ontario, Canada K1A OR6

As part of the 22nd Annual PTTI Meeting, this workshop was held as a discussion forum for hydrogen maser problems, particularly for those related to wall shift and wall relaxation effects. The chairman of the workshop was Jacques Vanier, National Research Council of Canada.

Following are brief summaries of the presentations made by the speakers together with some of the discussion that followed. These summaries were derived from tape recordings of the session and from notes made by Derek Morris.

J. Vanier (National Research Council of Canada)

In his opening remarks, Dr. Vanier stated that the wall effect in hydrogen masers was the main problem under discussion. He asked the speakers to speak frankly about results which they had found. He expressed the hope that frank discussion of the problem would suggest further experiments which might be tried to clarify the problem.

Dr. Vanier presented some data on two masers built at Laval University. The results represented 5 years of experiments, showing the line-Q (extrapolated to zero pressure) varying with time. For a 16.5 cm diameter bulb, the line Q was initially $6\text{-}7\times10^9$. However, it decreased with time and still had not stabilized after 5 years. A smaller bulb (11.5 cm diameter) showed a less rapid decrease in line-Q with time and the value appeared to stabilize. The reason for the behaviour was not clear.

Possibly there could be contamination from Viton O-rings used, or from silver solder used to braze the palladium leak valve. Both bulbs were coated with FEP-120 Teflon.

C. Audoin (Laboratoire de l'Horloge Atomique, France)

Dr. Audoin gave information on four hydrogen masers constructed at his laboratory. All had bulbs coated with FEP-120 Teflon. No wall shift measurements were made, but measurements of the transverse relaxation time T2 (proportional to the line-Q) were made. For one maser (built around 1970) which used metal gaskets throughout, T2 showed a continuous decrease from 515 ms to 320 ms. The maser eventually stopped oscillating, and the bulb was recoated in 1989 with Teflon purchased in 1978. After the recoating, T2 was measured as 515 ms again, i.e. it returned to its original value.

[1]Editors note: This summary was prepared by Dr. Morris from tapes of the workshop and from his notes. Time did not permit proofreading of the text by the various speakers, so if there is a question, please contact the individual speakers directly.

Later, three smaller masers were built for radioastronomy use. These use some Viton O-rings. The bulbs of these were coated in 1984 with the same batch of Teflon (bought in 1978). The value of T2 decreased more rapidly than for the older maser and the oscillation level decreased. This was particularly true for masers #2 and #3. In 1988 the bulb in maser #2 was recoated with the same batch of Teflon. Afterwards, T2 decreased very rapidly. In the last year or two, this bulb has been recoated, this time with new Teflon. So far, T2 seems to be more stable. For maser #3 it is not certain if T2 has changed further.

Dr. Audoin also mentioned that the masers at his laboratory are shut down for the whole of the month of August each year, with only the vacuum pumps and temperature controls left in operation. When they are set in oscillation again each September the oscillation level is found to be higher initially and then decreases within a few days. In discussion of this effect, it was suggested that contributing causes may be a change in the efficiency of the dissociator after start-up and/or surface absorption of hydrogen on the storage bulb.

H. Schweda (Observatoire Cantonal Neuchatel, Switzerland)

Dr. Schweda presented results for an EFOS hydrogen maser whose storage bulb had a bad coating. The line-Q (extrapolated to zero pressure) decreased from 2.1×10^9 to 1.4×10^9 over 140 days without apparent stabilization of the final value. In addition, the maser output decreased and the frequency (corrected for cavity tuning) showed a non-linear increase with time. The bulb was then recoated with FEP-120 using nominally the same procedure but with better control of parameters, and put back in the same maser with the same hydrogen source. This time the initial line-Q was 2.5×10^9. It decreased to 2.3×10^9 but had stabilized at this value after 180 days. Attempts are being made to characterize test specimens of Teflon coatings using infrared spectroscopy, electron spin resonance and photoelectron spectroscopy. During discussion on this paper, surprise was expressed that the frequency of the maser increased with time. Several other laboratories have found the frequency decreasing with time. In discussions as to possible causes of a "bad" coating, H.T.M. Wang (Hughes Research Laboratories) mentioned that in one case when a maser had stopped oscillating after two months operation, destructive testing on the bulb showed the presence of titanium on the wall (presumably sputtered from the ion pump).

A. Kirk (Jet Propulsion Laboratory, USA)

Mr. Kirk presented frequency data for six JPL (manufactured by SAO) masers located in different parts of the world as part of the Deep Space Network. Two masers are located at each site, so that one can be tuned against the other. In operation, the masers slowly drift in frequency and the procedure employed is to allow the frequency of a maser to drift until a limit is reached ($+ 5 \times 10^{-13}$). Then the field is checked, the maser is tuned, the line-Q is checked and the synthesizer is calibrated against the NIST time scale. Then the maser cavity is deliberately mistuned to give a maser frequency offset of -5×10^{-13} and the maser is left to run again for about a year before the procedure is repeated. Over the period 1978 to 1990 several masers have shown changes in the synthesizer frequency, indicating that the wall shift is changing. After correcting for the change due to cavity aging, the maser frequencies have all shown a decrease with time. A change of several parts in 10^{12} has occurred for the older VLG-10 masers; the newer VLG-11 units seem to have shown less effect. In one maser a bulb was recoated because the line-Q had deteriorated. The frequency was different by 1×10^{-12} afterwards. In all other cases, the line-Q was stable over the 12 year period.

In many cases, the masers were opened to the atmosphere prior to the tuning measurements in order to replace the ion pump elements. In the future, the maser parameters will be measured before and after replacement of the elements.

E.M. Mattison (Smithsonian Astrophysical Observatory, USA)

Dr. Mattison showed a transparency which replotted the data presented by A. Kirk and showed the frequency decrease of 1 to 2 $\times 10^{-15}$ per day due to wall shift change. He also showed the frequency change due to cavity dimensional changes, as derived from varactor voltage changes required to retune the cavity. The characteristic of this is a decreasing slope with time. All the cavities studied were made of Cervit, and the frequency changes found were consistent with the shrinkage of the actual material of the cavities.

R.F.C. Vessot (Smithsonian Astrophysical Observatory, USA)

Dr. Vessot discussed results obtained on the wall phase shift per collision, $\Delta\phi(T)$, as a function of the inverse of temperature. A change of slope occurs, which is indicative of the change of state of Teflon. In France, Dr. Desaintfuscien obtained data down to a temperature of 77 K. Dr. Vessot's group obtained data to 60 K before maser oscillation stopped. They found that further insight into the process occurring on the wall could be obtained by plotting $-T\Delta\phi(T)$ versus $1/T$. The energy of the interaction of the atom when it resides on the surface could be derived from the plot. The slope was 143.3/T. When carbon tetrafluoride was frozen on the bulb wall, a lower value of wall shift was found but the data on the plot showed the same slope as before. This indicates that the interaction energy was unchanged but that the surface area was changed by a factor of 3 or 4 compared to that of the Teflon.

The USSR material, Fluorocarbon F-10, has a lower wall shift than FEP-120, perhaps by a factor of 8. This may be due to a better surface area. Experiments with this material over a range of temperature are required in order to clarify this.

D. Morris (National Research Council, Canada)

Dr. Morris presented results showing a decrease in frequency of a hydrogen maser (after correction for cavity tuning) over a period of 10 years as compared with the NRC primary cesium clock CsV. This change in frequency is attributed to a change in wall shift of the bulb. This bulb was coated in 1980 with 4 coats of FEP-120 Teflon which had been purchased in 1965. The total frequency change which occurred in 10 years was 7.2 $\times 10^{-12}$, or about 2 $\times 10^{-15}$ per day. During the same period the line-Q at operating beam flux showed changes less than 19%. The maser used has many Viton O-rings. It was not run continuously for the whole period, but the cumulative time of oscillation was 7 years. Measurements over periods of 1 to 3 years on four other bulbs, three of which were coated with FEP-120 and one with Teflon 42, have also shown frequency decreases of approximately the same magnitude.

Recently, two new masers have been put into operation. These use metal gaskets throughout. The storage bulbs were coated in 1987 with a batch of FEP-120 purchased in 1985. No wall shift data are available, but one maser has shown a degradation in line-Q of about 30% in one year.

In comments, Dr. F. Walls (NIST) stated that in passive masers he has built they found changes in frequency less than 2×10^{-16} per day. He feels that careful filtering of the FEP-120 dispersion to remove any large particles is important.

H.E. Peters (Sigma Tau Standards Corporation, USA)

Mr. Peters stated that a number of design features of their masers were different to those built in other laboratories. For example, they use metal cavities, non-spherical storage bulbs, and cavity frequency switching servos. In addition they coat their bulbs differently; only one coat is used and the firing temperature is different. He showed results obtained at the U.S. Naval Observatory with Sigma Tau maser NAV-2 from one month after it was delivered in November 1989 up to August 1990. The frequency of this maser showed a slope of $+ 3.2 \times 10^{-15}$ per day initially versus TAI. This has decreased to $+ 9.4 \times 10^{-16}$ per day more recently. The increase in frequency with time is typical of all their masers. A second set of results was presented for 4 other masers over 90 days. All showed a drift of $+ 2 \times 10^{-15}$ per day relative to TAI. Mr. Peters said that it is conceivable that frequency changes might be due to a drift in the electronics but it is unlikely that, in this case, all the 24 masers that they have built would show a frequency change in the same direction. Therefore, he feels that either the wall shift is changing with time or the ratio of the hydrogen and cesium hyperfine frequencies is changing with time, which would imply that the fundamental constants are changing.

J. Ponsonby (University of Manchester, UK)

Dr. Ponsonby drew attention to a form of Teflon, designated Teflon AF, which dissolves in perfluorinated solvents. According to an article cited (Electronic Product Design, Vol. 1 1, No. 10, p. 22, October 1990) defect-free layers as thin as 0.2 μm can be put on using this material and can be removed with an appropriate solvent.

In discussion, Dr. R. Vessot (SAO) said that they had purchased some of this material and had used it to coat glass slides. It has a higher specific gavity than FEP-120. It was found to stick to glass only if the surface had been roughened by sandblasting. He felt that it would be worthwhile to try Teflon AF in hydrogen masers.

J.J. Suter (Johns Hopkins University, Applied Physics Laboratory, USA)

Dr. Suter described experiments to determine if exposure of a storage bulb coated with Teflon to nuclear radiation affected the line-Q. In one maser the bulb was recoated and the line-Q was measured. Then the bulb was removed and was irradiated in air by a commercial company with 10 krads of 1.25 MeV photons from a gamma ray source. After irradiation the bulb was put back in the maser, and it was found that the line-Q had increased by between 6% and 15%. He emphasized that this was based on just one experiment. They are planning to repeat this experiment on another hydrogen maser under more carefully controlled conditions.

They also have an ongoing program examining irradiated Teflon samples on quartz slides, using microscopy. He showed results obtained using an X-ray topography technique on such a slide before and after irradiation. The X-rays were focussed on a part of the slide where some lamellae of the Teflon could be seen. The measurements indicate that the density of the layer is decreased by the irradiation. He feels that a change in polymerization of the Teflon is occurring on irradiation, but he had expected

the line-Q to decrease rather than increase.

A.A.Uljanov ("QUARTZ" Research and Production Association, USSR)

Dr. Uljanov gave same details of the "QUARTZ" company. This company specializes in the development of measuring devices and medical instrumentation. It consists of a scientific institute, two laboratories and five production plants, and employs a total of 20,000 people. Dr. Uljanov is director of the company and director of the institute. The company produces frequency standards based on rubidium, cesium and hydrogen. The company has 15 years experience with hydrogen masers, and has produced the system used in the State Standard of Time and Frequency in the USSR.

N.A. Demidov ("QUARTZ" Research and Production Association, USSR)

Dr. Demidov stated that the stability of the wall shift in a hydrogen maser depends on the material used (they have used Fluorocarbon F-10 recently), on the method of application, and also on the level of residual gas in the storage bulb. He gave information on a poor coating. The bulb was operated at a temperature of 50°C, and the maser showed a large change in frequency with time at first. This is believed to be due to outgassing of the coating. The bulb was then operated at 37°C and the frequency change then diminished. Thereafter, the temperature of the bulb was raised to 50°C without removing it from the maser, and the stability of the wall shift improved. In their masers they use a three-section vacuum system. By improving the technology of their masers they have lowered the drift in wall shift. As described in the paper by N.B. Koshelyaevsky of VNIIFTRI given on December 4, the drift in wall shift of their masers was about 1×10^{-16} per day. No data are available for the latest masers but the results are expected to be about the same as this. Dr. Demidov feels that higher bulb operating temperatures tend to give rise to greater frequency drifts. Therefore, they are planning to put a CHI-75 maser in a refrigerator at VNIIFTRI to reduce the bulb temperature to 20°C. In addition to an increase in the stability of the resonator by this means, a reduction in wall shift drift should occur.

There were a number of questions regarding the F-10 coating material (made in Leningrad), which apparently has a smaller wall shift than FEP-120. Dr. Deniidov said that the material is in the form of a suspension in water with additional surfactants. Three layers are usually used on a storage bulb. The coating procedure is as follows: – a small amount of the suspension is placed in the bulb and the material is dried on the wall using a stream of dry nitrogen. The bulb is then baked at 120 - 140°C. A second coat is then applied in the same way, and, if possible, a third coat is applied. If the third coat cannot be put on successfully the coatings have to be removed and the complete procedure repeated. If the firing temperature is raised to 260°C after the first coat, it is not possible for a second coat to adhere. The average time to coat a bulb is from 3 to 7 days. Several patents have been obtained for the coating procedure.

He mentioned that in addition to the maser with a flexible storage bulb which he described in a paper on December 4 they are now working on an improved design of flexible storage bulb maser.

H.T.M. Wang (Hughes Research Laboratories, USA)

Dr. Wang discussed some results which, although not directly connected with the wall shift problem, were relevant to masers with Viton O-rings. In 1983 they built a small maser which used some O-rings, and was pumped by a getter pump and a small ion pump. The output frequency of the maser

was stable. When the ion pump was switched off the maser continued to oscillate but the frequency drifted. There was no detectable vacuum leak. However, when a residual gas analyzer was put on the system it was found that, with the ion pump off, the partial pressure of argon after five weeks rose to three times that of the hydrogen. This was attributed to argon permeation of the Viton seals. It was thought that this might be responsible for the frequency change that was found. Therefore, they have used metal gaskets on later masers.

Dr. Vessot (SAO) said that they had observed similar affects. For that reason, when they built a lightweight maser which had some O-rings, they baked it at 100°C for 3 weeks to outgas it, and used a small ion pump in addition to the sorption cartridge. Residual gas analysis showed that the argon contamination was greatly reduced. He does not feel that argon is causing wall shift problems. Contamination by hydrocarbons is a more likely cause. Both speakers agreed that it is desirable to use metal gaskets throughout the maser.

G.M.R. Winkler (U.S. Naval Observatory)

Dr. Winkler described the performance of 12 hydrogen masers (6 made by Sigma Tau Standards Corporation and 6 by the Smithsonian Astrophysical Observatory) in use at USNO. All of these masers have exhibited constant frequency drift rates. The masers are in five locations which are up to 200 m from the central monitoring location. Phase measurements between them are made at 100 s intervals, with a resolution of 5 ps. He discussed the possible effect of impurity atoms not only on the storage bulb wall but also on the dissociator. Impurities in the discharge may cause variations in the hydrogen flux which can cause output frequency variations, if the cavity is slightly detuned.

Nevertheless, under optimum conditions at USNO they have been able to reproduce the variations of an unknown maser oscillator over a period of 95 days within 1 ns with respect to the mean of the group. He stressed that any change in maser environment causes instability. He has found that, after an interruption, the subsequent re-establishment of various servos may cause changes which can last for a week.

Further discussion

Dr. L. Maleki (JPL) referred to a suggestion by Prof. Norman Ramsey that diamond films might make a good storage bulb coating material if the technology could be worked out, and asked if anyone knew if such films had been made. Dr. H.T.M. Wang (Hughes Research Laboratories) said that experiments were being carried out for the production of diamond films on substrates for integrated electronics. Dr. R. Vessot (SAO) said that he understood that there was a process available by which diamond films could be put on flat plates. So far, such films have not been tried on bulbs. He feels that perhaps a more promising material to try is Fomblin oil. This is a stable perfluorinated oil which Prof. Ramsey has used for storing polarized neutrons.

Closing remarks

In his concluding remarks Dr. J. Vanier said that, although there are still many unanswered questions regarding the wall shift problem in hydrogen masers, he felt that the presentations and discussion had been valuable in pointing out further avenues for exploration.

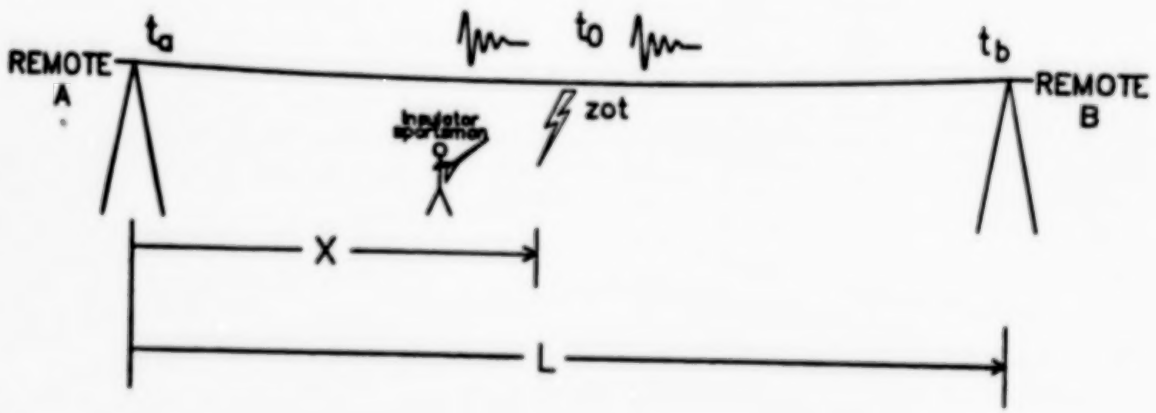
DELIVERY AND APPLICATION OF PRECISE TIMING FOR A TRAVELING WAVE POWERLINE FAULT LOCATOR SYSTEM

Michael A. Street
Telecommunications Systems Branch
Division of Electrical and Electronics Engineering
Bonneville Power Administration
Portland, Oregon

Abstract

The Bonneville Power Administration has successfully operated an in-house developed powerline fault locator system since 1986. The BPA fault locator system consists of remotes installed at cardinal power transmission line system nodes and a central master which polls the remotes for traveling wave time-of-arrival data. A power line fault produces a fast rise-time traveling wave which emanates from the fault point and propagates throughout the power grid. The remotes time-tag the traveling wave leading edge as it passes through the power system cardinal substation nodes. A synchronizing pulse transmitted via the BPA analog microwave system on a wideband channel synchronizes the time-tagging counters in the remote units to a differential accuracy of better than one microsecond. The remote units correct the raw time tags for synchronizing pulse propagation delay and return these corrected values to the fault locator master. The master then calculates the power system disturbance source using the collected time tags. The system design objective is a fault location accuracy of 300 meters. This paper describes BPA's fault locator system operation, error producing phenomena and method of distributing precise timing.

Figure 1 illustrates the basic principle of operation of the BPA fault locator system, which is known as the Fault Location Acquisition Reporter or FLAR system.



BASIC FAULT LOCATOR PRINCIPLE
FIGURE 1

Figure 1 illustrates a line of length L. A FLAR remote is coupled to each end of this line. A FLAR remote is actually a fancy electronic stopwatch. However, each remote timer is synchronized to a common timing standard. When a fault occurs at time to at a distance of X miles from an end of the line, the resulting arc (*ZOT!*) to ground or adjacent conductor causes transients with 2 to 10 microsecond leading edge rise–times to emanate from the fault point to the ends of the line at the finite velocity of 0.18628 miles per microsecond. The FLAR remotes time tag the transient arrival times to an accuracy of one microsecond. A microsecond time tagging accuracy will allow a fault location accuracy to as good as 1000 feet which is the typical distance between transmission line towers. By knowing the line length L and the time–of–arrival difference $(t_b - t_a)$, one can calculate the distance X, from the closest end by using the famous fault location equation:

$$X = \frac{[L - c \times (t_b - t_a)]}{2}$$

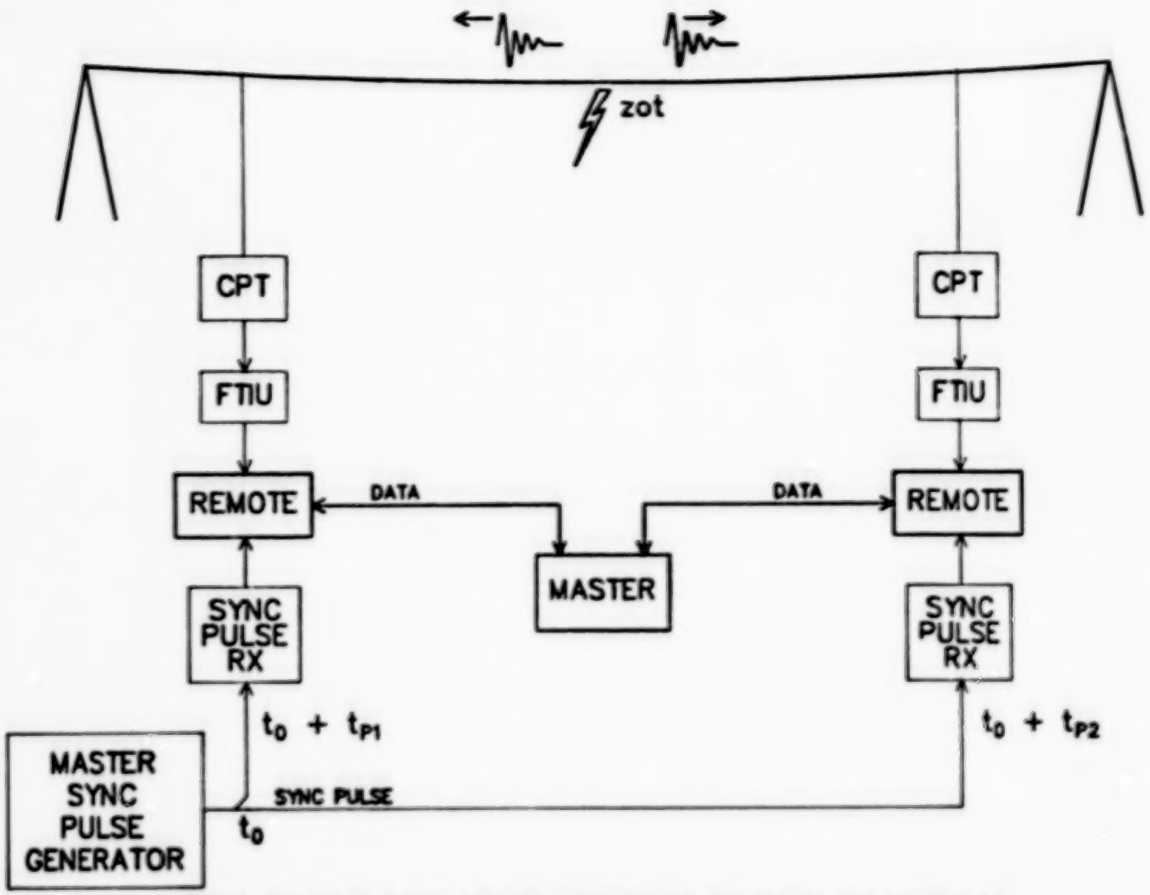
Where: L = Line length
c = Velocity of Propagation
= .18628 mi/usec
t_a = End A arrival time
t_b = End B arrival time

FAMOUS FAULT LOCATION EQUATION
FIGURE 2

Figure 3 shows a functional block diagram of the BPA fault locator system. The system master is located at the BPA Dittmer Control Center near Vancouver, Washington. Remotes are located at major nodes in a grid of 500 kV power transmission lines which cover the BPA service area of Oregon, Washington, Idaho and Western Montana. These nodes are called substations in the power utility business.

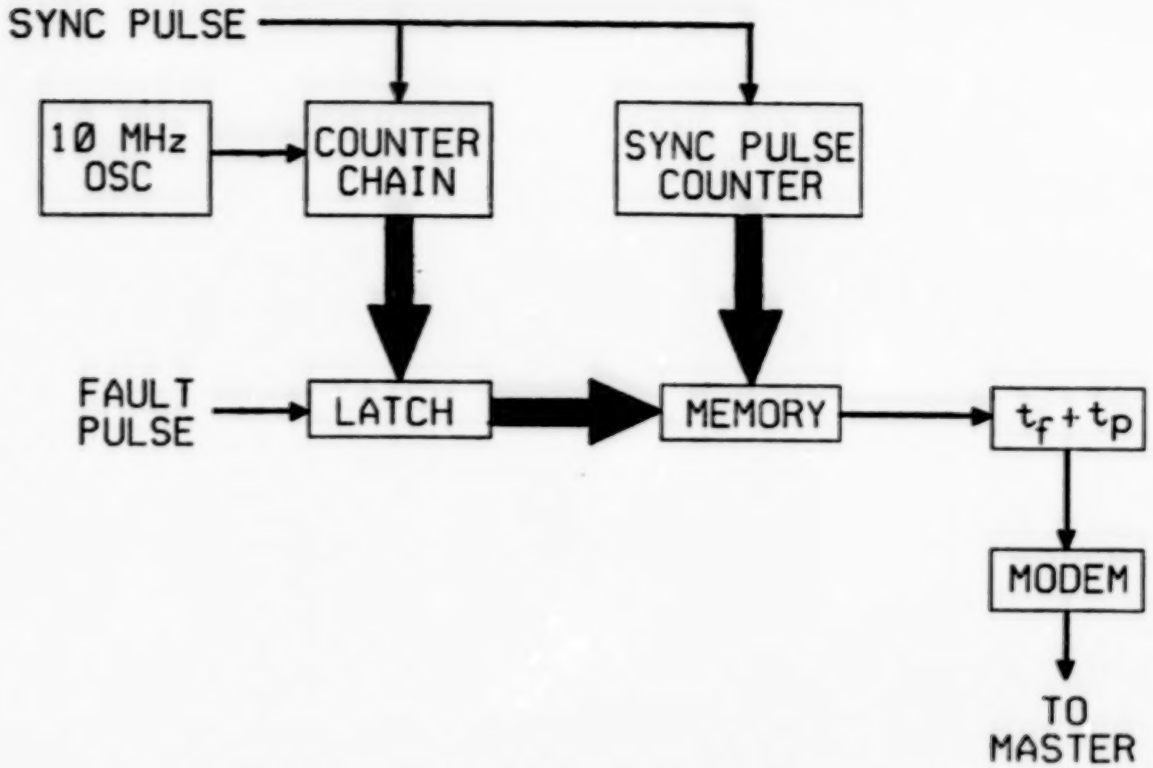
From the BPA Dittmer Control Center in Vancouver, Washington, 100 second period sync pulses, which synchronize each remote counter, are transmitted to the remotes via a wide bandwidth microwave channel on the BPA analog microwave network which covers the BPA service area.

At a substation equipped with a fault locator remote unit, fault pulses are coupled from the power lines to the fault locator remote via powerline coupling devices, known as Capacitive Potential Transformers (CPT). The CPT functions as an LC high pass filter which blocks 60 Hz energy, but passes the high frequency components of fault transients. The Fault Transient Interface Unit (FTIU) will accept transient pulses from up to three CPT's. When the FTIU detects a valid fault transient, it outputs a TTL pulse to the remote which time tags and stores the transient's arrival time. The Fault locator master retrieves the fault data by polling all remotes sequentially at the end of each 100 second period. The FLAR master then uses the transient arrival time data to calculate the fault location in response to operator commands.



BPA FAULT LOCATOR SYSTEM BLOCK DIAGRAM
FIGURE 3

Figure 4 illustrates a basic fault locator remote block diagram. The fault locator remote includes an accurate 10 MHz crystal oscillator. A divide-by-5 divider then produces a 2 MHz counter clock which drives a synchronous decade counter chain. This counter chain counts from 0 to 100 seconds in .5 microsecond increments. The counter is synchronized by the 100 second period sync pulses from the sync pulse receiver. This 0.01 Hz sync pulse train also acts as the reference frequency for an Electronic Frequency Control (EFC) loop which keeps the remote local oscillator locked to the master frequency reference from which the master sync pulse is derived. In normal operation, the counter will rollover from 99.999 999 5 seconds to zero at the same time a sync pulse is received. Re-starting the counter chain every 100 seconds minimizes accumulated time error while the local oscillator is acquiring lock. The master and all remotes also have a sync pulse counter which counts the sync periods since an absolute reference time. The master updates this reference time every three hours. A valid fault pulse received from the FTIU causes latches connected to the counter chain outputs to latch the instantaneous counter outputs. This stored count is the raw fault arrival time. The remote CPU then stores the raw fault time and corresponding sync pulse count in memory.



BASIC FAULT LOCATOR REMOTE BLOCK DIAGRAM
FIGURE 4

However, the remote counter time is delayed in respect to the master sync pulse time by the microwave free space propagation delay time (t_p) from the BPA control center to the remote site. Thus, the latched counter time must be corrected to master time by adding t_p to the raw value before it is used to calculate a fault location. This is done in the FLAR system at each remote during the process of transmitting the raw fault times to the master at each polling time. The propagation time correction is done at the remotes rather than the master to facilitate the future design of a time code interface unit which will provide accurate time code output from the FLAR remote unit. The remote then calculates the actual transient arrival time by adding the latched counter value plus 100 times the sync pulse counter to the base absolute time.

Sync Pulse Derivation

During the early years of the FLAR system, the master sync pulse was derived simply by dividing the output of a 10 MHz crystal oscillator by 109 to obtain the 100 second sync pulse period. Since the EFC loops in all the remotes caused all the remote local oscillators to track the master oscillator, the master oscillator drift requirements were not extremely tight. However, in 1987, BPA extended fault location coverage to a major power line which is jointly owned by BPA and The Montana Power Company. The far end of this line is not served by the BPA analog microwave system. Synchronizing the far end remote via the MPC digital microwave system did not prove successful.

Thus, BPA chose to use the Global Positioning System (GPS) as a timing source so that the BPA remotes and the remote at the MPC site were synchronized to a common timing source. Currently, the master sync pulse is supplied by a GPS timing receiver which is configured to output a sync pulse on the hour and every 100 seconds there after. This then allows an identical GPS receiver to synchronize

the fault locator remote located at the isolated MPC substation.

Sources of Fault Location Error

Fault location error results from three basic error sources:

- Fault Detection Error .5 to 5 microseconds
- Time Tagging Resolution 0 to .5 microseconds
- Sync Pulse transmission Jitter .15 to .35 microseconds

Fault Detection Error - Fault detection error is, by far, the most significant error producing phenomenon. As a fault transient propagates along a transmission line, its amplitude decreases and rise-time increases. The FTIU employs a level comparator to detect that a significant disturbance has occurred. A transient with a longer rise-time will experience a longer delay through the FTIU than a faster rise-time transient. A transient which occurs near the center of the line sections between two remotes will have similar rise-times after propagating to those remote sites. Thus, the additional error will cancel when the arrival time difference is calculated. However, when the fault location occurs closer to one remote relative to the other, the residual error difference will increase and produce a location calculation error.

Counter Resolution — Detected faults are time-tagged by the synchronous counter which counts in steps of .5 microseconds. Obviously, fault transients are asynchronous to the remote clock, thus the remote adds from 0 to .5 microseconds of waiting time error to the time tagged value.

Sync Pulse Jitter — A remote counter chain is reset to zero by a sync pulse received via the BPA analog (FDM) microwave system. Because the sync pulse is transmitted in the presence of additive white gaussian noise (AWGN), a certain amount of timing error jitter will occur. The measured value of this jitter varies from .15 to .35 microseconds RMS and increases with increasing microwave circuit distance from the BPA control center.

SUMMARY

The Bonneville Power Administration has successfully operated an in-house developed powerline fault locator system since 1986. This system has reduced the time required to find and repair power line outages. This translates into savings of both line maintenance personnel costs and lost power sales revenue. The BPA fault locator system consists of 23 remotes installed at cardinal power transmission line system nodes and a central master which polls the remotes for traveling wave time-of-arrival data. The remotes are fancy stopwatches which accurately time-tag disturbance arrival times to a microsecond level accuracy. An accurate sync pulse transmitted via the BPA analog microwave system synchronizes all remotes to a common timing reference. Future system plans include installing 15 additional remotes and developing a remote unit time code output interface to produce microsecond accurate time code for other substation time tagging requirements. The primary error sources are: Fault detection error, counter time tagging resolution and sync pulse transmission time jitter due to broadband noise.

Dr. Gernot Winkler, U. S. Naval Observatory: Where do you get the number of 250 nanoseconds for the GPS receivers?

Mr. Street: That is the specified number that we got from the manufacturers. We are actually getting numbers larger than that in practise, measuring two receivers side by side in our laboratory.

Dr. Winkler: What receivers were they?

Mr. Street: I prefer not to give specific manufacturer names in a public forum. If you see me later, I can discuss it with you.

PRECISE SYNCHRONIZATION OF PHASOR MEASUREMENTS IN ELECTRIC POWER SYSTEMS

Dr. A.G. Phadke
Virginia Polytechnic Institute and State University
Blacksburg, Virginia 24061–0111, U.S.A.

Abstract

Phasors representing positive sequence voltages and currents in a power network are the most important parameters in several monitoring, control, and protection functions in interconnected electric power networks. Recent advances in computer relaying have led to very efficient and accurate phasor measurement systems. When the phasors to be measured are separated by hundres of miles, it becomes necessary to synchronize the mesurement processes, so that a consistent description of the state of the power system can be established. GPS transmissions offer an ideal source for synchronization of phasor measurements. The paper describes the concept and implementation of this technique. Several uses of synchronized phasor measurements are also described. Among these are improved state estimation algorithms, state estimator enhancements, dynamic state estimates, improved control techniques, and improved protection concepts.

INTRODUCTION

Computer relaying is a well established field by now, and it has furnished a new insight into the technique of measuring power system quantities in real–time from sampled data. Voltage and current phasors in a three phase power system can be measured from waveform samples, and the measurement process can be made to be responsive to dynamically changing system conditions. For many new applications of phasor measurements now under consideration, measurement response times of 1–5 periods of the power frequency seem desirable. This paper will examine the concept of phasor measurements, and describe some practical considerations in achieving synchronous sampling of currents and voltages in different substations in a power system. We will also describe research now under way in the development of a phasor based protection and control system.

PHASORS FROM SAMPLED DATA

A phasor is a complex number which represents the fundamental frequency component of a waveform. Consider the samples x_k obtained from a signal (voltage or current) x(t). The phasor representation of the signal x(t) is related to the fundamental frequency component calculated by the Discrete Fourier Transform (DFT). If the phasor is X, and the fundamental frequency calculated by the DFT is X_1, then

$$X = \frac{1}{\sqrt{2}} X_1 = \frac{1}{\sqrt{2}} \frac{2}{K} \sum_{k=1}^{K} x_k \, \epsilon^{-jk\omega\Delta t} \qquad (1)$$

where K is the total number of samples (usually a multiple of the fundamental frequency period), and Δt is the sampling interval. One could drop the constant in front of the

summation sign in equation (1), and instead use cosine and sine sums of the sampled data to represent the phasor:

$$X = X_c - jX_s \tag{2}$$

where

$$X_c = \sum_{k=1}^{K} x_k \cos k\omega\Delta t \quad , \quad X_s = \sum_{k=1}^{K} x_k \sin k\omega\Delta t \tag{3}$$

If the actual frequency of the power system differs from the nominal frequency used in the sampling process, the phasor calculated by equation (2) is in error. For all practical frequency deviations, the error in the phasor calculation is negligible. If the phasors of the three phases are given by X_a, X_b, and X_c, the positive sequence quantity X_1 (not to be confused with the fundamental frequency component computed by the DFT) is given by

$$X_1 = X_a + \alpha X_b + \alpha^2 X_c \tag{4}$$

where α and α^2 are the usual phase shift operators of 120° and 240° respectively at the nominal frequency. An important use of the positive sequence voltage is the measurement of the power system frequency. If we write the positive sequence phasor in its polar form, the phase angle of the positive sequence phasor can be differentiated to obtain the incremental frequency of the input waveform over the nominal frequency. If φ is the phase angle of X_1, and ω_0 is the nominal frequency, then the actual frequency of the input signal is given by

$$\omega = \omega_0 + \frac{d\varphi}{dt} \tag{5}$$

Equation (5) is one of the most sensitive methods of measuring power system frequency.

SYNCHRONIZATION OF THE SAMPLING PROCESS

The phasor given by equation (1) uses the sampling instant of the first sample as the reference. The necessary accuracy of synchronization may be specified in terms of the prevailing phase angle differences between buses of a power network. Typically, these angular differences may vary between a few degrees, to perhaps 60° under extreme loading conditions. Under these circumstances, a precision corresponding to 0.1° seems to be desirable to measure angular differences corresponding to lightly loaded systems. Allowing for other sources of error in the measurement system, it seems certain that a synchronizing accuracy of about 1 μsecond would meet the needs of this measurement technique. A superior and satisfying solution to the synchronization problem is to use the 1 pulse–per–second (pps) transmission provided by the Global Positioning System (GPS) satellites.

IMPLEMENTATION FOR FIELD TRIALS

A typical phasor measurement system is shown in Figure 1. The GPS receiver is designed to provide the standard 1 pps, a phase–locked sampling pulse at the desired sampling frequency, and a time–stamp corresponding to the 1 pps. The three signals from the GPS receiver are connected to a microprocessor, which acquires the power system current and voltage input signals through the signal conditioning units and the Analog–to–Digital converter. The microprocessor chosen for the task is a 16–bit processor with a sufficient instruction speed to accommodate between 1000 and 2000 instructions within the sampling period. The A/D converters are typically 12–bit converters, and with careful design of the computation algorithms, provide measurements with very good precision. The measured phasor, its associated time–stamp, and other message codes of interest are communicated to the next hierarchical level

over a communication channel. The local display port and the connected terminal is used to provide a graphic and alphanumeric display of the measured phasors, the reference phasor, the local frequency, and the rate of change of frequency. The system time error can be calculated by counting the rotations of the measured positive sequence voltage phasor with respect to the true time reference provided by the GPS receiver.

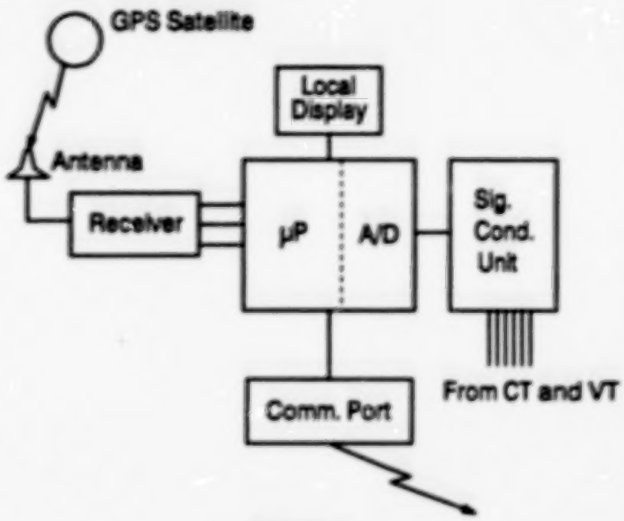


Figure 1.

Phasor Measurement System Block Diagram

USES OF SYNCHRONIZED PHASORS

State Estimation with Phasors

The collection of all positive sequence bus voltages of a power system is known as its state vector. A knowledge of the state vector is essential in many of the central control functions associated with power system operations. The present practice is to obtain measurements of various system quantities such as real and reactive power flow over transmission lines, real and reactive power injections, voltage magnitudes at system buses, line current magnitudes, etc., and estimate the state of the power system with a non–linear state estimator. The measurement vector $\mathbf{z}$ is a non–linear function of the state vector:

$$\mathbf{z} = \mathbf{h}(\mathbf{x}) + \boldsymbol{\epsilon} \tag{6}$$

where $\boldsymbol{\epsilon}$ is the measurement noise with a covariance matrix $\mathbf{W}$. One could obtain the weighted–least–square (WLS) estimate of the state with an iterative algorithm:

$$\hat{\mathbf{x}}_{k+1} = \hat{\mathbf{x}}_k + (\mathbf{H}^T\mathbf{W}^{-1}\mathbf{H})^{-1}\mathbf{H}^T\mathbf{W}^{-1}[\mathbf{z} - \mathbf{h}(\hat{\mathbf{x}}_k)] \tag{7}$$

where $\mathbf{H}(\mathbf{x})$ is the Jacobian matrix of the measurement functions:

$$\mathbf{H}(\mathbf{x}) = \frac{\partial}{\partial \mathbf{x}}\mathbf{h}(\mathbf{x}) \tag{8}$$

The iterations are continued until the measurement residual $[\mathbf{z} - \mathbf{h}(\mathbf{x}_k)]$ becomes smaller than a pre–selected tolerance. A state estimation procedure such as that described above can never represent the dynamic phenomena occurring on the power system during transient power swings. The data scan rates in use at present are rather slow, and the non–linear iterative algorithm also contributes to the slow response time of the estimation process.

The synchronized phasor measurement technique provides the system state with direct measurements. Let the complete measurement set consist of positive sequence voltages at buses, and currents in transmission lines and transformers. These measurements are ***linear*** functions of the state vector:

$$\mathbf{z} = \begin{bmatrix}\mathbf{E}\\ \mathbf{I}\end{bmatrix} = \mathbf{B}\mathbf{x} \tag{9}$$

The measurement matrix $\mathbf{B}$ now consists of two sub–matrices, the unity matrix, and a matrix relating the currents and the system state. This latter sub–matrix is similar to the familiar admittance matrix of the power system. In any case, the important point is that equation (9) is linear. Since $\mathbf{B}$ is a complex matrix, the WLS solution is now given by

$$\hat{\mathbf{x}} = (\mathbf{B}^\dagger\mathbf{W}^{-1}\mathbf{B})^{-1}\mathbf{B}^\dagger\mathbf{W}^{-1}\mathbf{z} \tag{10}$$

Equation (10) can be much simplified by using the known structure of the admittance matrix elements.

An interesting distinction of the phasor measurement technique is that a complete system–wide data scan is not needed to complete the estimation process. The measured positive sequence voltages, with appropriate data validation done at the source, can be used directly. Thus, if the partial state vector is useful is some applications, it can be put to use immediately. For example, the phase angle between two regions of a network may be measured directly, in order to assess the inter–regional power transfer, without having to measure the connecting network, and then estimating the phase angle. In the next two sections, other examples of uses of partial state vector measurements will be discussed.

Improved Control with Phasors

It is possible to improve post–disturbance power system performance using control schemes based on real–time phasor measurements. Present day controllers which act in such situations are restricted by the limited (local) nature of the measurements available to the controller. If synchronized phasor measurements from throughout the system are available, the quality of the control can be improved considerably. Such controllers for dynamic stability enhancement of AC/DC systems, and the application of real–time phasor measurements in generator exciter and speed governing system control has been reported in the technical literature. The key idea is to replace the non linear differential equation describing power system dynamics

$$\dot{\chi}(t) = f(\chi(t), u(t)) \tag{11}$$

by an equation that linearizes f, and then collects the remainder as a correction term

$$\dot{x} = A\,x + B\,u + [\,f(\chi_0 + x, u) - A\,x - B\,u] \tag{12}$$

Note that this equation (12) is not an approximation, it is in fact the same as equation (11). One may treat the term in the bracket

$$r(t) = f(\chi_0 + x, u) - A\,x - B\,u = \dot{\chi} - A\,x - B\,u \tag{13}$$

as a correction term, which is some unknown function of time. If sufficient observations of $x(t)$ are available, $r(t)$ can be predicted, and an optimal control law determined for the original system of equation (11). The resulting control law has several interesting properties, and it has been shown that the computational burden in the real–time control function can be accommodated in modern microcomputer based implementation.

In summary, we may say that real–time phasor measurements provide highly beneficial feedback to various controllers in use in power systems. Although a complete state vector feedback would be ideal, even partially observed states can help. With currently available communication channel speeds, the feedback can be obtained in a continuous data stream with state vector sampling periods of between 50 and 100 milliseconds. This makes the feedback most appropriate for controlling power system transients which lie in the frequency band of 0–5 Hz. Thus, most phenomena associated with electromechanical oscillations on power systems can be controlled with state vector feedback.

Protection with Phasors

Protection is a form of control. Phasors play an important role in protection system design. In fact, modern phasor measurement techniques originated in the field of computer relaying.

It has now become clear that synchronized phasor measurements can be of great use in many of the protection applications. Although phasors may be used in many relaying tasks, their full impact is felt in the new field of adaptive relaying. ***Adaptive Protection is a protection philosophy which permits and seeks to make adjustments in various protection functions automatically in order to make them more attuned to prevailing power system conditions.*** The idea of adaptive relaying is an old one. Thus, existing protection systems try to adapt to changing system conditions in a limited manner. However, the advent of computer relaying has added a new dimension to this idea. For the first time, it is possible to imagine protection systems which can have dynamic settings, in order to provide the best protection possible in a changing environment. Of course, not all relay characteristics are amenable to adaptive adjustments. And, one must take care that in case of failures of the adaptive features, the relays revert to their pre–adaptive mode of operation. A number of studies of adaptive relaying have appeared in the technical literature in recent years. We will consider one example to give the flavor of this new and exciting development.

Detection of Instability

This problem impacts many protection and control applications. As the power system undergoes oscillations of synchronizing power following a disturbance, it would be extremely useful to know in real–time whether the swing under development is going to lead to an instability. At present, this problem cannot be solved for a completely general system, but progress can be made in case of systems with two areas of concentrated load–generation complexes, connected together by somewhat weak interconnections. These systems behave like the classical two–machine system. The detection of instability for such a problem is equivalent to an evaluation of the balance between the accelerating and decelerating powers using the equal area criterion. If $\delta(t)$ is the angle between the two equivalent machines, the set of observations $\{\delta_k; k = 1 \cdots n\}$ can be used to predict the balance between the accelerating and decelerating areas on the P–δ plane. It has been observed that observations made over one quarter of the period of the electromechanical oscillation are sufficient to provide a reliable estimate of the outcome of a power swing.

As mentioned before, no such results for the general case of multi–machine oscillations exist at this time. Several promising approaches to this problem – such as the method of Potential Energy Boundary Surface, and Extended Equal Area – are currently under investigation.

SUMMARY AND CONCLUSIONS

Synchronized measurement of power system parameters is now achievable with the time transmissions of the GPS satellites. The hardware costs associated with such a measurement system are comparable to those of other relays and measurement systems in general use at present. The synchronized phasor measurement systems are likely to have a significant impact on all aspects of power system operations in the coming years, and will usher in an era of electric power networks operating with greater efficiency and security.

FOR FURTHER READING

Transactions of IEEE on Power Apparatus and Systems contain many of the research results described above. The book, ***"Computer Relaying for Power Systems"***, by A. G. Phadke and J. S. Thorp, gives a coherent account of some of these developments.

BLANK PAGE

TIME CONCURRENCY / PHASE-TIME SYNCHRONIZATION IN DIGITAL COMMUNICATIONS NETWORKS

Masami KIHARA and Atsushi IMAOKA
NTT Transmission Systems Laboratories

Abstract

Digital communications networks have the intrinsic capability of time synchronization which makes it possible for networks to supply time signals to some applications and services.

A practical estimation method for the time concurrency in terrestrial networks is presented. By using this method, time concurrency capability of the NTT (Nippon Telegraph and Telephone corporation) digital communications network is estimated to be better than 300 ns rms at a advanced level, and 20 ns rms at final level.

INTRODUCTION

In current digital telecommunication networks, highly stable frequency signals are distributed as a standard frequency. Master-slave synchronization is generally adopted to synchronize all nodes in these networks. A unique master node and other slave nodes compose a hierarchically topological tree structure which is gradually growing with the expansion of digital networks. In master-slave synchronization, however, this growth causes the extension of logical depth, namely an increase in the number of links. Consequently, the purity and stability of standard frequencies are being degraded.

There are two effective ways to prevent such degradation. One is a new standard frequency distribution system named the Primary Reference Clock developed by AT&T that receives GPS signals and can distribute a highly stable reference [1]. This system can reduce the number of links in a synchronization hierarchy since reference signals are regenerated in nodes dispersed throughout the U.S.

The other way is the phase-time synchronization described here. Traditional master-slave synchronization is actually syntonization, even though phase-locked loop systems are used in slave nodes. We suggest a new system which can provide true synchronization in both phase-time synchronization and time concurrency through reference time signal distribution.

Such distribution to all telephone offices and subscriber sites can also provide time concurrency for certain aspects of systems which are improved by accurate time signals, such as time management in network operation systems, time stamping in distributed computer systems, and navigation in digital mobile systems.

We assume that the present network synchronization (i.e. frequency synchronization) is being changed to accommodate time synchronization, in which reference time signals will be distributed over digital paths composed of optical transmission and digital radio systems. The high capability of the terrestrial digital network for time transfer is presented here.

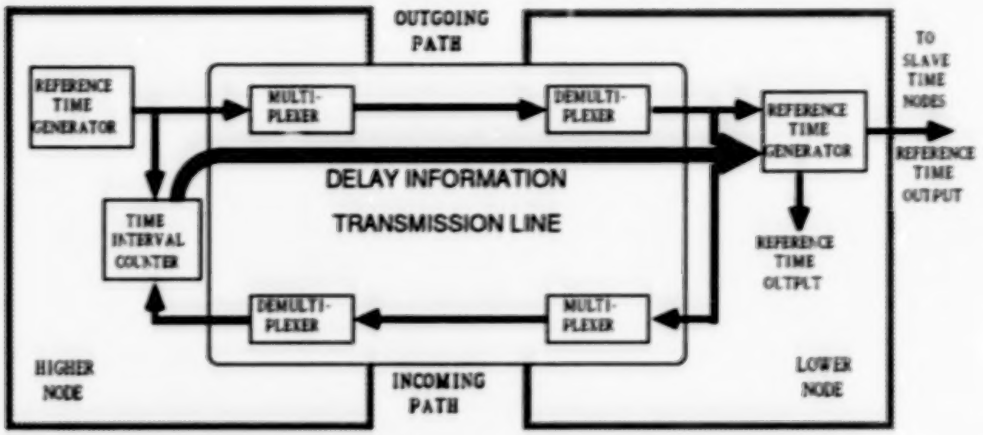


Fig. 1 Basic configuration of time distribution link

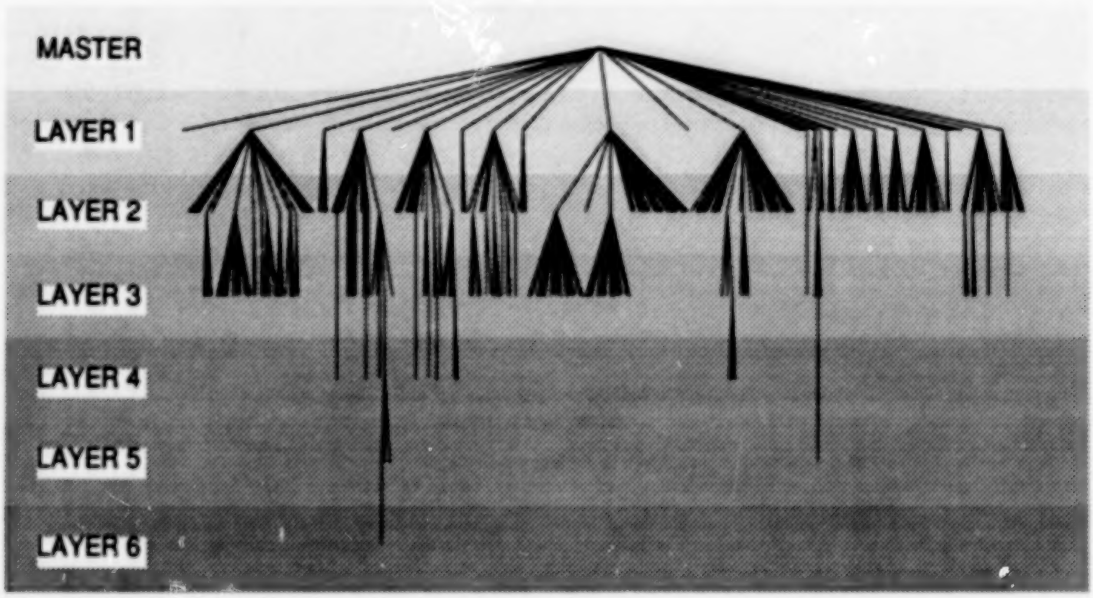


Fig. 2 Hierarchical tree for time synchronization analysis

PHASE-TIME SYNCHRONIZATION NETWORK

The performance of time synchronization can be evaluated by relative phase-time stability and absolute time concurrency. In our new synchronization system, these characteristics are simultaneously accomplished by transmission delay compensation. The measurement of the round-trip delay in digital paths allows a transmission delay correction because, for the most part, outgoing and incoming paths in digital transmission systems have the same transmission delay and are laid under the same circumstances.

Network topology for time synchronization follows the master-slave hierarchy, in which a unique time master node generates reference time signals that are distributed to other slave nodes. The basic configuration of the time distribution link is shown in Fig. 1. A higher node measures a round-trip delay and transfers the half-transmission delay as delay information to a lower node. The lower node compensates the time signal according to the received delay information.

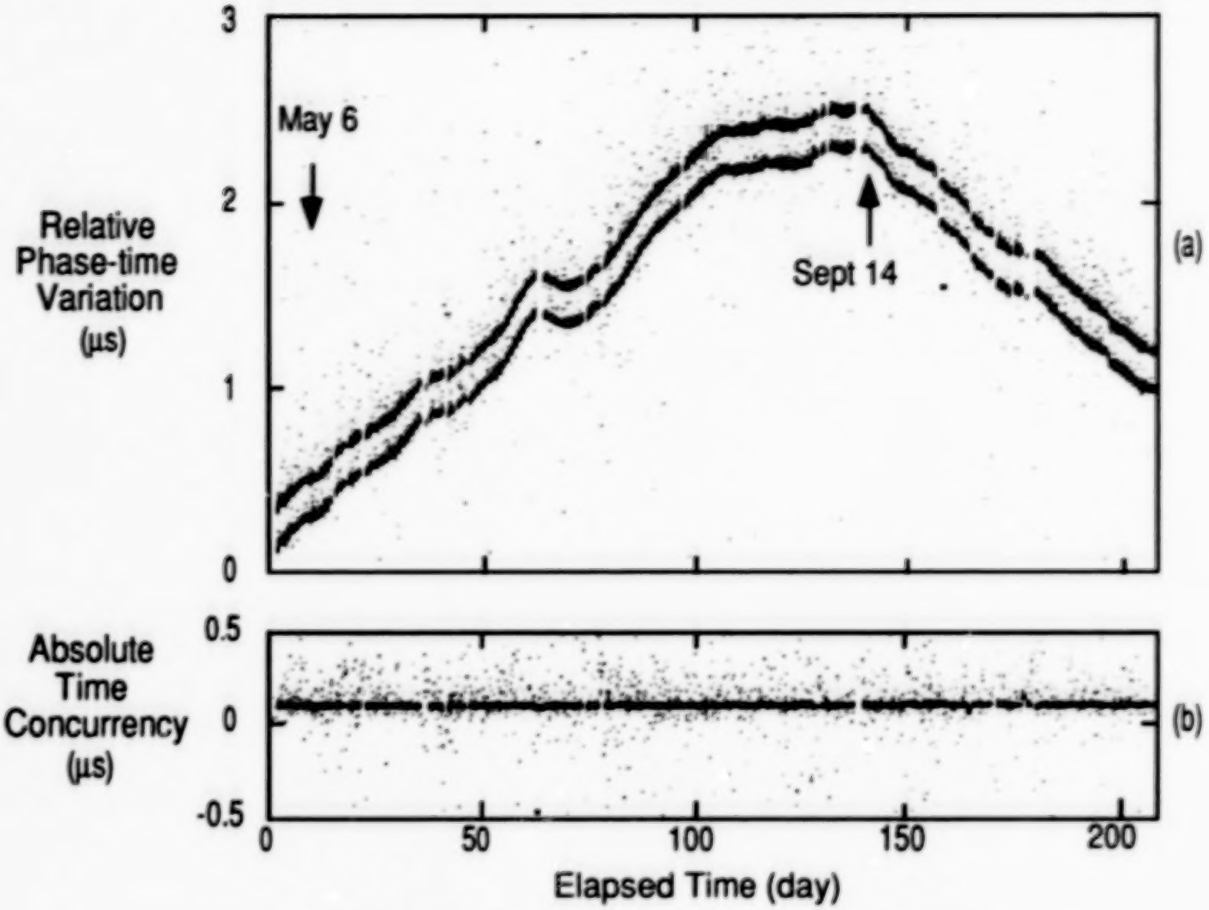


Fig. 3 (a) Measured wander and (b) compensated wander

TIME SYNCHRONIZATION CAPABILITY

Time synchronization topology

The topology of the master-slave method is mostly determined by geographical situations since node locations are settled independent of transmission systems. Therefore, characteristics of future time-synchronization networks can probably be estimated based on the analysis of the current syntonization system in an existing network. The hierarchical tree for the time synchronization network is shown in Fig. 2. For this topology we selected 400 nodes out of NTT's synchronized network. There are 7 layers. The top one is called the master layer and they are connected through 6 links.

Relative phase-time synchronization capability

Arrival time dispersion of time signals is determined by long-term delay variation in transmission lines due to temperature change in transmission cables originating from the environment. This variation, called wander, corresponds to relative phase-time synchronization stability and its influence can be reduced by measuring round-trip delay. Practical wander is on the order of micro seconds as shown in Fig. 3 (a). This is one of the results obtained through measuring an approximately 2400-km transmission path in the terrestrial NTT network for 7 months. The influence of this wander is compensated to be within 50 ns by the time distribution link, as shown in Fig. 3 (b). Furthermore, filtering, whose time constant is 100 to

1000 s, decreases timing jitter caused by multiplexers and demultiplexers, and can achieve about 2 ns relative time synchronization.

The accumulation of these measured results has yielded the experimental equation for the relation between the transmission path length,L in km, and the relative time synchronization, $\Delta T_{relative}$ in ns as follows:

$$\Delta T_{relative} = K_1 \cdot L + K_0 \quad (1)$$

Constants, K_1 and K_0 are 5×10^{-4} ns and 0.8 ns in the 6.312 Mb/s digital path. K_1 is the factor of the asymmetry in round-trip delay compensation. K_0 is the factor of the delay asymmetry in digital circuits. Relative time synchronization stability is consequently proportional to transmission length.

Absolute time synchronization capability

The above time compensation method simultaneously enables absolute time concurrency; however, residual time errors, which correspond to the difference between transmission delays of the outgoing and incoming paths in the round-trip compensation, degrade it [2]. The delay difference is caused by variations in the cable length which depends on the number of fiber fusion splices, fiber connections by connecters and the delay difference in connections between multiplexers. As time concurrency, the following model can be employed in the event time errors are not correlated:

$$\Delta T_{absolute} = \sqrt{K_{fs}^2 N_{fs} + K_{rc}^2 N_{rc} + K_{ic}^2 N_{ic}} \quad (2)$$

K_{fs}: time difference in fiber fusion splices
K_{rc}: time difference in the fiber connection of repeaters and multiplexers by connecters
K_{ic}: time difference due to multiplexer connections in an intra-office
N_{fs}: number of fiber fusion splices
N_{rc}: number of fiber connections
N_{ic}: number of multiplexer connections

In Fig. 3 (b), absolute time concurrency, $\Delta T_{absolute}$, is 100 ns. This value can be estimated on the condition that K_{fs} and K_{rc} are 2 ns rms, K_{ic} is 20 ns rms, N_{fs} is 1128, N_{rc} is 240 and N_{ic} is 64.

The time difference from UTC is not presented here. It is important not to guarantee UTC itself, which is maintained by governmental facilities, but rather to trace it. Guaranteeing UTC itself is beyond the work of telecommunication companies.

TIME CONCURRENCY PERSPECTIVES

Time synchronization performance is influenced by the transmission path configuration for transfer time signals and by timing clock systems which supplies timing clocks to digital systems in transmission paths. These constituent elements in networks classify the time concurrency. This classification also shows the transition stream of the progress in time synchronization. The different configurations shown in Figs. 4, 6 and 8 can be considered in terrestrial digital networks. The time transition is classified into 5 stages.

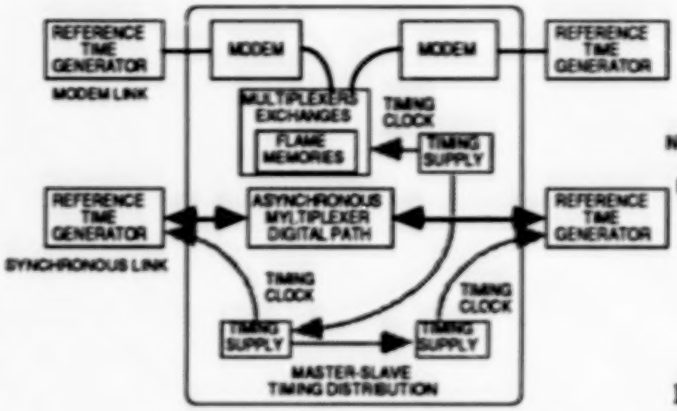


Fig. 4 Entry level time distribution configuration

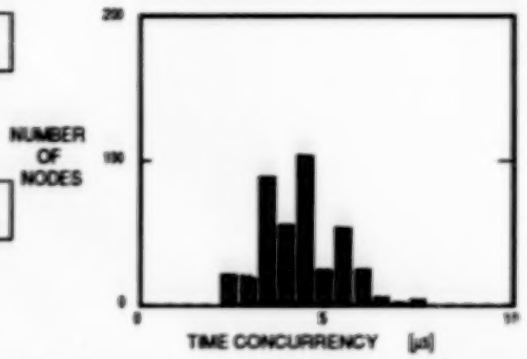


Fig. 5 Time concurrency distribution in stage 2

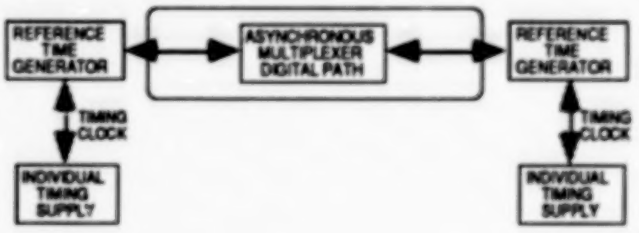


Fig. 6 Advanced level time distribution configuration

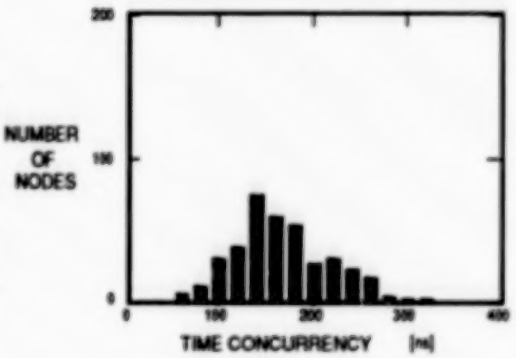


Fig. 7 Time concurrency distribution in stage 3

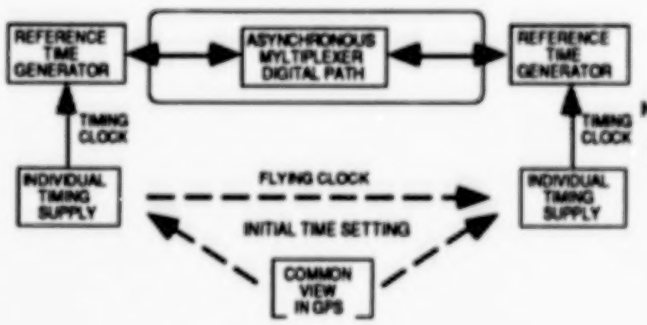


Fig. 8 Final level time distribution configuration

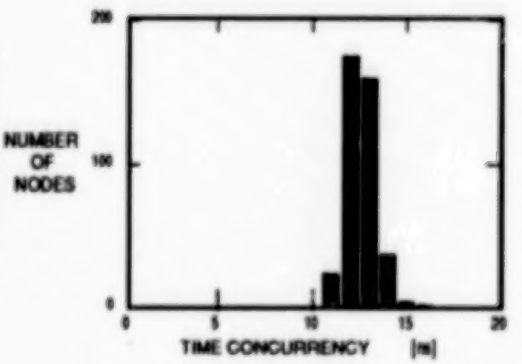


Fig. 9 Time concurrency distribution in stage 5

Entry level (Stages 1 and 2)

One of the most practical configurations is time transfer via low-speed digital paths such as the modem links and 64 kb/s ISDN shown in Fig. 4. Since these paths include synchronous digital multiplexers and exchanges, uncertainty in time concurrency is on the order of 100 μs and is equivalent to the amount of frame memories installed in those systems. Practical measurements in such systems have been shown by D. W. Allan and others [3][4]. Time concurrency in stage 1 can be estimated to be 100 to 200 μs.

It is possible to eliminate the influence of frame memories if paths are composed of asynchronous digital multiplexers using pulse justification up to the highest hierarchy. In these situations, phase-time variations of timing clocks remain in the total time uncertainty. Two timing clock configurations are possible at both ends of paths in time control systems: synchronized timing clocks supplied by the existing frequency synchronization (syntonization), and individual timing clocks generated by independent oscillators.

Wander appearing in synchronized timing clocks is gradually increasing according to digital network expansion. In stage 2, time concurrency can be estimated at this time to be within 10 μs using these clocks. If stage 2 is introduced in the existing networks, time concurrency distribution can be calculated in Fig. 5 based on the hierarchical tree shown in Fig. 2.

Advanced level (Stage 3)

Individual timing clocks can prevent the influence of network expansion in master-slave synchronization. These clocks can be indirectly synchronized in frequency by the phase-time synchronization shown in Fig. 1 (Fig. 6).

In stage 3, where there are multi-links of digital paths for the time transfer, time concurrency is determined by the number of repeaters and fusion splices in fiber connections, which varies with a transmission cable length, and by the number of connections between multiplexers in intra-offices. The factor of multiplexer connections is dominant in these situations and it can be estimated within 300 ns rms as shown Fig. 7.

Final level (Stages 4 and 5)

If the virtual container in SDH (Synchronous Digital Hierarchy) can be used for the time transfer, the single-linking of digital paths is possible (Stage 4). However, time concurrency can not be dramatically improved even if the single-link between time synchronized nodes is introduced. When the initial time setting is adopted together with the single-link configuration, time concurrency can obtain the highest performance (Fig. 8). Its distribution is shown in Fig. 9 and it is within 20 ns rms (Stage 5).

The first half of time concurrency in Fig. 9 results from uncertainty in the initial time setting. There are two ways for the initial time setting: flying clock and common view method in GPS. Uncertainty in the initial time setting here is expected to be within 10 ns in this estimation. Using conventional Cesium beam standards for flying clock method, the setting accuracy is now within 100 ns; however, it will be improved to 10 ns by applying new oscillators such as optically pumped Cesium standards. If the initial time setting can correct the residual time error, the second half of time concurrency shown in Fig. 9 is determined by relative phase-time synchronization calculated by Eq. (1). It can also be estimated to be within 10 ns rms.

Time concurrency transition

Time concurrencies in each level are shown in Fig. 10. The entry level providing time concurrency within 1 ms is an area in the application coping with 1 second. In the advanced level, time concurrency within 1 μs enables time stamping for distributed data-base and network operation systems, and provides time synchronization in comparatively lower speed digital signals. The final level is effective in future TDMA such as next-generation cellular phone systems, and can also contribute to academic applications such as geophysics and astronomy.

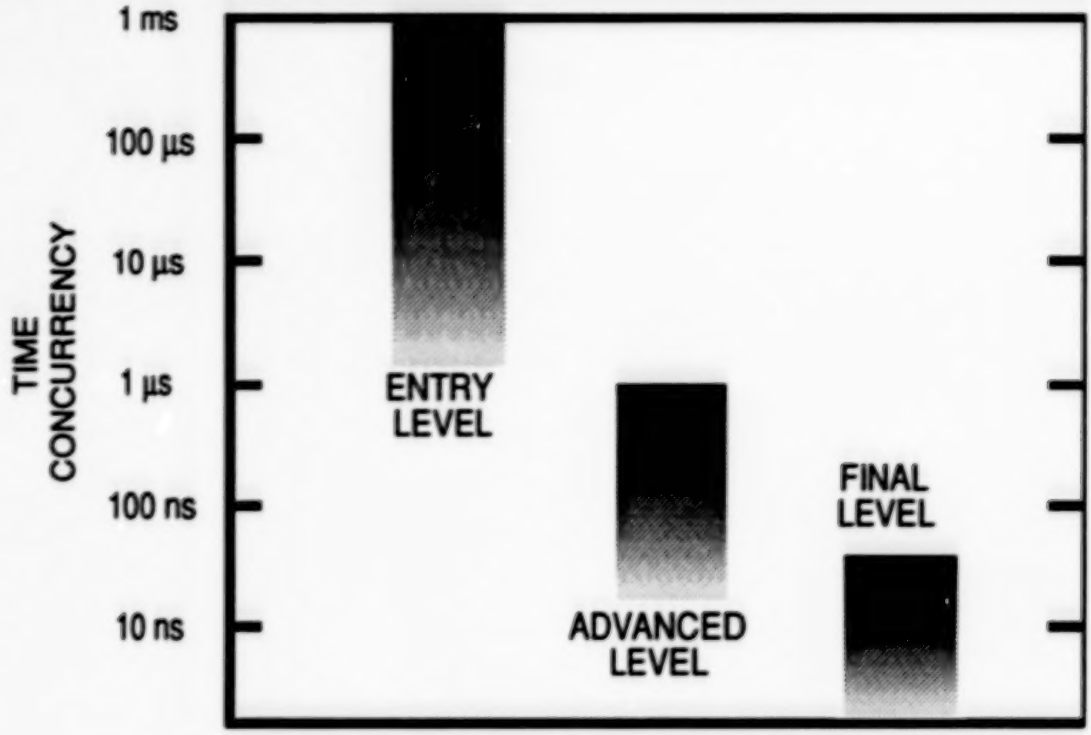


Fig. 10 Time concurrency transition stream

CONCLUSION

We presented the possibility of submicro-second time concurrency in a 400-node scale telecommunication network with a maximum transmission length of approximately 2400 km. This scale is similar to that of NTT networks in Japan; however, this estimation method can be applied to other networks in other countries.

ACKNOWLEDGEMENT

We are grateful to Dr. Tetuya Miki and Mr. Katsuaki Kikuchi of NTT Transmission Systems Laboratories for their encouragement. We would like to thank Mr. Kenji Hisadome of NTT Transmission Systems Laboratories for his help with the experiments.

REFERENCES

[1] E. W. Butterline and J. E. Abate and G. P. Zampetti:"Use of GPS to Synchronize the AT&T National Telecommunications Network", Proc. of the 20th Annual PTTI Applications and Planning Meeting, pp. 65-74, 1988.
[2] W. D. Grover and T. E. Moore:"Precision Time-Transfer in Transport Networks Using Digital Crossconnect Systems",GLOBECOM'88, 47.2, pp.1544-1548, 1988.
[3] D. W. Allan and D. D. Davis, J. Levine, M. A. Weiss, N. Hironaka and D. Okayama:"New Inexpensive Frequency Calibration Service From NIST", Proc. of 44th symposium on Frequency Control, 1990.
[4] M. Aida, T. Sato and S. Yamamori:"Time comparison using Telephone Line",Rev. of the Radio Research Laboratories, Vol.31, No.160, pp. 115-124, 1985.

QUESTIONS AND ANSWERS

David Allan, NIST: Did I understand you to say that you are planning to use time division multiplexing for communication networks?

Mr. Kihara: Yes, the most important application is time division multiplexing systems.

Mr. Allan: Can you tell us how much more efficiency you expect from this new system?

Mr. Kihara: I am not sure.

THE CABLE & WIRELESS APPROACH TO NETWORK SYNCHRONIZATION

Robert D. Calvert
Cable & Wireless plc.,
Summit House, 12, Red Lion Square,
London, WC1R 4QD, England.

Abstract

This paper presents the philosophy adopted by Cable and Wireless for the synchronization of its world-wide network. It identifies the architectures of some of the clock systems already deployed and how network synchronization has been implemented at selected locations. This includes some innovative designs as the network spans both first and third world countries with a combination of North American and European hierarchy equipment. Different parts of the global network are linked together by a combination of terrestrial microwave, submarine cable and satellite technology. The paper also addresses the impact of synchronization on Intelsat IDR operation and the restoration of submarine cable systems.

The paper does not attempt to identify details of all the clock systems deployed by Cable and Wireless and its subsidiary companies world-wide, rather a snapshot of some of these systems is presented.

The Cable and Wireless Network

The Cable and Wireless Group is one of the world's leading telecommunications operators. The company is establishing a global digital telecommunications network connecting the world's primary economic and financial centers. Private submarine fiber optic cables link the Group's operations in Europe, North America, and the Pacific Rim via Japan and Hong Kong. In the contiguous United States, Cable and Wireless Communications Incorporated provides an all-digital broadband network which is 90% fiber optic, and within reach of 80% of the US business population. In Bermuda, Cable and Wireless has interfaced its PTAT-1 cable with another submarine fiber optic cable CARAC. The CARAC cable interconnects with Tortola in the British Virgin Islands and from there south to Trinidad via the Group's Eastern Caribbean Microwave System. This connects with most of the fourteen nations the Group serves in the West Indies.

Cable and Wireless owns and operates many satellite earth stations in locations in the Atlantic, Pacific and Indian Ocean Regions of the Intelsat system.

Synchronization Philosophy

The Cable and Wireless Global Network is evolving into a fully digital network using Plesiochronous Digital Hierarchy (PDH) equipment. The network is split into separate regional or national networks, each of which is, or will be, synchronous at the primary rate (1544 kbit/s or 2048 kbit/s)

and below. Each Regional or National network is synchronized using the Hierarchical Master-Slave Synchronization method. Each network conforms to a network synchronization plan which has been formulated following CCITT Recommendations G.811 and G.812 (Red and Blue Books). As a result, the hierarchical clock performances comply with the following:

Level	Clock Performance Requirements		CCITT Recs	Remarks
	Drift/Day	Frequency Offset		
1	-	1×10^{-11}	G.811	Network Reference Clock co-located with International Switching Center.
2	1×10^{-9}	5×10^{-10}	G.812	Co-located with National trunk exchange.
3	2×10^{-8}	1×10^{-8}	G.812	Local Exchanges
4	-	5×10^{-5}	G.700 series	Primary rate multiplexers and Remote Line Units (RLU's)

Where the Local Exchange Clocks have a lower performance than that shown, additional synchronization links are provided to improve the availability of network timing traceable to the network reference clock. This ensures that timing performance in free-run or holdover meets the network requirements of Cable and Wireless.

This timing strategy also ensures that network timing meets the requirements necessary to achieve the end-to-end slip performance identified in CCITT Recommendation G.822, which calls for less than 5 slips in 24 hours on any 64 kbit/s connection.

Cable and Wireless have chosen to procure stand-alone reference clocks and Level 2 clocks, and to implement a Building Integrated Timing System approach to their deployment. This approach ensures independence of the synchronization system from the telecommunications equipment deployed. Additionally, it provides flexibility in expansion and avoids vendor dependence.

Each Regional or National network interworks with other regional or national networks plesiochronously. Buffers are incorporated in all equipment interfacing with international streams.

Typically, the Level 1 Reference clocks are either cæsium or Loran-C based. They have an accuracy which exceeds 7 parts in 10^{12} and are designed to meet an availability of 99.999%. The Level 2 clock systems are stand-alone network elements which typically exhibit a drift performance of less than 1 part in 10^{10} per day in holdover, and use digital phase lock loop timing recovery circuits. Each clock system can be operated manually to support maintenance and trouble shooting.

In each network, timing is distributed downstream through the synchronization hierarchy of clocks, using the traffic carrying primary rate streams. Clock recovery occurs at each node in the hierarchy. The streams chosen for distribution of timing are direct between synchronization network elements and avoid any intermediate processing at the primary rate and below. By this means all clocks in the network are timed traceable to the Network Reference Frequency Standard (NRFS) or Reference Clock. Jitter accumulation is reduced to a minimum by using timing recovery circuits equipped with phase lock loops with very low cut-off frequencies.

Cable and Wireless has adopted a philosophy of distributing the reference clock at more than one location primarily for strategic and security reasons. This approach is designed to enhance survivability and ensure the continuance of network timing traceable to a reference clock, even during periods of catastrophic failure.

Each clock sub-system is a hybrid Level 1 and Level 2 clock. At any point in time, only one of the sub-systems provides the network reference (Level 1 operation), the other sub-systems recover timing from incoming primary rate streams clocked from the reference sub-system's location (Level 2 operation). The architecture of a sub-system is as shown in Figure 1.

Control of this distributed reference clock system has been effected in two ways. Some of the systems already deployed use telemetry over modem channels, others utilize telemetry embedded in the primary rate frame.

The system deployed in the Eastern Caribbean Network makes use of the 2048 kbit/s primary rate frame structure. This has a number of spare bits available for use by the network provider. These are located within time slot zero of the frame not containing the frame alignment word. The system consists of three sub-systems, each being a hybrid Level 1 and 2 system. The status of each sub-system is signaled to the other two sub-systems using the spare bits.

The system deployed in Hong Kong has two sub-systems which communicate their status to each other over a modem channel. This philosophy is also being adopted for the system being deployed in Jamaica. The reason for this is that the Jamaica network is based on the North American digital hierarchy and there is no available integral telemetry facility embedded into the 1544 kbit/s standard frame structure at this time. (See below for Facilities Data Link).

A Loran-C based reference clock has been operating in the Bermuda network for three years without loss of timing. A fully redundant clock architecture is employed using the configuration shown in Figure 2. Two Loran-C receivers lock to different Loran chains and can automatically acquire a third chain if any of the selected chains fail. A similar system will shortly be installed in the Cayman Islands.

Each Level 2 clock has a fully redundant architecture with a configuration as shown in Figure 3. The timing recovery systems have selectable time constants, thereby allowing the phase lock loop cut-off frequency to be adjusted to optimize jitter and wander rejection. They have a capture range of 3 parts in 10^7. In holdover mode they can provide G.811 compatible performance for 10 hours or longer. This means that disruptions to the synchronization distribution network are transparent to the telecommunications traffic being carried by the network.

Cable and Wireless have adopted an approach of quality-marking 2048 kbit/s primary rate streams used to distribute synchronization. Such streams are at present marked to indicate traceability to the reference clock. Loss of traceability results in a simple bit flip from the 0 state to the 1 state. The bit chosen for this is bit 5 in time slot zero of the frame not containing the frame alignment word.

For networks based on the North American digital hierarchy, the 1544 kbit/s extended frame super-frame can be used to provide this facility. There is a 4 kbit/s data channel in this frame structure, and specific code words may be standardized for synchronization use. Although not available at present, the "facilities data link" will be used if it meets Cable and Wireless requirements.

For example, in the Eastern Caribbean Network, the timing quality of the stream is signaled to indicate whether it is traceable to cæsium or not. Each of the Cable and Wireless operated islands in the network have a slave clock, which is able to interrogate each synchronization stream and lock to whichever indicates its timing is traceable to the network reference.

Cable and Wireless operates the telecommunications of a number of small island nations where the only international routes are via the Intelsat satellite system. Typically, these systems now conform with the Intelsat Earth Station Standard (IESS) 308, which details the performance characteristics for Intermediate Data Rate (IDR) digital carriers. Where the location offers only analog services (Voice or voice band data) the IDR equipment is loop-timed to the distant end where a double Doppler buffer is employed on the receive equipment to absorb the Doppler delay variation. However, where the location operates a direct digital service, via IDR, to more than one destination, there is a need to provide a cost effective reference clock to meet the network's synchronization requirement. The solution may come in the form of a low cost GPS-based system, or alternatively a slave standard approach. In the latter case, it may be possible to extract and average timing from a number of IDR streams of known quality and drive a quartz standard to emulate the performance requirements imposed by CCITT Recommendation G.811.

Successful IDR operation requires an acceptable slip performance for the satellite section. The Doppler/plesiochronous buffer found within the IDR equipment must be clocked out by a clock traceable to a G.811 compatible reference. A typical configuration is shown on the attached drawing, Figure 4 (lower half). Here the clock is recovered from the 'transmit to satellite' stream (within the IDR equipment), and used to clock out the 'receive from satellite' stream from the buffers. However, some IDR modems are unable to perform this function and require a separate external clock input to the buffer. All digital streams at the primary rate and below are timed traceable to the reference clock. Therefore, the slip performance for a 2048 kbit/s or 1544 kbit/s primary rate IDR path will be of the order of 1 slip in 70 days.

Higher order multiplexers, such as the hybrid 2 Mbit/s to 45 Mbit/s multiplexers used in the transmission system, shown in Figure 4 (lower half), are not normally required to be timed traceable to the reference clock. These higher order multiplexers operate timed from their own internal quartz oscillators. These oscillators operate at a higher frequency than the combined aggregate tributary frequency and employ a technique known as bit stuffing or justification to maintain tributary synchronism. This ensures that the timing of the tributary stream is maintained transparent to the higher order multiplexer.

For restoration of a cable system it is more efficient to be able to restore at the highest bit rate, this is currently being performed at 45 Mbit/s. At the 45 Mbit/s rate, it is essential that the higher order multiplexer transmitting the 45 Mbit/s aggregate stream is timed traceable to the network reference clock (see Figure 4 upper half). Failure to do this will make the slip performance on the satellite section unacceptable. The reason for this is that within the higher order multiplexer the internal quartz clock has an accuracy of 20ppm. If this multiplexer is not externally timed the resulting slip performance may be as bad as 1 slip every 3 seconds. Additionally, because the frame of the 45 Mbit/s aggregate stream bears no relationship to the frame structure of the 2 Mbit/s tributary streams it transports, every slip at the 45 Mbit/s level will result in a re-frame at the 2 Mbit/s level.

To achieve acceptable slip performance during the period of cable restoration, the 2 Mbit/s to 45 Mbit/s higher order multiplexer feeding the 45 Mbit/s IDR modem must be timed from the reference clock. Cable and Wireless has achieved this by equipping clock systems with 45 MHz clock interfaces and feeding this to the external clock input of the multiplexer. This ensures that the 45 Mbit/s 'transmit to satellite' bit stream has acceptable timing. If the buffers within the IDR modems are centered at the start of the restoration period, they should not slip during the likely period of restoration; this is unlikely to last for longer than 15 days. All parties participating in a cable restoration via satellite must ensure that their 'transmit to satellite' streams are timed as shown in Figure 4 (Upper half).

Cable and Wireless wholly own or have capacity in a number of submarine cable systems. Some examples of wholly-owned systems are the Private TransAtlantic Cable, PTAT–1, and the Bermuda to Tortola cable, CARAC. Efficient restoration via satellite for such systems is of paramount importance.

The clock systems deployed in the Cable and Wireless network continue to operate satisfactorily. The Bermuda Loran-C system has operated fault-free since its installation in 1987. The reception of the Loran-C signal has been interrupted to one receiver during a very heavy rain storm on one occasion only. However, the fully redundant clock system architecture proved robust enough to maintain the timing signal outputs traceable to Loran-C continuously during this period. The quality of the timing signal output has been periodically compared with that from a portable cæsium and found to be at least as accurate.

The distributed cæsium-based Eastern Caribbean Clock System has operated satisfactorily since its installation in 1989. The system is designed to measure both phase and time interval error (TIE) between its own internal cæsium reference and the streams passing through it. TIE is measured in consecutive time periods using windows of duration of 100, 1000, and 10000 seconds. Phase is measured as a running total and so can be analyzed to give MRTIE over an extended period. The alarm system flags a TIE alarm on any stream which exceeds the CCITT Rec. G.811 mask.

The result of measurements in Tortola indicate that the MRTIE between the Cable and Wireless network and the AT&T timed streams passing through St. Thomas in the US Virgin Islands are within the CCITT Rec. G.811 mask. The MRTIE between Barbados, Antigua and Tortola, where the reference clock sub-systems are located, are within the resolution of the system. The system is consequently performing exceptionally well and indicates that the complete network is solidly synchronized.

The distributed cæsium-based system installed in Hong Kong Telecommunications' network is based on a two sub-system clock with one sub-system installed on Hong Kong Island and the other in Kowloon. The MRTIE measured between the two cæsiums is of the order of 2 parts in 10^{12}. The system has operated satisfactorily since its installation in 1987. Again the system is equipped to measure both TIE and phase.

Figure 1 DISTRIBUTED REFERENCE CLOCK SUB – SYSTEM

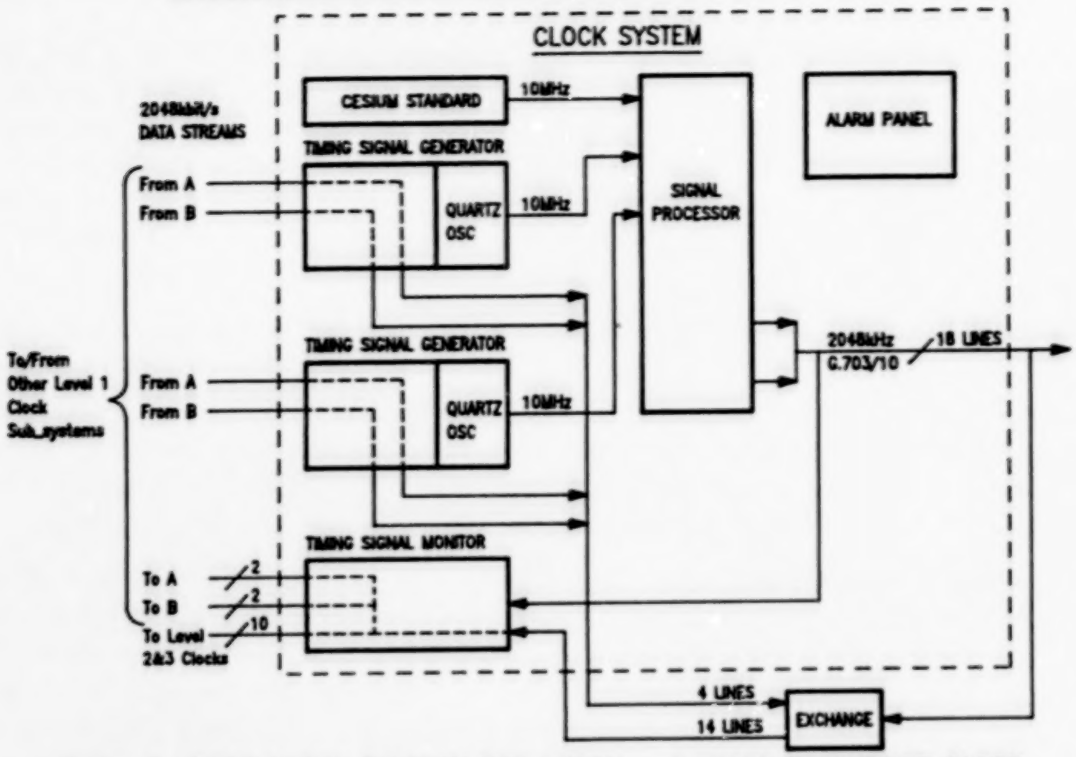


Figure 2 BASIC BLOCK DIAGRAM FOR LORAN – C BASED REFERENCE CLOCK

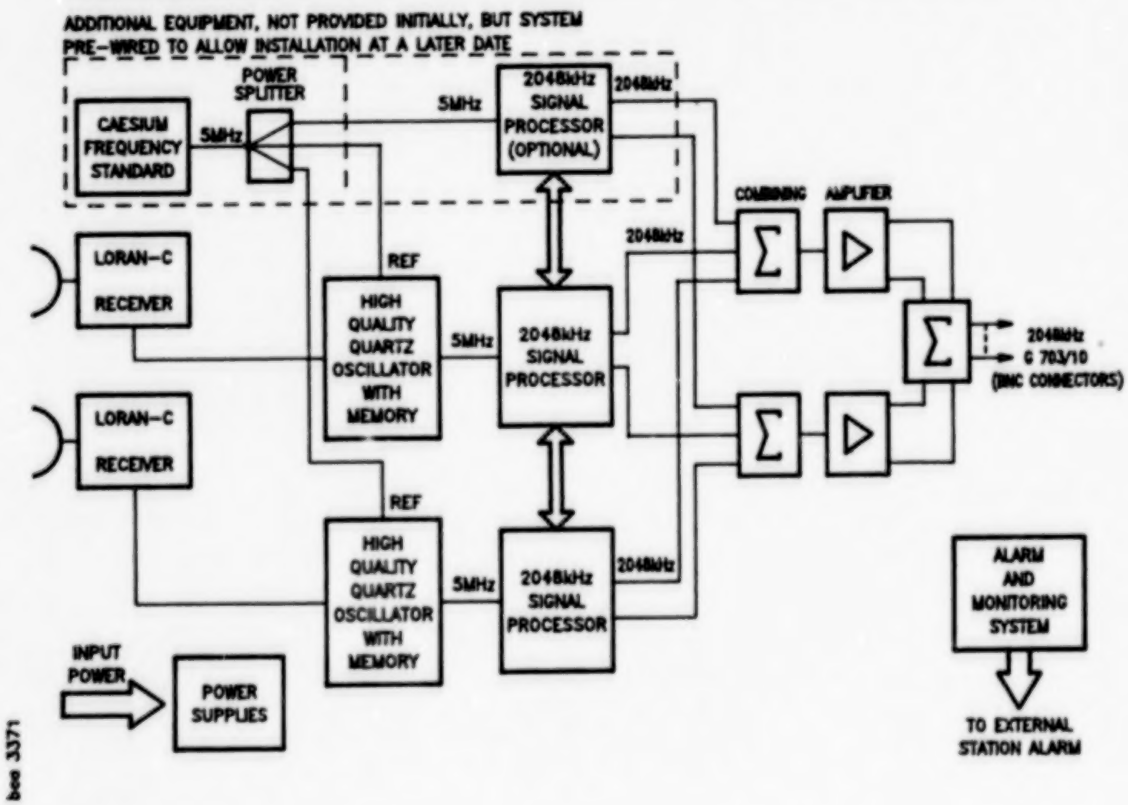


Figure 3 LEVEL 2 SYNCHRONISATION SYSTEM

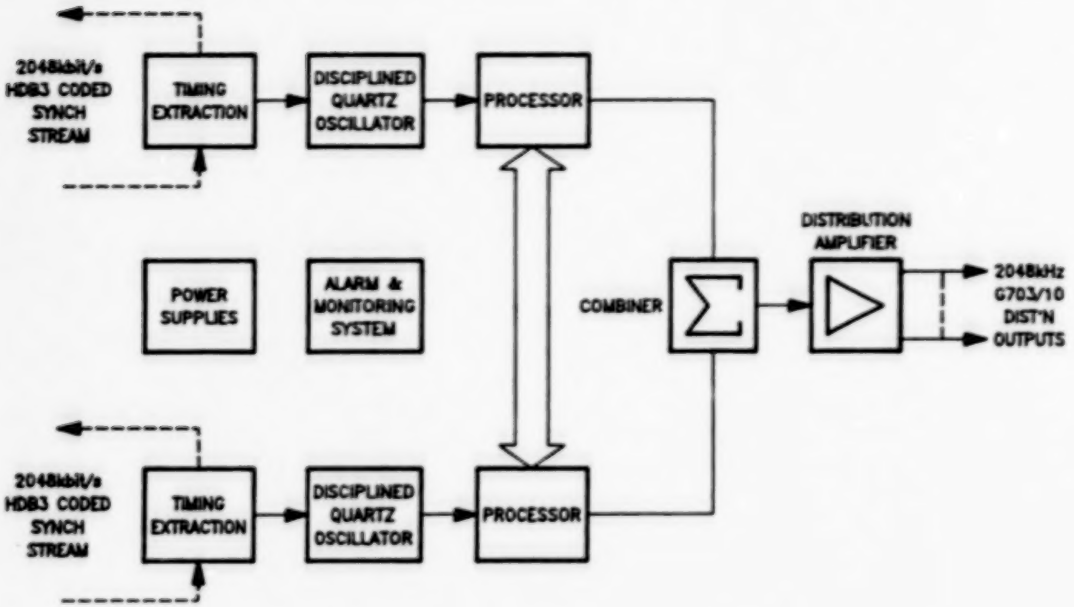
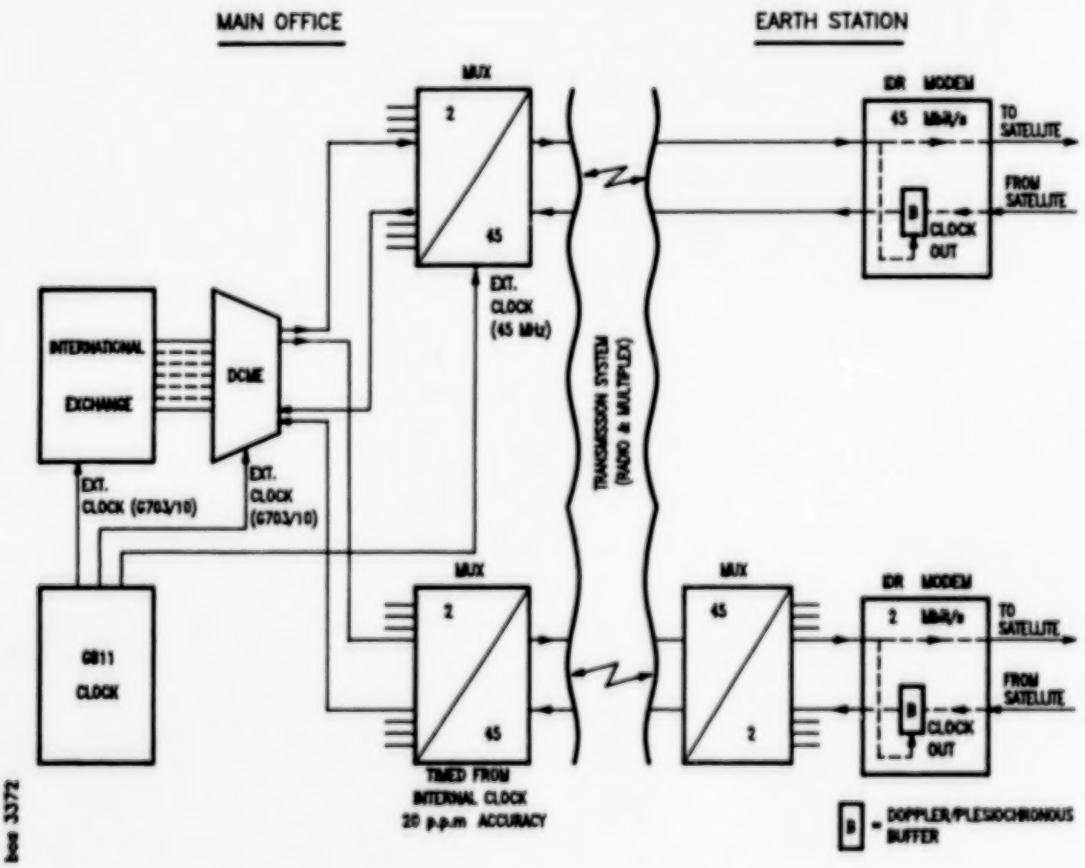


Figure 4 IDR OPERATION INCLUDING CABLE RESTORATION VIA SATELLITE



Unidentified Questioner: Have you measured the availability that you got out of your LORAN system?

Mr. Bodily: The only system that we have had running for any length of time is our system in Bermuda, which is LORAN based. Out of the three years that we have had the system in operation, we have had one occasion where we lost the signal, and that was due to a heavy rainstorm. Apart from that, there have been no outages. Almost 100% availability.

Unidentified Questioner from MCI: When the processor makes the choice between those input references, is that purely based on the quality marker?

Mr. Bodily: No. In the Level 1 system the quality markers tend to be ignored. The signal processor will measure the error between the outputs of the two oscillators, or each oscillator and the cesium standard. The quality marker is really for use in the Level 2 and Level 3 clocks. It gives a direct indication as to whether the cesium has actually failed.

INTERNATIONAL TWO–WAY SATELLITE TIME TRANSFERS USING INTELSAT SPACE SEGMENT AND SMALL EARTH STATIONS

L. B. Veenstra
International Telecommunications Satellite Organization
3400 International Drive, N.W.
Washington, D.C. 20008–3098

Abstract

The satellite system operated by the International Telecommunications Satellite Organization (INTELSAT) provides new and unique capabilities for the coordination of international time scales on a world wide basis using the two–way technique. A network of coordinated clocks using small satellite earth stations collocated with the time scales is possible. Antennas as small as 1.8 m at K–band and 3 m at C–band transmitting powers of less than 1 W will provide signals with timing jitters of less than 1 ns using existing spread spectrum modems.

One way time broadcasting is also possible, under the INTELSAT INTELNET system, possibly using existing international data distribution (press and financial) systems that are already operating spread spectrum systems.

The technical details of the satellite and requirements on satellite earth stations are given. The resources required for a regular operational international time transfer service is analyzed with respect to the existing international digital service offerings of the INTELSAT Business Service (IBS) and INTELNET. Coverage areas, typical link budgets, and a summary of previous domestic and international work using this technique are provided. Administrative procedures for gaining access to the space segment are outlined. Contact information for local INTELSAT signatories is listed.

The microwave time and ranging experiments (MITREX) modem is an efficient device for time transfer via satellite using spread spectrum techniques. International time transfer using satellite spread spectrum techniques regularly will probably require the use of an INTELSAT space segment. There are no substantial technical problems in such use. However, it is necessary to identify the operational issues of using this system in the INTELSAT environment. This paper describes the INTELSAT service compatible with spread spectrum time transfer and suggests how such a service could be implemented.

INTELSAT

INTELSAT, the International Telecommunications Satellite Organization, with headquarters in Washington, D.C., is an international cooperative of 119 member nations that owns and operates the global commercial communications satellite system used by over 178 countries around the world for international communications and by 35 countries for domestic communications. A fundamental characteristic

of the system, from the point of view of time transfer is that access to the INTELSAT space segment is controlled by various national entities, usually the members of INTELSAT. These entities are responsible for the operation of earth stations accessing INTELSAT space segment. In many cases, these entities, the posts, telephones and telegraphs (PT&T), are part of their national government or are chartered by their governments to provide access to INTELSAT. The earth stations may be owned directly by the entities, by common carriers or by the end users, depending on national policy. INTELSAT operates only the space segment and has no direct role in the operation of the ground segment. Thus, time transfer users will need to arrange with their national entities for earth station operation and for the right to use INTELSAT space segment. Appendix 1 of this paper contains contact points for these entities in countries of interest to the PTTI community.

Services

Two specialized INTELSAT services, IBS and INTELNET, are intended for digital links to small earth stations. INTELNET in particular, has enough flexibility in its technical description to allow the operation of a spread spectrum time transfer link.

INTELNET

INTELNET was designed to facilitate the operation of very small earth stations in one-way data broadcasting and two-way low speed data transfers. Spread spectrum operation is allowed, along with conventional BPSK or QPSK modulation. Operation under the INTELNET service description is specifically authorized for very small antennas.

Space segment is leased in "bulk" under the INTELNET service. This offering is defined in terms of specific transponder bandwidths with a corresponding allocation of power. Any required bandwidth may be used, with the resources scaled from the defined allocation. For example, at K-band, a lease of 100 Khz capacity would provide 8.6 dBW of transponder power. A lease of 2.25 MHz would provide 22.1 dBW. In general, the ratio of power to bandwidth is higher (excess power) than is needed for a single spread spectrum time transfer link. Both full time and occasional use service, with a minimum of 30 minutes per period, is available. Listed below are the basic lease powers, referenced to a 100 Khz bandwidth, available on the INTELSAT V series spacecraft.

Global	C-Band	-6.5 dBW
Hemi	C-Band	-5.5 dBW
Zone	C-Band	-5.5 dBW
Spot	K-Band	+8.6 dBW

INTELNET DATA BROADCAST FOR ONE WAY TIME TRANSFER

There are a variety of commercial services operating spread spectrum one way data broadcasting systems on INTELSAT. Many of these are operated in C-band on Global transponders, typically with a chip rate (spreading code rate) of 2.4576 MHz. Most are press news services, operating multiple time division multiplexed channels or low data rates, having an aggregate rate of either 9.6 or 19.2 kbit/s.

These broadcasts could be used for one way time dissemination if the transmitting stations chip rate was synchronized to a standard, and a low speed data subchannel was used to carry ephemeris and other correction information.

INTELSAT Business Service

Space segment for digital communications links can also be obtained under the INTELSAT Business Service (IBS) tariff. In this service the power and bandwidth supplied for a channel are defined in terms of reference links between standard sized earth stations. The reference link assumes conventional QPSK data transmission with either rate 3/4 or rate 1/2 forward error correction (F.E.C.). Sufficient power is available to provide better than 10^{-8} bit error rate performance under clear sky conditions. It is available under a full-time, part-time (scheduled at least 1 hour per day, 7 days per week), or occasional-use tariff. While the spread spectrum nature of the MITREX modem is outside the IBS technical description, the IBS service should be considered when it is necessary to provide communication links between standards sites. On most transponders where IBS is used, INTELSAT has reserved occasional use capacity. This bandwidth could be used to accommodate the MITREX modem operating under the INTELNET service as described below.

Operational Matters

Satellite Locations

INTELSAT operates 15 satellites, serving the three ocean regions, Atlantic, Indian, and Pacific. These locations in degrees East are:

AOR	IOR	POR
307.0	57.0	174.0
325.5	60.0	177.0
332.5	63.0	180.0
335.5	66.0	183.0
338.5		
341.5		
359.0		

Frequency Bands

At C-Band, INTELSAT satellites operate with both left and right circular polarization in the following frequency bands:

Ground Transmit: 5854 - 6423 MHz
Ground Receive: 3629 - 4198 MHz

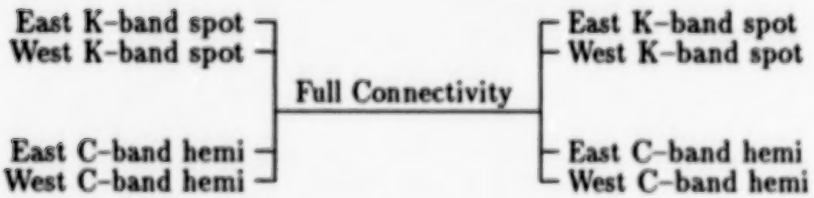
At K-Band, INTELSAT satellites operate with horizontal and vertical polarization in the following frequency bands:

Ground Transmit:	14,004 – 14,494 MHz
Ground Receive:	10,954 – 11,694 MHz
Ground Receive:	11,709 – 11,946 MHz (307 Deg. West only)
Ground Receive:	12,501 – 12,746 MHz (307 Deg. East only)

Transponder Configurations

Most of the Europe–North American IBS traffic is carried on the INTELSAT VA(F–13) located at 307o East. The following configurations of transponders are currently available:

East K–band spot	to	West K–band spot
West K–band spot	to	East K–band spot
East K–band spot	to	West C–band hemi
West C–band hemi	to	East K–band spot
West K–band spot	to	East C–band hemi
East C–band hemi	to	West K–band spot
East K–band spot	to	West C–band hemi
West C–band hemi	to	East K–band spot
West C–band zone	to	East C–band zone
East C–band zone	to	West C–band zone
West C–band hemi	to	West C–band hemi
East C–band zone	to	East C–band zone



The full–connectivity transponder configuration provides the most flexible environment for time transfer links. This consists of a set of four transponders, interconnected at the satellite so that a signal received on any of the four uplink beams is retransmitted on all four downlink beams simultaneously. Two of the beams operate at C–band. These are the West Hemi and the East Hemi. The K–band West spot covers the United States and southern Canada, and the East K–band beam covers western European be seen Figure 1 and 2. Figures 3 through 7 show the global coverage areas for all the C and K satellite antennas from the 307, 341.5 (typical AOR), 359, 63 (typical IOR) and 174 (typical POR). In addition to showing the coverage areas for the Spot, Hemi, and Zone antennas, the usable area is delimited by plots of the locations having 10, 5 and zero degree elevation look angles toward the satellite.

Full–connectivity operation can be used with spread spectrum code division multiple access (CDMA) to allow several time transfer links to be established simultaneously on the same frequency, with all

carriers visible to each user. This means that in a two-station, two-way transfer, it is possible for each site to monitor its own signal while receiving from the remote site.

Additional capacity in the form of East spot-West spot K-band capacity is available at the 325.5o East and 335.5o East locations. C-band capacity is assigned on the 325.5, 335.5 and 341.5o East locations serving the Atlantic Ocean region.

The Indian Ocean Region is served by satellites at 60 and 63o East with Global transponders and east/west zone capacity at C band. A cross strap connection WS/EZ provides a link a K-band in Europe to C-band to the Far East.

In the Pacific region at 174 and 180 degrees East, K-band capacity is available in the Pacific Ocean region between Korea or Japan and the West coast of the United States.

In all three ocean regions there are satellites with capacity reserved for occasional use. The reserved bandwidth is 3.173 MHz wide, sufficient for a 2.048 Mbits/s IBS carrier. These occasional use channels clearly would accommodate a spread spectrum link if the transmit spectrum were restricted by additional filtering. In the full-connectivity transponders, described above, the reserved capacity is in the form of two adjacent occasional-use channels, providing a bandwidth of 6.345 MHz. The operating frequencies for the occasional use channels are listed in Appendix 2.

Link Budgets for MITREX

The link budgets below show the required power for a time transfer link operating in the full-connectivity transponder. The transmitted power has been set to produce at least 54 dB-Hz to a small K-band (1.8 m) station. This same power will also be sufficient for use with a C-band 4.5 m antenna.

Uplink beam	WS	ES	EH	WH
Antenna size	1.8	1.8	4.5	4.5 meters
Hpa power	7.7	0.9	1.0	1.0 Watts
Hpa power	8.9	-0.4	0.0	-0.1 dBW
Antenna gain	46.0	46.0	47.7	47.7 dBi
E.I.R.P.	54.9	45.6	47.7	47.6 dBW
Downlink beam	WS	ES	EH	WH
Beam edge power	11.7	9.8	-4.1	-3.5 dBW
2.25 MHz lease	22.1	22.1	8.0	8.0 dBW

MITREX Modem Use

The simplest way to use the MITREX modem on INTELSAT would be to identify a tariffed INTELNET service that provides at least the necessary power and bandwidth. For regular PSK transmissions, the signal bandwidth at the -18 dB points is required to be within the allocated bandwidth. As can be seen in the attached spectrum analyzer plot. Figure 8 shows, the bandwidth of the MITREX modem is 3.5 MHz at the -18 dB point. The 6 dB bandwidth of the MITREX modem output is 2 MHz. It

is possible to apply additional filtering to the spread spectrum transmitted signal reducing its -18 dB bandwidth, and thus the nominal tariff. However with the spread spectrum operation at such low levels, the -18 dB bandwidth may not be appropriate for tariffing.

Earth Stations

The earth station requirements to operate a time transfer link are quite modest.

The presented link budgets assume the use of 1.8 m K-band stations as a minimum size. This certainly is not the absolute minimum, but it does represent a useful compromise of physical size, link power requirements, and sidelobe performance. Therefore a station equipped with a solid state amplifier would clearly be suitable. Links involving larger stations will need even less transmitting power. At C-Band earth stations in the range of 2.5 to 3 meter diameter are practical.

Any earth station classed as a standard INTELSAT antenna must satisfy the sidelobe gain limit described by the expression:

$$G = 32 - 25 \log i,$$

where G is the gain of the sidelobe envelope relative to an isotropic antenna in the direction of the geostationary orbit and is expressed in dBi, and i is the angle in degrees from the axis of the main lobe.

In addition antennas operating at C-band must use circular polarization with a voltage axial ratio that does not exceed 1.09. However C-band antennas with a diameter of 2.5 m or less are only required to have a voltage axial ratio of 1.3. To operate in the IBS service a K-band antenna must have a minimum G/T ratio of 25 dB/K, qualifying as a standard E1. At C-Band the G/T requirement is 22.7 dB/K and a minimum transmitting gain of 47.7 dBi to qualify as an F1 (nominal 4.5m diameter) standard antenna. To operate under the INTELNET service, there is no minimum G/T requirement.

Implementation

INTELSAT has always been willing to support innovative uses of satellite technology by granting free use of space segment for tests and demonstrations. A request for free use must be submitted through the national signatory for each station involved. The technical approval process for a test or demonstration has two parts:

1. Initially, the earth stations involved must be approved. Small stations not having the minimum G/T values (25 dB/K at K-band, 22.7 dB/K at C- Band) for IBS stations, would have to qualify under the standard G specification.

2. A transmission plan for the proposed experiment will have to be examined to see whether what is proposed will work with the resources requested and, finally, whether the proposed transmissions may cause harm to other users of the space segment.

After approval, the carrier powers are set up in accordance with a test plan issued by INTELSAT and the experiment will then proceed. At the conclusion of the experiment, the participating Signatories

are obligated to submit to INTELSAT a test report on the results. This report will be made available to any interested INTELSAT members.

One objective of such an experiment should be an evaluation of the compatibility of such a service with normal INTELSAT operations, with the view to proposing a tariffed technical description of spread spectrum time transfer. This could then be submitted to the INTELSAT Board of Governors for formal approval as a regular international service with the resources allocated and the consequent tariffs appropriate to the unique demands of spread spectrum time transfer.

Alternatively, commercial service could start immediately under the INTELNET service definition and tariffs. The occasional-use option would probably satisfy the requirements for periodic coordination links between various national standard labs.

Appendix 1.

INTELSAT Correspondent Representatives

Australia
Mr. Alan Ward
Intelsat Access Center
GPO Box 7000
Sydney NSW 2001, Australia
Tel. 2-287-5612
Tlx. 10162 OTCNA

Austria
Dipl. Ing. Wolfgang Schladofsky
Generaldirektion fur die Post-
und Telegraphenverwaltung
Abt. 21
Postgasse 8
A-1011 Vienna, Austria
Tel. 1-5125234
Tlx. 112300 GENT A

Canada
Mr. M. Stephens
Teleglobe Canada
680 Sherbrooke St West
Montreal, Quebec, H3A 2S4
CANADA
Tel. 514-289-7584
Tlx. 9224
Ms. G. Pazos 514-289-7771

China
Mr. Yang Xueming
Directorate General of Telecom
Ministry of the P&T
13 West Changan Ave.
100804 Beijing
Peoples Republic of China
Tel. 661390
Tlx. 222185 DGTEL

France
Mr. J. Meunier
France Telecom - D.T.R.E.
246 rue de Bercy
75584 Paris, FRANCE
Tel. 1-43426275
Tlx. 670372

Germany
Mr. A. Binzer
Referat S15
FTZ Darmstadt, GERMANY
Tel. 6151-833459
Tlx. 419201
Mr. G. Rudolf 6151-83-3383

Greece
Mr. S. Kontoleon
Hellenic Telecom. Org. (OTE)
International Comm. Dept
15 Stadiou Street
Athens 124. GREECE
Tel. 322-0899
Tlx. 219797

India
Mr. M.K.G. Nayar
Videsh Sanchar Nigam, Ltd.
Videsh Sanchar Bhavan
Matatma Gandi Road, Fort
Bombay - 400 001 India
Tel. 22-271819x307
Tlx. 11 2429 VSHN IN HQ BY

Italy
Dr. Luigi Ruspantini
Telespazio
Via Alberto Bergamini 50
00159 Rome, ITALY
Tel. 498-2355
Tlx. 610654

Japan
Mr. Naohiko Hattori, Director
Network Engineering Department
KDD Tokyo Network Headquarters
3-2 Nishi Shinjuku
2-Chome Shinjuku-ku
Tokyo 163, Japan
Tel. 3-347-6600
Tlx. 22500 KDD TOKYO

The Netherlands	Mr. Peter Essers PTT Telecommunicatie Directorate for Infrastructure (DIS) Prinses Beatrixlaan 9 P.O. Box 30000 2500 GA The Hague The Netherlands Tel. 70434725 Tlx. 32482 DIS NL
New Zealand	Mr. L. A. Watt International Relations Telecom Networks and Int'l. Ltd. Telecom Corp. of New Zealand Ltd. P.O. Box 1092 Wellington, New Zealand Tel. 4-738-444x8061 Tlx. 31688 TELINT NZ
Norway	Mr. Claus Svendsen Norwegian Telecommunications Admin PO Box 6701, St. Olavs Plass N-0130 Oslo 1, NORWAY Tel. 70434725 Tlx. 71203 Gentel N
Spain	Mr. J. Lorente TELEFONICA Plaza de Espana 4, Pta. 3 - 7th Floor Madrid 28008, Spain Tel. 1 241 9380 Tlx. 47793 Mr. A. Martin 1-522-2936
Sweden	Barbro Svensson Televerket S-123 86 Farsta SWEDEN Tel. 8-713-1568 Tlx. 14970 GENTEL S

Switzerland	Mr. P. Breu General Directorate PTT Radio and Television Main Division Satellite Communicatior Branch Speichergasse 6 CH-3030 Berne, Switzerland Tel. 31-623756 Tlx. 911025 Mr. P. Chablais 31-622533
USSR	Mr. G. Korolev, Director U.S.S.R. Satellite Communications Company Ministry Of Posts and Telecommunications 7 Gorky Street 103375 Moscow, U.S.S.R. Tel. 95-9255108 Tlx. 411120
United Kingdom	Mr. M. Seymour British Telecom, PLC Landsec House Room 407 23 New Fetter Lane London EC4A 1AE, England Tel. 1-492-3166 Tlx. 883739 Mr. Mike Perry 1-492-2263
United States	Mr. Calvin Harriott Communications Satellite Corp. 950 L. Enfant Plaza S.W. Washington D.C. 20024 Tel. 202-863-6427 Tlx. 892688
INTELSAT	Mr. Lester Veenstra INTELSAT 3400 International Drive, N.W. Washington, D.C. 20008 Tel. 202-944-7090 Tlx. 64290

Appendix 2.

Typical Occasional-Use Frequencies

Transponder Configuration		Uplink	Downlink	Satellite
11/71	WH/ES	5938.7425	10963.7425	(335)
71/11	ES/WH	14044.9975	3744.9975	(335)
11/11	WH/WH	5933.7700	3708.7700	(307)
41/41	WZ/WZ	5930.5975	3705.5975	(307)
41/41	WZ/WZ	5933.7700	3708.7700	(307)
41/51	WZ/EZ	5939.9625	3714.9625	(332)
51/41	EZ/WZ	5939.9625	3714.9625	(332)
62/72	WS/ES	4123.4025	11073.4025	(335)
72/62	ES/WS	4123.4025	11073.4025	(335)
43/53	WZ/EZ	6095.5975	3870.5975	(307)
53/43	EZ/WZ	6095.5975	3870.5975	(307)
13/373	WH/ES	6106.9825	12686.9825	(307)
73/13	ES/WH	14176.0425	3876.0425	(307)
23/163	EH/WS	6095.5975	11875.5975	(307)
63/23	WS/EH	14170.0000	3870.0000	(307)
14/24	WH/EH	6216.4225	3991.4225	(174)
24/14	EH/WH	6216.4225	3991.4225	(174)
64/54	WS/EZ	14296.2150	3996.2150	(174)
54/64	EZ/WS	6221.1925	11496.1925	(174)
64/54	WS/EZ	14264.2200	3964.2200	(63)
54/64	EZ/WS	6189.1975	11464.1975	(63)
61/171	WS/ES	14058.0000	12563.0000	(307)
71/161	ES/WS	14058.0000	11763.0000	(307)
69/79	WS/ES	14459.4075	11659.4075	(325)
69/79	ES/WS	14459.4075	11659.4075	(325)
38/38	GA/GA	6388.5925	4163.5925	(332)
86/86	GB/GB	6303.5975	4078.5975	(60)
12/22/62/72/162/172		Full Connectivity		
		6017.1600	3792.1600	(307)(Hemi)
		14092.1600	11797.1600	(307) (WS)
		12597.1600		(307) (ES)

FIGURE 1
INTELSAT V-A(F-13) at 307 Degrees East West Spot

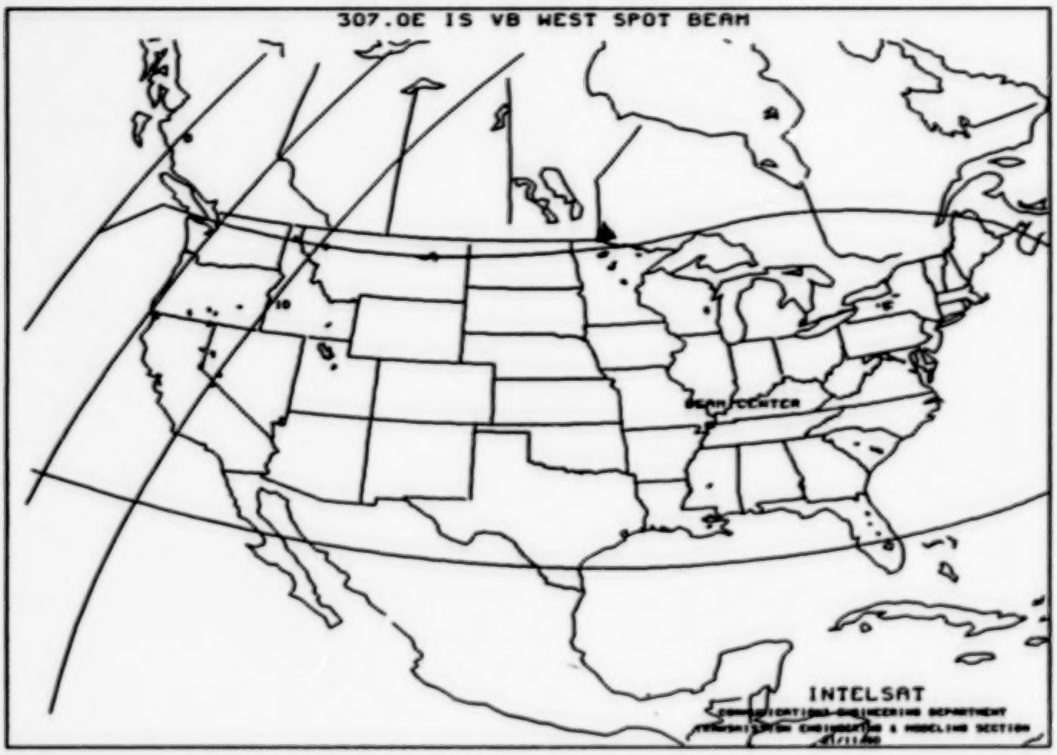


FIGURE 2
INTELSAT V-A(F-13) at 307 Degrees East East Spot

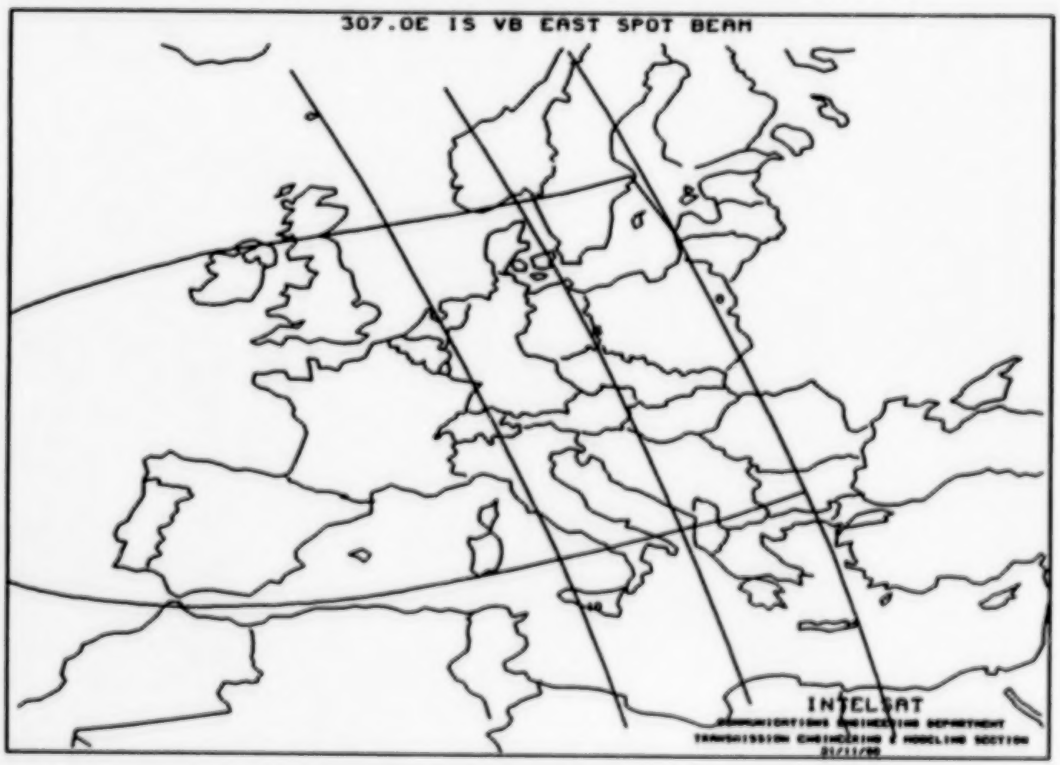
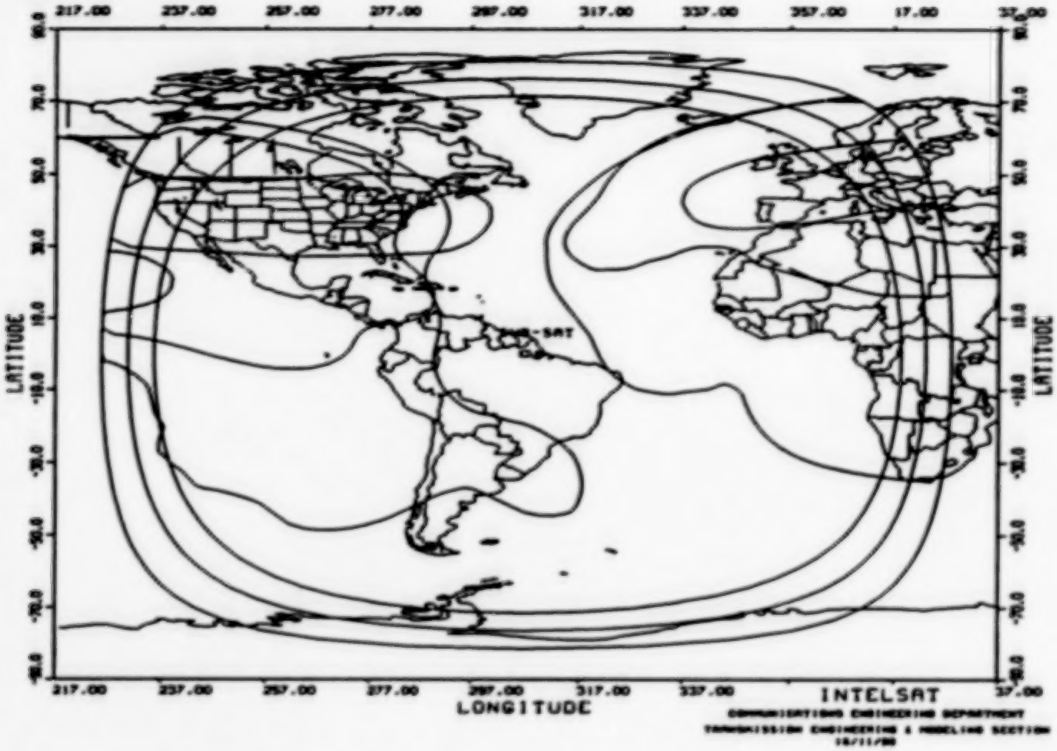


FIGURE 3
INTELSAT V-A(F-13) at 307 Degrees East



INTELSAT V(F-6) at 341.5 Degrees East

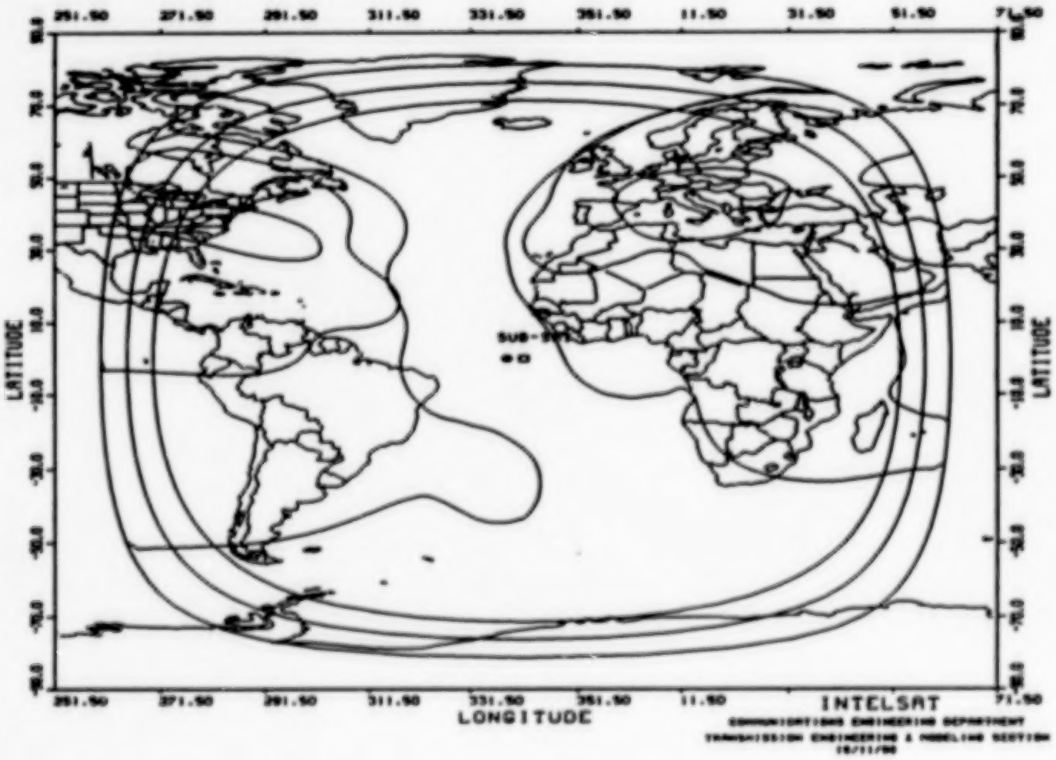


FIGURE 5
INTELSAT V-A(F-12) at 359.0 Degrees East

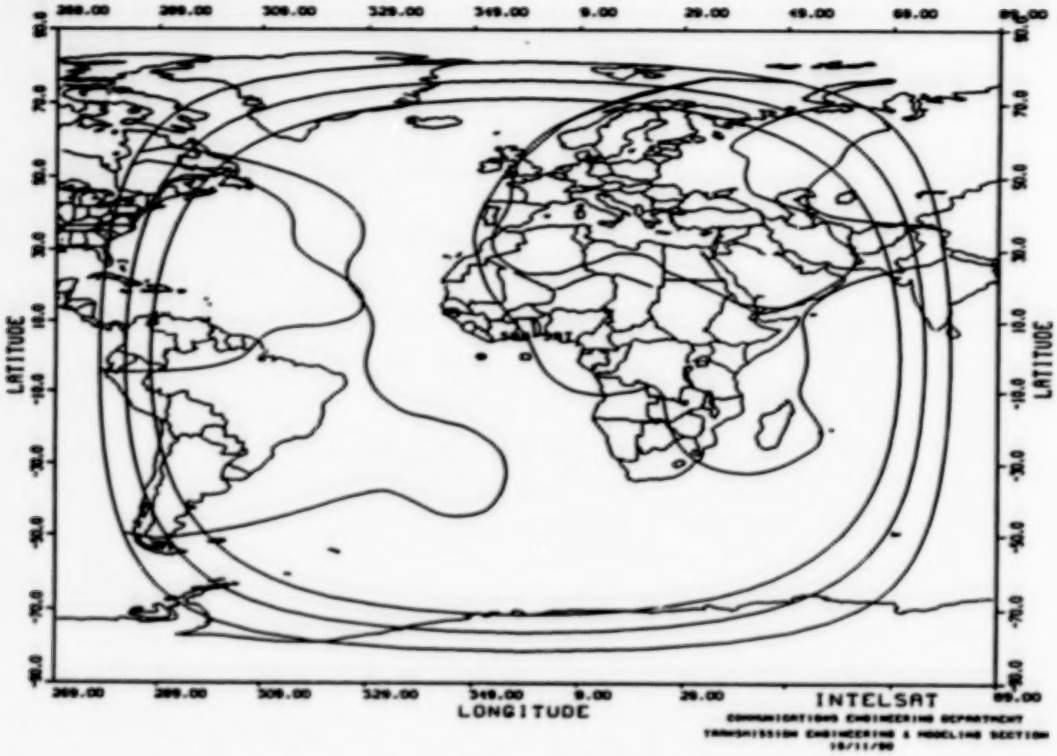


FIGURE 6
INTELSAT V(F-5) at 63 Degrees East

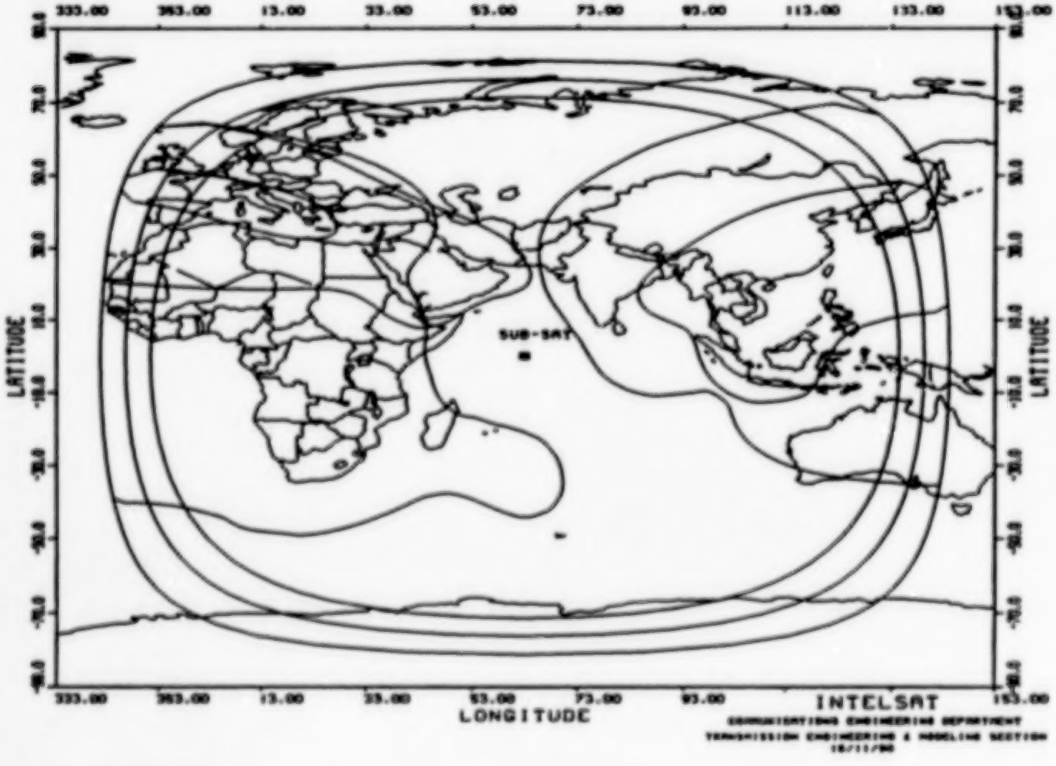
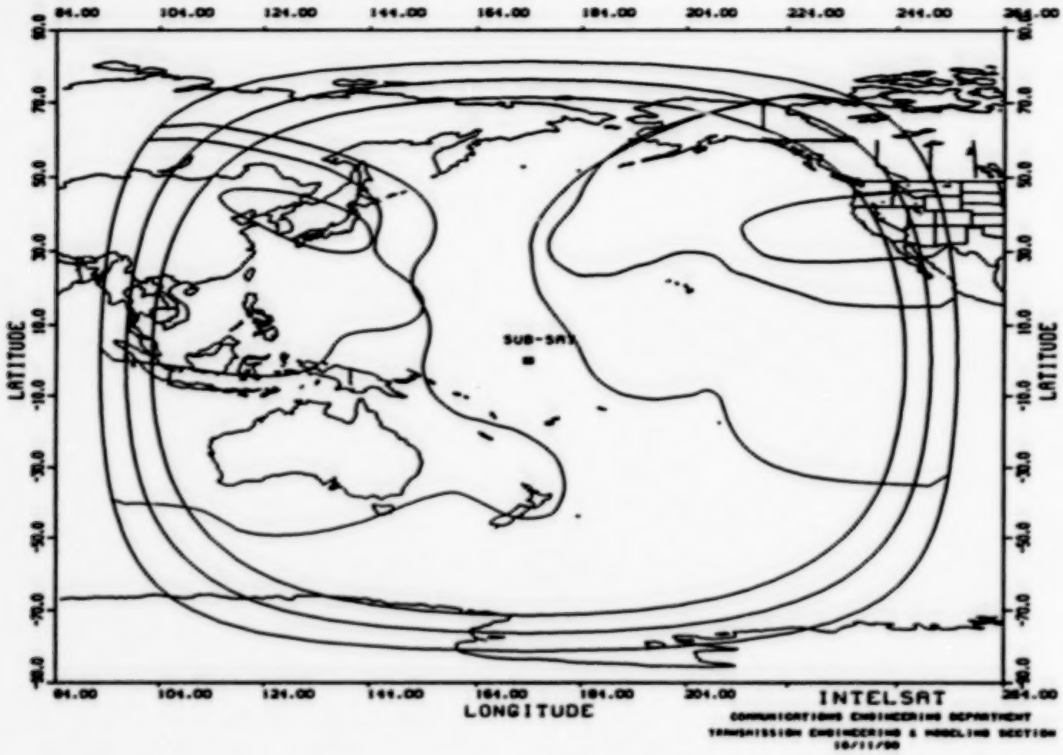
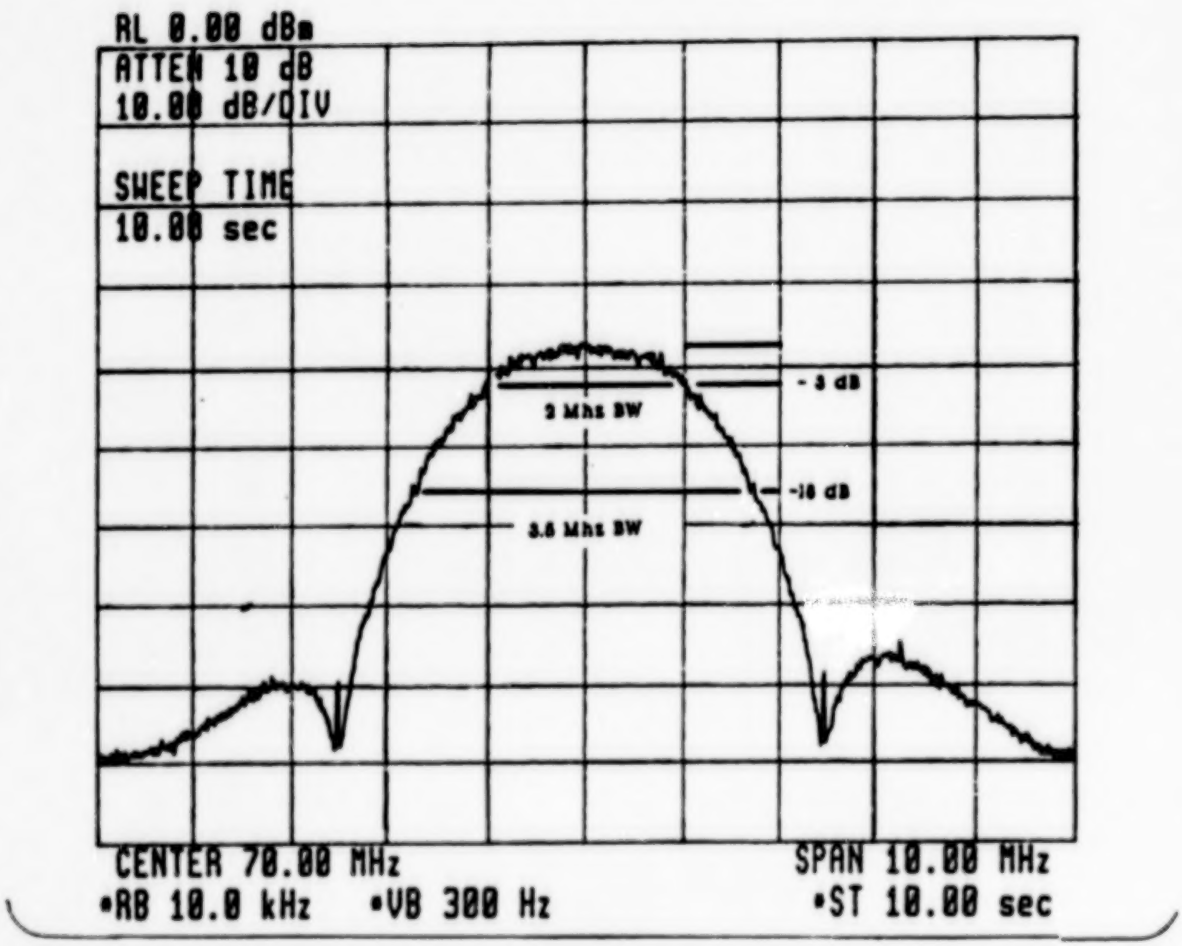


FIGURE 7
INTELSAT VA-(F-10) at 174 Degrees East





QUESTIONS AND ANSWERS

Dr. Gernot Winkler, U. S. Naval Observatory: If you used one of these occasional offerings of, say, a half an hour per week, and a bandwidth of 3.5 MHz, is there any restriction regarding the information other than just the time code. In other words, would there be a problem sending teletype messages also?

Mr. Veenstra: If we approach this as a time transfer sevice, it would be wise to say that the data channel which is being proposed on the newer spread spectrum modems is an order wire. Intelsat never charges for order wires. We know that earth stations need to talk to each other for coordination purposes. Unofficially and off the record to this minor group, I would suggest that you do not emphasize the fact that this is a data channel. I would suggest that you mention the fact that it is an order wire, a low data rate channel, that is used to coordinate at either end. That makes it easier for us to say that we will give this is a free channel because there is really no information being sent, they are transferring phase information. That is zero information so the bureaucrats do not think that you are transferring information for free. Call it an order wire and not a communications link.

BLANK PAGE

THE BBC NETWORK RADIO TIME AND FREQUENCY STANDARD AND ITS ROLE IN THE PROVISION OF THE GREENWICH TIME SIGNAL

Mr J. McIlroy
BBC Radio
Broadcasting House
Portland Place
London
W1A 1AA

Abstract

The BBC has broadcast the Greenwich Time Signal (GTS) on its networks since 1924. Up to February 1990 this signal was generated by the Royal Greenwich Observatory (RGO) in England and the BBC was informed that the RGO was moving its location to Cambridge and might not be able to continue to provide the Greenwich Time Service. The BBC in its role of a public service broadcaster believed that a long tradition of providing a time signal to its listeners should be upheld, and as such decided to seek alternative methods of provision.

In parallel with this activity an in-house requirement arose to re-engineer time switch equipment and provide new facilities for digital audio projects. As both requirements have a common engineering core, a decision was taken to design and procure a Time and Frequency Standard that could generate the Greenwich Time Signal to the same specification adhered to by the RGO, and provide additional time and frequency facilities. This paper discusses initially the concept of time and time/frequency dissemination as used in a broadcast network, and follows on to present the details of an engineering solution to the requirements of BBC Network Radio.

Trends in international broadcasting and the commercial telecommunications market place point towards the increased use of digital audio for studio networking and terrestrial links. The synchronisation requirements in this field are more stringent than that incurred in analogue distribution. This paper will consider what timing systems are needed in these applications and how these requirements are satisfied in the BBC Time and Frequency Standard.

Finally this paper will present a fringe benefit of the BBC Network Radio system. This is the ability to obtain UTC time from the system using a modem dial up method from any location in the world. This facility is currently under evaluation within the BBC; and if considered viable will be available to other organisations and companies in the near future.

Historical Background Of The Greenwich Time Signal (GTS)

The measurement and observance of time in advanced industrial societies in the present age merits a high priority. Yet this was not always so. Scientific interest in the measurement of time using

astronomical and other methods has an old and well established history, but the transfer of a standard time and time keeping to the general public was largely dominated by the railway companies.Quaint as it might have been in England to board a train at London time, and leave the same train on the same day at Plymouth time, these local variations were generally considered unhelpful to the operational management of England's railways.

Following the International Meridian Conference of 1884, a time zone system based on the Prime meridian at Greenwichwas adopted by many countries. Dissemination of time, particularly to the general public, was largely dominated by the "six pips" Greenwich Time Signal (GTS) which was conceived by Sir Frank Dyson, the ninth Astronomer Royal of the Royal Greenwich Observatory (RGO).

Following discussions with John Reith of the BBC, GTS was launched at 9:30 PM on the 5 February 1924 when six short pips were broadcast. The timescale reflected Greenwich Mean Time as determined from astronomical measurements. Initially the "pips" were derived from a Shortt pendulum clock, but in later years atomic clocks were employed. The timescale now adopted is UTC and GTS as heard today consists of five short pips of 100 ms duration and a final pip of 500 ms duration, the start of which marks the exact minute. The longer pip was introduced to make identification of the final pip a more exact process. See Reference 1 for further information.

Time And Frequency Dissemination Within The BBC Radio Network

From The Past To The Present Day

While the listeners were on the right time, courtesy of the RGO, it was equally important to ensure that all departments of BBC Radio were also on the same time. Different techniques for obtaining and disseminating time have evolved over the years. In the pre-microprocessor age cost has been a dominant factor, and a popular system has been the pendulum master impulse clock driving multiple slave units. This type of system has been used for many years at Broadcasting House although its days are numbered. A familiar problem with any oscillator is that of drift, and an ingenious mechanism is employed in this clock to correct the drift using GTS at 3:00 AM each morning. The synchronisation element was the addition or withdrawal of a carefully calculated weight from the pendulum, the effect of which caused the clock to run slow or fast as required.

In 1977 it was decided to upgrade time facilities at Broadcasting House by the installation of an off-air reference tuned to MSF60. This system fed selected technical areas of BBC Radio with a real time code that was used to drive display clocks and operate time switches.

Frequency dissemination in BBC Radio consisted of free running ovenised crystal oscillators which were installed as a component of specific equipments. Small groups of equipment were locked together as required, but no master frequency distribution existed as such.

From The Present To The Future

Two years ago a decision was taken to re-engineer all timing systems as current equipment was obsolete and inadequate for perceived future requirements. Concurrent with this period the RGO announced

they would be moving site from Sussex to Cambridgeshire and the continued provision of GTS was in doubt. As such it was decided to incorporate the means to generate GTS within the new system, and maintain it to the same degree of accuracy as that offered by the RGO.

Technology now available for the generation of studio quality digital audio has pointed the way forward to the all digital broadcast centre concept. The design of such a system required an AES/EBU code master clock with an accuracy greater than 1×10^{-7}. At this time no master distribution existed for this purpose. (AES/EBU abbreviations refer to Audio Engineering Society/European Broadcasting Union.)

The requirements of the new system were as follows:

General

To use equipment off-the-shelf wherever possible and to employ international standards for the dissemination of information, thus permitting easy expansion of the system without the additional work of building special interfaces.

Time

- Obtainment of an off-air time reference from at least two sources for UTC and TOD (Local Time Of Day).
- Generation of a broadcast standard timecode, locked to the off-air time reference, to disseminate time and date information within Broadcasting House.
- Generation of GTS to the same degree of accuracy as that of the RGO.
- Provision of a speaking clock.
- Provision of an AES/EBU digital audio master reference clock, with the inherent timecode locked to the off-air reference.
- Dissemination of UTC and TOD to other BBC sites, and other organisations as required.

Frequency

- Provision of an atomic oscillator system to sustain the Time Standard in the event of loss of off-air reception.
- Provision of frequency clocks, locked to the Frequency Standard, to satisfy user requirements as required.

System Management

- To use off-the-shelf computer hardware, thus providing a capital cost benefit and ease of maintenance by the use of standard boards.
- To use an industry standard operating system (OS) thus permitting flexible expansion of facilities.

System Solution

The system layout is illustrated in Figures 1 through 4. Each part is now described:

Time And Frequency Standard

TIME:

Time is received off-air from GPS and MSF. GPS is used as a UTC reference and to provide an accurate 1 PPS time mark for comparison with other equipment, while MSF is primarily used as a reference for British Time-Of-Day (TOD). A time voting switch (TVS) compares the time of all three receivers via their IRIG B outputs and provides two feeds of UTC and TOD in IRIG B format to the system management computer. If the voting process itself fails the TVS may be used as a stand alone generator to create UTC and TOD outputs as required until normal operation results. Refer to figure 1 for system diagram.

FREQUENCY:

Two GPS disciplined rubidium oscillators, each internally fitted within each GPS receiver, are used to form a dual redundant 10 MHz frequency standard. The long term stability of GPS is excellent and the drift/year of this system is typically 3×10^{-12}. As such this system provides a high degree of accuracy without the punitive maintenance costs of a Cesium system. Refer to Reference 3 for further details.

Dissemination Of Time

GENERAL:

Time dissemination facilities are built around the Leitch CSD5300 clock system controller which provides time output in a variety of formats. Refer to figure 2 for system diagram. These equipments may be controlled *via* a 300 baud RS232 interface or may be set manually via a front panel keyboard. A 10 MHz external frequency reference from the Frequency Standard is used to drive all time dissemination equipment thus ensuring tight control of each 1 PPS internal reference. The 1 PPS time mark in each clock unit is compared with the 1 PPS time mark reference from GPS and is set coincident, advanced or retarded according to user requirements.

Greenwich Time Signal

The Greenwich Time Signal is itself generated from a Leitch CSD5300 and its 1 PPS reference is advanced to compensate for the delay in the transmission path from Broadcasting House to the transmitter. Off-air measurements are made on GTS and the derived 1 PPS is again compared with the GPS RX 1PPS reference. BBC Network Radio aims to maintain GTS within ±2 ms of UTC on Radio 4 as transmitted on 198 kHz. GTS is also sent via private wire circuit to BBC World Service. At the moment GTS transmissions on the short wave network are not fully compensated for transmission channel delay.

TIMECODE DISTRIBUTION:

A realtime signal in the form of EBU Timecode is generated and distributed, to both technical and public areas of the building. This signal is used to drive self setting analogue and digital clocks, a digital voice announcer (speaking clock) and is also used as a timecode reference for audio tape recorders and time switches. As this signal spectrum falls within the audio band it is easily networked within a broadcast centre.

Refer to reference 4 for further details on this system.

REMOTE TIME:

A fringe benefit of the time dissemination facilities is the ability to obtain time via a modem link. This facility, which incorporates automatic path delay compensation, is used by various regional BBC premises to obtain a reference for their local clock control equipment, and has proved to be accurate for these purposes. Time transfer accuracy of ±1 ms ±modem error is quoted by Leitch. The BBC system employs CCITT tones and Hayes 1200 smart modems Experiments are in progress to judge the accuracy of this system. Dial-up time facilities are available for UTC and TOD.

Dissemination Of Frequency

FREQUENCY CLOCKS:

Frequency generators using Oscilloquartz VCXO's are employed to provide specific frequency clocks to user requirements. These generators are locked to the 10 MHz frequency standard, but in the event of a failure of this reference the modules may freewheel. On restoration of reference a long time constant is used to permit smooth operation of the PLL. The use of separate modules in this manner makes it simple to expand the system or locate modules of this type at another location.

AES/EBU MASTER CLOCK:

This module provides a digitally encoded stereo audio signal, with a bit rate of 3.072 Mb/s, locked to the 10 MHz frequency standard.

EBU Timecode carrying TOD information is also inserted into the bitstream. This signal is used as a master clock reference for digital audio studio areas and for multiplexed digital audio routing systems.

Refer to figure 3 for a system diagram.

System Computer

A modular based computer system is employed to read IRIG B format time signals and 1 PPS time mark reference from the TVS. Time Dissemination modules are then set to UTC, TOD or user specified time as required, and automatic monitoring is used to ensure that neither the set time nor the 1 PPS drifts out of time setting. As the system resides in an unmanned apparatus room an Ethernet interface

is used to convey control to the Network Radio Engineering Operations Centre, where control may be picked up by a number of operating positions.

Refer to figure 4 for system details.

Acknowledgements

The author would like to express his thanks to the Director of Engineering of the BBC for permission to publish this paper. In addition the author would like to express his thanks to Tony Seabrook, formerly of the Royal Greenwich Observatory at Herstmonceux, England, for his advice at the design stage of this project.

References

1. *BBC Engineering 1922-1972*, Edward Pawley, Published by BBC, ISBN 0 563 12127 0.

2. *An Off-air Observatory Time service*, A.R. Seabrook, Royal Greenwich Observatory, England, Proceedings of the Nineteenth Annual Precise Time and Time Interval (PTTI) Applications and Planning Meeting, December1-3, 1987.

3. *A GPS Disciplined Rubidium Clock*, Wayne Dewey, Kinemetrics/Truetime, Santa Rose, California, Proceeding of the Twenty First Annual Precise Time and Time Interval (PTTI) Applications and Planning Meeting, 27-30 November 1989.

4. *A Telephone-based Time Dissemination System*, Don Jackson, Leitch Video and R.J. Douglas, NRC, Canada, Proceedings of the Eighteenth Annual Precise Time and Time Interval (PTTI) Applications and Planning Meeting, 2-4 December 1986.

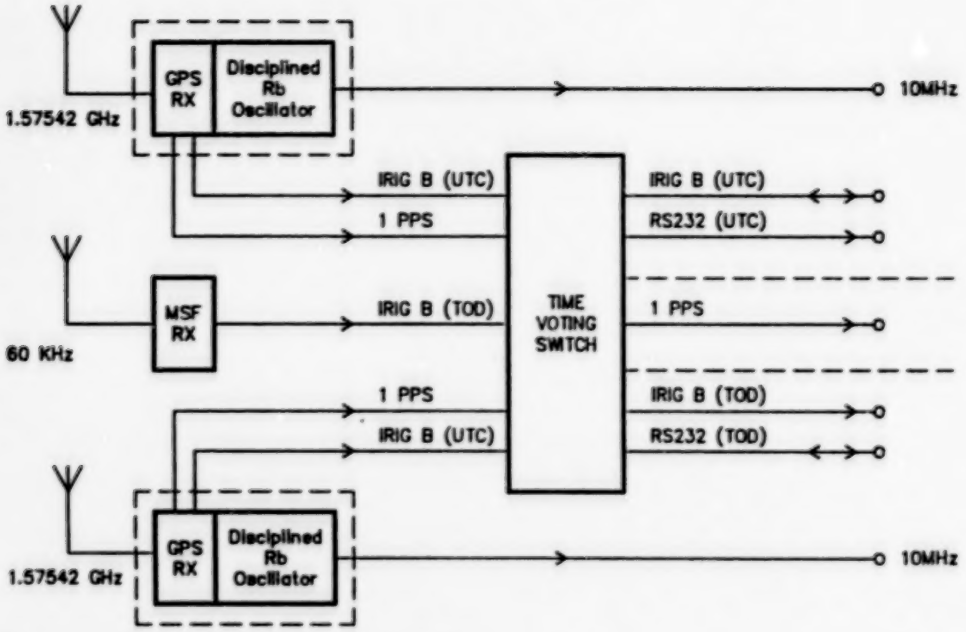


Figure 1: Time and Frequency Standard

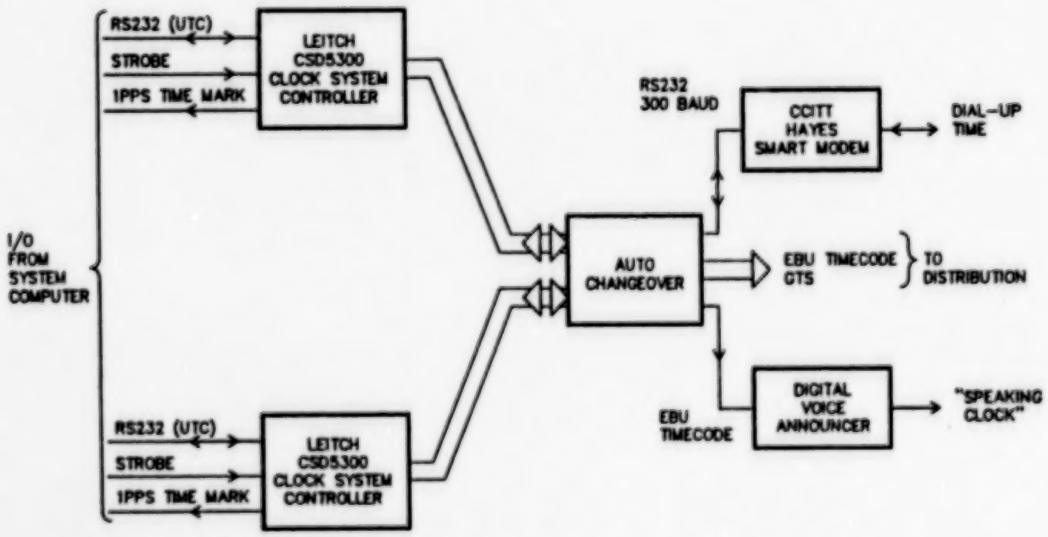


Figure 2: Time Dissemination

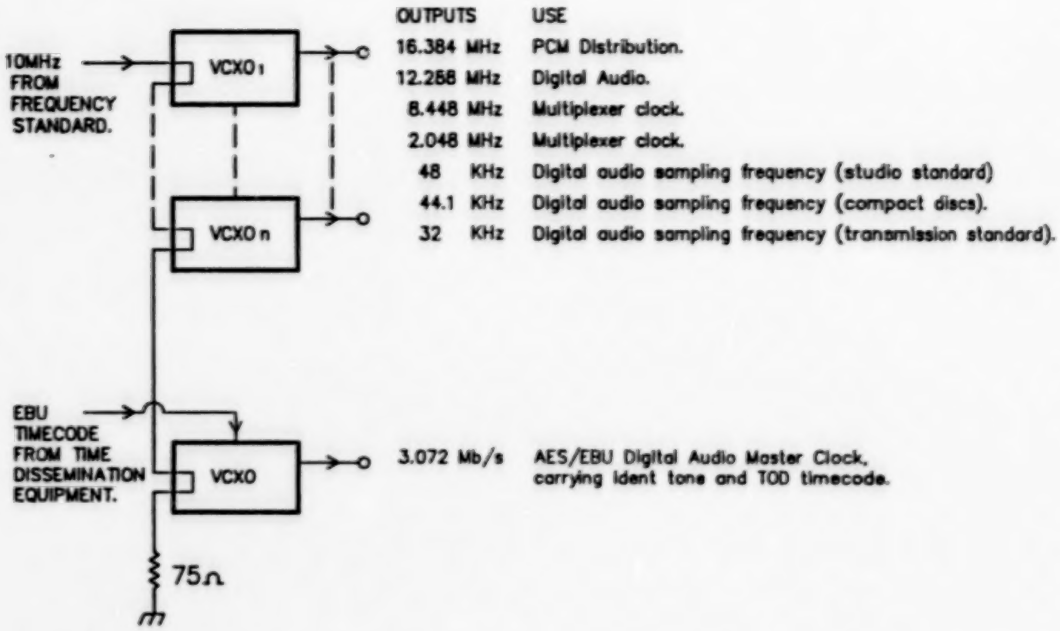


Figure 3 : Frequency Dissemination.

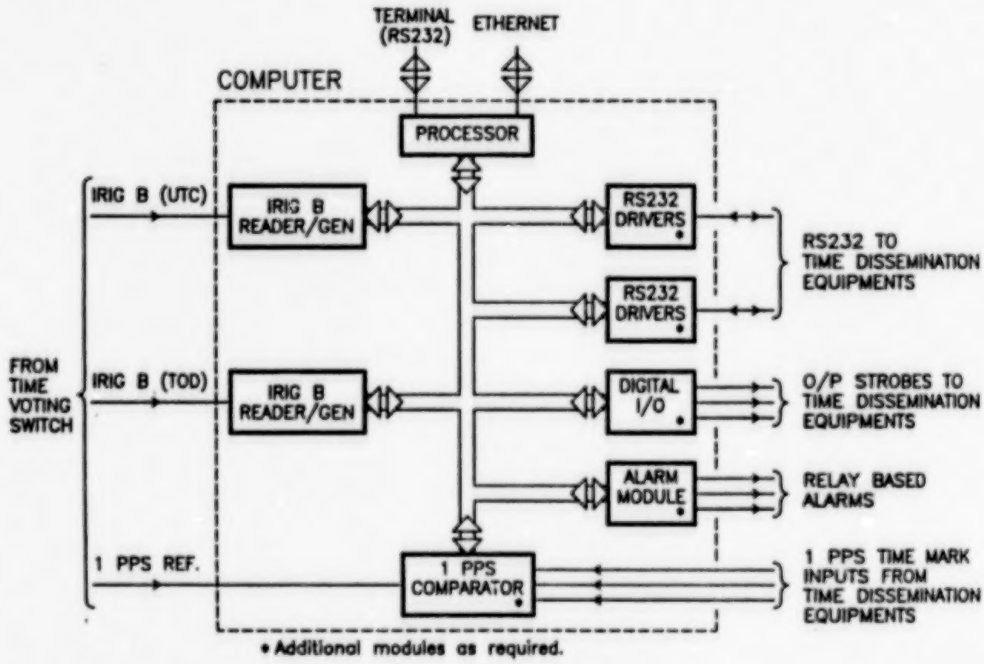


Figure 4: System Computer

SYNCHRONIZING COMPUTER CLOCKS USING A LOCAL AREA NETWORK

Judah Levine
Time and Frequency Division
and
Joint Institute for Laboratory Astrophysics
National Institute of Standards and Technology
Boulder, Colorado 80303

Abstract

We have completed the first tests of a method to synchronize the clocks of networked computers to the NIST time scale. The method uses a server computer to disseminate the time to other clients on the same local-area network. The server is synchronized to NIST using the ACTS protocol over a dial-up telephone line. The software in both the server and the clients constructs a statistical model of the performance of the local clock and of the calibration channel, and the parameters of this model are used to adjust the time of the local clock and the interval between calibration requests in a statistically optimum way. The algorithm maximizes the time between calibrations while at the same time keeping the time of the local clock correct within a specified tolerance. The method can be extended to synchronize computers linked over wide-area networks, and an experiment to test the performance of the algorithms over such networks is being planned.

Introduction

In 1988, the National Institute of Standards and Technology (NIST, formerly the National Bureau of Standards) introduced the Automated Computer Time Service. This service is a dial-up telephone service designed to provide digital access to the NIST time scale at accuracies approaching 1 ms. The service transmits time information at either 300 bits/s or 1200 bits/s. All of the lines support both transmission formats using standard modems. The data are transmitted using standard ASCII characters with 7 data bits, space parity and 1 stop bit. The current telephone number for the service is (303) 494-4774 (not toll-free). The transmitted data include the day number, the civil date and time and flags that give advance notification for the insertion of leap seconds and for the transition to and from Daylight Saving Time. See Levine et al. (1989) for more details.

In this paper we report on preliminary tests of a system to synchronize the time of networked computers that is based on this NIST service. Our method uses server computers to disseminate the time on the computer network. The servers in turn are synchronized using periodic calibrations from the NIST time scale. One of the most important features of the system is the statistical model that is incorporated into the software in both the server and client machines. These models dynamically adjust the interval between calibrations based on the desired synchronization accuracy, the jitter in the calibration link, the cost of each calibration and other factors. They make optimum use of the calibration data and optimize the performance of the network based on the specified accuracy requirements.

The Network Servers

The network servers are general-purpose computers and use a standard commercial multi-processing operating system. They are linked to a local-area network using standard hardware and also have an external modem that is connected to a voice-grade telephone circuit. The interface between the computer and the modem uses one of the RS-232 serial ports of the system. The time of the server is advanced automatically in response to hardware interrupts generated by an internal crystal-controlled oscillator. The interval between interrupts is 10 ms for our hardware, but periods ranging from 1 ms to 50 ms are often found in hardware from other suppliers. In addition to these hardware interrupts, the time of the server is adjusted by the software as described below. These adjustments are made to the software-maintained time registers only; the actual oscillator cannot be directly controlled.

The server software consists of two parts: the process that sets and maintains the time of the local clock and the process that transmits the time to other machines on the network. These two processes are independent, although they share access to a global set of parameters that define the state of the server. Both of the processes are normally activated as part of the start-up of the server. The process that controls the local clock runs as a dæmon in the background, while the transmitter is activated whenever a calibration request is received from a client machine. Neither process uses a significant fraction of the resources of a modest-sized workstation.

The clock control dæmon is divided into three sub-processes:

1. A process that measures the time difference between the server and NIST. The comparison is made using the dial-up telephone line and the ACTS protocol. The telephone connection time is typically 15 s. The accuracy of this calibration is about 10 ms and the repeatability is about 0.3 ms. This repeatability is achieved by careful design of the process, especially the algorithm to interpolate between the ticks of the local clock. This algorithm can reliably resolve intervals on the order of 1% of the period of the local clock (less than 1 ms on most systems).

2. A process that uses the time difference data to construct a model of the local oscillator. The principal parameters of the model are:

y	Clock Rate in seconds of deviation/second
D	Change in Clock Rate seconds/second^2
Δ	Interval between external calibrations
ϵ	Clock Noise
η	Channel noise
E_m	Maximum time error

   The model dynamically adjusts the first three parameters, (y, D and Δ), to optimize the performance of the clock in the presence of the two noise sources, ϵ and η. Specifically, the model attempts to maximize the interval between calibrations, Δ, while at the same time keeping the local time correct within the bounds specified by E_m.

3. A process that uses the model parameters to continuously correct the local clock. These corrections are implemented as 1 ms time steps in the appropriate direction. The interval between these corrections is at least 10 ms, so that the steering does not exceed 10% of the clock rate.

The Clock Model

The free-running performance of the server clock is modeled by

$$\begin{aligned} x(t_{j+1}) &= x(t_j) + y \times (t_{j+1} - t_j) \\ &\quad +0.5 \times D \times (t_{j+1} - t_j)^2 + \epsilon. \end{aligned} \tag{1}$$

This expression relates the time difference, x, between the server and NIST at time t_{j+1} to the difference at some earlier time t_j. Note that $\Delta = t_{j+1} - t_j$, and that Δ is not constant but is adjusted by the algorithm. The server constructs initial estimates for y and D by several successive calibrations separated by a time interval of between 1 and 2 hours. This interval is chosen long enough so that the channel noise η will not make a significant contribution to the rate and short enough so that D can be neglected and the clock noise ϵ can be modeled as a random process (even though all oscillators have a noise spectrum that shows increased variance at longer periods).

If the data are statistically consistent, then the server changes to a phase-lock mode. The time of the local clock is set (usually by slewing it at the maximum permitted frequency). When the local clock is on time, the rate estimate is used to apply periodic corrections to it as described above.

Subsequent calibrations are used to refine the parameters of the model. The calibration interval is gradually lengthened until the rms error of the model approaches the value of E_m. For any combination of oscillator and calibration channel, there is generally an optimum calibration interval and a corresponding minimum time error, E_m: the performance at shorter intervals is degraded because the random component of the measurement noise degrades the rate estimates, and the performance using longer intervals is degraded because the low-frequency components of the oscillator noise spectrum are not adequately predicted by the model. This optimum interval is usually about 24 hours for the crystal oscillators that are normally used in computer clocks, and the corresponding minimum time error is about 1 ms.

One important aspect of the algorithm is the reset logic. Most oscillators exhibit occasional glitches that are much larger than the standard deviation of their performance. Similar effects are often found in the performance of the calibration channel. It is important that these effects be recognized as unusual and that they not be allowed to corrupt the statistical model of the oscillator. If the error of a calibration exceeds twice the running average standard deviation for the previous day, then a reset algorithm is executed. The algorithm first repeats the calibration. If the two calibrations are statistically different, a channel error is assumed. If the two calibrations agree then either a time or frequency step is assumed. If the difference between the next two calibrations agrees with the long-term trend, then the problem is a time step only; if the subsequent calibrations are consistent with a new trend then a frequency step (including a possible time step) has occurred. If the subsequent calibrations cannot be modeled as a combination of a time step and a rate step, then a hardware failure is indicated. The algorithm attempts to re-initialize itself in this case; if that attempt fails then an unrecoverable error is signaled.

Server Test Results

We have conducted several tests to demonstrate the capabilities of the method. Fig. 1 show the free-running performance of the clock in node TILT. The time of the computer is compared periodically

with the NIST time scale using a dial-up connection and the ACTS protocol. The effect of the clock rate y, dominates the performance at this level.

The rate of the clock is then estimated using the first 4 hours of data, and the performance of the clock for the remainder of the month is predicted using (1). The subsequent difference measurements normally would be used to modify y, D and Δ, but this update loop was disabled for these tests.

Fig. 2 shows the residuals between the data of Fig. 1 and the predictions of the model. The short-term variance is 0.8 ms, (8% of a 10 ms tick) and the spectrum appears white. The performance of the ACTS system is considerably better than this (Allan et al., 1990), and we are probably being limited by jitter in both the modem equalizers and the interrupt latency of the server. This interrupt latency could be reduced by moving some of the code into the device driver for the RS-232 port, but we have not done this at this time. The longer-period fluctuations are due to changes in the rate of the clock oscillator; the relatively small diurnal changes probably result from temperature fluctuations while the longer term effect can be broadly characterized by a random-walk in frequency that is undoubtedly due to aging of the oscillator crystal. It is important to note, however, that the server does not deviate from the time predicted by the model by more than ± 20 ms for the entire observation period. If this level of performance was satisfactory, the server could run for at least 1 month with no additional external calibrations once the rate had been estimated.

Fig. 3 shows the locked performance of node TILT. The parameters of the lock algorithm have been tuned to lock the time to the minimum error E_m consistent with the channel and measurement noise spectra. The optimum calibration interval was about 18 hours, but Δ was fixed at 1.8 hours and the faster estimates were exponentially averaged to estimate the optimum rate.

Local Area Network Tests

The network tests were performed using a relatively large local-area network on the campus of the University of Colorado. The network consists of segments of thick-wire cable within buildings with bridges to connect the various buildings together. The maximum distance between buildings is about 3 km.

Two independent servers (named STRAIN and TILT) were locked to the NIST time scale using the methods outlined above. These servers responded to requests from any host on the network by sending the time together with flags providing advance notice of leap seconds and of upcoming transitions to and from Daylight Saving Time. A single character specifying the health of the server was also transmitted.

There are several different versions of the client software. The simplest version simply requests the time from the server and uses the data to set the time of the client if the server is healthy. A more complex client program utilizes the same algorithm as was described above for the server to keep the time of the client within a specified tolerance using periodic calibrations from the server. The client algorithm uses a somewhat different characterization for the channel noise parameter η since the client receives its calibration data over a packet network rather than over a single dial-up telephone circuit.

To test the performance of the network software, we used two servers and a single client. The client (named JILACK) periodically requests calibration data from both servers (named STRAIN and TILT) and computes the difference of the differences:

$$\begin{aligned} \delta t_s &= (\text{JILACK} + \epsilon_j - \text{TILT} + \eta_1) - (\text{JILACK} + \epsilon_j - \text{STRAIN} + \eta_2) \\ &\approx (\text{STRAIN} - \text{TILT} + \eta_1 - \eta_2) \end{aligned} \tag{2}$$

since the two requests are so close together in time that the fluctuations of JILACK can be neglected. Here ϵ_j is the unmodeled clock noise of node JILACK while η_1 and η_2 are the network delays between JILACK and the two calibration nodes. The times of nodes STRAIN and TILT are known with respect to the NIST time service since both are locked via periodic calibrations using the ACTS protocol:

$$\begin{aligned} (\text{STRAIN} - \text{ACTS}) &= E_s + \eta_{a1} \qquad \text{where } < E_s >= 0 \text{ and } < E_s^2 >= \sigma_s^2 \\ (\text{TILT} - \text{ACTS}) &= E_t + \eta_{a2} \qquad \text{where } < E_t >= 0 \text{ and } < E_t^2 >= \sigma_t^2 \end{aligned}$$

Here σ^2 is the variance of the clock noise and η_a is the noise in the ACTS calibration channel, which is assumed to be the same for both nodes (on the average). Thus the differential network delay can be estimated from

$$(\eta_1 - \eta_2) \approx \delta t_s - (E_s - E_t) + (\eta_{a1} - \eta_{a2}) \tag{3}$$

We found that the differential network delay varies by less than ± 1 ms over the range of network loads we have observed and that $< \delta t_s >= 0 \pm 2$ ms.

Expansion to Wide Area Networks

There is no difficulty in principle in expanding this system to wide area networks, and we are currently planning a wide-area network test. One practical limitation will be the characterization of the network delay parameter, η, which is likely to contain time-varying non-stationary components. It is also likely that the network delay will not be reciprocal so that the one-way delay between two points cannot be estimated by one-half of the round-trip time. Under these circumstances, a local-area network synchronized via a single server which is in turn calibrated using ACTS will have certain advantages over the same network synchronized using a wide-area network protocol because the telephone connections between the server and the NIST time scale are much easier to characterize and are much more likely to be stable and reciprocal. The additional cost of the charges for the toll calls is not high — one or two 15 s calls per day would be adequate for almost all applications, and lower-accuracy applications would require correspondingly less frequent calibrations.

Conclusions

We have designed and tested a method that can be used to synchronize the time of computers on computer networks using periodic calibrations from the NIST time scale. The method makes optimum use of the calibration data by constructing statistical models of the performance of the oscillators in both the server and client machines. The calibration of the servers uses dial-up telephone connections which are highly reciprocal and stable and are therefore much easier to characterize than dissemination methods which depend on a wide-area network for synchronization.

References

1. Allan, D. W., D. D. Davis, J. Levine, M. A. Weiss, N. Hironaka and D. Okayama, 1990. *New Inexpensive Frequency Calibration Service from NIST*, Proceedings of the Symposium on Frequency Control, in press.

2. Levine, J., M. Weiss, D. D. Davis, D. W. Allan and D. B. Sullivan, 1989. *The NIST Automated Computer Time Service*, J. Res. of NIST, 94, 311 – 321.

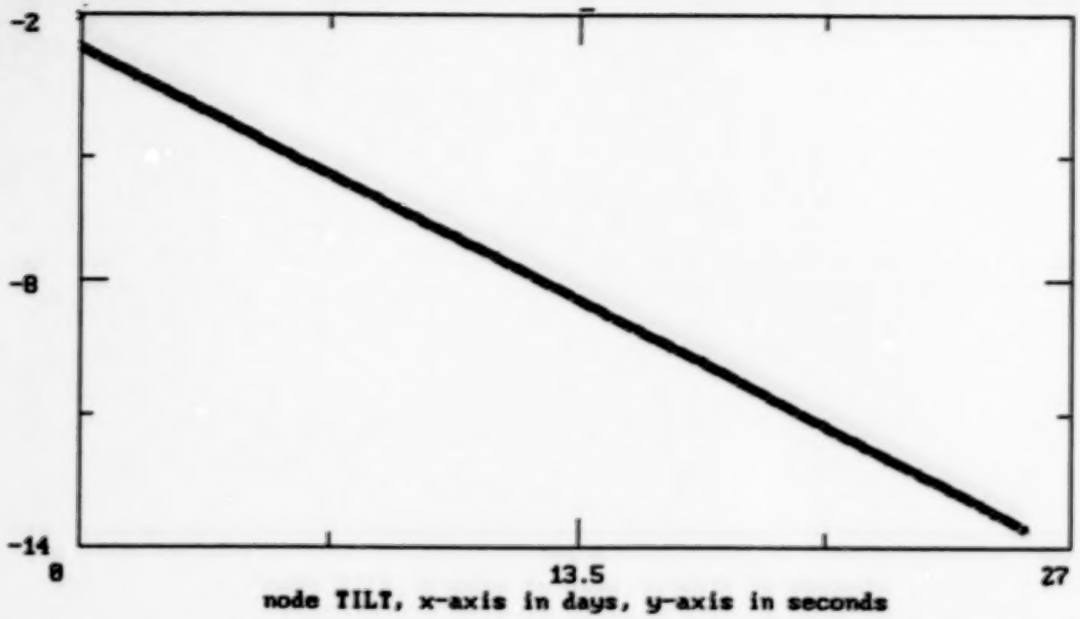


Fig. 1. Time of node TILT - NIST time scale. The time difference is measured using the ACTS time service over a dial-up telephone connection. The slope in these measurements shows the frequency offset of the free-running oscillator, and the deviations of the measurement line from a straight line are mainly due to measurement noise. (The width of the line is due to the size of the symbol used at each point.)

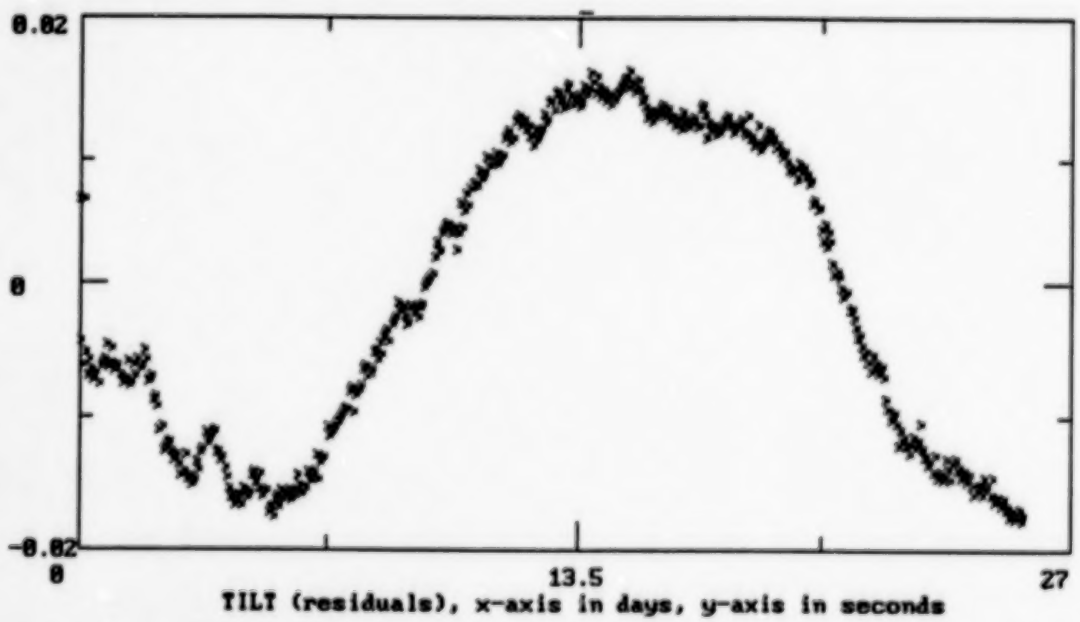


Fig. 2. Difference between the data in Fig. 1 and the predictions of the clock model. The rate of the oscillator was estimated from the first 4 hours of the data. The model parameters were locked at that point and the residuals between the modeled clock and NIST are shown in the figure.

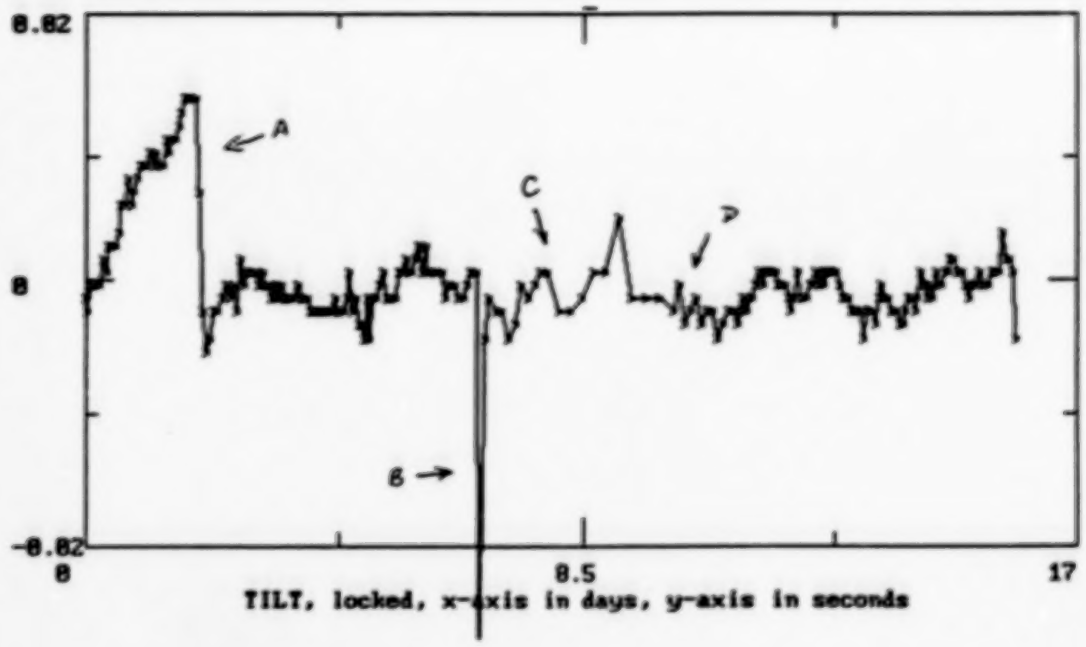


Fig. 3. Time of node TILT - NIST. The time of node tilt is adjusted in increments of ±1 ms. The interval between these software adjustments is derived from the model equation (1). The parameters of the model are updated periodically using calibrations via the ACTS time service over a dial-up telephone connection. Note the change from the parameter estimation mode to the locked mode at point A, the glitch at point B that was caused by the re-boot of the server following a short power failure. Note also the automatic adjustment of the interval between calibrations at points C and D.

QUESTIONS AND ANSWERS

Dr. Winkler, U. S. Naval Observatory: I miss, in your discussion, the substantial difference in timing in the computers depending on the operating system. In the PC, which has an increment of time in the timing registers of 16 milliseconds, usually, and the actual processor runs at 5 or 8 or 12 megaHertz, but the registers are not updated faster than every 16 milliseconds. Compare that to the OS-2 or the Unix systems where the actual time interval kept is in seconds, and the real-time system such as the HP system 1000. They are all completely different. It has been our experience that it is better not to fool around with the computer time internally, but to do everything externally. Make the time measurements externally and use the interupts to read the external time. I wonder how the different operating systems will affect that.

Mr. Allan: I am sure that they will. We have done experiments on Micro-Vaxes and on a Sun system. The same technique would work on a PC, just at a higher level.

BLANK PAGE

PHYSICAL ORIGIN OF THE FREQUENCY SHIFTS IN CESIUM BEAM FREQUENCY STANDARDS: RELATED ENVIRONMENTAL SENSITIVITY

C. AUDOIN, N. DIMARCQ, V. GIORDANO and J. VIENNET
Laboratoire de l'Horloge Atomique
Unité Propre de Recherche du CNRS
associée à l'Université Paris-Sud
Bât. 221 – Université Paris-Sud
91405 ORSAY Cedex – France

Abstract

When observed in a cesium beam frequency standard, the hyperfine transition frequency of the atoms differs slightly from the invariant transition frequency of the unperturbed atoms at rest. The various physical and technical origins of the frequency offsets are stated. They relate to fundamental physical effects, to the method of probing the atomic resonance and to the frequency control of the slaved oscillator. The variation of the frequency offsets under a change of the value of the internal operating characteristics is considered. The sensitivity to a change of the magnetic induction, the microwave power and the temperature is given. A comparison is made of the sensitivity of cesium beam frequency standards of the commercially available type, making use of magnetic state selection, and of devices under study, in which the state preparation and detection is accomplished optically. The pathways between the external stimuli and the physical origin of the frequency offsets are specified.

1. INTRODUCTION

According to a basic postulate of physics, the properties of atoms do not change with space and time (except for known relativistic effects). Therefore, the frequency delivered by atomic frequency standards should not vary with time and should not depend on perturbations applied such as constraints, change of temperature and humidity, etc.

However, although very slightly, this frequency varies during the device lifetime and depends on external factors. To understand this undesirable fact, one must not forget that the postulate mentioned implies that the atoms are assumed at rest, isolated and in free space. This is obviously not the case in actual devices: the atoms are moving at thermal velocities; although in a beam they are not isolated and, moreover, the two energy levels of interest pertain to manifolds; the atoms are subjected to fields. Furthermore, accessories are necessary to observe the microscopic properties of the cesium atoms. They are: an oven; state selectors; a microwave cavity; a set-up to generate the C-field; a detector; and electronic systems to probe the transition, to process the beam tube response and to frequency lock a quartz crystal oscillator.

These departures from the ideal conditions and some of these accessories can be sources of frequency offsets, the magnitudes of which depends on the technical choices made.

These frequency offsets couple the observed resonance frequency to the macroscopic world. Since macroscopic objects are usually sensitive to external factors such as temperature, the frequency offsets depend on environmental conditions and, consequently, the frequency of the standard does also. Frequency changes can thus be induced by a variation of the temperature, the humidity, the constraints, the fields, etc...applied to the device.

Although the frequency offsets are rather small, they are numerous in the cesium beam frequency standard. However we shall ignore the gravitational frequency offset, whose value is easily predictable and the frequency offsets whose change is negligible in the usual range of variation of the external factors.

The frequency offsets can be sorted out, more or less arbitrarily, into three categories depending on the principal origin of the offset. They are related to fundamental physical effects, to the resonance interrogation method and to possible imperfections in the electronic system. We shall give their order of magnitude and the possible cause of their change.

We shall consider commercially available cesium beam frequency standards, without reference to a specific model, but with plausible values of the characteristic parameters. In these devices, the static and the microwave magnetic fields are applied perpendicularly to the atomic beam axis. The length of each interaction region, l, is equal to about 1 cm. The separation, L, between the two oscillatory fields is of the order of 15 cm. State selection is presently accomplished by deflecting the atom trajectories in magnets. The velocity distribution function of the atoms detected depends on the design and it is not an universal function. We will therefore introduce a crude, but representative distribution of the interaction times τ in each oscillatory field region. It has the shape of a triangle shown in Figure 1a. The maximum of the distribution arises at $\tau_1 = 71\ \mu s$, corresponding to a velocity v_1 of 140 ms^{-1}[1]. For the purpose of comparison, we shall also consider the distribution of interaction times which is encountered in the simplest configuration of an optically pumped cesium beam frequency standard, using a single diode laser for the state preparation and the state detection. In that case, the velocity distribution is that of an effusive beam[2]. The related distribution of the interaction time is shown in Figure 1b. It peaks at $\tau_0 = 46.5\ \mu s$, assuming an oven temperature of 100°C. $\tau_0 = l/\alpha$ is the interaction time for atoms having the most probable velocity,α, in the oven.

We shall give the order of magnitude of the frequency offsets and the possible cause of their change. For that purpose, we shall rely mainly on results published in references 3 through 8, where credit is given to prior work. Frequency offsets whose value depend on the velocity distribution have been computed from equations derived in [8], assuming slow square wave frequency modulation, for simplicity. However, the main conclusions of this paper are valid for other types of modulation.

In the following, the frequency offsets are expressed in Hertz, the static magnetic induction is expressed in gauss ($1\ G = 10^{-4}\ T$) and ν_0 is the frequency of the unperturbed hyperfine transition of the cesium atom.

2. FREQUENCY OFFSETS DUE TO FUNDAMENTAL PHYSICAL EFFECTS

2.1. Second order Zeeman frequency offset

In the C-field region, a static magnetic induction is applied parallel to the main component of the microwave magnetic induction sustained in the interaction regions. It raises the degeneracy of the cesium atom hyperfine levels in the ground state and it enables $\Delta m_F = 0$ transitions to be induced. Its values is usually set around 60 mG, to separate sufficiently the second order field dependent $(F = 3,\ m_F = 0) \leftrightarrow (F = 4,\ m_F = 0)$ clock transition from the six other neighbouring, but first order field dependent, $\Delta m_F = 0$ transitions (see Figure 2).

a) Magnetic induction assumed uniform

The second order Zeeman offset of the frequency of the clock transition is given by:

$$\Delta\nu_B = 427.45\ B_0^2. \tag{1}$$

Assuming $B_0 = 6 \times 10^{-2}\ G$, the frequency offset amounts to about 1.54 Hz, or 1.67×10^{-10} in relative value. This is the largest frequency offset occuring in cesium beam frequency standards.

A change, dB_0, of the magnetic induction gives a change $d(\Delta\nu_B)$ of the frequency offset. We have:

$$d(\Delta\nu_B) = 855\ B_0\ dB_0. \tag{2}$$

For $B_0 = 6 \times 10^{-2}\ G$, $dB_0/B_0 = 3 \times 10^{-5}$ $(dB_0 = 1.8\ \mu G)$, we have $d(\Delta\nu_B)/\Delta\nu_B = 10^{-14}$. This means that the current source needed to generate the static magnetic induction must be of a sufficient quality, with a small sensitivity to temperature changes.

A transverse shielding factor of about 5×10^4 gives a sensitivity, equal to 10^{-13} per Gauss, to a change of the magnetic induction applied externally and orthogonally to the beam tube. However, one should be cautious in assuming that the frequency shift is proportional to the variation of the external induction since, at least in some models, non-linearities have been observed, as well as a lack of reproducibility of the effect of the variation.

A sensitivity to alternating magnetic fields has been observed. The DC frequency offset produced might be the result of some rectification effect related to non linearities occuring either in the shielding material or in electronic components used in the associated electronic sub-assemblies.

b) Effect of magnetic field inhomogeneities

Actually, the static magnetic induction is not uniform in the C-field region. The main reasons of this imperfection are the following. The permeability of the magnetic material is finite. There are holes in the magnetic shield (the largest one for the input waveguide). The static field created may simply be not uniform, at least in some tube designs.

The related frequency offset can be separated into two parts. The first one is associated to the field inhomogeneity in the space between the interaction regions. Let $B_0+\Delta B(z)$ be the magnetic induction along the beam path and $\Delta B(z)$ its fluctuation with quadratic mean value $\overline{\Delta B(z)^2}$. The frequency offset is equal to:

$$\Delta\nu'_B = 427\ \overline{\Delta B(z)^2} \tag{3}$$

Assuming a standard deviation of $2 \times 10^{-3}/G$, we have $\Delta\nu'_B/\nu_0 = 1.9 \times 10^{-13}$. The second source of frequency offset is the difference between the magnetic induction in the interval between the two interaction regions and the induction in these regions. We have:

$$\Delta\nu''_B = 214\frac{l}{L}(B_1^2 - B_2^2 - 2B_0^2)\ , \tag{4}$$

where B_1, B_2 and B_0 are the inductions in the first interaction region, in the second one and in the interval between them, respectively. The values of $\Delta\nu' \times B$ depends, but only slightly, on the microwave power and on the frequency modulation parameters. Assuming $B_1 = B_2 = 62\ mG$, $B_0 = 60\ mG$ and $l/L = 1/15$, we have $\Delta\nu''/\nu_0 = 7.6 \times 10^{-13}$, which is a significant frequency offset.

The frequency offset associated with the magnetic field inhomogeneities can change if the field distribution is modified by an externally applied magnetic field.

c) Effect of a magnetic field applied parallel to the beam tube

An external magnetic field applied parallel to the beam axis should not give a frequency shift. However, it has been observed that such an effect exists and that it is even larger than when the field is directed transverse to the tube[9,10].

A magnetic induction is added parallel to the beam axis in the C-field region (the shielding factor is smaller in the elongated direction). It is thus perpendicular to the main component of the microwave induction and it can induce neighbouring $\Delta m_F = \pm 1$ transitions, which may give rise to a frequency shift (see Section 2.2b). Furthermore, a distortion of the magnetic lines of force by the magnetic shields may create a small transverse component, dB_0, changing the value of the frequency offset $\Delta\nu_B$. Moreover, such a distortion may change the magnetic field inhomogeneities.

2.2. Neighbouring transitions

a) $\Delta m_F = 0$ transitions

Six intense, field dependent, $\Delta F = \pm 1$, $\Delta m_F = 0$ transitions are also present in the microwave spectrum of the cesium atom, as shown in Figure 2. The width of their pedestal is equal to about 15 to 20 kHz and their separation is approximately equal to 42 kHz when B_0 is close to 60 mG. The aisles of the pedestal of the $(F = 4,\ m_F = 1) \leftrightarrow (F = 3,\ m_F = 1)$ and of the $(F = 4,\ m_F = -1) \leftrightarrow (F = 3,\ m_F = -1)$ transitions overlap under the line of the $(F = 3,\ m_F = 0) \leftrightarrow (F = 4,\ m_F = 0)$ transition. In tubes where the state selection is accomplished magnetically, the field dependent lines, symmetrically placed around the central one, have significantly different amplitudes, as shown in Figure 2a. It follows that the shape of the central line is distorted by an added slanted base line, and that a

frequency offset arises. The properties of the latter depends closely on that of the aisles of the Rabi pedestal. Their amplitude is proportional to the microwave power and it is an oscillating function of their distance to the line center. Consequently, the frequency offset depends on the microwave power and on the value of the static magnetic induction. Furthermore, it depends on the population and of the velocity distribution of the atoms involved in the neighbouring transitions. The offset is also a function of the modulation parameters (*cf* Appendix). The Rabi pulling effect has been studied in detail by de Marchi[3,5]. He has found a frequency offset varying according to the previous statements in Cs beam frequency standards produced by a given manufacturer, as shown in Figure 3. Results obtained with standards of a different supply, using tubes of a different design and in which the frequency modulation scheme is different, were not has clear as that shown in Figure 3[11].

The relative frequency offset may amount to several 10^{12} and its change may be several 10^{-13} per dB of microwave power variation. When the influence of the neighbouring Rabi pedestals is clearly identified, there are magnetic field settings for which the frequency offset goes to zero as well as the sensitivity to a microwave power variation. In that case, it has been experimentally verified that Cs beam tubes tuned at one of these points show an improved long term stability[5,7]. However, most of the manufactured tubes are still operating at a different point. Then, the Rabi pulling effect contributes to their sensitivity to a change of their microwave power. A frequency shift may also occur if the beam composition varies (change of the beam optics and of the beam deflexion angle, Majorana transitions) and thus the asymmetry of the microwave spectrum. Similarly, a change of the velocity distribution of atoms in the sublevels $m_F = \pm 1$ of the ground states $F = 3$ and $F = 4$ can produce a frequency shift.

As shown in Figure 3, the Rabi pulling effect introduces a sensitivity to a change of the value of the C–field. However, this sensitivity is smaller than that related to the second order Zeeman effect and it can be neglected.

The Rabi pulling effect is specific to beam tubes with magnetic state selection. The related frequency offset and its sensitivity to the microwave power and to other factors should be absent in cesium beam tubes optically pumped with a linearly polarized light[12]. In that case, the microwave spectrum of the cesium atom is highly symmetrical around the central $(F = 3,\ m_F = 0) \leftrightarrow (F = 4,\ m_F = 0)$ line, as shown in Figure 2b. Furthermore, this property gives the opportunity to decrease the value of the C–field and thus the sensitivity to magnetic field changes.

b) $\Delta m_F = \pm 1$ transitions

A spurious component of the static magnetic field parallel to the beam tube axis, and therefore perpendicular to the main component of the microwave magnetic field can induce $\Delta m_F = \pm 1$ transitions. This component can be produced in the tube itself if the C–field region is poorly designed, or it can be the result of an externally applied magnetic field. The shape of the weak resonance features is similar to that of the $\Delta m_F = 0$ main lines. Such small lines can be seen in Figure 2a, in the dips between the $\Delta m_F = 0$ resonance patterns. Although weaker, they are closer than the neighbouring $\Delta m_F = 0$ lines. They may produce a frequency offset of the $\Delta m_F = 0$ clock transition when the populations of the $m_F = \pm 1$ sublevels are not identical. It depends on the microwave power level.

$\Delta m_F = \pm 1$ resonance features can take a different shape, as shown in Figure 2b at mid–distance between the $\Delta m_F = 0$ lines. This record has been obtained with a tube in which the apertures in the Ramsey cavity are larger than in conventional ones[12]. Moreover, the value of the C–field, and thus the separation between the lines, has been increased for the purpose of illustration. Although weak,

they are very likely present in all beam tubes, but they may be masked by the aisles of the intense $\Delta m_F = 0$ lines at the usual values of the C–field. Furthermore, they may not emerge from the noise.

The $\Delta m_F = \pm 1$ transitions shown in Figure 2b are likely due to the existence of components of the microwave magnetic field which are perpendicular to the static field, but have opposite directions at points symmetrically disposed around the waveguide axis[13]. In the E–plane microwave cavities considered here, these components are likely related to the distortion of the microwave magnetic lines of force, which is created by the holes.

Like the $\Delta m_F = 0$ ones, these transitions can have different intensities in cesium tubes with magnet state selectors. Thus the closest to the central line may induce a frequency offset. The effect of the $\Delta m_F = \pm 1$ transitions is being studied in detail[14].

2.3. Second order Doppler effect

The second order Doppler frequency offset is directly related to the time dilatation effect of the special theory of relativity. In the presence of a velocity distribution, the value of the relative frequency offset is given by:

$$\frac{\Delta\nu_D}{\nu_0} = -\frac{v_i^2}{2c^2}\Delta_D \,, \tag{5}$$

where v_i is equal to v_1 or α for cesium beam tubes with magnetic state selection or optical pumping, respectively. Δ_D depends on the parameters mentioned in the Appendix. Assuming slow square wave modulation, Figure 4 shows its variation versus the amplitude of the microwave induction for different values of the depth of the frequency modulation.

For the values of the operating parameters given in the Appendix, the relative frequency offset is equal to -1.1×10^{-13} and to -3.8×10^{-13} for the tubes with magnet state selection and optical pumping, respectively. A 1 dB change of the microwave power yields a small variation of the frequency offset, equal to 0.5×10^{-14} and 3.2×10^{-14}, respectively.

2.4 Spin exchange

Collisions between alkali atoms cause a relaxation of the population of the hyperfine energy levels and, also, a shift of the hyperfine transition frequency.

Collisions are present in a thermal beam. Their rate is approximately 1/3 that occuring in a vapor showing the same atom density. Furthermore, a background pressure of cesium vapor exists in a beam tube, mainly at the end of its life, when the getters get saturated.

However, the value of the spin exchange frequency shift cros–section of the cesium atom is not known at present. Work in this respect is desirable. It is thus not possible to give a quantitative estimate of the related frequency offset. However, it would be of interest to know whether spin–exchange can cause an ageing effect through a change of the background vapor pressure, or not.

2.5. Light shift

The frequency offset called the light shift is of course specific to optically pumped cesium beam tubes. It is due to a displacement of the hyperfine levels in the ground state, which is induced by transitions between the ground state and an excited state.

In a cesium beam tube, the photons emitted by the fluorescing atoms, and which propagate along the beam path, reach the microwave interaction region and perturb the transition frequency. Photons scattered from the laser pumping light can be efficiently eliminated by proper design of the optical part of the device.

An estimate of the magnitude of the light shift has been calculated by several authors[15–17]. For a small tube of the commercial type, it is predicted to be smaller than 10^{-13}, in relative value, using the D_2 line at 852 nm for the atom preparation and detection[17], and one order of magnitude smaller with the D_1 line at 894 nm[16]. No experimental result is available yet.

This frequency offset depends on the number of fluorescing atoms and thus on the atomic beam intensity. The latter can easily be maintained sufficiently stable. Moreover, the number of fluorescing atoms is not much sensitive to the intensity of the laser light beam when the optical pumping is almost complete in the two optical interaction regions. Thus, the stability of this intensity should not be critical.

3. FREQUENCY OFFSETS DUE TO THE INTERROGATION METHOD

A microwave signal is necessary to probe the atomic resonance, since the Cs beam frequency standard is a passive device. Frequency offsets are related to the implementation of a microwave cavity, with its two interaction regions, and to the presence of spurious spectral components in the interrogation signal.

3.1. Mean phase shift between the two oscillatory fields

A small amplitude travelling wave is superimposed to the cavity standing wave. It carries the energy lost in the waveguide walls and in the two terminations. This travelling wave couples any dissymmetry in the electrical properties of the two arms (unequal length, unequal losses, unequal reflections, asymmetry of the feeding junction) into a small phase difference between the two oscillatory fields. The resonance line is then distorted by an additional component which is an odd function of $(\nu - \nu_0)$. A frequency offset follows which can be thought as a residual first order Doppler effect.

Assuming a phase difference, ϕ, between the antinodes of the magnetic field in the two interaction regions, the frequency offset is given by:

$$\Delta\nu_\phi = -\frac{\phi}{2\pi T_i}\Delta_\phi \tag{6}$$

where T_i is a characteristic value of the time of flight of atoms between the two interaction regions.

We have chosen $T_i = T_1 = L/v_1$ for the tube with magnetic state selection and $T_1 = T_0 = L/\alpha$ for the tube with optical pumping. Δ_ϕ depends on the parameters listed in the Appendix.

In a short Ramsey cavity ($L = 15$ cm), a difference between the electrical length of the two arms equal to approximately 3×10^{-5} m gives $\phi = 10$ μrad. With the values of the operating parameters given in the Appendix, the relative frequency offset amounts to 1.5×10^{-13} and 2.9×10^{-13} for the tubes with magnetic state selection and optical pumping, respectively. A 1 dB change of the microwave power yields a relative frequency variation of 0.4×10^{-14} and 1.3×10^{-14}, respectively.

A differential dilatation of the length of the cavity arms, corresponding to a temperature unbalance of 1 K gives a change of the phase difference of 0.6 μrad and thus a negligible frequency offset of the order of 1×10^{-14}.

3.2. Distributed phase shift

In each interaction region, there exists a space dependent phase shift of the microwave magnetic field. It is due to the travelling wave component transporting the energy lost in the cavity walls. The distributed phase shift is present even if the phase difference between the centers of the interaction regions is equal to zero. It has a component in the direction transverse to the beam. A longitudinal component likely exists also. It is related to the presence of the holes which enable the atoms to cross the oscillatory field region.

Actually, the order of magnitude of the frequency offset associated with the transverse phase shift is the same as that due to the phase difference between the two cavity ends[18]. The longitudinal phase shift gives a frequency offset only if the two apertures and the two cut-off sections attached to the main waveguide show an asymmetry[8].

3.3. Cavity pulling

If the cavity is not exactly tuned at the atomic transition frequency, then the amplitude of the microwave field does not vary symmetrically when the atomic resonance is scanned. A frequency offset $\Delta\nu_r$ of the resonance frequency follows. It is given by:

$$\frac{\Delta\nu_r}{\nu_0} = \frac{T_c^2}{T_i^2}\Delta_c\frac{\Delta\nu_c}{\nu_0}\ , \tag{7}$$

where $\Delta\nu_c$ is the cavity mistuning. T_c is the cavity response time, equal to $Q_c/\pi\nu_0$ being the cavity quality factor. T_i has the same meaning as in Equation 6. Δ_c depends on the operating conditions, as described in the Appendix. The quantity $(T_c/T_i)^2$ is of the order of magnitude of $(Q_c/Q_l)^2$, where Q_l is the line quality factor. For slow square wave modulation, figure 5 shows the variation of Δ_c versus the amplitude of the microwave field, for different values of the depth of the frequency modulation. Assuming the operating conditions introduced previously, $Q_c = 5000$, $L = 15$ cm and a cavity mistuning of 0.1 MHz, the relative frequency offsets amounts to 1.1×10^{-13} for the classical tube and to 1.4×10^{-12} for the tube with optical pumping. The variation of the cavity pulling frequency offset, for a 1 dB change of the microwave power, is equal to 2.3×10^{-13} and 3.6×10^{-13} for the classical tube and the optically pumped tube, respectively.

Assuming b constant, the frequency shift related to a change ΔT of the cavity temperature is given by:

$$\frac{\Delta\nu_r}{\nu_0} = -\Delta_c \frac{T_c}{T_i} \alpha \Delta T \tag{8}$$

where α is the linear coefficient of expansion of the cavity material. With $\alpha = 1.6 \times 10^{-5}$ and $\Delta T = 1$K, we have: $\Delta\nu_r/\nu_0 = 1.6 \times 10^{-13}$ and 2.0×10^{-12} for the tube with magnetic state selection and optical pumping, respectively. Moreover, the cavity detuning changes the microwave power applied to the atoms, which must be taken into account[6]. Furthermore, the temperature change will vary the microwave power.

The cavity pulling frequency offset, and its variations, are larger for the optically pumped tube than for the traditional one. However, it can be reduced by decreasing the value of the cavity quality factor, since the frequency offset, and its changes, varies as Q_c^2. Similarly, it would be appropriate to increase the value of $b\tau_0$ towards the point where Δ_c goes to zero. It can be shown that, at that point, the DC content of the beam tube response shows a maximum, in the case of slow square wave modulation. Another, but more involved possibility consists in using two or three lasers instead of one. Implementation of detection *via* a cycling transition, and/or of pumping with two small power lasers, favors slow atoms[19,20]. This increases the mean time of flight, with a subsequent decrease of the related frequency shifts[21].

3.4. Majorana transitions

If the magnetic field varies along their path, the travelling atoms are subjected to a time dependent perturbation. It may have spectral components causing transitions between the m_F sublevels of the $F = 3$ and $F = 4$ manifolds. They are called Majorana transitions. They are usually avoided by trimming properly the magnetic field along the atom path.

Should they occur, the effect of these transitions is not completely understood yet[22]. However, they may give indirect frequency shifts, as briefly explained now. In practical magnetic state selectors, the deflection of a trajectory depends on the atom m_F value, besides the velocity. It follows that the occurence of Majorana transitions changes the trajectory of the atoms which are able to hit the hot wire detector and, therefore, their velocity distribution. The effect of these transitions is thus i) to modify the signal to noise ratio of the resonance detection, ii) to modify the amplitude of the neighbouring transitions and the related frequency offset, iii) to change the frequency offsets depending on the trajectory (such as that related to the transverse phase shift) and iv) to vary the frequency offsets depending on the velocity distribution.

In optically pumped tubes, Majorana transitions can be more easily avoided. Since, moreover, the atom deflection by light is very small, their effect should be negligible.

3.5. Spectral purity of the interrogation signal

The signal at 9.192 631... GHz, which is necessary to observe the resonance of the Cs passive frequency standard, is generated by the methods of frequency synthesis, starting from the output of a quartz crystal oscillator. Therefore, any spurious spectral component in the signal of this oscillator is enhanced

by the process of frequency multiplication. Furthermore, frequency mixing is necessary to create the frequency required and, usually, the final signal contains unwanted spectral components.

External factors can also be the source of spectral impurities. Sidebands at 50 or 60 Hz from the carrier come from the power supply. Other spectral components can be coupled to the interrogation signal in the presence of external signal generators. Vibrations perturb the quartz crystal resonator and are another source of spurious sidebands.

The additional spectral components give rise to virtual transitions which shift the energy levels of the $F = 3$, $m_F = 0$ and $F = 4$, $m_F = 0$ states. The complete analytical expression of this frequency offset is complicated in the case of a cesium beam tube[23]. We shall only consider here the effect of an additional spectral component whose frequency ν' is such that we have $|\nu' - \nu_0| \lesssim 20$ kHz. This means that this component is present outside the Rabi pedestal bandwidth. The frequency offset is then given by:

$$\Delta\nu_S^{(f)} = \frac{lb_1^2}{4\pi^2 L(\nu' - \nu_0)}\Delta_S^{(f)} \tag{9}$$

where b_1 is a measure of the amplitude of the spurious microwave induction. Its definition is similar to that of b (see Appendix). The quantity $\Delta_S^{(f)}$ is approximately equal to 0.65 for the operating conditions considered here and for both types of tube. Thus the frequency offset is proportional to the power of the added signal and inversely proportional to its separation from the carrier.

In many cesium beam frequency standards, a residual sideband is present at 12.6 MHz from the carrier. Taking into account the filtering effect of the cavity, and assuming $Q_c = 2000$, its power is approximately 20 dB below that of the carrier. We thus have $b_1 \cong 2 \times 10^3$ rad s^{-1}. With $l/L = 1/15$, the relative frequency offset is small, equal to 0.4×10^{-13}. It changes if the power of the side-band varies. It also depends on the power of the carrier in as much as the frequency mixing process binds the power of the side-band to that of the carrier. It is worth mentioning that the effect of a spurious side-band may be large for $|\nu' - \nu_0|$ comprised between approximately the half-width at half-maximum (HWHM) of the central fringe of the Ramsey pattern and the HWHM of the Rabi pedestal.

4. FREQUENCY OFFSETS DUE TO THE ELECTRONIC SYSTEM

4.1. Modulation and demodulation related frequency offsets

It can be shown that a false error signal is produced and therefore a frequency offset of the slaved quartz crystal oscillator results from the presence of the following imperfections[8]: i) the spectrum of the modulation waveform is distorted and comprises spectral components at frequencies $2p\nu_M$, p being an integer and ν_M the frequency of the modulation, ii) the amplitude of the microwave field applied to the atoms is not a constant and has spectral components at frequencies $(2p+1)\nu_M$ and iii) the spectrum of the demodulation waveform contains even harmonics of the modulation frequency ν_M whereas the even harmonics of the beam tube response are not sufficiently rejected.

Results have been given in the case of a sinusoidal modulation waveform[24]. For instance, a second harmonic distortion ratio of 10^{-5} gives a relative frequency offset of about 10^{-13}. We shall consider a slow square wave frequency modulation to exemplify the effect of a modulation of the amplitude of

the microwave field. If $b + \Delta b$ and $b - \Delta b$ are the values of that amplitude during the first and the second half of the modulation period, respectively, then the frequency offset is given by:

$$\Delta\nu_m = \frac{1}{T_i}\frac{\Delta b}{b}\Delta_m \tag{10}$$

Assuming $\Delta b/b = 10^{-6}$, which is a severe requirement, and the value of the operating parameters given in the Appendix, the relative frequency offset is equal to 0.3×10^{-14} and 2.1×10^{-13} for the traditional tube and the optically pumped tube, respectively. The sensitivity to a microwave power change is approximately 4×10^{-14} per dB for both types of tube. The quantities Δ_m and Δ_C are equal to zero for the same values of the operating parameters.

Alternating magnetic fields applied externally to the frequency standard, having a frequency equal to ν_M or its multiples, can add detrimental components to the beam tube response and/or perturb greatly the modulation and demodulation processes. They can be the cause of large frequency offsets.

4.2. Frequency offsets arising in the frequency control loop

Until now, analog electronics is implemented in most of the commercially available units to filter the beam tube response, to obtain the error signal and to realize the proper loop transfer function. However, operational amplifiers have a finite DC gain and show current and voltage offsets. The first of these imperfections translate a frequency offset of the free running quartz crystal oscillator (*e.g.* 10^{-7}) in relative value) into a frequency offset at the output of the standard (*e.g.* 10^{-13}). The latter is inversely proportional to the gain of the electron multiplier, which is known to change with time. The second imperfection, the voltage offset (*e.g.* 10 μvolts) also gives a frequency offset at the output (*e.g.* 10^{-13}) which depends on temperature, like the voltage offset. Such defects can be completely eliminated using a digital frequency control loop[25,26].

A drift of the quartz crystal oscillator, at a rate of 10^{-9} per day when it is free–running, gives a relative frequency offset equal to 10^{-14} assuming a first order loop with a time constant of 1 s. This effect disappears with a second order loop.

5. INFLUENCE OF THE ADJUSTEMENT OF THE INTERNAL PARAMETERS

Although we have given a plausible magnitude of the values of the various frequency offsets and of their possible change, the actual values depend on the particular adjustement of a given cesium beam frequency standard. This refers to the value of the C–field and of its inhomogeneities, the microwave power, the cavity mistuning, the cavity phase shift, the velocity distribution (*via* geometrical alignment), the level of the spectral impurities, the spurious modulation of the amplitude of the microwave induction, etc. Even the sign of the frequency offsets related to the cavity tuning and to the cavity phase shift may vary from unit to unit. The variability of the sensitivity to external factors[27→29], is therefore not surprising. We have noticed that optically pumped tubes should not be affected by the presence of neighbouring transitions, thanks to the symmetry of the microwave spectrum which can be achieved in that case. This symmetry has the additional advantage to allow one to decrease the value of the C–field and, consequently, to decrease the sensitivity to its change.

However, the sensitivity to the adjustment of other internal characteristics, such as the cavity tuning, is potentially larger than in traditional tubes. This is primarily due to the larger velocity of the atoms detected. The general cure is a better control of the misadjustments. In the particular case of the cavity pulling effect, a reduction of the value of Q_c will contribute to solve the difficulty. Nevertheless, one should be careful to improve the spectral purity of the signal at the output of the final frequency multiplier or mixer, since the filtering effect of the cavity will be decreased accordingly.

6. CONCLUSION—SENSITIVITY TO EXTERNAL FACTORS

Figure 6 shows the most efficient pathways from the external variables tothe physical origins of the largest change of the output frequency in the cesium beam frequency standard[6].

The effect of external DC and AC magnetic fields has been described in Section 2.1. A variation of the temperature can change, for instance: i) the current creating the static magnetic field and the properties of the shielding material, ii) the characteristics of the electronic components used in the generation of the microwave power and thus the level of this power, iii) the dimensions of the microwave cavity and thus its resonant frequency and iv) the voltage offset of operational amplifiers in the frequency control loop. Humidity can change the value of capacitances used in the tuning of the various stages of frequency synthesis chain and, consequently, the microwave power. It can also change leakage currents in the frequency control loop. A constant acceleration varies the position of the atomic trajectories with respect to the beam tube structure and, thus, the velocity distribution. However, its main effect is to change the free–runnning frequency of the quartz crystal oscillator. Vibrations create sidebands in the quartz crystal oscillator output. Most of the external variables are not independant ones[30]. A change of the humidity, of the atmospheric pressure, of the orientation of the unit in the earth gravity field and of the supply voltage will modify the internal temperature and/or temperature gradient and thus the temperature of the various sub–assemblies of the device.

APPENDIX

In the two separated oscillatory field method, the probability that a transition occurs depends on the amplitude of the microwave field and on the velocity distribution function of the atoms detected. It follows that most of the properties of a cesium beam frequency standard depends on these two parameters. Furthermore, the medium term frequency stability and a number of frequency offsets depend on the way the line shape is explored (frequency or phase modulation waveform, depth of the frequency or phase deviation and modulation frequency). These effects are considered in references [4,8,31].

It is convenient to characterize the amplitude of the microwave magnetic induction applied in the interaction regions by the quantity b, which has the dimension of rad s^{-1}. It is given by $b = \mu_B B/\hbar$, where B is the actual value of the amplitude of the microwave magnetic induction, μ_B is Bohr magneton and $\hbar$ is Planck constant divided by 2π.

Optimum operating conditions exist, depending on the criterion considered[8]. Considering the optimum amplitudes of the microwave field, they are all close to values such that we have $b\tau_1$ and $b\tau_0$ equal to 1.5, where τ_1 and τ_0 are defined in Section 1.

The amplitude of the frequency modulation which is needed to probe the atomic resonance is usually set close to its half width at half maximum. We have thus chosen $\omega_m T_1 = \omega_m T_0 = 1.5$, where $\omega/2\pi$ is the modulation depth. T_1 and T_0 are defined in Section 3.1.

REFERENCES

1. H. Hellwig, S. Jarvis Jr. D. Halford and H.E. Bell, *Evaluation and Operation of Atomic Beam Tube Frequency Standards Using Time Domain Velocity Selection Modulation*, Metrologia, vol. 9, pp. 107–112, 1973

2. A. Hamel, V. Giordano, P. Petit and C. Audoin, *Velocity Distribution Measurement in an Optically Pumped Cesium Beam Resonator* in Proc. 4th European Time and Frequency Forum, pp. 169–174, 1990

3. A. de Marchi, G.D. Rovera and A. Premoli, *Pulling by Neighbouring Transitions and its Effects on the Performance of Caesium-Beam Frequency Standards", Metrologia, vol. 20, pp. 37-47, 1984*

4. *A. de Marchi, G.D. Rovera and A. Premoli, Effects of Servo Loop Modulation in Atomic Beam Frequency Standards Employing a Ramsey Cavity" IEEE Trans. on Ultrasonics, Ferroelectrics and Frequency Control, vol. UFFC 34, n° 6, pp. 582-591, Nov. 1987*

5. *A. de Marchi, Rabi Pulling and Long-Term Stability in Cesium Beam Frequency Standards, IEEE Trans. on Ultrasonics, Ferroelectrics and Frequency Control, Vol. UFFC 34, n° 6, pp. 598-601, Nov. 1987*

6. *A. de Marchi, Understanding Environmental Sensitivity and Ageing of Cesium Beam Frequency Standards in Proc. 1st European Time and* Frequency Forum, pp. 288–293, 1987

7. A. de Marchi, *Improving the Long Term Stability of Cesium Beam Frequency Standards* in Proc. of the 4th European Forum on Time and Frequency, pp. 517–521, 1990

8. J. Vanier and C. Audoin, *The Quantum Physics of Atomic Frequency Standards*, Bristol, UK: Adam Hilger 1989, ch. 5, pp. 603–947

9. S. Iijima, K. Fujiwara, H. Kobayashi and T. Kato, *Effect of Environmental Conditions on the Rate of a Cesium Clock*, Annals of the Tokyo Astronomical Observatory, Vol. 17, n° 1, pp. 50–67, 1978

10. F.Deyzac, *Caractérisation en Environnement Perturbé des Horloges Atomiques au Césium*, La Recherche Aérospatiale, n° 2, pp. 145–148, Mars–Avril 1984

11. S.K. Karuza, W.A. Johnson, J.P. Hurrell and F.J. Voit, *Determining Optimum C-Field Settings That Minimize Output Frequency Variations in Cesium Atomic Frequency Standards* in Proc. 21st AnnualPrecise Time andTime Interval (PTTI). Applications and Planning Meeting, pp. 385–400, 1989

12. V. Candelier,, V. Giordano, A. Hamel, G. Théobald, P. Cérez and C. Audoin *Frequency Stability of an Optically Pumped Cesium Beam Frequency Standard*, Applied Physics B, vol. 49, pp. 365–370, 1989

13. A. Hamel, *Propriétés d'un résonateur atomique à jet de césium pompé optiquement et à structure de champ longitudinale*, Thèse de Doctorat, Université Paris-Sud, 1989

14. A. de Marchi, *Long Term Stability of Commercial Cesium Clocks*, Seminar at BIPM, 1990

15. A. Brillet, *Evaluation of the Light Shifts in an Optically Pumped Cesium Beam Frequency Standard*, Metrologia, Vol. 17, pp. 147–150, 1981

16. V.K. Egorov and V.A. Maslov, *Effect of Light Shift on the Accuracy of the Optically Pumped Cesium Atomic Beam Frequency Standards*, Soviet Physics Technical Physics, vol. 29, n° 3, pp. 334–338, 1984

17. J.Shirley, *Fluorescent Light Shift in Optically Pumped Cesium Standards* in Proc. 39th Annual Frequency Control Sympos, 1985

18. A. de Marchi and G.P. Bava, *On Cavity Phase Shift in Commercial Caesium- Beam Frequency Standards*, Metrologia, vol. 20, pp. 33–36, 1984

19. P. Cérez, G. Avila, E. de Clercq, M. de Labachelerie and M. Têtu, *Results on a Laser Diode Optically Pumped Cesium Beam* in Proc. of the 38th Annual Frequency Control Symposium, pp. 452–457, 1984

20. A. Derbyshire, R.E. Drullinger, M. Feldman, D.J. Glaze, D. Hilliard, D.A. Howe, L.L. Lewis and J.H. Shirley, *Optically Pumped Small Cesium Standards; a Status Report* in Proc. on the 39th Annual Symposium on Frequency Control, pp. 18–21, 1985

21. P. Tremblay, A. Michaud and C. Jacques, *Optical Pumping Rate Effects in Cesium Beam Frequency Standards* in CPEM'90 Digest, pp. 153–154, 1990

22. A. Bauch and T. Heindorff, *Experimental Studies on Majorana Transitions in a Cs Atomic Beam Frequency Standards* in Proc. 39th Annual Symposium on Frequency Control, pp. 8–12, 1985

23. C. Audoin, M. Jardino, L.S. Cutler and R.F. Lacey, *Frequency Offset Due to Spectral Impurities in Cesium-Beam Frequency Standards*, IEEE Trans. on Instr. and Meas., Vol. IM-27, n° 4, pp. 325–329, Dec. 1978

24. F.L. Walls, *Errors in Determining the Center of a Resonance Line Using Sinusoidal Frequency (Phase) Modulation*, IEEE Trans. on Ultrasonics, Ferroelectrics and Frequency Control, Vol. UFFC 34, n° 6, pp. 592–597, Nov. 1987

25. J. Rabian and P. Rochat, *Full Digital-Processing in a New Commercial Cesium Standard* in Proc. 2nd European Frequency and Time Forum, pp. 461–468, 1988

26. L.T. Sing, J. Viennet and C. Audoin, *Digital Synchronous Detector and Frequency Control Loop for Cesium Beam Frequency Standard*, IEEE Trans. on Instr. and Meas. , Vol. IM-39, n° 2, pp. 428–429, Apr. 1990

27. E. Bava, F. Cordara, V. Pettiti and P. Tavella, *Analysis of the Seasonal Effects on Cesium Clocks to Improve the Long-Term Stability of a Time Scale* in Proc. of the 19th Annual Precise Time and Time Interval (PTTI) Applications and Planning Meeting, pp. 185–202, 1987

28. J.E. Gray, M.E. Machlan and D.W. Allan, *The Effect of Humidity on Commercial Cesium Beam Atomic Clocks* in Proc. of the 42nd Annual Symposium on Frequency Control, pp. 514–518, 1988

29. R.L. Sydnor, T.K. Tucker, C.A. Greenhall, W.A. Diener and L. Maleki, *Environmental Tests on Cesium Beam Frequency Standards at the Frequency Standards Laboratory of the Jet Propulsion Laboratory* in Proc. of the 21st Annual Precise Time and Time Interval (PTTI). Applications and Planning Meeting, pp. 409–420, 1989

30. H. Hellwig, *Environmental Sensitivities of Precision Frequency Sources*, IEEE Trans. on Instr. and Meas., Vol. 39, n° 2, pp. 301–304, Apr. 1990

31. G.D. Rovera, A. de Marchi and E. de Clercq, *Estimation of Some Frequency Shifts in an Optically Pumped Clock Taking into Account Modulation Parameters* in Proc. of the Fourth European Frequency and Time Forum, pp. 161–162, 1990

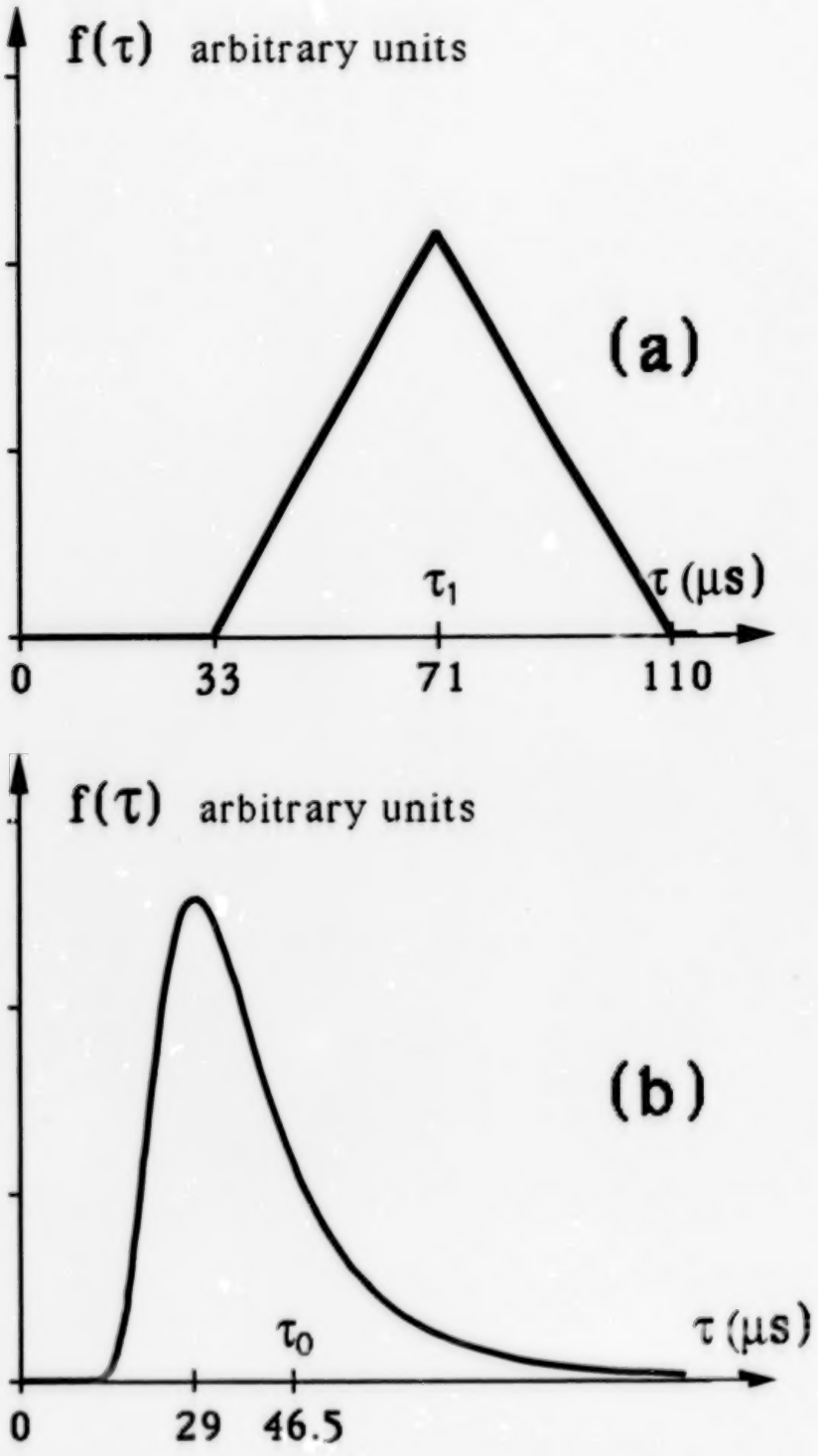


Figure 1. Distribution of interaction times
a) approximate distribution in a tube with magnet state selectors
b) distribution in a tube using a single laser for state selection and detection.

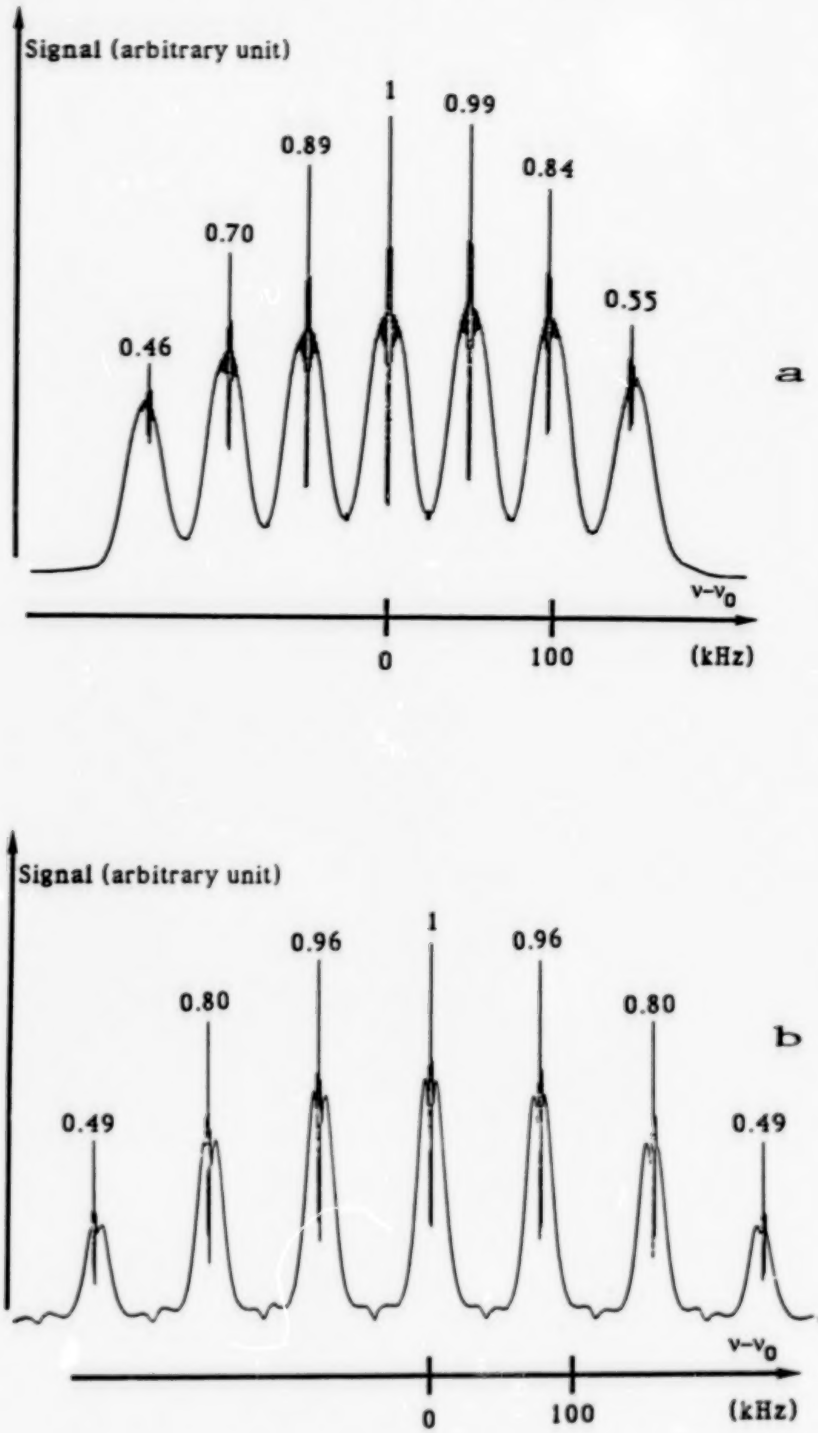


Figure 2. Microwave spectrum of cesium atoms in the ground state. The relative amplitude of the seven lines is shown

a) in a tube with magnet state selectors. B_o= 70 mG

b) in a tube using a single laser for state selection and detection. B_o = 110 mG.

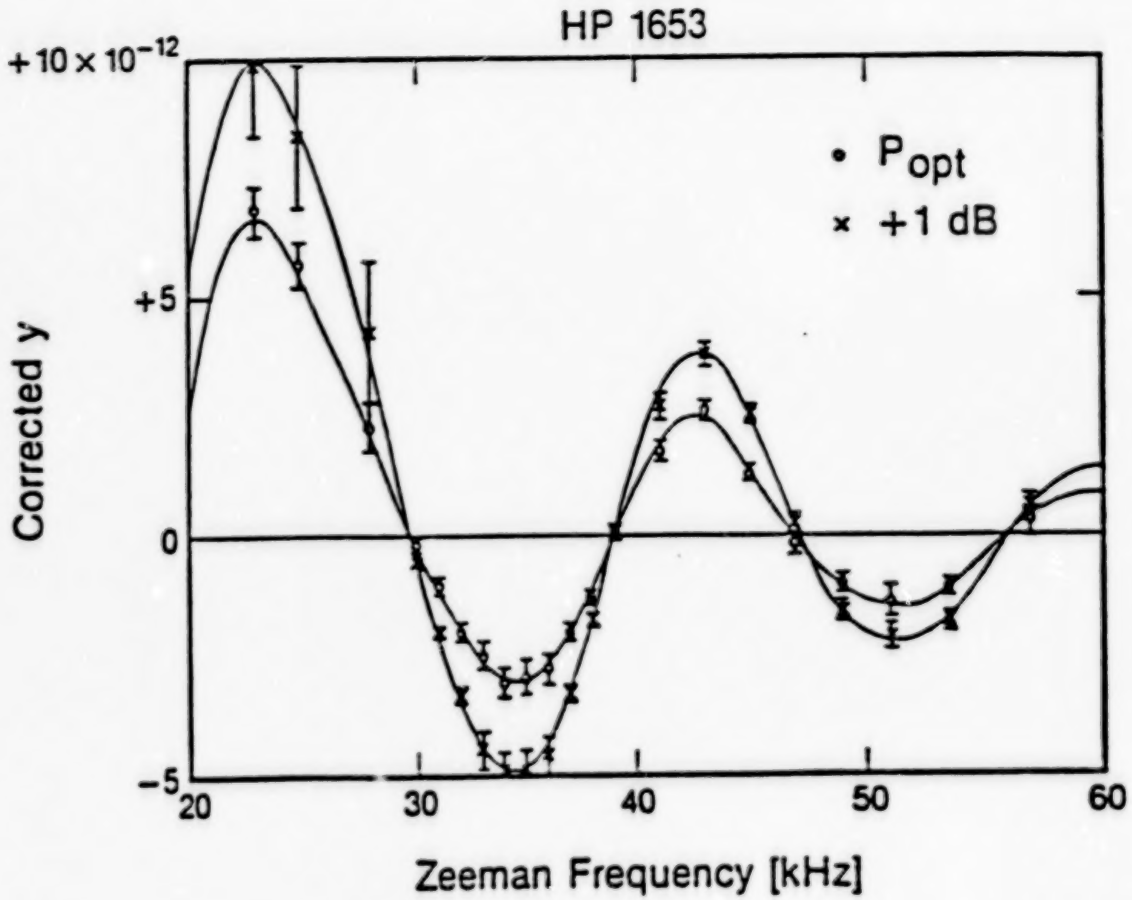


Figure 3. Example of measured Rabi pulling relative frequency offset versus a measure of the static magnetic induction (from ref. 5).

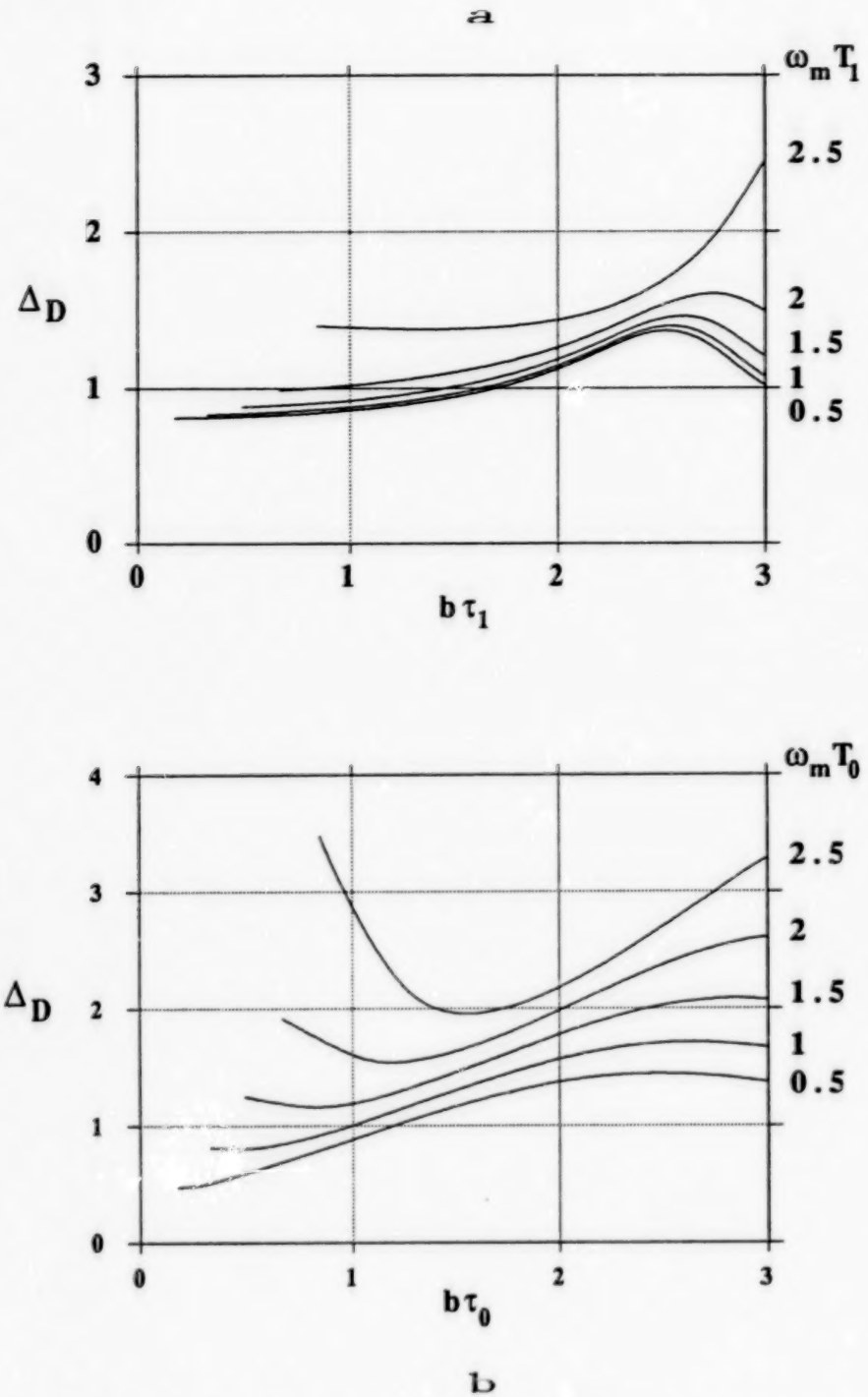


Figure 4. Second order Doppler effect, assuming slow square wave frequency modulation. Variation of Δ_D versus $b\tau_1$ or $b\tau_0$ for different values of $\omega_m T_1$ and $\omega_m T_0$.
a) Tube with magnet state selector
b) Tube using a single laser for state selection and detection.

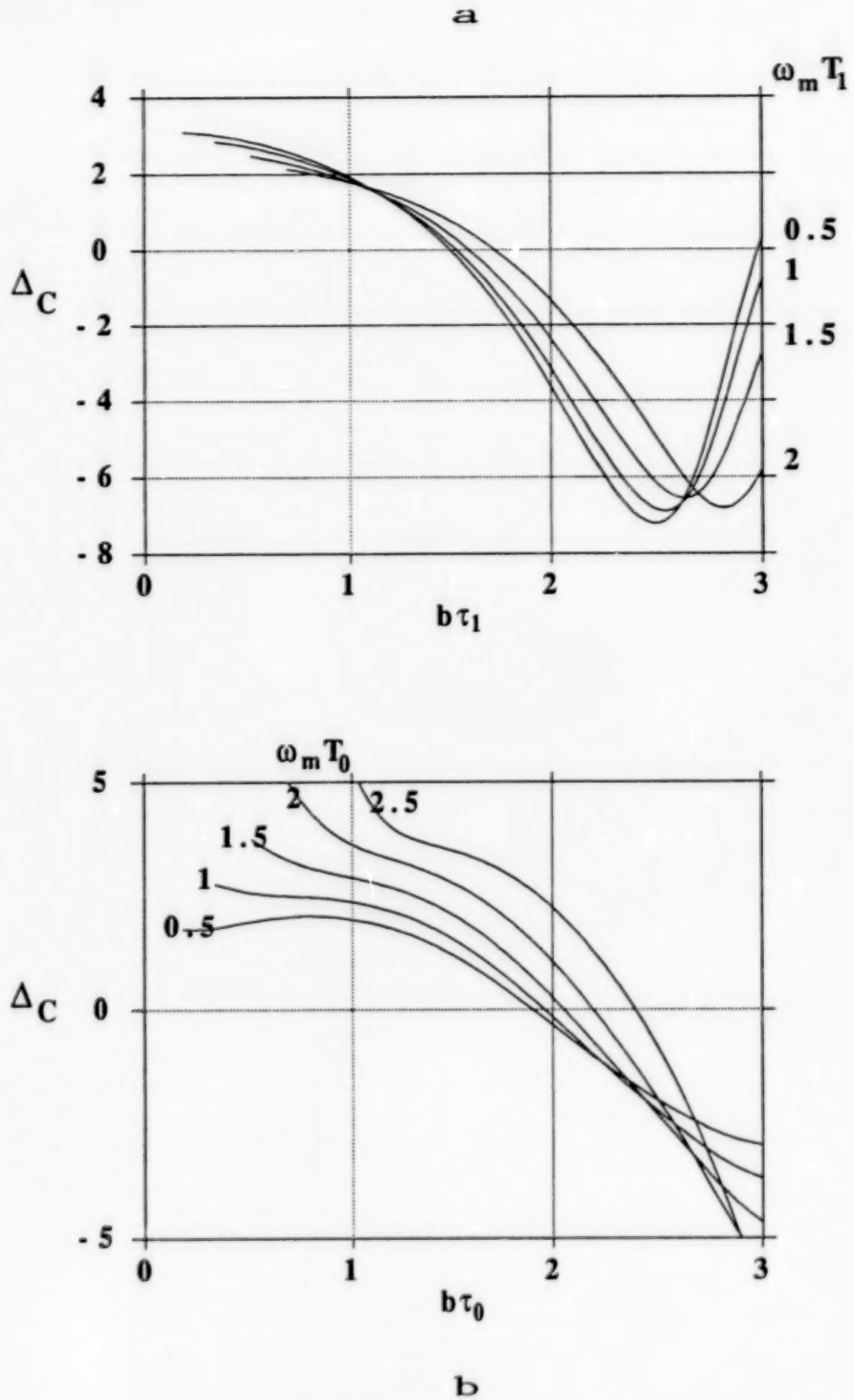


Figure 5. Cavity pulling, assuming slow square wave frequency modulation. Variation of Δ_c versus $b\tau_1$ and $b\tau_0$.

a) Tube with magnet state selector
b) Tube with a single laser for state selection and detection.

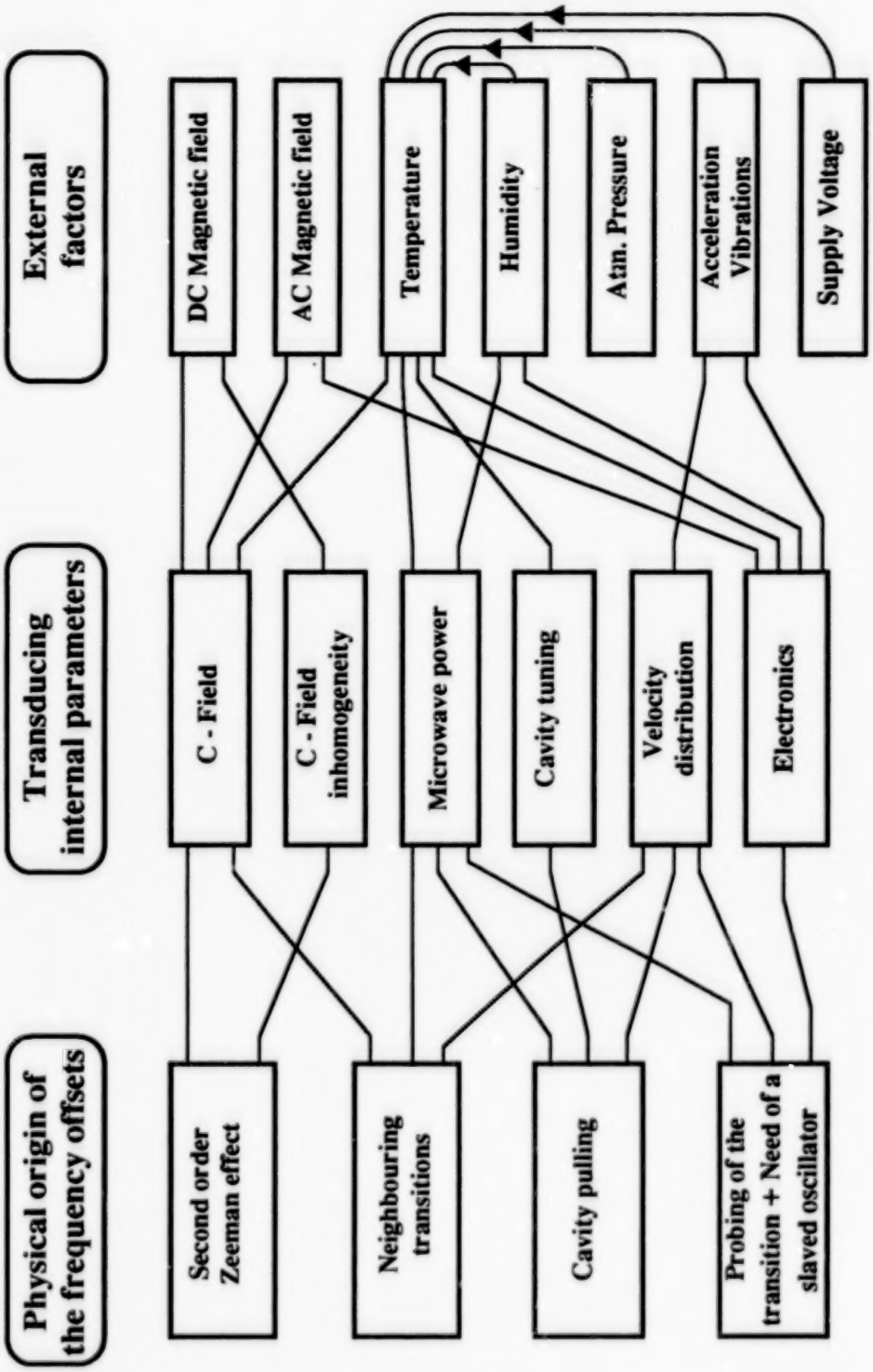


Figure 6. Pathways between the external stimuli and some of the physical origins of the frequency offsets, via internal characteristics of the device.

BLANK PAGE

THE PHYSICS OF THE ENVIRONMENTAL SENSITIVITY OF RUBIDIUM GAS CELL ATOMIC FREQUENCY STANDARDS

W. J. Riley
EG&G Frequency Products
Salem, MA 01970

Abstract

Environmental sensitivity is often the most significant limitation to the practical stability of rubidium frequency standards (RFS). For example, temperature sensitivity can cause a rapid frequency change of several parts in 10^{10} for a tactical RFS that has an aging of only $1x10^{-11}$/month. Other important environmental factors are barometric pressure, vibration, magnetic field, and nuclear radiation.

This paper considers the physical mechanisms that lie behind these environmental sensitivities, and relates them to the performance of actual rubidium frequency standards. It is part of an effort currently underway under NIST and IEEE sponsorship toward a standard characterizing such environmental sensitivities. For the systems designer, a better understanding of the reasons for RFS environmental sensitivity will help in making program tradeoffs. For the user of these devices, a better knowledge of the causes for Rb clock instability will aid in their testing and proper application. For the time and frequency specialist, a review of these factors may prove useful toward improving RFS design.

Some of the RFS environmental sensitivities are due to simple physical mechanisms like the effect of dc magnetic field on the Rb hyperfine resonance frequency. For these, an analysis can be based on physical principles and straightforward design factors. Other environmental factors, like temperature sensitivity, are more complex combinations of many effects, both physical and practical, and the analysis often takes the form of an error budget with large unit-to-unit variations.

Today's rubidium frequency standards span a wide performance range from small, inexpensive units with $pp10^{10}$ error budgets to larger, higher performance versions offering $pp10^{14}$ stabilities. For both extremes, however, environmental sensitivity can be the most significant performance limitation. This paper helps explain why, and offers some insight into how to make improvements.

INTRODUCTION

The rubidium gas cell atomic frequency standard has found widespread use since its introduction about thirty years ago. It offers the best combination of stability, size, weight, power, life, and cost for many commercial and military applications. In many of these applications, environmental sensitivity is the most significant performance limitation.[1, 2] This paper will attempt to summarize the physical basis of the environmental sensitivity of the rubidium frequency standard (RFS).

An understanding of the physical mechanisms that cause environmental sensitivity is of obvious concern to the RFS designer, especially since the device may be intended for a harsh tactical application.

But it is also important for the specifier and user of these devices to have a good understanding of the root causes of RFS environmental sensitivity.

The paper begins with an examination of the principal factors that contribute to RFS instability. These are the causes of environmental sensitivity. It then considers each environmental factor and relates it to the RFS sensitivities. Additional information is presented in the form of tables. The table columns cover the three major RFS sections, while the table rows relate similar sensitivity factors.

RFS SENSITIVITIES

The largest factors contributing to the environmental sensitivity of a rubidium frequency standard are shown in Table 1. Most of these factors are basic characteristics of the physics package (such as magnetic sensitivity) that become environmental sensitivities when the instabilities of the electronics circuits (such as the C-field current source) are considered.[3] Some of these RFS sensitivities are fixed (such as magnetic dependence), while others vary with operating conditions. For example, the effects of servo amplifier and rf chain offsets scale with the strength of the discriminator slope. Environmental constraints can, in turn, affect the realizable Rb signal. An RFS required to operate at an elevated ambient temperature must compromise its S/N ratio and discriminator signal by using an absorption cell oven setpoint higher than optimum.

TABLE 1 RFS SENSITIVITIES

PHYSICS PACKAGE	CRYSTAL OSCILLATOR	ELECTRONICS
C-FIELD SENSITIVITY: Magnetic Bias Field Residual Oven Heater Field		C-FIELD STABILITY: Volt Ref & Current Source Temp Controller Heater Current
LIGHT SHIFT: Light Intensity & Spectrum		LAMP EXCITER: Lamp Excitation Power
TEMPERATURE COEFFICIENTS: Lamp TC Filter Cell TC Absorption Cell TC C-Field Coil Resistance TC Cavity TC		TEMPERATURE CONTROLLERS: Thermal Gain DC Amplifier Stability Thermistor Self-Heating Thermistor Stability Bridge Resistor Stability
RF POWER COEFFICIENT: Buffer Gas Confinement Line Inhomogeneity C-Field Inhomogeneity Abs Cell Temperature Gradient		RF CHAIN: Microwave Excitation Power RF Spurious Components Modulation Distortion
BAROMETRIC COEFFICIENT: Abs Cell Buffer Gas Offset Abs Cell Envelope Deflection		
DISCRIMINATOR SIGNAL: Discriminator Slope	SERVO LOOP: Static & Dynamic Tracking Error	SERVO AMPLIFIER: Finite Gain & Phase Error Static & Dynamic Offsets Mod Deviation Change 2nd Harmonic Ripple
OPTICAL PATH: Light Beam Motion	CRYSTAL: G-Sensitivity	SERVO AMPLIFIER: Servo Interference

Magnetic Field Sensitivity: The magnetic field sensitivity of an RFS is a result of the hyperfine magnetic resonance on which it depends. The physics package uses an internal longitudinal dc magnetic bias field to orient the Rb atoms and separate the Zeeman sublevels. The "field independent" clock transition has a quadratic dependence $\Delta f = 573\,H^2$, where Δf is the frequency change in Hz and H is the magnetic field in Gauss. The incremental magnetic sensitivity varies linearly with the magnetic bias field $\frac{\Delta f}{f} = \frac{1146}{f_o}\,H\,\Delta H$, where $\frac{\Delta f}{f}$ is the fractional frequency change, f_o is the Rb frequency ($\approx$6835 MHz), and ΔH is the magnetic field change. The fractional magnetic sensitivity therefore varies as $\frac{\Delta f}{f} = 1.68\text{x}10^{-7}\,H^2\,\frac{\Delta H}{H}$, where $\frac{\Delta H}{H}$ is the fractional field change.

Light Shift: Light shift is one of the fundamental stability limitations of the rubidium frequency standard.[4] Because optical pumping is usually done in the same place, and at the same time, as interrogation of the Rb atoms, asymmetry in the pumping light spectrum causes a frequency offset.[5] For good performance, it is necessary to operate the unit at the condition of zero light shift (ZLS) where the frequency is independent of light intensity. This is accomplished by adjustment of the Rb lamp isotopic ratio for an integrated cell and adjustment of the length and/or temperature of a discrete filter cell.[6] The condition of zero light intensity coefficient, zero lamp TC, and zero lamp rf excitation power coefficient are not exactly the same, and there is always some residual light shift sensitivity.

Temperature Coefficients: A closely related fundamental RFS limitation is lamp and cell temperature sensitivity. Lamp and filter cell TCs are light shift effects. Absorption cell TC is primarily due to buffer gas effects. Two configurations offer overall optimization of RFS physics package operating conditions.[4] For the integrated cell, optimization of the lamp isotopic mix and the cell buffer gas mix can provide an overall zero light shift/zero TC condition.[7] For the discrete filter cell, an Rb^{87} lamp with a Rb^{85} filter cell and a Rb^{87} absorption cell, with the two cells in the same oven, and with optimized operating temperatures and buffer gas mixes, provides an overall ZLS/ZTC condition.[8] An RFS physics package using this arrangement can be easily adjusted for optimum operating conditions by setting the lamp oven temperature (light intensity) for zero cell oven TC and setting the cell oven temperature (hyperfine filtration) for zero lamp oven TC (ZLS). This also provides a homogeneous light spectrum for low rf power sensitivity. Typical residual TCs are a few $pp10^{11}$/°C for the RFS lamp and cell ovens. A wall coated cell without buffer gas has a relatively large TC ($\approx 2pp10^{10}$/°C).

RF Power Coefficient: RFS rf power sensitivity is due primarily to inhomogeneity within the absorption cell.[9] The microwave field strength is not uniform within the cavity, and most of the signal comes from whatever region has the optimum rf level. The buffer gas confines a particular Rb atom to a small region of the cell. If some other frequency-determining variable, such as C-field, temperature, light intensity, or light spectrum, is also inhomogeneous, then a change in rf power that shifts the region of optimum signal will also cause a frequency change.

Barometric Coefficient: The primary RFS pressure sensitivity is due to volumetric change of the absorption cell envelope. This is caused by the pressure shift coefficient of the buffer gas,[10] and scales with the net buffer gas frequency offset. Typical buffer gas offsets range from a few 100 Hz to a few kHz. An RFS using a wall-coated cell with no buffer gas would have a lower barometric sensitivity.

Modulation Distortion: Modulation distortion is a primary cause of frequency offsets and instability in passive atomic frequency standards. Low frequency phase modulation (PM or FM) is applied to the physics package rf excitation to produce an ac discriminator signal. This error signal is synchronously detected and used to generate a control voltage to lock a crystal oscillator to the atomic resonance. Even-order modulation distortion shifts the center of gravity (CG) of the microwave excitation and causes a frequency offset; any change in this offset causes a frequency change.

This effect may be understood by considering the spectrum resulting from distortionless FM at f_{mod} and $2f_{mod}$. The 1st order upper and lower FM sidebands have opposite sense while the 2nd order sidebands have the same sense. Thus, with 2nd harmonic distortion, the lower 2nd order sidebands subtract and the upper 2nd order sidebands add, shifting the CG of the overall spectrum toward a higher frequency. This shifts the locked frequency in the opposite direction by an amount given by $\frac{\Delta f}{f} = \frac{\delta_2}{2Q_l}$, where δ_2 is the relative amount of 2nd harmonic distortion and Q_l is the Rb line Q.[4] For a −70 dB 2nd harmonic distortion level in an RFS with a 300 Hz line width, this produces a fractional frequency offset of 7×10^{-12}. A 15% change in the amount of distortion, due to an environmental effect, would result in a frequency change of 1×10^{-12}. Another way to visualize this is to consider the effect of even-order distortion on the shape of a fundamental sinusoidal modulation waveform. For worse-case phasing, one side of the waveform is flattened, causing a shift in the average frequency.

Modulation distortion can be introduced in several ways: Distortion on the modulation signal itself, distortion in the phase modulator, and distortion introduced by asymmetrical rf selectivity and AM-to-PM conversion in the multiplier chain. The modulation signal can be made very pure (free from even-order distortion) by generating it from a precise square-wave followed by passive filtration and/or integration. Low-distortion phase modulation is possible with a hyperabrupt tuning varactor in an all-pass network. The latter also suppresses AM, which helps avoid subsequent AM-to-PM conversion. The phase modulation should be done at a relatively low rf frequency where the required deviation is low. An active phase modulator, such as a phase-lock loop (PLL), can introduce distortion because of coherent ripple in the modulation transfer function, and a passive network is generally better.

Many subtle modulation distortion effects can occur in a rf multiplier chain. Each stage of a harmonic multiplier enhances the PM index and can suppress AM by limiting. AM-to-PM and PM-to-AM conversion can cause frequency sensitivity to rf stage tuning and level. PLL multipliers can have problems due to finite loop bandwidth and phase detector distortion. Step recovery diode (SRD) multipliers exhibit sensitivity to drive and bias conditions. The first stages in a multiplier chain are usually the most critical since that is where the AM and PM indices are closest and the spurious components are closest to the carrier. Interstage selectivity is critical in a harmonic multiplier chain; it is vital to avoid spectral asymmetry caused by complex mixing between subharmonic components. The output of each stage must be well-filtered before driving the next stage, and yet selective networks must be symmetrical and stable against temperature and drift. It is especially important to have a pure drive signal to the final SRD multiplier. A direct multiplier chain is preferable to one using mixing to avoid asymmetrical microwave spectral components. Modulation of the VCXO by 2nd harmonic ripple from the servo amplifier has the same effect as even-order modulation distortion, producing a frequency offset that is subject to change versus environmental conditions.

Amplitude Modulation: Amplitude modulation on the microwave excitation is another form of modulation distortion that can cause frequency offset and instability. AM at the fundamental servo modulation rate on the microwave excitation will produce a spurious fundamental component on the recovered signal that the servo will null by making a corresponding frequency offset.

The frequency offset caused by AM at the servo modulation frequency is given by $\frac{\Delta f}{f} = \frac{\alpha_1}{2Q_l}$, where α_1 is the relative amount of AM.[4] As for the 2nd harmonic PM distortion, a −70 dB AM level with a line Q of 23×10^6 results in a frequency offset of 7×10^{-12}.

Spurious RF Components: Spurious rf spectral components can pull the locked frequency by causing a shift in the CG of the microwave excitation. The amount of pulling depends on the relative spurious level, its asymmetry, and its separation from the carrier. The change in frequency due to a

spurious component is given by $\frac{\Delta f}{f} = \frac{1}{2} \cdot \frac{\gamma H^2}{4\pi^2 f_o (f_o - f_2)}$, where γ is the ratio of Larmor frequency to magnetic field and H is the spurious microwave magnetic field at frequency f_2.[11, 12] Experiments have shown that an interfering signal equal to the normal microwave excitation at a separation of 5 MHz causes a frequency offset of 5×10^{-13}. Those values may be scaled to predict the pulling at other relative amplitudes and separations. For example, a SSB component with a 25 kHz separation at a level of −98 dBc at 13.4 MHz would, after multiplication by 510 to the Rb resonant frequency, have a relative level of −44 dBc and would cause a frequency offset of 1×10^{-13}. Such a pulling effect could be caused by slightly asymmetrical sidebands due to ripple from a switching power supply.

Subharmonics: Subharmonics are a particularly bothersome spectral component in the drive signal to the SRD multiplier. Subharmonic spectral components introduce time jitter between the impulses that generate the microwave energy, and can change the average rf power as the spectrum changes versus temperature or some other environmental condition. The period of the Rb microwave excitation is about 150 psec, so time jitter of the SRD multiplier drive waveform on the order of 10 psec can have a significant effect on its amplitude. The average of two waveforms differing in phase by 10/150 = 7% or 24° reduces the effective amplitude by 1−cos(24°) = 9%, or about −0.8 dB. Changes in rf power will give frequency shift on the order of $1 \text{pp} 10^{10}$/dB, which corresponds to a frequency change of 8×10^{-11} for the example above. For a typical multiplication factor of 80, this corresponds to a PM index, m, of $10 \cdot 2\pi/(150 \cdot 80) = 5 \times 10^{-3}$ rad, or a subharmonic level of −52 dBc. Thus even a relatively "clean" SRD multiplier drive spectrum can introduce significant frequency offsets.

ENVIRONMENTAL FACTORS

Magnetic Field: The inherent RFS sensitivity to dc magnetic field is useful for initial frequency calibration and to correct for aging, but it also causes external magnetic sensitivity. Magnetic shielding is the primary means to reduce this sensitivity. It is also desirable to operate the unit at the lowest possible value of C-field. This requires a tight tolerance on absorption cell buffer gas fill pressure or the use of a frequency synthesizer for tuning.

At a C-field of 250 mG (a typical value that provides a total frequency adjustment range of about 5×10^{-9}), the incremental C-field sensitivity is $\frac{\Delta f}{f} = 4.19 \times 10^{-8} \Delta H$. For a magnetic sensitivity of 1×10^{-11}/Gauss, this dictates a maximum internal field change of 240 μG and a shielding factor of about 4200. This can be realized with two nested magnetic shields.

The design of magnetic shields is outside the scope of this paper,[13] but it is worthwhile to mention some important considerations. The RFS magnetic sensitivity is greatest along the optical axis of the physics package (the direction of the internal C-field). Generally at least one shield is located directly around the physics package. The longitudinal shielding factor of nested shields depends critically on their end spacings. Rounded corners are desirable to avoid fringing. The shielding factor depends on the applied field strength since the permeability of the shielding material is nonlinear.

RFS magnetic sensitivity can be reduced by periodically switching the polarity of the C-field, thus obtaining 1st order cancellation of the external field.[14] While this may be effective under some circumstances, there is no entirely satisfactory way to perform the switching.

Internal residual magnetism, if stable and uniform, is not especially critical for Rb frequency standards. Residual magnetic fields from oven heaters can be an important consideration however. The latter can

cause a "pseudo-TC" effect as the ambient temperature and heater power varies. The most significant factors contributing to RFS magnetic sensitivity are shown in Table 2.

TABLE 2 RFS MAGNETIC SENSITIVITIES

PHYSICS PACKAGE	CRYSTAL OSCILLATOR	ELECTRONICS
C-FIELD: Magnetic Sensitivity Residual Oven Heater Field	NONE	TEMPERATURE CONTROLLERS: Oven Heater Current

Pressure: The volumetric change in the absorption cell that causes barometric pressure sensitivity is due mostly to "oil-can" deflection of the end windows. This deflection scales with the 4th power of the cell diameter and inversely with the cube of the window thickness. Cell window thickness is limited by glassworking and dielectric loading considerations, and the typical barometric sensitivity is about $1x10^{-10}$/atm. This sensitivity can be a very significant contributor to RFS frequency instability in an otherwise benign environment. Atmospheric barometric fluctuations of 5% cause $5x10^{-12}$ frequency fluctuations that limit the RFS noise floor. The absence of this form of environmental disturbance is an important factor in the excellent stability of GPS Rb clocks.[15] The barometric sensitivity can also be important for aircraft applications, and may dictate the use of a hermetically sealed unit.[16]

Another RFS pressure sensitivity mechanism is change in convective and conductive heat transfer. The latter does not change significantly until the barometric pressure is reduced to below about 1 Torr. All devices with non-negligible power dissipation must be conductively heat sunk. Within the physics package, thermal gradients change, oven power drops, and the stabilization factor improves in vacuum. An RFS does not use high voltages and can be safely operated throughout the full pressure range from sea level to hard vacuum without any corona discharge hazard. The most significant factors contributing to RFS pressure sensitivity are shown in Table 3.

TABLE 3 RFS PRESSURE SENSITIVITIES

PHYSICS PACKAGE	CRYSTAL OSCILLATOR	ELECTRONICS
ABSORPTION CELL: Envelope Deflection		
LAMP & CELL OVENS: Thermal Effects	CRYSTAL & OTHER DEVICES: Thermal Effects	ELECTRONIC DEVICES: Thermal Effects

Temperature: Temperature sensitivity is often the most significant environmental sensitivity of a rubidium frequency standard. A stability of $3x10^{-10}$ is typical for a small tactical RFS over a military temperature range, whereas the unit will not have that much frequency aging over several years. Furthermore, there is considerable unit-to-unit variation of this important parameter, which is not necessarily monotonic and which may have regions of high incremental sensitivity. Many physical mechanisms can contribute to RFS temperature sensitivity, and large unit-to-unit variations are often observed since the performance of a particular unit may be the algebraic sum of several factors. The most significant factors contributing to RFS temperature sensitivity are shown in Table 4.

These TC mechanisms are categorized as involving either the Rb physics package, the crystal oscillator, or the electronics. In most cases, it is physics package sensitivity that causes an electronic sensitivity. Each of the physics package elements (lamp, filter cell, and absorption cell or combined filter/absorption cell) has an intrinsic TC, but the overall Rb physics package can be designed so that it has low temperature sensitivity. Consider, for example, a classic design using a Rb^{87} lamp, a discrete Rb^{85} filter cell, and a Rb^{87} absorption cell. A change in lamp temperature causes a change in light intensity, which, due to the light shift effect, can cause a frequency change. This sensitivity can

be nulled by proper filter cell length and operating temperature. But, at this ZLS condition, the filter cell will have a relatively large negative TC ($\approx -1x10^{-10}$/°C). The absorption cell TC, however, can be changed from a significant positive to a significant negative TC by adjusting its buffer gas mix.

TABLE 4 RFS TEMPERATURE SENSITIVITIES

PHYSICS PACKAGE	CRYSTAL OSCILLATOR	ELECTRONICS
LAMP TC: Light Intensity/Spectrum Rb Vapor Pressure		LAMP OVEN TEMP CONTROLLER: Thermal Gain Temperature Setpoint
FILTER CELL TC: Light Shift Hyperfine Filtration		FILTER TEMP CONTROLLER: Thermal Gain Temperature Setpoint
ABSORPTION CELL TC: Buffer Gas TC		CAVITY TEMP CONTROLLER: Thermal Gain Temperature Setpoint
LAMP EXCITATION SENSITIVITY: See Lamp TC		LAMP EXCITER TC: RF Power Oscillator/Regulator
CAVITY RF POWER COEFF: Spatial Inhomogeneity		RF CHAIN: RF Power/ALC
C-FIELD SENSITIVITY: Magnetic Bias		C-FIELD SOURCE: Volt Ref/Current Source
RF SPECTRUM: CG Change		RF CHAIN: Mod Distortion, Spurious
CAVITY PULLING: Line Q/Cavity Q Ratio		CAVITY TEMP CONTROLLER: Thermal Gain, Setpoint
	CRYSTAL OSC TC: Static & Dynamic Tracking Error	SERVO AMPLIFIER: Static & Dynamic Servo Gain

Suppose, then, that the filter and absorption cells share the same thermal environment (oven). Then the absorption cell TC can be made to cancel that of the filter cell giving an overall net zero TC. In fact the situation is particularly favorable because, on a unit-to-unit basis, the lamp oven TC can easily be nulled by adjusting the cell oven temperature to the ZLS condition while the cell oven TC can simultaneously be nulled by adjusting the lamp oven temperature. (The latter is possible because the magnitude of the negative filter cell TC varies with the light intensity while the positive TC of the absorption cell is constant.) The residual TC of each oven can easily be held to $\pm$ 2x10^{-11}/°C. This approach, along with ovens having a modest stabilization factor (200), can thus reduce the overall physics package TC to $\pm$ 4x10^{-13}/°C, or about 10% of the temperature error budget for a small tactical RFS.

Another significant physics package consideration is rf power shift. Any resonance line spatial inhomogeneity or asymmetry will make the locked frequency vary with rf power. Spatial inhomogeneity gives a different frequency versus rf power as the position of maximum signal moves within the microwave cavity. Use of a discrete filter cell is critical here to avoid spatial inhomogeneity due to nonuniform light shift within the resonance cell. Other factors are C-field uniformity (use a Helmholtz coil configuration), a clean, symmetrical rf spectrum (avoid synthesis and mixing), and employment of a high thermal conductivity oven to avoid temperature gradients along the absorption cell. Still another physics package TC factor is residual magnetic field from the oven heaters (see above).

However, the most significant TC mechanisms are likely to be electronic. Items of particular concern are C-field stability, RF power stability, modulation distortion, and servo offsets. Temperature sensitivity due to the C-field current source is dependent on the C-field setting. At 250 mG, the fractional

C-field sensitivity is about $1x10^{-10}$/%. For a tactical RFS with a $3x10^{-10}$ stability requirement over a −55°C to +75°C temperature range the C-field current must be stable to about 100 ppm/°C. C-field temperature compensation can cause disparate frequency-temperature characteristics at different frequency adjustments.

A typical RFS rf power coefficient is about $1pp10^{10}$/dB. This imposes a stringent requirement on the stability of the rf power that excites the Rb physics package.

Cavity pulling is usually a negligible contributor to RFS temperature sensitivity. Vanier and Audoin[4] derive a cavity pulling factor $P = \frac{Q_c}{Q_l} \cdot \frac{\alpha}{1+S} \approx 10^{-7}$, where Q_c is the cavity loaded Q (≈ 200), Q_l is the Rb line Q ($\approx 10^7$, α is the maser gain parameter ($\approx 10^{-2}$), and S is the rf saturation factor (≈ 2 for optimum discriminator slope). It should be noted that P is not equal to $\frac{Q_c}{Q_l}^2$ as is often assumed for a passive atomic frequency standard because the maser gain parameter, although small, is not negligible. A cavity TC of 200 kHz/°C and an oven stabilization factor of 300 yields an RFS TC of about $1x10^{-14}$/°C.

Another minor cavity-related temperature sensitivity is caused by rf power variations due to cavity detuning. An rf power shift coefficient of $5x10^{-11}$/dB with the same cavity mistuned at the −3 dB point would cause an RFS TC of about $2x10^{-14}$/°C.

Servo offset can be a significant contributor to RFS TC. A typical value for the discriminator slope at the input of the servo integrator is 1 $mV/pp10^{11}$. Servo offset can be introduced by integrator dc offset or by pickup of synchronous detector reference drive. A 10% change in a 1 mV servo offset would cause a $1x10^{-11}$ frequency change.

Exposure to rapid temperature change can impose significant stress on an RFS. A particularly severe case is warmup after a cold soak. Nevertheless, a well-designed RFS can withstand thousands of such cycles with little effect on long-term stability.[17] Rapid change in ambient temperature can also produce pseudo frequency offset due to rate-of-change-of-phase in selective circuits such as crystal filters, or VCXO tracking error due to finite servo gain.

Shock: The most significant factors contributing to RFS shock sensitivity are shown in Table 5. Exposure of an RFS to mechanical shock can cause timing error and permanent frequency offset. Movement of optical elements can cause light shifts, movement of rf elements can cause rf power shifts, and movement of thermal elements can cause TC shifts.

TABLE 5 RFS SHOCK SENSITIVITIES

PHYSICS PACKAGE	CRYSTAL OSCILLATOR	ELECTRONICS
LAMP ASSEMBLY: Lamp Movement		LAMP EXCITER: Component/Wiring Disturbance
OPTICAL PATH: Movement of Optical Element	CRYSTAL: Frequency Change or Damage	SERVO AMPLIFIER: Finite Static & Dynamic Gain
SRD MULTIPLIER: Microwave Power		RF CHAIN: Component/Wiring Disturbance
LAMP & CELL OVENS: Thermistor Stress		TEMP CONTROLLERS: Temperature Setpoint

Acceleration: The most significant factors contributing to RFS acceleration sensitivity are shown in Table 6. An RFS does not have an inherent static acceleration sensitivity. It may, however, show frequency change due to static acceleration or orientation because of thermal effects. Frequency change is also possible due to redistribution of molten rubidium in the lamp under high static g forces.

Dynamic acceleration can have a profound effect on the stability and purity of an RFS, as discussed in the Vibration section below. The most significant factors contributing to RFS acceleration sensitivity are shown in Table 6.

TABLE 6 RFS ACCELERATION SENSITIVITIES

PHYSICS PACKAGE	CRYSTAL OSCILLATOR	ELECTRONICS
	CRYSTAL: G-Sensitivity	SERVO AMPLIFIER: Finite Static Servo Gain
RB LAMP/LIGHT PATH: Rb Movement (Light Shift) Movement of Optical Element		SERVO AMPLIFIER: Servo Offset (Δ Gain)
SRD MULTIPLIER: Microwave Power		RF CHAIN: RF Power

Vibration: The most significant factors contributing to RFS vibration sensitivity are shown in Table 7. The stability and purity of an RFS are affected by mechanical vibration primarily because of the acceleration sensitivity of the quartz crystal used in the VCXO. Direct vibrational modulation of the crystal oscillator at vibration frequencies higher than the servo bandwidth affects the RFS phase noise and spectral purity without producing a frequency offset. Spurious components are produced at $\pm f_{vib}$ at a dBc level of $\mathcal{L}(f_{vib}) = 20\log_{10}\left[\frac{\gamma f_o G}{2 f_{vib}}\right]$, where γ is the crystal acceleration coefficient, f_o is the carrier frequency, and G is the peak acceleration. The Allan deviation frequency stability is degraded to $\sigma_y(\tau) = \gamma G\left[\frac{\sin^2(\pi f_{vib}\tau)}{\pi f_{vib}\tau}\right]$, where τ is the averaging time. Vibrational modulation of the VCXO at the 2nd harmonic of the servo modulation rate, however, can cause a large frequency offset. Low frequency vibrational modulation of the crystal oscillator can cause a frequency offset due to loss of microwave power. These XO effects are reduced by a high modulation rate, a wide servo bandwidth, and a low crystal g-sensitivity.

RFS stability can also be affected by vibrational modulation of the physics package light beam at or near the servo modulation rate. This problem is reduced by rigid physics package construction. Circuit board and wiring microphonics can also affect RFS stability. The most significant factors contributing to RFS vibration sensitivity are shown in Table 7.

TABLE 7 RFS VIBRATION SENSITIVITIES

PHYSICS PACKAGE	CRYSTAL OSCILLATOR	ELECTRONICS
	CRYSTAL: G-Sensitivity ($2f_{mod}$)	SERVO AMPLIFIER: Interference
SRD MULTIPLIER: Microphonics, AM	OSCILLATOR CIRCUIT: Microphonics ($2f_{mod}$)	RF CHAIN: Microphonics, Carrier Power
RB LAMP: Rb Movement (Light Shift)		SERVO AMPLIFIER: Servo Offset (Δ Gain)
OPTICAL PATH: Lightbeam Motion (f_{mod})		SERVO AMPLIFIER: Interference

Radiation: The radiation sensitivity of an RFS is essentially that of its electronic circuits since the Rb physics package is inherently quite hard.[18] Survivability can be a critical requirement for both transient and total dose radiation environments. RFS radiation hardening is a specialized area that requires specific design techniques, careful analysis, and expert advice.[19]

Under transient radiation, an RFS may be required to "operate through" or to quickly recover frequency accuracy; in all cases it must not suffer latchup, burnout, or other permanent degradation.

Passive "flywheeling" using a high-Q passive circuit is one technique to maintain a continuous output under transient radiation. The most critical parts for latchup are usually CMOS devices; all circuits may require resistors or other means for current limiting.

Total dose radiation hardening requires careful analysis (based on piece part test data). The most critical devices are usually servo amplifier and temperature controller op amps and the C-field voltage reference. The most critical part for neutron fluence is usually the silicon photodetector, which loses output due to lattice damage. The most significant factors contributing to RFS radiation sensitivity are shown in Table 8.

TABLE 8 RFS RADIATION SENSITIVITIES

PHYSICS PACKAGE	CRYSTAL OSCILLATOR	ELECTRONICS
C-FIELD: Magnetic Sensitivity		C-FIELD SOURCE: Volt Ref, Current Source
PHOTODETECTOR: Detectivity Loss	CRYSTAL: Frequency Change	SERVO AMPLIFIER: Servo Offset (Δ Gain) Transient Recovery, Static Error

Electromagnetic Interference: The most significant RFS EMI susceptibility is usually power supply ripple and transients. Ripple susceptibility is generally worst at the RFS servo modulation rate; large frequency offsets are possible due to interference with the servo. RFS radiated susceptibility depends critically on the shielding and filtering of the RFS package and leads. The requirements for reverse and overvoltage transient protection vary depending on the characteristics of the external power supply. RFS turn-on (in-rush current) and turn-off (voltage spike) transients can be a problem for the host system. The most significant factors contributing to RFS EMI sensitivity are shown in Table 9.

TABLE 9 RFS EMI SENSITIVITIES

PHYSICS PACKAGE	CRYSTAL OSCILLATOR	ELECTRONICS
NONE	OSCILLATOR: Spurious Components	LAMP EXCITER: Light Modulation (f_{mod})
		SERVO AMPLIFIER: Interference (f_{mod})
		POWER SUPPLY: Ripple Attenuation

Humidity: RFS moisture sensitivity is most often associated with high impedance servo amplifier synchronous detector/integrator circuits. For an unsealed unit, performance under humidity or salt fog depends on the adequacy of the conformal coating and encapsulating processes used. The capability to withstand immersion is seldom a requirement for an RFS, and requires a sealed case and connectors. The most significant factors contributing to RFS humidity sensitivity are shown in Table 10.

TABLE 10 RFS HUMIDITY SENSITIVITIES

PHYSICS PACKAGE	CRYSTAL OSCILLATOR	ELECTRONICS
NONE	NONE	SERVO AMPLIFIER: Detector/Integrator Leakage
		TEMPERATURE CONTROLLERS: Temperature Setpoint

Supply Voltage: RFS sensitivity to supply voltage can occur due to a large number of factors. The dc input is often used directly as the supply voltage for the oven heaters, and changes associated with

the RFS temperature controllers (dc offsets, thermistor self-heating, heater magnetic field, etc.) can cause supply voltage sensitivity. Significant electronic supply sensitivity is also possible in the lamp exciter and rf circuits. An important distinction is between actual voltage sensitivity and thermal effects due to a change in supply voltage. The most significant factors contributing to RFS voltage sensitivity are shown in Table 11.

TABLE 11 RFS VOLTAGE SENSITIVITIES

PHYSICS PACKAGE	CRYSTAL OSCILLATOR	ELECTRONICS
C-FIELD: Residual Oven Heater Field	NONE	TEMP CONTROLLERS: Heater Current Thermistor Self-Heating
		LAMP EXCITER: Lamp Excitation Power
		RF CHAIN: RF Power/ALC
		MOD GENERATOR: Modulation Deviation

Storage: Exposure to wide temperature extremes during storage is generally not a problem for a well-designed RFS. Besides the obvious material considerations, Rb redistribution within the lamp and cells during prolonged hot storage can be a factor for subsequent lamp starting and frequency restabilization. This may worsen lamp starting, lower cavity Q, obstruct the light path, and generally cause a longer restabilization time. Storage within normal operating temperatures does not have any significant effect on subsequent RFS performance. Test data indicates that an RFS "freezes out" during storage, and, when turned on again, quickly assumes the previous frequency and aging. Electronic failure rates are lower during storage, since electrical and thermal stresses are removed, but chemical processes still continue (at a lower rate).

Retrace: A well-designed RFS has an excellent frequency retrace characteristic ($pp10^{11}$) that is non-accumulative with little dependency on temperature, off time, or restabilization time.[17] Frequency retrace is, by definition, measured by returning the unit to exactly the same operating conditions to exclude other environmental sensitivities.

Relativity: Relativistic effects due to velocity and gravitational potential are ordinarily negligible for Rb clocks except for those in a spacecraft environment.[20] Time dilation causes the frequency of a moving clock to appear to run more slowly by an amount $\frac{\Delta f}{f} \approx -\frac{v^2}{2c^2}$, where v is the clock velocity and c is the velocity of light. For a GPS satellite in a 12-hour circular orbit, the fractional frequency change is -8.35×10^{-11}. Gravitational redshift causes a clock to run more slowly in a stronger gravitational field by an amount $\frac{\Delta f}{f} = \frac{\mu}{c^2}\left(\frac{1}{R} - \frac{1}{r}\right)$, where μ is the Earth's gravitational constant, R is the Earth's radius, and r is the orbital radius. It is about $1pp10^{16}$/meter at the Earth's surface. For a GPS satellite, the gravitational redshift is 5.28×10^{-10} and the net relativistic frequency change is $+4.45 \times 10^{-10}$.

ACKNOWLEDGMENTS

The author wishes to acknowledge the efforts of J. Vig and H. Hellwig who are leading the current effort to study the environmental sensitivities of precision frequency sources. Obviously the physical understandings that underlie the environmental sensitivities of rubidium gas cell frequency standards are the result of the efforts of many persons, whom the author gratefully acknowledges.

REFERENCES

1. T. Lynch, W. Riley and J. Vaccaro, "The Testing of Rubidium Frequency Standards," Proc. 43rd Ann. Symp. on Freq. Control, pp. 257-262, May 1989.
2. H. Hellwig, "Environmental Sensitivities of Precision Frequency Sources," Proc. 3rd European Time and Frequency Forum, pp. 5-10, March 1989.
3. J.C. Camparo, "A Partial Analysis of Drift in the Rubidium Gas Cell Atomic Frequency Standard," Proc. 18th Ann. Precise Time and Time Interval (PTTI) Appl. and Planning Meeting, pp. 565-588, Nov. 1986.
4. C. Audoin and J. Vanier, *The Quantum Physics of Atomic Frequency Standards*, Adam Hilger, Bristol, 1989.
5. T.C English, E. Jechart and T.M. Kwon, "Elimination of the Light Shift in Rubidium Gas Cell Frequency Standards Using Pulsed Optical Pumping," Proc. 10th Ann. Precise Time and Time Interval (PTTI) Appl. and Planning Meeting, pp. 147-168, Nov. 1978.
6. J. Vanier, et al, "On the Light Shift in Optical Pumping of Rubidium 87; The Techniques of 'Separated' and 'Integrated' Hyperfine Filtering," Can. J. Phy., Vol. 60, pp. 1396-1403, 1982.
7. E. Jechart, "Gas Cell Atomic Frequency Standard Having Selected Alkali Vapor Isotope Ratios," U.S. Patent No. 3,903,481, Sept. 1975.
8. S. Goldberg, "Miniaturized Atomic Frequency Standard Having Both Filter Cell and Absorption Cell in Resonator Cavity," U.S. Patent No. 4,494,085, Jan. 1985.
9. A. Risley, S. Jarvis, Jr. and J. Vanier, "The Dependence of Frequency Upon Microwave Power of Wall-Coated and Buffer-Gas-Filled Gas Cell Rb^{87} Frequency Standards," J. Appl. Phy., Vol. 51, No. 9, pp. 4571-4576, Sept. 1980.
10. G. Missout and J. Vanier, "Pressure and Temperature Coefficients of the More Commonly Used Buffer Gases in Rubidium Vapor Frequency Standards," IEEE Trans. Instrum. and Meas., Vol. 24, No. 2, pp. 180-184, June 1975.
11. J.H. Shirley, "Some Causes of Resonant Frequency Shifts in Atomic Beam Machines. II. The Effect of Slow Frequency Modulation on the Ramsey Line Shape," J. Appl. Phys., Vol. 34, No. 4, Part 1, pp. 789-791, April 1963.
12. N.F. Ramsey, "Resonance Transitions Induced by Perturbations at Two or More Frequencies," Phy. Rev., Vol. 100, No. 4, pp. 1191-1194, Nov. 1955.
13. S.A. Wolf, D.U. Gubser and J.E. Cox, "Shielding of Longitudinal Magnetic Fields with Thin, Closely Spaced, Concentric Shells, with Applications to Atomic Clocks," Proc. 10th Ann.Precise Time and Time Interval (PTTI) Appl. and Planning Meeting, pp. 131-146, Nov. 1978.
14. A. Stern, A. Hertz, Y. Zarfaty and A. Lepek, "A Novel Compact Rubidium Frequency Standard with a Low Sensitivity to Magnetic and Vibrational Disturbances," Proc. 42nd Ann. Symp. on Freq. Control, pp. 519-524, June 1988.
15. F. Danzy and W. Riley, "Stability Test Results for GPS Rubidium Clocks," Proc. 19th Ann. Precise Time and Time Interval (PTTI) Appl. and Planning Meeting, pp. 267-274, Dec. 1987.
16. M.E. Ferking and D.E. Johnson, "Rubidium Frequency and Time Standard for Military Environment," Proc. 26th Ann. Symp. on Freq. Control, pp. 216-222, June 1972.
17. W. Riley and J. Vaccaro, "A Rubidium-Crystal Oscillator," Proc. 40th Ann. Freq. Cont. Symp., pp. 452-464, May 1986.
18. T.C. English, H. Vorwerk and N.J. Rudie, "Radiation Hardness of Efratom M-100 Rubidium Frequency Standard," Proc. 14th Ann. Precise Time and Time Interval (PTTI) Appl. and Planning Meeting, pp. 547-575, Nov. 1982.
19. T. Flanagan, et al, "Hardening Frequency Standards for Space Appl.," IEEE Trans. Nucl. Sci., Vol. NS-24, No. 6, pp. 2252-2258, Dec. 1977.
20. P.S. Jorgensen, "Special Relativity and Intersatellite Tracking," Navigation, Vol. 35, No. 4, pp. 429-442, Winter 1988-89.

PHYSICS OF SYSTEMATIC FREQUENCY VARIATIONS IN HYDROGEN MASERS

Edward M. Mattison
Smithsonian Astrophysical Observatory
Cambridge, Massachusetts

ABSTRACT

The frequency stability of hydrogen masers for intervals longer than 10^4 seconds is limited at present by systematic processes. We discuss the physics of frequency-determining mechanisms internal to the maser that are susceptible to systematic variations, and the connections between these internal mechanisms and external environmental factors. Based upon estimates of the magnitudes of systematic effects, we find that the primary internal mechanisms currently limiting long-term maser frequency stability are cavity pulling, at the level of parts in 10^{15} per day, and wall shift variations, at the level of parts in 10^{16} to parts in 10^{15} per day. We discuss strategies for reducing systematic frequency variations.

INTRODUCTION

The hydrogen maser is the most stable frequency standard currently available, providing fractional frequency stabilities of better than 1×10^{-15} for averaging intervals on the order of 10^4 seconds. The fundamental mechanisms limiting maser frequency stability are well know: additive thermal noise entering the maser's r.f. receiver[1] causes the two-sample (Allan) deviation $\sigma(\tau)$ to vary with the averaging interval τ as τ^{-1}, and is the dominant mechanism typically for $\tau< 100$ seconds, while thermal noise within the atomic linewidth[2] causes $\sigma(\tau)$ to vary as $\tau^{-1/2}$, and typically dominates the stability for $100<\tau<10^4$ seconds[3]. For intervals longer than roughly 10^4 seconds, $\sigma(\tau)$ generally increases with τ, due to systematic processes affecting the frequency. In this regime, typical plots of the Allan deviation show $\sigma(\tau)\sim\tau^1$, indicating domination by linear frequency drift. When linear drift is removed from the frequency data, $\sigma(\tau)$ often varies as $\tau^{1/2}$, which is characteristic of random-walk of frequency. Random walk frequency variations are likely to result from the simultaneous action of several quasi-independent processes; an underlying $\tau^{1/2}$ variation of $\sigma(\tau)$ suggests that a number of systematic effects are at work in addition to the dominant long-term process.

In order to improve the long-term frequency stability of hydrogen masers, systematic frequency-varying processes must be identified and reduced. At the present level of maser performance, not one, but many such processes must be dealt with in order to achieve a substantial improvement in long-term stability. The aim of the present work is three-fold: first, to identify sources of systematic frequency variation; second, to estimate the magnitudes of the various combinations of effects on the frequency stability; and third, to identify strategies for minimizing these systematic effects.

SOURCES OF SYSTEMATIC FREQUENCY VARIATION

The sources of systematic frequency variation in hydrogen masers can be organized into three groups, as shown in Table. 1: (i) the basic internal mechanisms that determine the maser's frequency[4], including cavity pulling, internal magnetic fields and field gradients, wall shift, collisional frequency shifts, and second order Doppler effect; (ii) environmental variables, including ambient temperature, magnetic field, humidity, barometric pressure, vibration, gravity, and time; and (iii) the myriad structures and systems within the maser that can connect, or transduce, environmental changes to the internal mechanisms. Time is included as an environmental or driving mechanism because many components, both mechanical and electronic, are observed to vary slowly, or "age," without direct external intervention.

Table 1 — Schema of Frequency-determining Mechanisms

Maser Frequency Physics (Internal)		**Driving Mechanisms (External)**
Cavity frequency (pulling) Magnetic field (internal) Wall shift Collisional shifts 2nd Order Doppler shift (dPhase/dt)	⇐**Transducing**⇐ **Mechanisms**	Time Temperature Magnetic field (external) Humidity Vibration Barometric pressure Gravity

Transducing mechanisms, and their connections between environmental drivers and internal maser physics, are listed in Table 2. As indicated in Table 2, the links between environmental and internal mechanisms are multiple, with many environmental drivers acting upon several physical mechanisms, often through several different transducing effects, and many internal mechanisms affected by more than one environmental force. Because all active masers necessarily employ systems that accomplish similar ends, the list of transducers is relatively general; the magnitudes of systematic frequency variations, however, can differ by orders of magnitude, depending upon the specifics of maser design.

Relevant to practical considerations of maser frequency stability, but not included in the list of Table 2, are noise and phase variations introduced by the comparison system used to measure maser frequencies. Thermal and mechanical disturbance of signal-carrying cables, and thermal noise in amplifiers and mixers, can introduce phase changes that are difficult to separate from maser frequency variations; these effects are most important in relatively short-term comparisons (under 30 minutes), and will be particularly important when comparing cryogenic masers, which are projected to have stabilities in the range of 10^{-17} to 10^{-18}.

Table 2 — Connections Among Frequency-determining Mechanisms

Internal Mechanism	Transducing Mechanism	Time	Temp	Humid	Baro	MagFld	Vib
Cavity Frequency	Bulb Dielectric coef		X				
	Cavity bulk thermal expansivity		X				
	Cavity coating thermal expansivity		X				
	Tuning diode voltage	?	X	?			
	Cavity joint shrinkage	X					X
	Cavity bulk shrinkage	X					
	Coupling circuit/isolator	?	X	??			
	Thermistors/resistors	X					
	Beam flux variation	?	X	?			
	Barometric pressure				X		
Magnetic Field magnitude & gradients	External mag fld variation	X				X	
	Internal field current var.		X				
	Magnetic shield aging	?					X
	Atomic state distribution						
Wall Shift	Storage bulb contamination	X					
	Coating changes	X					
Collisional Shifts	State distrib. changes	?	?			X	
	Beam flux variation	?	X				
2nd order Doppler	Temperature		X				

Some of the transducing effects of Table 2 require explanation. An important internal maser frequency-determining mechanism is cavity pulling: a change Δf_c of the maser's resonant cavity frequency produces a change Δf_m in the maser frequency given by

$$\Delta f_c = \Delta f_m(Q_c/Q_{line}) \qquad (1)$$

where Q_c is the loaded cavity Q and Q_{line} is the atomic line Q. The main factor affecting the cavity's resonance frequency is the cavity's size: the resonance frequency of a typical cavity varies with cavity length at a rate of roughly 10 MHz/cm, so that for $Q_c/Q_{line} \sim 10^{-5}$, a typical value, a fractional change in the maser frequency of 10^{-15}, which is readily measurable, is produced by a cavity length change of roughly one Angstrom, or the size of an atom. The cavity's dimensions are affected by the thermal

expansivity α of the material of which the cavity is constructed ($\alpha \sim 10^{-8}$ °C^{-1} for low-expansion materials like Cervit or Zerodur, and $\alpha \sim 2\times10^{-5}$ °C^{-1} for metals such as copper or aluminum); contraction of the joints between the cavity's cylinder and endplates over periods of months to years[5]; thermal expansivity of the cavity's metallic coating (for non-metallic cavity materials); change in the coating's internal stress[6]; and shrinkage of the cavity's (bulk) structural material over years[7,8,9]. The cavity's resonance frequency is also affected by thermally-induced changes in the quartz storage bulb's dielectric coefficient and by changes in the cavity's varactor tuning diode voltage, which can result from temperature changes in the diode voltage reference or voltage divider circuit (or digital-to-analog converter [DAC], if used), and from aging of the reference, divider, or DAC.

Internal magnetic fields affect the maser's frequency primarily through the quadratic dependence of the hydrogen hyperfine energy upon magnetic field, and also, in masers that are not properly tuned, through magnetic-gradient line broadening, which can change the amount of cavity pulling by varying the line Q. In addition, the internal field affects the magnetic gradient shift[10], which depends upon the d.c. magnetic field gradient, asymmetry in the r.f. magnetic field, and the state distribution in the atomic beam. Variations in the internal magnetic field can result from changes in the external (ambient) magnetic field, which is never perfectly excluded by the maser's magnetic shields; from changes in the shielding factor of the shields that may result from vibration or, possibly, from aging; and from changes in the current that supplies the solenoid that generates the uniform internal field. The solenoid current is susceptible to many of the environmental mechanisms that can affect the tuning diode voltage.

Slow changes in maser frequency due apparently to variations in the wall shift have been observed. Wall shift changes might be caused by contamination of the storage surface by materials outgassed from other parts of the maser or entering the storage bulb from the hydrogen dissociator; by outgassing of contaminants from the bulb surface (cleanup); and by physical or chemical changes in the fluorocarbon storage coating itself.

Frequency shifts due to collisions between stored hydrogen atoms — spin-exchange shifts and so-called Crampton-Verhaar shifts — are affected by variations in the hydrogen beam flux intensity and by changes in the magnetic fields in the region between the state-selection magnets and the resonant cavity, which can vary the distribution of atomic states entering the storage bulb.

The second-order Doppler shift affects the maser frequency directly through the speed, and therefore the temperature, of the hydrogen atoms in the storage bulb.

ESTIMATION OF SYSTEMATIC EFFECTS

APPROACH TO ESTIMATION

In estimating the magnitude of the many frequency-varying effects, both analytical and experimental approaches are used. Some effects can be analysed from physical principles; for example, the second-order Doppler shift Δf_D is directly related to the temperature of the storage bulb, while the change in the cavity resonance frequency due to cavity expansion can be expressed as a

function of the cavity's temperature and the cavity material's thermal expansion coefficient α. Other effects are difficult or impossible to analyse from first principles, and must be measured; examples are cavity joint shrinkage, and cavity frequency changes resulting from variation in the length of the coaxial cable coupling the cavity to the r.f. output circuit. Some effects, such as magnetic field sensitivity or thermal variations, can be measured in controlled, relatively short-term tests; others, notably the wall shift and cavity shrinkage, require very long-term observations and measurements.

For all effects, estimating absolute frequency variations requires assumptions about the construction of the maser, the effectiveness of its control systems, and the magnitudes of environmental variations. Here we assume an active maser with a low-expansivity resonant cavity; thermal control that maintains the maser's cabinet air temperature constant to 0.1 °C and the cavity temperature constant to 2×10^{-5} °C; and passive magnetic shields with a shielding factor $S = \Delta H_{ext}/\Delta H_{int} \sim 4\times10^{4}$. As discussed in a later section, cavity autotuning and other environmental control mechanisms, which are not assumed here, have the potential of significantly reducing some systematic frequency variations.

DISCUSSION OF SPECIFIC EFFECTS

Cavity coupling circuit. In addition to being a function of internal mechanisms such as the bulb dielectric coefficient and the cavity's dimensions, the cavity's resonance frequency is affected by the external circuit that couples r.f. power out of the cavity. Because the circuit terminator, usually a ferrite isolator, cannot be perfectly matched to its input coaxial cable, changes in the cable's length can alter the amount of r.f. power reflected back to the cavity, and consequently change the cavity frequency. As shown in Fig. 1, which represents measurements using a particular isolator, cable, and cavity coupling coefficient, the sensitivity of maser frequency to cable length can be as much as several parts in 10^{12} per cm if the cable's length is not adjusted optimally, or nominally zero if the cable's length is properly chosen. The choice of cable length affects not only the maser's sensitivity to the cable itself, but also its sensitivity to changes in the terminating isolator. This effect may play a part in the sensitivity to changes in ambient humidity, discussed below.

Cavity dimension changes The cavity resonance frequencies of many masers increase monotonically with time. Figure 2 shows the change in maser frequency due to cavity resonance frequency variations in Smithsonian Astrophysical Observatory (SAO) masers over periods of up to ten years[11]. The data were obtained from the variations in the tuning diode voltages required to keep the maser cavities spin-exchange tuned[12], and were translated to a common origin for ease of comparison. The frequencies almost invariable increase, at rates that generally decrease with time, and lie between roughly 2×10^{-15}/day and 7×10^{-15}/day. A possible source of such behavior has been suggested to be shrinkage of the polished, although not optically contacted, joints between the cavity cylinder and endplates. Optically contacted joints in similar materials have been shown to shrink at roughly exponentially decreasing rates, with characteristic times on the order of months[5]. The continuing increase in cavity frequencies over many years, however, suggests shrinkage of the bulk cavity material itself. Such shrinkage has been observed in gauge-blocks of Zerodur[7] and ULE[9] and in Zerodur and ULE laser etalons[8], and is summarized in Table 3. Column 3 of the table gives the equivalent maser frequency change that would result from the material shrinkage, assuming

$Q_c/Q_{line} \sim 10^{-5}$. The substantially lower shrinkage rate observed in a ULE etalon provides reason to believe that a proper choice of cavity material can result in a significant decrease in cavity frequency variation.

Table 3 — Shrinkage Rates of Low-expansivity Cavity Materials			
Material		Material creep $(1/L)(dL/dt)$ (day^{-1})	Maser freq change $(1/f)(df/dt)$ (day^{-1})
Zerodur[1]	initial	-1.8×10^{-9}	3.6×10^{-14}
	after 10 yrs	-2.9×10^{-11}	5.8×10^{-16}
Zerodur[2]	initial[3]	-3.9×10^{-10}	7.6×10^{-14}
	after 900 days	-1.8×10^{-10}	3.6×10^{-15}
ULE[2]	initial	-3.7×10^{-9}	9.3×10^{-15}
	after 20 days	-4.6×10^{-11}	9.2×10^{-16}
[1]Ref. 7. [2]Ref. 8. [3]1.5 years after heat treatment			

Wall Shift Even after changes in cavity frequency are accounted for by spin-exchange tuning, masers are observed to have long-term frequency drifts that are generally ascribed to changes in the wall shift. Figure 3 shows the frequencies of 7 hydrogen masers measured after tuning[13]. (The tunings and frequency measurements were generally done after the masers had been opened to the atmosphere for changing of their vacuum pump elements.) The tuned maser frequencies were compared with UTC by means of GPS common-view measurements or, in the case of the early measurements, transportable cesium clocks. (For this reason the early measurements have relatively large uncertainties.) The frequencies of most of the masers decrease with time, at rates between roughly -6×10^{-16}/day to -2×10^{-15}/day. Some of the more recently built masers, on the other hand, appear to increase slightly in frequency, at rates of up to $+6\times10^{-16}$/day. These wall shift changes may be due to chemical or physical alterations in the coating materials, or to adsorption or desorption of contaminants. In addition, wall shift changes have been observed that result from changes in the hydrogen flux intensity entering the storage buib. Wall shift variations cannot be removed by cavity retuning or servo control, and represent what is likely to be the dominant systematic effect on long-term maser frequency stability. Research into improved wall coating materials is called for, building upon Soviet work that has yielded coatings with up to 10 times less wall shift than previous materials[14].

Gravity Gravity affects the frequency of the hydrogen maser both through the relativistic effects to which all clocks are subject, and through deformations of the maser's structure, primarily the microwave cavity. In particular, many masers are sensitive to tilt; the measured sensitivity of one maser[15], for example, is 3.6×10^{-14}/degree. While tilt sensitivity should not affect the frequency stability of a maser located on a solid, it does limit the resettability of a maser after being moved, and requires masers to be carefully repositioned or retuned after being moved.

Humidity High-stability cesium and hydrogen clocks have been observed to be sensitive to humidity. Changes in humidity might affect a maser's frequency by altering the thermal conductivity of the air within the maser cabinet and thus affecting its temperature control systems, or by altering

the surface conductivity of the high-impedance circuits supplying the tuning diode voltage; there is also evidence suggesting that humidity may affect the maser's output isolator or coaxial coupling cable[16].

SUMMARY OF RESULTS

The results of measurements and calculations of a variety for systematic effect are summarized in Fig 4. The black lines give ranges of sensitivities for effects that can be estimated with a reasonable degree of confidence; gray lines represent values for which precision is lacking, or for which parameters, such as cavity detuning, can vary over a substantial range and depend upon specific maser operation. Lack of space prevents presentation of detailed derivations; details are available elsewhere[17]. It can be seen from Fig. 4 that, under the assumptions made here, the major systematic contributions to maser frequency variation arise from dimensional aging of the cavity material and from wall shift variation, contributing frequency variations on the order of parts in 10^{16}/day. A variety of other effects are expected to come into play at the level of parts in 10^{16}, and as a matter of observation, frequency stabilities currently appear limited, even after removal of linear frequency drift and rate of change of drift, to several parts in 10^{15} for periods of days to weeks[3].

STRATEGIES FOR REDUCING SYSTEMATIC FREQUENCY VARIATIONS

A variety of approaches to reducing systematic frequency variations in hydrogen masers have been implemented or proposed. Cavity pulling in active masers has been addressed by means of servo systems that lock the cavity's resonance frequency to the atomic masing frequency[18,19,20]. Active servo control has also been applied to the reduction of magnetic field effects; one such system concentrates and senses the magnetic field within the outermost magnetic shield and controls a solenoid to compensate for ambient field changes[19]. Single-state hydrogen beam state selection systems[21,22,23] can improve magnetic performance as well as reduce cavity pulling. By preventing hydrogen atoms in undesired hyperfine states from entering the storage region these systems reduce spin-exchange relaxation, thereby increasing the line Q and decreasing cavity pulling; in addition, they substantially reduce collisional frequency shifts that make the maser susceptible to magnetic field variations[24].

Electronic control systems and servos, including the temperature, hydrogen flux, tuning diode, and magnetic field controllers used in all masers, are potentially subject to long-term changes due to aging of components such as voltage references, thermistors, setpoint resistors, varactor diodes, and isolators. The effects of such aging on maser frequency stability has not been reported, and will require lengthy and careful investigation to quantify.

Wall shift variations cannot be reduced by incorporating new maser systems, but rather by improving the chemical and physical properties of the wall coating material, and perhaps by identifying and reducing contaminating materials in the maser.

A different approach to improving maser frequency stability is available for use with masers that are employed as medium-term flywheel oscillators or frequency references. The drift rate of a maser can be established by spin-exchange tuning the maser at intervals of weeks to months, or by comparing the maser's frequency with international references by means of GPS common-view measurements. Using a phase-continuous digital synthesizer in the maser receiver system, the output frequency of the maser receiver can be varied in steps of less than 10^{-17} to compensate for the maser drift. The tuning diode is then reset at intervals of weeks to months to the tuned cavity condition, at which time the synthesizer frequency is adjusted simultaneously to keep the maser's output frequency constant.

CONCLUSIONS

At the present state of the art, hydrogen maser frequency stability appears limited to a few parts in 10^{15} for intervals of days to weeks. Improvement of long-term stability will require careful attention to a variety of systematic effects. An advantageous approach to dealing with these effects appears to be to identify and reduce systematic processes as much as possible, and then to employ active servo control systems to reduce them further, taking care that the control systems do not, themselves, introduce other systematic variations.

ACKNOWLEDGEMENTS

For providing data and for helpful discussions I am grateful to J. Eler, A. Kubik, J. Mueller, and P. Wheeler (United States Naval Observatory), J. Hall (Joint Institute for Laboratory Astrophysics), A. Kirk (Jet Propulsion Laboratory), H. Peters (Sigma Tau Standards Corporation), R. Vessot (Smithsonian Astrophysical Observatory) and H. Wang (Hughes Research Corporation). Support for this work was provided in part by the Smithsonian Institution and by the Jet Propulsion Laboratory.

REFERENCES

1 R.Vessot, L. Mueller, and J. Vanier, "The specification of oscillator characteristics from measurements made in the frequency domain," *Proc. IEEE* **54**, 199 (1966).

2 W.A. Edson, "Noise in oscillators," *Proc. IRE* **48**, 1454 (1960).

3 A. Uljanov, N. Demidov, E. Mattison, R. Vessot, D. Allan, and G. Winkler, "Performance of Soviet and U.S. hydrogen masers," *Proc 22nd Annual Precise Time and Time Interval (PTTI) Applications and Planning Meeting* (this issue) (1990).

4 The operation of the maser is discussed in D. Kleppner, H.C. Berg, S.B. Crampton, N.F. Ramsey, R.F.C. Vessot, H.E. Peters, and J. Vanier, "Hydrogen maser principles and techniques," *Phys. Rev. A* **138**, 972 (1965), and in J. Vanier and C. Audoin, *The quantum physics of atomic frequency standards*, Adam Hilger (1989).

[5] J.W. Berthold III, S.F. Jacobs, and M.A. Norton, "Dimensional stability of fused silica, invar, and several ultralow thermal expansion materials," *Applied Optics* **15**, 1898 (1976), and S.F. Jacobs, "Dimensional stability measurements of low thermal expansivity materials using an iodine stabilized laser," *Proc. 2nd Frequency Standards and Metrology Symposium*, Copper Mountain, CO, p. 296 (1976).

[6] E.M. Mattison and R.F.C. Vessot, "Time and temperature stability of silver-coated ceramics for hydrogen maser resonant cavities," *Proc 20th Annual Precise Time and Time Interval (PTTI) Applications and Planning Meeting*, p. 313 (1988).

[7] F. Bayer-Helms, H. Darnedde, and G. Exner, "Längenstabilität bei Raumtemperatur von Proben der Glaskeramik 'Zerodur'," *Metrologia* **21**, 49 (1985).

[8] D. Hils and J.L. Hall, "Ultra-stable cavity-stabilized lasers with subhertz linewidth," *Frequency Standards and Metrology* , p. 162 (1989).

[9] B. Justice, "Precision measurements of the dimensional stability of four mirror materials," *Journal of Research of the National Bureau of Standards – A. Physics and Chemistry* **79A**, 545 (1975).

[10] S.B. Crampton and H.T.M. Wang, "Density-dependent shifts of hydrogen maser standards," *Proc. 28th Frequency Control Symposium*, p. 355 (1974).

[11] A. Kirk, Jet Propulsion Laboratory, private communcation (1990).

[12] S.B. Crampton, "Spin-exchange shifts in the hydrogen maser," *Phys. Rev.* **158**, 57 (1967).

[13] A. Kirk, Jet Propulsion Laboratory, Pasadena, California. Private communication.

[14] N.A. Demidov, E.M. Yezhov, V.A. Fedodorov, and A.A. Uljanov, "The search for new materials in the hydrogen generator," *UDK* 621.317.7.6.089.69.

[15] SAO VLG-11 maser.

[16] A. Kirk, Jet Propulsion Laboratory. Private communication.

[17] E.M. Mattison and R.F.C. Vessot, "A study on the feasibility of development of a state-of-the-art hydrogen maser," Final report on contract 958019, prepared for Jet Propulsion Laboratory, Pasadena, California.

[18] C. Audoin, "Fast cavity auto-tuning systems for hydrogen masers," *Revue Phys. Appl.* **16**, 125 (1981).

[19] H. Peters, H. Owings, and P. Koppang, "Atomic hydrogen masers with self auto-tune system and magnetic field cancellation servo," *Proc 20th Annual Precise Time and Time Interval (PTTI) Applications and Planning Meeting*, p. 337 (1988).

[20] R. Hayes and H. Wang, "A subcompart Q-enhanced active maser," *Proc 18th Annual Precise Time and Time Interval (PTTI) Applications and Planning Meeting*, p. 611 (1986).

[21] E.M. Mattison and R.F.C. Vessot, "Single-state selection system for hydrogen masers," *Proc. 40th Annual Frequency Control Symposium*, p. 422 (1986).

[22] C. Audoin, M. Desaintfuscien, P. Petit, and J-P. Schermann, "Design of a double focalization in a hydrogen maser," *IEEE Trans. on Instr. and Meas.* **IM-17**, 351 (1968).

[23] S. Urabe, K. Nakagiri, Y. Ohta, M. Kobayashi, and Y. Saburi, "Majorana effect on atomic frequency standards," *IEEE Trans. on Instr. and Meas.* **IM-29**, 304 (1980).

[24] E.M. Mattison and R.F.C. Vessot, "Performance of SAO model VLG-12 advanced hydrogen masers," *Proc. 44th Annual Frequency Control Symposium*, p. 71 (1989).

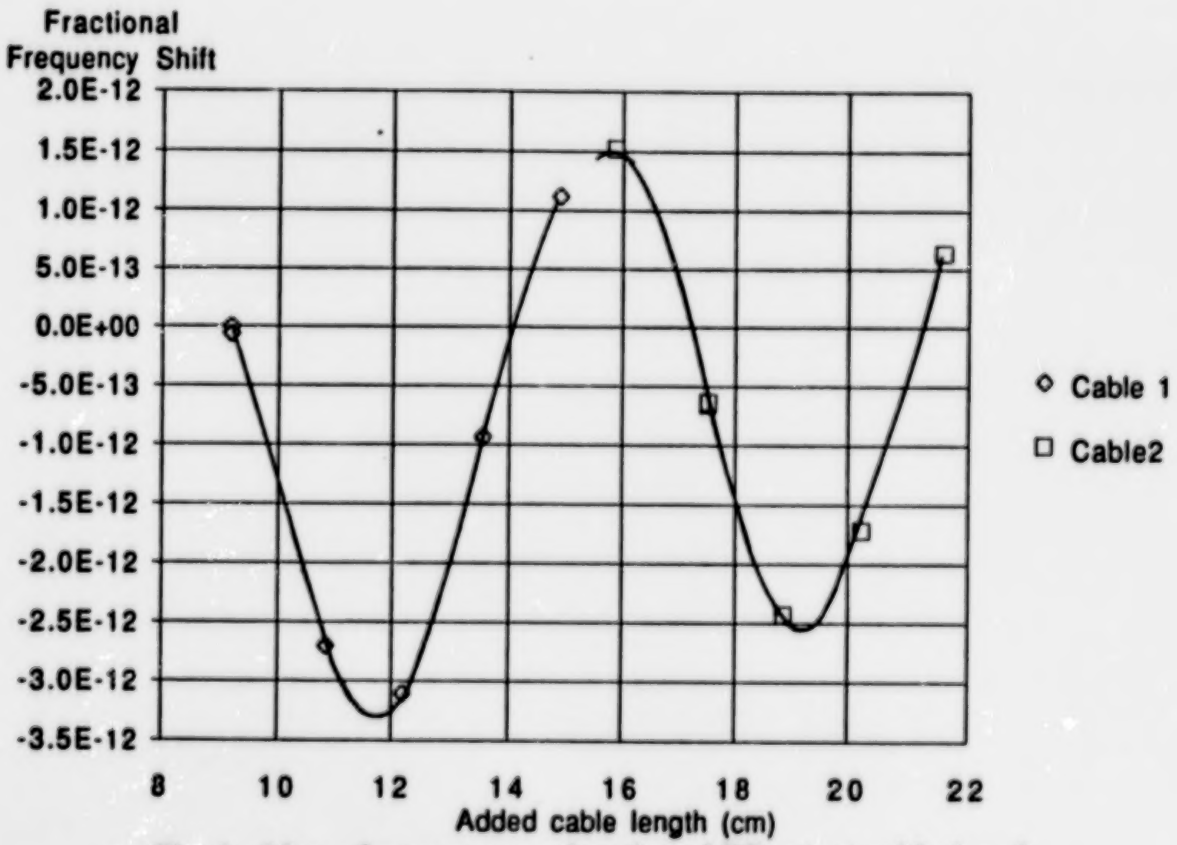


Fig. 1. Maser frequency as a function of RF output cable length.

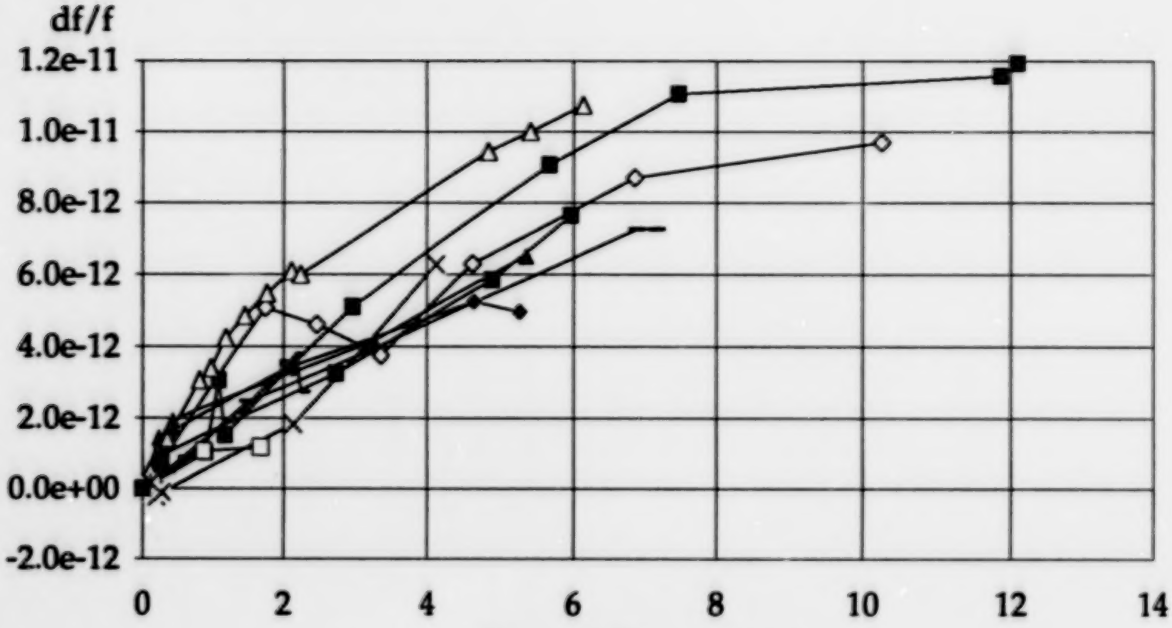


Fig. 2. Maser output frequency vs. time due to cavity resonance frequency variation

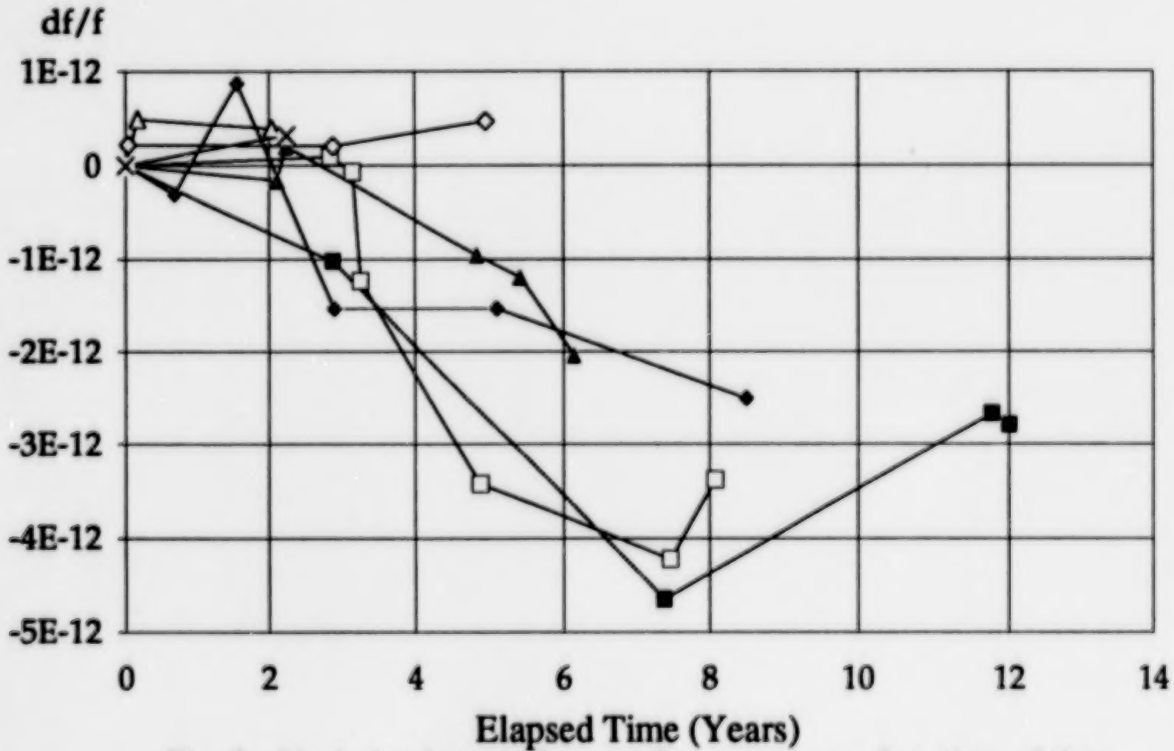


Fig. 3. Variation in tuned maser frequency as a function of time

BLANK

PAGE

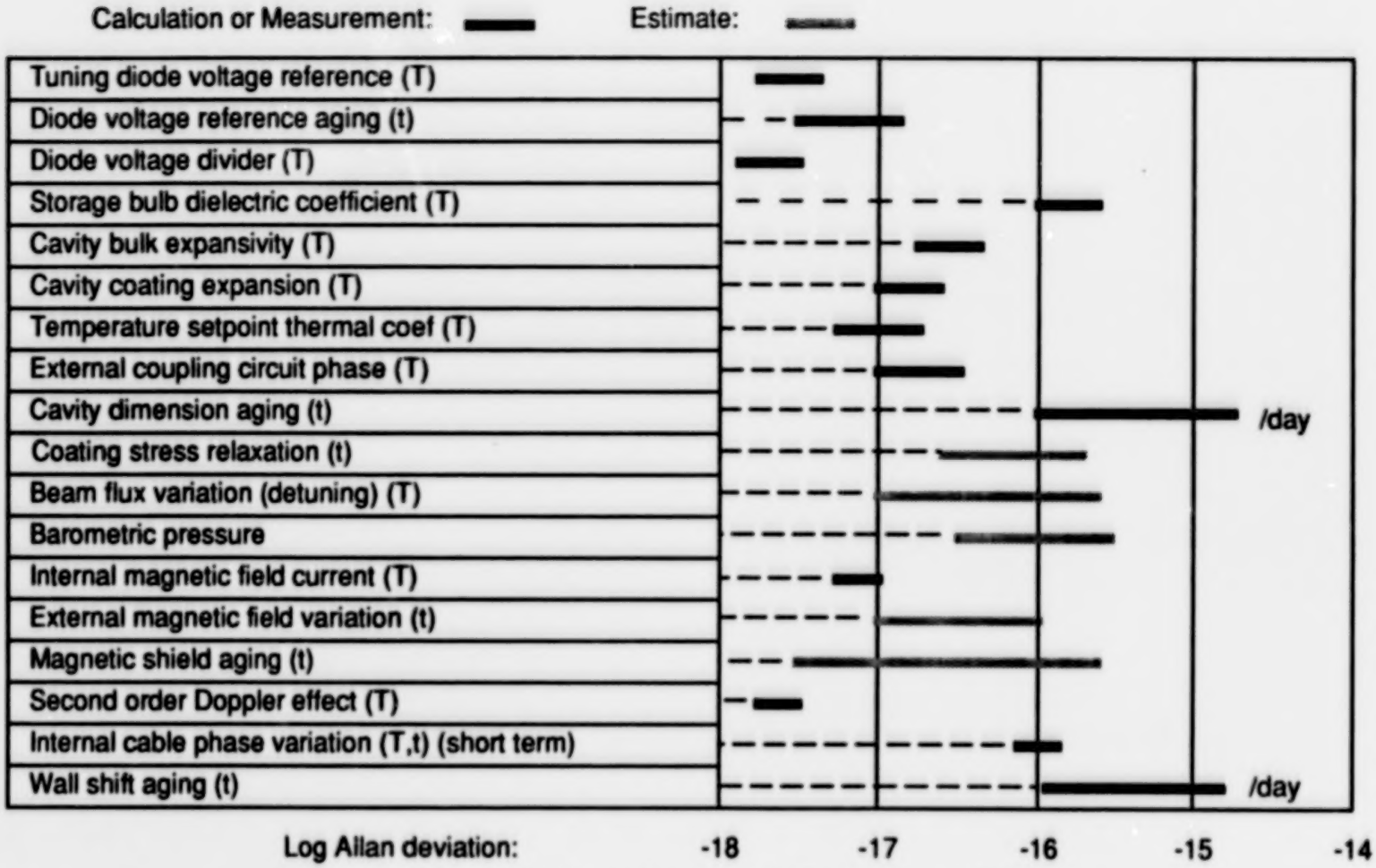


Fig. 4. Summary of estimated systematic frequency variations.

Environmental Sensitivities of Quartz Crystal Oscillators

Fred L. Walls
Time and Frequency Division
325 Broadway
Boulder, Colorado 80303

Abstract

The frequency, amplitude, and noise of the output signal of a quartz-crystal-controlled-oscillator is affected by a large number of environmental effects. This paper examines the physical basis for the sensitivity of precision oscillators to temperature, humidity, pressure, vibration, magnetic field, electric field, load, and radiation. The sensitivity of crystal oscillators to radiation is a very complex topic and poorly understood. Therefore only a few general results are mentioned. The sensitivity to most external influences often varies significantly from one oscillator type to another and from one unit of a given type to another. For a given unit, the sensitivity to one parameter often depends on the value of other parameters and history. Representative sensitivity to the above parameter will be given.

I. Introduction

Quartz crystal oscillators are a fundamental element in many areas of frequency metrology affecting applications such as communication and navigation. Their frequency, output level, amplitude noise, and phase noise are generally critical parameters that determine the overall performance of a system. In many applications their performance is significantly less than that obtained under ideal environmental conditions. In this paper I will briefly outline the physical basis and representative values for the sensitivity of quartz crystal oscillators to environmental parameters. The most important of these are temperature, humidity, pressure, vibration, magnetic field, electric field, load, and radiation. The sensitivity of quartz oscillators to radiation is a very complex and poorly understood topic and therefore only a few general results are mentioned. For a given oscillator the sensitivity to one parameter often depends on the value of other parameters, and the history of the device. It is often difficult to separate the influence of one parameter from that of another. Several methods for characterizing the environmental sensitivities of both quartz resonators and oscillators are discussed in [1]. Much more effort is needed in this area.

II. Model of a Quartz Controlled Oscillator

Figure 1 shows a simplified diagram of a quartz-crystal-controlled oscillator. The well known oscillation conditions are that the phase around the loop be an integral multiple of 2π and that the loop gain be 1 [2-5]. Small changes in the loop phase, $d\phi$, are compensated by a change in oscillation frequency of

$$\Delta\nu/\nu_0 = (1/2Q)\, d\phi, \tag{1}$$

where ν_0 is the oscillation frequency and Q is the loaded Q-factor of the resonator. Small changes in the frequency of the resonator are directly translated into changes in the frequency of the oscillator since the rest of the electronics is generally very broadband compared to the resonator, that is,

$$\Delta\nu/\nu_{0_{\text{oscillator}}} = d\nu/\nu_{0_{\text{resonator}}}. \tag{2}$$

These two equations provide the basis for understanding how the various environmental conditions affect both the short-term and the long-term frequency stability of the oscillators.

III. Changes Within the Resonator

Environmental effects that change the frequency of the resonator have been investigated by many people in much more detail than can be described in this paper. The most important environmentally driven changes within the resonator are driven by changes in temperature, level of excitation (rf amplitude), stress, adsorption and desorption of material on the surface, vibration, radiation, electric field, and magnetic field.

The frequency shifts due to these effects are universal to the extent that a given change in resonator frequency causes the same change in oscillator frequency in the limit that the oscillator loop is broadband. Different oscillator designs have an influence on the apparent isolation of the resonator from the environmental parameters.

A. Temperature and Temperature Changes

Temperature variations change the value of the elastic constants and, to a lesser degree, the dimensions of the resonator. The change in resonator frequency with temperature varies greatly with crystallographic cut and orientation [6-21]. Figure 2 shows a typical static frequency versus temperature curve for precision quartz resonators [16]. The actual values depend on the resonator cut, overtone, frequency, diameter, and mounting technique. Temperature changes and temperature gradients often cause frequency changes that are large compared to the slope of the static curve [6-22]. Typical coefficients for the frequency-temperature effect for 5 MHz resonators are

$$\Delta\nu/\nu_0 = 10^{-9}\, \Delta T^2 - 10^{-5}\, dT/dt \tag{3}$$

for 5th overtone AT-cuts, and

$$\Delta\nu/\nu_0 = 10^{-9}\, \Delta T^2 + 10^{-7}\, dT/dt \tag{4}$$

for 3rd overtone SC-cuts. Here ΔT is the temperature difference in K from turnover and dT/dt is the rate of change of temperature in K/s.

The dynamic temperature effect leads to hysteresis in the experimental measurements of temperature coefficients as shown in Figs. 3 and 4. This effect makes it difficult to locate the exact turn-over point. This in turn leads to oscillators with finite frequency changes even for slow, small temperature excursions, especially for AT-cut resonators. Table 1 shows typical temperature coefficients for an AT-cut resonator as a function of the error in setting the oven to the exact turn-over point. Table 2 shows typical temperature coefficients for an SC-cut resonator as a function of the error in setting the oven to the exact turn-over point. The actual change in temperature may be driven by changes in atmospheric pressure and/or humidity thereby changing the thermal conductance and temperature gradients within the oscillator package [22-24]. Deposited radiative energy can also change the temperature of the resonator. The performance potential of AT-cut resonators is extremely difficult to attain due to their very high dynamic temperature coefficient. Sulzer was the first to attain a performance $\sim 3 \times 10^{-13}$ from AT-cut resonators, and it was many years before it was generally realized that the reason for the excellent performance was an oven design with extremely low thermal transients [25]. The reduction in the dynamic temperature coefficient for SC-cut resonators as compared to the earlier AT- and BT-cut resonators represents a major advance in the practical application of quartz crystal oscillators in nonideal environments using only simple ovens. Much better thermal performance can be obtained using multiple ovens [26], aged high-performance thermistors [27], and compensated oven designs [28]. The tradeoff is increased complexity, size, weight, and cost.

Temperature generally does not affect the phase noise or short-term frequency stability of an oscillator. However, in cases where the sustaining electronics is not temperature controlled, slight changes in gain and noise figure with temperature will be reflected in the output phase noise. Reviews of the correlation of output phase noise with the noise performance of the sustaining stage and output amplifier are given in [2-5, 29].

Another important effect, especially with AT-cut resonators, is activity dips. Activity dips are due to the accidental overlap of some other mode of the resonator with the resonance mode. This coupling to the unwanted mode leads to increased losses and hence a reduction in the oscillator amplitude. The frequency of the resonator is also pulled by the coupling to the other mode, which usually has much higher sensitivity to temperature than the primary mode of oscillation. This leads to temperature-frequency coefficients that vary rapidly with temperature over very narrow ranges in temperature of the resonator [30-34]. Figure 5 shows the frequency-versus-temperature performance of the primary clock in the Ginga satellite [33]. The nonlinear thermal coefficient near $18°C$ make it very difficult to model to accurately recover clock timing. SC-cut resonators and some types of lateral field resonators show much reduced incidence of activity dips and their associated quirks in the temperature coefficients [34-36].

The dynamic temperature effect and the possibility of an activity dip significantly complicates the specification and measurement of oscillator temperature coefficients. For critical applications the frequency must be measured over the entire operating temperature range using a model of the actual temperature profiles.

B. RF Excitation Level

The frequency of the resonator is also a function of amplitude of the signal level as shown in Fig. 6 [16, 18-20, 34, 37-39]. The sensitivity to this effect, usually called the amplitude-frequency effect, is a function of the blank curvature as shown in Fig. 7 [34]. Typical sensitivities to this parameter range from approximately $10^{-9}/\mu W$ for 5th overtone AT- or BT-cut resonators to parts in $10^{-11}/\mu W$

for 3rd overtone, SC-cut resonators at 5 MHz. The primary environmental drivers for this effect are temperature, humidity, or radiation changing the excitation level through interaction with the automatic gain control (AGC) and the gain of the sustaining stage. Changes in the dc supply voltage can also affect the amplitude of oscillation by changing the AGC circuitry.

C. Stress (Force)

Stress on the resonator blank changes the resonance frequency through the nonlinear piezoelectric coefficients [11-21, 34, 40-44]. Stress is transmitted to the resonator through the mounting structure. It can originate from temperature-driven dimensional variations in the vacuum enclosure, or changes in the pressure surrounding the vacuum enclosure, changes in the magnetic field causing a change in the mounting force due to the use of magnetic components. The stress on the resonator, due to the use of electrodes directly plated onto the resonator, can change with resonator drive, temperature, radiation exposure, and time. The stress due to the electrode has been estimated [12-13, 20], but the changes with environmental effects such as vibration and temperature cycling are very difficult to estimate. Figure 8 shows the change in frequency of a traditional AT-cut plate due to diametrically opposed forces in the plane of the resonator as a function of the angle between the applied force and the x axis [29]. BVA resonators are probably less sensitive to this effect due to their unique mounting arrangement [20-21].

D. Adsorption-Desorption

Changes in the quantity or distribution of molecules on the surface of the resonator can lead to very large changes in the frequency of the resonator [6, 16, 46-48]. One monolayer added to a 5 MHz resonator amounts to roughly 1 part per million change in the frequency [16]. Major drivers of changes in the background pressure and in the movement of adsorbed gasses are temperature changes and enclosure outgassing or leaks.

The background pressure of helium inside the resonator enclosure can significantly increase if the vacuum enclosure is glass and the resonator is operated in an environment with large amounts of helium. A typical helium leak rate for a glass enclosure operating at $80°C$ in a pure helium environment is $5 \times 10^{-3} Pa/s$. Even in air at $80°C$ the helium builds up at a rate of approximately $2 \times 10^{-8} Pa/s$ or about $0.7 Pa/yr$ [49]. The use of metal enclosures greatly reduces the helium leak rate, but most metals outgas significant amounts of hydrogen and may contribute to the drift of some oscillators [29,49]. A typical sensitivity for an AT-cut resonator to a non-reactive gas is $10^{-7}/Pa$ ($0.7 \times 10^{-10}/Torr$). Ceramic enclosures that reduce the helium and hydrogen leak rates to negligible values have been developed [46]. There also is some question as to what portion of the residual phase noise in quartz resonators is due to time varying rates of collisions with the background gas [48].

E. Acceleration/Vibration

Although a large shock and/or vibration can change the long-term frequency of the resonator, the dominant effect is usually the instantaneous change in the frequency of the resonator due to changes in the stress applied to the resonator through the mounting structure [6,14,16,18-21,52-57]. The frequency change depends on orientation and is linear with applied acceleration or vibration up to approximately 50 g [19]. See Fig. 9. The maximum sensitivity is typically of order $2 \times 10^{-9}/g$. Significant effort has

been expended in minimizing this effect through compensation [52-54], mounting techniques [20- 21,49-50,52], and resonator fabrication techniques [20-21]. The net sensitivity for specially compensated or fabricated oscillators ranges from approximately 10^{-11} to 3×10^{-10} per g. The change in frequency due to inversion "2g tipover test" is often biased due to changes in the temperature gradient as shown in Fig. 10. Although not commonly mentioned, magnetic field sensitivity can also bias the test since the magnetic field effect also is a function of position and motion [58-59].

The phase noise of a resonator subjected to vibration is increased by an amount

$$\mathcal{L}(f) = \frac{1}{4}\left(\frac{\nu^2}{f^2}\right)\Gamma^2 A^2, \tag{5}$$

where Γ is acceleration sensitivity and A is the applied acceleration. Figure 11 shows the quiescent phase noise of a 100 MHz oscillator and that obtained with $\Gamma = 2 \times 10^{-9}/g$ and $A = 2\cos 2\pi ft$. The increase in phase noise over that obtained under quiescent conditions is approximately 70 dB at a Fourier frequency of 10 kHz. Even with $\Gamma = 1 \times 10^{-11}/g$ the degradation would be about 30 dB.

F. Radiation

Radiation interacts with the resonator in many ways. Although not fully characterized for each resonator type and oscillator, it is possible to list some common aspects. A more detailed summary is found in [16].

Pulse Irradiation Results

1. For applications requiring circuits hardened to pulse irradiation, quartz resonators are the least tolerant element in properly designed oscillator circuits.
2. Resonators made of unswept quartz or natural quartz can experience a large increase in series resistance, R_s, following a pulse of radiation; the radiation pulse can even stop the oscillation.
3. Resonators made of properly swept quartz experience a negligible change in R_s when subjected to pulsed ionizing radiation (the oscillator circuit does not require a large reserve of gain margin).

Steady-State Radiation Results

1. At doses <100 rad, frequency change is not well understood. Radiation can induce stress relief. Surface effects such as adsorption, desorption, dissociation, polymerization and charging may be significant. The frequency change is nonlinear with dose.
2. At doses >1 Krad, frequency change is quartz impurity dependent. The ionizing radiation produces electron-hole pairs; the holes are trapped by the impurity Al sites while the compensating cation (e.g. Li or Na) is released. The freed cations are loosely trapped along the optic axis. The lattice near the Al is altered, and the elastic constant is changed; therefore, the frequency shifts. Ge impurities are also troublesome.
3. At 10^6 rad dose, frequency change ranges from 10^{-11} per rad for natural quartz to 10^{-14} per rad for high quality swept quartz.

4. Frequency change is negative for natural quartz; it can be positive or negative for cultured and swept cultured quartz.

5. Frequency change saturates at doses $> 10^6$ rads.

6. The Q degrades if the quartz contains a high concentration of alkali impurities; the Q of resonators made of properly swept cultured quartz is unaffected.

7. Frequency change anneals at $T > 240°C$ in less than 3 hours.

8. Preconditioning (e.g., with doses $> 10^5$ rads) reduces the high dose radiation sensitivities upon subsequent irradiations.

9. High dose radiation can also rotate frequency-vs.-temperature characteristic.

G. Electric Field

The frequency of certain resonator cuts are directly affected by the application of even small electric fields through changes in dimension and effective mass and through interaction with the nonlinear coefficients [58-63]. The application of electric fields also tends to cause ions within the crystal to move which changes the frequency. The net result is that the change in frequency generally has a fast component due to the interaction with the crystal constants and one or more slower components associated with the movement of ions as shown in Fig. 12. The slower time constants depend exponentially on temperature. This electric field effect has been used to vibration compensate SC cut resonators [54] and to create an ultra-linear phase modulator [60]. Sensitivities to this effect are highly cut and material dependent and range from approximately 10^{-11} to 10^{-8} per volt applied across the resonator. Large electric fields and elevated temperatures are sometimes used to "sweep" ions out of the quartz bar prior to fabrication resonators [16,60-63]. This is most often used on resonators for radiation environments.

H. Magnetic Field

The inherent magnetic field sensitivity of quartz resonators is probably smaller than $10^{-11}/T$ [1,64-66]. Most resonators are, however, constructed with magnetic holders. As the magnetic field changes the force on the various components of the resonator. This causes a frequency shift through the force-frequency coefficient discussed above.

IV. Changes Within the Loop Electronics

Many environmental parameters cause change in the phase around the oscillator loop. The most important are temperature, humidity, pressure, acceleration/vibration, magnetic field, voltage, load, and radiation. This environmental sensitivity often leads to increases in the level of wide-band phase noise in the short-term, random-walk frequency modulation in the medium-term, and drift in the long-term. The value of loop phase shift are not universal, but critically depend on the circuit design and the loaded Q-factor of the oscillator.

A. Tuning Capacitor

The frequency of the oscillator is generally fine-tuned using a load capacitor, C_L, of order 20 to 32 pF. In practice this capacitor is often made up of a fixed value (selected at the time of manufacture), a mechanically tuned capacitor for coarse tuning; a varactor for electronic tuning, and a contribution from the input capacitance of the sustaining stage and matching networks. The frequency change for small changes in C_L are

$$\Delta\nu/\nu = \frac{C_1/2}{C_0 + C_L}\frac{dC_L}{C_0 + C_L}, \tag{6}$$

where C_0 is the parallel capacitance and C_1 is the motional capacitance. It is not uncommon for the first term in Eq. 5 to be of order 10^{-3} [16]. In this case a change in C_L of only 10^{-6} results in a frequency change of 10^{-9}. Primary environmental parameters which change C_L are temperature, humidity, pressure, and shock/vibration. Humidity and pressure change the ratio between convection and conduction cooling. See Figs. 10 and 13. Pressure changes in a hermetically sealed oscillator can also be driven by temperature. This changes the temperature gradients and thereby the temperature of the tuning capacitor (and also the temperature of the resonator.) Shock and vibration can change the mechanical capacitor, if present. Changes in the supply voltage, AGC and temperature all change the input capacitance of the sustaining stage and the varactor diode. Humidity can change the value of the dielectric coefficient and losses in the capacitors and even the circuit board. Radiation can change the gain and offsets of the AGC and the sustaining stage and thereby change the effective input capacitance.

B. Mode Selection/Tuned Circuits

Most oscillators use matching circuits and filters to adjust the loop phase to approximately 0π and, especially with SC-cut resonators, to suppress unwanted modes. The phase shift across a transmission filter is given approximately by Eq. 1 with the Q in this case being that of the tuned circuit, Q_c. The fractional change in output frequency due to small changes in either circuit inductance, L_c, or circuit capacitance, C_c, is approximately given by

$$\Delta\nu/\nu \sim \frac{1}{2Q} \sim \frac{Q_c}{Q}\frac{dc}{C_c} + \frac{dL}{L_c}. \tag{7}$$

Far from resonance the change in loop phase with change in filter capacitance or inductance is generally much less than that given by Eq. (1). This suggests that the use of notch filters to suppress unwanted modes is probably superior to the use of narrow-band transmission filters.

The values of most resistors, inductors and capacitors, and even parameters associated with the active junctions, are a function of temperature, humidity, current, or voltage. Significant improvements in the medium-term frequency stability can often be obtained merely by sealing an oscillator to prevent changes in the humidity and pressure [22-23]. Figure 13 shows the frequency change of a high performance oscillator due to a change in relative humidity from approximately 20% to 100% [22-23]. This fractional change of frequency is about 1000 times the normal 1 s frequency stability of 3×10^{-13}.

C. External Load

If the external load of the oscillator changes, there is a change in the amplitude and/or phase of the signal reflected back into the oscillator. The portion of this reflected signal that reaches the oscillating loop changes the phase of the oscillation and hence the output frequency by an amount given by Eq. (1) and reexpressed in Eq. (8). In this case we can estimate the maximum phase change as just the square root of the isolation. For example 40 dB of isolation corresponds to a maximum phase deviation of 10^{-2} radians.

$$\Delta\nu/\nu \sim \frac{1}{2Q} d\phi \sim \frac{q}{2Q}\sqrt{\text{isolation}} \tag{8}$$

For $Q \sim 10^6$ and isolation of 40 dB, the maximum pulling is approximately $\Delta\nu/\nu = 5 \times 10^{-9}$. This is an approximate model for most 5 MHz oscillators. As the frequency increases the problem of load pulling becomes much worse because both the Q-factor and the isolation decrease.

D. Acceleration, Vibration, and Magnetic Fields

Acceleration and vibration can distort the circuit substrate and the position of components leading to changes in the stray inductance and/or capacitance and thereby changes in the frequency. Virtually none of the presently available oscillators have magnetic shielding. The presence of magnetic field complicates matters significantly since changes in orientation within the magnetic field lead to frequency shifts and motion dependent effects. Therefore movement, acceleration, and or vibration certainly leads to induced electric and magnetic fields that disturb the quiescent performance of the oscillator. In most cases such effects are very difficult to separate from other motion induced effects. Acceleration and vibration of circuit elements in the absence of a magnetic field lead to phase/frequency modulation. These effects are difficult to separate from those due to changes of stress applied to the resonator, but are no doubt present and may in some cases prevent accurate measurements on some low-g-sensitive resonators [1,56,57,64-66].

Discussion

The frequency stability of quartz-crystal-controlled oscillators has been refined to the point that small changes in a wide variety of environmental parameters are now significant. The most important environmental parameter is probably acceleration and vibration at frequencies less than approximately 100 Hz. All of the other environmental drivers can be significantly reduced by appropriate attention to circuit design and/or shielding. Among the remaining environmental drivers, temperature is probably the most significant. Most oscillator ovens could be significantly improved using better circuits and better insulation. Magnetic shielding may be necessary to actually realize the full performance of low-g sensitivity resonators. Pressure and humidity effects can be very serious in open oscillators. Fortunately these effects can be eliminated by hermetically sealing the oscillator. The sensitivity to low doses of radiation is not well understood. More work needs to be done to refine the characterization of sensitivity to various environmental parameters.

Acknowledgements

I am particularly grateful to A. Ballato, R. Besson, R. Filler, J. J. Gagnepain, and J. Vig for many discussions of systematic effects in quartz crystal-controlled oscillators.

References

[1]† J. J. Gagnepain "Characterization Methods for the Sensitivity of Quartz Oscillators to the Environment", Proc. of 43rd Annual Symposium on Frequency Control, 1989, pp. 242–247.

[2] D. B. Leeson, "A Simple Model of Feedback Oscillator Noise Spectrum", Proc. of the IEEE, 54, 329–330 (1966).

[3]† T. E. Parker, "Characteristics and Sources of Phase Noise in Stable Oscillators", Proc. of the 41st Annual Symposium on Frequency Control, 1987, pp. 99–110.

[4]† G. S. Curtis, "The Relationship Between Resonator and Oscillator Noise, and Resonator Noise Measurement Techniques", Proc. of the 41st Annual Symposium on Frequency Control, 1987, pp. 420–428.

[5] B. Parzen, Design of Crystal and Other Harmonic Oscillators, John Wiley & Sons, New York, 1983.

[6] Precision Frequency Control (Ed. by E. A. Gerber and A. Ballato, Academic Press, New York, 1985).

[7]* A. Ballato, J. Vig., "Static and Dynamic Frequency-Temperature Behavior of Singly and Doubly Rotated, Oven-Controlled Quartz Resonators", Proc. 32nd Annual Symposium on Frequency Control, 1978, pp. 180–188.

[8] R. Holland, "Non Uniformly Heated Anisotropic Plates : I Mechanical Distortions and Relaxation", IEEE Trans. Sonics and Ultrasonics, SU-21, 1974.

[9] R. Holand, "Non Uniformly Heated Anisotropic Plates : II Frequency Transients in AT and BT Quartz Plates", Ultrasonics Symp. Proc. IEEE Cat. # 74 CHO 896-ISU 1974.

[10]* G. Théobald, G. Marianneau, R. Prétot and J. J. Gagnepain, "Dynamic Thermal Behavior of Quartz Resonators", Proc. 33rd Annual Symposium on Frequency Control, 1979, pp.239–246.

[11] J. Kusters, "Transient Thermal Compensation for Quartz Resonators", IEEE Trans. Sonics and Ultrasonics, SU-23, 273–276 (1976).

[12] J. A. Kusters, J. G. Leach, "Further Experimental Data on Stress and Thermal Gradient Compensated Crystals", Proc. IEEE, 282–284 (1977).

[13]* E. P. EerNisse, "Quartz Resonator Frequency Shifts Arising from Electrode Stress", 29th Proc. of Annual Symposium on Frequency Control, pp. 1–4, (1975).

[14] A. Ballato, "Static and Dynamic Behavior of Quartz Resonators", IEEE Trans. Sonics and Ultrasonics, SU-26, 299 (1979).

[15]* B. K. Sinha, H. F. Tiersten, "Transient Thermally Induced Frequency Excursions in Doubly-Rotated Quartz Thickness Mode Resonators", Proc. of 34th Annual Symposium on Frequency Control, 1980, pp. 393–402.

[16] J. R. Vig, "Quartz Crystal Resonators and Oscillators for Frequency Control and Timing Applications, A Tutorial", June 1990.

[17]* J. P. Valentin, G. Théobald, and J. J. Gagnepain, "Frequency Shifts Arising from In-Plane Temperature Gradient Distribution in Quartz Resonators", Proc. of 38th Annual Symposium on Frequency Control 1984, pp. 157–163.

[18] J. J. Gagnepain, R. Besson, "Nonlinear Effects in Piezoelectric Quartz Crystal", Physical Acoustics, W.P. Mason Ed. Vol XI, 245–288, Academic Press 1975.

[19]* J. J. Gagnepain "Nonlinear Properties of Quartz Crystal and Quartz Resonators: A Review", Proc. of 35th Annual Symposium on Frequency Control, 1981, pp. 14–30.

[20]* R. Besson, "A New Piezoelectric Resonator Design", Proc. 30th Annual Symposium on Frequency Control, 1976, pp.78–83.

[21]* R. Besson and U. R. Peier "Further Advances on B.V.A. Quartz Resonators", Proc. 34th Annual Symposium on Frequency Control, 1980, pp.175–182.

[22]* F. L. Walls, "The Influence of Pressure and Humidity on the Medium and Long-Term Frequency Stability of Quartz Oscillators", Proc. of the 42nd Annual Symposium on Frequency Control, 1988, pp. 279–283.

[23] F. L. Walls, "Environmental Effects on the Medium and Long Term Frequency Stability of Quartz Oscillators", Proc. of the 2nd European Frequency and Time Forum, Neuchatel, Switzerland, March, 1989, pp. 719–727.

[24]* J. P. Valentin, G. Théobald, and J. J. Gagnepain "Frequency Shifts Arising From In-Plane Temperature Gradient Distribution in Quartz Resonators", Proc. 38th Annual Symposium on Frequency Control, 1984, pp. 157–163.

[25]† M. B. Bloch, J. C. Ho, C. S. Stone, A. Syed, and F. L. Walls, "Stability of High Quality Quartz Crystal Oscillators: An Update", Proc. of 43rd Annual Symposium on Frequency Control, 1989, pp. 80–84.

[26]* G. Marianneau and J. J. Gagnepain, "Digital Temperature Control for Ultrastable Quartz Oscillators", Proc. of 34th Annual Symposium on Frequency Control, 1980, pp.52–57.

[27] J. F. Schooley Thermometry, CRC Press, Inc. Boca Raton, Florida, 1986.

[28]† F. L. Walls, "Analysis of High Performance Compensated Thermal Enclosures", Proc. of 41st Annual Symposium on Frequency Control, 1988, 439–443.

[29] F. L. Walls and J.J. Gagnepain, "Special Applications, Precision Frequency Control", Chapter 15 in Precision Frequency Control, (Ed. by E. A. Gerber and A. Ballato, Academic Press, New York, 1985) pp. 287–296.

[30]* A. F. B. Wood and A. See, "Activity Dips in AT-Cut Crystals", Proc. 21st Annual Symposium on Frequency Control, 1967, pp. 420–435.

[31]* C. Franx, "On Activity Dips of AT Crystals at High Levels of Drive", Proc. of 22nd Annual Symposium on Frequency Control, 1967, pp. 436–454.

[32]* J. Birch, D. A. Weston, "Frequency/Temperature, Activity/Temperature Anomalies in High Frequency Quartz Crystal Units", Proc. of 30th Annual Symposium on Frequency Control, 1978, pp. 32–39.

[33] J. E. Deeter and H. Inoue, "Temperature Dependence of the Ginga Clock Rate", ISAS Research Note 430, January 1990.

[34] J. A. Kusters, "The SC-Cut Crystal — An Overview", Proc. IEEE Ultrasonics Symposium, 1981, pp. 402–409.

[35]* A. W. Warner, Jr. and B. Goldfrank, "Lateral Field Resonators", Proc. 39th Annual Symposium on Frequency Control, 1985, pp. 473–474.

[36]* A. W. Warner, "Measurement of Plano-Convex SC Quartz Blanks Using Lateral Field Excitation", Proc. 42nd Annual Symposium on Frequency Control, 1988, pp. 202–204.

[37]* J. J. Gagnepain, J. C. Poncot, C. Pégeot, "Amplitude-Frequency Behavior of Doubly Rotated Quartz Resonators", Proc. of 31st Annual Symposium on Frequency Control, 1977, pp. 17–22.

[38]* R. L. Filler, "The Amplitude-Frequency Effect in SC-Cut Resonators", Proc. 39th Annual Symposium on Frequency Control, 1985, pp. 311–316.

[39] R. J. Besson, J. M. Groslambert, and F. L. Walls, "Quartz Crystal Resonators and Oscillators, Recent Developments and Future Trends", Ferroelectrics 43, 57–65 (1982).

[40] J. M. Ratajski, "Force-Frequency Coefficient of Singly-Rotated Vibrating Quartz Crystals", IBM J. Res. Dev. 12, 92 (1968).

[41]* C. R. Dauwalter, "The Temperature Dependence of the Force Sensitivity of AT-Cut Quartz Crystals", Proc. of 26th Annual Symposium on Frequency Control, 1972, pp. 108–112.

[42]* A. Ballato, E. P. Eernisse, T. Lukaszek, "The Force-Frequency Effect in Doubly Rotated-Quartz Resonators", Proc. of 31st Annual Symposium on Frequency Control, 1977, pp. 8–16.

[43] A. Ballato, "Force-Frequency Compensation Applied to Four-Point Mounting of AT-Cut Resonators", IEEE Trans. Sonics and Ultrasonics, SU-25, 233 (1978).

[44]* E. P. EerNisse, "Temperature Dependence of the Force Frequency Effect for the Rotated X-Cut", Proc. of 33rd Annual Symposium on Frequency Control, 1979, pp. 300–305.

[45]* J. J. Gagnepain, M. Olivier, and F. L. Walls, "Excess Noise in Quartz Crystal Resonators", Proc. of 37th Annual Symposium on Frequency Control, 1983, pp. 218–225.

[46] R. L. Filler, L. J. Keres, T. M. Snowden, and J. R. Vig, "Ceramic Flatpack Enclosed AT and SC-Cut Resonators", Proc. IEEE Ultrasonics Symposium, 1980.

[47] J. R. Vig, "UV/Ozone Cleaning of Surfaces", J. Vac. Sci. Technol. A 3, 1027–1034, 1985.

[48]* Y. K. Yong and J. R. Vig, "Resonator Surface Contamination — A Cause of Frequency Fluctuations", Proc. of the 42nd Annual Symposium on Frequency Control, 1988, pp. 397–403.

[49] W. G. Perkins, "Permeation and Outgassing of Vacuum Materials", J. Vac. Sci. Technol., 10, 543–556 (1973).

[50]* A. Ballato, "Resonators Compensated for Acceleration Fields", Proc. of 33rd Annual Symposium on Frequency Control, 1979, pp. 322–336.

[51] R. L. Filler, "The Effect of Vibration on Quartz Crystal Resonators", R&D Technical Report DELET-TR-80-10, US Army Electronics Research and Development Command, Fort Monmouth, NJ 07703.

[52] F. L. Walls and R. Vig, "Acceleration Insensitive Oscillator", United States Patent - No. 4,575,690, 1986.

[53]* J. M. Pryjemski "Improvement in System Performance Using a Crystal Oscillator Compensated for Acceleration Sensitivity", Proc. of 32nd Annual Symposium on Frequency Control, 1978, pp. 426–430.

[54]* V. J. Rosati and R. L. Filler, "Reduction in the Effects of Vibration on SC-Cut Quartz Oscillators", Proc. of 35th Annual Symposium on Frequency Control, 1981, pp. 117–121.

[55]† Y. S. Zhou and H. F. Tiersten, "On the Influence of a Fabrication Imperfection on the Normal Acceleration Sensitivity of Contoured Quartz Resonators with Rectangular Supports," Proc. of 44th Annual Symposium on Frequency Control, 1990, pp. 452–453. See also H. F. Tiersten and Y. S. Zhou, "An Analysis of the In-Plane Acceleration Sensitivity of Contoured Quartz Resonators with Rectangular Supports", same proceedings, pp. 461–467.

[56] J. R. Vig, M. Driscal, E. P. EerNisse, R. L. Filler, M. Garvey, W. Riley, R. Smythe, and R. D. Weglein, "Acceleration Effects", Labcom Tech Report, 1991, available from U.S. Army, Electronics Technology and Devices Laboratory, Labcom, Fort Monmouth, NJ 07703.

[57]† M. H. Watts, E. P. EerNisse, R. W. Ward, and R. B. Wiggins, "Technique for Measuring the Acceleration Sensitivity of SC-Cut Quartz Resonators", Proc. of 42nd Annual Symposium on Frequency Control, 1988, pp. 442–446.

[58] C. K. Hruska and M. Kucera, "The Dependence of the Polarizing Effect on the Frequency of Quartz Resonators", Journal of the Canadian Ceramic Society, 55, 39–41 (1986).

[59]† R. Brendel, J. J.Gagnepain, J. P. Aubry, "Impurity Migration Study in Quartz Crystal Resonators by Using Electroelastic Effect", Proc. of 40th Annual Symposium on Frequency Control, 1986, pp. 121–126.

[60] J. Lowe and F. L. Walls, "Ultralinear Small Angle Phase Modulator", to be published in Proc. 5th Annual European Forum on Time and Frequency, 1991.

[61]* R. Brendel, and J. J. Gagnepain, "Electroelastic Effects and Impurity Relaxation in Quartz Resonators", Proc. 36th Annual Symposium on Frequency Control, 1982, pp.97–107.

[62] J. J. Martin, "Electrodiffusion (Sweeping) of Ions in Quartz", IEEE Transactions on Ultrasonics, Ferroelectrics, and Frequency Control, 35, 288–296 (1988); J. G. Gualtieri.

[63] "Sweeping Quartz Crystals", Proc. of 1989 IEEE Ultrasonics Symposium, 1989, pp. 381–391.

[64]† R. Brendel, C. El Hassani, M. Brunet, and E. Robert, "Influence of Magnetic Field on Quartz Crystal Oscillators", Proc. of 43rd Annual Symposium on Frequency Control, 1989, pp. 268–274.

[65] F. Deyzac, "Magnetic Sensitivity of Quartz Oscillators", Proc. 4th Annual European Forum on Time and Frequency, March 1990, 255–258.

[66]* A. Ballato, T. J. Lukaszek, and G. J. Iafrate, "Subtle Effects in High Stability Vibrators", Proc. 34th Annual Symposium on Frequency Control, 1980, pp.431–444

* Copies available from National Technical Information Service, Sills Bldg., 5285 Port Royal Road, Springfield, VA 22116.

† Copies available from Institute of Electrical & Electronics Engineers, 445 Hoes Lane, Piscataway, NJ 08854.

Table 1. Typical frequency versus temperature coefficients for an AT-cut resonator with a turnover temperature of $85°C$ as a function of oven parameters. Frequency stability of 1×10^{-13} requires $\Delta T/dt < 10nK/s$.

$$\Delta\nu/\nu \simeq 3 \times 10^{-8}\Delta T^2 + 10^{-5}\, dT/dt$$

Oven Offset	Oven Change			
mK	±100 mK	±10 mK	± 1 mK	± 0.1 mK
0	3×10^{-10}	3×10^{-12}	3×10^{-14}	3×10^{-15}
1	3×10^{-10}	5×10^{-12}	2×10^{-13}	6×10^{-15}
10	5×10^{-10}	2×10^{-11}	6×10^{-13}	6×10^{-14}
100	2×10^{-9}	6×10^{-11}	6×10^{-12}	6×10^{-13}

Table 2. Typical frequency versus temperature coefficients for a SC-cut resonator with a turnover temperature of $85°C$ as a function of oven parameters. Frequency stability 1×10^{-13} requires $\Delta T/dt < 330nK/s$.

$$\Delta\nu/\nu = 4 \times 10^{-9}T^2 + 3 \times 10^{-7}dT/dt$$

Oven Offset	Oven Change			
mK	±100 mK	±10 mK	±1 mK	±0.1 mK
0	4×10^{-11}	4×10^{-13}	2×10^{-15}	4×10^{-17}
1	4×10^{-11}	6×10^{-13}	2×10^{-14}	8×10^{-16}
10	6×10^{-11}	2×10^{-12}	8×10^{-14}	8×10^{-15}
100	2×10^{-10}	8×10^{-12}	8×10^{-13}	8×10^{-14}

Table 1. Typical frequency versus temperature coefficients for an AT-cut resonator with a turnover temperature of 85°C as a function of oven parameters. Frequency stability of 1×10^{-13} requires $\Delta T/dt < 10$ nK/s.

$$\Delta\nu/\nu \simeq 3 \times 10^{-8}\Delta T^2 + 10^{-5}\, dT/dt$$

Oven Offset	Oven Change			
mK	±100 +mK	± 10 mK	± 1 mK	± 0.1 mK
0	3×10^{-10}	3×10^{-12}	3×10^{-14}	3×10^{-15}
1	3×10^{-10}	5×10^{-12}	2×10^{-13}	6×10^{-15}
10	5×10^{-10}	2×10^{-11}	6×10^{-13}	6×10^{-14}
100	2×10^{-9}	6×10^{-11}	6×10^{-12}	6×10^{-13}

Table 2. Typical frequency versus temperature coefficients for a SC-cut resonator with a turnover temperature of 85°C as a function of oven parameters. Frequency stability 1×10^{-13} requires $\Delta T/dt < 330$ nK/s.

$$\Delta\nu/\nu \simeq 4 \times 10^{-9}\Delta T^2 + 3 \times 10^{-7}\, dT/dt$$

Oven Offset	Oven Change			
mK	±100 mK	± 10 mK	± 1 mK	± 0.1 mK
0	4×10^{-11}	4×10^{-13}	2×10^{-15}	4×10^{-17}
1	4×10^{-11}	6×10^{-13}	2×10^{-14}	8×10^{-16}
10	6×10^{-11}	2×10^{-12}	8×10^{-14}	8×10^{-15}
100	2×10^{-10}	8×10^{-12}	8×10^{-13}	8×10^{-14}

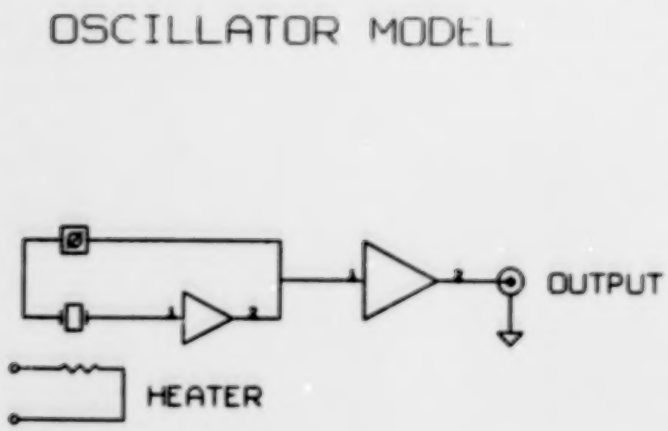


Fig. 1 Simplified block diagram of a quartz-crystal-controlled-oscillator. Loop gain = 1 and loop phase = n2π n = 0,1,2....

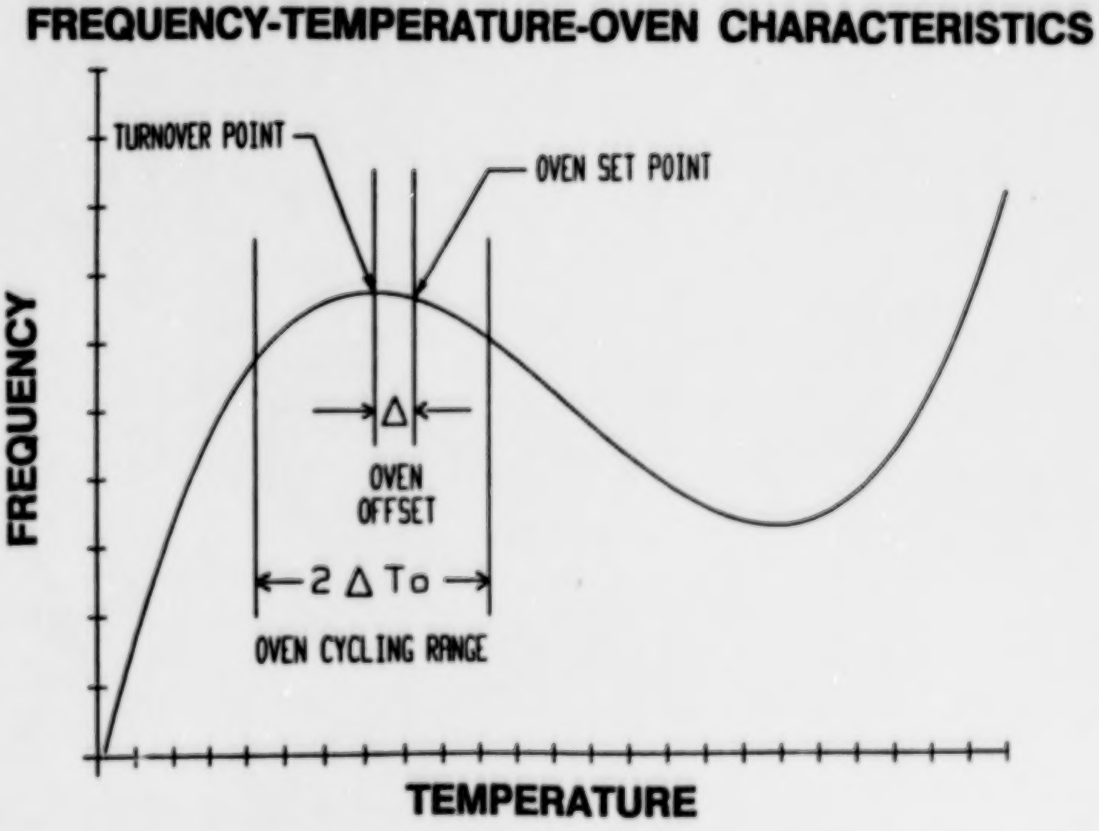


Fig 2. Idealized frequency versus temperature curve for a quartz resonator. The turnover point and the oven offset from turnover are indicated. From [16].

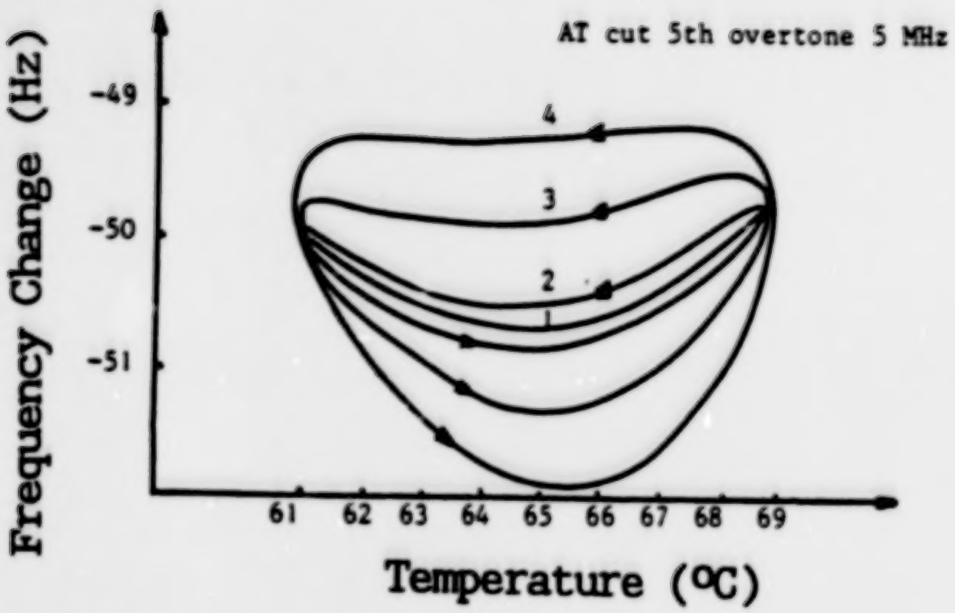


Fig. 3. Frequency versus temperature for a 5 MHz AT-cut resonator. The static temperature curve is shown in curve 1. The other curves show the response with ±4°C sinusoidal temperature cycling at a sweep frequency of 9.2×10^{-5} Hz-curve 2, 3.7×10^{-4} Hz-curve 3, and 7.4×10^{-4} Hz- curve 4. A model fit to the curves yields a dynamic temperature coefficient of -1.3×10^{-5} s/°C. From [10].

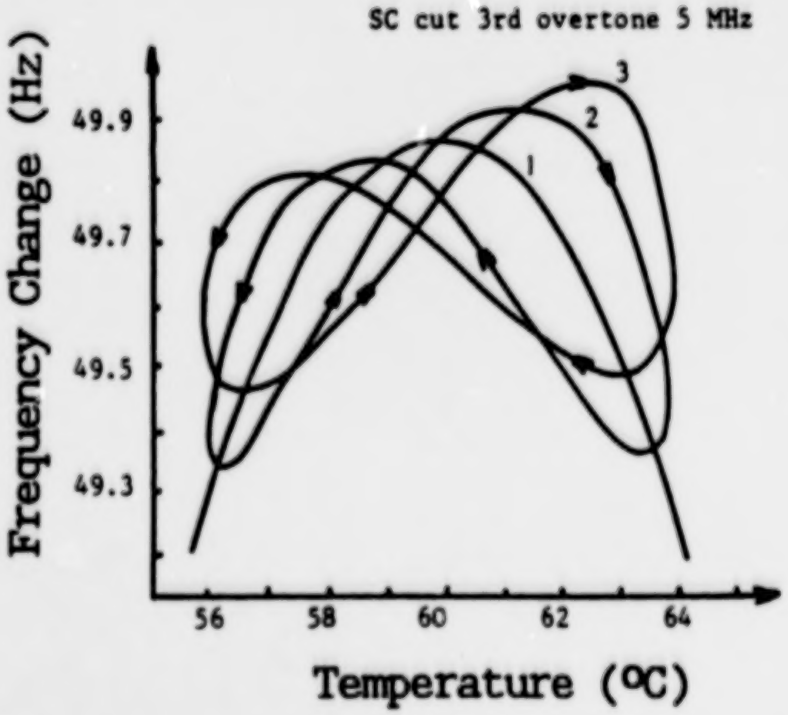


Fig. 4. Frequency versus temperature for a 5 MHz SC-cut resonator. The static temperature curve is shown in curve 1. The other curves show the response with ± 4°C sinusoidal temperature cycling at a sweep frequency of 9.1×10^{-4} Hz-curve 2, and 1.8×10^{-3} Hz-curve 3. A model fit to the curves yields a dynamic temperature coefficient of 3×10^{-7} s/°C. From [10].

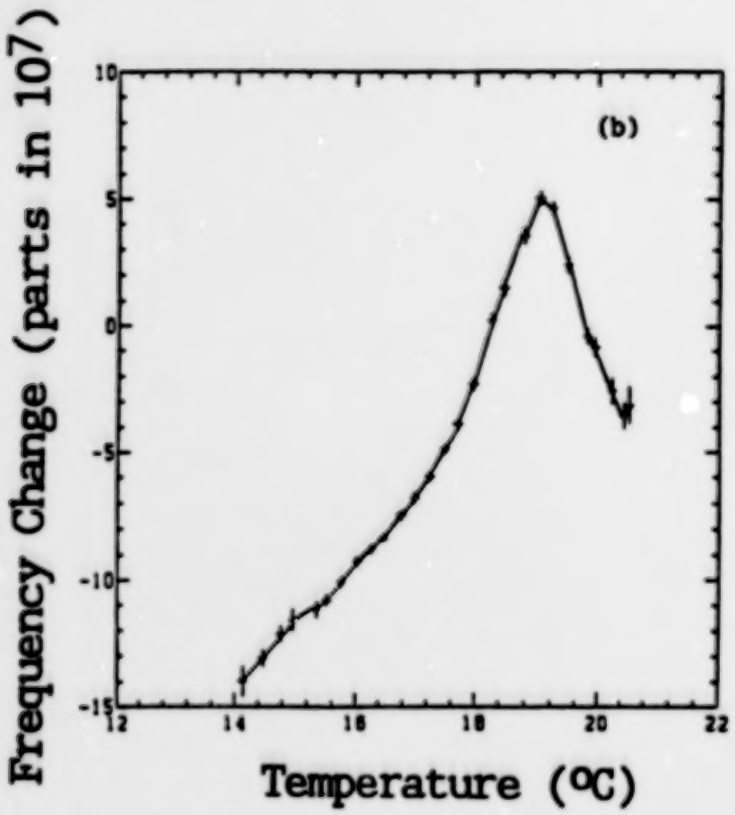


Fig. 5. Frequency versus temperature for the primary timing clock of the Ginga satellite. From [33].

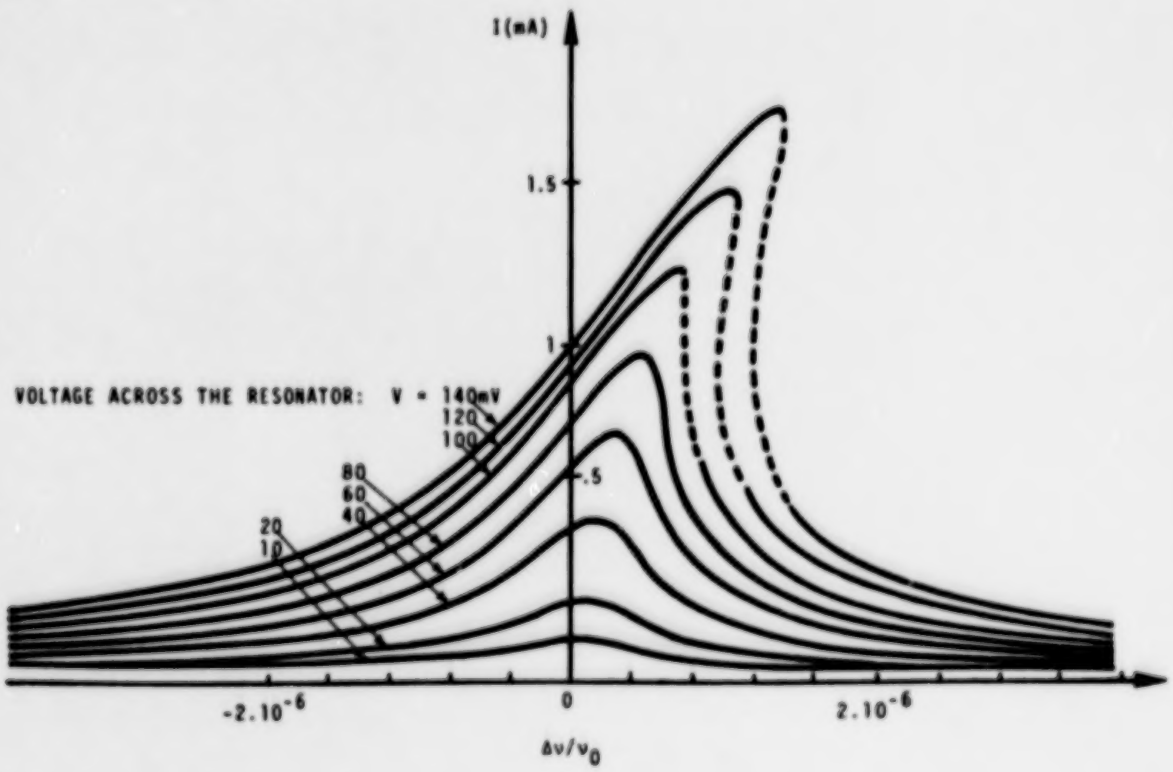


Fig. 6. Frequency versus the rf excitation level for a 5 MHz AT-cut resonator. From [19].

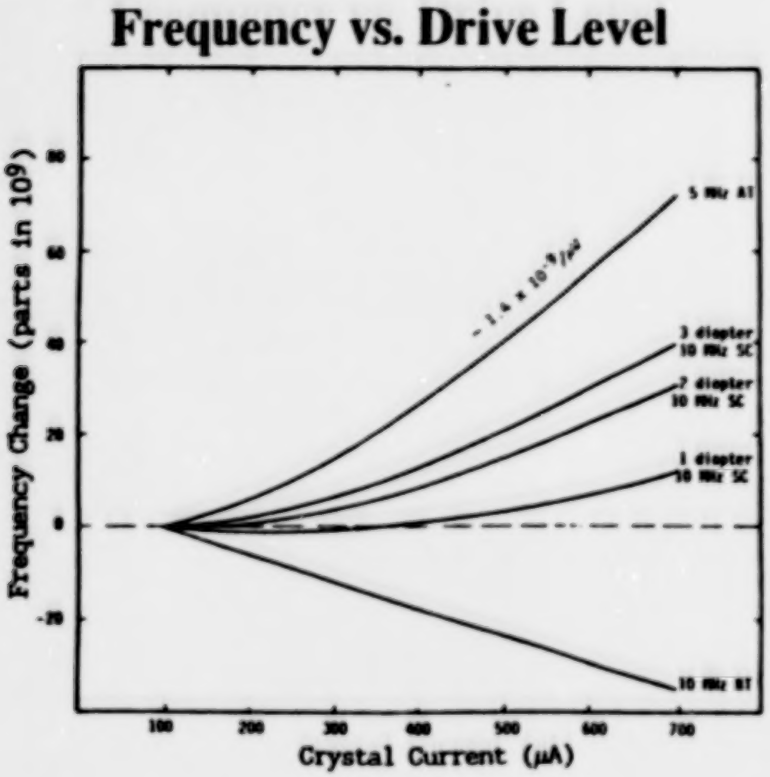


Fig. 7. Frequency versus the rf excitation level for AT-, BT-, and several SC-cut resonators. The approximate power levels are indicated on the left margin. From [16, 33].

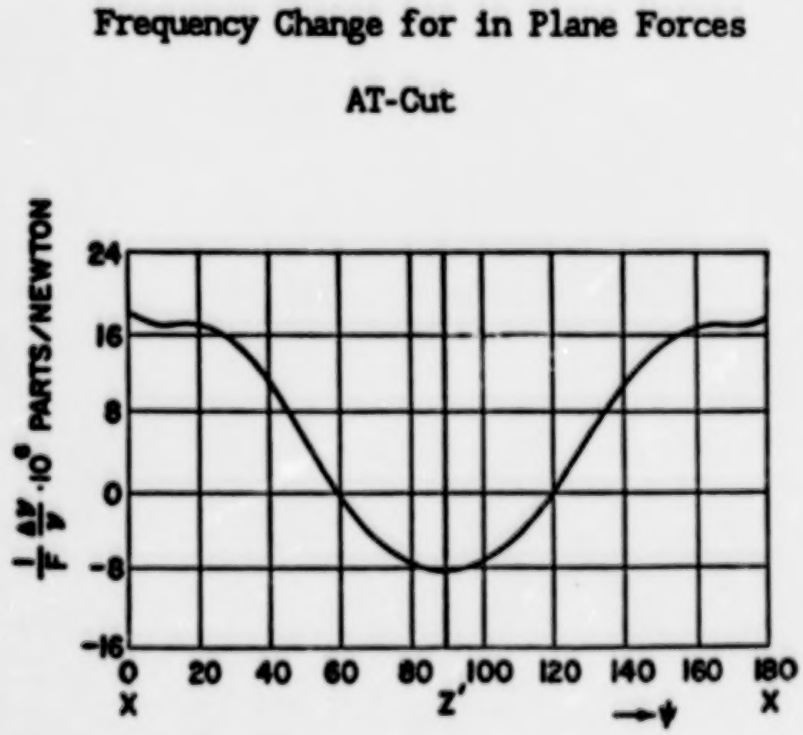


Fig. 8. Frequency shift versus diametrically opposed forces in the plane of the resonator as a function of the angle between the force and the azimuthal axis. From [28].

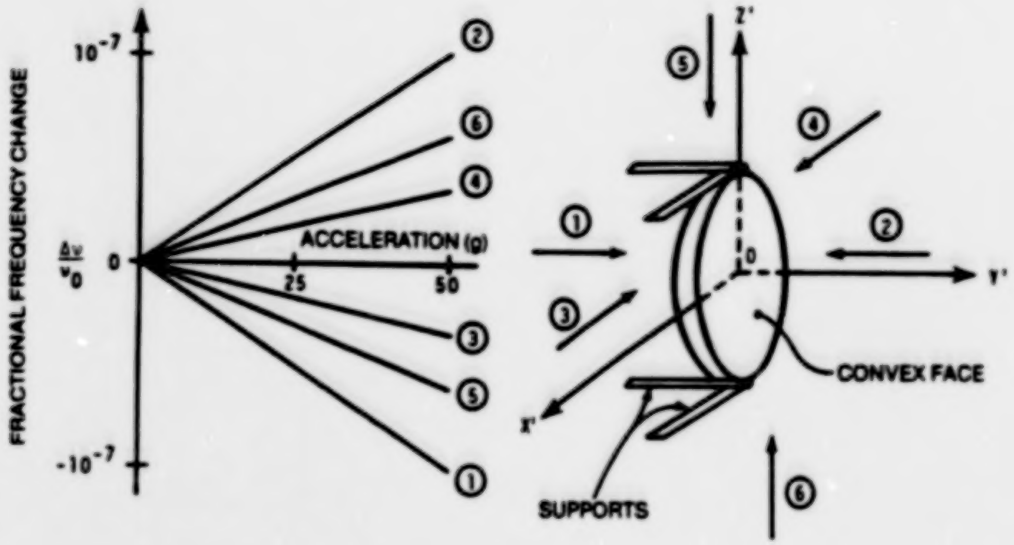


Fig. 9. Typical sensitivity of a AT-cut resonator to acceleration as a function of direction. From [19].

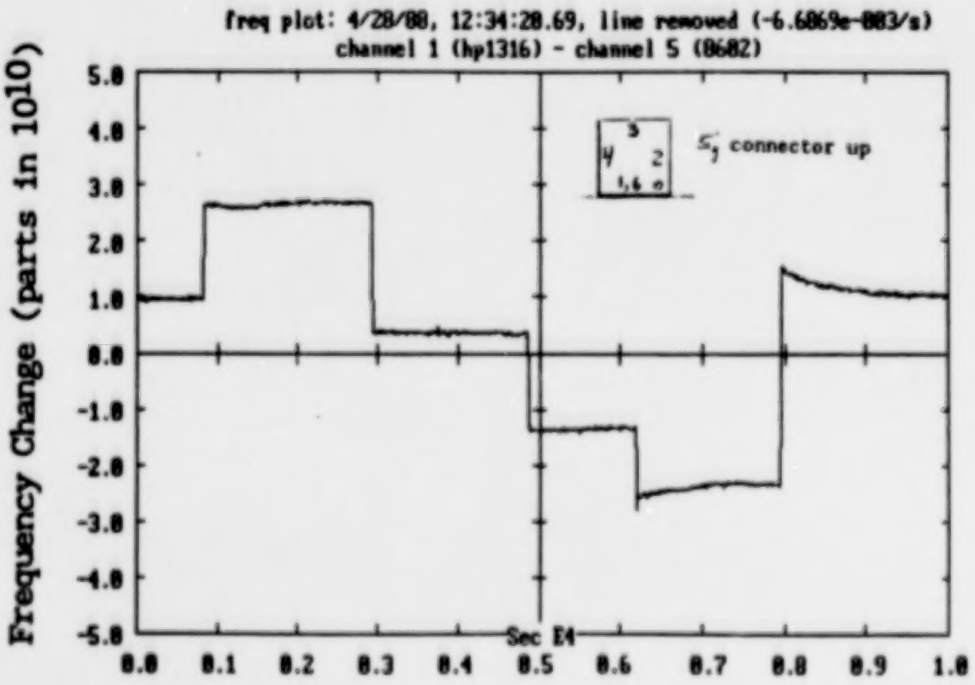


Fig. 10. Frequency of a precision oscillator as a function of orientation. Position 1 and 6 are the same. Note the slow change of frequency immediately after the rotation. This is likely due to small changes in the temperature gradient within the oscillator. From [23].

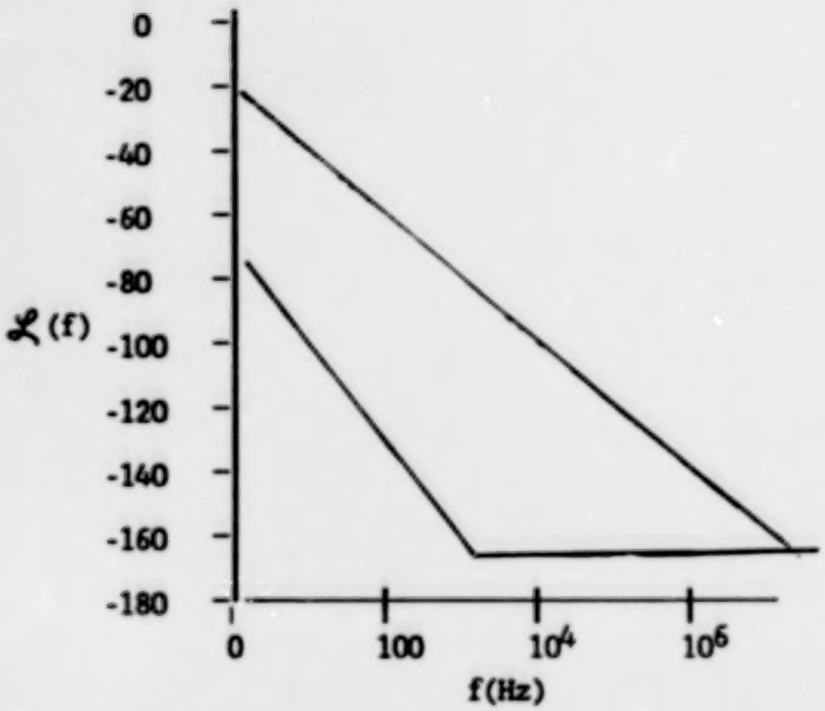


Fig. 11. Quiescent phase noise of a high quality 100 MHz oscillator and the induced phase noise from the application of sinusoidal acceleration at amplitude 2 g. An acceleration sensitivity of $2 \times 10^{-9}/g$ has been assumed.

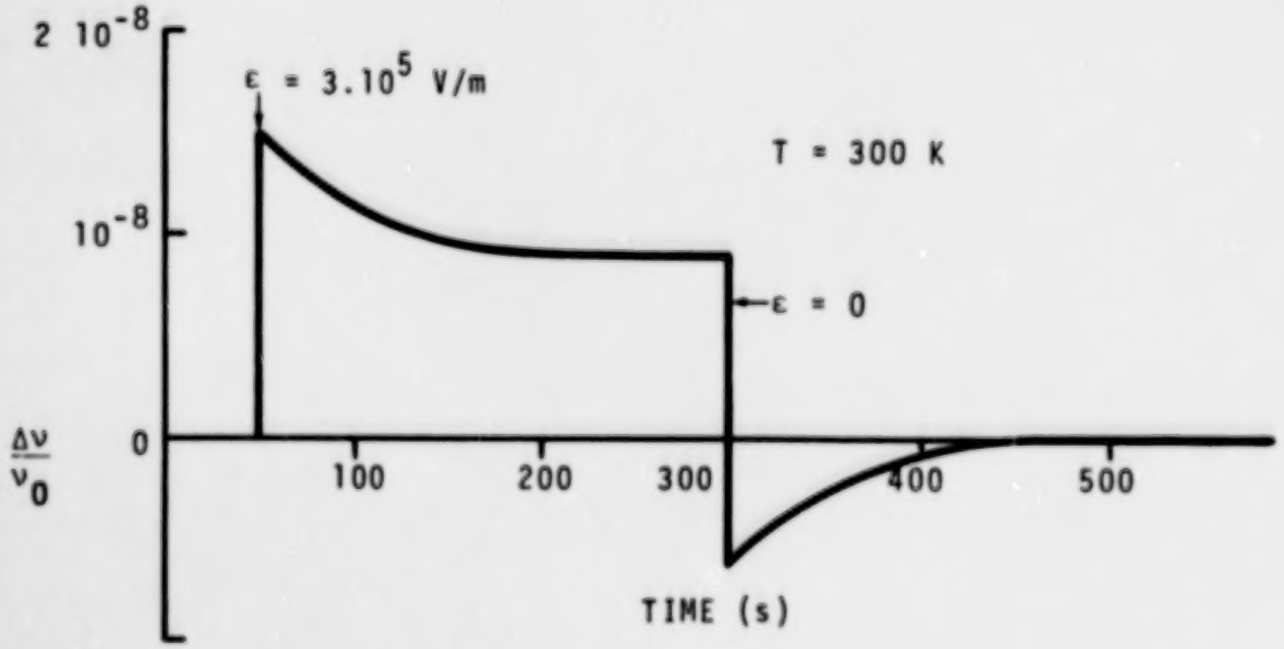


Fig. 12. Frequency of a function of applied voltage. The slow variation after the change in voltage is due to the movement of ions within the resonator. From Gagnepain [1].

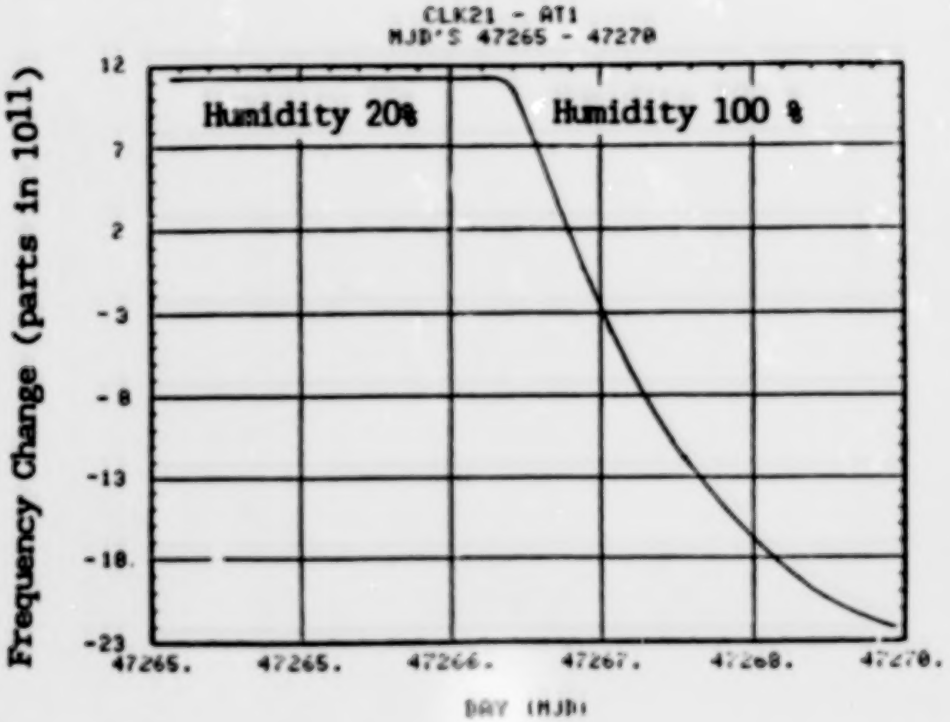


Fig. 13 Frequency change of quartz controlled oscillator due to a change in humidity. Fractional stability is approximately 2×10^{-13} at 1 s. From [22].

LOCAL OSCILLATOR INDUCED DEGRADATION OF MEDIUM–TERM STABILITY IN PASSIVE ATOMIC FREQUENCY STANDARDS*

G. J. Dick, J. D. Prestage, C. A. Greenhall, and L. Maleki

California Institute of Technology
Jet Propulsion Laboratory
4800 Oak Grove Drive
Pasadena, California 91109

Abstract

As the performance of passive atomic frequency standards improves, a new limitation is encountered due to frequency fluctuations in an ancillary local oscillator (L.O.). The effect is due to time variation in the gain of the feedback which compensates L.O. frequency fluctuations. The high performance promised by new microwave and optical trapped ion standards may be severely compromised by this effect.

We present an analysis of this performance limitation for the case of sequentially interrogated standards. The time dependence of the sensitivity of the interrogation process to L.O. frequency fluctuations is evaluated for single–pulse and double–pulse "Ramsey" RF interrogation and also for amplitude modulated pulses. The effect of these various time dependencies on performance of the standard is calculated for an L.O. with frequency fluctuations showing a typical $1/f$ spectral density. A limiting $1/\sqrt{\tau}$ dependent deviation of frequency fluctuations is calculated as a function of pulse lengths, dead time, and pulse overlap.

We also present conceptual and hardware–oriented solutions to this problem which achieve a much more nearly constant sensitivity to L.O. fluctuations. Solutions involve: use of double–pulse interrogation; alternate interrogation of multiple traps so that the "dead time" of one trap can be covered by operation of the other; and the use of double–pulse interrogation for two traps, so that during the time of the RF pulses, the increasing sensitivity of one trap tends to compensate for the decreasing sensitivity of the other. A solution making use of amplitude–modulated pulses is also presented which shows nominally zero time variation.

INTRODUCTION

As the performance of passive atomic frequency standards improves, a new limitation is encountered due to frequency fluctuations in the local oscillator (L.O.) from which RF interrogation signals are derived[1–3]. This limitation continues to the longest times, giving frequency deviations which show the same $1/\sqrt{\tau}$ dependence on measuring time τ as the inherent performance of the standard itself. It is due to periodic time variation of the gain in the feedback which keeps the L.O. frequency locked

*This work was carried out at the Jet Propulsion Laboratory, California Institute of Technology, under a contract with the National Aeronautics and Space Administration.

to the atomic line. The varying gain aliases higher frequency L.O. fluctuations to frequencies near zero frequency, and these low frequency detected signals are improperly compensated by the feedback process.

Practical atomic interrogation processes show a sensitivity to L.O. frequency which is not constant with time. This arises because e.g. the high and low frequency sides of the atomic absorption line are alternately interrogated to compensate for signal strength variability. Furthermore, a "dead time" with consequent zero sensitivity is characteristic of newly developed standards using sequential interrogation. These include both microwave and optical frequency versions of the trapped–ion standard. The higher performance promised by these new standards is severely compromised by presently available L.O. capability.

In the following sections we examine the time dependence of the sensitivity to L.O. frequency which is inherent in single– and double–pulse (Ramsey) sequential RF interrogation processes. Details of the electromagnetic transition are calculated using a conventional spin–flip analogue. This treatment allows the effect of time–varying phase or amplitude of the exciting RF signal to be calculated by means of appropriate solid–body rotations of an initial state vector.

We propose the use of several alternately–interrogated collections of atoms or ions (several "traps") to allow a net sensitivity which is much more nearly constant in time. Detailed strategies are developed, including one which uses amplitude modulated RF pulses with a particular form which can give a net sensitivity for the two traps which shows nominally zero time variation.

The effect of any given time varying sensitivity on performance of the atomic standard depends on the spectrum of frequency fluctuations for the L.O. We present the results of numerical and analytical calculations for the effect of an L.O. with flicker frequency noise and consequent flat Allan deviation as a function of measuring time τ.

Finally, block diagrams are shown for implementations of a trapped mercury ion frequency standard with two ion collections, including one with two ion collections in a single linear trapping structure. Various systematics are addressed, including sensitivities to signal strengths and RF phase shift values.

BACKGROUND

Passive atomic and ionic frequency standards presently provide greater long–term stability than any other frequency sources. They include the new Trapped Mercury Ion standards[4–6], more conventional Rubidium[7] and Cesium standards[8,9], and the optical standards[10] which are proposed for even higher stability. These standards have an inherent advantage for long term stability which derives from the energy gain which is available from atomic transitions which can be linked in a causal way. Thus, a low energy microwave photon may be absorbed in an ultra–stable atomic transition process that then makes possible the scattering of optical photons with energy increased by more than 10^4. This makes possible a tremendous increase in sensitivity and allows passive standards to operate with very small numbers of atoms or ions. By the use of electromagnetic traps, these few atoms or ions can be isolated from each other and from their environment much more effectively than can the many atoms or ions required by active standards. This isolation reduces the effects of time–varying external variables on the operating frequency, and allows the frequency of the standard to more closely approximate the inherent unvarying atomic transition frequency of a single isolated atom or ion.

However, by the nature of this process, passive frequency sources do not themselves emit a signal at

their operational frequency as do active sources. Instead, they require a secondary frequency source to interrogate the very narrow absorption line in the isolated atoms or ions. This interrogation process necessarily takes a certain amount of time, during which time the secondary local oscillator (L.O.) acts alone to provide frequency stability. Information obtained in the interrogation processes is then used to adjust the frequency of the L.O. by feedback and to stabilize it over long periods of time with great precision.

The consequence of this is most easily understood with respect to a portion of the interrogation cycle called "dead time". During this time the local oscillator's frequency is not sensed by the atomic interrogation process and so local oscillator frequency fluctuations during those times are not corrected by the feedback process. The cumulative effect of oscillator phase wander during the dead time for each cycle reduces the long term stability obtainable with the atomic standard. If the dead time could be reduced to zero, the long term instability induced by the L.O. could also be reduced.

The dead time cannot be eliminated, however, because interrogation of the atoms or ions necessarily involves processes which degrade the Q and shift the frequency of the atomic line. The strategy which allows the highest ultimate stability is to perform these processes during dead times to minimize their interference with operation of the standard. The processes include; illumination with an intense optical beam which prepares the quantum state of the atoms or ions and which induces light scattering, the intensity of which is analyzed to determine frequency errors in the local oscillator and to correct them; adding more ions to the trap to make up for those that have been lost; and other similar processes such as vibrating the ion cloud to measure the number of ions in order to hold the number very nearly constant in time.

TIME DEPENDENCE OF FREQUENCY SENSITIVITY

Definition of a Time–Dependent Frequency Sensitivity

The lineshape, bandwidth, and resolving power for an atomic transition induced by means of electromagnetic (RF) pulses are well known[11]. Of importance to frequency standard applications is the frequency resolving power which can be written in terms of a dimensionless frequency sensitivity parameter g as

$$\frac{dp}{d\nu} = \pi g t_i, \tag{1}$$

where p is the probability for the transition, t_i is the time for the RF interrogation process, and ν is the applied RF frequency. For the case of single π–pulse interrogation and for atoms initially in the ground state, the conventional lineshape[11] gives $p = 1$ at the resonant frequency, and a resolving power described by

$$g_\pi \approx 0.60386 \tag{2}$$

at the half–bandwidth points ($p = 0.5$). Double pulse (Ramsey) interrogation using two $\pi/2$–pulses shows a narrower bandwidth and increased resolving power compared to single pulse excitation[12]. In the limit of very short excitation pulses at the beginning and end of the interrogation period, the frequency sensitivity approaches a limit of

$$g_{max} = 1. \tag{3}$$

The conventional treatment, however, does not allow a study of the effect of a frequency which varies during the excitation process. In order to accomplish this task, we generalize the frequency sensitivity

g to allow time variation during the interrogation process. If the phase fluctuations involved in the frequency variation are small ($\delta\phi << 1$), we can assume that fluctuations at all points in the process combine linearly. For this case we can generalize Eq. 1 to describe the variation in transition probability δp due a time–varying frequency error $\delta\nu(t)$ in terms of an integral over the RF interrogation time

$$\delta p = \pi \int_{RF} \delta\nu(t)\, g(t)\, dt. \tag{4}$$

Application of a non–varying $\delta\nu$ to Eq. 4 recovers Eq. 1 by relating the constant g to an integral over $g(t)$ as

$$g\, t_i = \int_{RF} g(t)\, dt. \tag{5}$$

Eq. 1 may be rewritten

$$g = 2\frac{dp}{d(\Delta\phi)} \tag{6}$$

where $\Delta\phi \equiv 2\pi\,\nu\, t_i$ is the phase progression during the course of the interrogation. In order to evaluate the time–dependent $g(t)$ for Eq. 4, let $\delta\nu(t)$ be zero except for a phase step of size ϵ at time t' given by $\phi = \epsilon\,\sigma(t - t')$, where $\sigma(x) = 1$ for $x \geq 0$ and is zero otherwise. Since $2\,\pi\,\delta\nu = d\phi/dt$, this corresponds to a frequency variation $\delta\nu(t) = (\epsilon/2\pi)\delta(t - t')$, where $\delta(t - t')$ is the Kronecker delta function. Eq. 4 gives the response

$$\begin{aligned} \delta p(t', \epsilon) &= \pi \int_{RF} \frac{\epsilon}{2\pi}\delta(t - t')\, g(t)\, dt & (7) \\ &= \frac{\epsilon}{2}\, g(t'), & (8) \end{aligned}$$

so that $g(t')$ can be written in terms of the effect of a small phase step at time t'

$$g(t') = 2\frac{\delta p(t', \epsilon)}{\epsilon}. \tag{9}$$

That is, $g(t)$ describes the sensitivity of the final atomic state to a small phase step in the interrogating field at the time t. This dependence may be calculated directly by means of a detailed look at the quantum–mechanical transition process.

Analysis of L.O. Phase Step in Rotating System

The processes which determine the rate of excitation of atoms or ions from one energy state to another are explicitly quantum–mechanical. Following Kusch and Hughes[11] we find the time dependence of the phase and amplitude for the excited state by a magnetic spin–flip analogue. For the case where the two–level system consists of a particle with spin 1/2 in a magnetic field, there exists a one–to–one correspondence between the expectation values of quantum–mechanical picture and the classical picture of a magnetic moment precessing in its applied field. Only the absolute phase, a physically meaningless quantity, is missing from the classical picture. Since all weakly–coupled two–level quantum mechanical systems may be treated with identical formalism, the magnetic–moment precession analogue is generally applicable to calculate the details of transition amplitudes and phase in quantum–mechanical two level systems.

In this analogue as depicted in Fig. 1a), a vertical magnetic field $H_o = \omega_o/\gamma$ generates an energy difference between "down" and "up" states of a moment with magnitude γ and direction I. A transverse microwave field H_1 at frequency ω_{rf} is approximately tuned to the precession rate of the moment in the presence of the field H_o. Transformation to a reference frame rotating at ω_{rf} removes the rapid time variation due to spin precession in the large field H_o, leaving only a slow precession in the rotating frame. The transition problem can thus be treated entirely by the use of solid-body rotations.

In this context, detuning of the microwave frequency results in incomplete cancellation of the vertical dc field. The remaining, uncompensated, part of the vertical field combines with the transverse rf field H_1 to give an effective field in the rotating frame H_{eff}. The time dependent solutions are (slow) precessions of the magnetic moment I about this effective field at an angular rate ω_{eff} which is proportional to the magnitude of that field. Phase deviations due to the L.O. give rise to rotations about the z-axis.

All starting vectors lie in the plane, including the starting position of the unit vector $I_{initial}$, a fact which makes the algebraic relationships between the various frequencies apparent. The quantum-mechanical correspondence for the precession of I about ω_{eff}, identifies a correspondence between the vertical component of a unit vector $\hat{I}_{final}$ with the transition probability; more specifically, it is equal to the fractional occupation difference between upper and lower states at the end of the transition.

Figure 1b) shows the precession of I for the case of a π pulse on resonance. Figure 2 shows a three dimensional view of the effect of this same pulse when detuned to the half-signal point. Vertical lines are drawn from $z = 0$ plane to the arc which describes the time evolution of the atomic state. This arc is traversed by I at a uniform angular velocity during the interrogation process.

Figures 3 and 4 describe the processes used to calculate $g(t)$ for single π pulse excitation via Eq. 9. Here, I precesses about H_{eff} for a fraction of the interrogation process (until time t), a small phase step is introduced in the RF field (rotation about the z axis), and then the precession about H_{eff} is completed. The phase steps give rise to variation in the z component of the I_{final} which depends on where the step takes place; and this dependence defines $g(t)$.

Solutions

Details of the calculations for $g(t)$ based on the rotation transformations just described have been previously presented[1]. Figure 5 shows the results for three different interrogation processes. The cycle time t_c, interrogation time t_i, and dead time t_d are identified.

The functional form for the sensitivity $g(t)$ for the case of a single π-pulse at the half-bandwidth point as indicated in Figs. 2, 3, and 4 and as shown in Fig. 5a) is given by

$$g(t) = \frac{\Delta}{(1+\Delta^2)^{3/2}} \left[\sin(\Omega_1(t))(1-\cos(\Omega_2(t)) + \sin(\Omega_2(t))(1-\cos(\Omega_1(t))\right] \tag{10}$$

$$\begin{aligned} \text{where} \quad \Omega_1(t) &= \Omega \cdot \left(\frac{t}{t_i}\right), \\ \Omega_2(t) &= \Omega \cdot \left(1 - \left(\frac{t}{t_i}\right)\right), \end{aligned} \tag{11}$$

$$\Omega = \Omega(\Delta) = \pi\sqrt{1+\Delta^2}, \tag{12}$$

and where $\Delta \equiv 2\delta\nu\, t_i$ is detuned to the half signal point $\Delta = \Delta_{half} \approx 0.798685$. For this case the

angle of H_{eff} from the z axis (Figure 1a)) is given by

$$\theta = \theta(\Delta) = \pi/2 + \arctan \Delta. \tag{13}$$

It is worthy of note that integration of $g(t)$ as given by Eq. 10 returns the value given by Eq. 2 for this same interrogation process, i.e.

$$\int_0^{t_i} g(t)\, dt = 0.60386\, t_i. \tag{14}$$

The case of double $\pi/2$-pulse RF excitation at the resonant frequency and with a $\pi/2$ phase shift between pulses gives maximum sensitivity of the resulting measurement to frequency deviations of the L.O., and shows a particularly simple form for the time dependence of the sensitivity. As shown in Fig. 5b) its form is given by

$$\begin{aligned} g(t) &= \sin(\pi t/2t_p) && 0 < t < t_p, \\ &= 1 && t_p < t < t_i - t_p, \\ &= \sin(\pi \tfrac{t_i - t}{2t_p}) && t_i - t_p < t < t_i, \end{aligned} \tag{15}$$

where t_p is the short pulse time, and t_i the interrogation time as before.

Figure 5c) shows the time dependence for double-pulse interrogation with very narrow RF pulses to be essentially constant except for the dead time.

Use of Two Traps for More Nearly Constant Sensitivity

While a substantial "dead time" is required for a single trap, use of several, separately interrogated, sets of atoms or ions (several traps) would allow interrogation of one trap during the other's dead time. In this way the interrogation process could be almost seamless, thus apparently approaching the goal of continuous interrogation. Two traps are usually sufficient since a duty factor of $\Delta_d > \approx 50\%$ can be obtained for each trap. If it cannot, more traps could be used.

The duty cycles shown in Figure 5 point the way to interrogation strategies for two traps. Single-pulse interrogation as shown in 5a) shows large variability, even without the effect of dead time. In contrast, the two pulse example shown in 5c) represents some kind of ideal. Here the infinitesimally short RF pulses give an unvarying sensitivity except for the dead time. However, RF pulse lengths cannot be shortened arbitrarily due to the increasing RF power required and the necessity to average out effects of the thermal motion of the atoms or ions[4]. Thus Fig. 5b), with functional form as given in Eq. 15 and with explicit consideration of turn-on and turn-off effects for double-pulse interrogation allows us to examine the effects of RF pulse lergth and of various strategies of pulse timing. It seems clear that the starting pulse for one trap should more or less coincide with the ending pulse for the other.

Figure 6 shows the sensitivity variation for several interrogation strategies using two traps. Parts b), c), and d) show examples of the way double-pulse interrogation could be used. A comparison of parts b) and c) shows that overlapping the pulses for the two traps gives a somewhat more constant sensitivity. In addition, we can calculate an optimum overlap by equating the areas above and below the line given by $g(t) = 1$. This condition minimizes the effect of the lowest frequency L.O. fluctuations and results in a sequence where the starting pulse for one trap begins slightly later than the ending pulse for the other, for a total combined pulse time $4/\pi$ times longer than a single pulse. Fig. 6d) shows that the deviation of the sensitivity from unity has been substantially reduced.

A strategy using amplitude modulated RF pulses

As a final enhancement, the use of amplitude–modulated pulses with particular shapes would allow a sensitivity with no deviation from unity, even during the time of the overlapping pulses. The requirement is, of course, that the two sensitivities not vary. One approach is to have the pulses overlap completely, and to adjust the RF amplitudes in the two traps $A_1(t)$ and $A_2(t)$ so that the sensitivities for the two traps obey

$$g_1(t) + g_2(t) = 1 \tag{16}$$

during the time of the overlap. During other times one trap would have the constant sensitivity required while the other would experiencing its dead time. Without derivation, we present the results of a generalization of the calculation in [1] which gave rise to Eq. 15. This more general calculation shows that Eq. 15 can be rewritten for amplitude–modulated RF pulses over the time interval $0 \leq t \leq t_p$ as;

$$g_1(t) = \sin\left(\frac{\pi}{2\,t_p}\int_0^t A_1(t)\,dt\right) \tag{17}$$

for the trap which is just beginning its interrogation, and

$$g_2(t) = \cos\left(\frac{\pi}{2\,t_p}\int_0^t A_2(t)\,dt\right) \tag{18}$$

for the second trap which is ending its interrogation and which will now begin housekeeping tasks. Here, $A_1(t) = A_2(t) = 1$ recovers the solutions given by Eq. 15. Solutions of Eqs. 17 and 18 which also satisfy Eq. 16 are not unique. However, analytical solutions can be found for a particularly symmetric form for the two contributions which satisfy Eq. 16 and which have the sine–squared and cosine–squared dependencies

$$g_1(t) = \sin^2\left(\frac{\pi t}{2\,t_p}\right) = \frac{1}{2}\left[1 - \cos\left(\frac{\pi t}{t_p}\right)\right] \tag{19}$$

for the starting pulse of trap 1 and

$$g_2(t) = \cos^2\left(\frac{\pi t}{2\,t_p}\right) = \frac{1}{2}\left[1 + \cos\left(\frac{\pi t}{t_p}\right)\right] \tag{20}$$

for the ending pulse of trap 2 for times $0 \leq t \leq t_p$. Solution of the integral equations 17 and 18 for these examples yields

$$A_1(t) = \frac{2}{\sqrt{1 + \left(\sin\frac{\pi t}{2\,t_p}\right)^{-2}}} \tag{21}$$

for the beginning pulse and

$$A_2(t) = \frac{2}{\sqrt{1 + \left(\cos\frac{\pi t}{2\,t_p}\right)^{-2}}} \tag{22}$$

for the ending pulse.

Details of pulse timing for this example of amplitude modulated RF excitation are shown in Fig. 7b).

L.O.–INDUCED PERFORMANCE LIMITATION

Phase Noise Downconversion

A simplified block diagram of the frequency–locked loop is shown in Figure 8. Here the time dependence of the sensitivity of the measured atomic transition rate is combined with the microwave duty cycle to give an effective time dependent modulation $g(t)$ of the loop gain as shown. In this model, frequency noise $S_y^{LO}(f)$ in the *Local Oscillator* as partially compensated by feedback from the *Integrator* results in *Signal Output* from the locked local oscillator with frequency fluctuations $S_y^{LLO}(f)$. Compensation to achieve high long term stability is accomplished by a feedback circuit in which the *Signal Output* frequency fluctuations are first converted into voltage fluctuations $S_v^d(f)$ by the action of a high Q *Discriminator* and then to $S_v^m(f)$ by the action of the *Modulator*. This voltage is then integrated to provide a correction to the frequency of the *Local Oscillator*.

We identify a loop time constant t_ℓ for the integrator; assuming that for high frequencies $f \gg 1/(2\pi t_\ell)$ the loop gain is approximately zero, while for low frequencies $f \ll 1/(2\pi t_\ell)$ the loop gain is much greater than unity. Thus, high frequency fluctuations will be uncompensated by the action of the loop, so that $S_y^{LLO}(f) = S_y^{LO}(f)$ for $f \gg 1/(2\pi t_\ell)$. However, low frequency fluctuations, as detected, are nearly completely compensated. Thus any down–conversion of high frequency components of $S_v^d(f)$ to low frequency components in $S_v^m(f)$ will result in an identical transformation in the locked loop from high frequency components of $S_y^{LO}(f)$ to low frequency components of $S_y^{LLO}(f)$ subject to a requirement of "low" frequency as given above.

Depending on the harmonic content of $g(t)$, the modulator will introduce such down–conversion for "high" frequencies very near integral multiples of $f_c = 1/t_c$ to frequencies near $f = 0$. We assume $t_c \ll t_\ell \ll \tau$, where τ is the time over which the stability of the *Signal Output* is measured. The down–converted signals must be compared to the average value of $g(t)$, the which characterizes the strength with which the modulator passes signals near $f = 0$. For $g(t)$ symmetric about $t = 0$, coefficients g_n for frequency down–conversion of noise amplitudes near the nth harmonic of f_c can be written:

$$g_n = \frac{1}{t_c}\int_0^{t_c} g(t)\cos\left(\frac{2\pi\, n\, t}{t_c}\right) dt, \tag{23}$$

with the average value given by

$$g_0 = \frac{1}{t_c}\int_0^{t_c} g(t)dt. \tag{24}$$

The coefficients g_n depend on the nature of the RF excitation used and can be calculated from forms for $g(t)$ given by Eqs. 10 or 15.

Assuming complete compensation by the loop for the down–converted fluctuations, "white" noise in the narrow range about each harmonic, (and taking into account fluctuations at frequencies both above and below harmonics nf_c,) the low frequency contribution to $S_y^{LLO}(f)$ is given by

$$g_0^2 S_y^{LLO}(0) = 2 \cdot \sum_{n=1}^{\infty} g_n^2 S_y^{LO}(nf_c). \tag{25}$$

The consequences of this relation depend in detail on the nature of the noise which characterizes the

local oscillator and on the time dependence of the duty factor. If, for example, L.O. noise increases rapidly with frequency, the sum may not converge.

Modeling Quartz oscillator performance by a flat Allan Deviation σ_q over the time range of interest allows its flicker frequency noise to be calculated as[13–15]

$$S_y^{LO}(f) = \frac{1}{2\ln(2)} \frac{\sigma_q^2}{f}. \tag{26}$$

Correspondingly, the limiting Ion Standard variance as measured at cycle time t_c can be related to the white noise of the locked loop $S_y^{LLO}(0)$ by

$$\sigma_c^2 = \frac{S_y^{LLO}(0)}{2t_c}. \tag{27}$$

Combining Equations 25–27 allows us to calculate a performance ratio R between the limiting frequency standard performance at the cycle time t_c and the (constant) Quartz oscillator performance given by

$$R^2 \equiv \frac{\sigma_c^2}{\sigma_q^2} = \frac{1}{2\ln(2)} \frac{1}{g_0^2} \sum_{n=1}^{\infty} \frac{g_n^2}{n}. \tag{28}$$

Performance Degradation due to Quartz L.O.

Figure 9 shows the limitations to medium term performance for a trapped mercury ion standard presently under development[5] in terms of the dimensionless parameter R. The effect of conventional feedback limitations due to feedback attack time are also indicated[16,17]. For this L.O. performance[18,19] the value of R would need to be reduced to $R = 0.02$ for this example in order to achieve the stability which is inherent in the standard.

Figure 10 shows the results of numerical calculations of the dependence of R on dead time and pulse time based on Eq. 28 for waveforms shown in Figures 5 and 6. They show that relatively small reduction in R is possible for single pulse RF interrogation, with $R \geq 0.305$ for all values of the dead time. The situation is improved by the use of two (very narrow) pulses where R approaches zero as the dead time is reduced. However, even in that case the requirement of $R \leq 0.02$ to match available quartz L.O.'s to the trapped mercury ion source (from Fig. 9) requires an impractically low dead time of $\Delta_d \approx 0.01$. At present, a minimum value for the trapped mercury ion standard is $\Delta_d \approx 0.1$–0.3.

Cryogenic (superconducting) oscillators[20] are presently available with performance which would match and complement that of the new trapped mercury ion standard. These sources show performance of $\sigma_y(\tau)|_{L.O.} \leq 10^{-14}$ for measuring times 1 second $< \tau <$ 1000 seconds. While they are presently relatively complex and expensive, this may improve; furthermore, if trapped ion performance continues to improve, cryogenic oscillator performance may be required.

The performance improvement made possible by the use of two traps is even greater than may first be apparent. This is because the length of the RF pulse sequence for two traps may be reduced simply by applying more RF power (typically microwatts) and properly synchronizing pulses for the two traps (typically milliseconds). A pulse length of 0.1 second, can be combined with an overall interrogation

time of 10 seconds to give a RF pulse time fraction of $\Delta_{rf} = 0.01$. In contrast, reduction of the dead time much below 1 second in a single trap may prove very difficult on account of the various tasks that must be accomplished during that time. For example, in present versions of the trapped ion standard, a discharge lamp requires approximately 1.0–1.5 seconds for optical interrogation and state preparation during each cycle.

TWO–TRAP CONFIGURATIONS AND SCENARIOS

General Considerations

For two traps in separate and isolated RF environments, Fig. 10 shows that the *optimally overlapping* strategy described in Figs. 6d) and 7a) offers a great advantage, with reduction of L.O. influence on the long–term standard performance by almost 100 times compared to straightforward double–pulse interrogation. *Amplitude modulated* pulses might also be used, for nominally zero effect of the L.O. on medium–term performance.

However, many economies are brought about by combining the vacuum and trapping elements of the two traps. Because trap elements and spacings may be approximately the same size as the wavelength of the exciting radiation, RF isolation between the two traps is likely to be poor. This would require the *100% overlap* strategy described by Fig. 6c), with simultaneous excitation of both traps. As shown in Fig. 10, an RF pulse time of $\Delta_{rf} = 0.01$ would make possible L.O. coupling as low as $R = 0.005$.

Isolated Traps

Figure 11 shows a hardware configuration using two completely independent traps. This design features high RF isolation between traps and great flexibility of operation, so that almost any interrogation scenario could be supported. While this configuration is designed for use with trapped mercury ions in which the RF hyperfine transition at 40.5 GHz is interrogated, similar configurations are applicable to other cases using, e.g. interrogation of optical transitions, state preparation, and/or cooling by the use of lasers at one or more wavelengths. Only those aspects relating to the interrogation process itself are presented: not shown are trapping electrodes and voltage sources, ion sources, etc.

Figure 12 shows a state diagram representing the details of an interrogation scenario using *amplitude modulated* pulses, for the hardware configuration shown in Fig. 11. A similar scenario could be used for any of the other pulse strategies.

Four cycles with length t_c make up this scenario as opposed to two cycles for previously published single trap cases[4–6]. Two cycles are needed for each trap so that a reversal of the RF phase progression can be used to cancel dependence of the frequency on the absolute intensity of signals in the optical system. Thus, for trap #1, the 90° phase advance between RF pulses in cycles 1 and 2 gives rise to a negative dependence of the reading of the counter in cycle 2 (C_2) on the L.O. frequency, while the opposite variation between cycles 3 and 4 gives rise to a corresponding positive dependence of the counter reading in cycle 4.

In this commonly used technique, frequency error is then inferred by the difference between the values of the counts obtained in cycles 2 and 4, or $C_4 - C_2$. Combining the values for the two traps gives an inferred frequency error for the L.O. $\Delta f_{L.O.} \propto C_1 - C_2 - C_3 + C_4$. With appropriate weighting

and filtering, this value is used by the *Control* element of Fig. 11 to adjust the frequency of the *Local Oscillator*, and so compensate and correct its deviations.

Combined Traps in a Linear Structure

Figure 13 shows a configuration that combines two ion collections in linear trapping structure so that a single optical system (lamp and detector) can be used. This configuration is shown in somewhat more detail than the previous one, and the traps share the same RF environment to some extent, so that RF fields must be simultaneously applied to the two traps. Here, electrostatic fields are used to separate and manipulate a linear ion cloud in such a way that its two halves can alternately extend into a central region where optical pumping and detection take place. Electrostatic elements are placed as shown at nodes (zeros) of the RF trapping fields generated by the four circular rods.

Completely overlapping pulses are implemented by the state diagram shown in Fig. 14 with the beginning RF pulse for one trap being one and the same as the ending pulse of the other. Here the phase progression of the RF pulses must extend to 180° in order to provide insensitivity of the frequency to the absolute value of optical signals. This example again gives frequency error in terms of fluorescent light counts in the various cycles as $\Delta f_{L.O.} \propto C_1 - C_2 - C_3 + C_4$.

In the previous configuration, matching values of forward and reverse phase progression ($\pm \approx 90°$) in each trap give a first order cancellation of sensitivity to the actual value of the progression. A similar cancellation here requires that the phase steps at the ends of cycles 1 and 3 match, and also those at the ends of cycles 2 and 4. This could be accomplished by use of two separate 90° phase shifters in series, actuated in an appropriate sequence.

The state diagram for this configuration includes electrostatic potentials for the electrodes which move the ions into and out of the central region for optical illumination. No electrodes are placed in this region because the light they would scatter would degrade performance of the frequency standard. Instead, main electrodes 1 and 4 attract and repel the ions from storage regions at either end where they are subject to RF pulses to begin and end their respective clock cycles. "Cap" electrodes 2 and 3 contain and separate the ion clouds and prevent either ion cloud from mixing with the other. Not shown are electrodes at the trap ends which prevent escape of the ions. Critical aspects of this scenario include stability of the trapping configuration during the clock time "b-e" of either ion cloud as indicated in Fig. 14 while the other cloud is being moved. This is because of a configuration-dependent frequency shift due to second-order Doppler effects[4].

Economies of this configuration include use of one component rather than two for many functions. These components include most of the expensive and performance-sensitive parts of the trap; and include vacuum housing, trap structure, trap excitation electronics, amplitude (pulse) modulator, state pumping lamp and excitation electronics, scattered light detector, and photon counter. The added electrodes complicate the trap structure, but their control with DC potentials is not difficult.

CONCLUSIONS

Improved performance of trapped-ion frequency standards is jeopardized by medium-term instabilities generated by down-conversion of local oscillator frequency fluctuations. These instabilities show a $1/\sqrt{\tau}$ dependence on measuring time τ, and are due to periodic time-variation of the frequency

sensitivity of the RF interrogation process.

We have presented an analysis of the time-variation of this sensitivity for both single- and double-pulse sequential RF interrogation processes based on a spin-flip analogue of the electromagnetic transition process. The consequence of this variation was then numerically calculated for a quartz-crystal type local oscillator with flicker-frequency noise characteristics.

Results of these calculations show that for interrogation processes with large sensitivity variations, e.g. single pulse interrogation with a 50% dead time, the $1/\sqrt{\tau}$ performance of the standard is degraded to a value approximately equal to that of the L.O. when measured at the cycle time for the interrogation process.

Performance can be improved in several ways: (1) Use of an L.O. with ultra-stable short term performance such as the cryogenic SCMO gives a good match to projected Trapped mercury Ion standard performance for almost any interrogation process. (2) Double pulse interrogation with short pulses and with a relatively short dead time (10% or less) can reduce the effect substantially, so that the best Quartz crystal oscillators may not greatly degrade presently observed Trapped Ion performance. (3) Use of several traps with overlapping double-pulse interrogations could greatly reduce, and possibly eliminate, this effect.

Available performance improvement is limited by the inherent stability of the standard, which shows this same time $1/\sqrt{\tau}$ dependence, and by an L.O.-induced "feedback limitation" which decreases more rapidly (as $1/\tau$) with increasing measuring time. Thus the greatest impact on performance takes place at medium and long measuring times ($\tau \geq 1000$ seconds). However, a strength of the trapped ion technology is at these longer times where the great stability achievable with relatively few (isolated) ions can be expressed. Considerations discussed here may also be applicable to future optical trapped ion standards where sequential interrogation is likely to be used, and where L.O. phase noise is also a major concern.

ACKNOWLEDGEMENTS

The authors would like to express their thanks to R. L. Sydnor for his encouragement of this work and to L. S. Cutler for pointing out the problem.

REFERENCES

[1] G. J. Dick, "Calculation of Trapped Ion Local Oscillator Requirements," *Proc. 19th Annual Precise Time and Time Interval (PTTI) Applications and Planning Meeting*, 133-147 (1988).

[2] "A Limit to the Frequency Stability of Passive Frequency Standards," C. Audoin, V. Candelier, and N. Dimarcq, presented at *Conference on Precision Electromagnetic Methods (CPEM)*, Ottawa, Canada, June 11-14, 1990.

[3] F. L. Walls and S. R. Stein "Servo Techniques in Oscillators and Measurement Systems," NBS Technical Note 692, (1976).

[4] J. D. Prestage, G. J. Dick, and L. Maleki, "New Ion Trap for Frequency Standard Applications," *J. Appl. Phys.* **66** (3), 1013-1017, 1989.

[5] J. D. Prestage, G. J. Dick, and L. Maleki, "Linear Ion Trap based Atomic Frequency Standard," *Proc. 44rd Ann. Symp. on Frequency Control*, 82-88 (1990).

[6] L. S. Cutler, R. P. Giffard, P. J. Wheeler, and G. M. R. Winkler, "Initial Operational Experience with a Mercury Ion Storage Frequency Standard," *Proc. 41st Ann. Symp. Freq. Control*, IEEE Cat. No. 87Ch2427-3, 12-19 (1987).

[7] J. Vanier and L. G. Bernier, "On the Signal-to-Noise Ratio and Short-Term Stability of Passive Rubidium Frequency Standards," *IEEE Proc. Instrum. Meas.* **IM-30**, 277-282 (1981).

[8] J. Vanier and C. Audoin, "Atomic Frequency Standards and Clocks," *J. Phys. E* **9**, 697-720 (1976).

[9] J. Vanier and C. Audoin, *The Quantum Mechanics of Atomic Frequency Standards*, Bristol: Adam Hilger, 804 (1989).

[10] D. J. Wineland, J. C. Bergquist, J. J. Bollinger, W. M. Itano, D. J. Heinzen, S. L. Gilbert, C. H. Manney, and C. S. Weimer, "Progress at NIST Toward Absolute Frequency Standards using Stored Ions," it Proc. 43rd Ann. Symp. on Frequency Control, 143-150 (1989).

[11] Kusch, P. and Hughes, V. W., "Atomic and Molecular Beam Spectroscopy," in "Handbuch der Physik," Ed. S. Flügge, Vol. XXXVII/1, p. 55, (1959).

[12] N. F. Ramsey, *Molecular Beams*, London, England, Oxford University Press, (1956).

[13] L. S. Cutler and C. L. Searle, "Some Aspects of the Theory and Measurement of Frequency Fluctuations in Frequency Standards," *Proc. IEEE* **54**, 136-154 (1966).

[14] D. W. Allan, "Statistics of Atomic Frequency Standards," *Proc. IEEE* **54**, 221-230 (1966).

[15] D. W. Allan, "The Measurement of Frequency and Frequency Stability of Precision Oscillators," *Proc. 6th Ann. Precise Time and Time Interval (PTTI) Applications and Planning Meeting*, 109-142 (1974).

[16] J. Vanier, M. Tetu, and L. G. Bernier, "Transfer of Frequency Stability from an Atomic Frequency Reference to a Quartz-Crystal Oscillator," *IEEE Proc. Instrum. Meas.* **IM-28**, 188-193 (1979).

[17] A. De Marchi, G. D. Rovera, and A. Premoli, "Effects of Servo Loop Modulation in Atomic Beam Frequency Standards Employing a Ramsey Cavity," *IEEE Trans. Ultrasonics, Ferroelectrics, and Frequency Control* **UFFC-34**, 582-591 (1987).

[18] Austron BVA Quartz Crystal Oscillator Model 8600, Option 03.

[19] M. B. Bloch, J. C. Ho, C. S. Stone, A. Syed, and F. L. Walls, "Stability of High Quality Quartz Crystal Oscillators: an Update," *Proc. 43rd Ann. Symp. on Frequency Control*, 80-84 (1989).

[20] R. T. Wang and G. J. Dick, "Improved Performance of the Superconducting Cavity Maser at Short Measuring Times," *Proc. 44rd Ann. Symp. on Frequency Control*, 89-93 (1990).

FIGURE CAPTIONS

Figure 1 Field and frequency diagrams for a spin with moment I in the rotating reference system. The general case is shown in a) where the applied frequency ω_{rf} does not match the internal transition frequency $\omega_o = \gamma H_o$, giving rise to an effective field in the rotating frame H_{eff} which differs from the applied RF field H_1. Time evolution of the electromagnetic transition corresponds to a three-dimensional rotation of I about H_{eff}. b) shows evolution during a π pulse at the resonant frequency ω_o.

Figure 2 Three dimensional view of time evolution of I during single-pulse interrogation at a half-bandwidth frequency offset, i.e. final excitation probability is 50%.

Figure 3 Phase variations in the Local Oscillator correspond to rotations about the z axis. Here, an L.O. phase step half-way through the interrogation process causes I_{final} to deviate from the mid-plane (50% excitation probability). L.O. frequency noise can be mathematically represented by a series of such (infinitesimal) phase steps.

Figure 4 Changing the time of the phase step gives differing deviations of the final state from the midplane. Shown are phase steps at 10%, 20%, 40% 60%, 80%, and 90% of the RF pulse time. Phase steps near the middle of the interrogation have a greater effect on excitation probability as represented by the z component of I_{final}.

Figure 5 Time dependence of the sensitivity g(t) of the final state to L.O. frequency variations for several interrogation types. Here, a) corresponds to a sequential appli- cation of single-pulse interrogation as described in detail by Figs. 2, 3, and 4; and b) and c) to double-pulse (Ramsey) interrogation with pulse widths of 20% and 0%, respectively. RF pulses beginning and ending the interrogations are labeled 'b' and 'e'.

Figure 6 Time variability of g(t) may be reduced by the use of alternatively interrogated traps. Here a) shows alternate single-pulse interrogations as Fig. 5a); and b), c), and d) show double-pulse strategies as Fig. 5b) with varying overlap between the beginning pulse for one trap and the ending pulse for the other.

Figure 7 Details of RF pulse sequences for optimally overlapping pulses a) and amplitude-modulated pulses b). Optimally overlapping pulses have a short delay between the ending pulse for one trap and the beginning pulse of the other. Coincident amplitude-modulated pulses with proper waveform give unvarying g(t).

Figure 8 Simplified block diagram of frequency feedback in sequentially interrogated atomic standard. Frequencies near harmonics of t_c^{-1} are aliased to near zero frequency by action of the modulator. High loop gain at long integration times improperly 'corrects' for these perceived low frequency fluctuations.

Figure 9 The effect of aliased (white) low frequency noise can be described in terms of a dimensionless parameter R which describes consequent $1/\sqrt{\tau}$ dependent frequency deviation in relation to L.O. stability and the cycle time t_c. For this example, a value of $R \leq 0.02$ is required to prevent degradation of inherent performance of the source.

Figure 10 Numerical calculations of R for L.O. with flat deviation as shown in Fig. 9 (flicker frequency noise). R is plotted as a function of the fractional dead time Δ_d for one-trap scenarios shown in Figs. 5a) and c); and as a function of fractional RF pulse time Δ_{rf} for two-trap scenarios

described in Figs. 6b), c), and d). Two–trap scenarios show advantage of low–lying curves in addition to ability to reduce $\Delta_{rf} < 0.1$.

Figure 11 Block diagram of a trapped ion frequency standard using two completely independent traps, each including its own phase and amplitude control, state pumping lamp and scattered light detector for maximum flexibility. Excellent RF isolation allows use of complex interrogation scenarios.

Figure 12 State diagram showing a time sequence for the frequency standard as shown above which uses amplitude modulated pulses for nominally zero sensitivity of medium term performance of the standard to L.O. fluctuations. Four cycle scenario allows insensitivity of operating frequency to signal intensity, phase shift error.

Figure 13 Block diagram of a trapped ion frequency standard with two ion collections combined in a single linear quadrupole trapping structure. Added electrostatic elements 1–4 separate the ions into two collections and alternately allow each collection to extend into a central region where a state–pumping lamp and scattered light detector are located. Poor RF isolation indicates use of common constant–amplitude RF pulses.

Figure 14 State diagram showing a time sequence for the frequency standard shown above. 180° phase shift range is necessary for insensitivity to signal intensity for both ion collections. Two 90° phase shifters in series can also give independence to phase shift error. V1–V4 show potentials applied to electrostatic electrodes 1–4.

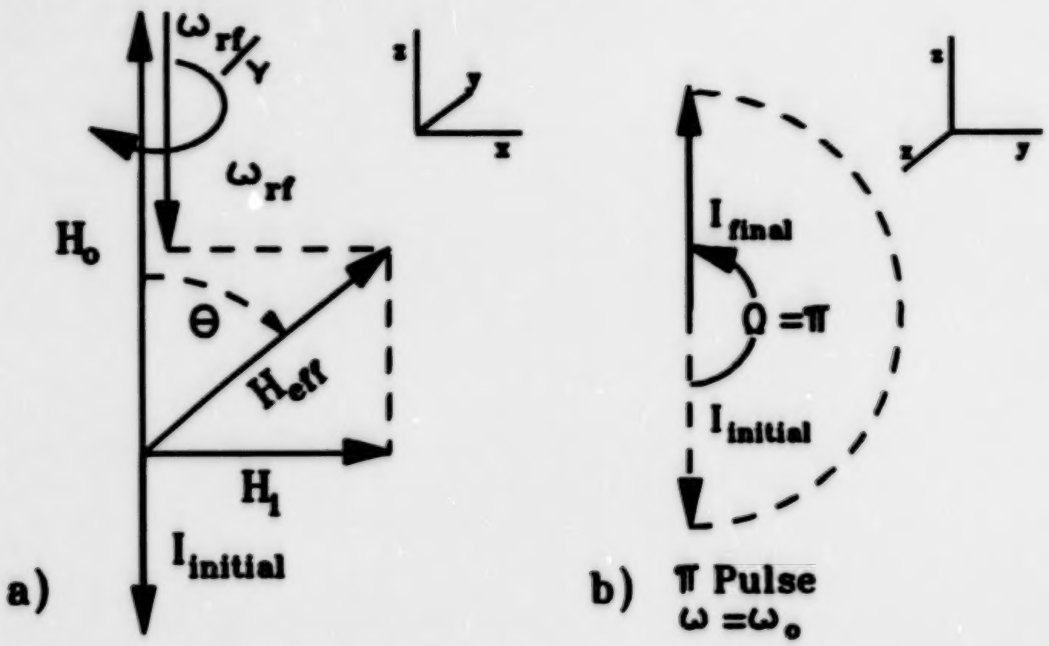


Figure 1: Field and frequency diagrams for a spin with moment I in the rotating reference system. The general case is shown in a) where the applied frequency ω_{rf} does not match the internal transition frequency $\omega_o = \gamma H_o$, giving rise to an effective field in the rotating frame H_{eff} which differs from the applied RF field H_1. Time evolution of the electromagnetic transition corresponds to a three-dimensional rotation of I about H_{eff}. b) shows evolution during a π pulse at the resonant frequency ω_o.

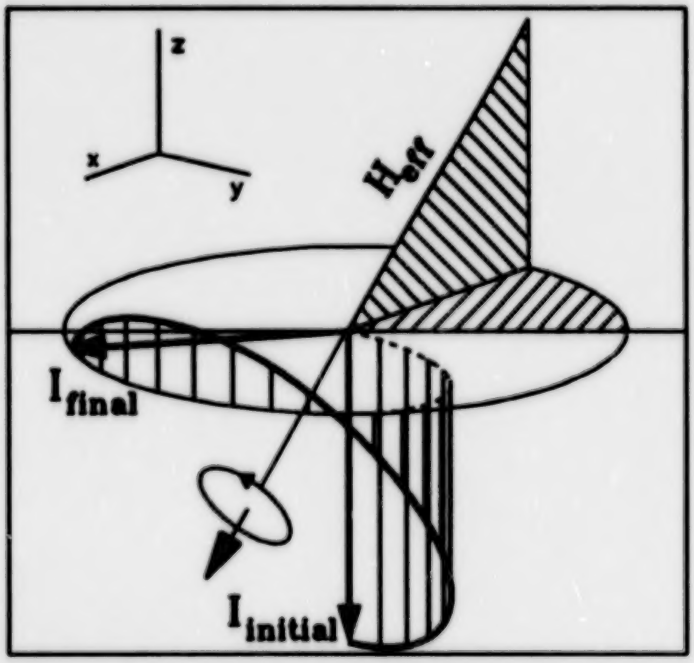


Figure 2: Three dimensional view of time evolution of I during single-pulse interrogation at a half-bandwidth frequency offset, i.e. final excitation probability is 50%.

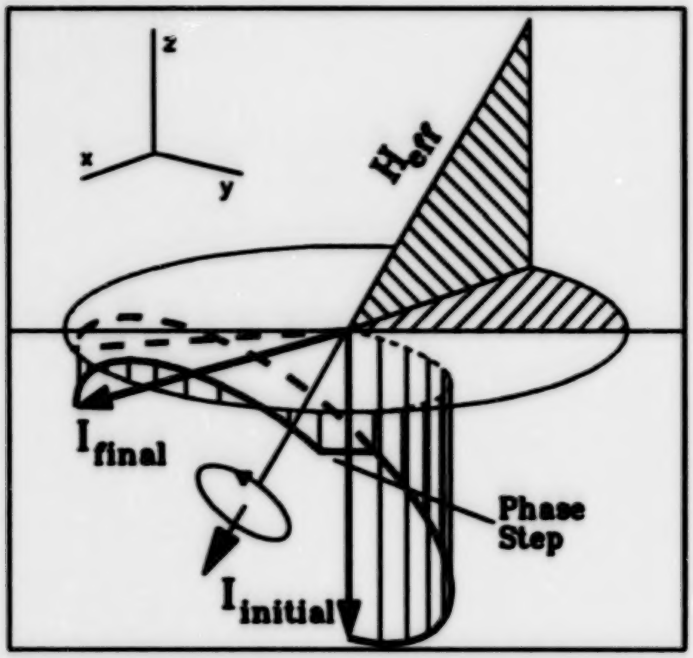


Figure 3: Phase variations in the Local Oscillator correspond to rotations about the **z** axis. Here, an L.O. phase step half-way through the interrogation process causes I_{final} to deviate from the mid-plane (50% excitation probability). L.O. frequency noise can be mathematically represented by a series of such (infinitesimal) phase steps.

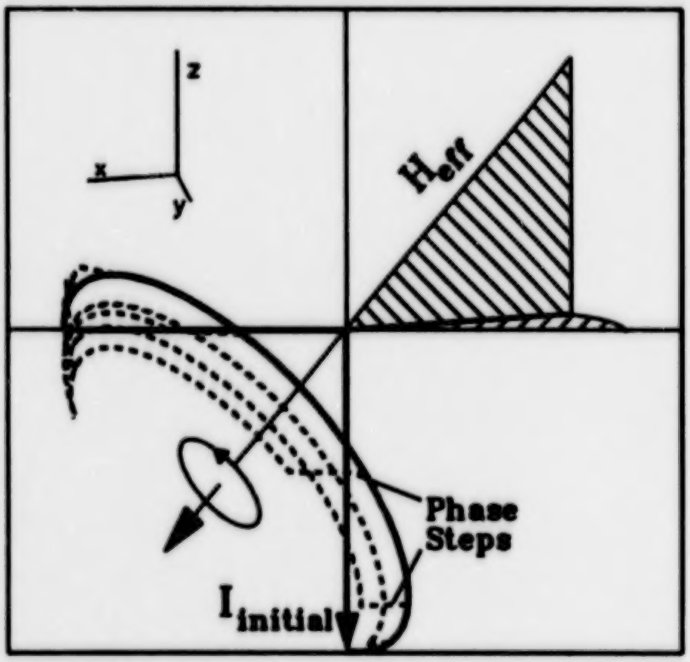


Figure 4: Changing the time of the phase step gives differing deviations of the final state from the midplane. Shown are phase steps at 10%, 20%, 40% 60%, 80%, and 90% of the RF pulse time. Phase steps near the middle of the interrogation have a greater effect on excitation probability as represented by the **z** component of I_{final}.

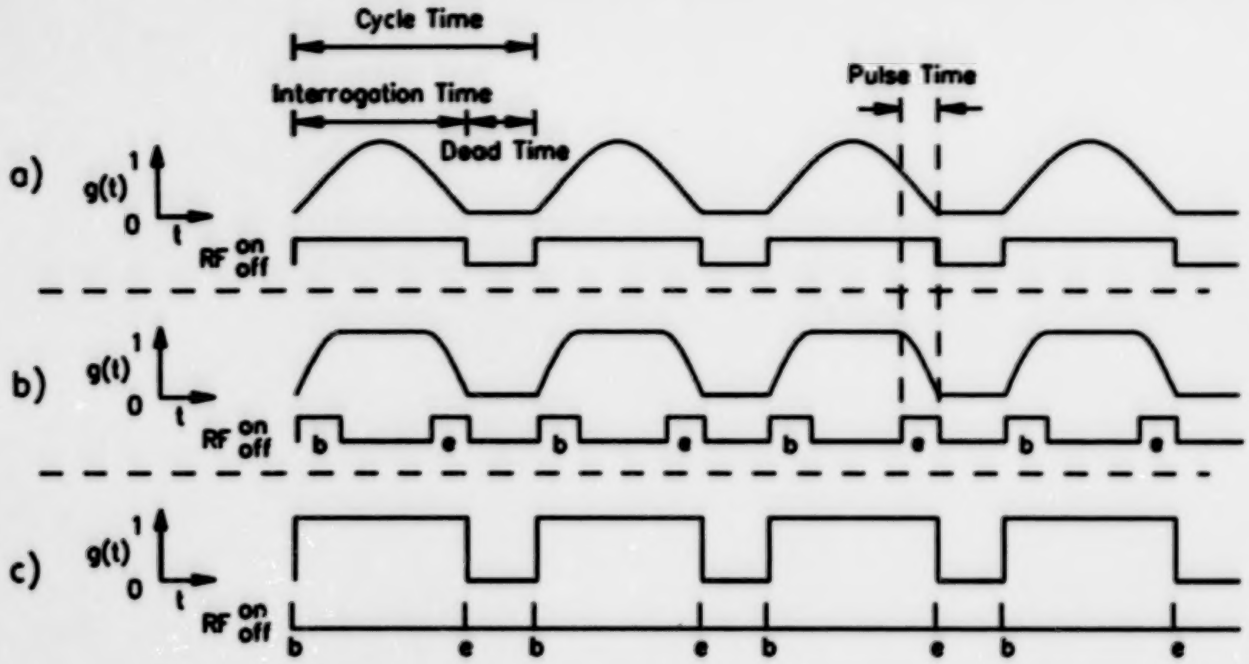


Figure 5: Time dependence of the sensitivity g(t) of the final state to L.O. frequency variations for several interrogation types. Here, a) corresponds to a sequential application of single-pulse interrogation as described in detail by Figs. 2, 3, and 4; and b) and c) to double-pulse (Ramsey) interrogation with pulse widths of 20% and 0%, respectively. RF pulses beginning and ending the interrogations are labeled 'b' and 'e'.

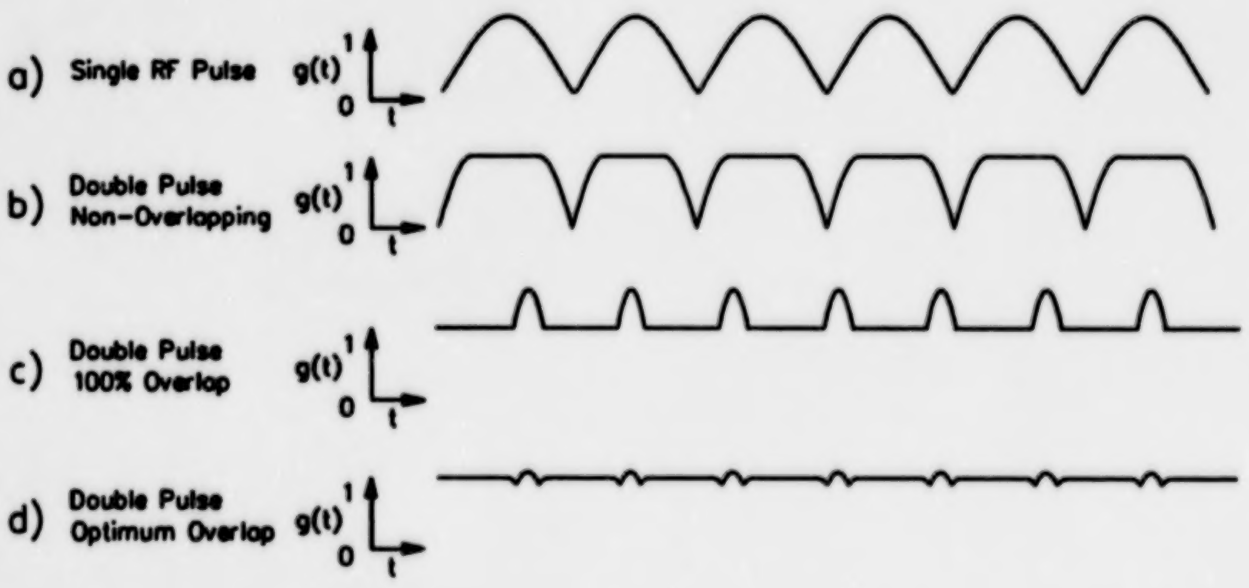


Figure 6: Time variability of g(t) may be reduced by the use of alternatively interrogated traps. Here a) shows alternate single-pulse interrogations as Fig. 5a); and b), c), and d) show double-pulse strategies as Fig. 5b) with varying overlap between the beginning pulse for one trap and the ending pulse for the other.

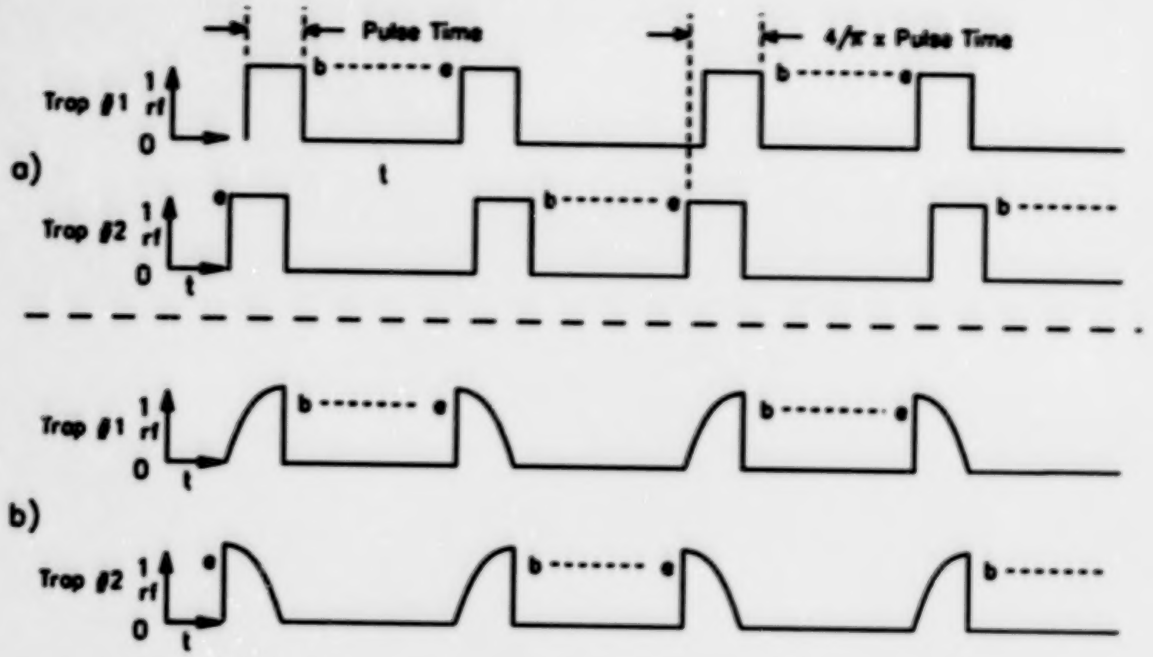


Figure 7: Details of RF pulse sequences for optimally overlapping pulses a) and amplitude-modulated pulses b). Optimally overlapping pulses have a short delay between the ending pulse for one trap and the beginning pulse of the other. Coincident amplitude-modulated pulses with proper waveform give unvarying g(t).

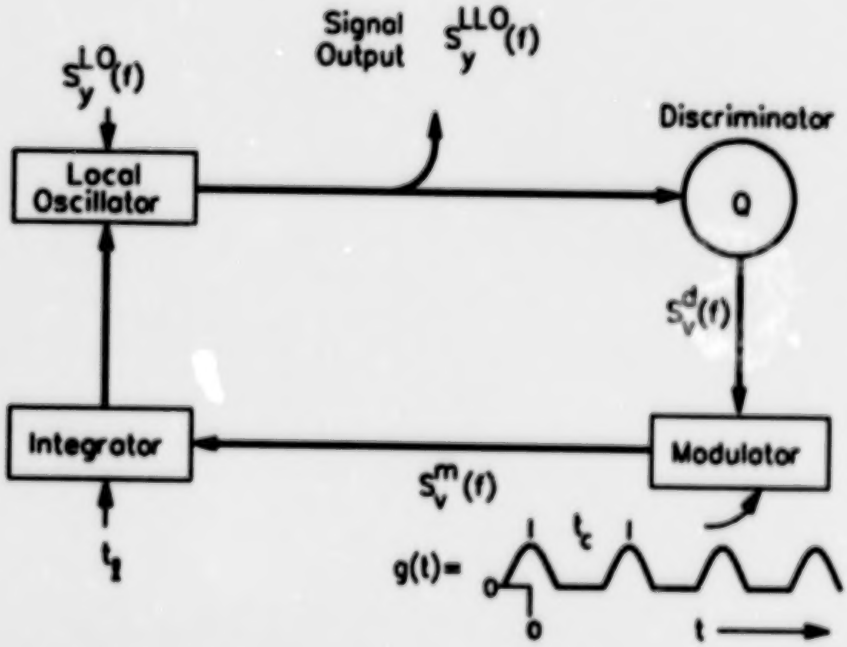


Figure 8: Simplified block diagram of frequency feedback in sequentially interrogated atomic standard. Frequencies near harmonics of t_c^{-1} are aliased to near zero frequency by action of the modulator. High loop gain at long integration times improperly 'corrects' for these perceived low frequency fluctuations.

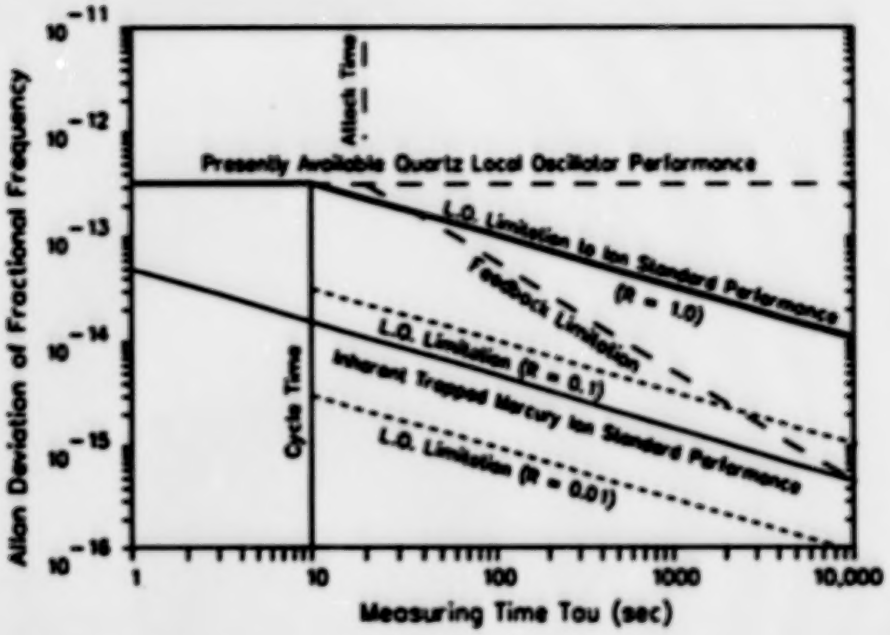


Figure 9: The effect of aliased (white) low frequency noise can be described in terms of a dimensionless parameter **R** which describes consequent $1/\sqrt{\tau}$ dependent frequency deviation in relation to L.O. stability and the cycle time t_c. For this example, a value of $R \leq 0.02$ is required to prevent degradation of inherent performance of the source.

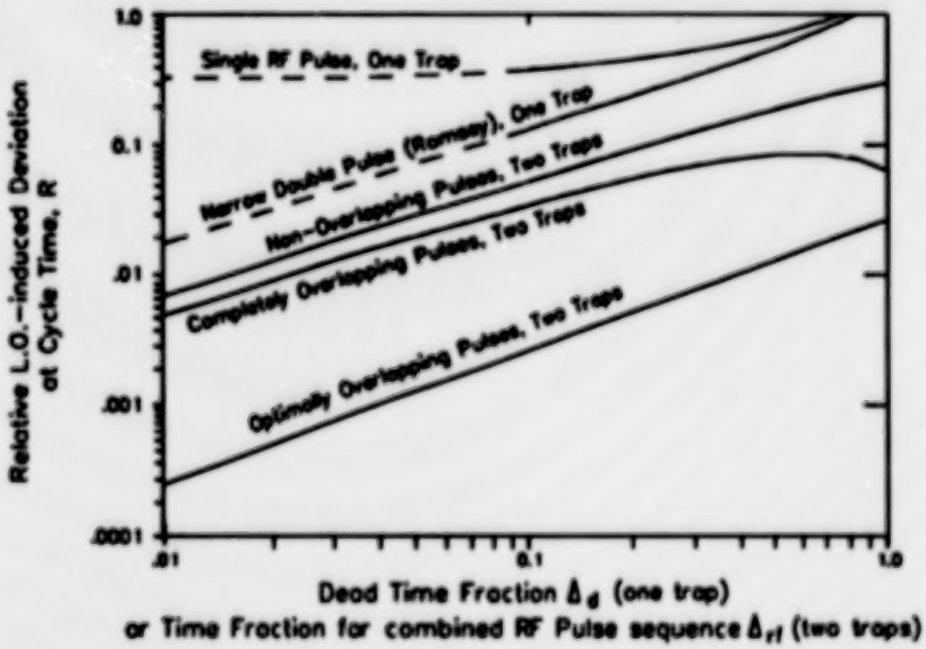


Figure 10: Numerical calculations of **R** for L.O. with flat deviation as shown in Fig. 9 (flicker frequency noise). **R** is plotted as a function of the fractional dead time Δ_d for one-trap scenarios shown in Figs. 5a) and c); and as a function of fractional RF pulse time Δ_{rf} for two-trap scenarios described in Figs. 6b), c), and d). Two-trap scenarios show advantage of low-lying curves in addition to ability to reduce $\Delta_{rf} < 0.1$.

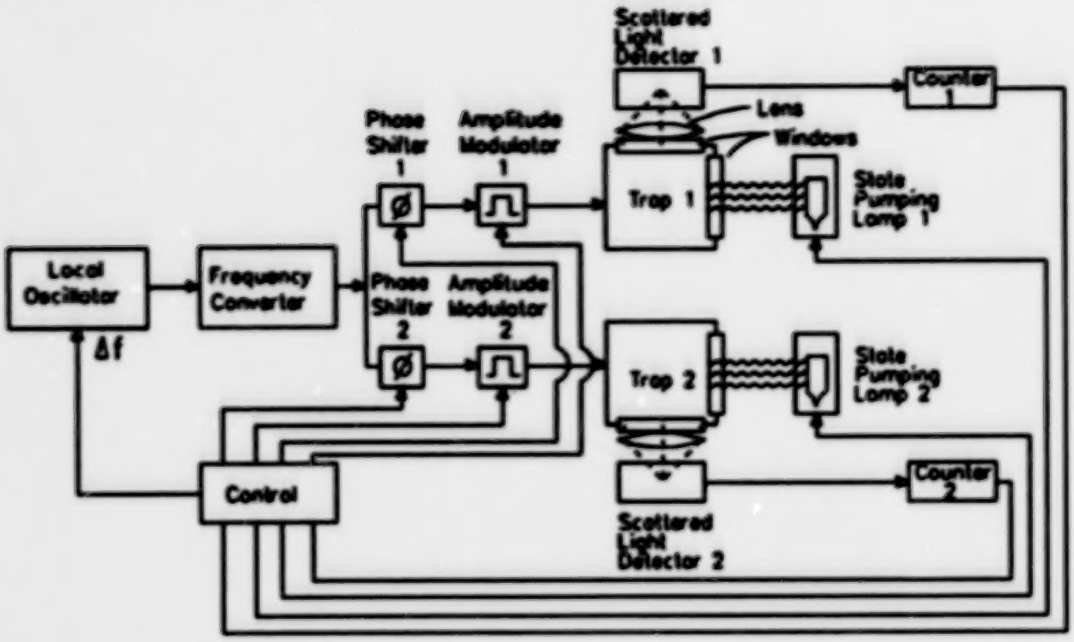


Figure 11: Block diagram of a trapped ion frequency standard using two completely independent traps, each including its own phase and amplitude control, state pumping lamp and scattered light detector for maximum flexibility. Excellent RF isolation allows use of complex interrogation scenarios.

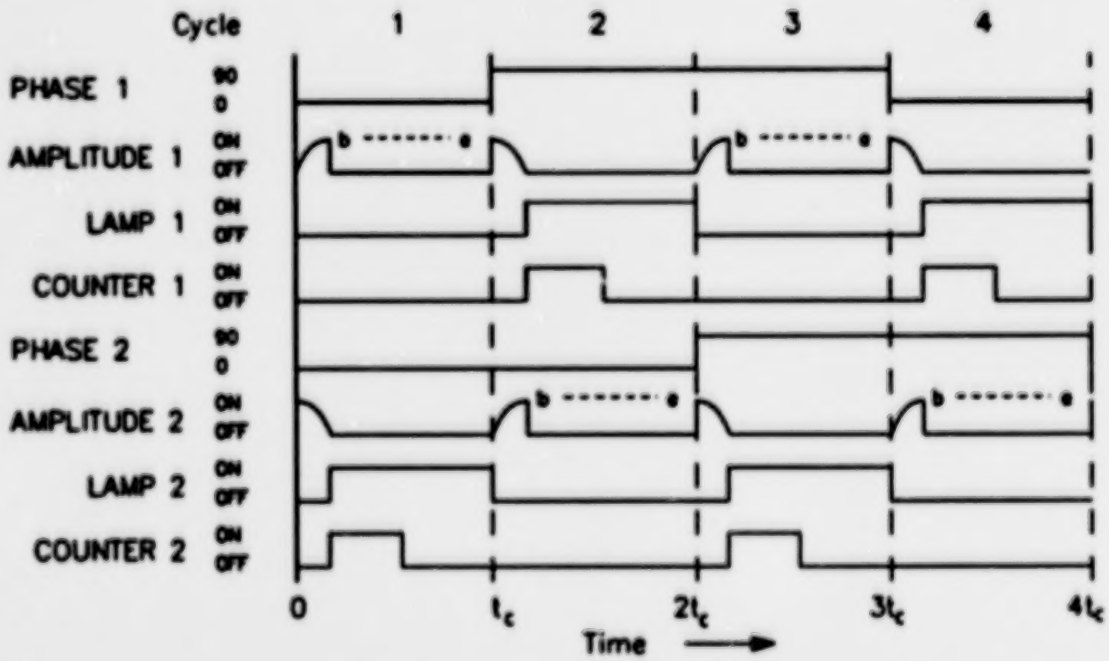


Figure 12: State diagram showing a time sequence for the frequency standard as shown above which uses amplitude modulated pulses for nominally zero sensitivity of medium term performance of the standard to L.O. fluctuations. Four cycle scenario allows insensitivity of operating frequency to signal intensity, phase shift error.

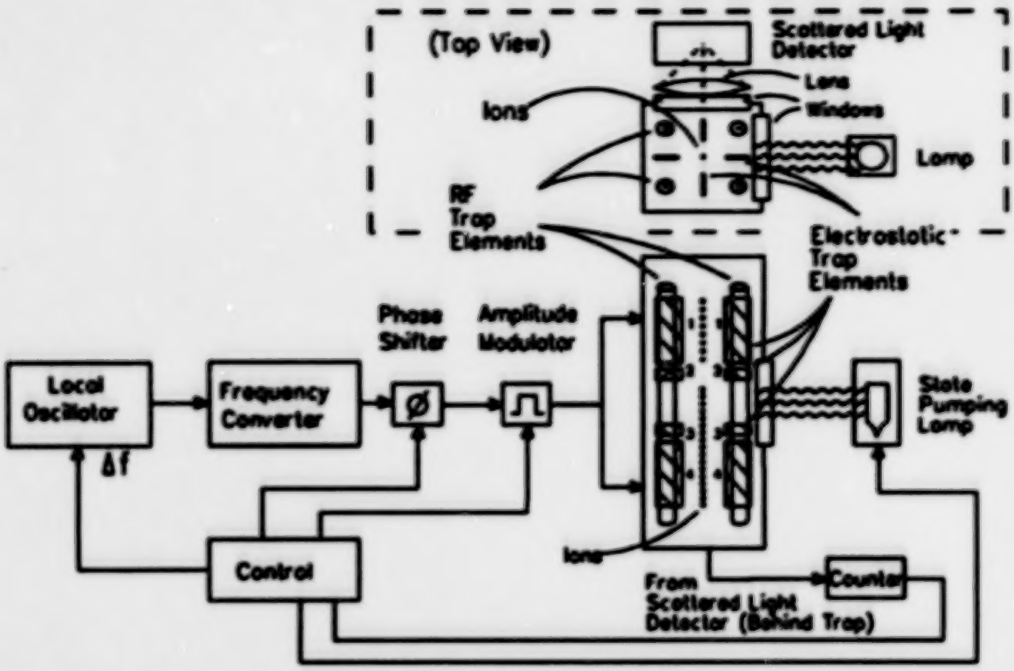


Figure 13: Block diagram of a trapped ion frequency standard with two ion collections combined in a single linear quadrupole trapping structure. Added electrostatic elements 1-4 separate the ions into two collections and alternately allow each collection to extend into a central region where a state-pumping lamp and scattered light detector are located. Poor RF isolation indicates use of common constant-amplitude RF pulses.

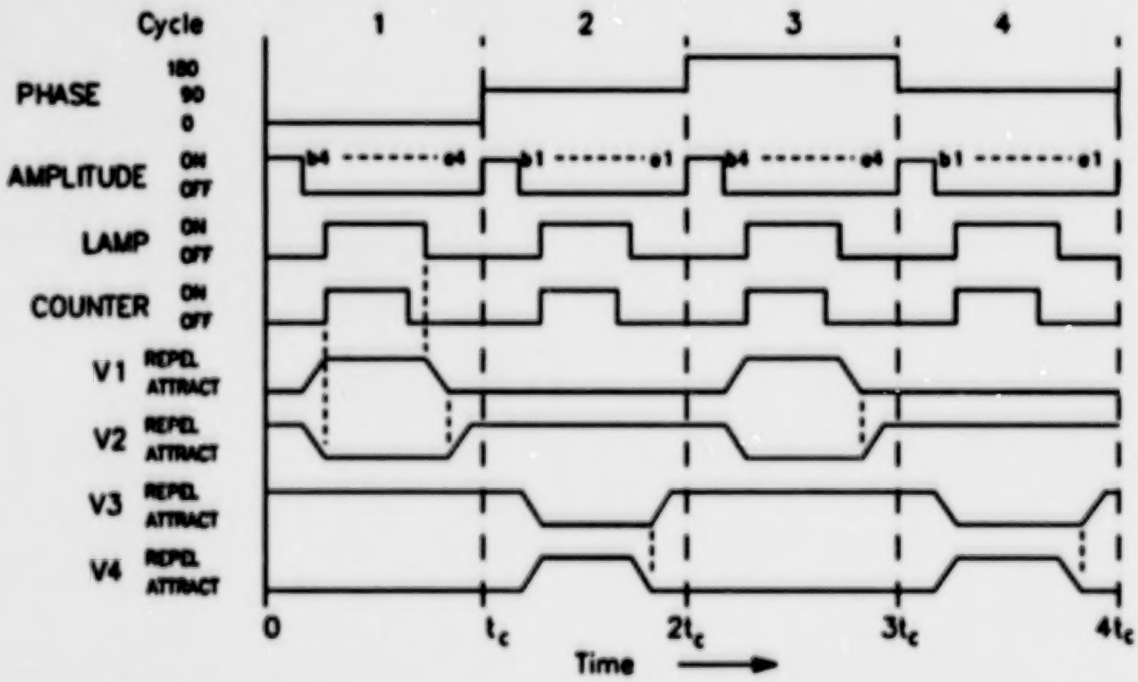


Figure 14: State diagram showing a time sequence for the frequency standard shown above. 180° phase shift range is necessary for insensitivity to signal intensity for both ion collections. Two 90° phase shifters in series can also give independence to phase shift error. V1-V4 show potentials applied to electrostatic electrodes 1-4.

PERFORMANCE OF SOVIET AND U.S. HYDROGEN MASERS

Adolf A. Uljanov and Nikolai A. Demidov
"Quartz" Research and Production Association, Gorkii, USSR

Edward M. Mattison and Robert F. C. Vessot
Smithsonian Astrophysical Observatory, Cambridge, Massachusetts, USA

David W. Allan
National Institute of Standards and Technology, Boulder, Colorado, USA

Gernot M. R. Winkler
United States Naval Observatory, Washington, D.C., USA

ABSTRACT

The frequencies of Soviet- and U.S.-built hydrogen masers located at the Smithsonian Astrophysical Observatory and at the United States Naval Observatory (USNO) were compared with each other and, via GPS common-view measurements, with three primary frequency-reference scales. The best masers were found to have fractional frequency stabilities as low as 6×10^{-16} for averaging times of approximately 10^4 s. Members of the USNO maser ensemble provided frequency prediction better than 1×10^{-14} for periods up to a few weeks. The frequency residuals of these masers, after removal of frequency drift and rate of change of drift, had stabilities of a few parts in 10^{-15}, with several masers achieving residual stabilities well below 1×10^{-15} for intervals from 10^5 s to 2×10^6 s. The fractional frequency drifts of the 13 masers studied, relative to the primary reference standards, ranged from -0.2×10^{-15}/day to $+9.6\times10^{-15}$/day.

INTRODUCTION

A welcome consequence of *glasnost*, the Soviet movement to openness, has been the recent availability of Soviet-built hydrogen masers for testing in the United States. In September 1990, two atomic hydrogen masers built by the Gorkii Instrument-Making Research and Development Institute were shipped to the Smithsonian Astrophysical Observatory (SAO) for comparison with U.S.-built masers and with time scales throughout the world. This unprecedented event was a result of discussions among officials of the U.S. National Institute of Standards and Technology (NIST), the Soviet "Quartz" Research and Production Association, and SAO.

Because of the previous scarcity of information on Soviet masers, the initial and primary interest of the comparisons was on the performance of the Soviet masers; however, for two reasons the scope of the work expanded to include other frequency standards. First, the frequency of a clock cannot be evaluated in isolation, but must be measured relative to accepted primary references; thus it was important to compare the masers at SAO with international time scales. Second, the use of common-view Global Positioning System (GPS) comparisons made it possible to include in the study an ensemble of nine hydrogen masers located at the United States Naval Observatory (USNO). In addi-

tion to being used to extend the TAI time scale over the period of observation, these masers represent a cohort of state-of-the art frequency standards whose performance has not previously been reported on. Thus we have evaluated a substantial number of hydrogen masers produced by manufacturers worldwide.

MASERS STUDIED

Four of the masers under study were located at the SAO Maser Laboratory. Two of these, serial numbers P13 and P26, are model VLG-11 masers built by the SAO Maser Group. The Soviet masers[1,2] at SAO were a model Ch1-75 active maser and a model Ch1-76 passive maser[3]. All masers other than Ch1-76 were active oscillators. Maser Ch1-75 is equipped with an autotuning system designed to stabilize the resonance frequency of the maser's microwave cavity, and thus reduce frequency variations due to cavity pulling. The autotuner, which was operated during part of this study, employs linewidth modulation by means of alternation of the internal magnetic field gradient at intervals of 100 s; a high-stability signal from another maser is used as a reference for the system. Masers P13 and P26 do not use cavity autotuners.

Nine masers at the USNO were studied. Three were SAO VLG-11 masers, serial numbers P18, P19, and P22; two were SAO VLG-12 masers[4], numbers P24 and P25; and four were commercial masers[5], serial numbers N2, N3, N4, and N5.

The masers were compared with each other and with three primary time scales, TAI, NIST(AT1), and UTC(PTB). TAI (International Atomic Time) is maintained by the Bureau International des Poids et Mesures (BIPM) in Sevres, France; it incorporates time and frequency data from about 180 clocks located in more than 50 standards laboratories throughout the world. NIST(AT1) is an unsteered, unsyntonized cesium-generated time scale maintained by the NIST Time and Frequency Division, Boulder, Colorado. Its generating algorithm, AT1, is optimized for frequency stability and minimum time prediction error. UTC(PTB), generated at the Physikalische-Technische Bundesanstalt in Braunschweig, Germany, is controlled by PTB primary cesium standard Cs-1.

TIME AND FREQUENCY COMPARISON SYSTEMS

Several time and frequency comparison systems were employed to link the masers and the time scales, and to provide measurements of frequency stability over both short and long time spans.

Three systems were used at SAO to compare the masers located there (Fig. 1). Frequency difference measurements for intervals of 0.8 s and longer were made with SAO's beat-frequency measurement facility, which permits two or three masers to be compared simultaneously. The masers' frequency synthesizers are offset from one another, and their receiver output signals are multiplied to 1.2 GHz and mixed in highly isolated double-balanced mixers. The periods of the resulting beat signals are measured by a three-channel, zero-deadtime counter and stored in a computer. Typically the frequency synthesizers are offset from one another by approximately 1.4 Hz at 1.42 GHz; after division to the 1.2 GHz comparison frequency, the beat frequency is approximately 1.18 Hz, corresponding to a beat period of approximately 0.84 s. When three masers are compared using

this system, one synthesizer is set approximately 1.4 Hz higher than the second, and the third approximately 1.4 Hz lower; thus the beat frequencies between the first and second masers and between the second and third masers are approximately 1.2 Hz, while the beat frequency between the first and third masers is approximately 2.4 Hz.

A second comparison system used at SAO is a time-difference measurement system[6] (TDMS). This system, which does not require synthesizer offsets, permits simultaneous phase comparisons of up to 24 clocks. For averaging times greater than roughly 10^4 s its measurement noise is below typical maser frequency instability, making it suitable for long-term comparisons.

In addition to comparisons by the TDMS, the relative phase of the Soviet masers was measured with the masers' one-pulse-per-second (1 pps) outputs. The time delay between the 1 pps signals was measured by a commercial time-interval counter and by a counter incorporated in Ch1-75.

The masers at SAO were compared with the external time scales by means of GPS common-view measurements. Throughout the observation period, Ch1-75's 5 MHz output provided the frequency reference for a GPS receiver located at SAO that was monitored via modem by NIST. These measurements related Ch1-75 to NIST's AT1 time scale; the measurements at SAO between Ch1-75 and the other masers at SAO then permitted comparison between the other masers and NIST(AT1).

NIST also carried out GPS common-view measurements with PTB and USNO (not indicated in Fig. 1). The USNO data linked the other clocks (at SAO, NIST, and PTB) to TAI and, by means of a TDMS at USNO, to the individual masers at USNO.

At the time the calculations reported here were made, TAI time was not available over the entire observation period; as a consequence we extrapolated TAI forward by means of hydrogen masers at USNO. To do this we characterized the masers at USNO in terms of their frequency drift and rate of change of drift relative to TAI over several months prior to modified Julian date (MJD) 48189, the last date for which TAI was available. The mathematical models used are given in Appendix A. The predicted times for the four most stable masers (N2, N4, P24, and P25) were then calculated forward to MJD 48215 using the models, and the average time was taken as representative of TAI for that period.

MEASUREMENT PROCEDURE

The Soviet masers were delivered to SAO on 24 September 1990. After they were installed in the Maser Laboratory's clock room and all of the masers had time to equilibrate, initial measurements were made from 28 September to 7 October to assess the masers and the measurement systems.

Formal measurements were carried out from 7 October to 28 November (MJD 48171 to 48223). Ch1-75's autotuning system, which is designed to improve its long-term frequency stability, was operated from 7 October to 16 November (MJD 48211). From 16 November to 28 November frequency comparisons were made with Ch1-75's autotuner off.

During the observation period the TDMS at SAO measured and recorded the phase of the masers at SAO at intervals of 500 s. The SAO beat comparison system measured the 0.84-s beat periods and calculated Allan deviations for averaging intervals of 0.84 s and longer; the beat period measurements were averaged in groups of 10 (84 s) and stored for later processing. The time interval between the Ch1-75 and Ch1-76 1-pps signals was recorded continuously on a chart recorder and measured digitally once per day. Both the TDMS and the beat system were interrupted occasionally for data backup and because of power-line spikes and software errors.

FREQUENCY VARIATION AS A FUNCTION OF TIME

The frequency behavior of clocks can be characterized by graphing pair-wise frequency differences as a function of time, and by plotting the Allan deviation, $\sigma_y(\tau)$, as a function of averaging interval τ. Figure 2 shows the time variation of Ch1-75's frequency against the primary frequency reference scales NIST(AT1), UTC(PTB), and TAI. The data are Kalman-smoothed estimates from GPS common-view measurements among the standards laboratories and SAO. Respective common-view measurement noises were 0.8 ns for TAI, 3 ns for UTC(PTB), and 2 ns for NIST(AT1). As discussed above, the TAI data were extrapolated forward by means of the masers at USNO. The general trends of Ch1-75 against the three time scales are consistent, indicating that the major frequency variations are due to Ch1-75 and that the scales are in good long-term agreement with one another.

NIST(AT1) was used as the independent standard frequency reference for estimating the frequency drifts of the masers at SAO. The frequency stability of NIST(AT1) is better than 10^{-14} for integration times of interest for this paper; its average frequency drift over the past few years with respect to either TAI or UTC(PTB) has been less than 1×10^{-16}/day. Annual variations of a few parts in 10^{14} have been observed between NIST(AT1) and UTC(PTB) or TAI. The source and cause of these variations have been studied but are not understood[7,8]. For the present work, the frequency drift of NIST(AT1) was estimated versus TAI and UTC(PTB) for the periods over which data were available and that best corresponded to our measurement period; these were MJD 48172 to 48215 for TAI (using the masers at USNO for extrapolation) and MJD 48172 to 48222 for UTC(PTB). Unfortunately, our measurements occur during what appears to be a period of steep annual frequency variation. The frequency drift of NIST(AT1) relative to TAI during the observation period was $+2.1\times10^{-16}$/day, and relative to UTC(PTB) was $+2.3\times10^{-16}$/day.

The frequencies of the masers at SAO against NIST(AT1) are shown in Fig. 3; their drift rates relative to NIST(AT1), calculated by means of linear regressions on the frequencies over the entire observation period, are given in Table 1. The Ch1-75–NIST(AT1) frequency difference was obtained from the GPS common-view measurements. The frequencies of P13 and P26 relative to NIST(AT1) were then calculated using the frequency differences between those masers and Ch1-75 measured by the SAO beat frequency measurement system; the values plotted represent one-hour averages observed once per day. Daily measurements of the Ch1-75–Ch1-76 time difference yielded the data for Ch1-76. The frequency excursions and subsequent recoveries seen in Fig. 3 for P13 and P26 at MJD 48201 were due to a two-hour power failure that affected those masers but not Ch1-75 or

Ch1-76. With the exception of the P13 and P26 excursions on MJD 48201, fluctuations that correlate among the data for Ch1-76, P26, and P13 are probably due to the GPS common-view time transfer or to NIST(AT1); such fluctuations, which appear across the data length, amount to roughly 1-2 ns per day, which is consistent with the level of previously observed common-view time transfer noise. The fluctuations are absent from the Ch1-75 graph because Ch1-75 was the clock controlling the GPS receiver, and its data were Kalman filtered with respect to NIST(AT1). The correlated fluctuations are difficult to identify in Ch1-76's frequency graph prior to MJD 48200, probably because they are obscured by Ch1-76's frequency variations.

Table 1
Drift rates of masers at SAO vs. NIST(AT1)

Maser	Frequency Drift (1×10^{-15}/day)
Ch1-75	–8.6
Ch1-76	–3.1
P13	+0.7
P26	+9.6

The frequency of Ch1-75 versus P26 is shown in Fig. 4. A frequency offset of roughly 1×10^{-11} has been removed for convenience in plotting. The two spikes at MJD 48215 and MJD 48221, which correspond to phase jumps of about 0.5 ns, were apparently caused by the time-difference measurement system; they did not appear in data from the beat-frequency system. Ch1-75's autotuner, which operated until 16 October (MJD 48211), clearly adds short- and intermediate-term frequency instability. Within the confidence of estimate of the data of Figs. 2–4, Ch1-75's drift seems unaffected by the operation of its autotuner. The two-month test is probably too short to establish with confidence the autotuner's long-term effect on Ch1-75's frequency.

FREQUENCY STABILITY

Short-term frequency stability measurements of the active masers at SAO, as expressed by the Allan deviation $\sigma_y(\tau)$, were obtained from the beat-frequency measurements system and are shown in Fig. 5. The measure used in Fig. 5 is the reduced Allan deviation, $\tilde{\sigma}_y(\tau) \equiv \sigma_y(\tau)/\sqrt{2}$, for the frequency pair. If two oscillators contribute equal amounts of noise, then $\tilde{\sigma}_y(\tau)$ represents the frequency variability of the individual oscillators; if, however, one oscillator contributes considerably more noise than the other, as in the case of Ch1-75 with autotuner on, then $\sigma_y(\tau)$, rather than $\tilde{\sigma}_y(\tau)$, represents the variability of the noisier oscillator. Figure 5 gives $\tilde{\sigma}_y(\tau)$ for the frequency differences P26–Ch1-75 and P26–P13 over two nine-day intervals. During interval A, 11 October – 20 October (MJD 48175 – 48184), Ch1-75's autotuner was operating; during interval B, 16 October – 25 October (MJD 48211 – 48220), the autotuner was turned off. By the beginning of interval B, P13 and P26 had restabilized following the power interruption on 6 November. Curves *a* and *b* in Fig. 5 show the stability of P26 vs Ch1-75 with the autotuner on and off (during intervals A and B), respectively. A relative drift of 1.68×10^{-14}/day has been removed from curve *a*, and a drift of 1.24×10^{-14}/day from curve *b*. The peak in curve *a* at approximately τ=100 s probably results from

modulation of Ch1-75's internal magnetic field at a period of 100 s for the autotuner. Curve *c* is the reduced Allan deviation for P26–P13 during interval 3; a relative drift of 6.45×10^{-15}/day has been removed. The drift-removed stability of P26–P13 during interval A was not significantly different from curve *c*. The effect of removing frequency drift is seen by comparison with curve *d*, which gives the reduced Allan deviation for P26–P13 without drift removal. Curves *b* and *c* show that the drift-removed stability levels of the Soviet (autotuner–off) and SAO masers are comparable for averaging times between a second and a day.

Comparison of $\tilde{\sigma}_y(\tau)$ with the line segments included in Fig. 5 shows that $\tilde{\sigma}_y(\tau)$ [and thus $\sigma_y(\tau)$] is proportional to τ^{-1} for $\tau<100$ s and to $\tau^{-1/2}$ for $100<\tau<7\times10^3$ s; as predicted theoretically[9], this behavior is due to additive noise in the maser receivers and noise within the atomic linewidth, respectively. For $\tau>10^4$ s, $\tilde{\sigma}_y(\tau)$ is proportional to τ^1 for P26–P13 with drift not removed; this form of $\tilde{\sigma}_y(\tau)$ is characteristic of linear frequency drift. In the case of the drift-removed data, portions of the graphs are approximately proportional to $\tau^{1/2}$, which is identified with random walk of frequency; this behavior may result from the simultaneous action of several quasi-independent frequency-determining mechanisms in the masers.

The long-term frequency stability of Ch1-75 against the three time scales, with drift removed, is shown in Fig. 6. (In Figs. 6–11 the Allan deviation $\sigma_y(\tau)$ is used, rather than the reduced deviation $\tilde{\sigma}_y(\tau)$.) The data for AT1 and PTB cover the entire observation period, MJD 48171 to 48223, while the TAI values cover MJD 48171 to 48215. Due to the Kalman filtering, the values for 1- and 2-day averaging intervals are artificially low, by perhaps a factor of 2; however, the data for $\tau\geq4$ days are representative of the performance of the clocks. That the drift rate for Ch1-75 against TAI is greater than the rates against AT1 and PTB may be due to the fact that the shorter time span over which the TAI data were available corresponded to an interval during which Ch1-75's drift was greater than its average value for the entire observation period. The Allan deviation of the three scales relative to one another is shown in Fig. 7. The stability of AT1 versus TAI, in particular, is considerably lower than the values in Fig. 6, indicating that the latter values represent the stability of Ch1-75.

The long-term stabilities of the clocks at SAO are shown in Fig. 8. The data were obtained from the TDMS at SAO, with interruptions spanned by linear interpolation. The calculations for Ch1-75–P13 and for P26–P13 are based on frequency data obtained from MJD 215.8 to 221.7; those for Ch1-75–P26, on data taken from MJD 211.5 to 223.7; and those for Ch1-75–Ch1-76, on data taken from MJD 204.9 to 223.8. Thus the plots not involving Ch1-76 represent data taken with Ch1-75's autotuner not operating, while the Ch1-75–Ch1-76 plot includes data with Ch1-75's autotuner both on and off; however, because Ch1-76's stability is considerably less than that of Ch1-75, $\sigma_y(\tau)$ for the Ch1-76–Ch1-75 frequency difference is not significantly affected by the operation of Ch1-75's autotuner.

Figures 9 and 10 show the stabilities of the individual masers at USNO in the ensemble used to extrapolate TAI. $\sigma_y(\tau)$ was obtained for each clock from an N-cornered hat calculation from the Allan variance of the frequency differences with frequency drift and rate-of-change of drift removed. The stability of a cesium clock with little frequency drift is included for comparison. Although the N-cornered hat procedure is theoretically exact for population variances, in practice it yields differences

between pairs of sample variances observed over finite times; consequently, the calculated variances σ_y^2 for the best clocks of the group can (randomly) be negative numbers, which are omitted in Figs. 9 and 10. The least stable clocks of the group are well characterized, while for the most stable clocks, N2, N4, N5, P24, and P25, one can say only that their stabilities are below 1×10^{-15} for intervals from 10^5 s to 3×10^6 s.

DISCUSSION

From the observations presented here, it is apparent that maser frequency stabilities of a few parts in 10^{15} and below are achieved for averaging intervals from one day to about two weeks, levels that are an order of magnitude lower than those attained perhaps ten years ago. These stabilities require removal of frequency drift and, in some cases, rate of change of drift.

The frequency prediction capability of hydrogen masers seems to be somewhat better than 10^{-14} for extrapolation over a few weeks. In our case, the forward prediction from MJD 48189 to 48218 showed modelling errors of less than 1×10^{-14}, and for some masers a few parts in 10^{15}. The prediction errors were calculated by subtracting the frequency residuals between different pairs of USNO masers after removing their respective parameterized models. Figure 11 shows the residual errors between four pairs of masers, expressed in terms of $\sigma_y(\tau)$ calculated from MJD 48172 to 48218; these results demonstrate unprecedented oscillator predictability.

The time scale instabilities evident in Fig. 7, of about 10^{-14} at one day intervals, are due principally to the cesium standards involved. Our drift-removed data show about an order-of-magnitude advantage of hydrogen masers over cesium devices at integration times of one day.

ACKNOWLEDGEMENTS

We thank the Frequency and Timing Engineering group of the NASA Jet Propulsion Laboratory for enabling us to include maser P26 in this comparison; Mr. Lee Erb for the loan of measurement equipment; Dr. Marc Weiss, Mr. Tom Weissert, and Ms. Trudi Peppler (NIST) and Dr. Lee Breakiron (USNO) for assistance with data analysis; and Mr. Richard Nicoll and Mr. Donald Graveline (SAO) and Mr. Sergei Kozlov and Mr. Gherman Chernov ("Quartz" Research) for assistance with maser setup and operation. We are grateful to the Smithsonian Institution for its support of the activity at SAO.

APPENDIX A -- EXTRAPOLATION OF TAI TIME SCALE

At the time this analyis was done, the time differences between UTC(USNO) and TAI were available only through MJD 48189. The TAI time scale was represented over the entire observation period (MJD 48172 to 48215) by modelling hydrogen masers at USNO over periods prior to MJD 48189 during which they were well characterized against the known values of TAI, and extending the models to MJD 48215. Since each of the masers is measured against UTC(USNO), they can be related to TAI through the TAI–UTC(USNO) time difference data. Each maser was modelled by a three-parameter expression,

$$y(n) = [C_0 + C_1\, n + C_2\, n^2] \times 10^{-15} \qquad (1)$$

Here $y(n) = y_{maser} - y_{TAI}$ is the normalized frequency offset of the maser from TAI at day n, where n is the day count relative to the reference date given in Table 2. C1 is the maser's frequency drift rate, and C2 its rate of change of frequency drift, relative to TAI. N in Table 2 is the number of frequency measurements, each representing a 10-day average, used to establish the coefficients from BIPM circular-T 10-day data. Masers N2–N5 use cavity autotuning systems that employ modulation of the cavity resonance frequency[5]; masers P18–P25 do not use cavity autotuning.

Table 2
Parameters of model for USNO masers vs. TAI

Clock	Reference Date	C_0	C_1	C_2	N	Rms of residuals (10^{-15})
N2	48024	–1199.1	1.21	–0.003	34	15.5
N3	48159	–1190.1	0.01	----	6	3.0
N4	48174	550.5	–0.20	----	4	2.9
N5	48164	212.7	0.16	----	6	11.0
P18	48039	–82.2	0.62	----	31	12.3
P19	48099	–9.8	2.15	–0.004	19	8.8
P23	48129	–125.3	1.62	–0.008	13	11.1
P24	48029	7684.0	3.20	–0.006	33	15.1
P25	48129	784.4	5.12	–0.012	13	9.6
Cs2485	48074	922.2	0.057	----	24	18.1

REFERENCES

1 B.A. Gaygerov, L.P. Yelkina and S.B. Pushkin, "Metrological characteristics of a group of hydrogen clocks." *Measurment Technology* **25**, 23 (1982).

2 N.A. Demidov and A.A. Uljanov, "Design and industrial production of frequency standards in the USSR." *Proc. 22nd Precise Time and Time Interval (PTTI) Applications and Planning Meeting* (this issue) (1990).

3 A.A. Belyaev, N.A. Demidov, B.A. Sakharov, V.Yu. Maksimov, M. Yu. Fedotov, and A.E. Yampol'skii, "Ch1-76 small-size passive hydrogen frequency and time." *Measurement Techniques* **30**, 767 (1987).

4 E. M. Mattison and R. F. C. Vessot, "Performance of model VLG-12 advanced hydrogen masers." *Proc. 44th Annual Freq. Control Symposium*, p. 66 (1990)

[5] H.E. Peters, H.B. Owings, and P.A. Koppang, "Atomic hydrogen masers with self auto-tune system and magnetic field cancellation servo." *Proc. 20th Annual Precise Time and Time Interval (PTTI) Applications and Planning Meeting*, p. 337 (1988)

[6] Erbtec Corporation, Boulder, Colorado.

[7] D.W. Allan, "A study of long-term stability of atomic clocks." *Proc. 19th Annual Precise Time and Time Interval (PTTI) Applications and Planning Meeting*, p. 375 (1987).

[8] D.W. Allan, M.A. Weiss, and T.K. Peppler, "In search of the best clock." *IEEE Trans. Inst. and Meas.* **38**, 624 (1989).

[9] R.F.C. Vessot, M.W. Levine, and E.M. Mattison, "Comparison of theoretical and observed hydrogen maser stability limitation due to thermal noise and the prospect for improvement by low-temperature operation." *Proc. 9th Annual Precise Time and Time Interval (PTTI) Applications and Planning Meeting*, p. 549 (1977).

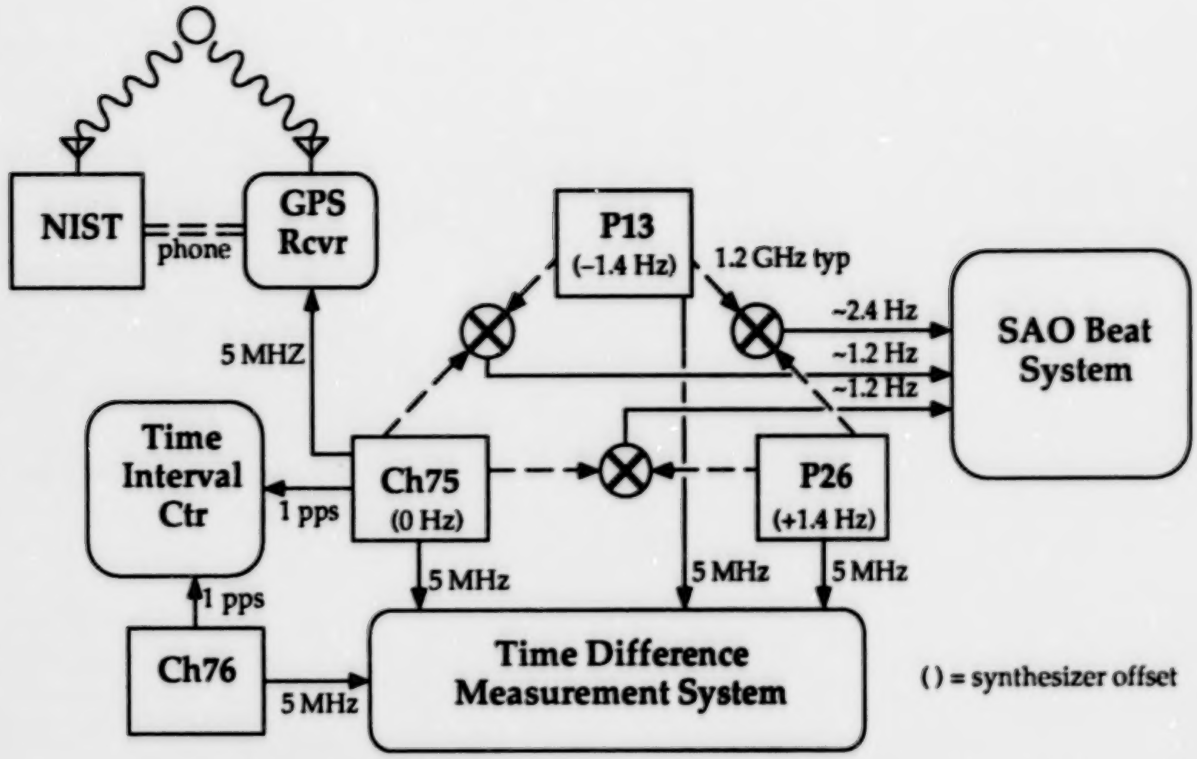


Fig. 1a. Comparison systems at SAO with Ch1-75 autotuner off

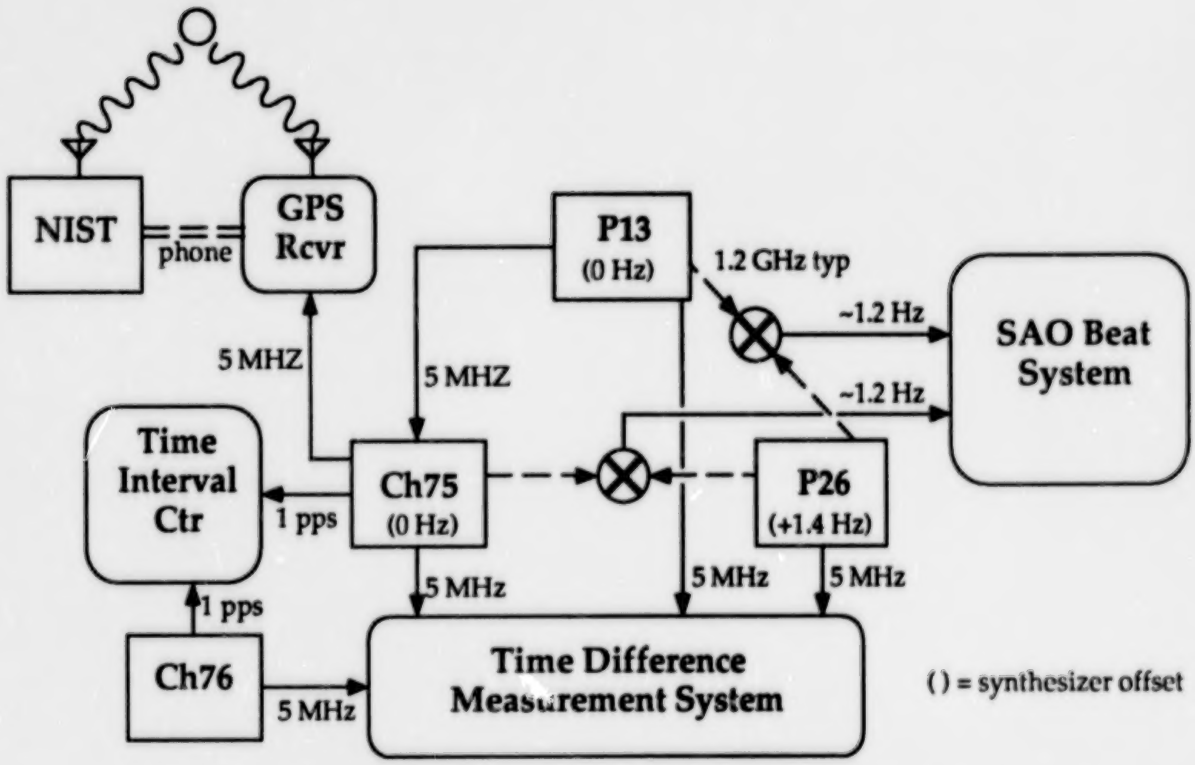


Fig. 1b. Comparison systems at SAO with Ch1-75 autotuner on

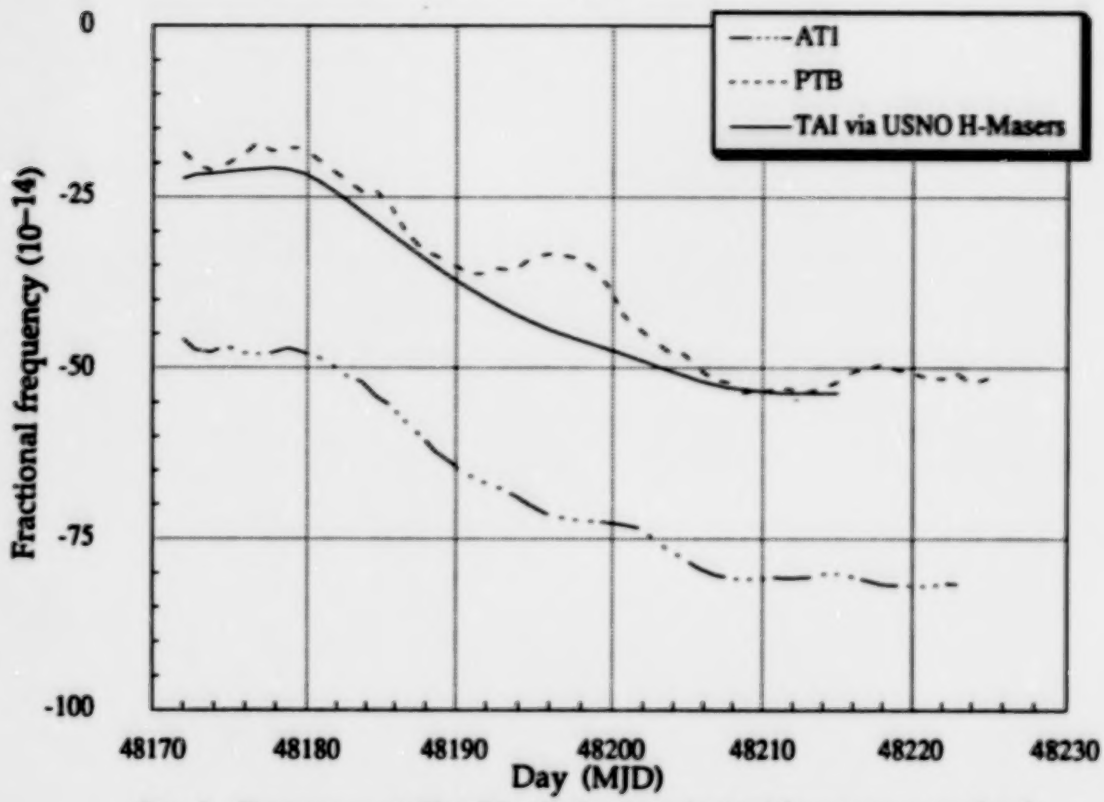


Fig. 2. Frequency of Ch1-75 relative to principal frequency standards (Kalman smoothed)

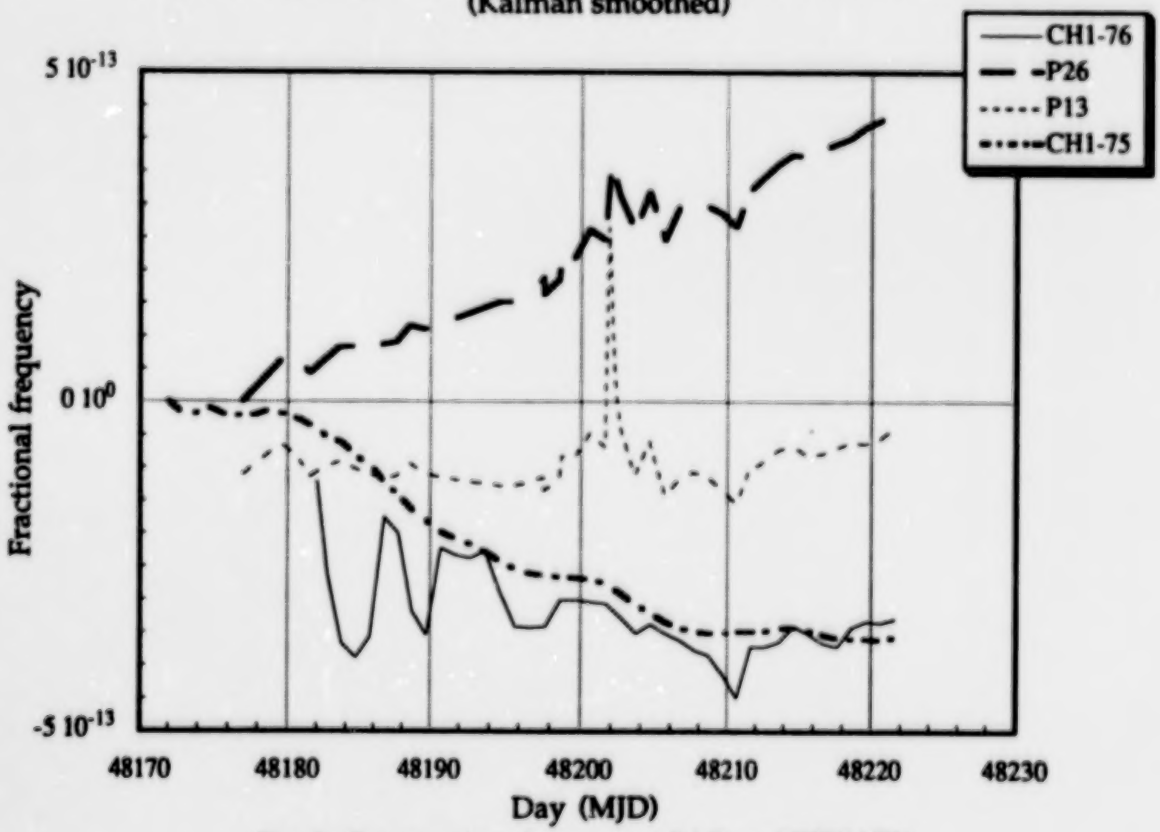


Fig. 3. Frequencies of masers at SAO vs. NIST(AT1)

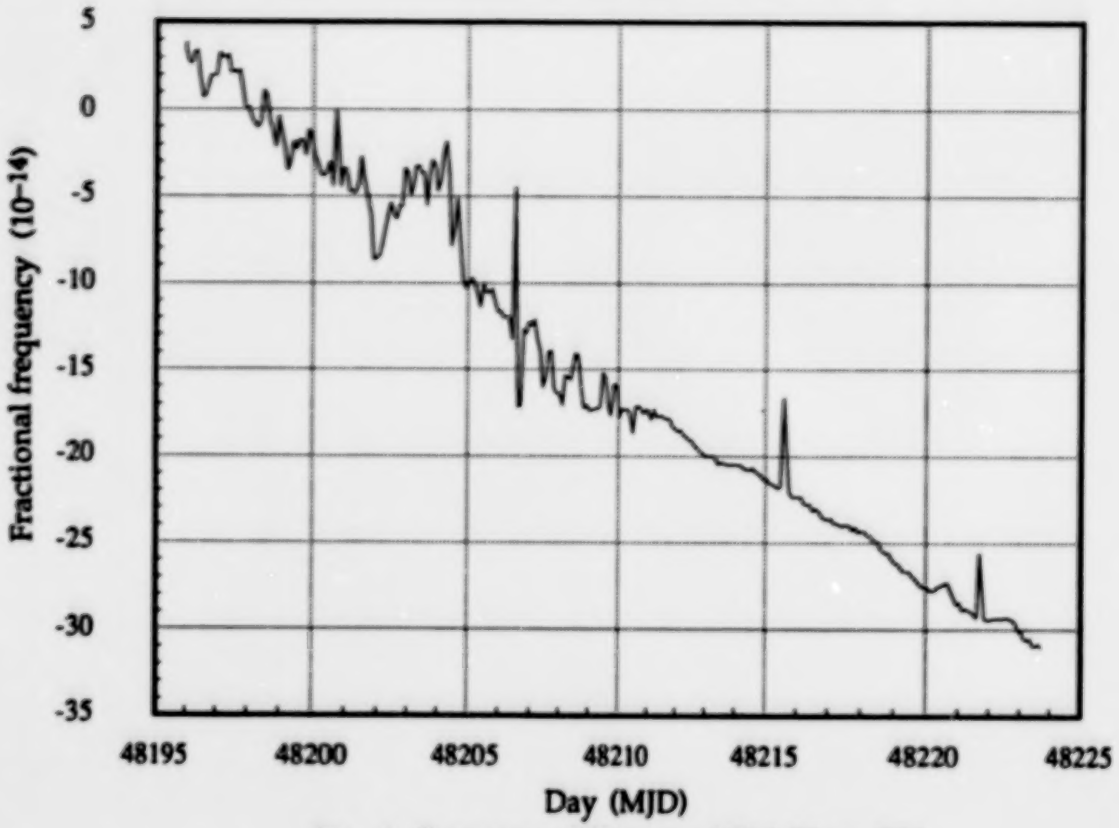


Fig. 4. Frequency difference of Ch1-75 vs. P26

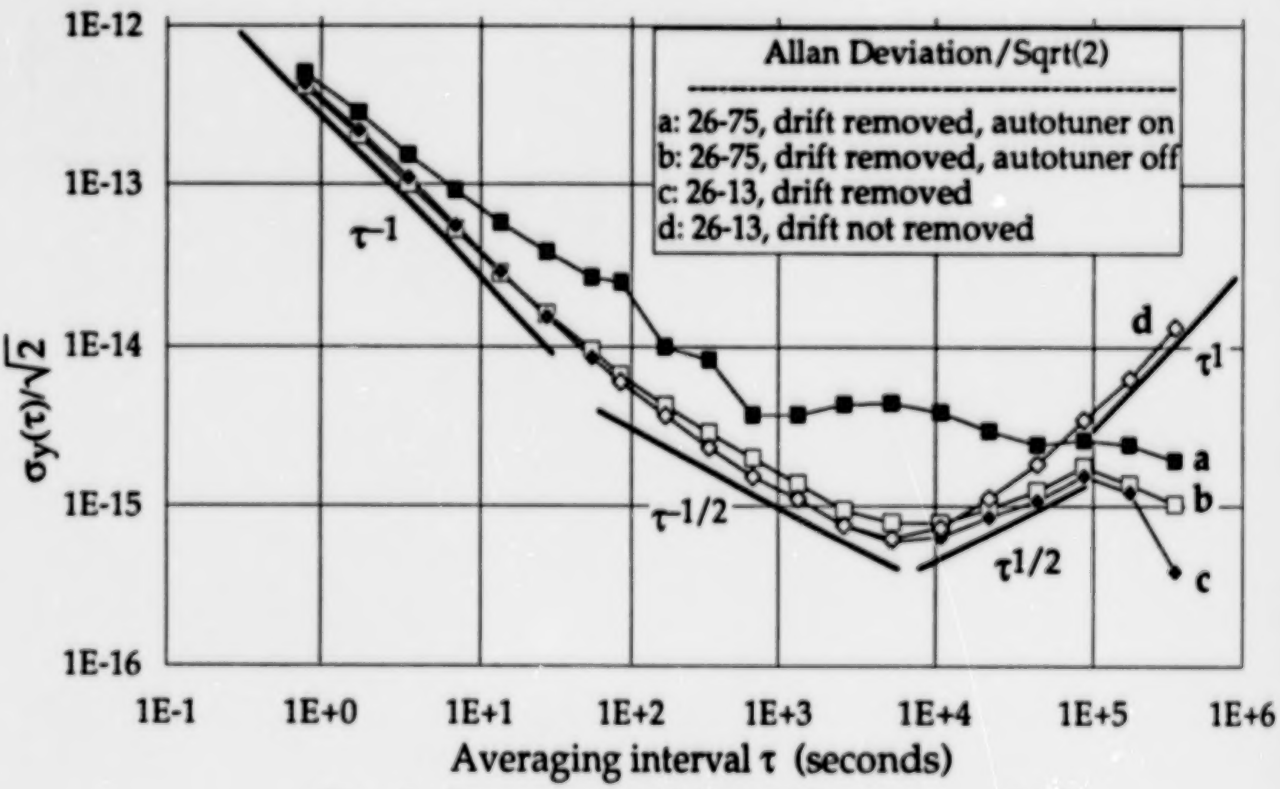


Fig. 5. Frequency stabilities of masers at SAO

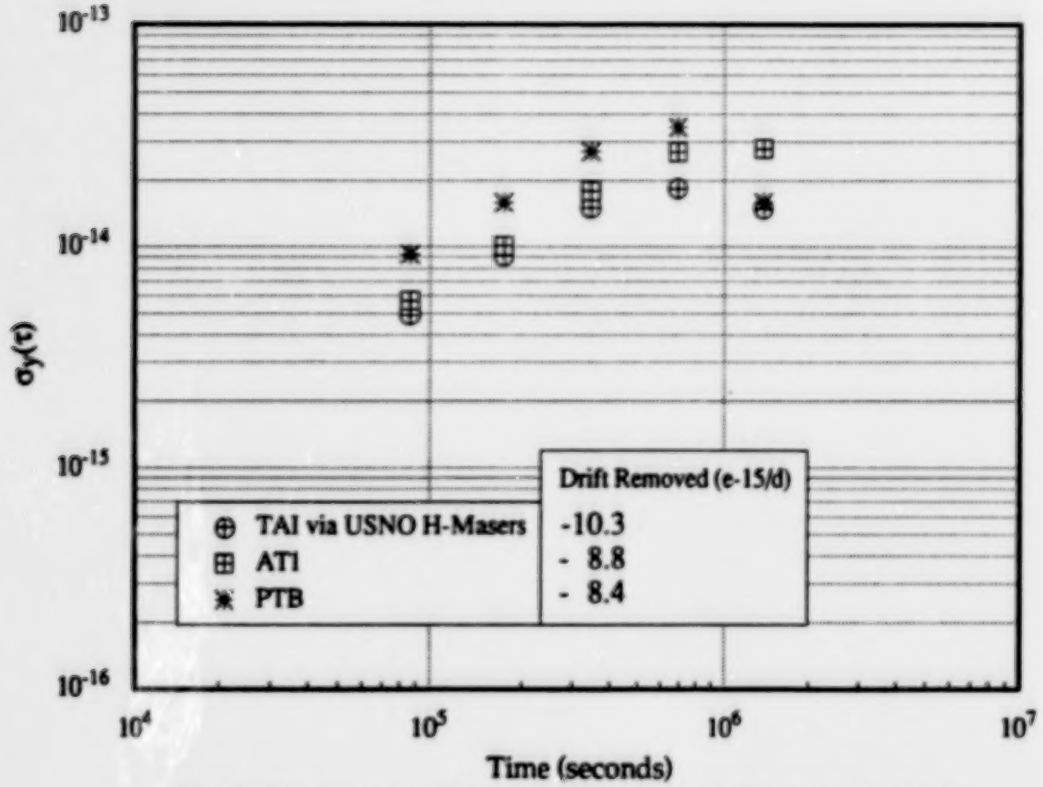


Fig. 6. Frequency stabilities of Ch1-75 vs. frequency standards (Kalman smoothed)

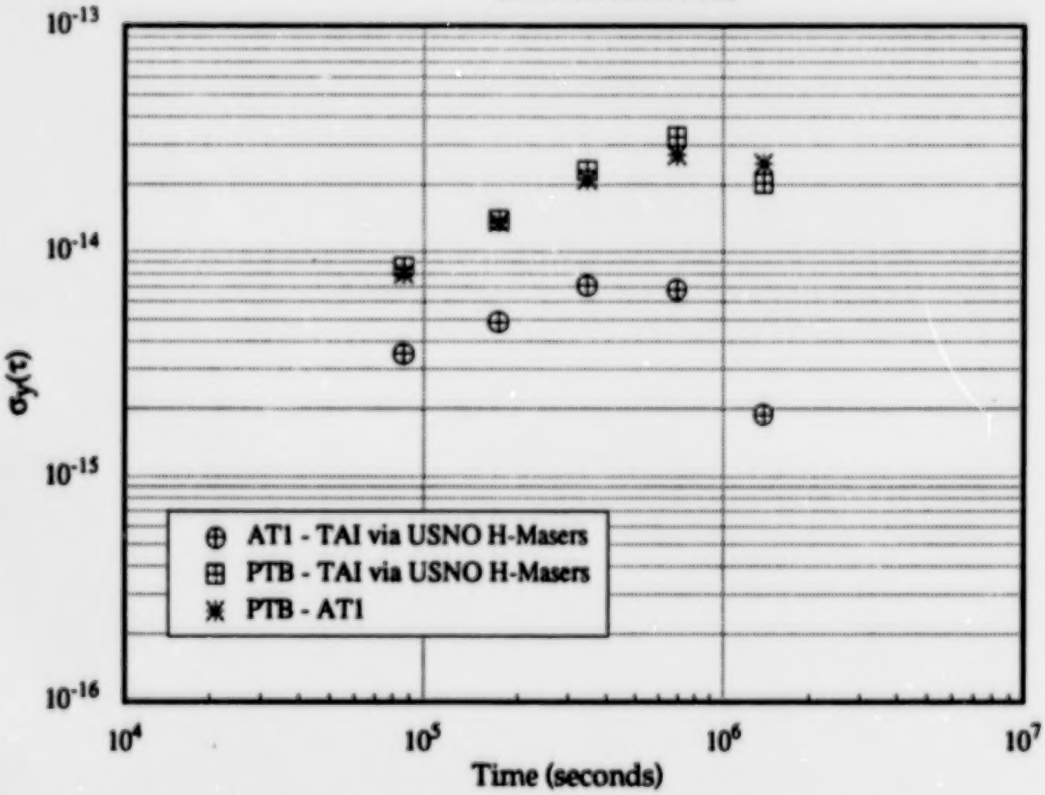


Fig. 7. Relative frequency stabilities of frequency references (Kalman smoothed)

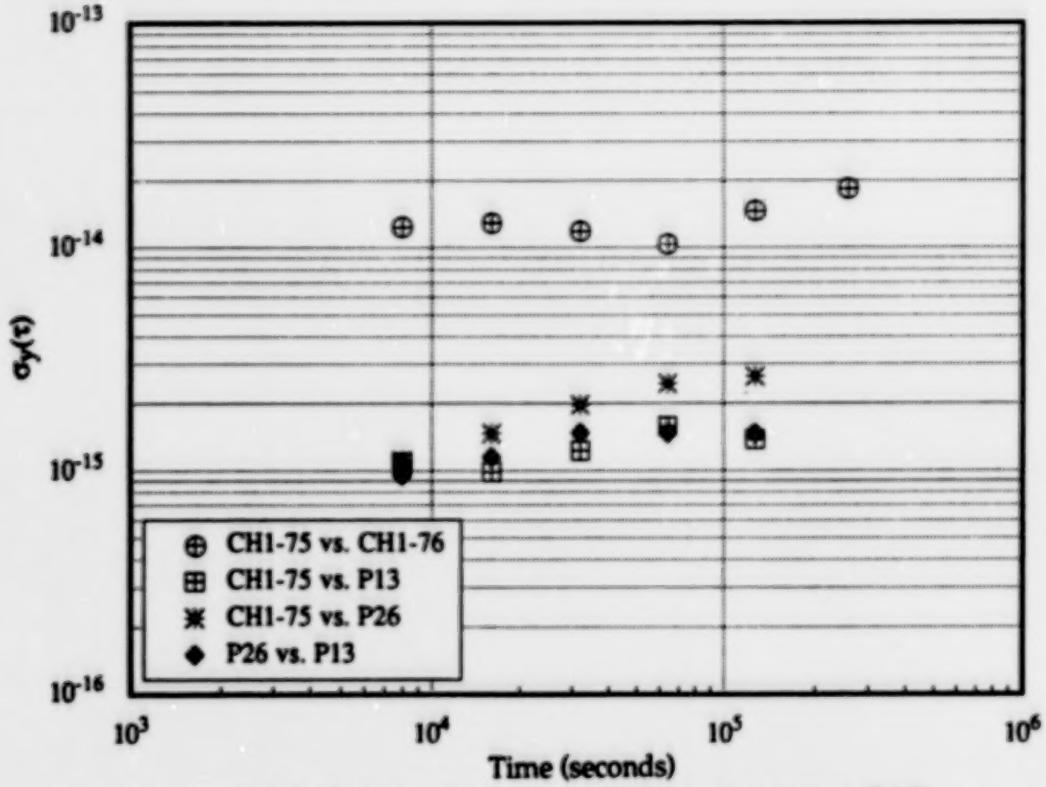


Fig. 8. Relative frequency stabilities of masers at SAO (drift removed)

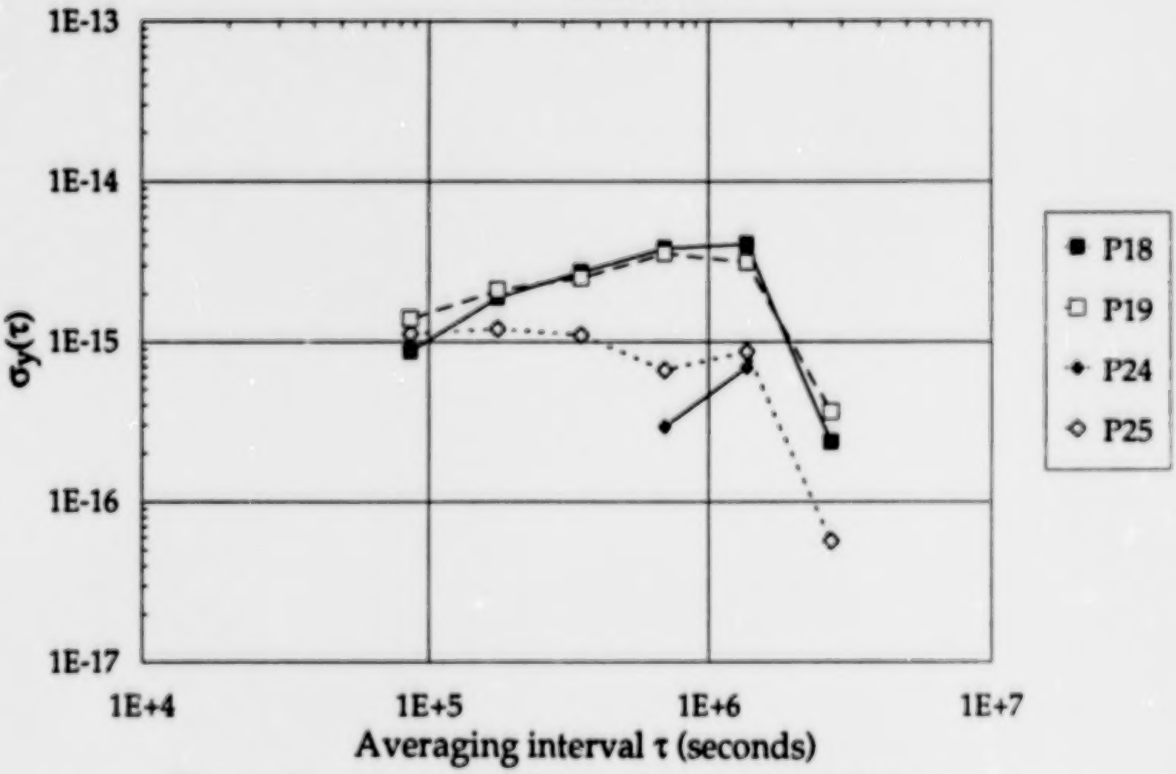


Fig. 9. Frequency stabilities of masers at USNO, from N-corner hat calculation

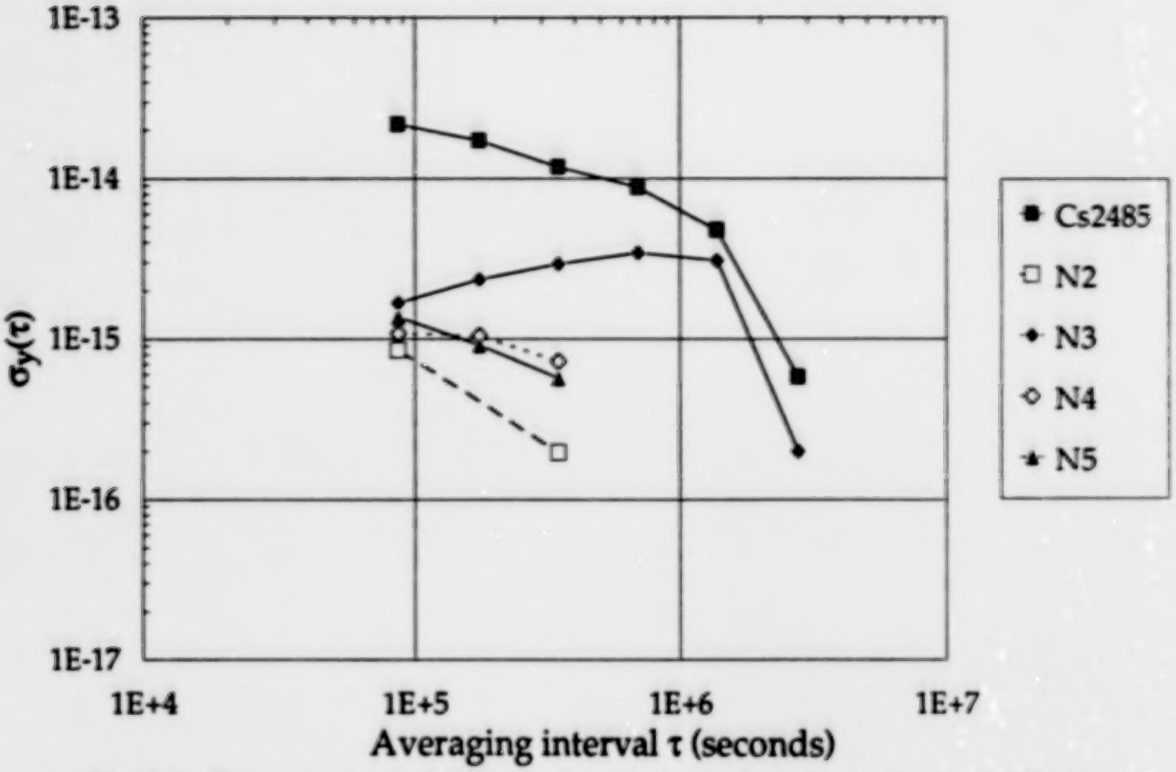


Fig.10. Frequency stabilities of masers and cesium clock at USNO, from N-corner hat calculation

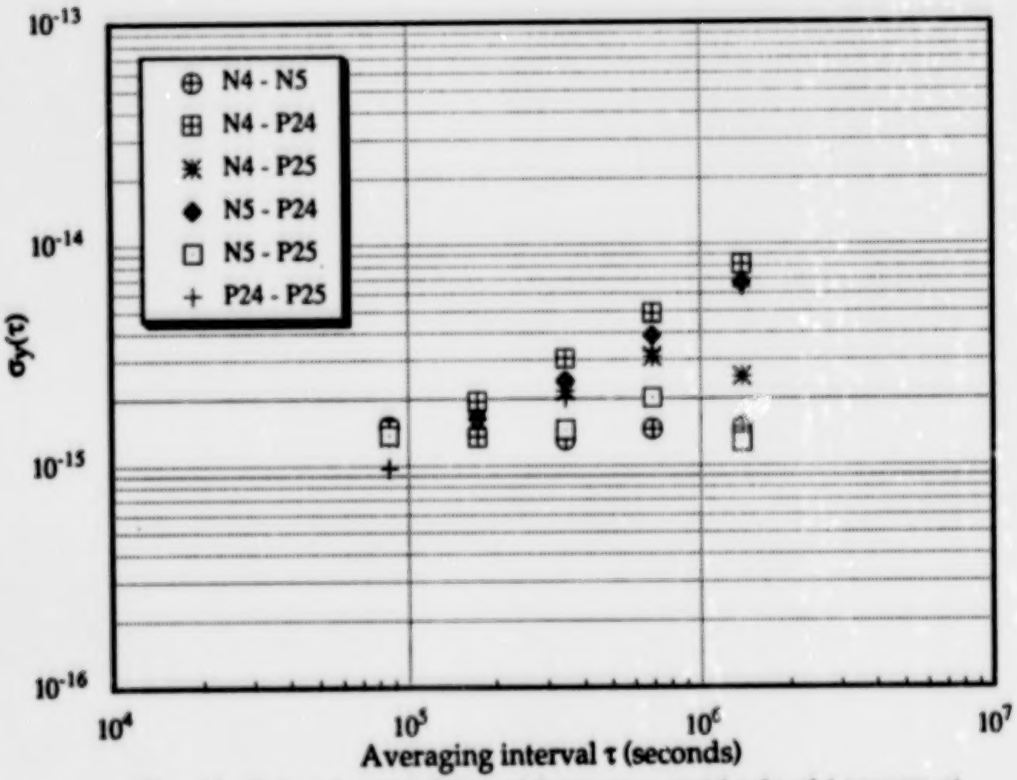


Fig. 11. Pair-wise stabilities of frequency residuals of 4 masers at USNO, with clock models removed

BLANK PAGE

THE NATIONAL- AND INTERNATIONAL-WIDE PROSPECTS OF FUTURE IMPROVEMENTS OF POSITION LOCATION AND TIME SYNCHRONIZATION SYSTEMS AND AIDS

Prof. Yuri G. Gouzhva, Prof. Boris N. Balyasnikov,
Dr. Vladimir V. Korniyenko, Irina G. Pushkina,
Prof. Valentin S. Shebshayevich
Leningrad Scientific Research Radiotechnical Institute (LSRRI), USSR

Vladimir I. Denisov "Interradionavigation" Com., Moscow, USSR
Prof. Alexander P. Reutov, USSR Ministry of Radio Industry

Abstract

The concept being designed by LSRRI of united positioning and timing service on the basis of the utilization of long-range and global radionavigation and common time systems and aids for different users is described. The estimate of proposals of its utilization on the national—as well as on international—scale is given.

1. INTRODUCTION

The main direction of Leningrad Scientific Research Radio Technical Institute (LSRRI) activities is the designing and improvement of position location and time synchronization systems and aids for different branches of national economy as well as for scientific research.

The general principle of systems and aids to be developed by LSRRI is a generation and/or utilization of high-precision position and time data for long-range and global radionavigation, synchronization of remote clocks and other goals of this kind.

The most significant directions of LSRRI's activities comprise:

- designing of equipment for transmitting and monitor-and
- correction stations and other aids of ground-based long-range and global pulse-phase and phase radionavigation systems;
- creation of aids for State System of Common Time and Standard Frequencies, including monitoring sites of different accuracy classes for specific users;
- development of quartz oscillators and atomic frequency standards with optical (laser) pumping on the basis of atomic beam discriminators and hydrogen masers;
- designing of on-board equipment and ground-based aids for GLONASS Satellite radionavigation system (SRNS);
- development of position-timing user equipment operating via ground-based-as well as space based systems for sea, airspace and land vehicles;
- realization of scientific researches.

2. STATE–OF–THE–ART OF SOVIET SYSTEMS AND AIDS PROVIDING POSITIONING AND TIMING SERVICE

Up to date, the task of realization of the positioning and timing service with desired performances for different platforms was being solved in the USSR on the basis of a separate development of aids for position determinations and that for time determinations. The those conditions, for position determinations was the navigation equipment being designed, and for time determinations was the timing equipment being developed. As much as no one of systems to be mentioned above enables the achievement of desired positioning and timing service, this task is solved on the basis of utilization of a system mix to be optimal for any region over a certain time interval. As far as we know, the US specialists are of the same opinion. It is proven by US Federal Radionavigation Plan.

While developing the similar program for long–term improvement of radionavigation systems and aids in the USSR, LSRRI had already in early '70 years has proposed idea about a generation of common global radionavigation field as a source of the universal position–timing data for any user with the achievement of desired values from the standpoint of accuracy, availability, reliability and integrity. This approach was developed on implementation of the concept for the common positioning and timing service. This concept has later been approved and enlarged by a series of scientific research institutes of the USSR Academy of Sciences as well as by ones of different branches of national economy.

3. MAIN CONCEPT PRINCIPLES (SUBSTANTIATION OF METHODOLOGY)

The basis of our concept of providing a joint positioning and timing service is a community of principles of position (coordinates) and time determinations and, as a consequence. a possibility to treat these determinations as being two sides of a single physical process to be connected with signal transfer and generation of corresponding data. As an example, one can use the main navigation equations connecting the increments of space coordinates with time increments to be correspondent with signal transfer between the points to be compared. In such a case, navigation data are determined as being data referring to relative coordinates of bodies (i.e. sets of material points) within a four–dimensional space-time variety. In its turn, the relative coordinates are the functions of mass center mutual location and mutual orientation of corresponding axes as well as of its derivatives of different degrees. Under these conditions, in order to determine the space–time interval setting a relative position of four dimensional points or, in other words, to compare the events to be taken place at those points, it is necessary to use a material data bearer moving within a four dimensional framework. While providing the data relating to origins of frames of reference, the radio signals appear to be such a bearer. The other performances of navigation–time data depend on metrical properties of frame wherein the signal moves. Such an approach enables to formulate a general definition of any positioning and timing service as a common set of space–remote technical aids and natural space sources to be used for generation of corresponding data.

4. FUTURE NATIONAL–WIDE POSITIONING AND TIMING SERVICE (PRINCIPLES OF ORGANIZATION AND OPERATION)

The Unified State System of Positioning and Timing Service (USS PTS) will be implemented on the basis of existing and deploying ground-and space-based navigation and timing systems and aids by means of institutional and methodical coordination of operation of such aids with application of equipment to be designed for solving the user problems. This is equally valid for the equipment of Joint position-timing complexes.

A specific feature of such a system is its openness, permitting a possibility of including as well as exclusion of certain aids. The other important feature is a possibility of generation of unified positioning-timing basis providing a performing of determinations in the unified frame of reference with a possible gradation in accordance with accuracy classes and with a subsequent transition to any frame of reference to be convenient.

From the organizational standpoint, USS PTS might consist of four subsystems as follows:

- fundamental bases of space and time frame of reference;
- generation and transfer of position-timing data;
- control and monitoring of system operation;
- users.

The important feature of the system to be proposed is that it isn't merely a set of technical aids or an organization operating in accordance with the set of rules to be prescribed, but that is a technical system of a top level. Such a system may be considered as a *synergetic one permitting to realize a new quality-the presentation of space-time data with ensuring the values of accuracy, availability, reliability and integrity to be necessary for defined users while solving all the problems, including specific ones.

The USS PTS implementation on the basis of RNS to be already in operation and to be deployed would enable to set in foreseeable future a global positioning-time field with accuracy level of 10m (1m locally) and synchronization error of 50ns, thus providing a possibility of solving the widest class of problems for all users, including a short-range navigation task with landing approach and landing itself.

5. PROSPECTS OF INTERNATIONAL COOPERATION WITHIN THE FIELD OF GLOBAL PTS CREATION

From our point of view, the national-wide principles of PTS organization to be considered above would be used as the basis of concept of global PTS implementation — of course, with taking into account a number of factors relating to foreign political situation, USSR and USA national priority systems, specific roles of certain regions as well as existing machineries for attainment of agreements. The advantages of an open positioning and timing service may be realized only in conditions of "open" international community, i.e. such a community wherein the relations between the countries-participants are based on the whole mutual confidence. With regard to this, how can one estimate the relations between the superpowers, the USSR and the USA, and its influence on prospects of global PTS creation?

With the beginning of current decade, the world to come in the initial period of the new non-confrontation era, but this period is complicated and contradictory, because the past tries to keep its positions and the future carries the non-predictable dangers. The nuclear arsenals lose its sense, but its improvement is going on. The space-based PTS aid that appear to be intended for the main mole on future PTS implementation on a national-wide as well as on international-wide scale were being created in the USSR and in the USA, in conditions of competition for the defense agencies with taking into account its tasks in the first place. The very concept of defense sufficiency gives today only certain quantity cut of armaments, while not providing an ending of its quality improvement. It is equally true for the supporting subsystems, including PTS aids.

In such a situation, the only possible way to overcome a distrust to be accumulated over the preceding decades of the "Cold War" is that to be based on an improvement of a machinery for generation and adoption of Joint solutions.

From our point of view, it should prefer any form of cooperation, including ramified membership in different institutions, creation of cross groups and parallel institutes, partly duplicating its functions, but permitting at the same time to achieve the best mutual understanding as a result.

At the present time, LSRRI's practical activities include examples of cooperation with the USA and Western European state agencies as well as with different companies.

The development and the substantiation of a concept with taking into account the demands of different branches of national economy as well as the needs of scientific researches are being carried on LSRRI over a series of years. In November of 1990, in Leningrad, the Fist All-Union Scientific and Technical Conference on problems relating to the common positioning and timing service was held at LSRRI. It is planned for such conferences to be the regular ones in future.

In conclusion, I would like to note that there is a sufficiently powerful factor permitting an optimistic estimate for the prospects of realization of global PTS. This factor is a belonging of such a system realizing the needs of the civilized community on a global scale to the values common to humanity and, consequently, its incontestable priority. The support of a safe operation of such a system will undoubtedly need the highest art not only with regard to scientific technical sphere, but also to human contacts. We would like to hope the good will of all participants would enable a successful solving of this problem.

GPS COMPOSITE CLOCK SOFTWARE PERFORMANCE

A. L. Satin, W. A. Feess, H. F. Fliegel, and C. H. Yinger
The Aerospace Corporation
Los Angeles, CA 90009

ABSTRACT

Computer software for ensembling all the space vehicle (SV) and ground clocks of the Global Positioning Systems (GPS) was implemented at the Master Control Station (MCS) on 17 June 1990. Improved GPS time stability and steering control are predicted. This paper assesses the perceptions of both Air Force and outside users and compares current performance to theoretical predictions.

GPS SYSTEM DESCRIPTION

The Global Positioning System is a Department of Defense space-based navigation and timing dissemination system currently under deployment. By 1993 it will consist of a constellation of 24 space vehicles (SVs) supported by a control segment (CS) that tracks the SVs with its monitor stations (MSs), determines SV ephemeris states and SV and MS clock states at the Master Control Station (MCS) and periodically uploads the SVs with predicted SV states that users require to navigate and/or determine their time. At this stage in the buildup, the constellation consists of six block I SVs and nine block II SVs. The CS MSs are located at Kwajalein Island, Diego Garcia Island, Hawaii, Ascension Island, and Colorado Springs, Colorado.

SV range measurements (i.e., pseudorange) are a function of the SV(i)–MS(j) geometric range and the phase offset between the SV(i) and MS(j) clocks, where i and j are the ith SV and the jth MS, respectively. The accuracy with which a user can navigate (i.e., determine his position and clock state) depends on the accuracy of his measured pseudorange and the accuracy of the predicted SV ephemeris and clock information generated and uploaded by the CS. The latter source of error is fundamental to GPS operation and is quantified by the User Range Error (URE). URE is defined as the difference between the range-to-a-user computed using predicted states and the "true" range-to-a-user computed using the latest Kalman estimates of ephemeris and clock. Operationally, the MCS computes UREs every 15 min (the Kalman filter update cycle) for each SV, taking a root sum of squares (RMS) of individual UREs to a fixed set of grid locations on the earth that have visibility to the SV.

The CS, by solving for SV and MS clock phase and frequency states from the pseudorange measurements, effectively synchronizes the system to GPS time. Originally the GPS time reference was taken to be one of the MS clocks. States for that MS (i.e., the master MS) were defined to be fixed at zero and, hence, were not included in the filter state vector. Clock state offsets estimated by the filter were then relative to master clock (GPS) time. When the filter is allowed to estimate all clock states (i.e., including states for what used to be the master MS), the configuration is called a composite or ensemble clock system. Since June of this year, the time reference for the system clocks (i.e., GPS time) has been a composite clock.

Since the MCS has so many SV states to estimate (11 per SV x 24) it was decided long ago to "partition" the SVs among several filters each capable of handling up to six of them and each containing, of course, the complete complement of MS states: 3 per MS x 4 for a master clock configuration and 3 per MS x 5 for the composite clock case.

COMPOSITE CLOCK IMPLEMENTATION AND THEORY

When additional states are added to the Kalman filter, for what was the master MS, the GPS system becomes explicitly unobservable. This is because a constant bias shift in all clock phase states would not affect pseudorange and hence, would be unobservable to the filter. The existence of this unobservable component of state causes the clock phase covariance matrix to grow linearly with time even though the system is completely stable with well behaved filter gains. See Reference 1 for further discussion of these characteristics. Since a growing covariance matrix will eventually cause numerical problems, a method for reducing the covariance matrix without degrading filter performance was introduced. The method chosen was reduction via pseudomeasurement update (Reference 2).

Covariance Reduction

This update takes the standard Kalman form

$$P' = P - [PH^T(HPH^T + R)^{-1}]\, HP \qquad (1)$$

where P′ is the covariance matrix resulting from the update (i.e., the reduced covariance matrix) and R is the pseudomeasurement noise variance. The matrix P in Equation 1 is the full n x n covariance matrix of ephemeris and clock states for the SVs and MSs of a particular partition. All filter partitions undergo independent covariance reductions every filter update cycle. The n x 1 column vector H^T is constructed by inserting each element of an m x 1 column vector $\hat{H}^T$ into the appropriate position in an n x 1 vector of zeros. $\hat{H}^T$ is given by

$$\hat{H}^T = B^{-1}u/[u^TB^{-1}u] \qquad (2)$$

where B is the m x m submatrix of P corresponding to clock phase states only and u is an m x 1 column vector of elements, all of which are one. Each clock in a partition, then, has an ensembling weight in the column vector H (ordered as P is ordered), whereas each ephemeris state has weight zero. By the construction of H, the sum of all weights is one. Equation 2 assigns to each clock a normalized set of phase and frequency weights that are inversely proportional to the magnitude of estimation error variance (i.e., the diagonals of B). Because of the particular form of H^T, however, the correction term in Equation 1, i.e., the second term on the right side of the equation has nonzero elements corresponding to ephemeris states and, hence, this method of covariance reduction is not a transparent variation on filter operation. A simulation of this algorithm was performed (Reference 3) using real pseudorange measurement data from the MCS in order to assess the impact of the algorithm on Kalman states and URE. RMS UREs were shown to be very good with the algorithm and states changed only slightly. Ephemeris states with composite clock operation are unchanged from

what they were with the master clock configuration—with or without the reduction algorithm (Reference 3).

Partition Reconciliation

Partition reconciliation is required to ensure that composite clock time for the various filter partitions is consistent. Uploads built for SVs from different partitions must have very nearly the same reference time for clock phase and frequency offsets contained in the navigation message. Any difference in reference times maps into URE. The reconciliation process, since it is an adjustment of reference time for the partition, does not affect filter gains or measurement residuals because it amounts to a constant shift of all the clock phase and frequency states in the partition. Each partition will have a different shift as computed by the reconciliation algorithm. Partition reconciliation is possible only because the MS clocks are common to each partition. It requires that a specified weighted sum of MS states be the same for each partition, where the same weights are used to compute the sum for each partition. The value of the weighted sum is itself a weighted average of MS and SV states. The computation proceeds as follows:

First the vectors $\bar{b}_i$ are computed for each partition according to (References 2, 4)

$$\bar{b}_i = [(H^*)^T C^{-1} H^*]^{-1} (H^*)^T C^{-1} \begin{bmatrix} \hat{\phi}_i^1 \\ \cdot\cdot \\ \hat{\phi}_i^5 \end{bmatrix} \tag{3}$$

where $\hat{\phi}_i^j$ are the MS_j clock states for the i^{th} partition and H^* is a 10 x 2 matrix of five 2 x 2 identity matrices. C is a 10 x 10 matrix obtained by summing the MS clock covariance submatrices from the various partitions. Note from Equation 3 that the linear combination of MS states is taken for each partition. Next, the vector $\bar{b}$ that the $\bar{b}_i$ are reconciled to, is computed according to Equation 4 below:

$$\bar{b} = W^{-1} \sum_{i=1}^{N} w_i \bar{b}_i \tag{4}$$

where $$w_i = \sum_{j=1}^{n_i} [p_i^j]^{-1}, \quad W = \sum_{i=1}^{N} w_i$$

N = the number of partitions, and n_i = the number of SVs in partition i.

$$p_i^j = \begin{bmatrix} q_1^j \tau + q_2^j \tau^3/3 & q_2^j \tau^2/2 \\ q_2^j \tau^2/2 & q_2^j \tau \end{bmatrix} \tag{5}$$

for the j^{th} SV in partition i. In Equation 5, q_1^j and q_2^j are the phase and frequency process noise covariances, respectively, and τ is the update interval (15 min). The adjustment (Δb_i) that gets applied to each clock phase state in partition i is then computed by

$$\Delta b_i = \bar{b} - \bar{b}_i$$

After the adjustments are made to each partition, a recomputation of the $\bar{b}_i$ would yield $\bar{b}$ for all partitions. This means that GPS time for each partition is now the same, i.e., after reconciliation the weighted average of MS states for each partition is the same.

Stability of GPS Time

One of the primary reasons for ensembling the GPS clocks (i.e., constructing a composite clock) is to gain stability in GPS time. Clock ensembling is a proven technology most prominently used by the U.S. Naval Observatory (USNO) and National Institute of Standards and Technology (NIST). The enhancement of stability for a system of n clocks, each of which is stable to say 1E-13, goes as $1/\sqrt{n}$. For the current system of 19 clocks, operating with a Kalman filter configured for the composite clock option, the stability of GPS time is predicted to be of the order of 2.3E-14. This assumes that the three MCS filter partitions (with 5, 5 and 4 SVs in partitions 1, 2, and 3, respectively) are being reconciled perfectly and states do not differ appreciably from what they would be if the MCS were operating with the 14 SVs in one partition.

Steering of GPS Time

The composite clock software package provides a new GPS time steering algorithm that automatically determines and applies the appropriate clock drift rate steer to all clock states when enabled by operator directive. The operator need only input daily USNO updates of GPS-UTC phase offset. A bang-bang controller (Reference 4) has been implemented. Allowable steering rates are $\pm 2E{-}19 s/s^2$ and 0. Three steering modes are provided as follows: steer out the GPS-UTC offset as computed by the MCS from "raw" USNO measurements; steer out a particular GPS-UTC offset input by the operator; or steer GPS time to one of the MS clocks. Simulations of this control loop, carried out by The Aerospace Corporation (Reference 5), predict an RMS steady state control error of the order of 10 ns assuming the GPS time stability is 3E–14s/s at 1 day (Figure 1).

COMPOSITE CLOCK PERFORMANCE (ACTUAL)

Transition to the composite clock was initiated on 17 June 1990 by including the master MS clock states as estimated states in the filter partitions. This act causes the state component covariances to then be Q'd (i.e., process noise added in the filter propagation operation) every 15 min.

UREs

RMS UREs for all age-of-data were as good, if not better, than what they were with the master clock configuration. For one upload per day per SV these RMS values were in the range of 2 to 4 m. Note that UREs are very insensitive to GPS time stability. They are primarily due to SV clock phase/frequency variations over the upload interval.

Steering of GPS Time

At 23:30 on 25 June 1990 (MJD48067), a directive was input to the system to begin steering GPS time to drive the GPS-UTC internally computed offset to zero. Figure 2 shows a history of GPS-UTC obtained from the USNO GPSV1 file. The steering achieved is not as good as clock ensembling can theoretically achieve. Control is not able to reduce the large amplitude (± 100 ns) of the offset. It is apparent that the underlying stability of GPS time (without steering) must be considerably worse than 2.3E-14 and/or some other unknown type of aging-like effect, perhaps caused by system model errors, must be going on. Table 1 shows the time steer history from 0000 6 January 1980 to 0630 22 October 1990. Note that steer control values (i.e., ±2.00E-19 or 0.00E+00) only change at times that are multiples of 15 min. (the Kalman filter update interval).

Table 1. Time Steer History

Day	Month	Year	Modified Julian Date	Time	Steer Control Value
6	Jan	1980	44244	00:00:00	+0.00E+00
25	Jun	1990	48067	23:30:00	+2.00E-19
11	Jul	1990	48083	22:30:00	-2.00E-19
12	Jul	1990	48084	15:00:00	+2.00E-19
13	Jul	1990	48085	15:00:00	-2.00E-19
13	Jul	1990	48085	21:45:00	+2.00E-19
16	Jul	1990	48088	01:15:00	-2.00E-19
16	Jul	1990	48088	18:30:00	+2.00E-19
17	Jul	1990	48089	05:15:00	-2.00E-19
17	Jul	1990	48089	17:30:00	+2.00E-19
19	Jul	1990	48091	17:00:00	-2.00E-19
17	Aug	1990	48120	16:15:00	+0.00E+00
27	Aug	1990	48130	23:45:00	-2.00E-19
28	Aug	1990	48131	06:30:00	+2.00E-19
28	Aug	1990	48131	17:00:00	-2.00E-19
29	Aug	1990	48132	09:30:00	+2.00E-19
29	Aug	1990	48132	22:15:00	+0.00E+00
4	Sep	1990	48138	16:45:00	+2.00E-19
17	Sep	1990	48151	14:15:00	+0.00E+00
21	Sep	1990	48155	12:15:00	+2.00E-19
21	Sep	1990	48155	12:45:00	-2.00E-19
5	Oct	1990	48169	18:30:00	+0.00E+00
9	Oct	1990	48173	07:15:00	-2.00E-19
20	Oct	1990	48184	11:15:00	+0.00E+00
22	Oct	1990	48186	06:30:00	

When the steering from Table 1 is backed out of the GPS-UTC plot of Figure 2, along with a mean slope of 4 ns/day, the underlying behavior of GPS-UTC is evident (Figure 3). Ideally Figure 3 should look like random walk with a small amplitude starting from 250 ns offset. The oscillatory nature of this curve needs to be understood. The only source of perturbation on GPS time (or GPS-UTC) must come via the Kalman filter and will occur when the filter is "lied to." For example, if a Rubidium clock (e.g., SV 16) has a large frequency jump and the clock frequency state is not Q'd sufficiently to absorb the variation, then GPS time will be perturbed. It would also be perturbed if an MS suffers a phase or frequency step that goes unnoticed and so the clock covariance is never Q-bumped to allow the filter to solve for the new phase or frequency. GPS time is perturbed because the corrected clock (i.e., the clock time corrected by the filter state offset) represents GPS time, and if the state doesn't correctly compensate for true clock behavior, the "corrected" clock, or GPS time will be perturbed. In the course of these investigations perturbations in both MS and SV clock states were evident, and it is only necessary to see how the filter was handled (e.g., was the covariance matrix Q-bumped or process noise increased at these times) in order to assess whether or not a perturbation in GPS time was likely. An attempt was made to correlate state perturbations occurring in the interval 2 October to 15 October with the slope discontinuities of Figure 3. On 2 October the Multiple Frequency Standard System (i.e., the MFSS of six Cesium clocks operated by the U. S. Naval Research Laboratory (NRL)) at Falcon Air Force Base became the primary standard for the Colorado Springs Monitor Station (COSPM). At the time of the switch, a large jump in the COSPM frequency state was apparent. Hopefully the jump was simultaneous with a large Q-bump of the COSPM clock states, however, the distinct change in slope of GPS-UTC at that time is evidence to the contrary.

SV Clock Stability

Although GPS time is being perturbed, due to unmodeled filter processing, the stability of the SV clocks is up to expectations. Figure 4, provided by D. Allan of NIST, is a plot of Allan's variance for five SVs in the constellation. SV 16, the outlier, was having problems during this interval of time (12 August to 11 September 1990). The other four block II SVs are operating better than their specification of 2E-13 at tau equals 1 day. Figures 5 and 6 show SVN 18 clock phase behavior (with a straight line removed) and corresponding Allan variance for tau between 15 min and 1 day. These were computed from MCS Kalman filter data. A 12-hr, unmodeled, periodic variation in phase is evident in Figure 5. It's peak-to-peak amplitude is about 2 m. This periodicity produces the sharp breaks in the Allan variance plot of Figure 6. The 1-day value of the variance, 8E–14, is uncorrupted by the periodicity, since 1 day is a multiple of 12 hr.

Stability of GPS Time

It should come as no surprise, because of the oscillatory behavior of GPS-UTC evidenced in Figure 3, that GPS stability relative to UTC (in the interval 31 May to 8 September 1990) would not be as good as predicted from the theory (2.3E-14). This is apparent from Figure 7, another of D. Allan's contributions. Stability is more like 8E-14; comparable to the performance of a master MS configuration.

It should be noted that in the time span of Figure 7, SV 16 had a large frequency jump and in addition its aging state was not being Q'd in the filter. This could have had a significant impact on GPS time. Another impression, however, of GPS time stability is gained when one looks at the Colorado Springs monitor station clock phase state. This state is an estimate of the phase offset between the MFSS ensemble (stable to 2E-14 relative to UTC) and GPS time. The phase state from partition No. 1 is plotted in Figure 8 and its Allan variance is shown in Figure 9. The 1-day GPS stability (with the MFSS stability removed) is 4E-14. The difference between this assessment (based on the current time phase state) and that of D. Allan (based on the predicted phase state) is considerable. The 1-day Allan variance is close to our theoretical expectation. Figure 10, an Allan variance plot for the Kwajalein MS, also supports the idea that GPS time stability is better than 4E-14 at 1 day. The 24-hr periodicity inherent in the clock phase of Kwajalein (and all other MS clocks to a greater or lesser degree) causes the Allan variance to be larger at 12 and 36 hr than at 24 hr. Figure 11 shows this periodicity with peak-to-peak amplitude of 4 m or so. If the clocks are really cycling daily (e.g., because of temperature and/or humidity changes), and the filter estimates only reflect a portion of the amplitude, it is possible that GPS time stability will be degraded for taus that are not a multiple of 24 hr (as Figures 9 and 10 indicate). On the other hand, augmenting the clock model with a sinusoid term would remove the performance degradation. It is also possible that the unmodeled sinusoid is hindering our ability to steer GPS time. This is being investigated by simulation.

As mentioned earlier, each filter partition has its own GPS time reference, and these are reconciled every 15 min for a common value. The effectiveness of this reconciliation is measured by differencing corresponding MS phase states from two partitions. One of these differences for the Kwajalein MS and partitions No.1 and 3 is plotted in Figure 12. Excursions are generally between ± 2m. The Allan variance of the difference, a direct measure of the stability of partition No.1 GPS time relative to partition No. 3, is 4E-14 at 1 day (Figure 13). The inferred absolute stability of each relative to a "perfect" clock would be $4/\sqrt{2}$ E-14, or 2.7E-14. The stability of GPS time for each partition looks good in terms of Allan variance, but the MS phase difference of ± 2 m may be a problem. This is being investigated further.

CONCLUSIONS

GPS time, constructed from the composite clock software, is being perturbed by unmodeled or improperly modeled clock phase behavior. Analysis of Kalman filter MS clock phase estimates shows a daily periodic signature with peak-to-peak amplitude of 4 m that varies somewhat from MS to MS. GPS time stability, inferred from Allan variances of MS clock phase estimates, in the interval 2 to 22 October 1990 very nearly measures up to expectations. This means that the filter clock states are by and large reflecting true clock behavior and, hence, are isolating GPS time from clock perturbations in this interval. Further studies are needed to explain the behavior of GPS-UTC in the interval prior to 2 October when SV 16 was having its problems.

REFERENCES

1. A. L. Satin and C. T. Leondes "Ensembling Clocks of the Global Positioning System (GPS)," IEEE Transactions on Aerospace and Electronic Systems, Vol. 26, No. 1 (January 1990).
2. K. Brown, "Optimal Ensembling for GPS and Other Systems of Clocks," IBM Federal Systems Division Draft (14 July 1987).
3. A. L. Satin, "Ensembling Clocks of the Global Positioning System," Masters Thesis, Department of Mechanical, Aerospace and Nuclear Engineering, University of California, Los Angeles (1988).
4. Ephemeris/Clock Development Specification, CP-MCSEC-302C, SCN04, Part I, App. A, Navstar GPS Joint Program Office, U.S. Air Force Space Systems Division (1 September 1989).
5. C. H. McKenzie, et al., *GPS-UTC Time Synchronization*, Proceedings of the 21st Annual PTTI Applications and Planning Meeting (28–30 November 1989).

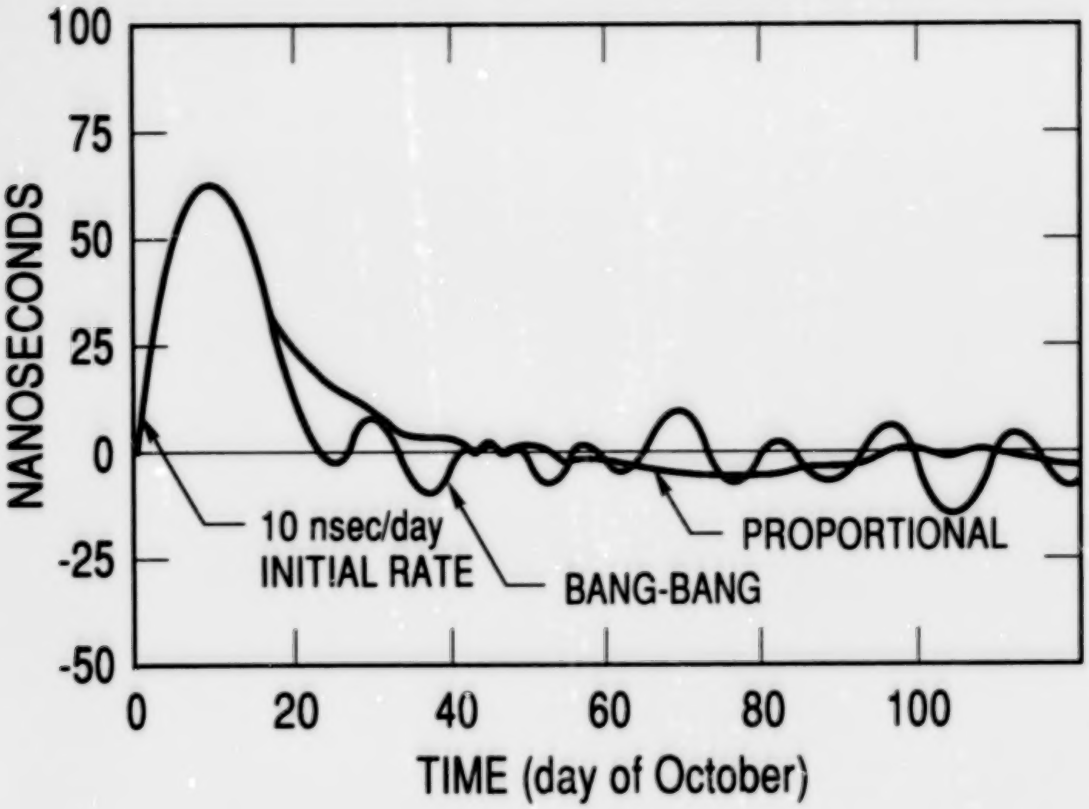


Figure 1. Transient Responses to Bang-Bang and Proportional Steering Control Laws.

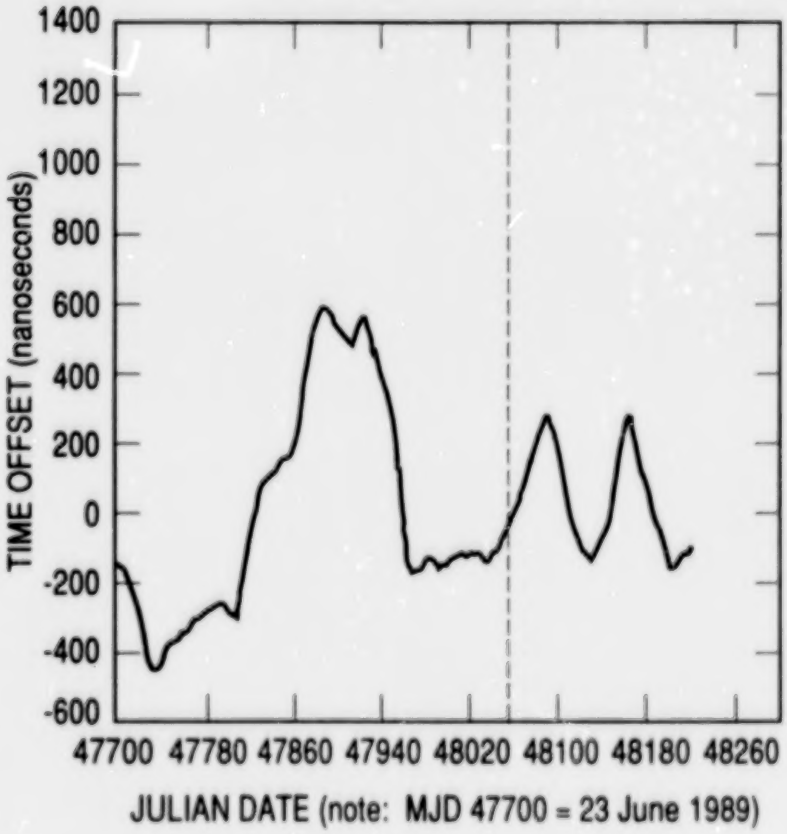


Figure 2. UTC(USNO) Reference — GPS Time

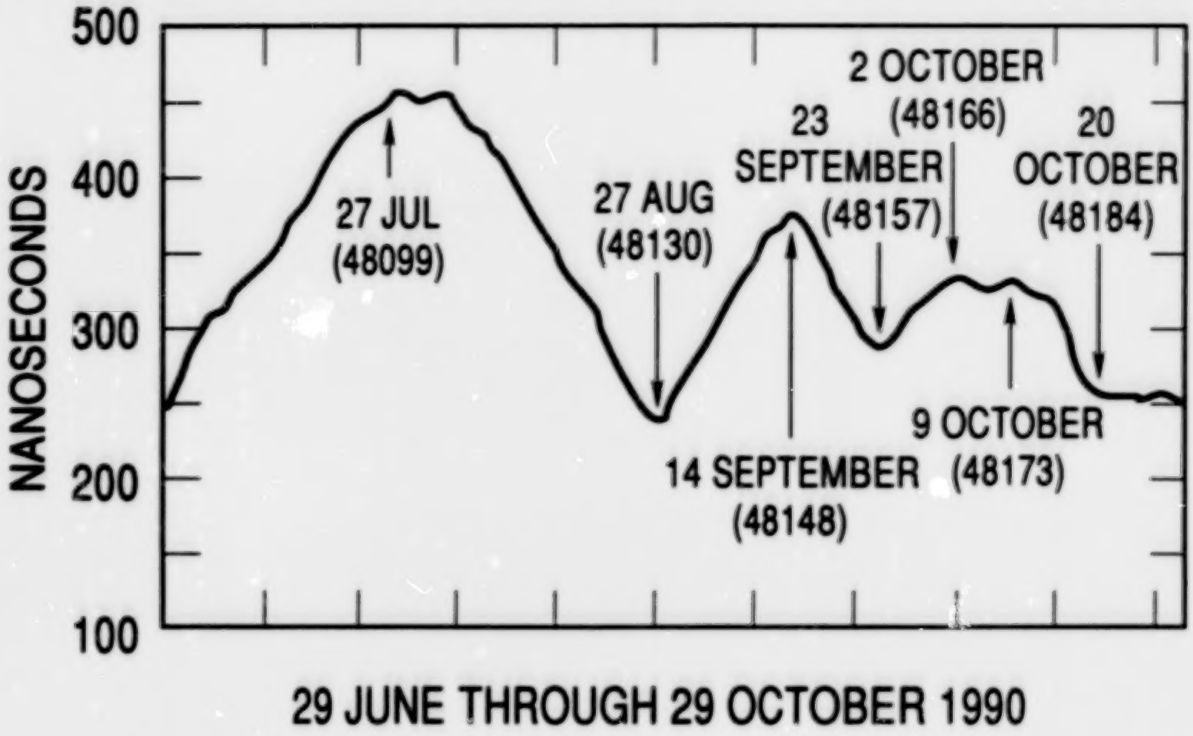


Figure 3. GPS-UTC(USNO) with GPS Time Steering and Mean Slope Removed (4 ns/day).

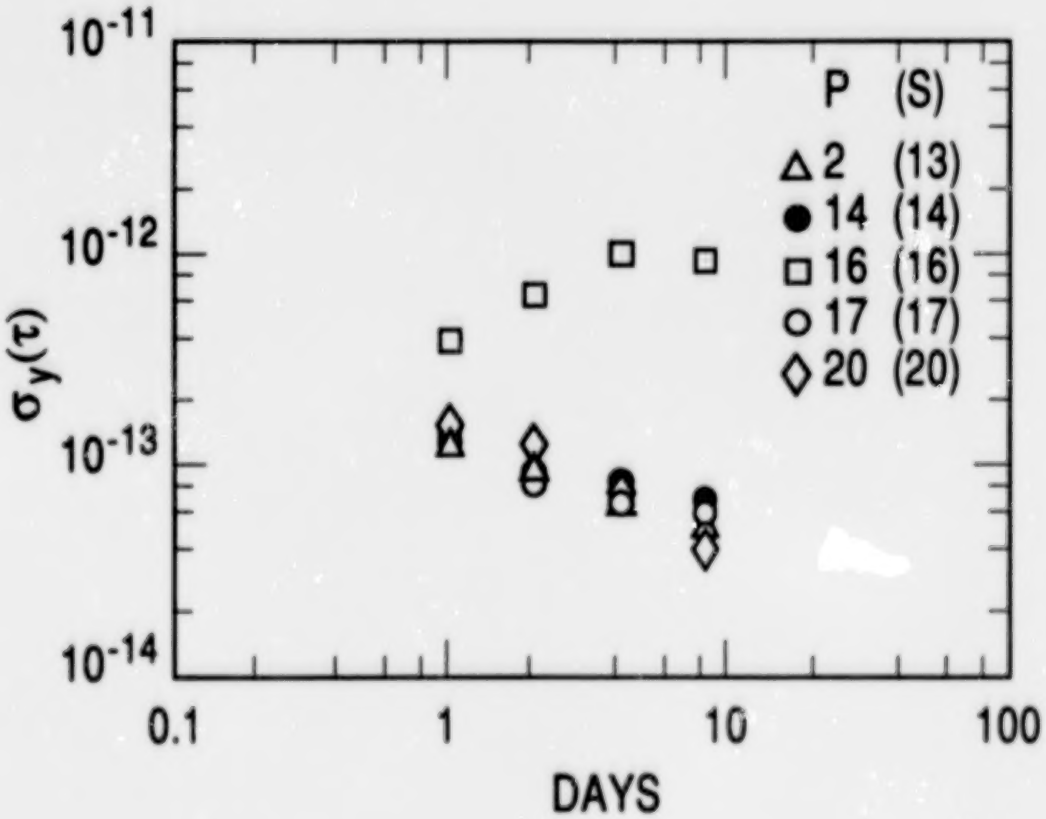


Figure 4. PRN(SVN) Clock – UTC(NIST) 12 August to 11 September 1990.

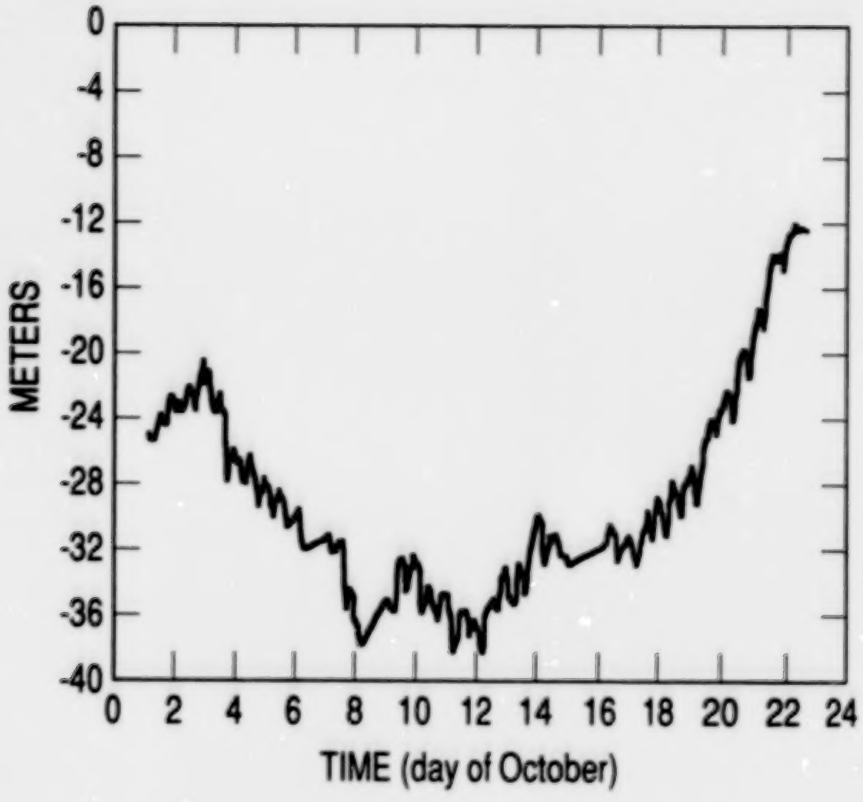


Figure 5. SVN 18 Clock Phase Estimate (2-22 October 1990).

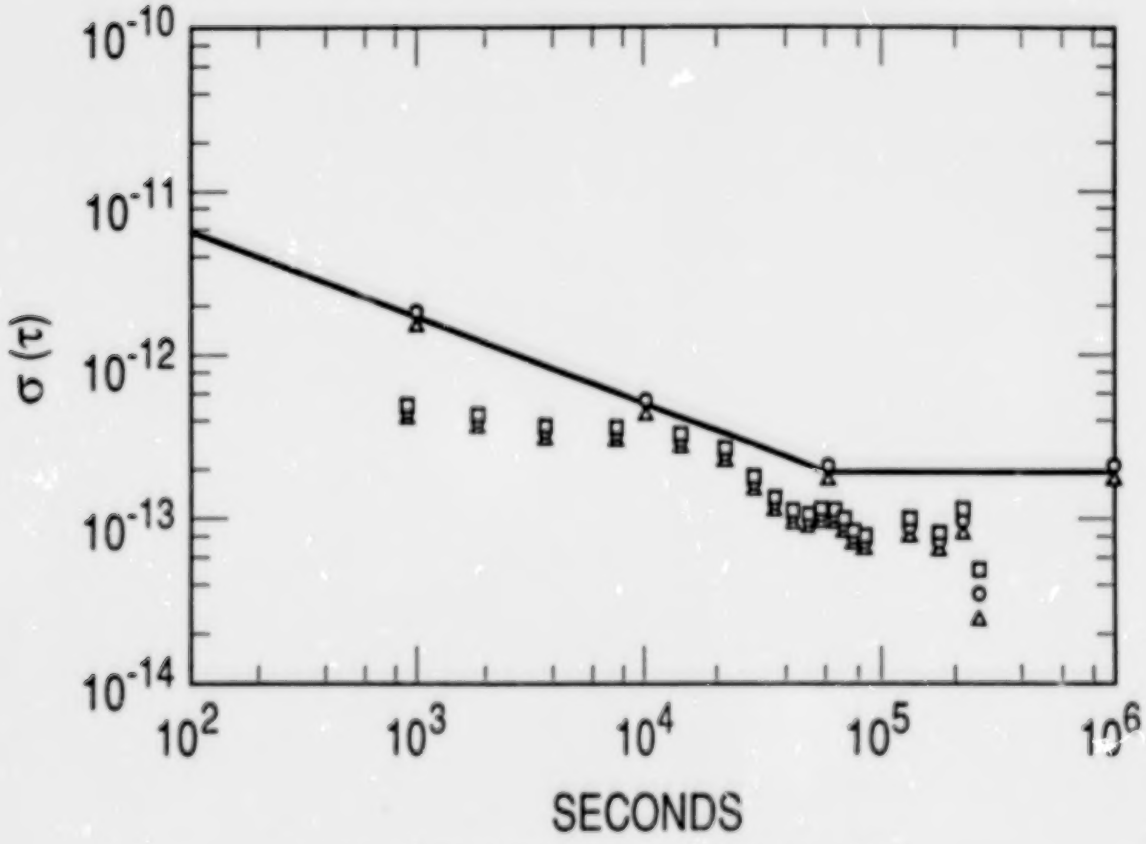


Figure 6. SVN 18 Allan Variance (2–22 October 1990).

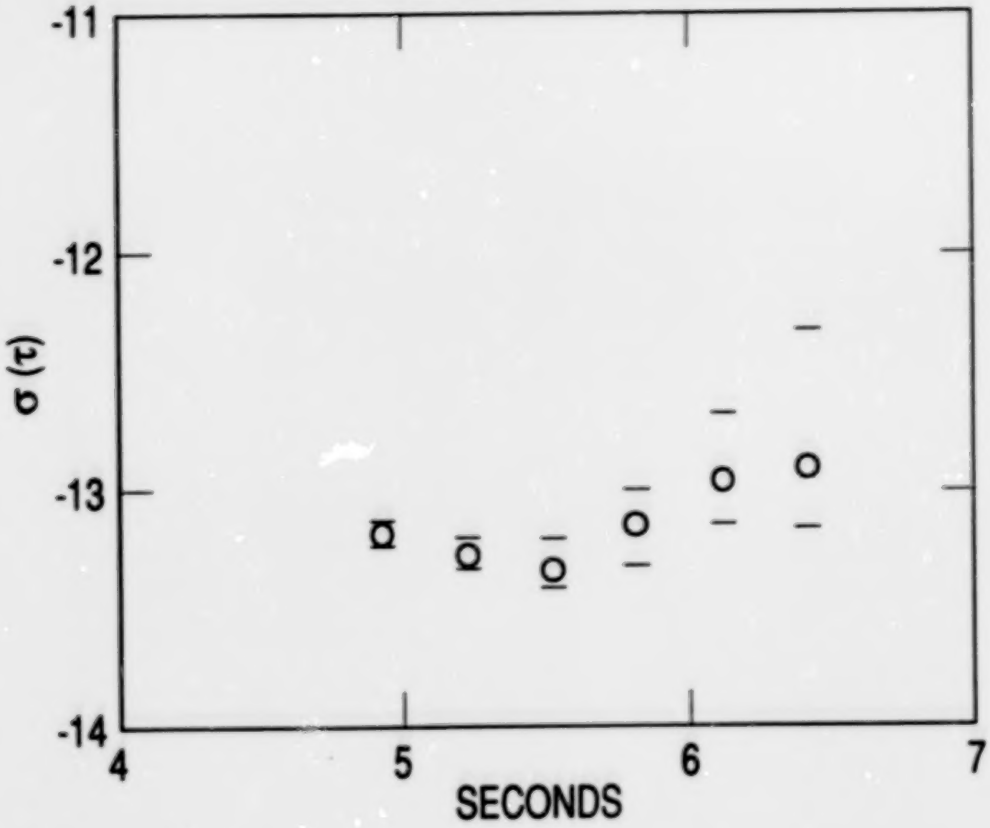


Figure 7. GPS System Time − UTC(USNO MC) (31 May to 8 September 1990).

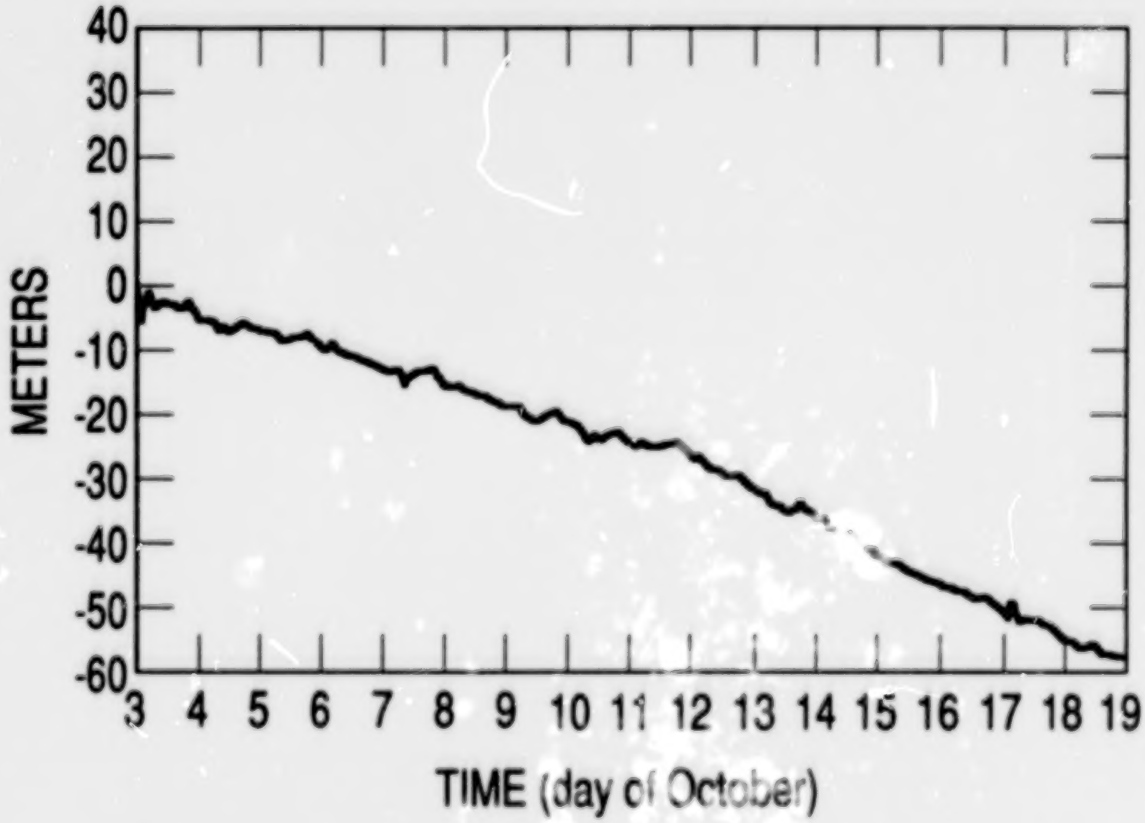


Figure 8. Colorado Springs Monitor Station Clock Phase Estimate (Partition No. 1).

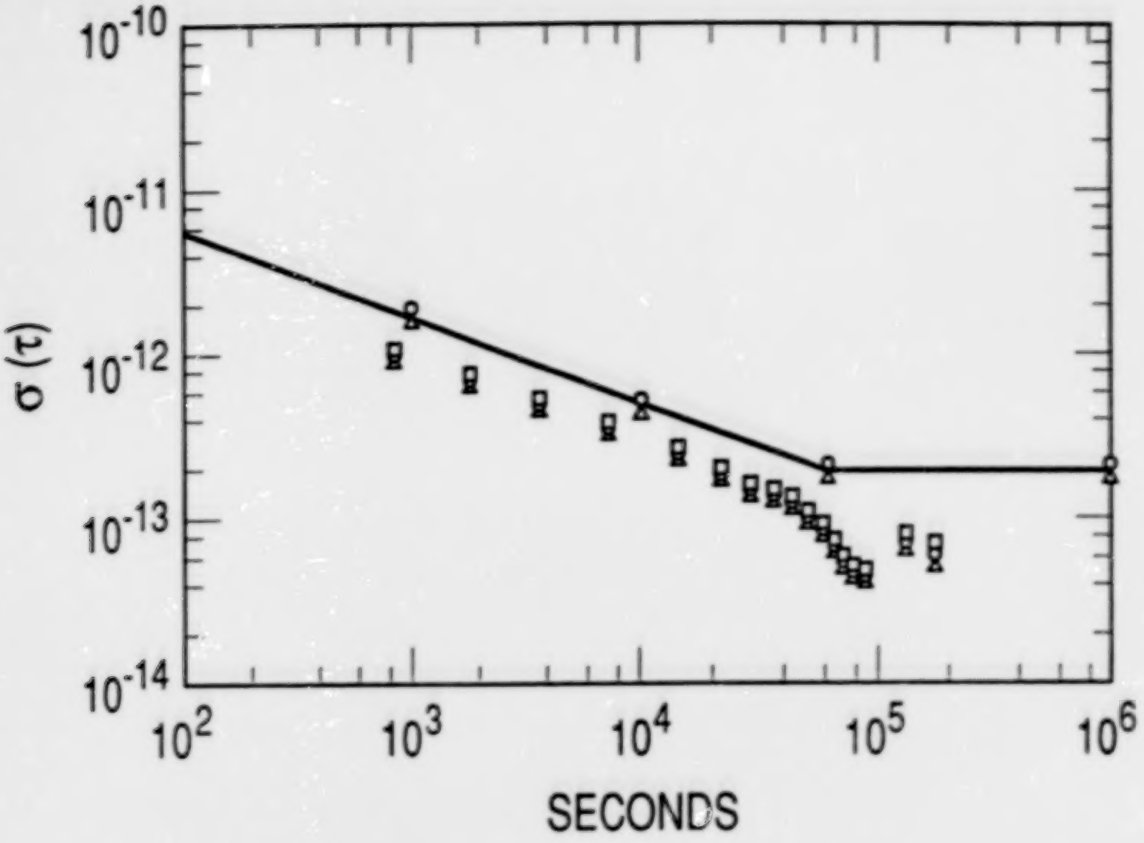


Figure 9. Colorado Springs Monitor Station Allan Variance (Partition No. 1).

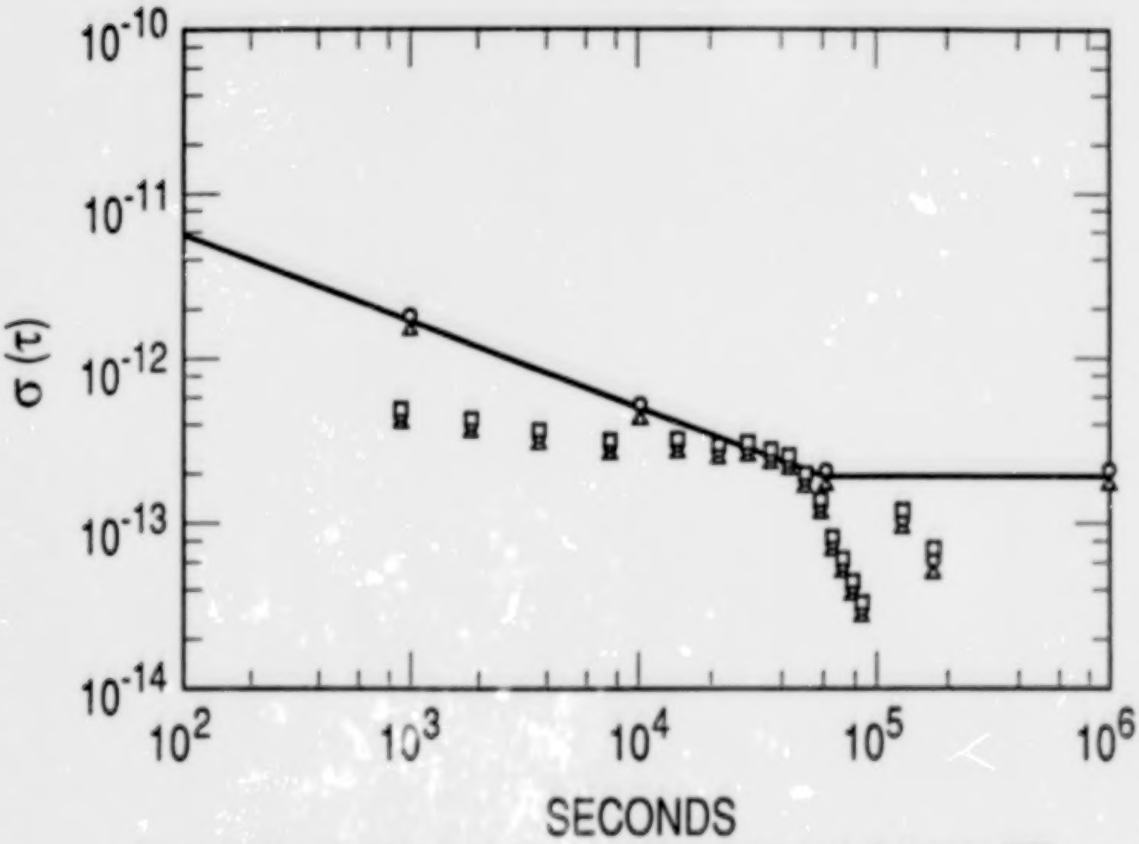


Figure 10. Kwajalein Monitor Station Clock Phase Estimate (3–19 October 1990).

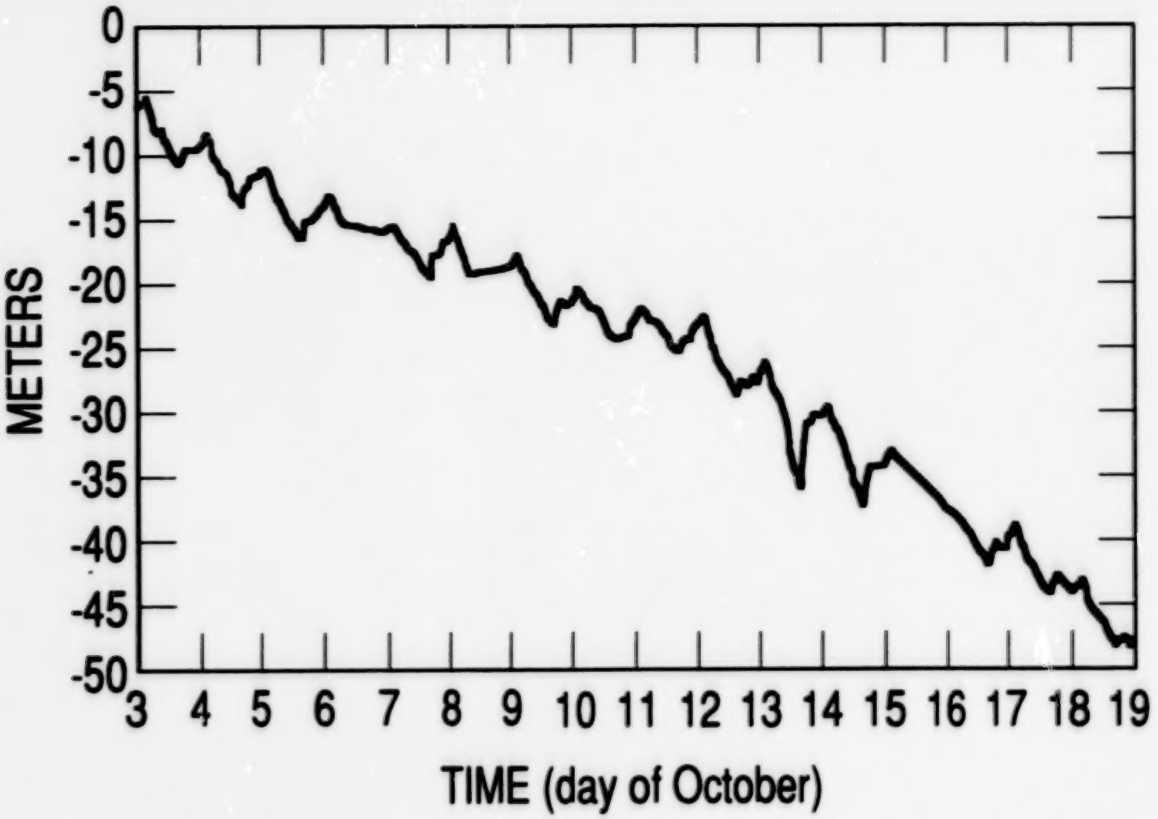


Figure 11. Kwajalein Monitor Station Clock Phase Estimate (3–19 October 1990).

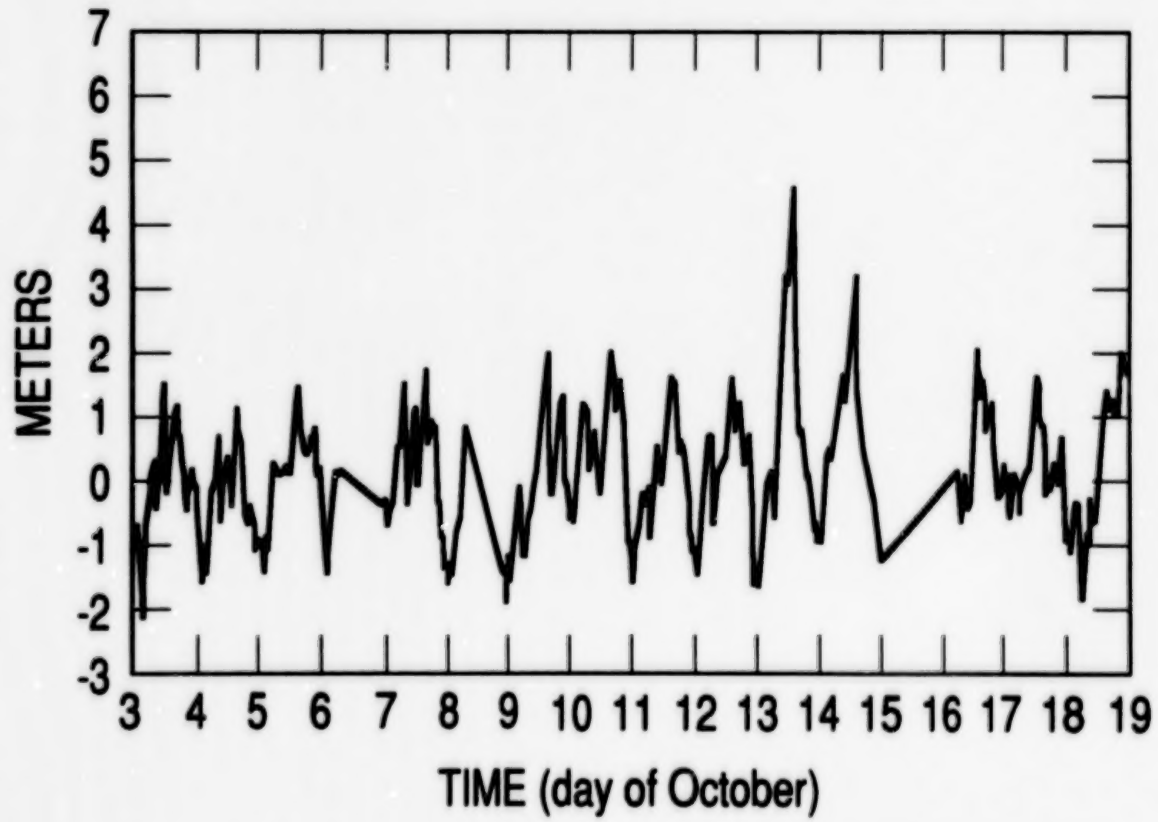


Figure 12. Partition 1 Minus Partition 3 Kwajalein Monitor Station Clock Phase Difference.

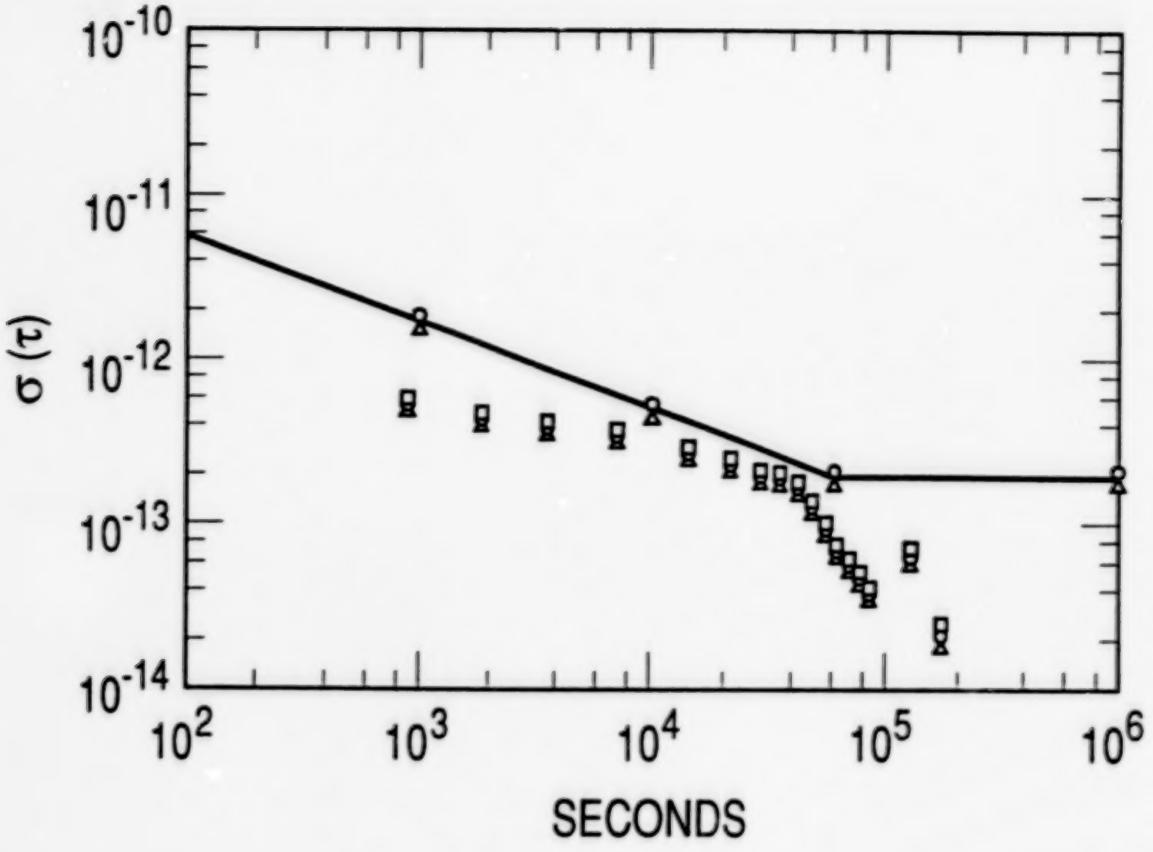


Figure 13. Allan Variance of Partition 1 Minus Partition 3 Kwajalein Monitor Station Clock Phase Difference.

QUESTIONS AND ANSWERS

Professor Alley, University of Maryland: You mentioned that there was a variation. Did that have a 12 hour or a 24 hour period?

Mr. Satin: That did not have any definite periodicity to it. It does look like the station frequency has a 24 hour periodicity to it. We think that the periodicity is caused by humidity.

Professor Alley: You mentioned a 12 hour period also.

Mr. Satin: That is in the satellite, they have a 12 hour orbit. That is a temperature variation effect.

Dr. Winkler, U. S. Naval Observatory: What was the rationale which led to the decision to use a bang-bang steering to UTC? And what is the dead-band in that control?

Mr. Satin: I can't answer the question about the dead-band right now. We investigated several different algorithms for the control. The bang-bang takes out large initial offsets much quicker than the others.

Dr. Winkler: At the expense of much larger frequency changes, and that is, of course, detrimental to its time usage.

Mr. Satin: All the simulations show that there is no problem there.

David Allan, NIST: On your last view-graph, the cesium performance of $\tau^{-1/2}$ from 10^{-12} down to 10^{-13} is pretty typical of the space cesiums. How can you have a τ^{-1} type of behavior out at 10^5 seconds? That is not typical of cesiums or anything in the system.

Mr. Satin: We think that that is related to the periodicity in the monitor stations. In other words, at the 24 hour point you don't see the 24 periodicity and things get better, but you do see it at other points.

Mr. Allan: You are saying that this is an aliasing?

Mr. Satin: Yes, that is right.

Mr. Allan: But if you have a periodicity, it will increase the noise over $\tau^{-1/2}$, it will not decrease it. The curve would have an increase at 12 hours, and no increase at 24 hours. You have a $\tau^{-1/2}$ curve, so I don't see any aliasing affect.

Dr. Henry Fliegel, The Aerospace Corporation: We believe that the strange appearance of the sigma-tau curve is because we do have 24 hour periodicities and they alias at 12 and 36 hours. As far as I know, that completely explains the appearance of the curve.

Dr. Claudine Thomas, BIPM: Why are you using that set of filters and the clocks are not

independent, when with one Kalman filter you could handle everything?

Mr. Satin: It is computationally more efficient to use three smaller filters. When the system was first designed, we didn't have the number-crunching capability to handle the single Kalman filter. That would be 24 satellites, 11 states per satellite for a total of hundreds of states.

Dr. Thomas: Yes, but the clocks which are involved in your filters are not independent.

Mr. Satin: Right, it is sub-optimal. That is correct, but we did a study to determine what the effect would be to use one, two, or three filters because we are making a large software change and could change the filters, but the gain was essentially zero.

Sam Stein, Ball Corp.: I am afraid, Henry, that I would have to agree with Dave Allan and disagree with you. We calculated the exact effect of a periodicity on σ_y. Its effect, if you have a 24 hour periodicity, would be an elevation of σ_y over the white frequency noise level, due to the ensemble, at 12 hours, a decrease back to the white frequency noise level at 24 hours, and then it would come back up afterwards. If you look at the very short term, if you look at the numbers at 1000 seconds, you can see where the $\tau^{-1/2}$ level is. Whatever this phenomenon is, it causes a decrease below the noise level that one would attribute to the ensemble, and that is surprising. We often see this when there is a small amount of data, but if those are error bars that I see on the curve, it would indicate that there is an adequate amount of data and one should not see such a large effect.

Mr. Satin: We have approximately 20 days of data, so we should have a pretty good estimate of the one day variance.

Tom McCaskill, Naval Research Laboratory: I would just like to make some comments. If you look at the short term data, you start out at 900 seconds, which is 15 minutes. If you follow that out, you have the same slope out to what corresponds to the time for one pass of a satellite. Then there is the time when you are switching to another satellite and you get a different type of behavior. I agree with the other gentlemen about the effect of the periodicity, but this is not that effect.

BLANK PAGE

THE USE OF PRECISE EPHEMERIDES, IONOSPHERIC DATA AND CORRECTED ANTENNA COORDINATES IN A LONG–DISTANCE GPS TIME TRANSFER

W. Lewandowski, G. Petit, C. Thomas
Bureau International des Poids et Mesures
Pavillon de Breteuil
92312, Sèvres Cedex
France

and

M. A. Weiss
Time and Frequency Division, 576
National Institute of Standards and Technology
325, Broadway
Boulder, Co 80303
USA

Abstract

Over intercontinental distances the accuracy of GPS time transfers ranges from 10 to 20 ns. The principal error sources are the broadcast ionospheric model, the broadcast ephemerides and the local antenna coordinates.

Previous work has already shown the impact of correcting each of these error sources individually, using either measured ionospheric delays, precise GPS satellite ephemerides, or improved antenna coordinates. Ionospheric delay measurements can be provided by dual frequency codeless ionospheric calibrators. Precise GPS satellite ephemerides are now available from the U.S. Defense Mapping Agency (DMA), and others. GPS receiver antenna coordinates should be accurately linked to stations of the IERS Terrestrial Reference Frame. If such a link is not available from geodetic methods, accurate differential positioning, between GPS antennas, can be realized over short distances, using the BIPM method.

For the first time, the three major error sources for GPS time transfer can be reduced simultaneously for a particular time link. Ionospheric measurement systems of the NIST type are now operating on a regular basis at the National Institute of Standards and Technology in Boulder (Colorado, USA) and at the Paris Observatory in Paris (France). Broadcast ephemerides are currently recorded for time–transfer tracks between these sites, this being necessary for using precise ephemerides. At last, corrected local GPS antenna coordinates are now introduced in GPS receivers at both sites. This paper shows the improvement in precision for this long–distance time comparison resulting from the reduction of these three error sources.

INTRODUCTION

The excellence of worldwide unification of time depends on the means of time comparison. The rapid development of the Global Positioning System since 1983 has led to a major improvement in the precision and accuracy of time metrology. Using commercially available C/A Code GPS time receivers, time comparisons can easily be performed with an accuracy of 10 to 20 nanoseconds over intercontinental distances. However, it should be possible to improve this performance greatly by removing systematic errors[1]. In GPS time transfers the three principal error sources are the local antenna coordinates, the broadcast ionospheric model and the broadcast ephemerides. Previous work shows the impact of correcting each of these error sources individually[2, 3, 4]. We show here the first example of long-distance time comparison where all three errors may be reduced simultaneously. This experiment concerns the time link between the Paris Observatory (Paris, France) and the National Institute of Standards and Technology (Boulder, Colorado, USA), which corresponds to 7400 km baseline. In following sections the experiment is first presented in detail, then the results are analyzed.

1–THE EXPERIMENT

The difference UTC(OP) – UTC(NIST) is computed using the common-view method[5], for a 67-day period, from 1990 June 14 (MJD 48056) to 1990 August 20 (MJD 48123). The GPS data taken at the two sites correspond to the international GPS schedule n°15, issued by the Bureau International des Poids et Mesures, and implemented on 1990 June 12 (MJD 48054), see table 1.

TABLE 1: Daily scheduled common views between Europe and West North America (MJD 48054)

PRN	Cl	h	m	El(from OP)	El(from NIST)
14	00	00	16	37	30
13	08	01	36	44	41
13	09	02	08	39	33
3	08	04	16	14	68
16	08	05	36	41	48
12	08	09	20	59	30
20	19	11	28	58	18
2	08	21	04	36	23
14	01	23	44	26	25

Nine tracks, spread over 14 hours, are scheduled each day, four of which correspond to Block I satellites and five to Block II satellites, so we have 603 potential common views for the period under study. However the elevation of satellite 3 was too low from Paris and became observable only at mid-July due to its rephasing maneuver.

For one part of the period under study (1990 June 14 to 1990 August 10), the intentional degradation of GPS signals, known as Selective Availability (SA), was turned on for the Block II satellites. It can be shown however that it affected only the satellite clocks, producing a phase jitter which is completely removed by strict common views[6] (same start time and same track length). In our experiment we found 576 perfect common views. Moreover, the two GPS receivers come from the same maker and

use the same software for treating the short-term data. This further helps remove the clock dither and enhances the symmetry of the experiment.

The values UTC(OP) – UTC(NIST) are obtained for each observed satellite at the time, Tmid, of the midpoint of the track.

1–1 ACCURATE ANTENNA COORDINATES

Accurate antenna coordinates can be obtained with uncertainties of a few centimeters through geodetic methods[7] by relative positioning between the antenna and the nearest IERS site. The BIPM has also developed a method of differential positioning between GPS antennas, using the data of the time comparisons themselves[2]. The consistency of the coordinates obtained by this method is within 50 cm for distances up to 1000 km. Using these two techniques together, over the last few years, all national laboratories equipped with GPS have been linked to IERS sites. On 1990 June 12 at 0h00 UTC (MJD 48054), as suggested by the BIPM, these corrected coordinates were introduced into the GPS time receivers, ensuring worldwide homogenization of the coordinates in the IERS Terrestrial Reference Frame (ITRF).

Thus, at the beginning of our experiment, the NIST GPS antenna has coordinates known with an uncertainty of 30 cm. They were obtained by GPS geodetic differential positioning with respect to Platteville VLBI site in July 1989[7]. For OP, the coordinates were obtained by the BIPM differential positioning method, with respect to the Grasse ITRF SLR site. They are derived from data covering 1987 December 15 to 1988 June 21[2] and are given with an uncertainty of 50 cm.

1–2 MEASURED IONOSPHERIC DELAY

In the usual GPS data file, the correction used for ionospheric refraction comes from a model[8], the parameters of which are included in the GPS message. At radio-frequencies, however, the ionosphere is a dispersive medium so that its effect on time comparison between local and GPS satellite clocks can be estimated by dual-frequency methods. Dual-frequency receivers, which do not depend on knowledge of the P-code have recently been developed[9, 10]. They give measurements of ionospheric delay along the line of sight of satellites with uncertainties of 1 to 2 ns. The gain in precision for long-distance time comparisons has already been shown when the two branches of the link are corrected with measured ionospheric values[11]. The gain in accuracy was also pointed out from the study of the closure around the world via NIST, OP and CRL through the use of such measurements[3].

The two sites involved in this study are equipped with similar codeless dual-frequency GPS receivers of the NIST type[10] (NIST Ionospheric Measurement System). In their present configuration, these devices are stand-alone units, with values of ionospheric delay for all satellites in view available as often as every 15 seconds. These data are stored after a linear fit over 15 minutes, at times Ti corresponding to round quarters of hours: 0h00 UTC, 0h15 UTC, 0h30 UTC,... etc. From these data it is necessary to estimate the value of the measured ionospheric delay for a given tracking (satellite s and middle-time Tmid). In the general case, we use several measurements for the same satellite s, surrounding Tmid. A polynomial fit is then performed (linear to cubic depending on the number of values which are used). The estimated value is deduced for Tmid by interpolation. This polynomial fit is never extrapolated and measurements from other satellites are never used. If only one value is available for s, it is used only if its reference time, Ti, is less than 7.5 minutes away from Tmid. The ionospheric measure for Ti and the slope of the 15-minute linear fit, computed in the receiver over

15-second ionospheric measurements, are then processed to estimate the ionospheric delay at Tmid.

With the available data from both sites, 393 strict common views were corrected for the ionospheric delay during the period under study.

1-3 PRECISE EPHEMERIDES

The GPS precise ephemerides were computed at the U.S. Naval Surface Warfare Center (NSWC) from the beginning of 1986 to 1989 July 29. Since then they have been produced by the Defense Mapping Agency (DMA). These ephemerides are received on a regular basis at the BIPM. Their estimated accuracy is of the order of 3 meters. At present time, the delay of access of precise ephemerides is about three months, so that the period we are studying here is limited to the end of August 1990.

In practice, computations with precise ephemerides require knowledge of the broadcast ephemerides used by the receiver software in order to apply differential corrections[4]. The BIPM started the regular collection of GPS broadcast ephemerides in May 1990. Another difficulty is the possible change of ephemeris parameters during the usual 13-minute tracking period. The software of the GPS receivers used in this experiment was modified in order to retain a single ephemeris for the full duration of the tracking. The available ephemerides data collected by the BIPM could be used for correcting 454 strict common views between OP and NIST for the period under study.

The precise ephemerides PEi are provided in Cartesian coordinates at times Ti corresponding to round quarters of hours: 0h00 UTC, 0h15 UTC, 0h30 UTC, 0h45 UTC...etc. It is then necessary to compute from the broadcast Keplerian elements, the positions BE1, BE2 and BE3 for three times T1, T2 and T3, such that:

$$T1 < Tstart < T2 < Tstop < T3$$

where Tstart and Tstop are the start time and the stop time of the usual 13-minute tracking. The ephemeris corrections PEi – BEi, for i = 1,2,3, are transformed in a frame linked to the satellite (On-track, Radial, Cross-track) and a quadratic polynomial in time is computed to represent each component. A quadratic representation is also computed in the same frame for the vector satellite-station. The inner product of these quadratic representations provides the corrections to GPS measurements each 15 seconds. A linear fit on these short-term corrections gives the correction at Tmid of the values UTC(Lab) – GPS for each laboratory.

2 RESULTS

For the period under study, 314 perfect common views between OP and NIST could be corrected simultaneously with measured ionospheric delays and precise ephemerides. The results given here only involve the values UTC(OP) – UTC(NIST) corresponding to these particular trackings, whether the tracks include the corrections or not.

The corrections to the antenna coordinates being already introduced, four different cases are emphasized in this study:

- raw values,

- corrected values for ephemerides only,
- corrected values for ionosphere only,
- corrected values for ephemerides and ionosphere together.

For each case, a Vondrak smoothing[12] is performed on the values UTC(OP) – UTC(NIST). The standard deviation of the residuals to the smoothing for the complete period is as follows:

raw values:	7.53 ns
corrected values for ephem.:	5.39 ns
corrected values for iono.:	6.46 ns
corrected values for ephem. + iono.:	3.22 ns

Each correction decreases the total standard deviation with a clear improvement where both of the corrections are applied.

The residuals to the smoothing for each data point are presented in Fig. 1 to 4. The comparison of these figures gives the evidence of the improvement of the 'precision of reading UTC(OP) – UTC(NIST)' when correcting one or the other error source. The effect is yet more clear with the use of precise ephemerides together with measured ionospheric delays. In this case, the daily standard deviations of the residuals (see Fig. 5) unquestionably drop. They collapse to values below 4 ns for nearly the entire period under study.

Some comments should be added to this general overview:

During the period under study, SA was on from the beginning till 1990 August 10 (MJD 48113). Fig. 1 shows that it did not affect our computations using strict common views. This is in agreement with Ref 6. Among others, satellite 12 presented very large residuals for some days in August. This effect completely disappears only when corrections for precise ephemerides are applied (Fig. 2). These very poor broadcast ephemerides for satellite 12 are observed during its eclipse season. This phenomena was already observed[4] for satellites equipped with rubidium clocks, which are more sensitive to thermal environment. However, this explanation does not seem to be valid here since the satellite 12 was probably equipped with a cæsium clock at that time.

The examples of satellites 12 and 13, underlined on Fig. 1 to 4, show that the use of precise ephemerides helps to smooth the daily residuals for each common view track while the use of ionospheric measurements tends rather to decrease the biases between satellites. These two effects were already shown individually[4, 11]; here they combine to reduce the uncertainty of the time comparison (Fig. 4).

The favorable effect of applying these two corrections is linked to the particular long baseline (7400 km) between the two sites. This baseline requires that common view observations often have low elevations so that precise knowledge of satellite positions and of ionospheric conditions are needed.

Daily values of UTC(OP) – UTC(NIST), at 0h00 UTC, have been estimated from the smoothed data points. The changes brought by the application of corrections to these values are shown on Fig. 6. The ionospheric measurements, which improve the estimate of the signal delay over the ionospheric model, cause a global shift of about 7 ns. Precise ephemerides correct anomalies due to some satellites with poor broadcast ephemerides. Though we have here no absolute test, the accuracy of the time transfer is probably improved[3].

The Allan deviation of the daily raw and corrected values of UTC(OP) – UTC(NIST) at 0h00 UTC is given on Fig.7 and 8 with a basic sample duration equal to one day. It is impossible to get an estimate of the Allan deviation on a shorter evenly-spaced time interval since the scheduled common views OP–NIST are spread over 14 hours each day. Raw data is affected by white phase noise whose origin is the time difference measurements. It is smoothed out by averaging over 5 to 6 days. When corrections for precise ephemerides and measured ionospheric delays are applied, the measurement noise is already smoothed out when averaging over one day. The real performance of the local clocks, white frequency modulation for that averaging time, is then accessible.

CONCLUSIONS

A two-month study of time transfers between OP and NIST shows that the consistency of long-distance GPS time comparisons is largely improved by the use of accurate antenna coordinates, precise satellite ephemerides and measured ionospheric delays. The average of the daily biases between satellites drops to 3 ns. At that level of precision, the local time scales are completely accessible for averaging time of the order of one day. This performance competes with that is observed for short-distance time comparisons[1].

Very soon, it may be necessary to refine the conditions of operation: calibration of GPS receivers, unification of receiver software, control of multipath interferences, use of ultra-precise ephemerides, use of Earth tides model...etc.

Another experiment with a third laboratory in Japan in which the three links could be corrected for precise ephemerides and ionospheric measurements is now in progress; it should give an interesting test of the accuracy of GPS time transfer.

ACKNOWLEDGMENTS

The authors are grateful to Dr. Pierre Uhrich from the Laboratoire Primaire du Temps et des Fréquences (Paris, France), for his kindness in collecting ionospheric measurements from the NIST Ionospheric Measurement System set at LPTF and sending them to the BIPM.

REFERENCES

1. B. Guinot, W. Lewandowski and C. Thomas, *A review of recent advances in GPS time comparisons*, in Proc. 4th European Frequency and Time Forum, pp. 307–312, 1990.

2. B. Guinot and W. Lewandowski, *Improvement of the GPS time comparisons by simultaneous relative positioning of the receiver antennas*, Bulletin Géodésique, 63, pp. 371–386, 1989.

3. M. Weiss, T. Weissert, C. Thomas, M. Imae and K. Davies, *The use of ionospheric data in GPS time transfer*, in Proc. 4th European Frequency and Time Forum, pp.327–333, 1990.

4. W. Lewandowski and M. A. Weiss, *The use of precise ephemerides for GPS time transfer*, in Proc. 21st PTTI, pp. 95–106, 1989.

5. D. W. Allan and M. Weiss, *Accurate time and frequency transfer during common-view of a GPS satellite*, in Proc. 34th Ann. Symp. on Freq. Cont., pp.334-346, 1980.

6. D. W. Allan, M. Granveaud, W. J. Klepczynski and W. Lewandowski, *GPS time transfer with implementation of Selective Availability*, in Proc. 22nd PTTI, 1990, accepted.

7. W. Lewandowski, R. J. Douglas, W. J. Klepczynski, W. Strange, J. Suter and M. A. Weiss, *Positioning of GPS antennas in time-keeping laboratories of North America*, in Proc. 43rd Ann. Symp. on Freq. Cont., pp. 218-224, 1989.

8. J. A. Klobuchar, *Ionospheric correction for the single frequency users of the Global Positioning System*, IEEE Trans. NTS,1982.

9. M. Imae, W. Lewandowski, C. Thomas and C. Miki, *A dual frequency GPS receiver measuring ionospheric effects without code demodulation and its application to time comparisons*, in Proc. 20th PTTI, pp.77-86, 1988.

10. D. Davis, M. A. Weiss and M. Vidmar, *A codeless ionospheric calibrator for time transfer applications*, in Proc. 2nd Intern. Meeting Inst. of Navigation, 1989.

11. M. Imae, M. Miranian, W. Lewandowski and C. Thomas, *A dual frequency codeless GPS receiver measuring ionospheric effects and its application to time comparison between Europe and USA*, in Proc. 3rd European Frequency and Time Forum, pp. 89-93, 1989.

12. J. Vondrak, Bull. Astron. Inst. Czechoslovakia, 20, 349, 1969.

ACRONYMS

BIPM	Bureau International des Poids et Mesures
C/A-Code	Coarse/Acquisition Code
CRL	Communications Research Laboratory
DMA	Defense Mapping Agency
IERS	International Earth Rotation Service
ITRF	IERS Terrestrial Reference Frame
LPTF	Laboratoire Primaire du Temps et des Fréquences
MJD	Modified Julian Date
NIST	National Institute of Standards and Technology
NSWC	Naval Surface Warfare Center
OP	Observatoire de Paris
P-Code	Precision Code
SLR	Satellite Laser Ranging

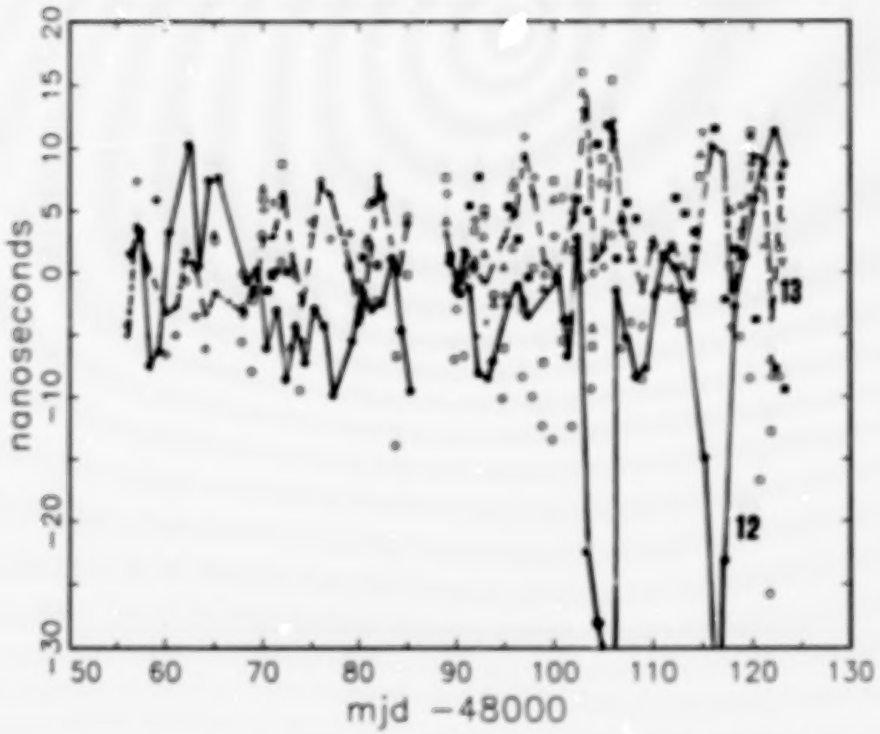


Figure 1. GPS time transfer UTC(OP) - UTC(NIST): residuals to the smoothed raw values (two points corresponding to PRN 12 are outside the frame).

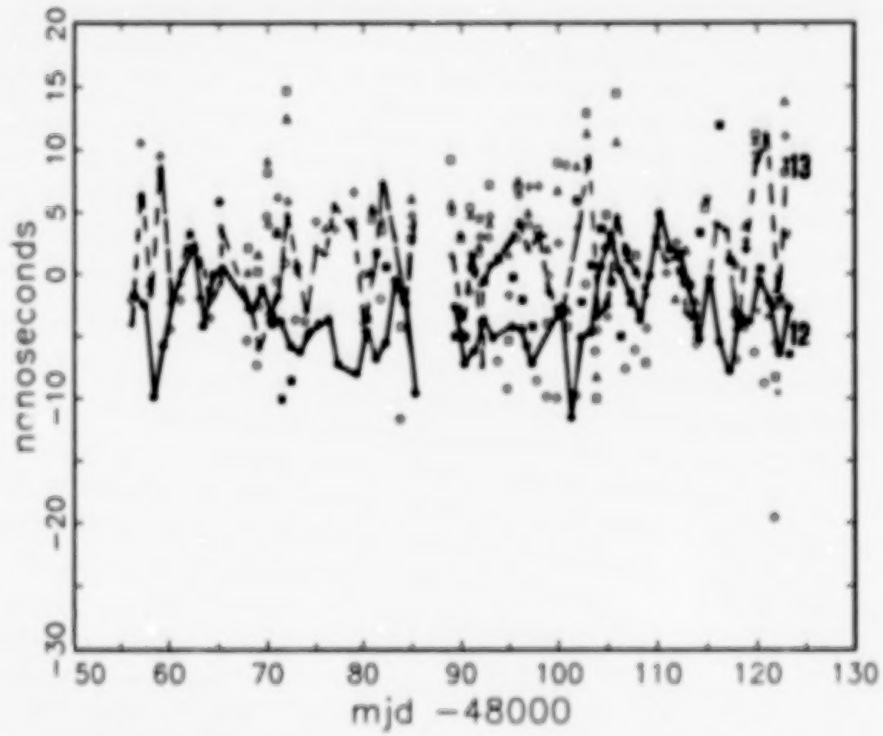


Figure 2: GPS time transfer UTC(OP) - UTC(NIST): residuals to the smoothed values previously corrected for precise satellite ephemerides.

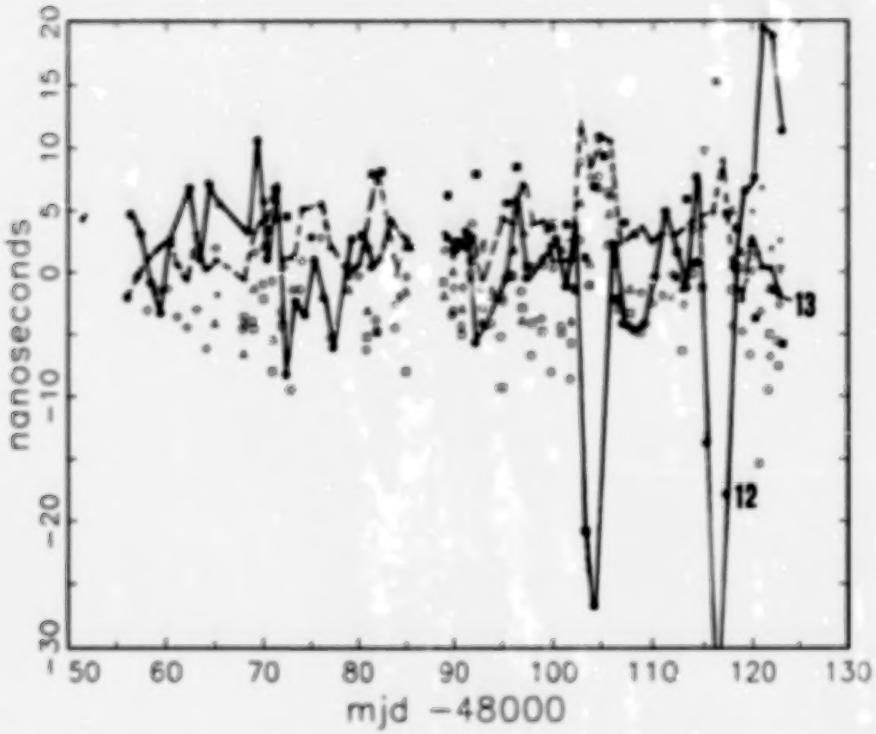


FIGURE 3: GPS time transfer UTC(OP) - UTC(NIST): residuals to the smoothed values previously corrected for measured ionospheric delays.

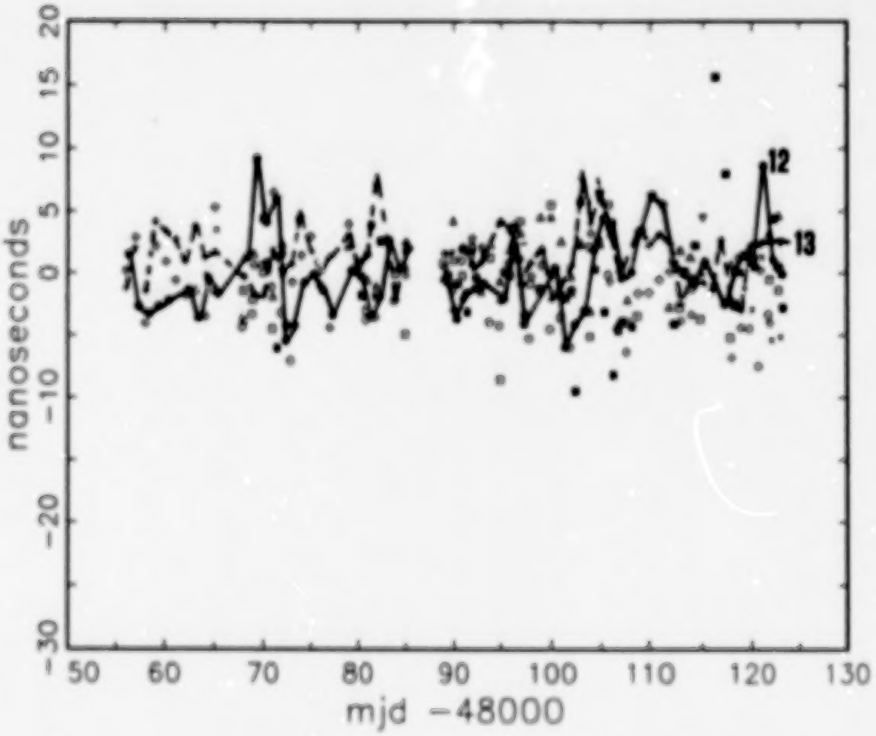


FIGURE 4: GPS time transfer UTC(OP) - UTC(NIST): residuals to the smoothed values previously corrected for precise ephemerides and measured ionospheric delays.

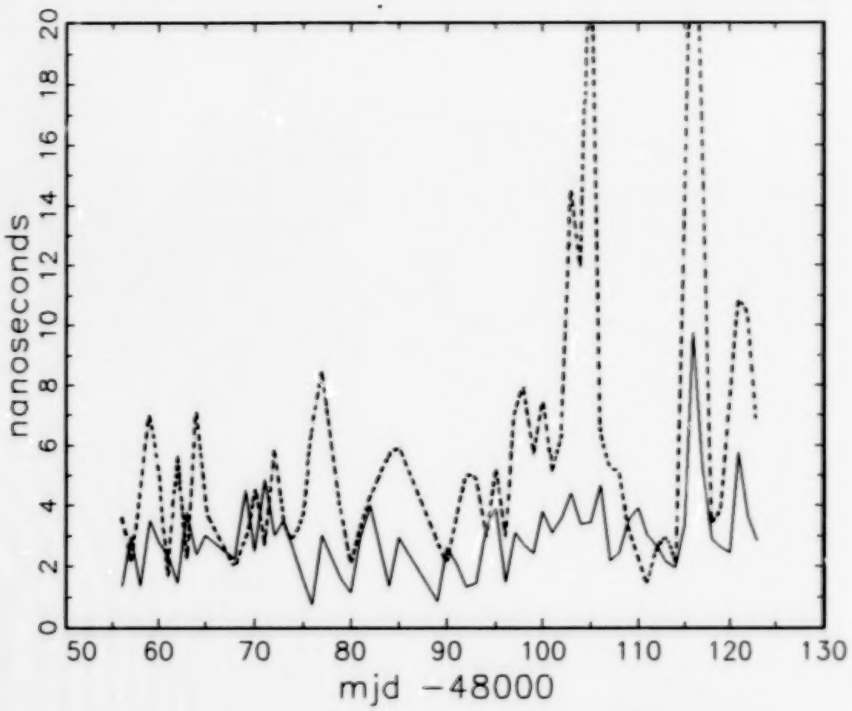


FIGURE 5: GPS time transfer UTC(OP) - UTC(NIST): daily standard deviations of the residuals obtained with:
--------- raw data,
——————— data corrected for precise ephemerides and measured ionospheric delays.

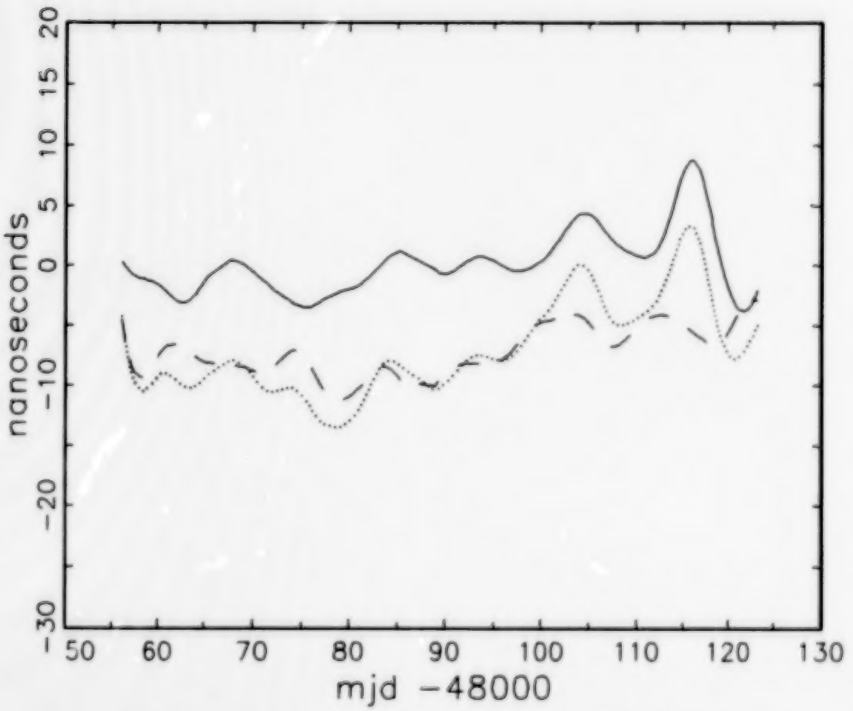


FIGURE 6: Difference between the corrected and the raw values UTC(OP) - UTC(NIST). The corrected values UTC(OP) - UTC(NIST) are obtained with:
——————— precise ephemerides,
— — — — measured ionospheric delays,
..... precise ephemerides and measured ionospheric delays.

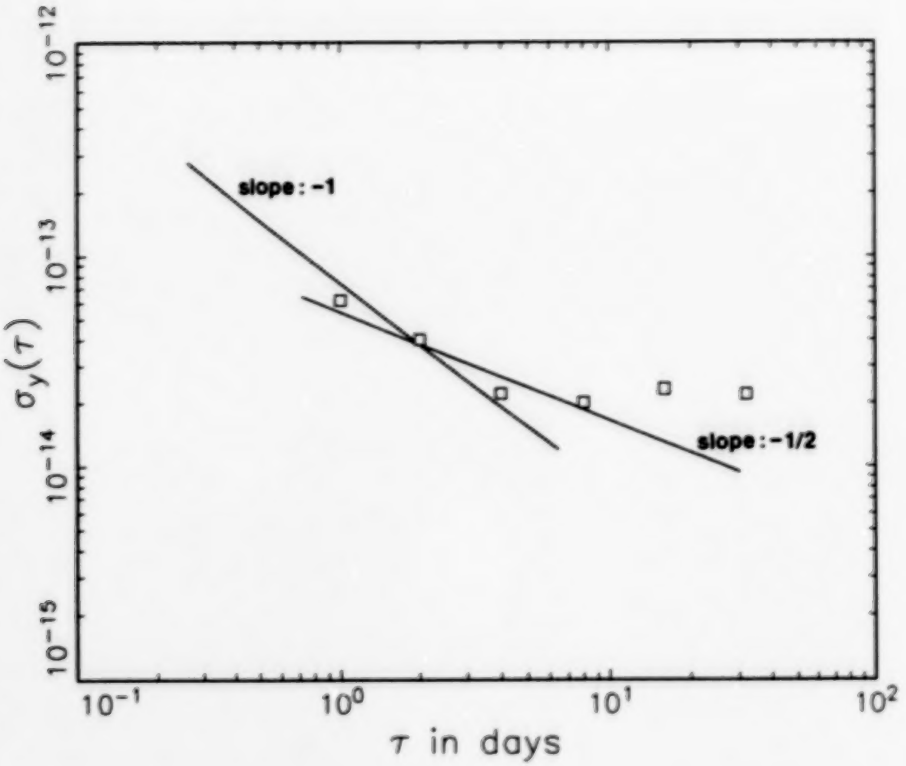


FIGURE 7: Allan deviation of the raw values UTC(OP) - UTC(NIST).

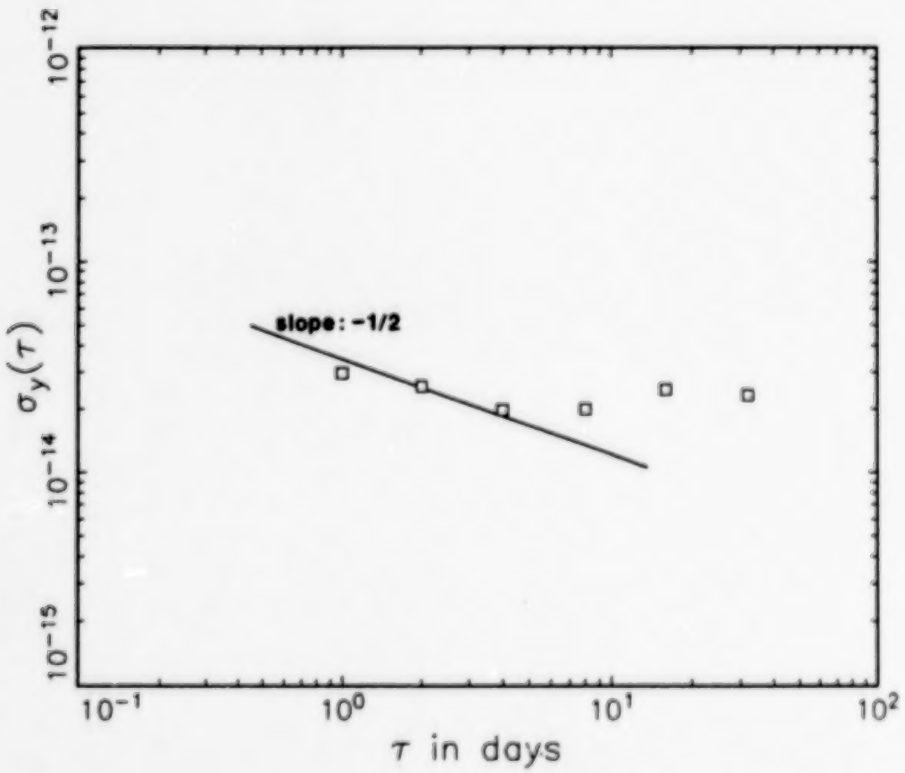


FIGURE 8: Allan deviation of the values UTC(OP) - UTC(NIST) after correction for precise ephemerides and measured ionospheric delays.

QUESTIONS AND ANSWERS

David Allan, NIST: How do you combine the nine readings of each satellite each day?

Dr. Thomas: We did smoothing and then took the value each day at zero hours, UTC.

Mr. Allan: Are all values treated equally?

Dr. Thomas: Yes.

Anthony Liu, The Aerospace Corporation: By what method do you use the differential correction for your ephemeris?

Dr. Thomas: We get the parameters for the precise ephemeris each 15 minutes. It is a little difficult to explain here, but it is in the paper.

Mr. Liu: What is the general magnitude of the correction in meters or other units?

Dr. Lewandowski: It can reach 10 meters. Generally it is not more than 3 to 5 meters.

Unknow Voice: I would add that the uncertainty of the DMA precise ephemerides are about three meters. A study that was made last year showed that the broadcast ephemerides differed by an average of about 5 or 6 meters. For rubidium equipped satellites, this difference can get to 30 meters during eclipses.

Michel Grandveaud, Paris Observatory: I would like to know whether the same filtering was used on the data and the corrected data and whether you observed a bias between the results of these two filterings?

Dr. Thomas: The filtering was the same for both cases. Yes, there was some bias. It is shown in the paper.

Tom McCaskill, Naval Research Laboratories: We are looking at the use of precision clocks in a fairly complex system. What we have seen on the frequency stability profile in what you have presented and in the previous paper and you can identify from the slopes of the frequency stability profile the types of noise on the clocks. The clocks have been very well characterized in terms of the types of behavior. If you use the data to determine the slope, then you can identify the random noise process. If the alopes do not agree with the known behavior of the clock, then the noise is coming from some other part of the system. This sort of behavior tells you that it is a non-clock process, or at least that it is not a well behved clock.

GPS/Loran–C Interoperability for Time and Frequency Applications—A Survey of the Times of Arrival of Loran–C Transmissions via GPS Common Mode/Common View Satellite Observations

Bruce Penrod, Richard Funderburk, Peter Dana–Consultant
Austron, Inc.
P.O. Box 14766
Austin, Texas 78761

I. Introduction

Since the advent of GPS satellite based time and frequency transfer the role of Loran–C in this application has been greatly diminished. The capabilities of undegraded GPS are indeed superior to those of the Loran–C system in most respects including coverage, absolute timing accuracy, and ease of use. However potential drawbacks of GPS to the time and frequency user exist, such as higher cost, more complex hardware and non–civilian control of the system. This last has brought us the specter of Selective Availability (SA), an on again–off again, intentional degradation of the accuracies obtainable from the GPS. Though not the focus of this report, it should be noted that the medium term (τ =780 seconds) frequency stability of the Loran–C transmissions, for reasonably close transmitters, is almost two orders of magnitude better than that of the GPS transmissions observed under SA—reason enough to keep Loran–C in mind for frequency control purposes.

This paper surveys the absolute time setting performance achievable from seven distinct transmitters in four North American chains via the Loran–C Time of Coincidence (TOC) with UTC synchronization technique. Motivation for this undertaking consisted of both frustration with SA and strong curiousity about how well the propagation path of the Loran–C signals could be modeled and how well the transmitters are synchronized to UTC as a result of the enactment in 1987 of Public Law 100–223[2] requiring synchronization at the 100 ns level. Navigation users desiring to combine GPS with Loran–C to enhance the overall reliability of their systems would prefer to treat the Loran–C signals analogously to those from the satellites, i.e. as pseudo–ranges rather than as time differences (TD's), the input to the traditional Loran–C hyperbolic navigation solution. Multi–chain Loran–C navigation is also facilitated by absolute time synchronization as well.

The propagation modeling techniques applied in this study were intentionally limited to those which could be implemented in a modern, low cost microprocessor based instrument and therefore do not include the terrain inclusive, full wave integral approach. The results presented here support development of a new Loran–C timing receiver with internal propagation path correction and multiple chain capability offering precise time setting at the 500 ns level. While this performance is just comparable

to that of GPS under SA for absolute timing, the frequency stability is far superior and the equipment cost is much less.

II. Approach

The equipment for the experiment consists of an Austron Model 2201 GPS Timing and Frequency receiver, an Austron Model 2100T Loran-C Timing receiver, an HP-85 desktop computer for controlling the 2100T receiver, an antenna ambient temperature recorder and various PC's for processing and presenting the data. The 2201 GPS receiver is operated in the NIST/USNO time transfer mode where both the tracking of satellites and the processing of the acquired data are to the NIST/USNO specified format. Adherence to these specific requirements allows a differential time transfer mode of operation with various time standards laboratories worldwide who maintain receivers which track to the same specifications and make that data available to the public. The benefit of this common mode/common view operation is of course the complete removal of the satellite clock error and partial removal of orbital and ionospheric errors. Significant reduction of SA induced errors is also realized since they are a combination of satellite clock and ephemeris dithering.

Knowledge of the receiver positions at both ends of the link is of course required for this to work. Austron's position was transferred, via a differential GPS carrier phase survey, from the position of the Applied Research Laboratories of the University of Texas at Austin which is known to the one meter level in WGS 84. The time transfer accuracies attainable under these conditions are at the 10 ns level under the non-SA conditions experienced during the duration of the data taking.

The 2100T Loran-C receiver is operated in a sequence mode of operation under the control of the HP-85 desktop computer via the IEEE-488 bus. The HP-85 takes care of the parameter set-up for each of the ten Loran-C transmissions tracked over the data acquisition period. These include setting the Group Repetition Interval (GRI), secondary coding delays, and TOC synchronization times. All error messages generated by the 2100T such as blink, cycle error and loss of signal are logged by the HP-85 as well in order to facilitate outlier removal.

Data was acquired in both three hour and twenty-four hour dwell modes, according to this pattern: one ten day, three hour dwell period followed by one twenty day, twenty-four hour dwell period and finally one ten day, three hour dwell period. Additional data was then taken for about six days on the two weakest stations, Carolina Beach and Searchlight, to make up for significant gaps due to skywave tracking problems during the sequencing periods, and also on Dana to resolve GRI related anomalies in the TOA's which were noted during the sequencing periods.

After acquiring the Loran-C pulse and selecting the third cycle, the 2100T waits for the next TOC to synchronize its 1 PPS output to the arrival time of the UTC synchronized Loran-C pulse. If the Loran-C pulse does indeed arrive at the scheduled time then the receiver indicates that a successful TOC synchronization has occurred and sets its 1 PPS output to that time of arrival. This 1 PPS output is input to the 2201 GPS receiver which measures its relation in time to the received satellite currently being tracked and logs the data in the NIST/USNO format. Approximately twenty-four hours later the corresponding USNO track data is available for downloading over a modem and used to correct the previously acquired raw satellite data. These differential TOA's, now referenced to the USNO master clock, are then corrected for propagation path delays and analyzed with the temperature data.

III. Loran–C TOA Predictions

A. Background

All positions and path corrections are in the WGS–84 geodetic datum[1]. The Austron antenna position for both GPS and Loran–C is:

Receiver	Latitude	Longitude
Austron Site	+30:27:15.47	- 97:39:45.72

The Loran–C transmitters and their positions[2] are shown in Table 1.

TABLE 1. Loran–C Transmitter Locations

Transmitter	Latitude	Longitude
Malone	+30:59:38.870	– 85:10:08.751
Grangeville	+30:43:33.149	– 90:49:43.046
Raymondville	+26:31:55.141	– 97:49:59.539
Jupiter	+27:01:58.528	– 80:06:52.875
Carolina Beach	+34:03:46.208	– 77:54:46.100
Dana	+39:51:07.658	– 87:29:11.586
Searchlight	+35:19:18.305	–114:48:16.881

The conductivity data used for these predictions is a set of disk files: the FCC data base for microcomputers[3]. The FCC M3 map file data shown in Figure 1 is based on a study of effective ground conductivity for the United States[4]. The data, in the form of line segments that define conductivity boundaries, was accessed by a program written for this project that returns the conductivity for any latitude and longitude.

An ellipsoidal ray path is computed[5] from the Austron site to the Loran–C transmitter and with an arbitrary step size a set of latitudes and longitudes is created for looking up conductivities. The prediction program produces a list of ranges and conductivities along the path from receiver to transmitter.

The phase delay of a ground wave can be separated into two components: the primary phase and the secondary phase. The primary phase is the result of propagation through the air while the secondary phase is the result of propagation over a conducting surface with terrain variations. National Bureau of Standards Circular 573[7] defines the primary and secondary phase for the low frequency groundwave over homogeneous paths. The primary ground wave phase can be described as:

$$pf = \frac{dn}{c_0} \tag{1}$$

where:

$$pf = \text{primary phase (seconds)} \tag{2}$$

d = range meters
c_0 = speed of light in vacuo (meters/sec)
n = index of refraction of air

The index of refraction of air is influenced by pressure, temperature, and humidity[9]:

$$n = 1 + 0000776(P/T + 4810e/T^2) \tag{3}$$

where:

T = temperature (°K) (4)
P = atmospheric pressure (millibars)
e = partial water vapor pressure

For most ground wave predictions, Loran-C in particular, a value for n is assumed to be 1.000338[7]. The value can change from 1.0002 to 1.0004[10]. The wave velocity at 100 kHz at the surface for a perfectly conducting ground and $n = 1.000338$ is then:

$$c = \frac{c_0}{n} = 299691162 \; meters/second. \tag{5}$$

The secondary phase correction may be computed using the methods provided by NBS 573. The methods involve time consuming solutions of Legendre polynomials and Hankel functions. Faster methods have been developed for receiver implementation.

B. Brunavs' Polynomials

A faster method of obtaining secondary phase corrections from distance and conductivity in a real time receiver uses Brunavs' formulas[8]. The corrections applied here employ the eight coefficient implementation offering residual fit errors at the six meter level. The correction returned by the Brunavs formula, Eq. 6 is added to the primary phase correction to give the total path delay.

$$p = c_1 + c_2 s + (c_3 s + c_4)e^{c_5 s} + \frac{c_6}{1 + c_7 s + c_8 s^4} + \frac{2.277}{s}, \tag{6}$$

where:

s = range (meters)/100000 (7)
p = phase lag (meters)
c_i = eight coefficients for each conductivity

Application of Brunavs' formula to the mixed conductivity paths typically encountered is performed using three approaches: average conductivity, average complex impedance, and the Millington-Pressy[9]

technique. The first two techniques are essentially range segment length weighted averages of either the conductivity (real) or the impedance (complex) along the receiver to transmitter path. The impedance method requires the additional step of converting back to conductivity after the path integration[11]. The third approach is a heuristic method which has historically given good results near distinct impedance boundaries (coastlines), where it reproduces the localized phase disturbances near those boundaries. Table 2 presents the path data for each transmitter.

TABLE 2. Propagation Path Characteristics

Transmitter	Range (km)	Pri. Phase (μs)	Sec. Phase (μs)		
			Cond.	Imp	Mil-Pres.
Malone	1197.479	3995.710	6.881	6.550	5.847
Grangeville	656.048	2189.082	3.119	3.076	2.924
Raymondville	435.021	1451.563	1.618	1.598	1.560
Jupiter	1753.507	5851.047	6.546	5.490	5.970
Carolina Bch	1900.259	6340.725	9.953	9.741	9.569
Dana	1393.296	4649.107	6.188	6.102	5.910
Searchlight	1689.677	5638.062	7.520	7.464	7.052

C. Propagation Model Evaluation

1. Correction of Chain Timing Errors

As previously alluded, TOA data on some of the dual rated Loran-C transmitters exhibited anomalous behavior, i.e. a 5 μs difference between the same transmitter on a different chain GRI. Since there could be no path differences in these transmissions and since the receiver will only track positive zero crossings of the 100 kHz carrier, a flag was raised concerning phasing of the chain. This characteristic was observed on transmissions from Dana on GRI's 89700 and 99600 and from Carolina Beach on GRI's 79800 and 99600. In each case, the transmissions from the 99600 GRI were 5 μs later than the other GRI. The transmissions from Malone on GRI's 79800 and 89700 did not exhibit such a large difference, however. They differed by less than a microsecond. The transmissions from Searchlight on GRI 99400 fall in line with those from the North East chain on GRI 99600.

Conversations with the Loran-C timing personnel at the USNO and measurements made by them on November 28-29, 1990 confirmed these anomalies on Dana, Seneca and Carolina Beach[13]. The USNO measurements, made with an Austron Model 2100T receiver, place the transmissions on GRI 99600 on-time relative to the USNO Master Clock. Those from the 89700 and 79800 GRI's are 5 μs early. Based on this information, all data from these early arriving GRI's was corrected prior to further processing by the addition of exactly 5 μs to their TOA's.

2. Model Evaluation

Performance of each of the techniques on actual Loran-C TOA data taken from the Austron site is shown in Figures 2 and 3, which present data from two consecutive ten day twenty-four hour dwells on seven Loran-C transmitters, three of which are dual rated and seen twice each ten days. Each data trace has been corrected for propagation delay using one of the three methods described previously.

Regression analysis on the entire forty-seven days of data, corrected by each of the three methods, is summarized in Figure 4. The complex impedance approach yields the tightest cluster of TOA's with a residual RMS scatter of 463 ns. It also yields a TOA midway between those of the other two models. Since the Austron location is not near any significant impedance boundary, any advantages yielded by the Millington-Pressy approach may not be visible. In fact the method performs the most poorly of the three with a residual RMS scatter of 732 ns. The average conductivity approach is slightly better at 669 ns. The remainder of the data and analysis makes use only of the average complex impedance path correction.

IV. Results

A. Overall Performance

More than one thousand TOA's were logged over forty-seven days of testing. The vast majority of these NIST/USNO formatted points were complete 780 second tracks. For each of these time-tagged points an antenna temperature reading was collected. Figure 5 shows all of the data collected over the experiment, including the temperature trace. Linear regression analysis on this propagation corrected data versus time and temperature yields a frequency offset of 10.8 ns/day with +/-1.4 ns/day one sigma points, a temperature coefficient of -1.1 ns/deg C with +/-2.2 ns/deg C one sigma points (no significant temperature coefficient in this mixed data), and a residual standard deviation of 463 ns. From the regression data, the predicted GPS and Loran-C antenna, cable and receiver delays would be 53.418 μs at the time of the first data point on MJD 48169 (October 5, 1990).

The actual delays measured on the two receivers were:

Model 2201 GPS receiver	.047 μs	
Model 2100T Loran-C receiver	51.760 μs	(includes third cycle tracking delay)

The difference of these delays, 51.713 μs, should be the expected offset of the received Loran-C TOA's, as measured by the GPS receiver, from USNO via the common mode/common view technique. This implies that the realized absolute time transfer accuracy over the period of this test, including transmitters nearly two thousand kilometers away, is:

$$53.418\mu s - 51.713\mu s = 1.705\mu s \pm 1\sigma = .463\mu s$$

B. Individual Transmitter Performances

Figures 6 and 7 show two consecutive ten day periods of propagation delay corrected, twenty-four hour dwell TOA data with the antenna temperature shown on the bottom trace. Inspection of these charts shows that there are varying levels of temperature correlation in the received signals from the different transmitters as well as definite biases in the TOA's. Linear regression analyses on both time and temperature for each transmitter's set of data yield the results graphed in Figures 8 through 12.

Figure 8 shows the regressed TOA's at test startup, MJD 48169 (October 5, 1990) and the residual standard deviations for each transmitter. These TOA's vary from 52.8 μs to 53.9 μs across the transmitters while the residual standard deviations vary from less than 100 ns to over 500 ns.

Figures 9 and 10 show the regression coefficients (slopes) for time and temperature along with their standard deviations. The temporal slope varies from 2 ns/day to 18 ns/day (low parts in 10^{13} fractional frequency offset), and the temperature coefficients range from -2 ns/deg C to almost 45 ns/deg C. This latter level, from the Searchlight transmitter, is almost certainly not actually temperature induced but is more likely skywave induced. The levels of the other six transmitters, ranging from -2 ns/deg C to 8 ns/deg C are in reasonable agreement with those reported in previous proceedings of this conference[12].

Since the data taken for this survey covers transmitters located from 400 km to nearly 2000 km from the Austron site, some correlation should be observable between both the residual standard deviations of the TOA's and the temperature coefficients. Figure 11 plots the regression residual standard deviation against the range in kilometers divided by the square root of the peak radiated power in watts (very much a first order approximation to received signal to noise ratio). Though not perfectly correlated, especially in the more distant transmitters, a definite relationship is evident. Figure 12 plots the regression temperature coefficient versus range. Here as well a strong overall trend is evident. The Jupiter transmitter with its very small and negative coefficient, whose path contains the only sea water of the transmitters tracked, falls completely out of line with the other transmitters. The Dana transmitter also displays unexpectedly good temperature insensitivity considering the length of the path.

V. Conclusions

The results from this survey (even ignoring the systematic 5 μs error) clearly indicate that the GPS time transfer capability is superior to that of the Loran-C system for absolute timing accuracy, and that even with the most careful calibration of the Loran-C receiver delay and propagation path, inexplicable TOA biases remain which are larger than the variations across all of the transmitters. Much more data covering years would be needed to show that these biases were stable enough to be removed with a one time site calibration.

The syntonization of the transmissions is excellent, all showing low parts in 10^{13} offsets versus the USNO master clock. With the exception of the Searchlight transmitter, all of the transmissions exhibit timing stabilities over the entire period of less than 300 ns RMS which is at the observed levels of GPS under SA. As previously mentioned though, the Loran-C phase instabilities take place over a much greater time interval than those being forced onto the GPS signals under SA, providing far better medium to short term frequency stability. This is shown in Figure 13 where 780 second observations of the Loran-C received fractional frequency offsets have been combined in a RMS sense and plotted versus transmitter and range/square root power ratio. From this data it can be seen that all but the most distant transmitters offer better than three parts in 10^{11} stability at this averaging time. It is in the frequency control area where GPS/Loran-C interoperation will offer some synergistic advantages over GPS alone under SA.

Synchronization of the chains to UTC as required by Public Law 100-223 has obviously not been accomplished at this time.

VI. References

1. Department of the Air Force, WGS 84 Defining Parameters and Derived Constants, HQ USAF Space Division, Los Angeles, 1987.

2. U.S. Coast Guard, Radionavigation Bulletin, Number 23, U.S. Department of Transportation, Washington, DC, 1990.

3. FCC, FCC M3 Map Data File for Microprocessors, NTIS PB87- 222253, Washington, DC, 1981.

4. Fine, H., *An Effective Ground Conductivity Map for Continental United States,* Proceedings of the IRE, September, 1954.

5. Snyder, J. P., Map Projections Used by the U.S. Geological Survey, USGS 1532, Washington, DC, 1982.

6. U.S. Coast Guard, Specification of the Transmitted Loran-C Signal, USCG COMDTINST MI6562.4, U.S. Department of Transportation, Washington, DC, July, 1981.

7. Johler, J. R., et al, Phase of the Low Frequency Ground Wave, NBS Circular 573, Washington, DC, 1956.

8. Brunavs, P., Phase Lags of 100kHz Radiofrequency Groundwave and Approximate Formulas for Computation, Canadian Hydrographic Service Internal Report, 1977.

9. Samaddar, S. N., *The Theory of Loran-C Ground Wave Propagation—A Review,* Journal of the Institute of Navigation, Vol. 26, No. 3, Washington, DC, 1979.

10. Doherty, R. H., L. W. Campbell, S. N. Samaddar and J. R. Johler, *A Meteorological Prediction Technique for Loran-C Temporal Variations,* Wild Goose Association, Williamsburg, VA, 1979.

11. Johler, J. R., Loran-C Pulse Transient Propagation, U.S. Dept. of Transportation, NTIS AD A077551, Washington, DC, 1979.

12. Markovic, Zoran M., *Meteorological Influences on Loran-C Propagation Over Sea and Land in Mediterranean Sea Chain,* Proceedings of the Twentieth Annual Precise Time and Time Interval (PTTI) Applications and Planning Meeting, Washington, DC, 1988.

13. Telecons with Mihran Miranian of the USNO, November 21-30, 1990.

FIG. 1--ECC M3 Conductivity Map

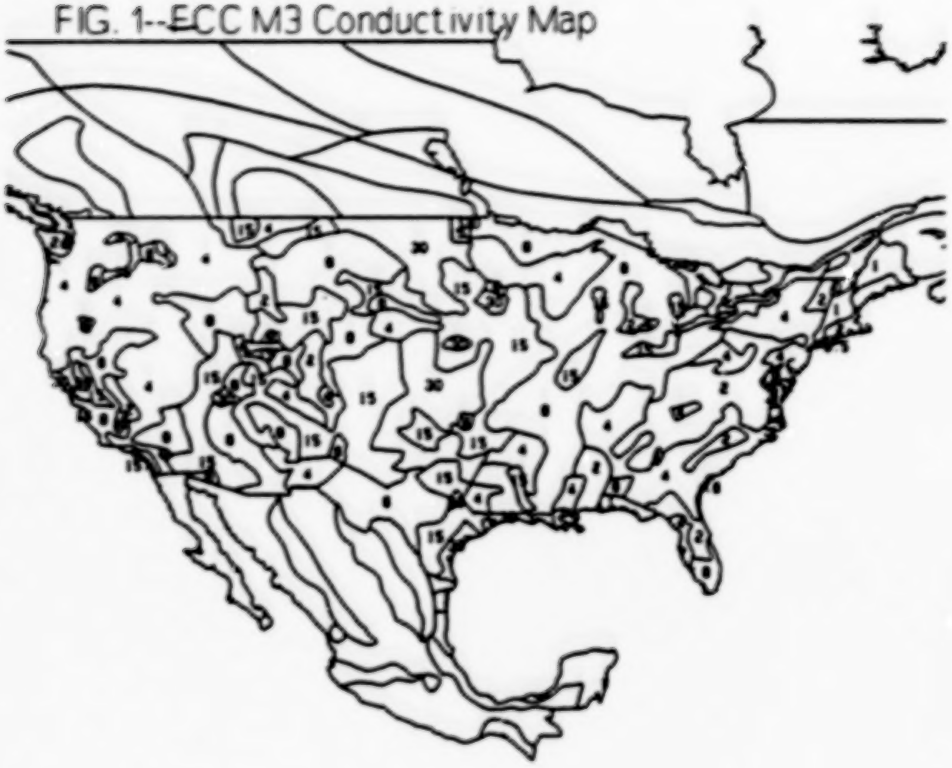


FIG. 2--Loran-C TOA's, 24 Hour Duells,
Various Propagation Models

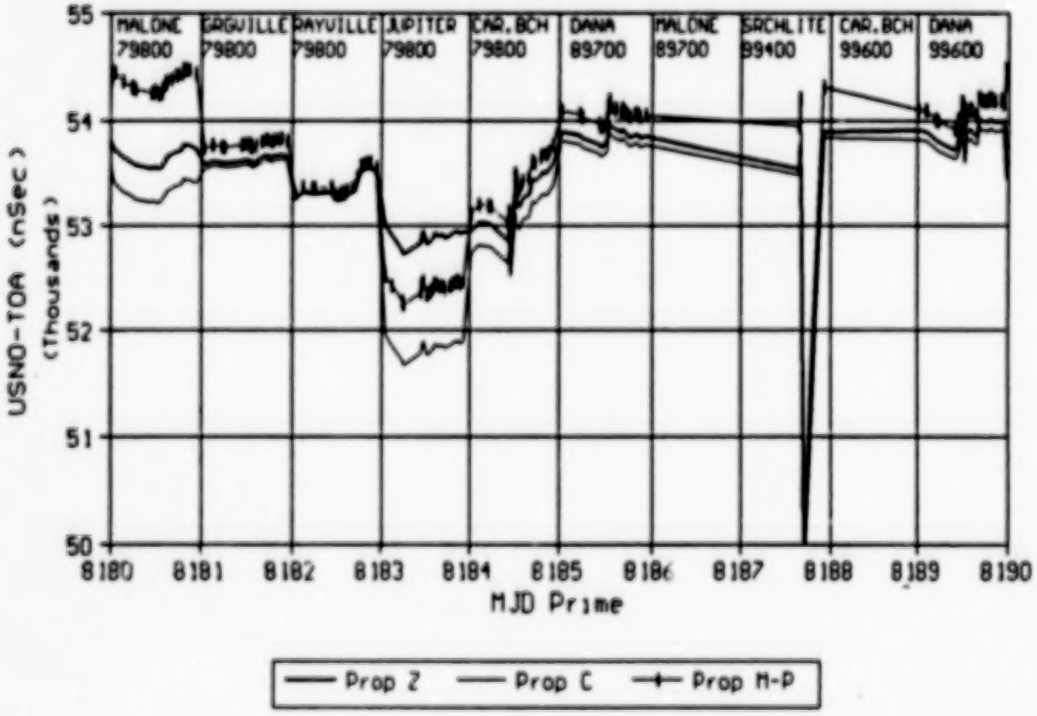


FIG. 3--Loran-C TOA's, 24 Hour Duells,
Various Propagation Models

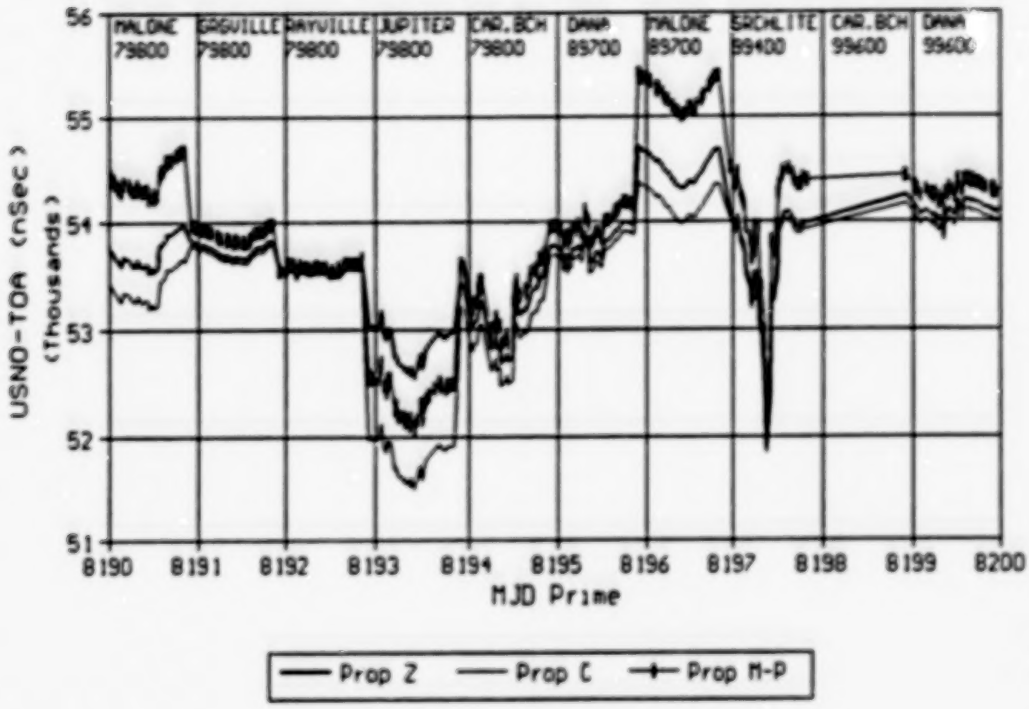


FIG. 4--Loran-C TOA's, Residual RMS,
from Time/Temp Regression

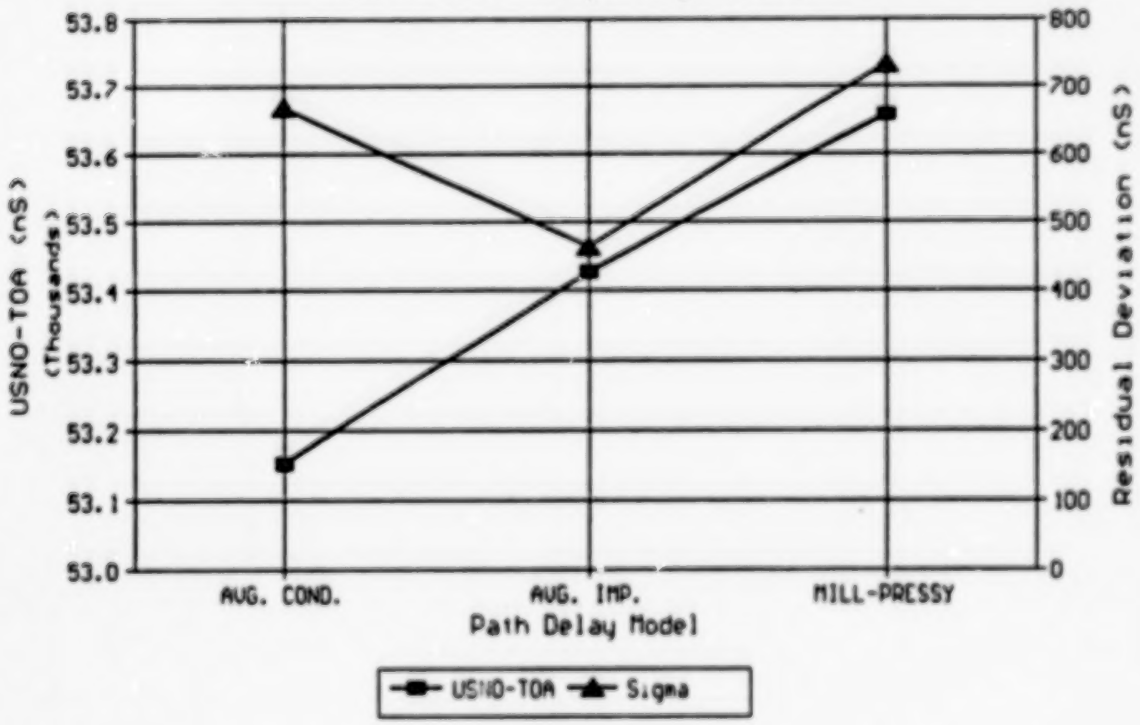


FIG. 5--Loran-C TOA's, 3 Hour/24 Hour Duells vs Antenna Temperature

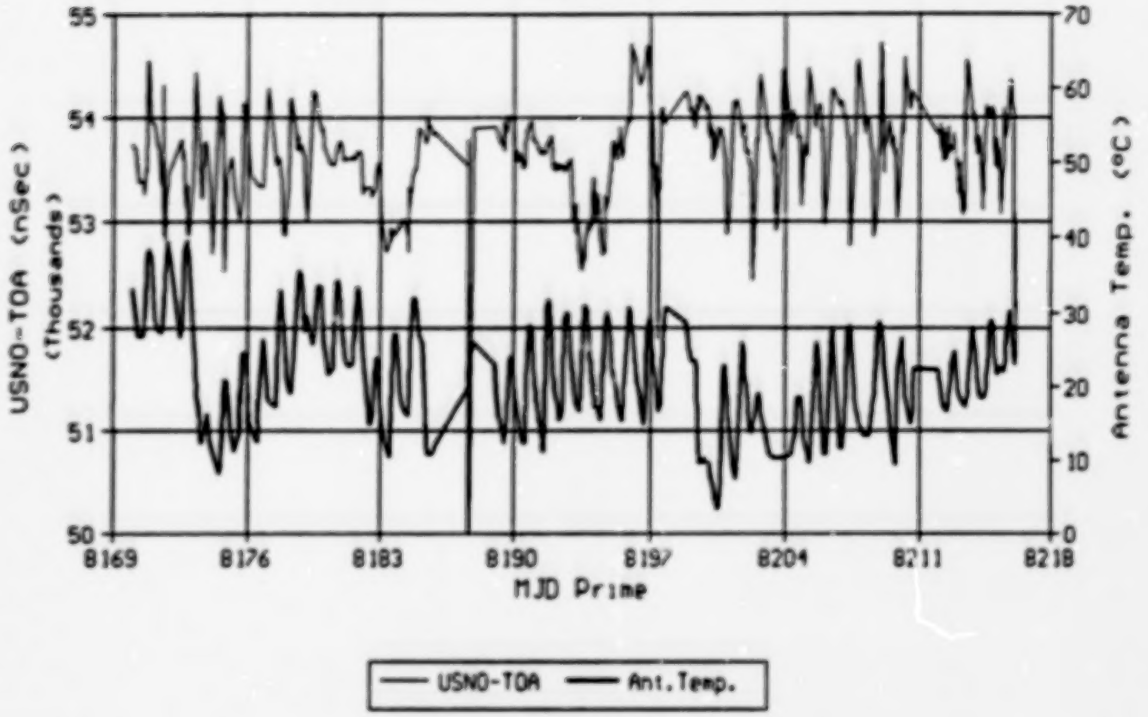


FIG. 6--Loran-C TOA's, 24 Hour Duells vs Antenna Temperature

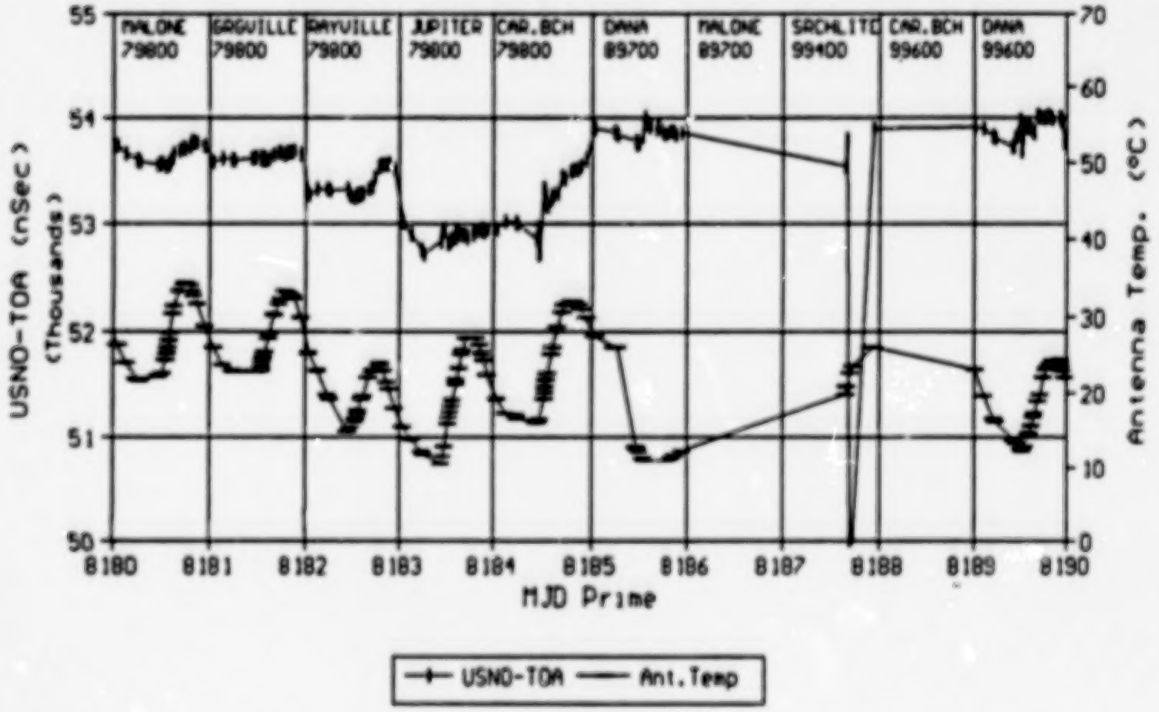


FIG. 7--Loran-C TOA's, 24 Hour Dwells
vs Antenna Temperature

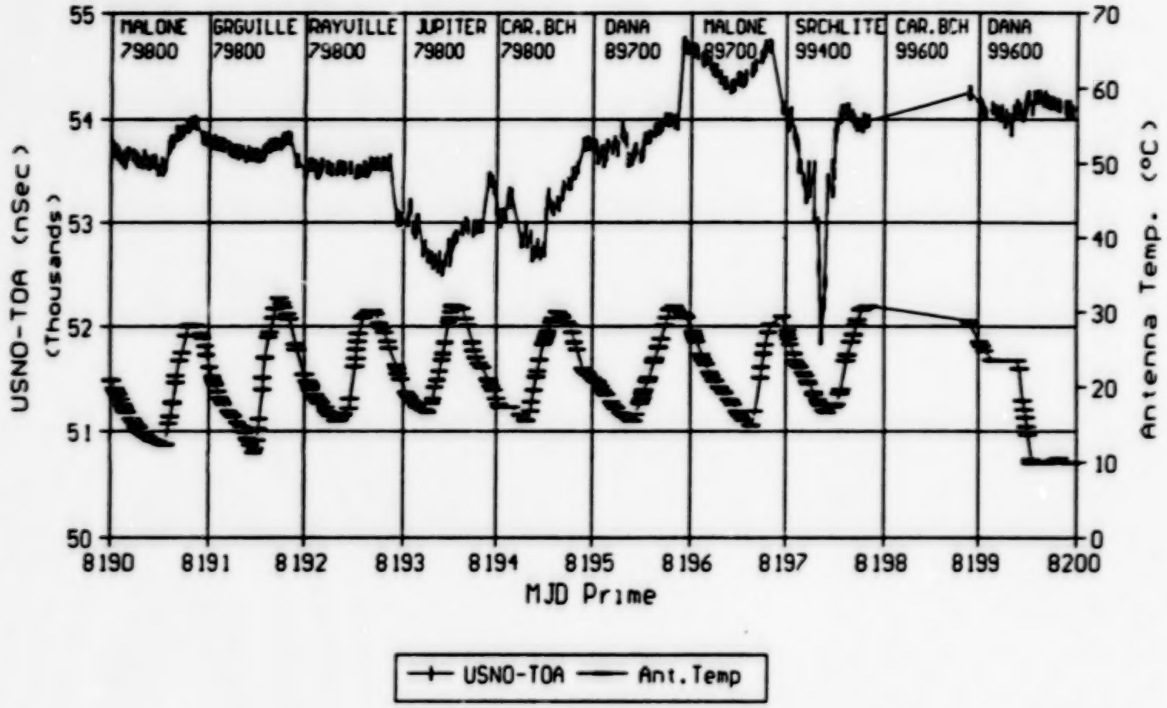


FIG. 8--Loran-C TOA's and Residual RMS
from Time/Temp Regression

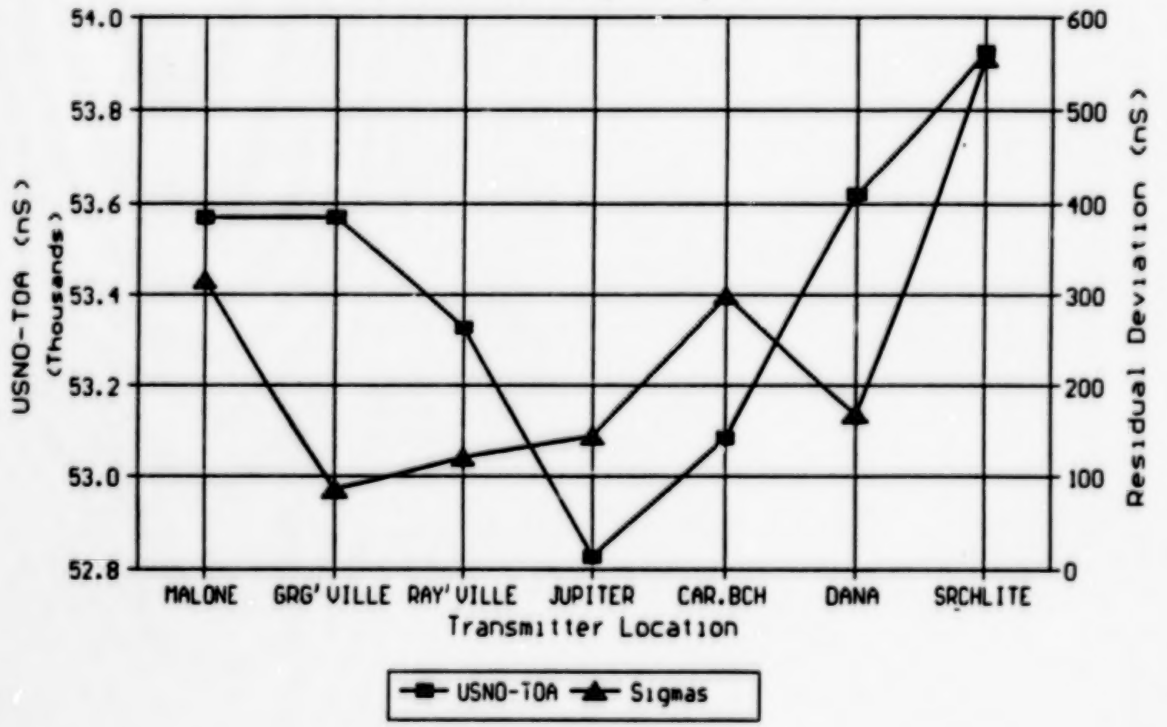


FIG. 9--Loran-C δ(USNO-TOA)/δt and Sigma from Time/Temp Regression

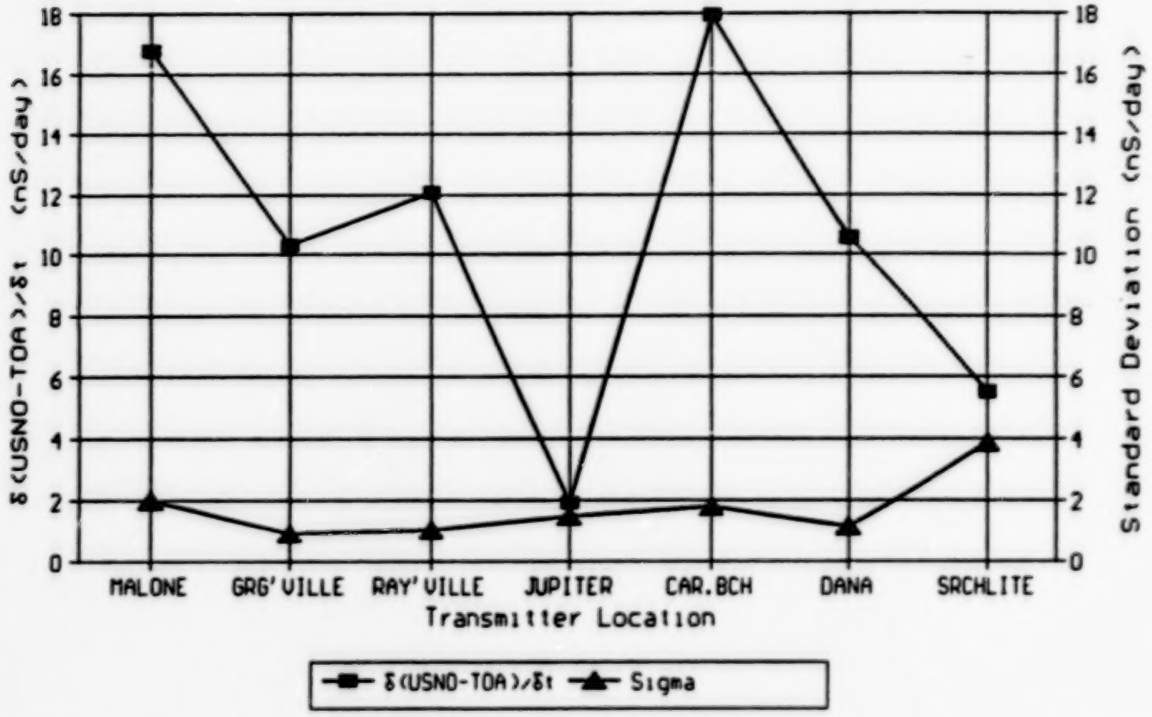


FIG. 10--Loran-C δ(USNO-TOA)/δT and Sigma from Time/Temp Regression

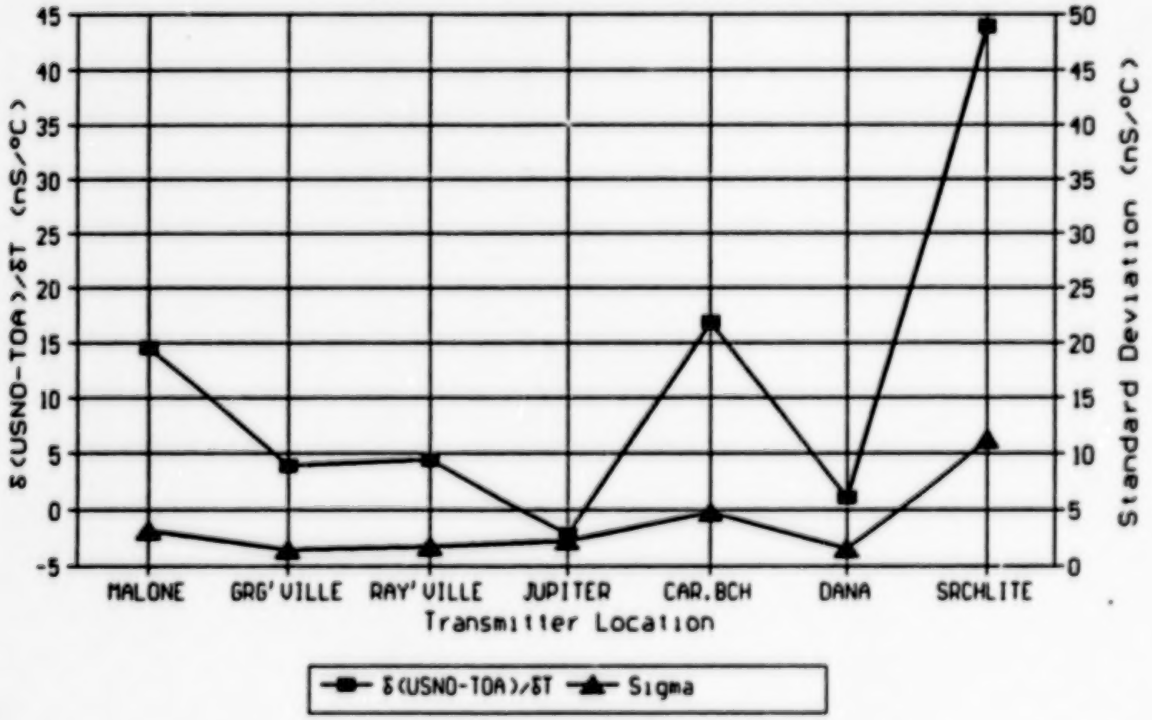


FIG. 11--Loran-C Residual RMS vs. R/√P
from Time/Temp. Regression

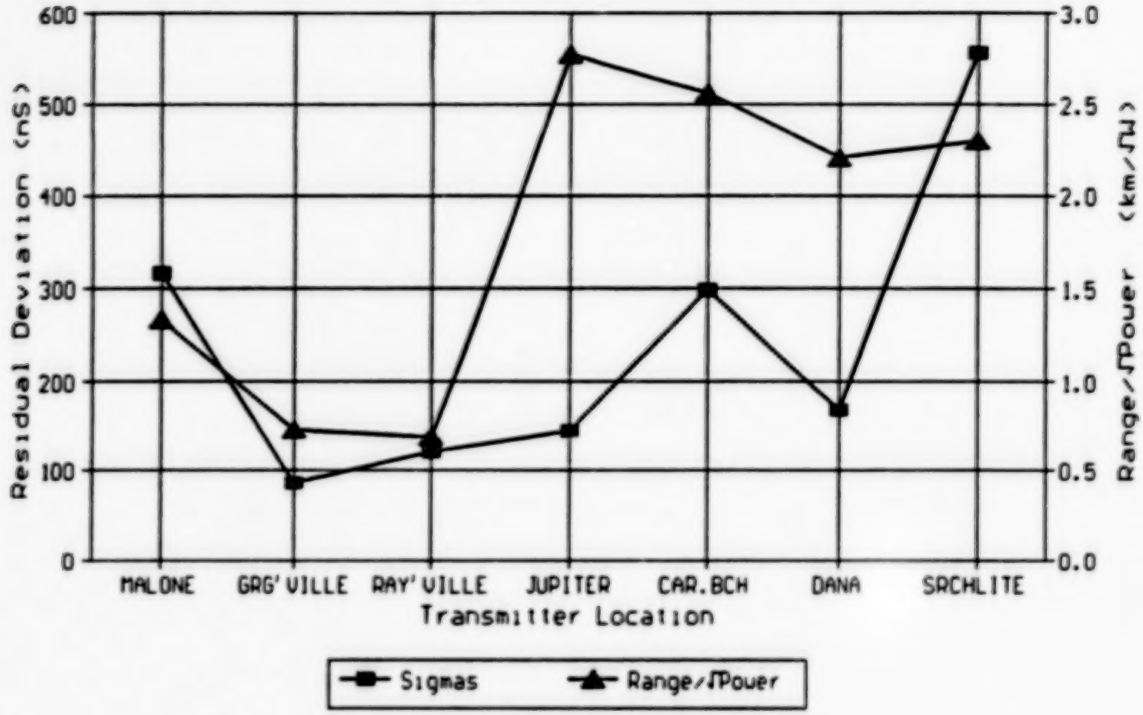


FIG. 12--Loran-C δ(USNO-TOA)/δT vs Range
from Time/Temp. Regression

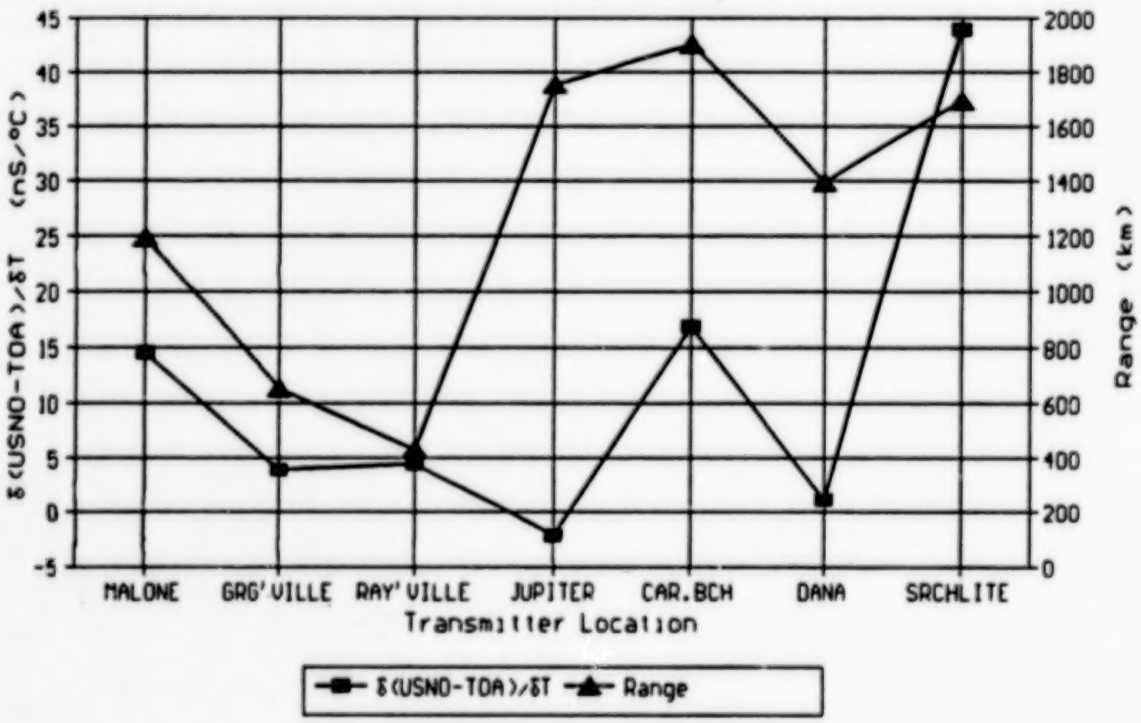
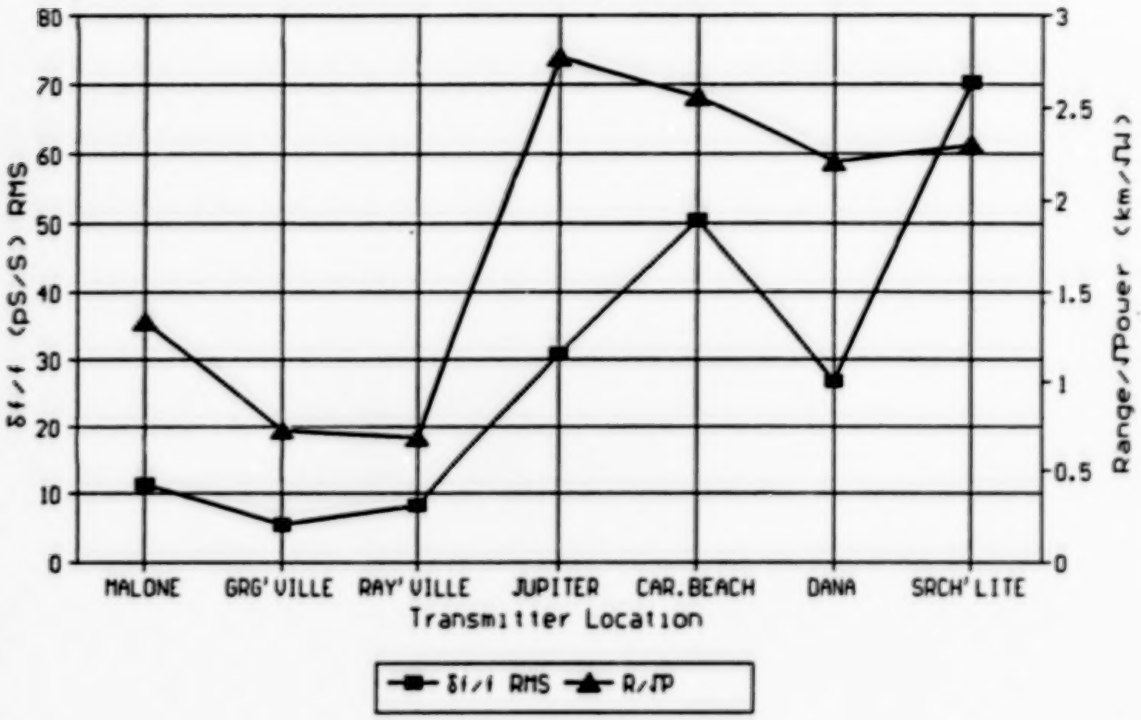


FIG. 13--Loran-C RMS $\delta f/f$ @ γ=780 sec
from GPS Time Transfer Data



QUESTIONS AND ANSWERS

Dr Winkler, U. S. Naval Observatory: I would like to make some comments regarding your interesting presentation. Number one, your conclusions are completely consistent with my own. I think that you have done an excellent job. Number two, I would suggest that, in addition to the disturbances and causes for noise which you have mentioned, there is one which is particularly important in the Washington metropolitan area. That is interference. Interference, as it comes on and goes off, will, depending on the position of the filters in the preamplifiers, affect the bias in the receivers. This is quite a problem and it is part of our efforts to improve our capabilities in our monitoring. That leads me to the third point and that is your conclusion that the Public Law requirement has not been realized. I would say 'not yet been realized' because there are considerable efforts going on which have been hampered by the lack of funding. Congress passed a law without regular and well organized funding procedure. Under the funding limitations which now exist, the problems of truly synchronizing all of the chains to within 100 nanoseconds has only been partially attacked. Part of the problem, as you have seen, is the 5 microsecond ambiguity. That has a historical reason. Many of the loop antennas which were used in the past had the arrow pointed in the wrong direction. If you have stations which have the 5 microsecond offset, my recommendation would be to simply turn the loop around and the receiver will lock on. Except, it not quite as simple as that because the offset also affects the envelope synchronization. You have alluded to that problem. Let me say that all these things have to be precisely nailed down before you can make an adjustment. As funding becomes available, these questions will be resolved.

LASSO, two-way and GPS time comparisons: a (very) preliminary status report

C. Veillet, D. Féraudy, J.M. Torre, J.F. Mangin (OCA)
P. Grudler, F. Baumont (OCA)
J. Gaignebet, J.L. Hatat (OCA)
W. Hanson, A. Clements, J. Jespersen, M. Lombardi (NIST)
D. Kirchner (TUG)
G. Kirchner, H. Ressler, S. Fassl (Space Res. Inst. Graz)
W.J. Klepczynski, P.J. Wheeler, W. Powell, A.Davis (USNO)
M. Granveaud, P. Uhrich (LPTF)

Abstract

This very preliminary report briefly presents the first results on the time transfer experiments between TUG (Graz, Austria) and OCA (Grasse, France) using common view GPS, and two-way stations at both sites. The present data, providing a rms of the clock offsets of 2 to 3 nanoseconds for a three months period, have to be further analysed before any conclusions on the respective precision and accuracy of these techniques can be drawn.

Two years after its start, the LASSO experiment is finaly giving its first results at TUG and OCA. The first analysis of three common sessions permitted us to conclude that the LASSO package on board of Meteosat P2 is working staisfactorily, and that time transfer using this method should provide clock offsets at better than 1 nanosecond precision, and clock rates at better then 10^{-12} s/s in a 5 to 10 minutes session. A new method for extracting this information from the raw data sent by LASSO should enhance the performances of this experiment, exploiting the stability of the on-board oscillator.

1 - Introduction

After the failure of the SIRIO 2 launch, and the subsequent unavailability of the LASSO experimental equiipment package (hereafter referred to as LASSO), a new phase started in Summer 1988, when a new geosynchronous satellite, Meteosat P2, carrying a new LASSO experiment, was launched successfully. In spite of the work made at various sites in order to obtain results from LASSO data, and after a short move of the satellite across the Atlantic (up to 50° W) and back to 0° in early 1990, no real results were obtained before November 1990.

During 1990, in order to compare various techniques transfering time at a few nanoseconds supposed accuracy, GPS and two-way time transfer were achieved between TUG (Graz, Austria) and OCA (Grasse, France). The first, very preliminary, results of these GPS and two-way results will be given. But most of this presentation will be devoted to LASSO.

2 - Two-way and GPS

With the help of NIST and USNO, a VSAT two-way time transfer equipment has been installed close to the laser stations on the «Plateau de Calern», observing site of the «Observatoire de la Côte dAzur» (hereafter OCA). With a dish of 1.8m in diameter, it permitted us to achieve common sessions three times a week with TUG (Graz, Austria) starting on June 22, 1990.

A typical clock offset measurement plot is shown on Fig. 1. The rms value of the offsets (a linear fit has been made through the data) is 0.7 ns. Most of the sessions are at this level of precision, smaller rms values being obtained using larger dishes (like in the NIST/USNO experiments).

At the same time, GPS time transfer using common view satellites has been performed. Fig.

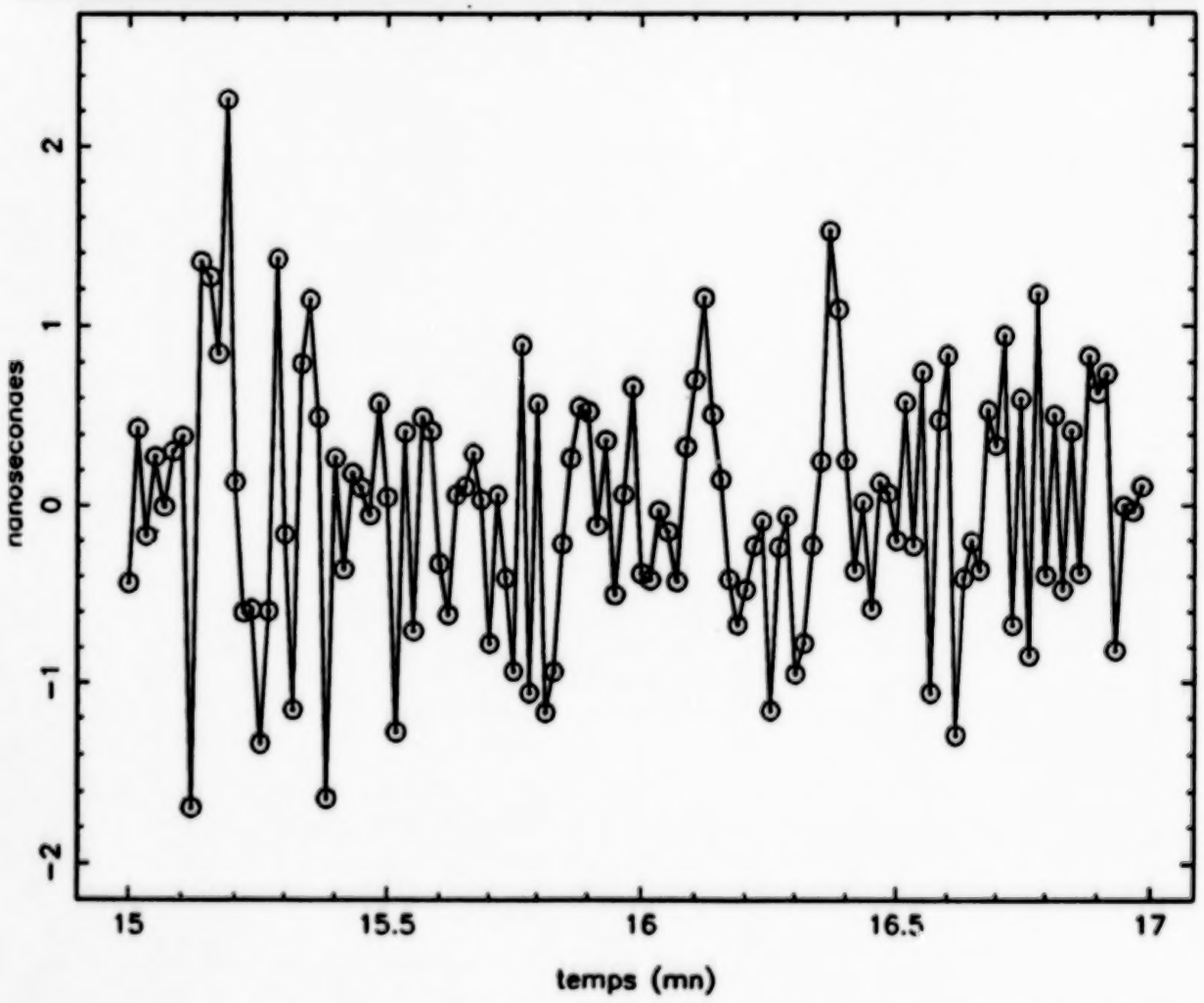


Fig. 1 - *A two minutes two-way session between TUG and OCA (1990 Nov 9). Each point is a clock offset measurement. A linear fit has been made through the data. The rms of the values around the fit is 0.70 ns.*

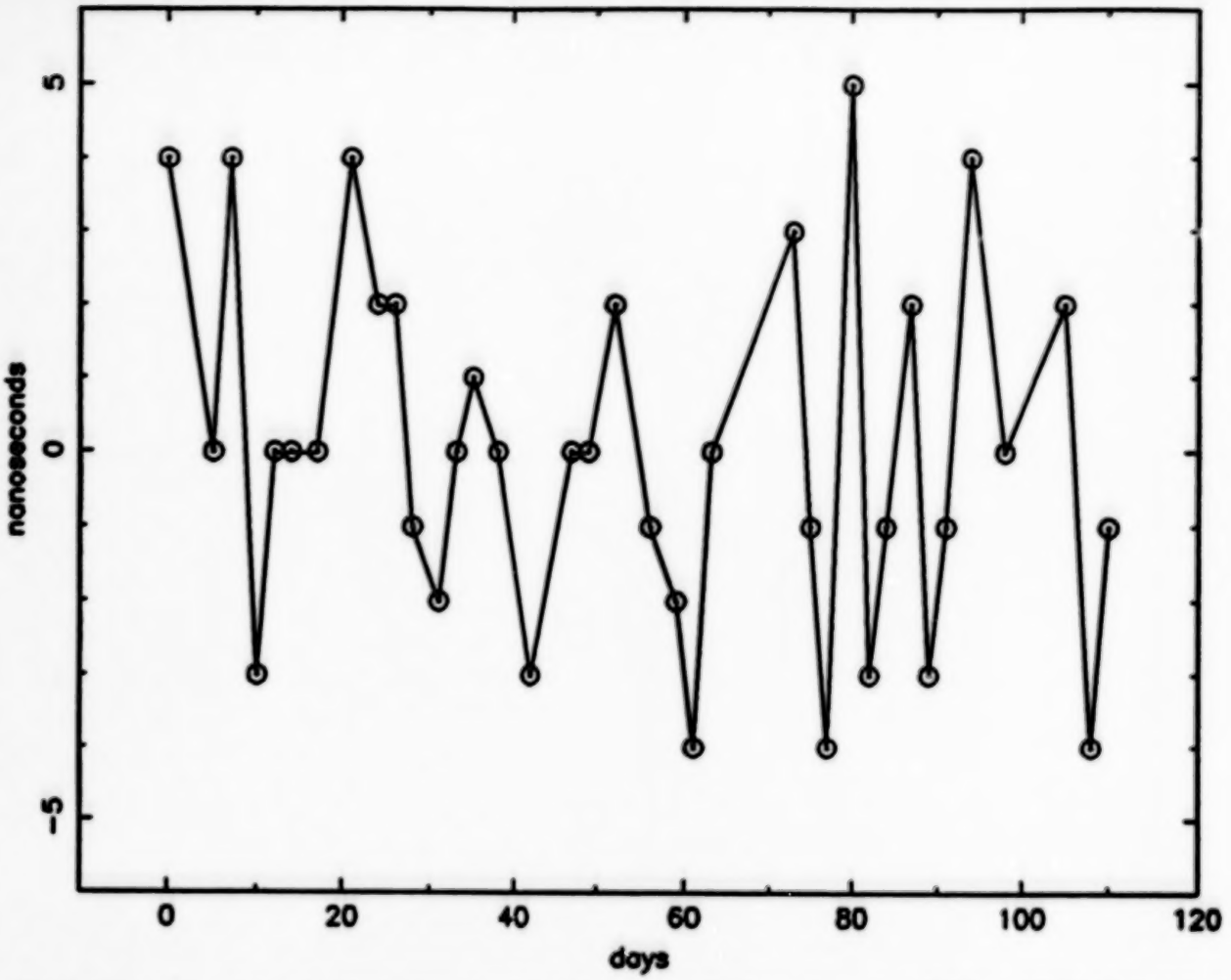


Fig. 2 - *Plot of the clock offsets differences determined using GPS and two-way at TUG and OCA. The period shown covers three months from 1990 June 22 up to October 10. The rms of the differences (bias removed) is 2.5 ns..differences*

2 shows a plot of the differences of the clock offsets obtained using both the GPS and two-way techniques. These results are very preliminary. Many things have to be looked at, especially the way in which the GPS data are interpolated to match the epoch of the two-way sessions. More on this analysis will be presented in a subsequent paper.

3 - LASSO

3.1 - How does it work ?

On board a geosynchronous satellite, Meteosat P2, an active package is able to detect and record oby an event-timer the arrival time of a laser pulse sent from a ground-based station. Retroreflectors, installed above the receiver, send back to the transmitting station part of the incoming light, so that the station can record the start and return time of the laser pulse.

Both firing and echo times are measured using the station time scale, but the detection time on board of Meteosat is determined using an oscillator which is stable enough to insure that there will be a drift of less than one nanosecond in a few milliseconds. For comparing the time scales at two different Earth stations, it is sufficient to organize the firing times at both sites so that the arrival times at LASSO be within a few milliseconds. By its specifications, the on-board oscillator should not introduce any error at the nanosecond level. Direct clock comparison is achieved every time two pulses from two different stations give two detection times on board the satellite in a common window (that is, within a few milliseconds ...), when one also has an echo time at each participating station. Fig. 3 gives a schematic view of the time transfer method used for LASSO.

3.2 A brief review of the LASSO experiment steps since 1988 ...

A short time after the launch of

Meteosat P2, echoes were obtained at the OCA Lunar Laser Ranging station. A few months were sufficient to be sure that the LASSO package was working properly, after the correction of encoding errors in the data transmission between the satellite and the Earth. With the time passing and the attempts from various sites remaining unsuccesfsul, it became clear that only a few stations were able to get echoes from Meteosat P2. Beside the OCA Lunar Laser Ranging (LLR) station, for which a satellite, even geosynchronous, is an easy target, only the TUG satellite station, equipped especially for LASSO with a ruby laser, and the Katzively station (Crimea, USSR), (another potential LLR site), can really contribute to LASSO as a two-way station. Both of these stations are able to get both detection on-board Meteosat, and echoes from its retroreflectors.

The first echoes, as well as on-board detections, were obtained with TUG station in September 1989. In late October 1989, Meteosat P2 was moved to 50° West, in order to provide meteorological information to the United States. Two stations (Mc Donald, Texas, and University of Maryland / Goddard Space Flight Center optical facility, Greenbelt, Maryland) started to study how to work with LASSO, and OCA LLR station obtained echoes in spite of the very low position of the satellite as seen from Grasse (17° elevation). Meteosat P2 started a journey back over Europe in late December 1989, and a new European phase of LASSO has been organized in January 1990.

Due to various problems in Graz, only OCA LLR station ranged successfully LASSO between January and August. TUG was back at work at that time, as well as Katzively. The latter station got echoes in September, and the first common sessions with both TUG and OCA finally succeeded on 1990 November 7 and 8.

3.3 The first results

The following analysis has been made using the processing of the satellite raw data files made at OCA for the sessions of November 7 and 8 1990.

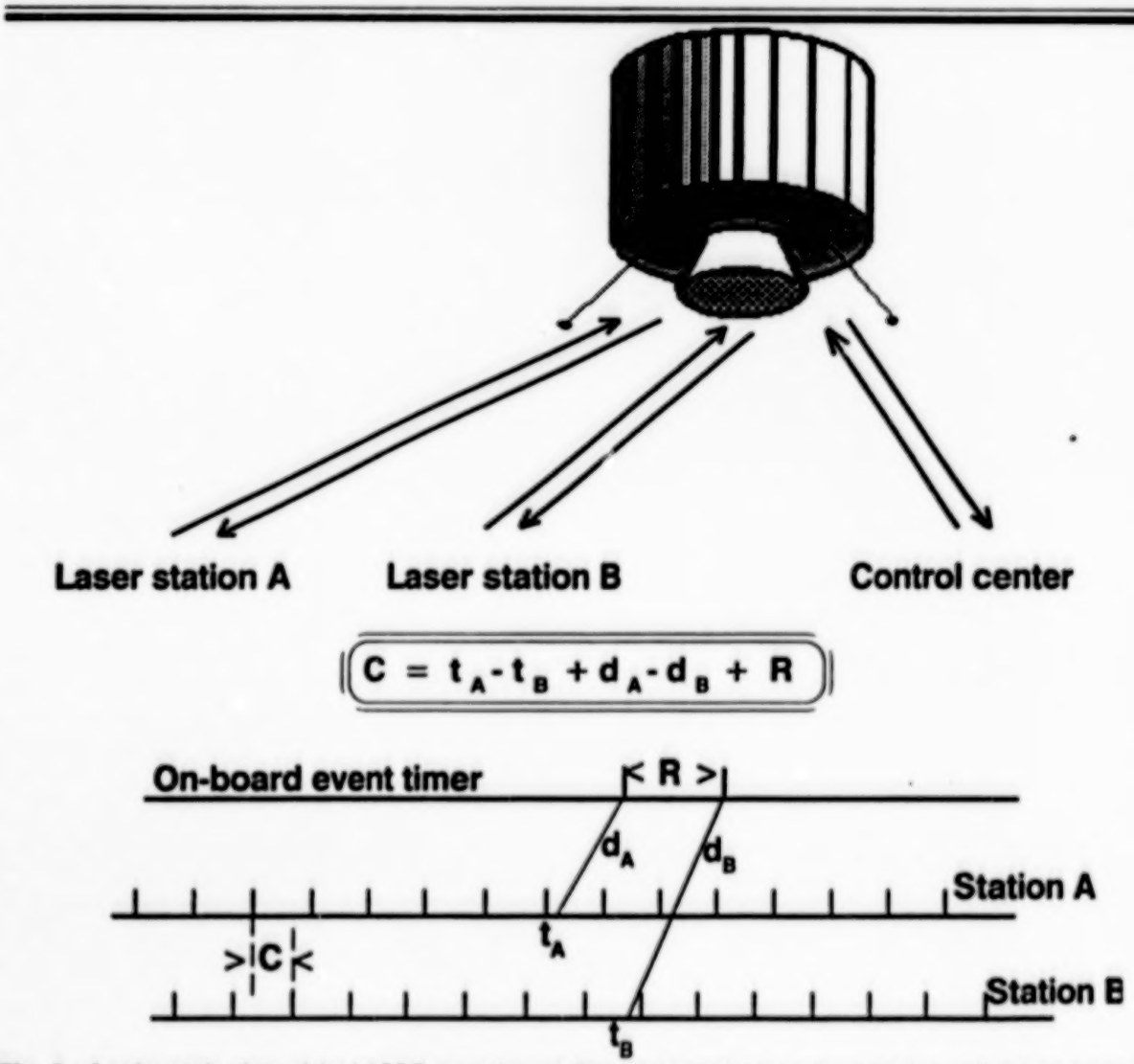


Fig. 3 - *A schematic view of the LASSO experiment. The time transfer is performed through the on-board oscillator which provides an intermediate time scale for the determination of the offset of the station clocks.*

From these files, and using the station data , it is possible to identify triplets, i.e. laser pulse start time, detection time on LASSO and echo time back at the considered station, for a given session typically 10 minutes long. These triplet data lead to the identification of common windows, a couple of triplets from TUG and OCA with close detection times on the satellite.

In order to check the quality of the LASSO package in terms of time stability, the echo times have been analysed, and compared to the detection times (on the on-board time scale) at a given station. Fig. 4 show show these echo times look for TUG as a function of the firing times. The high rms found after a polynomial fit is as high as the rms values found using the detection times with the same data. It simply reflects the fact that TUG used at that time (this is no longer the case) an event timer with only a 10 ns resolution. The same analysis with OCA results (Fig. 5 and 6) shows that the rms values for the detection times (in LASSO time scale) is only twice as large as that for the echo times (in station time scale), and still much below 1 ns. The conclusion is that the LASSO equipment doesn't degrade too much the laser signal, and is really suitable for a sub-nanosecond timing.

Using these triplets, only 12 common windows have been found for November 8 first session. It leads to 12 individual clock offset determinations which are plotted on Fig. 7. The rms of these values against a linear fit over the four minutes of the run is 4 ns, and comes mainly from the poor resolution of the Graz time measurements at the time of the session. The same analysis made on three sessions on November 7 yields to a rms of 5 ns over 100 minutes and 12 common windows.

3.4 Another approach

Since the beginning of LASSO in 1988, it appeared from the detection times recorded on board that the oscillator is quite stable over 10

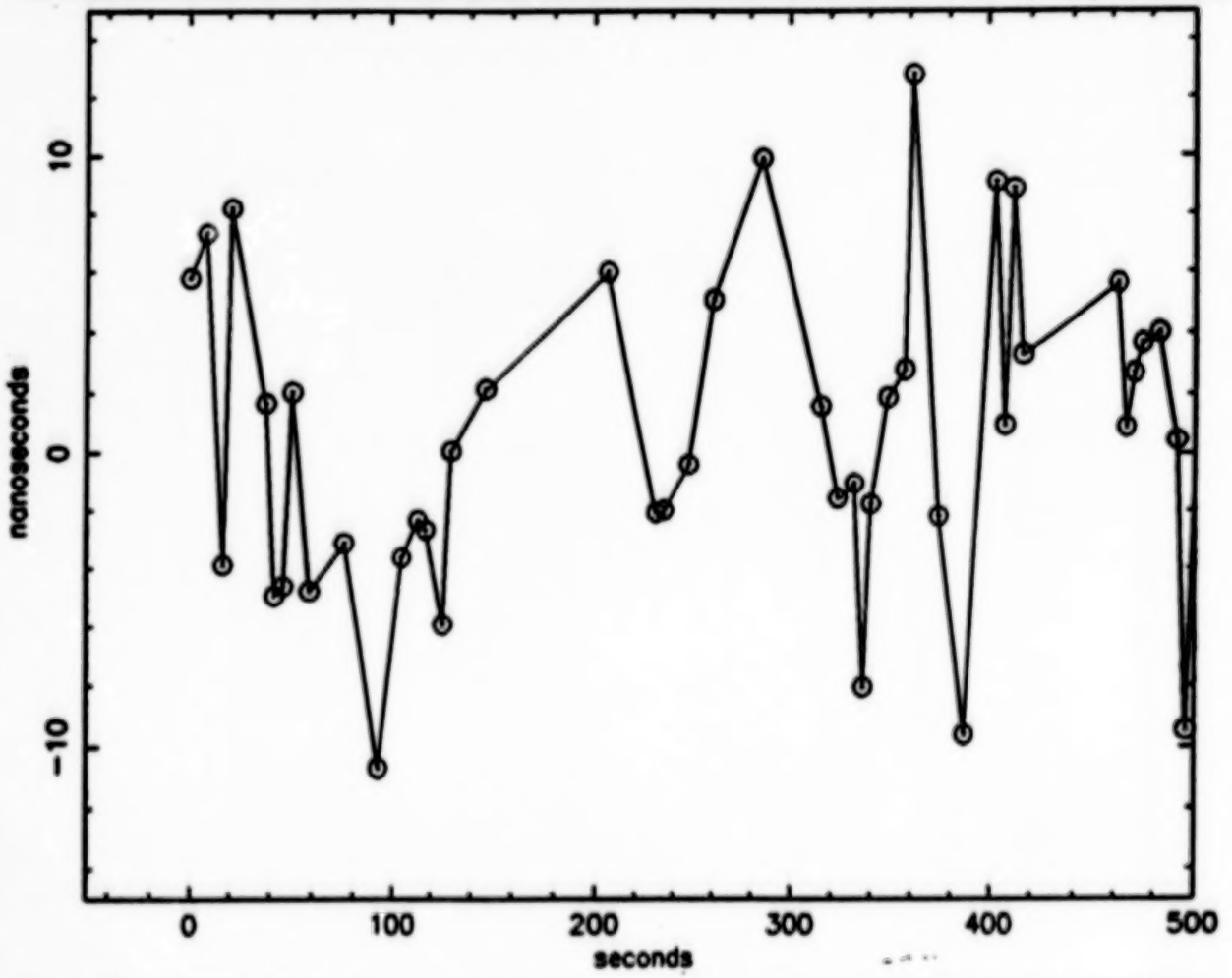


Fig. 4 - *Plot of the residuals on the range measurements relative to a polynomial fit - First session on 1990 Nov. 8 - TUG data. The high rms, 4.7 ns, reflects the poor resolution (10 ns) of the event-timer used at that time in*

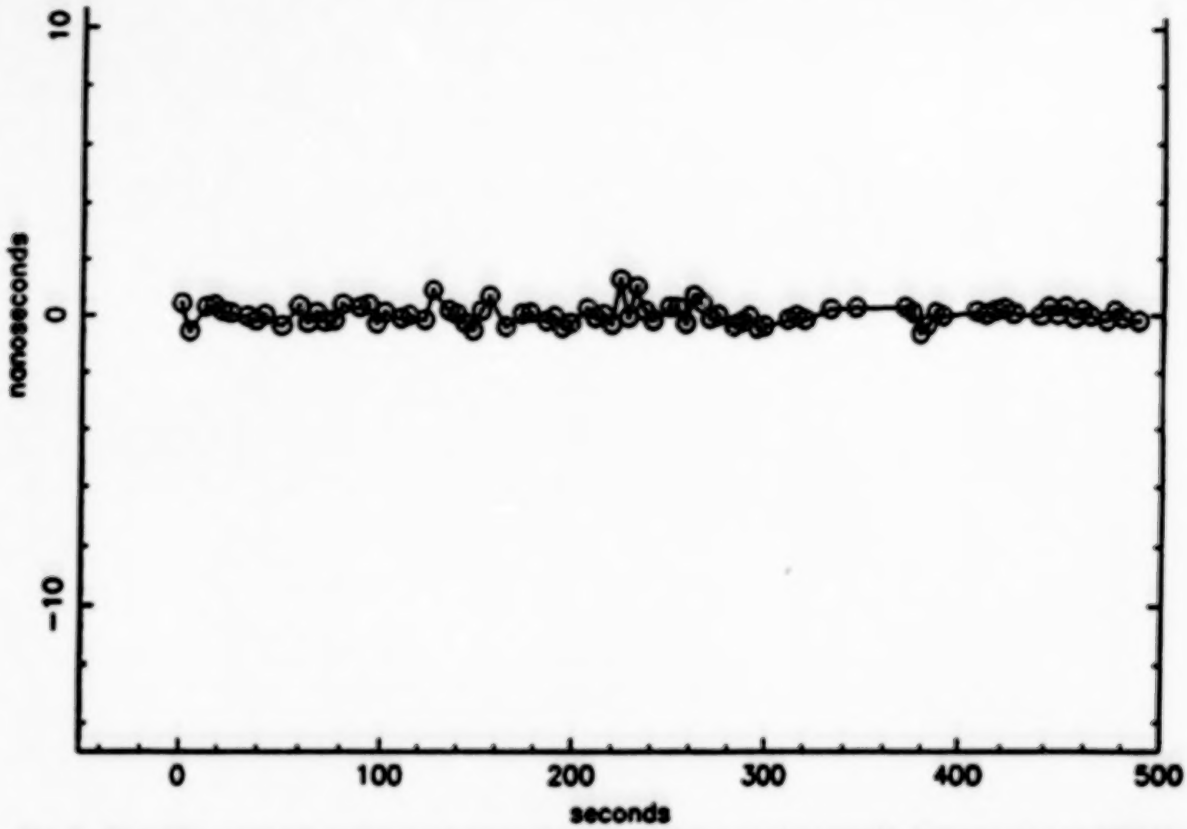


Fig. 5 - *Plot of the residuals on the range measurements relative to a polynomial fit - First session on 1990 Nov. 8 - OCA data. The rms, 0.33 ns, is typical of ranging measurements made on satellites with the OCA/CERGA Lunar Laser Ranging station.*

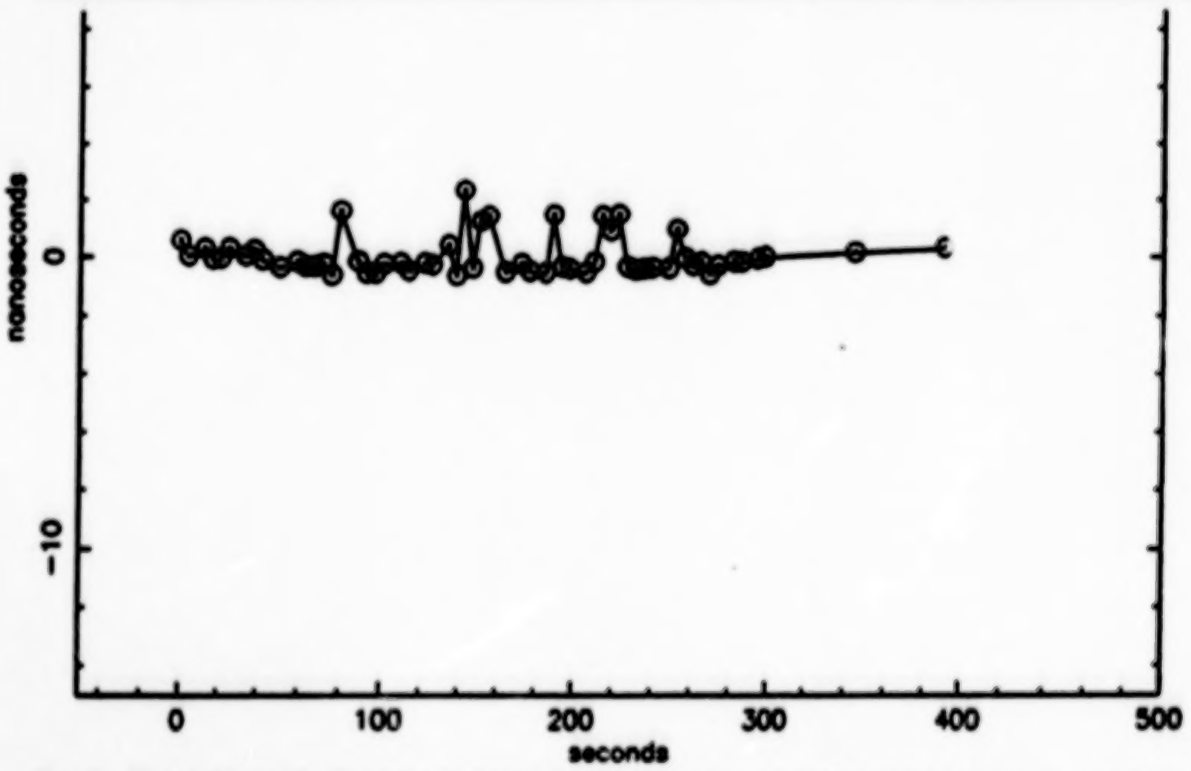


Fig. 6 - *Plot of the residuals on the on-board detection times as a function of the firing times relative to a polynomial fit - First session on 1990 Nov. 8 - OCA data. The rms, 0.67 ns, is only twice as large as that for the echo times. It shows that the jitters on board of LASSO are largely at a sub-nanosecond level, and that the oscillator has no suspect behaviour.*

minutes. As only a small number of common windows are seen in a session (12 for 10 minutes on November 8, 1990), an other treatment of the data was made at OCA in order to exploit the high number of triplets obtained (37 from TUG and 59 from OCA) and to use the good quality of the observerd LASSO time scale. At every session (5 to 10 minutes), the triplets from a given station are used for determining both the LASSO oscillator rate and the offset relative to the on-site clock. The difference between the clock offsets relative to the same LASSO scale will provide the clock offset between the two stations. The rate of a clock compared to the other one could also be determined if the data are sufficiently accurate, or the analysis could enforce the clock rates at the two sites to be equal.

Table 1 presents the results of this global analysis using the sessions on November 7 and 8 compared to those obtained with the common windows analysis previously planned for LASSO analysis. It is clear that the uncertainty on the clock offsets is much smaller with the global analysis, mainly because the number of data used is much larger. The TUG poor timings doesn't permit to reach the precision of LASSO. This precision should, from the results obtained using OCA data, be less than half a nanosecond for the clock offset, and 10^{-12} s/s for the clock rate.

3.5 Conclusion

Experiments in the near future, with a TUG station using a subnanosecond resolution event timer, should confirm that a time transfer at a subnanosecond level can be achieved with LASSO. Other stations could be involved, like Katzively (USSR) and Wettzell (Germany). After a calibration of the three methods used simultaneously, (GPS, two-way and LASSO), a comparison of their precision and accuracy could be possible at the nanosecond level, assuming that a H_2 maser is available at the concerned stations. As both two-way time transfer and

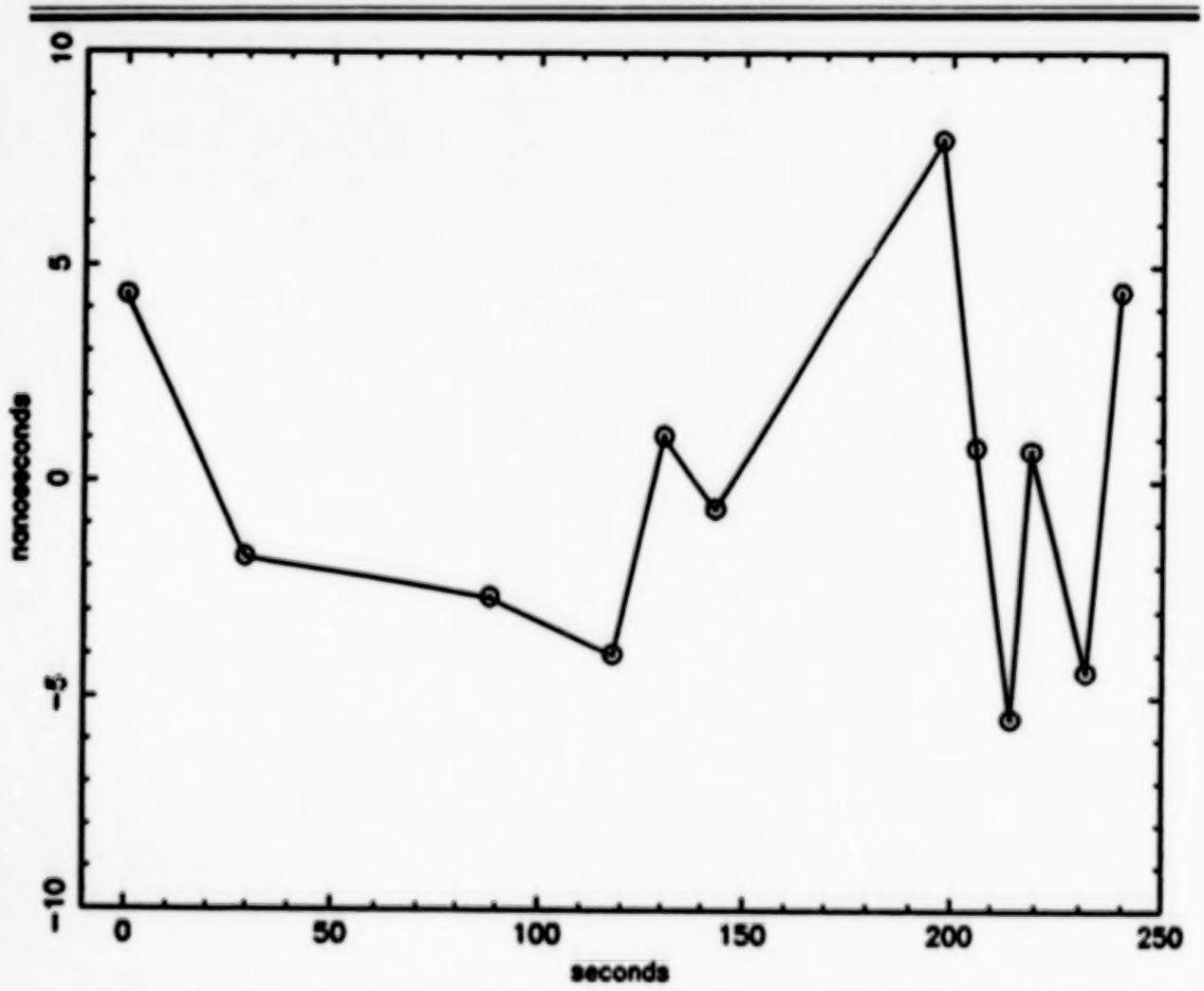


Fig. 7 - *Plot of the clock offsets between TUG and OCA determined using 12 LASSO common windows on the first session of 1990 Nov. 8. The scatter of the results is mainly dominated by the poor TUG timing resolution at the time of the session.*

LASSO act like a snapshot of the clock offset at a given epoch, the only way to compare them at the nanosecond level is to employ a time keeping device, like a maser, able to reach less than one nanosecond over two or three days. However OCA and Wettzell are the only sites at which a maser is in operation.

In the middle of 1991, Meteosat P2 could be moved again at 50° West, permitting a time transfer experiment between Europe (OCA) and United States. Waiting for this eventual move, the months to come will be used as much as possible to achieve time transfer between the European sites able to range Meteosat P2.

		1990 Nov. 7			Nov. 8
Session time (UTC)		**19h 25**	**19h 45**	**22 h 05**	**19h 35**
Triplet number	**OCA**	**15**	**23**	**61**	**59**
" "	**TUG**	**37**	**18**	**17**	**37**
With same clock rate at TUG and OCA					
LASSO clock rate (ps/s)		**-10252.7**	**-10228.5**	**- 10240.2**	**- 10239.6**
uncertainty		**6.8**	**9.3**	**1.7**	**2.6**
Clock offset (ns)		**8059.0**	**8060.6**	**8053.5**	**6006.6**
uncertainty		**1.6**	**1.3**	**0.7**	**0.7**
With different clock rates at TUG and OCA					
LASSO / OCA rate (ps/s)		**- 10248.9**	**- 10246.5**	**- 10238.7**	**- 10246.8**
uncertainty		**2.3**	**1.5**	**0.4**	**0.9**
LASSO / TUG rate (ps/s)		**- 10252.8**	**- 10215.3**	**- 10249.5**	**- 10235.9**
uncertainty		**8.6**	**18.1**	**9.8**	**5.1**
Clock offset (ns)		**8059.3**	**8060.6**	**8053.3**	**6006.6**
uncertainty		**1.0**	**1.5**	**1.3**	**0.9**

Table 1 - *Preliminary global analysis of the four sessions on 1990 Nov. 7 and 8, where data were obtained at TUG, OCA and on-board Meteosat P2. Each session is 5 to 10 minutes long. Further studies have to be made on the processing of these first LASSO data, but these preliminary results demonstrate that LASSO time transfer is possible at subnanosecond level, and clock rate measurements in a session at better than 10^{-12}.*

RECENT DEVELOPMENTS OF LORAN-C IN EUROPE

Sigfrido Leschiutta Enrico Rubiola

Politecnico di Torino
Torino, Italy

Summary

Even if recent developments, both technical and political, are affecting the satellite GPS and GLONASS navigation systems, alone, in conjunction, or with a possible civilian overlay via INMARSAT or other satellites, the time proven that Loran-C can be still a viable solution for many problems.

The aims of this paper are twofold, to present a panorama of the most recent developments in the World and mostly in Europe, and to consider some technical aspects of two problems regarding the Mediterranean Sea chain.

This chain is at moment based on four stations, two in Italy, one in Spain and in Turkey. The fate of the station in Turkey is known, in the sense that this station will not operate when the U.S. support will cease; the future of the Spanish station it is not yet known, while Italy has expressed its intention to operate the two remaining stations. Consequently two problems are to be solved if it will be needed to assure at least the coverage of Italy and of the eastern Mediterranean Sea.

1 Recent Developments of Loran-C

Since this paper is unique during this XXIV PTTI Meeting in addressing Loran-C topics, it seems appropriate to present an overview of the recent developments of this navigation system.

In order to avoid misunderstandings, care will be taken by differentiating between *activities underway*, *existing programs* and *tentative studies*.

1.1 America

As regards the American continent, starting from North, **Canada** is taking an active part in the North-European Loran-C Policy Group — to be introduced later in section 2.2.2 — in order to secure, by the possible upgrading of a station, a better coverage of the waters south of Greenland.

A research activity is performed [1] in order to validate, using GPS, the distortion of the Loran-C grid due to variations of the secondary phase factor, for land navigation applications.

In the **U.S.A.**, as it is well known, for mid 1991 it is expected the coast to coast coverage of the continental States.

Along the large industrial production of airborne Loran-C navigators, combined Loran-C/GPS receivers were announced and there are hopes that a suitable combination of GPS with Loran-C could became the sole mean for air navigation in order to abandon, in some future, the system VOR/DME.

Tests were performed on the use of GPS to obtain the Loran-C secondary phase errors [2] for land navigation.

In **Mexico** some studies are being performed in regard to a possible National coverage.

In **Venezuela** a decision was taken to install a national chain with four stations covering the whole Country and its coastal areas with emphasis on the inland waterways, such as the Orinoco river.

In **Brazil**, very preliminary investigations into coverage for the Amazon basin are underway.

No other activities are known in southern America.

1.2 Asia

In Asia, starting from the far east, studies are underway in **Korea**, also with on-field measurements, concerning the upgrading of the two existing stations witch have been take over by Korea, and the possibility to obtain a national chain, with the construction of an additional station.

Japan hosts four stations and, following in some extent the approach of France, is reported to considering the build-up of a national chain, mostly for defense purposes; at any rate the take-over of the existing stations is planned in a few years time.

In **China**, were in the recent years a chain was constructed in the southern part of the Yellow Sea, another chain with three stations is under construction in the northern part of the coastline to complete its eastern coastal coverage. Since some years a powerful Loran-C station (not a chain) is active inland in the Shaanxi province.

Consequently, if Korea will go along with its plans, a continuous coverage will be secured along all the approaches of Asia from the Pacific Ocean.

A **technical working group** has been formed with representative from China, USSR, South-Korea and Japan in order to coordinate present and future Loran-C activities in the area. Chairman of this working Group is the Secretary General of IALA. IALA stands for *International Association of Lighthouses Authorities*, an informal Organization, with seat in Paris, formed by representatives of all the seafaring nations.

As regards **North-Pacific**, it is worth to be noticed the agreement reached on May 1988 between U.S.A. and USSR for a joint operation of their Loran-C/CHAIKA chains in North Pacific ocean and the Bering Sea areas. Following this agreement, to be realized in two steps between 1990 and 1992 a joint radionavigation chain will be formed using stations in Attu, Alaska, Petropavlovsk, Aleksandrovsk, and Kurilsk.

India has decided the installation of two short range Loran-C chains along the eastern and western coast of the subcontinent, to replace the DECCA chains covering the approaches of Calcutta and Bombay.

In the Arabic Peninsula, one of the two existing chains was temporarily turned off before the current confrontation. It is expected to be returned in operation soon.

A short range Loran-C chain is being installed in Dubai, to support a vehicle location system already in operation there, which previously had relied on the Saudi system signals.

In Africa, **Egypt** is keeping in service the low-power Loran-C chain formed by three stations and serving the Suez Canal.

The news gathered in this two sections were collected attending various meetings, or excerpted from the U.S. Radio Navigation Plan (1988 issue), the open literature, the IALA Reports [3,4,5,6,7],

the Volumes of CCIR, the Records of IFRB, the "Wild Goose Gazette" and from conversations with individuals active in the field.

2 European Approaches for Loran-C

2.1 Situation Prior to 1985

The coverage of European waters prior 1985, is reported in every receiver manual, and was based on the North Sea and the Mediterranean Sea chains.

In the late eighties the Ukrainian or Bielorussian CHAIKA chain was officially recorded in the IFRB (International Frequency Registration Board) and CCIR (Comitè Consultatif International pour les Radiocommunications) publications, but the coordinates of two stations only were given at that time:

Briansk	53°13′ N	34°24′ E
Syzran	32°11′ N	49°46′ E

This chain has the GRI of 80.0 ms and is formed by four stations; their signals are well received in our Laboratory, located in North-West of Italy.

The European coverage of Loran-C about 1985 is qualitatively given in Fig. 1.

2.2 Situation After 1985

In 1985, started the activity of two Loran-C stations in France, to be used in the ρ-ρ mode, mostly for military purposes. Obviously these two stations, if operated with the Group Repetition Rate (or with a double rate) of a nearby chain, can constitute a standard hyperbolic Loran-C chain.

The news of the U.S.A. decision to terminate at some time around 1994 the direct or indirect support of the chains operating outside the U.S.A. territories, had meanwhile promoted in 1984, the formation of a North-European Loran-C Working Group, under the Chairmanship of Mr. Steenset, deputy Director General of the *Norwegian Defense Communication and Data Services Administrations* (NODECA). Mr. K. Enerstadt of Norway being the secretary of the Group.

2.2.1 The North-European Working Group

The terms of reference of the Group were:

- to study future requirements for Loran-C chains in the North Atlantic and Norwegian Sea areas,
- to investigate on other navigation options, present or future,
- to study, if Loran-C should be retained, all the relevant technical problems, in the phases of transition and operation,
- to study the organization of future system operation and administration, including chain control and allocation of responsibilities,
- to propose an operation structure, with a relevant budget,
- to formulate proposals about the repartition of the financial charges between the various Nations.

The Final Report, July 1985, concluded with the following recommendations:

1. The present Loran-C system in Northern Europe, should continue to operate beyond 1994.
2. An Organization, as indicated in the Report, should be appointed / established.
3. A Meeting with representatives from the involved Countries should be called to reach agreement as to the formation and term of reference, of the necessary mechanism to have the Organization recommended,
4. Norway should take the initiative to call the proposed meeting.

That Meeting was called in Oslo in May 1987, when a Loran-C Policy Group was formally established.

2.2.2 The North-European Policy Group

The aims of this Group were as follows:

1. To seek agreement between Nations concerned in the continued operation and enhancement of the present Loran-C system in N.W. Europe. Such agreement to include take over of present U.S. Coast Guard Loran-C Stations in the area, utilization of non-U.S.A. stations and Loran-C stations to be established and operation on a cooperative basis.
2. To agree and sign a memorandum of understanding between Governments participating in the System before proceeding with the actual work.

The present membership of this Policy Group with the status of a full member is Canada, Denmark, France, Germany, Iceland, Ireland, Norway, U.K., and, as observer, U.S.A., the Commission of the European Communities in Brussels and IALA.

The Working and the Policy groups meet in total eleven times (the last in Oslo in July 1990, the next in Ottawa in January 1991), and at the moment the text of a Memorandum of Understanding is available and discussed.

2.2.3 Two timing approaches: System Area Monitors, Versus Time of Transmission

Of particular interest for the Time and Time interval community is the fact that the system control, as proposed for the three planned chains, is not based in the traditional *System Area Monitors* (SAM) approach — monitoring stations located in specific points and charged to maintain mutual and internal synchronization of the chain — but on the so-called *Time Of Transmission* (TOT) concept. Following this approach the clocks of all the stations are referred independently to a common reference, such as UTC.

Both approaches, SAM and TOT are equally good in monitoring the transmitters timing errors.

As regards the variations in the propagation delays, SAM enables error minimization, but only in selected areas, while TOT distributes errors more evenly. TOT is more costly in the implementation (more atomic clocks and GPS receivers, but the running cost is less. The TOT approach can present some drawbacks for Time users and Geophysicist, but can provide historical data for delays of propagation.

In U.K., in an official press release in April 1990 of the Department of Transport, it was announced that, at the termination of the public support for the DECCA System, U.K. will participate in the

Loran-C coverage of North-West of Europe sea with a new station in North-East of the Country. This decision will hold if certain considerations will be met. One of these conditions was that Loran-C system should preserve its international flavor and that an acceptable repartition of the charges will be found.

If these conditions are not met, U.K. may reconsider its position.

In the proposals of the Policy Group, is also planned the construction of an additional station in Ireland. This later station, operating with the two French transmitters and with the southernmost station of the North Sea Chain in Sylt, could cover the Channel, the Gulf of Biscay and in general all the western approaches of Europe.

2.2.4 A New Chain in Eastern Europe?

For land and air navigation, some activity is performed Eastern Europe. Indeed a new CHAIKA chain is planned between Eastern Germany, Hungary and Bulgaria; the planned positions of this new proposed chain were:

Eastern Germany	Damgarten	12°27′ E	54°15′ N
Hungary	Esztergam	18°45′ E	47°46′ N
Hungary	Kunmadaras	20°48′ E	47°26′ N
Bulgaria	Pleven	25°04′ E	43°20′ N

No news are available about the status of the new proposed chain nor about the consequences of recent political changes. At any rate it can be stated that, at least from July-August 1990, no activity was observed from our Laboratory at the GRI of 49.60 ms, proposed for the new chain.

2.2.5 An Iberian Chain?

Inside IALA, a small working group, composed by France, Portugal, Spain and U.K. was formed with the task to study the possibility and the interest, with a station in north-west of Spain, or possibly in the Azores, to cover the Portuguese waters and the access to the Mediterranean from the Atlantic Ocean.

A station in Ortegal, in N.W. Spain, with the southernmost French station Soustons and with Estartit, the westernmost of the Mediterranean, double rated, could indeed cover the Iberian peninsula.

The Group should prepare a financial and technical report no later than March 1991, with practical chain configurations, meeting the requirements for Iberian and Atlantic area, including Azores and Canaries.

A possible coverage, for Europe, Mediterranean excluded, is qualitatively given in Fig. 2.

2.3 Mediterranean Sea Chain

Always inside IALA another group, with the chairmanship of Italy, is studying the future of the chain in the Mediterranean area. The membership of this Group includes all the Nation around the Mediterranean Sea, with the exception of Cyprus, Israel, Lebanon, and Turkey .
Concerning the Nations hosting at the moment the chain:

Italy (two stations) has announced in 1988 the intention to assume the operation of the stations when the U.S. support will cease,

Turkey (one station) has announced in 1990, that the service will not continue,

Spain (one station), has not, insofar, announced officially any the decision, but informally, the opinion is that, provided some support will be granted and the operations of the two Italian stations will be secured, the activity of the Estartit station will be extended.

If the above scenario will become reality, two situations are to be considered :

1. if the operations of Estartit station will not secured, Italy will have to make a decision, whether to drop the coverage of Loran-C around Italy, or to form a national chain with the two existing stations of Sellia Maria and Lampedusa and the addition of a third new station,
2. if the coverage of central-eastern Mediterranean must be ensured, another new station in the area must be erected.

The technical aspects only of possible solutions to the two problems will be presented in what follows.

3 A New Transmitter, Where?

As well known, a Loran-C transmitter is to be placed in on an high conductivity soil in order to achieve a reasonable radiated to loss power ratio. This is due also to the dimensions of the practical antennas, that are small compared to the wavelength (3 km); a "small" antenna presents a "low" radiation resistance and consequently the overall resistance of the earth system must be as "low" as possible.

Only a few places with suitable soil conductivity exist in the eastern Mediterranean. Keeping in mind that signal coverage and geometrical dilution of precision requirements are to be met, the set of possible places is further reduced. As regards the Italian solution, more severe constraints arise from the Country shape.

Some hypothesis are considered here and summarized in Fig. 3 and Table 1, in which the approximate considered positions are given, along the existing M, X, Y and Z.

Stations C, T, N or E are proposed as a possible replacement for the Turkish Y.

If a fully national system is indeed to be implemented, V or W can be chosen, in conjunction with the existing M and X. One of these stations was initially proposed as a possible extension of the chain, and a technical study is available [3].

A transmitter located around Genova (north west Italy), as sometimes proposed in [8], has not been considered because of the soil conductivity of the area; moreover, being the region highly populated, it would be very difficult to find a site.

Finally, political consideration, not included here, could still reduce the set of possible sites.

4 Coverage and Related Problems

4.1 Signal Strength

The groundwave signal strength is evaluated for all the proposed and existing stations using a computer program especially written for this purpose. The program is based on the data available in the CCIR report 717-1 [9], converted in a digital map with a resolution of 0.5° in latitude and longitude, and the method therein proposed for mixed paths.

IDENT.	LAT. (deg)	LON (deg)	POWER (kW)	BASELINE (km)	SITE	COUNTRY
M ¶	38.9	16.7	165	n. a.	Sellia Marina	Italy
X ¶	35.5	12.5	325	525	Lampedusa	Italy
Y ¶	41.0	27.9	165	980	Kargabarun	Turkey
Z ¶	42.1	3.2	165	1195	Estartit	Spain
C †	35.2	24.5	165	800	Creta	Greece
T †	40.8	24.6	165	710	North East	Greece
E †	31.5	26.2	165	1190	North West	Egypt
N †	31.2	33.2	165	1725	Nylus delta	Egypt
V ‡	44.5	12.2	165	730	Po delta	Italy
W ‡	45.4	13.4	165	770	North East	Italy
¶ existing † replaces Y ‡ Italian system						

Table 1: Existing and proposed Loran-C transmitters in the Mediterranean area.

The proposed transmitters are supposed to be quite similar to the existing ones, with the same radiated power and 190 m top vertical monopole; only Lampedusa (Y) is different.

The output of the program is the groundwave electric field for all the transmitters, evaluated at each cross point of a 1° spaced grid for the region 5–35° W and 30–50° N.

4.2 Noise

A single value of the atmospheric noise is adopted in the whole analysis, 47.5 dB over 1 μV/m in a two sided band of 20 kHz. This figure, based on the CCIR report 322-2 [10] and taken from an earlier analysis [3], is evaluated for the point 40° N, 15° E, in the middle of the region shown in Fig. 3. It is the average noise power in the worst case as regards the season (Summer and Autumn) and daytime (00 ... 04 Local Time).

The average value, versus the season and daytime, spans over about 30 dB; upper and lower deciles, in the same conditions, are 10–15 dB apart from the average. In the whole area the variations of the average value never exceed 2–3 dB. The man made noise and the coherent interferences are not considered here.

4.3 Geometry

The relation between positioning and timing errors, known as GDOP (geometrical dilution of precision), involves two concepts:

Sensitivity. Considering two transmitters, the sensitivity S is the ratio of positioning error vector p divided by the timing error t, and is given by $S = c/2\cos\psi$; S is a vector perpendicular to the hyperbola, c the speed of light, ψ the angle at the receiver site delimited by the direction lines towards the transmitters.

Crossing angles. Being the position obtained as the intersection of two hyperbolae, each generated by a couple of transmitters, its error is the sum of the two vectors given by the sensitivities and the timing errors.

It is a common practice to evaluate the GDOP with a scalar formula, assuming that timing errors are originated by Gaussian white noise, uncorrelated for each time difference.

In our opinion the GDOP should be considered as the sum of two error vectors because the most important sources of errors are the systematic or seasonal propagation effects, that are not white noise. Moreover, the white noises on the two time differences are correlated because one transmitter is common.

5 Two Hypothesis for the Future of the Chain

5.1 A National Navigation System for Italy

A national system, based on Sellia, Lampedusa and W will provide a fair signal to noise ratio, as shown in Fig. 4. Most of the national area lies in the shadowed area, where the evaluated S/N ratio is 10 dB or better. Since most receivers work reasonably with S/N = 0 dB, there is a sufficient margin.

The geometrical dilution of precision is shown in Fig.5, where the module and angle of the sensitivities are plotted for the triad M-X-W.

The extreme north-eastern Italy and a small southern region near the continuation of the line from X to M are not covered because of the sensitivity. In most of the peninsular area the sensitivity spans from 200 to 500 m/ns and the crossing angles are near 90°, which is the best. In a small region, at south west of Sardinia island, the positioning will be difficult because of the crossing angle near 180°, despite of the "good" sensitivity and S/N.

The solution V, not shown, will provide a slightly better signal coverage, but the north eastern blind area will considerably increased and shifted from outside to the Country.

5.2 A Loran-C Coverage for Eastern Mediterranean

In the case that the central-eastern basin of Mediterranean should be covered, four possible sites were investigated: these sites are listed in Table 1 and shown in Fig. 3. In all the cases the criteria of sections 3 and 4 were taken into account.

As regards station C, in the north coast of Crete island, there are some flat lands along the sea side , the same conditions are met for station T planned in the North-East border of Greece, about 230 km West of the present site of Y station.

The two proposed sites in Egypt were chosen with the following criteria; the eastern site in order to cover most of the eastern basin of the Mediterranean, the western one because the former "Egyptian" site would require an high power transmitter, being the baseline with the master of about 1700 km.

The investigations about geometrical and signal to noise problems, were repeated for all the proposed sites, using as a Master the present one.

From the investigations, it seem that the best site is C, on the island of Crete, because the resulting baselines are adequate and the geometry of the first Mediterranean Sea chain — before the shift of Matratin station in Libya to Lampedusa — is somehow restored.

In Fig. 6, for this latter solution are given the plots of constant signal/noise ratio, including the existing M and X. In the shadowed areas, the sensitivities are less or equal than 600 and 1000 m/μs.

From the results of this study it can be pointed out that with only one additional station both of the problems cannot be solved.

Obviously, if the new proposed chain in Bulgary and Hungary will became a reality, the problem should be fully reconsidered.

6 Final Remarks

It must be stressed that in this analysis nor economical nor political considerations were taken in to account.

Moreover, this research was supported by University founds only and no implication must be made about a possible construction of any of the considered stations.

Political considerations apart, it can be stressed that Loran-C still provides an useful service and that is to be considered as an economical solution when a regional navigation service must be provided.

References

[1] G. Lachapelle and B. Townsend, "En-route coverage validation and calibration of Loran-C with GPS," in *Proc. ION GPS '90*, Colorado Springs (U.S.A.), September 1990.

[2] J. Pisano, P. Levin and P. Enge, "Using GPS to calibrate Loran-C," in *Proc. ION GPS '90*, Colorado Springs (U.S.A.), September 1990.

[3] "A proposed European Loran-C system", *Proc. of IALA (International Association of Lighthouse Authorities) Special Radionavigation Conference*, London (UK), 11–12 March 1987, pp. 58-79.

[4] IALA Loran-C Meeting for Mediterranean Countries, Paris (France), 17–18 January 1989.

[5] IALA Loran-C Meeting for Mediterranean Countries, Madrid (Spain), 19–20 June 1989.

[6] IALA Loran-C Meeting for Mediterranean Countries, Marseille (France), 21–22 November 1989.

[7] IALA Loran-C Meeting for Mediterranean Countries, Paris (France), 9–10 may 1990.

[8] E. Rubiola, "A possible extension of the Mediterranean Sea Loran-C chain," in *Proc. NAV 88, Radionav 2000 — a European Dimension*, Conference of the Royal Institute of Navigation, London (UK), 22–24 March 1988, paper no. 22.

[9] "World atlas of ground conductivities," CCIR report 717-1, Dubrovnik 1986.

[10] "Characteristics and applications of atmosferic radio noise data," CCIR report 322-1, Dubrovnik 1896.

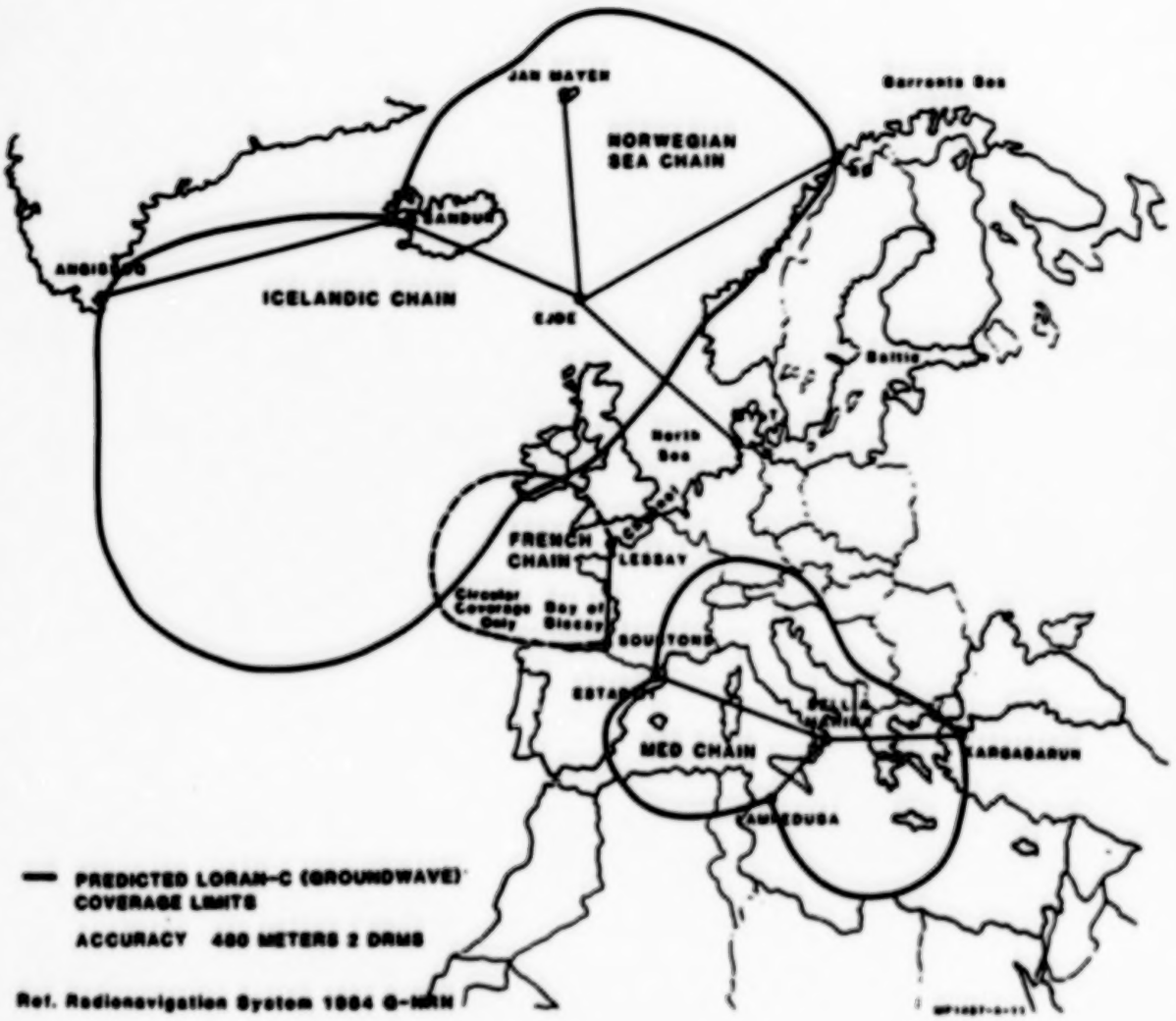


Figure 1: Loran-C european coverage in 1985.

BLANK

PAGE

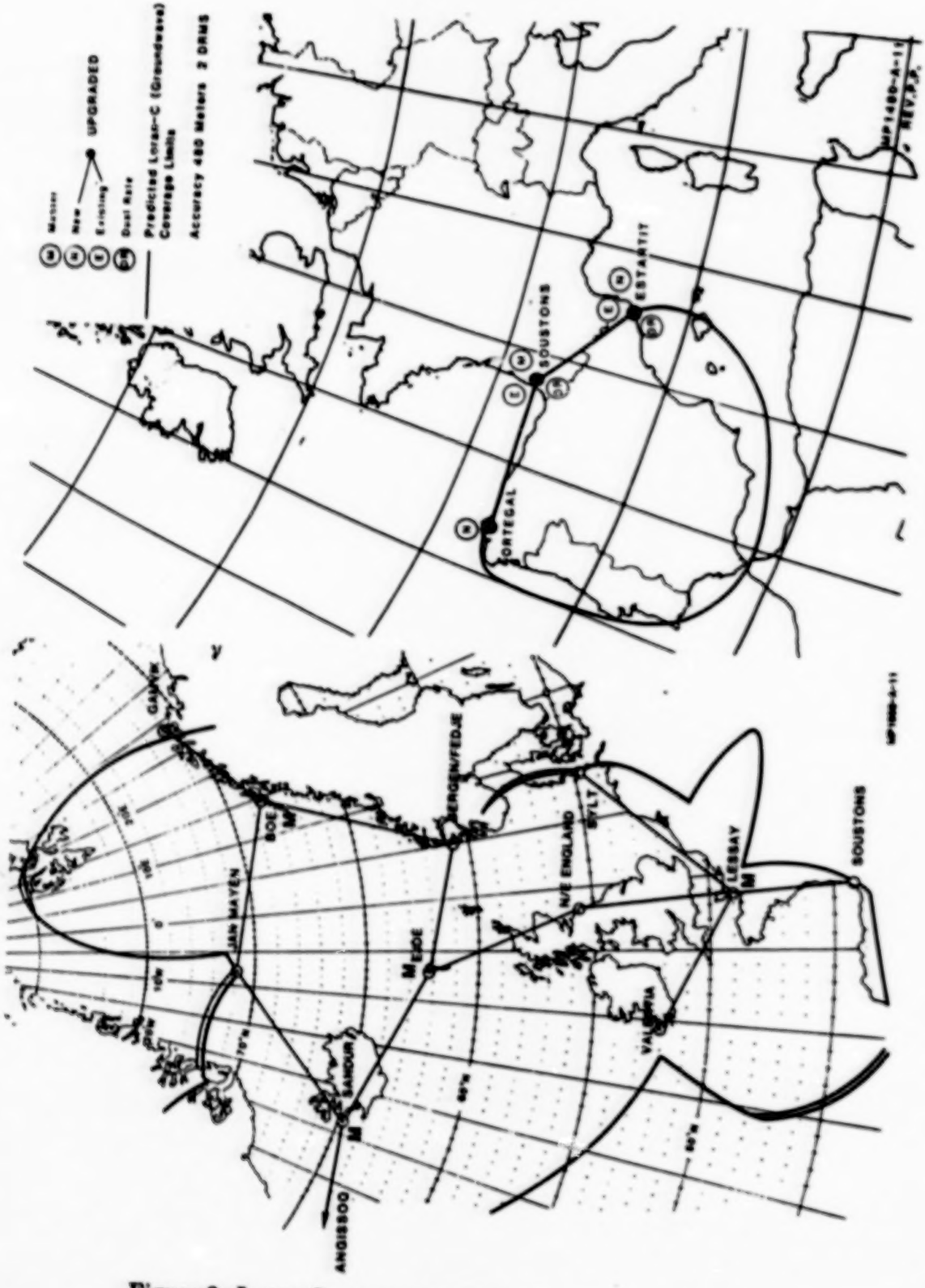


Figure 2: Loran-C european possible coverage about 1995

593

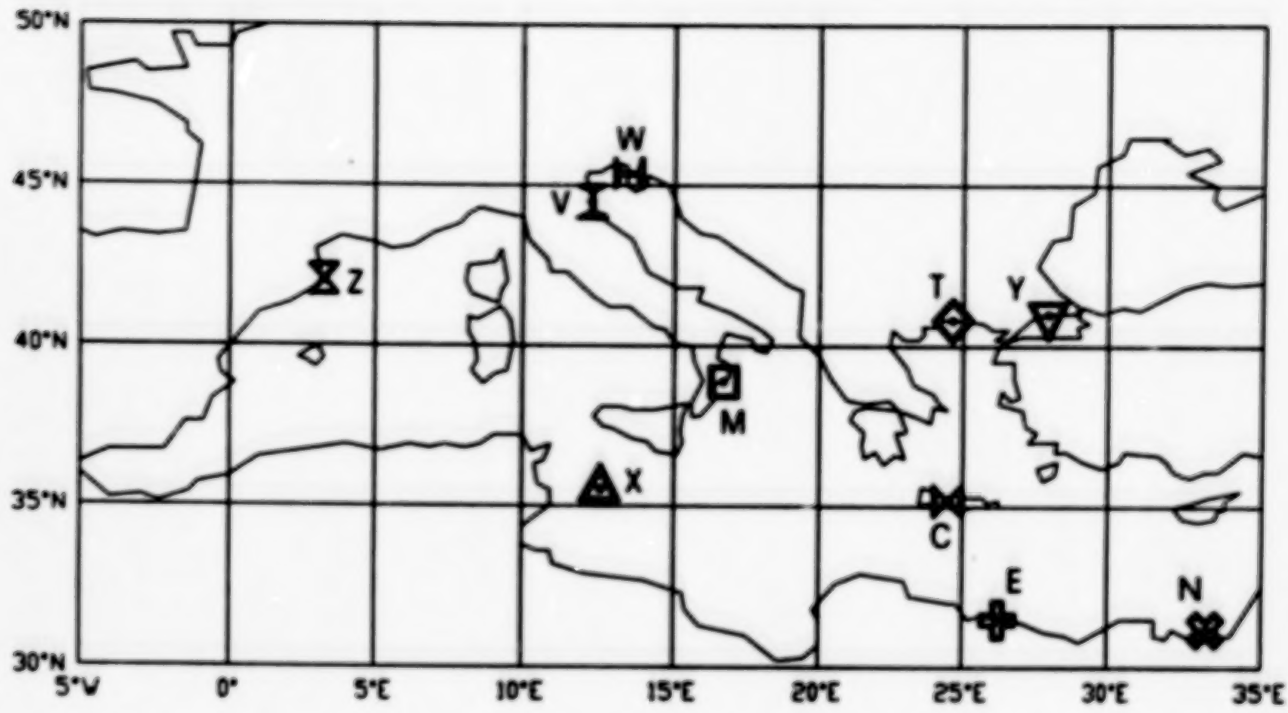


Figure 3: Existing and proposed Loran-C transmitters in the Mediterranean area.

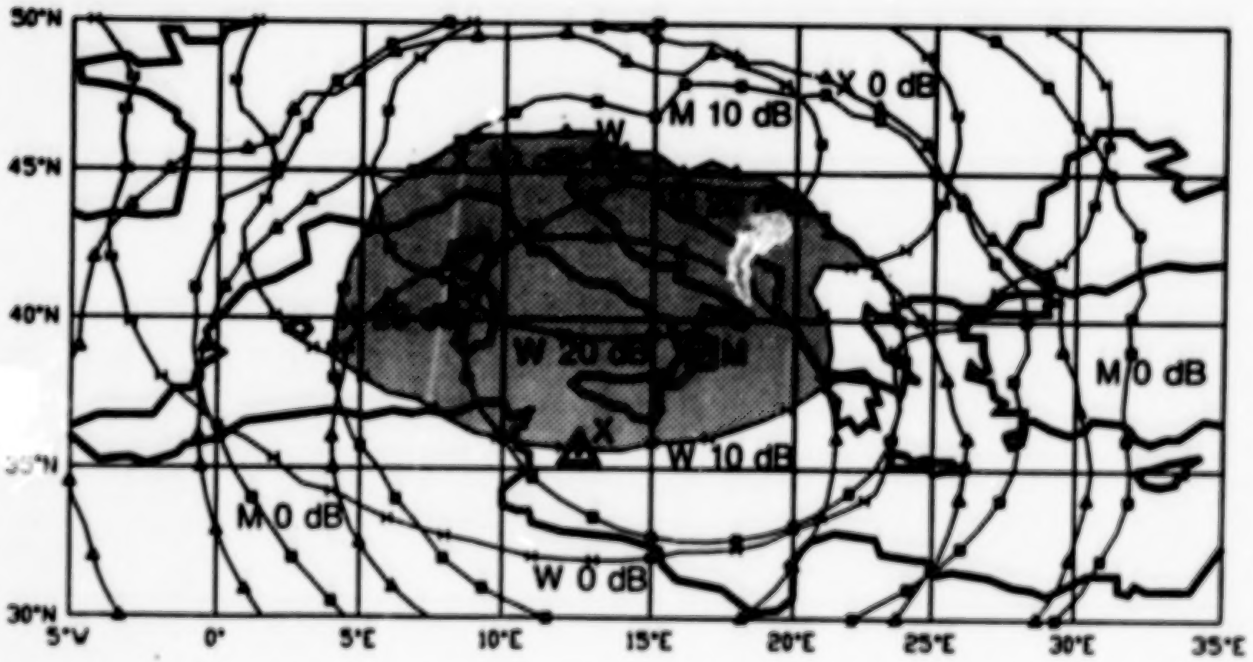


Figure 4: Calculated S/N ratio for the hypothesis of an Italian national system in which the station W is added.

BLANK

PAGE

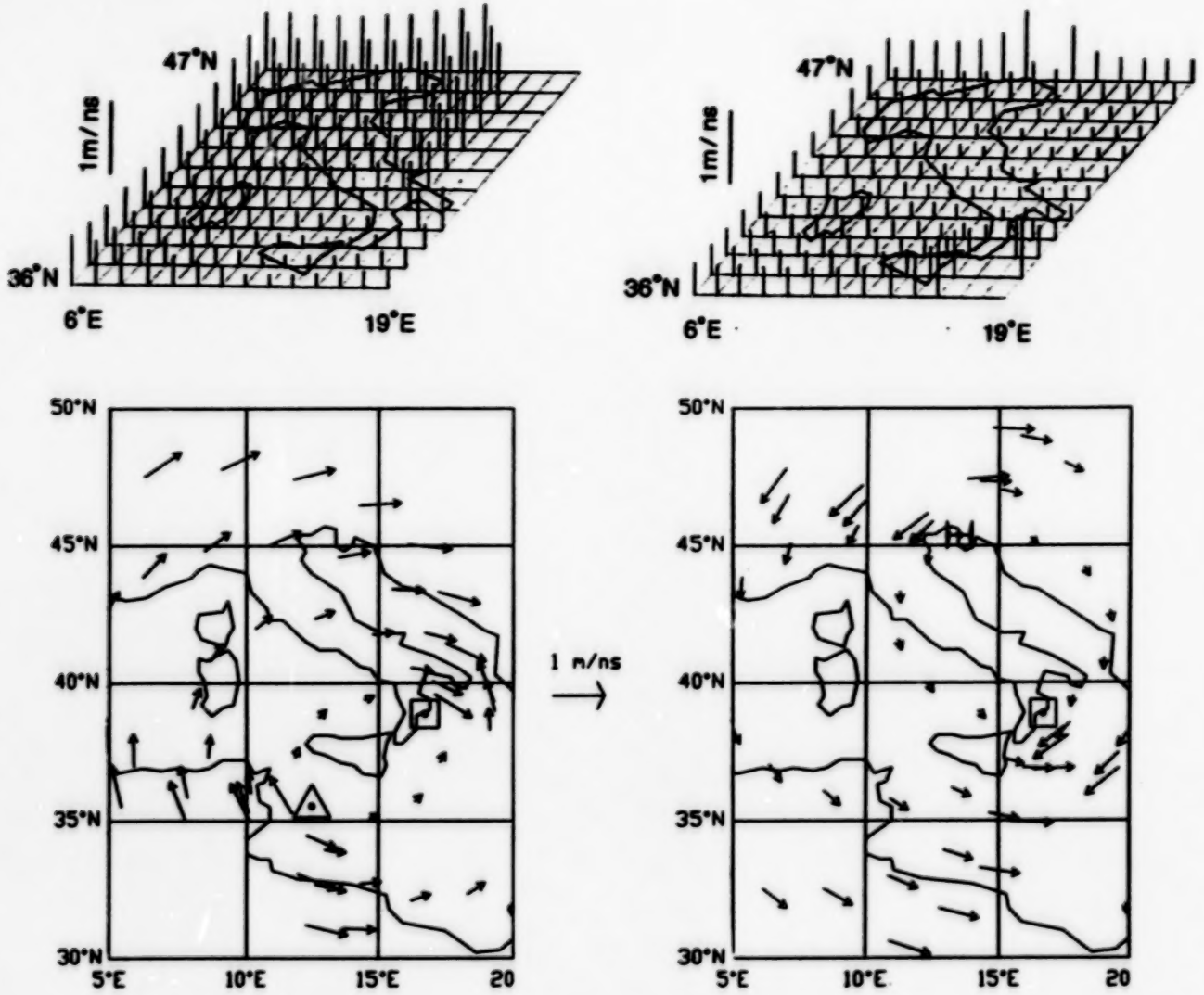


Figure 5: Sensitivity for the stations M, X and W. Top: module, the reference segment is 1 m/ns; all the values above 1.2 m/ns are suppressed. Bottom: angles; they are not distorted as the map.

595

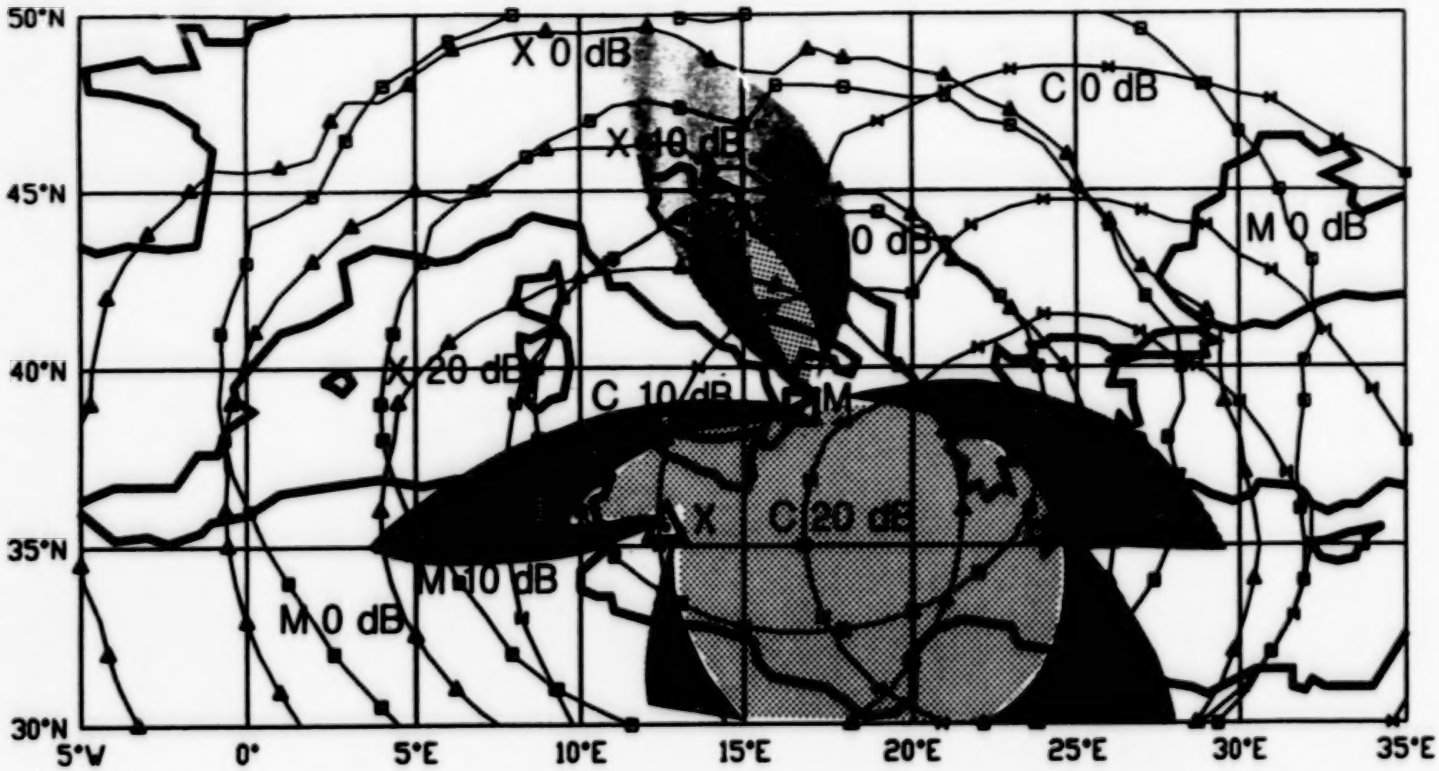


Figure 6: Geometrical and Noise limited coverage for a possible eastern Mediterranean chain, with a slave in Crete.

QUESTIONS AND ANSWERS

Unidentified Questioner: I understand that this band from 90 to 100 kiloHertz is allocated differently in Europe than it is in the United States.

Professor Leschiutta: You are completely right. That is a problem, but it can be solved. I am not speaking about metrological use, but about those who are interested in navigation.

BLANK PAGE

On the Line Q Degradation in Hydrogen Masers

L. G. Bernier, G. Busca, H. Schweda
Observatoire de Neuchâtel, Switzerland

Abstract

In hydrogen masers, the atomic resonance quality factor is largely determined by the properties of the Teflon coating on the quartz storage bulb. Normally a good Teflon coating will last many years. On the other hand, there may be a relatively fast degradation of the quality factor if the Teflon coating is bad. This paper updates a series of observations and measurements performed on an hydrogen maser that had successively a bad and a good Teflon coating.

1.0 Introduction: A Pathological Case

In hydrogen masers, the atomic resonance quality factor is largely determined by the properties of the Teflon coating on the quartz storage bulb. Normally a good Teflon coating will last many years and will show an extremely slow degradation of the atomic quality factor. On the other hand, once upon a time the Teflon coating happens to be "bad" which is characterized by a reasonable initial value of the atomic line quality factor followed by a fast degradation. The physico-chemical composition and structure of Teflon coatings is not well known. Empirical evidence shows that the atomic hydrogen consumed during normal maser operation plays a role in the degradation mechanism of a bad coating [1] and that the curing process is as important as the raw material in the preparation of a successful Teflon coating. This paper updates a series of observations and measurements performed on our hydrogen maser EFOS-7, operated in Sweden at Onsala Space Observatory, that had successively a bad and a good Teflon coating [2].

2.0 The Effect of Air on a Bad Teflon Coating

In the past, we observed once that any intervention on a certain maser would temporarily cure its amplitude decay problem, whatever the intervention was. It was finally suspected that the simple fact of exposing the storage bulb to air, during the intervention, would temporarily improve the quality factor. More recently this past observation lead us to deliberately try the experiment on a maser that suffered a fast degradation of the line Q. The only intervention made on the maser between the 2 measurements of the quality factor reported below consisted of filling the maser with air and then

pumping down again. The atomic line quality factor was 1.20×10^9 before and 1.44×10^9 after exposure to air. The cure produced by exposure to air was temporary and the decay continued as before.

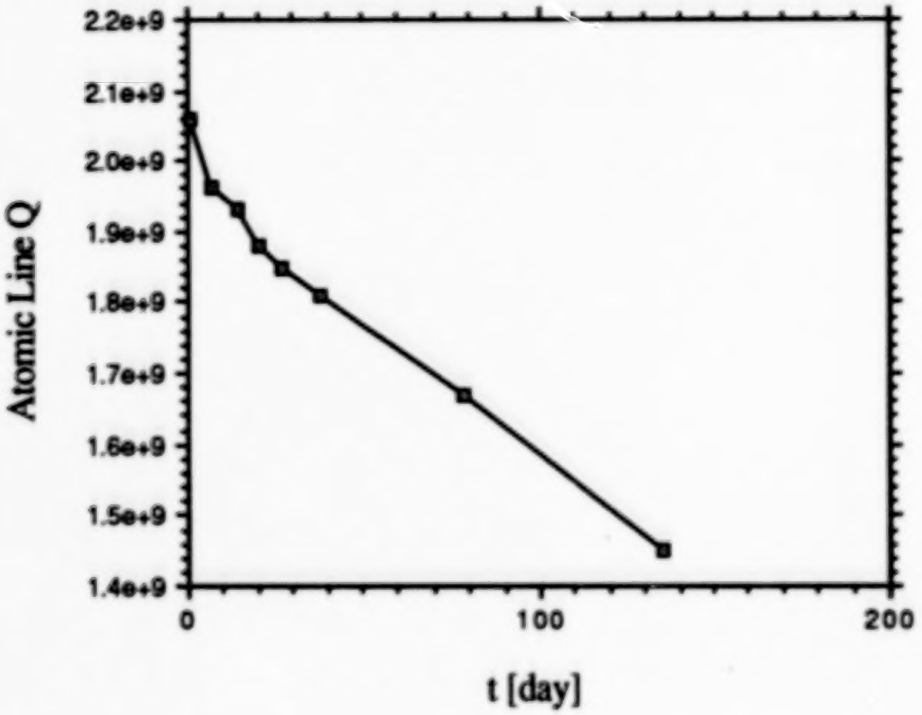


Figure 1
Atomic Line Quality Factor vs Time

3.0 The Time Behavior of a Bad Teflon Coating

The effect of a bad Teflon coating on the maser behavior was observed for several months. Figure 1 shows the evolution of the line Q starting just after the re-coating of the storage bulb. The origin of the time axis is the first day of oscillation. It can be observed that there is a decelerating degradation, during the first days, and then the degradation rate stabilizes. Figure 2 shows a linear regression of the linear part of the line Q degradation. The equation of the linear regression is as follows: $Q = 1.9528\times10^9 - 3.7052\times10^6$ t [day]. The relative degradation rate is 0.19 %/day. Figure 3 shows the amplitude of the maser signal versus time. By amplitude we mean the detected peak amplitude at the 5.7 kHz last IF in the receiver. Again there is a decelerating decay, at first, and then the rate of decay stabilizes. The amplitude steps are due to hydrogen pressure resettings. Figure 4 shows the linear part of the curve with the amplitude steps corrected by translation of the constant hydrogen pressure segments. A linear regression of the data points yields: $A\ [V] = 11.741 - 4.0735\times10^{-2}$ t [day]. The rela-

tive rate of decay is 0.35 %/day. Figure 5 shows the normalized frequency $y(t) = \Delta\nu(t)/\nu_0$. The beat frequency $\Delta\nu(t)$ was measured by comparing the maser frequency ν_0 with the frequency of a reference maser.

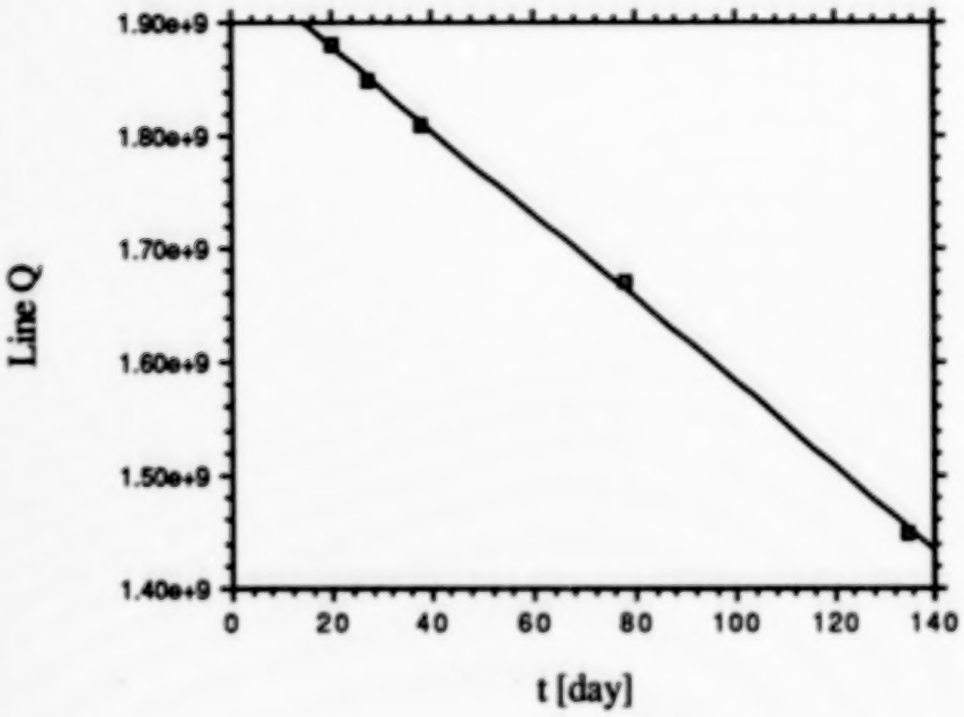


Figure 2
Linear Part of Atomic Line Q vs Time

A periodical spin-exchange tuning of the cavity showed that the microwave cavity was not drifting. The big frequency step on the curve is due to the initial spin-exchange tuning of the microwave cavity. The small steps are due to the imperfect resetting of the varactor voltage after each verification of the correct spin-exchange tuning. Figure 6 shows the y versus t curve with the frequency steps corrected by translation of the constant cavity tuning segments. The residual frequency change is approximately logarithmic. The analytic curve shown on the figure is given by: y(t) = -1.7693×10-12 + 2.8426 LOG(t [day]). If the frequency change were due exclusively to the time varying cavity pulling effect associated with the line Q degradation, one would expect a linear drift. Thus the observed non-linear drift seems to indicate a wall shift evolution associated with the Teflon degradation.

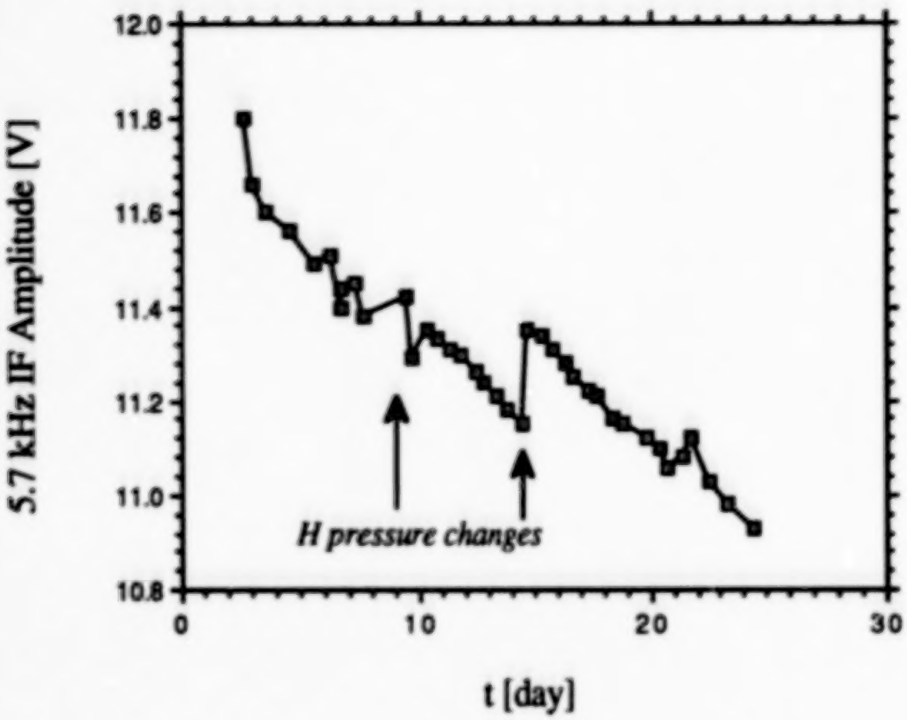


Figure 3
Signal Amplitude vs Time

4.0 Discussion: Present Situation

The storage bulb of the same maser described above was re-coated and put back into operation with the same hydrogen dissociator as before. The signal is now higher (-104 dBm, i.e. 12.0 V amplitude peak at the 5,7 kHz last IF) for a smaller hydrogen flux (0.1 mBar of hydrogen in the dissociator, i.e. V_p = 6,5 [V] at the pirani gauge output, with a ϕ 0.15 mm × 1.5 mm collimator). After several months of operation there is no sign of signal decay. This means that the bad coating was entirely responsible for the signal decay observed before. The fact that the signal is now stronger for a lower hydrogen pressure in the dissociator is a sign that, as expected, the threshold flux is lower with the good coating. The operating quality factor is now stabilizing at about $Q = 2.3\times10^9$ (with 0.1 mBar in the dissociator) with an initial value of $Q = 2.5\times10^9$ as shown on figure 7.

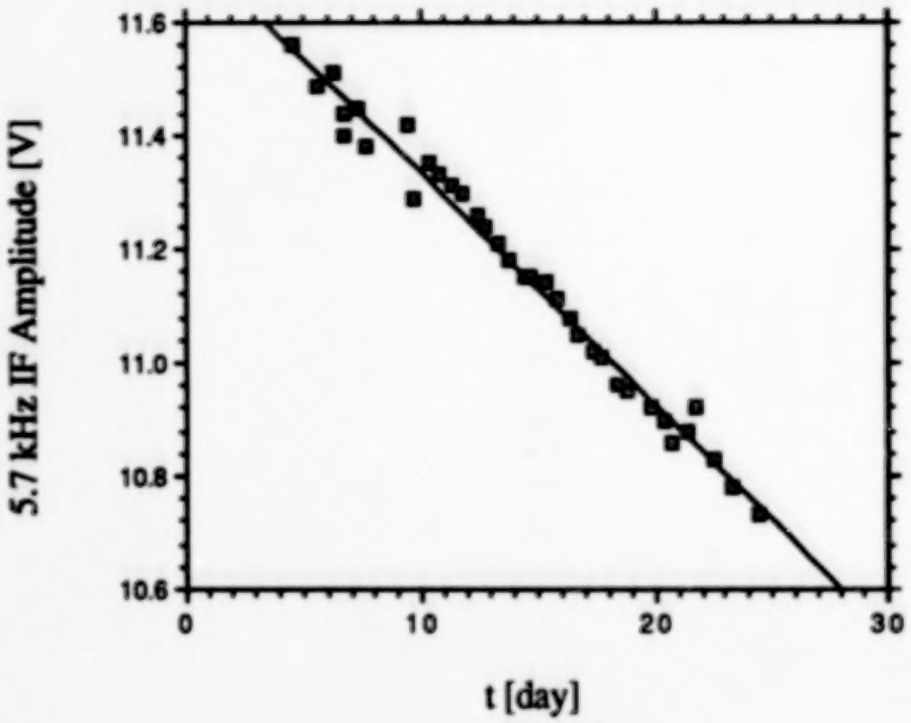


Figure 4
Signal Amplitude vs Time
Corrected for Constant Hydrogen Pressure

5.0 Conclusion: Investigations at ON on the Teflon Coating

The properties of the coating and possible ways to test the Teflon before actual use in a maser are under investigation at Neuchâtel Observatory. From a practical point of view, we believe that it is equally important to control both the properties of the initial Teflon coating solution as well as the conditions of the drying and curing process if reliable coatings are to be produced.

For example, the thickness of the coating is determined by the concentration of the Teflon resin in the coating solution. The concentration may be estimated from a measurement of the specific weight of the commercial solution which is normally about 1.42 according to Du Pont. Our experience shows that the actual Teflon resin concentration may vary largely from sample to sample, simply because the solution has a tendency to separate when stored for some time. The solution is originally conditioned by Du Pont into 13 kg buckets. If a sample of the solution is poured from a large to a small container, which is always the case since a few cubic centimeters are sufficient for the coating of a storage bulb, the concentration of the sample is strongly dependent upon the storage time of the large

container if the solution is not perfectly mixed before pouring. On the other hand, the commercial solution cannot be stored for more than a few months because the residual of the initiator , left after the polymerization process, causes the solution to separate. Therefore it is not possible to select a good solution and keep it forever for the coating of future masers.

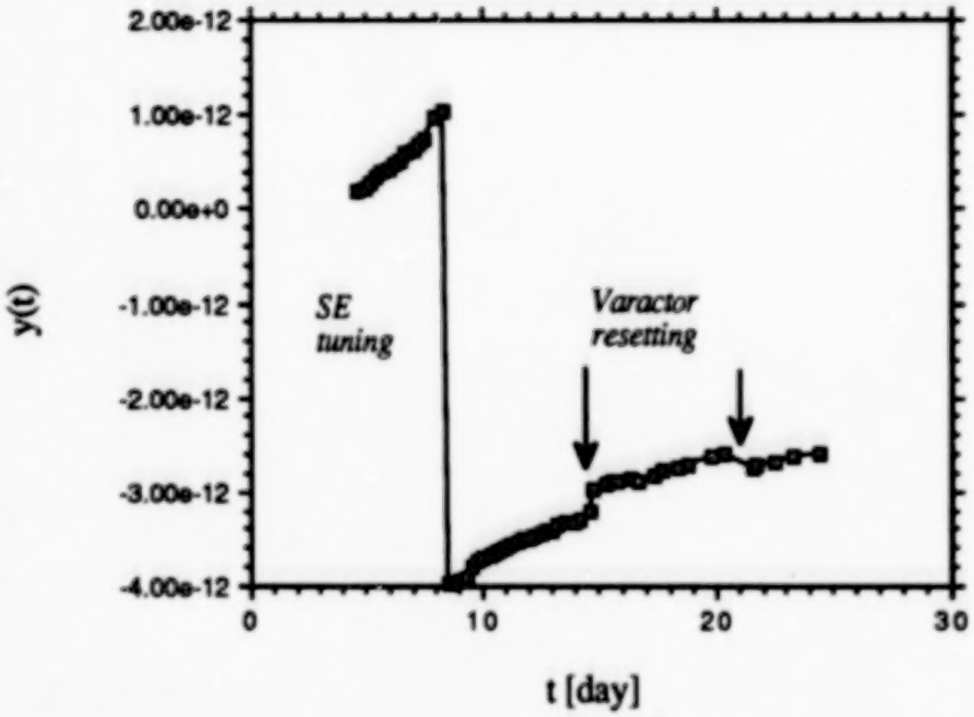


Figure 5
Normalized Frequency y vs Time

In conclusion there is a definite need for a method that would permit to determine the performance of a coating without actually testing it into an oscillating maser. The possibility of testing coating samples with Electron Spin Resonance (ESR), Infrared Spectroscopy (IS) and Photon Spectroscopy (XPS) is now under investigation at Neuchâtel Observatory. Preliminary results with ESR testing shows that there is a sizable difference in free electron spins between different Teflon samples. However we suspect that the differences are determined more by the curing process than by a difference of composition between different batches of the Teflon solution. A very tight control of all the parameters of the curing process would be necessary in order to demonstrate differences between different Teflon batches.

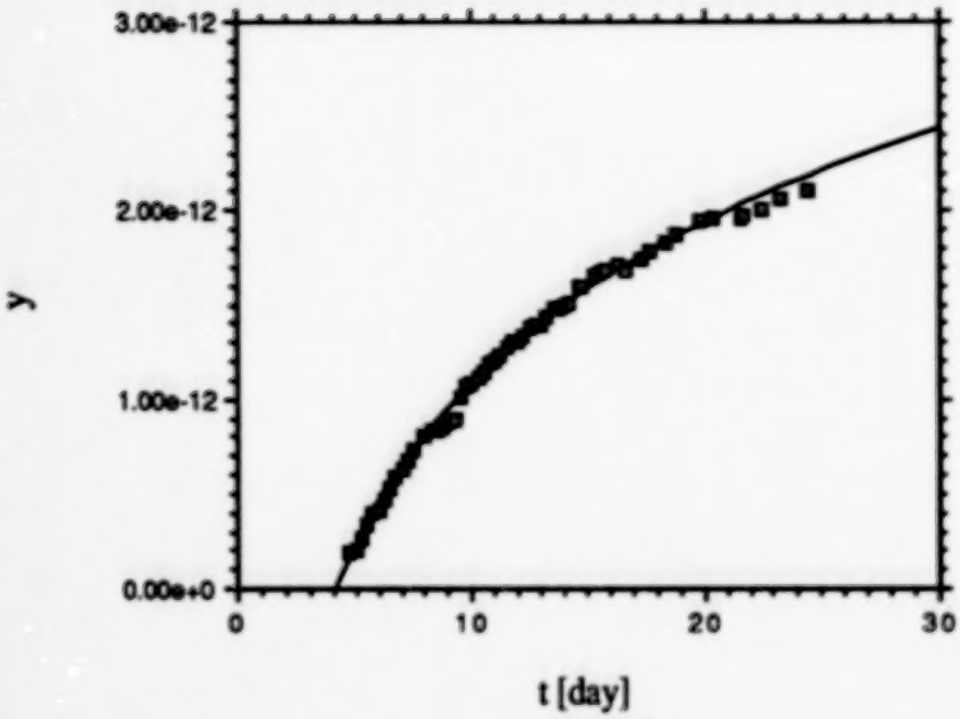


Figure 6
y vs Time
Corrected for Constant Cavity Tuning

[1] Mattison E. M., Vessot R.F.C., Bain C., Wasserman S., Whiteside G. "Surface Interaction of Atomic Hydrogen with Teflon," *Proc. 41st Annual Symposium on Frequency Control*, Philadelphia, May 1987, pp. 95-98.

[2] Bernier L.G., Busca G., "Some Results on the Line Q Degradation in Hydrogen Masers", *4th European Time and Frequency Forum*, Neuchâtel, March 1990, pp. 713-714.

Acknowledgements

We want to thank Prof. Schweiger of the Laboratorium für Physikalische Chemie, ETH Zürich, for his ESR measurements on the Teflon samples and Joel Elldér of Onsala Space Observatory in Sweden for his field line Q measurements on the EFOS-7 maser.

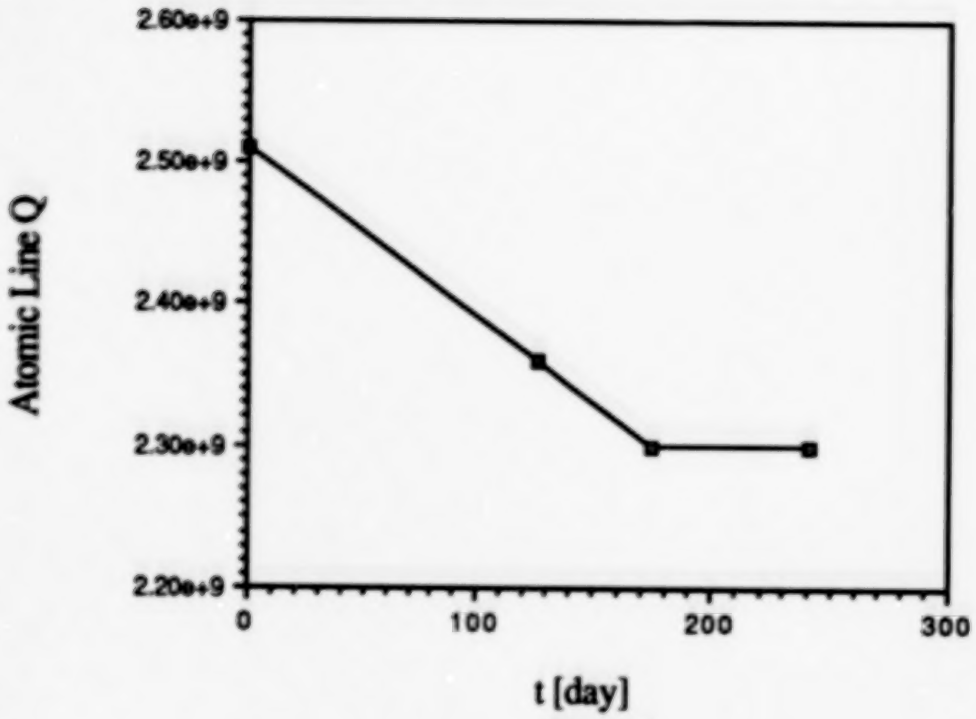


Figure 7
Atomic Line Q with Good Coating

1990 PTTI CONFERENCE
ATTENDEES LIST

David W. Allan
National Institute of Standards and Technology
Time and Frequency Division
325 Broadway
Boulder, CO 80303 USA
303/497-5637

Carroll O. Alley
University of Maryland
Department of Physics and Astronomy
College Park, MD 20742 USA
301/405-6098

Brad Anderson
Stanford Telecommunications
2421 Mission College Boulevard
Santa Clara, CA 95056-0968 USA
408/987-5506

Leigh A. Archbold
U.S. Coast Guard
7323 Telegraph Road
Alexandria, VA 22310 USA
703/866-3862

Tim R. Armstrong
DSIR-Physical Sciences
P.O. Box 31-313
Lower Hutt NEW ZEALAND
64 4 666 919

John C. Arnold
Bendix Field Engineering Corporation
One Bendix Road, MS/VLBI
Columbia, MD 21045 USA
301/964-7931

Claude L. Audoin
Laboratoire de
L'Horloge Atomique
Batiment 221 Universit
Paris-sud, Orsay FRANCE
1 69 41 78 45

Joshua P. Auzenne
GPS Joint Program Office
SSD/MZUF
Los Angeles, CA 90009 USA
213/363-6359

Rob Avery
Telecom Solutions
85 West Tasman Drive
San Jose, CA 95134 USA
408/433-0910

Richard G. Bailey
Datum, Inc.
1363 S. State College
Anaheim, CA 92806 USA
714/533-6333

Anthony P. Baker
ITT Aerospace
492 River Road
Nutley, NJ 07110 USA
201/284-2312

James A. Barnes
Austron, Inc.
3011 Broadway
Boulder, CO 80304 USA
303/440-7282

Thomas R. Bartholomew
TASC
1190 Winterson Road
Linthicum, MD 21090 USA
301/850-0070

Andrews P. Baugh
Pan Am World Services
P.O. Box 1413
APO San Francisco, CA 96555 USA
805/238-7994

Francoise S. Baumont
Observatoire de la Cote D'Azur
OCA/CERGA
Avenue Nicolas Cpernic
F-06130 Grasse, FRANCE
33 93 365849

Cynthia L. Beagle
SSD/MZS
Los Angeles AFB
P.O. Box 92960
Los Angeles, CA 90009-2960 USA
213/363-6363

Ronald L. Beard
Naval Research Laboratory
4555 Overlook Avenue, SW, MS 8320
Washington, DC 20375-5000 USA
202/767-2595

Roger E. Beehler
National Institute of Standards and Technology
325 Broadway
Boulder, CO 80303 USA
303/497-3281

Albert Benjaminson
General Technical Services
105 Clermont Avenue
Alexandria, VA 22304 USA
703/751-0955

Robert N. Blackwood
TRAK Systems
1835-G Forest Drive
Annapolis, MD 21401 USA
301/261-1904

Scott S. Blake
NASA
Goddard Space Flight Center
Code 531.3
Greenbelt, MD 20771 USA
301/286-3224

Eirik Bliksrud
Norwegian Telecom
P.O. Box 6701
Olso 0130 NORWAY
47 2 488 990

Martin Bloch
FEI
55 Charles Lindbergh Boulevard
Mitchel Field, NY 11553 USA
516/794-4500

Mark A. Bodily
Cable and Wireless
Mercury House
Theobalds Road, London, WC1 UNITED KI
071/315-4500

Jim Bohac
Stanford Telecommunications
2421 Mission College Boulevard
Santa Clara, CA 95056-0968 USA
408/987-5506

Dan E. Brannen
HRB Systems
P.O. Box 60, Science Park
State College, PA 16804 USA
814/238-4311

Erland Brannstrom
Swedish Telecom Radio
S-136 80 Haninge SWEDEN
46 8 707 5197

Lee A. Breakiron
U.S. Naval Observatory
Time Service Department
34th and Massachusetts Avenue, NW
Washington, DC 20392-5100 USA
202/653-1888

Danny R. Bridges
U.S. Army
906 Dayton Drive
Scottsboro, AL 35768 USA
205/842-8538

Archie W. Brown
Bendix Field Engineering Corporation
One Bendix Road MS/VLBI
Columbia, MD 21045 USA
301/964-7570

Ellis H. Bryant, Jr.
5400 New PeachTree Drive
Atlanta, GA 30341 USA
404/458-6267

James A. Buisson, III
Naval Research Laboratory
4555 Overlook Avenue, SW, MS 8320
Washington, DC 20375-5000 USA
202/767-2095

Martin Buoncristiani
National Aeronautics and Space Administration
Langley Research Center, MS 468
Hampton, VA 23665 USA
804/864-1569

Edward E. Burkhardt
Burkhardt Monitoring Service
P.O. Box 1411
Glen Allen, VA 23060 USA
804/261-1800

Dr. Giovanni Busca
Observatoire Cantonal de Neuchatel
3 Avenue de Beauregard
CH-2036 Cormondreche SWITZERLAND
38 24 18 61

Edgar W. Butterline
AT&T, Room 3C130E
Routes 202 and 206 North
Bedminster, NJ 07921 USA
908/234-4545

Ernest Byron
John Hopkins University
Applied Physics Laboratory
Johns Hopkins Road
Laurel, MD 20723-6099 USA
301/953-6420

Malcolm D. Calhoun
Jet Propulsion Laboratory
4800 Oak Grove Drive
Pasadena, CA 91109 USA
818/354-9763

J. Richard Carlson
Communications Security Estab.
Dept. of National Defense
P.O. Box 9703 Terminal
Ottawa, Ontario K1G 3Z4 CANADA
613/991-7214

Harold A. Chadsey
U.S. Naval Observatory
Time Service Department
34th and Massachusetts Avenue, NW
Washington, DC 20392-5100 USA
202/653-1888

David N. Chalmers
U.S. Naval Observatory
Time Service Department
34th and Massachusetts Avenue, NW
Washington, DC 20392-5100 USA
202/653-1412

Mark J. Chandler
BMC Associates
235 Congress Avenue
Lansdowne, PA 19050 USA
215/622-2833

Laura G. Charron
U.S. Naval Observatory
Time Service Department
34th and Massachusetts Avenue, NW
Washington, DC 20392-5100 USA
202/653-1529

Lee A. Chenoweth, Jr.
Ball Corporation
Efratom Division
3 Parker
Irvine, CA 92718 USA
714/770-5000

Randolph T. Clarke, III
U.S. Naval Observatory
Time Service Depa[illegible]
34th and Massach[illegible]venue, NW
Washington, DC 2[illegible]0 USA
202/653-0485

Debra Coleman
Bonneville Power
Administration
P.O. Box 3621-E
Portland, OR 97208-362[illegible] USA
503/230-4533

609

Franco Cordara
Istituto Elettrotecnico
Nazionale G. Ferraris
42 Corso Massimo D'Azeglio
Torino, 10126 ITALY
39-11-3488933

Tracy Crane
Creative Marketing Associates
9140-H Guilford Road
Columbia, MD 21046 USA
301/880-4161

John Cuesta
Odetics, Inc.
12819 Kettering Drive
Herndon, VA 22071 USA
703/860-0170

John C. Cutherbertson
Ball Corporation
Efratom Division
9601 Riverdale Place
Manassas, VA 22110 USA
703/284-5400

Leonard S. Cutler
Hewlett-Packard Laboratories
P.O. Box 10350, MS 26M-9
Palo Alto, CA 94303-0867 USA
415/857-5259

Peter Daly
University of Leeds
Department of Electrical Engineering
Leeds, LS2 9JI UNITED KINGDOM
0532 332073

James E. Danaher
35 Navigation
23141 Plaza Pointe Drive
Laguna Hills, CA 92653 USA
714/830-3777

Angela M. Davis
U.S. Naval Observatory
Time Service Department
34th and Massachusetts Avenue, NW
Washington, DC 20392-5100 USA
202/653-1528

Gerrit De Jong
Van Swinden Laboratory
P.O. Box 654
Delft 2600 AR NETHERLANDS
31 15 631 623

Nikolai A. Demidov
Department of Gorki R&D
Instrument Making-Institute
176 Gagarin Avenue
Gorki 603009 USSR
65 22 93

Edoardo Detoma
SEPA S.p.A
Corso Giulio Cesare 294
Torino 10154 ITALY
39 11 2682 523

G. John Dick
Jet Propulsion Laboratory
4800 Oak Grove Drive
Pasadena, CA 91109 USA
818/354-6393

Irvin Diegel
Bendix Field Engineering Corporation
One Bendix Road
Columbia, MD 21045 USA
301/964-7343

William A. Diener
Jet Propulsion Laboratory
4800 Oak Grove Drive, Building 298
Pasadena, CA 91109 USA
818/354-9762

Thomas P. Donaher
Spectracom Corporation
101 Despatch Drive
East Rochester, NY 14445 USA
716/381-4827

Chauncey P. Dunn
Computer Sciences Raytheon
P.O. Box 4127
Patrick Air Force Base FL 32925-0127 USA

Frank E. Easton
U. S. Air Force
Systems Command
FTD/SDMSS Wright-Patterson AFB
Dayton, OH 45433-6508 USA
513/257-4113

Edward Eng
Lockheed Missiles and Space Company
P.O. Box 3504
Sunnyvale, CA 94088-3504 USA
408/756-3989

Sheila C. Faulkner
U.S. Naval Observatory
Time Service Department
34th and Massachusetts Avenue, NW
Washington, DC 20392-5100 USA
202/653-1460

Scott D. Feairheller
U.S. Air Force
Systems Command
WP AFB, OH 45433-5608 USA
513/257-4113

Raymond L. Filler
U.S. Army LABCOM
SLCET-EQ
Fort Monmouth, NJ 07703 USA
908/544-2467

Richard H. Flamm
Lockheed
Kennedy Space Center
Mail Unit 350, FL 32780 USA
407/867-3145

Henry F. Fliegel
The Aerospace Corporation
2350 El Segundo Boulevard
El Segundo, CA 90237 USA
213/336-1710

Joe E. Flores
Computer Sciences Corporation
P.O. Box 446
Edwards AFB, CA 93523 USA
805/377-6130

D. Earl Fossler
TRAK Systems
4726 Eisenhower
Tampa, FL 33634 USA
813/884-1411

Roger S. Foster
Naval Research Laboratory
Code 4200
Washington, DC USA
202/767-0669

Dan D. Friel
Leitch Video of America
825 K Greenbrier Circle
Chesapeake, VA 23320 USA
804/424-7920

Hugo Fruehauf
Ball Corporation
Efratom Division
3 Parker
Irvine, CA 92718 USA
714/770-5000

Jean C. Gaignebet
Observatoire de la Cote D'Azur
OCA/CERGA
Avenue Nicolas Coeprnic
F-06130 Grasse, FRANCE
33 93 365849

Joseph M. Gardner
Leitch Video of America
825 K Greenbrier Circle
Chesapeake, VA 23320 USA
804/424-7920

Michael R. Garvey
Frequency and Time Systems, Inc.
34 Tozer Road
Beverly, MA 01915 USA
508/927-8220

611

Guy A. Gifford
Naval Research Laboratory
4555 Overlook Avenue Southwest, MS 8320
Washington, DC 20375-5000 USA
202/767-2595

Norman J. Gillaspie
ISS Engineering
1047 Elwell Court
Palo Alto, CA 94303 USA
415/967-0833

William M. Golding
Naval Research Laboratory
4555 Overlook Avenue
Washington, DC 20375 USA
202/767-2595

Erhard P. Graf
Oscilloquartz SA
16 Brevards
Neuchatel CH-2002 SWITZERLAND
41 38 25 85 01

Michel P. Granveaud
Observatoire de Paris
Laboratoire Primaire du Temps
61, Av. Observatoire
75014 Paris FRANCE
33 14 05 12723

Joe C. M. Green
Bendix Aerospace Corporation
129 North Hill Avenue
Pasadena, CA 91101 USA
818/584-4612

Charles A. Greenhall
Jet Propulsion Laboratory
4800 Oak Grove Drive
Pasadena, CA 91109 USA
818/354-5434

Captain James B. Hagen
U.S. Naval Observatory
34th and Massachusetts Avenue, NW
Washington, DC 20392-5100 USA
202/653-1538

Shinichi Hama
Communications Research Laboratory
University of California/RA Lab, 601 Campbell
Berkeley, CA 94720 USA
415/642-5128

Robert J. Hamell
Jet Propulsion Laboratory
4800 Oak Grove Drive
Pasadena, CA 91109 USA
818/354-4944

William P. Hanson
Piezo Crystal Company
100 K Street
Carlisle, PA 17013 USA
717/249-2151

Wayne Hanson
National Institute of Standards and Technology
325 Broadway
Boulder, CO 80303 USA
303/497-5233

Walter R. Harding
Navel Electronic Systems Engineering Center
P.O. Box 55
Portsmouth, VA 23705-0055 USA
804/396-7992

Robert W. Harris
Telecom Australia Research Laboratories
770 Blackburn Road
Clayton Victoria 3168 AUSTRALIA
613 541 6124

Ilan Havered
Datum, Inc.
1363 South State College Boulevard
Anaheim, CA 92806-5790 USA
714/533-6333

Helmut W. Hellwig
Department of the Air Force
Office of Scientific Research
Bolling Air Force Base
Washington, DC 20332-5448 USA
202/767-5017

Robert J. Hesselberth
Spectracom Corporation
101 Despatch Drive
East Rochester, NY 14445 USA
716/381-4827

Quyen Hua
Stanford Telecommunications
2421 Mission College Boulevard
Santa Clara, CA 95056-0968 USA
408/987-5506

Jeffrey S. Ingold
Bendix Field Engineering Corporation
One Bendix Road
Columbia, MD 21045 USA
301/964-7188

Bernardo Jaduszliwer
The Aerospace Corporation
P.O. Box 92557 M2-253
Los Angeles, CA 90009-2957 USA
213/336-9257

Nicolette M. Jardine
U.S. Naval Observatory
Time Service Department
34th and Massachusetts Avenue, NW
Washington, DC 20392-5100 USA
202/653-1662

James Jespersen
National Institute of Standards and Technology
325 Broadway
Boulder, CO 80303 USA
303/497-3849

Andrew C. Johnson
U.S. Naval Observatory
Time Service Department
34th and Massachusetts Avenue, NW
Washington, DC 20392-5100 USA
202/653-1561

William B. Johnson
Bell South Services
WIGI, 3535 Columbia Parkway N
Birmingham, AL 35243 USA
205/977-5085

Larry S. Johnson
Bendix Field Engineering Corporation
One Bendix Road
Columbia, MD 21045 USA
301/461-7463

Edward C. Jones
Naval Research Laboratory
4555 Overlook Avenue, SW, MS 8320
Washington, DC 20375-5000 USA
202/767-2595

Kevin S. Judge
Magnavox Advanced Products
2829 Maricopa Street
Torrance, CA 90505 USA
213/618-1200

Kurt B. Kaiser
EG&G Frequency Products
35 Congress Street
Salem, MA 01970 USA
508/745-3200

Sarunas K. Kaurza
The Aerospace Corporation
2350 East El Segundo Boulevard
El Segundo, CA 90245-4691 USA
213/336-6837

Clement D. Ketchum
U.S. Coast Guard
OMEGA System Center
6510 Caualier Drive
Alexandria, VA 22307 USA
703/866-3822

Masami Kihara
NTT Transmissions Systems Laboratory
1-2356 Take
Yokosuka, Kanagawa 238-03 JAPAN
81 468 59 3164

Dieter Kirchner
Technical University Graz
Inffeldgasse 2
Graz A-8010 AUSTRIA
316/873-7459

Albert Kirk
Jet Propulsion Laboratory
4800 Oak Grove Drive
Pasadena, CA 91109 USA
818/354-3038

William J. Klepczynski
U.S. Naval Observatory
Time Service Department
34th and Massachusetts Avenue, NW
Washington, DC 20392-5100 USA
202/653-1521

Douglas E. Koch
Naval Space Surveillance Center
Dahlgren, VA 22448 USA
703/663-8561

Paul A. Koppang
Sigma Tau Standards Corporation
1711 Holt Road
Tuscaloosa, AL 35404 USA
205/553-0038

Vladimer V. Korniyenko
Leningrad Scientific
Research Radiotechnical Institute
2, Rastrelli Square
Leningrad 193124 USSR
2719309

Greg J. Kret
Kinemetics/Truetime
3243 Santa Rosa Avenue
Santa Rosa, CA 95407 USA
707/528-1230

Frank S. Kroc
Loral Western Development Labs
7100 Standard Drive
Hanover, MD 21076 USA
301/796-3474

Paul F. Kuhnle
Jet Propulsion Laboratory
4800 Oak Grove Drive
Pasadena, CA 91109
818/354-2715

Emil R. Kursinski
Jet Propulsion Laboratory
4800 Oak Grove Drive
Pasadena, CA 91109 USA
818/354-7533

Paul J. Kushmeider
Bendix Field Engineering Corporation
One Bendix Road
Columbia, MD 21045 USA
301/964-7672

Jack Kusters
Hewlett-Packard
5301 Stevens Creek Boulevard
Santa Clara, CA 95052-8059 USA
408/553-2041

Joe C. Lamb
U.S. Air Force
Edward AFB, CA 93523 USA
301/275-8302

Graybill P. Landis
Naval Research Laboratory
4555 Overlook Avenue, SW, MS 8320
Washington, DC 20375-5000 USA
202/767-2095

Marie Largay
Naval Research Laboratory
4555 Overlook Avenue, SW MS 8320
Washington, DC 20375-5000 USA
202/767-2095

Leonard R. Lathrem
Bendix Field Engineering Corporation
One Bendix Road
Columbia, MD 21045 USA
301/964-7187

Julius C. Law
Jet Propulsion Laboratory
4800 Oak Grove Drive, MS 298-100
Pasadena, CA 91030 USA
818/354-2988

Felix Lazarus
Hewlett-Packard
150 Route Du Nant D'Avril
CH-1217 Meyrin 2 SWITZERLAND

Sigfrido M. Leschiutta
Politecnico-Elettronica
Corso Abbruzzi 24
Torino 10123 ITALY
38 11 556 7235

614

Martin W. Levine
Timing Decision, Inc.
P.O. Box 1513
Manchester, MA 01944 USA
508/526-4218

Wlodzimierz W. Lewandowski
Bureau International des Poids et Mesures
Pavillon de Breteuil
92312 S FRANCE
33 1 45 07 7063

Frank B. Lifsey
Locus, Inc.
2560 Huntington Avenue
Alexandria, VA 22303 USA
703/960-1000

Anthony S. Liu
The Aerospace Corporation
2350 El Segundo Boulevard
El Segundo, CA 90245-4691 USA
213/336-5069

Gene E. Long
Odetics, Inc.
P.O. Box 2727
La Plata, MD 20646 USA
301/879-3311

Pete R. Lopez
TRAK Systems
4726 Eisenhower Boulevard
Tampa, FL 33634-6391 USA
813/884-1411

Carl F. Lukac
U.S. Naval Observatory
Time Service Department
34th and Massachusetts Avenue, NW
Washington, DC 20392-5100 USA
202/653-1527

Edward M. Lukacs
U.S. Naval Observatory
Time Service SubStation
11820 SW 166th Street
Miami, FL 33177 USA
305/235-0515

George H. Luther
U.S. Naval Observatory
Time Service Department
34th and Massachusetts Avenue, NW
Washington, DC 20392-5100 USA
202/653-1022

Lute Maleki
Jet Propulsion Laboratory
4800 Oak Grove Drive
Pasadena, CA 91109 USA
818/354-3688

Victoria Manymules
Jet Propulsion Laboratory
4800 Oak Grove Drive
Pasadena, CA 91109 USA
818/354-7055

Kenneth E. Martin
Bonneville Power Administration
18905 NE Davis Road
Brush Prairie, WA 98606 USA
206/254-3049

Demetrios Matsakis
U.S. Naval Observatory
Time Service Department
34th and Massachusetts Avenue, NW
Washington, DC 20392-5100 USA
202/653-0585

Edward M. Mattison
Smithsonian Astrophysical Observatory
60 Garden Street, MS-59
Cambridge, MA 02138 USA
617/495-7265

Thomas B. McCaskill
Naval Research Laboratory
4555 Overlook Avenue, SW MS 8320
Washington, DC 20375-5000 USA
212/767-2595

Terence J. McGurn
U.S. Government
11225 Handlebar Road
Reston, VA 22091 USA
703/860-0806

James W. McHale
Contel
FSS
P.O. Box 235
Las Cruces, NM 88004-1235 USA
505/525-6924

Jim J. McIlroy
BBC Radio
Room 2057, Broadcasting House
1 Portland Place
London W1A 1AA ENGLAND
071 927 4090

Jack S. McNabb
TRAK Systems
4722 Eisenhower Boulevard
Tampa, FL 33634 USA
813/884-1411

Marvin P. Meirs
Frequency Electronics, Incorporated
55 Charles Lindbergh Boulevard
Mitchell Field, NY 11553 USA
516/794-4500

Alan L. Milton
Computer Sciences
Raytheon
P.O. Box 4127
Patrick AFB, FL 32925-0127 USA

Gilles Missout
Hydro Quebec
1800 Montee Ste Julie
Varennes, Quebec J3X 151 CANADA
514/652-8084

Don Mitchell
Austron, Incorporated
P.O. Box 14766
Austin, TX 78761-4766 USA
512/251-2313

Theodore W. Mogey
Rockwell International
Satellite and Space Electronics Division
Stop 82
Falcon AFB, CO 80912-5000 USA
719/550-2950

Kenneth W. Monington
University of Delaware
412 Wharton Drive
Newark, DE 19711 USA
302/731-1648

Craig R. Moore
The Johns Hopkins University
Applied Physics Laboratory
Johns Hopkins Road
Laurel, MD 20732-6099 USA
301/953-5920

Derek Morris
National Research Council
Montreal Road
Ottawa Ontario K1A OR6 CANADA
613/993-9340

Ruzbeh Mossavati
National Physical Laboratory
Queens Road
Teddington, London TW1101W UNITED KI
81 943 6094

Frank Mullen
Frequency and Time Systems
34 Tozer Road
Beverly, MA 01915 USA
508/927-8220

Robert E. Murphy
FTS
34 Tozer Road
Beverly, MA 01983 USA
508/887-8235

William J. Murphy, Jr.
Computer Sciences Corporation
P.O. Box 446
Edwards AFB, CA 93523 USA
805/227-2004

James A. Murray
Naval Research Laboratory
SFA, Code 8320
Washington, DC 20375-5000 USA
202/404-7056

Dr. Robert A. Nelson
W. L. Pritchard Company, Inc.
7315 Wisconsin Avenue
Bethesda, MD 20706 USA
301/907-7070

Orville J. Oaks
Naval Research Laboratory
4555 Overlook Avenue, SW, MS 8320
Washington, DC 20375-5000 USA
202/767-2595

Karen F. O'Donoghue
Naval Surface Warfare Center
Code N35
Dahlgren, VA 22405 USA
703/663-1567

David P. Opie
College of William and Mary
Department of Physics
Williamsburg, VA 23185 USA
804/221-3560

Skip W. Osborne
Allen Osborne Associates
756 Lakefield Road, Building J
Thousand Oaks, CA 91361 USA
805/495-8420

Robert W. Osborne
Allen Osborne Associates
756 Lakefield Road, Building J
Thousand Oaks, CA 91361 USA
805/495-8420

Allan Oster
Air Force Space Systems Division
Worldway Postal Center, Box 92960
Los Angeles, CA 90009 USA
213/363-2240

Terry N. Osterdock
Stellar Navigation, Inc.
19075 Skyline Boulevard
Los Gatos, CA 95030 USA
408/354-0733

Joseph W. Quellete
The Aerospace Corporation
P.O. Box 92957, M4-895
Los Angeles, CA 90009-2957 USA
213/336-1048

Angel L. Padilla
U. S. Army
TMDE Activity
AMCTM - S - ED, Building 5435
Redstone Arsenal, AL 35898 USA
205/842-8529

Ralph E. Partridge
Los Alamos National Laboratory
Group J-8, MSP947, P.O. Box 1663
Los Alamos, NM 87545 USA
505/665-1617

Ian Pascaru
Frequency Electronics, Incorporated
55 Charles Lindbergh Boulevard
Uniondale, NY 11553 USA
516/794-4500

Peter Z. Paulovich
NAVELEX Systems Engineering Command
P.O. Box 55
Portsmouth, VA 23320 USA
804/547-4768

Rolando Penabade
TRAK Systems
4726 Eisenhower Boulevard
Tampa, FL 33634-6391 USA
813/884-1411

Bruce Penrod
Austron, Incorporated
P.O. Box 14766
Austin, TX 78761-4766 USA
512/251-2313

617

James C. Perry
National Aeronautics and Space Administration
Greenbelt Road
Greenbelt, MD 20771 USA
301/286-3471

Harry E. Peters
Sigma Tau Standards Corporation
1711 Holt Road, P.O. Box 1877
Tuscaloosa, AL 35403 USA
205/553-0038

Gerard Petit
Bureau International des Poides et Mesures
Pavillon de Breteuil
92312 Sevres Cedex, FRANCE
33 1 45 07 7067

Arun G. Phadke
Virginia Polytechnic Institute
Department of Electrical Engineering
Blacksburg, VA 24061 USA
703/231-7029

David H. Phillips
2901 Accokeek Road, W
Accokeek, MD 20607 USA
301/283-2747

John B, Ponsonby
University of Manchester
Nuffield Radio Astronomy Lab
Jodrell Bank
Macclesfield, Cheshire SK1190DL UNITED KI
44 477 71321

William M. Powell
U.S. Naval Observatory
Time Service Department
34th and Massachusetts Avenue, NW
Washington, DC 20392-5100 USA
202/653-1528

Edward D. Powers, Jr.
Naval Research Laboratory
4555 Overlook Avenue, SW, MS 8320
Washington, DC 20375-5000 USA
202/767-2095

John D. Prestage
Jet Propulsion Laboratory
4800 Oak Grove Drive
Pasadena, CA 91109 USA
818/354-3515

Robert E. Price
Bendix Field Engineering Corporation
One Bendix Road
Columbia, MD 21043 USA
301/964-7437

Norman F. Ramsey
Harvard University
Lyman Physics Laboratory
Cambridge, MA 02138 USA

Richard A. Rayos
Computer Sciences Raytheon
Patrick AFB, FL 32925 USA
407/494-7176

Donald A. Rhine
Bendix Field Engineering Corporation
1720 Yorkland Road
Finksburg, MD 21048 USA
301/876-1672

William J. Riley
EG&G Frequency Products
35 Congress Street
Salem, MA 09170 USA
508/745-3200

Per Rise
OMEGA Norway
N-8730 Bratland NORWAY
47 86 93109

Paul N. Risinger
Telecom Solutions
85 West Tasman Drive
San Jose, CA 95134 USA
408/943-9403

Ron Roloff
Austron, Incorporated
P.O. Box 14766
Austin, TX 78761-4766 USA
512/251-2313

Lauren J. Rueger
The Johns Hopkins University
Applied Physics Laboratory
1415 Glen Allan Avenue
Silver Spring, MD 20902 USA
301/942-7733

Harry W. Sadler
Bendix Field Engineering Corporation
One Bendix Road
Columbia, MD 21045 USA
301/964-7425

Stephen F. Sandford
National Aeronautics and Space Administration
La RC, MS 474
Hampton, VA 23665 USA
804/864-1832

Arthur L. Satin
The Aerospace Corporation
2350 East El Segundo Boulevard
Los Angeles, CA 90009 USA
213/336-4499

Hartmut S. Schweda
Observatoire Cantonal de Neuchatel
58 Rue De l'Observatoire
CH-2000 Neuchtel SWITZERLAND
41 38 31 8831

Amitav SenGupta
National Institute of Standards and Technology
325 Broadway
Boulder, CO 80303 USA
303/497-3207

Sarah J. Sirois
The Mitre Corporation
R350 Burlington Road
Bedford, MA 01730 USA
617/271-6238

Armin Soering
German Telekom
FTZ Darmstadt
P.O. Box 100003
6100 Darmstadt GERMANY
49 6151 83 4549

Sarah Stebbins
Naval Research Laboratory
4555 Overlook Avenue, SW, MS 8320
Washington, DC 20375-5000 USA
202/767-2595

Samuel R. Stein
Timing Solutions Corporation
555 Jack Pine Court
Boulder, CO 80304-1711 USA
303/443-5152

Charles S. Stone
Brightline Corporation
P.O. Box 1299
Cedar Park, TX 78613 USA
512/258-3701

Emil R. Straka
Hewlett-Packard
5301 Stevens Creek Boulevard
Santa Clara, CA 95051 USA
408/553-2887

Michael A. Street
Bonneville Power Administration
P.O. Box 3621
Portland, OR 97208 USA
503/230-4363

Joseph J. Suter
The Johns Hopkins University
Applied Physics Laboratory
Johns Hopkins Road
Laurel, MD 20723-6099 USA
301/953-5826

Richard L. Sydnor
Jet Propulsion Laboratory
4800 Oak Grove Drive
Pasadena, CA 91109 USA
818/354-2763

Philip E. Talley
The Aerospace Corporation
2350 East El Segundo Boulevard
El Segundo, CA 90245-4691 USA
213/336-0484

Erik A. Tangen
Norwegian Defence
Communications Administration
Oslo Mil/Akershus
0015 Oslo 1 NORWAY

Patrizia Tavella
Istituto Elettrotecnico Nazionale
91 Strada Delle Cacce
Torino 10135 ITALY
39-11-3488933

Physikalisch-Technische
Bundesanstalt
Library
Bundesallee 100, P.O. Box 3345
D-3300 Braunschweig GERMANY FED REP

Dorsey L. Thacker
Interferometrics, Incorporated
8150 Leesburg Pike, Suite 1400
Vienna, VA 22182 USA
703/790-8500

Jimmie B. Thigpen
Naval Space Surveillance Center
Building 183, NSWC
Dahlgren, VA 22448 USA
703/663-8561

James E. Thomas
Southern Company Services, Incorporated
P.O. Box 2625
Birmingham, AL 35202 USA
205/870-6742

Dr. Claudine Thomas
Bureau International des Poids et Mesures
Pavillon de Breteuil
92312 Sevres Cedex, FRANCE
33 1 45 07 7073

Michael R. Tope
Kinemetrics/Truetime
3243 Santa Rosa Avenue
Santa Rosa, CA 95407 USA
707/528-1238

Adolph A. Uljanov
Measuring Instruments and Systems
176 Prospect Gagarina
Gorkij 603009 USSR
65 22 06

M. J. Van Melle
Rockwell International
P.O. Box 3644 SN85
Seal Beach, CA 90740 USA
213/797-3459

Jacques Vanier
National Research Council
Montreal Road
Ottawa, Canada KIA OR6 CANADA
613/993-9326

Francine N. Vannicola
U.S. Naval Observatory
Time Service Department
34th and Massachusetts Avenue, NW
Washington, DC 20329-5100 USA
202/653-1525

Vinicio Vannicola
U.S. Coast Guard
10024 Ranger Road
Fairfax, VA 22030 USA
703/866-3840

Lester B. Veenstra
INTELSAT
3400 International Drive, NW
Washington, DC 20008-3098 USA
202/944-7090

Christian J. L. Veillet
Observatoire de La Cote D'Azur
OCA/CERGA
Avenue Nicolas Copernic
F-06130 Grasse FRANCE
33 93 365849

Robert F. C. Vessot
Harvard-Smithsonian Center for Astrophysics
60 Garden Street
Cambridge, MA 02138 USA
617/495-7276

Jerome R. Vetter
The Johns Hopkins University
Applied Physics Laboratory
Johns Hopkins Road
Laurel, MD 20723 USA
301/953-5000

Peter Vlitas
Frequency and Time Systems
34 Tozer Road
Beverly, MA 01915 USA
508/988-8220

Frank J. Voit
The Aerospace Corporation
2350 East El Segundo Boulevard
El Segundo, CA 90245-4691 USA
213/336-6837

Eric P. Vondran
Eastern Space and Missile Center
Systems Development
Building 981, ESMC/DVEC
Patrick AFB, FL 32935 USA
407/494-5107

Fred L. Walls
National Institute of Standards and Technology
325 Broadway
Boulder, CO 80303 USA
303/497-3207

Ben-Chun Wang
University of Maryland
Department of Physics and Astronomy
College Park, MD 20742 USA
301/405-6102

Harry T. Wang
Hughes Research Labs
3011 Malibu Canyon Road
Malibu, CA 90265 USA
213/317-5431

Samuel C. Ward
2258 Midlothian Drive
Altadena, CA 91001 USA
818/794-3491

S. Clark Wardrip
Bendix Field Engineering Corporation
726 Foxenwood Drive
Santa Maria, CA 93455 USA
805/865-3214

Toney C. Warren
Telecom Solutions
85 West Tasman Drive
San Jose, CA 95134 USA
408/943-9403

Werner A. Weidemann
Ball Corporation, Efratom Division
3 Parker
Irvine, CA 92718-1605 USA
714/770-5000

Marc A. Weiss
National Institute of Standards and Technology
325 Broadway
Boulder, CO 80303 USA
303/497-3261

Paul J. Wheeler
U.S. Naval Observatory
Time Service Department
34th and Massachusetts Avenue, NW
Washington, DC 20392-5100 USA
202/653-0516

Joe D. White
Naval Research Laboratory
4555 Overlook Avenue, SW, MS 8320
Washington, DC 20375-5000 USA
202/767-2095

Mark S. Whitty
MCI
12369 Sunrise Valley Drive
Reston, VA 22102 USA
703/648-8156

Warren L. Wilson
Lockheed Missiles and Space Company
707 Spindrift Drive
San Jose, CA 95134-1346 USA
408/743-1213

David J. Wineland
National Institute of Standards and Technology
325 Broadway
Boulder, CO 80303 USA
303/497-5286

Dr. Gernot M. R. Winkler
U.S. Naval Observatory
Time Service Department
34th and Massachusetts Avenue, NW
Washington, DC 20392-5100 USA
202/653-1520

Valerie A. Wooden
Johnson Controls
World Services, Incorporated
401 Wynn Drive
Huntsville, AL 35801 USA
205/721-3750

Clark E. Woodward
Pacific Bell
2600 Camino Ramon, Room 3S400
San Ramon, CA 94583 USA
415/823-2359

Woody Wordsworth
Austron, Inc.
1930 Isaac Newton Square, Suite 11
Reston, VA 22090 USA
703/471-7963

James L. Wright
C S R
Box 4127
Patrick AFB, FL 32937 USA
407/494-2014

Nicholas F. Yannoni
Rome Air Development Center
Hanscom Air Force Base
Bedford, MA 01731 USA
617/377-2206

Eric C. Youngberg
Hewlett-Packard Company
5301 Stevens Creek Boulevard, MS 16
Santa Clara, CA 95052 USA
408/553-2308

George P. Zampetti
AT&T
Crawfords Connor Road, Room 3M-529
Hamson, NJ 07737 USA
908/544-1092

NASA
National Aeronautics and Space Administration

Report Documentation Page

1. Report No.	2. Government Accession No.	3. Recipient's Catalog No.
NASA CP-3116		

4. Title and Subtitle	5. Report Date
22nd Annual Precise Time and Time Interval (PTTI) Applications and Planning Meeting	May 1991
	6. Performing Organization Code: 534.3

7. Author(s)	8. Performing Organization Report No.
Richard L. Sydnor, Editorial Committee Chairman	91B00084
	10. Work Unit No.

9. Performing Organization Name and Address	11. Contract or Grant No.
Goddard Space Flight Center Greenbelt, Maryland 20771	
	13. Type of Report and Period Covered: Conference Publication

12. Sponsoring Agency Name and Address	14. Sponsoring Agency Code
National Aeronautics and Space Administration Washington, D. C. 20545-0001	

15. Supplementary Notes: The theme for the technical papers in this document is Precise Time and Time Interval Techniques in Military, Scientific and Industrial Applications. Emphasis is on the practical employment of precise timing and time synchronization technology to enhance the efficiency and effectiveness of communications, power distribution, geo-positioning, space navigation, and earth science activities.

16. Abstract: This document is a compilation of technical papers presented at the 22nd Annual PTTI Applications and Planning Meeting, December 4 through 6, 1990, at the Sheraton Premiere Hotel in Vienna, Virginia. Papers are in the following categories:

- Recent developments in rubidium, cesium, and hydrogen-based frequency standards, and in cryogenic and trapped-ion technology.
- International and transnational applications of precise time and time interval technology with emphasis on satellite laser tracking networks, GLONASS timing, intercomparison of national time scales and international telecommunications.
- Applications of precise time and time interval technology to the telecommunications, power distribution, platform positioning, and geophysical survey industries.
- Applications of PTTI technology to evolving military communications and navigation systems.
- Dissemination of precise time and frequency by means of GPS, GLONASS, MILSTAR, LORAN, and synchronous communications satellites.

17. Key Words (Suggested by Author(s))	18. Distribution Statement
Masers, Frequency Standards, Time Synchronization, Precise Time, GPS Timing, Satellite Clocks	Unclassified - Unlimited Subject Category 70

19. Security Classif. (of this report)	20. Security Classif. (of this page)	21. No. of pages	22. Price
Unclassified	Unclassified	616	A99

NASA FORM 1626 OCT 86

NASA-Langley, 1991

END

6 — 19 — 91